TNO innovation for life

RFOIL.v.3.0 user's manual

RFOIL

TNO Public › TNO 2025 R10388
13 February 2025

Energy & Materials
Transition
www.tno.nl
+31 88 866 50 65
info@tno.nl

TNO 2025 R10388 – 13 February 2025

RFOIL

RFOIL.v.3.0 user's manual

Author(s)	A. Koodly Ravishankara, A. Sahoo, M. Caboni
Classification report	TNO Public
Number of pages	930 (excl. front and back cover)
Number of appendices	3

All rights reserved
No part of this publication may be reproduced and/or published by print, photoprint, microfilm or any other means without the previous written consent of TNO.

© 2025 TNO

Summary

This document is RFOIL.v.3.0 user's manual. The first part of this document consists of the user's manual for RFOIL.v.3.0, while the second part provides a validation of the code using experimental data.

Contents

Summary 3

1 Introduction 5

2 User's manual 6
2.1 License activation 6
2.2 Operating RFOIL 7
2.3 Airfoil Panelling 8
2.4 Performing calculations 10
2.5 Output and data processing 14

3 Validation 17
3.1 Tested codes 17
3.2 Results 17

References 19

Appendices

Appendix A: Sample input files for RFOIL.v.3.0 20

Appendix B: Comparison between experimental and numerical polars for the ATG database's airfoils and the AVATAR-DU00-W-212 airfoil 26

Appendix C: Comparison between experimental and numerical pressure distributions for the AVATAR-DU00-W-212 airfoil 501

1 Introduction

RFOIL is a tool which is used extensively by the wind turbine industry in airfoil design. The tool was originally developed in 1996 by ECN, TUDelft and NLR as a “wind turbine modification” of the aerospace code XFOIL [1]. The first version of RFOIL, denoted by RFOIL.v1.1, improved the robustness of boundary layer computations, improved accuracy of predictions near stall and introduced the rotational effects within boundary layer. A shortcoming of RFOIL.v1.1 inherited from XFOIL was the underprediction of the drag coefficient. In 2016 ECN developed a new version of RFOIL, named RFOIL.v3.0 [2], which aimed to overcome this drawback.

In this report we include the user manual for RFOIL.v3.0 and we present the assessment of the code’s accuracy using a database of wind tunnel measurements. The results from RFOIL.v3.0 have been validated with measurements on multiple airfoils, usually at 3 Reynolds numbers or even more. The validation is based on lift and drag measurements of known quality from the so-called ATG database, an internal database of airfoil lift, drag and moment coeffient experimental data. High quality measurements of pressure distributions from the AVATAR project up to Reynolds numbers of 15 million are also included.

Chapter 2 describes how to activate the RFOIL.v3.0’s license and the various options available to perform the airfoil analysis, while Chapter 3 presents the validation of RFOIL.v3.0. The present version includes very minor upgrades to RFOIL.v3.0 and hence will be referred to as RFOIL.v3.04.

2 User's manual

2.1 License activation

Please find below details of the installation package of TNO software tool RFOIL:

The current RFOIL version requires a 64-bit operating system to function. The program is compatible with the latest Windows versions.

1. Inside, the folder 'RFOIL_exe' you will receive two folders 'RFOIL' and 'RFOIL Activation'. To use all features of the software, TNO will share a licence key which is used to activate the software.

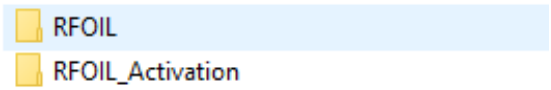

Figure 2.1: File structure.

2. From the 'RFOIL Activation' folder, run Activation.exe. There are two options for activating the licence for this software, either online which requires communication with a server or offline.
3. Online activation of the tool is possible by filling the product key (XXXXX-XXXXX-XXXXX-XXXXX-XXXXX) that will be shared by TNO and pressing Activate button.

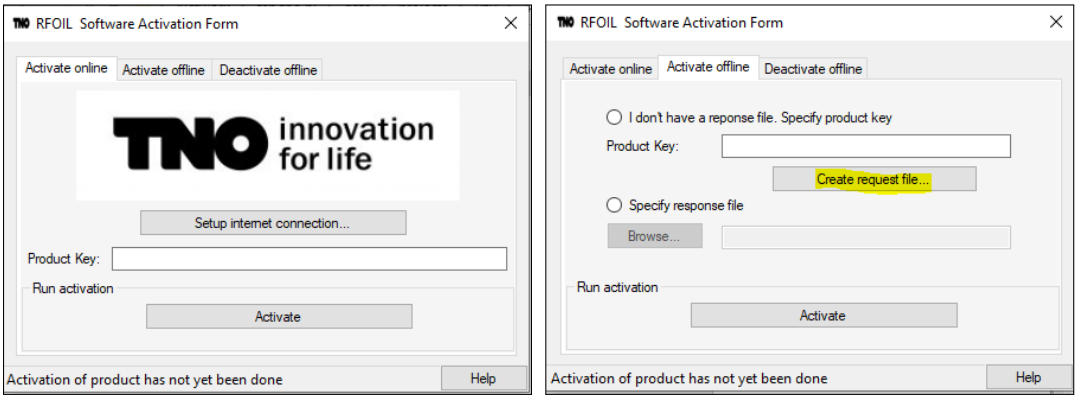

Figure 2.2: Activation of the license.

4. Upon pressing the Activate button, in case a network error occurs, an error message would appear. This means that communication with the server is not possible because the host computer is connected to a proxy server. In this case, the user needs to specify the proxy details by pressing the Setup Internet Connection... button in the main screen and retry the activation. Please note that not all fields are required to specify the proxy server but in all cases the server and port are required.
5. In case offline activation is preferred, a request .txt file has to be generated from the user after specifying the product key. The request file needs to be sent to TNO in order to

generate a response .dat file which is delivered back to the user. The generated .dat file is specified by the user by browsing and choosing its location to activate the product offline.

2.2 Operating RFOIL

RFOIL can be operated in two modes —interactively through command line prompts, or in batch mode using an input file. For both operating modes, all input files (e.g. airfoil coordinate file) must be present in the directory where the RFOIL executable is located. All user output files (e.g. polar file) will also be saved in the same directory.

Batch mode operation is performed via Command Prompt on Windows. The input file is a plain text file with the list of commands. It must be in the same directory as the RFOIL executable. In a Command Prompt terminal opened in the directory where the RFOIL executable is located, enter the following command.

```
C:\user\workdir> RFOIL.exe < rfoilinput.txt
```

In this example `C:\user\workdir` is where the RFOIL executable and input file are located. `rfoilinput.txt` is the filename of the batch mode input file. Accepted file extentsions are `.txt` and `.inp`.

Some sample input files for batch mode operation are presented in appendix A. The text in the file are the commands to be executed and the line breaks indicate wherever the user would press the '`Enter`' key during interactive operation. The rest of this user guide describes interactive mode operation. Every command in the interactive mode can be provided in the input file for batch mode.

When RFOIL is launched in interactive mode, the following top level menu and prompt appear:

Listing 2.1: RFOIL start menu

```
 ===============================================================
 RFOIL Version 3.0 with thick airfoil drag correction
 TNO (tno.nl)
 ===============================================================

 QUIT Exit program
 OPER Direct operating point(s)
 MDES Complex mapping design routine
 QDES Surface speed design routine
 GDES Geometry design routine
 SAVE Write airfoil to generic disk file
 ISAV Write airfoil to ISES coordinate file
 LOAD Read buffer airfoil from generic disk file
 ILOA Read buffer airfoil from ISES coordinate file
 NORM Switch toggle for buffer airfoil normalization
 NAC4 Set NACA 4-digit airfoil and buffer airfoil
 NAC5 Set approx. NACA 5-digit airfoil and buffer airfoil
 PANE Regenerate paneled airfoil from buffer airfoil
 SHOW Show airfoil paneling
 PPAR Change airfoil paneling parameters and re-panel
```

```
SIZE Change plot size
NAME Change airfoil name


RFOIL c>
```

The banner on top displays the RFOIL version being used. Each level and sublevel of RFOIL has its own command menu that appears when the user enters that level. The list of possible inputs of the current level can be accessed any time by entering '?' into the prompt. To go to a higher level menu from a current sub-menu, press the '`Enter`' key in the prompt.

A typical RFOIL calculation session goes as follows. The typical context menus used during calculations are described in sections 2.4.1 and 2.4.2.

1. Defining the airfoil to be analyzed.
2. Performing calculations by entering the `OPER` menu.
3. Saving data if necessary, and exiting.

Commands

`load`
Load airfoil coordinates from a text file in the working directory. The user is prompted for the filename containing the coordinates after this. Relative path to files can be provided.

`nac4/nac5`
Generate a 4 digit or 5 digit NACA airfoil for analysis. The user is then prompted for the airfoil number e.g. `0018` or `24012`.

`ppar`
Enter the menu to change airfoil panelling parameters like number of panels, refinement location, and so on. The terminal prompt turns into
`Change what ? (<cr> if nothing else)  c>`
instead of
`RFOIL  c>`

`oper`
Enter the operating point menu to perform airfoil analysis.

2.3 Airfoil Panelling

RFOIL can load airfoil coordinates from a user-specified file, as well as generate NACA 4 digit and 5 digit series airfoils. After setting an airfoil, the user sees the message shown in Figure 2.2. The message displays panelling parameters used to panel the airfoil. These parameters can be changed by entering the `ppar` menu from the main menu.

Listing 2.2: Airfoil panelling message

```
Number of input coordinate points: 160
Clockwise ordering
Blunt trailing edge
```

```
Paneling parameters used:
Number of panel nodes 160
Panel bunching parameter 0.50000000
TE/LE panel density ratio 1.00000000
Refined area/LE panel density ratio 0.20000000
Suction side refined area x/c limits 1.00000000 1.00000000
Pressure side refined area x/c limits 1.00000000 1.00000000

Maximum panel corner angle = 4.73433399 at i,x,y = 71 0.00487871 0.03063674
```

2.3.1 Airfoil Coordinate File

The airfoil file to be loaded must be a generic text file (`.txt` or `.dat`) containing only the X and Y coordinates in separate columns (without headers). The points must start from the trailing edge, go round the leading edge, and back to the trailing edge (both clockwise and counter-clockwise numbering are acceptable). fig. 2.3 shows an airfoil represented with coordinate points with clockwise numbering.

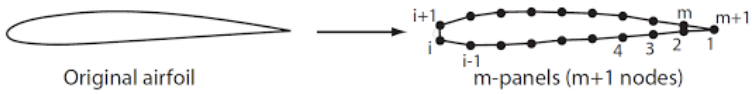

Figure 2.3: An airfoil represented with discrete coordinate points numbered in clockwise order starting from the trailing edge

2.3.2 Paneling parameters

Entering the `ppar` menu shows the current paneling parameters as well as the commands to change them (listing 2.3 shows the default values). The panelling parameters are described below along with their respective commands in brackets. It is recommended to use the `pane` command after exiting the paneling sub menu to ensure the airfoil paneling is set properly. An example of an airfoil with paneling parameters modified from default values is represented in fig. 2.4.

- Number of nodes `n` **(default value = 160)**
  The total number of panels set by the user are redistributed by the rest of the paneling parameters. A higher number is recommended for airfoils with large curvature and also to accurately capture effects like flow separation, stagnation, transition, etc. RFOIL supports maximum 300 panel nodes.
- Panel bunching parameter `p` **(default value = 0.5)**
  This describes the ratio between the number of panels in high curvature areas to the number of panels in low curvature areas of the airfoil. The default value is 0.5. A higher value can be used to accurately capture the leading edge stagnation point, for example.
- Trailing edge panel density `t` **(default value = 1.0)**
  This controls the number of panels in the trailing edge by setting the ratio of number of panels at the trailing edge to the number of panels at the leading edge.
- Suction side `xs` and pressure side `xp` refinement location **(default values = 1.0, 1.0 for both)**

These parameters can be used to define a high panel density on the suction or pressure side to capture aerodynamic effects in specific areas of interest. The user is prompted to provide refinement limits in terms of x/c —first the point closer to leading edge, then the point closer to trailing edge.

- Density ratio `r` **(default value = 0.2)**
  The density ratio sets the ratio of the number of panels in the refined area(s) to the number of panels at the leading edge.

Listing 2.3: Paneling parameters with commands and default values

```
   Present paneling parameters:
N Number of panel nodes 160
P Panel bunching parameter 0.50000000
T TE/LE panel density ratio 1.00000000
R Refined area/LE panel density ratio 0.20000000
XS Suction side refined area x/c limits 1.00000000 1.00000000
XP Pressure side refined area x/c limits 1.00000000 1.00000000
```

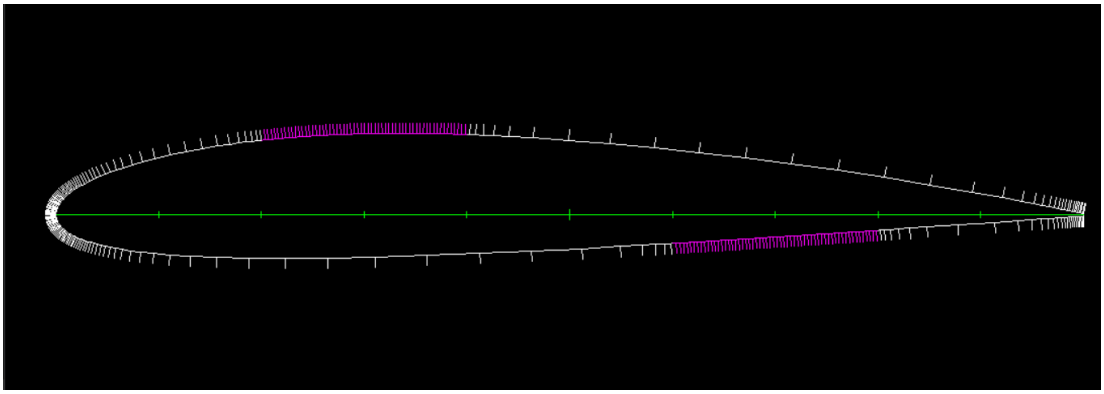

Figure 2.4: A NACA 2412 panelled using 300 nodes with a panel bunching parameter of 10.0 and a TE/LE panel density ratio of 0.75. The user specified refined area is highlighted between $x/c = 0.2$ to $x/c = 0.4$ on the suction side and between $x/c = 0.6$ to $x/c = 0.8$ on the pressure side. The refined area to LE panel density ratio is 0.2.

2.3.3 Frequently encountered errors

- The most common error is `LE not found. Continuing...`
  Common causes of this error is
  1. An error in the format of the airfoil coordinate, for example if there is a header in the coordinate file,
  2. Errors in LE curvature when generating new airfoils during an optimization routine.
- Number of points is greater than 300.

2.4 Performing calculations

2.4.1 The OPER menu

Polar calculations are performed by entering the `oper` menu from the main menu. By default, the calculations are inviscid. The prompt turns to '`OPERi c>`' with the '`i`' representing inviscid mode.

Commands

`visc`
Enables viscous calculations and turns the prompt to '`OPERv c>`'. The user is prompted to enter a Reynolds number (in numeric or scientific notation) for the boundary layer calculations.

`pacc`
Save the calculated aerodynamic properties for each angle of attack in a single file during operation alongside seeing them on the terminal. The user is prompted to specify the filenames for a save file and a dump file to store the results. If RFOIL detects that a savefile already exists, the user is prompted to either use the same file or specify a new file (see listing 2.4).
Note: the `pacc` command has to be used before `alfa` or `aseq` to store the calculated values. The polar file then makes a record of the angle of attack, the C_L, C_D, and C_M values, and the operating conditions. Depending on the version of RFOIL, the stagnation point and the transition point data may also be stored. The dump file is a binary file containing information about the current simulation. Similar to the polar file, RFOIL first checks if a dump file with the same name exists and prompts if it needs to be appended or overwritten. The writing of dump file is optional. when prompted to give the filename for the dump file, users can hit `Enter` or leave an extra blank line in the input file to skip writing the dump file.

Caution

Users need to be aware of the extra prompts when running in batch mode. When a file with the same name exists, the input file needs to account for the extra prompts for the calculations to proceed.

Listing 2.4: Message when polar file already exists

```
 OPERv c> pacc

Current polar save filename: p

Enter new filename OR <return> for current filename f> newpolar.txt

New polar save file available

Enter polar dump filename OR <return> f>

Polar dump file will NOT be written

Auto polar accumulation enabled to available save and/or dump files
```

`alfa`
Calculate aerodynamic properties for a single angle of attack. The user is prompted to specify the angle of attack (in degrees). The result of the calculation is displayed in the terminal after the calculation converges (a sample result is shown in listing 2.5).

`aseq`
Calculate aerodynamic properties for a series of angle of attacks The user is prompted to provide a starting angle of attack, an ending angle of attack, and the increment between the angles (all in degrees).

Listing 2.5: Example of a viscous calculation for a single angle of attack

```
Side 1 free transition at x/c = 0.39898428 44
Side 2 free transition at x/c = 0.46493679 47
N+NW 224 NBL(2) 148
   7 rms: 0.47099620E-04 max: 0.64793357E-03 D at 75 2
      a = 0.00000000E+00 CL = 0.25228506E+00
     Cm = -0.71847484E-01 CD = 0.10629558E-01 CDp = 0.60514244E-02
      Tail side 1 and 2 at 78 84
```

`cl`, `cseq`, `cli`
The same as `alfa` and `aseq` but specifying C_L value(s) instead of angle of attack. `cli` is used for inviscid mode.

`mach`
Modify the Mach number.

`vels`
Display the dimensionless velocity components u/U_∞ and v/U_∞, pressure coefficient C_p, and the dynamic pressure divided by the freestream velocity q/U_∞ calculated at the last angle of attack at any user specified point. The user is prompted to enter the points as x/c and y/c

`vpar`
Modify boundary layer properties.

2.4.2 Boundary layer properties and the VPAR sub menu

The `VPAR` sub menu provides options to configure the boundary layer parameters for the calculation of the integral boundary layer quantities like displacement thickness (δ^*), momentum thickness (θ), shape factor (H), kinetic energy shape factor (H_k), skin friction coefficient (C_f), pressure coefficient (C_P), and so on. These parameters can influence the lift and drag calculations for the airfoil. The `VPAR` menu also allows to control the rotational corrections [3, 4, 5, 6], transition to turbulence for the boundary layer via forced transition or via free transition with the e^N method [7].

The boundary layer parameters can be displayed using the `show` command in the `VPAR` sub menu (listing 2.6). The commands to change the parameters can be displayed using the '`?`' command in the `VPAR` sub menu (listing 2.7).

Commands

`re`
Modify Reynolds number

`xtr` **(default values = 1.0, 1.0 on both suction and pressure side)**
Set the forced transition location (in form of x/c) on the suction and pressure sides.

`n` **(default value = 9.0)**
Set the amplification factor N_{crit} for the e^N free transition method [7].

`turb`
Turn on fully turbulent simulation (see section 2.4.3)

`drag` and `lift`
Toggle the improved drag and lift calculations respectively.

The calculated integral boundary layer quantities can be saved in the `OPER` menu using the `arbl` and `svbl` commands. `arbl` instructs RFOIL to store the calculated quantities in memory when performing calculations. `svbl` saves the quantities to a file whose username has to be supplied by the user. `svbl` provides two options — either saving the integral boundary layer quantities over the whole airfoil, or saving acoustic quantities for analysis in a tool like SILANT [8].

Listing 2.6: Default Boundary layer parameters displayed from the VPAR menu

```
Re = 0.30000000E+07 (fixed Re)
Xtr/c = 1.00000000 suction side
Xtr/c = 1.00000000 pressure side
Turb = 0
iTurb = 1 suction side
iTurb = 5 pressure side
Ncrit = 9.00000000 ( 0.07013526 % turb. level )
Vacc = 0.05000000

Parameters for rotational effects:
f0 = 1.00000000
c/r = 0.00000000
c/Rtip = 0.00000000
rf1 = 1.00000000
rf2 = 1.00000000
rf3 = 0.00000000
DRAG Corr = T
Lift Corr = F

..VPAR c> ?

  <cr> Return to OPER menu
  SHOW Display viscous parameters
```

Listing 2.7: Boundary layer parameters than can be changed in the VPAR menu

```
  RETY Change type of Re variation with CL
  XTR Change trip positions Xtr/c
  TURB Set fully turbulent simulation
  iTUR Change the trip location wrt stagnation point
  N Change critical amplification exponent Ncrit
  VACC Change Newton solution acceleration parameter
  F Change f0 parameter rotational effects
  CR Change c/r (chord to radius) ratio
  CRT Change c/Rtip (chord to tipradius) ratio
        (include radial pressure gradient)
  RF1 Change factor higher higher effects
  RF2 Change factor transpiration velocity
  RF3 Change factor rad. pressure gradient
  INIT BL initialization flag toggle
  DRAG Toggle drag correction for thick airfoils
  LIFT Toggle lift correction for thick airfoils
```

2.4.3 Fully turbulent feature

RFOIL versions 3.0 and later also have the possibility to perform a fully turbulent simulation instead of manually tripping the boundary layer to turbulence at a user specified location. This feature was introduced to enable comparisons with fully turbulent CFD simulations. The fully turbulent feature automatically trips the boundary layer at a location after the stagnation point. The commands are found within the `vpar` menu.

Commands

`turb`
Set fully turbulent simulation on or off

`itur` **(default value = 1 on suction side and 5 on pressure side)**
Set the number of nodes after stagnation point where the boundary layer will become turbulent.

2.4.4 Rotational parameters

One of the main modifications of RFOIL include the addition of rotational effects to the boundary layer equations. These modifications are turned off by default and can be changed by the commands in the `vpar` menu. The details of the equations can be found in [5]

Commands

`F` **default value = 1.0**
Contribution of rotational speed to the total freestream velocity. For a wind turbine without yaw, this is

$$f_0 = \sqrt{\left([1-a]\frac{R}{\lambda r}\right)^2 + (1+a')^2}$$

`CR` **default value = 0.0**
Ratio of local chord to radial position ($\frac{c}{r}$). If $\frac{c}{r} = 0$, which is the default, the standard 2D non-rotating boundary layer equations will be used.

`CRT` **default value = 0.0**
Ratio of local chord to tip radius, $\frac{c}{R_{tip}}$

`RF1, RF2, RF3` **default values = 1.0,1.0,0.0**
Parameters to control influence of higher order radial terms in the 3D boundary layer equations. $RF1$ and $RF2$ control the radial non-dimensional pressure coefficient gradient and $RF3$ controls the radial gradient of integral quantities. For more details see Bosscher et al [5].

2.5 Output and data processing

2.5.1 Polar

The polar output file saved with the `pacc` command stores the operating conditions and the polar data calculated at all the user defined angles of attack. The header of the file containing the operating conditions is shown in listing 2.9 and the calculated polars are shown in listing 2.10. The file header displays the location of forced transition.

2.5.2 Dump file

The header of the dump file contains information about the Mach number, Reynolds number, critical amplification ratio (N_{crit}), rotational correction information. The dump file first writes the the coordinates of the airfoil currently being used. Once calculation starts, the information about the force coefficients and boundary layer parameters like δ^*, θ, C_f, C_P, C_τ at each panel on the airfoil and wake per angle of attack are added to the dump file.

2.5.3 Pressure coefficient

`svcp`
Save the pressure distribution calculated at the last angle of attack. The user is prompted for a filename for the saved file.

2.5.4 Boundary layer properties

`arbl` and `svbl`
Save the pressure distributions and integral boundary layer quantities calculated for every angle of attack specified during calculation. The user is prompted first to choose either to save integral boundary layer quantities over the whole airfoil, or to save acoustic quantities for analysis in a tool like SILANT [8] (see listing 2.8). The user is then prompted for the filename for the saved file(s).
Note: The commands must be used in this specific order because the `arbl` command initialises the data array which is saved by the `svbl` command. Figure 2.8 also shows the error message when the `svbl` command is used without the `arbl` command.

Listing 2.8: Options with the svbl command

```
 OPERv c> arbl
Fill Boundary Layer -array enabled

 OPERv c> svbl

Do you want a Silant file format with TE-parameters (0)
 or 4 files with BL-parameters along the surface (1) : i> 0

Enter filename for TE boundary layer thicknesess : f> bl

 OPERv c> arbl
Fill Boundary Layer -array disabled

 OPERv c> svbl
Impossible, Array not filled (=ARBL).
```

The boundary layer quantities are stored in separate files. Four files are generated with separate extensions for four different quantities — δ^* (`.dst`), θ (`.tet`), C_P (`.cpx`), and C_f (`.cfx`). The header of each file mentions the angles of attack in the first line. The header is shown in listing 2.11.

Each of these files are stored as tab separated text files that can be viewed and processed using any text editor. The data can be plotted with any plotting program of the user's choice.

Listing 2.9: Header of the polar output file

```
     RFOIL Version 3.0

Calculated polar for: airfoil

1 Reynolds number fixed

xtrf = 0.30000001 (suction) 1.00000000 (pressure)
Rot. Parameters: f0 = 1.00000000 c/r = 0.00000000
Mach = 0.00000000 Re = 3.00000000 e 6 Ncrit = 9.00000000
```

Listing 2.10: Polars saved in the output file

```
  alpha CL CD Re(CL) CM S_xtr P_xtr CDp I_stag X_stag
 ------- -------- --------- --------- -------- ------- ------- --------
0.40000000E+01 0.10996485E+01 0.16511071E-01 0.30000000E+01 -0.14758258E+00
    ↪ 0.25372204E+00 0.44608071E+00 0.85227564E-02 177 0.55220495E-02
0.45000000E+01 0.11675278E+01 0.16140392E-01 0.30000000E+01 -0.14968047E+00
    ↪ 0.24872142E+00 0.45136937E+00 0.82348287E-02 178 0.67318338E-02
0.50000000E+01 0.12354345E+01 0.16010774E-01 0.30000000E+01 -0.15179996E+00
    ↪ 0.24448134E+00 0.45595077E+00 0.81887087E-02 179 0.81616761E-02
```

Listing 2.11: Example of the header of a C_f output file

```
 0.00000000E+00 0.00000000 0.50000000 1.00000000 1.50000000 2.00000000
    ↪ 2.50000000 3.00000000 3.50000000 4.00000000 4.50000000 5.00000000
    ↪ 5.50000000 6.00000000 6.50000000 7.00000000 7.50000048 8.00000000
    ↪ 8.50000000 9.00000000 9.50000000 10.00000000 10.50000000 11.00000000
    ↪ 11.50000000 12.00000000 12.50000000 13.00000000 13.50000000
    ↪ 14.00000000 14.50000000 15.00000095 15.49999905 16.00000000
    ↪ 16.50000000 17.00000000 17.50000000 18.00000000 18.50000000
    ↪ 19.00000000 19.50000000 20.00000000 20.50000000 21.00000000
    ↪ 21.50000000 22.00000000 22.50000000 23.00000000 23.50000000
    ↪ 24.00000000 24.50000000 25.00000000 25.50000000 26.00000000
    ↪ 27.50000000
 0.000000E+00 146 147 147 148 149 150 151 152 153 155 156 157 157 158 159 160
    ↪  161 162 163 163 164 165 165 166 166 167 167 167 167 167 167 167 168
    ↪ 168 168 169 169 169 170 170 171 171 172 172 173 173 174 174 175 175
    ↪ 176 177 177 176
```

3 Validation

The goal of the present chapter is to present the validation of RFOIL.v3.04. The accuracy of RFOIL.v3.04 was assessed using a database of wind tunnel data. A selection of the ATG database (made excluding the airfoil data having a numerical source) provides experimental polar data for 30 airfoils commonly used in wind energy applications. Data are given for different Reynolds numbers, resulting in around 100 experimental polars all used in the validation. The internal database of airfoils, known as the ATG database, has been integrated with the recent 2D high Reynolds number measurements carried out on the DU00-W-212 airfoil within the AVATAR project [9]. Moreover, the numerical results obtained by means of RFOIL.v3.04 were verified against those otained from XFOIL.v6.99, and RFOIL.v1.1.

3.1 Tested codes

Details on the tested XFOIL and RFOIL versions are depicted in Table 3.1. XFOIL.v.6.99 is the last XFOIL [1]. RFOIL.v.1.1 is the original RFOIL version written in Fortran 77 [10], while RFOIL.v.3.04 is the version featuring an improved formulation of drag estimation. In the former versions of RFOIL (i.e., before RFOIL.v.3.0) it was found that drag under-prediction was significant. In RFOIL.v.3.0 and onwards, the improved drag formulation predicts the drag more accurately for airfoils with reasonably small trailing edge thickness. The derivation of drag correction is based on the difference between the actual momentum loss thickness based on free stream velocity and the one based on the velocity at the edge of the boundary layer. Details of this implementation can ge found in [2].

Table 3.1: Tested codes.

	name	version	short description
1	XFOIL	6.99 (2013)	last XFOIL version
2	RFOIL	1.1 (1996)	original RFOIL version in F77
4	RFOIL	3.04 (2024)	RFOIL version featuring drag prediction improvement

3.2 Results

The validation plots are included in Appendix B and Appendix C. Appendix B presents the results of the comparison between experimental and numerical polars for the ATG database's airfoils. The database has been integrated with the polars of the DU00-W-212 airfoil measured within the AVATAR project. The ATG database contains both measured and synthesized polars. For the present validation only measured data has been used.

RFOIL's numerical polars have been obtained using input files similar to the one depicted in Appendix A. For each polar, Ncrit has been setup according to the available information on the turbulence intensity of the wind tunnel the experimental polars have been obtained. Mack formula [11] has been used to relate the wind tunnel turbulence intensity to Ncrit.

For each validation case (i.e., one polar of a given airfoil at a given Reynolds number), Appendix B presents three figures showing a) the comparison between experimental and numerical polars as a function of the angle of attack (giving execution time and the number of converged polar

points), b) the differences between experimental and numerical polars as a function of the angle of attack and c) the comparison between experimental and numerical pressure and skin friction distributions.

Appendix C presents the comparison between experimental and numerical pressure distribution for the AVATAR- DU00-W-212 airfoil.

References

[1] M. Drela. “XFOIL: An Analysis and Design System for Low Reynolds Number Airfoils.” In: *Proceedings of the Conference Notre Dame*. Notre Dame, USA, 1989.

[2] G. Ramanujam, H. Ozdemir, and H. Hoeijmakers. “Improving Airfoil Drag Prediction.” In: *Journal of Aircraft* 53.6 (2016), pp. 1844–1852.

[3] H. Snel. “Scaling laws for the boundary layer flow on rotating wind turbine blades.” In: *4th IEA Symposium on Aerodynamics for Wind Turbines*. 1991.

[4] H. Snel, R. Houwink, and J. Bosschers. “Sectional prediction of lift coefficients on rotating wind turbine blades in stall.” In: *Ecn-C–93-052* (1994).

[5] J. Bosscher, B. Montgomerie, A. J. Brand, and R. van Rooy. “Influence of blade rotation on the sectional aerodynamics of rotational blades.” In: *The twenty-second European Rotorcraft Forum* (1996).

[6] J. Bosschers. “Modelling of rotational effects with a 2D viscous inviscid interaction code.” In: *NLR Contract Report CR* 96521 (1997), p. 50.

[7] J. L. Van Ingen. “The eN method for transition prediction. Historical review of work at TU Delft.” In: *38th AIAA Fluid Dynamics Conference and Exhibit* (2008). DOI: 10.2514/6.2008-3830.

[8] K. Boorsma and J. Schepers. “Enhanced wind turbine noise prediction tool SILANT.” In: *Fourth International Meeting on Wind Turbine Noise*. April. 2011, pp. 1–16.

[9] J. S. O. Ceyhan et al. “Latest results from the EU project AVATAR: Aerodynamic modelling of 10 MW wind turbines.” In: *Journal of Physics: Conference Series*. Vol. 753. 2. IOP Publishing. 2016, p. 022017.

[10] R. A. van Rooij. *Modification of the boundary layer calculation in RFOIL for improved airfoil stall prediction*. IW-96087R. TU Delft, 1996.

[11] L. M. Mack. *Transition and Laminar Instability*. 77-15. National Aeronautics and Space Administration, 1977.

Appendix A

Sample input files for RFOIL.v.3.0

Listing A.1: Example of RFOIL.v.3.0 input file for free transition analysis

```
load
geo.dat
airfoil
isav
isav.dat


oper
visc
3e+06
Mach
0
vpar
N
12

pacc
polar.dat

arbl
aseq
-5
20
0.5
svbl
1
bl
pacc


quit
```

Listing A.2: Example of RFOIL.v.3.0 input file for fully turbulent analysis

```
load
geo.dat
airfoil
isav
isav.dat


oper
visc
3e+06
Mach
0
vpar
N
12
turb
1
itur
2
6

pacc
polar.dat

arbl
aseq
-5
20
0.5
svbl
1
bl
pacc


quit
```

Listing A.3: Example of coordinate file for an airfoil (DU97-W-300)

```
+1.000000000000 +0.008700000000
+0.993499000000 +0.010475000000
+0.984793000000 +0.012864000000
+0.973903000000 +0.015792000000
+0.961300000000 +0.019089000000
+0.947670000000 +0.022555000000
+0.933240000000 +0.026152000000
+0.918373000000 +0.029824000000
+0.903318000000 +0.033520000000
+0.888175000000 +0.037223000000
+0.873011000000 +0.040915000000
+0.857862000000 +0.044590000000
+0.842739000000 +0.048239000000
+0.827650000000 +0.051861000000
+0.812603000000 +0.055448000000
+0.797611000000 +0.058995000000
+0.782636000000 +0.062504000000
+0.767680000000 +0.065977000000
+0.752768000000 +0.069404000000
+0.737878000000 +0.072786000000
+0.723012000000 +0.076122000000
+0.708174000000 +0.079408000000
+0.693367000000 +0.082642000000
+0.678605000000 +0.085816000000
+0.663897000000 +0.088925000000
+0.649207000000 +0.091972000000
+0.634573000000 +0.094949000000
+0.619998000000 +0.097847000000
+0.605436000000 +0.100675000000
+0.590944000000 +0.103418000000
+0.576483000000 +0.106077000000
+0.562067000000 +0.108651000000
+0.547709000000 +0.111130000000
+0.533396000000 +0.113514000000
+0.519142000000 +0.115797000000
+0.504938000000 +0.117976000000
+0.490807000000 +0.120044000000
+0.476747000000 +0.121995000000
+0.462722000000 +0.123832000000
+0.448800000000 +0.125544000000
+0.434992000000 +0.127121000000
+0.421290000000 +0.128558000000
+0.407687000000 +0.129850000000
+0.394212000000 +0.130991000000
+0.380839000000 +0.131974000000
+0.367583000000 +0.132796000000
+0.354457000000 +0.133451000000
+0.341458000000 +0.133934000000
+0.328618000000 +0.134240000000
+0.315956000000 +0.134362000000
+0.303491000000 +0.134295000000
```

```
+0.291234000000 +0.134033000000
+0.279209000000 +0.133573000000
+0.267439000000 +0.132909000000
+0.255937000000 +0.132039000000
+0.244719000000 +0.130955000000
+0.233702000000 +0.129642000000
+0.222764000000 +0.128085000000
+0.211881000000 +0.126284000000
+0.201007000000 +0.124233000000
+0.190150000000 +0.121937000000
+0.179330000000 +0.119402000000
+0.168598000000 +0.116640000000
+0.157972000000 +0.113655000000
+0.147491000000 +0.110458000000
+0.137197000000 +0.107061000000
+0.127100000000 +0.103465000000
+0.117223000000 +0.099680000000
+0.107599000000 +0.095719000000
+0.098259000000 +0.091596000000
+0.089234000000 +0.087325000000
+0.080539000000 +0.082915000000
+0.072211000000 +0.078392000000
+0.064280000000 +0.073776000000
+0.056780000000 +0.069098000000
+0.049735000000 +0.064385000000
+0.043187000000 +0.059681000000
+0.037147000000 +0.055017000000
+0.031648000000 +0.050446000000
+0.026708000000 +0.046018000000
+0.022320000000 +0.041767000000
+0.018458000000 +0.037713000000
+0.015087000000 +0.033871000000
+0.012170000000 +0.030249000000
+0.009674000000 +0.026850000000
+0.007539000000 +0.023643000000
+0.005731000000 +0.020620000000
+0.004217000000 +0.017753000000
+0.002967000000 +0.015011000000
+0.001960000000 +0.012372000000
+0.001193000000 +0.009800000000
+0.000640000000 +0.007271000000
+0.000275000000 +0.004778000000
+0.000068000000 +0.002321000000
+0.000000000000 -0.000073000000
+0.000080000000 -0.002493000000
+0.000315000000 -0.005012000000
+0.000719000000 -0.007626000000
+0.001311000000 -0.010341000000
+0.002119000000 -0.013167000000
+0.003162000000 -0.016131000000
+0.004456000000 -0.019256000000
+0.006030000000 -0.022560000000
```

```
+0.007937000000 -0.026075000000
+0.010221000000 -0.029848000000
+0.012942000000 -0.033918000000
+0.016165000000 -0.038336000000
+0.019934000000 -0.043115000000
+0.024276000000 -0.048224000000
+0.029230000000 -0.053646000000
+0.034792000000 -0.059344000000
+0.040906000000 -0.065224000000
+0.047503000000 -0.071191000000
+0.054539000000 -0.077180000000
+0.061996000000 -0.083162000000
+0.069815000000 -0.089088000000
+0.077967000000 -0.094925000000
+0.086427000000 -0.100655000000
+0.095163000000 -0.106256000000
+0.104110000000 -0.111689000000
+0.113210000000 -0.116912000000
+0.122432000000 -0.121910000000
+0.131774000000 -0.126673000000
+0.141251000000 -0.131213000000
+0.150840000000 -0.135519000000
+0.160528000000 -0.139588000000
+0.170267000000 -0.143401000000
+0.180001000000 -0.146938000000
+0.189684000000 -0.150179000000
+0.199315000000 -0.153121000000
+0.208869000000 -0.155764000000
+0.218315000000 -0.158095000000
+0.227651000000 -0.160117000000
+0.236879000000 -0.161828000000
+0.246026000000 -0.163234000000
+0.255171000000 -0.164343000000
+0.264353000000 -0.165168000000
+0.273579000000 -0.165706000000
+0.282913000000 -0.165960000000
+0.292364000000 -0.165934000000
+0.301944000000 -0.165622000000
+0.311689000000 -0.165020000000
+0.321653000000 -0.164122000000
+0.331890000000 -0.162928000000
+0.342361000000 -0.161444000000
+0.353052000000 -0.159667000000
+0.364018000000 -0.157589000000
+0.375251000000 -0.155220000000
+0.386753000000 -0.152557000000
+0.398555000000 -0.149605000000
+0.410690000000 -0.146359000000
+0.423168000000 -0.142839000000
+0.435829000000 -0.139099000000
+0.448702000000 -0.135132000000
+0.461802000000 -0.130949000000
```

```
+0.475127000000 -0.126561000000
+0.488709000000 -0.121975000000
+0.502526000000 -0.117216000000
+0.516526000000 -0.112318000000
+0.530643000000 -0.107314000000
+0.544867000000 -0.102215000000
+0.559194000000 -0.097029000000
+0.573688000000 -0.091744000000
+0.588338000000 -0.086385000000
+0.602989000000 -0.081019000000
+0.617590000000 -0.075685000000
+0.632075000000 -0.070414000000
+0.646401000000 -0.065240000000
+0.660609000000 -0.060156000000
+0.674666000000 -0.055185000000
+0.688544000000 -0.050349000000
+0.702247000000 -0.045662000000
+0.715780000000 -0.041134000000
+0.729132000000 -0.036779000000
+0.742282000000 -0.032616000000
+0.755214000000 -0.028662000000
+0.767905000000 -0.024938000000
+0.780345000000 -0.021459000000
+0.792562000000 -0.018229000000
+0.804591000000 -0.015247000000
+0.816457000000 -0.012514000000
+0.828182000000 -0.010027000000
+0.839750000000 -0.007791000000
+0.851101000000 -0.005822000000
+0.862262000000 -0.004125000000
+0.873297000000 -0.002691000000
+0.884187000000 -0.001521000000
+0.894962000000 -0.000616000000
+0.905620000000 +0.000031000000
+0.916082000000 +0.000415000000
+0.926314000000 +0.000535000000
+0.936250000000 +0.000399000000
+0.945777000000 +0.000007000000
+0.954915000000 -0.000642000000
+0.963638000000 -0.001533000000
+0.971951000000 -0.002665000000
+0.979867000000 -0.004008000000
+0.987234000000 -0.005505000000
+0.993980000000 -0.007111000000
+1.000000000000 -0.008700000000
```

Appendix B

Comparison between experimental and numerical polars for the ATG database's airfoils and the AVATAR-DU00-W-212 airfoil

B.1 AVATAR DU00-W-212

Figure B.1: Comparison between experimental and numerical polars for the AVATAR-DU00-W-212 airfoil at a Reynolds number of 12000000. Simulation time to generate the polars by means the different codes and the number of converged polar points are depicted between parentheses.

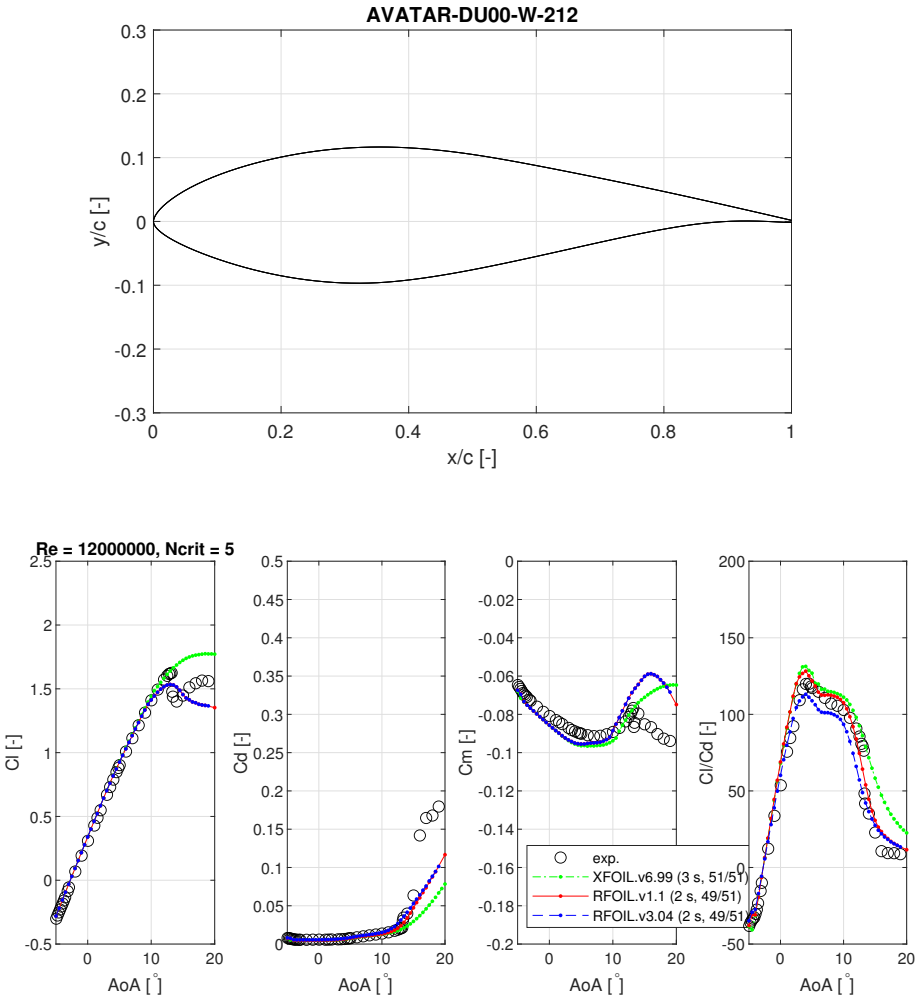

Figure B.2: Differences between experimental and numerical polars for the AVATAR-DU00-W-212 airfoil at a Reynolds number of 12000000. Vertical black lines in the middle subplot indicate, from left to right, the angle of attack corresponding to the minimum drag coefficient, maximum lift to drag ratio and maximum lift coefficient, respectively.

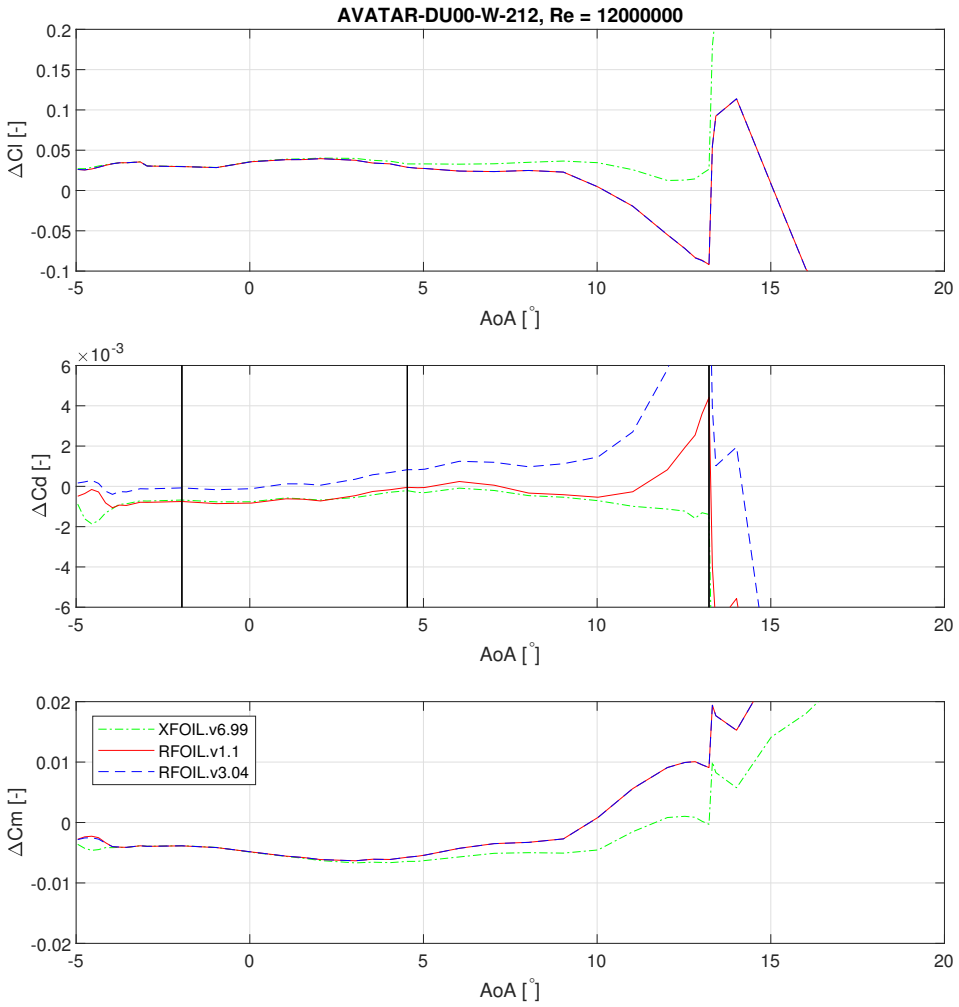

Figure B.3: Comparison between experimental and numerical pressure and skin friction distributions for the AVATAR-DU00-W-212 airfoil at a Reynolds number of 12000000 and at the design angle of attack.

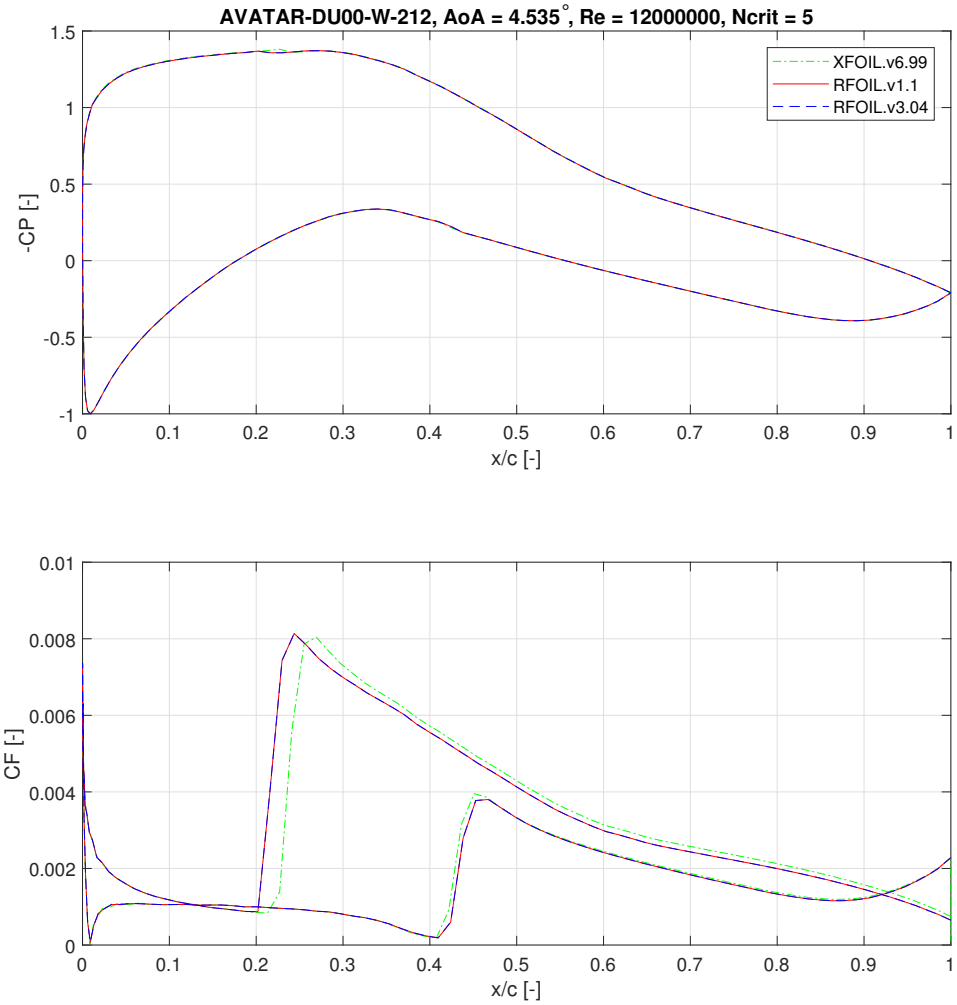

Figure B.4: Comparison between experimental and numerical polars for the AVATAR-DU00-W-212 airfoil at a Reynolds number of 15000000. Simulation time to generate the polars by means the different codes and the number of converged polar points are depicted between parentheses.

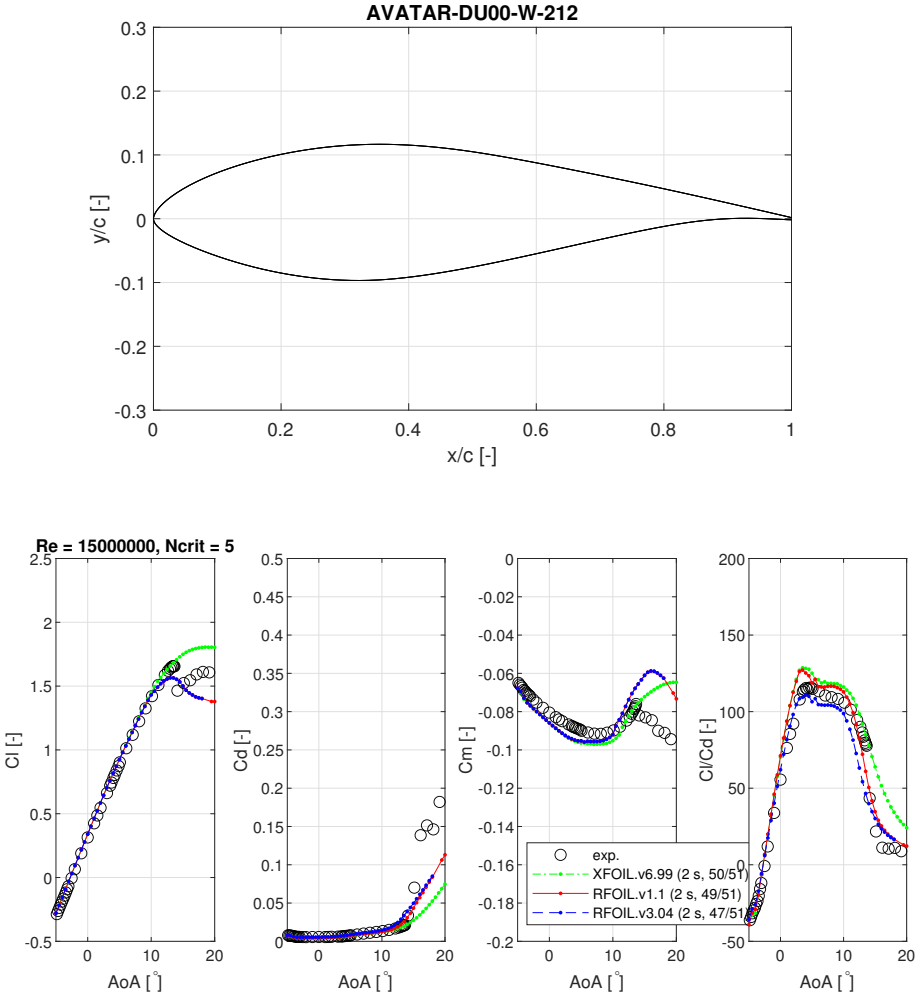

Figure B.5: Differences between experimental and numerical polars for the AVATAR-DU00-W-212 airfoil at a Reynolds number of 15000000. Vertical black lines in the middle subplot indicate, from left to right, the angle of attack corresponding to the minimum drag coefficient, maximum lift to drag ratio and maximum lift coefficient, respectively.

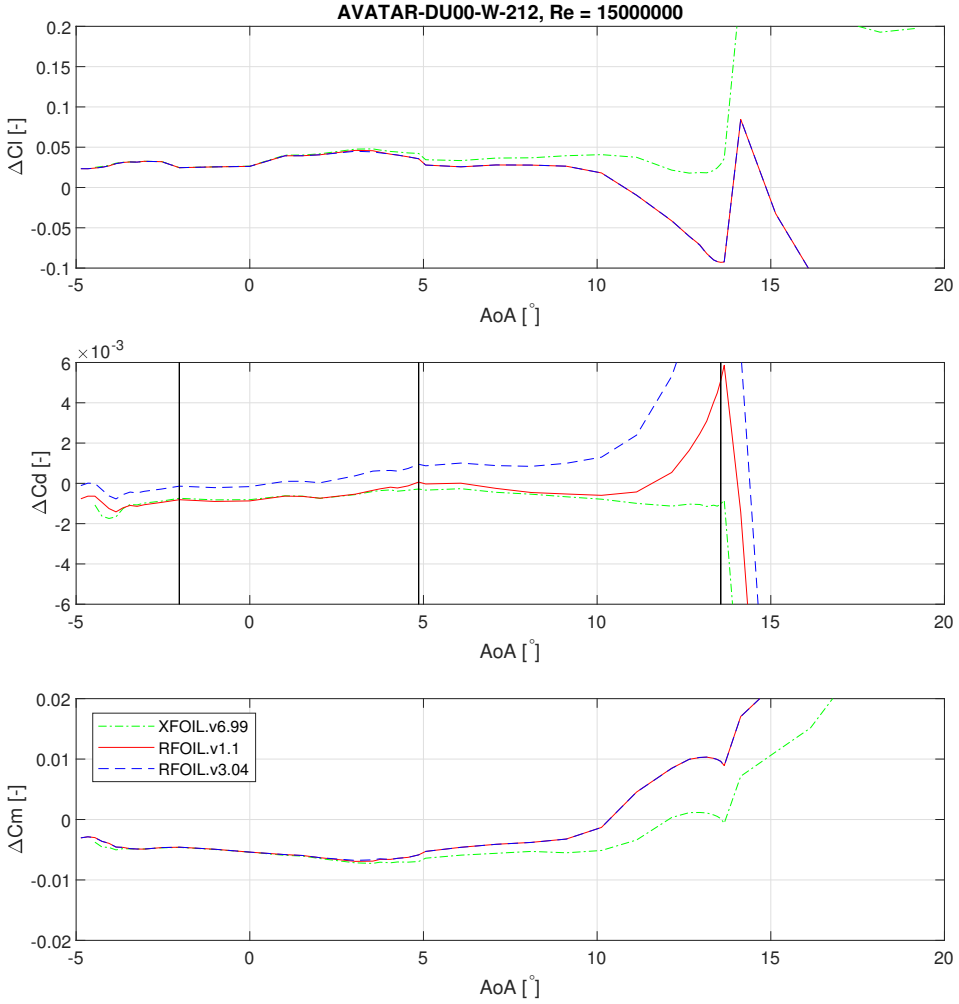

Figure B.6: Comparison between experimental and numerical pressure and skin friction distributions for the AVATAR-DU00-W-212 airfoil at a Reynolds number of 15000000 and at the design angle of attack.

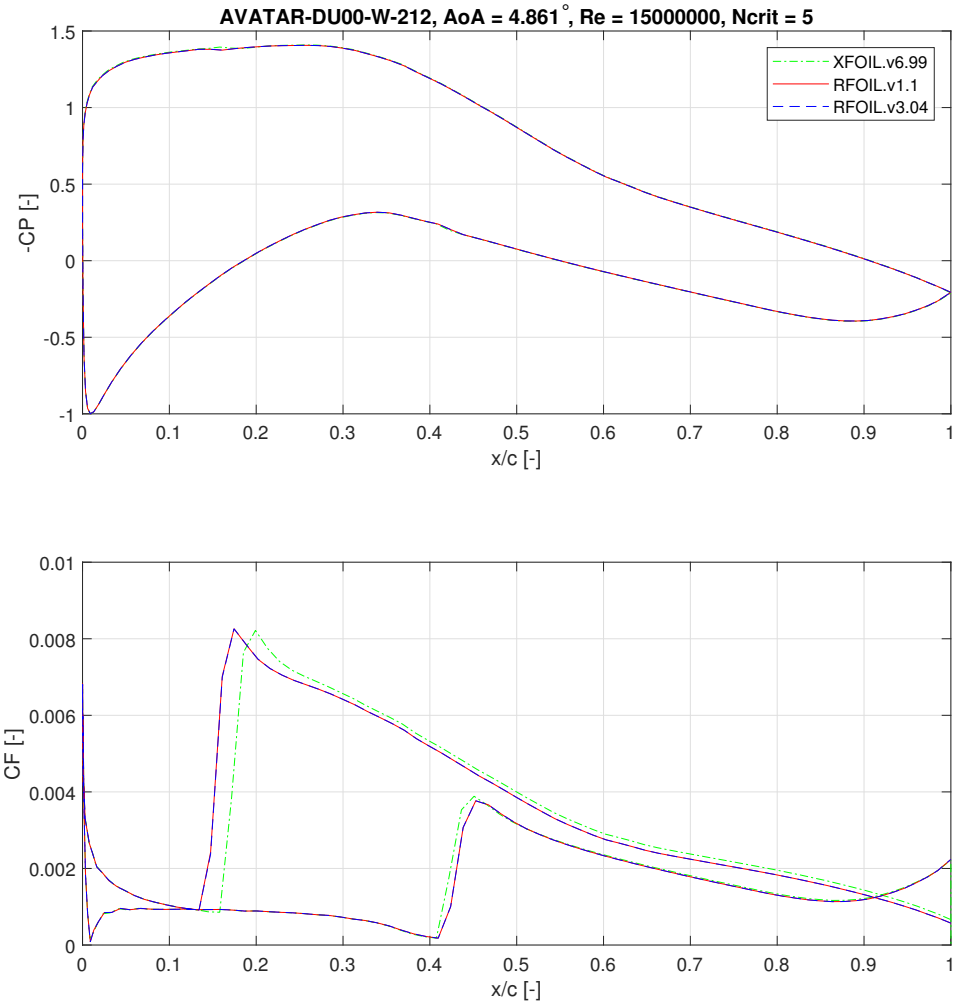

Figure B.7: Comparison between experimental and numerical polars for the AVATAR-DU00-W-212 airfoil at a Reynolds number of 3000000. Simulation time to generate the polars by means the different codes and the number of converged polar points are depicted between parentheses.

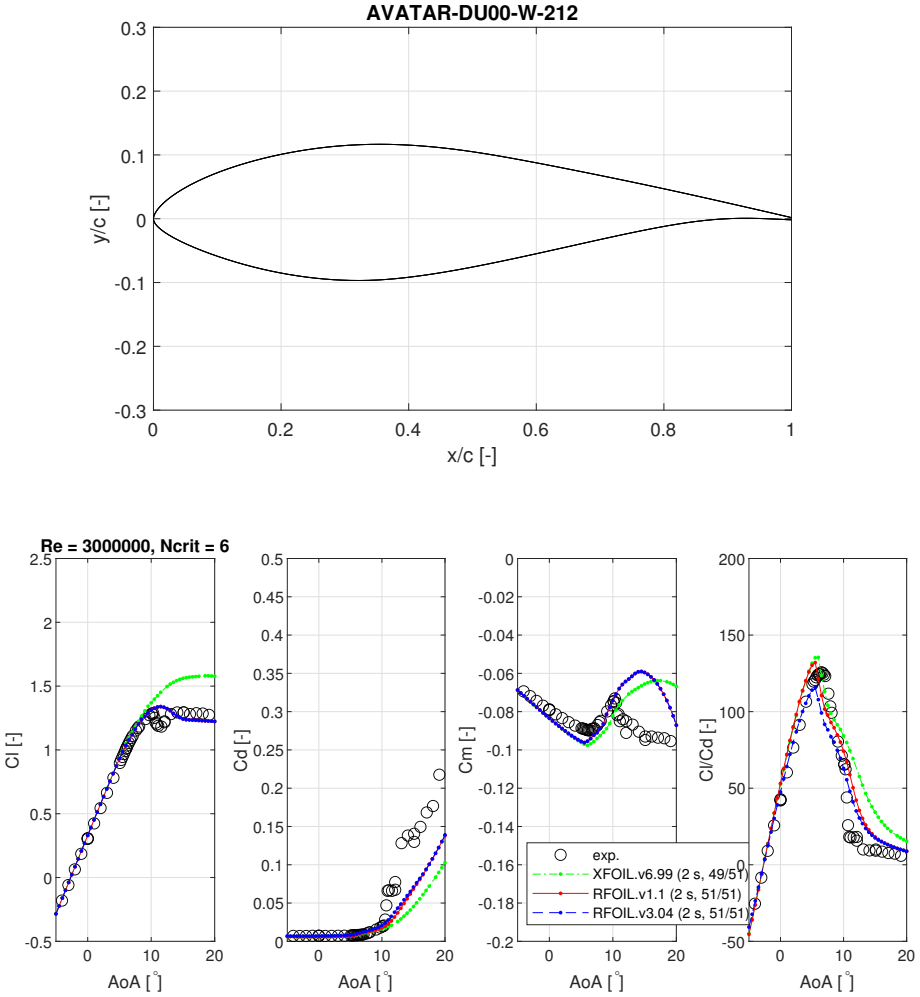

Figure B.8: Differences between experimental and numerical polars for the AVATAR-DU00-W-212 airfoil at a Reynolds number of 3000000. Vertical black lines in the middle subplot indicate, from left to right, the angle of attack corresponding to the minimum drag coefficient, maximum lift to drag ratio and maximum lift coefficient, respectively.

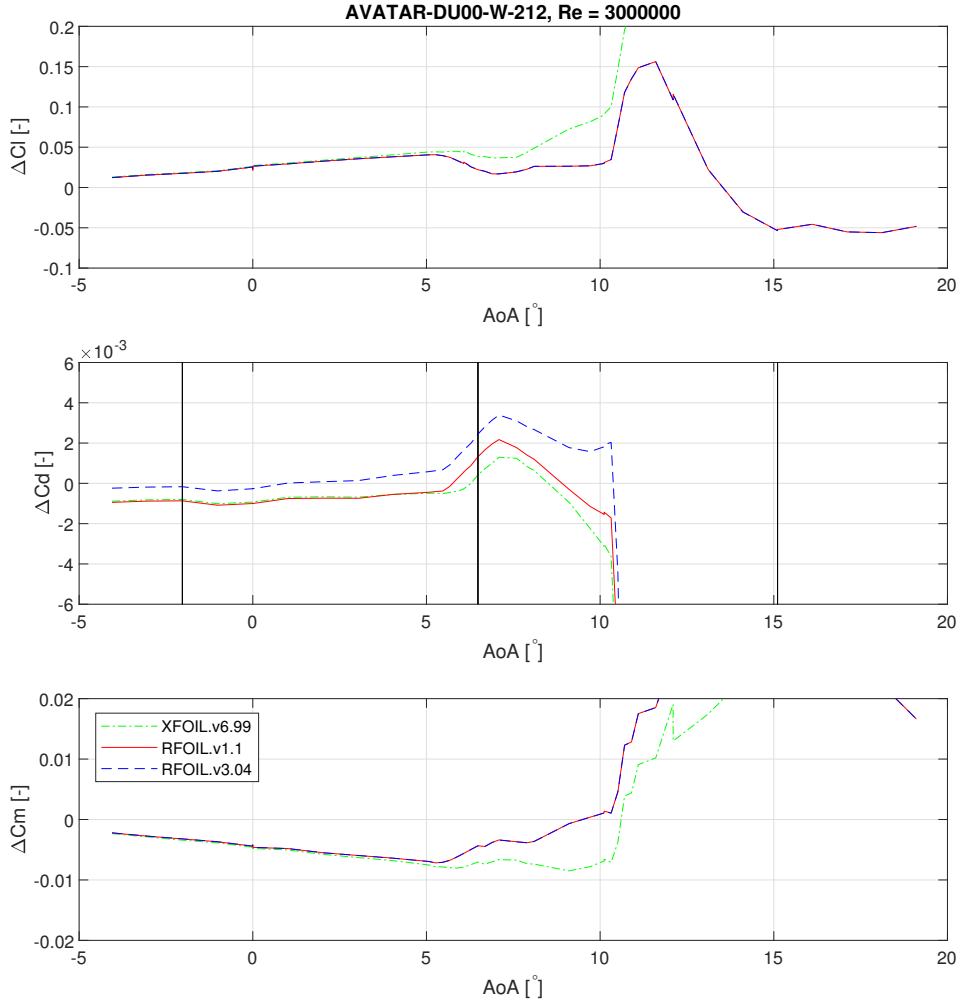

Figure B.9: Comparison between experimental and numerical pressure and skin friction distributions for the AVATAR-DU00-W-212 airfoil at a Reynolds number of 3000000 and at the design angle of attack.

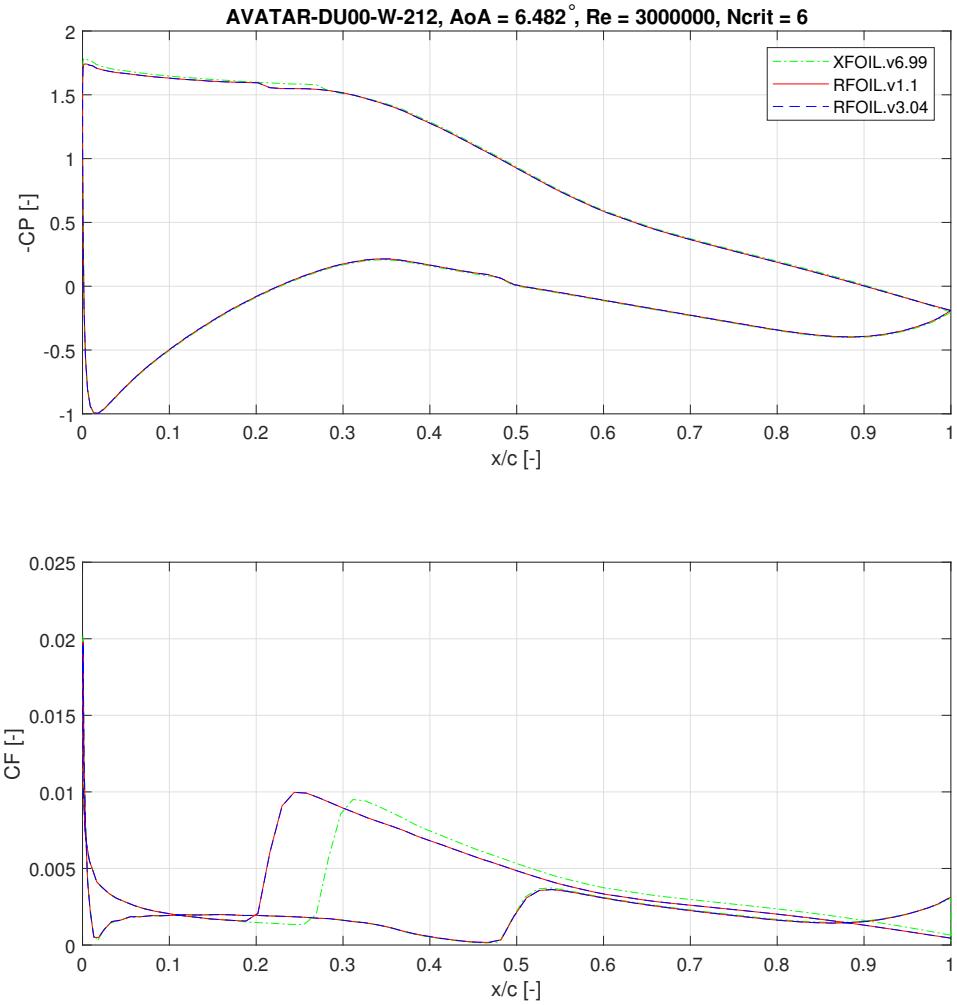

Figure B.10: Comparison between experimental and numerical polars for the AVATAR-DU00-W-212 airfoil at a Reynolds number of 6000000. Simulation time to generate the polars by means the different codes and the number of converged polar points are depicted between parentheses.

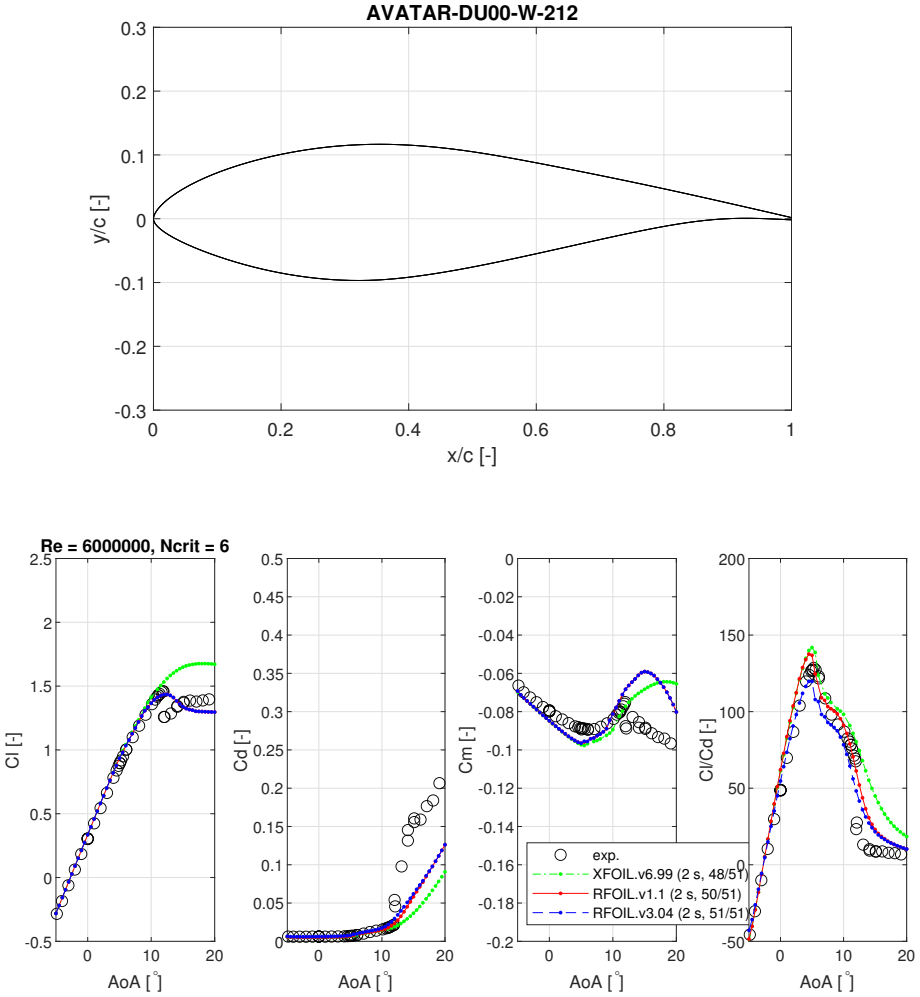

Figure B.11: Differences between experimental and numerical polars for the AVATAR-DU00-W-212 airfoil at a Reynolds number of 6000000. Vertical black lines in the middle subplot indicate, from left to right, the angle of attack corresponding to the minimum drag coefficient, maximum lift to drag ratio and maximum lift coefficient, respectively.

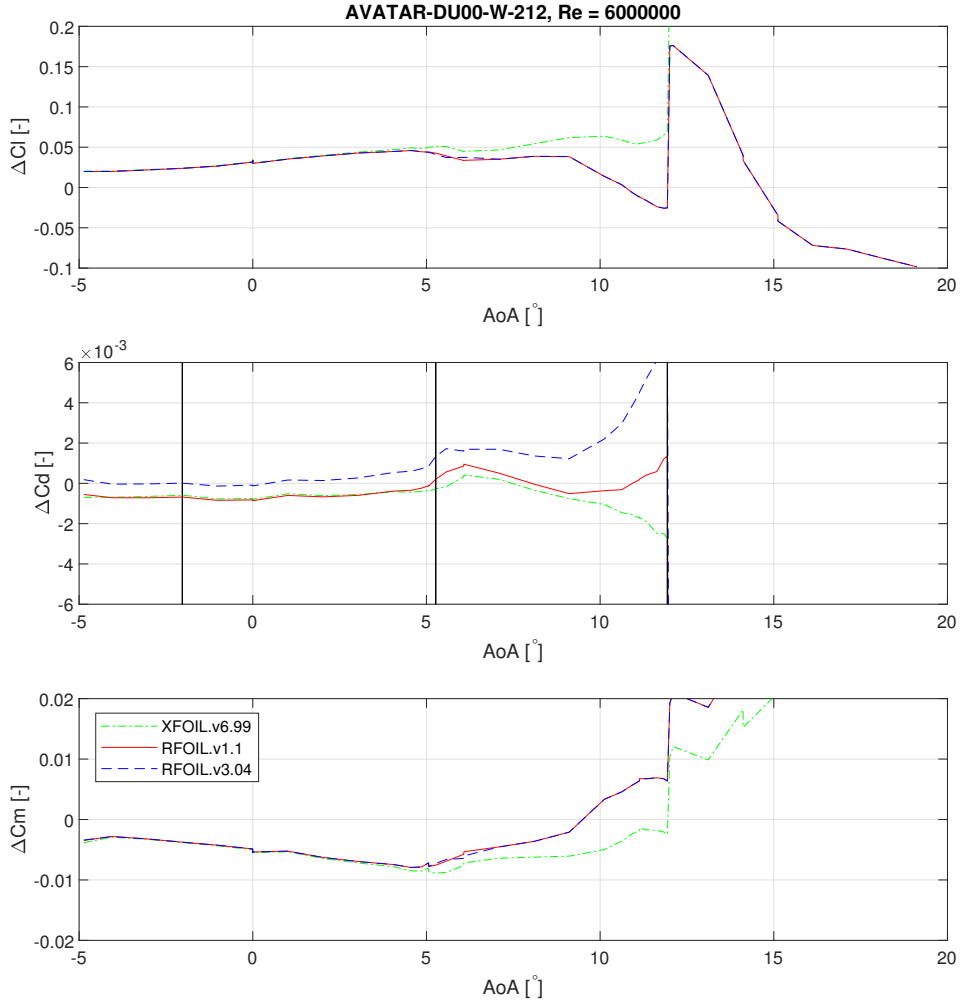

Figure B.12: Comparison between experimental and numerical pressure and skin friction distributions for the AVATAR-DU00-W-212 airfoil at a Reynolds number of 6000000 and at the design angle of attack.

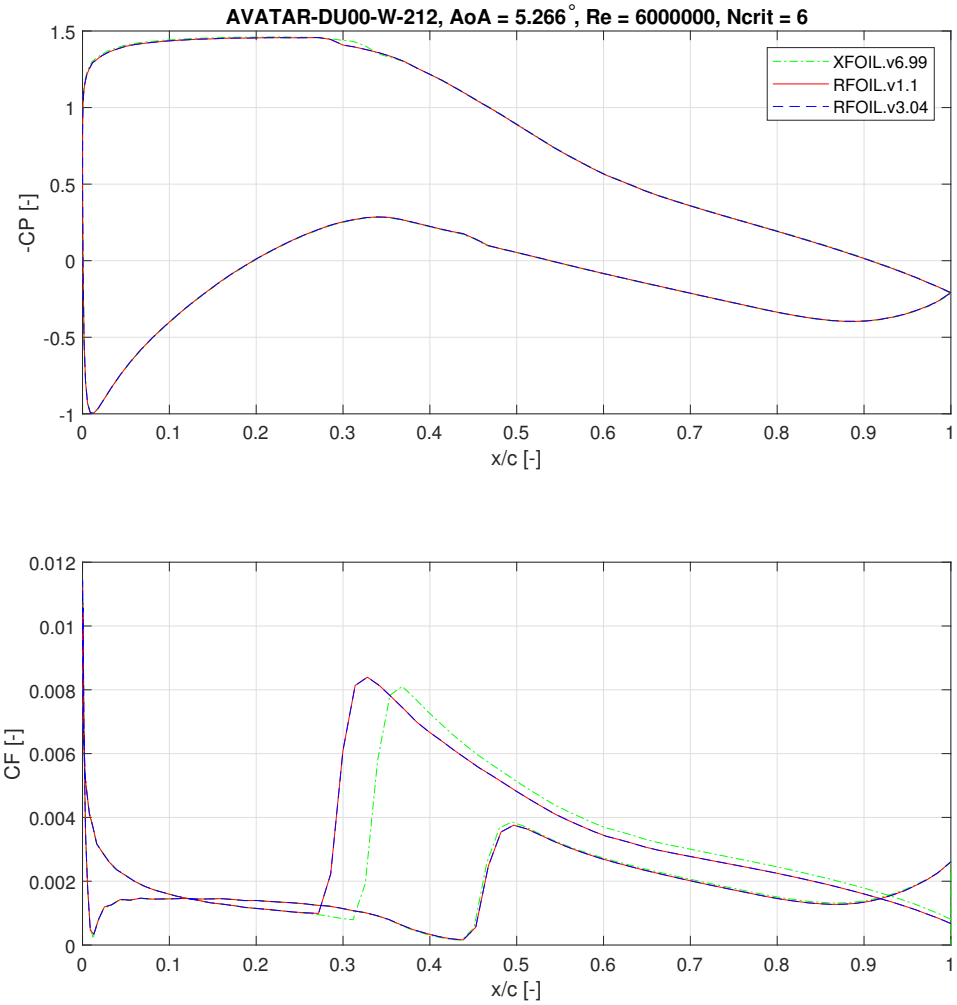

Figure B.13: Comparison between experimental and numerical polars for the AVATAR-DU00-W-212 airfoil at a Reynolds number of 9000000. Simulation time to generate the polars by means the different codes and the number of converged polar points are depicted between parentheses.

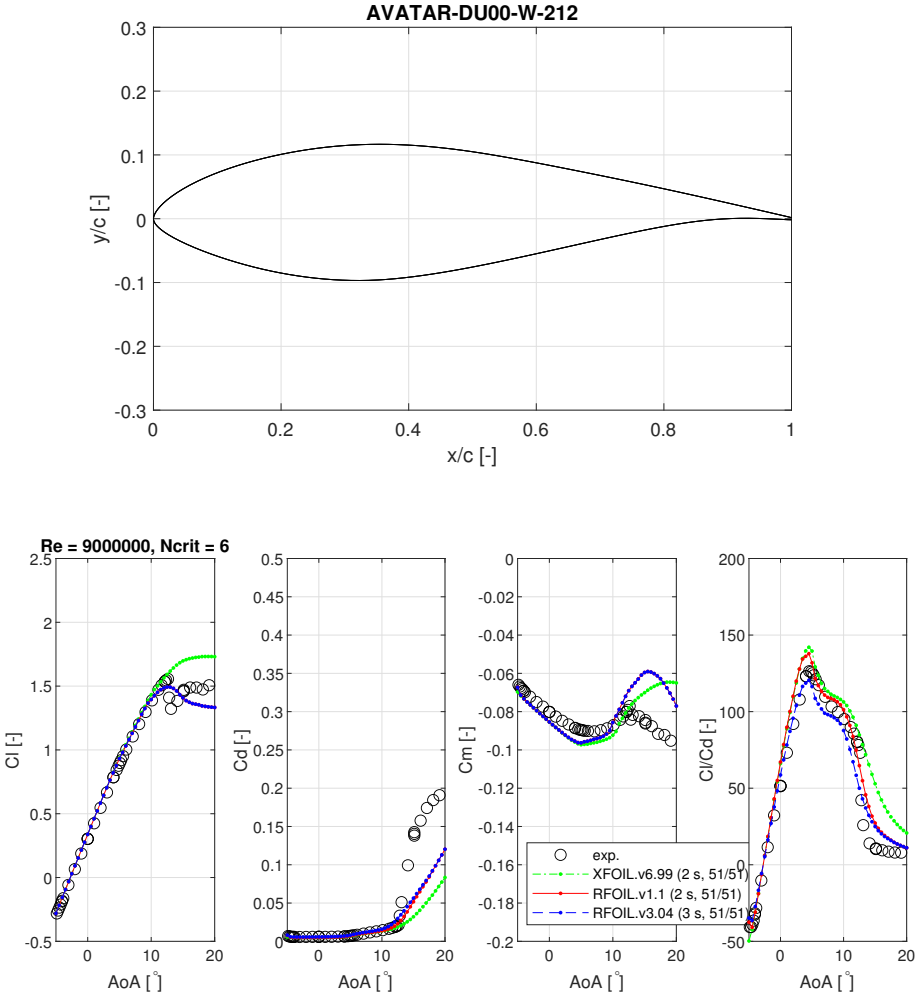

Figure B.14: Differences between experimental and numerical polars for the AVATAR-DU00-W-212 airfoil at a Reynolds number of 9000000. Vertical black lines in the middle subplot indicate, from left to right, the angle of attack corresponding to the minimum drag coefficient, maximum lift to drag ratio and maximum lift coefficient, respectively.

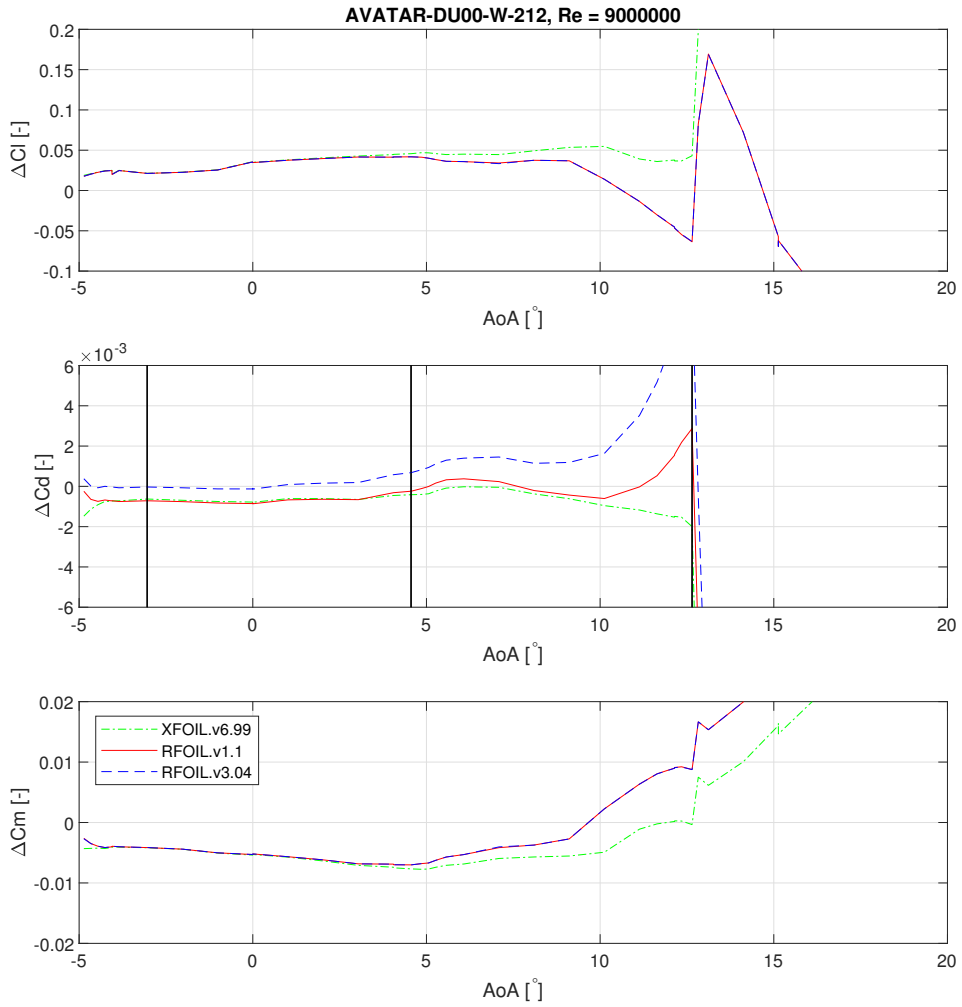

Figure B.15: Comparison between experimental and numerical pressure and skin friction distributions for the AVATAR-DU00-W-212 airfoil at a Reynolds number of 9000000 and at the design angle of attack.

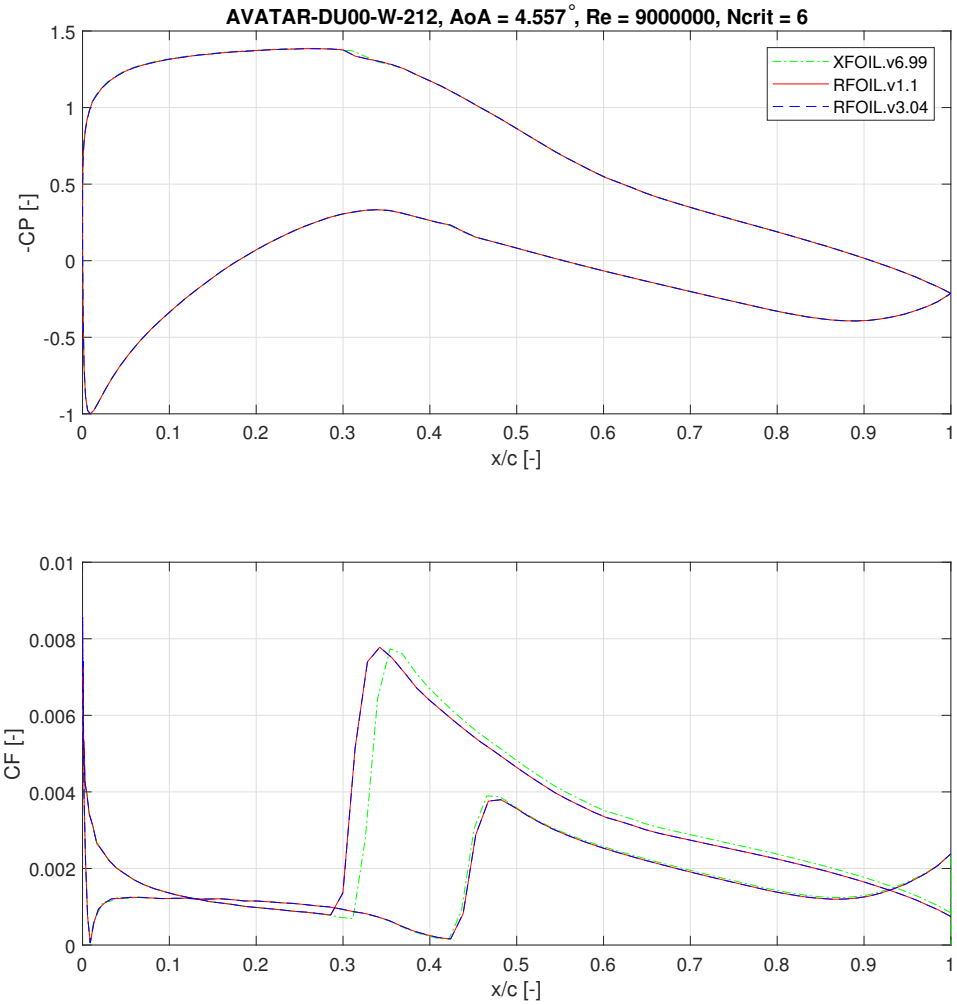

B.2 DU series airfoils

Figure B.16: Comparison between experimental and numerical polars for the DU00-W-212 airfoil at a Reynolds number of 3000000. Simulation time to generate the polars by means the different codes and the number of converged polar points are depicted between parentheses.

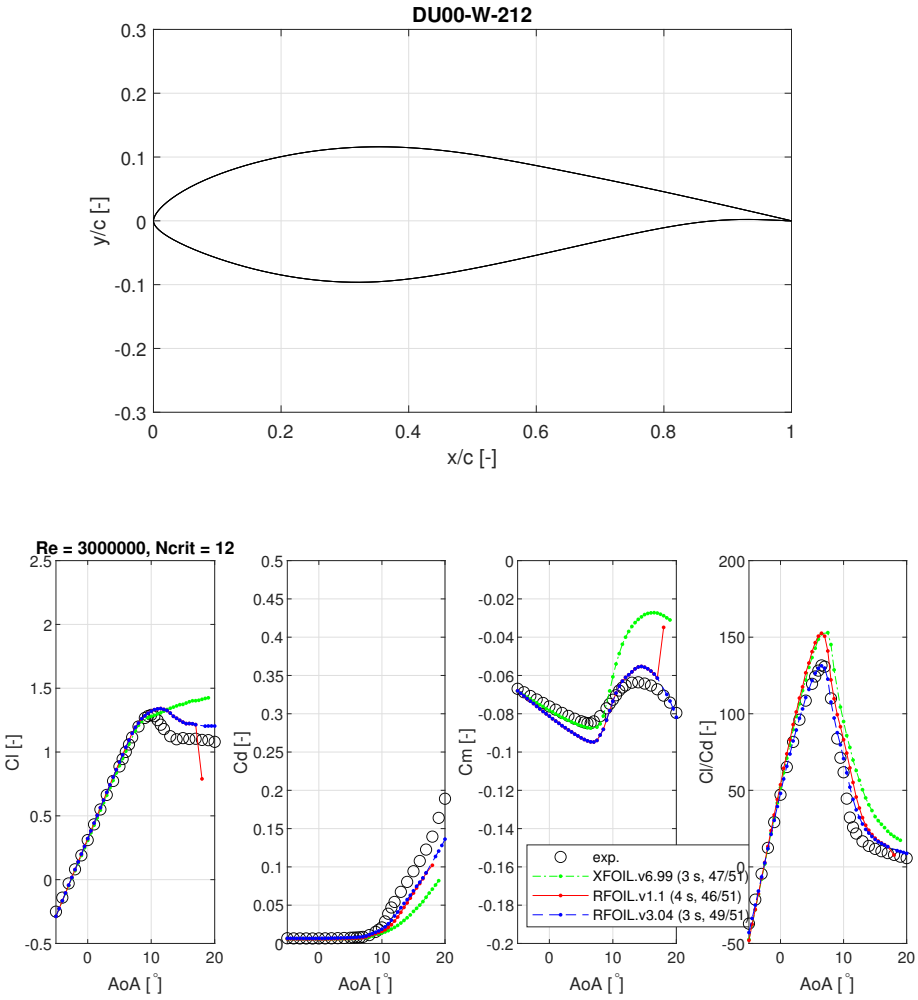

Figure B.17: Differences between experimental and numerical polars for the DU00-W-212 airfoil at a Reynolds number of 3000000. Vertical black lines in the middle subplot indicate, from left to right, the angle of attack corresponding to the minimum drag coefficient, maximum lift to drag ratio and maximum lift coefficient, respectively.

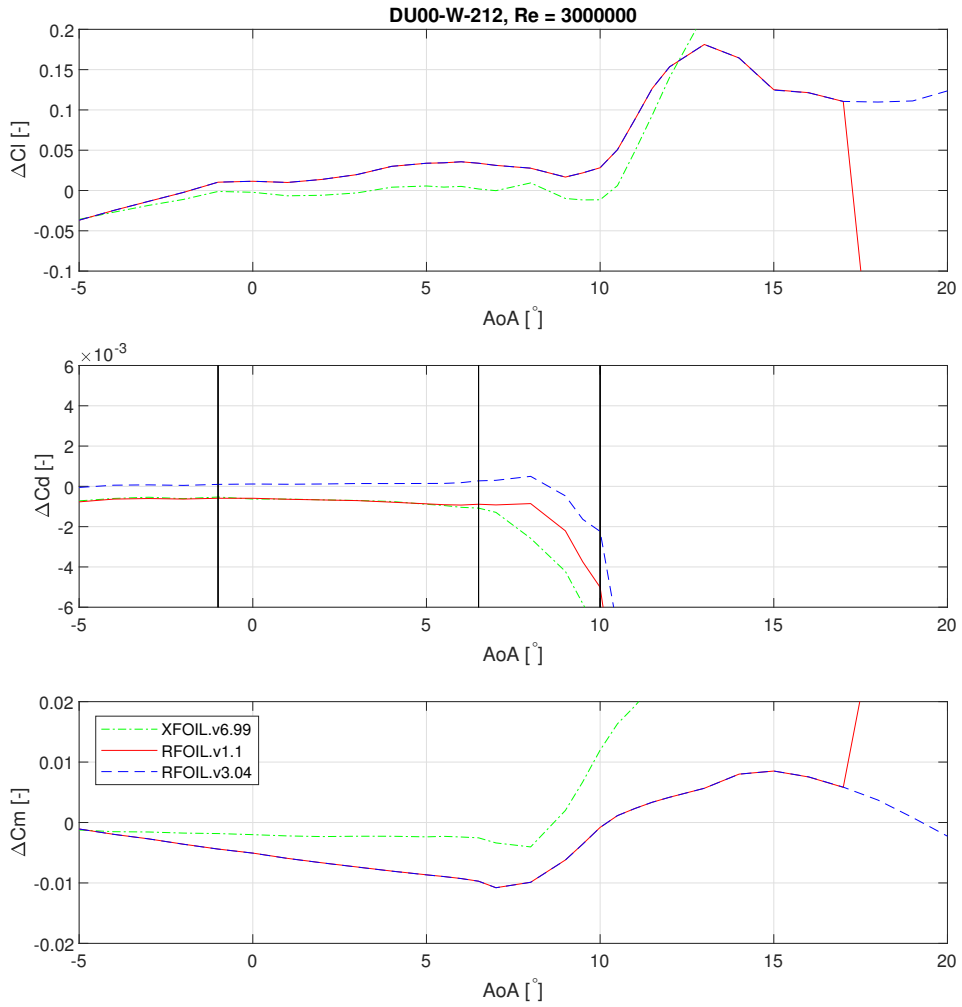

Figure B.18: Comparison between experimental and numerical pressure and skin friction distributions for the DU00-W-212 airfoil at a Reynolds number of 3000000 and at the design angle of attack.

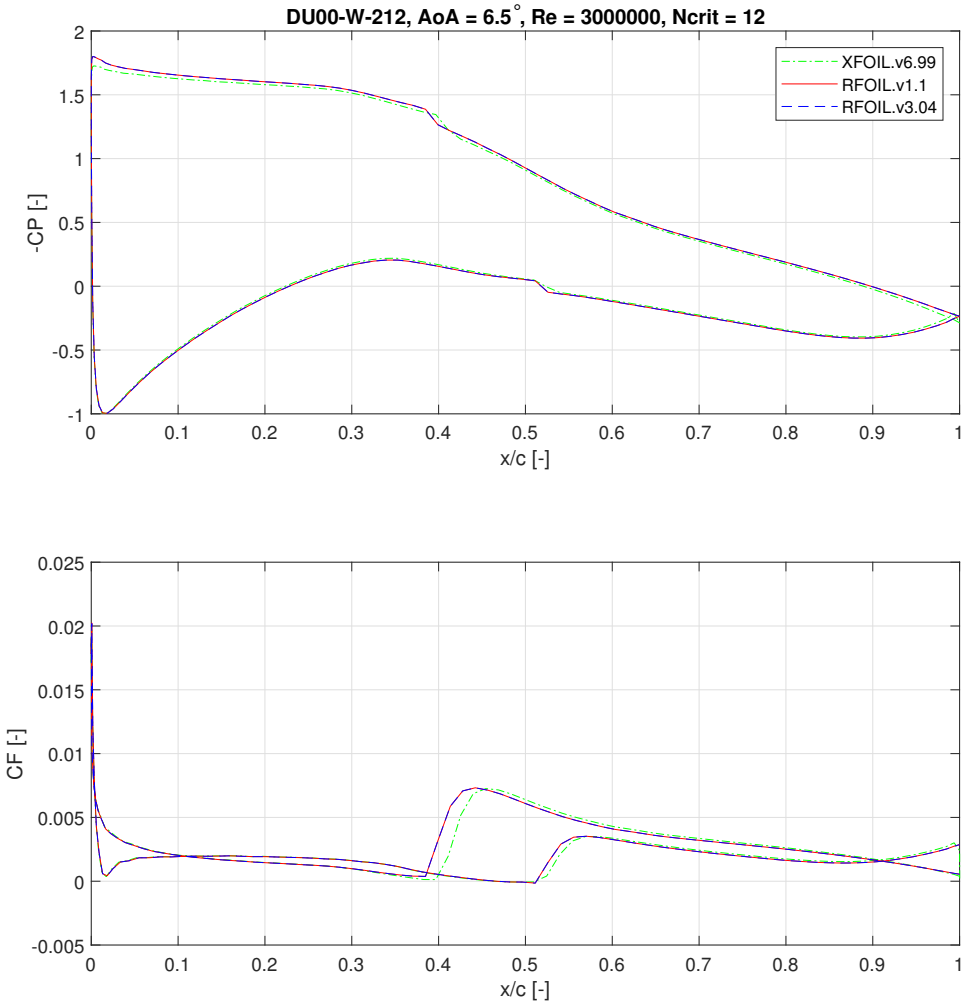

Figure B.19: Comparison between experimental and numerical polars for the DU00-W-212 airfoil at a Reynolds number of 7000000. Simulation time to generate the polars by means the different codes and the number of converged polar points are depicted between parentheses.

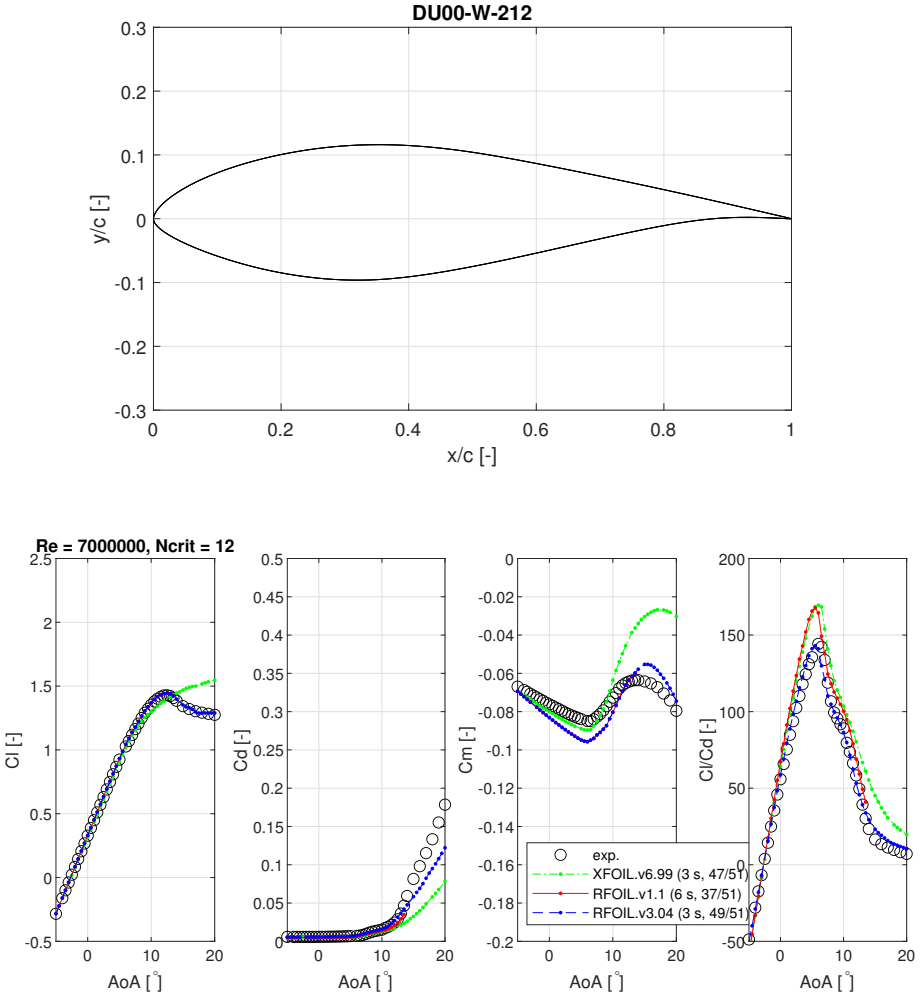

Figure B.20: Differences between experimental and numerical polars for the DU00-W-212 airfoil at a Reynolds number of 7000000. Vertical black lines in the middle subplot indicate, from left to right, the angle of attack corresponding to the minimum drag coefficient, maximum lift to drag ratio and maximum lift coefficient, respectively.

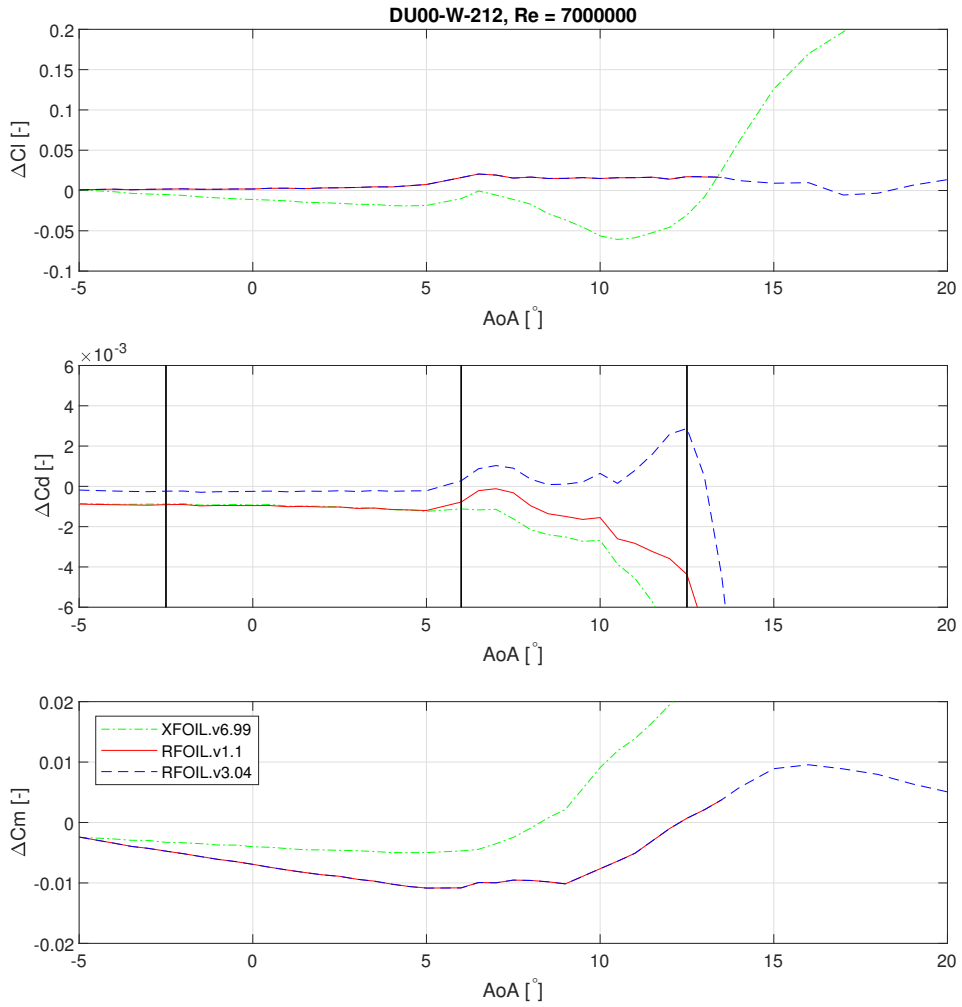

Figure B.21: Comparison between experimental and numerical pressure and skin friction distributions for the DU00-W-212 airfoil at a Reynolds number of 7000000 and at the design angle of attack.

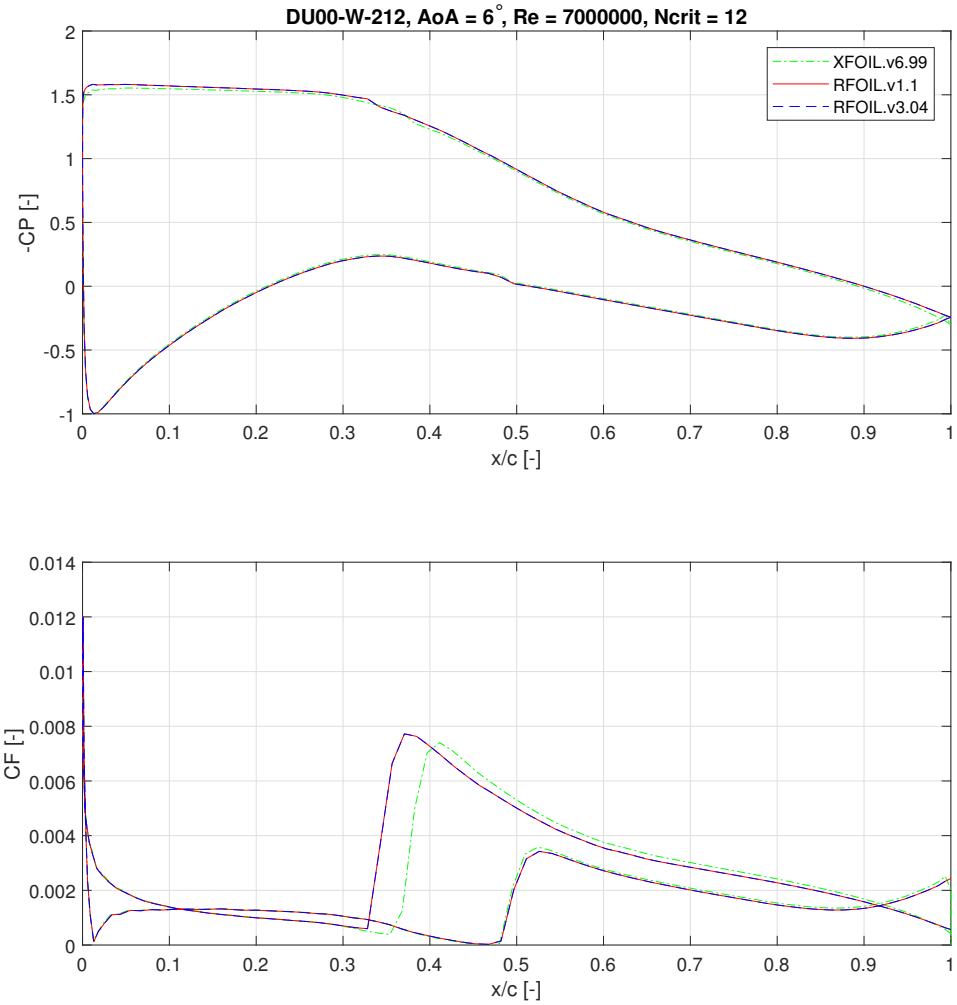

Figure B.22: Comparison between experimental and numerical polars for the DU00-W2-350 airfoil at a Reynolds number of 3000000. Simulation time to generate the polars by means the different codes and the number of converged polar points are depicted between parentheses.

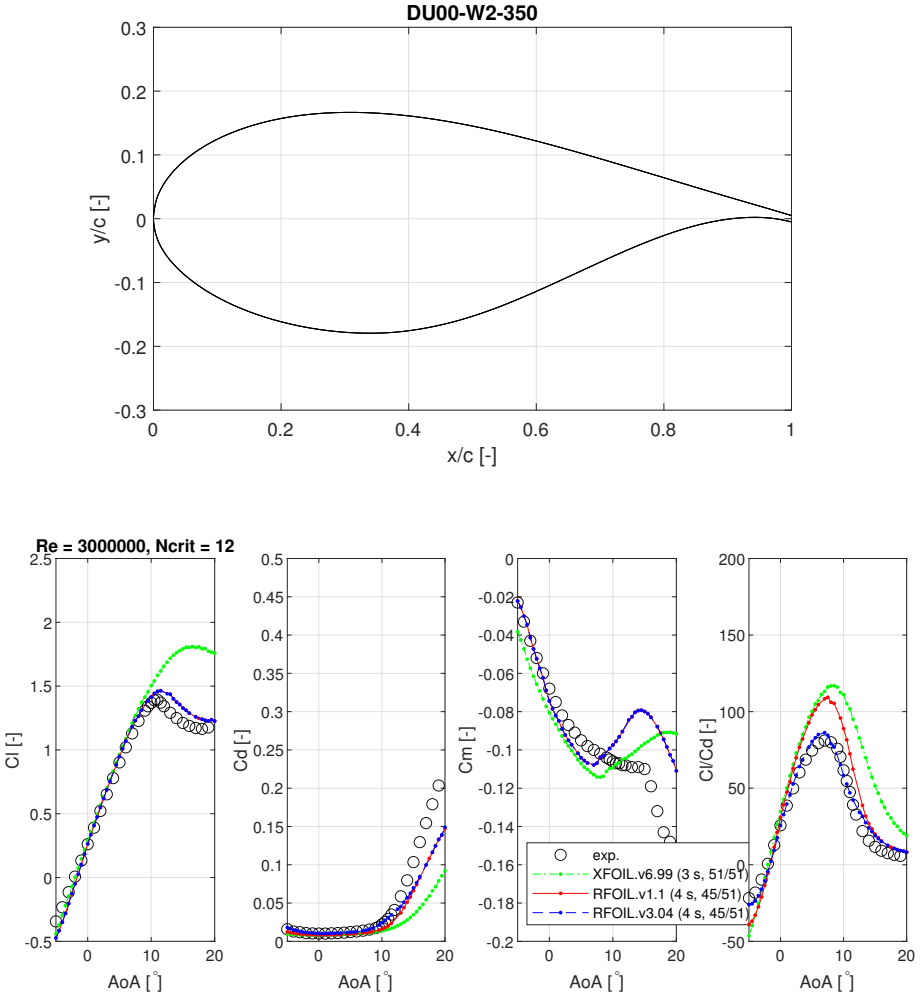

Figure B.23: Differences between experimental and numerical polars for the DU00-W2-350 airfoil at a Reynolds number of 3000000. Vertical black lines in the middle subplot indicate, from left to right, the angle of attack corresponding to the minimum drag coefficient, maximum lift to drag ratio and maximum lift coefficient, respectively.

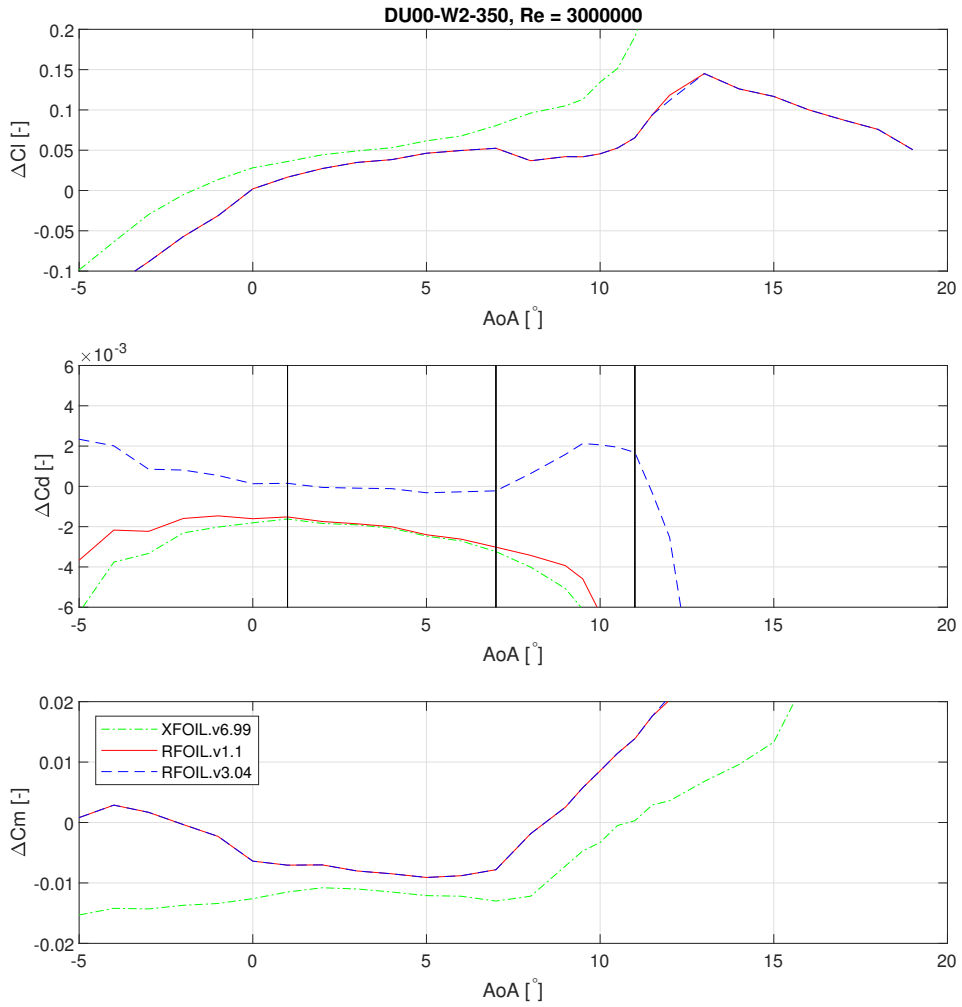

Figure B.24: Comparison between experimental and numerical pressure and skin friction distributions for the DU00-W2-350 airfoil at a Reynolds number of 3000000 and at the design angle of attack.

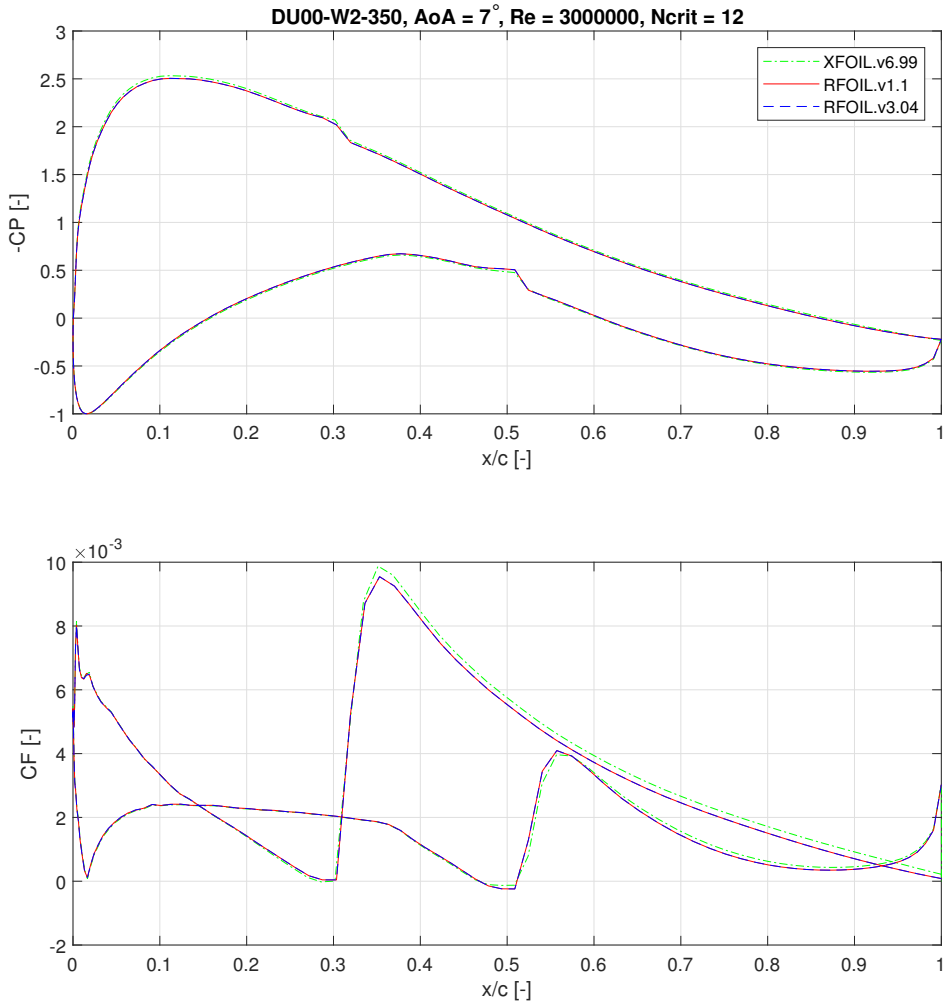

Figure B.25: Comparison between experimental and numerical polars for the DU00-W2-350 airfoil at a Reynolds number of 7000000. Simulation time to generate the polars by means the different codes and the number of converged polar points are depicted between parentheses.

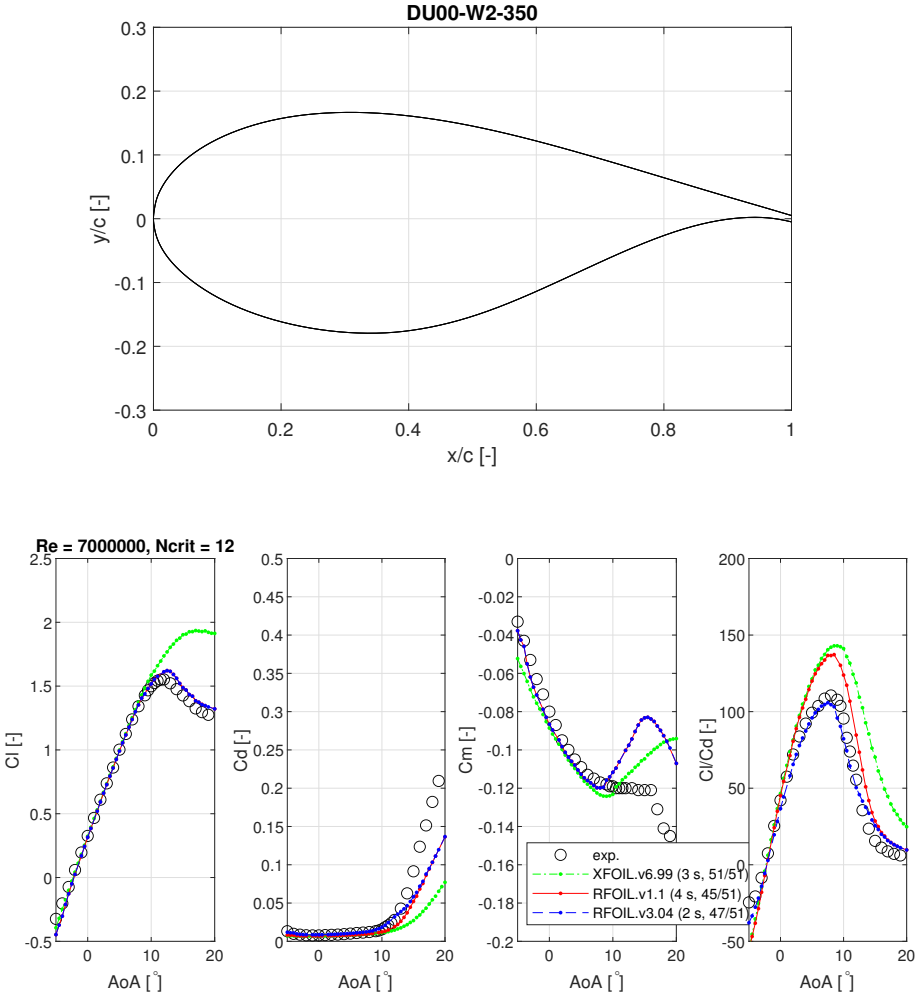

Figure B.26: Differences between experimental and numerical polars for the DU00-W2-350 airfoil at a Reynolds number of 7000000. Vertical black lines in the middle subplot indicate, from left to right, the angle of attack corresponding to the minimum drag coefficient, maximum lift to drag ratio and maximum lift coefficient, respectively.

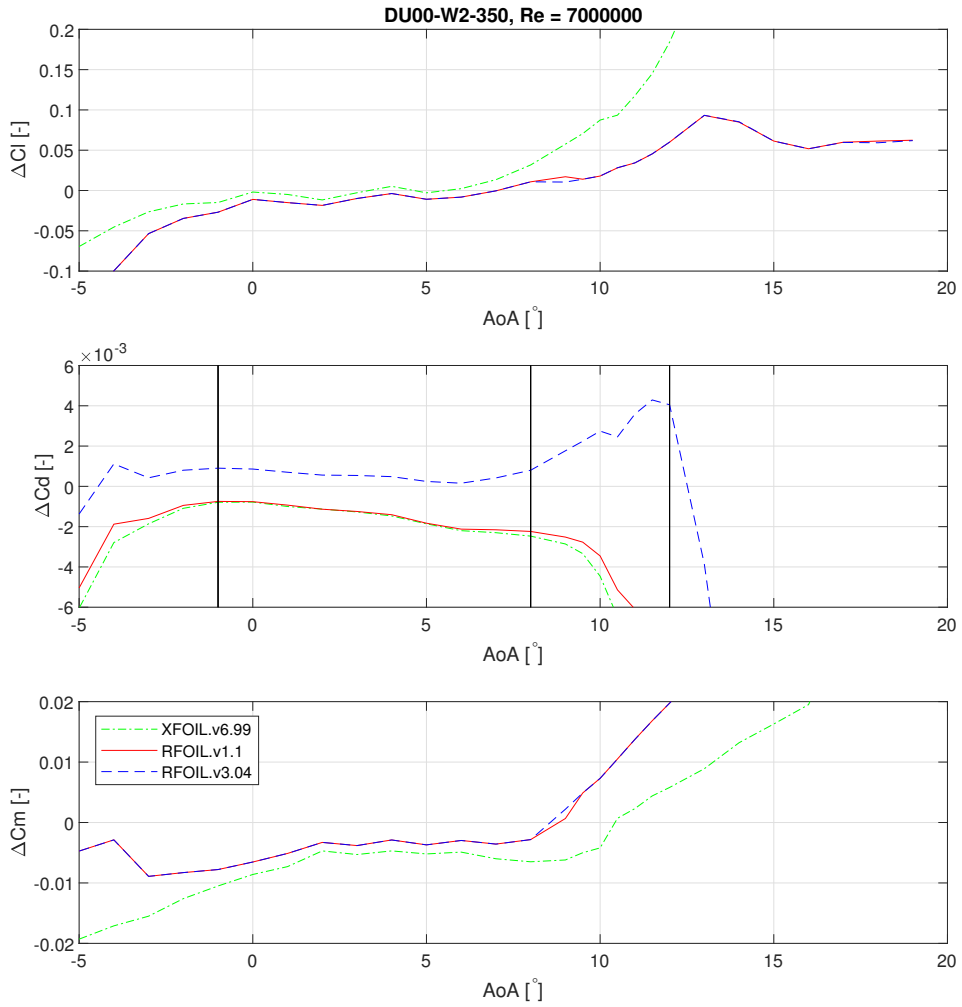

Figure B.27: Comparison between experimental and numerical pressure and skin friction distributions for the DU00-W2-350 airfoil at a Reynolds number of 7000000 and at the design angle of attack.

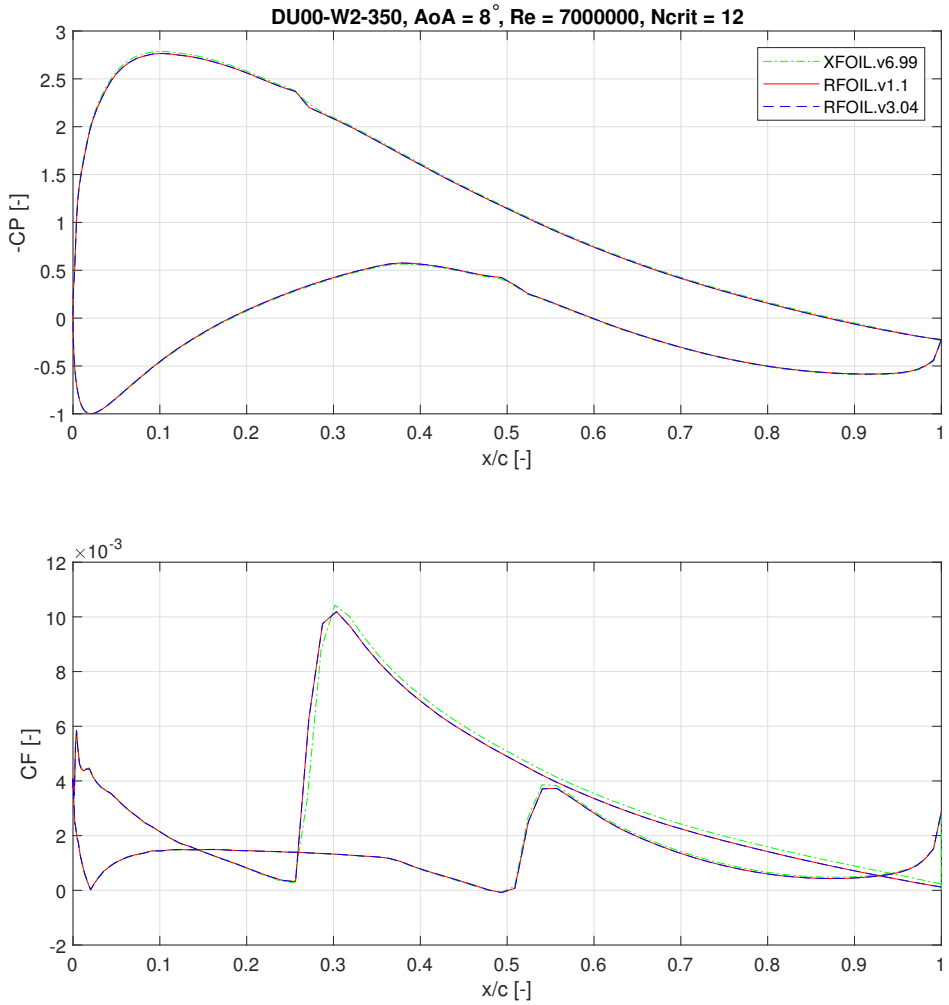

Figure B.28: Comparison between experimental and numerical polars for the DU00-W2-401 airfoil at a Reynolds number of 1000000. Simulation time to generate the polars by means the different codes and the number of converged polar points are depicted between parentheses.

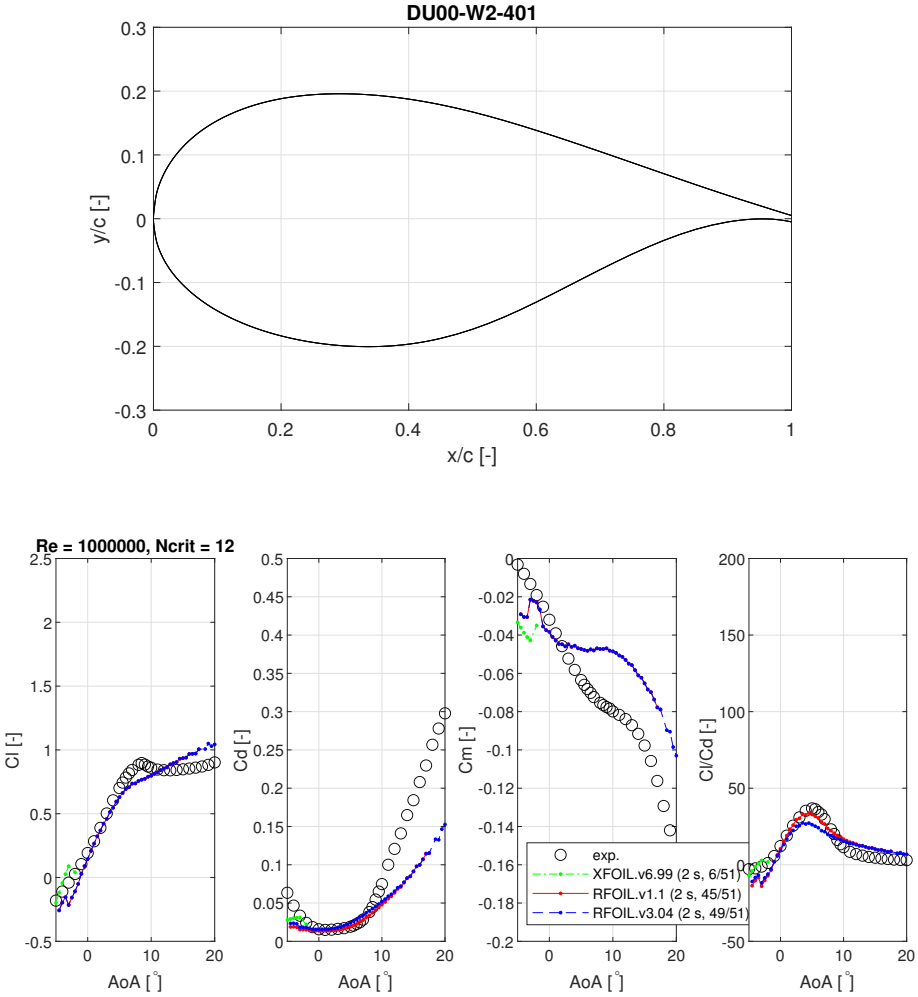

Figure B.29: Differences between experimental and numerical polars for the DU00-W2-401 airfoil at a Reynolds number of 1000000. Vertical black lines in the middle subplot indicate, from left to right, the angle of attack corresponding to the minimum drag coefficient, maximum lift to drag ratio and maximum lift coefficient, respectively.

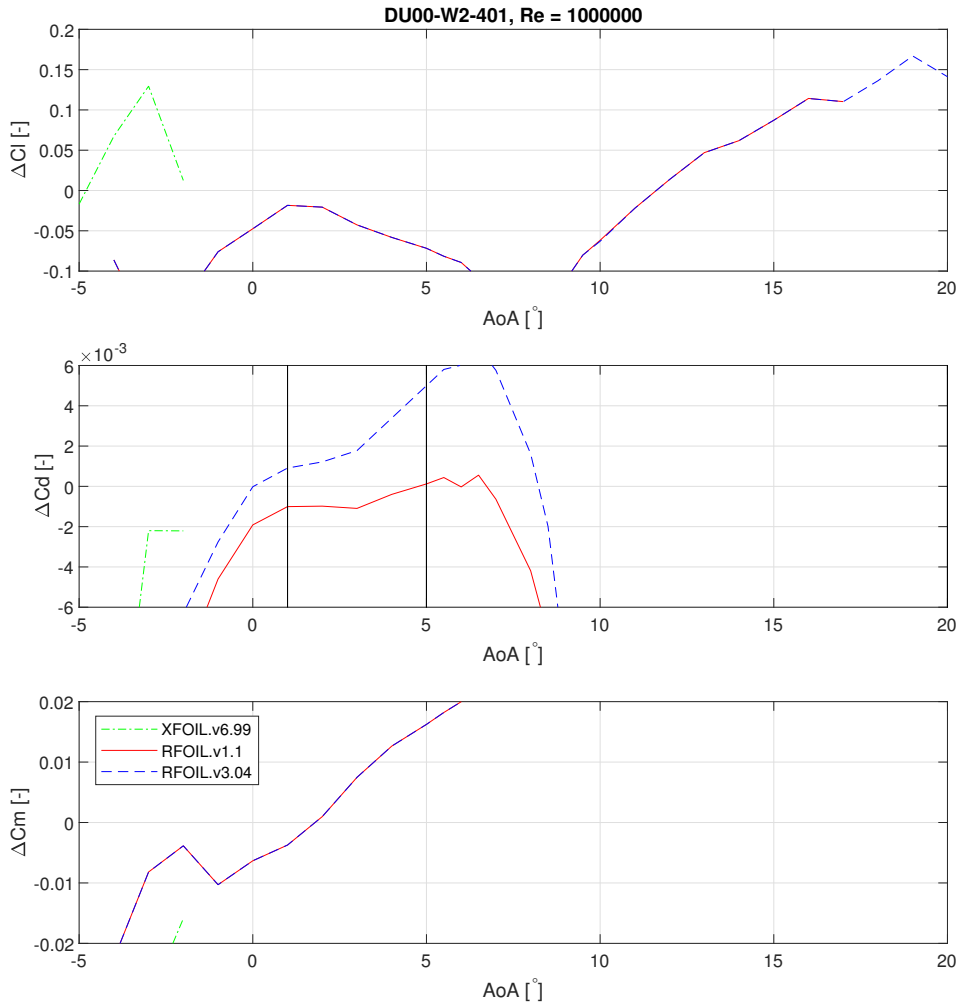

Figure B.30: Comparison between experimental and numerical pressure and skin friction distributions for the DU00-W2-401 airfoil at a Reynolds number of 1000000 and at the design angle of attack.

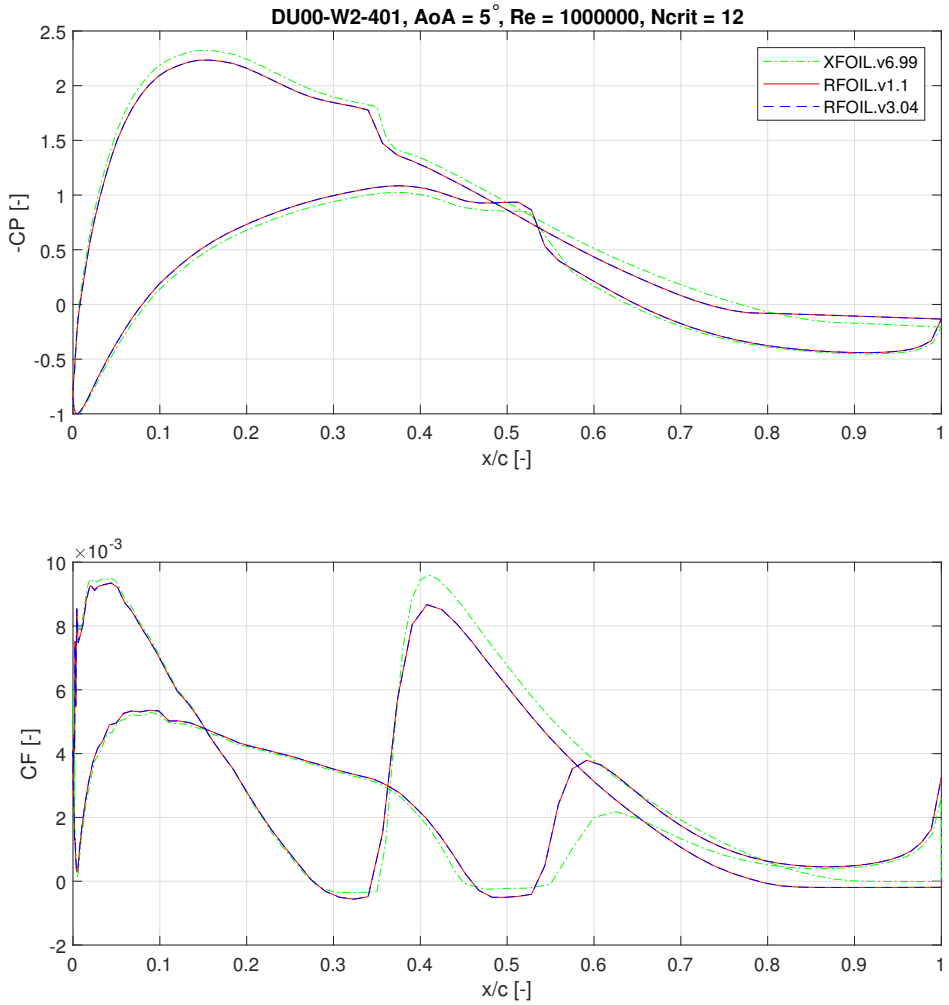

Figure B.31: Comparison between experimental and numerical polars for the DU00-W2-401 airfoil at a Reynolds number of 3000000. Simulation time to generate the polars by means the different codes and the number of converged polar points are depicted between parentheses.

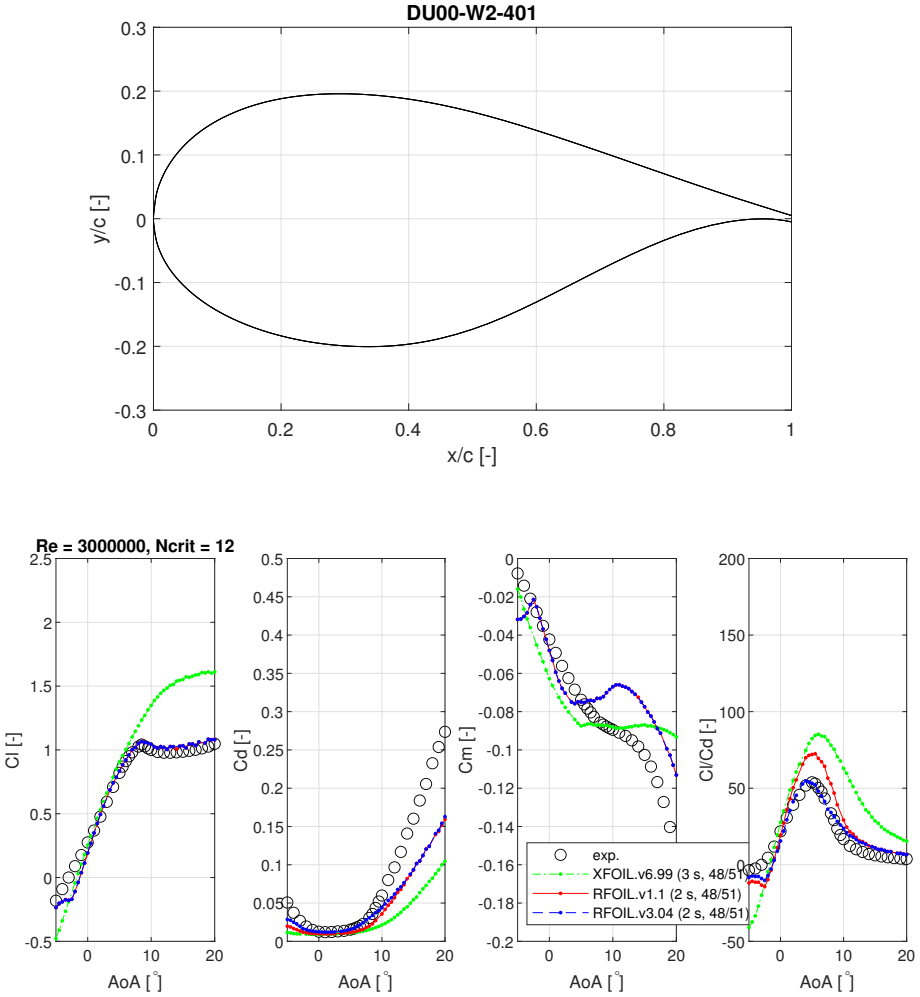

Figure B.32: Differences between experimental and numerical polars for the DU00-W2-401 airfoil at a Reynolds number of 3000000. Vertical black lines in the middle subplot indicate, from left to right, the angle of attack corresponding to the minimum drag coefficient, maximum lift to drag ratio and maximum lift coefficient, respectively.

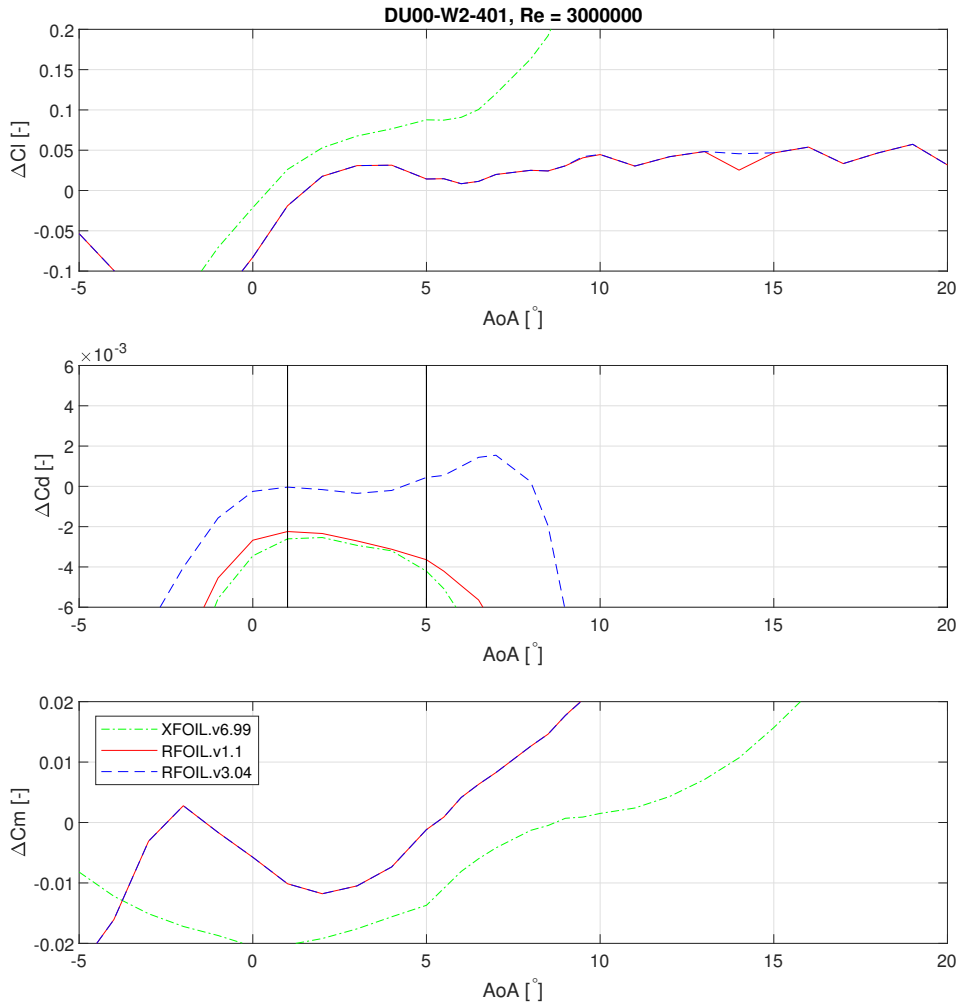

Figure B.33: Comparison between experimental and numerical pressure and skin friction distributions for the DU00-W2-401 airfoil at a Reynolds number of 3000000 and at the design angle of attack.

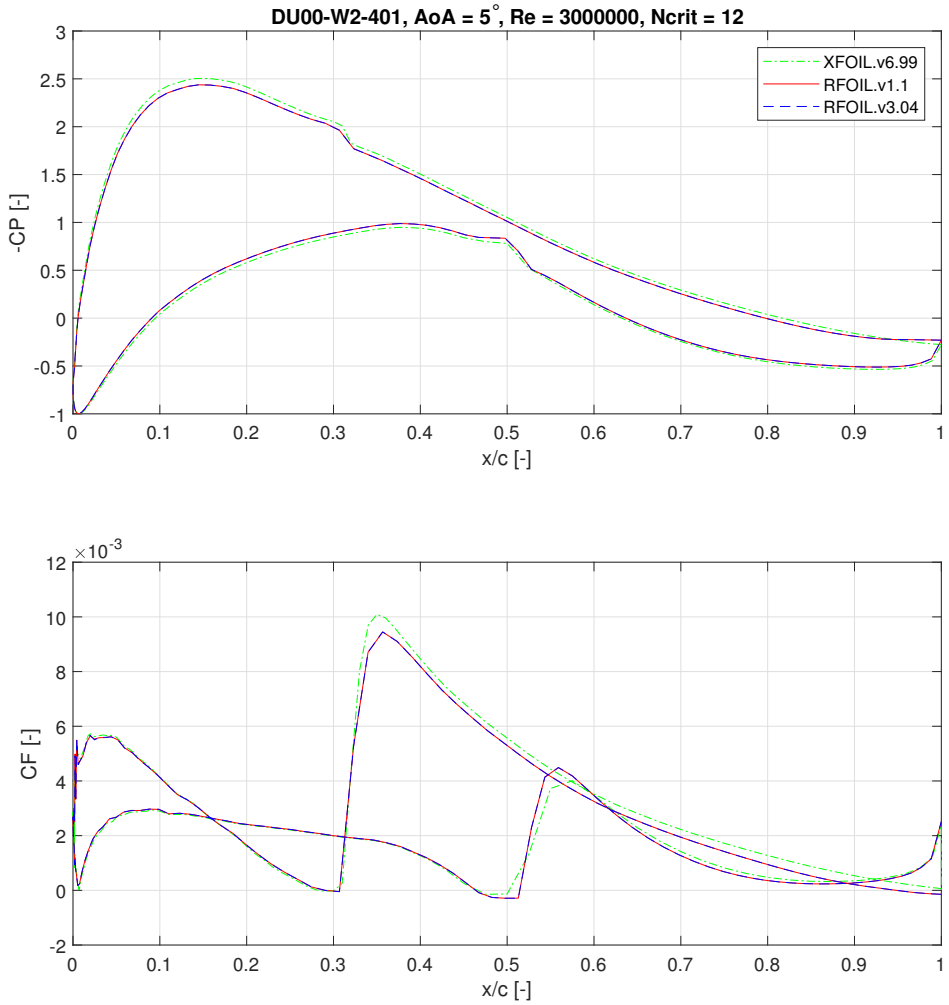

Figure B.34: Comparison between experimental and numerical polars for the DU00-W2-401 airfoil at a Reynolds number of 7000000. Simulation time to generate the polars by means the different codes and the number of converged polar points are depicted between parentheses.

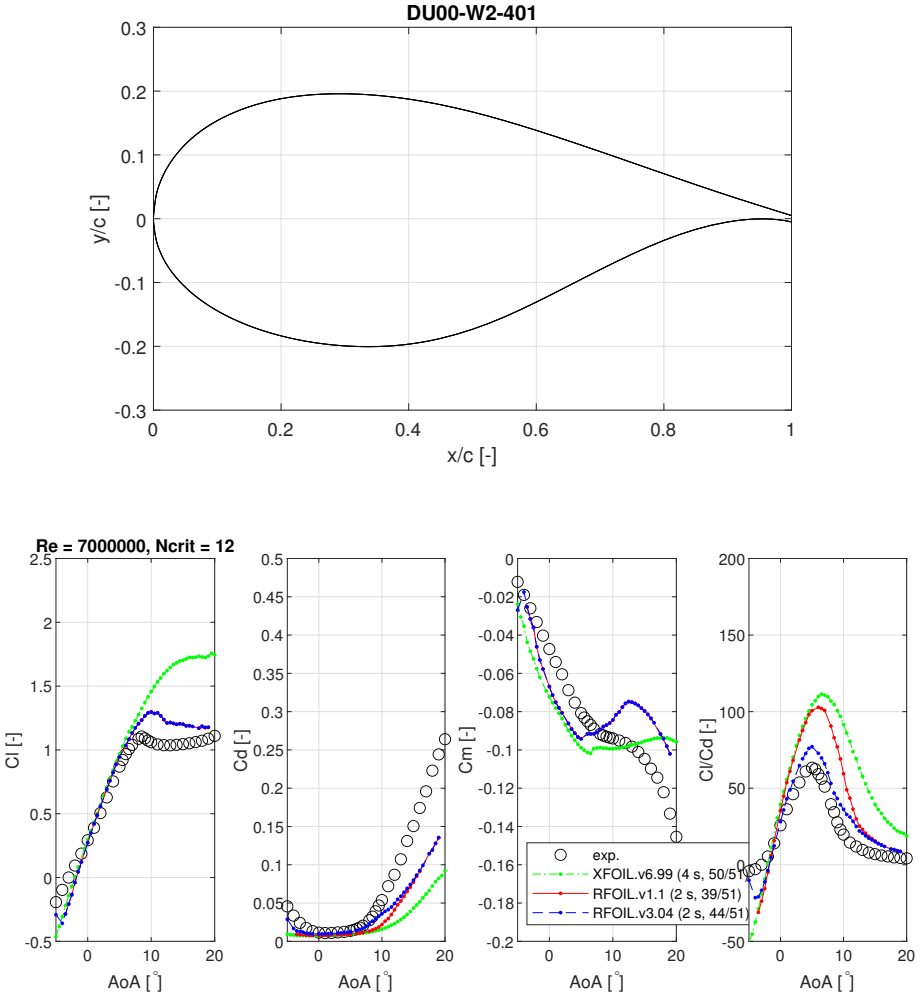

Figure B.35: Differences between experimental and numerical polars for the DU00-W2-401 airfoil at a Reynolds number of 7000000. Vertical black lines in the middle subplot indicate, from left to right, the angle of attack corresponding to the minimum drag coefficient, maximum lift to drag ratio and maximum lift coefficient, respectively.

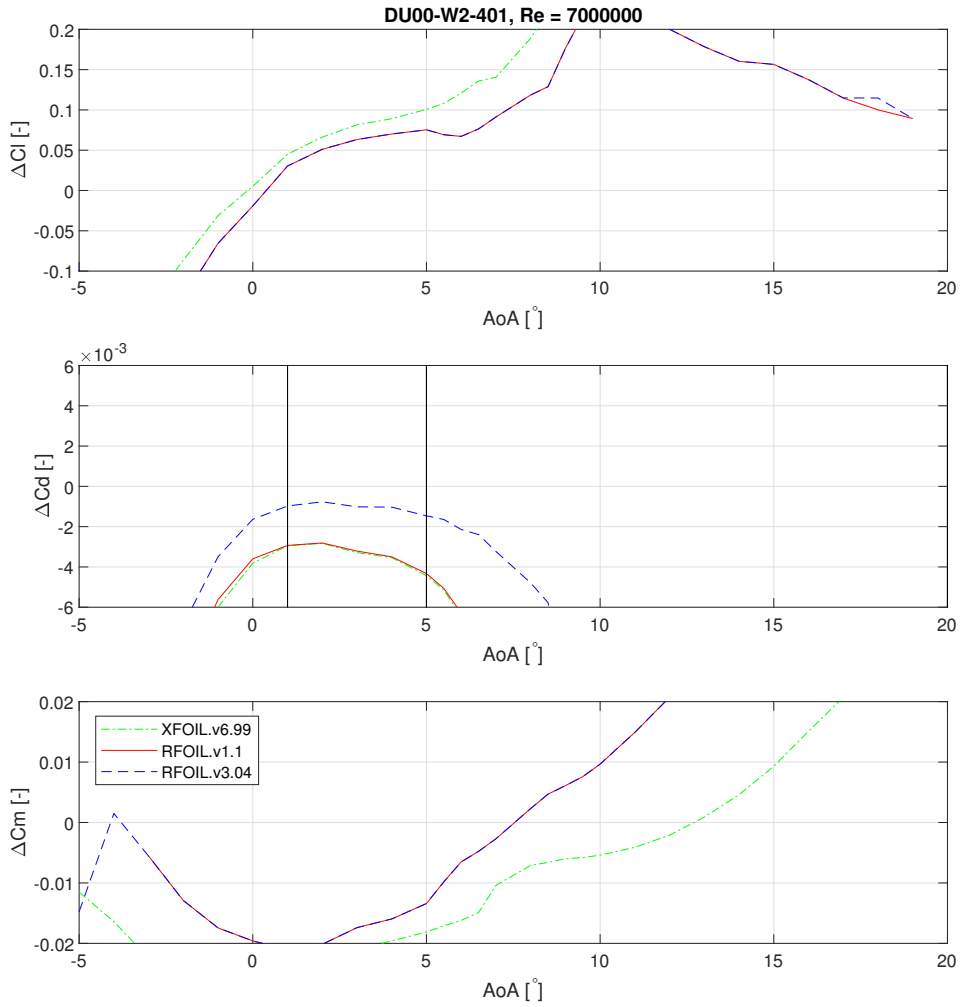

Figure B.36: Comparison between experimental and numerical pressure and skin friction distributions for the DU00-W2-401 airfoil at a Reynolds number of 7000000 and at the design angle of attack.

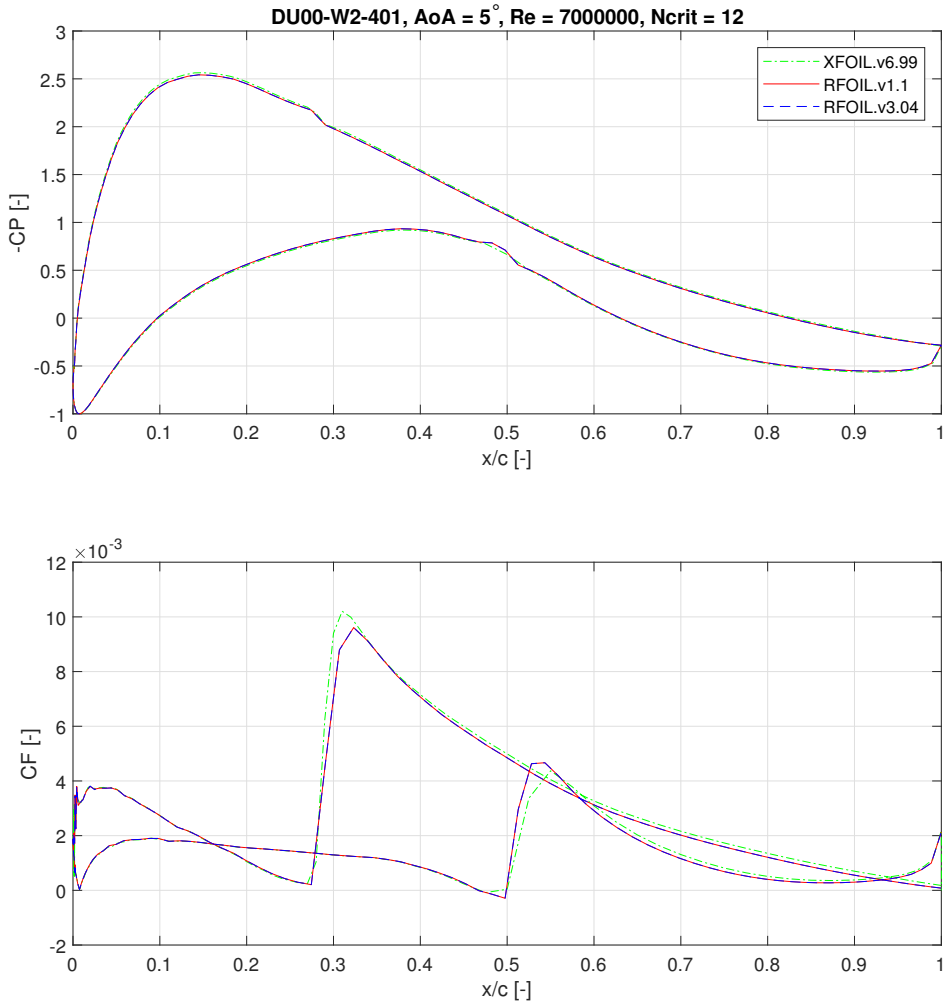

Figure B.37: Comparison between experimental and numerical polars for the DU91-W2-250 airfoil at a Reynolds number of 1000000. Simulation time to generate the polars by means the different codes and the number of converged polar points are depicted between parentheses.

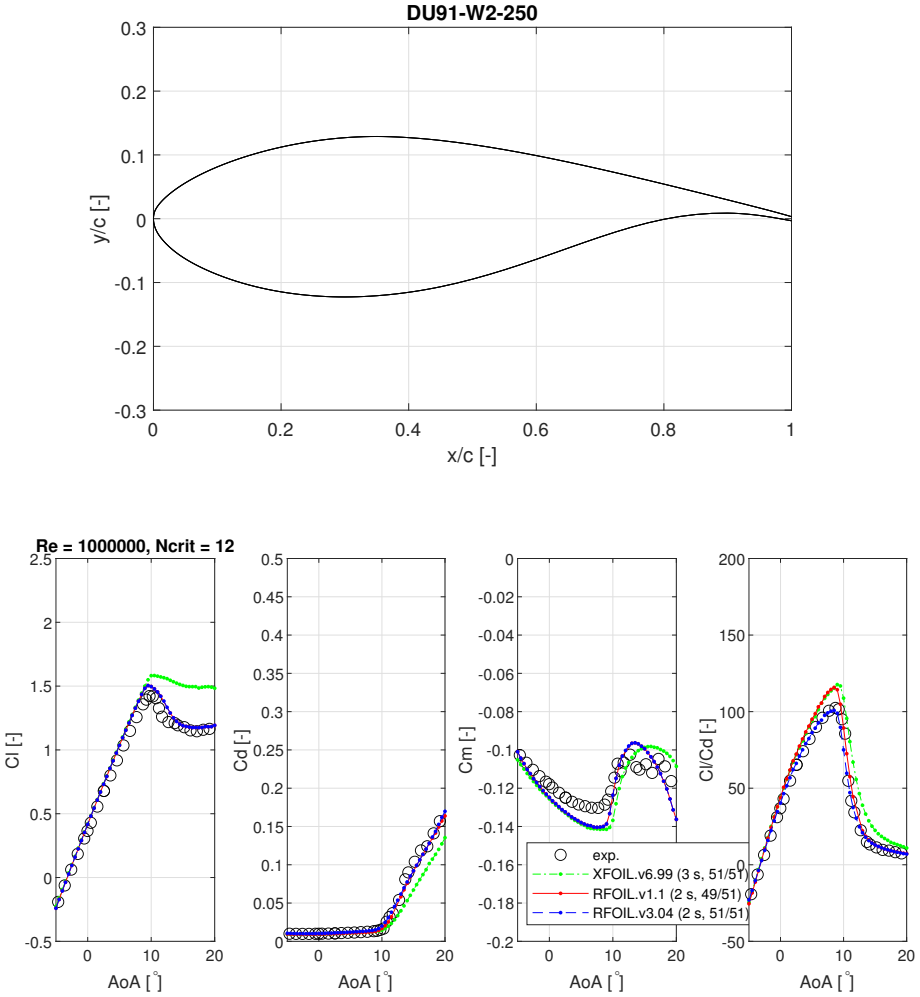

Figure B.38: Differences between experimental and numerical polars for the DU91-W2-250 airfoil at a Reynolds number of 1000000. Vertical black lines in the middle subplot indicate, from left to right, the angle of attack corresponding to the minimum drag coefficient, maximum lift to drag ratio and maximum lift coefficient, respectively.

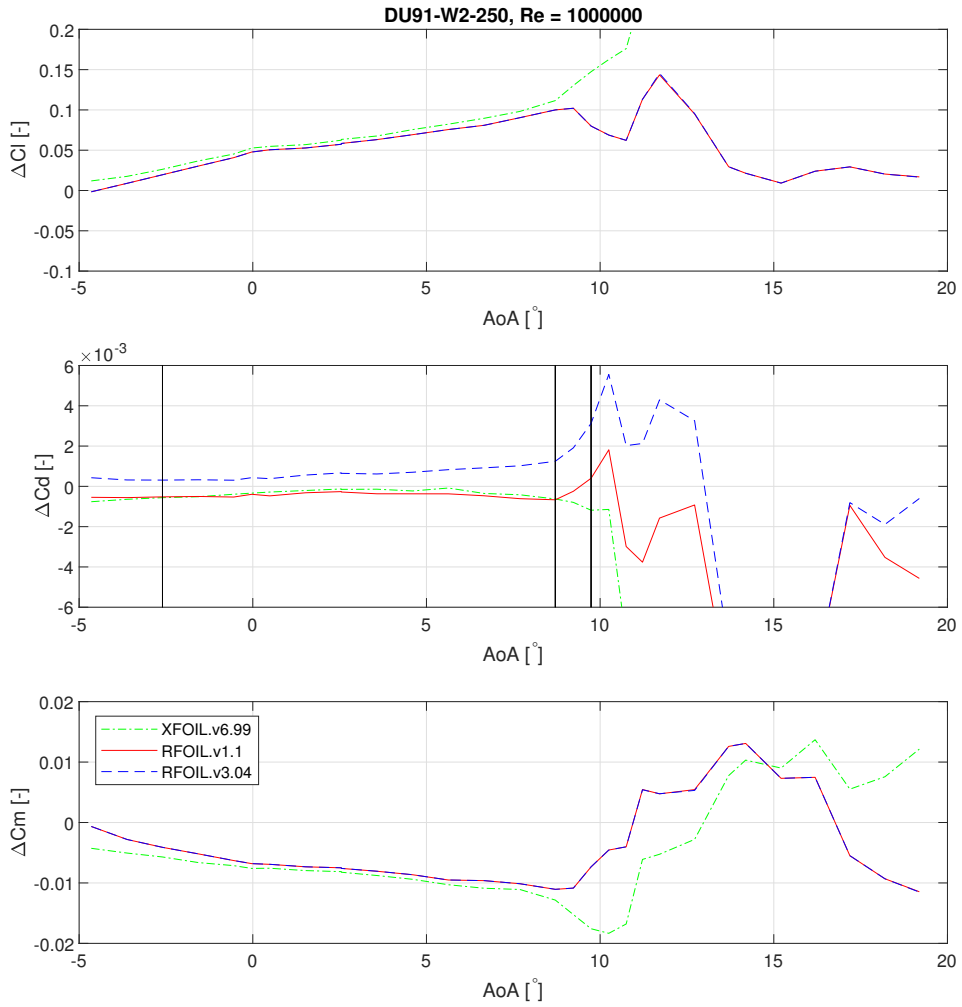

Figure B.39: Comparison between experimental and numerical pressure and skin friction distributions for the DU91-W2-250 airfoil at a Reynolds number of 1000000 and at the design angle of attack.

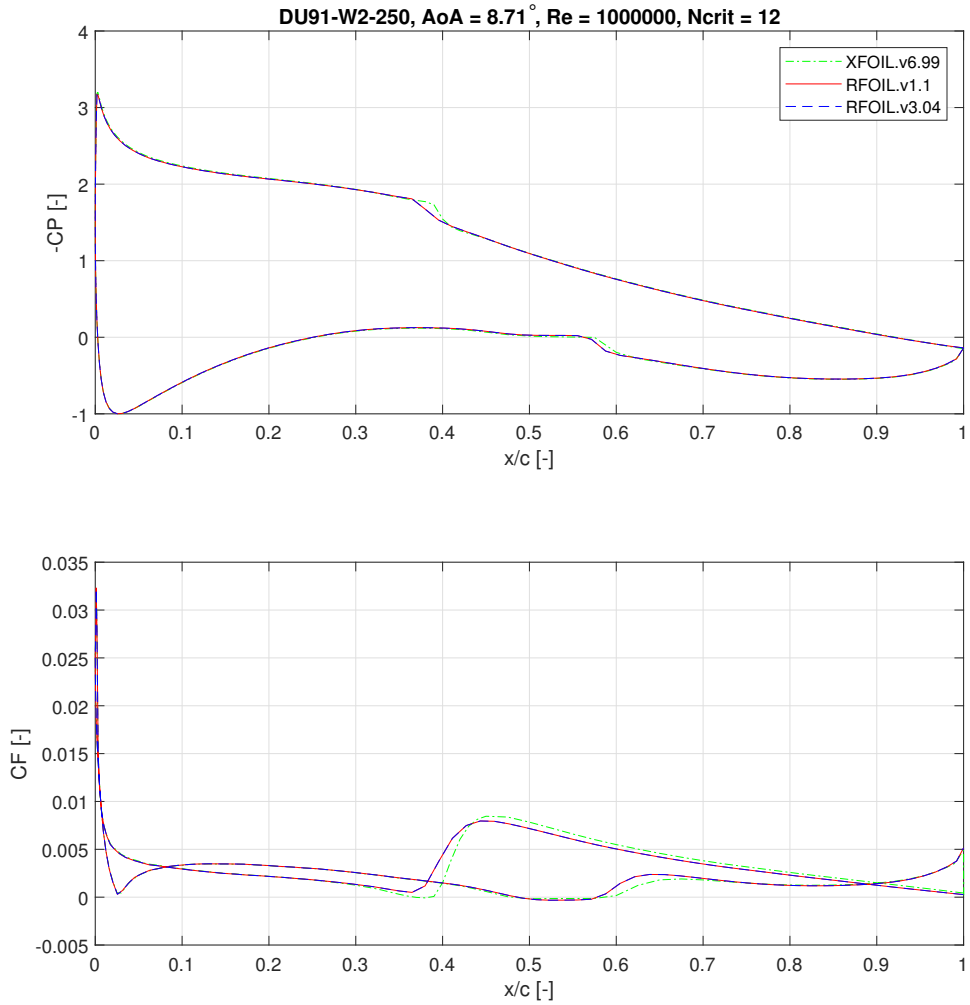

Figure B.40: Comparison between experimental and numerical polars for the DU91-W2-250 airfoil at a Reynolds number of 2000000. Simulation time to generate the polars by means the different codes and the number of converged polar points are depicted between parentheses.

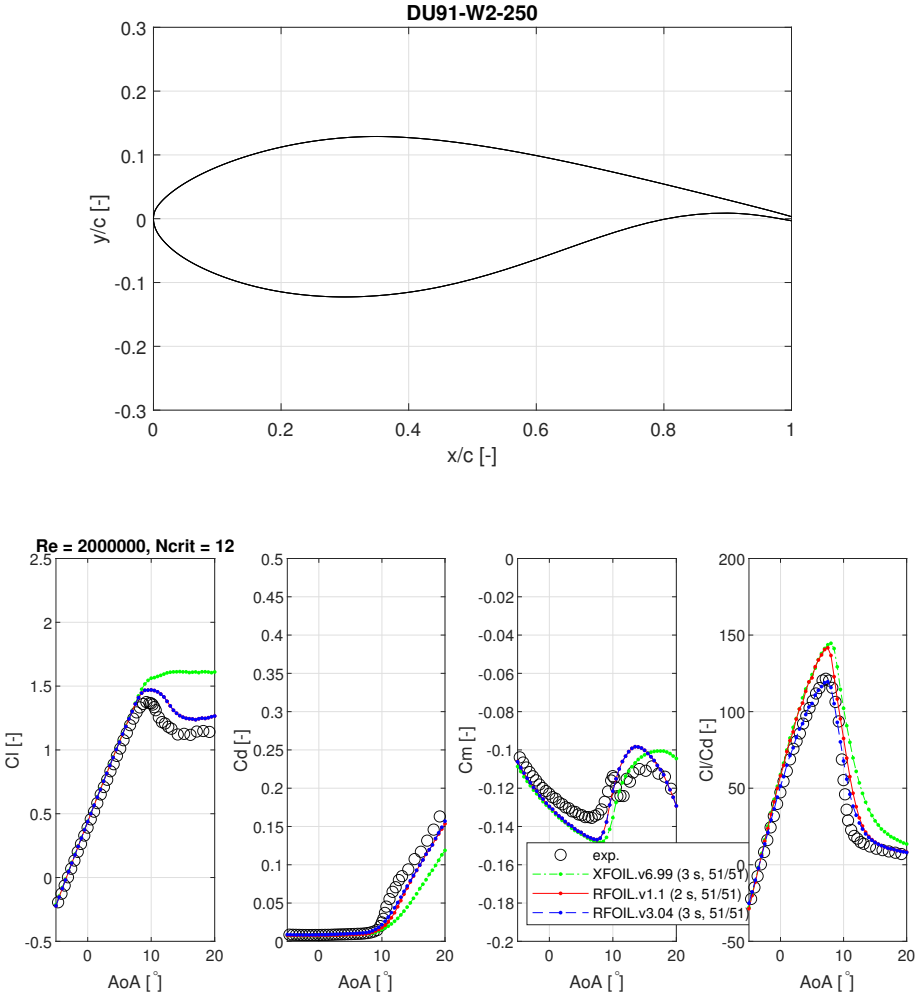

Figure B.41: Differences between experimental and numerical polars for the DU91-W2-250 airfoil at a Reynolds number of 2000000. Vertical black lines in the middle subplot indicate, from left to right, the angle of attack corresponding to the minimum drag coefficient, maximum lift to drag ratio and maximum lift coefficient, respectively.

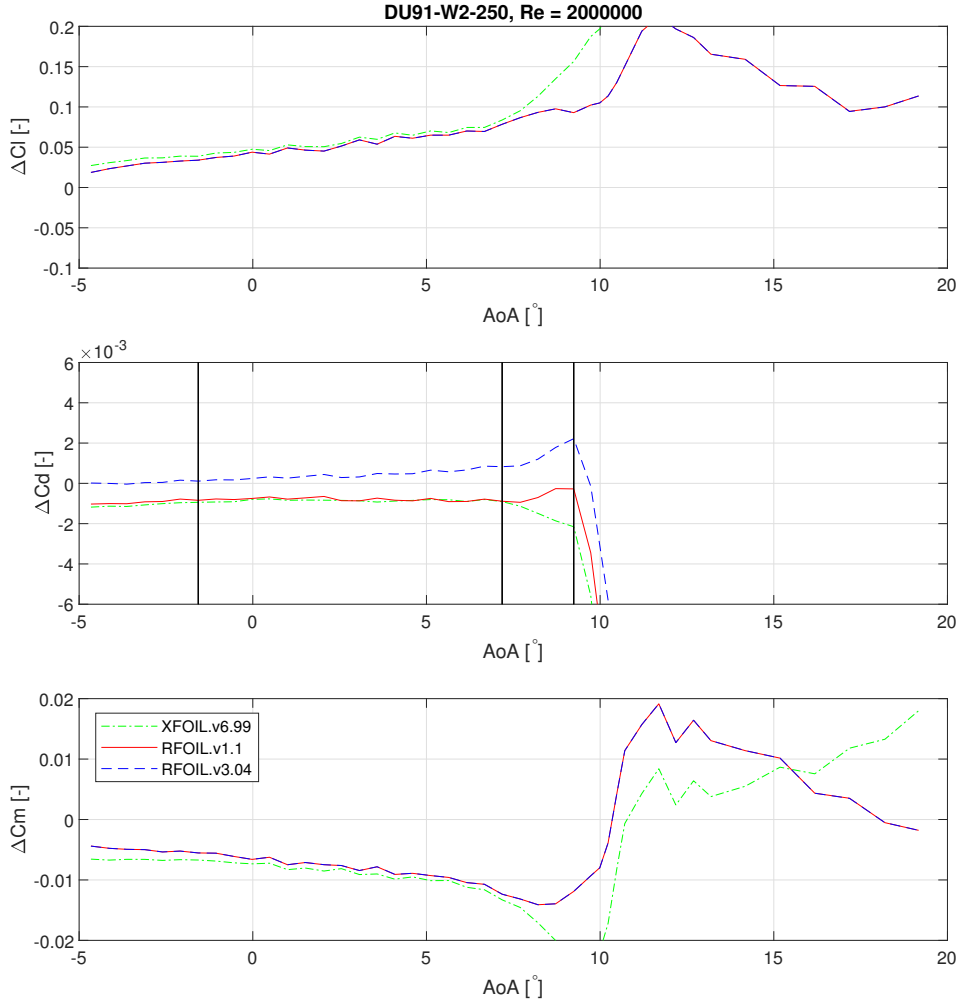

Figure B.42: Comparison between experimental and numerical pressure and skin friction distributions for the DU91-W2-250 airfoil at a Reynolds number of 2000000 and at the design angle of attack.

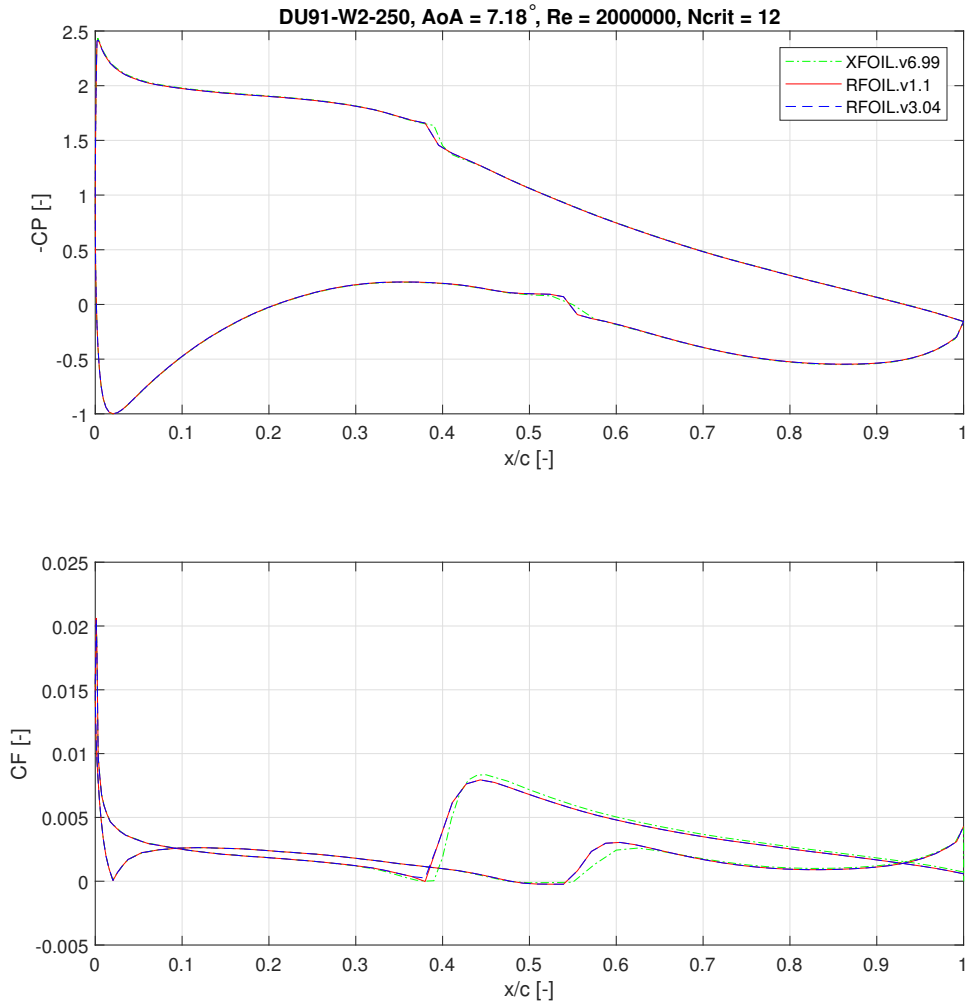

Figure B.43: Comparison between experimental and numerical polars for the DU91-W2-250 airfoil at a Reynolds number of 3000000. Simulation time to generate the polars by means the different codes and the number of converged polar points are depicted between parentheses.

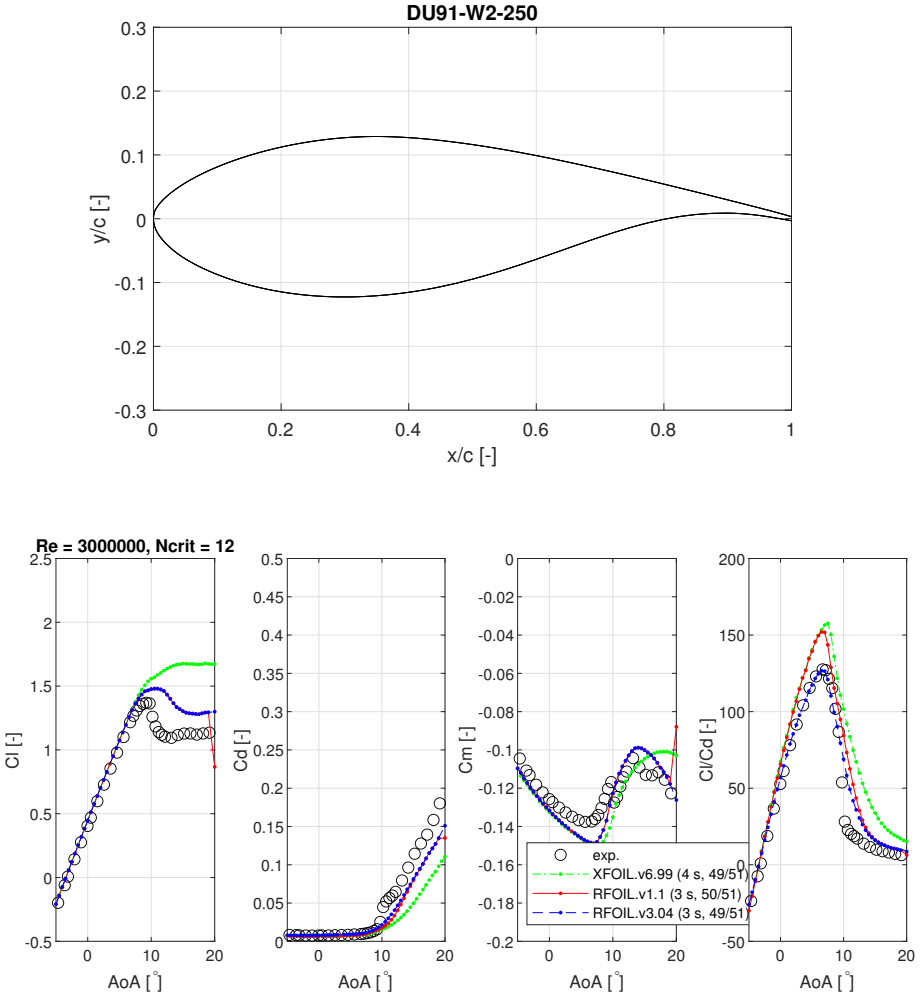

Figure B.44: Differences between experimental and numerical polars for the DU91-W2-250 airfoil at a Reynolds number of 3000000. Vertical black lines in the middle subplot indicate, from left to right, the angle of attack corresponding to the minimum drag coefficient, maximum lift to drag ratio and maximum lift coefficient, respectively.

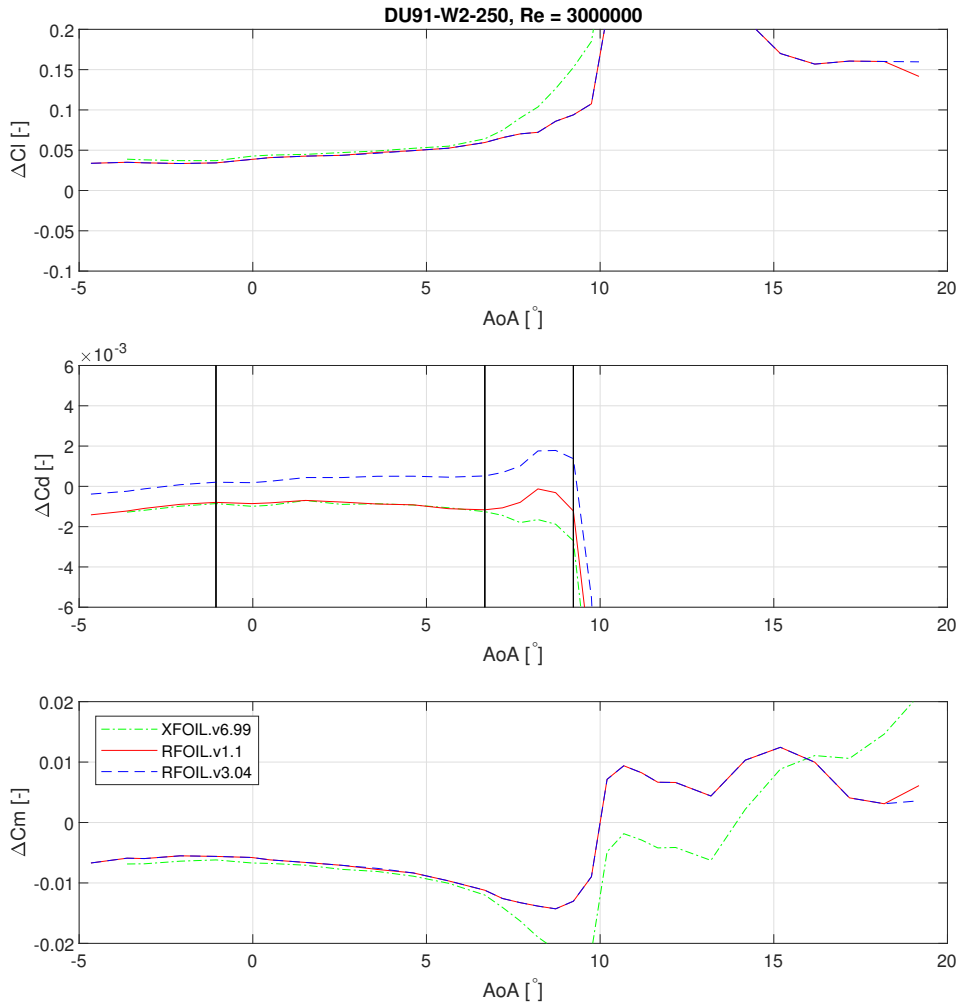

Figure B.45: Comparison between experimental and numerical pressure and skin friction distributions for the DU91-W2-250 airfoil at a Reynolds number of 3000000 and at the design angle of attack.

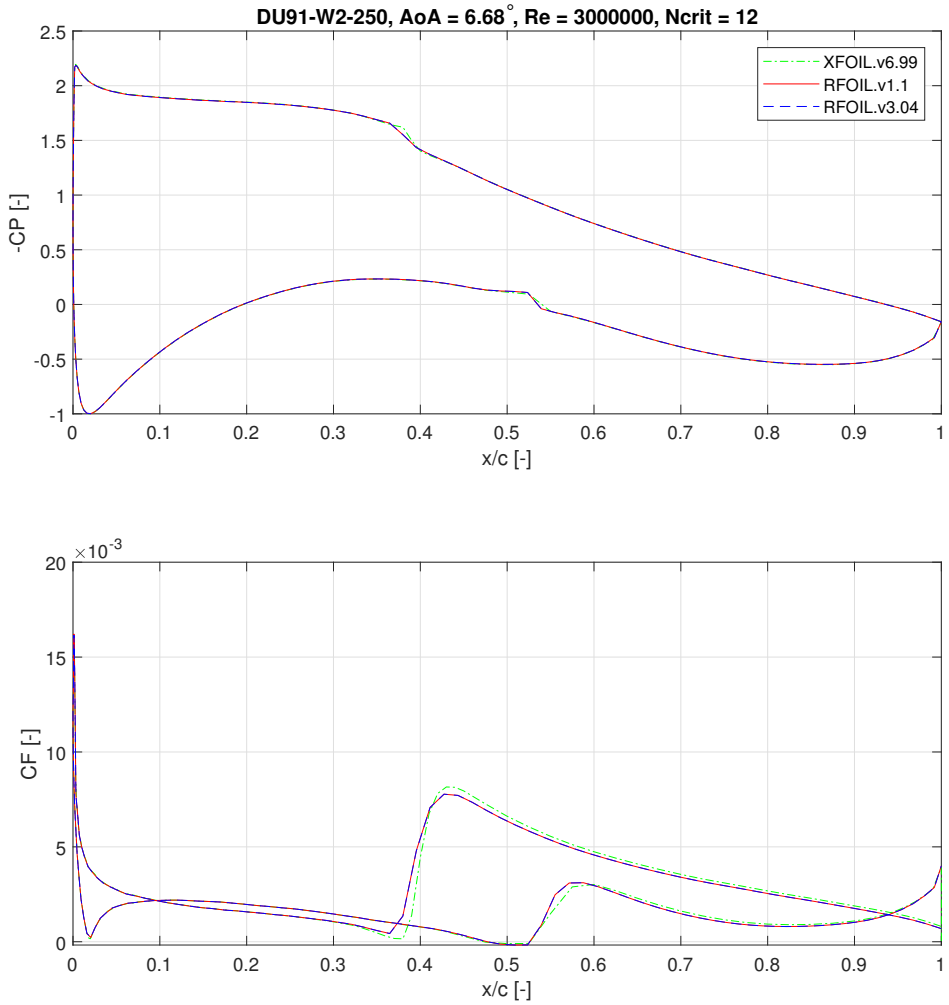

Figure B.46: Comparison between experimental and numerical polars for the DU91-W2-250 airfoil at a Reynolds number of 7000000. Simulation time to generate the polars by means the different codes and the number of converged polar points are depicted between parentheses.

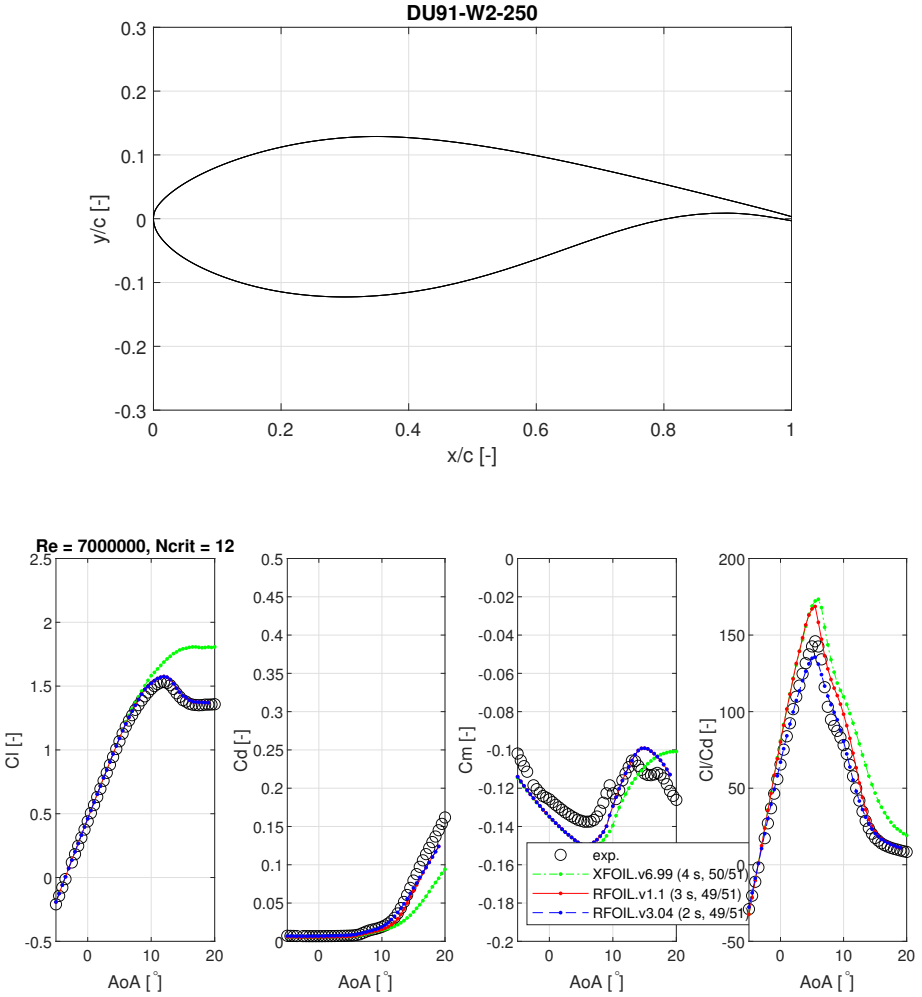

Figure B.47: Differences between experimental and numerical polars for the DU91-W2-250 airfoil at a Reynolds number of 7000000. Vertical black lines in the middle subplot indicate, from left to right, the angle of attack corresponding to the minimum drag coefficient, maximum lift to drag ratio and maximum lift coefficient, respectively.

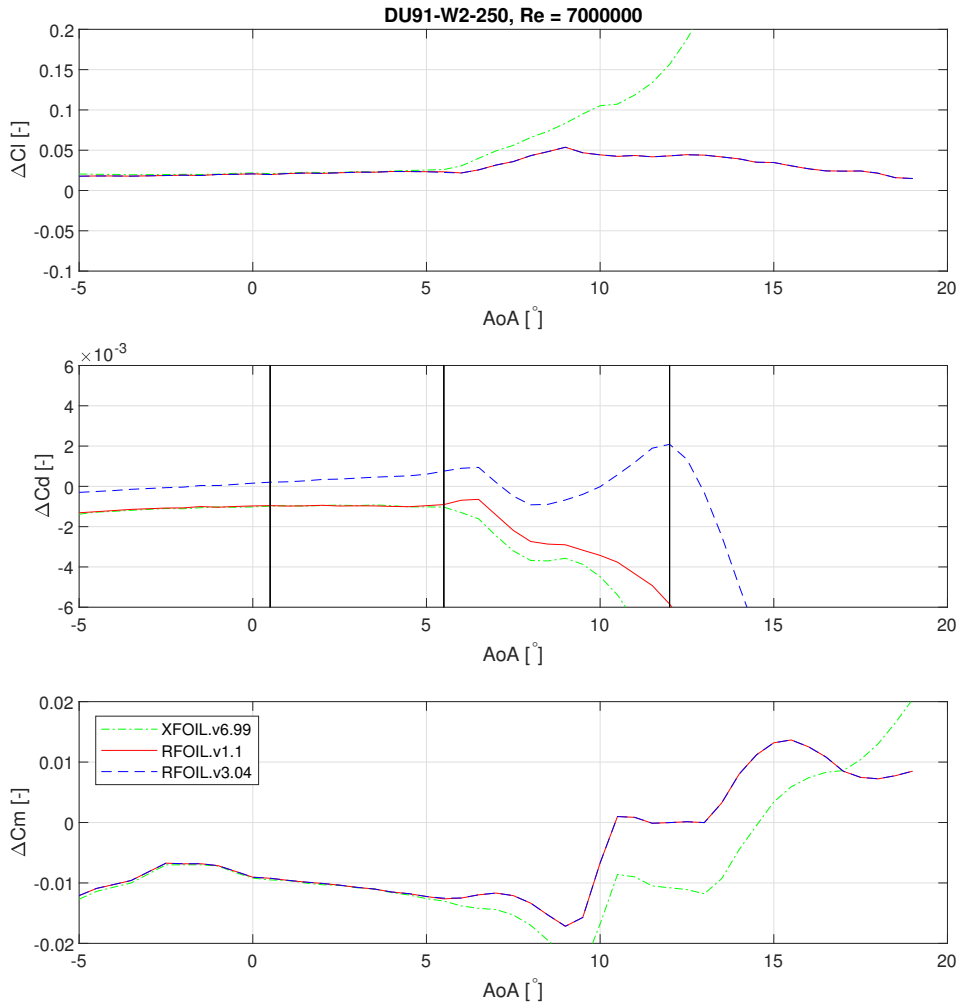

Figure B.48: Comparison between experimental and numerical pressure and skin friction distributions for the DU91-W2-250 airfoil at a Reynolds number of 7000000 and at the design angle of attack.

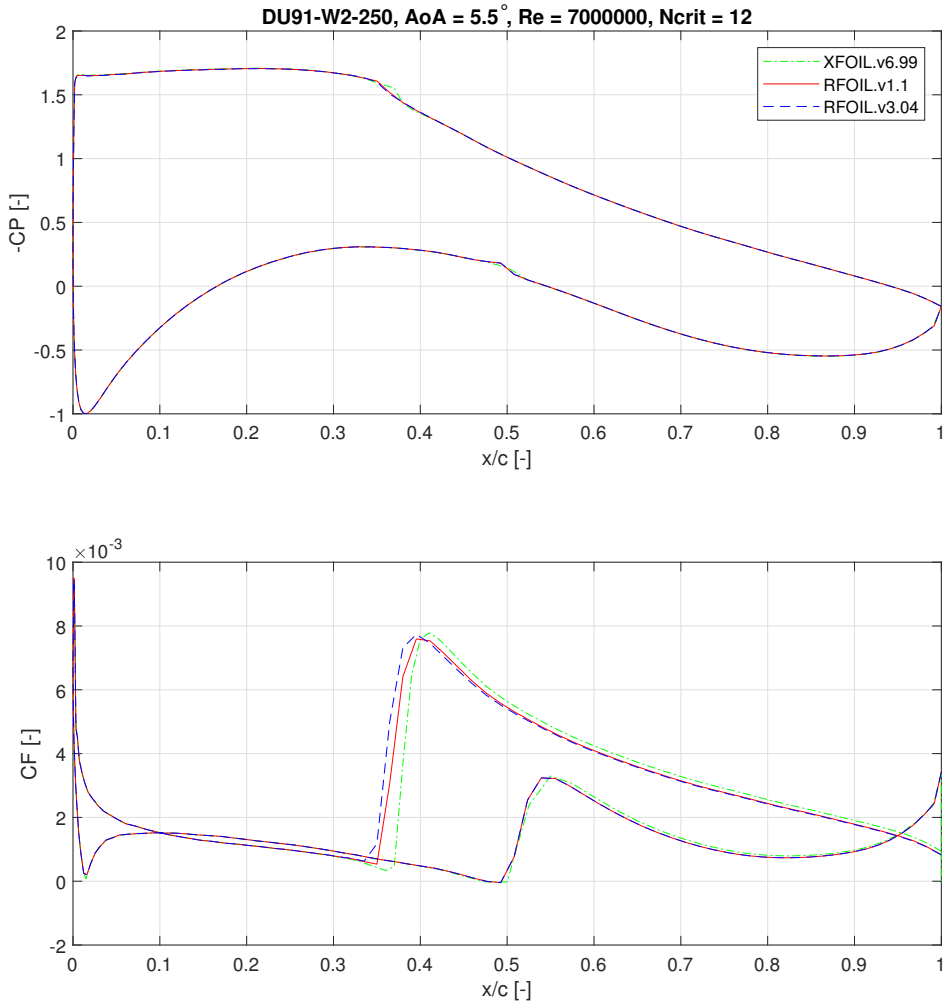

Figure B.49: Comparison between experimental and numerical polars for the DU91-W2-250 airfoil at a Reynolds number of 9900000. Simulation time to generate the polars by means the different codes and the number of converged polar points are depicted between parentheses.

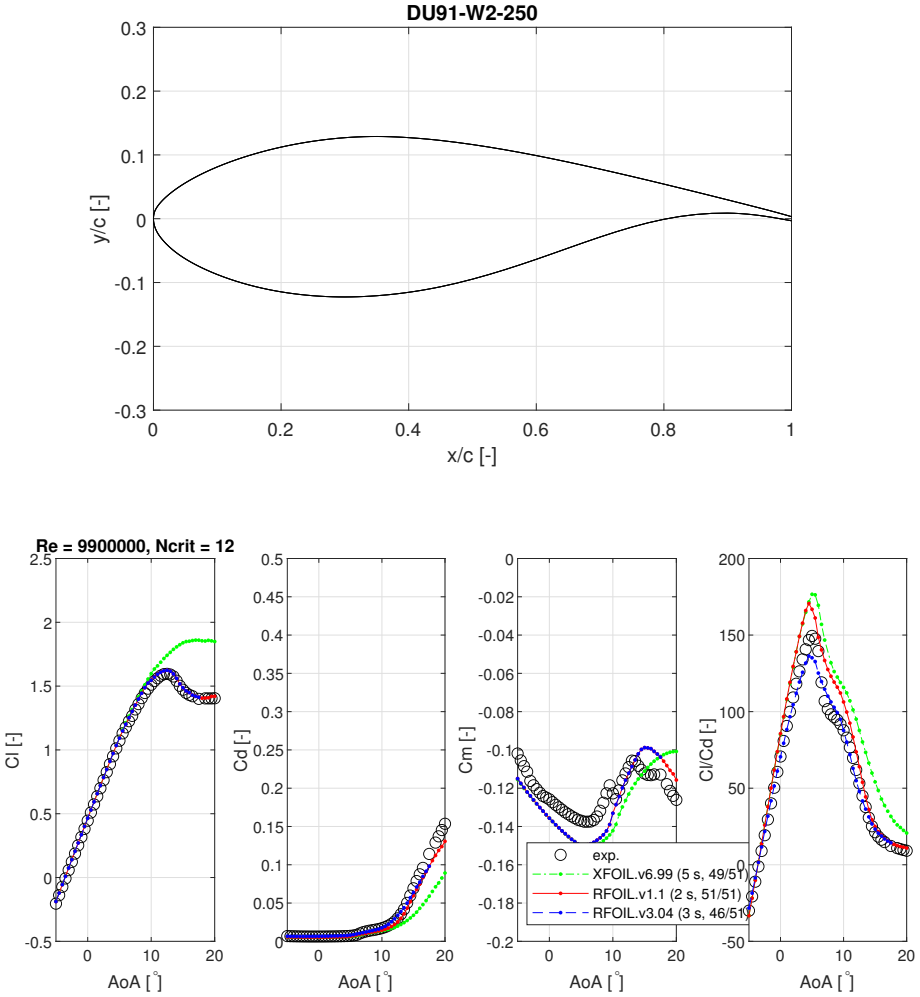

Figure B.50: Differences between experimental and numerical polars for the DU91-W2-250 airfoil at a Reynolds number of 9900000. Vertical black lines in the middle subplot indicate, from left to right, the angle of attack corresponding to the minimum drag coefficient, maximum lift to drag ratio and maximum lift coefficient, respectively.

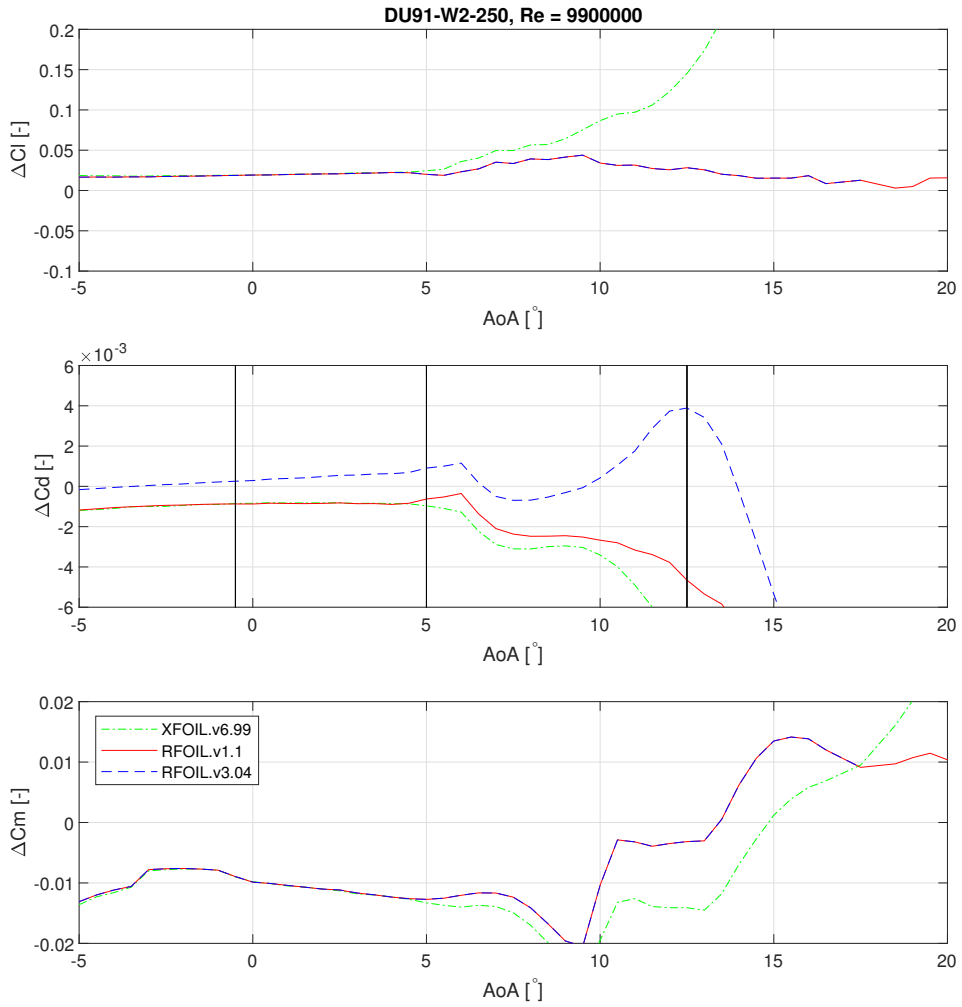

Figure B.51: Comparison between experimental and numerical pressure and skin friction distributions for the DU91-W2-250 airfoil at a Reynolds number of 9900000 and at the design angle of attack.

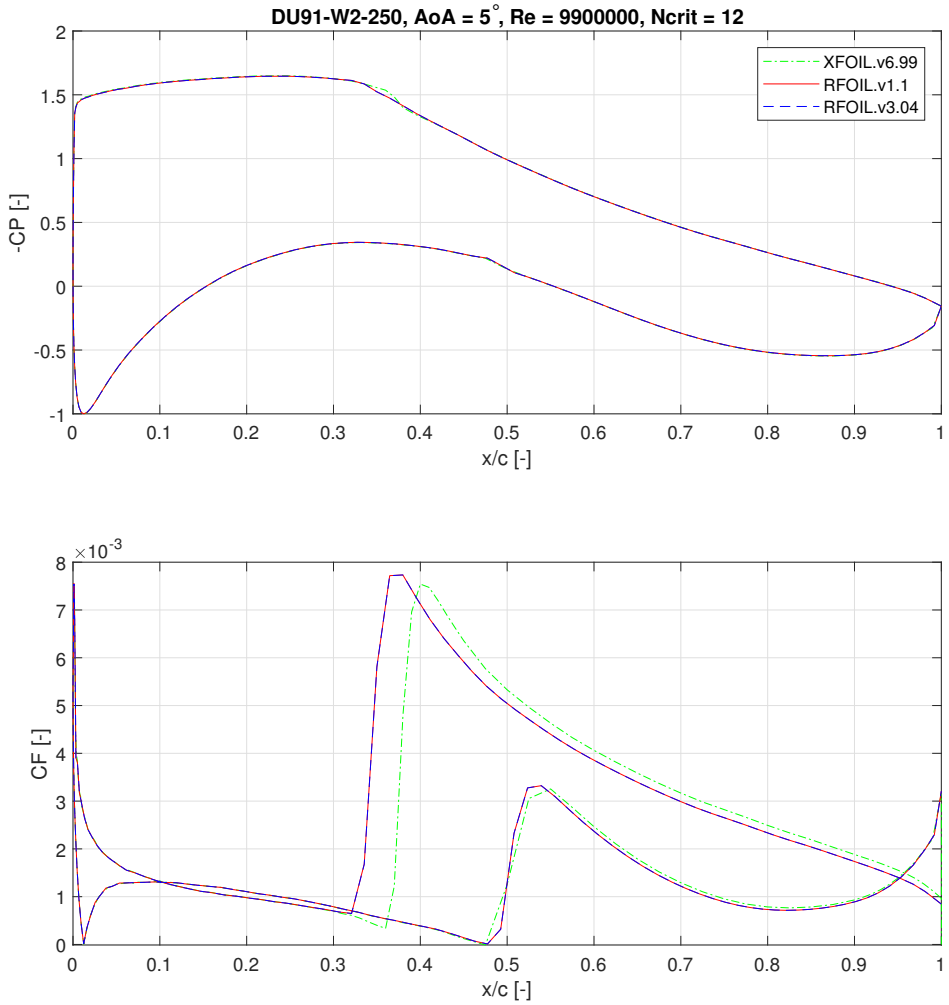

Figure B.52: Comparison between experimental and numerical polars for the DU93-W-210-S180 airfoil at a Reynolds number of 1000000. Simulation time to generate the polars by means the different codes and the number of converged polar points are depicted between parentheses.

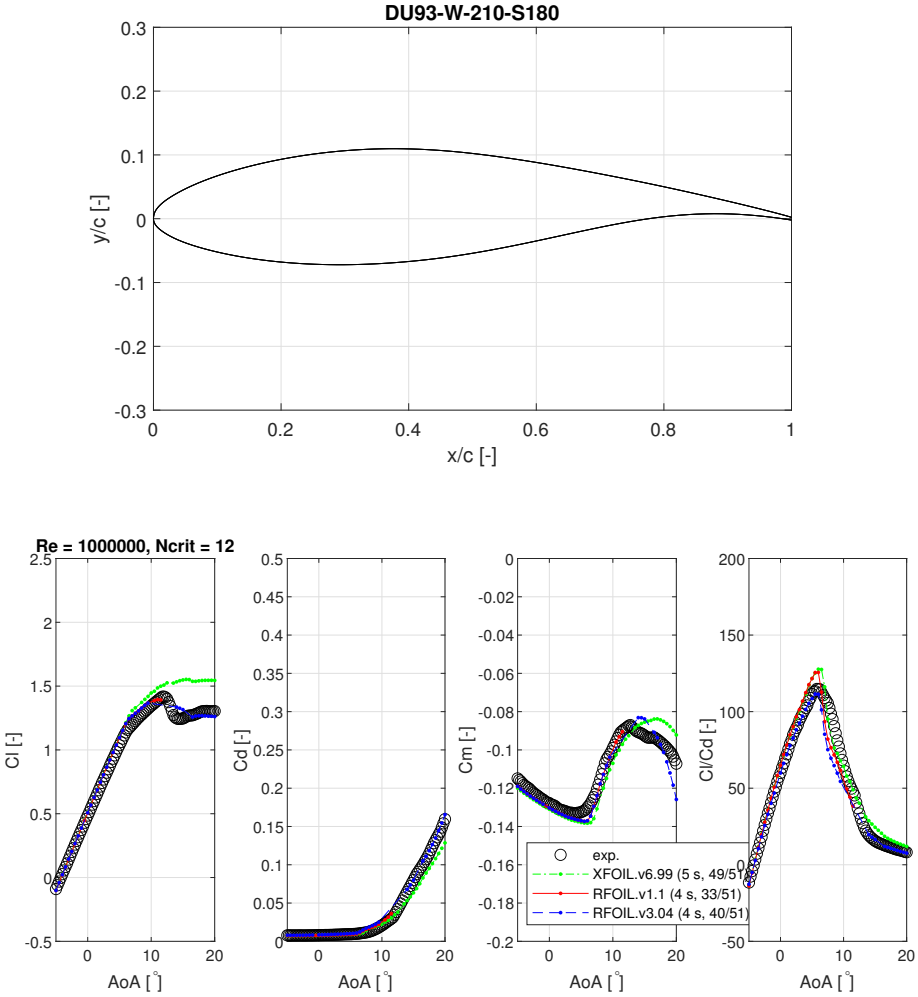

Figure B.53: Differences between experimental and numerical polars for the DU93-W-210-S180 airfoil at a Reynolds number of 1000000. Vertical black lines in the middle subplot indicate, from left to right, the angle of attack corresponding to the minimum drag coefficient, maximum lift to drag ratio and maximum lift coefficient, respectively.

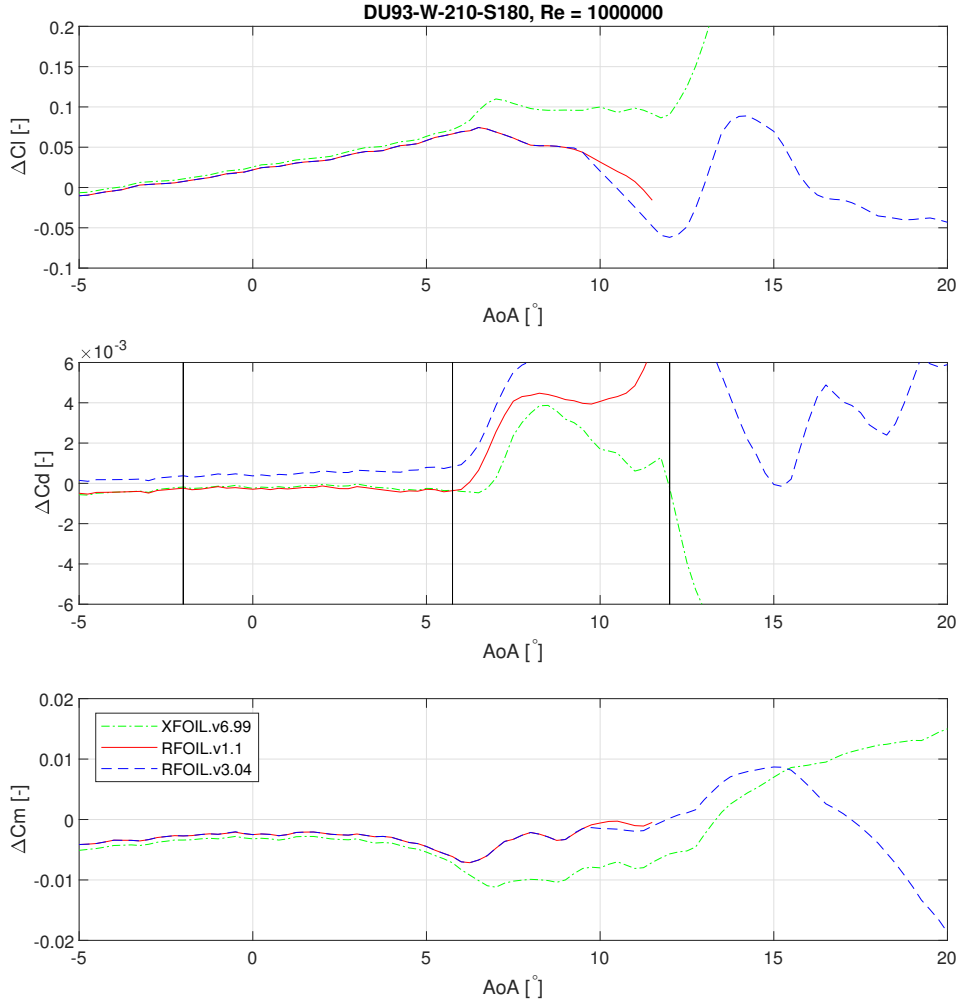

Figure B.54: Comparison between experimental and numerical pressure and skin friction distributions for the DU93-W-210-S180 airfoil at a Reynolds number of 1000000 and at the design angle of attack.

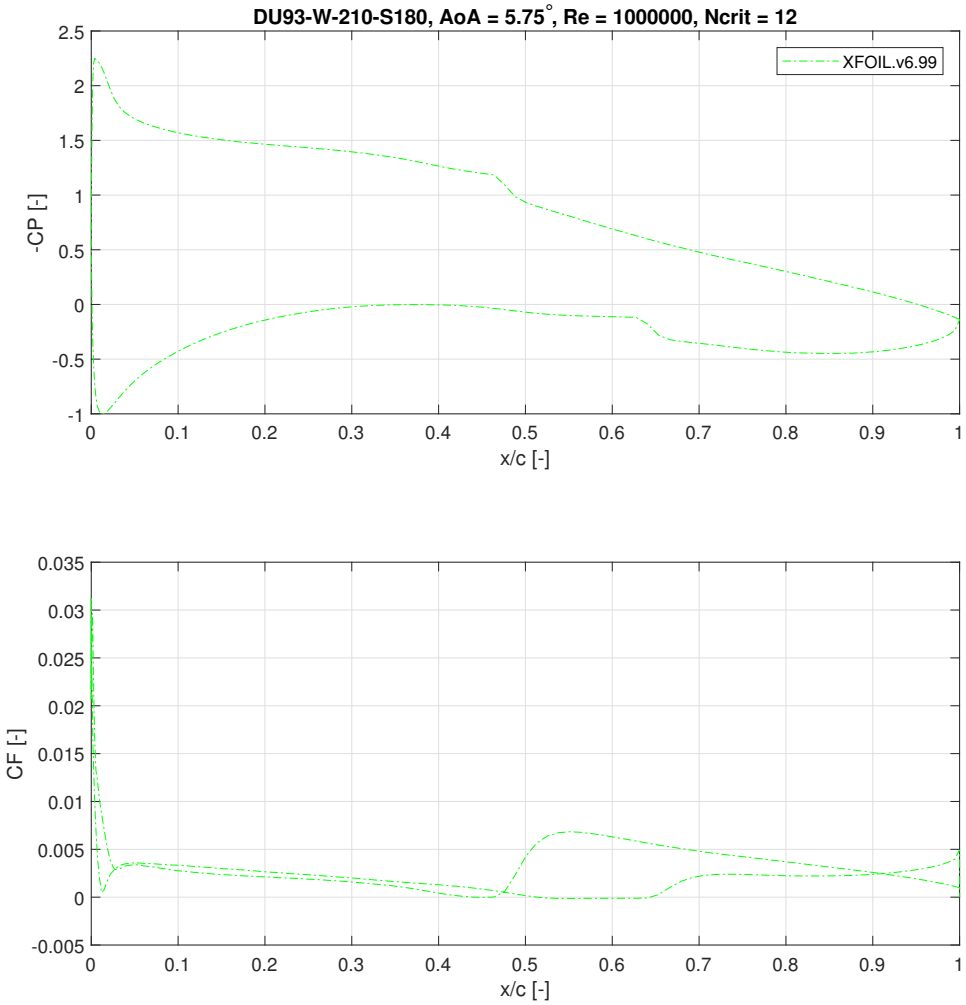

Figure B.55: Comparison between experimental and numerical polars for the DU93-W-210-S180 airfoil at a Reynolds number of 1500000. Simulation time to generate the polars by means the different codes and the number of converged polar points are depicted between parentheses.

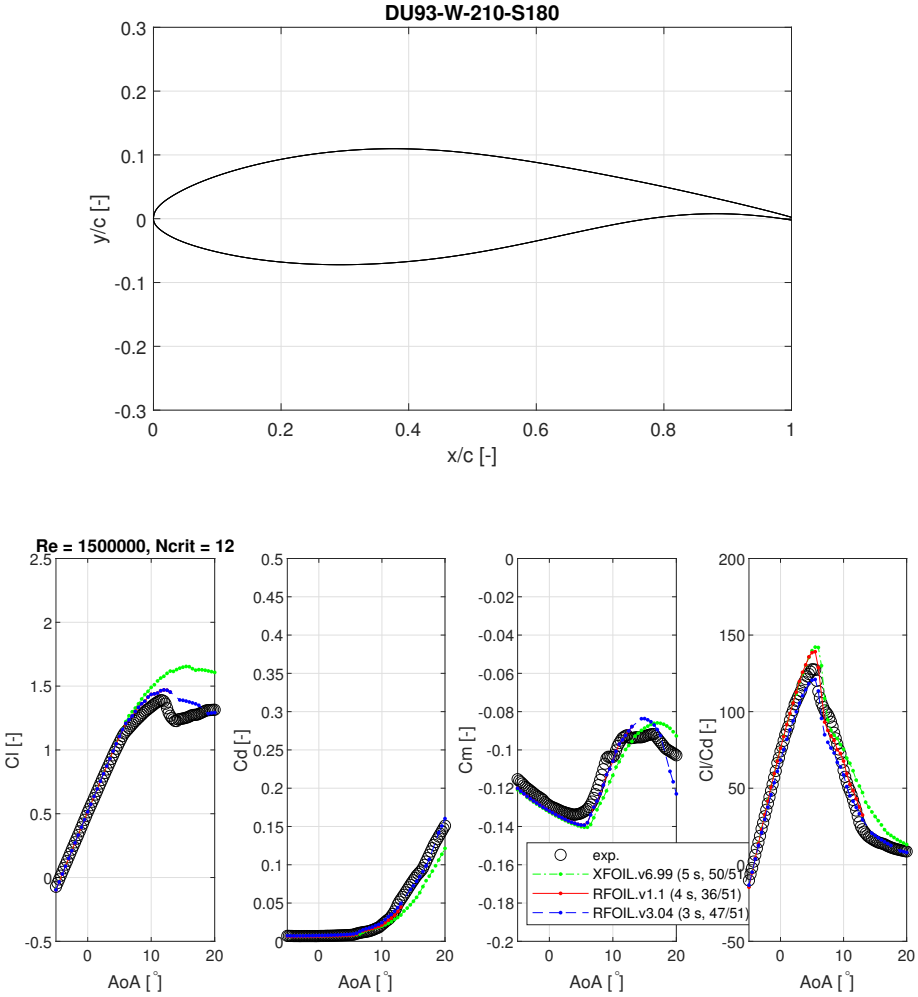

Figure B.56: Differences between experimental and numerical polars for the DU93-W-210-S180 airfoil at a Reynolds number of 1500000. Vertical black lines in the middle subplot indicate, from left to right, the angle of attack corresponding to the minimum drag coefficient, maximum lift to drag ratio and maximum lift coefficient, respectively.

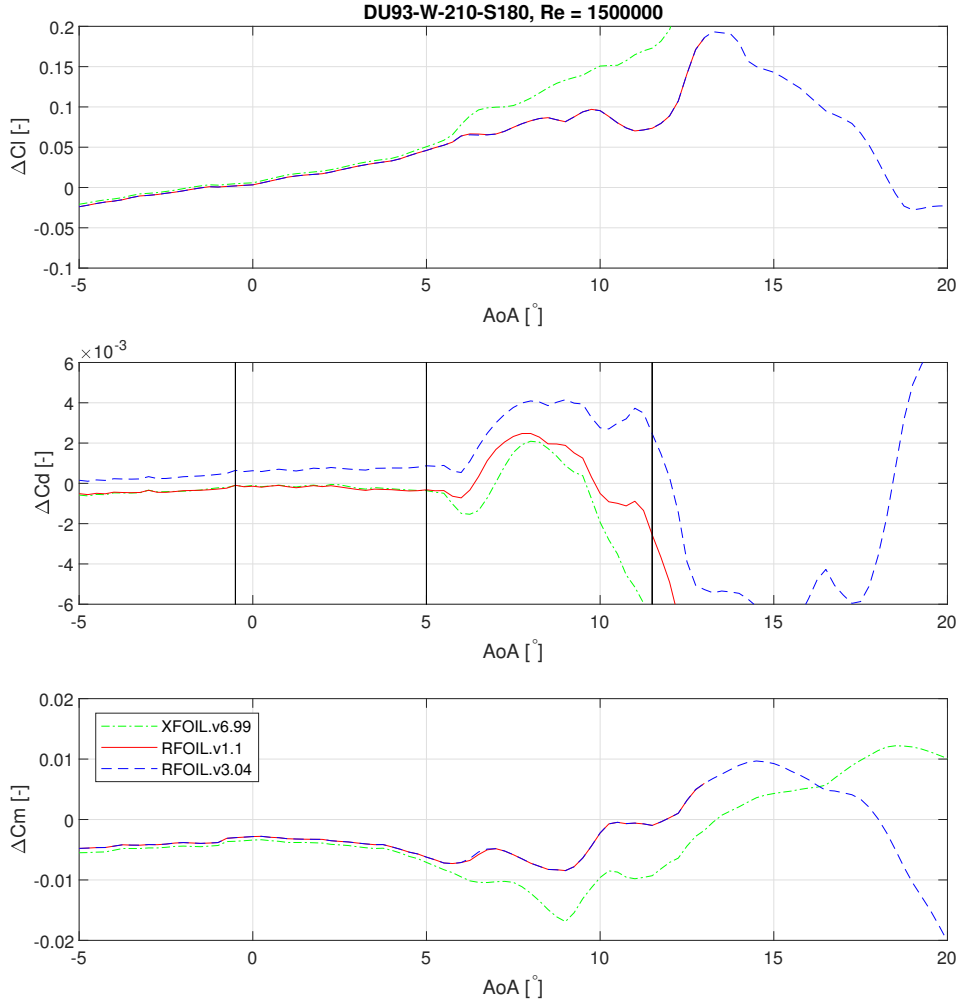

Figure B.57: Comparison between experimental and numerical pressure and skin friction distributions for the DU93-W-210-S180 airfoil at a Reynolds number of 1500000 and at the design angle of attack.

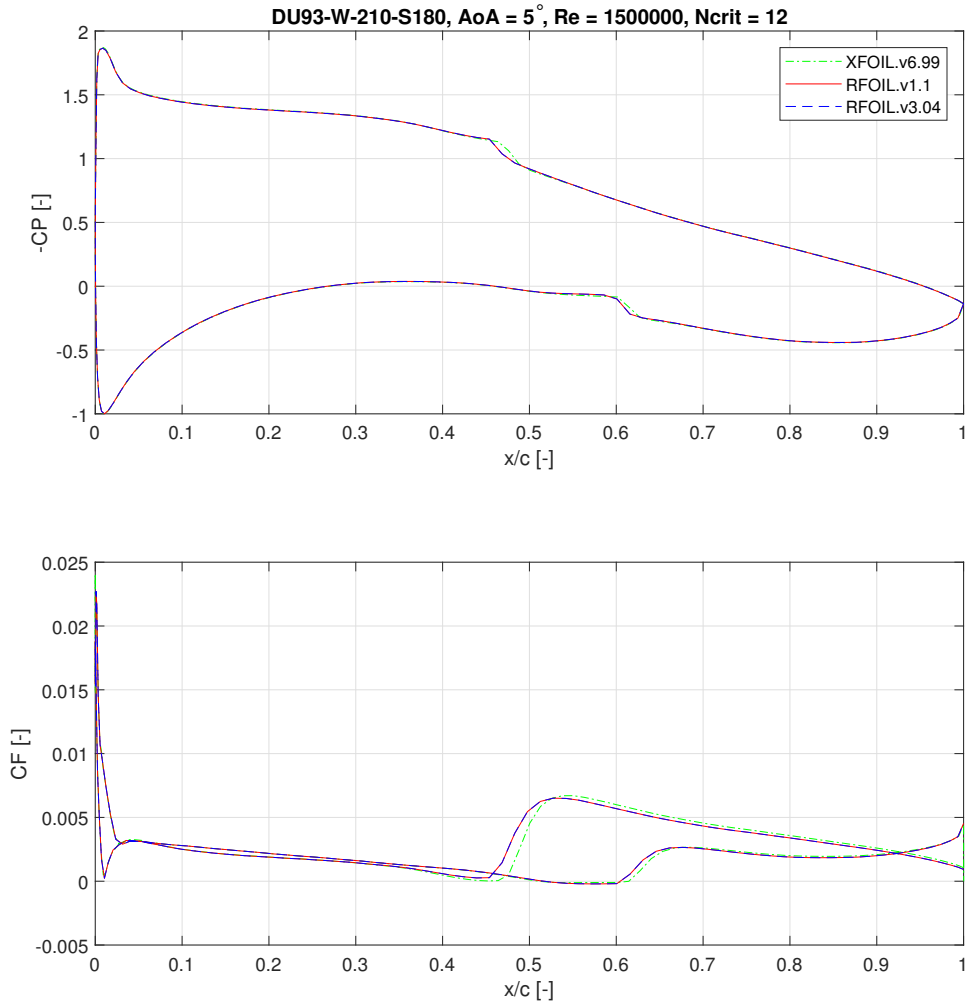

Figure B.58: Comparison between experimental and numerical polars for the DU93-W-210-S180 airfoil at a Reynolds number of 2000000. Simulation time to generate the polars by means the different codes and the number of converged polar points are depicted between parentheses.

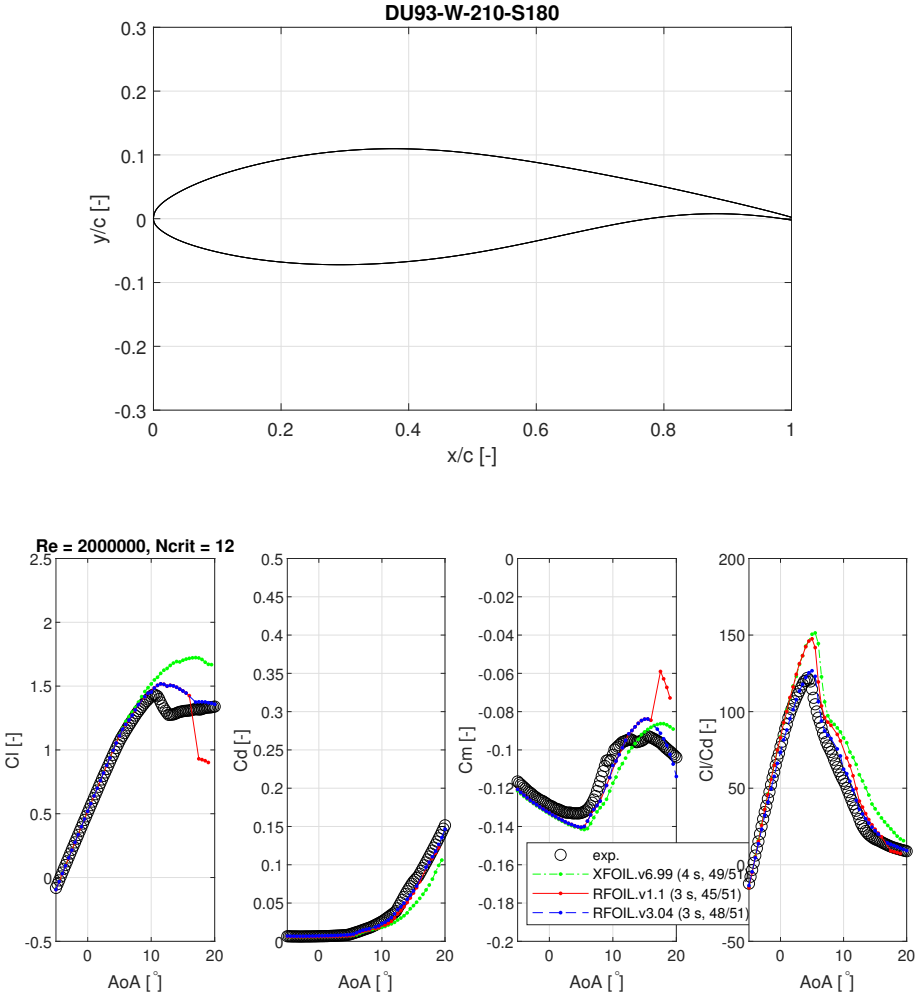

Figure B.59: Differences between experimental and numerical polars for the DU93-W-210-S180 airfoil at a Reynolds number of 2000000. Vertical black lines in the middle subplot indicate, from left to right, the angle of attack corresponding to the minimum drag coefficient, maximum lift to drag ratio and maximum lift coefficient, respectively.

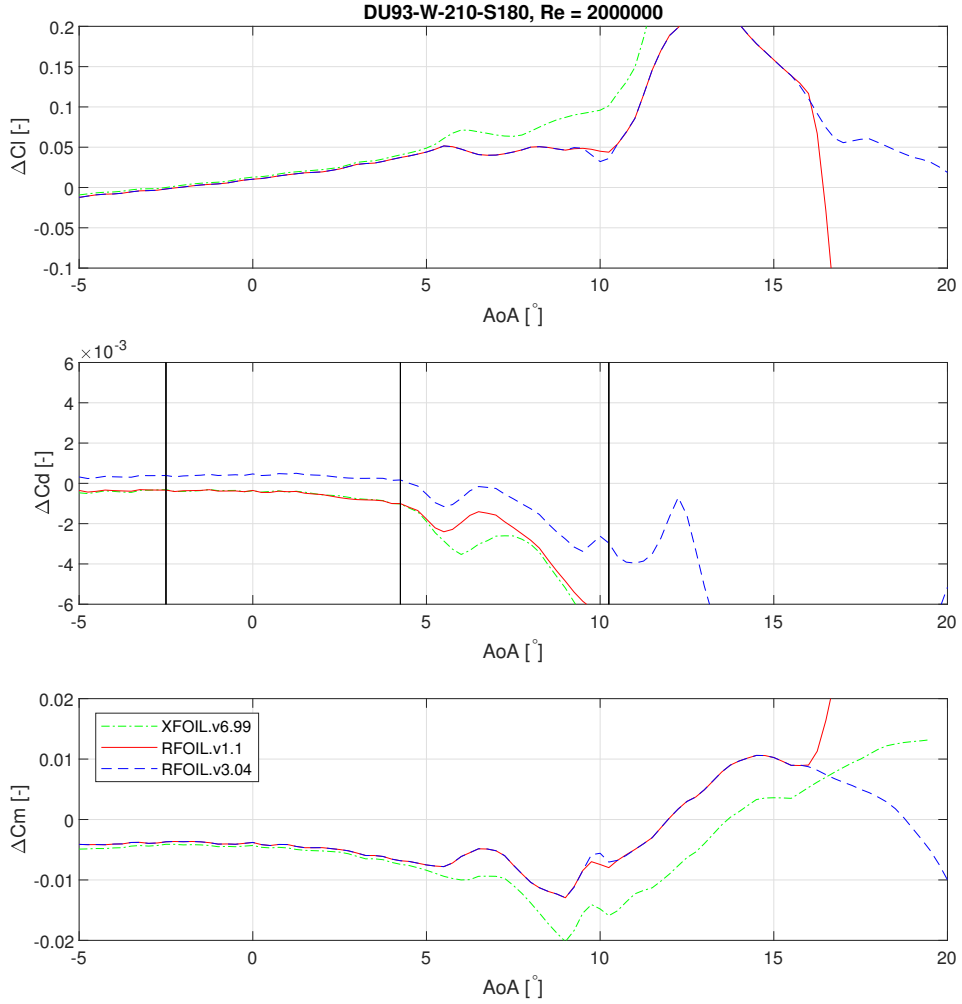

Figure B.60: Comparison between experimental and numerical pressure and skin friction distributions for the DU93-W-210-S180 airfoil at a Reynolds number of 2000000 and at the design angle of attack.

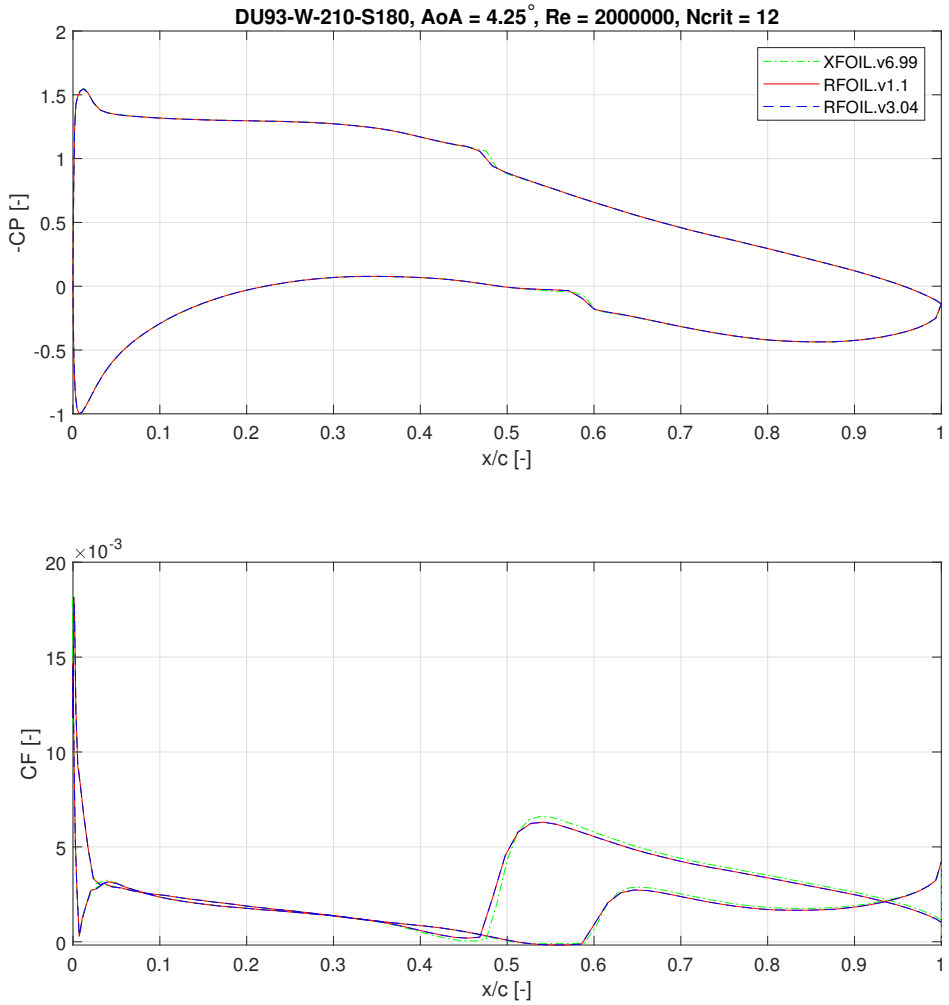

Figure B.61: Comparison between experimental and numerical polars for the DU93-W-210 airfoil at a Reynolds number of 1000000. Simulation time to generate the polars by means the different codes and the number of converged polar points are depicted between parentheses.

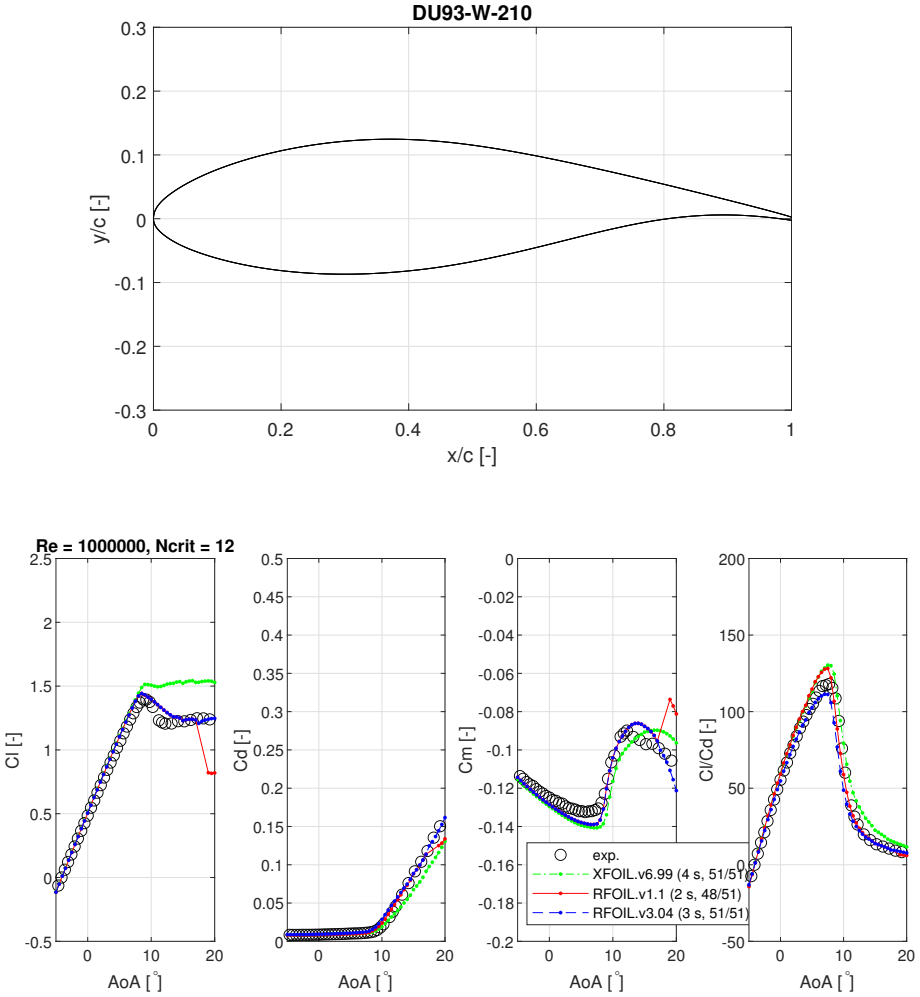

Figure B.62: Differences between experimental and numerical polars for the DU93-W-210 airfoil at a Reynolds number of 1000000. Vertical black lines in the middle subplot indicate, from left to right, the angle of attack corresponding to the minimum drag coefficient, maximum lift to drag ratio and maximum lift coefficient, respectively.

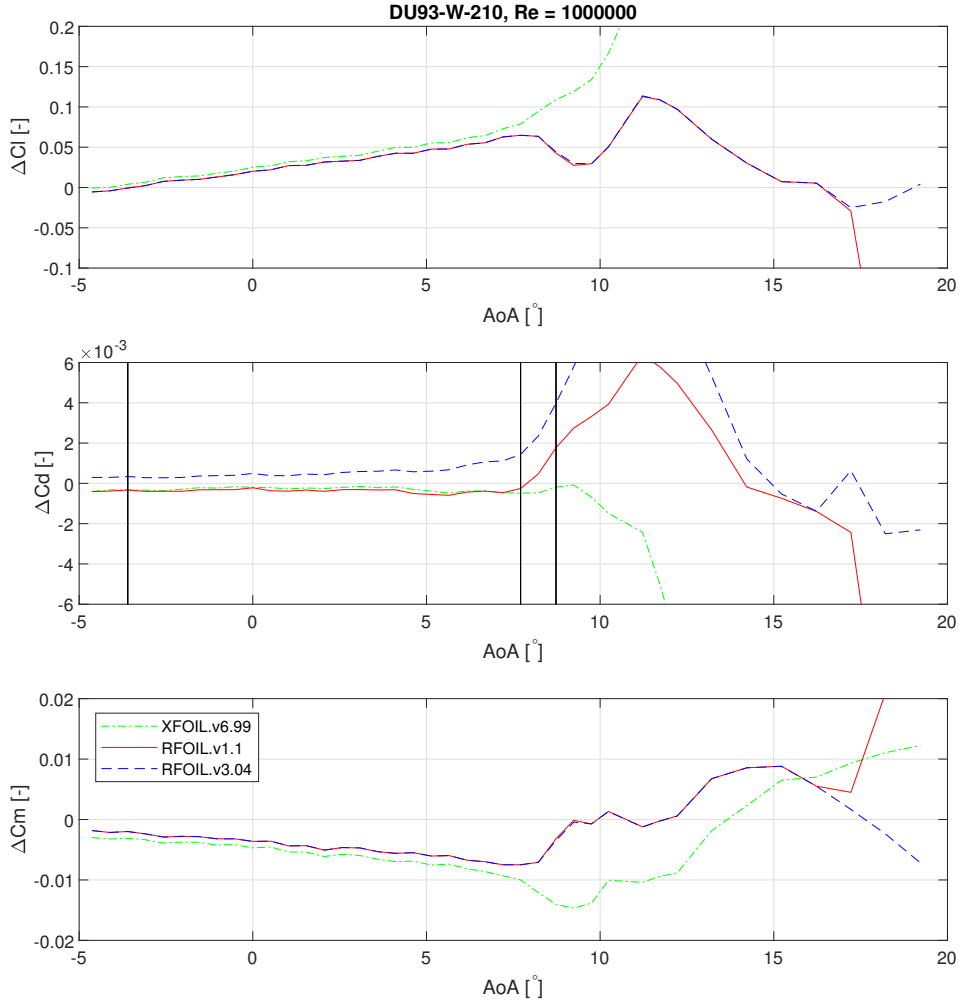

Figure B.63: Comparison between experimental and numerical pressure and skin friction distributions for the DU93-W-210 airfoil at a Reynolds number of 1000000 and at the design angle of attack.

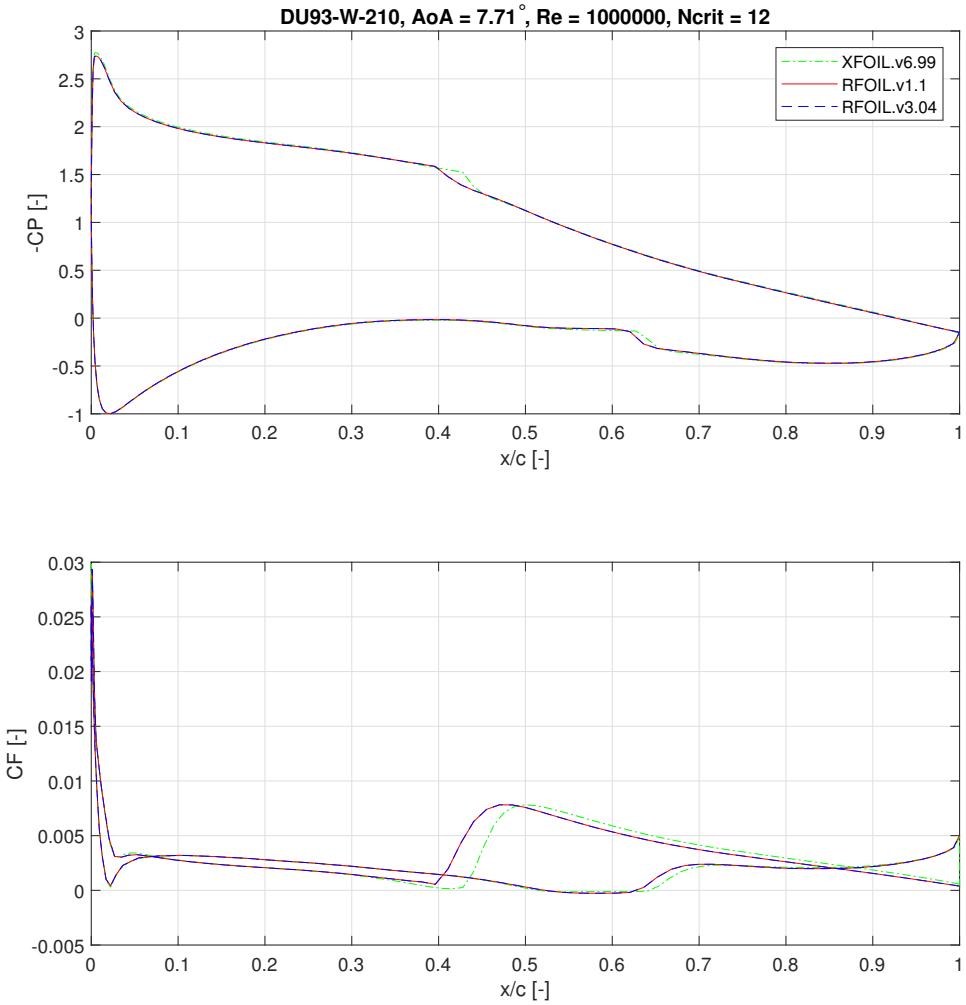

Figure B.64: Comparison between experimental and numerical polars for the DU93-W-210 airfoil at a Reynolds number of 1500000. Simulation time to generate the polars by means the different codes and the number of converged polar points are depicted between parentheses.

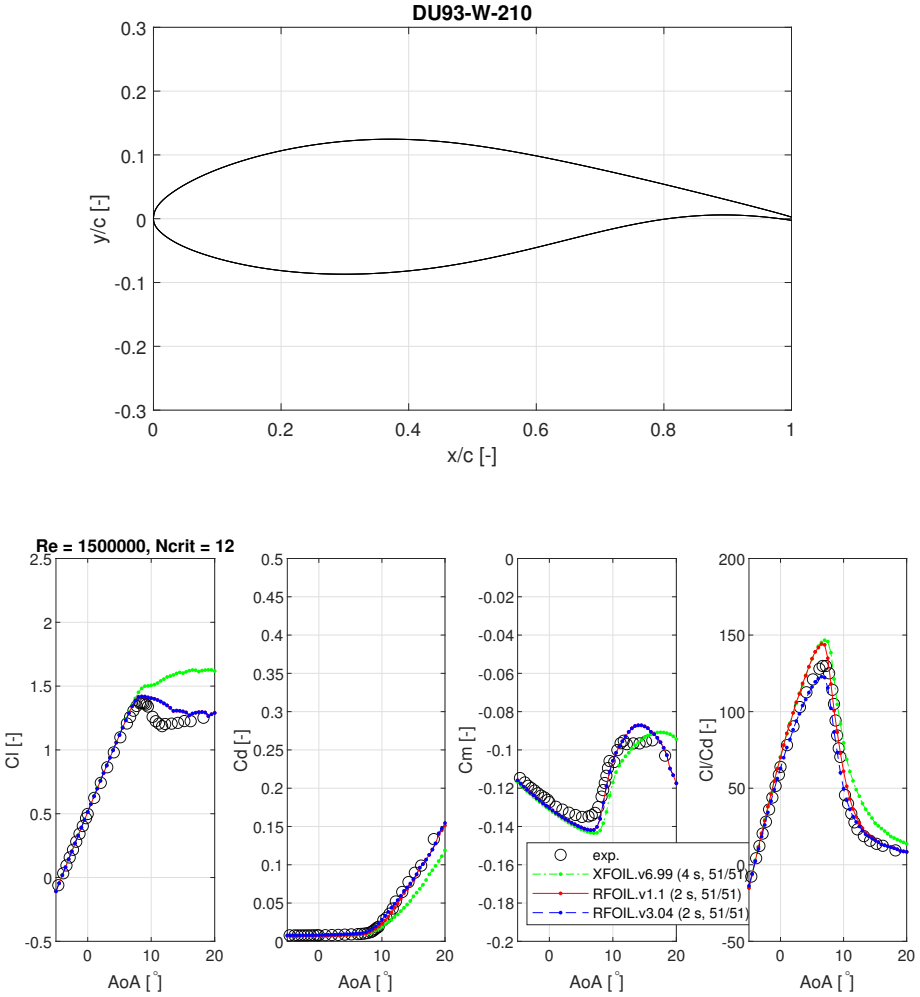

Figure B.65: Differences between experimental and numerical polars for the DU93-W-210 airfoil at a Reynolds number of 1500000. Vertical black lines in the middle subplot indicate, from left to right, the angle of attack corresponding to the minimum drag coefficient, maximum lift to drag ratio and maximum lift coefficient, respectively.

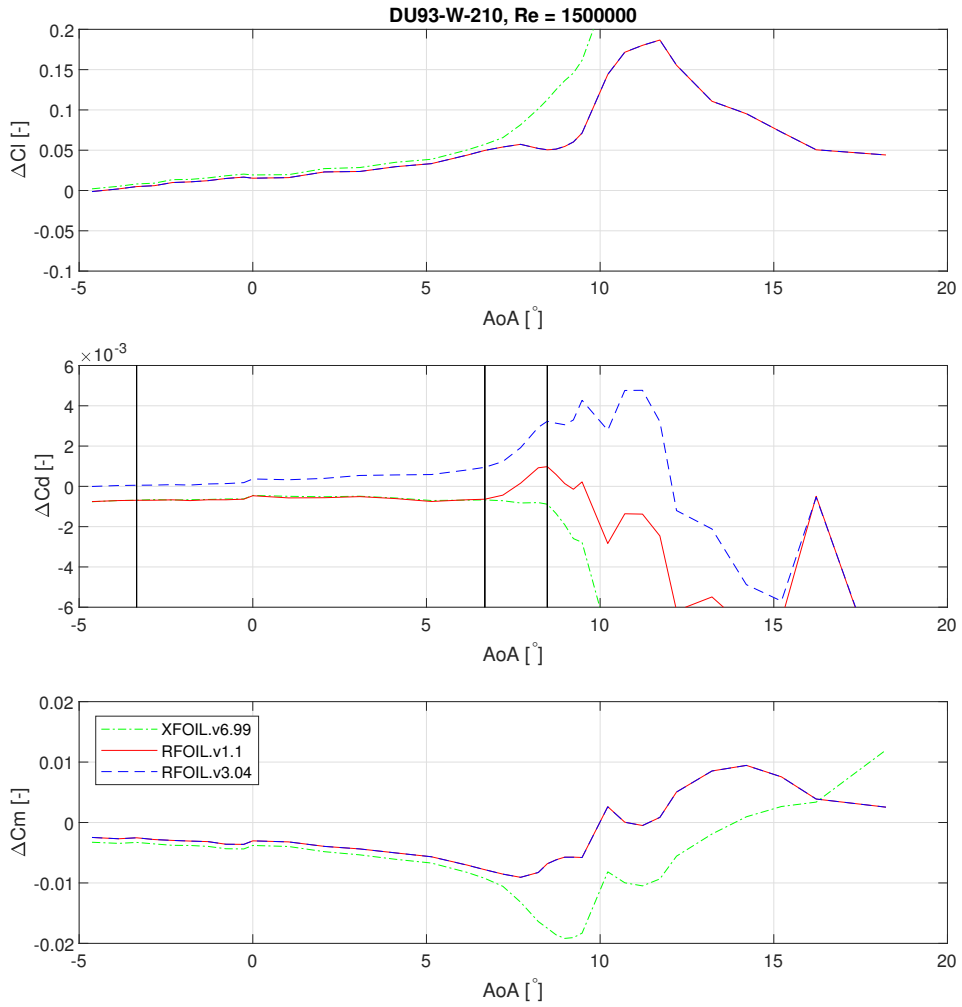

Figure B.66: Comparison between experimental and numerical pressure and skin friction distributions for the DU93-W-210 airfoil at a Reynolds number of 1500000 and at the design angle of attack.

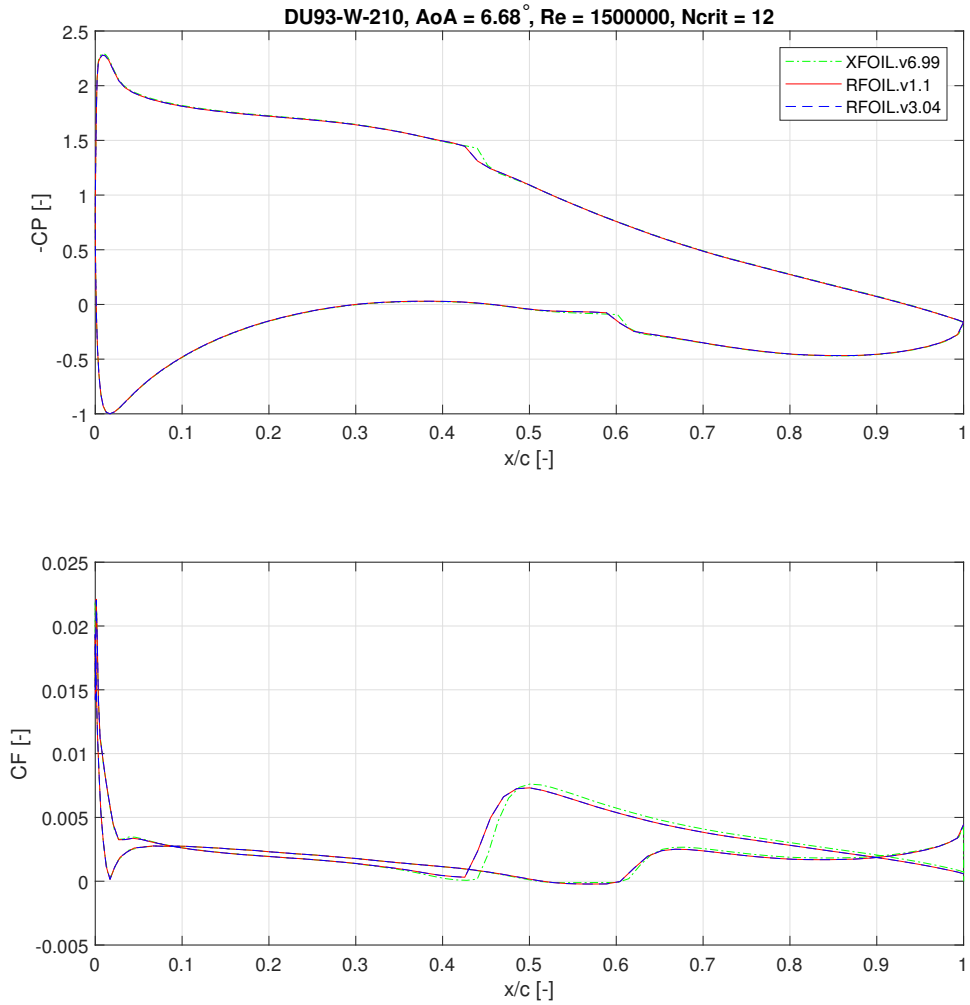

Figure B.67: Comparison between experimental and numerical polars for the DU93-W-210 airfoil at a Reynolds number of 2000000. Simulation time to generate the polars by means the different codes and the number of converged polar points are depicted between parentheses.

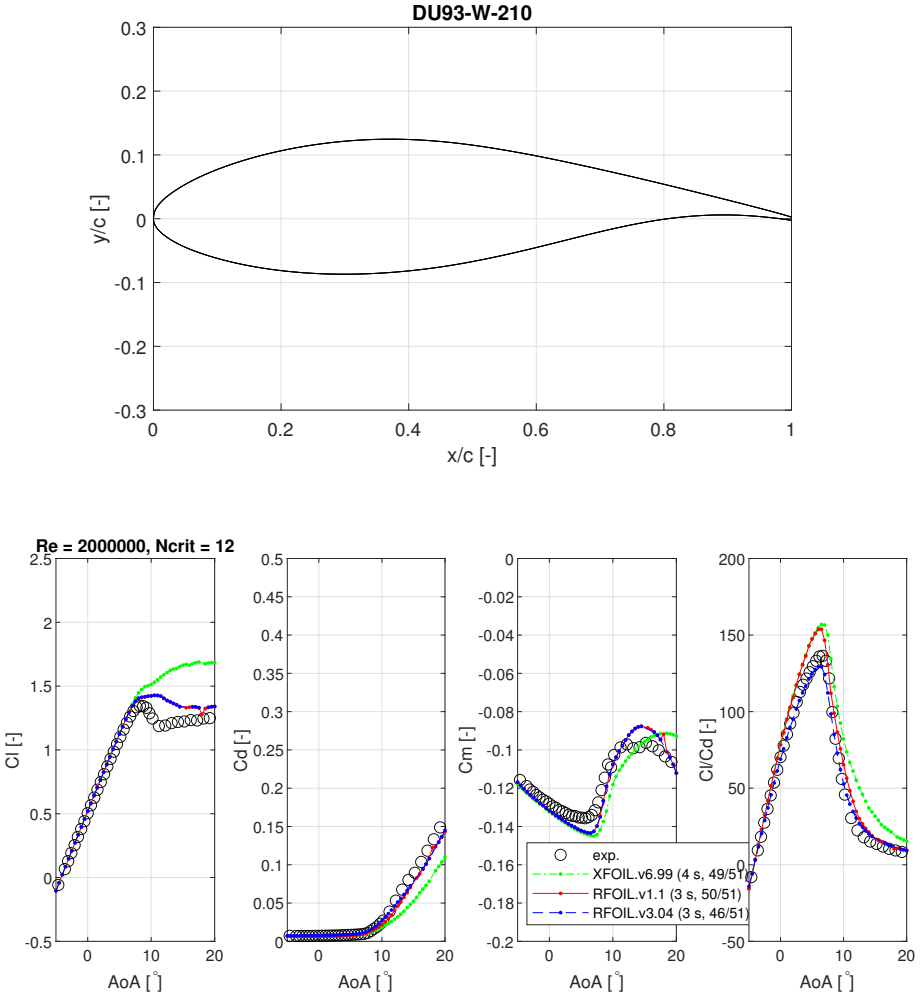

Figure B.68: Differences between experimental and numerical polars for the DU93-W-210 airfoil at a Reynolds number of 2000000. Vertical black lines in the middle subplot indicate, from left to right, the angle of attack corresponding to the minimum drag coefficient, maximum lift to drag ratio and maximum lift coefficient, respectively.

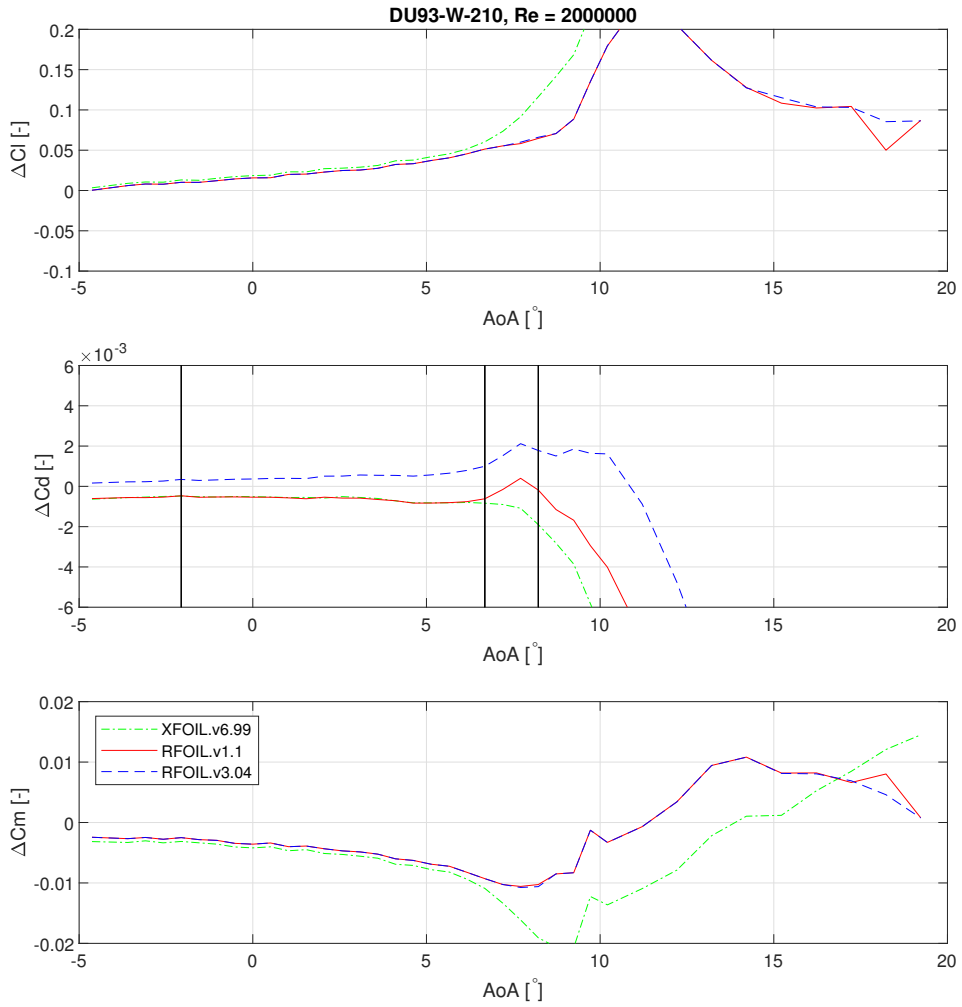

Figure B.69: Comparison between experimental and numerical pressure and skin friction distributions for the DU93-W-210 airfoil at a Reynolds number of 2000000 and at the design angle of attack.

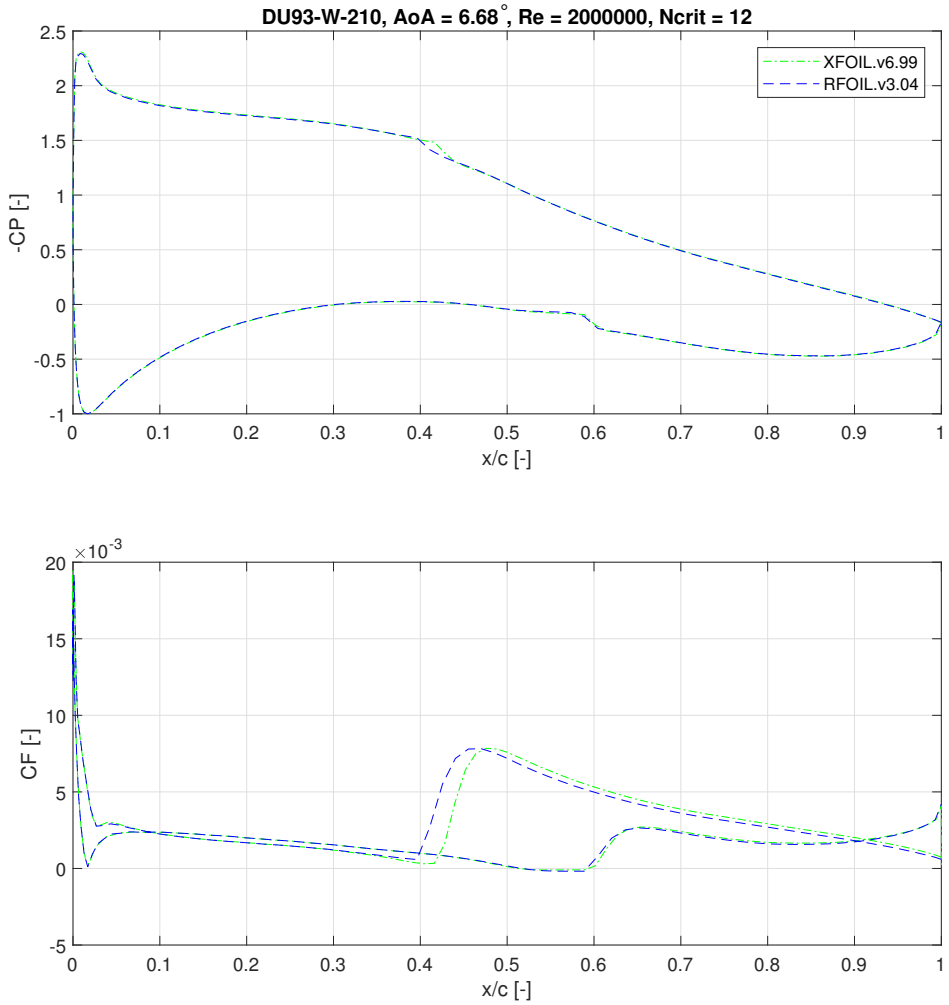

Figure B.70: Comparison between experimental and numerical polars for the DU93-W-210 airfoil at a Reynolds number of 3000000. Simulation time to generate the polars by means the different codes and the number of converged polar points are depicted between parentheses.

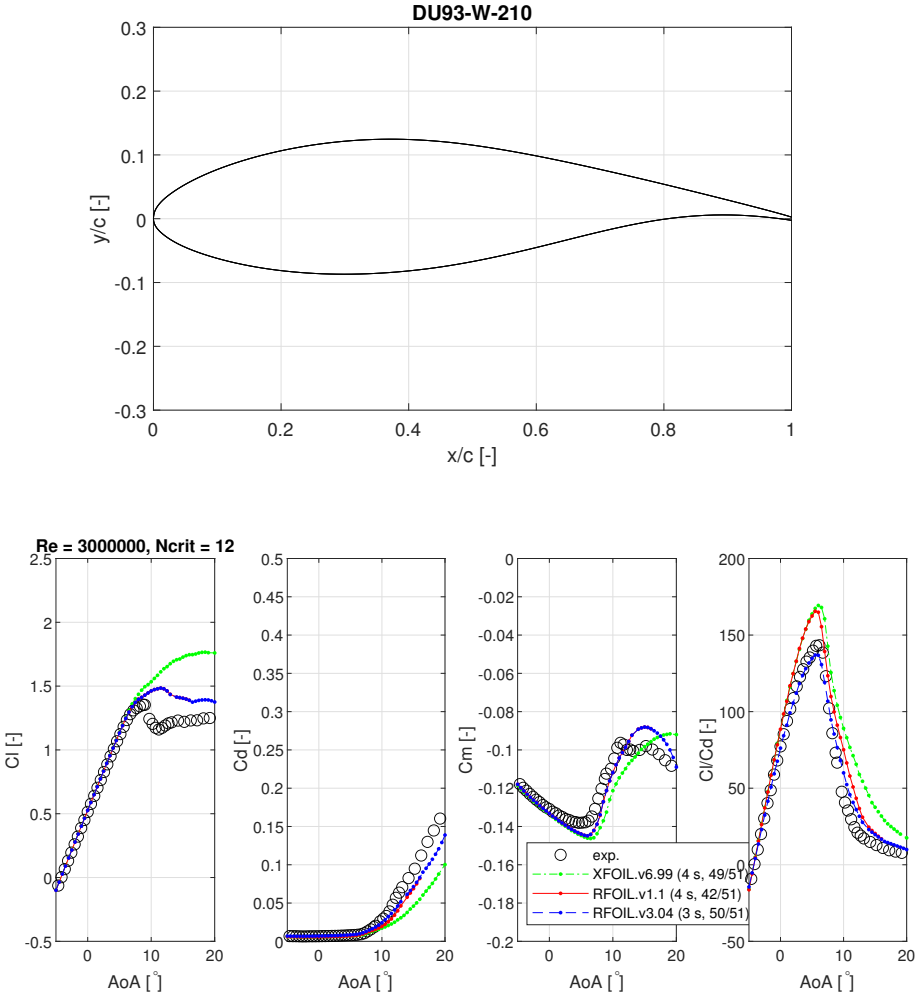

Figure B.71: Differences between experimental and numerical polars for the DU93-W-210 airfoil at a Reynolds number of 3000000. Vertical black lines in the middle subplot indicate, from left to right, the angle of attack corresponding to the minimum drag coefficient, maximum lift to drag ratio and maximum lift coefficient, respectively.

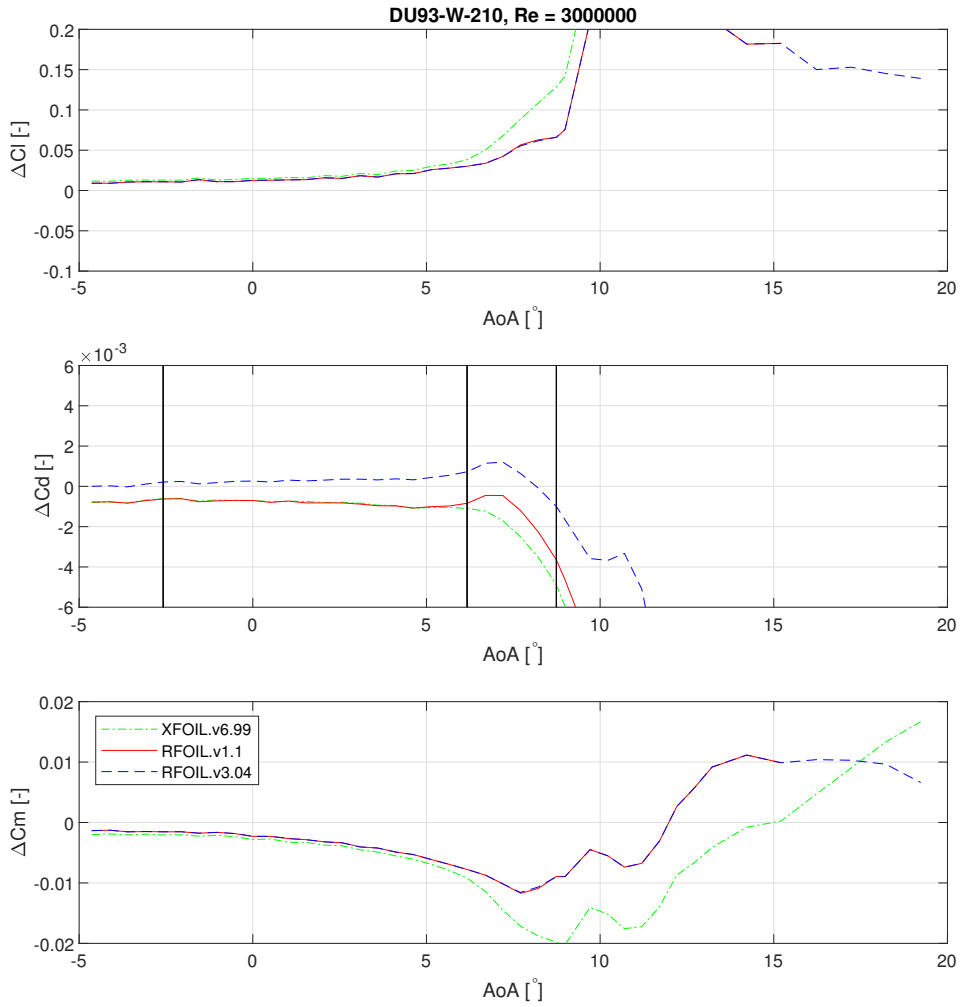

Figure B.72: Comparison between experimental and numerical pressure and skin friction distributions for the DU93-W-210 airfoil at a Reynolds number of 3000000 and at the design angle of attack.

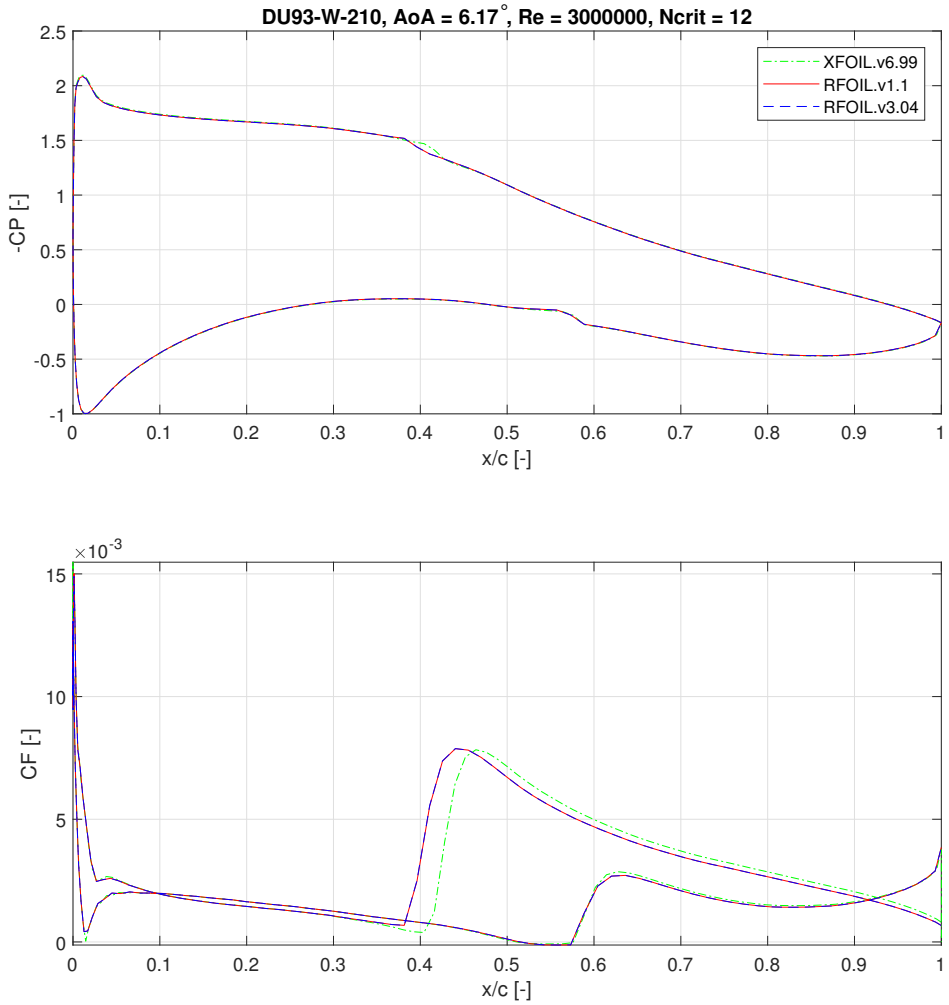

Figure B.73: Comparison between experimental and numerical polars for the DU95-W-180-S150 airfoil at a Reynolds number of 1000000. Simulation time to generate the polars by means the different codes and the number of converged polar points are depicted between parentheses.

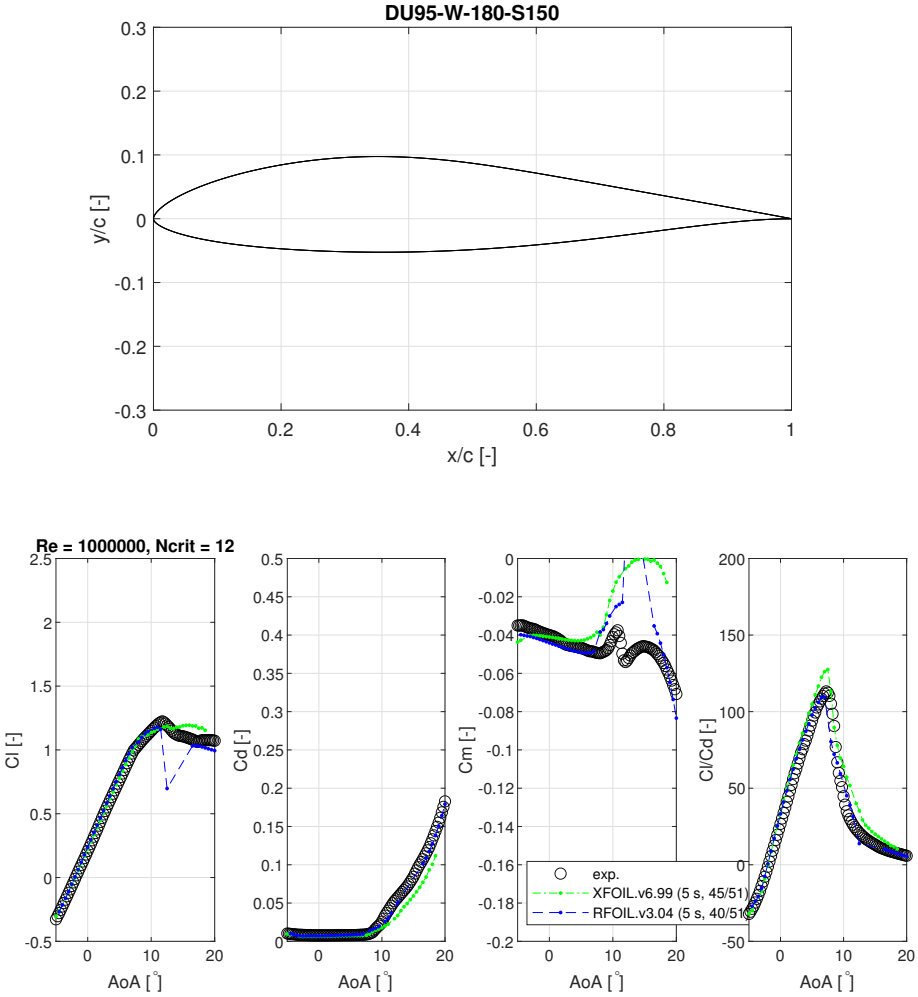

Figure B.74: Differences between experimental and numerical polars for the DU95-W-180-S150 airfoil at a Reynolds number of 1000000. Vertical black lines in the middle subplot indicate, from left to right, the angle of attack corresponding to the minimum drag coefficient, maximum lift to drag ratio and maximum lift coefficient, respectively.

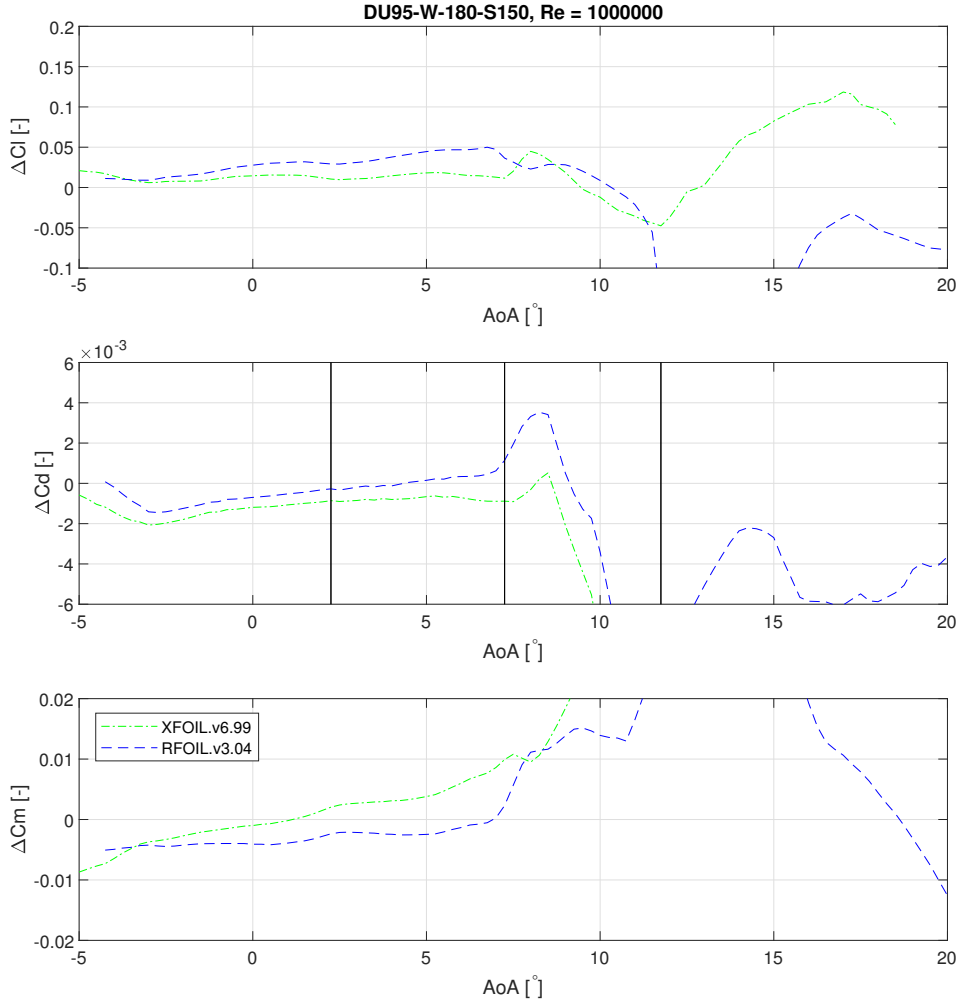

Figure B.75: Comparison between experimental and numerical pressure and skin friction distributions for the DU95-W-180-S150 airfoil at a Reynolds number of 1000000 and at the design angle of attack.

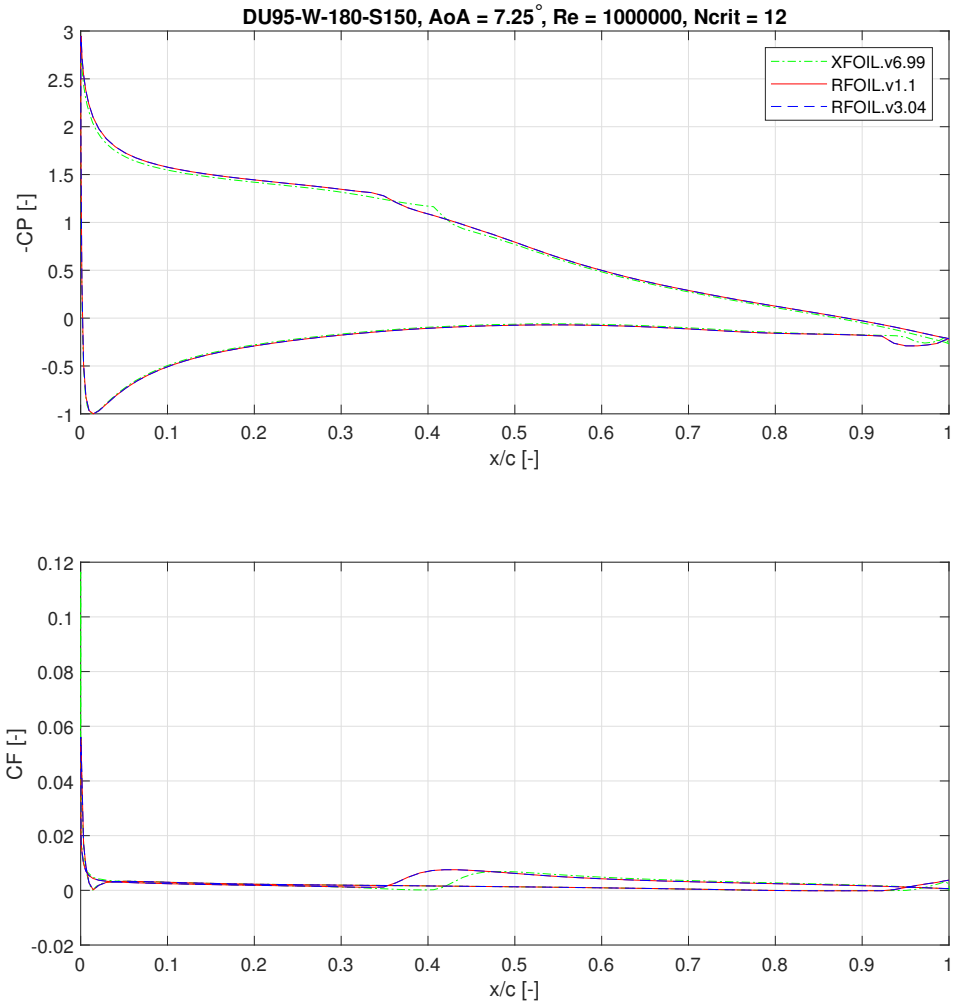

Figure B.76: Comparison between experimental and numerical polars for the DU95-W-180-S150 airfoil at a Reynolds number of 2000000. Simulation time to generate the polars by means the different codes and the number of converged polar points are depicted between parentheses.

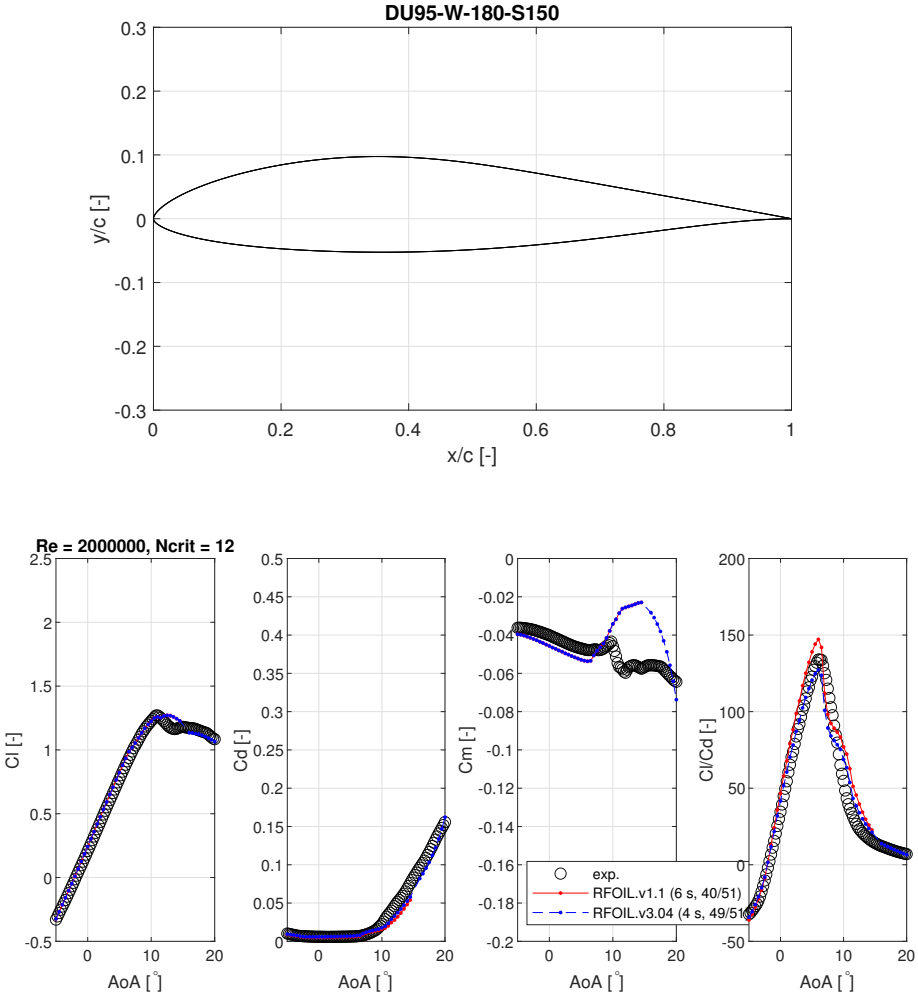

Figure B.77: Differences between experimental and numerical polars for the DU95-W-180-S150 airfoil at a Reynolds number of 2000000. Vertical black lines in the middle subplot indicate, from left to right, the angle of attack corresponding to the minimum drag coefficient, maximum lift to drag ratio and maximum lift coefficient, respectively.

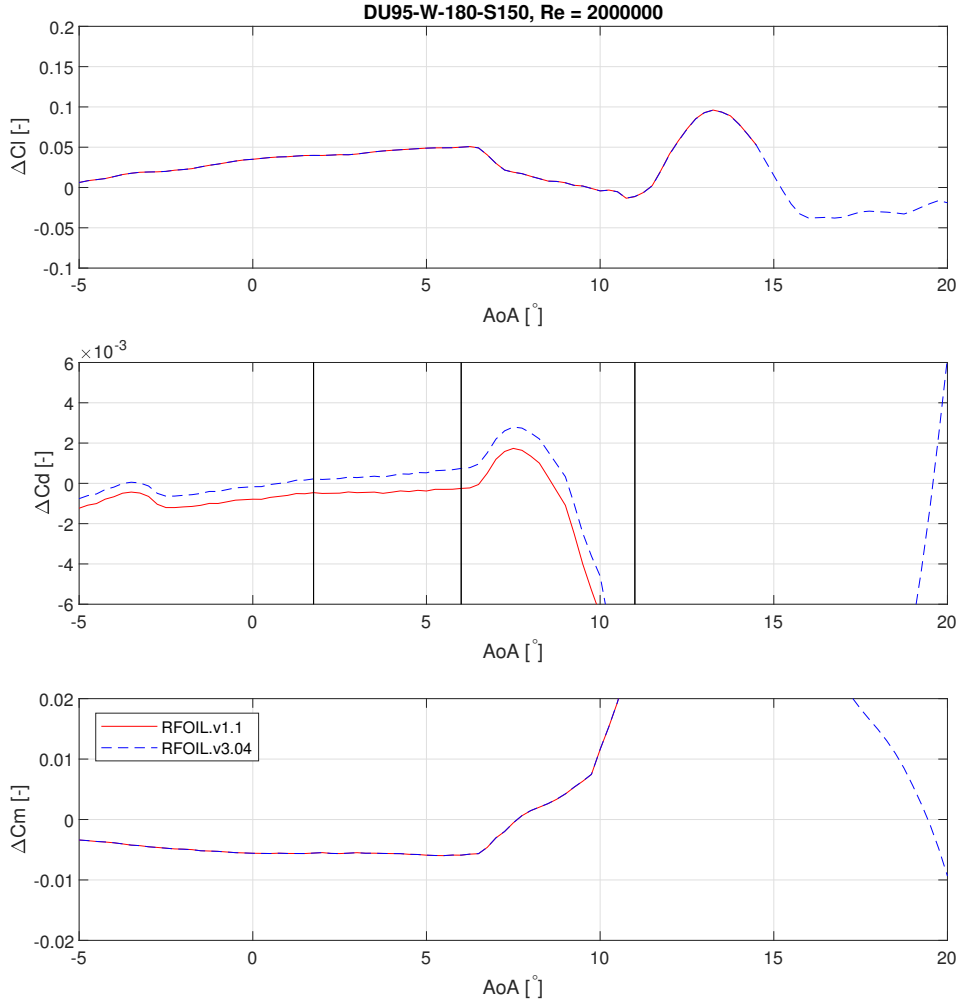

Figure B.78: Comparison between experimental and numerical pressure and skin friction distributions for the DU95-W-180-S150 airfoil at a Reynolds number of 2000000 and at the design angle of attack.

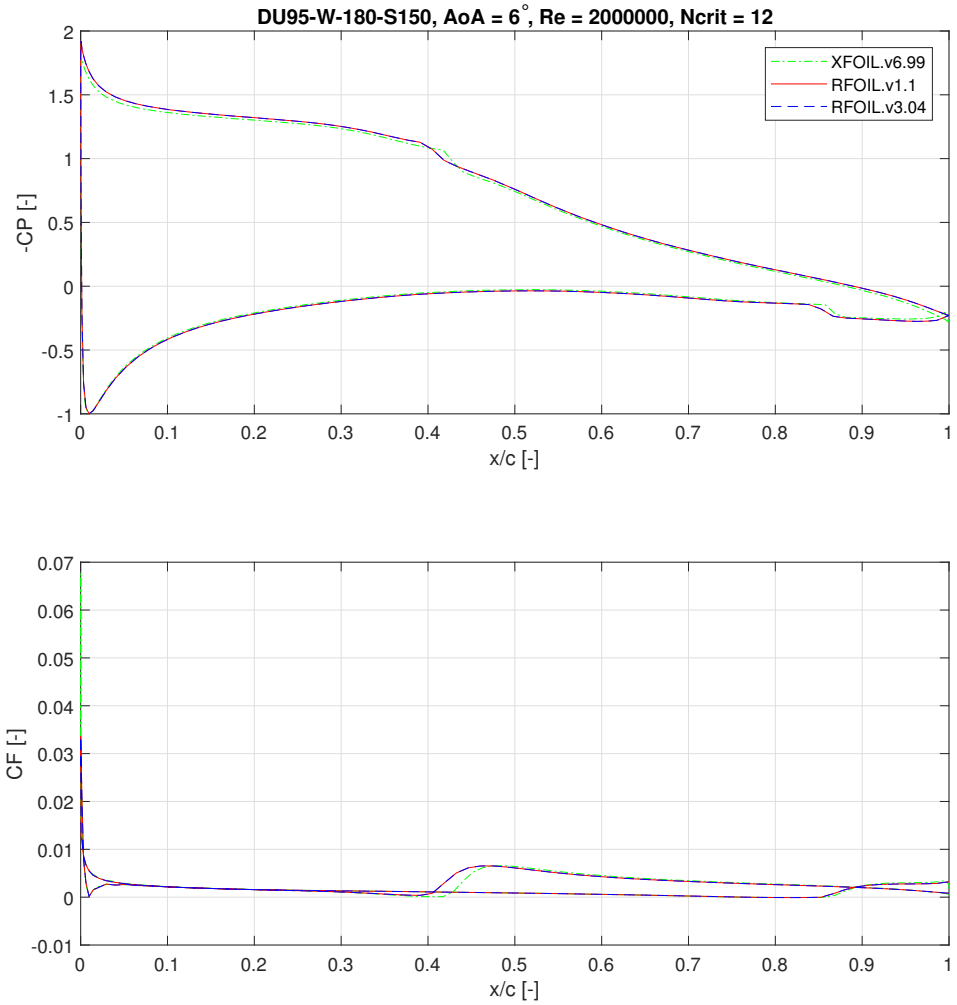

Figure B.79: Comparison between experimental and numerical polars for the DU95-W-180-S150 airfoil at a Reynolds number of 3000000. Simulation time to generate the polars by means the different codes and the number of converged polar points are depicted between parentheses.

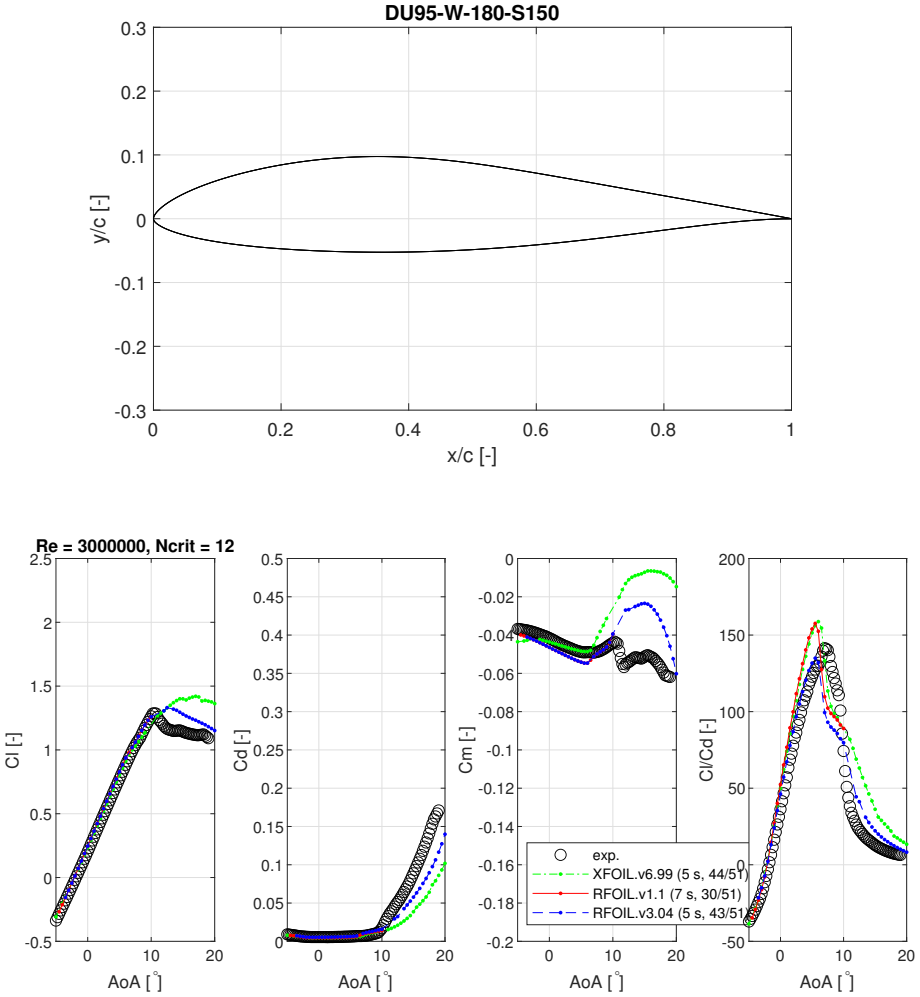

Figure B.80: Differences between experimental and numerical polars for the DU95-W-180-S150 airfoil at a Reynolds number of 3000000. Vertical black lines in the middle subplot indicate, from left to right, the angle of attack corresponding to the minimum drag coefficient, maximum lift to drag ratio and maximum lift coefficient, respectively.

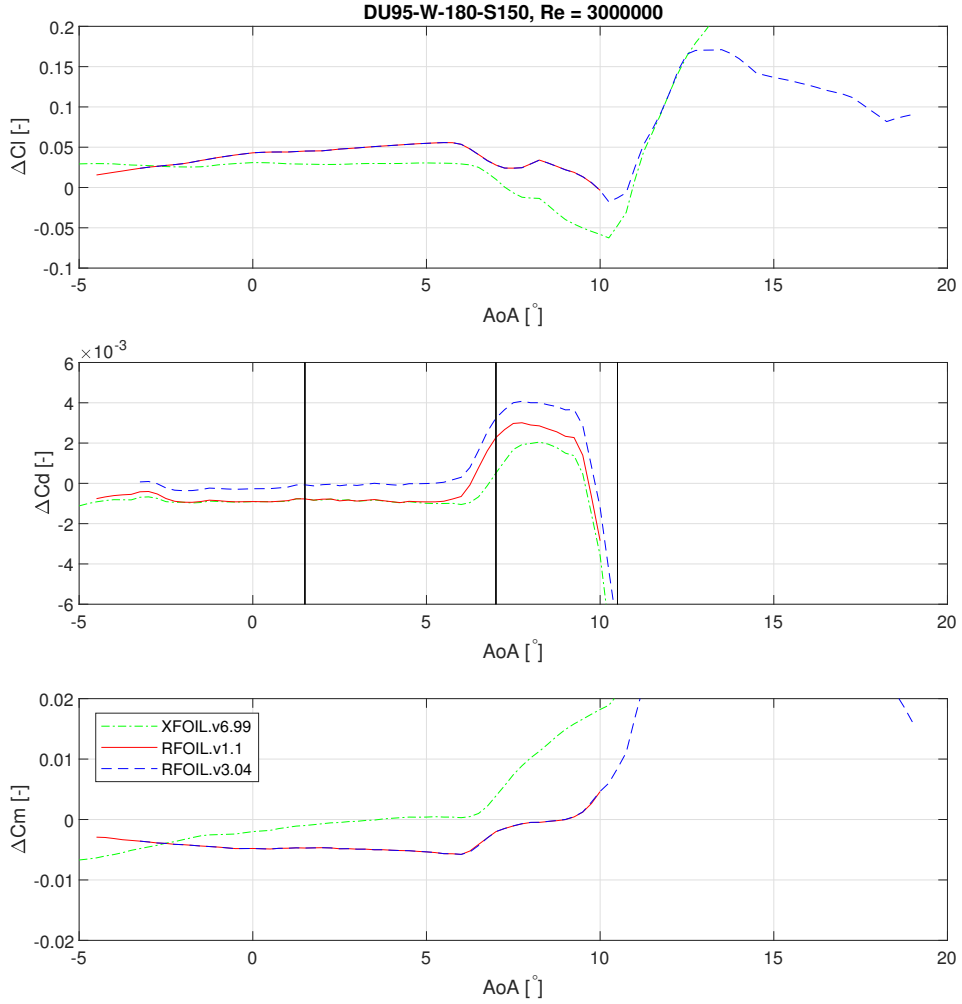

Figure B.81: Comparison between experimental and numerical pressure and skin friction distributions for the DU95-W-180-S150 airfoil at a Reynolds number of 3000000 and at the design angle of attack.

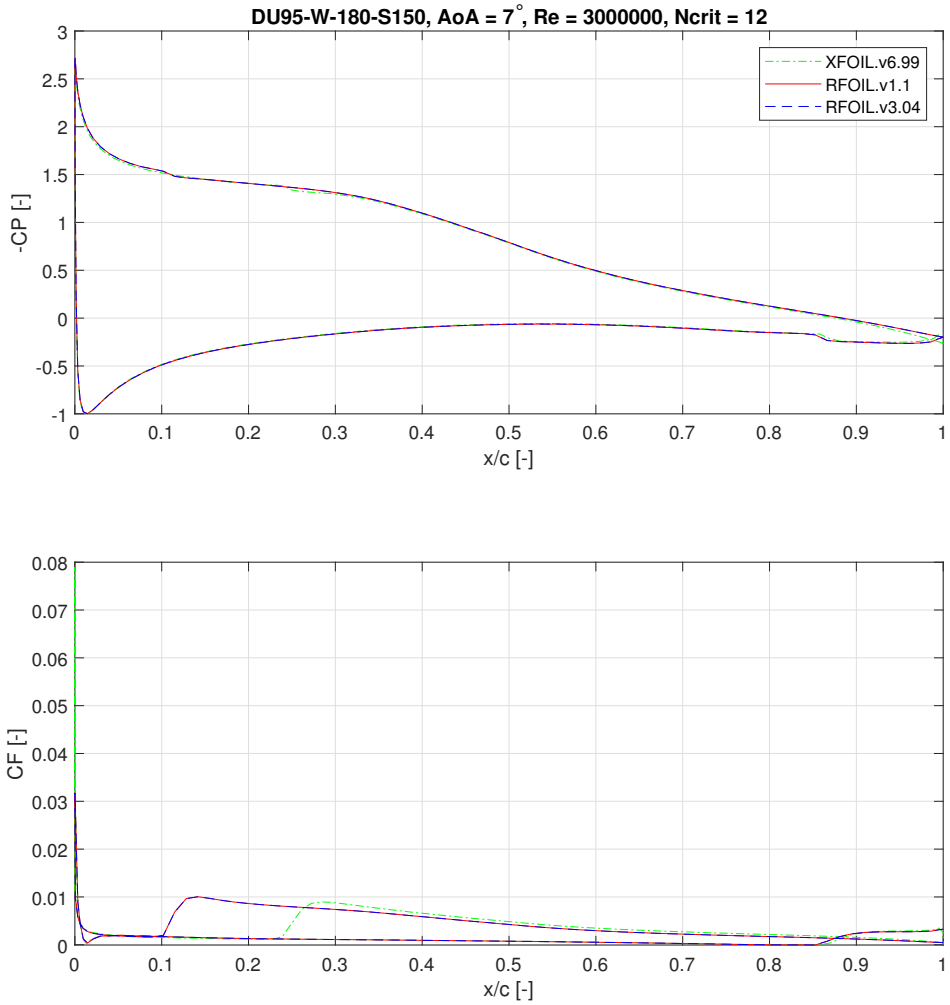

Figure B.82: Comparison between experimental and numerical polars for the DU95-W-180-S210 airfoil at a Reynolds number of 1000000. Simulation time to generate the polars by means the different codes and the number of converged polar points are depicted between parentheses.

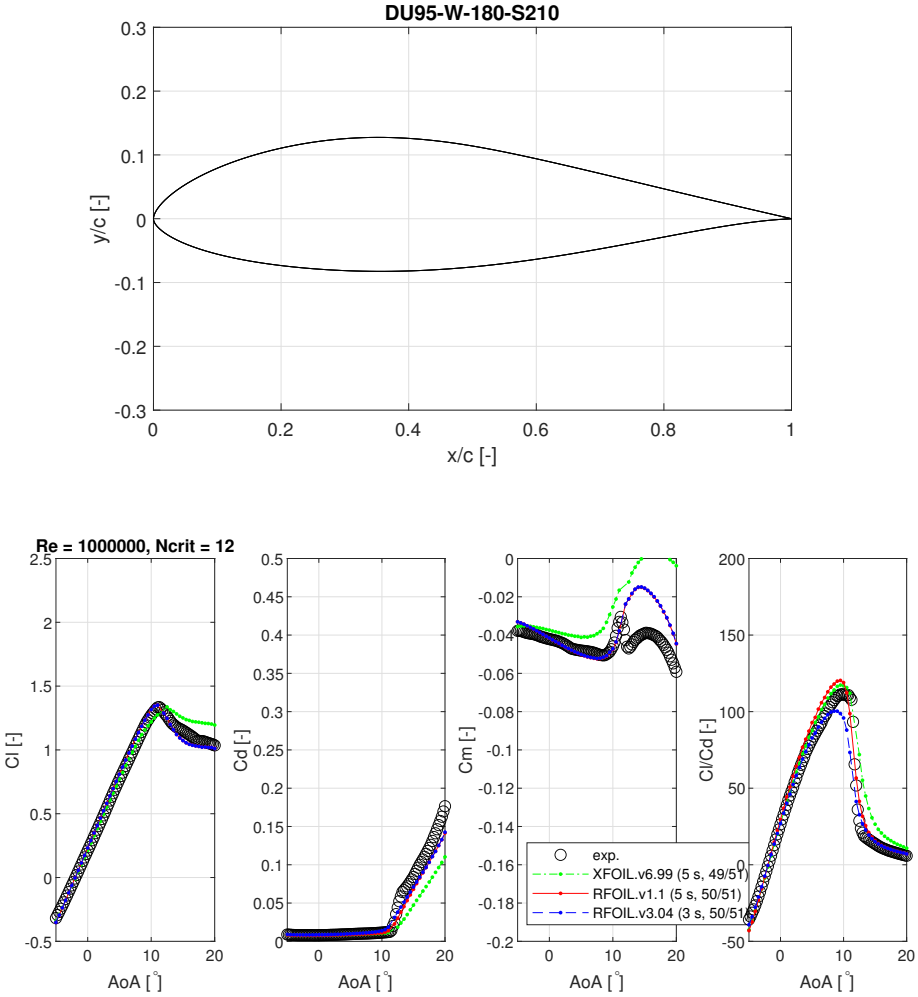

Figure B.83: Differences between experimental and numerical polars for the DU95-W-180-S210 airfoil at a Reynolds number of 1000000. Vertical black lines in the middle subplot indicate, from left to right, the angle of attack corresponding to the minimum drag coefficient, maximum lift to drag ratio and maximum lift coefficient, respectively.

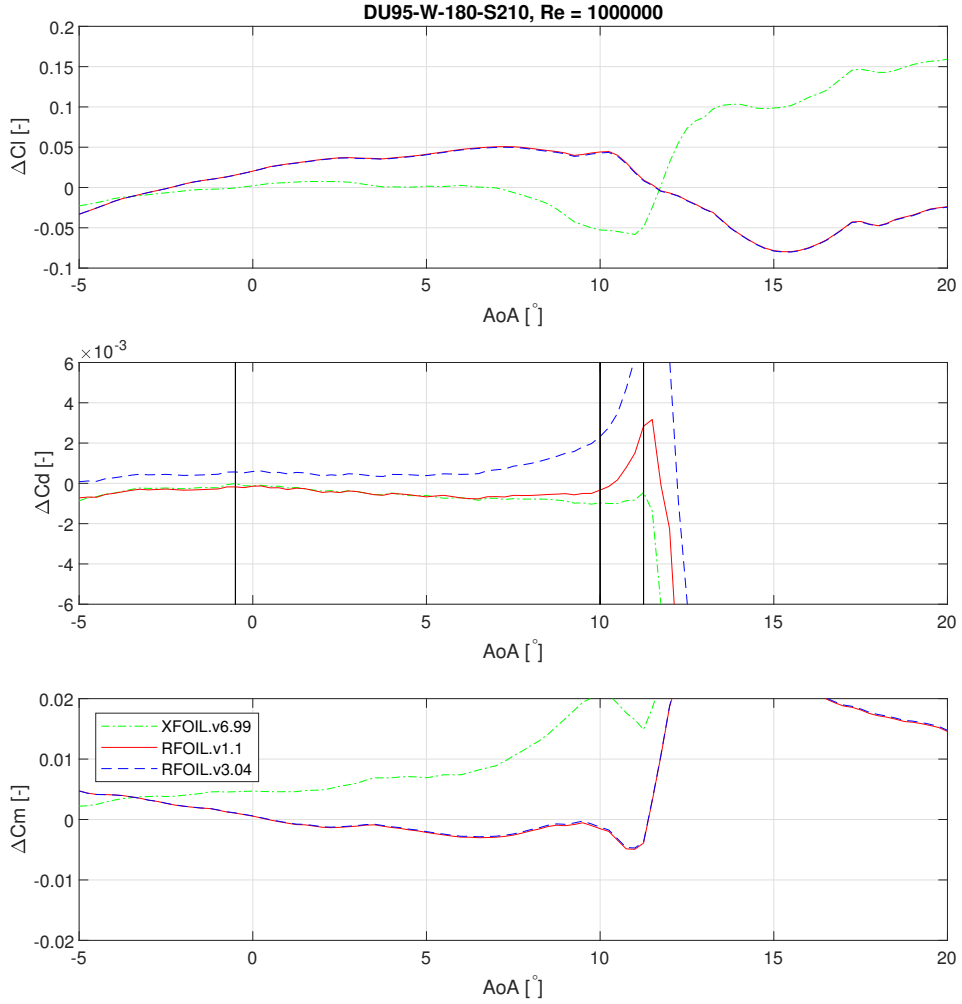

Figure B.84: Comparison between experimental and numerical pressure and skin friction distributions for the DU95-W-180-S210 airfoil at a Reynolds number of 1000000 and at the design angle of attack.

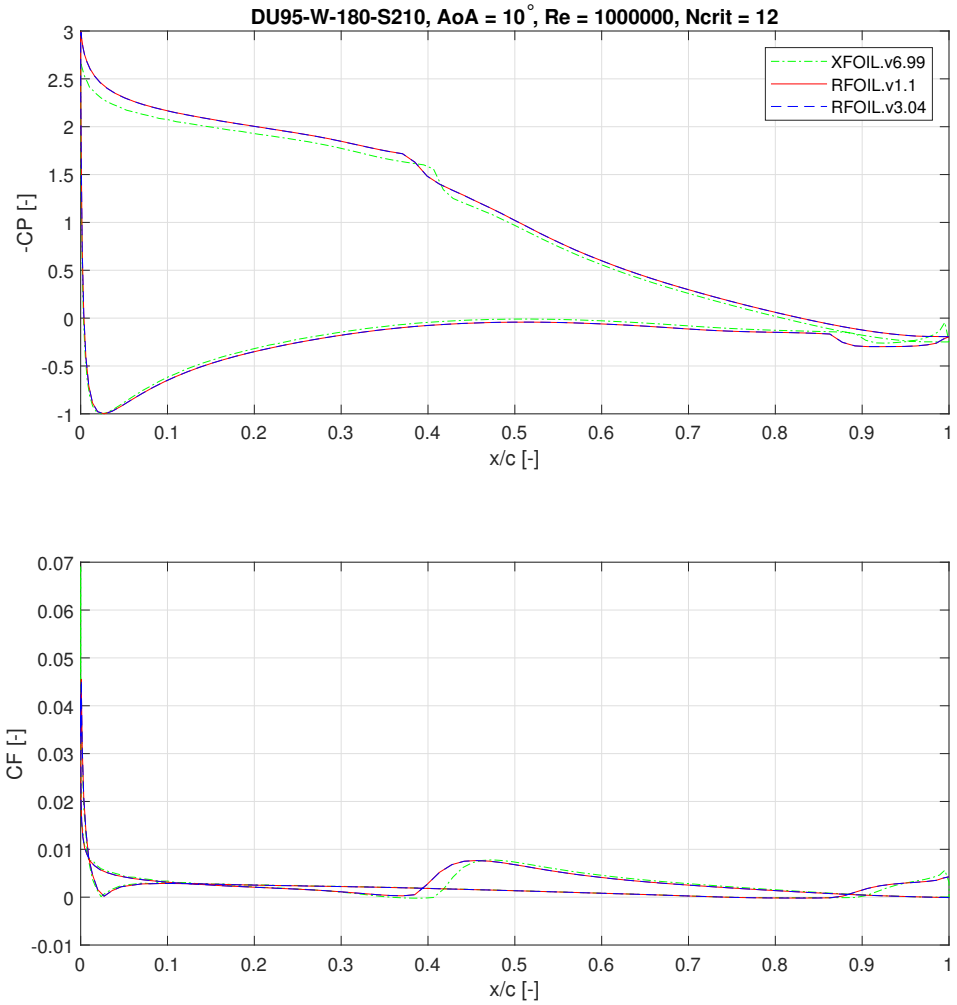

Figure B.85: Comparison between experimental and numerical polars for the DU95-W-180-S210 airfoil at a Reynolds number of 2000000. Simulation time to generate the polars by means the different codes and the number of converged polar points are depicted between parentheses.

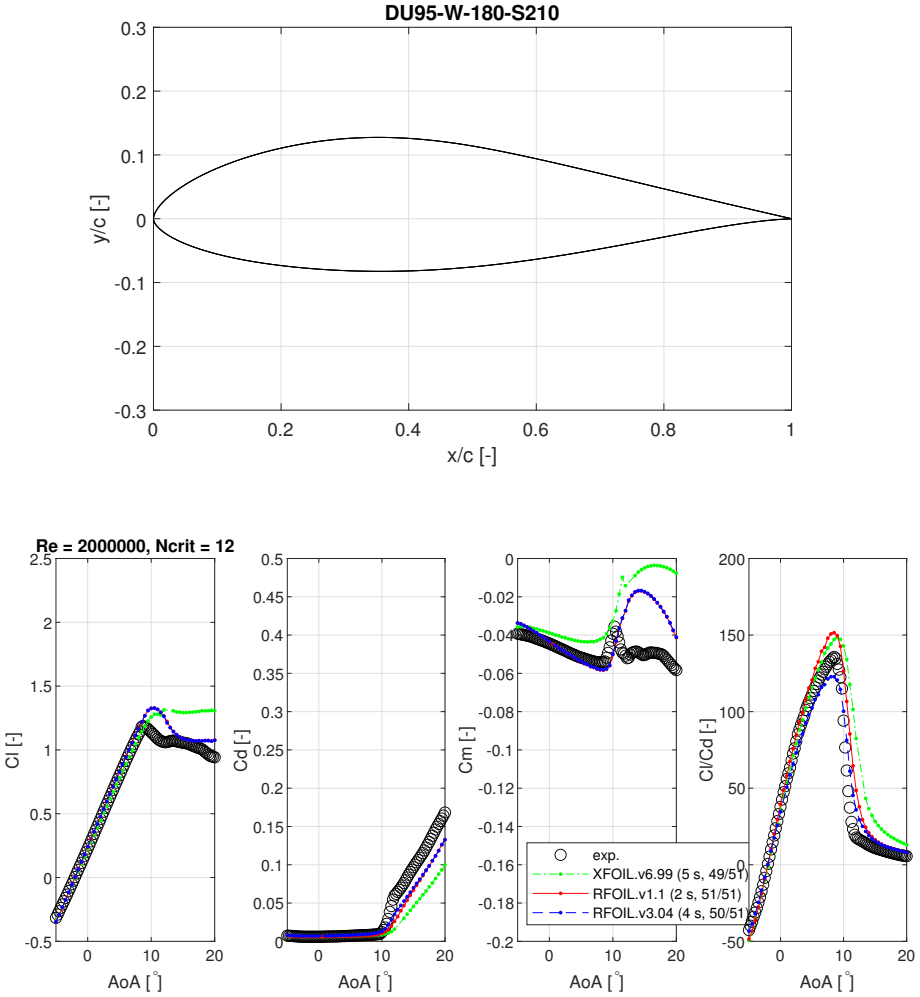

Figure B.86: Differences between experimental and numerical polars for the DU95-W-180-S210 airfoil at a Reynolds number of 2000000. Vertical black lines in the middle subplot indicate, from left to right, the angle of attack corresponding to the minimum drag coefficient, maximum lift to drag ratio and maximum lift coefficient, respectively.

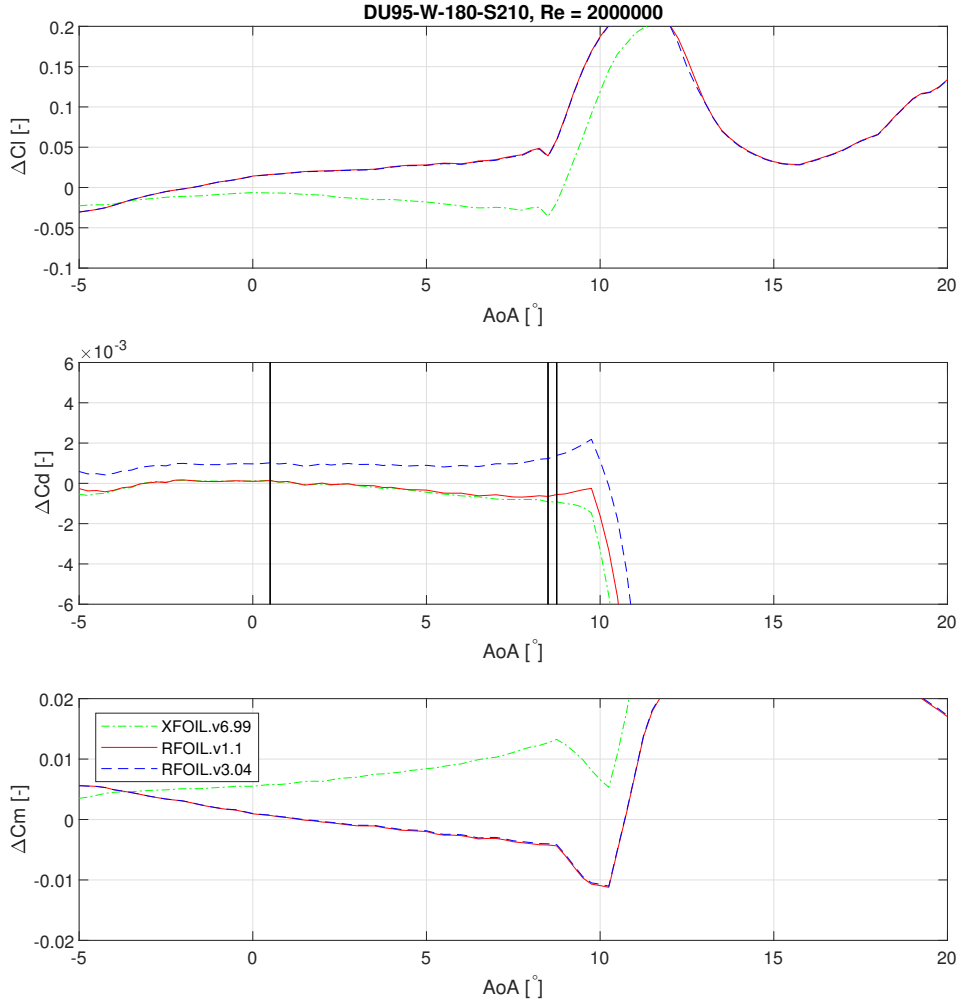

Figure B.87: Comparison between experimental and numerical pressure and skin friction distributions for the DU95-W-180-S210 airfoil at a Reynolds number of 2000000 and at the design angle of attack.

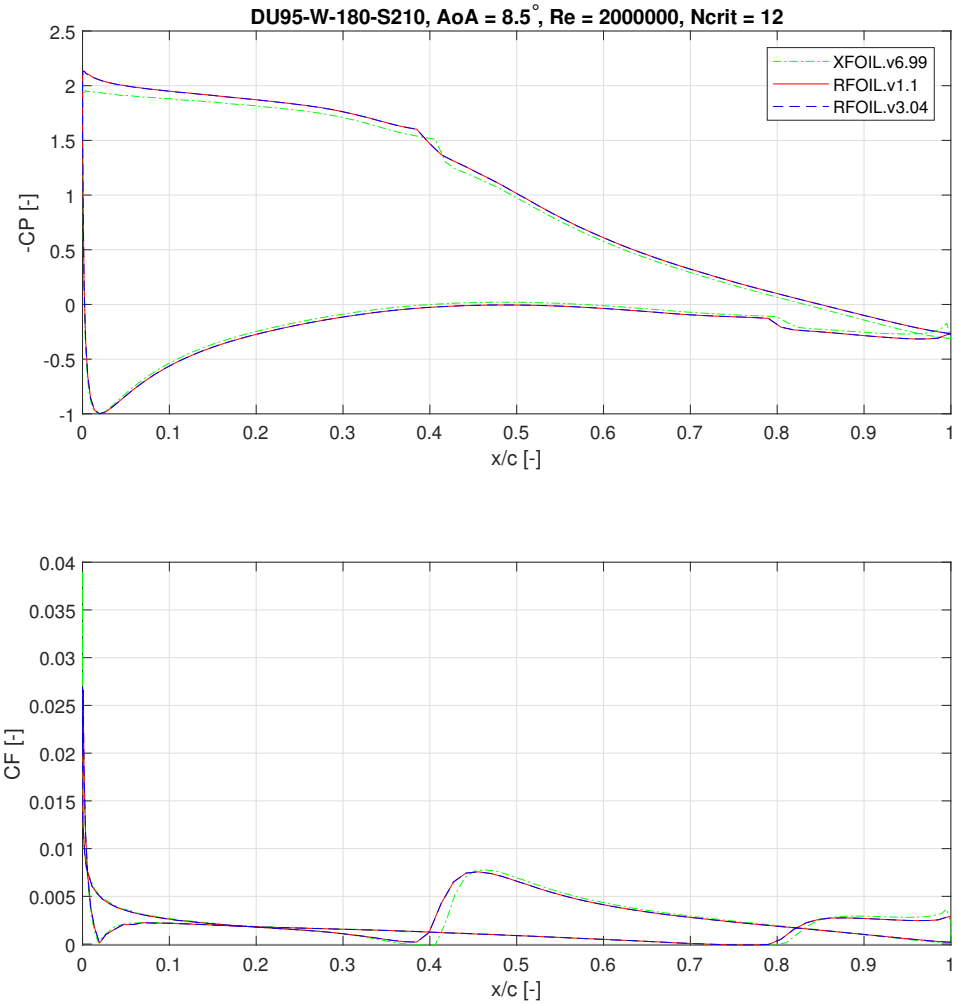

Figure B.88: Comparison between experimental and numerical polars for the DU95-W-180-S210 airfoil at a Reynolds number of 3000000. Simulation time to generate the polars by means the different codes and the number of converged polar points are depicted between parentheses.

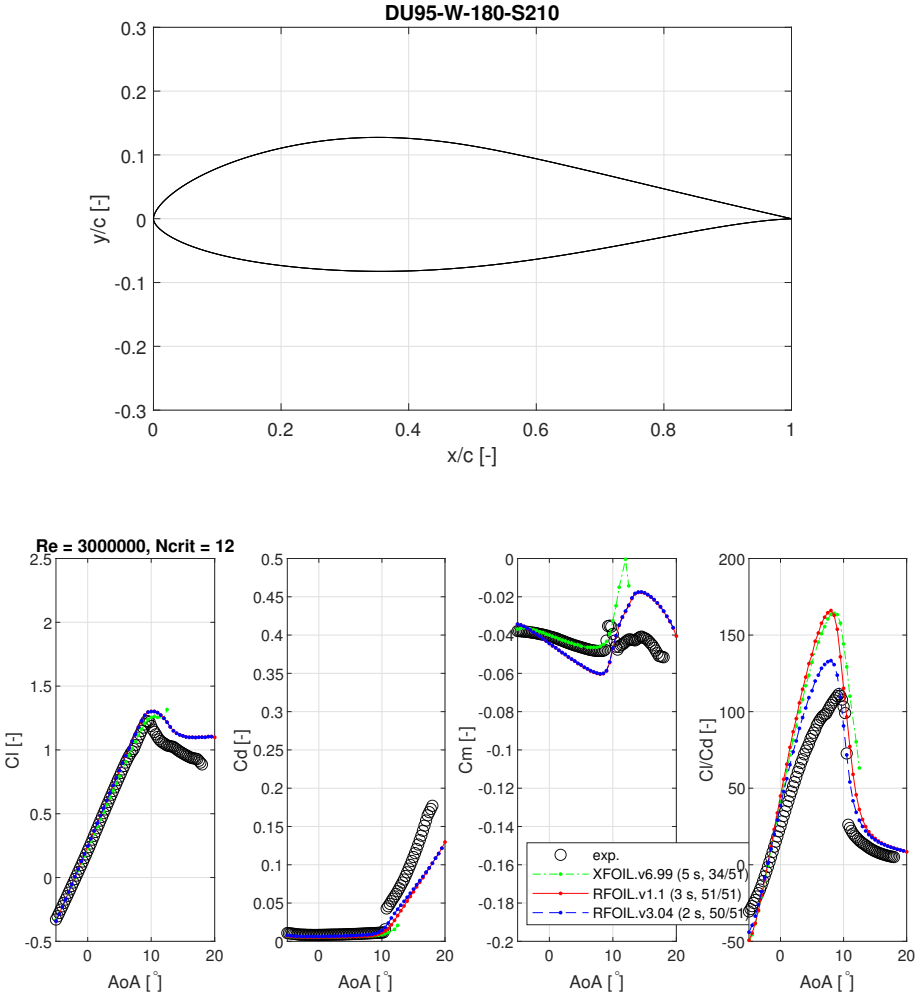

Figure B.89: Differences between experimental and numerical polars for the DU95-W-180-S210 airfoil at a Reynolds number of 3000000. Vertical black lines in the middle subplot indicate, from left to right, the angle of attack corresponding to the minimum drag coefficient, maximum lift to drag ratio and maximum lift coefficient, respectively.

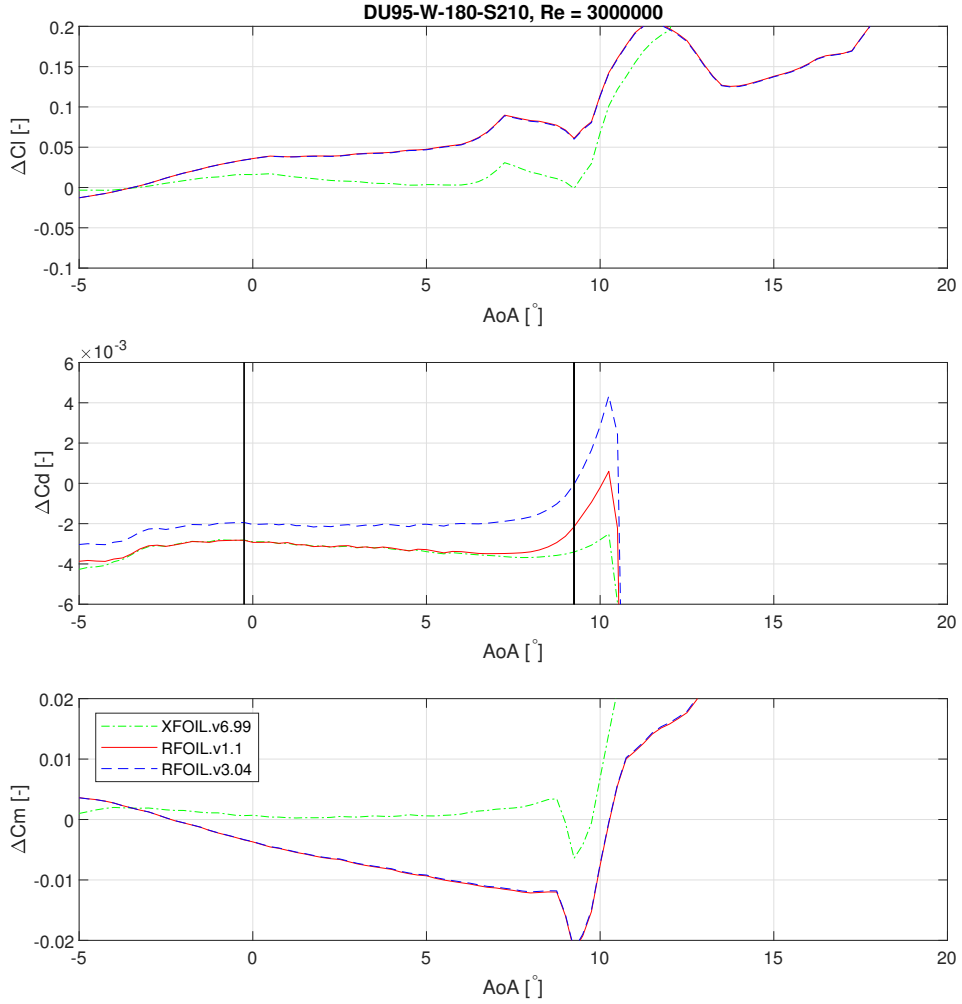

Figure B.90: Comparison between experimental and numerical pressure and skin friction distributions for the DU95-W-180-S210 airfoil at a Reynolds number of 3000000 and at the design angle of attack.

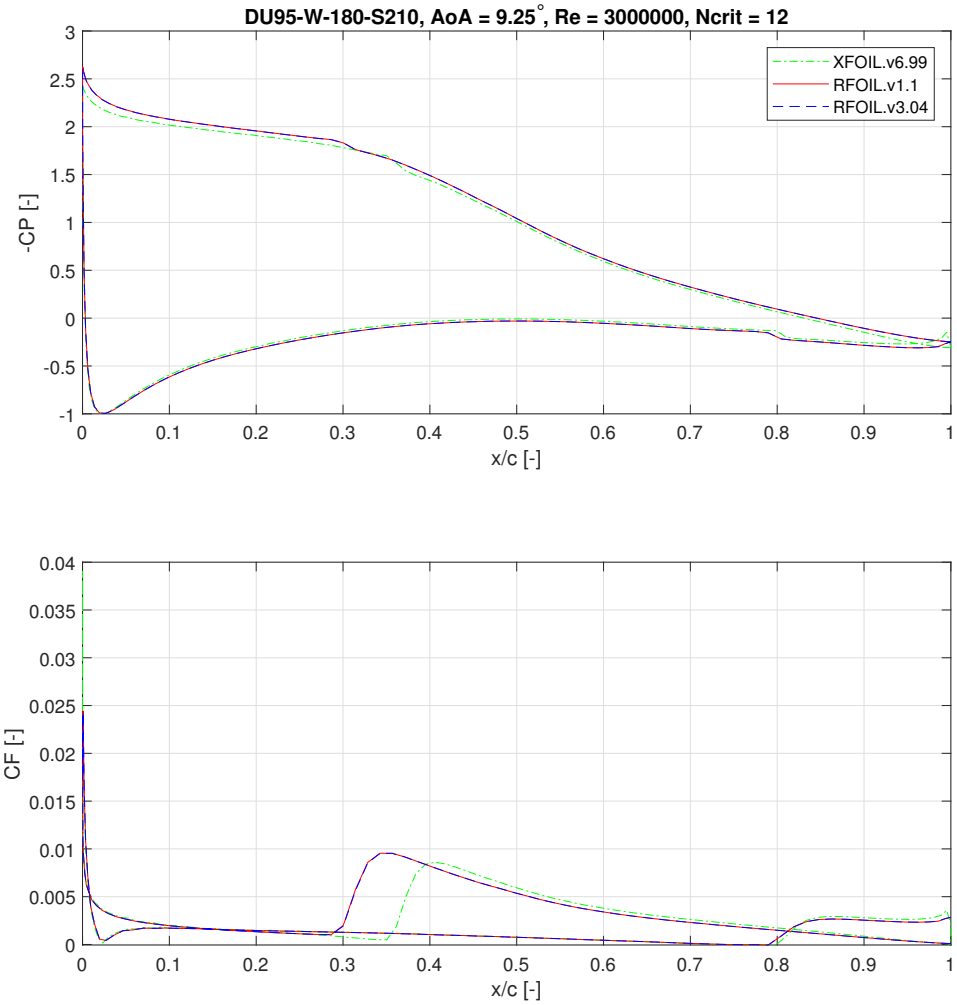

Figure B.91: Comparison between experimental and numerical polars for the DU95-W-180 airfoil at a Reynolds number of 1000000. Simulation time to generate the polars by means the different codes and the number of converged polar points are depicted between parentheses.

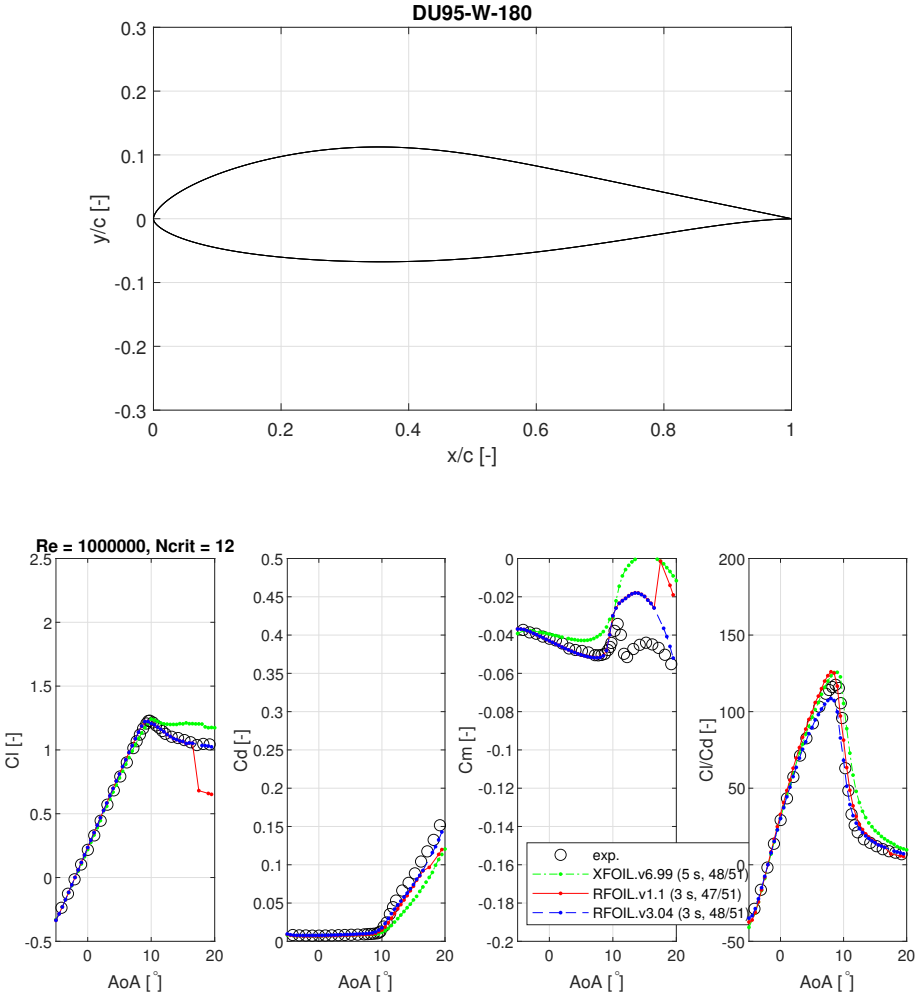

Figure B.92: Differences between experimental and numerical polars for the DU95-W-180 airfoil at a Reynolds number of 1000000. Vertical black lines in the middle subplot indicate, from left to right, the angle of attack corresponding to the minimum drag coefficient, maximum lift to drag ratio and maximum lift coefficient, respectively.

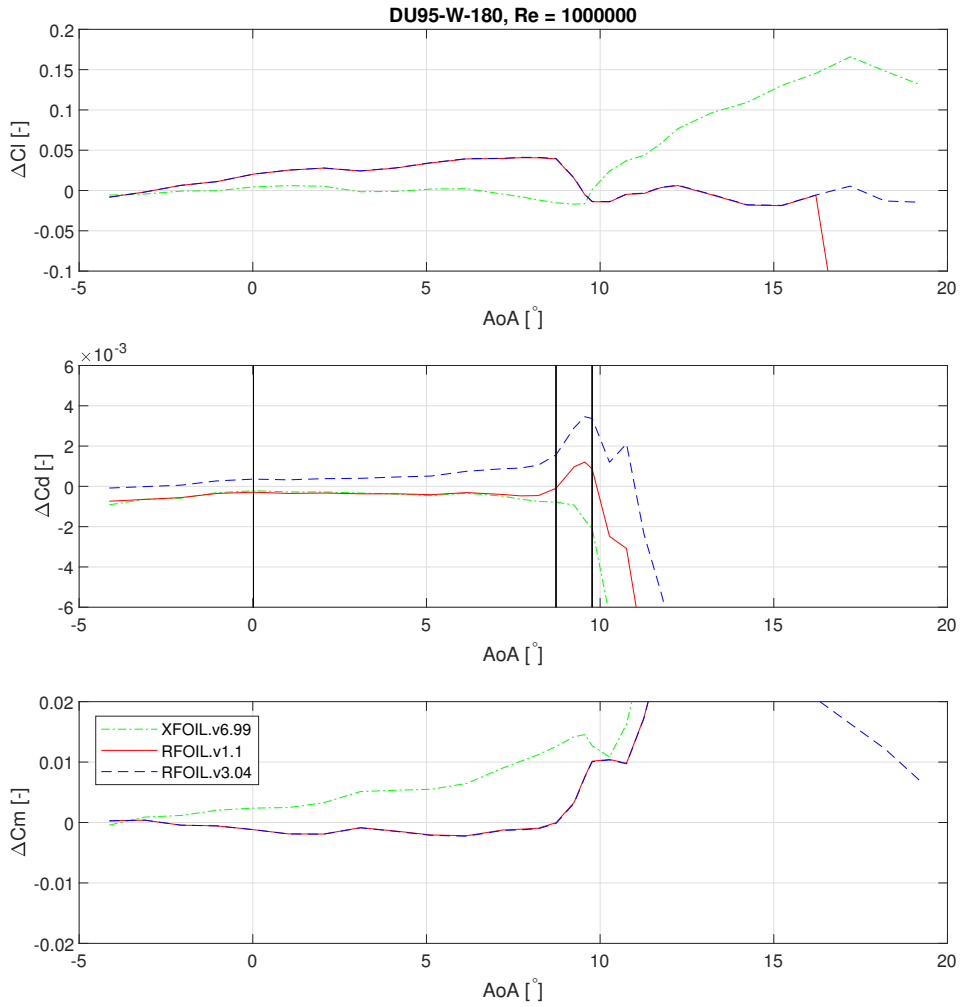

Figure B.93: Comparison between experimental and numerical pressure and skin friction distributions for the DU95-W-180 airfoil at a Reynolds number of 1000000 and at the design angle of attack.

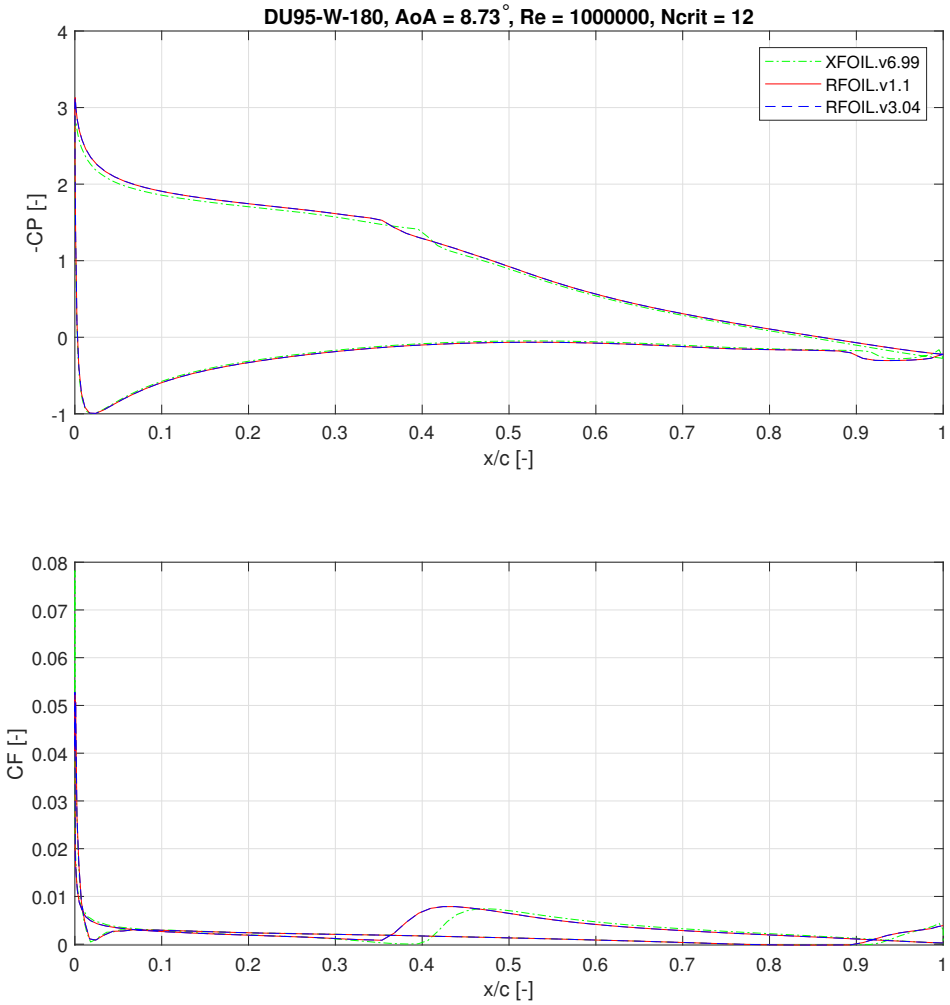

Figure B.94: Comparison between experimental and numerical polars for the DU95-W-180 airfoil at a Reynolds number of 2000000. Simulation time to generate the polars by means the different codes and the number of converged polar points are depicted between parentheses.

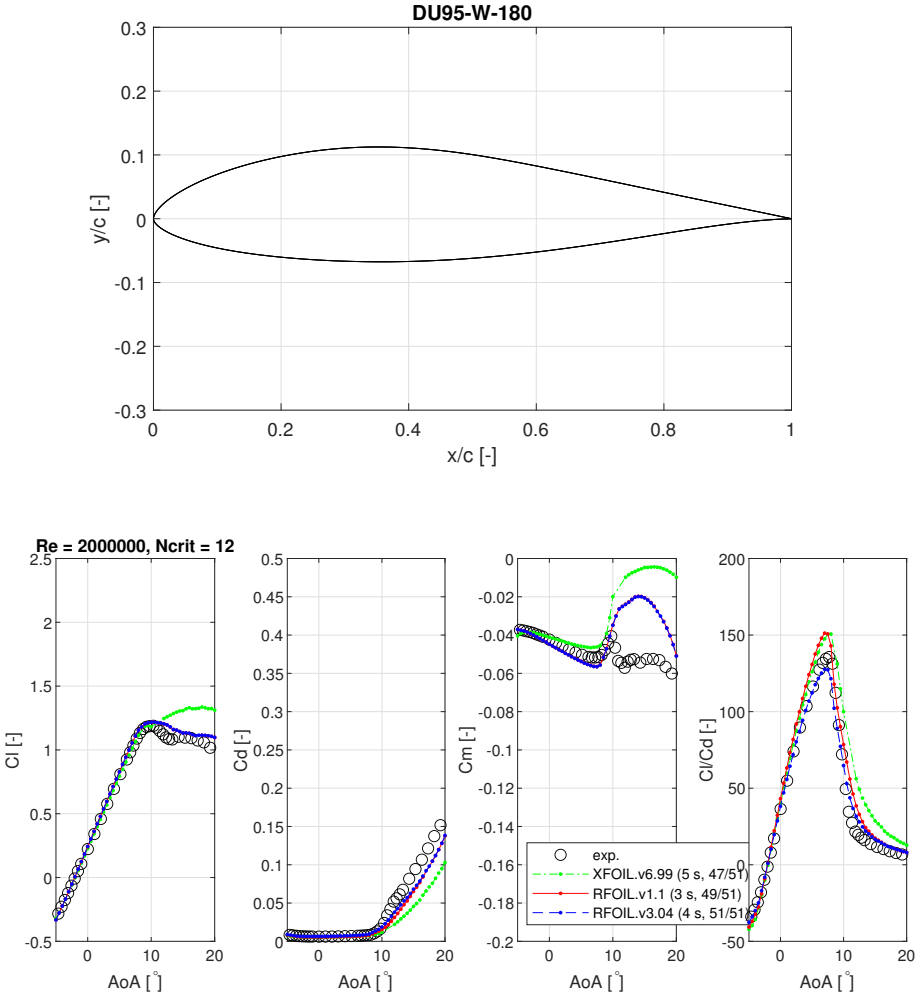

Figure B.95: Differences between experimental and numerical polars for the DU95-W-180 airfoil at a Reynolds number of 2000000. Vertical black lines in the middle subplot indicate, from left to right, the angle of attack corresponding to the minimum drag coefficient, maximum lift to drag ratio and maximum lift coefficient, respectively.

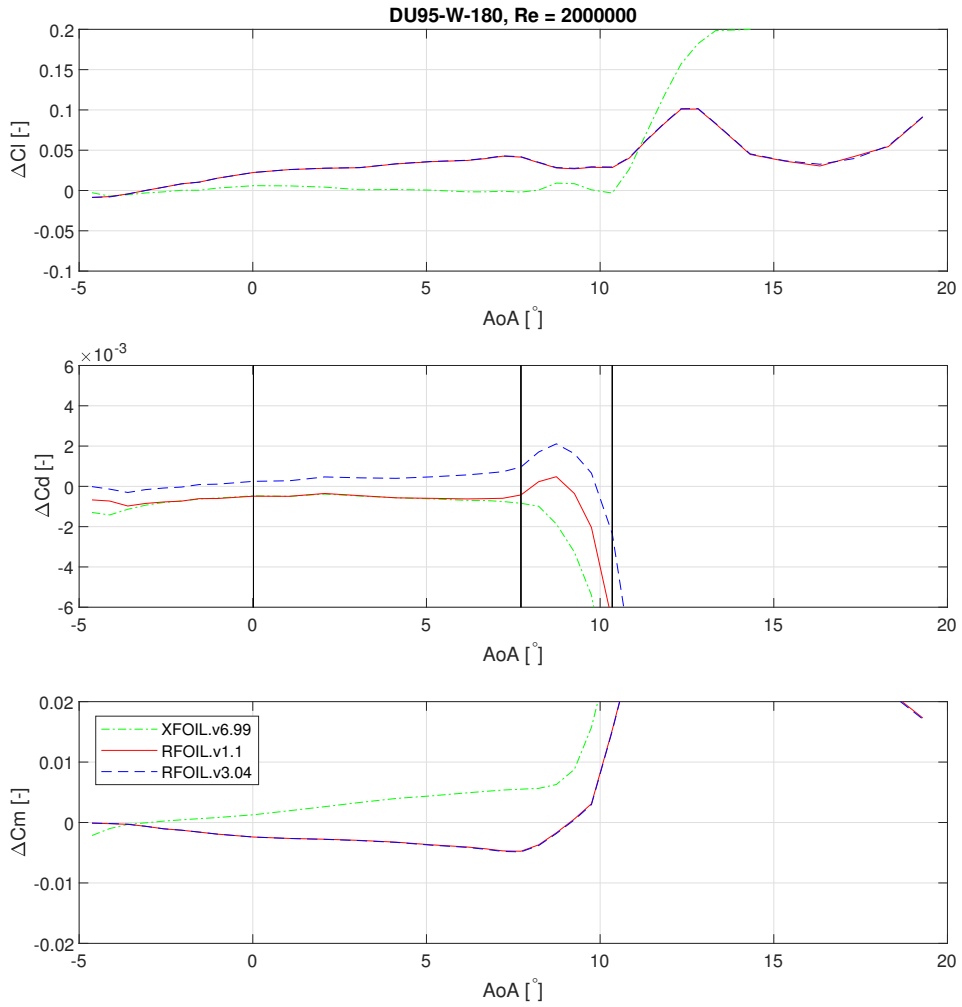

Figure B.96: Comparison between experimental and numerical pressure and skin friction distributions for the DU95-W-180 airfoil at a Reynolds number of 2000000 and at the design angle of attack.

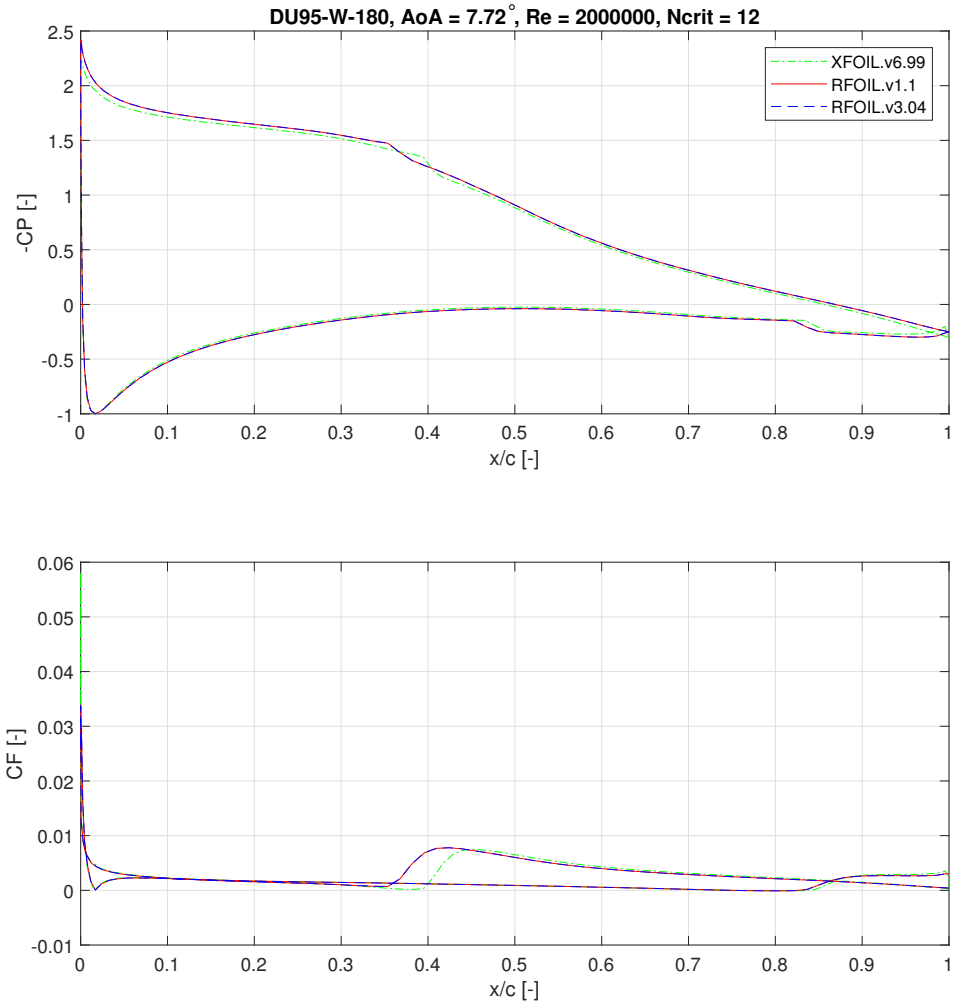

Figure B.97: Comparison between experimental and numerical polars for the DU95-W-180 airfoil at a Reynolds number of 3000000. Simulation time to generate the polars by means the different codes and the number of converged polar points are depicted between parentheses.

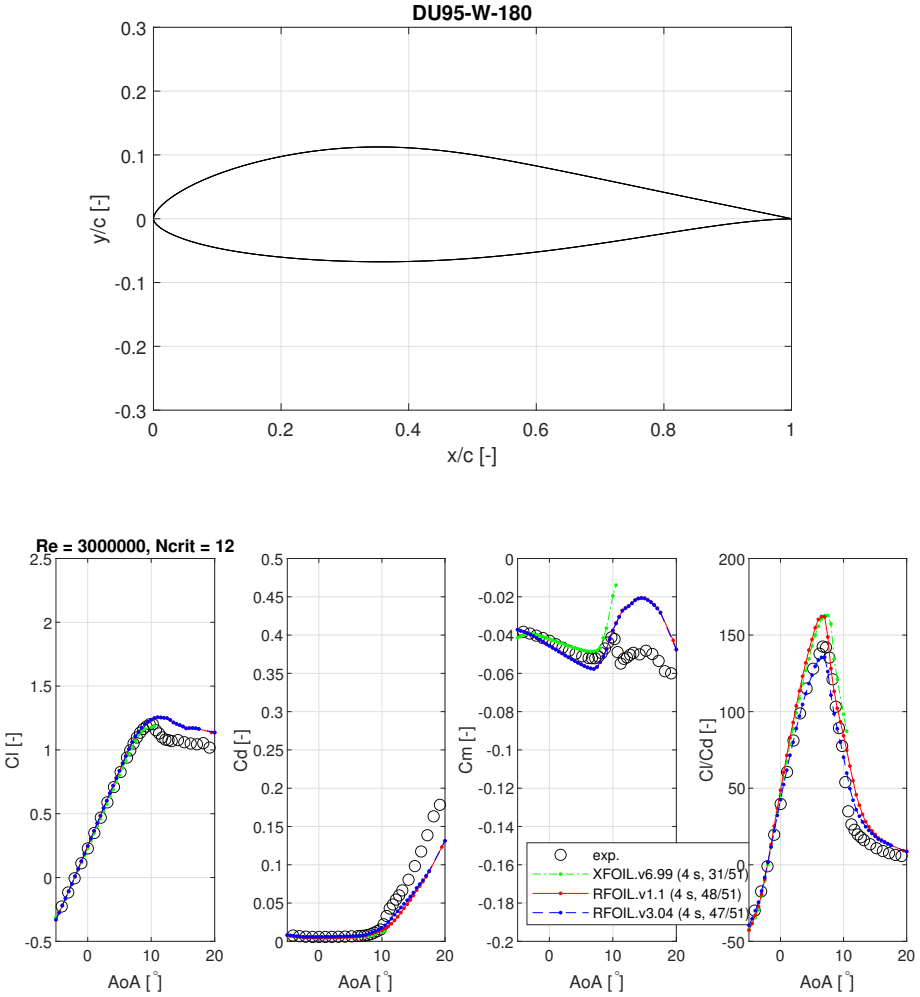

Figure B.98: Differences between experimental and numerical polars for the DU95-W-180 airfoil at a Reynolds number of 3000000. Vertical black lines in the middle subplot indicate, from left to right, the angle of attack corresponding to the minimum drag coefficient, maximum lift to drag ratio and maximum lift coefficient, respectively.

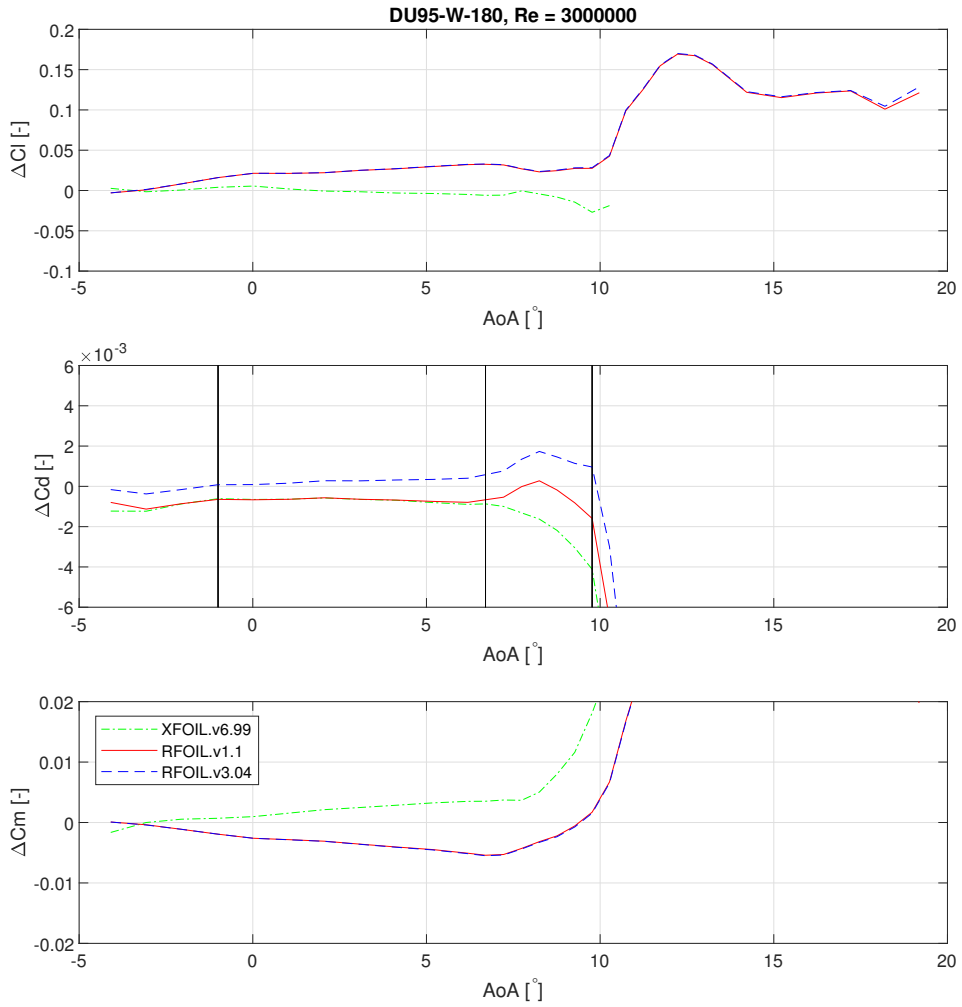

Figure B.99: Comparison between experimental and numerical pressure and skin friction distributions for the DU95-W-180 airfoil at a Reynolds number of 3000000 and at the design angle of attack.

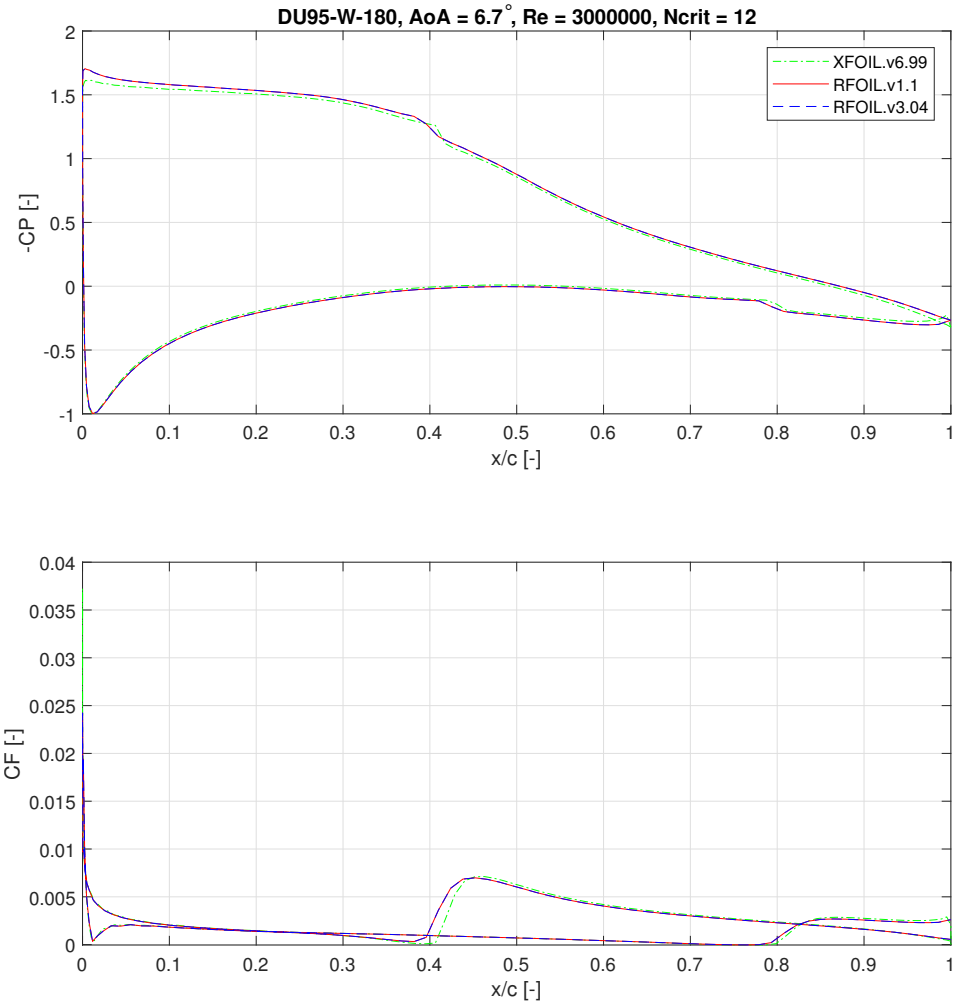

Figure B.100: Comparison between experimental and numerical polars for the DU96-W-180-S150 airfoil at a Reynolds number of 1000000. Simulation time to generate the polars by means the different codes and the number of converged polar points are depicted between parentheses.

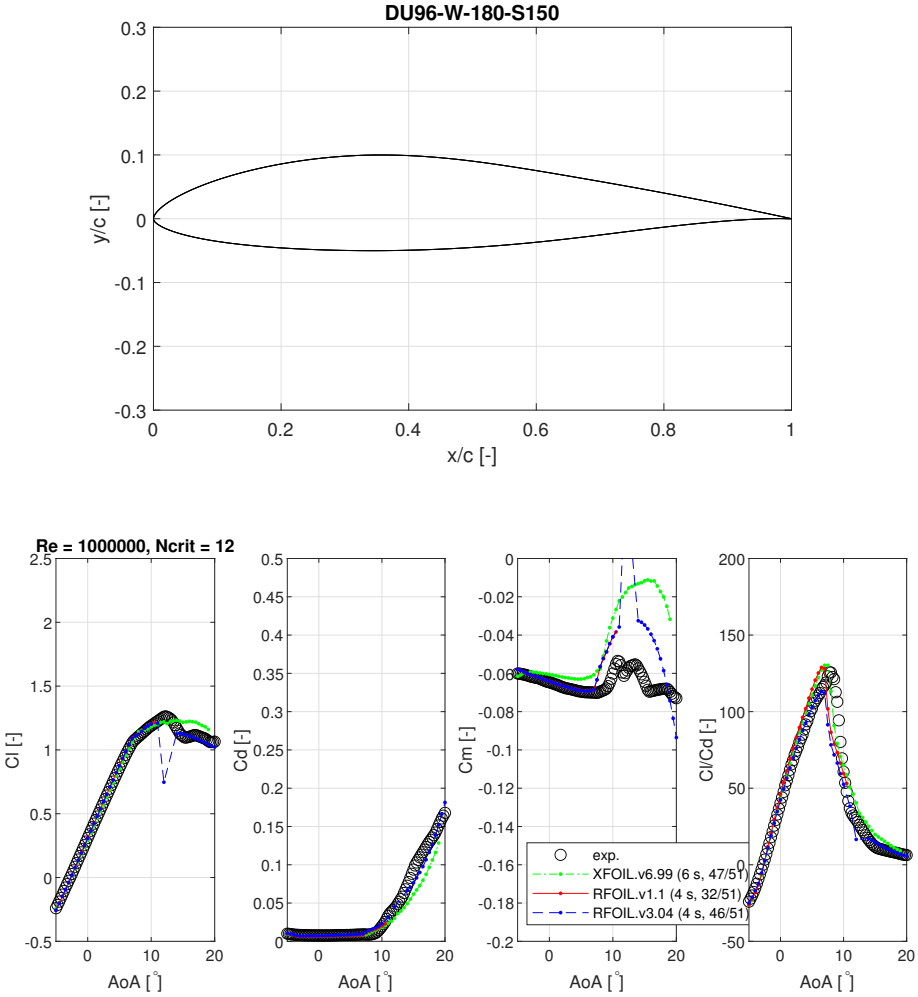

Figure B.101: Differences between experimental and numerical polars for the DU96-W-180-S150 airfoil at a Reynolds number of 1000000. Vertical black lines in the middle subplot indicate, from left to right, the angle of attack corresponding to the minimum drag coefficient, maximum lift to drag ratio and maximum lift coefficient, respectively.

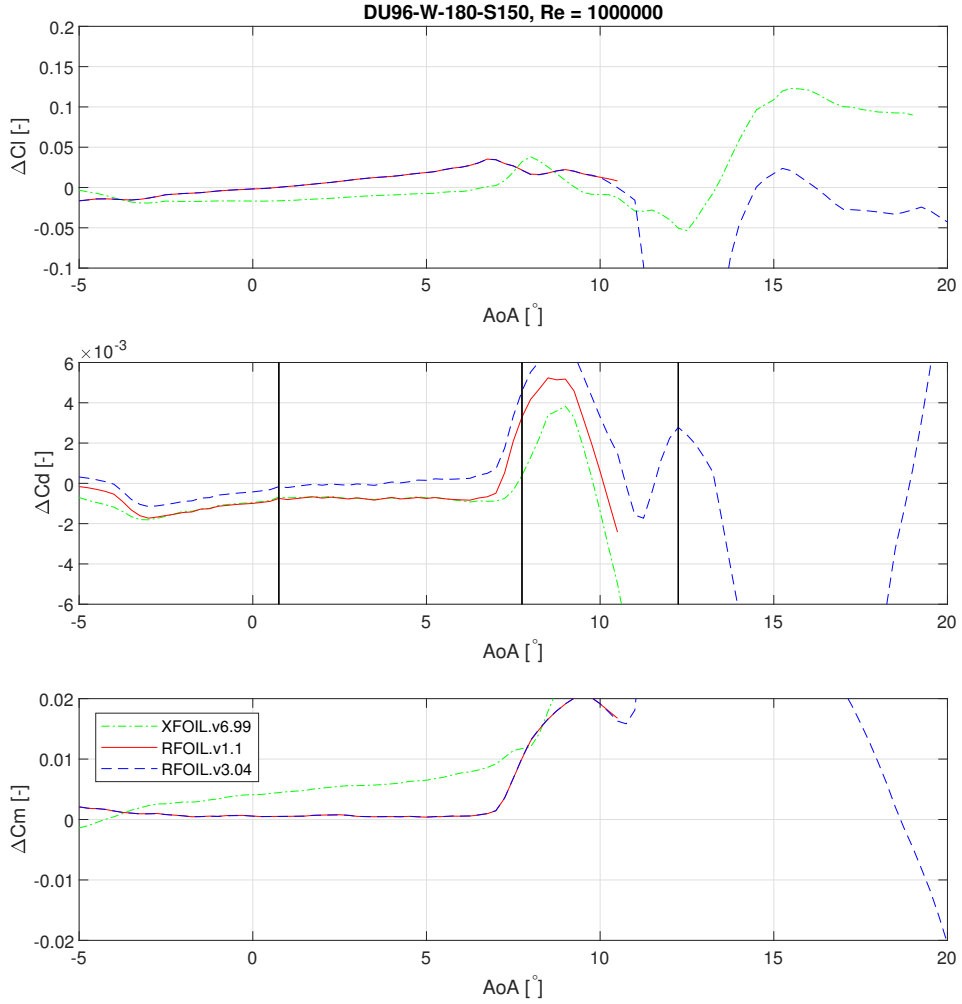

Figure B.102: Comparison between experimental and numerical pressure and skin friction distributions for the DU96-W-180-S150 airfoil at a Reynolds number of 1000000 and at the design angle of attack.

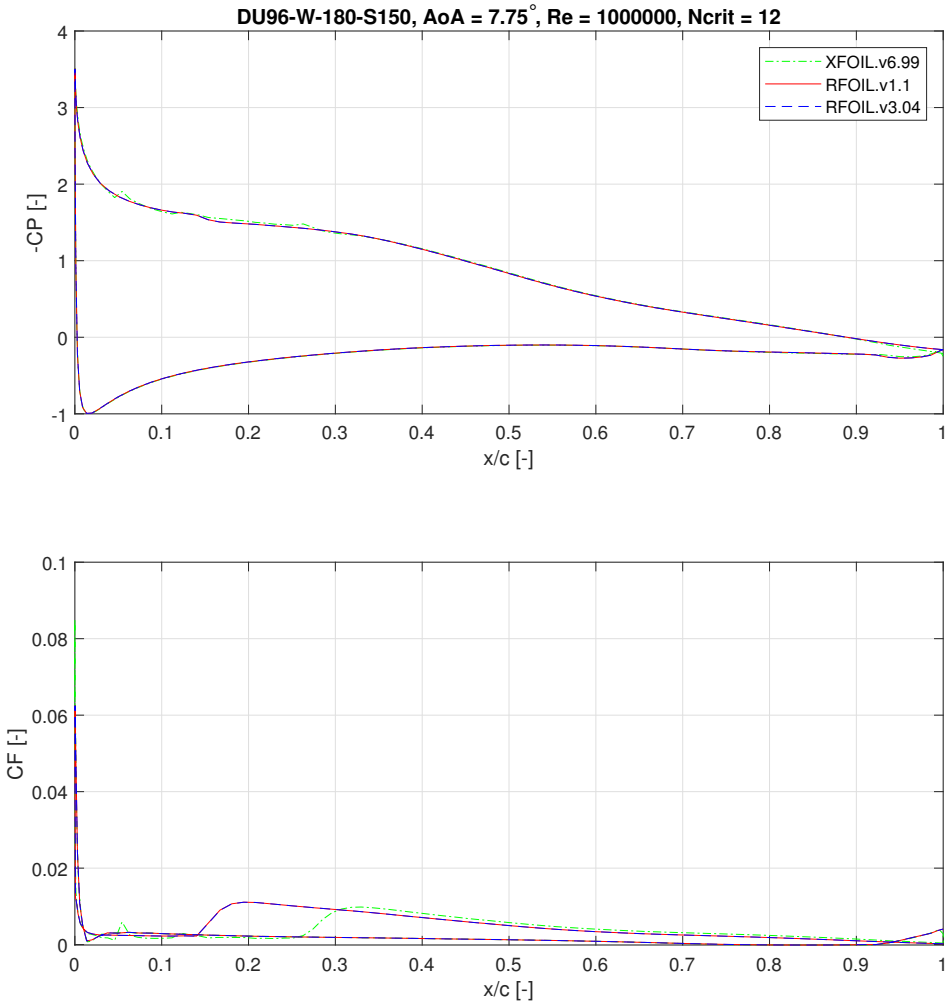

Figure B.103: Comparison between experimental and numerical polars for the DU96-W-180-S150 airfoil at a Reynolds number of 2000000. Simulation time to generate the polars by means the different codes and the number of converged polar points are depicted between parentheses.

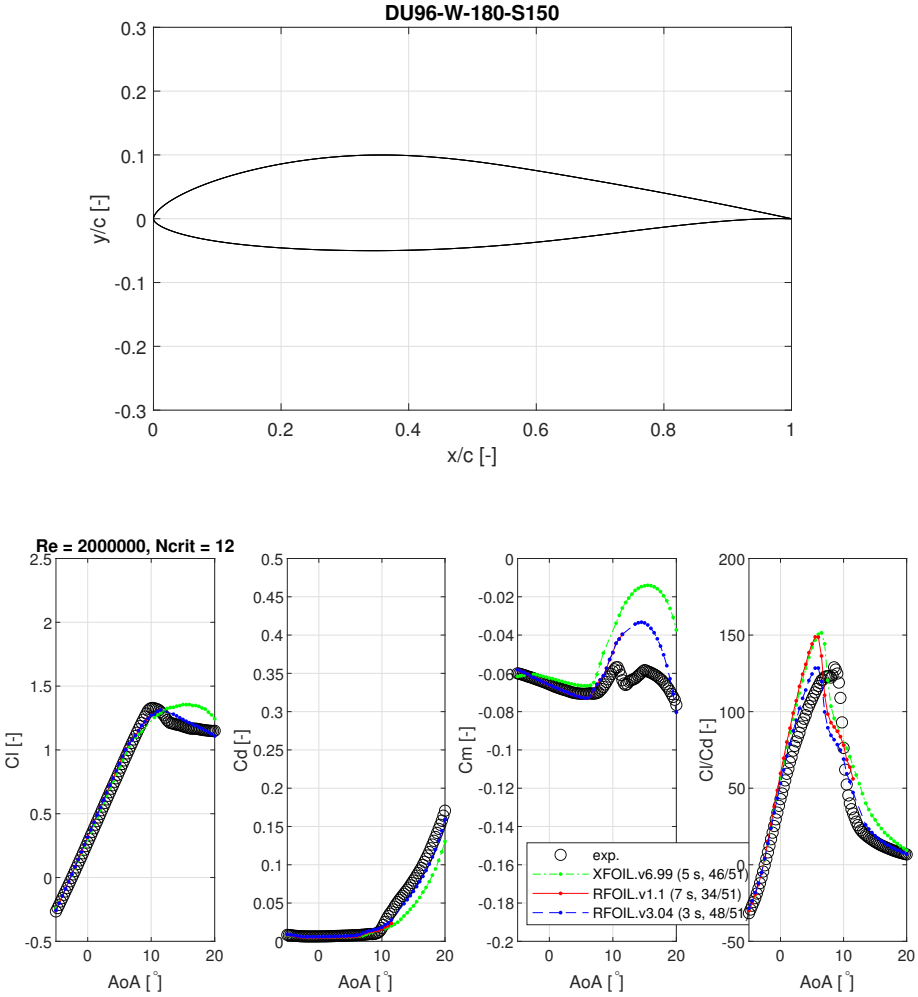

Figure B.104: Differences between experimental and numerical polars for the DU96-W-180-S150 airfoil at a Reynolds number of 2000000. Vertical black lines in the middle subplot indicate, from left to right, the angle of attack corresponding to the minimum drag coefficient, maximum lift to drag ratio and maximum lift coefficient, respectively.

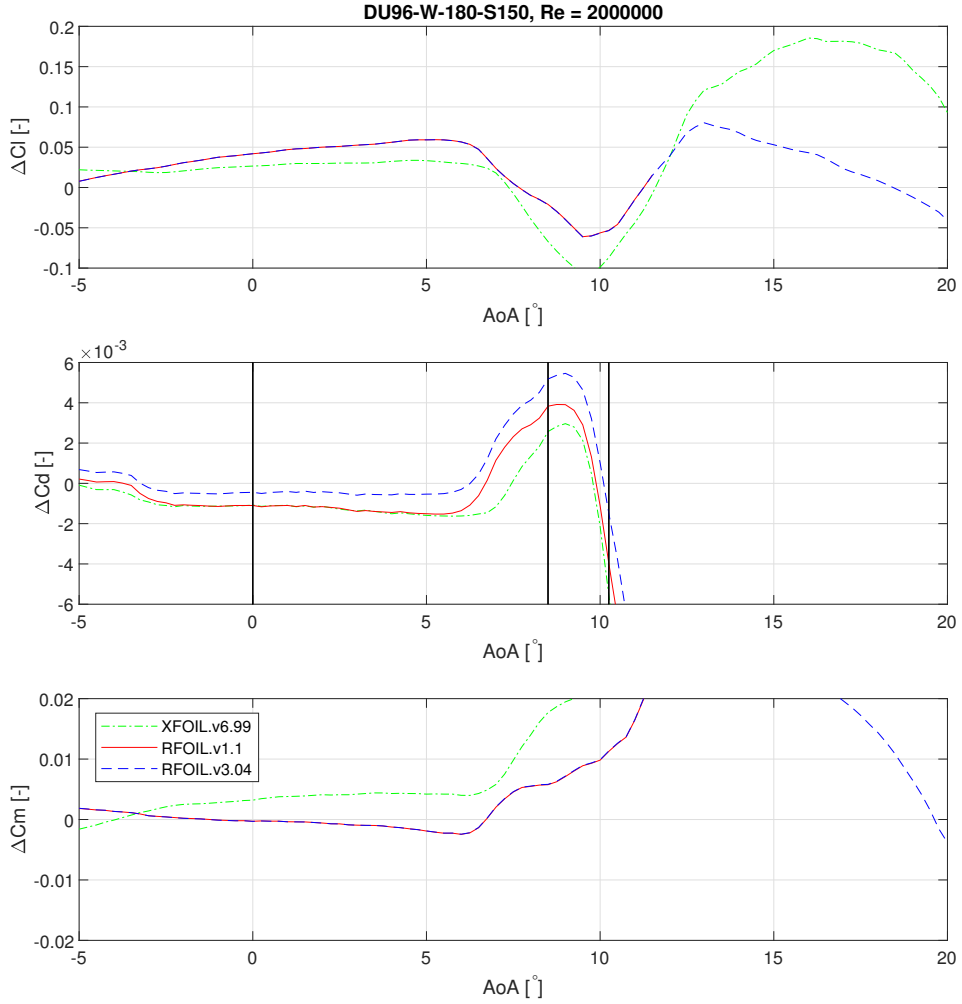

Figure B.105: Comparison between experimental and numerical pressure and skin friction distributions for the DU96-W-180-S150 airfoil at a Reynolds number of 2000000 and at the design angle of attack.

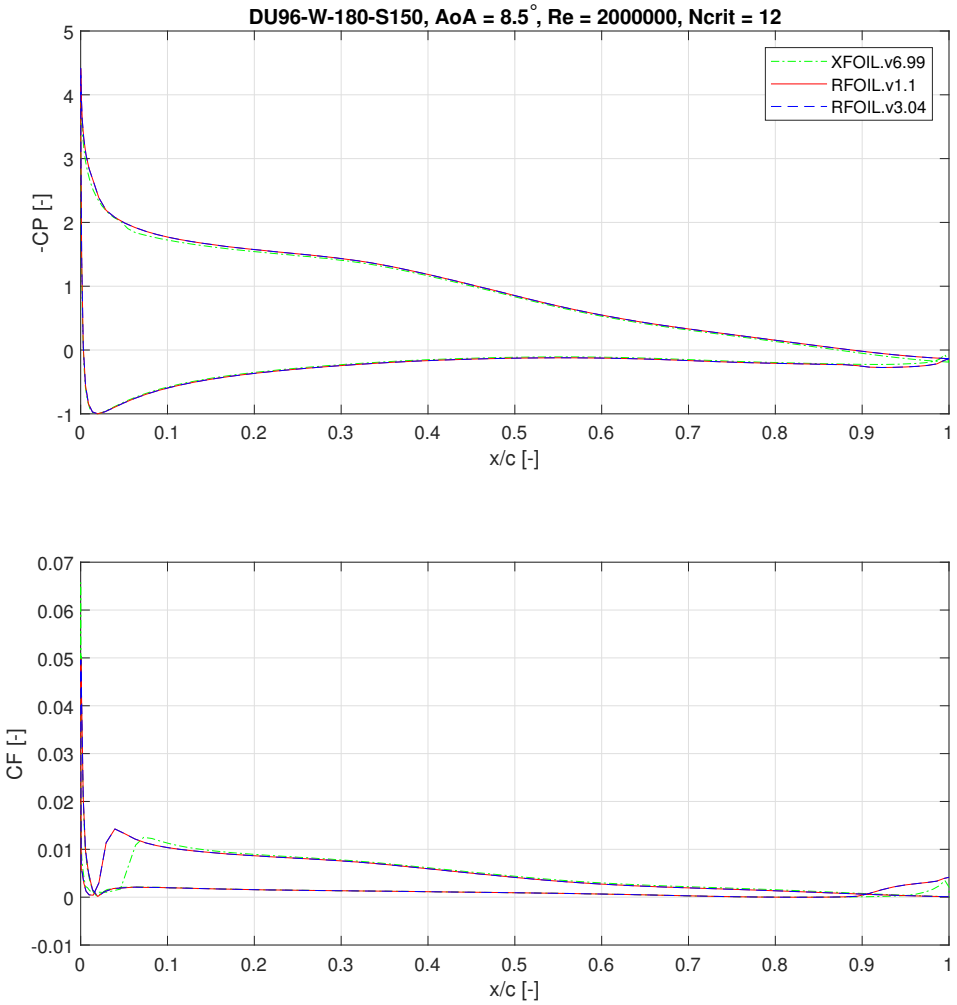

Figure B.106: Comparison between experimental and numerical polars for the DU96-W-180-S210 airfoil at a Reynolds number of 1000000. Simulation time to generate the polars by means the different codes and the number of converged polar points are depicted between parentheses.

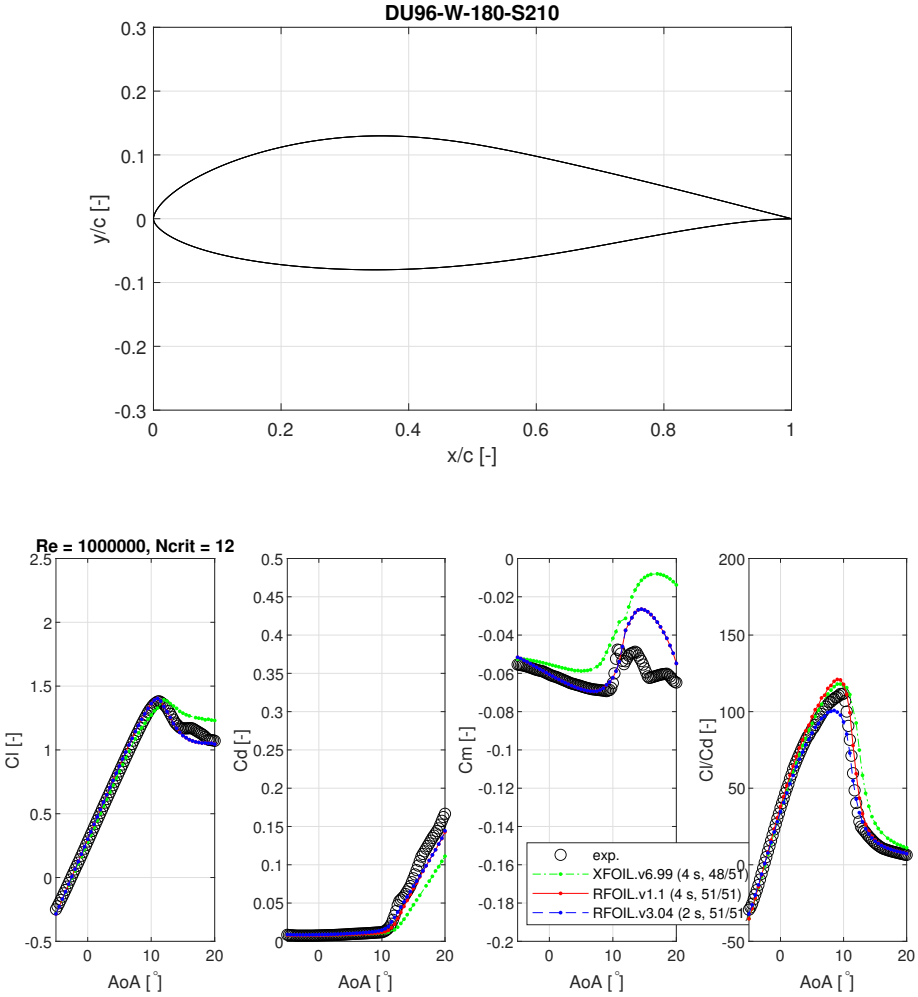

Figure B.107: Differences between experimental and numerical polars for the DU96-W-180-S210 airfoil at a Reynolds number of 1000000. Vertical black lines in the middle subplot indicate, from left to right, the angle of attack corresponding to the minimum drag coefficient, maximum lift to drag ratio and maximum lift coefficient, respectively.

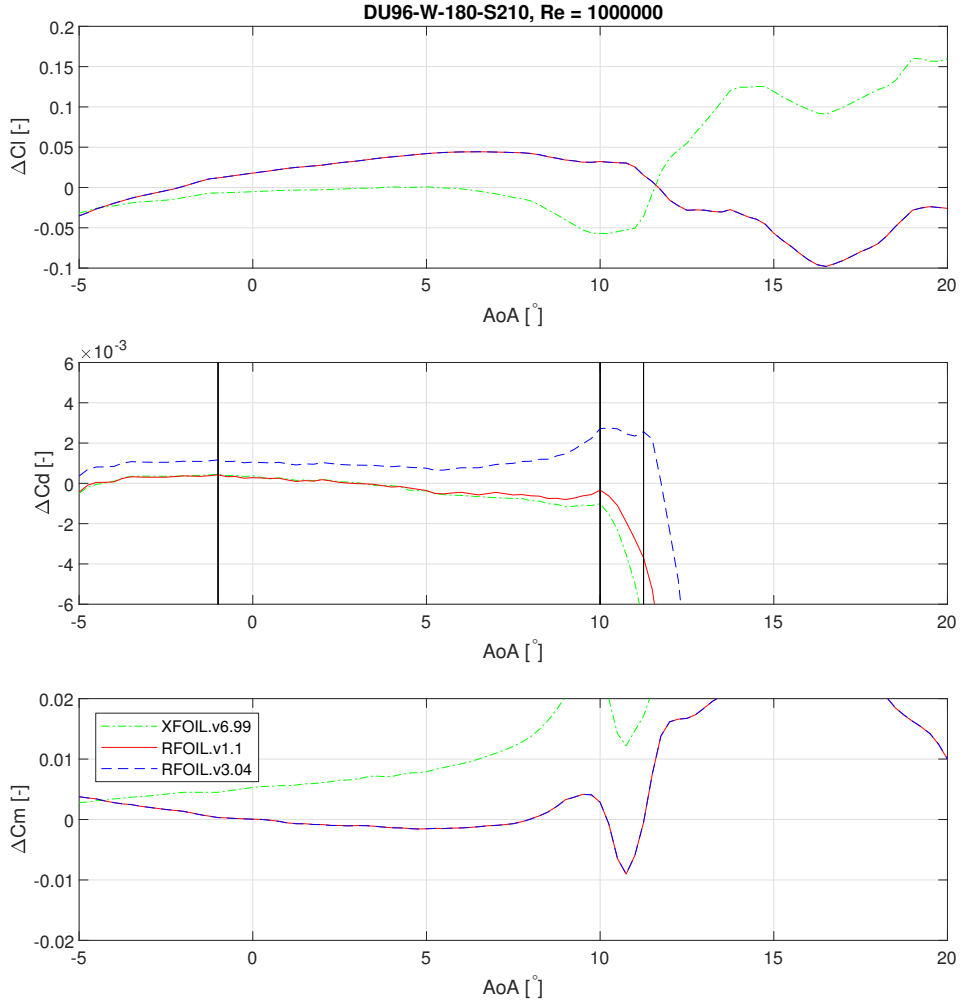

Figure B.108: Comparison between experimental and numerical pressure and skin friction distributions for the DU96-W-180-S210 airfoil at a Reynolds number of 1000000 and at the design angle of attack.

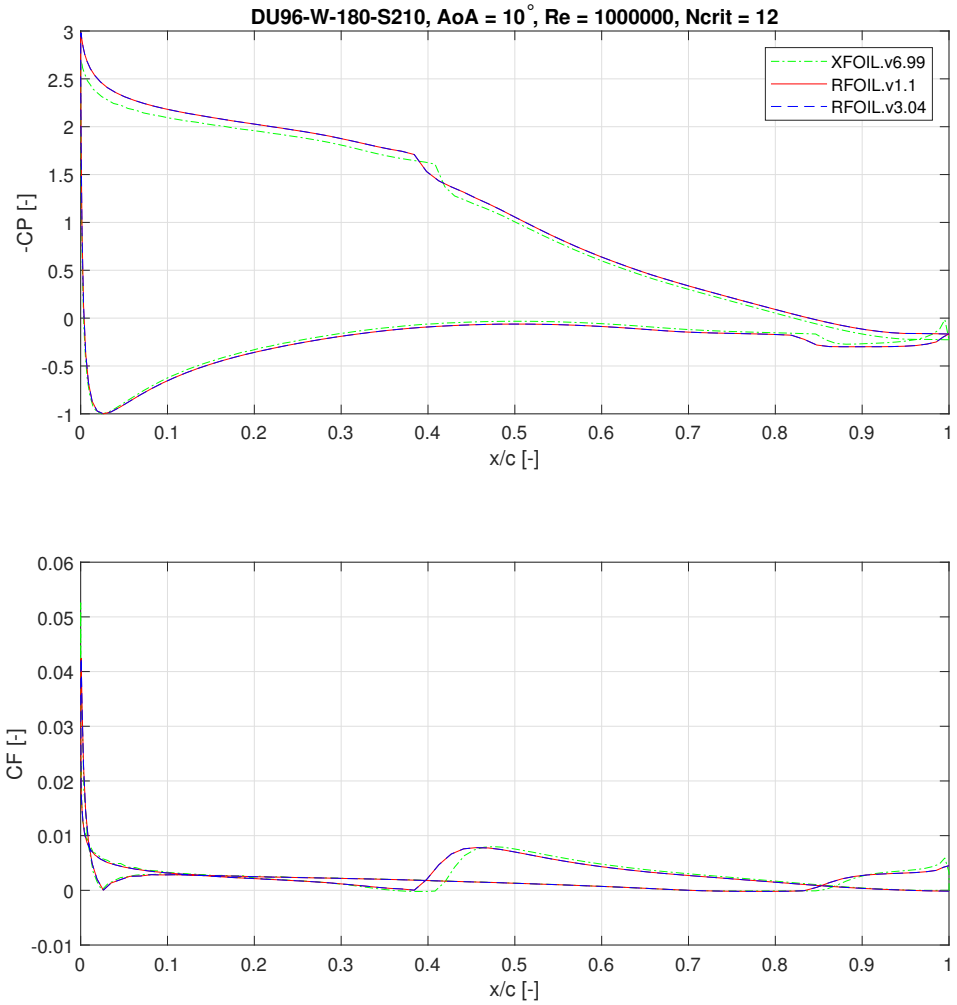

Figure B.109: Comparison between experimental and numerical polars for the DU96-W-180-S210 airfoil at a Reynolds number of 2000000. Simulation time to generate the polars by means the different codes and the number of converged polar points are depicted between parentheses.

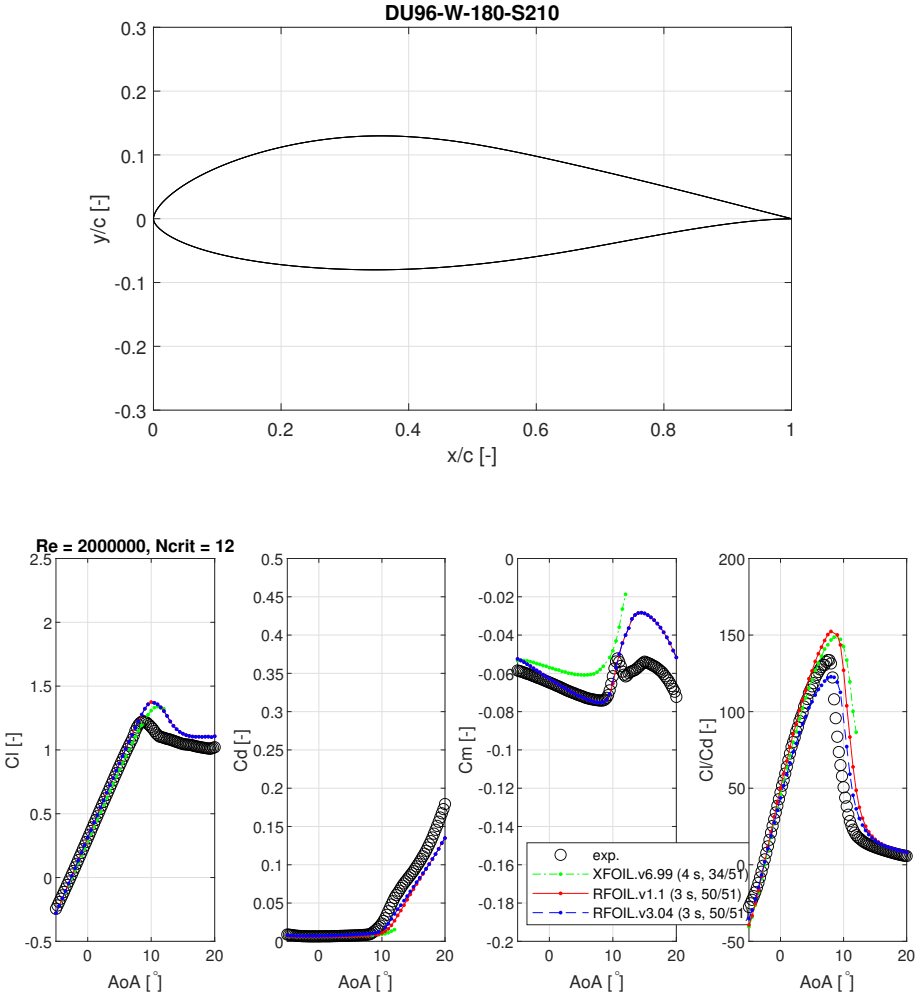

Figure B.110: Differences between experimental and numerical polars for the DU96-W-180-S210 airfoil at a Reynolds number of 2000000. Vertical black lines in the middle subplot indicate, from left to right, the angle of attack corresponding to the minimum drag coefficient, maximum lift to drag ratio and maximum lift coefficient, respectively.

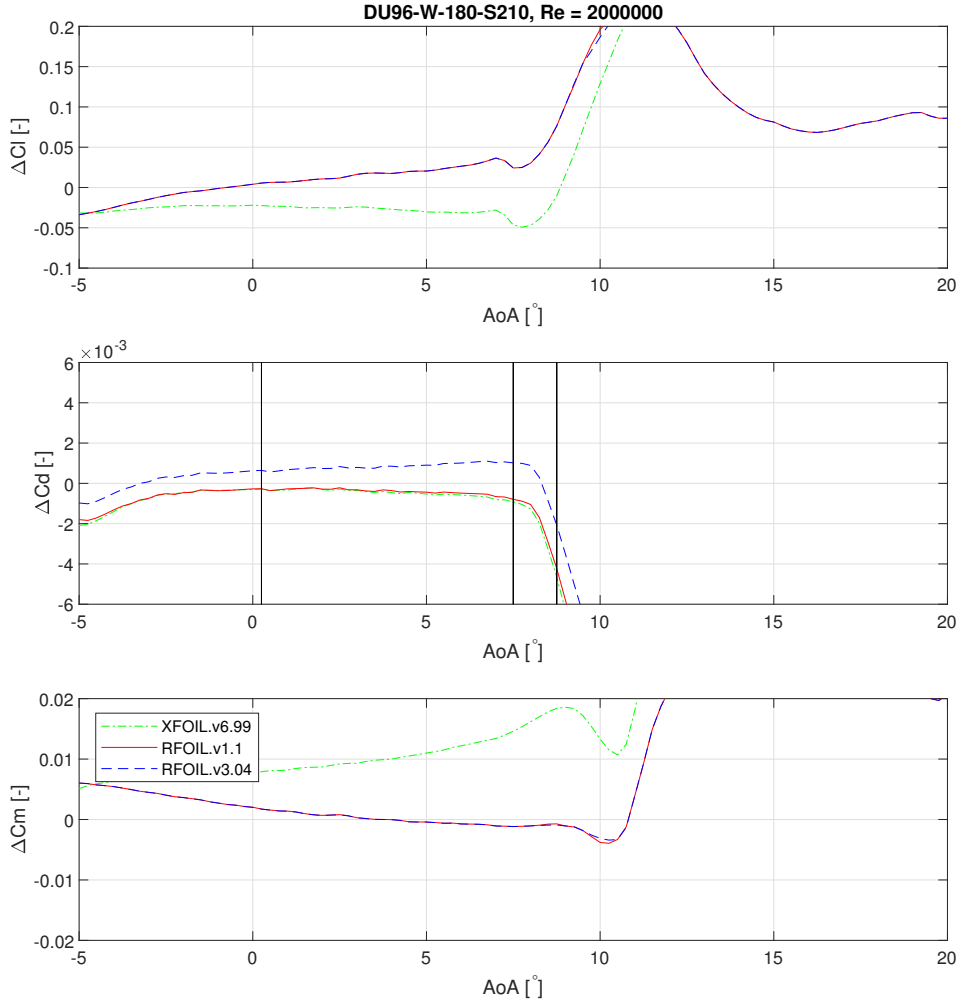

Figure B.111: Comparison between experimental and numerical pressure and skin friction distributions for the DU96-W-180-S210 airfoil at a Reynolds number of 2000000 and at the design angle of attack.

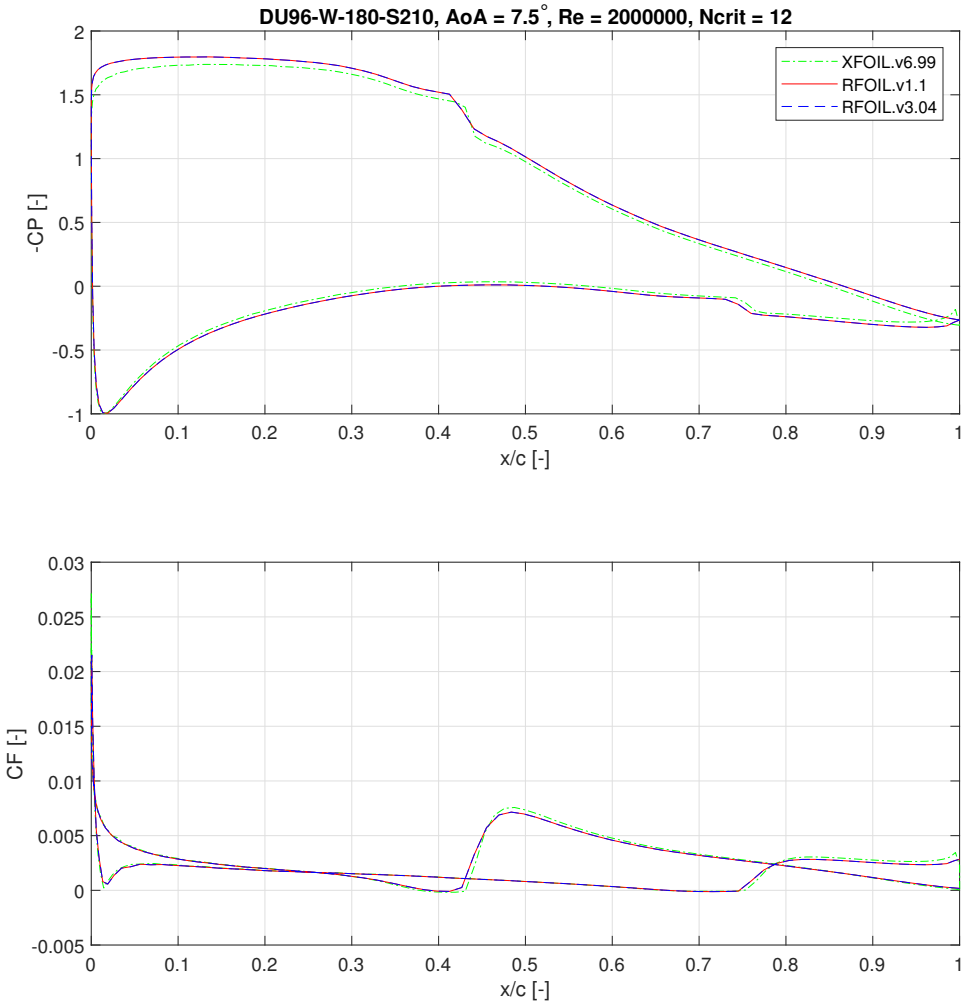

Figure B.112: Comparison between experimental and numerical polars for the DU96-W-180 airfoil at a Reynolds number of 1000000. Simulation time to generate the polars by means the different codes and the number of converged polar points are depicted between parentheses.

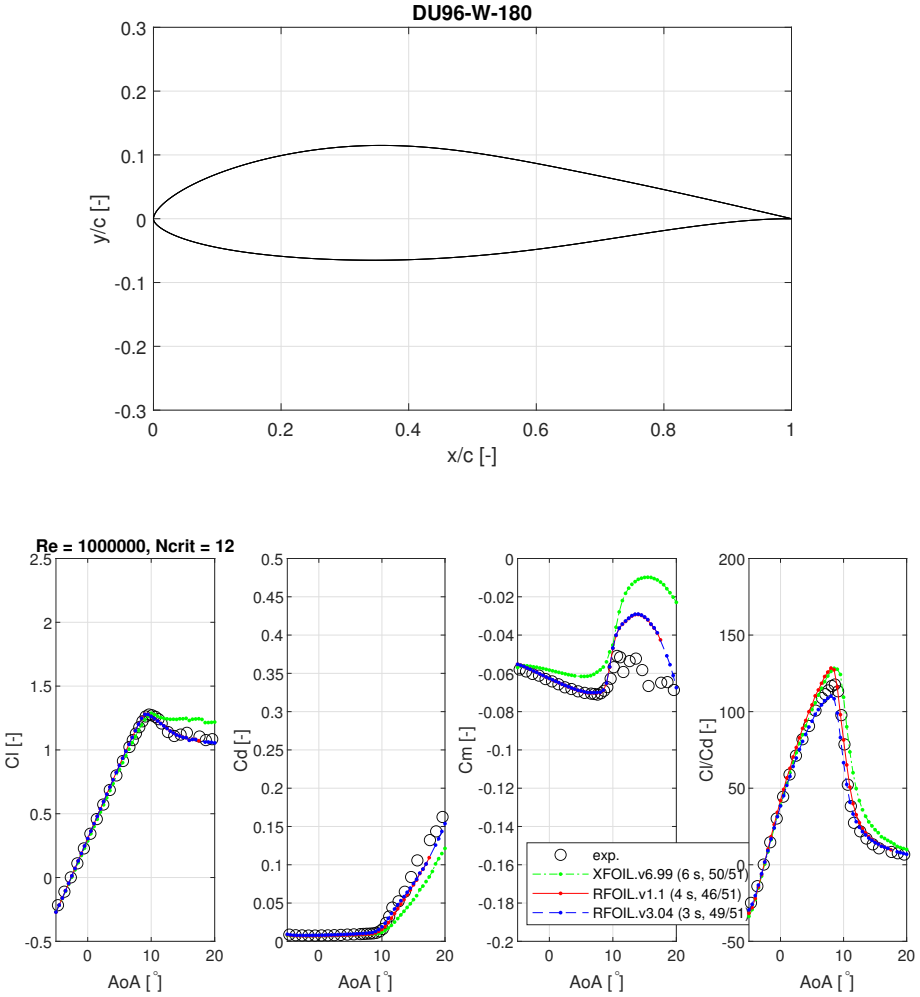

Figure B.113: Differences between experimental and numerical polars for the DU96-W-180 airfoil at a Reynolds number of 1000000. Vertical black lines in the middle subplot indicate, from left to right, the angle of attack corresponding to the minimum drag coefficient, maximum lift to drag ratio and maximum lift coefficient, respectively.

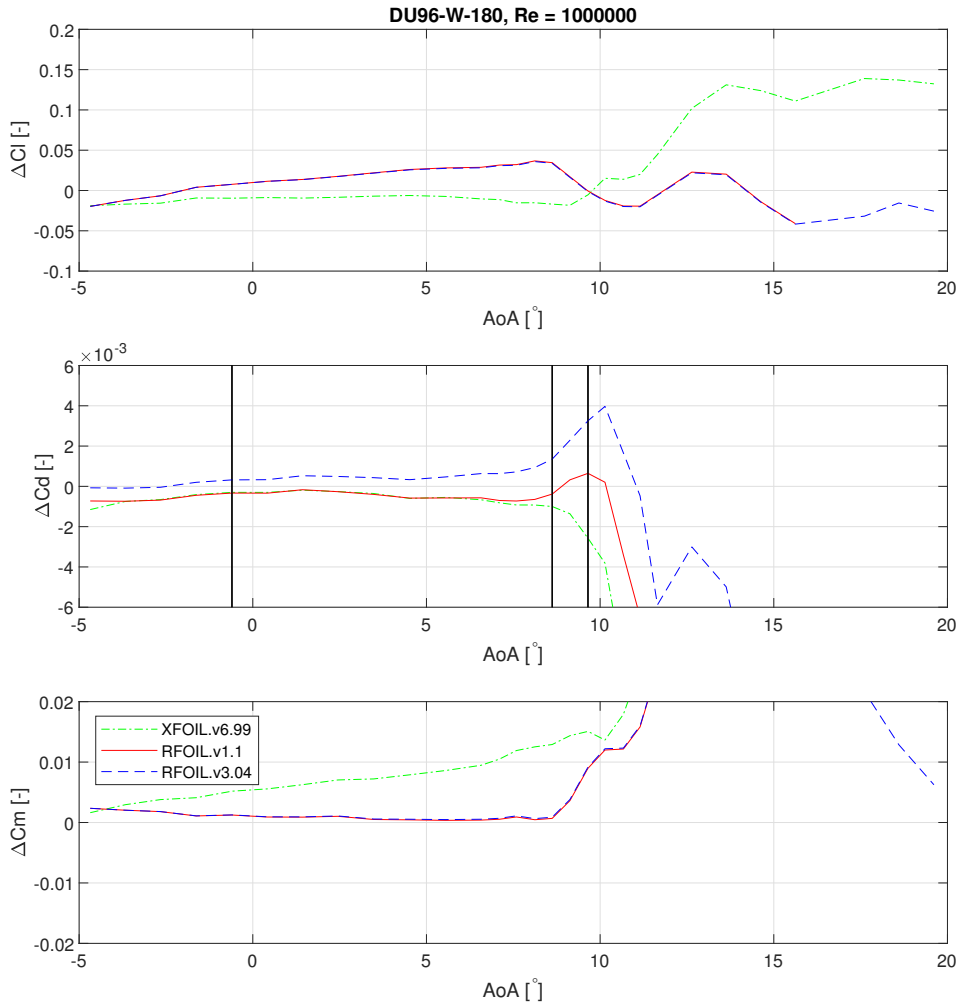

Figure B.114: Comparison between experimental and numerical pressure and skin friction distributions for the DU96-W-180 airfoil at a Reynolds number of 1000000 and at the design angle of attack.

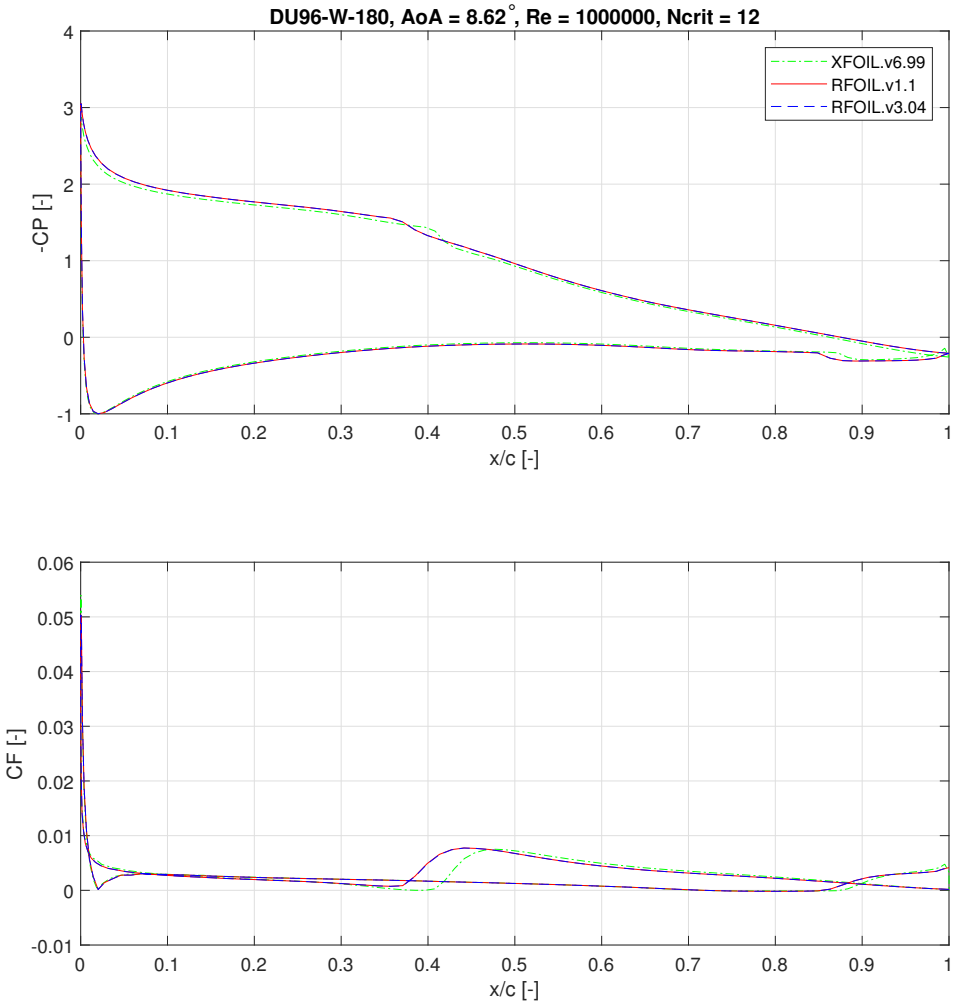

Figure B.115: Comparison between experimental and numerical polars for the DU96-W-180 airfoil at a Reynolds number of 2000000. Simulation time to generate the polars by means of the different codes and the number of converged polar points are depicted between parentheses.

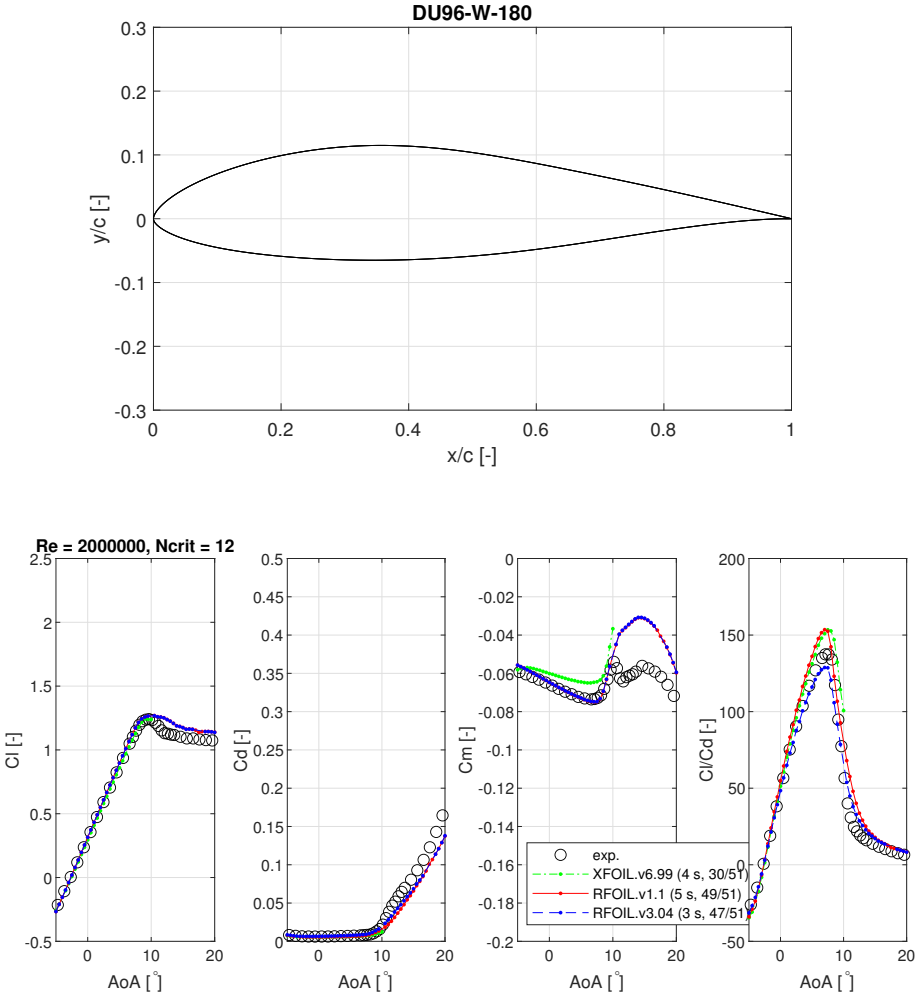

Figure B.116: Differences between experimental and numerical polars for the DU96-W-180 airfoil at a Reynolds number of 2000000. Vertical black lines in the middle subplot indicate, from left to right, the angle of attack corresponding to the minimum drag coefficient, maximum lift to drag ratio and maximum lift coefficient, respectively.

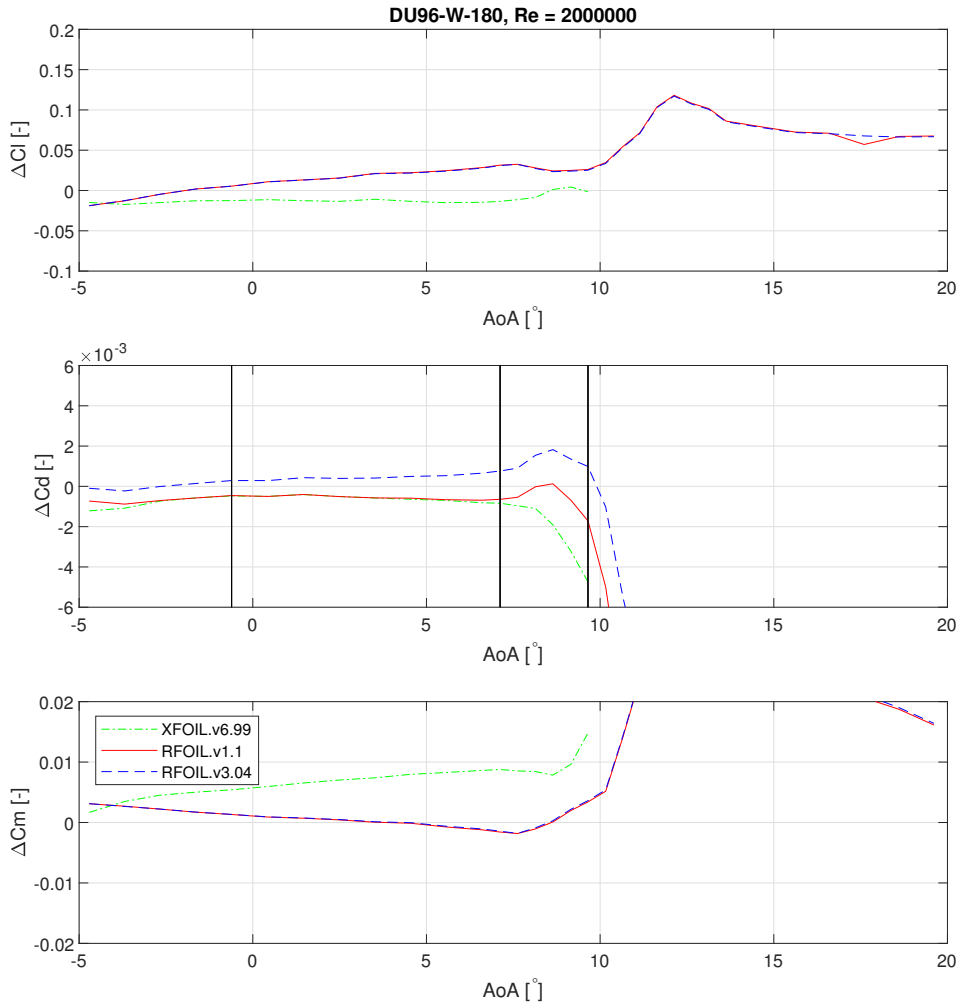

Figure B.117: Comparison between experimental and numerical pressure and skin friction distributions for the DU96-W-180 airfoil at a Reynolds number of 2000000 and at the design angle of attack.

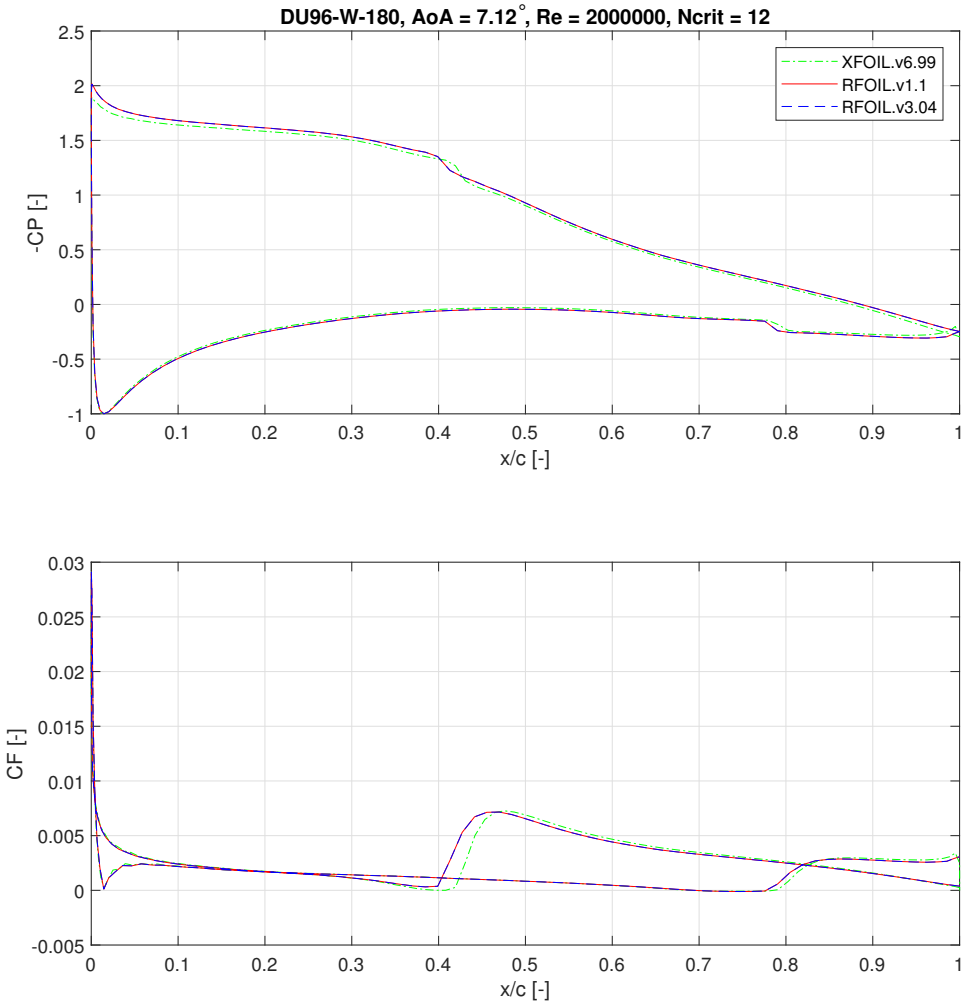

Figure B.118: Comparison between experimental and numerical polars for the DU96-W-180 airfoil at a Reynolds number of 3000000. Simulation time to generate the polars by means the different codes and the number of converged polar points are depicted between parentheses.

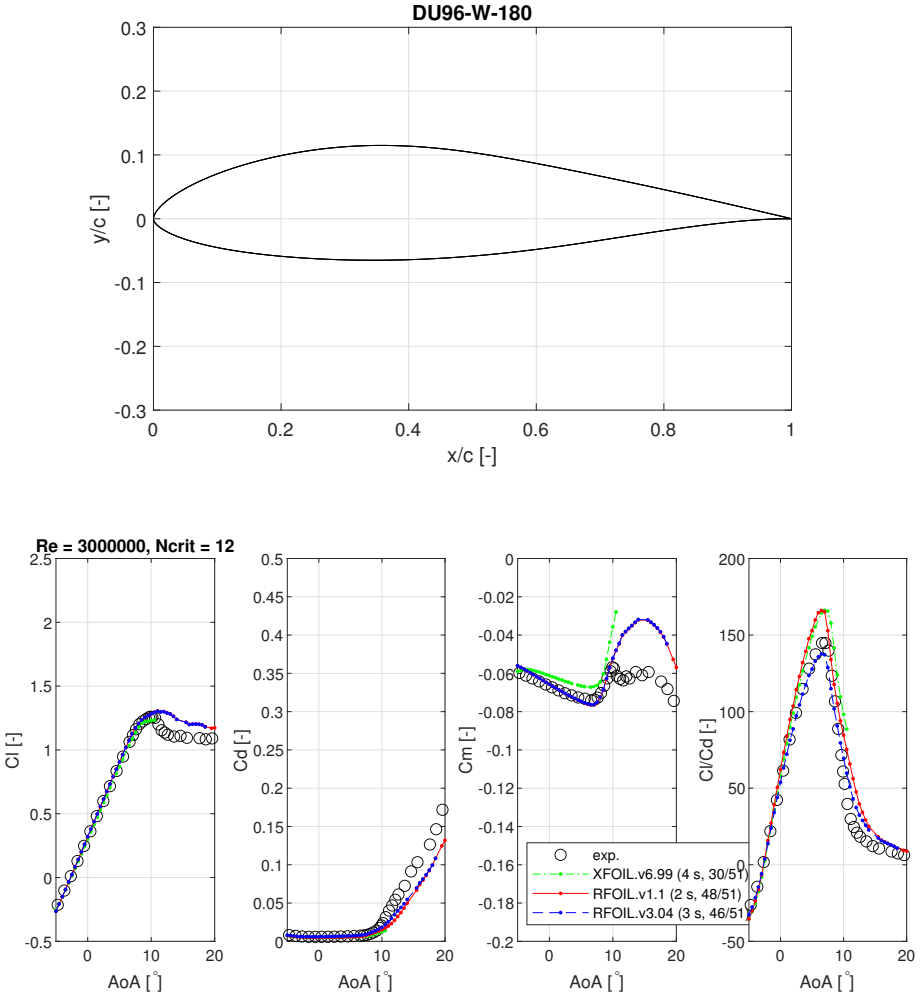

Figure B.119: Differences between experimental and numerical polars for the DU96-W-180 airfoil at a Reynolds number of 3000000. Vertical black lines in the middle subplot indicate, from left to right, the angle of attack corresponding to the minimum drag coefficient, maximum lift to drag ratio and maximum lift coefficient, respectively.

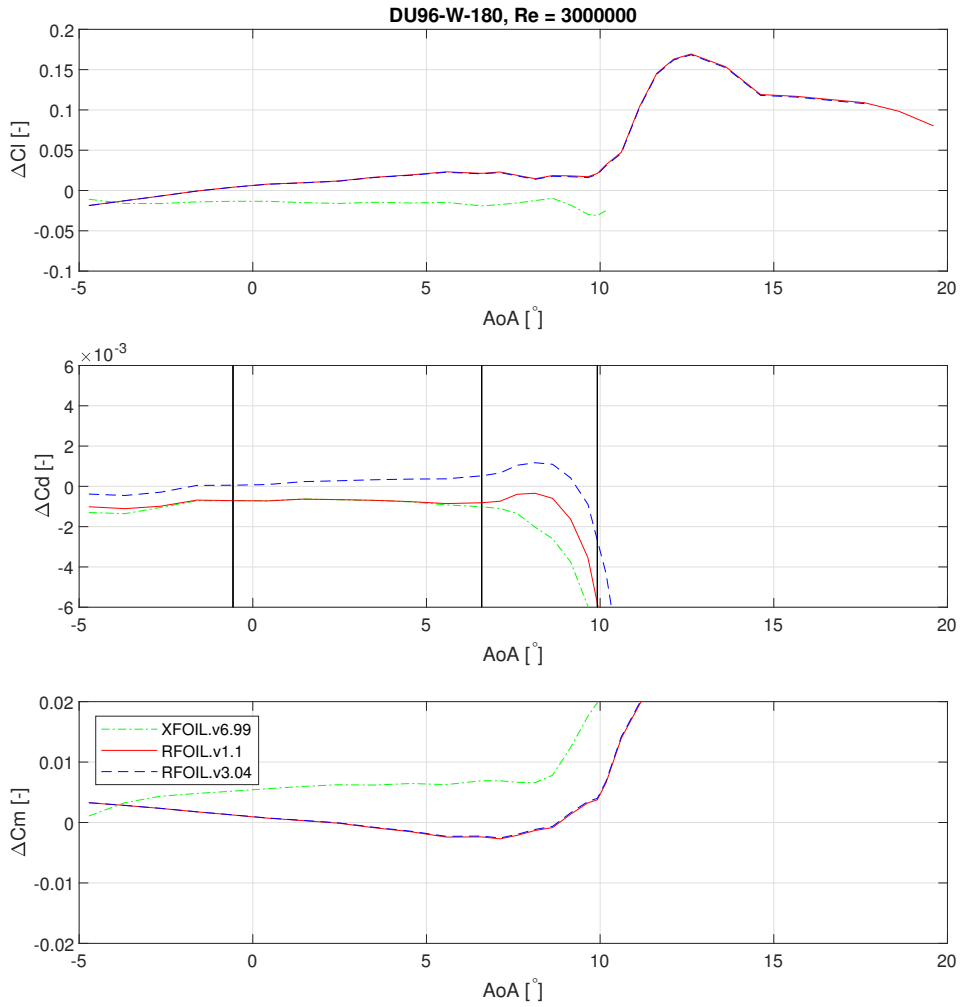

Figure B.120: Comparison between experimental and numerical pressure and skin friction distributions for the DU96-W-180 airfoil at a Reynolds number of 3000000 and at the design angle of attack.

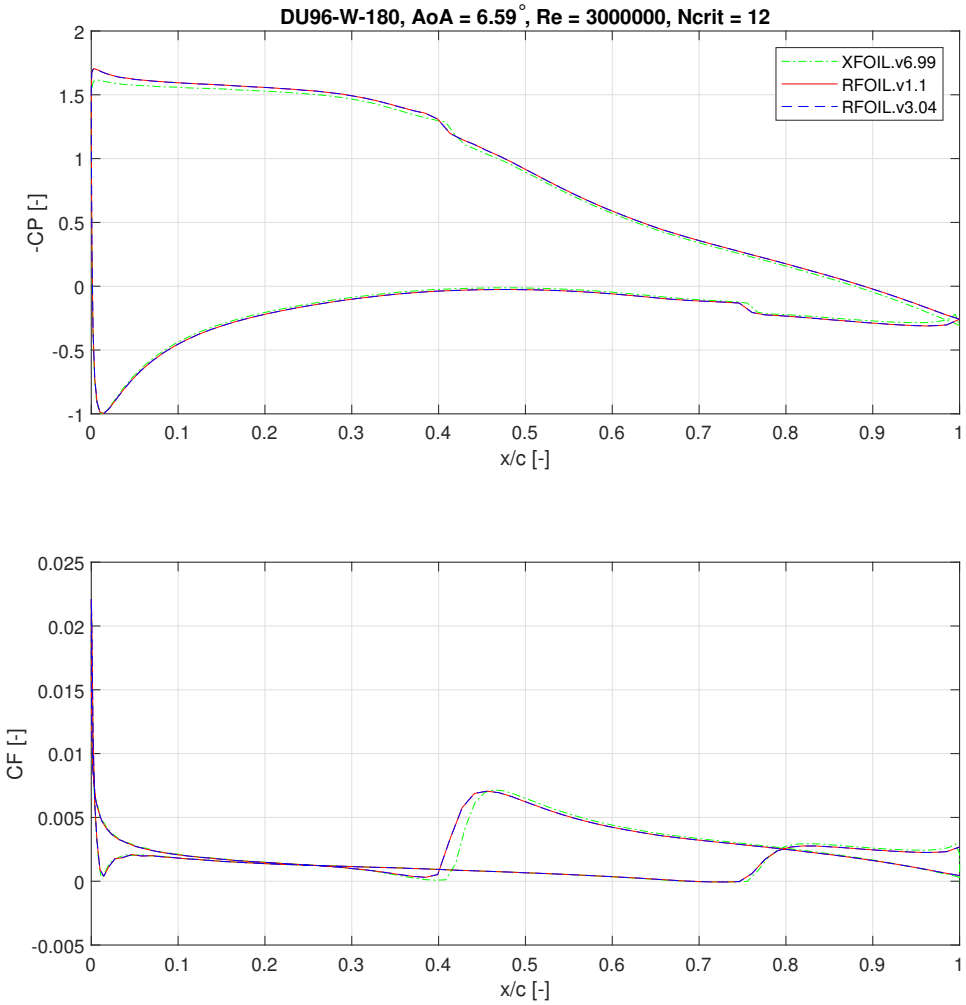

Figure B.121: Comparison between experimental and numerical polars for the DU97-W-300 airfoil at a Reynolds number of 1000000. Simulation time to generate the polars by means the different codes and the number of converged polar points are depicted between parentheses.

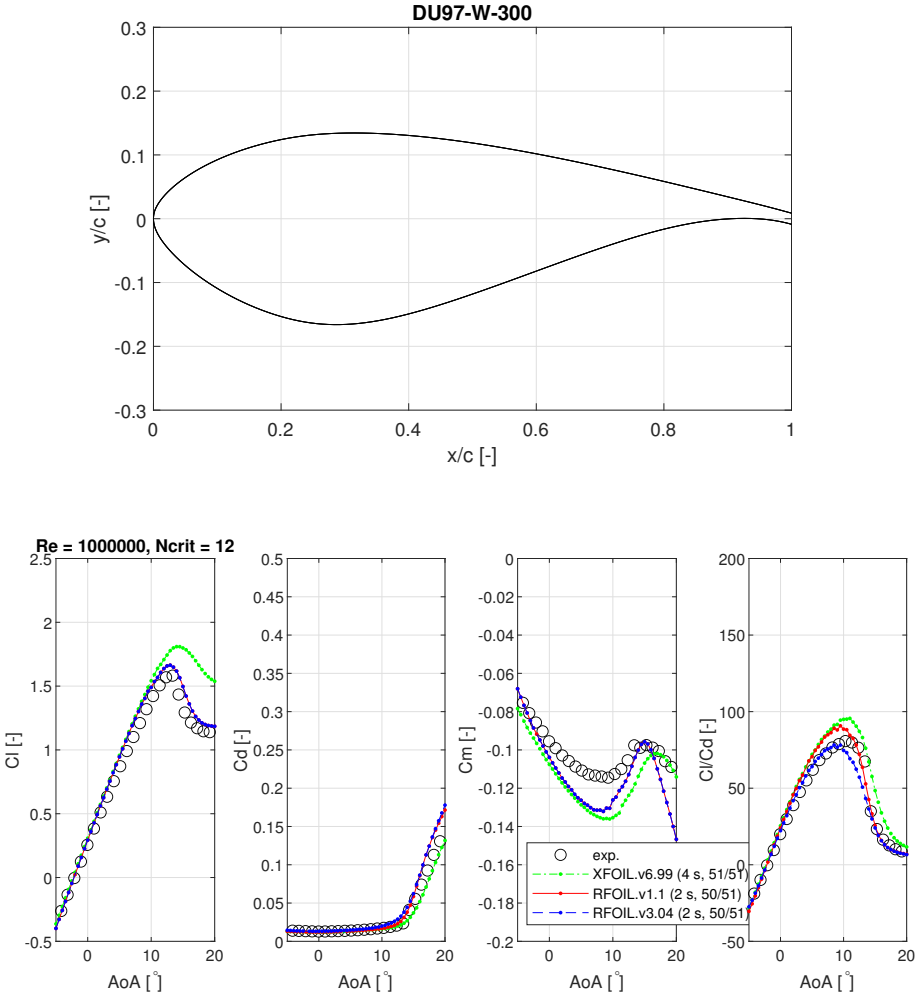

Figure B.122: Differences between experimental and numerical polars for the DU97-W-300 airfoil at a Reynolds number of 1000000. Vertical black lines in the middle subplot indicate, from left to right, the angle of attack corresponding to the minimum drag coefficient, maximum lift to drag ratio and maximum lift coefficient, respectively.

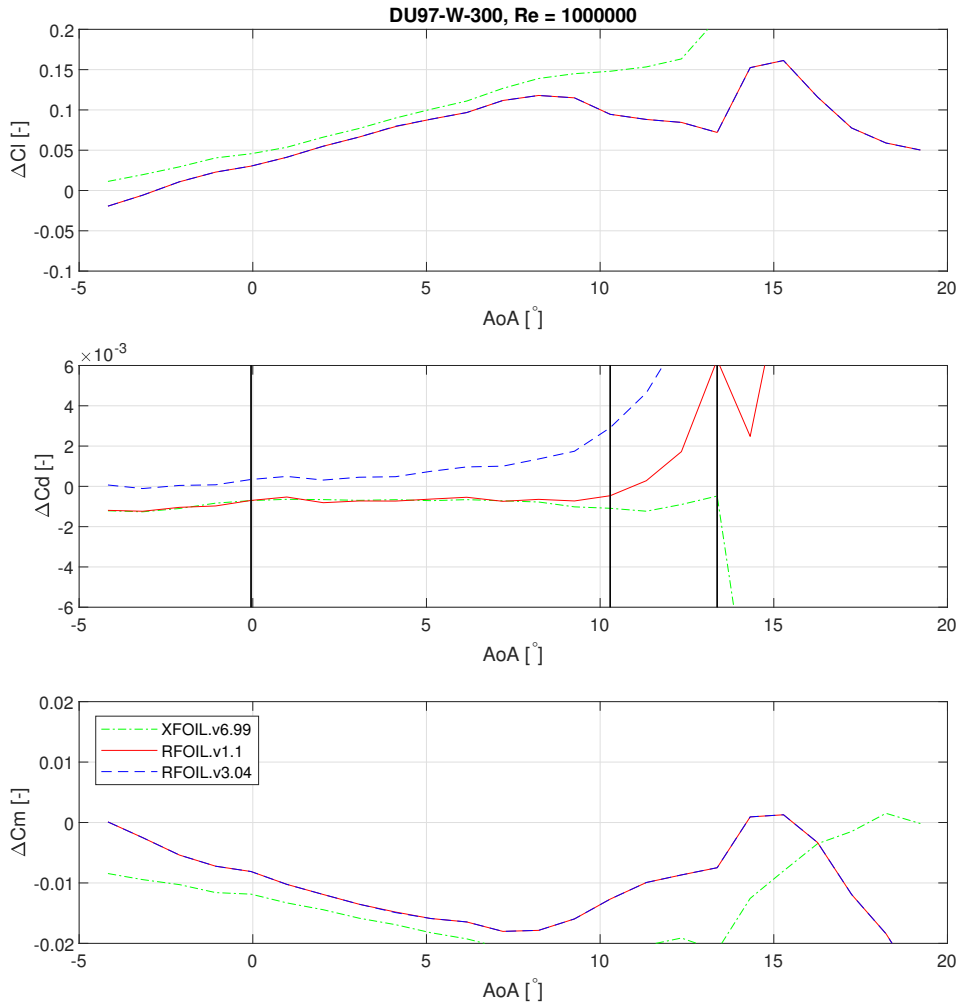

Figure B.123: Comparison between experimental and numerical pressure and skin friction distributions for the DU97-W-300 airfoil at a Reynolds number of 1000000 and at the design angle of attack.

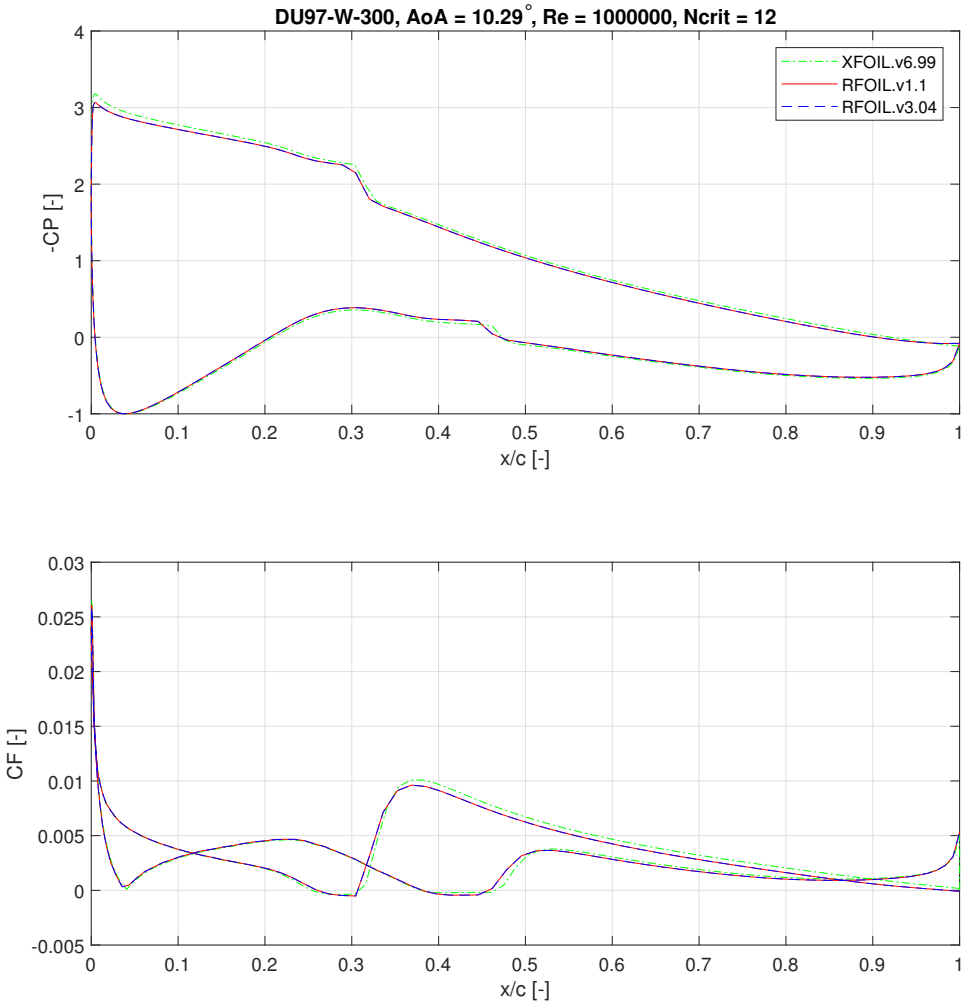

Figure B.124: Comparison between experimental and numerical polars for the DU97-W-300 airfoil at a Reynolds number of 2000000. Simulation time to generate the polars by means the different codes and the number of converged polar points are depicted between parentheses.

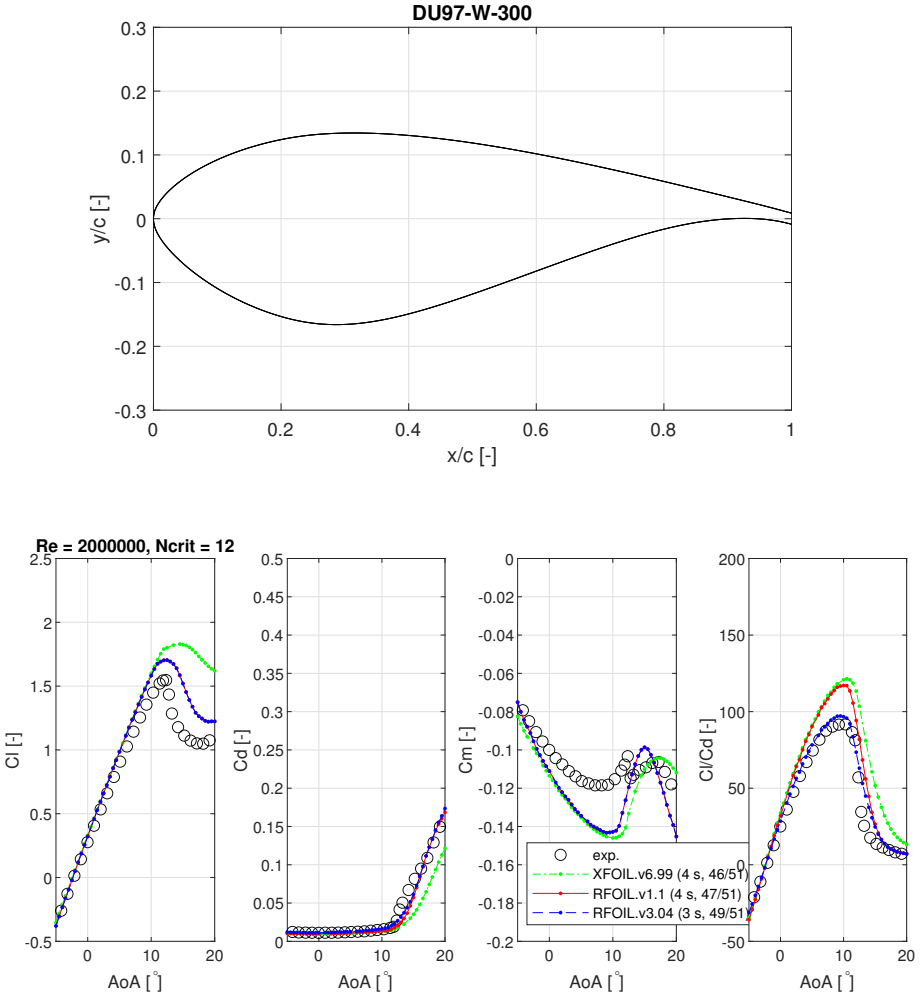

Figure B.125: Differences between experimental and numerical polars for the DU97-W-300 airfoil at a Reynolds number of 2000000. Vertical black lines in the middle subplot indicate, from left to right, the angle of attack corresponding to the minimum drag coefficient, maximum lift to drag ratio and maximum lift coefficient, respectively.

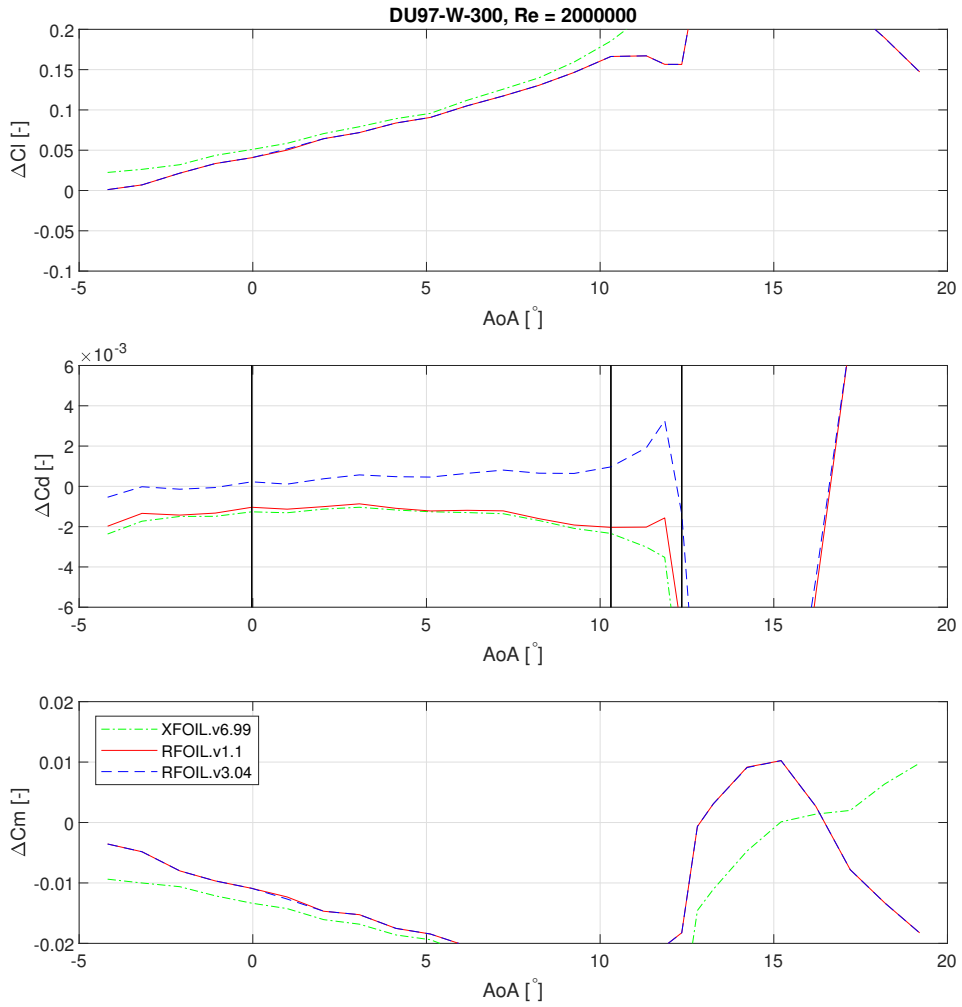

Figure B.126: Comparison between experimental and numerical pressure and skin friction distributions for the DU97-W-300 airfoil at a Reynolds number of 2000000 and at the design angle of attack.

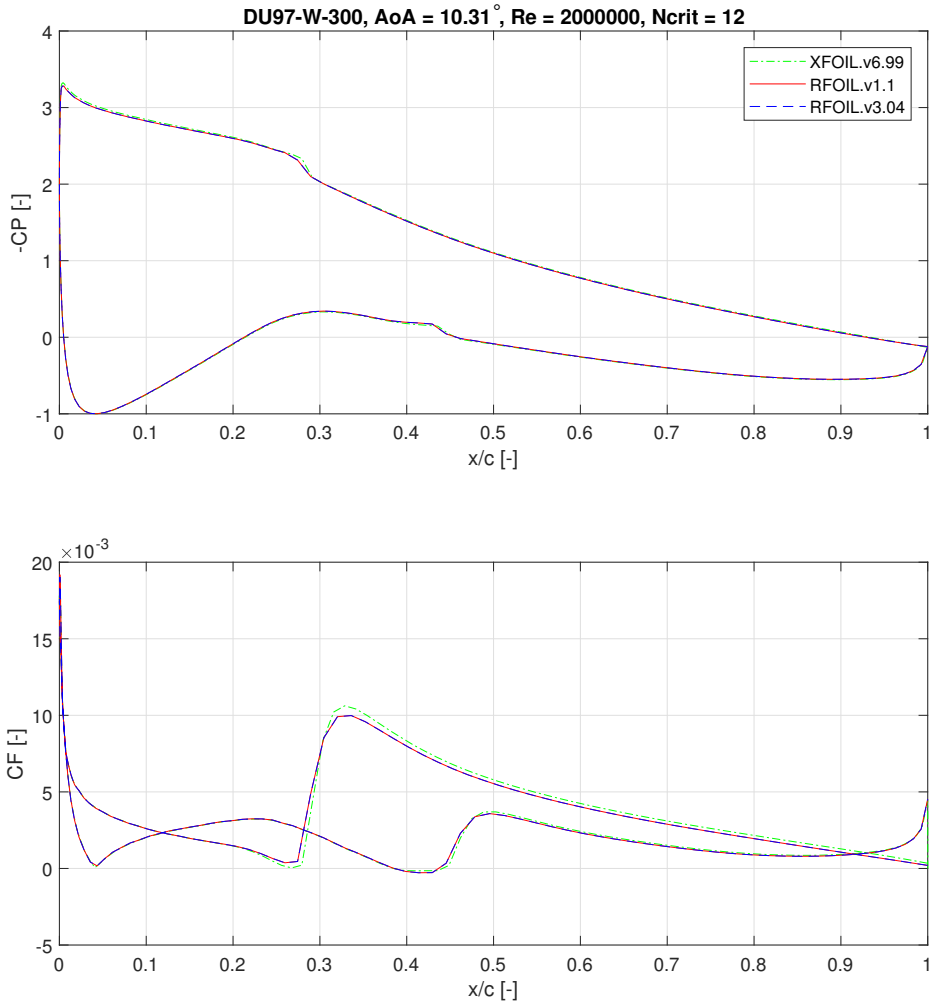

Figure B.127: Comparison between experimental and numerical polars for the DU97-W-300 airfoil at a Reynolds number of 3000000. Simulation time to generate the polars by means the different codes and the number of converged polar points are depicted between parentheses.

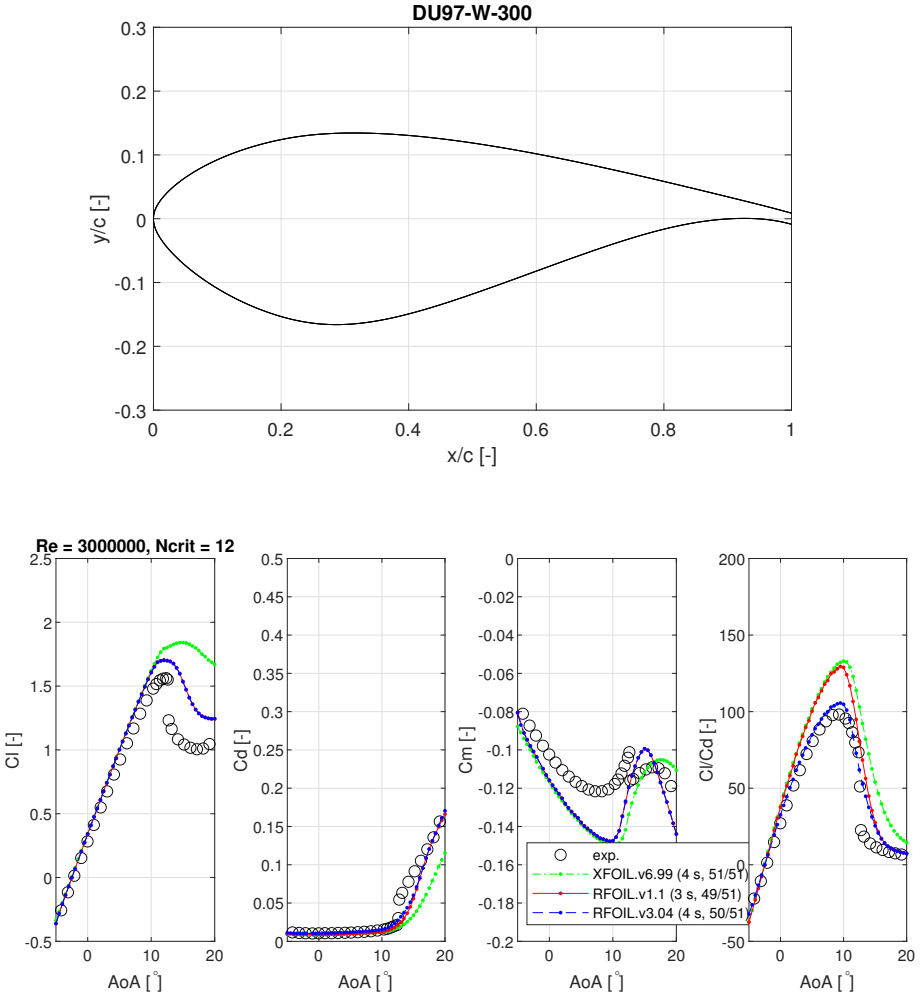

Figure B.128: Differences between experimental and numerical polars for the DU97-W-300 airfoil at a Reynolds number of 3000000. Vertical black lines in the middle subplot indicate, from left to right, the angle of attack corresponding to the minimum drag coefficient, maximum lift to drag ratio and maximum lift coefficient, respectively.

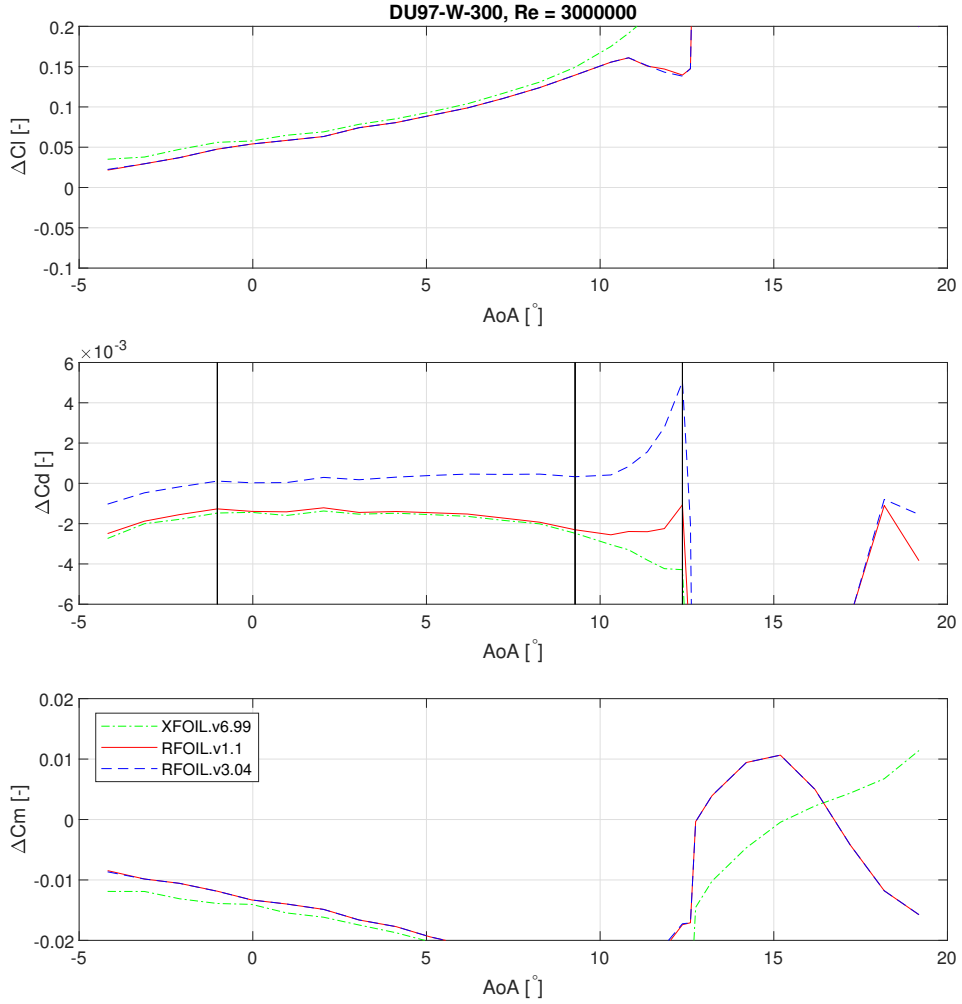

Figure B.129: Comparison between experimental and numerical pressure and skin friction distributions for the DU97-W-300 airfoil at a Reynolds number of 3000000 and at the design angle of attack.

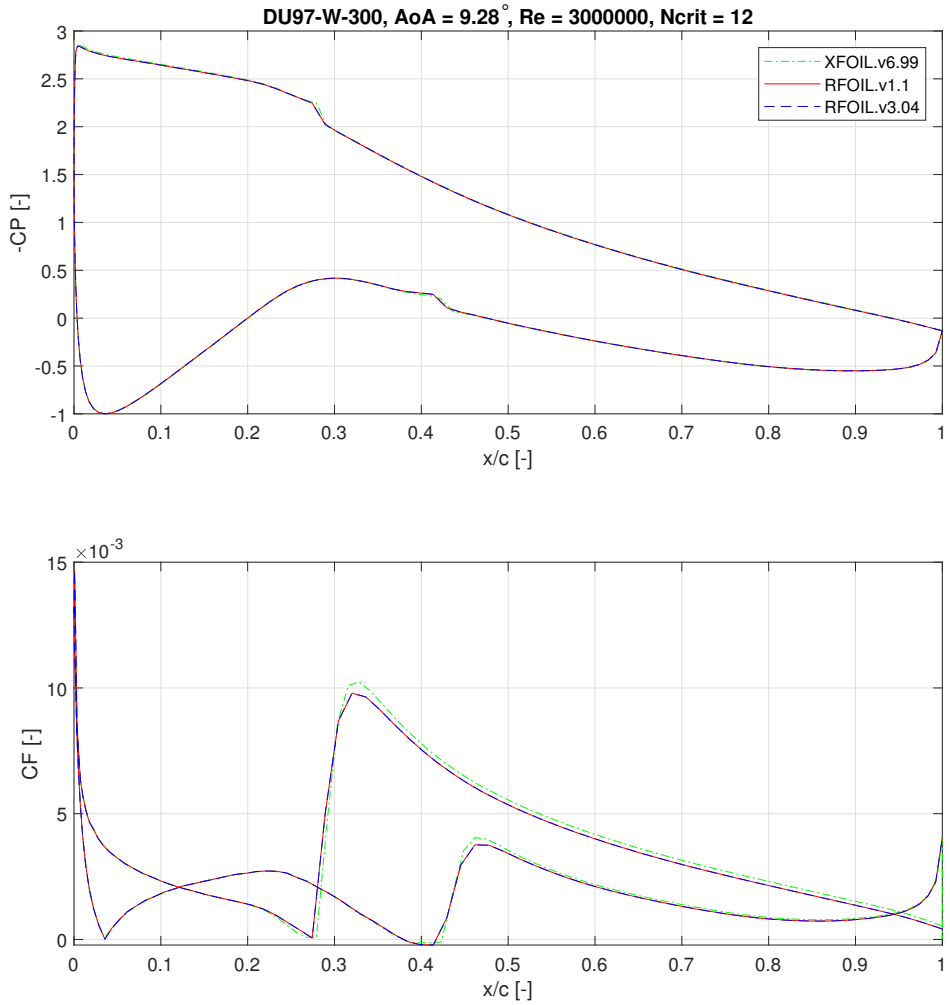

Figure B.130: Comparison between experimental and numerical polars for the DU97-W-300 airfoil at a Reynolds number of 7000000. Simulation time to generate the polars by means the different codes and the number of converged polar points are depicted between parentheses.

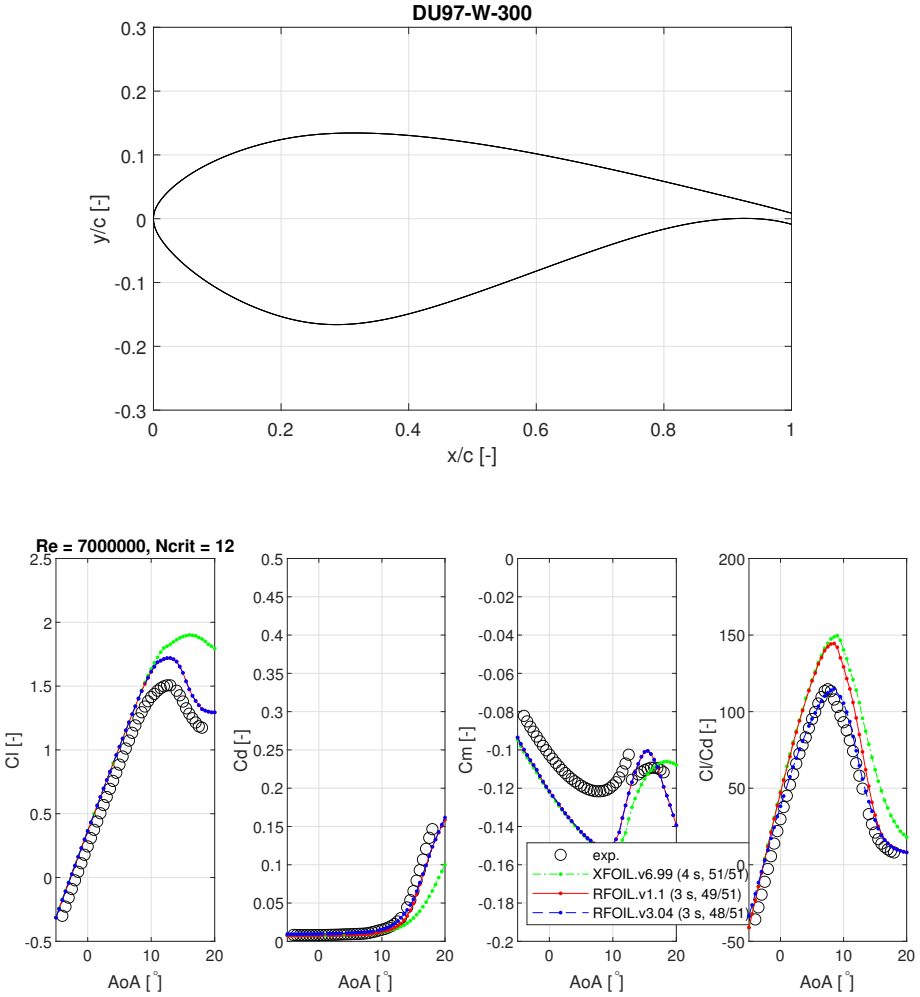

Figure B.131: Differences between experimental and numerical polars for the DU97-W-300 airfoil at a Reynolds number of 7000000. Vertical black lines in the middle subplot indicate, from left to right, the angle of attack corresponding to the minimum drag coefficient, maximum lift to drag ratio and maximum lift coefficient, respectively.

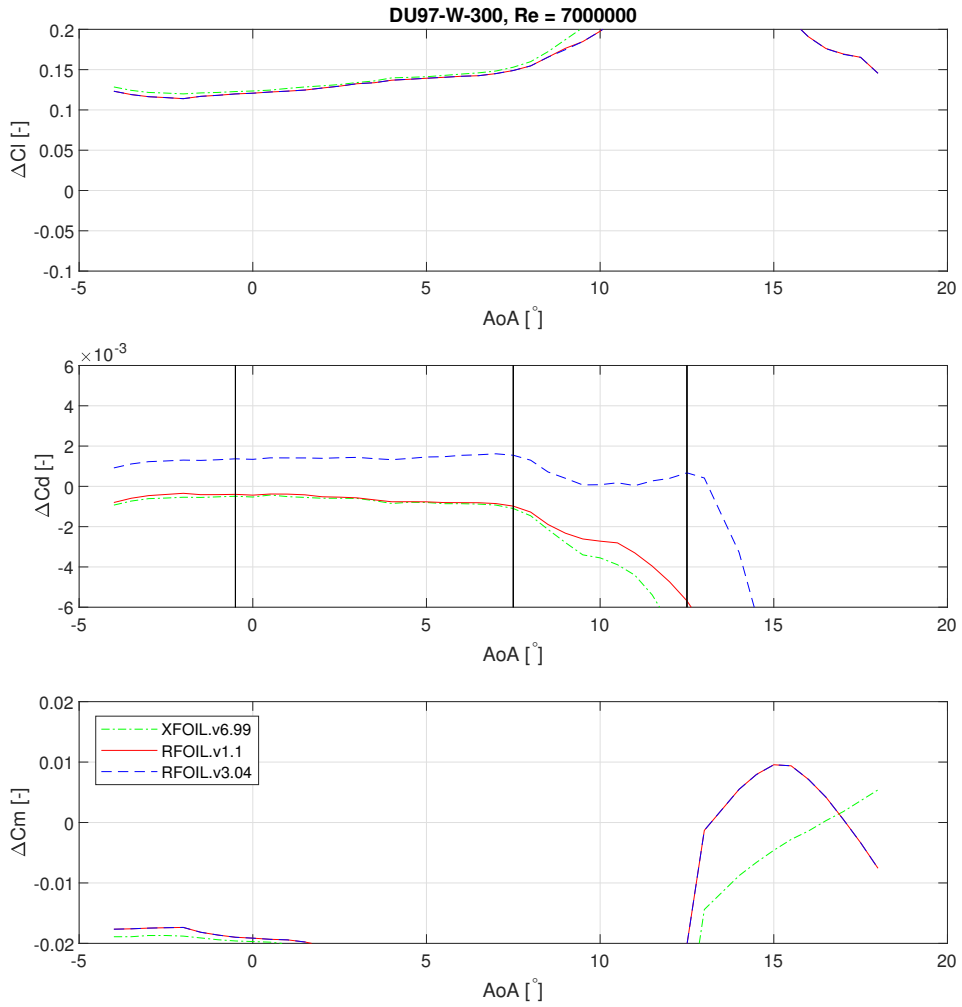

Figure B.132: Comparison between experimental and numerical pressure and skin friction distributions for the DU97-W-300 airfoil at a Reynolds number of 7000000 and at the design angle of attack.

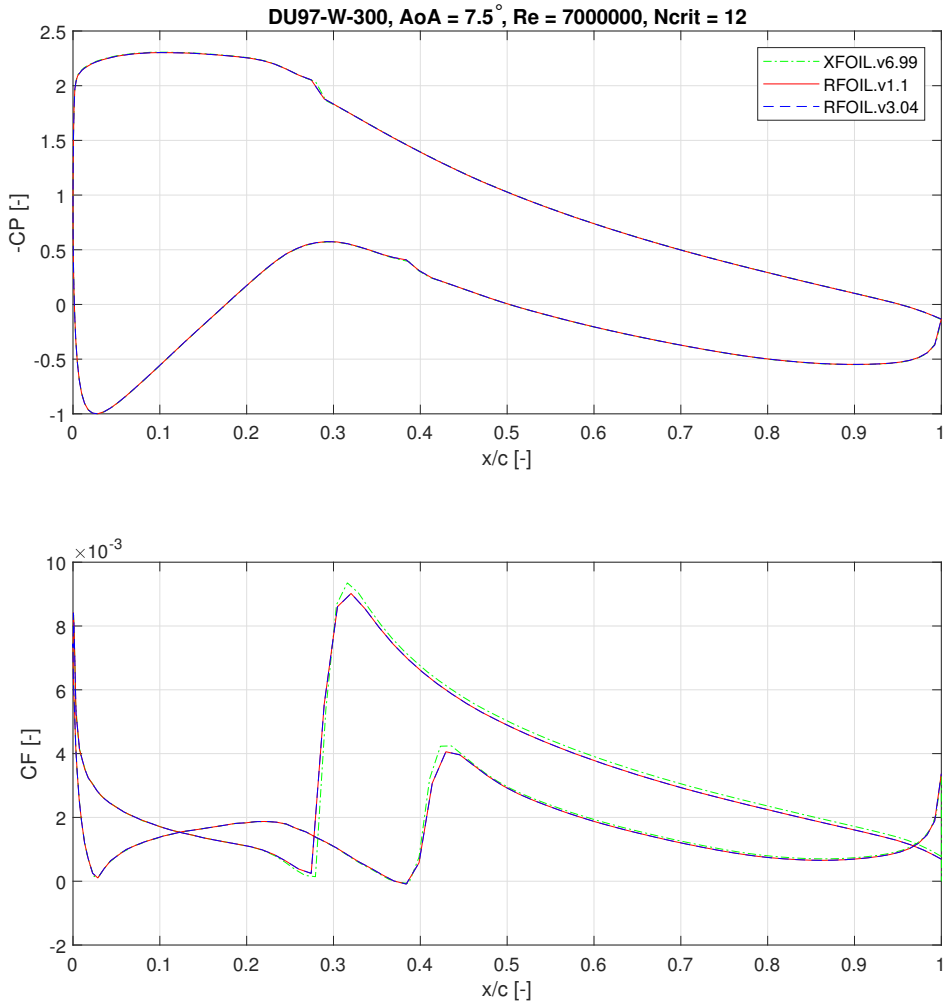

Figure B.133: Comparison between experimental and numerical polars for the DU97-W-300 airfoil at a Reynolds number of 9800000. Simulation time to generate the polars by means the different codes and the number of converged polar points are depicted between parentheses.

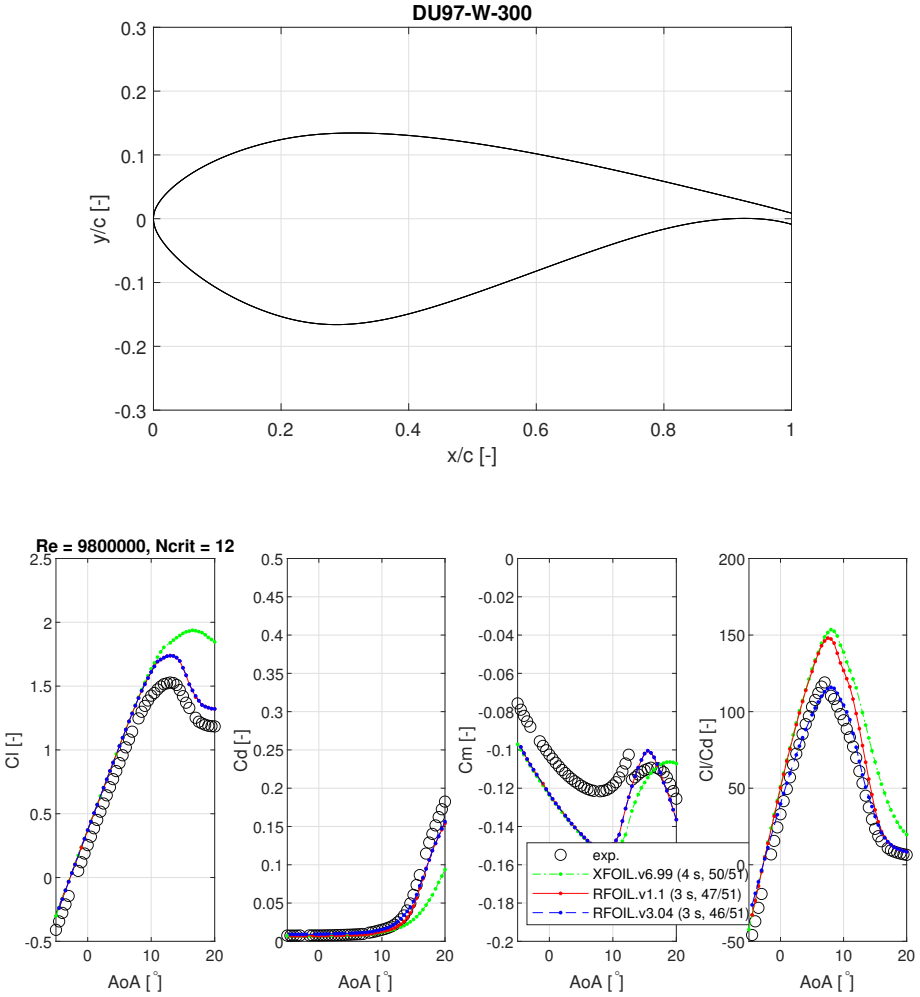

Figure B.134: Differences between experimental and numerical polars for the DU97-W-300 airfoil at a Reynolds number of 9800000. Vertical black lines in the middle subplot indicate, from left to right, the angle of attack corresponding to the minimum drag coefficient, maximum lift to drag ratio and maximum lift coefficient, respectively.

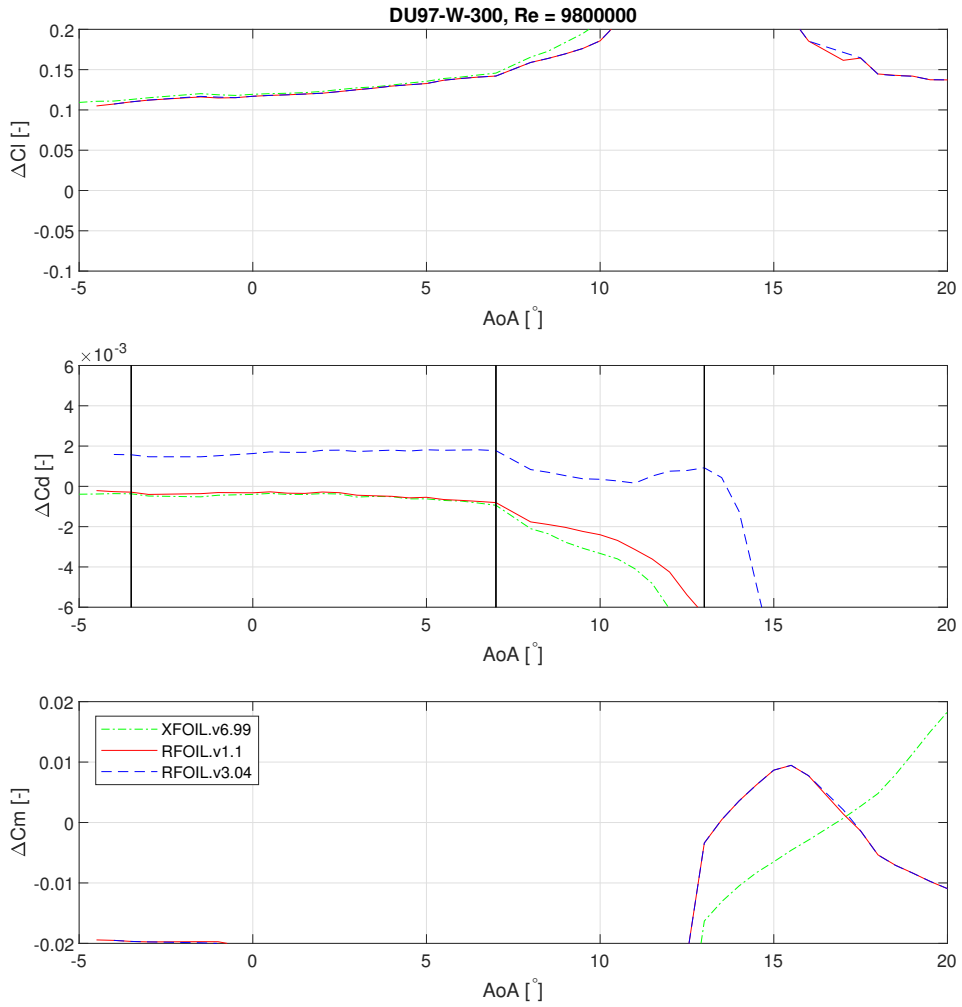

Figure B.135: Comparison between experimental and numerical pressure and skin friction distributions for the DU97-W-300 airfoil at a Reynolds number of 9800000 and at the design angle of attack.

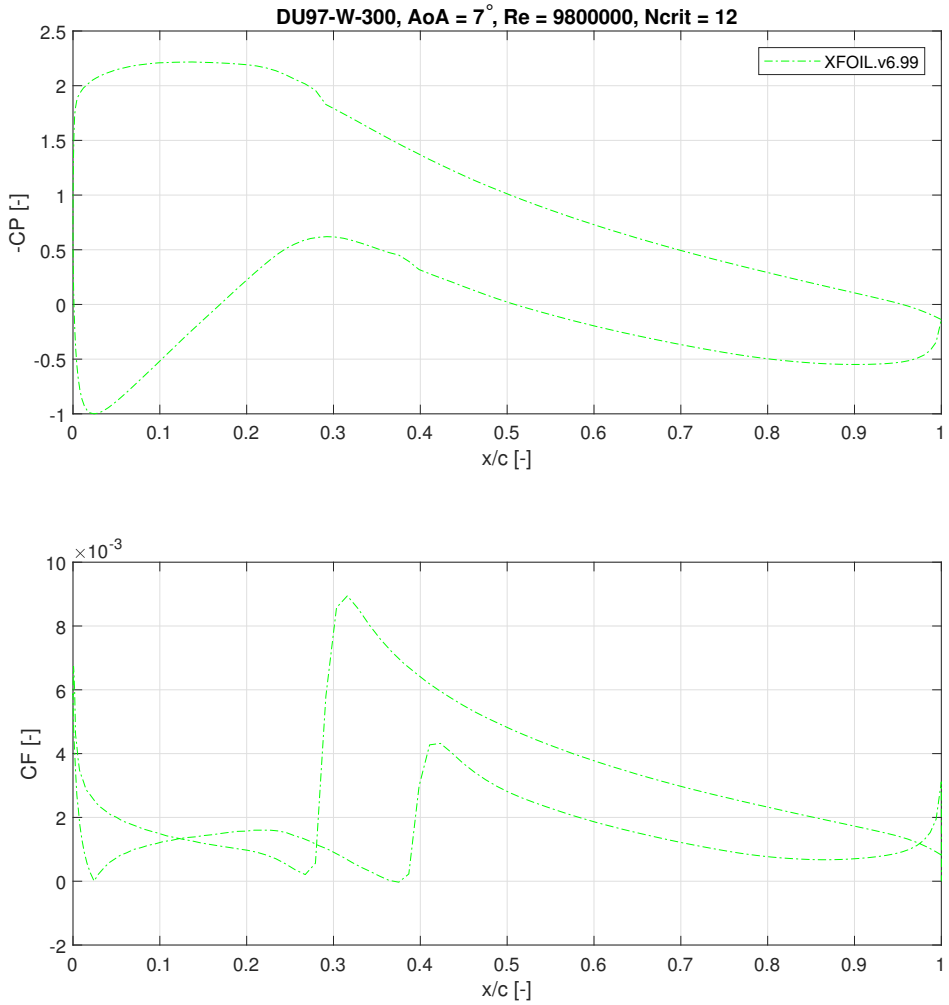

B.3 FFA Airfoils

Figure B.136: Comparison between experimental and numerical polars for the FFA-W3-211 airfoil at a Reynolds number of 1800000. Simulation time to generate the polars by means the different codes and the number of converged polar points are depicted between parentheses.

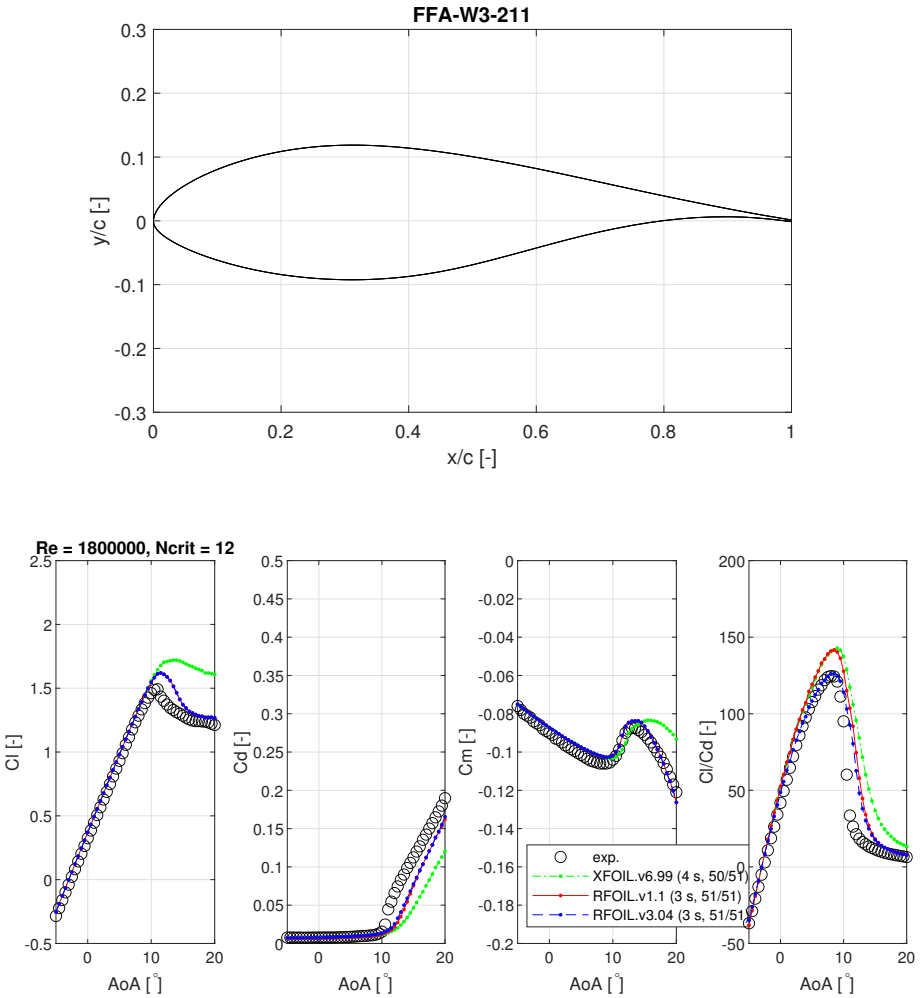

Figure B.137: Differences between experimental and numerical polars for the FFA-W3-211 airfoil at a Reynolds number of 1800000. Vertical black lines in the middle subplot indicate, from left to right, the angle of attack corresponding to the minimum drag coefficient, maximum lift to drag ratio and maximum lift coefficient, respectively.

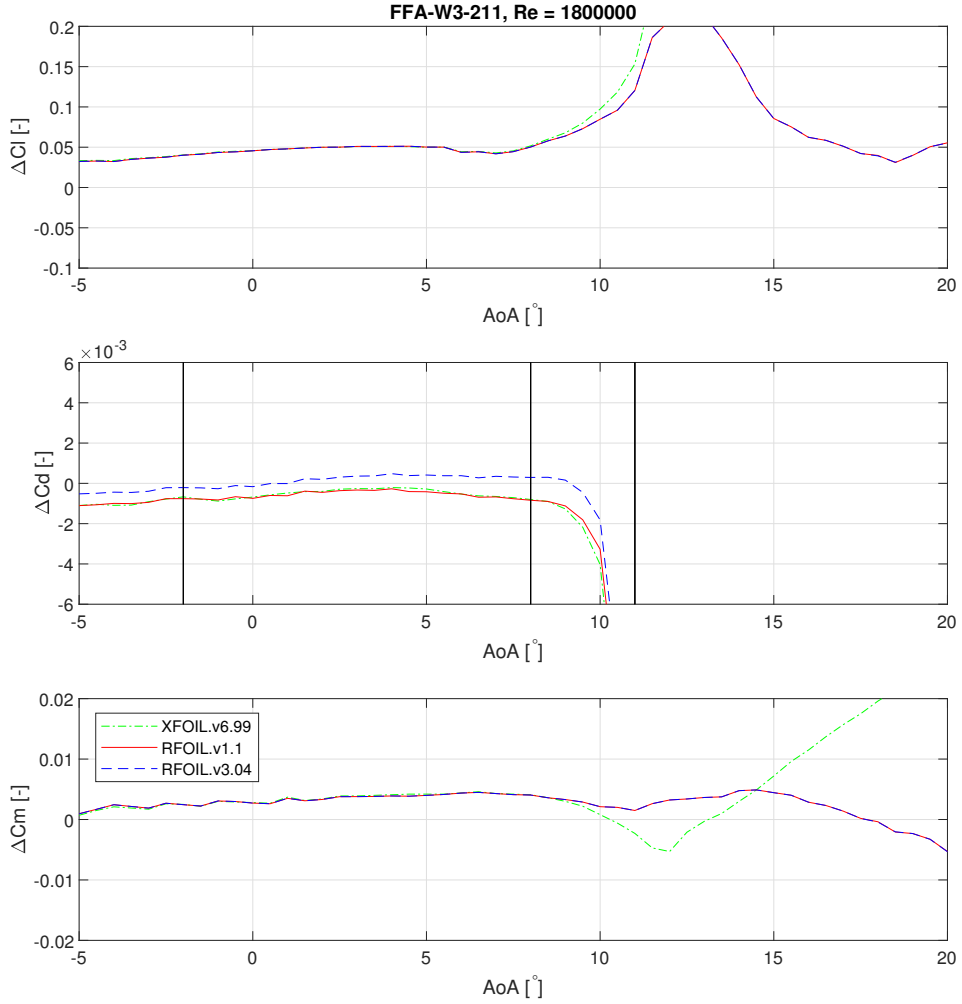

Figure B.138: Comparison between experimental and numerical pressure and skin friction distributions for the FFA-W3-211 airfoil at a Reynolds number of 1800000 and at the design angle of attack.

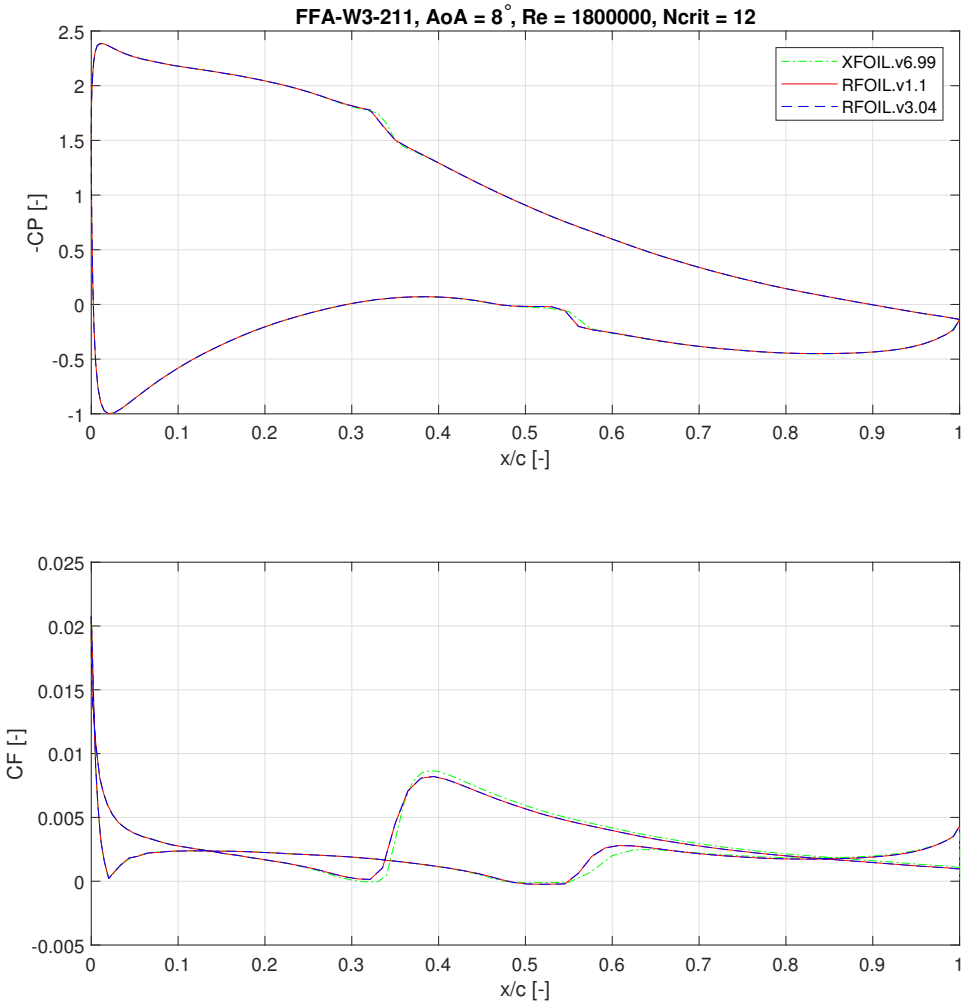

Figure B.139: Comparison between experimental and numerical polars for the FFA-W3-211 airfoil at a Reynolds number of 4000000. Simulation time to generate the polars by means the different codes and the number of converged polar points are depicted between parentheses.

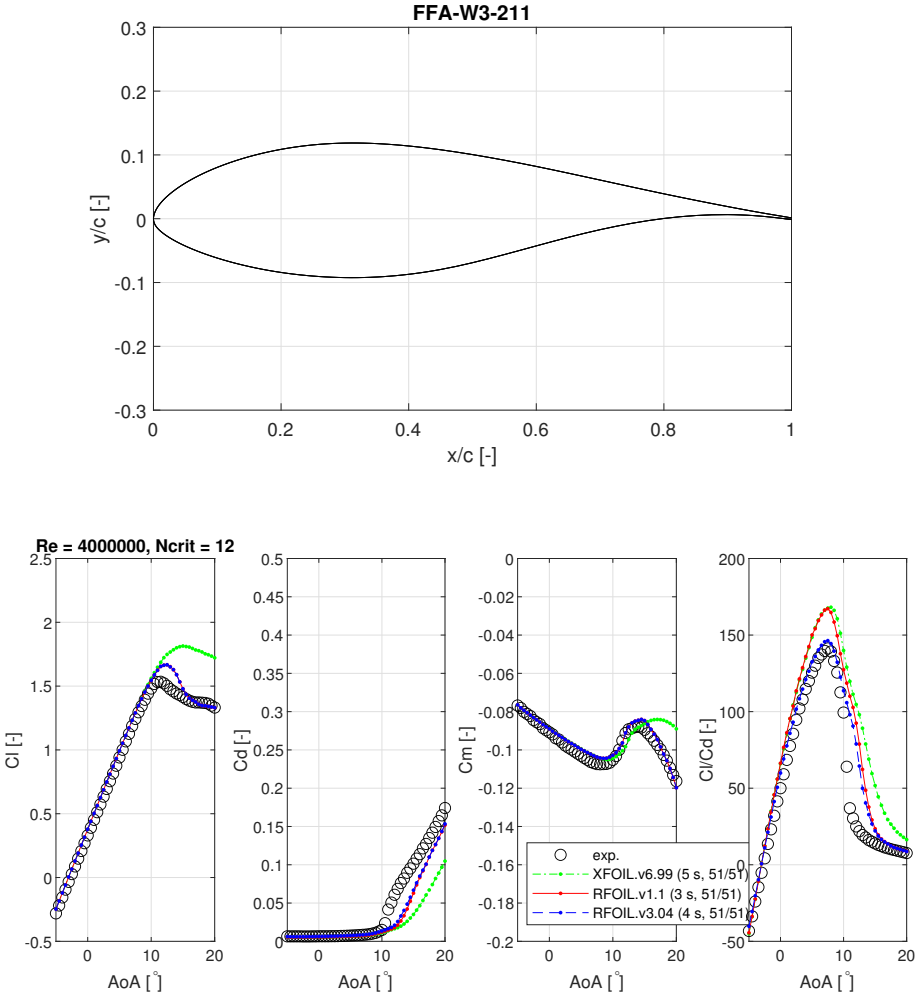

Figure B.140: Differences between experimental and numerical polars for the FFA-W3-211 airfoil at a Reynolds number of 4000000. Vertical black lines in the middle subplot indicate, from left to right, the angle of attack corresponding to the minimum drag coefficient, maximum lift to drag ratio and maximum lift coefficient, respectively.

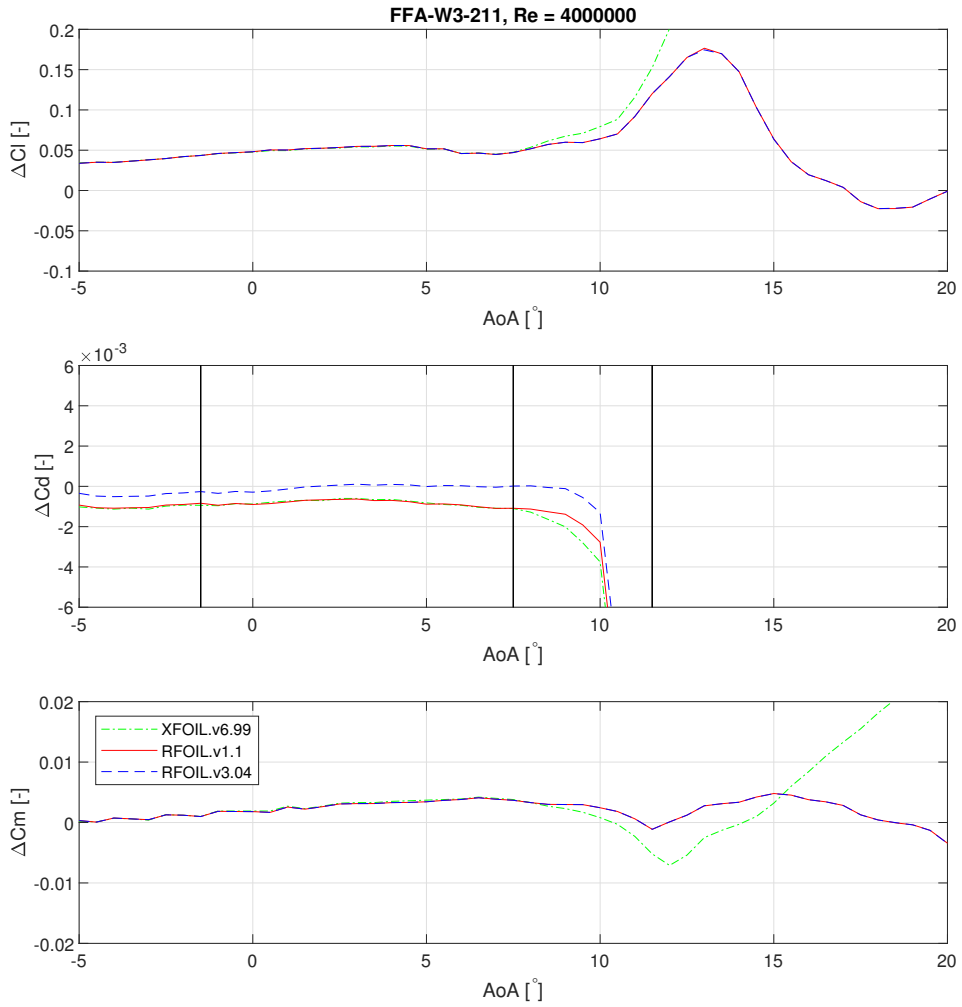

Figure B.141: Comparison between experimental and numerical pressure and skin friction distributions for the FFA-W3-211 airfoil at a Reynolds number of 4000000 and at the design angle of attack.

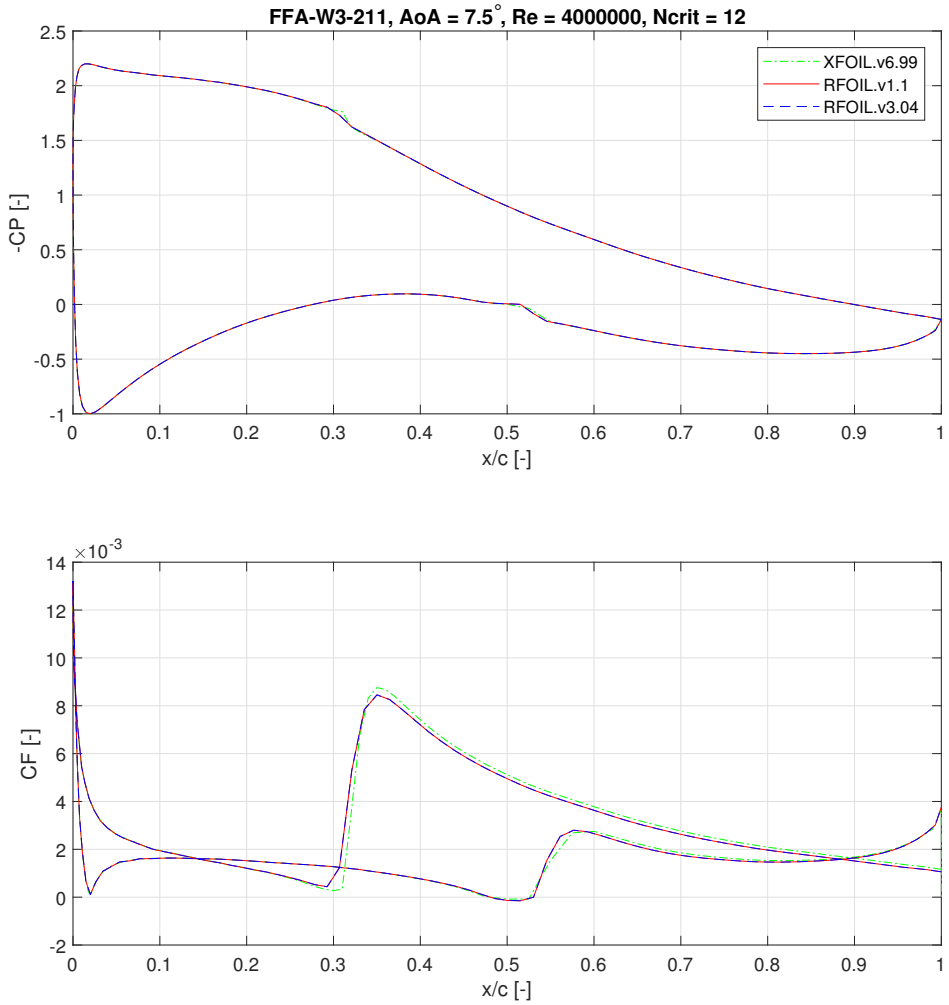

Figure B.142: Comparison between experimental and numerical polars for the FFA-W3-211 airfoil at a Reynolds number of 6000000. Simulation time to generate the polars by means the different codes and the number of converged polar points are depicted between parentheses.

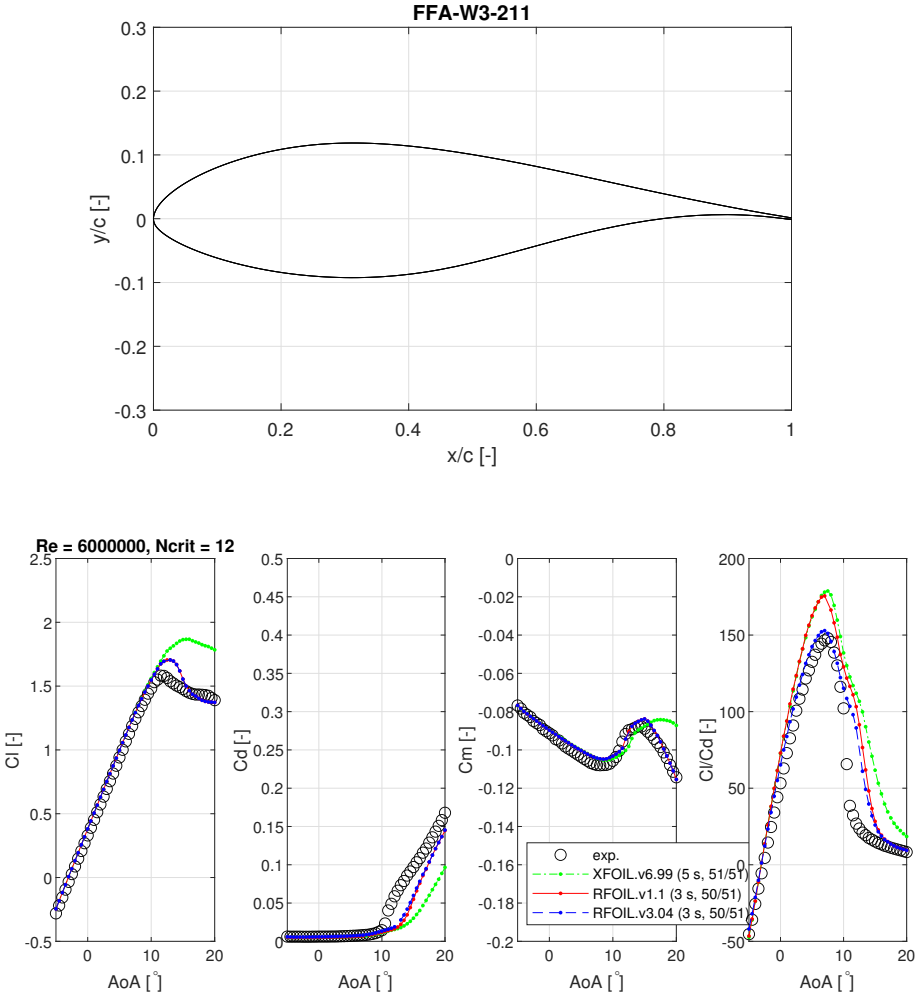

Figure B.143: Differences between experimental and numerical polars for the FFA-W3-211 airfoil at a Reynolds number of 6000000. Vertical black lines in the middle subplot indicate, from left to right, the angle of attack corresponding to the minimum drag coefficient, maximum lift to drag ratio and maximum lift coefficient, respectively.

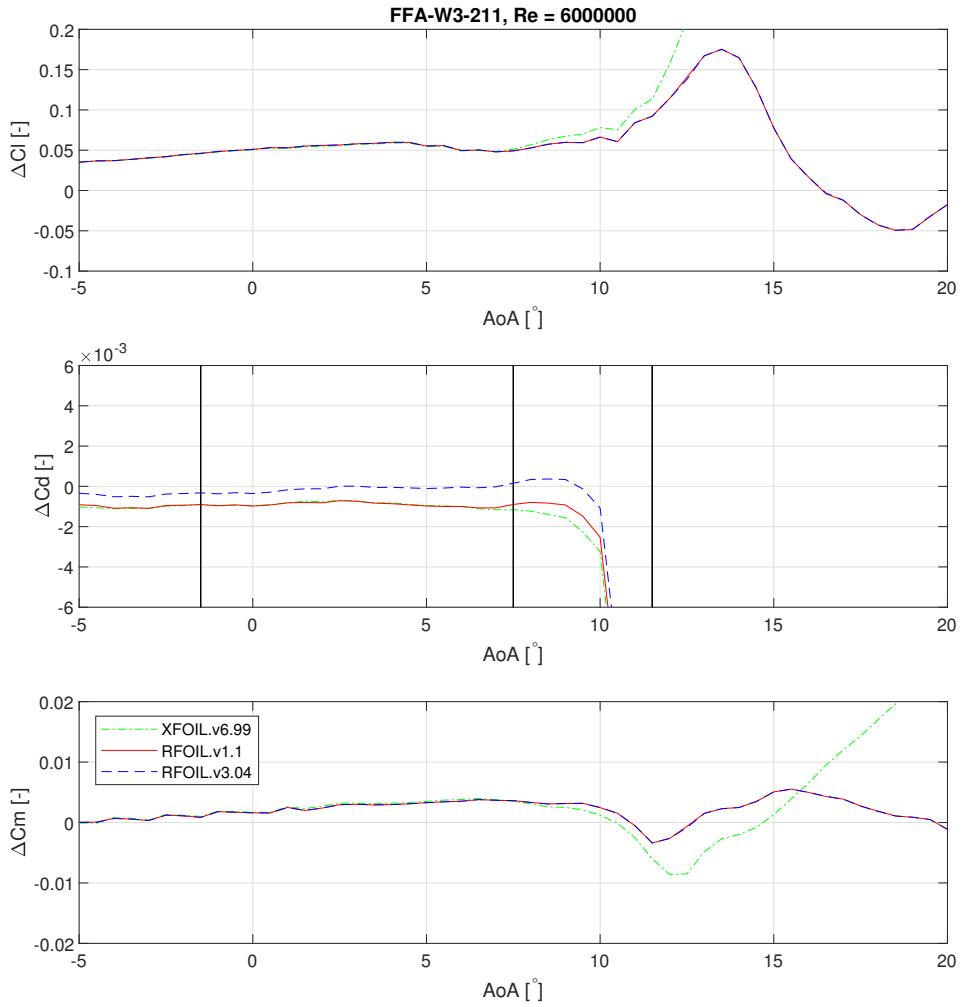

Figure B.144: Comparison between experimental and numerical pressure and skin friction distributions for the FFA-W3-211 airfoil at a Reynolds number of 6000000 and at the design angle of attack.

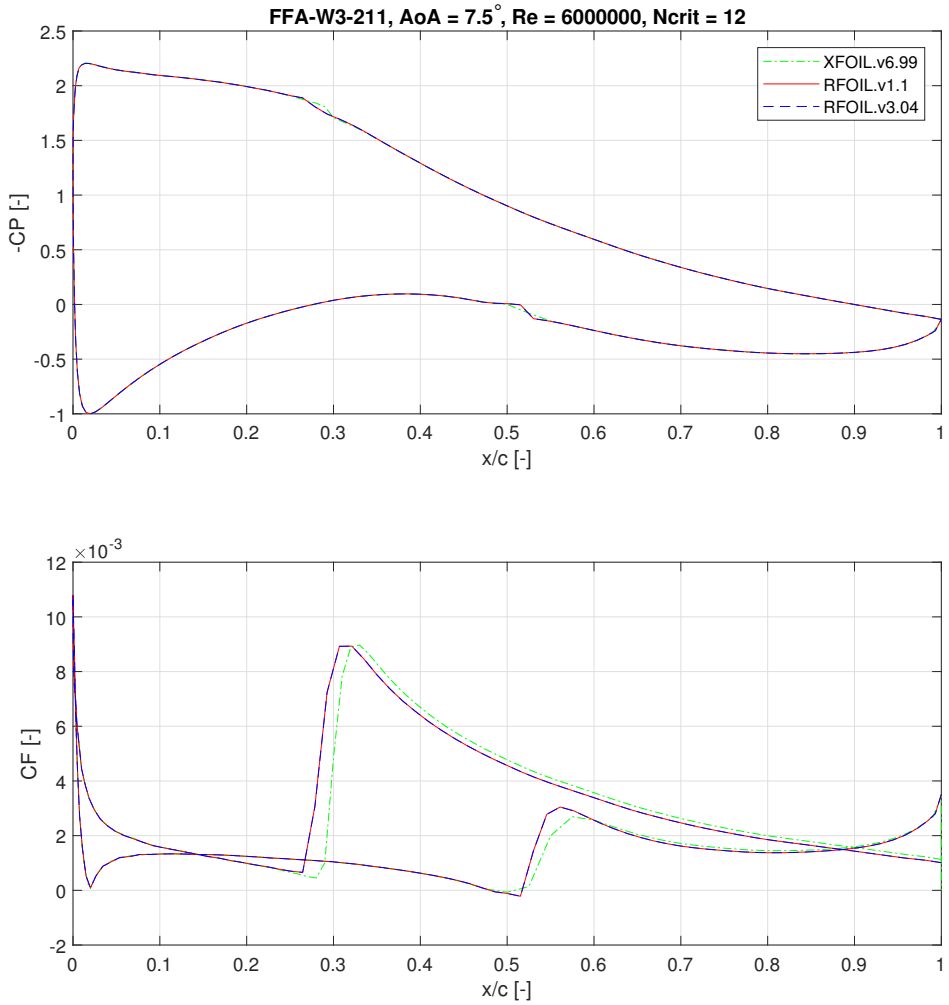

B.4 FX series airfoils

Figure B.145: Comparison between experimental and numerical polars for the FX83-W-108 airfoil at a Reynolds number of 1000000. Simulation time to generate the polars by means the different codes and the number of converged polar points are depicted between parentheses.

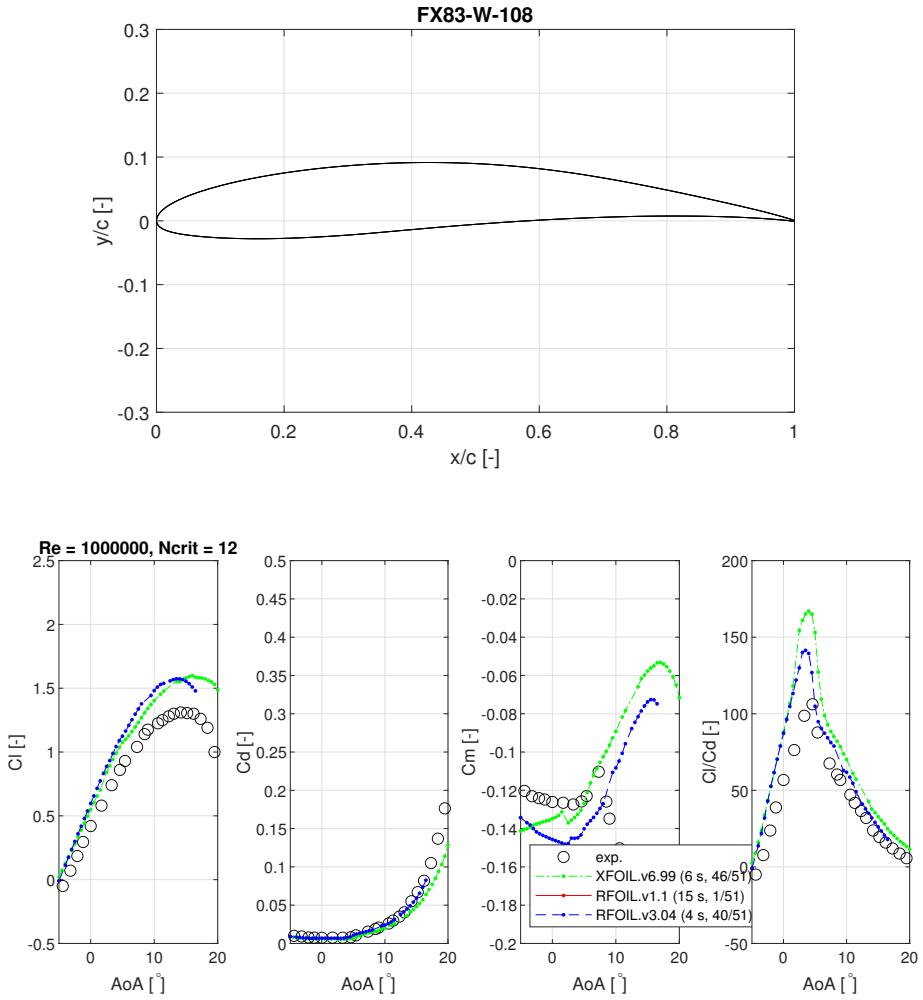

Figure B.146: Differences between experimental and numerical polars for the FX83-W-108 airfoil at a Reynolds number of 1000000. Vertical black lines in the middle subplot indicate, from left to right, the angle of attack corresponding to the minimum drag coefficient, maximum lift to drag ratio and maximum lift coefficient, respectively.

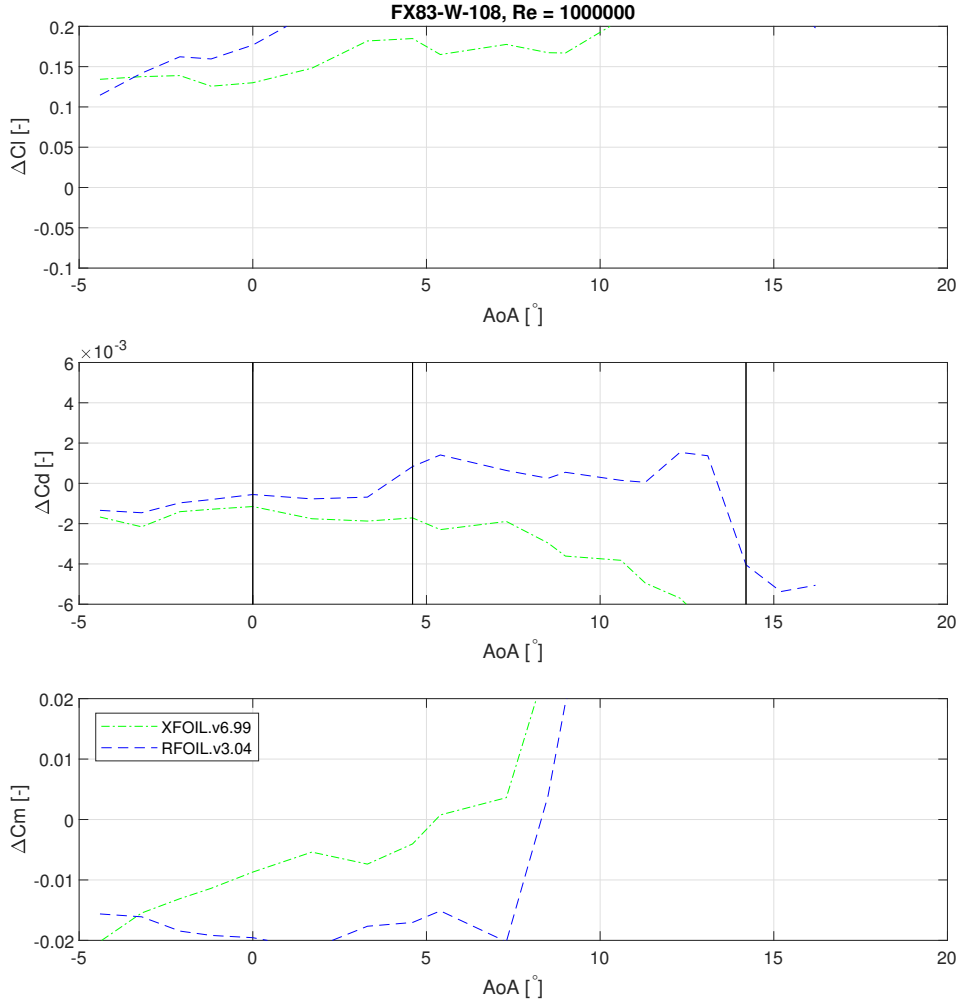

Figure B.147: Comparison between experimental and numerical pressure and skin friction distributions for the FX83-W-108 airfoil at a Reynolds number of 1000000 and at the design angle of attack.

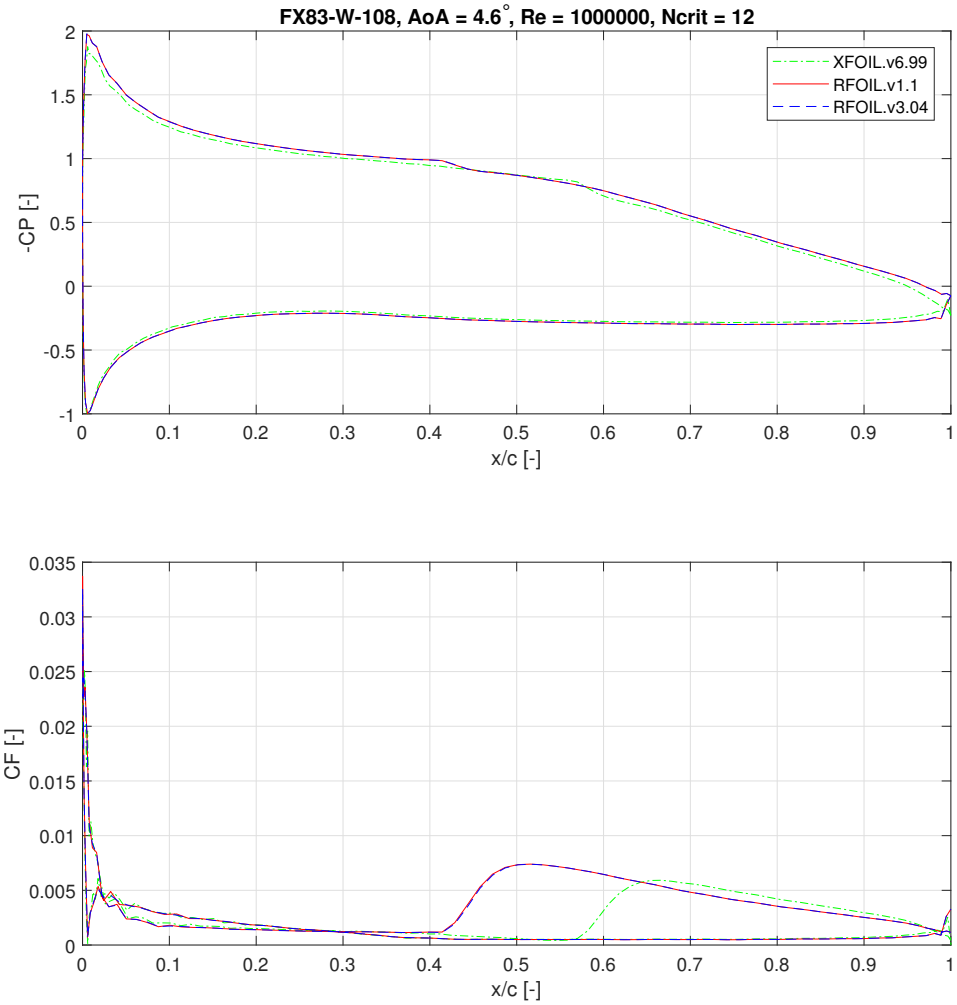

Figure B.148: Comparison between experimental and numerical polars for the FX83-W-108 airfoil at a Reynolds number of 1200000. Simulation time to generate the polars by means the different codes and the number of converged polar points are depicted between parentheses.

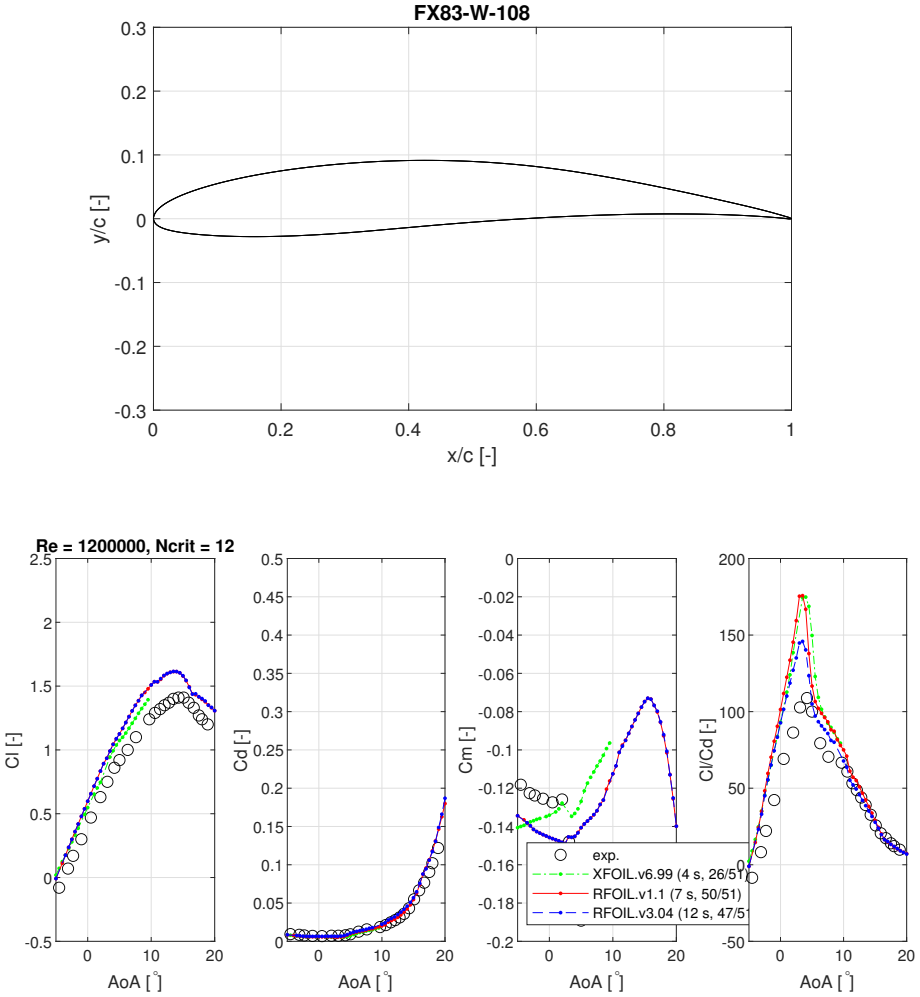

Figure B.149: Differences between experimental and numerical polars for the FX83-W-108 airfoil at a Reynolds number of 1200000. Vertical black lines in the middle subplot indicate, from left to right, the angle of attack corresponding to the minimum drag coefficient, maximum lift to drag ratio and maximum lift coefficient, respectively.

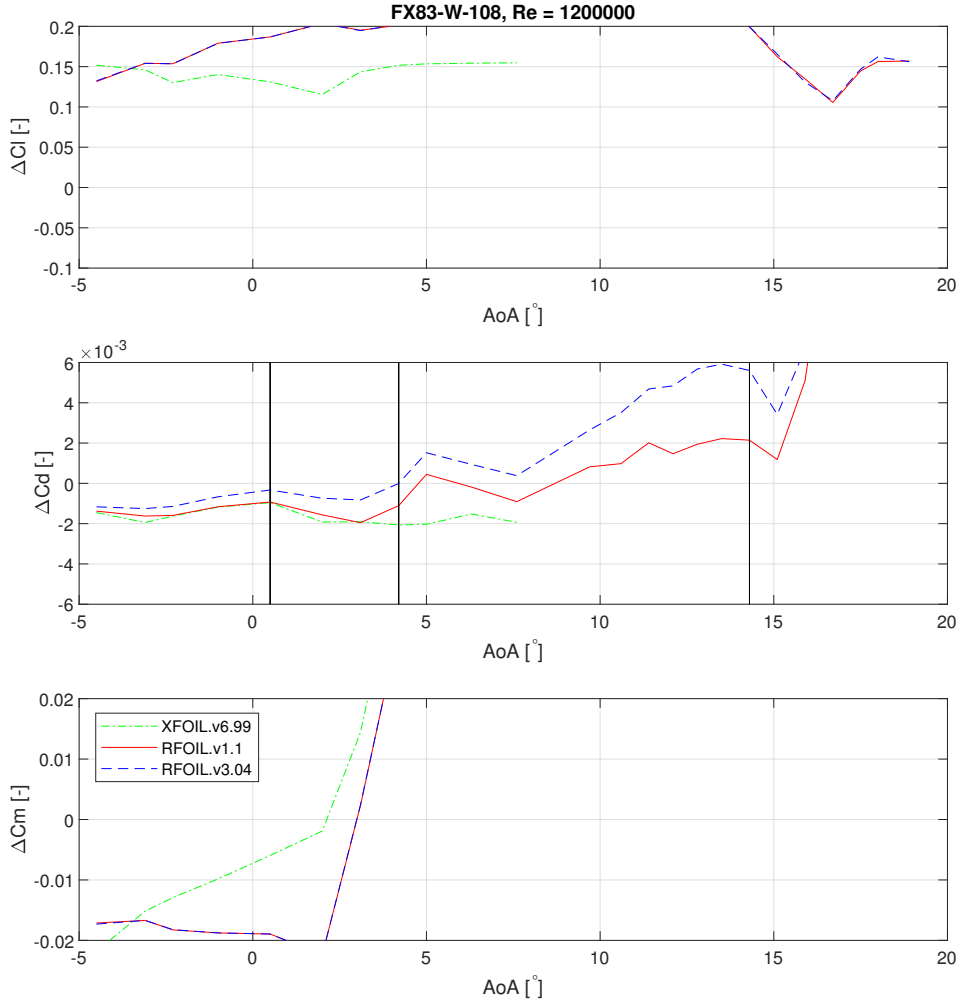

Figure B.150: Comparison between experimental and numerical pressure and skin friction distributions for the FX83-W-108 airfoil at a Reynolds number of 1200000 and at the design angle of attack.

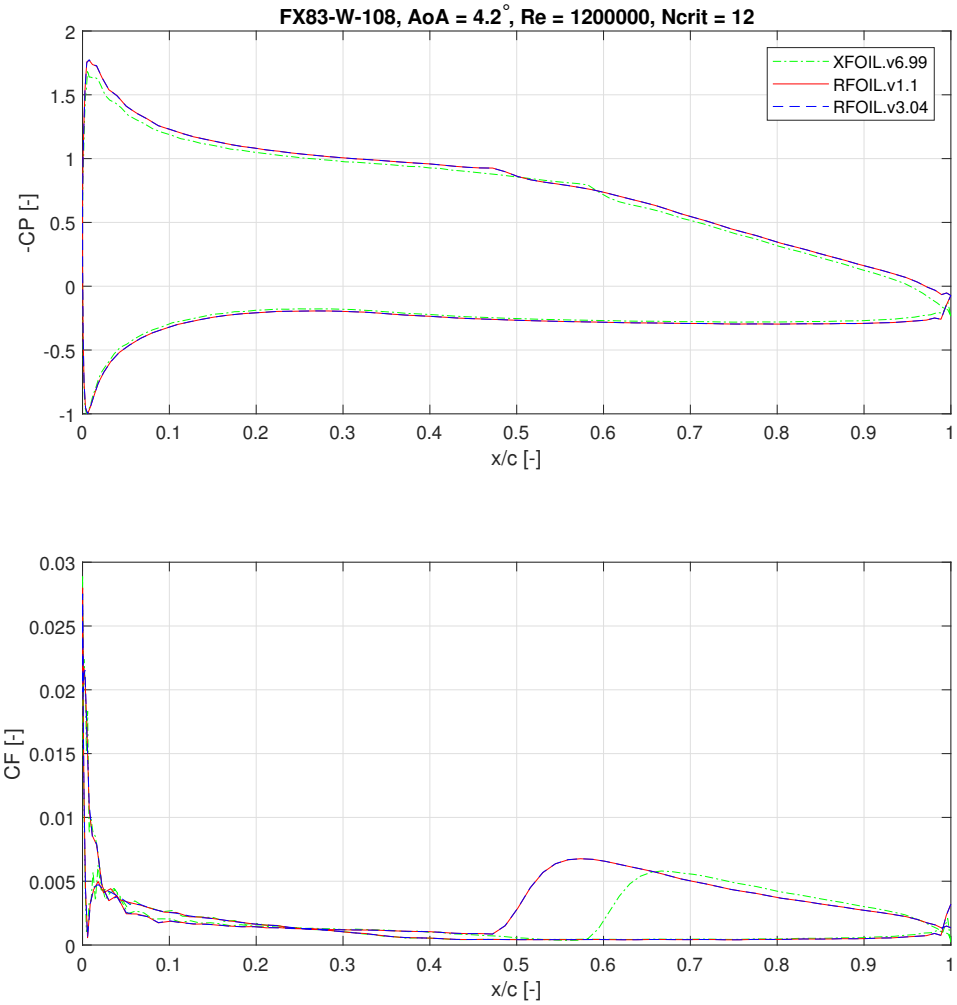

Figure B.151: Comparison between experimental and numerical polars for the FX83-W-108 airfoil at a Reynolds number of 500000. Simulation time to generate the polars by means the different codes and the number of converged polar points are depicted between parentheses.

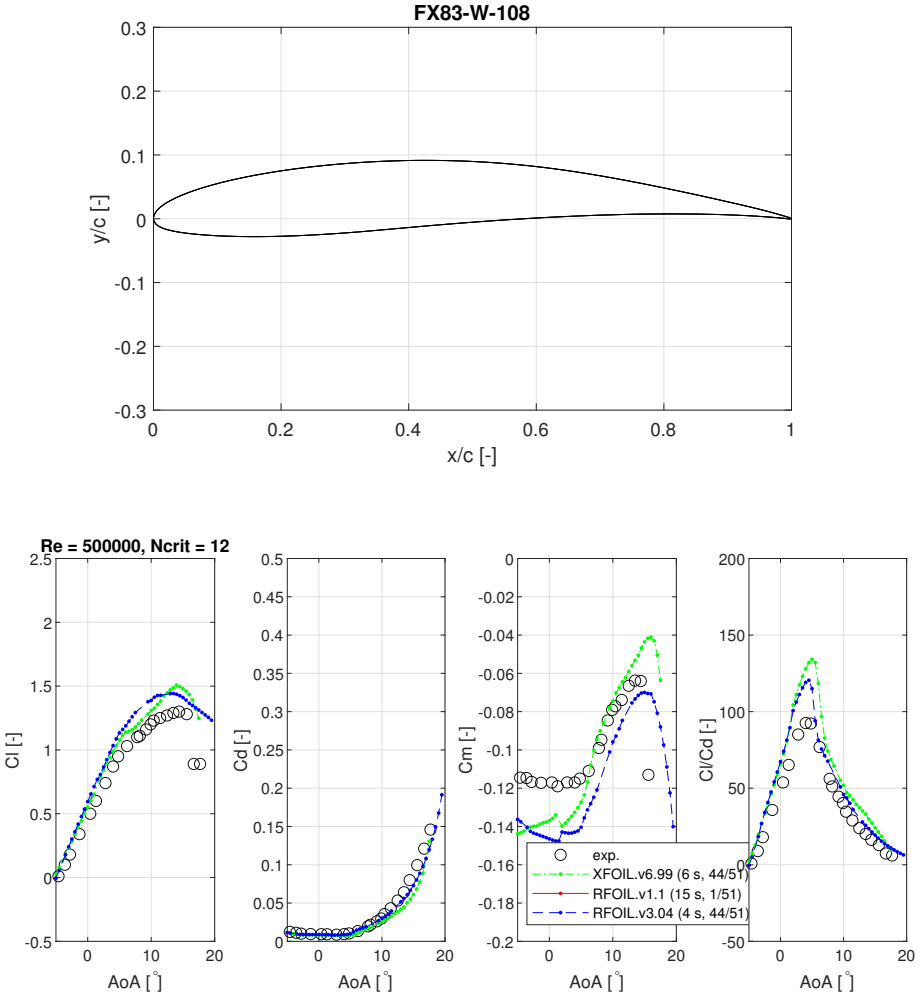

Figure B.152: Differences between experimental and numerical polars for the FX83-W-108 airfoil at a Reynolds number of 500000. Vertical black lines in the middle subplot indicate, from left to right, the angle of attack corresponding to the minimum drag coefficient, maximum lift to drag ratio and maximum lift coefficient, respectively.

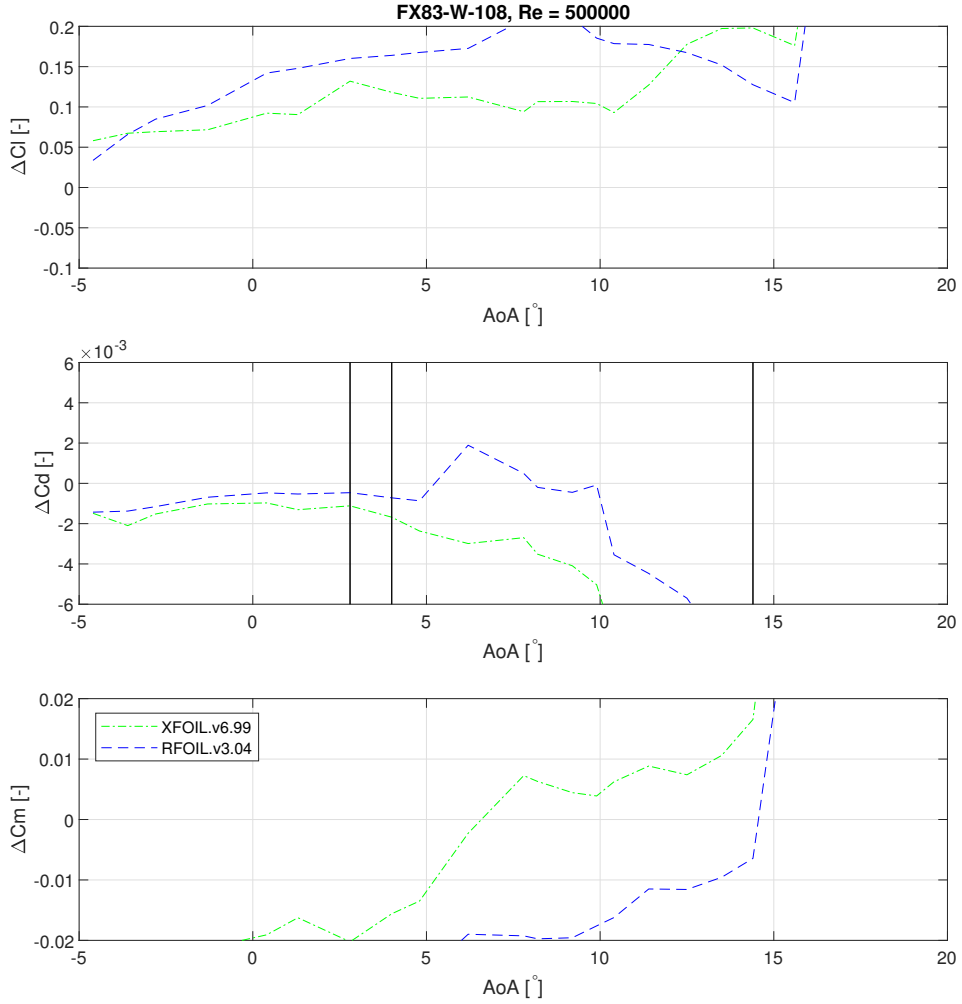

Figure B.153: Comparison between experimental and numerical pressure and skin friction distributions for the FX83-W-108 airfoil at a Reynolds number of 500000 and at the design angle of attack.

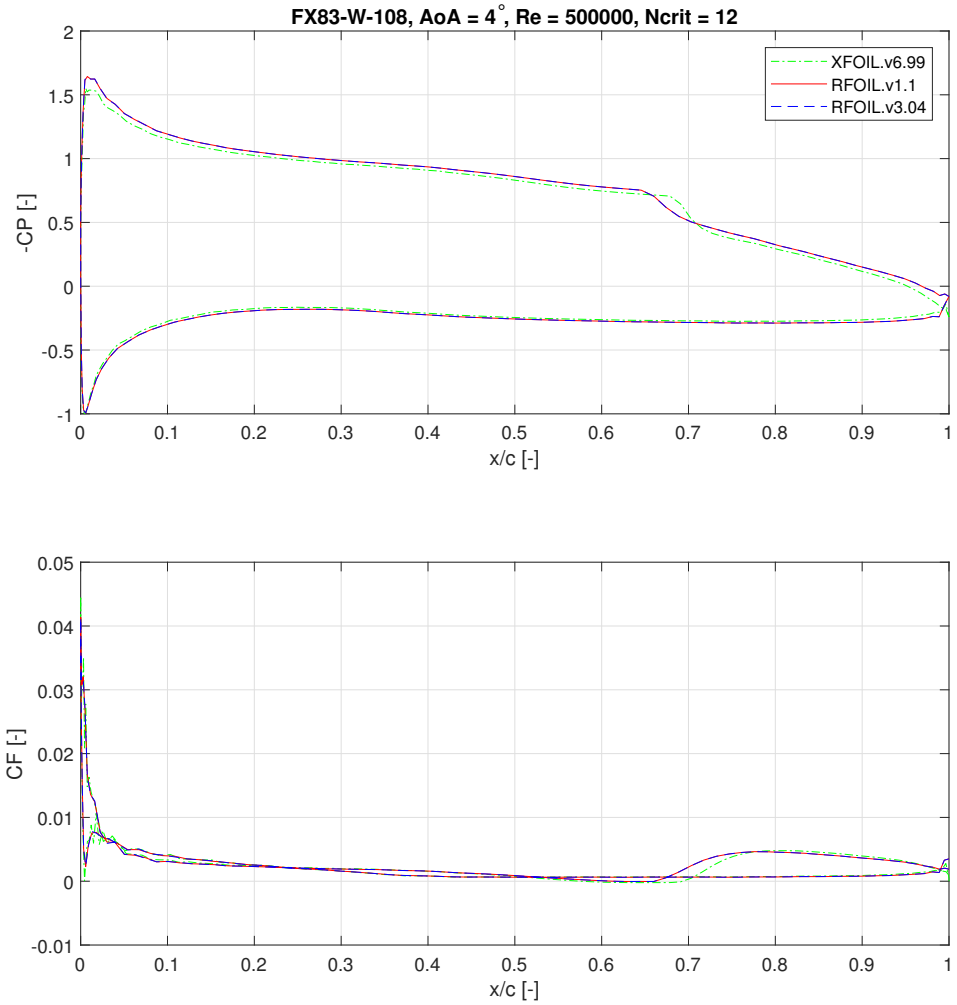

Figure B.154: Comparison between experimental and numerical polars for the FX83-W-160 airfoil at a Reynolds number of 1000000. Simulation time to generate the polars by means the different codes and the number of converged polar points are depicted between parentheses.

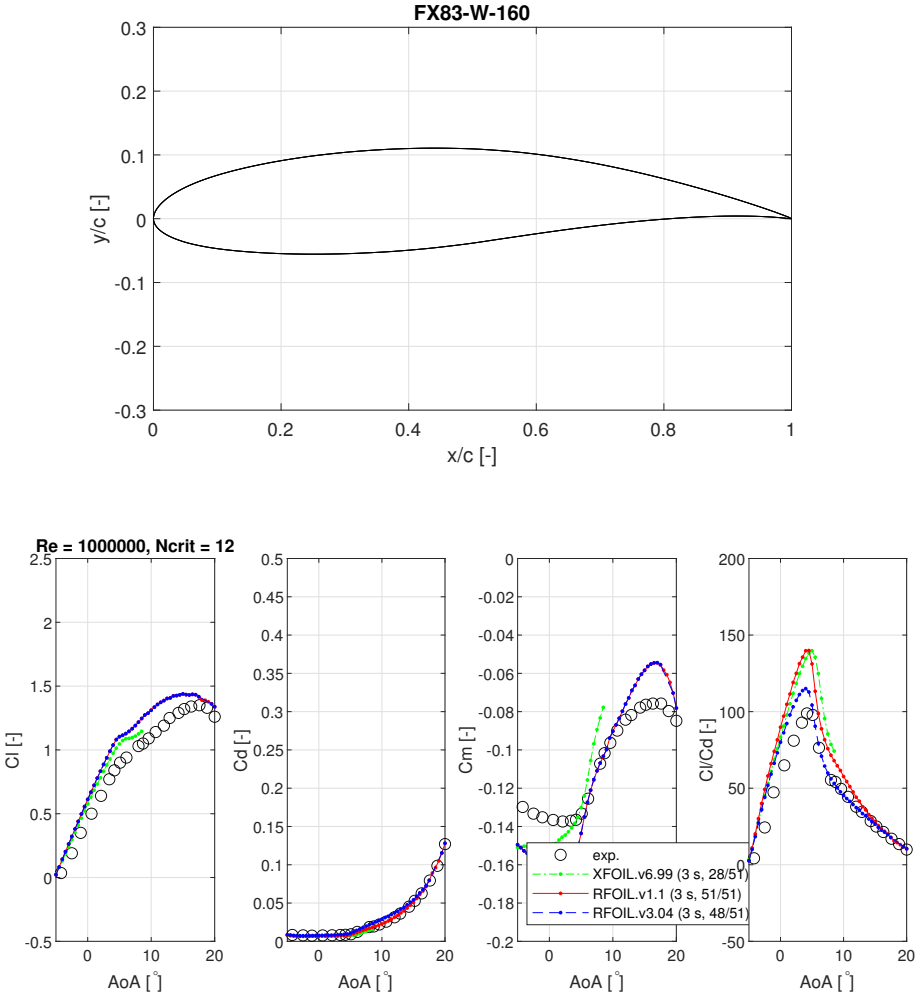

Figure B.155: Differences between experimental and numerical polars for the FX83-W-160 airfoil at a Reynolds number of 1000000. Vertical black lines in the middle subplot indicate, from left to right, the angle of attack corresponding to the minimum drag coefficient, maximum lift to drag ratio and maximum lift coefficient, respectively.

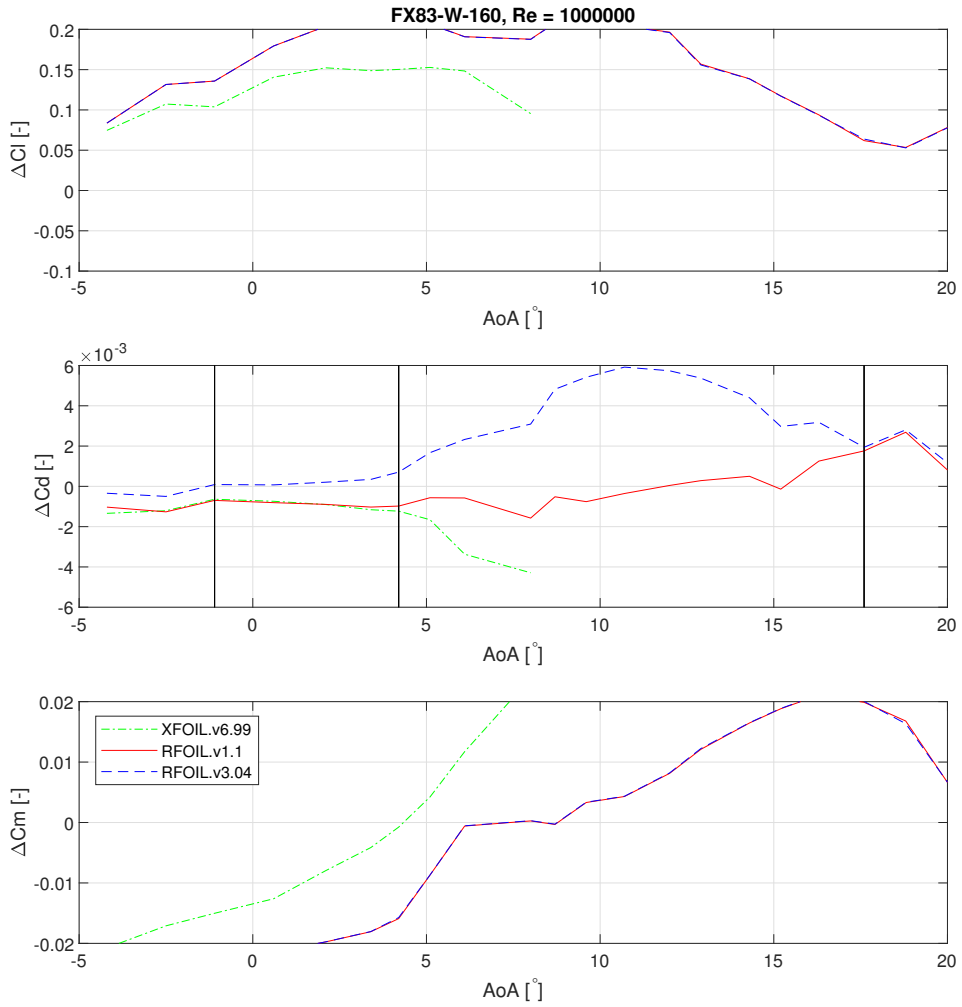

Figure B.156: Comparison between experimental and numerical pressure and skin friction distributions for the FX83-W-160 airfoil at a Reynolds number of 1000000 and at the design angle of attack.

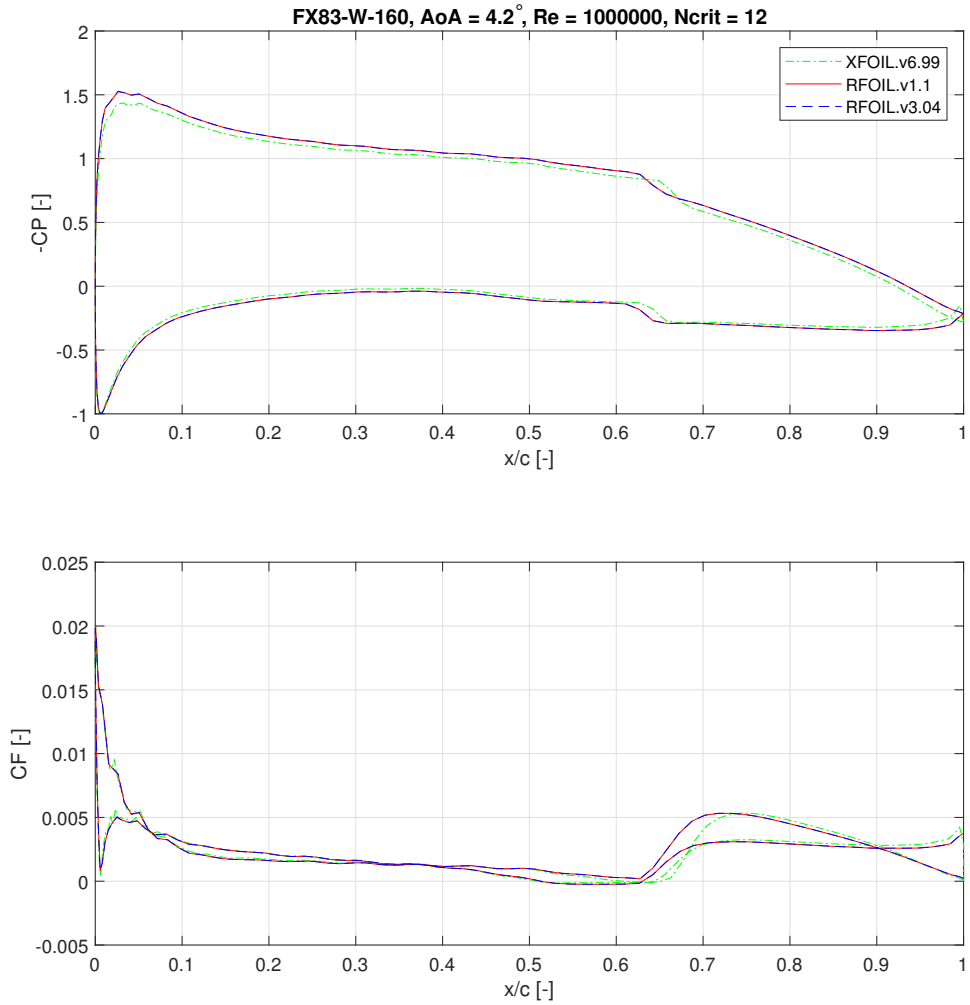

Figure B.157: Comparison between experimental and numerical polars for the FX83-W-160 airfoil at a Reynolds number of 1500000. Simulation time to generate the polars by means the different codes and the number of converged polar points are depicted between parentheses.

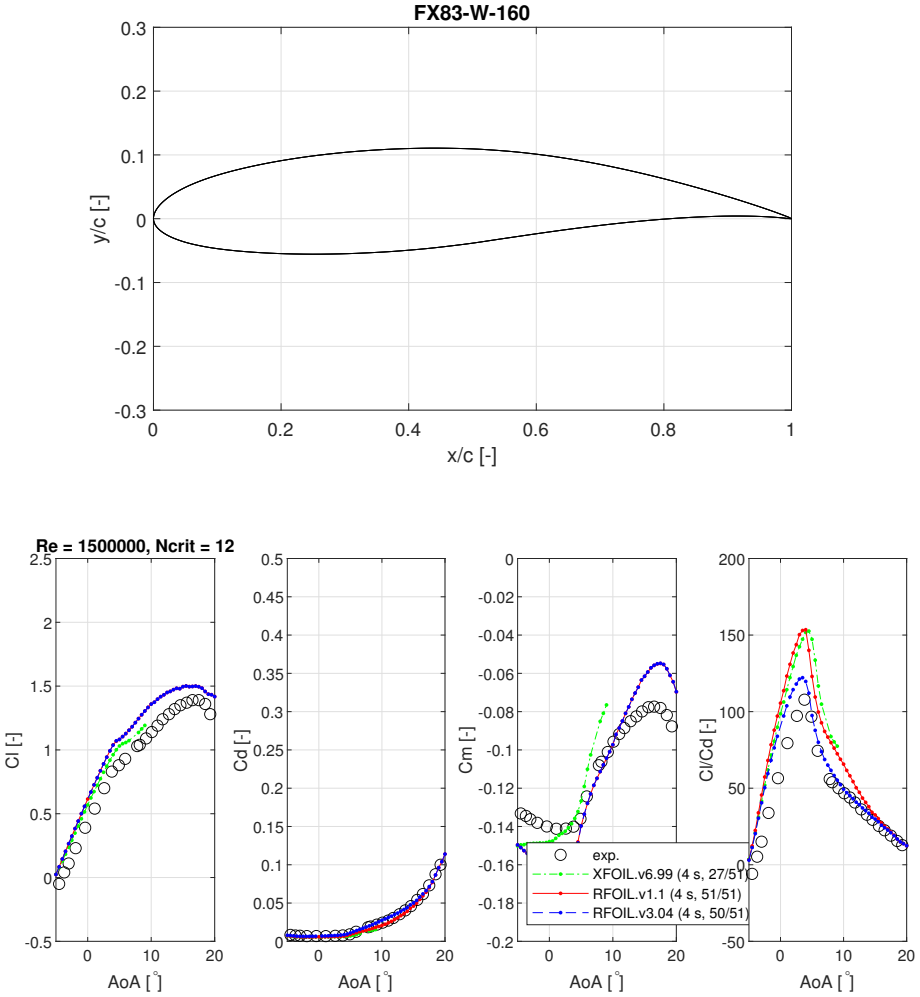

Figure B.158: Differences between experimental and numerical polars for the FX83-W-160 airfoil at a Reynolds number of 1500000. Vertical black lines in the middle subplot indicate, from left to right, the angle of attack corresponding to the minimum drag coefficient, maximum lift to drag ratio and maximum lift coefficient, respectively.

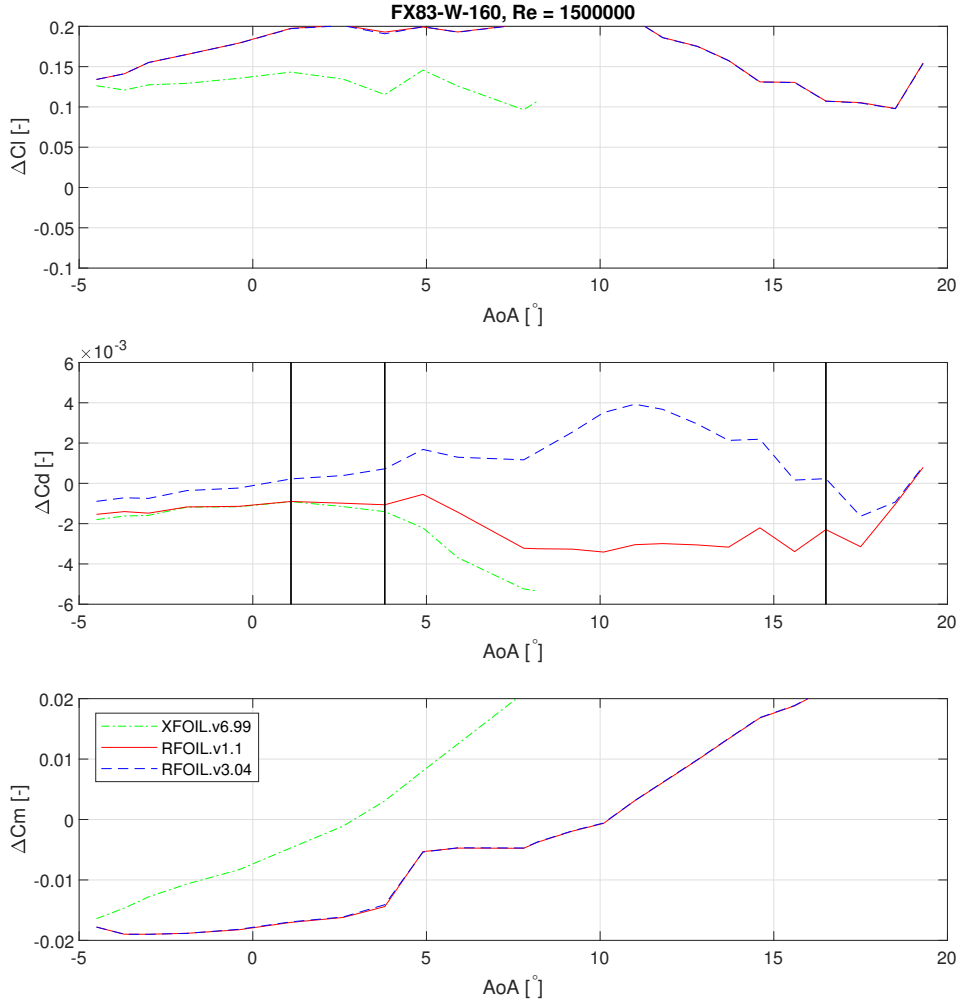

Figure B.159: Comparison between experimental and numerical pressure and skin friction distributions for the FX83-W-160 airfoil at a Reynolds number of 1500000 and at the design angle of attack.

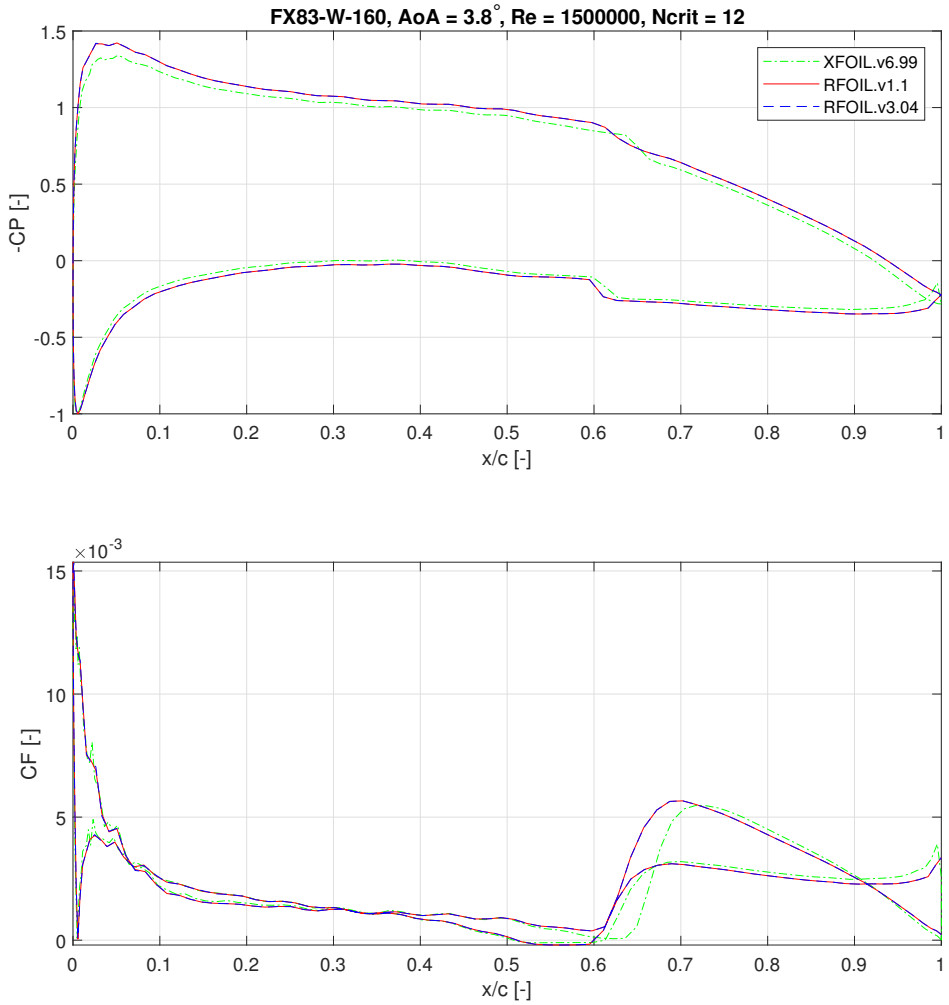

Figure B.160: Comparison between experimental and numerical polars for the FX83-W-160 airfoil at a Reynolds number of 500000. Simulation time to generate the polars by means the different codes and the number of converged polar points are depicted between parentheses.

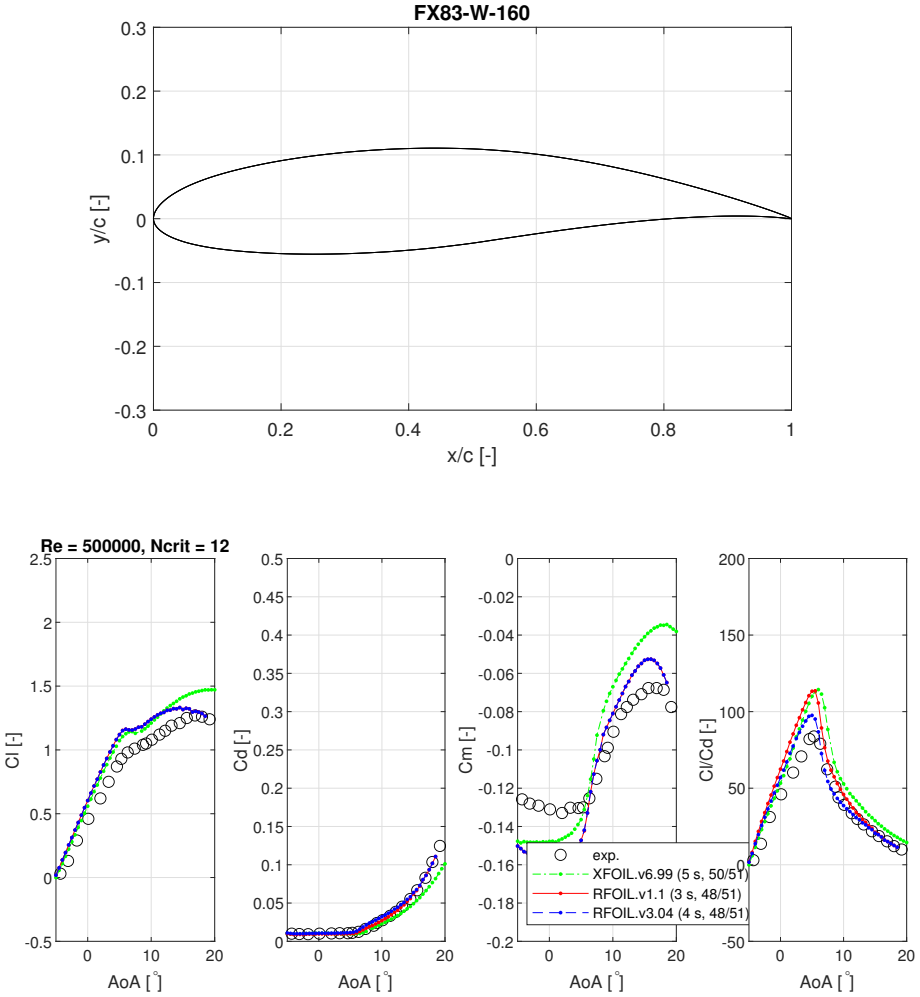

Figure B.161: Differences between experimental and numerical polars for the FX83-W-160 airfoil at a Reynolds number of 500000. Vertical black lines in the middle subplot indicate, from left to right, the angle of attack corresponding to the minimum drag coefficient, maximum lift to drag ratio and maximum lift coefficient, respectively.

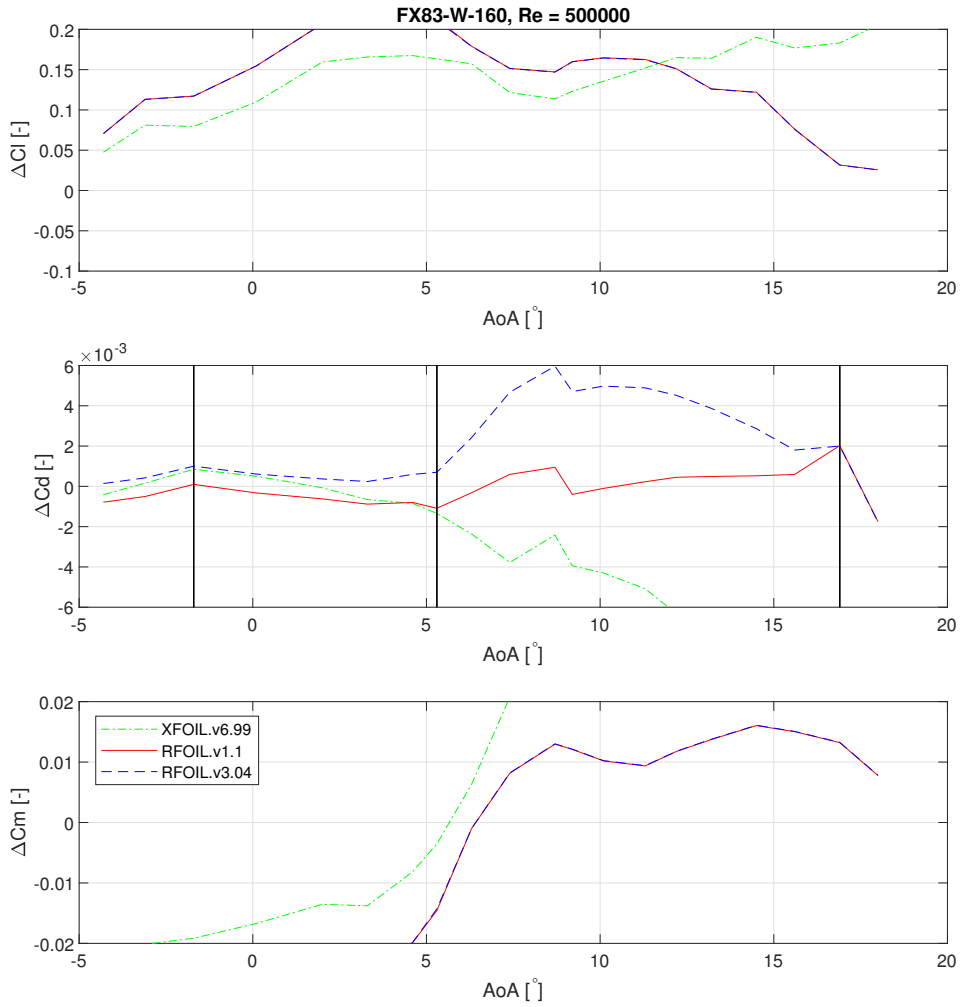

Figure B.162: Comparison between experimental and numerical pressure and skin friction distributions for the FX83-W-160 airfoil at a Reynolds number of 500000 and at the design angle of attack.

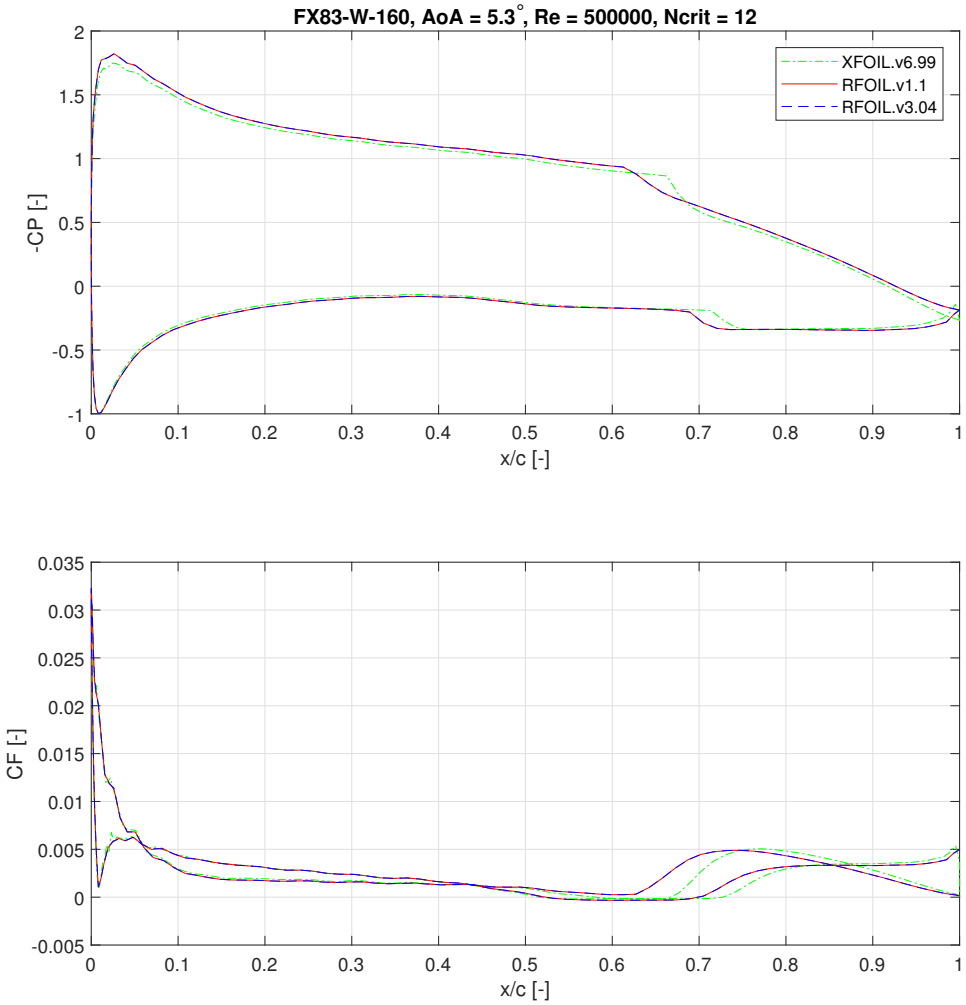

Figure B.163: Comparison between experimental and numerical polars for the FX84-W-175 airfoil at a Reynolds number of 1000000. Simulation time to generate the polars by means the different codes and the number of converged polar points are depicted between parentheses.

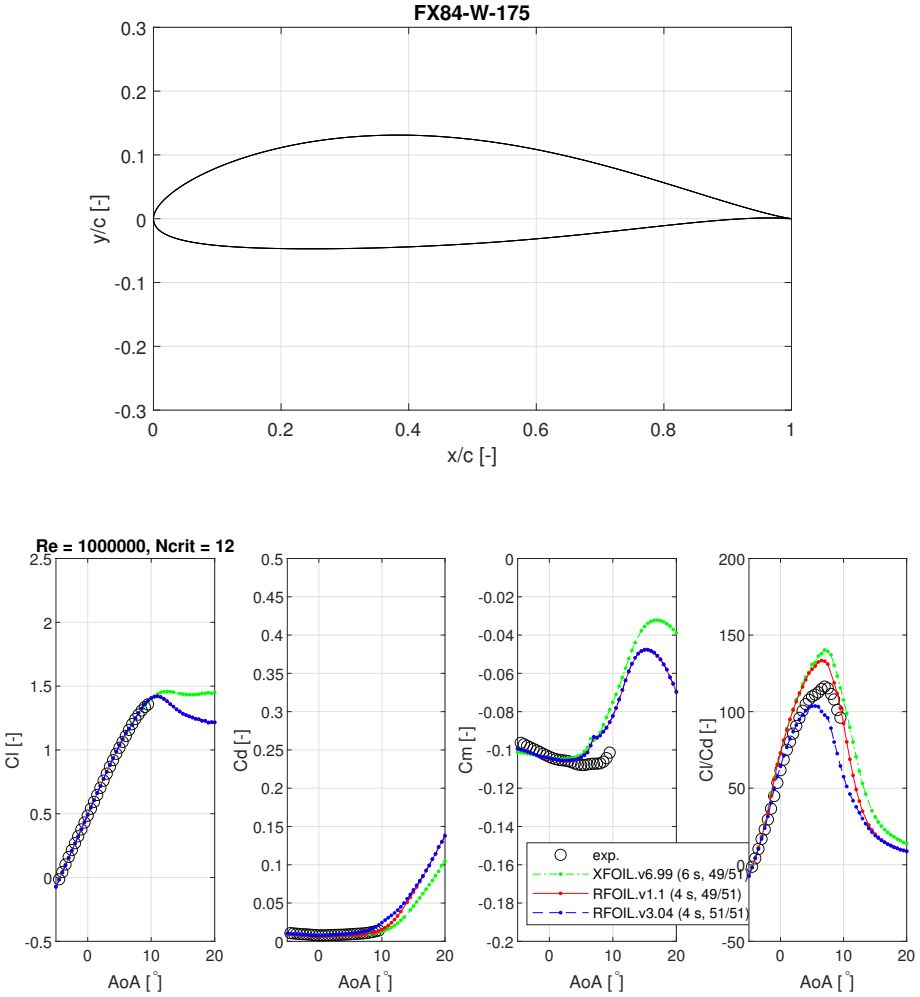

Figure B.164: Differences between experimental and numerical polars for the FX84-W-175 airfoil at a Reynolds number of 1000000. Vertical black lines in the middle subplot indicate, from left to right, the angle of attack corresponding to the minimum drag coefficient, maximum lift to drag ratio and maximum lift coefficient, respectively.

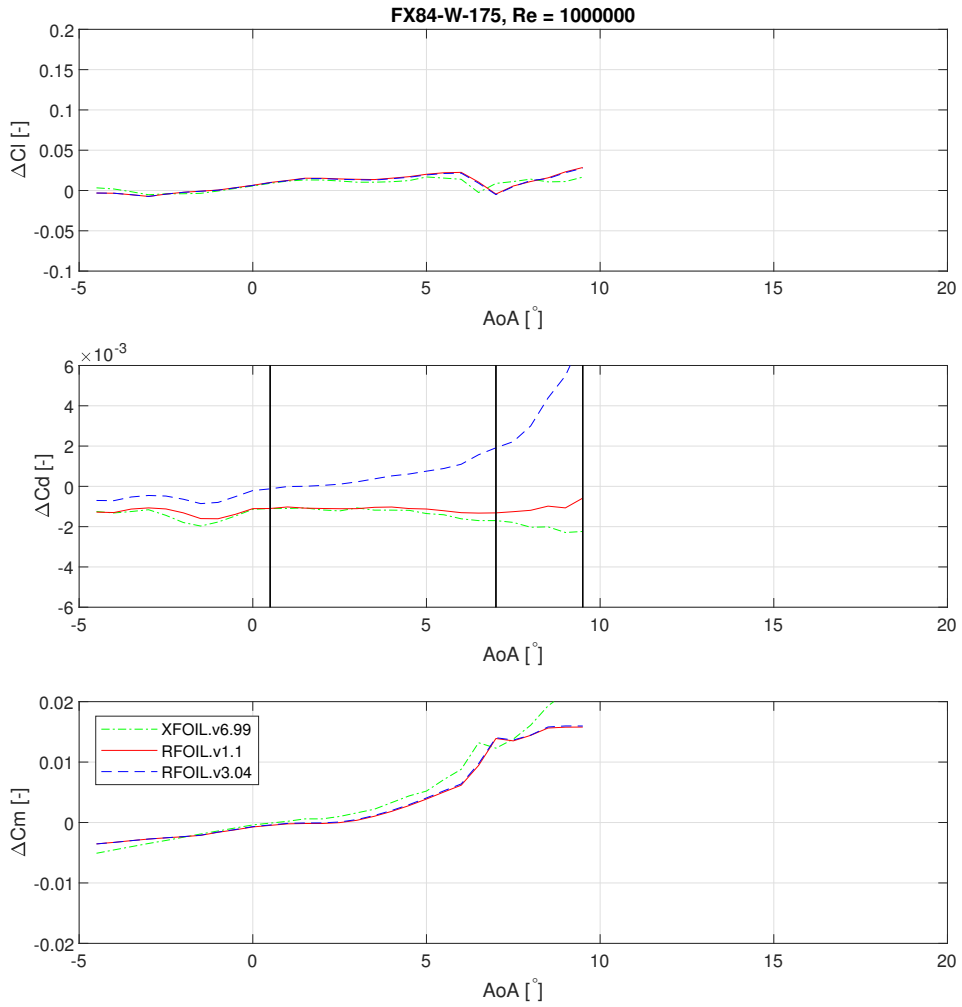

Figure B.165: Comparison between experimental and numerical pressure and skin friction distributions for the FX84-W-175 airfoil at a Reynolds number of 1000000 and at the design angle of attack.

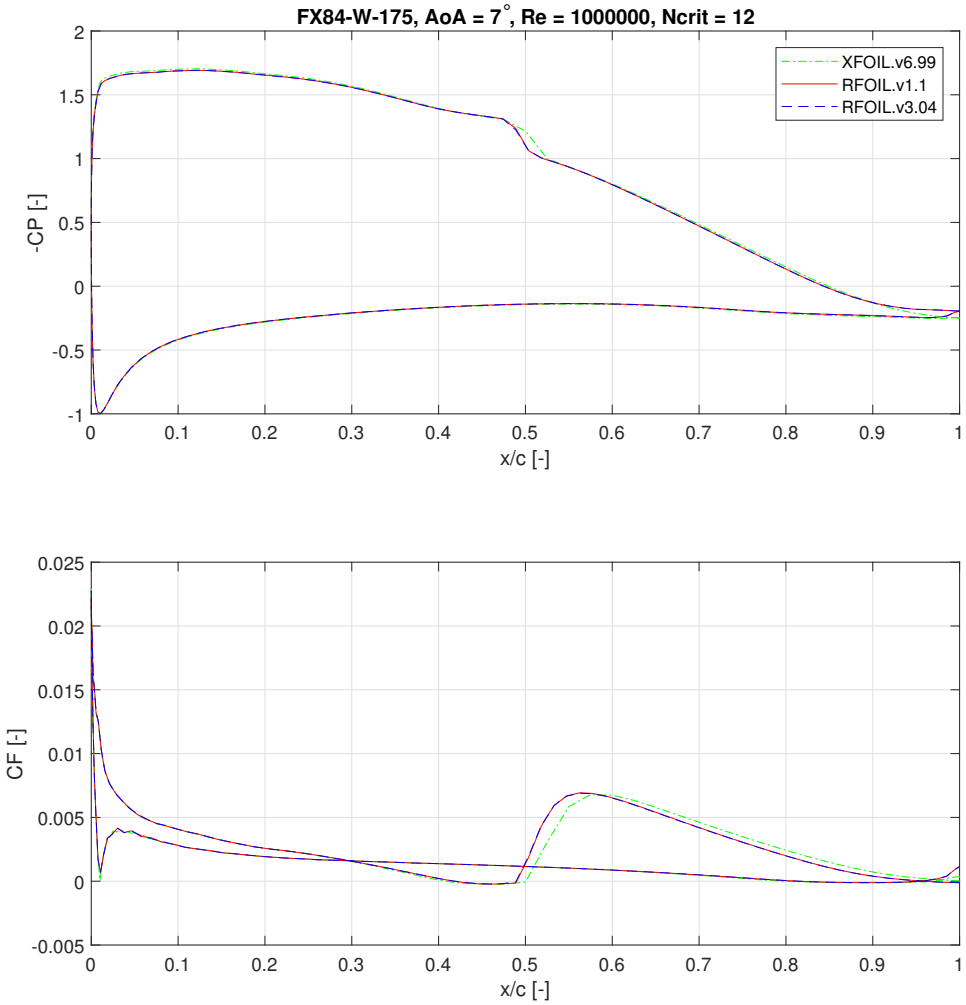

Figure B.166: Comparison between experimental and numerical polars for the FX84-W-175 airfoil at a Reynolds number of 1500000. Simulation time to generate the polars by means the different codes and the number of converged polar points are depicted between parentheses.

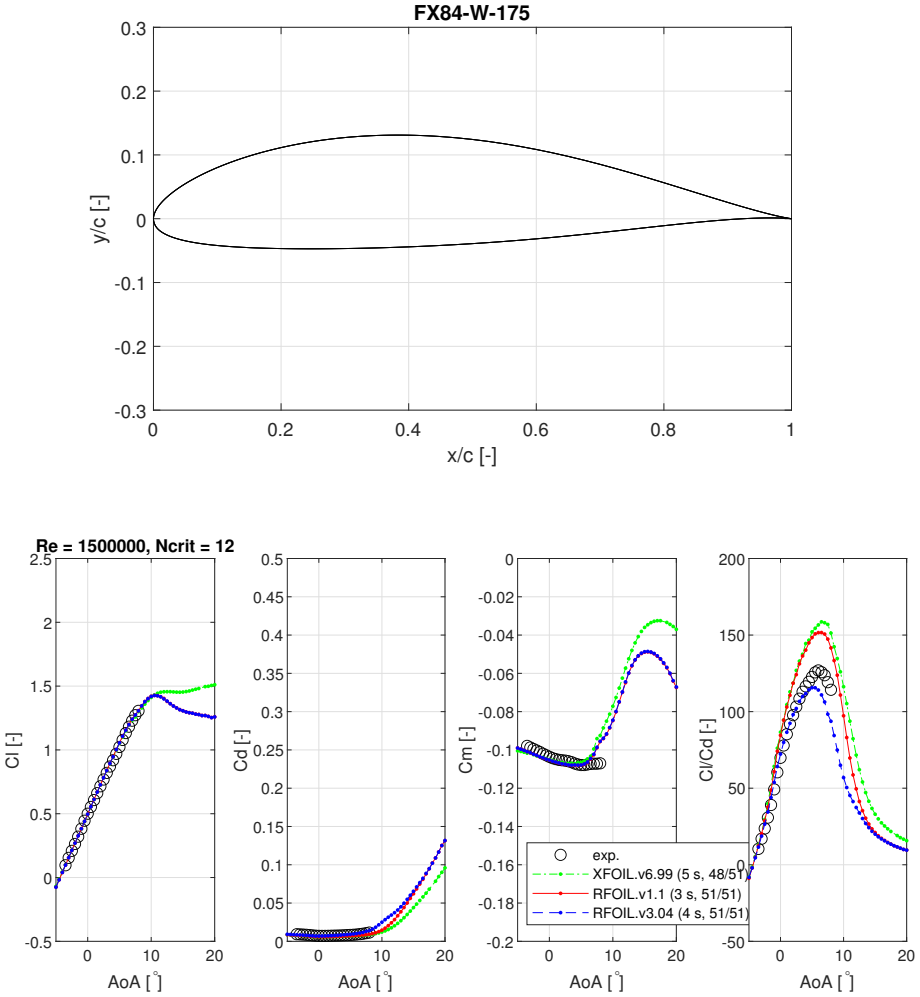

Figure B.167: Differences between experimental and numerical polars for the FX84-W-175 airfoil at a Reynolds number of 1500000. Vertical black lines in the middle subplot indicate, from left to right, the angle of attack corresponding to the minimum drag coefficient, maximum lift to drag ratio and maximum lift coefficient, respectively.

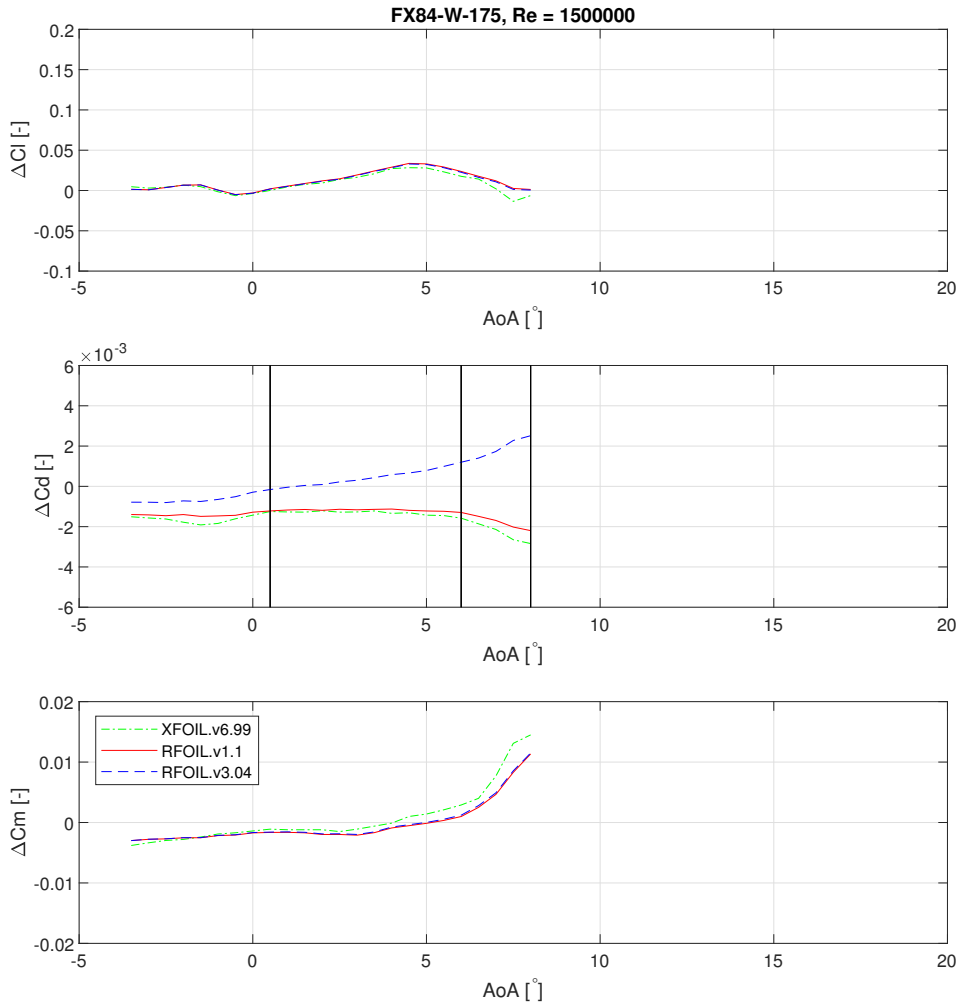

Figure B.168: Comparison between experimental and numerical pressure and skin friction distributions for the FX84-W-175 airfoil at a Reynolds number of 1500000 and at the design angle of attack.

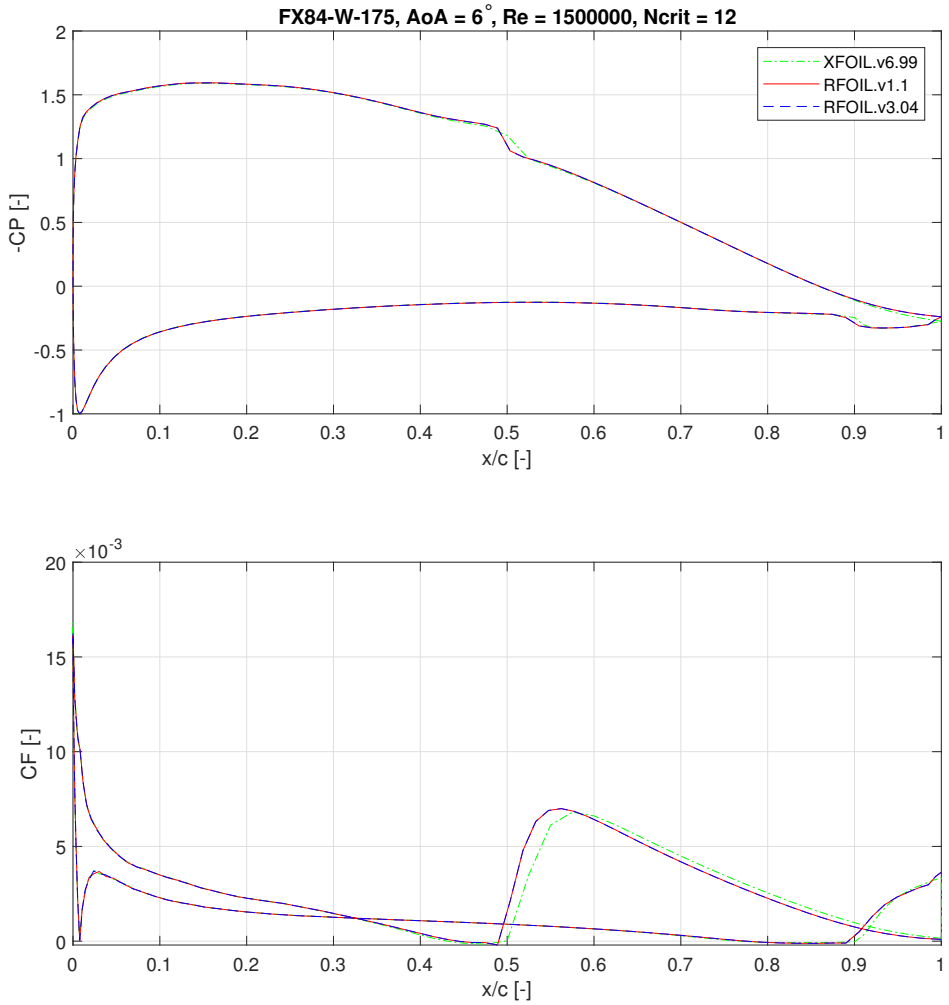

Figure B.169: Comparison between experimental and numerical polars for the FX84-W-218 airfoil at a Reynolds number of 1000000. Simulation time to generate the polars by means the different codes and the number of converged polar points are depicted between parentheses.

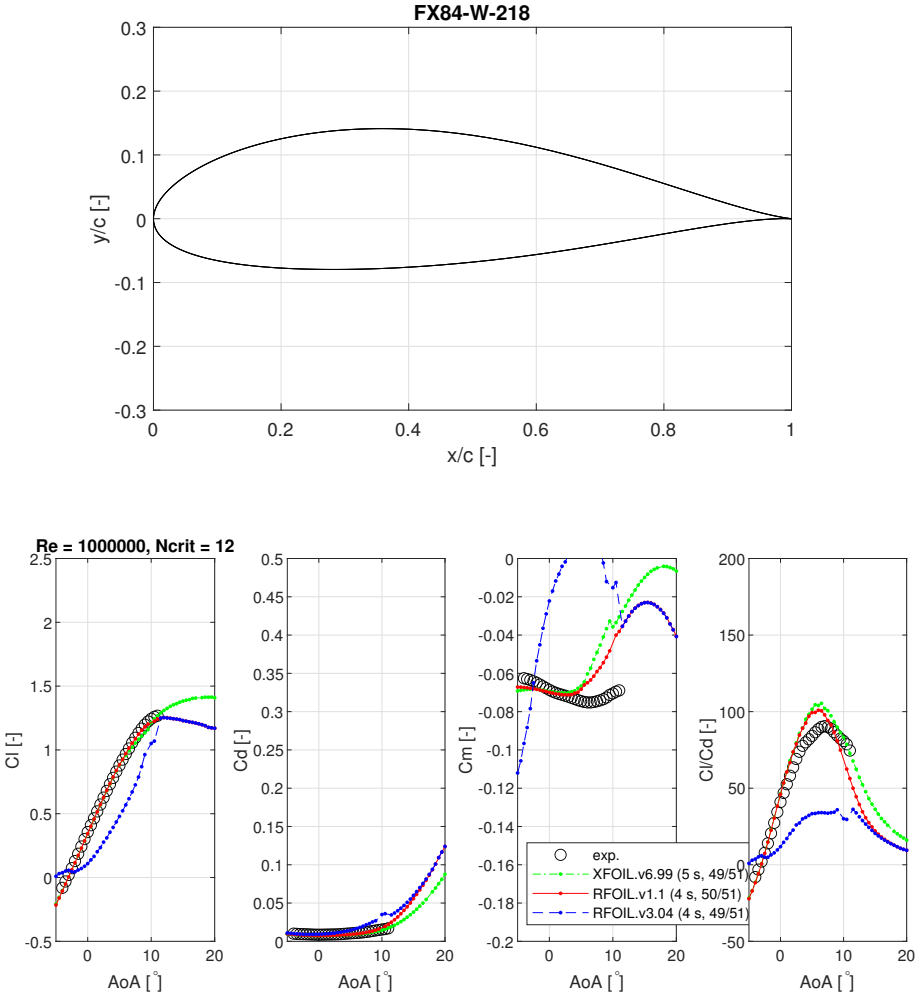

Figure B.170: Differences between experimental and numerical polars for the FX84-W-218 airfoil at a Reynolds number of 1000000. Vertical black lines in the middle subplot indicate, from left to right, the angle of attack corresponding to the minimum drag coefficient, maximum lift to drag ratio and maximum lift coefficient, respectively.

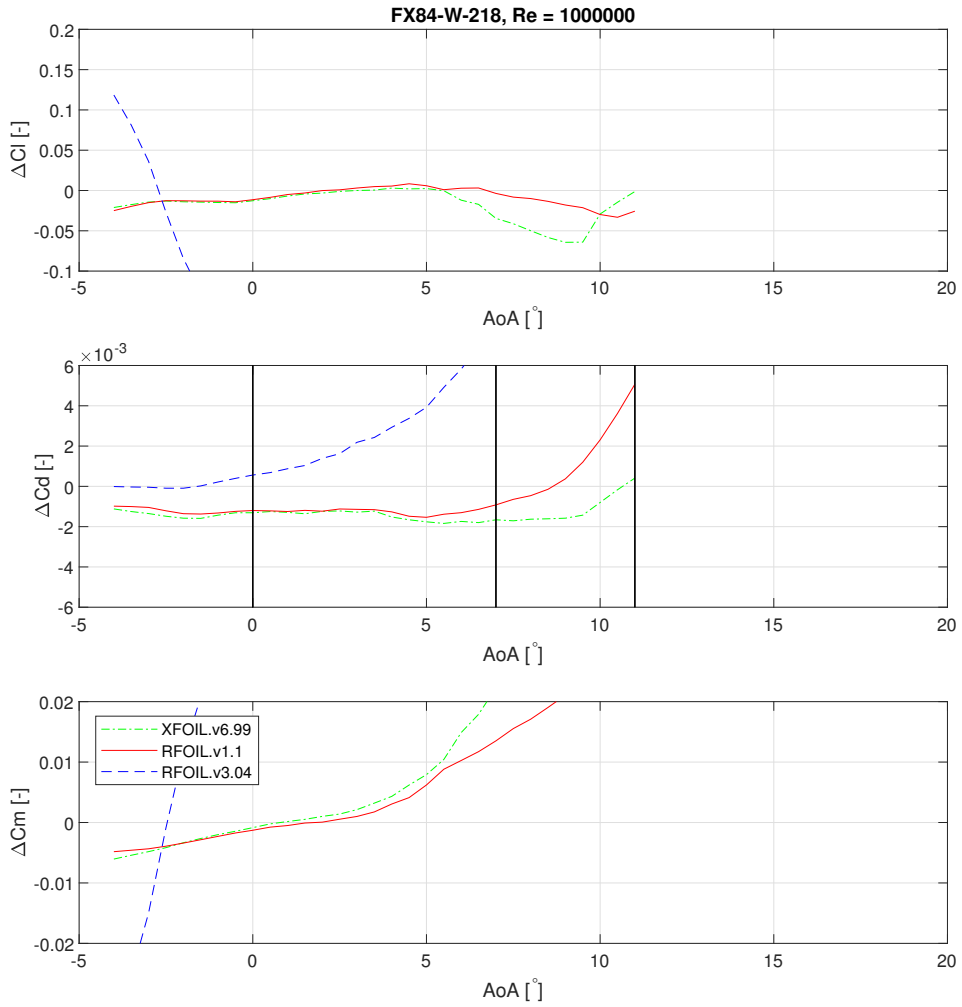

Figure B.171: Comparison between experimental and numerical pressure and skin friction distributions for the FX84-W-218 airfoil at a Reynolds number of 1000000 and at the design angle of attack.

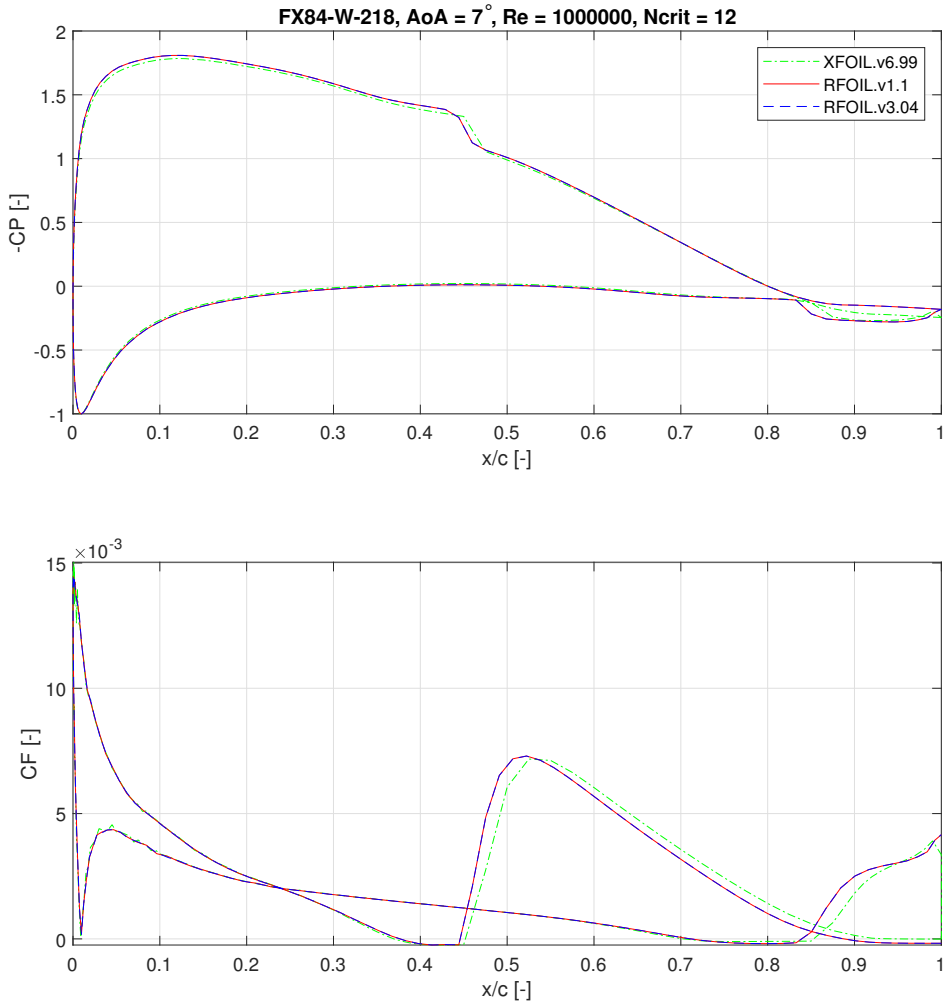

Figure B.172: Comparison between experimental and numerical polars for the FX84-W-218 airfoil at a Reynolds number of 1500000. Simulation time to generate the polars by means the different codes and the number of converged polar points are depicted between parentheses.

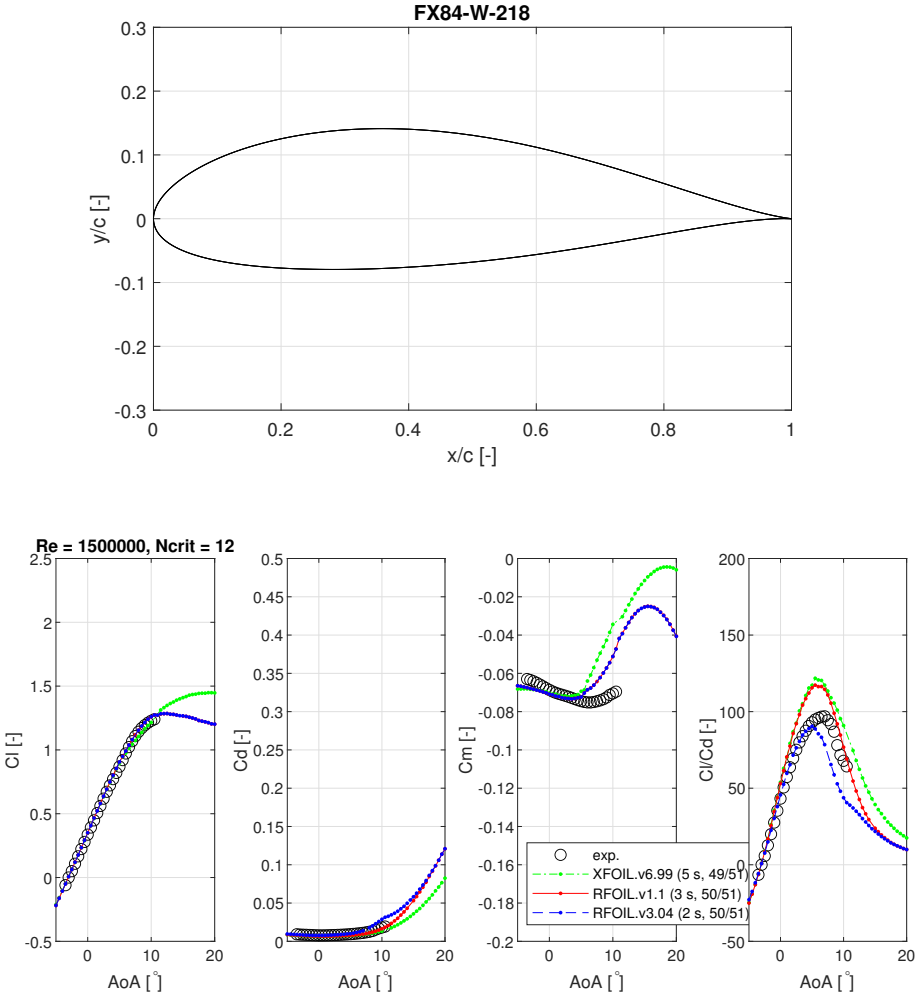

Figure B.173: Differences between experimental and numerical polars for the FX84-W-218 airfoil at a Reynolds number of 1500000. Vertical black lines in the middle subplot indicate, from left to right, the angle of attack corresponding to the minimum drag coefficient, maximum lift to drag ratio and maximum lift coefficient, respectively.

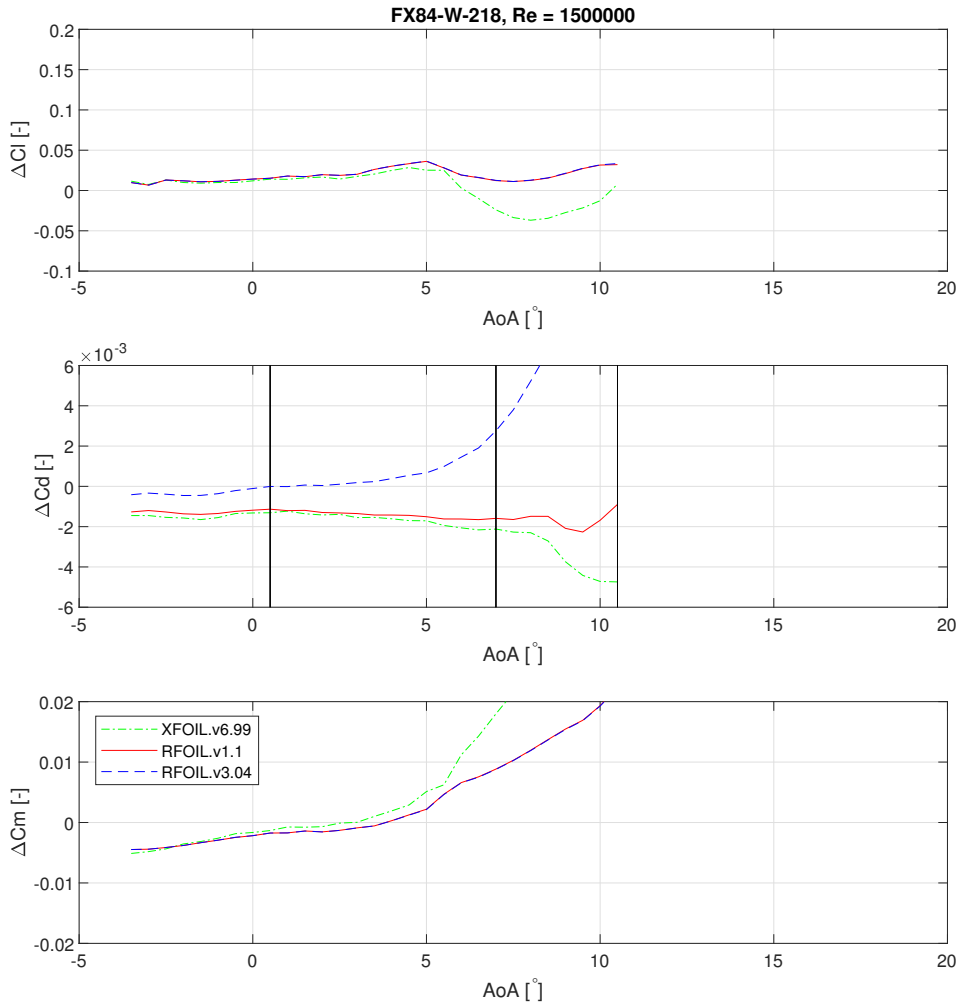

Figure B.174: Comparison between experimental and numerical pressure and skin friction distributions for the FX84-W-218 airfoil at a Reynolds number of 1500000 and at the design angle of attack.

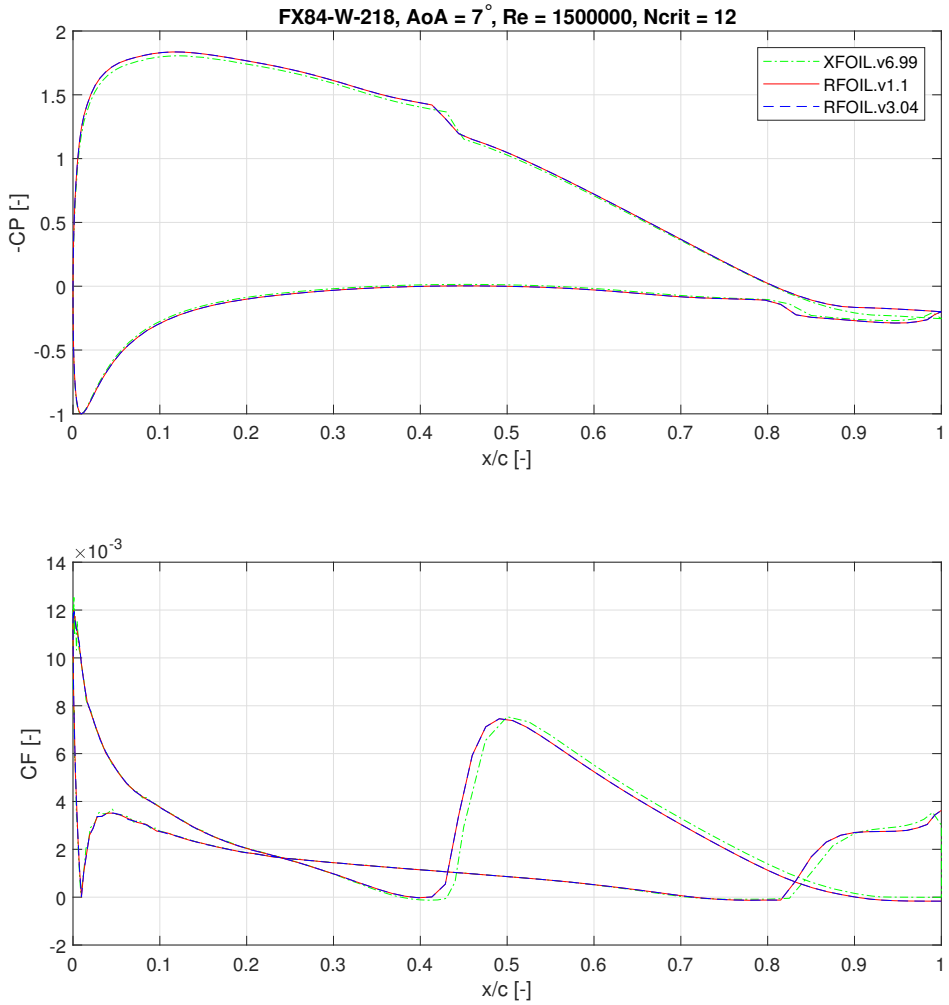

B.5 LS1 series airfoils

Figure B.175: Comparison between experimental and numerical polars for the LS1-0417 airfoil at a Reynolds number of 2100000. Simulation time to generate the polars by means the different codes and the number of converged polar points are depicted between parentheses.

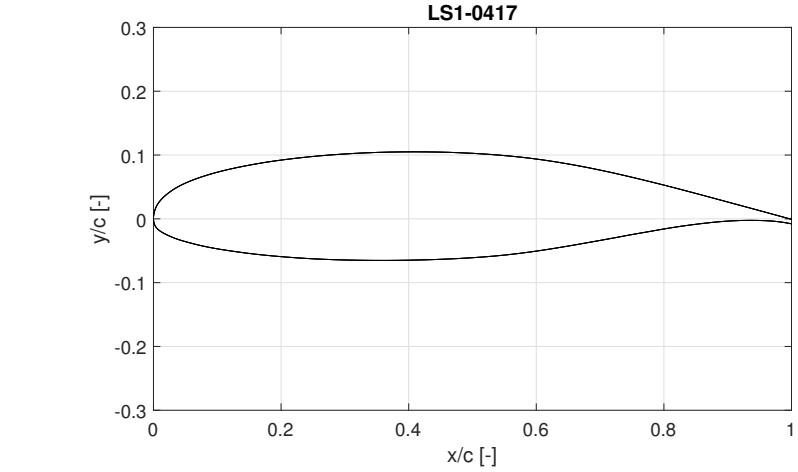

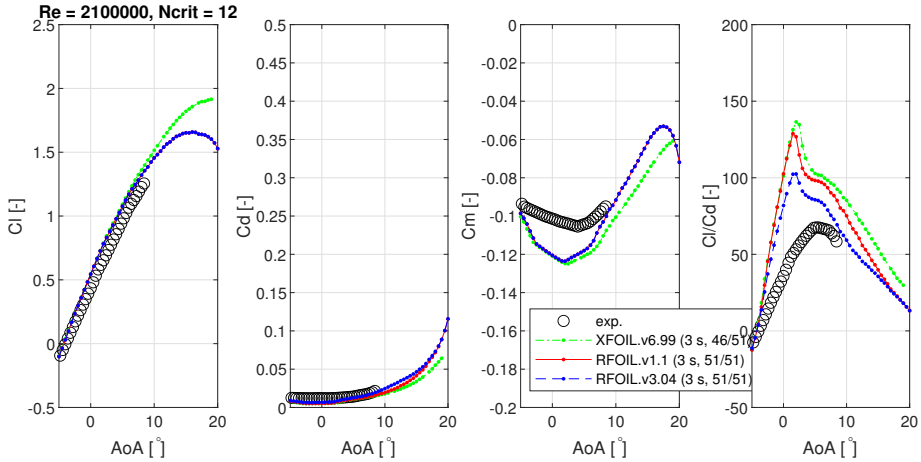

Figure B.176: Differences between experimental and numerical polars for the LS1-0417 airfoil at a Reynolds number of 2100000. Vertical black lines in the middle subplot indicate, from left to right, the angle of attack corresponding to the minimum drag coefficient, maximum lift to drag ratio and maximum lift coefficient, respectively.

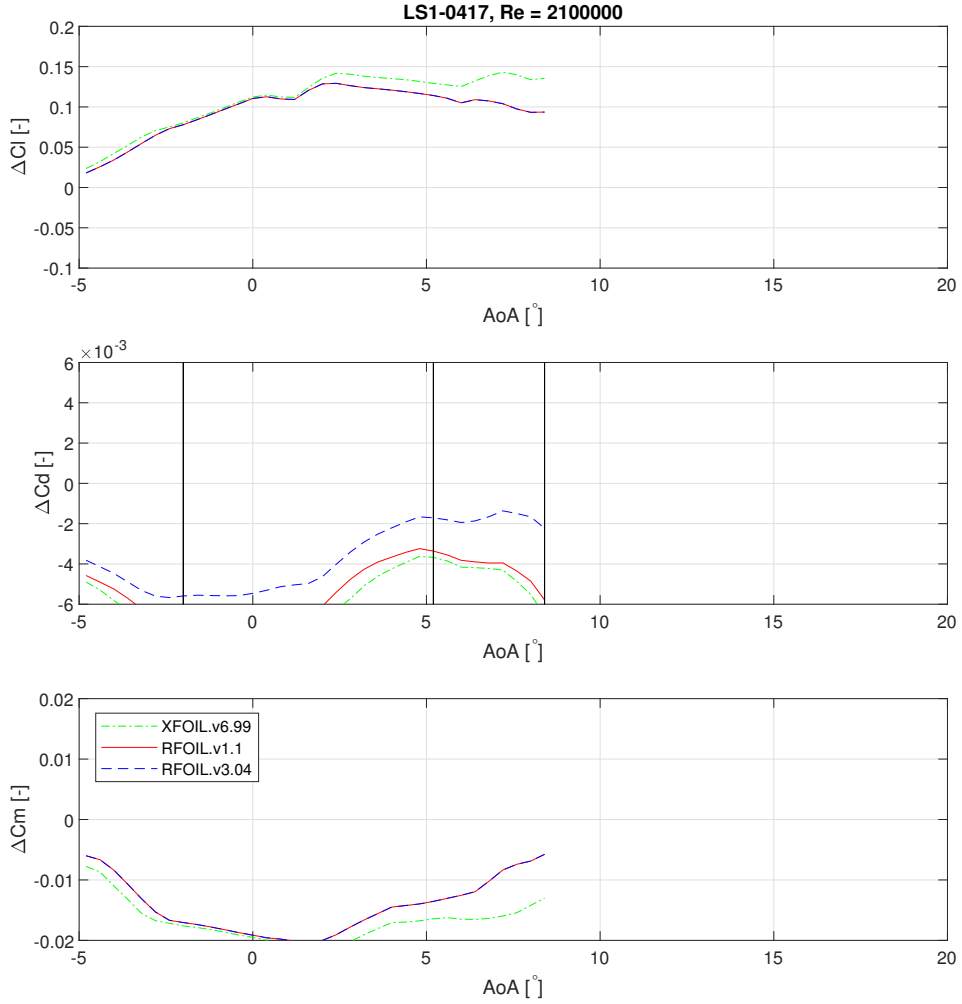

Figure B.177: Comparison between experimental and numerical pressure and skin friction distributions for the LS1-0417 airfoil at a Reynolds number of 2100000 and at the design angle of attack.

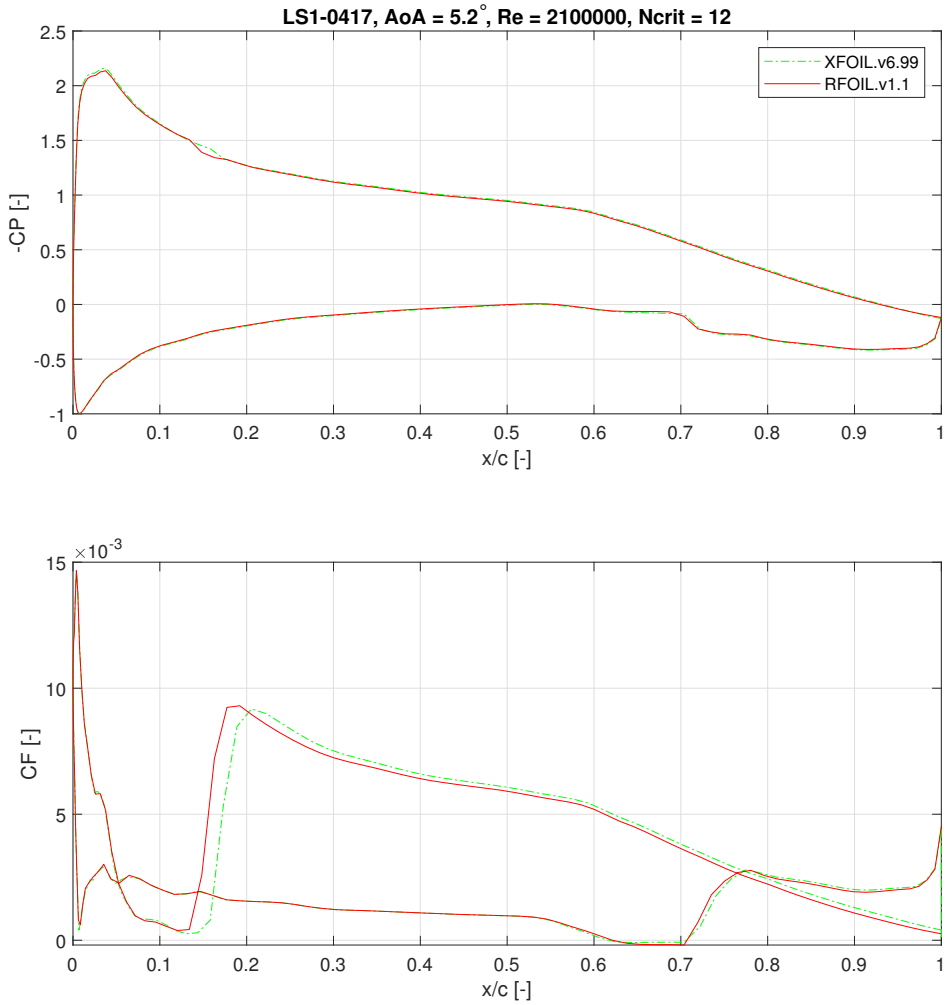

Figure B.178: Comparison between experimental and numerical polars for the LS1-0417 airfoil at a Reynolds number of 4300000. Simulation time to generate the polars by means the different codes and the number of converged polar points are depicted between parentheses.

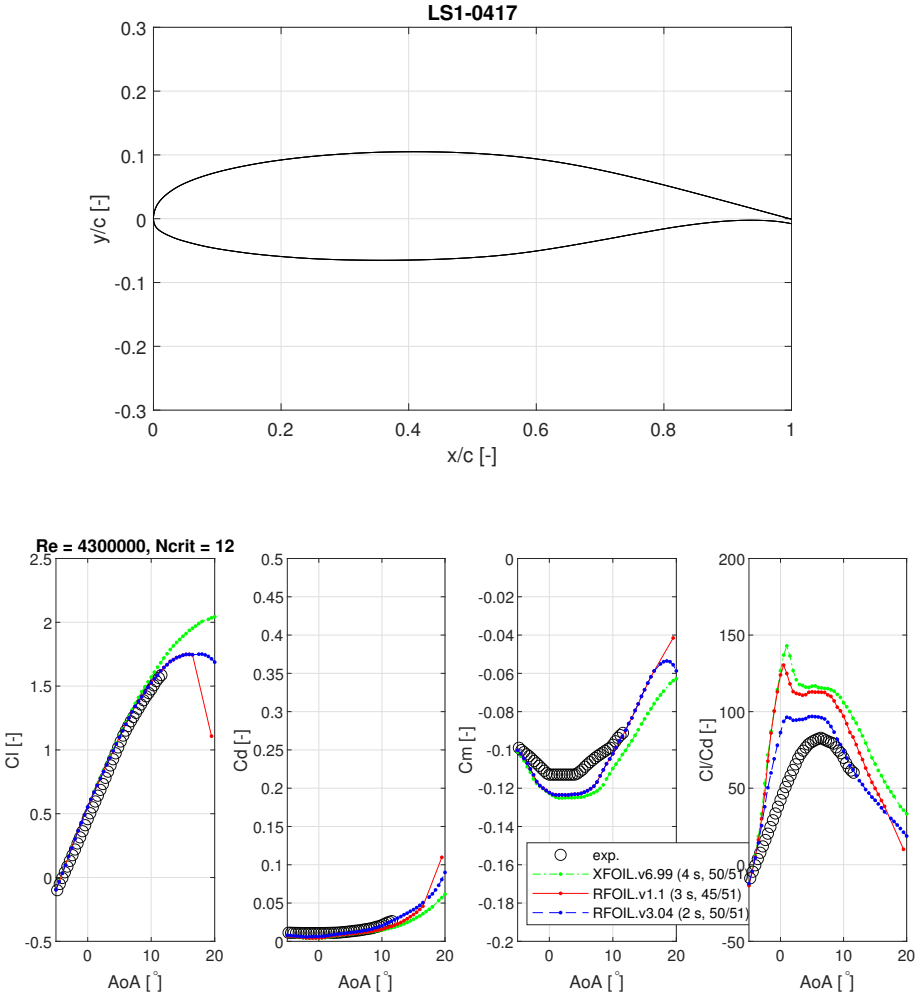

Figure B.179: Differences between experimental and numerical polars for the LS1-0417 airfoil at a Reynolds number of 4300000. Vertical black lines in the middle subplot indicate, from left to right, the angle of attack corresponding to the minimum drag coefficient, maximum lift to drag ratio and maximum lift coefficient, respectively.

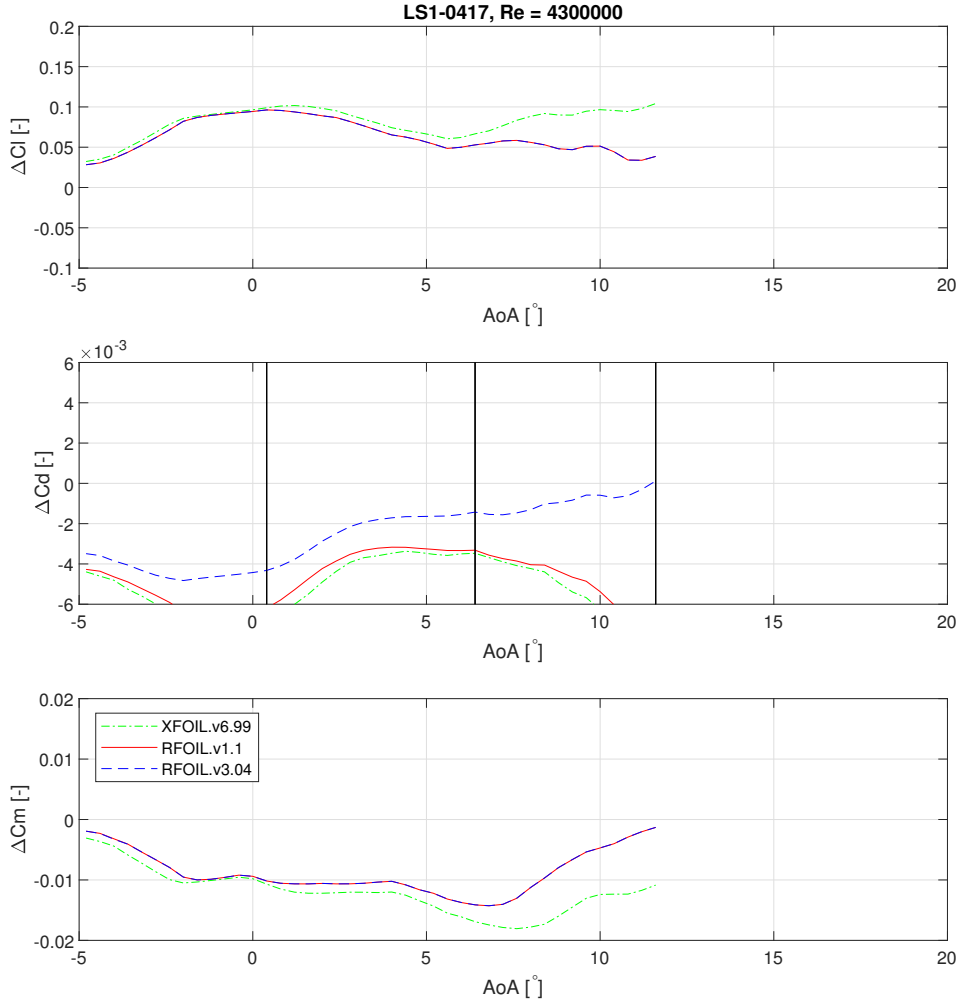

Figure B.180: Comparison between experimental and numerical pressure and skin friction distributions for the LS1-0417 airfoil at a Reynolds number of 4300000 and at the design angle of attack.

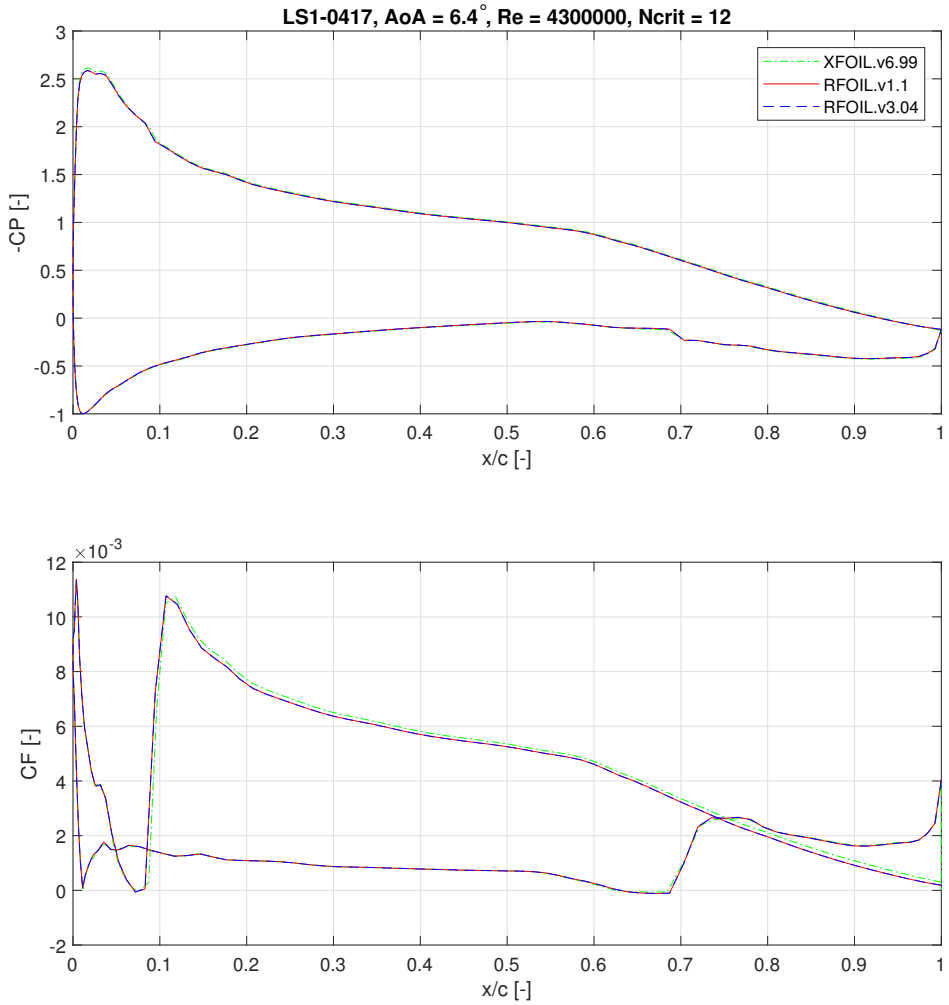

Figure B.181: Comparison between experimental and numerical polars for the LS1-0417 airfoil at a Reynolds number of 6300000. Simulation time to generate the polars by means the different codes and the number of converged polar points are depicted between parentheses.

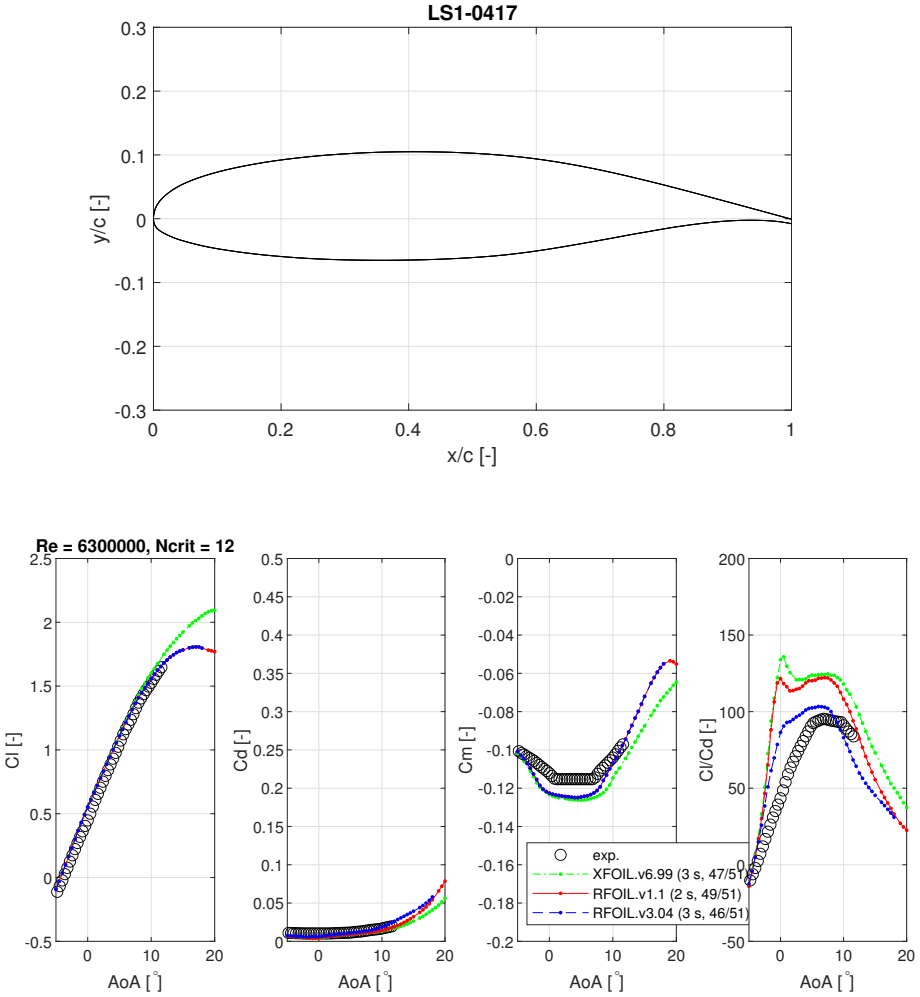

Figure B.182: Differences between experimental and numerical polars for the LS1-0417 airfoil at a Reynolds number of 6300000. Vertical black lines in the middle subplot indicate, from left to right, the angle of attack corresponding to the minimum drag coefficient, maximum lift to drag ratio and maximum lift coefficient, respectively.

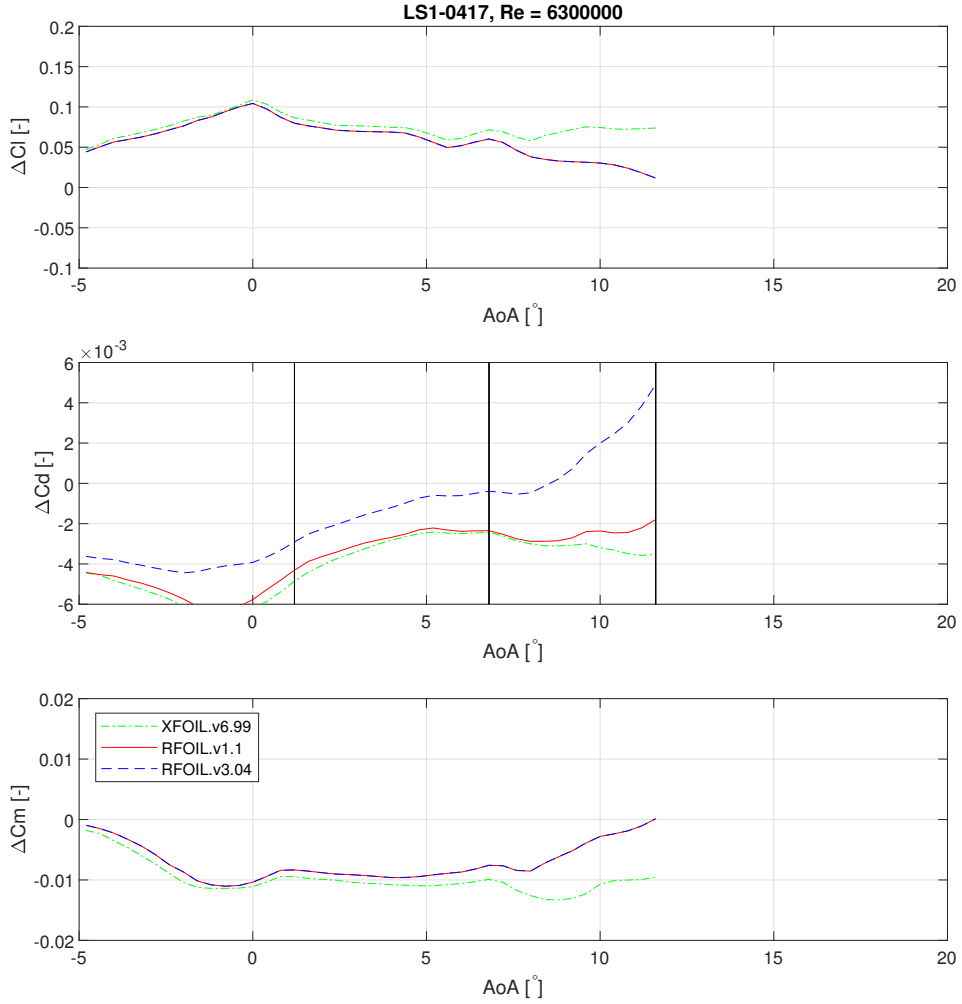

Figure B.183: Comparison between experimental and numerical pressure and skin friction distributions for the LS1-0417 airfoil at a Reynolds number of 6300000 and at the design angle of attack.

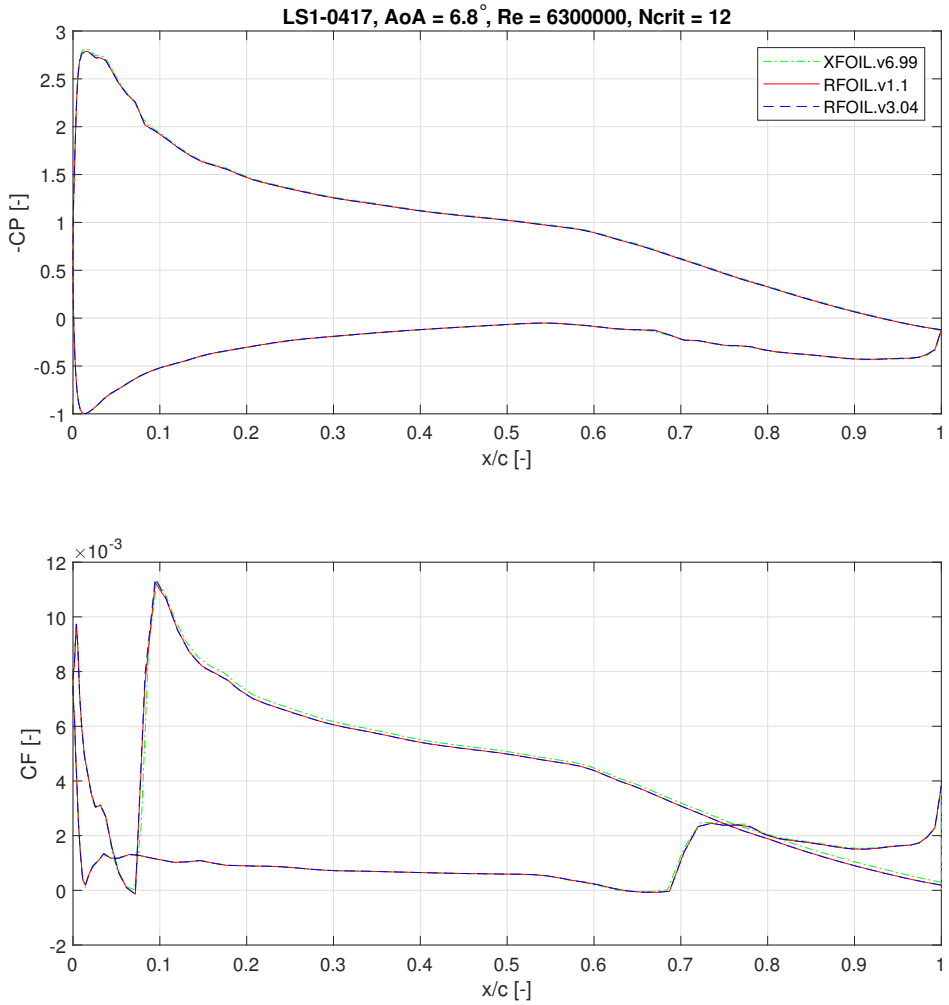

Figure B.184: Comparison between experimental and numerical polars for the LS1-0421 airfoil at a Reynolds number of 2000000. Simulation time to generate the polars by means the different codes and the number of converged polar points are depicted between parentheses.

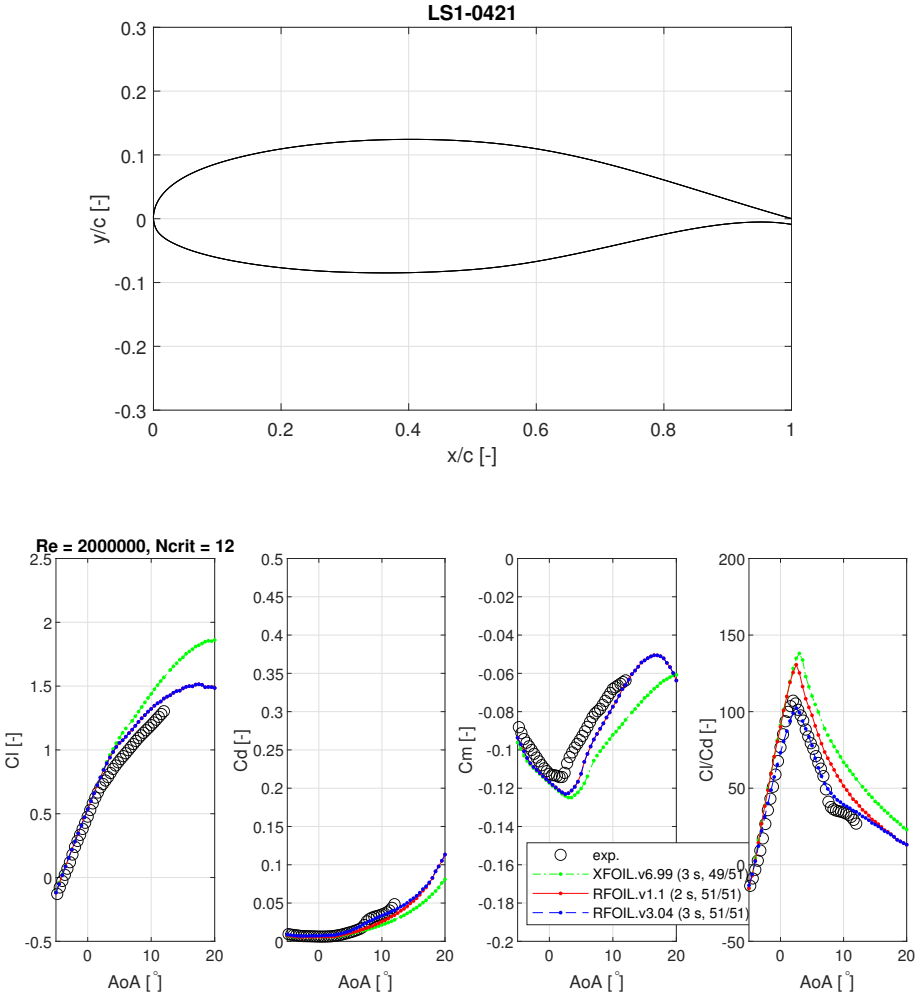

Figure B.185: Differences between experimental and numerical polars for the LS1-0421 airfoil at a Reynolds number of 2000000. Vertical black lines in the middle subplot indicate, from left to right, the angle of attack corresponding to the minimum drag coefficient, maximum lift to drag ratio and maximum lift coefficient, respectively.

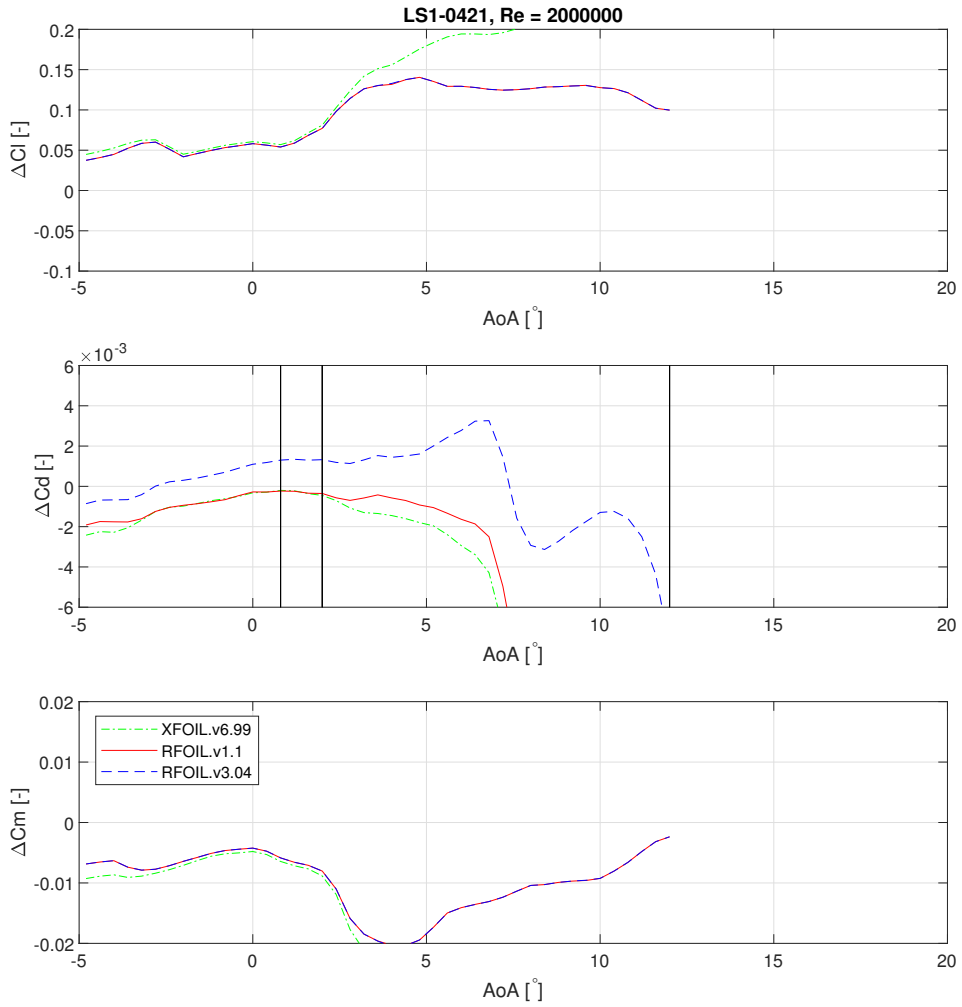

Figure B.186: Comparison between experimental and numerical pressure and skin friction distributions for the LS1-0421 airfoil at a Reynolds number of 2000000 and at the design angle of attack.

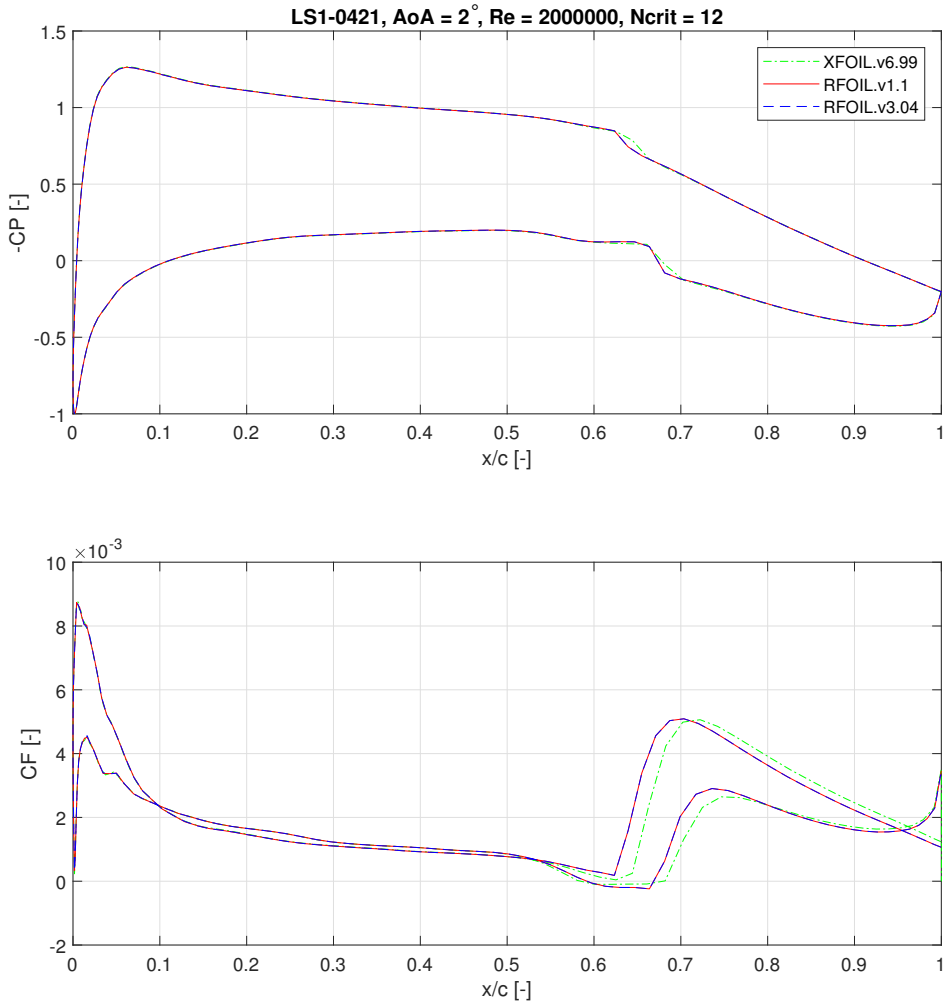

Figure B.187: Comparison between experimental and numerical polars for the LS1-0421 airfoil at a Reynolds number of 3000000. Simulation time to generate the polars by means the different codes and the number of converged polar points are depicted between parentheses.

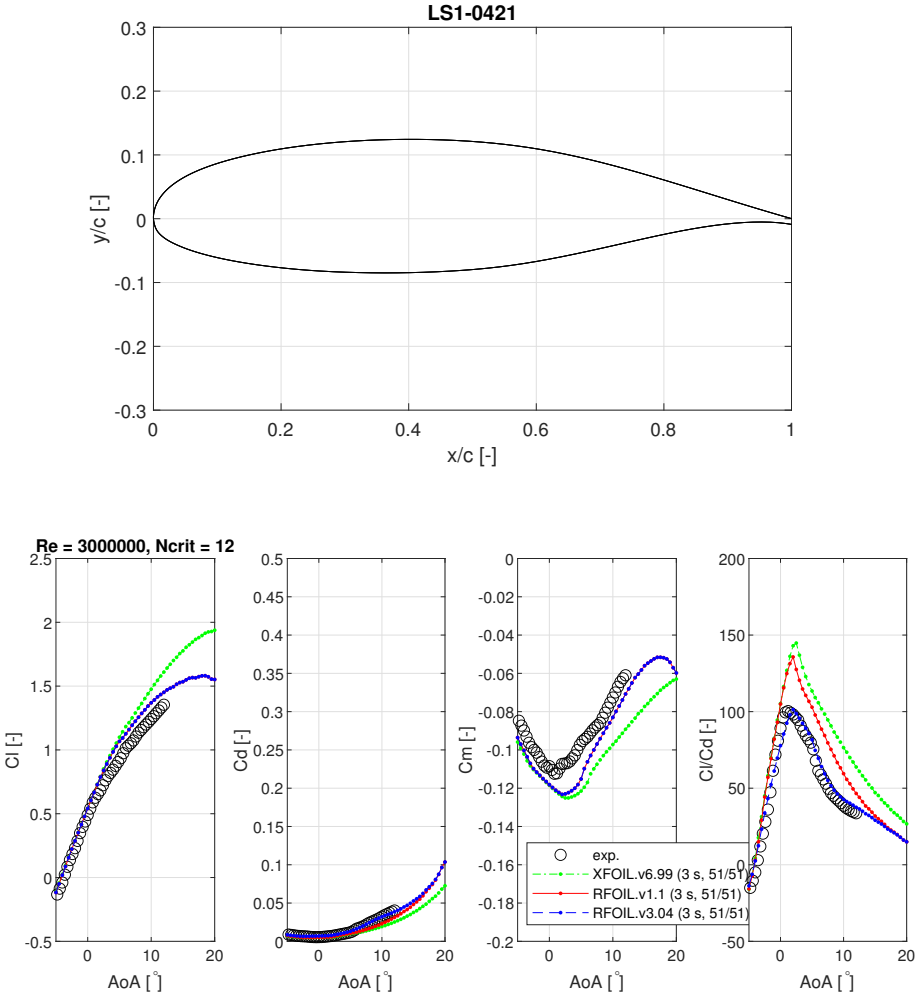

Figure B.188: Differences between experimental and numerical polars for the LS1-0421 airfoil at a Reynolds number of 3000000. Vertical black lines in the middle subplot indicate, from left to right, the angle of attack corresponding to the minimum drag coefficient, maximum lift to drag ratio and maximum lift coefficient, respectively.

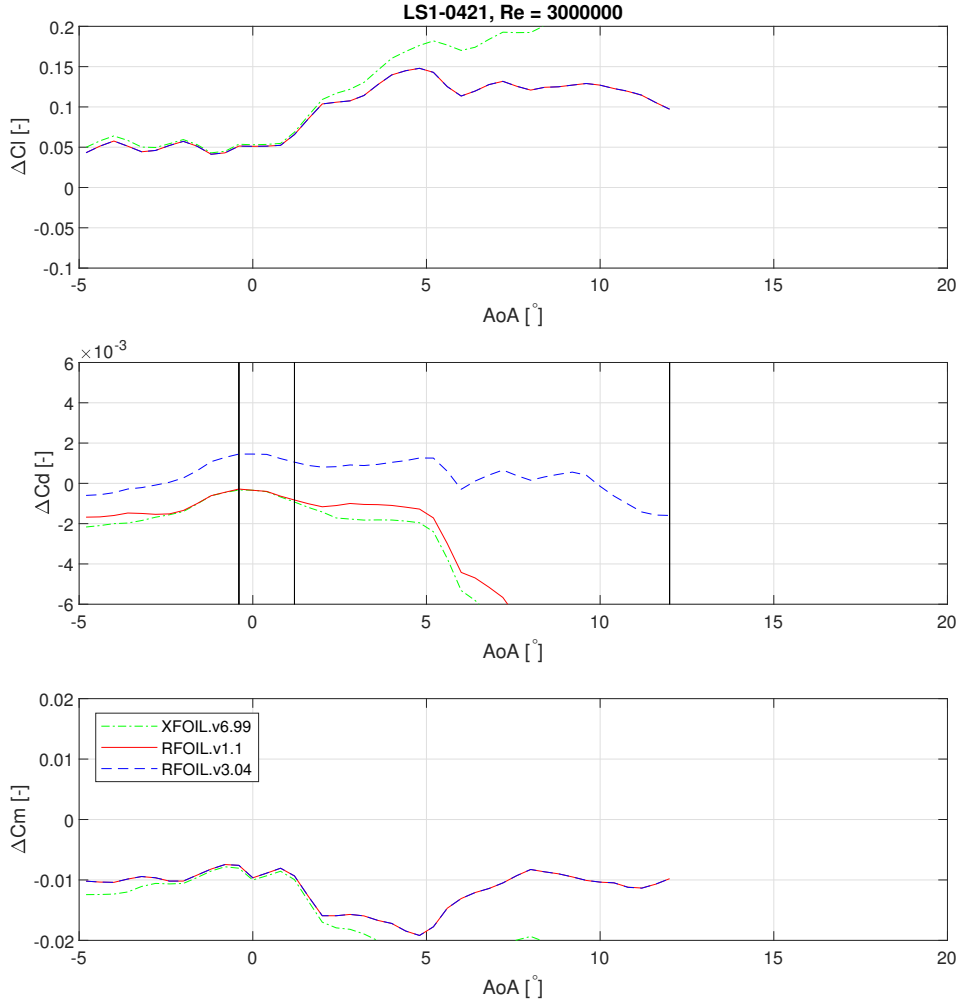

Figure B.189: Comparison between experimental and numerical pressure and skin friction distributions for the LS1-0421 airfoil at a Reynolds number of 3000000 and at the design angle of attack.

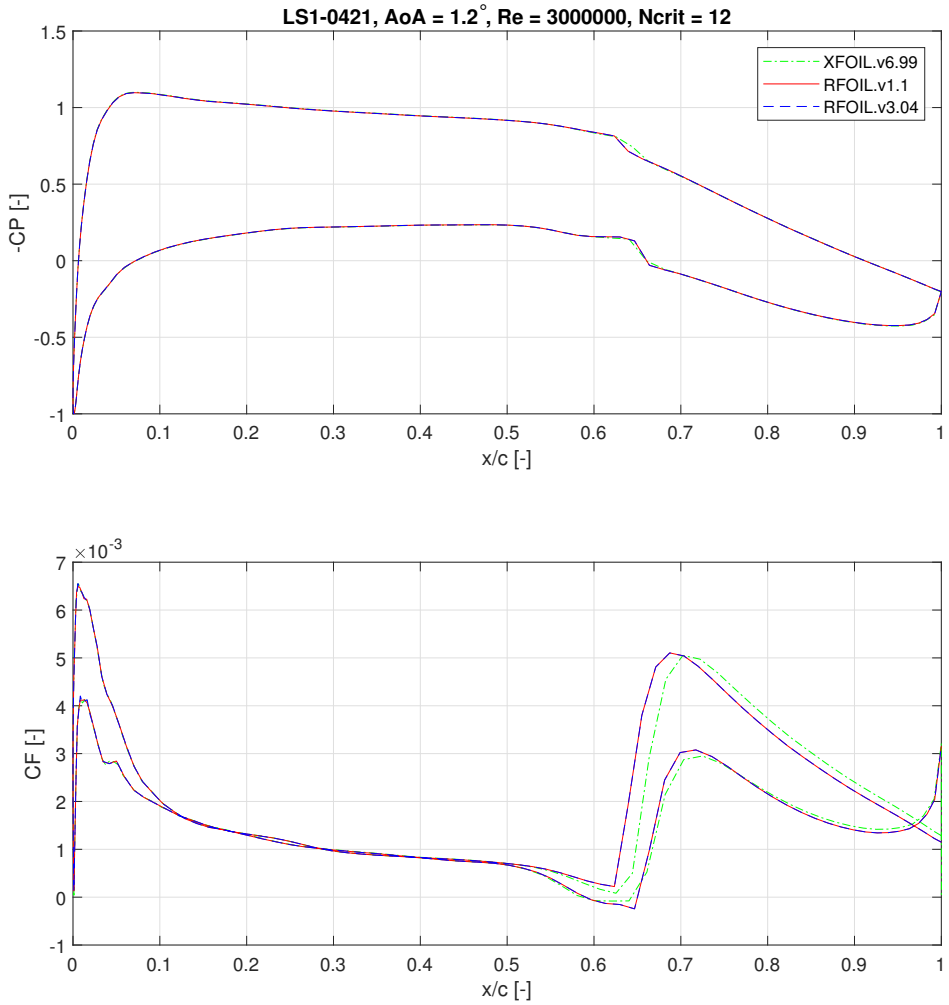

Figure B.190: Comparison between experimental and numerical polars for the LS1-0421 airfoil at a Reynolds number of 4000000. Simulation time to generate the polars by means the different codes and the number of converged polar points are depicted between parentheses.

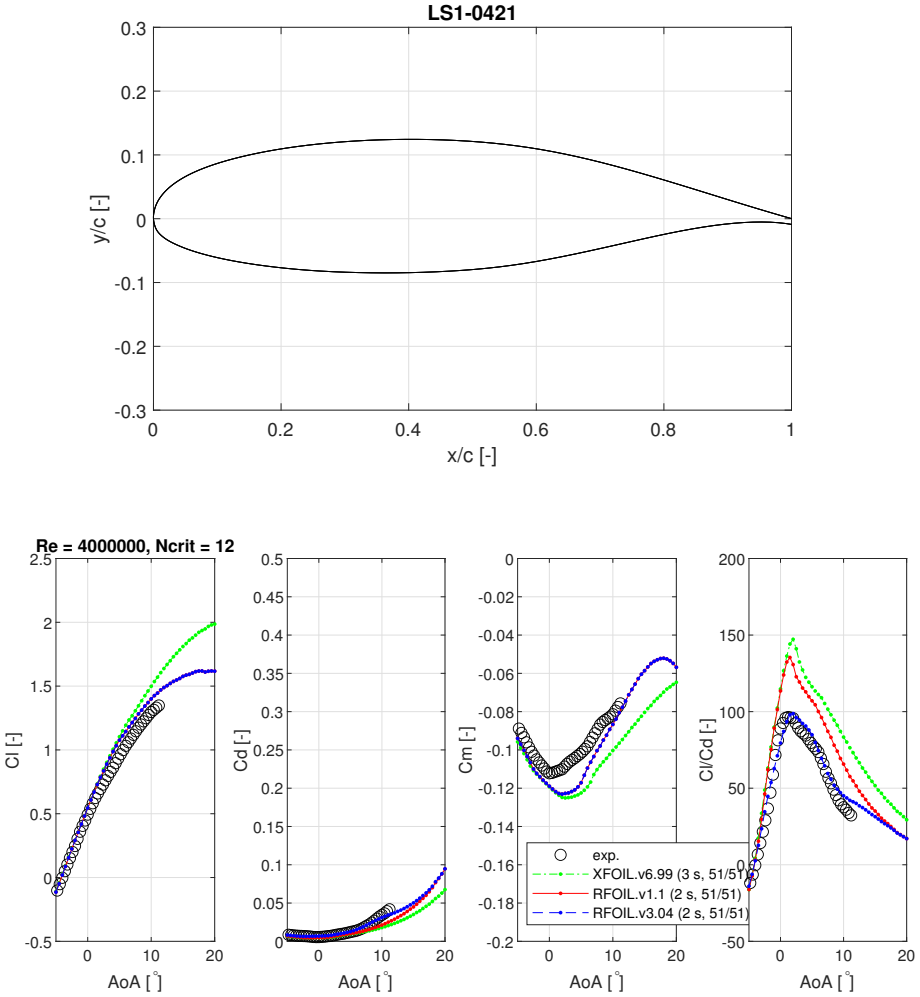

Figure B.191: Differences between experimental and numerical polars for the LS1-0421 airfoil at a Reynolds number of 4000000. Vertical black lines in the middle subplot indicate, from left to right, the angle of attack corresponding to the minimum drag coefficient, maximum lift to drag ratio and maximum lift coefficient, respectively.

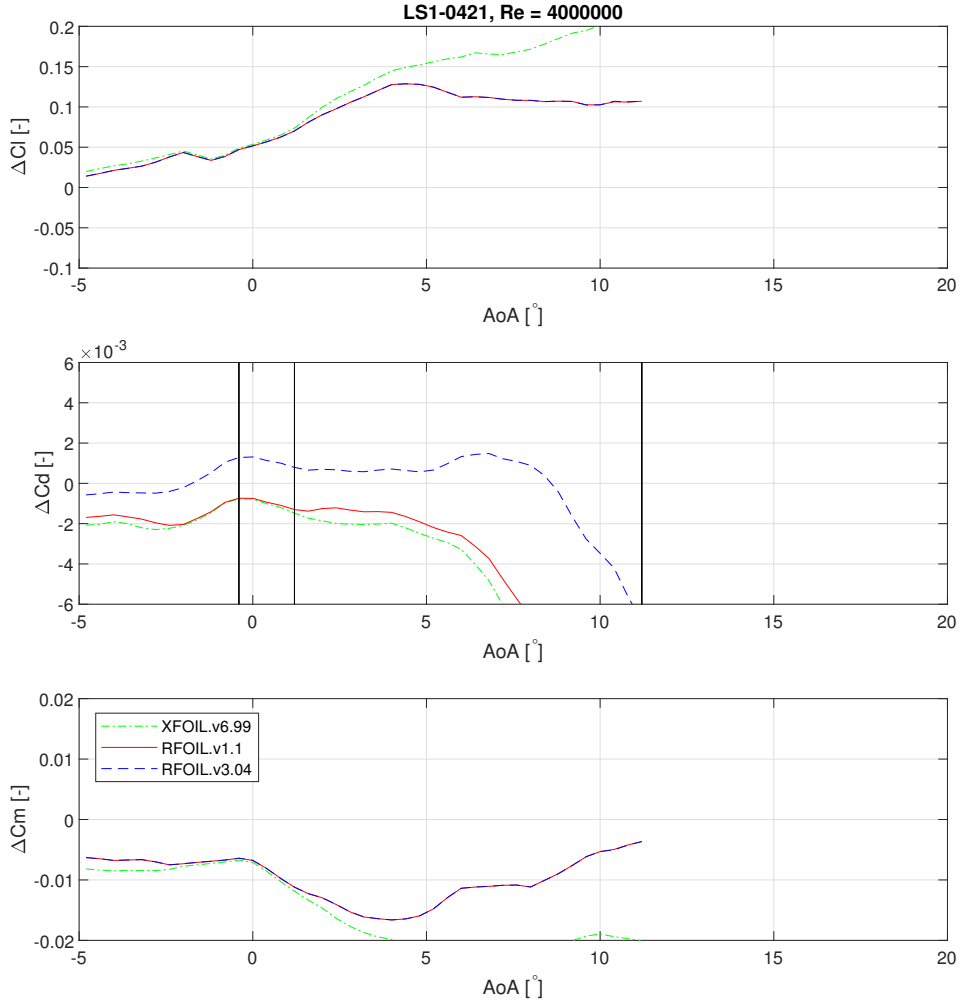

Figure B.192: Comparison between experimental and numerical pressure and skin friction distributions for the LS1-0421 airfoil at a Reynolds number of 4000000 and at the design angle of attack.

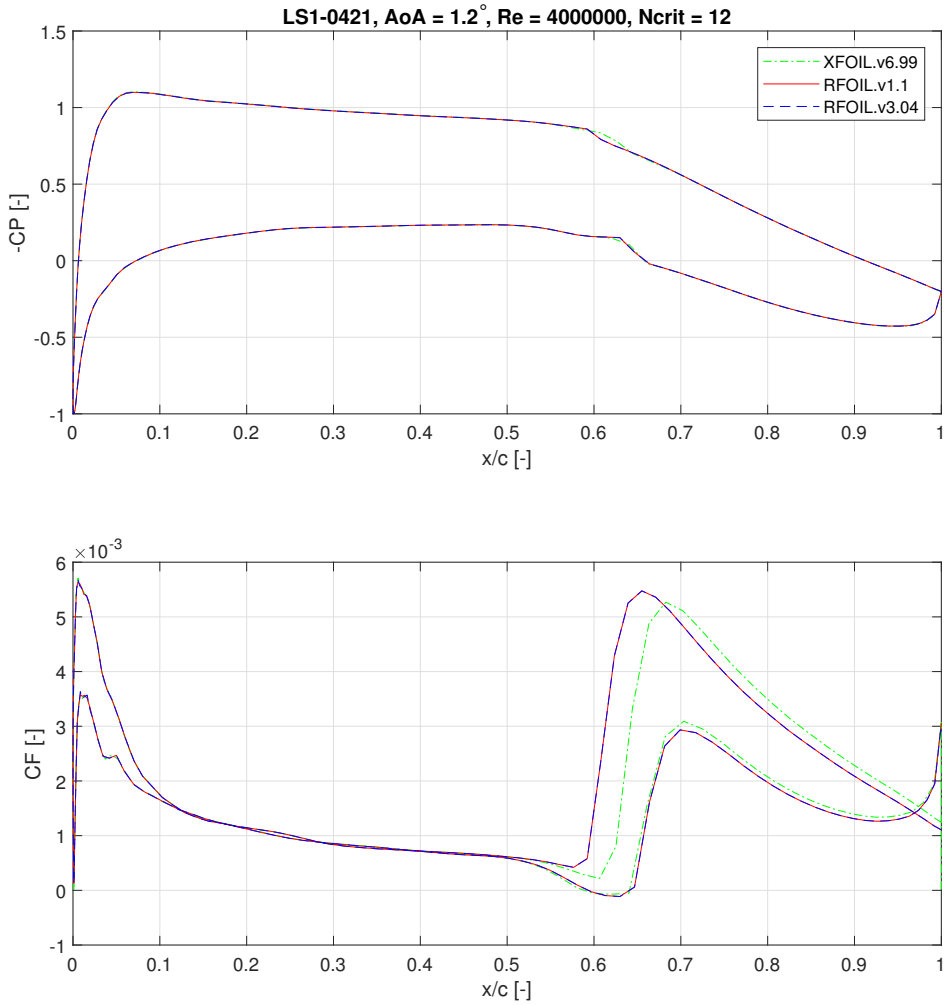

Figure B.193: Comparison between experimental and numerical polars for the LS1-0421 airfoil at a Reynolds number of 6000000. Simulation time to generate the polars by means the different codes and the number of converged polar points are depicted between parentheses.

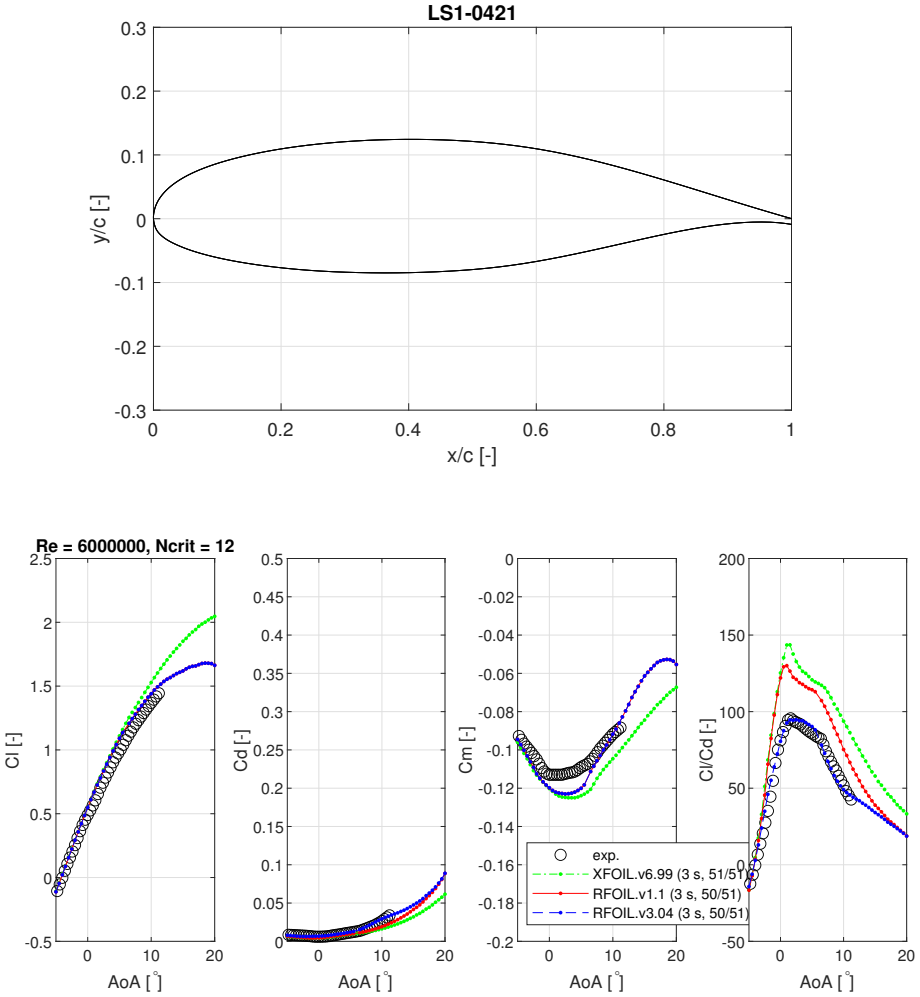

Figure B.194: Differences between experimental and numerical polars for the LS1-0421 airfoil at a Reynolds number of 6000000. Vertical black lines in the middle subplot indicate, from left to right, the angle of attack corresponding to the minimum drag coefficient, maximum lift to drag ratio and maximum lift coefficient, respectively.

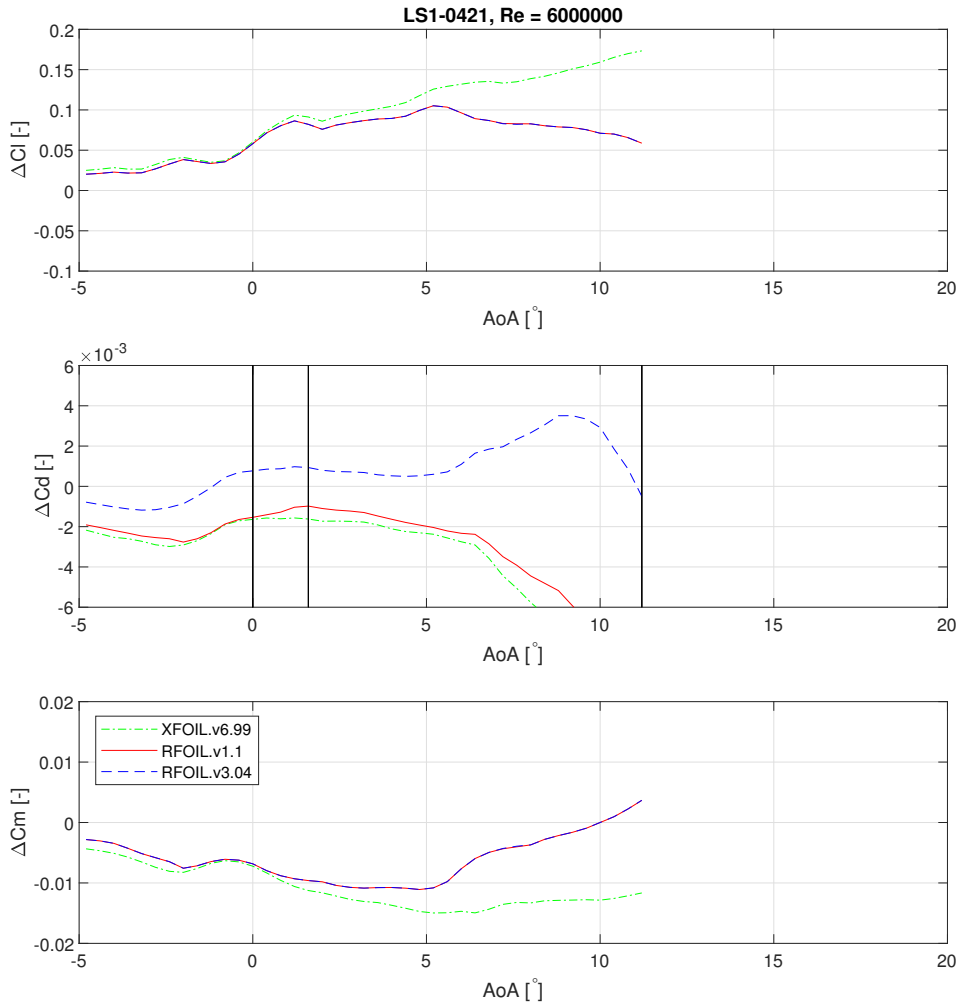

Figure B.195: Comparison between experimental and numerical pressure and skin friction distributions for the LS1-0421 airfoil at a Reynolds number of 6000000 and at the design angle of attack.

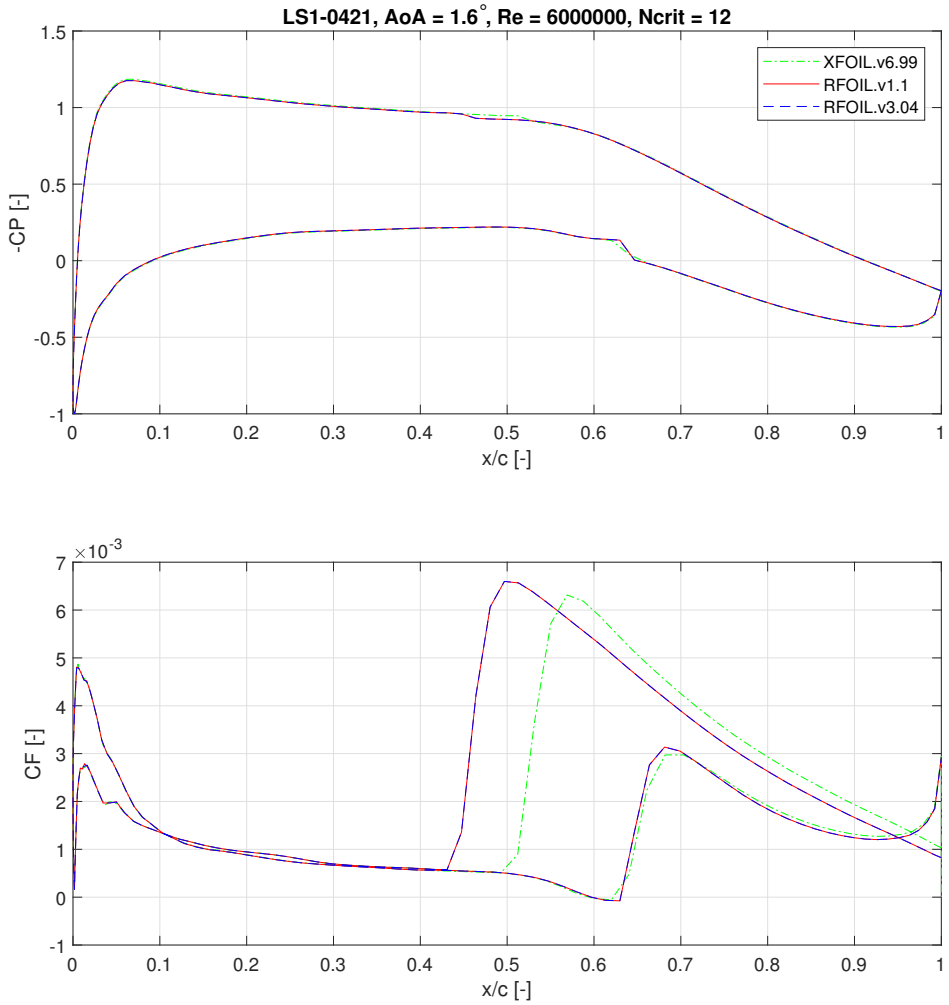

Figure B.196: Comparison between experimental and numerical polars for the LS1-0421 airfoil at a Reynolds number of 9000000. Simulation time to generate the polars by means the different codes and the number of converged polar points are depicted between parentheses.

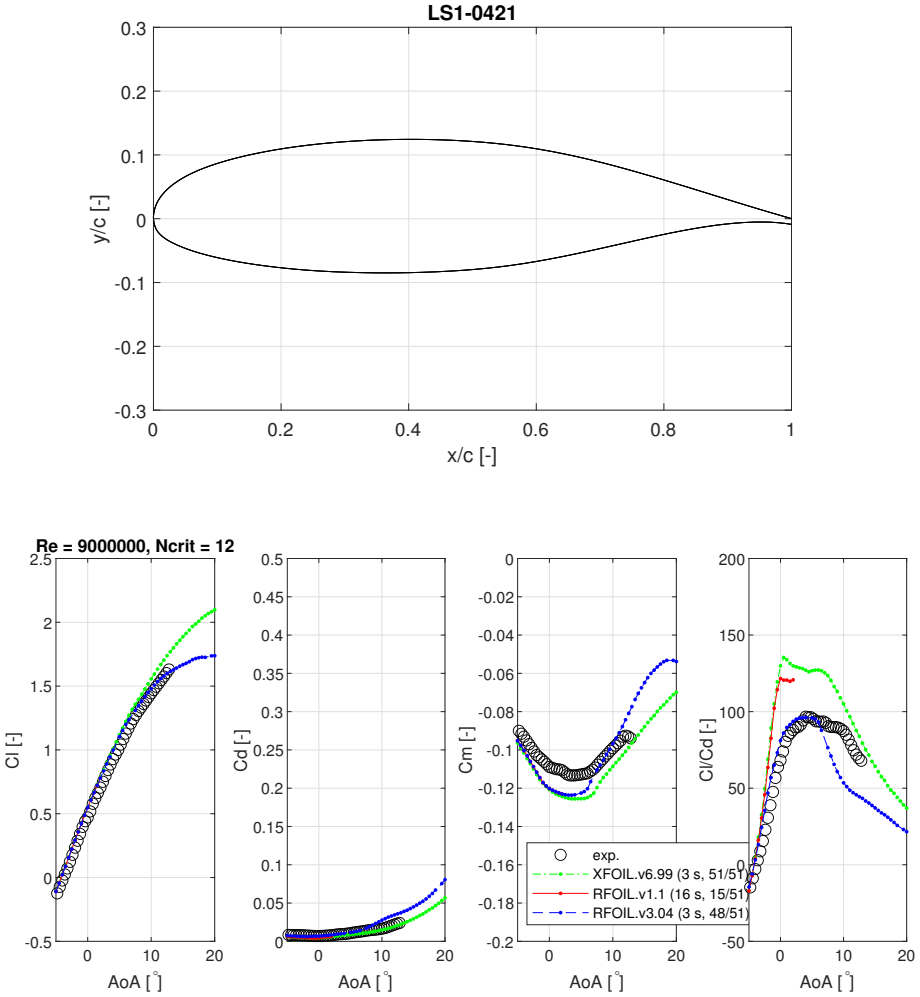

Figure B.197: Differences between experimental and numerical polars for the LS1-0421 airfoil at a Reynolds number of 9000000. Vertical black lines in the middle subplot indicate, from left to right, the angle of attack corresponding to the minimum drag coefficient, maximum lift to drag ratio and maximum lift coefficient, respectively.

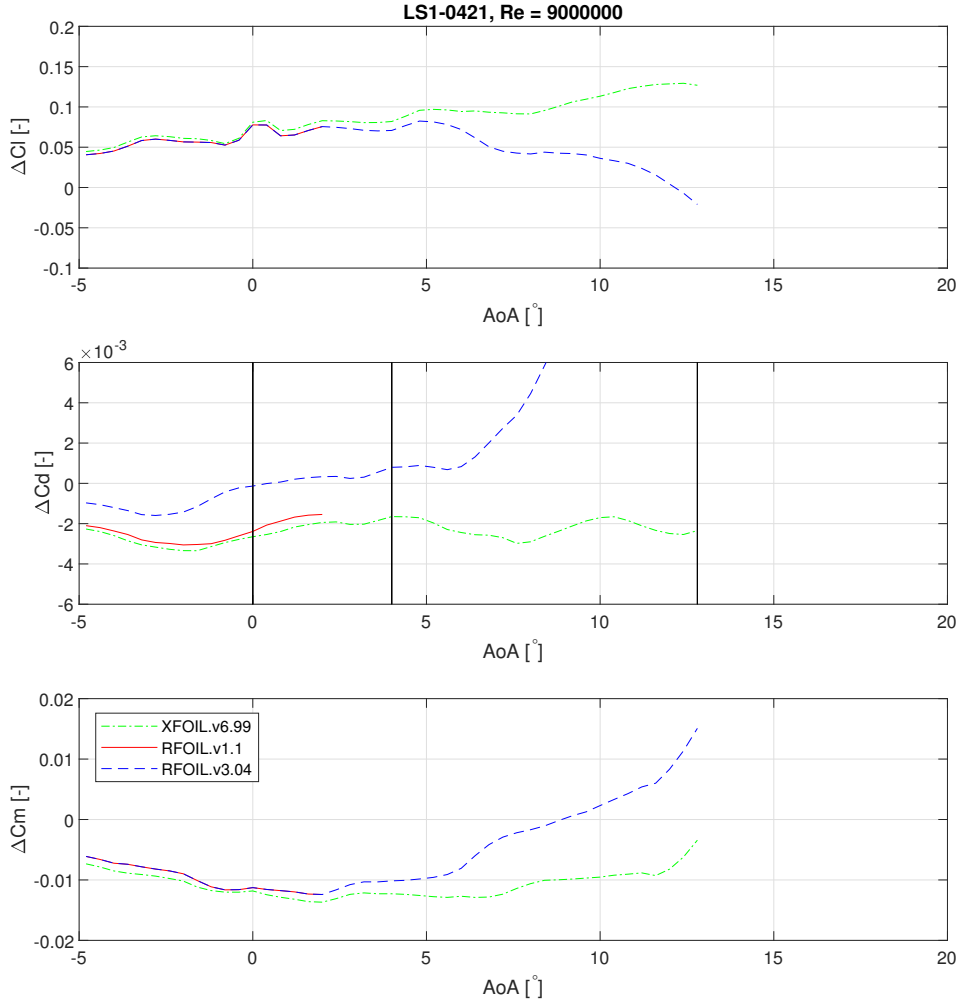

Figure B.198: Comparison between experimental and numerical pressure and skin friction distributions for the LS1-0421 airfoil at a Reynolds number of 9000000 and at the design angle of attack.

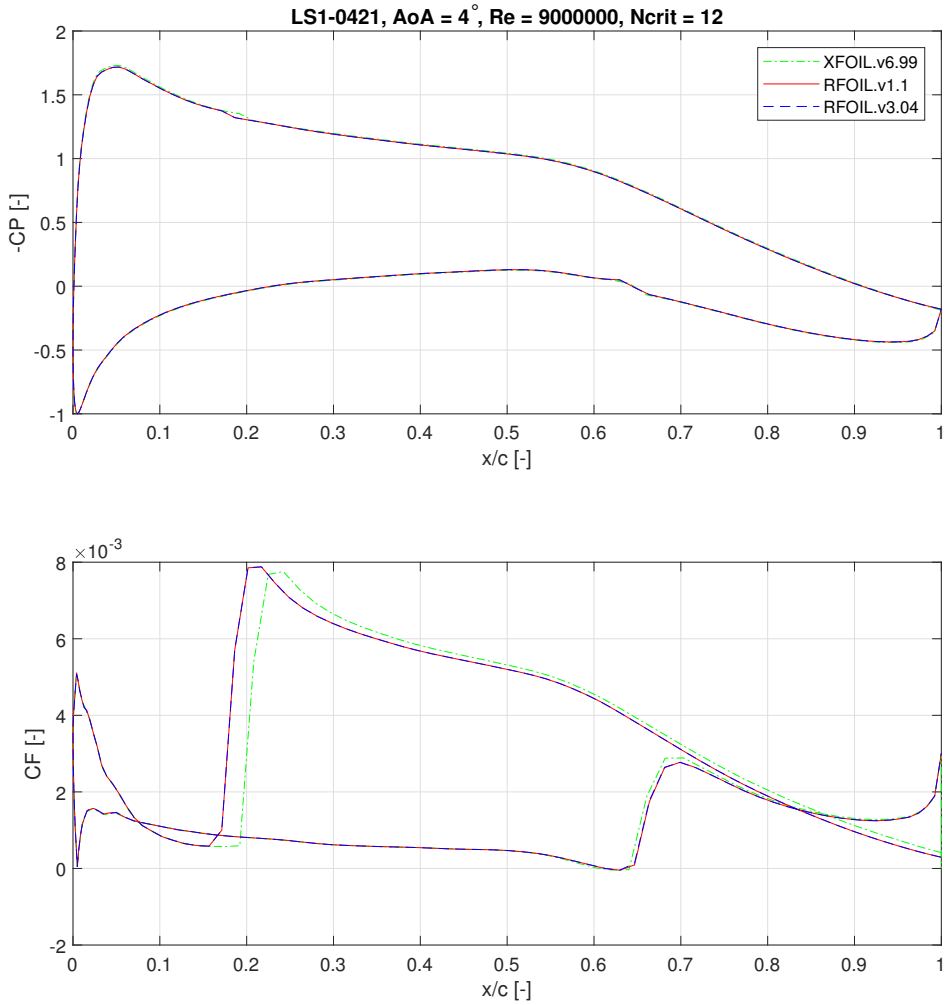

B.6 NACA series airfoils

Figure B.199: Comparison between experimental and numerical polars for the NACA-23012 airfoil at a Reynolds number of 1000000. Simulation time to generate the polars by means the different codes and the number of converged polar points are depicted between parentheses.

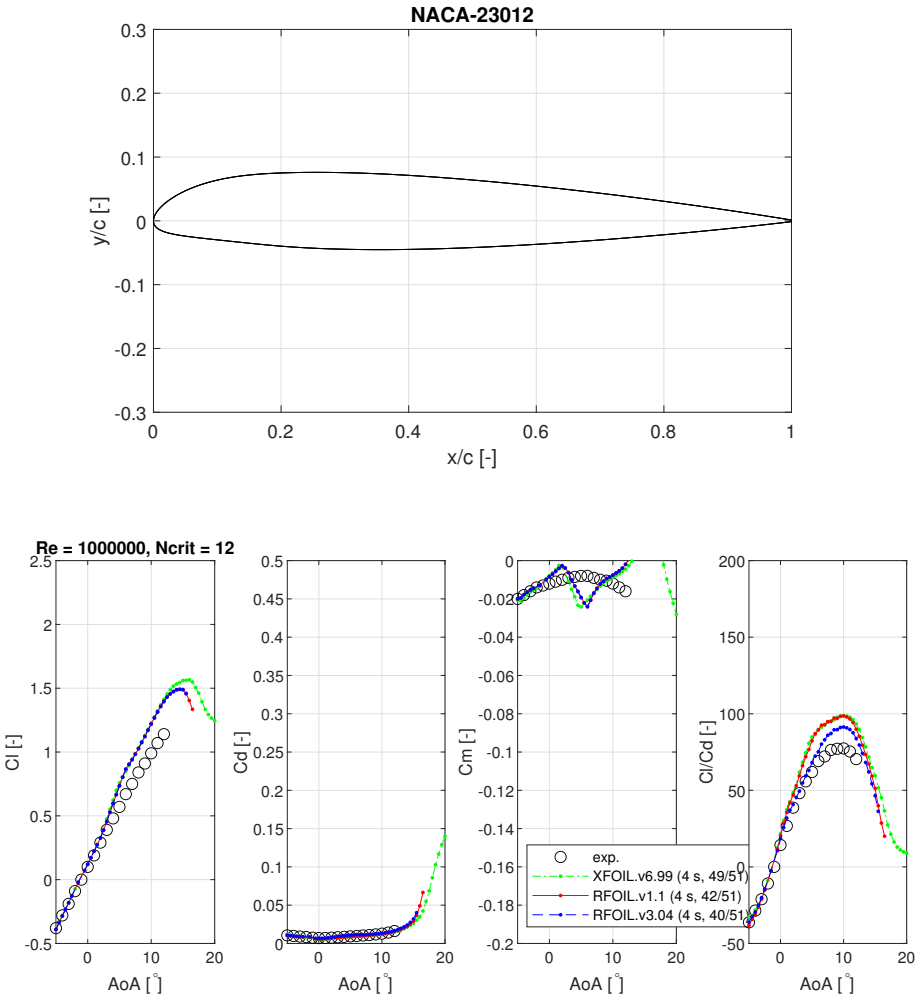

Figure B.200: Differences between experimental and numerical polars for the NACA-23012 airfoil at a Reynolds number of 1000000. Vertical black lines in the middle subplot indicate, from left to right, the angle of attack corresponding to the minimum drag coefficient, maximum lift to drag ratio and maximum lift coefficient, respectively.

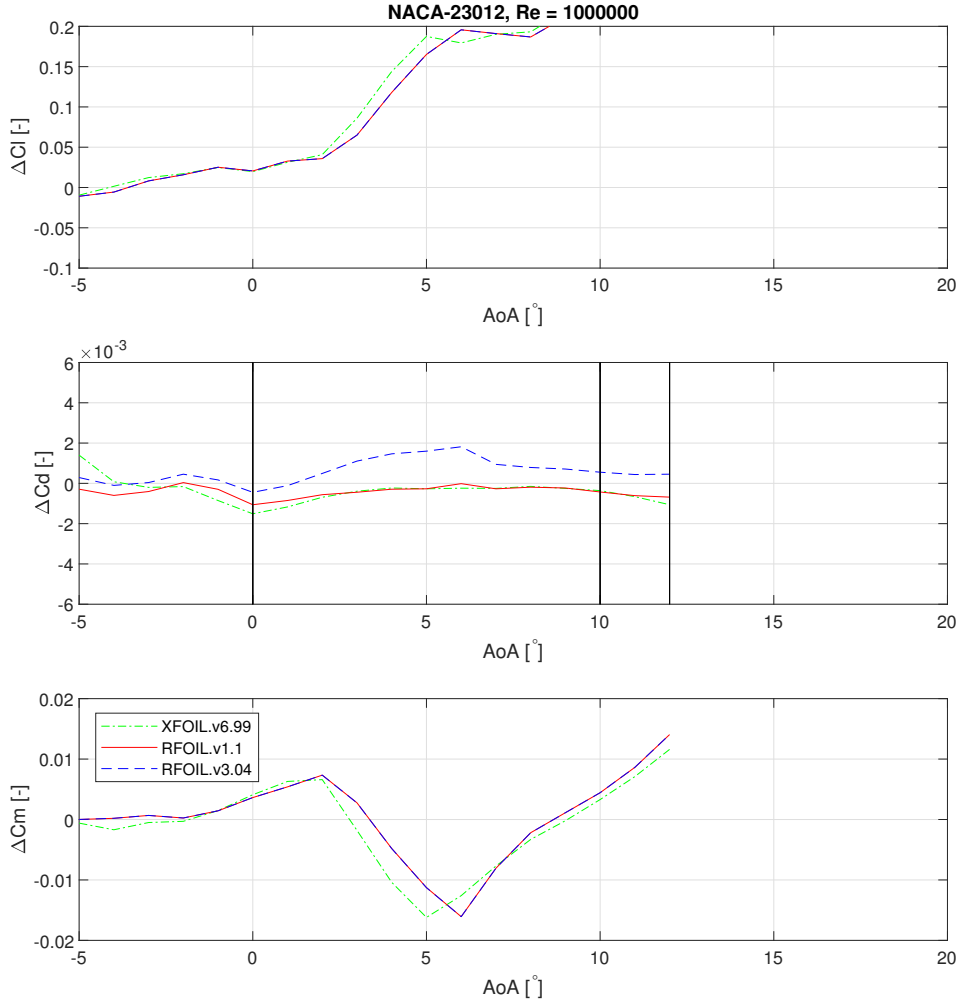

Figure B.201: Comparison between experimental and numerical pressure and skin friction distributions for the NACA-23012 airfoil at a Reynolds number of 1000000 and at the design angle of attack.

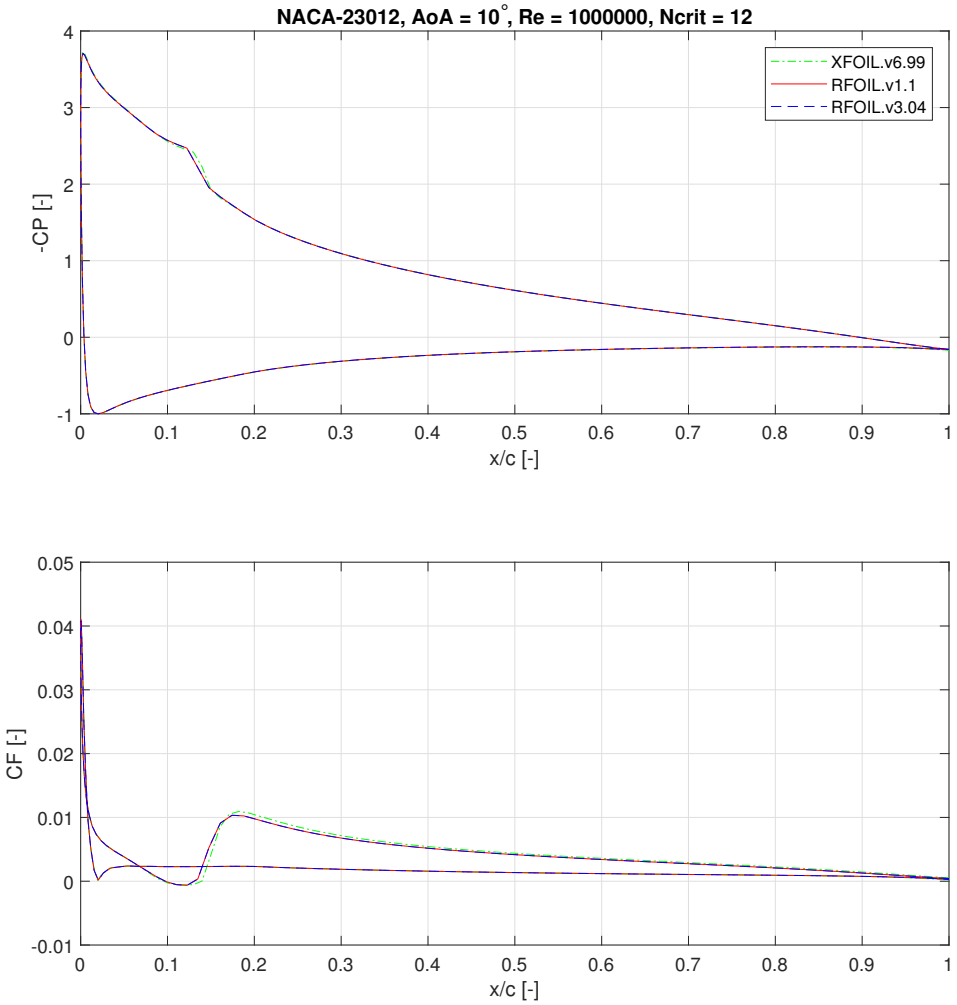

Figure B.202: Comparison between experimental and numerical polars for the NACA-23012 airfoil at a Reynolds number of 1500000. Simulation time to generate the polars by means the different codes and the number of converged polar points are depicted between parentheses.

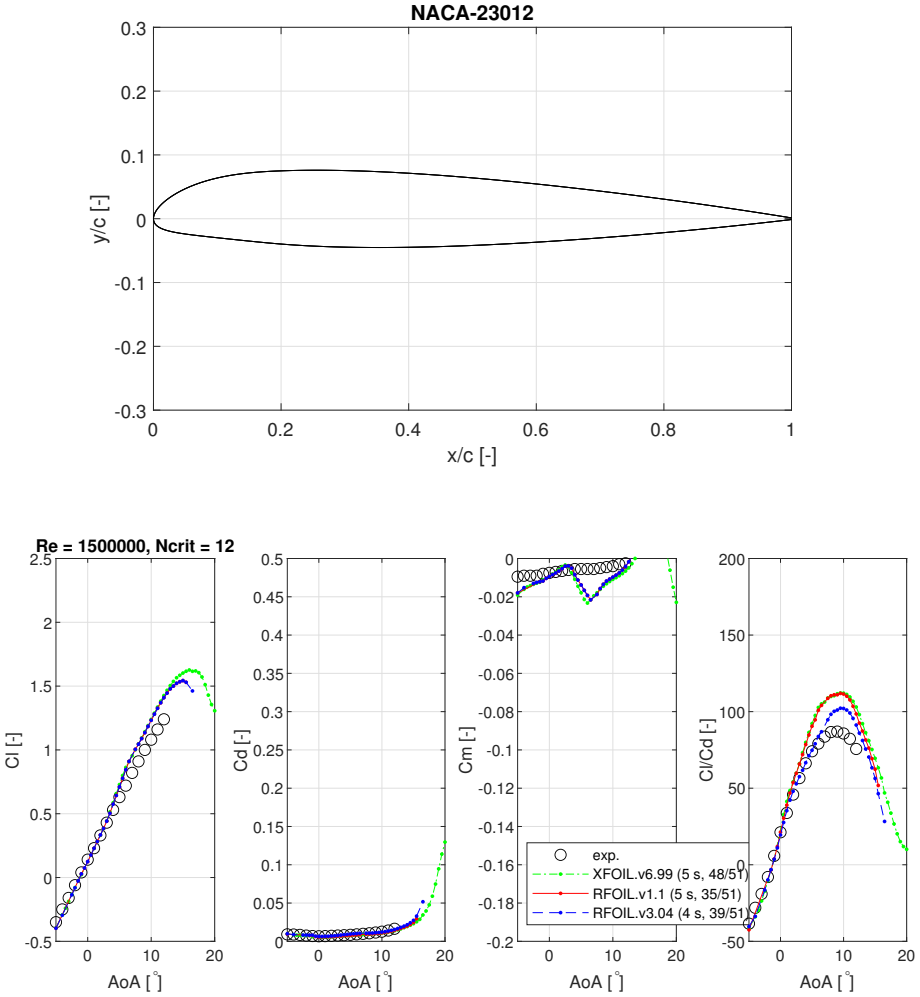

Figure B.203: Differences between experimental and numerical polars for the NACA-23012 airfoil at a Reynolds number of 1500000. Vertical black lines in the middle subplot indicate, from left to right, the angle of attack corresponding to the minimum drag coefficient, maximum lift to drag ratio and maximum lift coefficient, respectively.

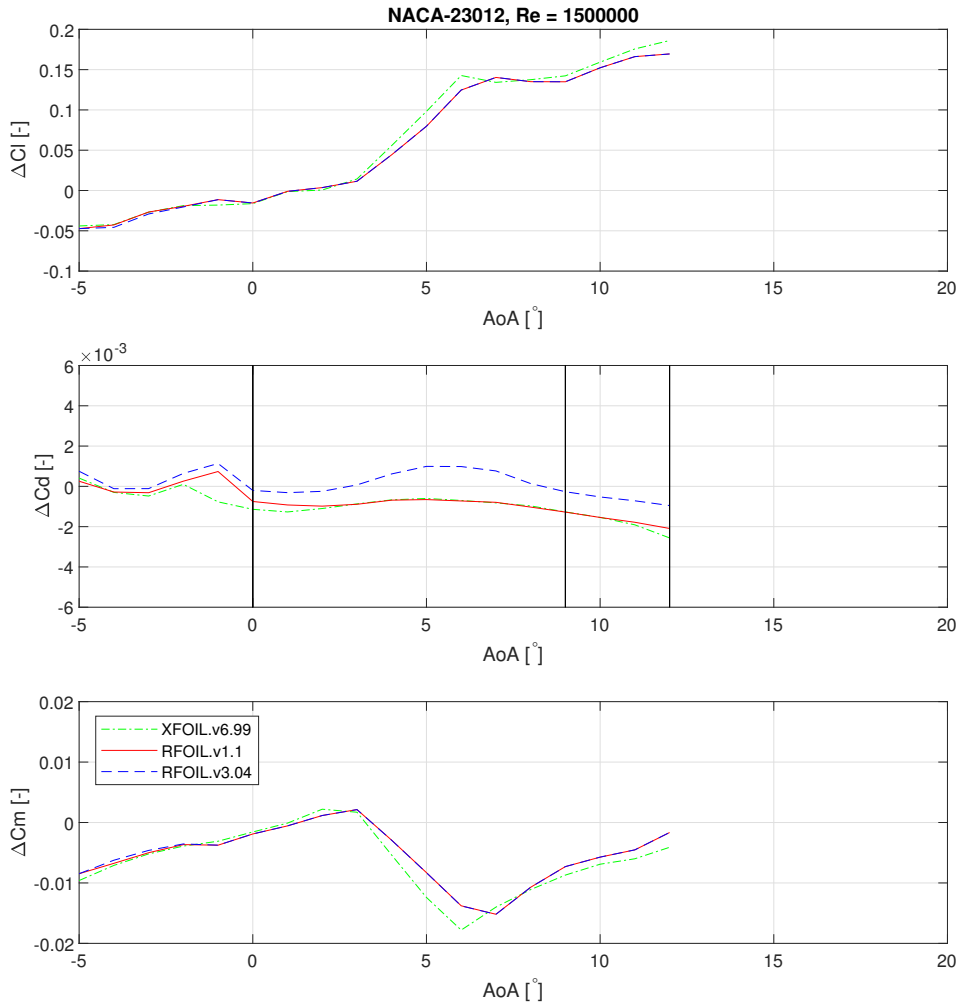

Figure B.204: Comparison between experimental and numerical pressure and skin friction distributions for the NACA-23012 airfoil at a Reynolds number of 1500000 and at the design angle of attack.

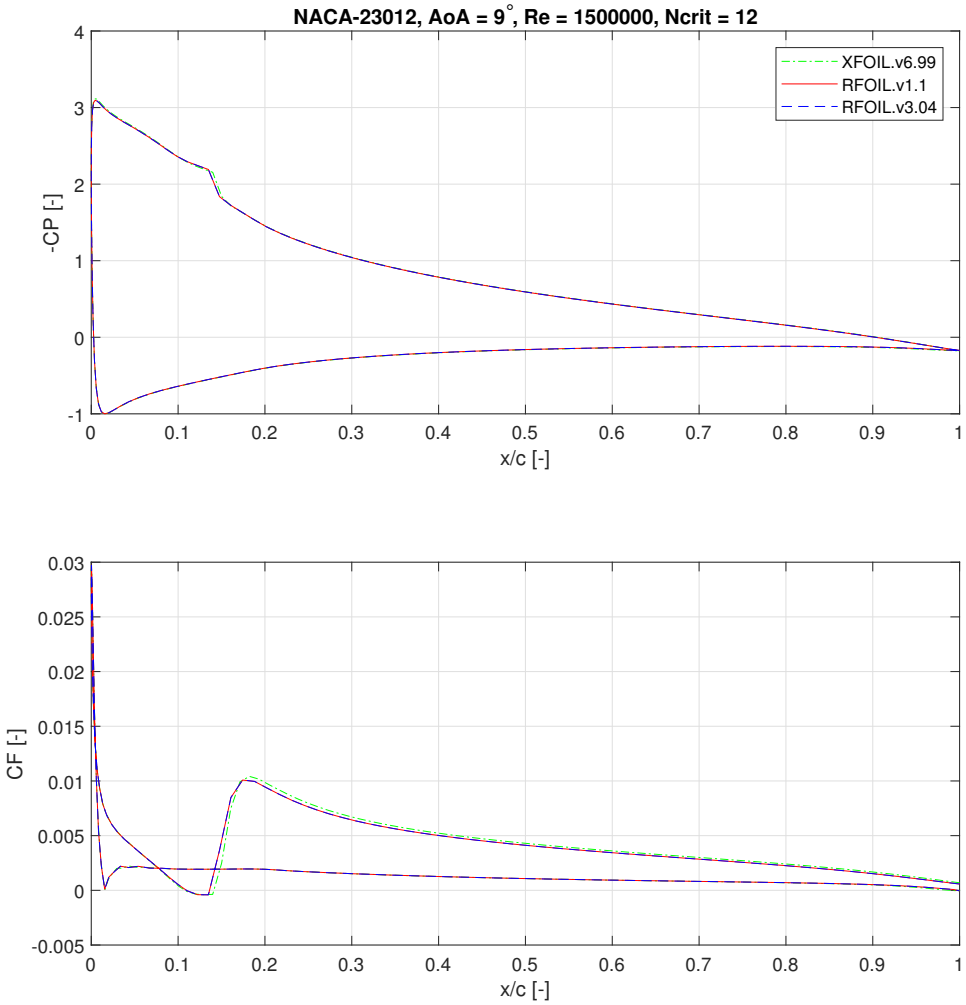

Figure B.205: Comparison between experimental and numerical polars for the NACA-23012 airfoil at a Reynolds number of 2000000. Simulation time to generate the polars by means the different codes and the number of converged polar points are depicted between parentheses.

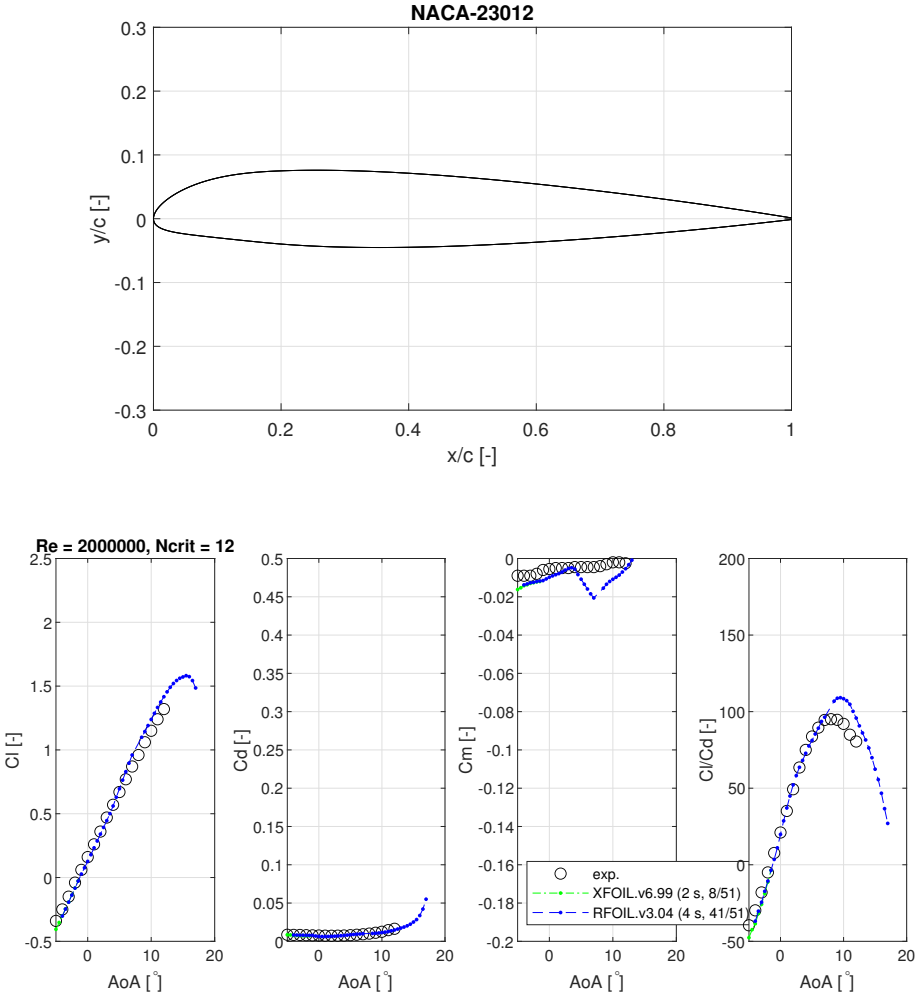

Figure B.206: Differences between experimental and numerical polars for the NACA-23012 airfoil at a Reynolds number of 2000000. Vertical black lines in the middle subplot indicate, from left to right, the angle of attack corresponding to the minimum drag coefficient, maximum lift to drag ratio and maximum lift coefficient, respectively.

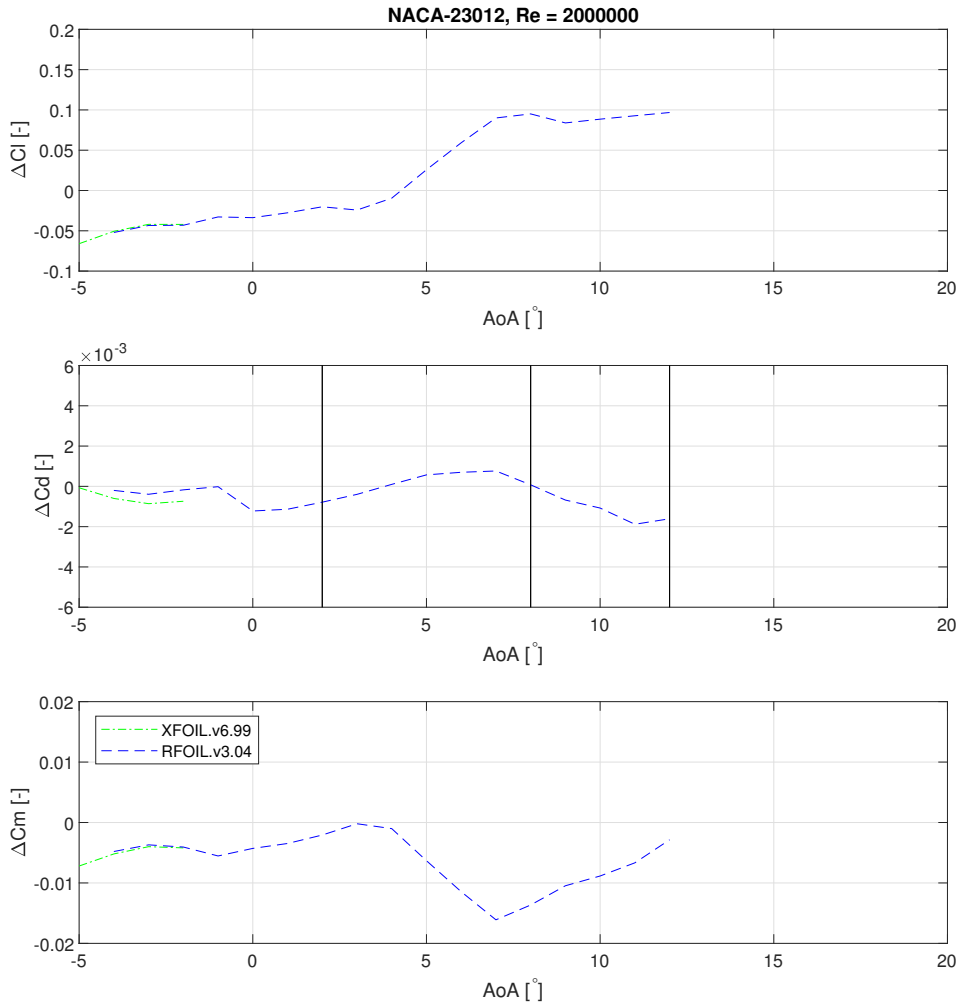

Figure B.207: Comparison between experimental and numerical pressure and skin friction distributions for the NACA-23012 airfoil at a Reynolds number of 2000000 and at the design angle of attack.

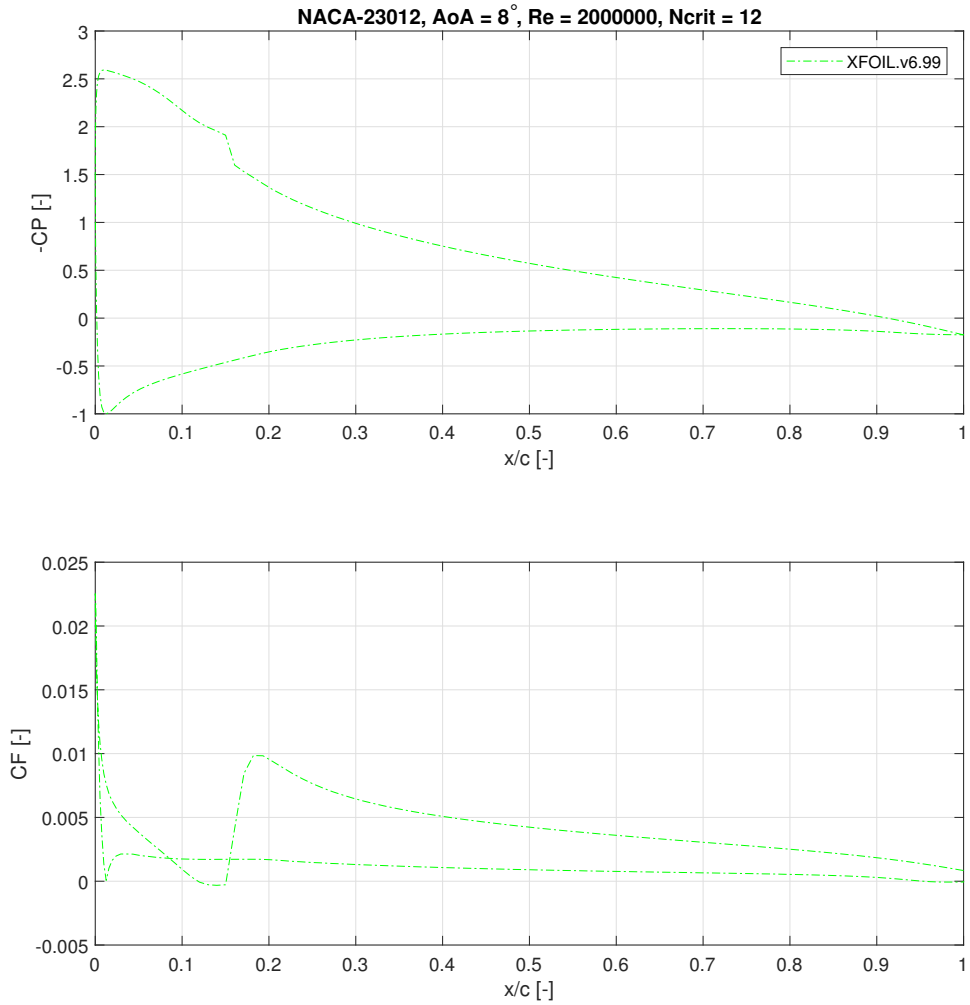

Figure B.208: Comparison between experimental and numerical polars for the NACA-23012 airfoil at a Reynolds number of 3000000. Simulation time to generate the polars by means the different codes and the number of converged polar points are depicted between parentheses.

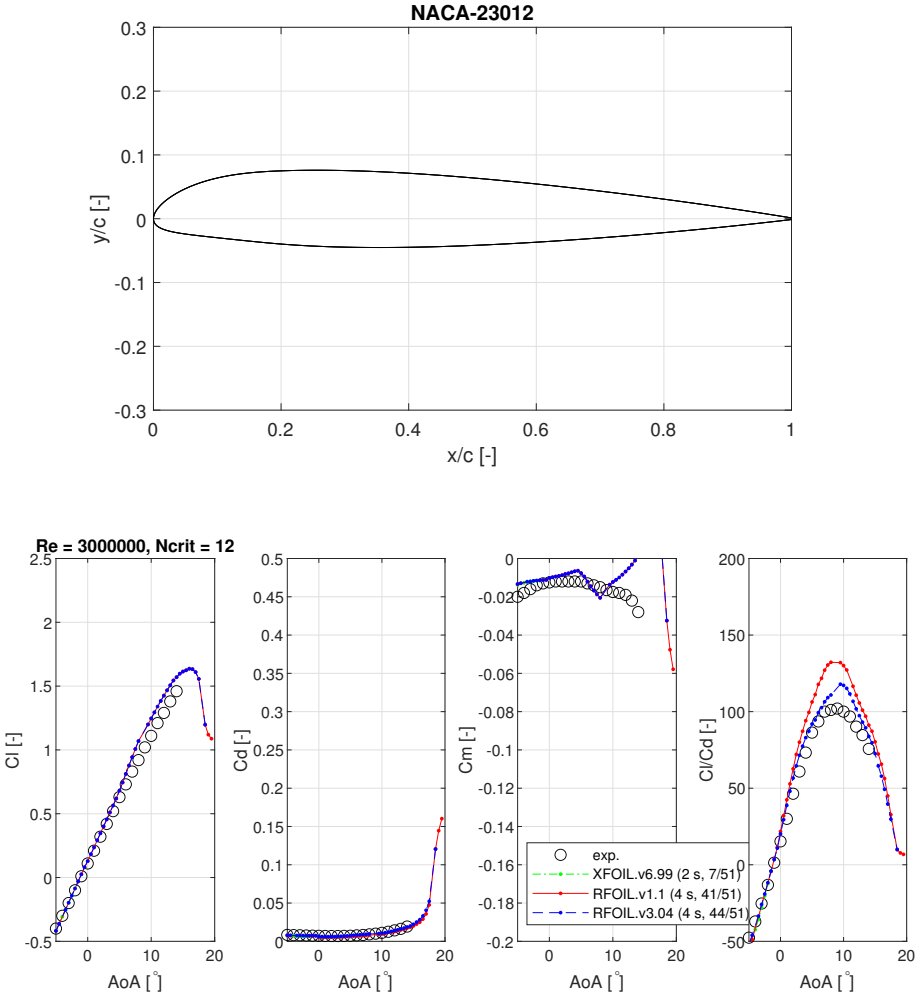

Figure B.209: Differences between experimental and numerical polars for the NACA-23012 airfoil at a Reynolds number of 3000000. Vertical black lines in the middle subplot indicate, from left to right, the angle of attack corresponding to the minimum drag coefficient, maximum lift to drag ratio and maximum lift coefficient, respectively.

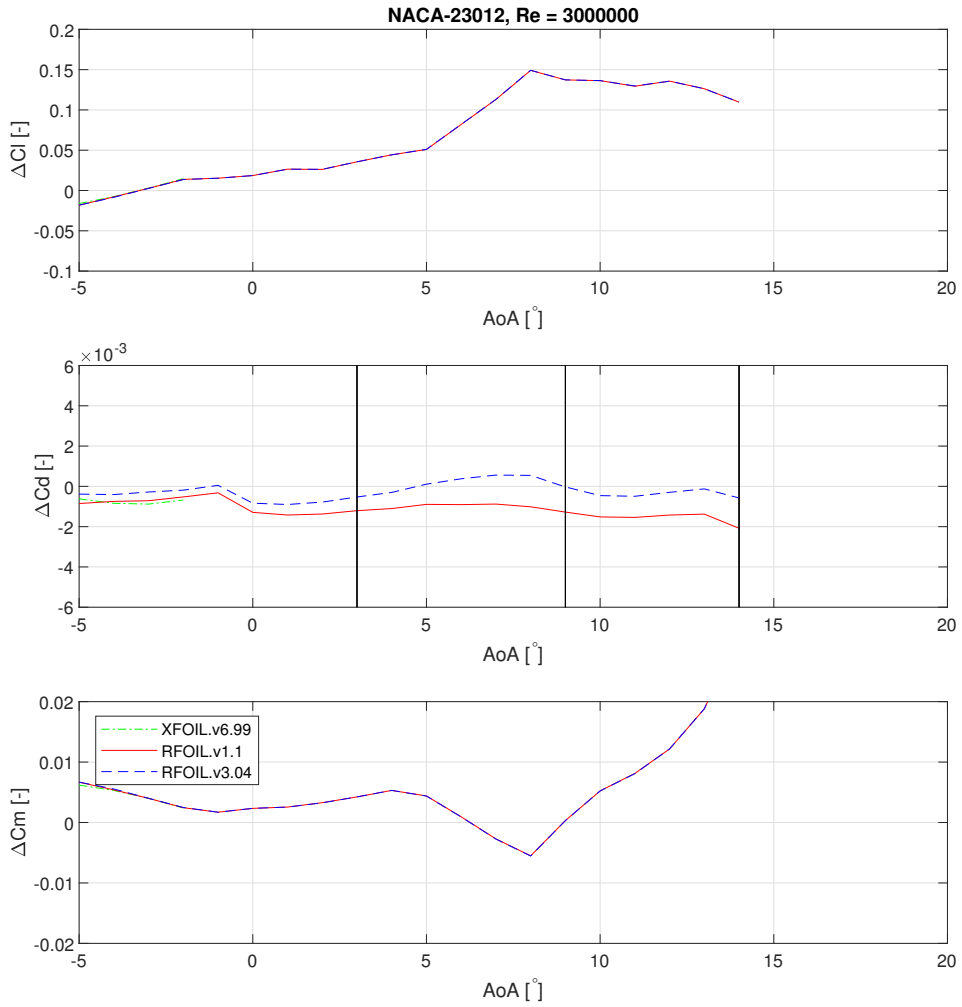

Figure B.210: Comparison between experimental and numerical pressure and skin friction distributions for the NACA-23012 airfoil at a Reynolds number of 3000000 and at the design angle of attack.

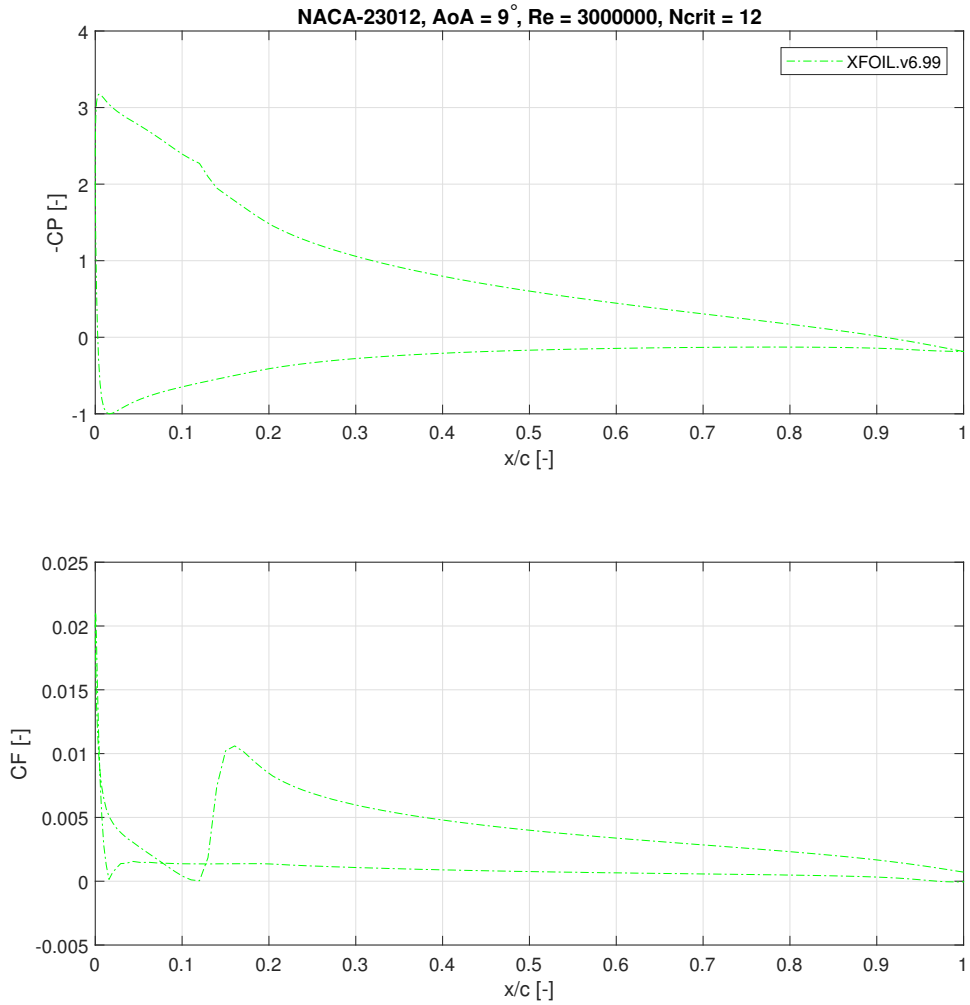

Figure B.211: Comparison between experimental and numerical polars for the NACA-23012 airfoil at a Reynolds number of 700000. Simulation time to generate the polars by means the different codes and the number of converged polar points are depicted between parentheses.

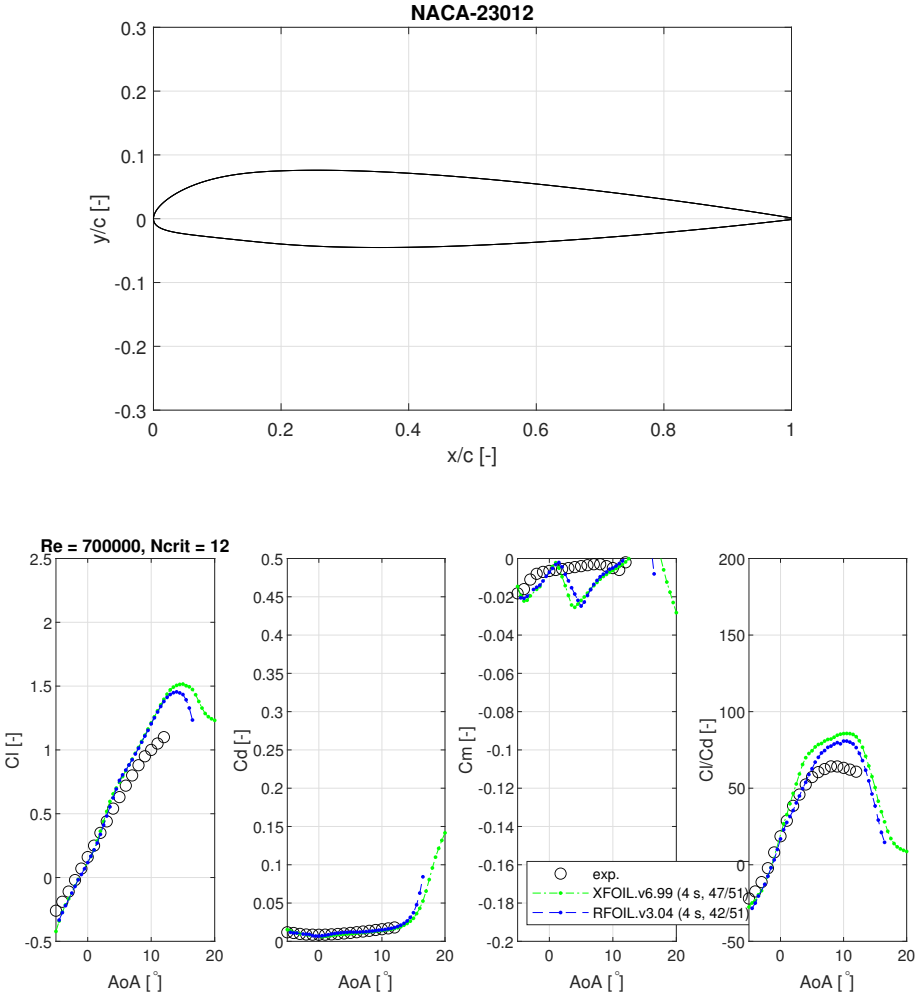

Figure B.212: Differences between experimental and numerical polars for the NACA-23012 airfoil at a Reynolds number of 700000. Vertical black lines in the middle subplot indicate, from left to right, the angle of attack corresponding to the minimum drag coefficient, maximum lift to drag ratio and maximum lift coefficient, respectively.

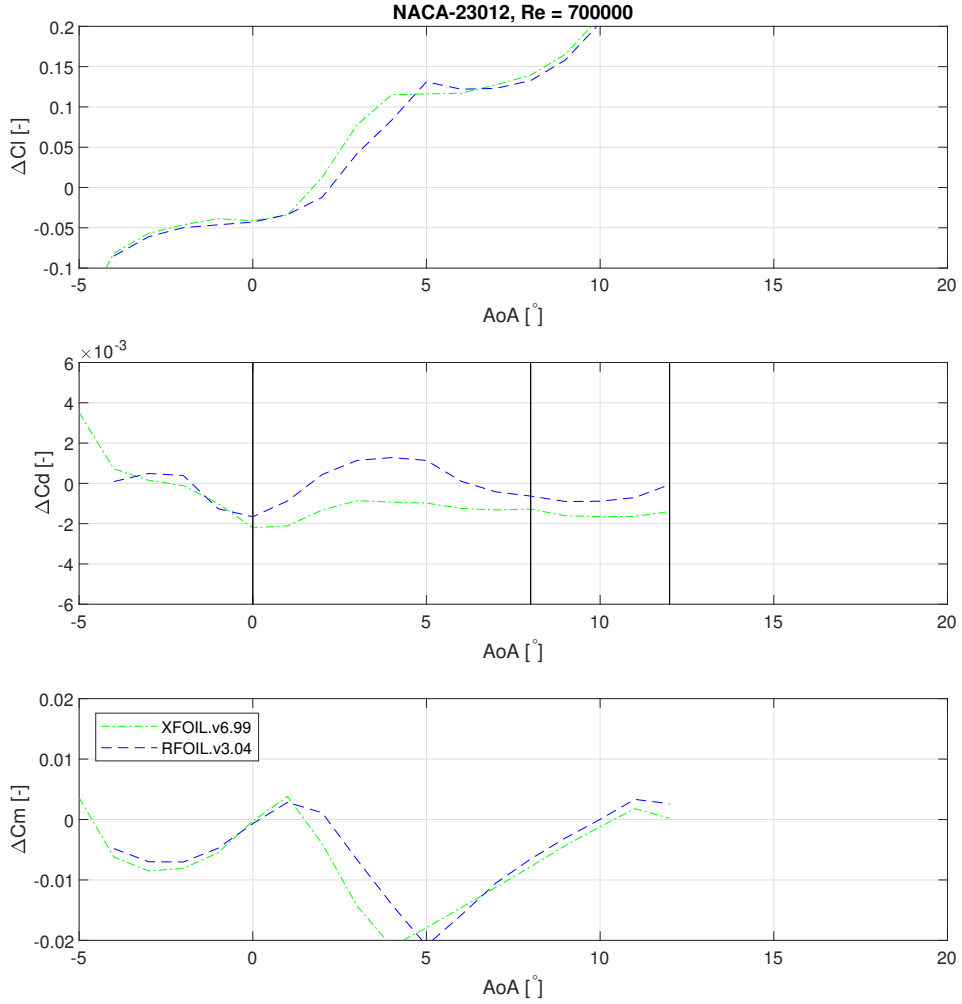

Figure B.213: Comparison between experimental and numerical pressure and skin friction distributions for the NACA-23012 airfoil at a Reynolds number of 700000 and at the design angle of attack.

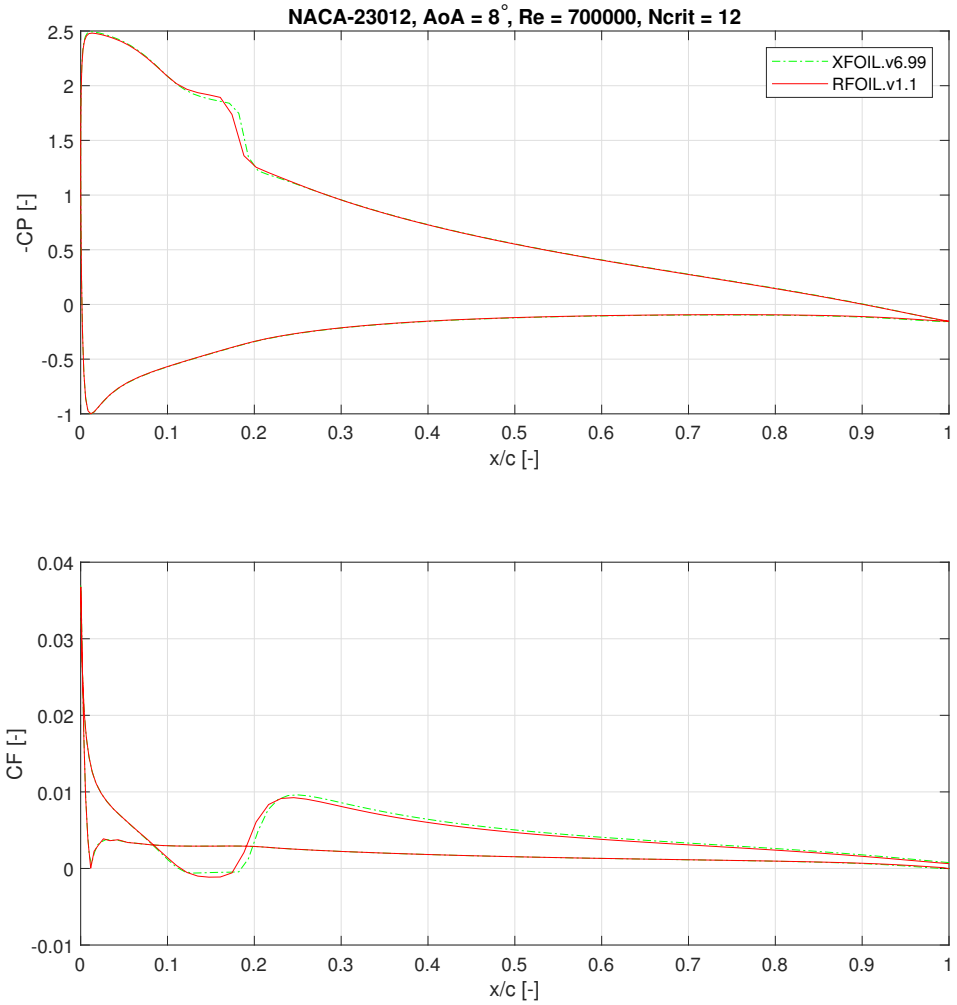

Figure B.214: Comparison between experimental and numerical polars for the NACA-23015 airfoil at a Reynolds number of 1000000. Simulation time to generate the polars by means the different codes and the number of converged polar points are depicted between parentheses.

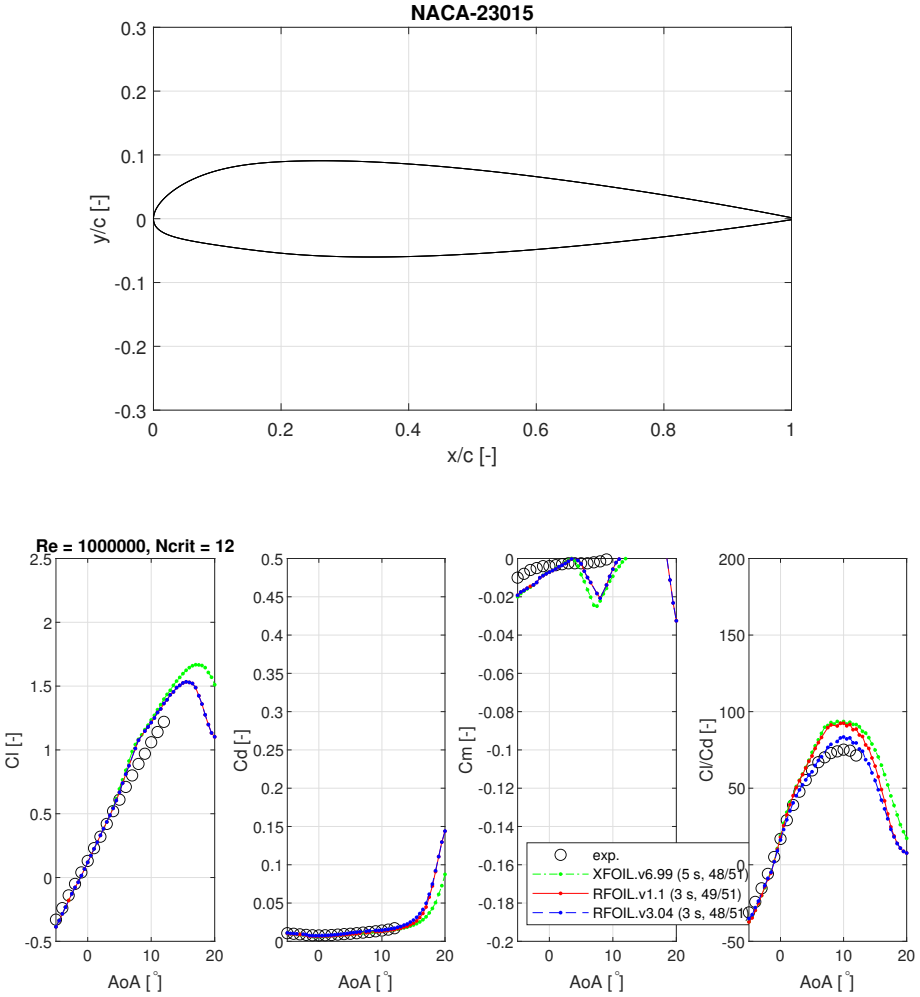

Figure B.215: Differences between experimental and numerical polars for the NACA-23015 airfoil at a Reynolds number of 1000000. Vertical black lines in the middle subplot indicate, from left to right, the angle of attack corresponding to the minimum drag coefficient, maximum lift to drag ratio and maximum lift coefficient, respectively.

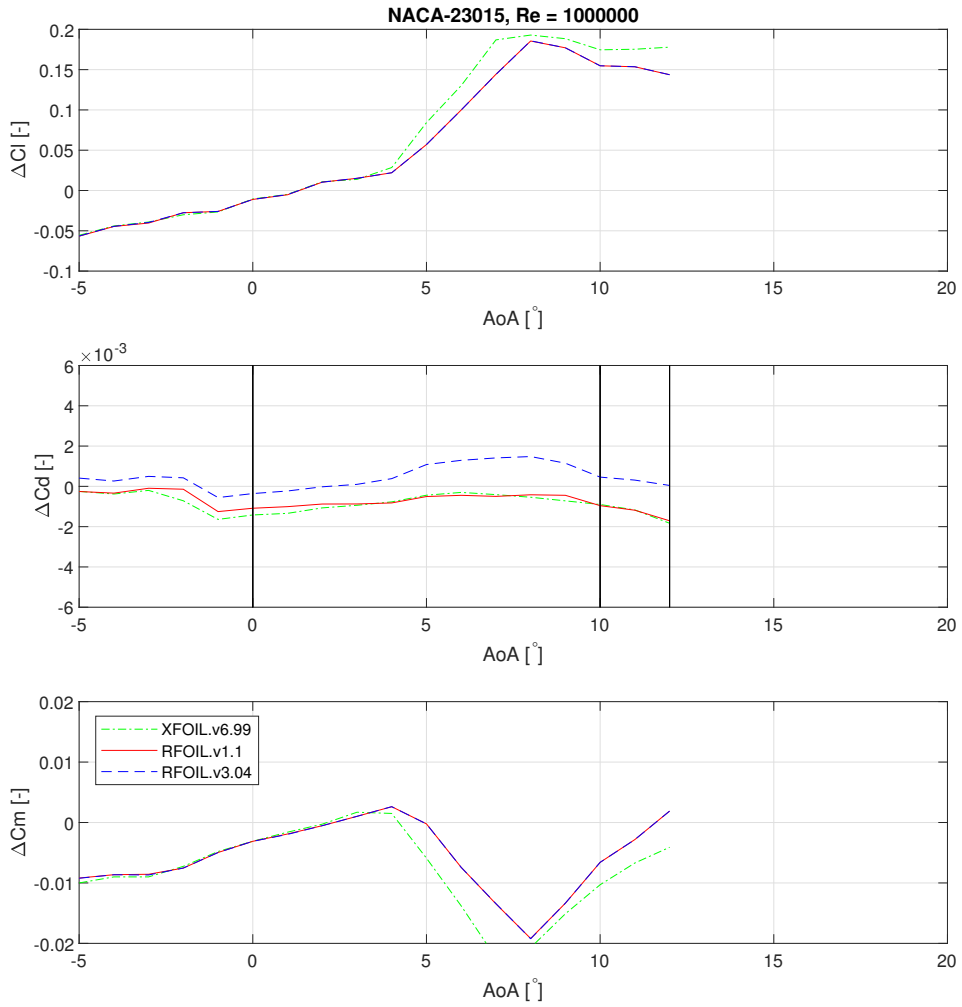

Figure B.216: Comparison between experimental and numerical pressure and skin friction distributions for the NACA-23015 airfoil at a Reynolds number of 1000000 and at the design angle of attack.

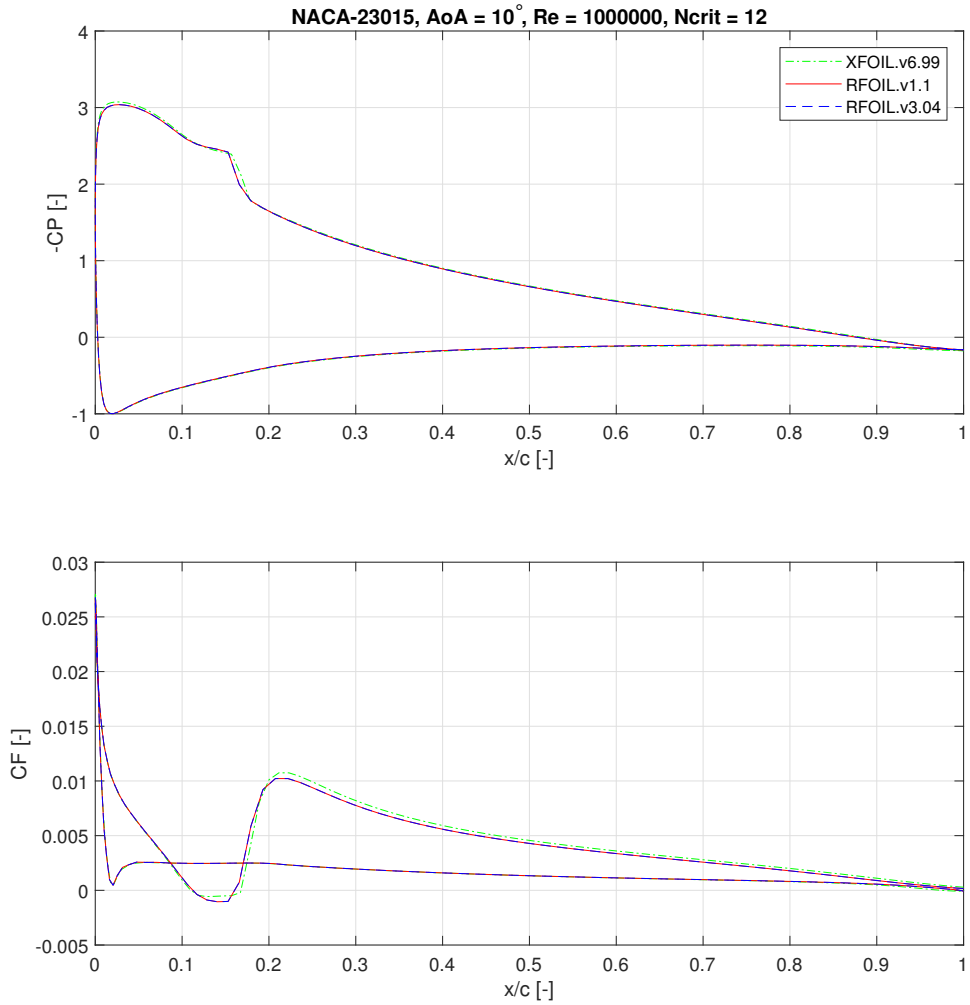

Figure B.217: Comparison between experimental and numerical polars for the NACA-23015 airfoil at a Reynolds number of 1500000. Simulation time to generate the polars by means the different codes and the number of converged polar points are depicted between parentheses.

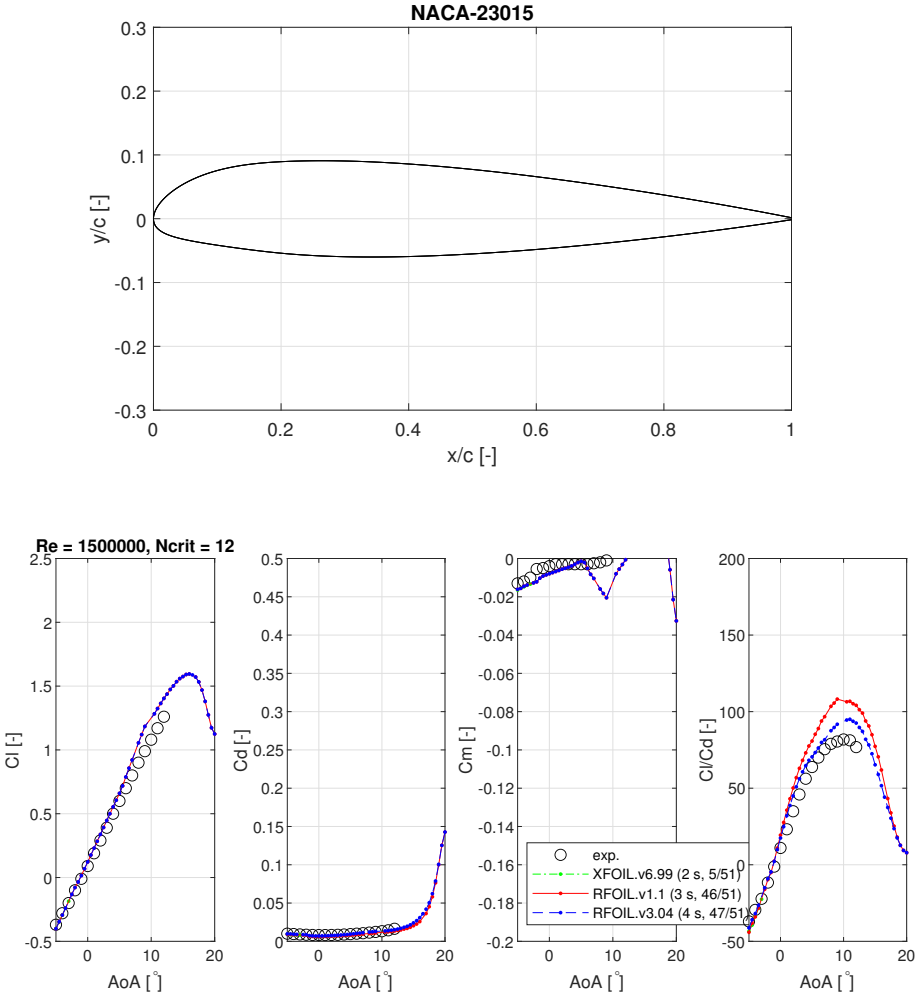

Figure B.218: Differences between experimental and numerical polars for the NACA-23015 airfoil at a Reynolds number of 1500000. Vertical black lines in the middle subplot indicate, from left to right, the angle of attack corresponding to the minimum drag coefficient, maximum lift to drag ratio and maximum lift coefficient, respectively.

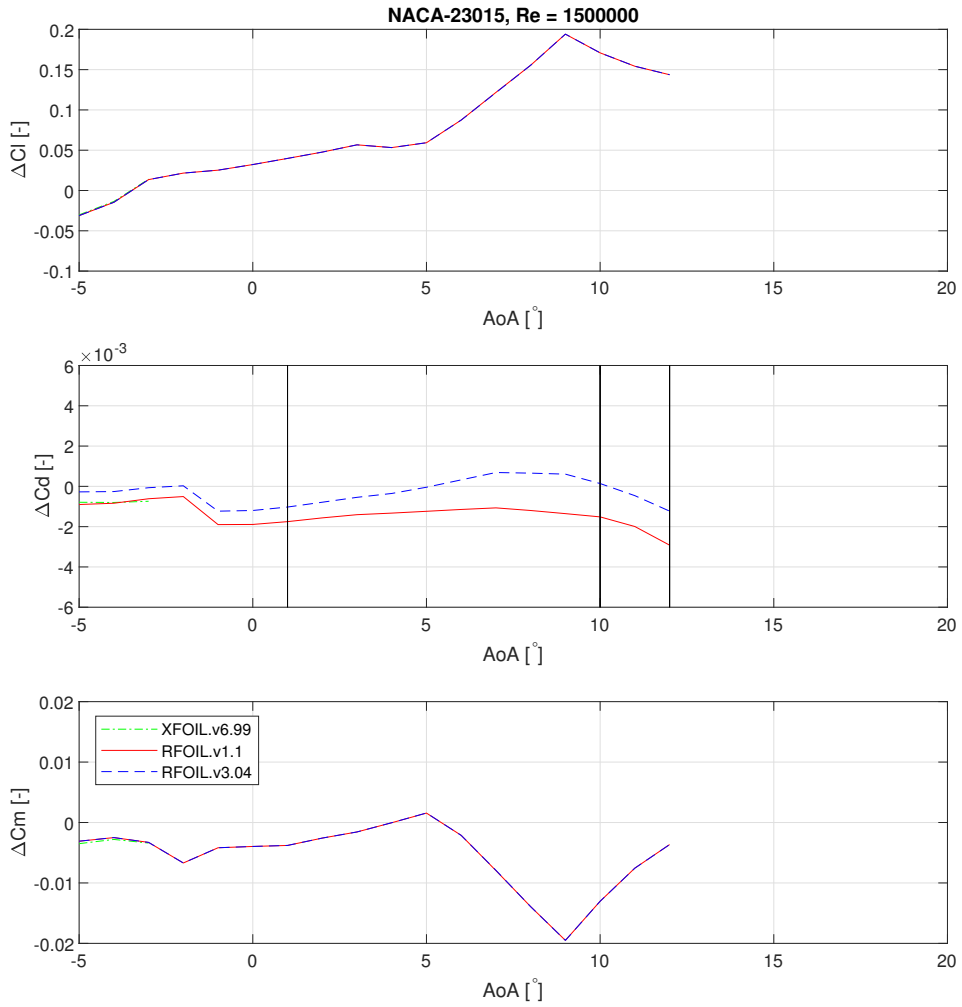

Figure B.219: Comparison between experimental and numerical pressure and skin friction distributions for the NACA-23015 airfoil at a Reynolds number of 1500000 and at the design angle of attack.

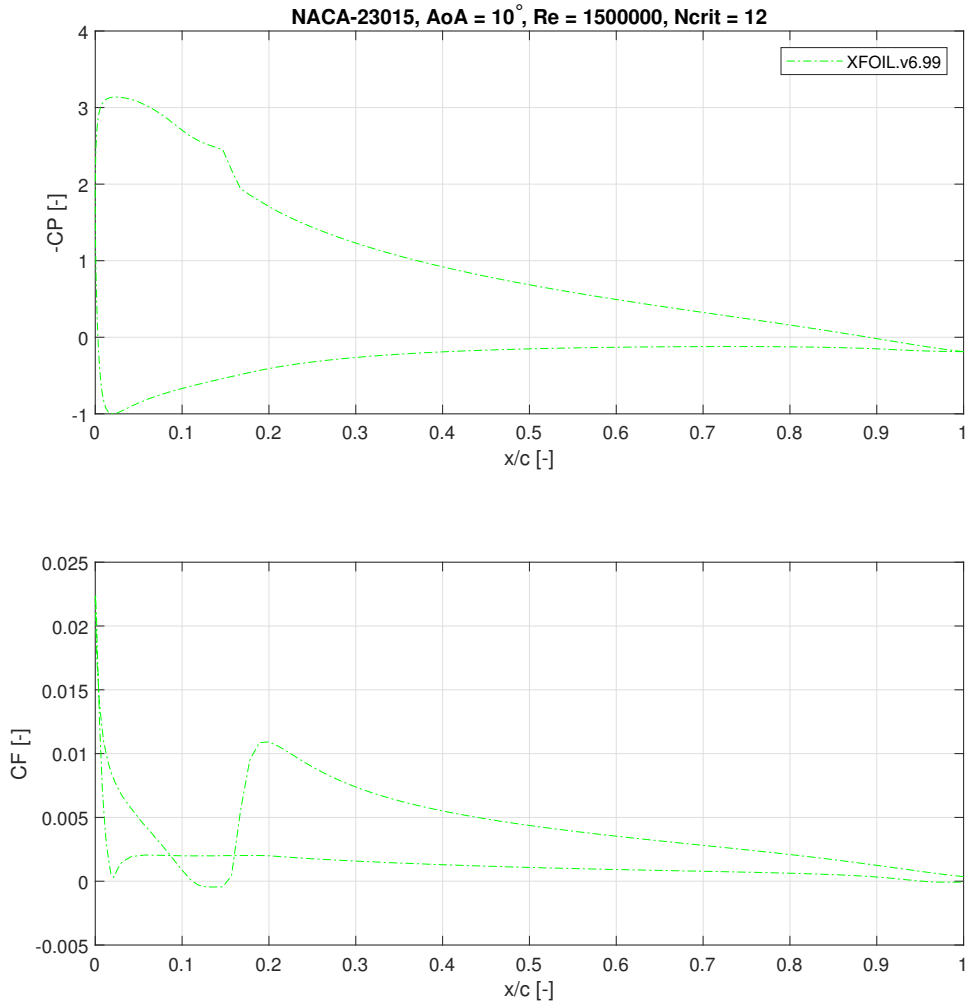

Figure B.220: Comparison between experimental and numerical polars for the NACA-23015 airfoil at a Reynolds number of 2000000. Simulation time to generate the polars by means the different codes and the number of converged polar points are depicted between parentheses.

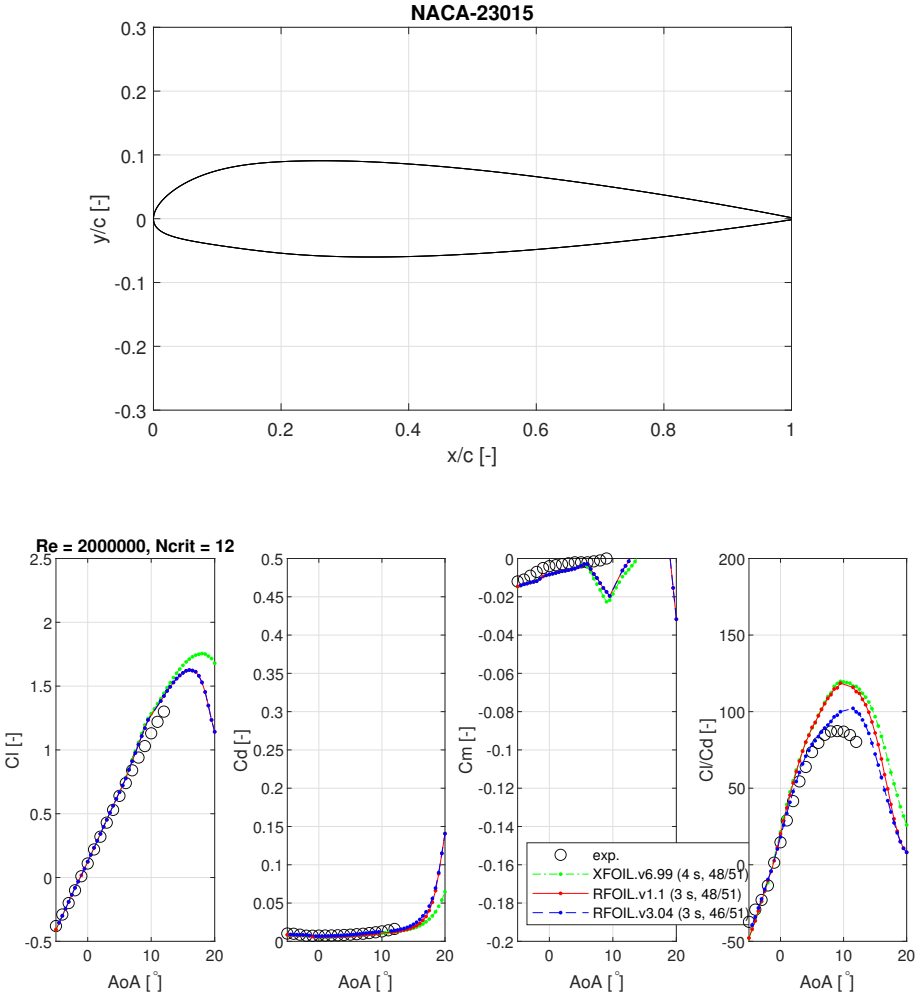

Figure B.221: Differences between experimental and numerical polars for the NACA-23015 airfoil at a Reynolds number of 2000000. Vertical black lines in the middle subplot indicate, from left to right, the angle of attack corresponding to the minimum drag coefficient, maximum lift to drag ratio and maximum lift coefficient, respectively.

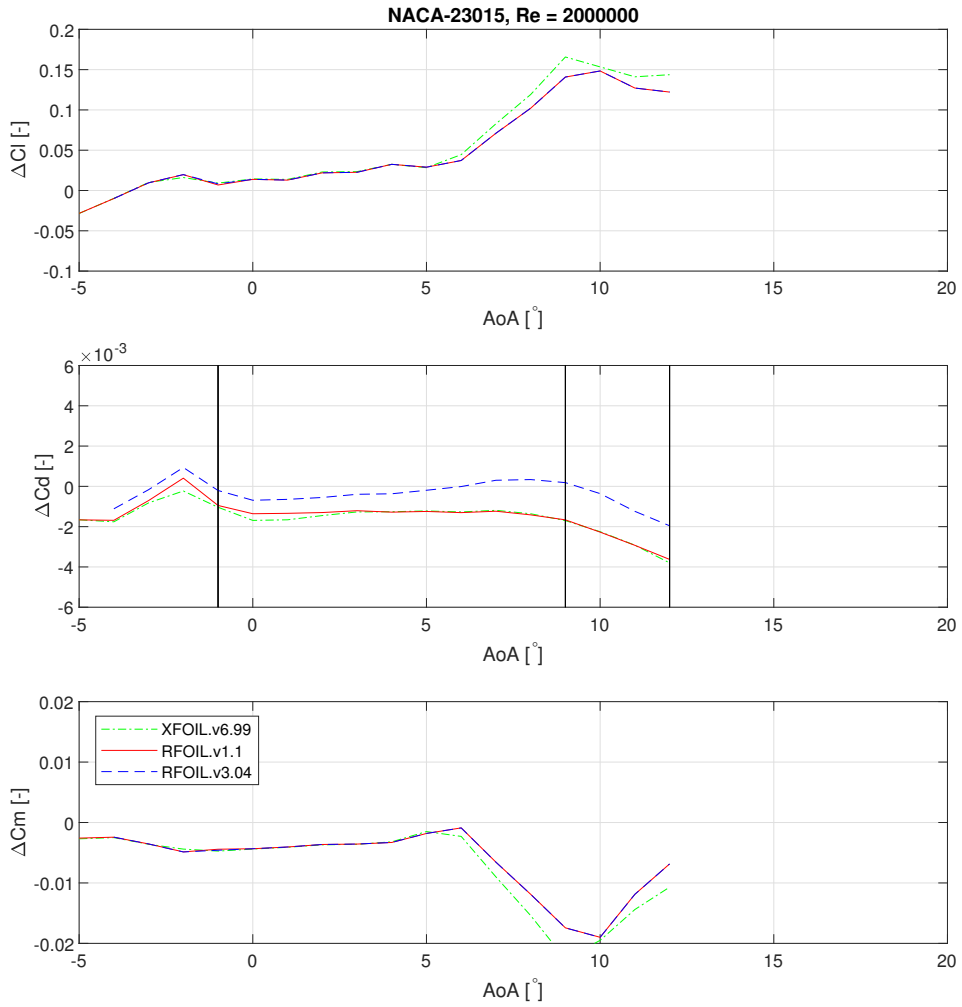

Figure B.222: Comparison between experimental and numerical pressure and skin friction distributions for the NACA-23015 airfoil at a Reynolds number of 2000000 and at the design angle of attack.

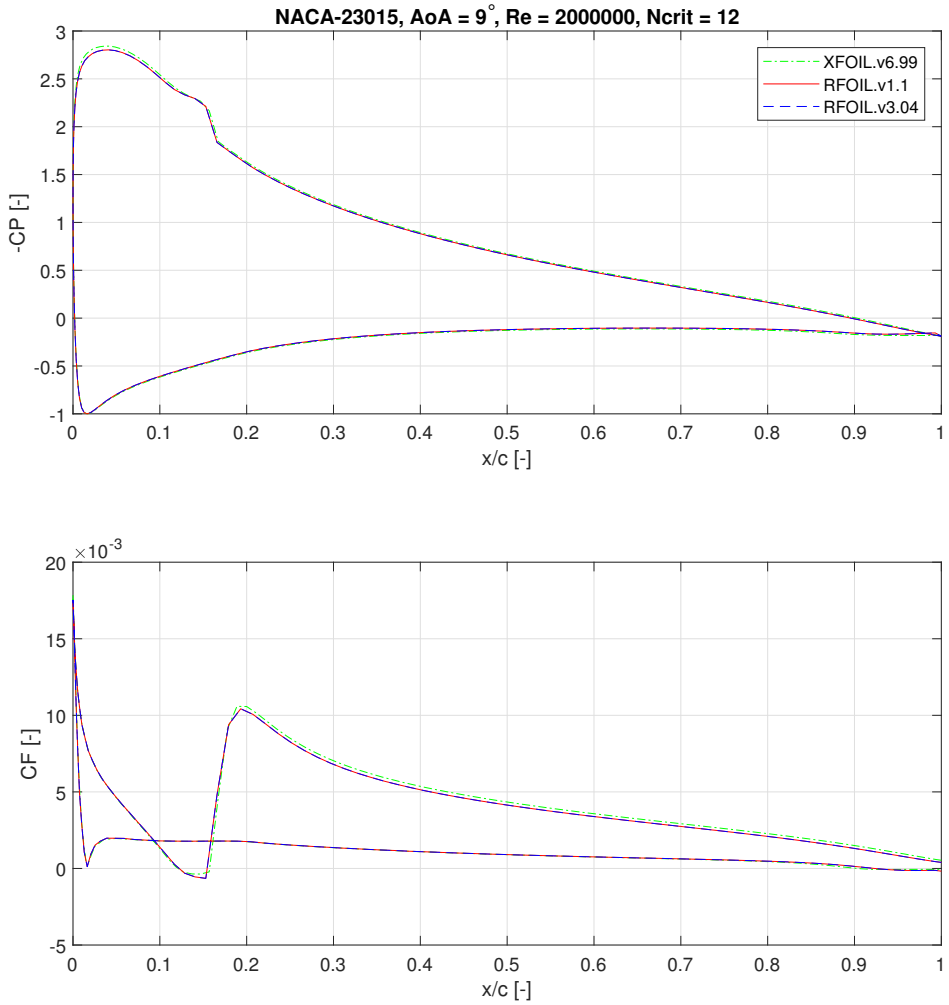

Figure B.223: Comparison between experimental and numerical polars for the NACA-23015 airfoil at a Reynolds number of 3000000. Simulation time to generate the polars by means the different codes and the number of converged polar points are depicted between parentheses.

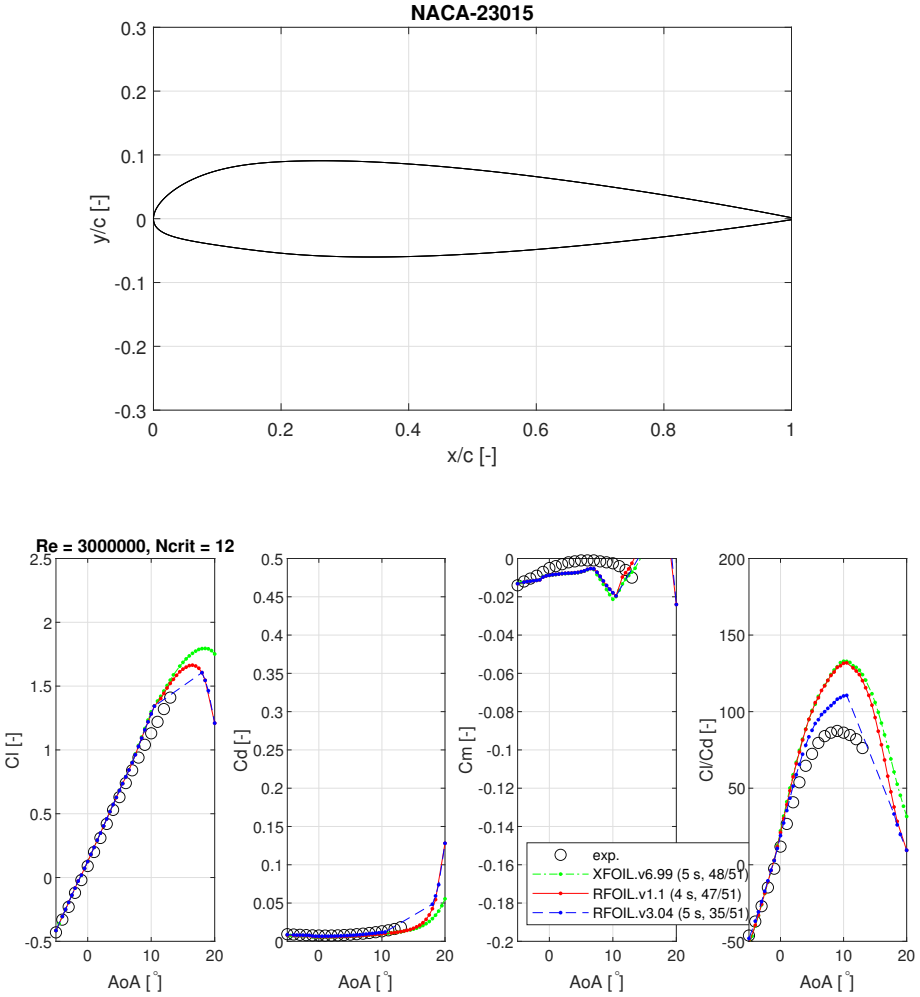

Figure B.224: Differences between experimental and numerical polars for the NACA-23015 airfoil at a Reynolds number of 3000000. Vertical black lines in the middle subplot indicate, from left to right, the angle of attack corresponding to the minimum drag coefficient, maximum lift to drag ratio and maximum lift coefficient, respectively.

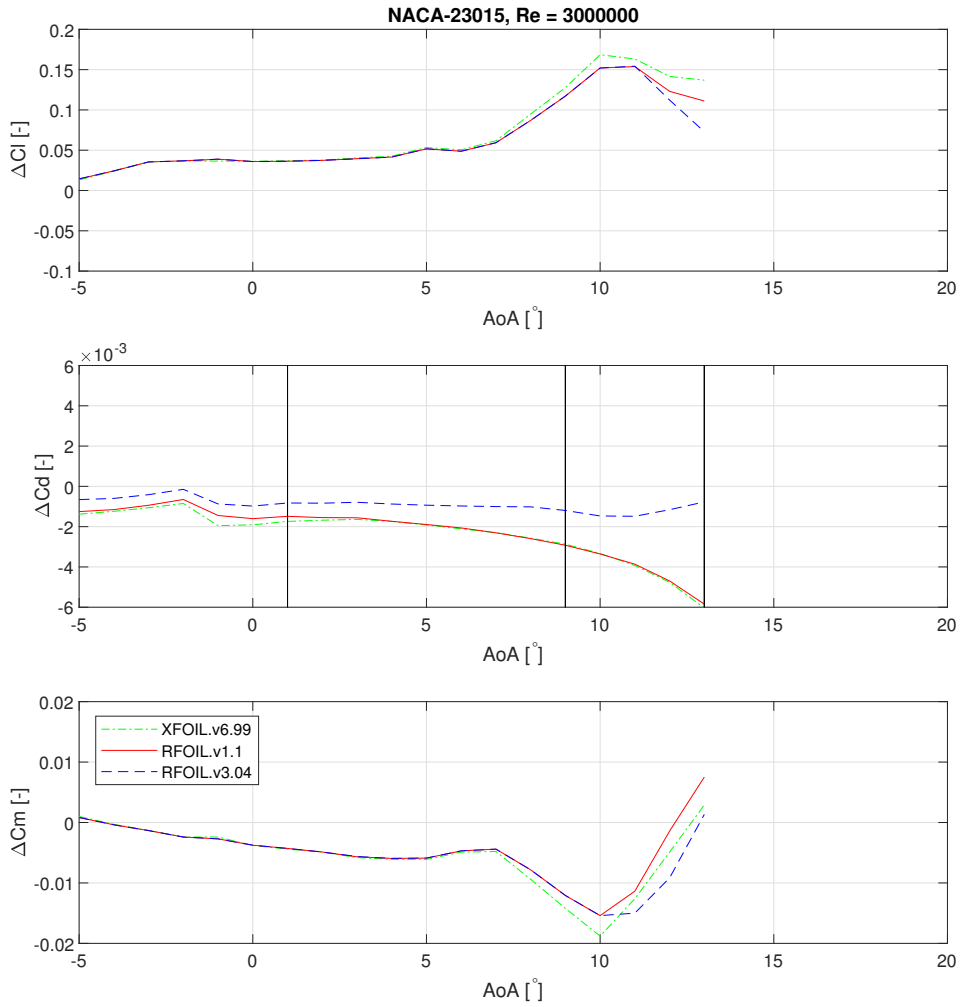

Figure B.225: Comparison between experimental and numerical pressure and skin friction distributions for the NACA-23015 airfoil at a Reynolds number of 3000000 and at the design angle of attack.

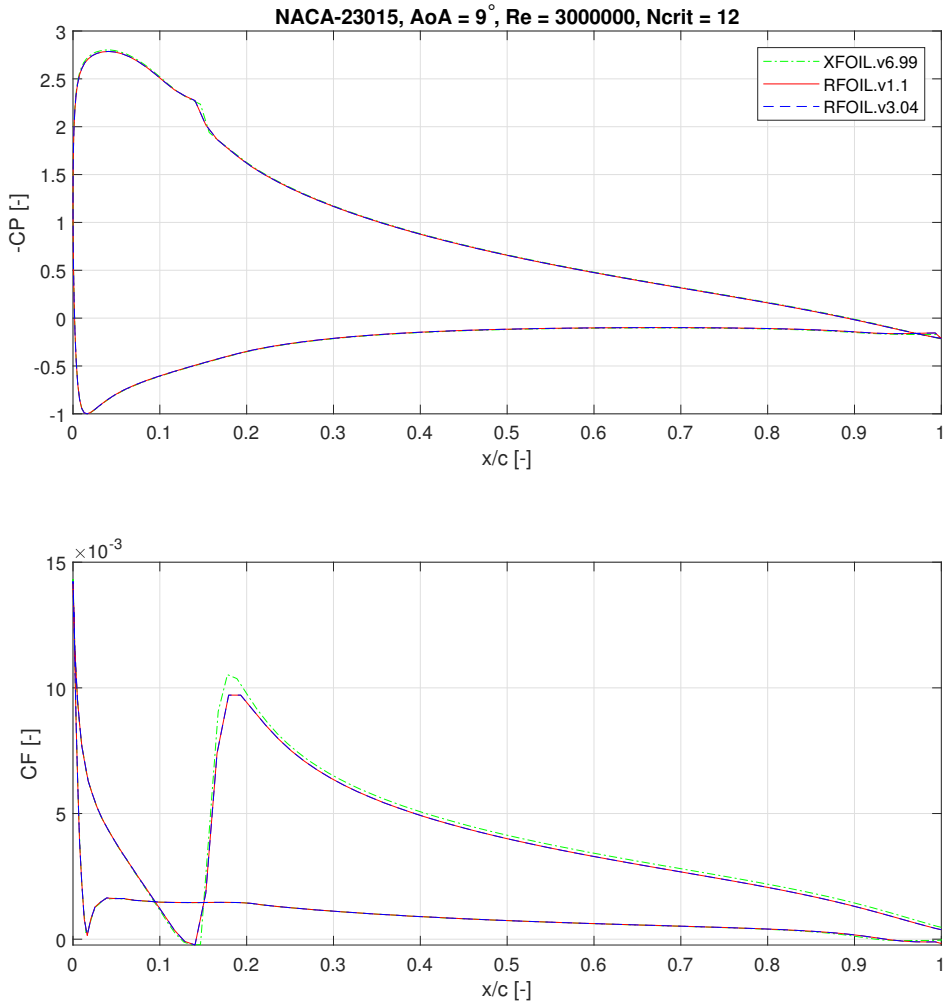

Figure B.226: Comparison between experimental and numerical polars for the NACA-23015 airfoil at a Reynolds number of 700000. Simulation time to generate the polars by means the different codes and the number of converged polar points are depicted between parentheses.

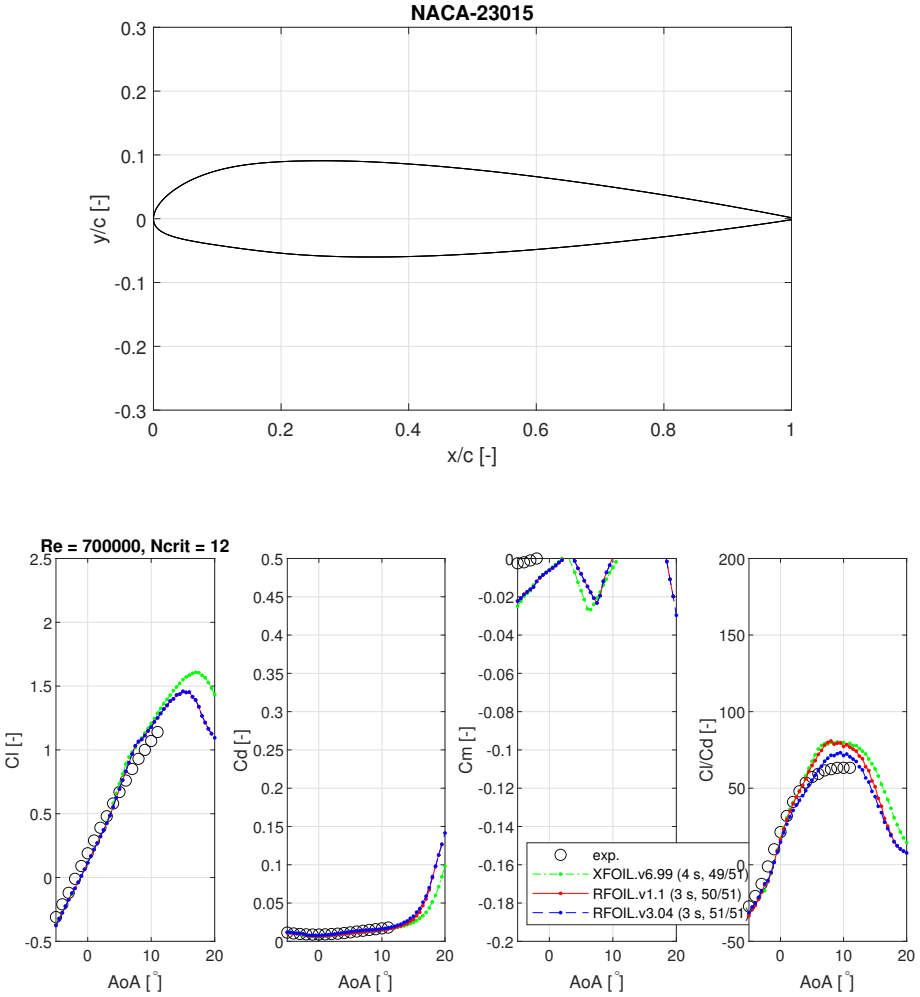

Figure B.227: Differences between experimental and numerical polars for the NACA-23015 airfoil at a Reynolds number of 700000. Vertical black lines in the middle subplot indicate, from left to right, the angle of attack corresponding to the minimum drag coefficient, maximum lift to drag ratio and maximum lift coefficient, respectively.

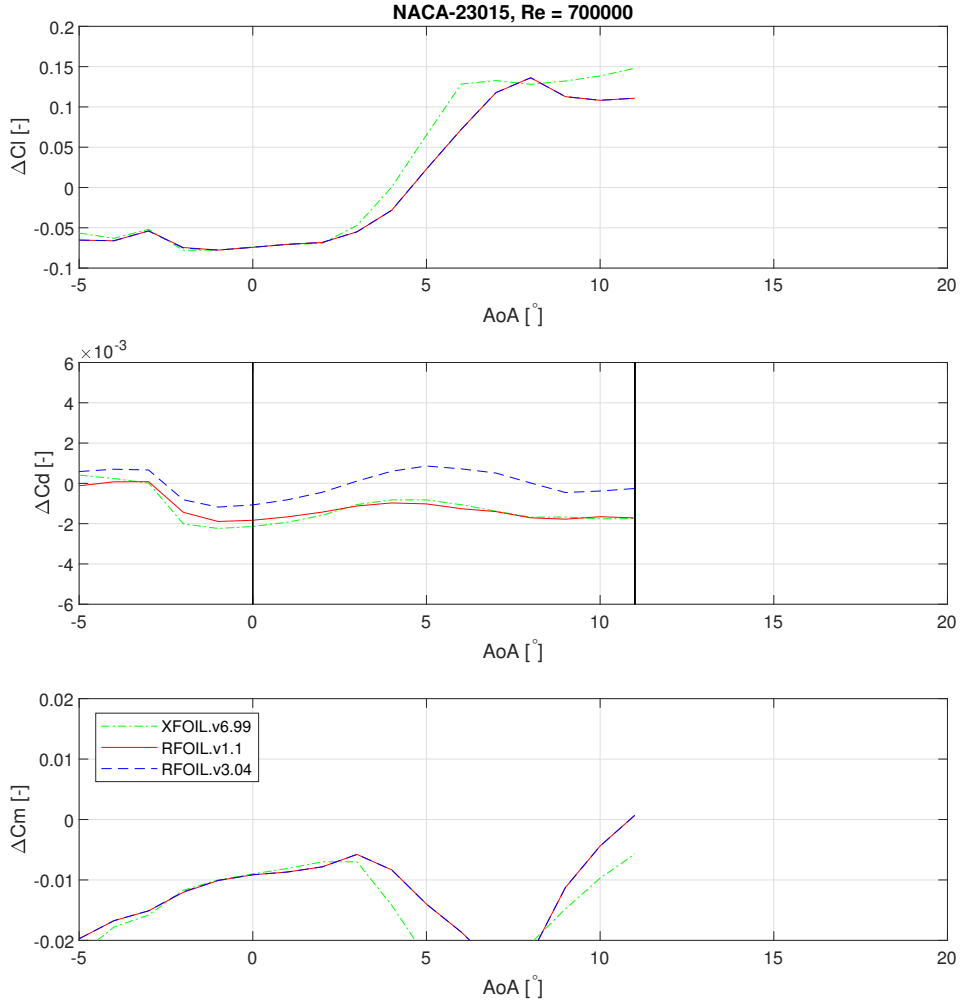

Figure B.228: Comparison between experimental and numerical pressure and skin friction distributions for the NACA-23015 airfoil at a Reynolds number of 700000 and at the design angle of attack.

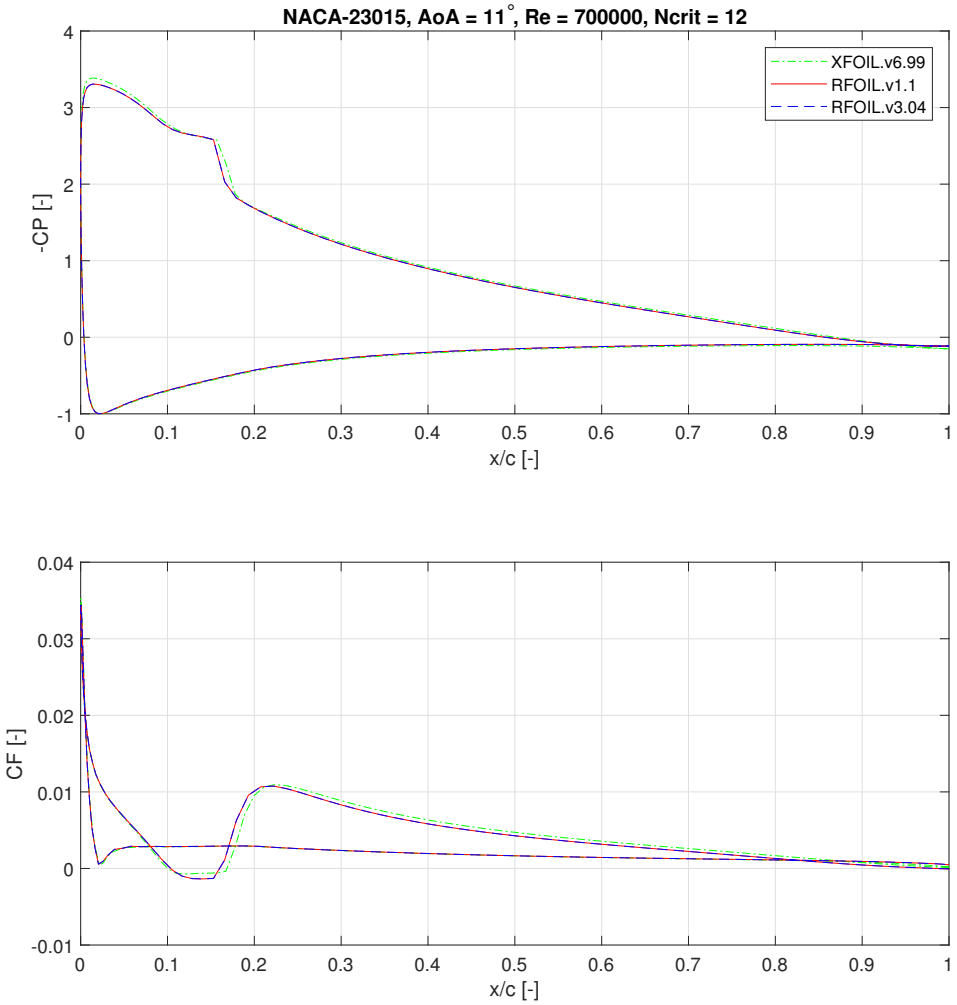

Figure B.229: Comparison between experimental and numerical polars for the NACA-2412 airfoil at a Reynolds number of 1300000. Simulation time to generate the polars by means the different codes and the number of converged polar points are depicted between parentheses.

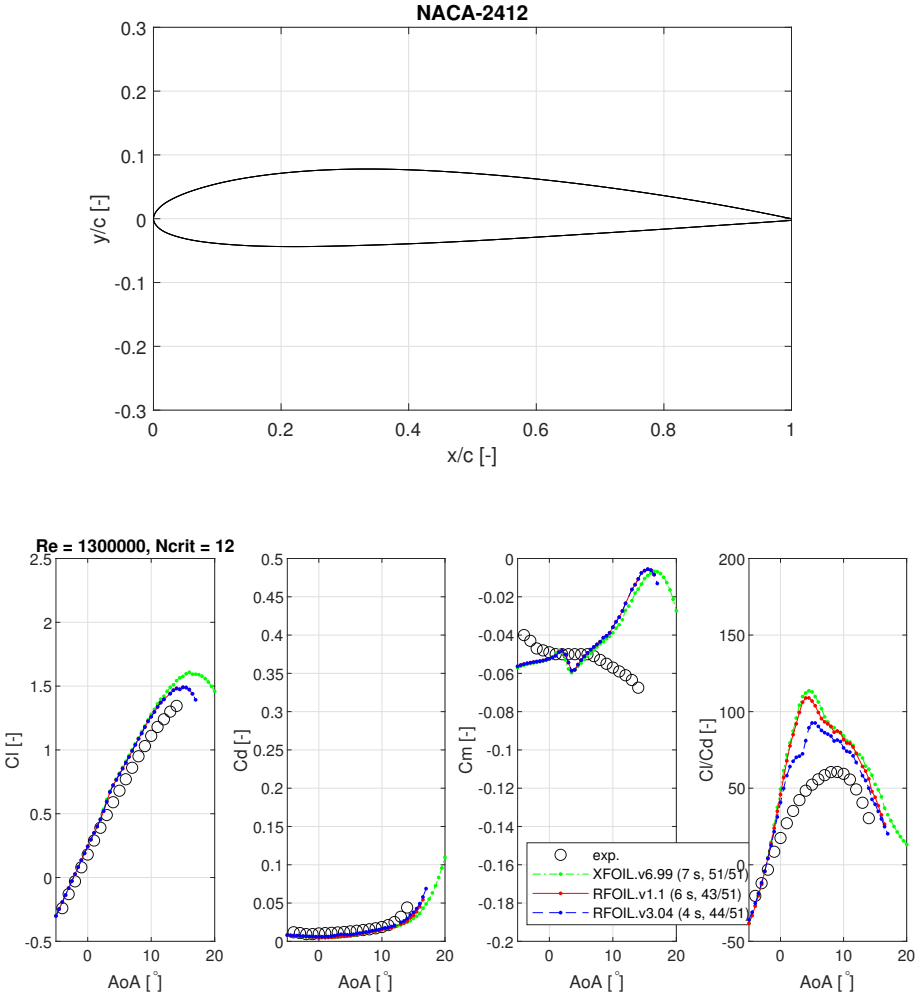

Figure B.230: Differences between experimental and numerical polars for the NACA-2412 airfoil at a Reynolds number of 1300000. Vertical black lines in the middle subplot indicate, from left to right, the angle of attack corresponding to the minimum drag coefficient, maximum lift to drag ratio and maximum lift coefficient, respectively.

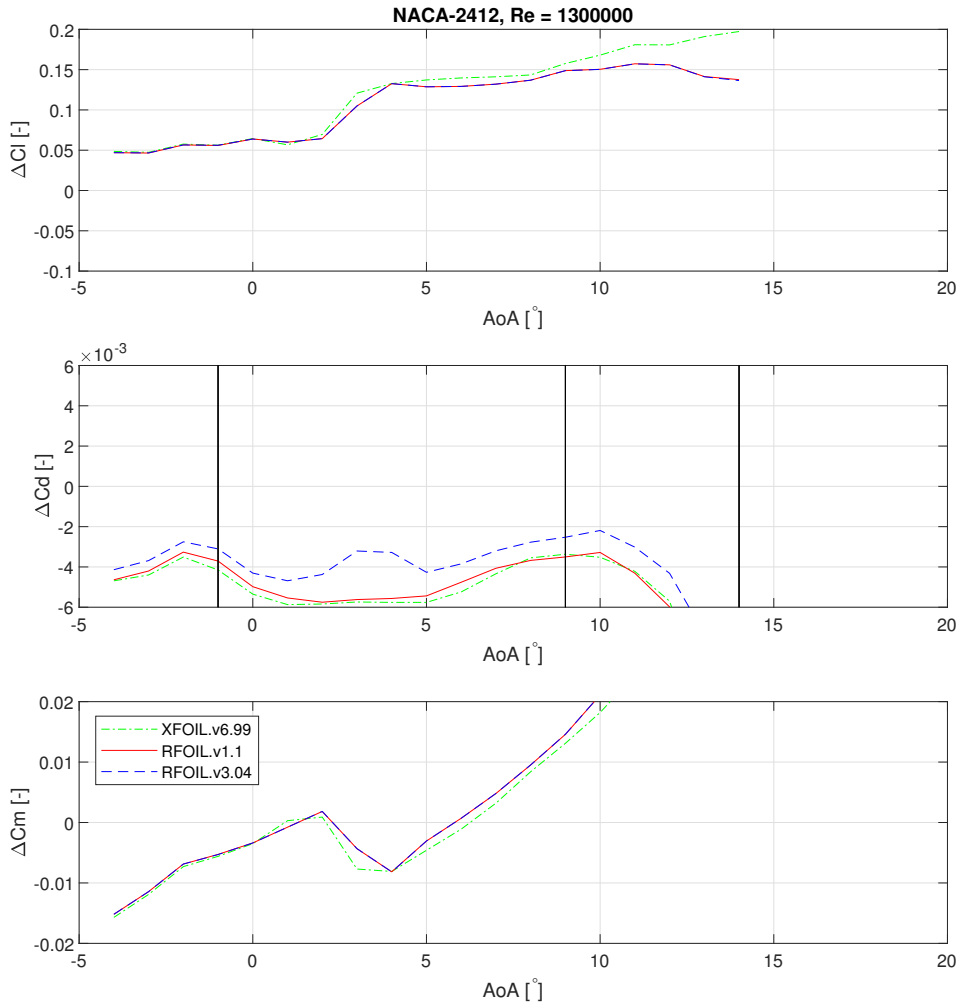

Figure B.231: Comparison between experimental and numerical pressure and skin friction distributions for the NACA-2412 airfoil at a Reynolds number of 1300000 and at the design angle of attack.

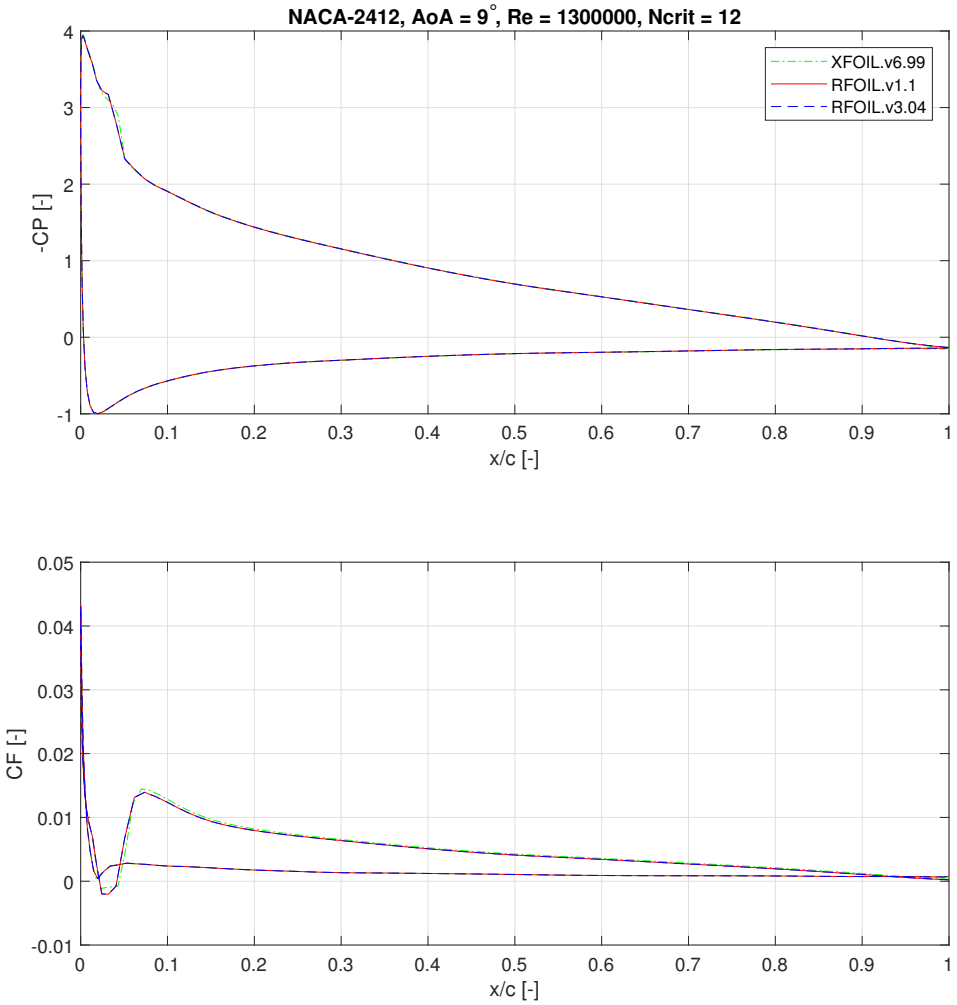

Figure B.232: Comparison between experimental and numerical polars for the NACA-2412 airfoil at a Reynolds number of 2300000. Simulation time to generate the polars by means the different codes and the number of converged polar points are depicted between parentheses.

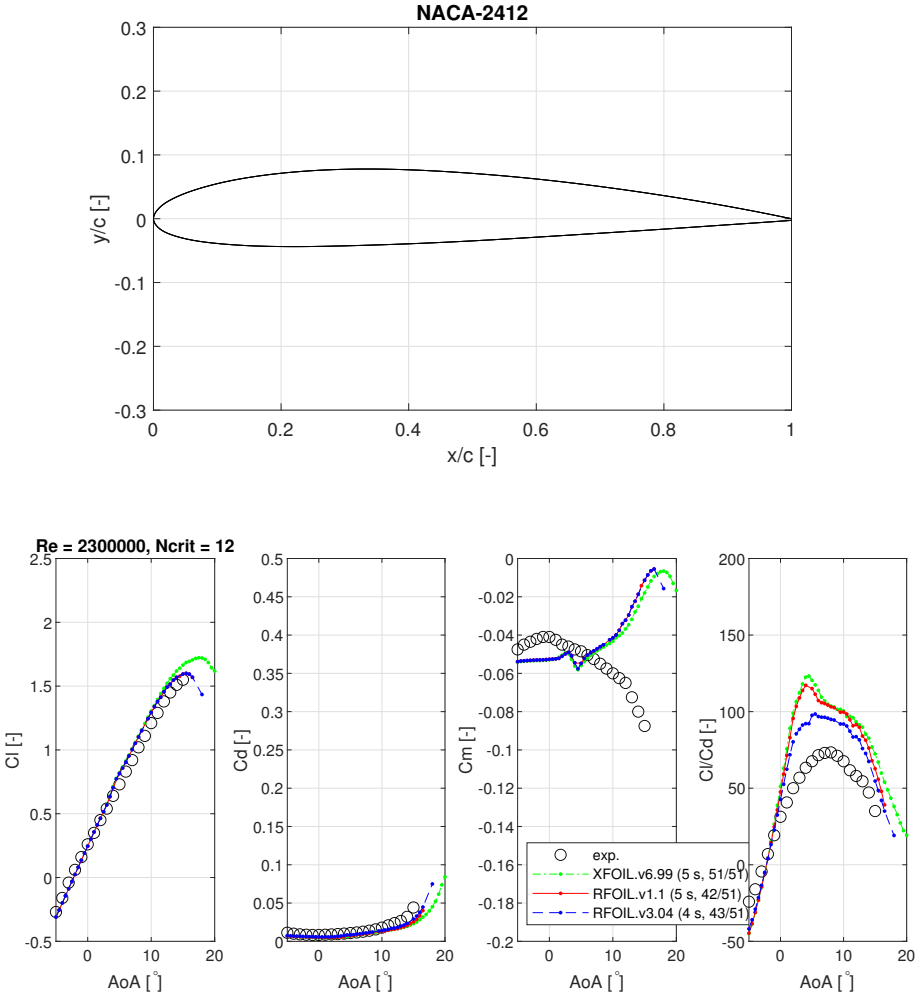

Figure B.233: Differences between experimental and numerical polars for the NACA-2412 airfoil at a Reynolds number of 2300000. Vertical black lines in the middle subplot indicate, from left to right, the angle of attack corresponding to the minimum drag coefficient, maximum lift to drag ratio and maximum lift coefficient, respectively.

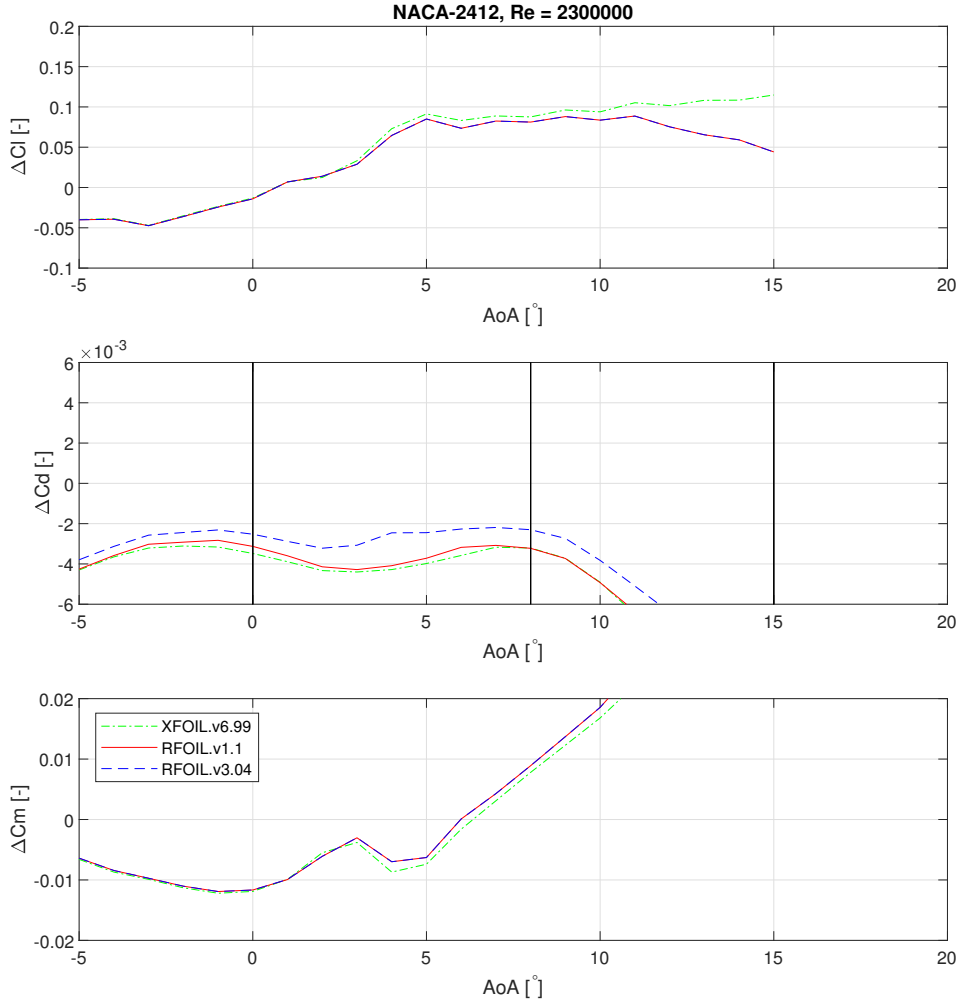

Figure B.234: Comparison between experimental and numerical pressure and skin friction distributions for the NACA-2412 airfoil at a Reynolds number of 2300000 and at the design angle of attack.

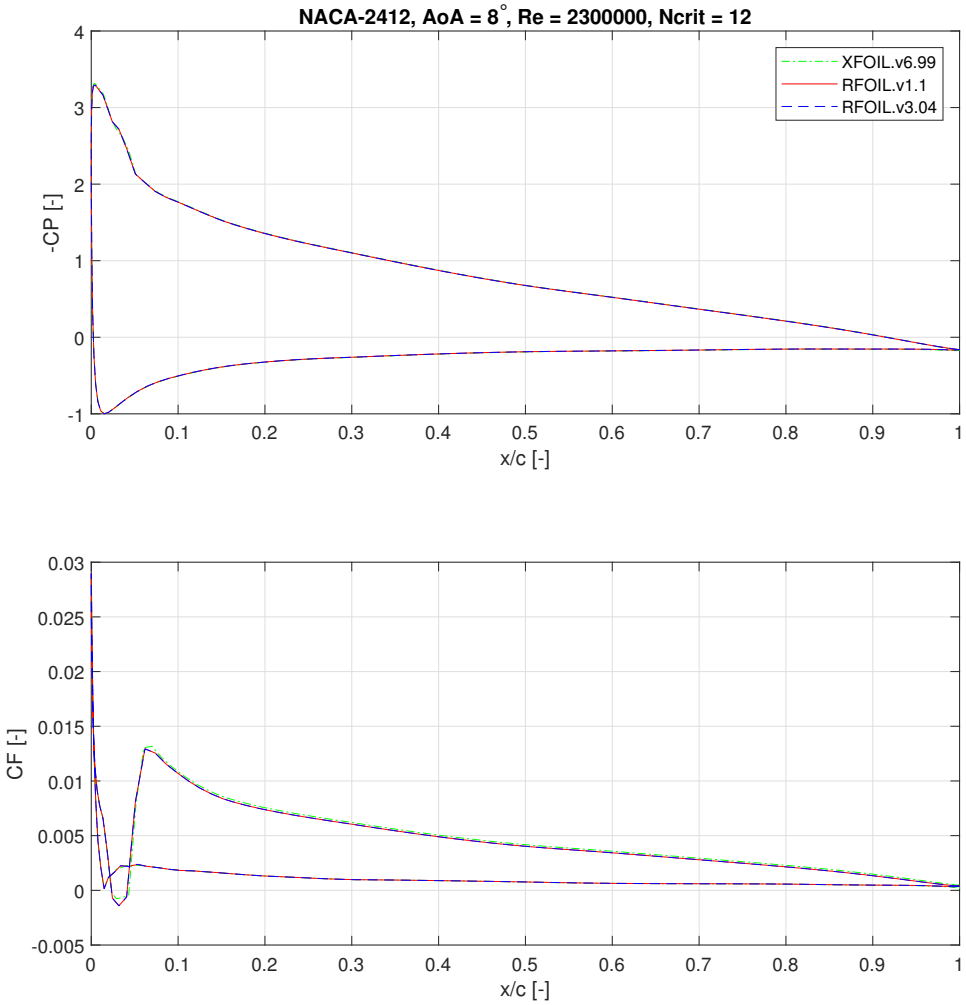

Figure B.235: Comparison between experimental and numerical polars for the NACA-2412 airfoil at a Reynolds number of 3100000. Simulation time to generate the polars by means the different codes and the number of converged polar points are depicted between parentheses.

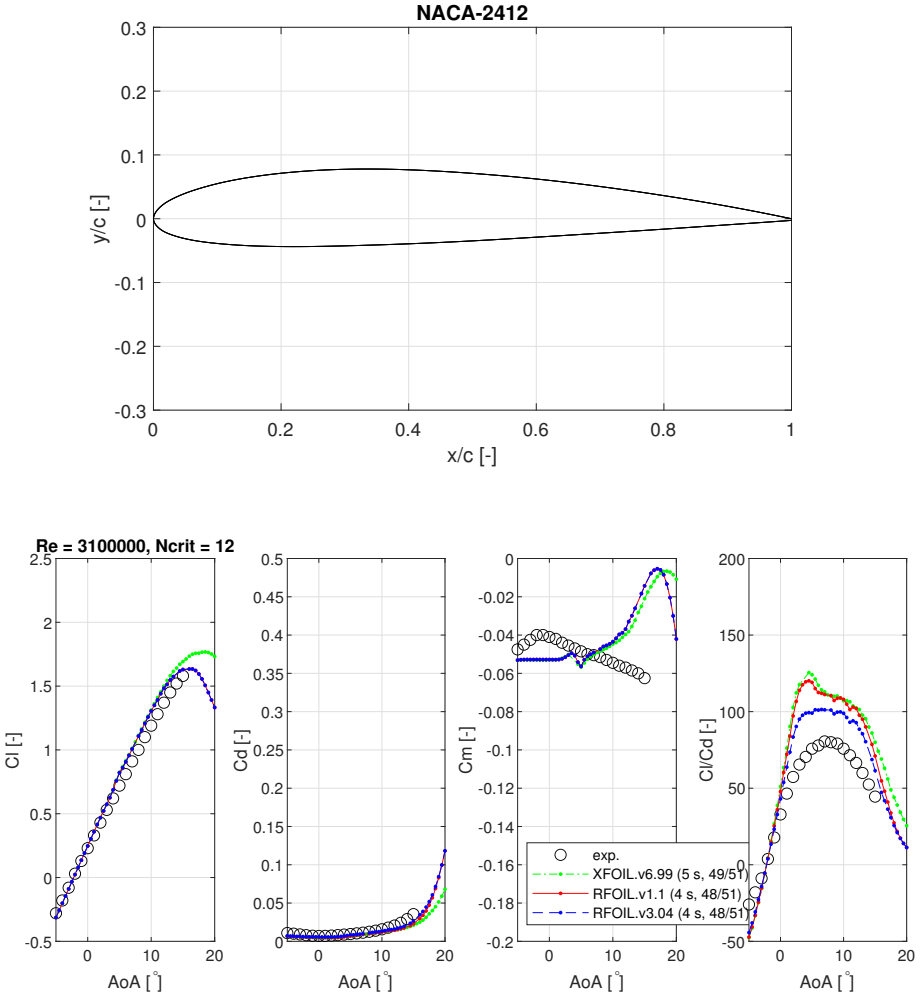

Figure B.236: Differences between experimental and numerical polars for the NACA-2412 airfoil at a Reynolds number of 3100000. Vertical black lines in the middle subplot indicate, from left to right, the angle of attack corresponding to the minimum drag coefficient, maximum lift to drag ratio and maximum lift coefficient, respectively.

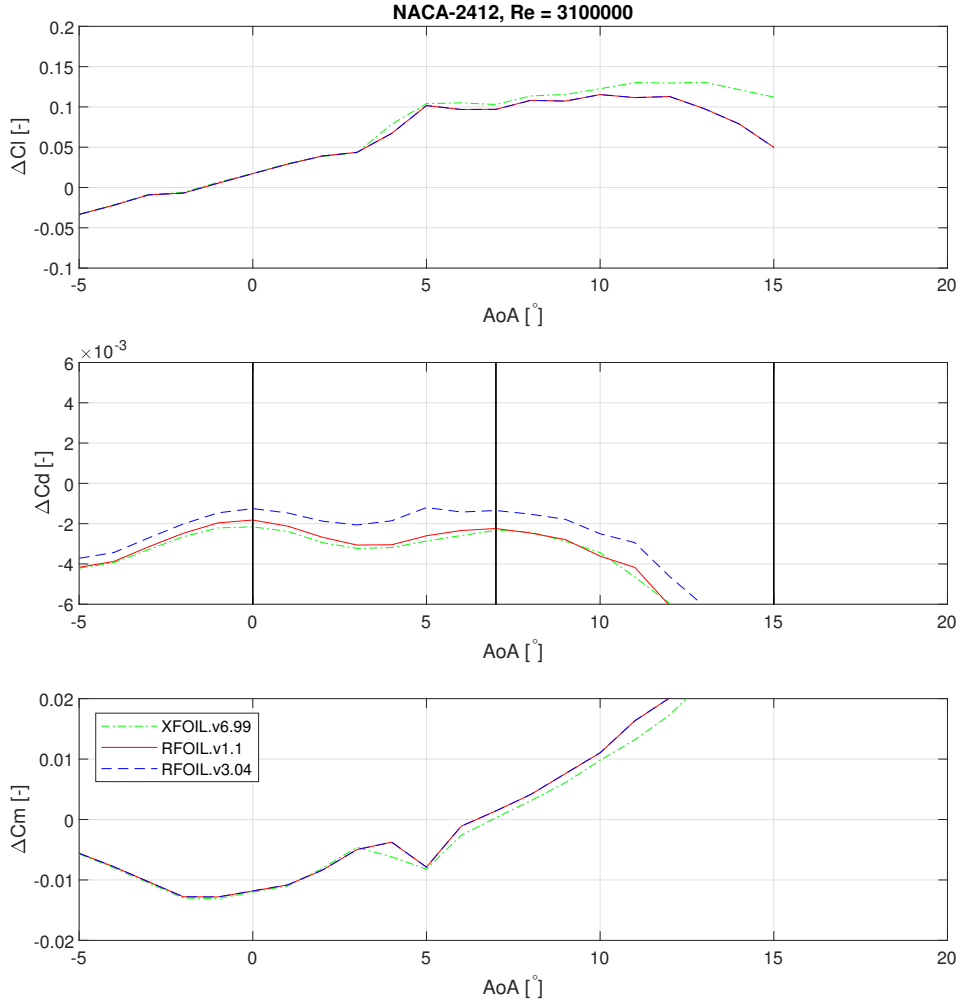

Figure B.237: Comparison between experimental and numerical pressure and skin friction distributions for the NACA-2412 airfoil at a Reynolds number of 3100000 and at the design angle of attack.

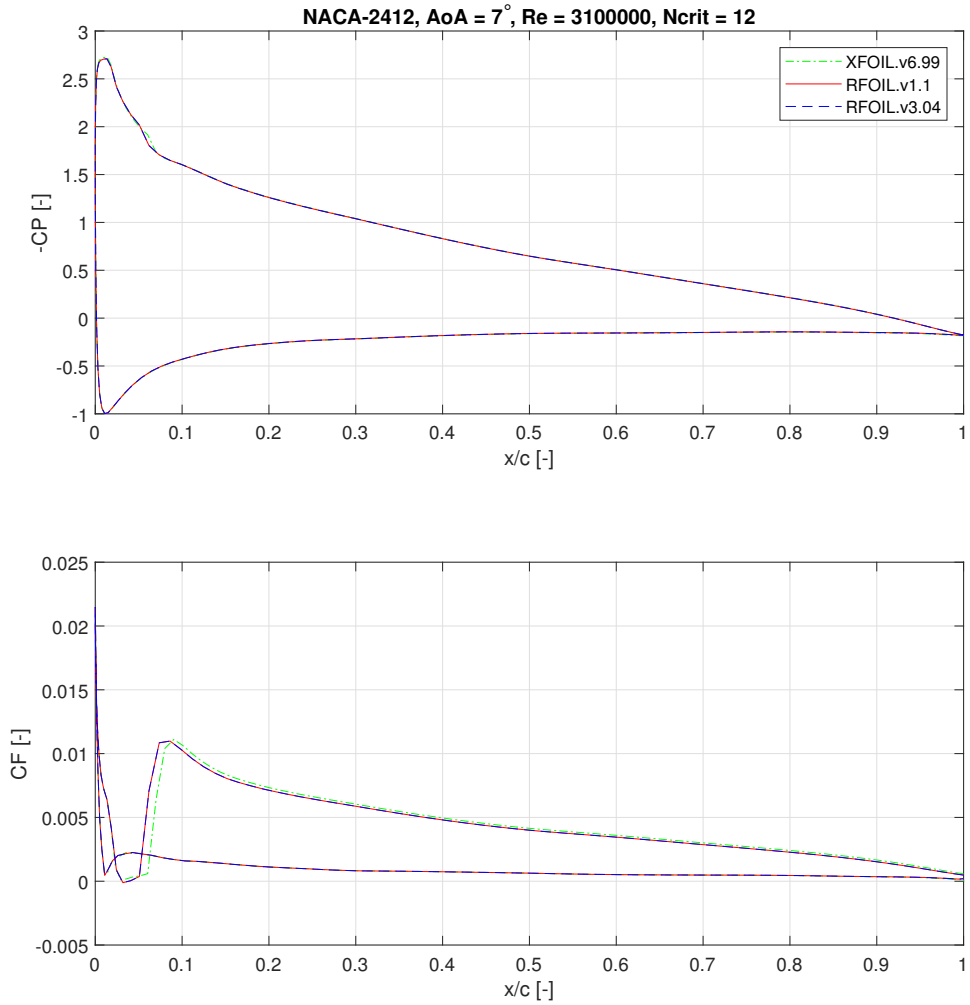

Figure B.238: Comparison between experimental and numerical polars for the NACA-2412 airfoil at a Reynolds number of 600000. Simulation time to generate the polars by means the different codes and the number of converged polar points are depicted between parentheses.

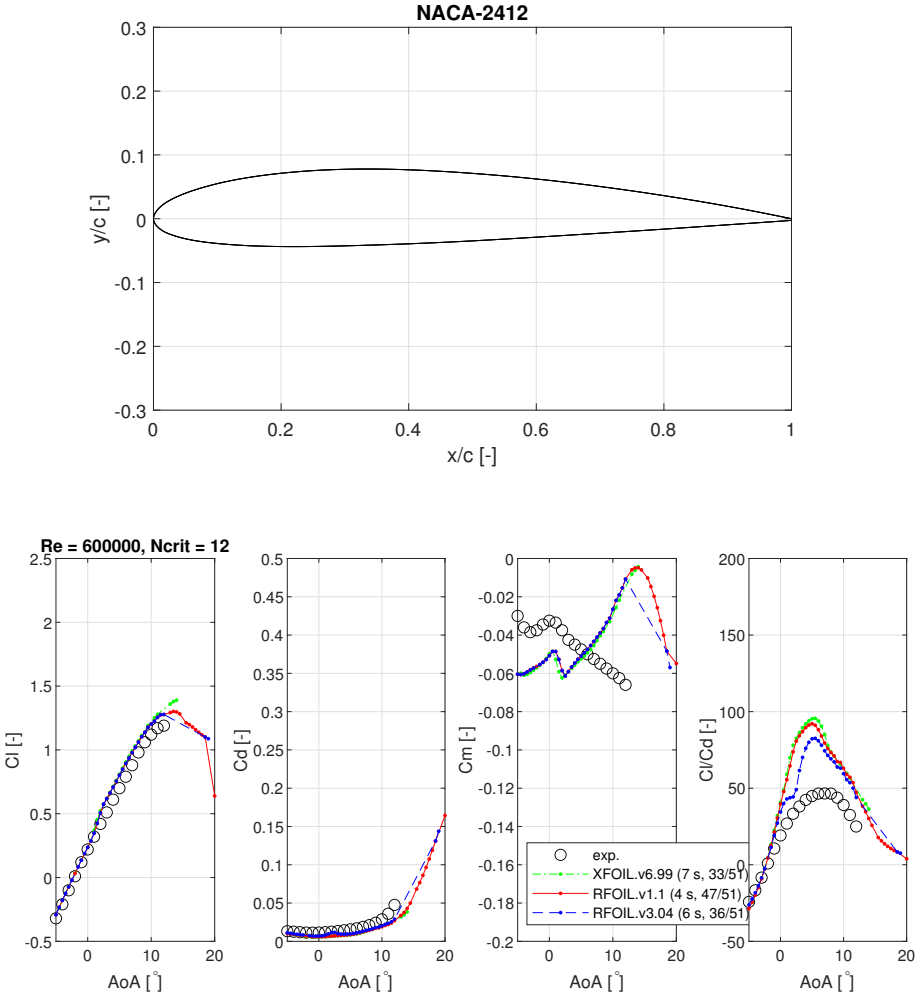

Figure B.239: Differences between experimental and numerical polars for the NACA-2412 airfoil at a Reynolds number of 600000. Vertical black lines in the middle subplot indicate, from left to right, the angle of attack corresponding to the minimum drag coefficient, maximum lift to drag ratio and maximum lift coefficient, respectively.

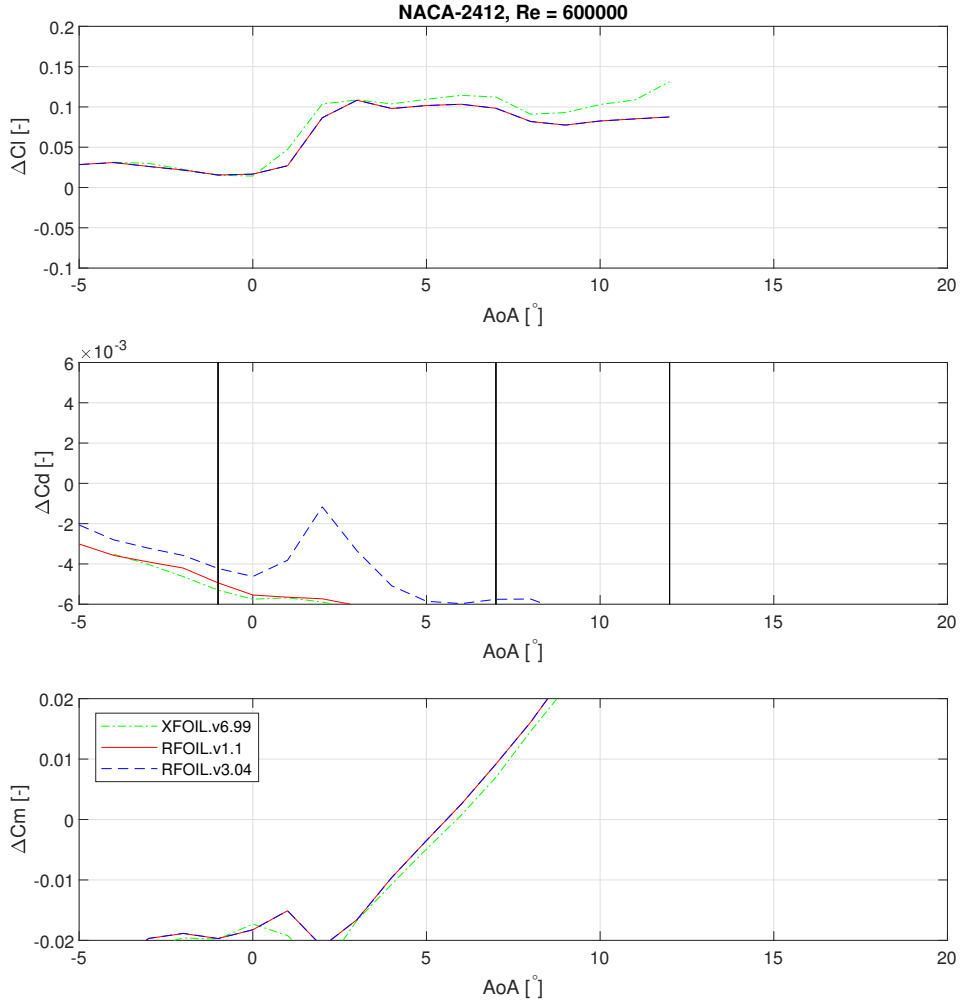

Figure B.240: Comparison between experimental and numerical pressure and skin friction distributions for the NACA-2412 airfoil at a Reynolds number of 600000 and at the design angle of attack.

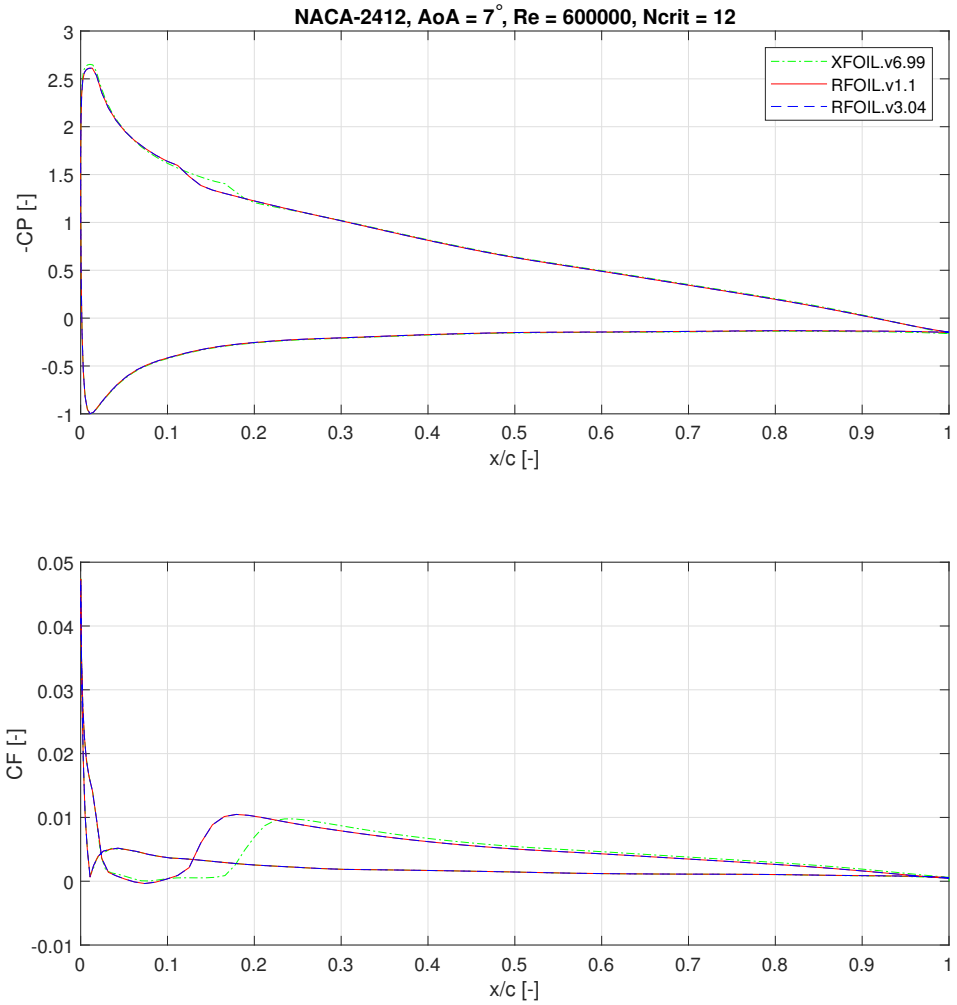

Figure B.241: Comparison between experimental and numerical polars for the NACA-4409 airfoil at a Reynolds number of 2300000. Simulation time to generate the polars by means the different codes and the number of converged polar points are depicted between parentheses.

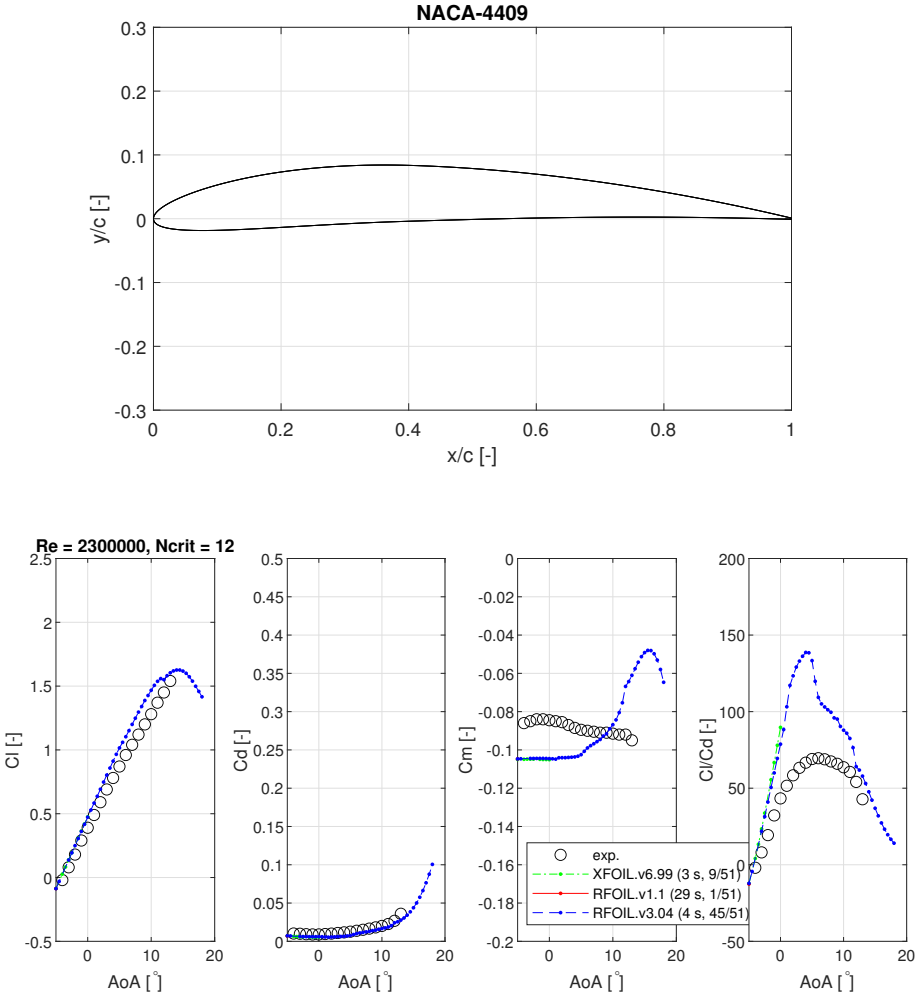

Figure B.242: Differences between experimental and numerical polars for the NACA-4409 airfoil at a Reynolds number of 2300000. Vertical black lines in the middle subplot indicate, from left to right, the angle of attack corresponding to the minimum drag coefficient, maximum lift to drag ratio and maximum lift coefficient, respectively.

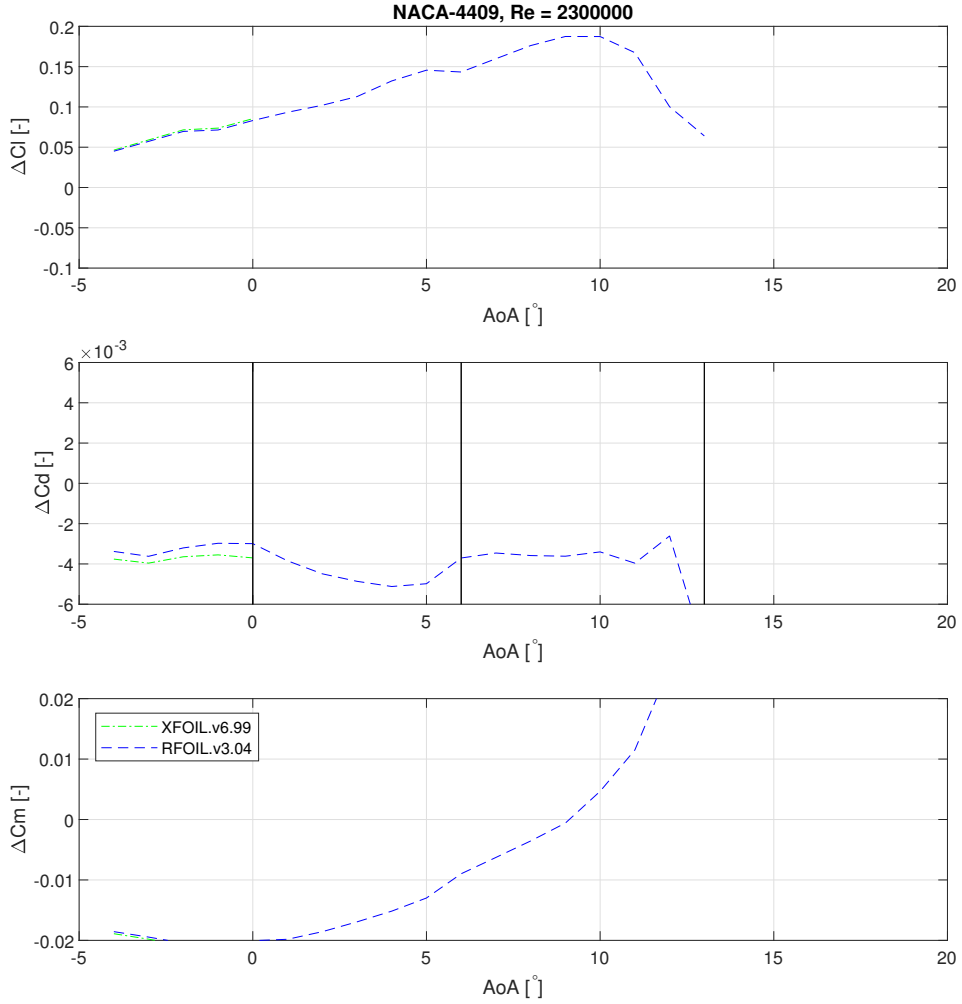

Figure B.243: Comparison between experimental and numerical pressure and skin friction distributions for the NACA-4409 airfoil at a Reynolds number of 2300000 and at the design angle of attack.

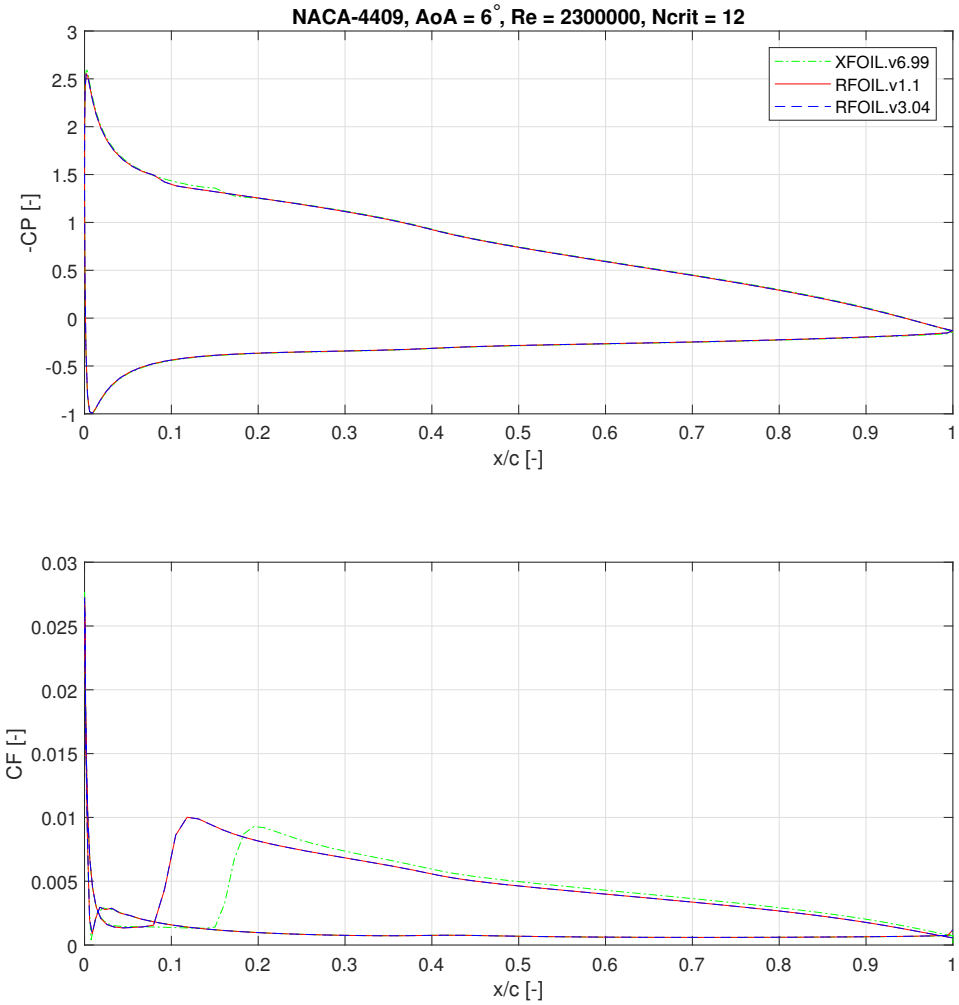

Figure B.244: Comparison between experimental and numerical polars for the NACA-4409 airfoil at a Reynolds number of 3100000. Simulation time to generate the polars by means the different codes and the number of converged polar points are depicted between parentheses.

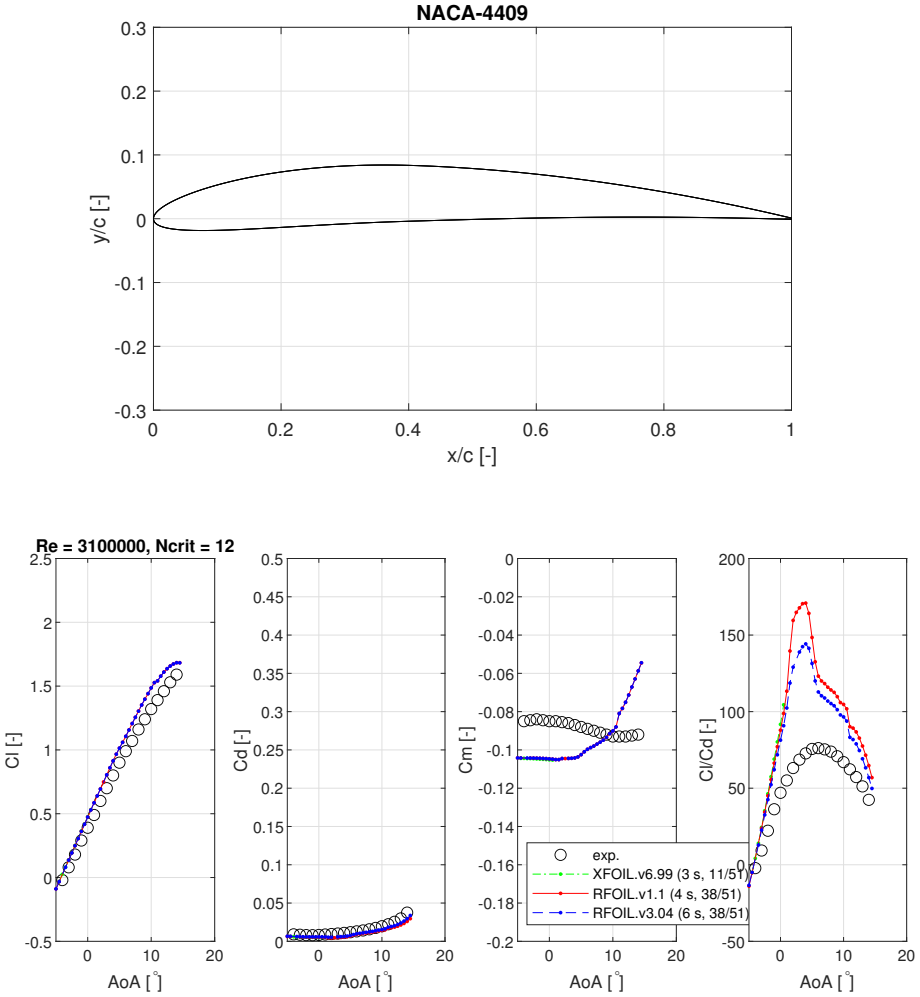

Figure B.245: Differences between experimental and numerical polars for the NACA-4409 airfoil at a Reynolds number of 3100000. Vertical black lines in the middle subplot indicate, from left to right, the angle of attack corresponding to the minimum drag coefficient, maximum lift to drag ratio and maximum lift coefficient, respectively.

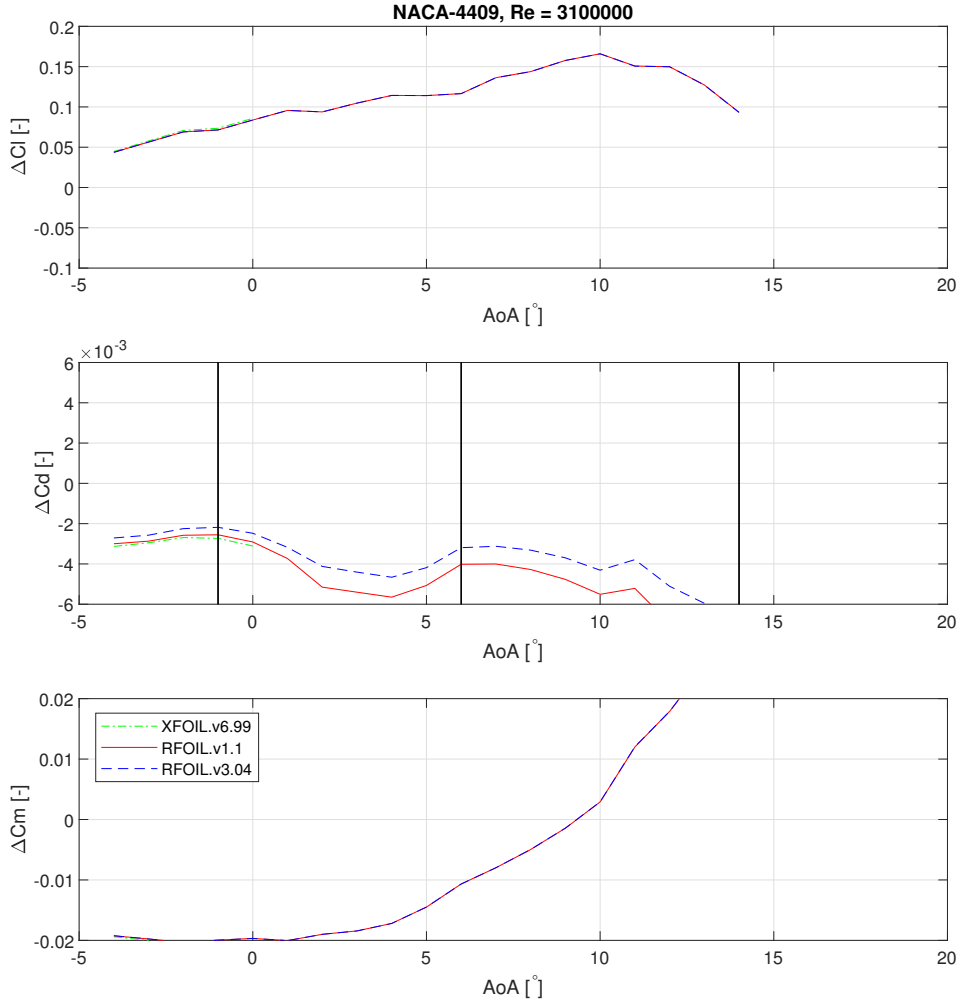

Figure B.246: Comparison between experimental and numerical pressure and skin friction distributions for the NACA-4409 airfoil at a Reynolds number of 3100000 and at the design angle of attack.

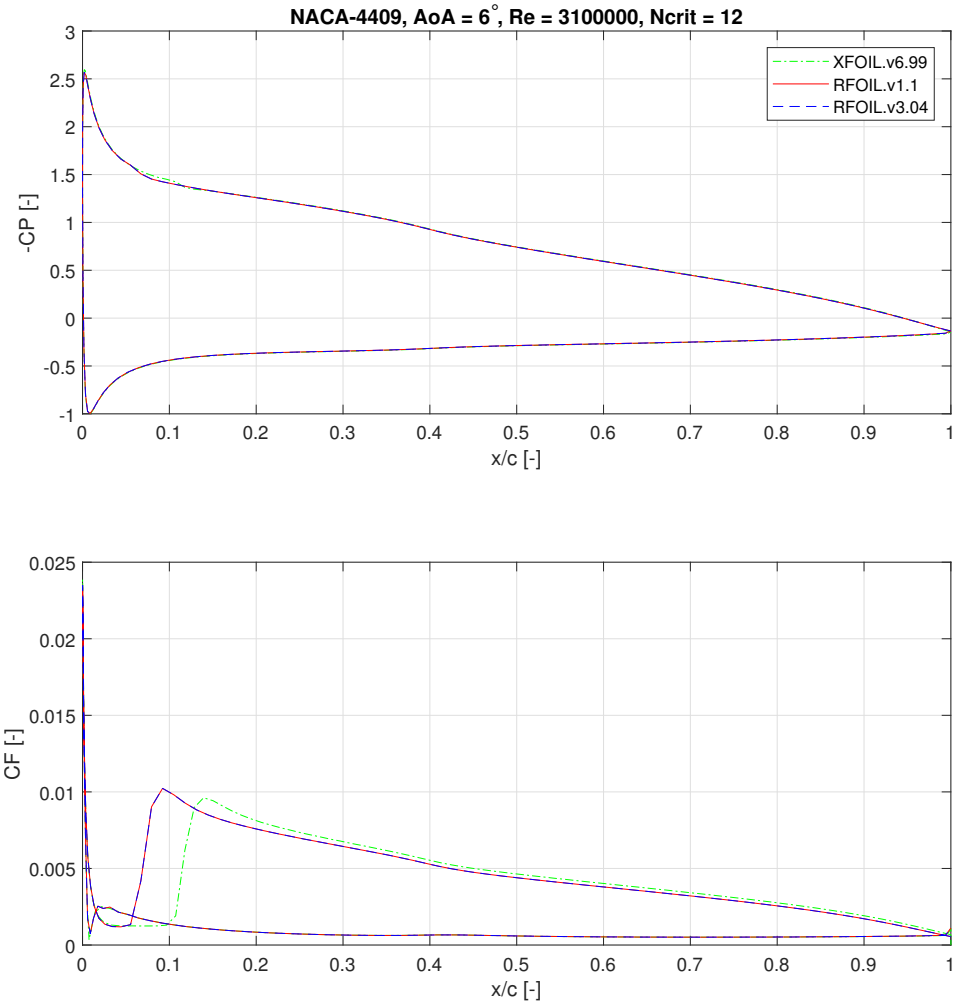

Figure B.247: Comparison between experimental and numerical polars for the NACA-4409 airfoil at a Reynolds number of 600000. Simulation time to generate the polars by means the different codes and the number of converged polar points are depicted between parentheses.

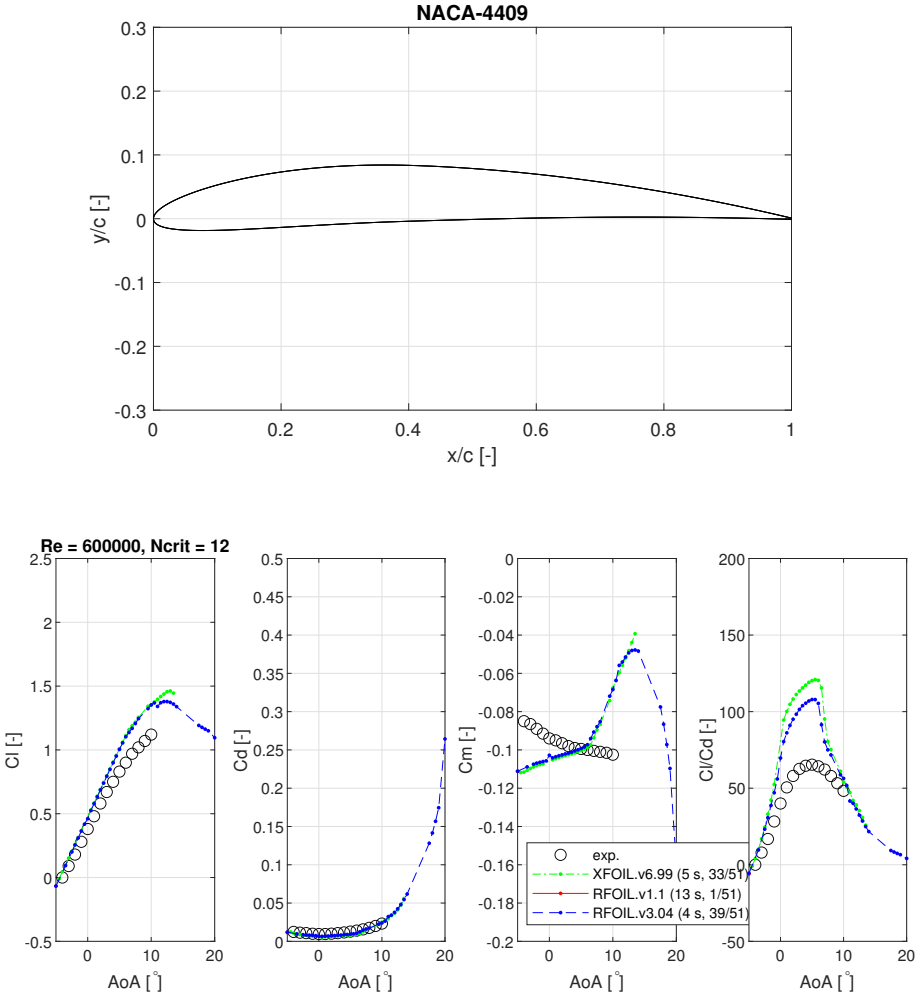

Figure B.248: Differences between experimental and numerical polars for the NACA-4409 airfoil at a Reynolds number of 600000. Vertical black lines in the middle subplot indicate, from left to right, the angle of attack corresponding to the minimum drag coefficient, maximum lift to drag ratio and maximum lift coefficient, respectively.

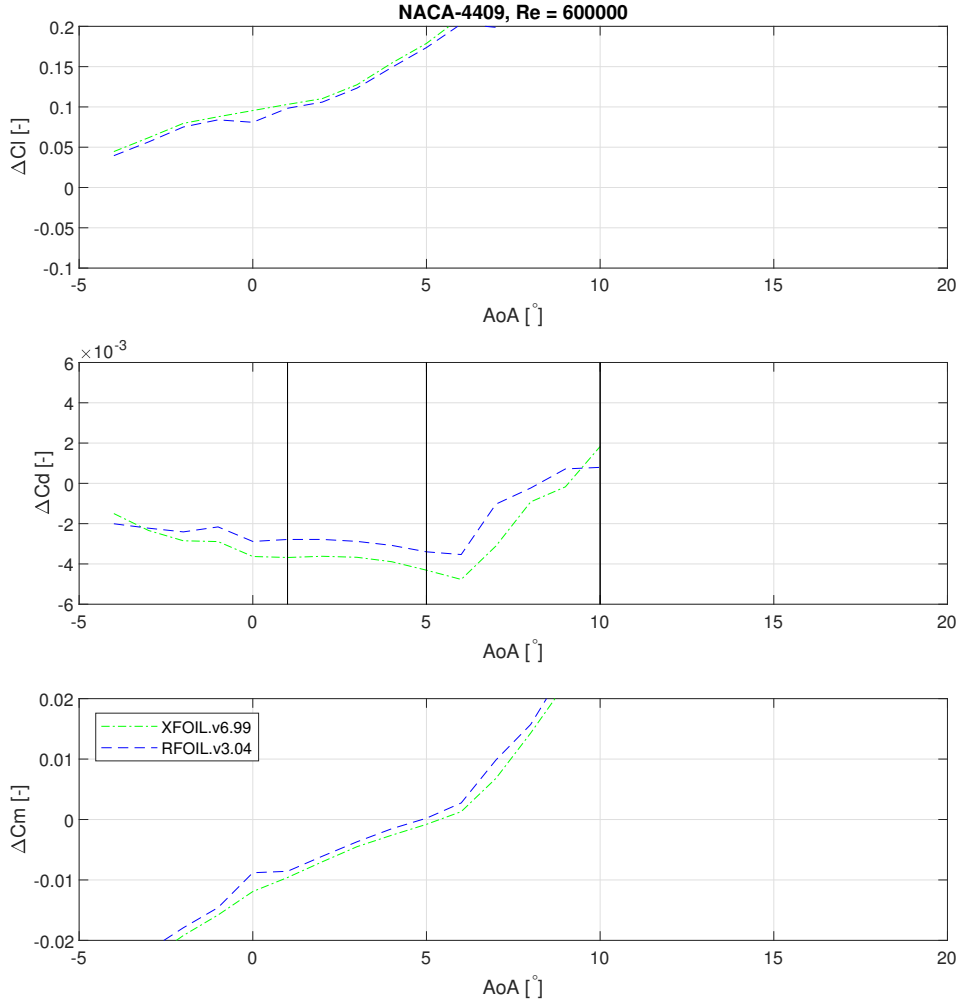

Figure B.249: Comparison between experimental and numerical pressure and skin friction distributions for the NACA-4409 airfoil at a Reynolds number of 600000 and at the design angle of attack.

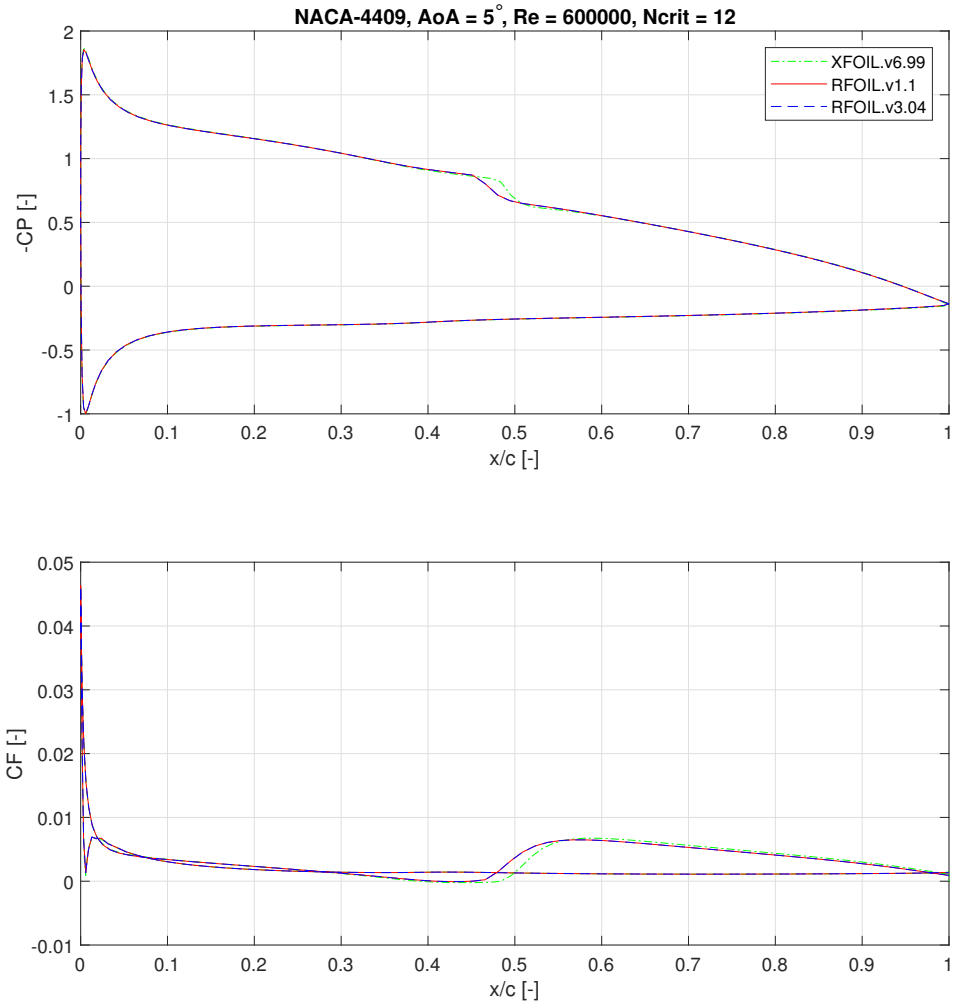

Figure B.250: Comparison between experimental and numerical polars for the NACA-4412 airfoil at a Reynolds number of 1000000. Simulation time to generate the polars by means the different codes and the number of converged polar points are depicted between parentheses.

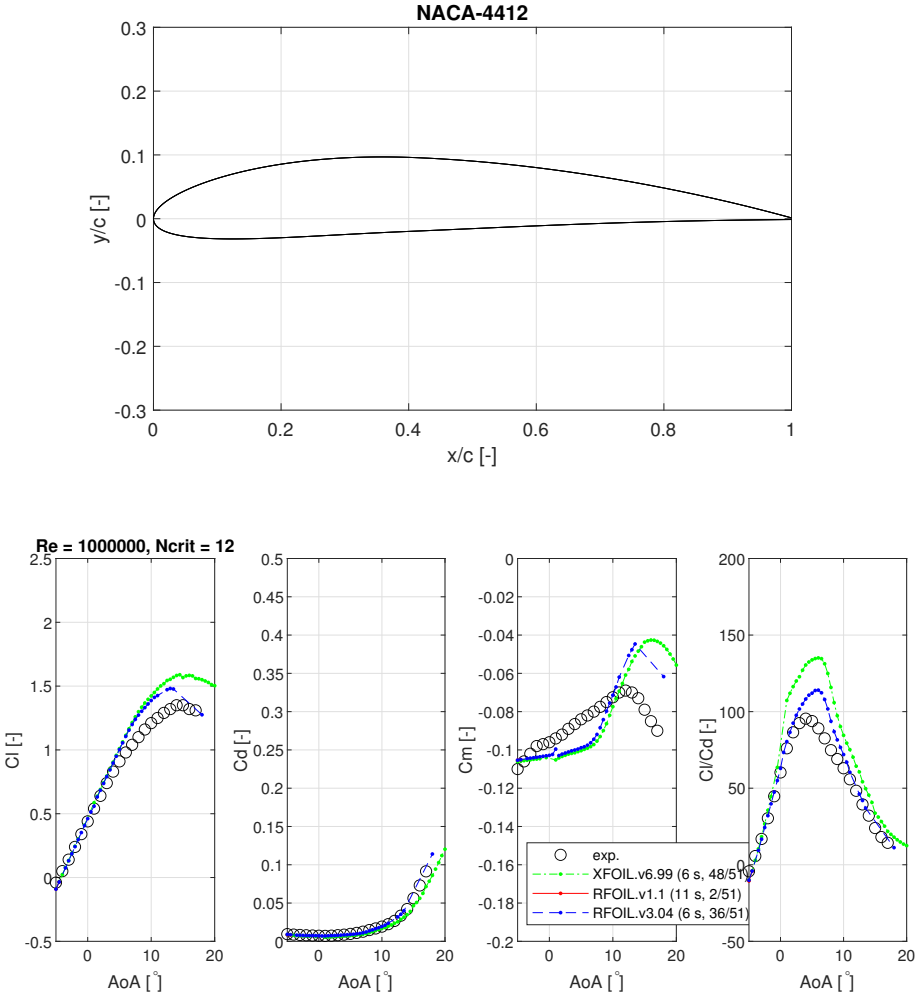

Figure B.251: Differences between experimental and numerical polars for the NACA-4412 airfoil at a Reynolds number of 1000000. Vertical black lines in the middle subplot indicate, from left to right, the angle of attack corresponding to the minimum drag coefficient, maximum lift to drag ratio and maximum lift coefficient, respectively.

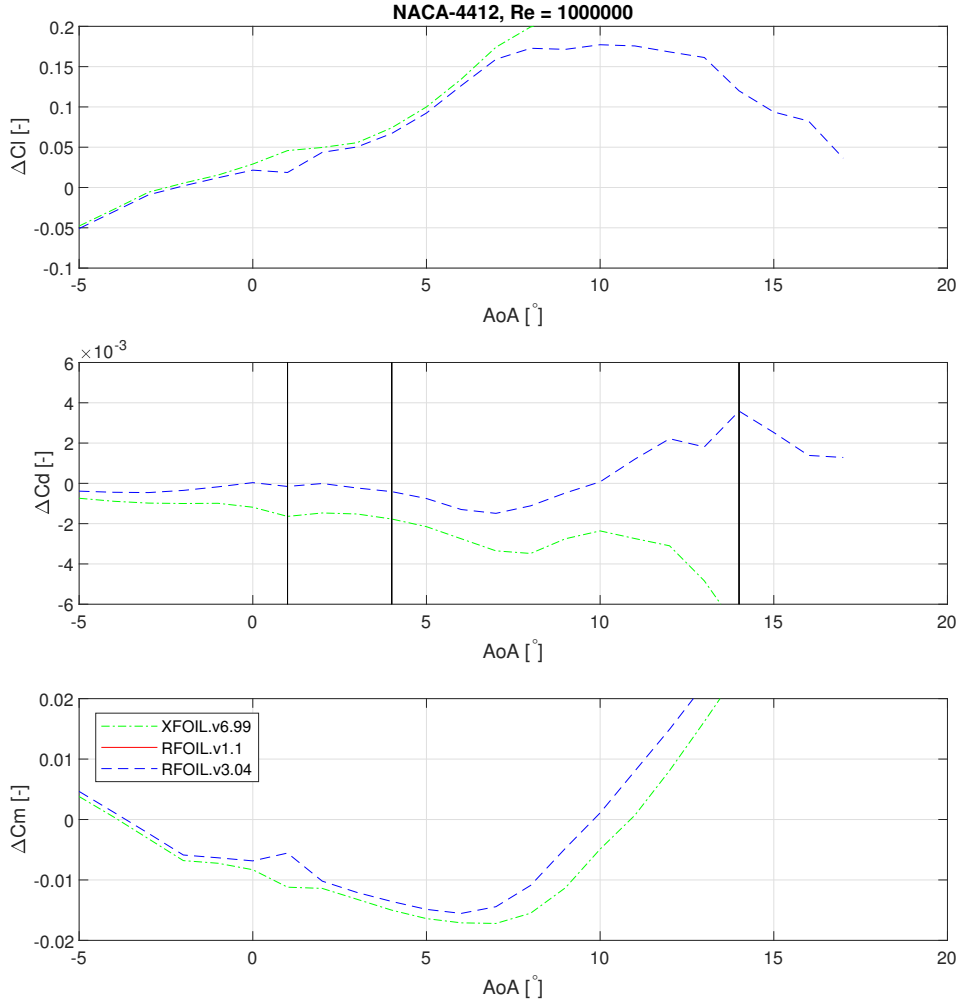

Figure B.252: Comparison between experimental and numerical pressure and skin friction distributions for the NACA-4412 airfoil at a Reynolds number of 1000000 and at the design angle of attack.

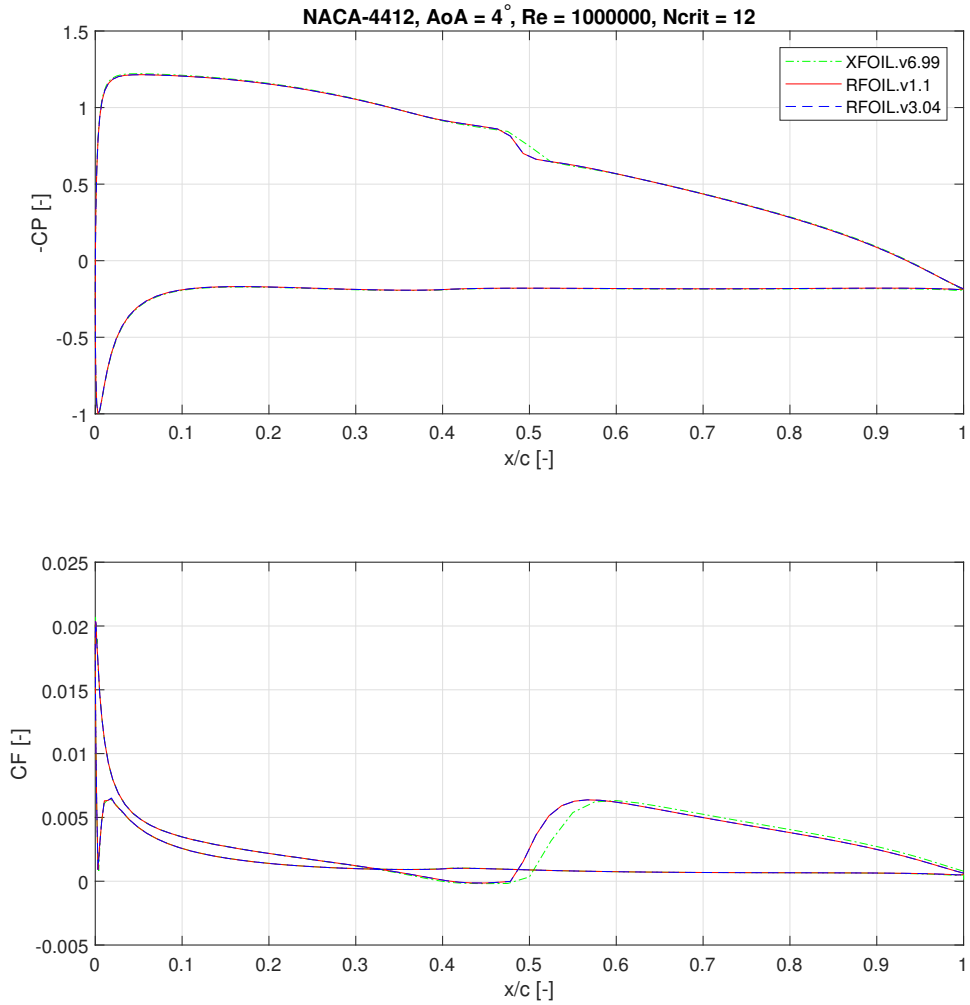

Figure B.253: Comparison between experimental and numerical polars for the NACA-4412 airfoil at a Reynolds number of 1500000. Simulation time to generate the polars by means the different codes and the number of converged polar points are depicted between parentheses.

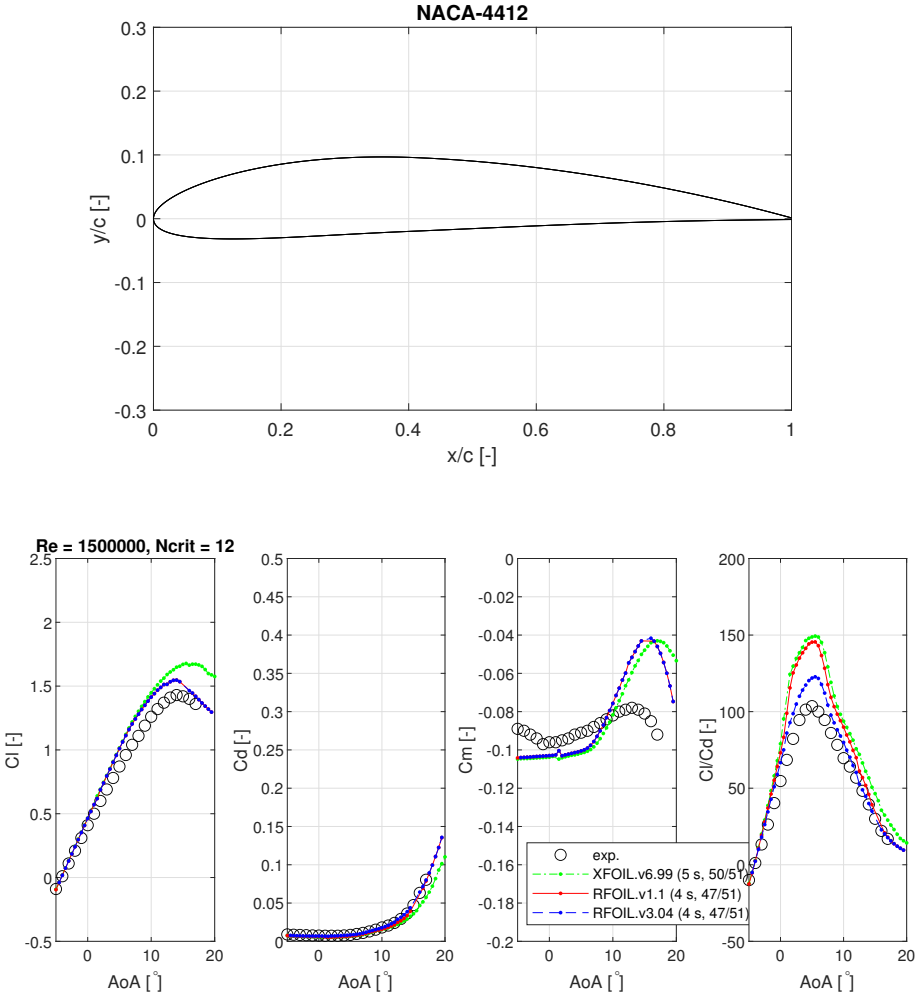

Figure B.254: Differences between experimental and numerical polars for the NACA-4412 airfoil at a Reynolds number of 1500000. Vertical black lines in the middle subplot indicate, from left to right, the angle of attack corresponding to the minimum drag coefficient, maximum lift to drag ratio and maximum lift coefficient, respectively.

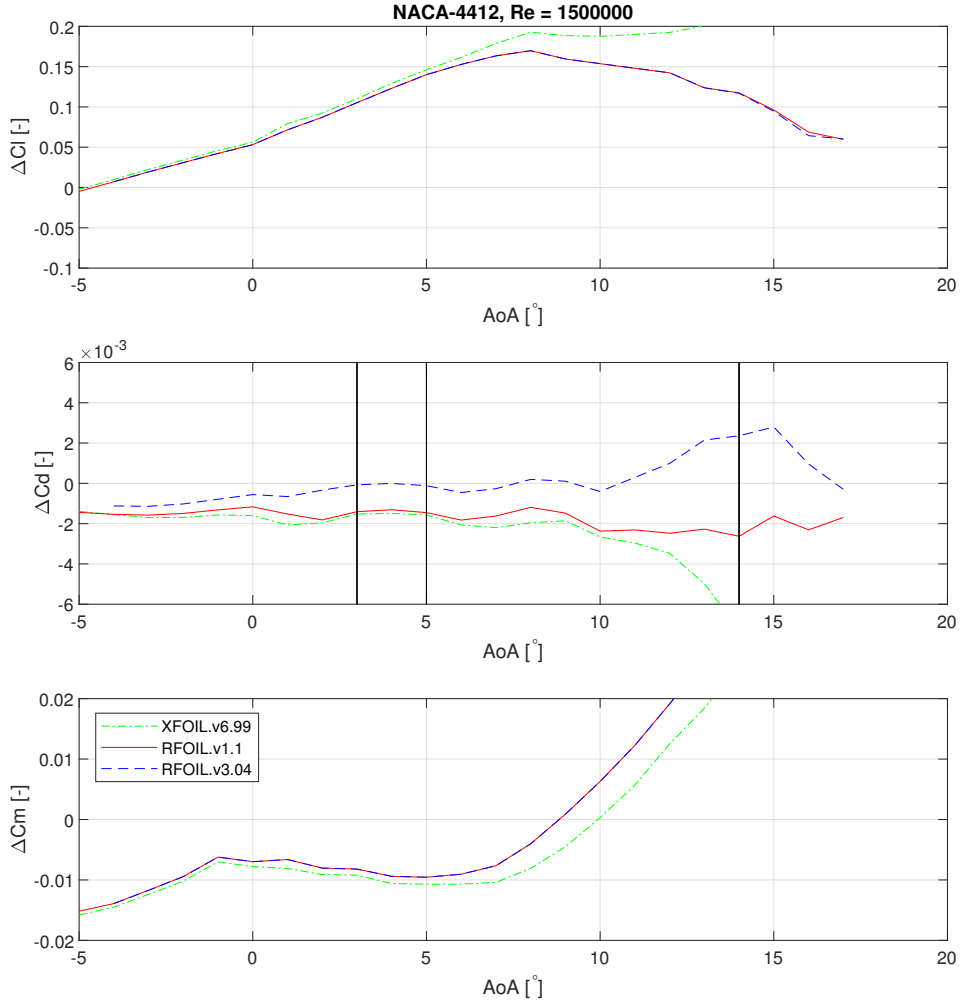

Figure B.255: Comparison between experimental and numerical pressure and skin friction distributions for the NACA-4412 airfoil at a Reynolds number of 1500000 and at the design angle of attack.

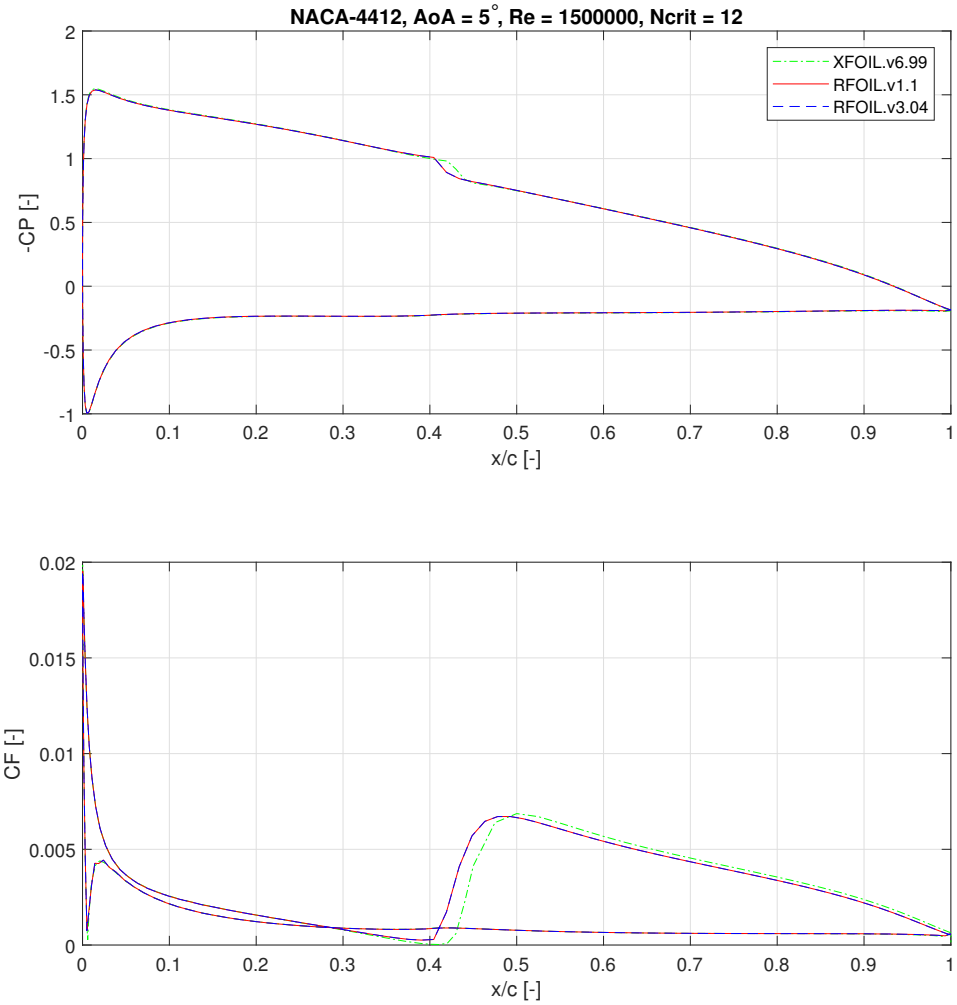

Figure B.256: Comparison between experimental and numerical polars for the NACA-4412 airfoil at a Reynolds number of 2000000. Simulation time to generate the polars by means the different codes and the number of converged polar points are depicted between parentheses.

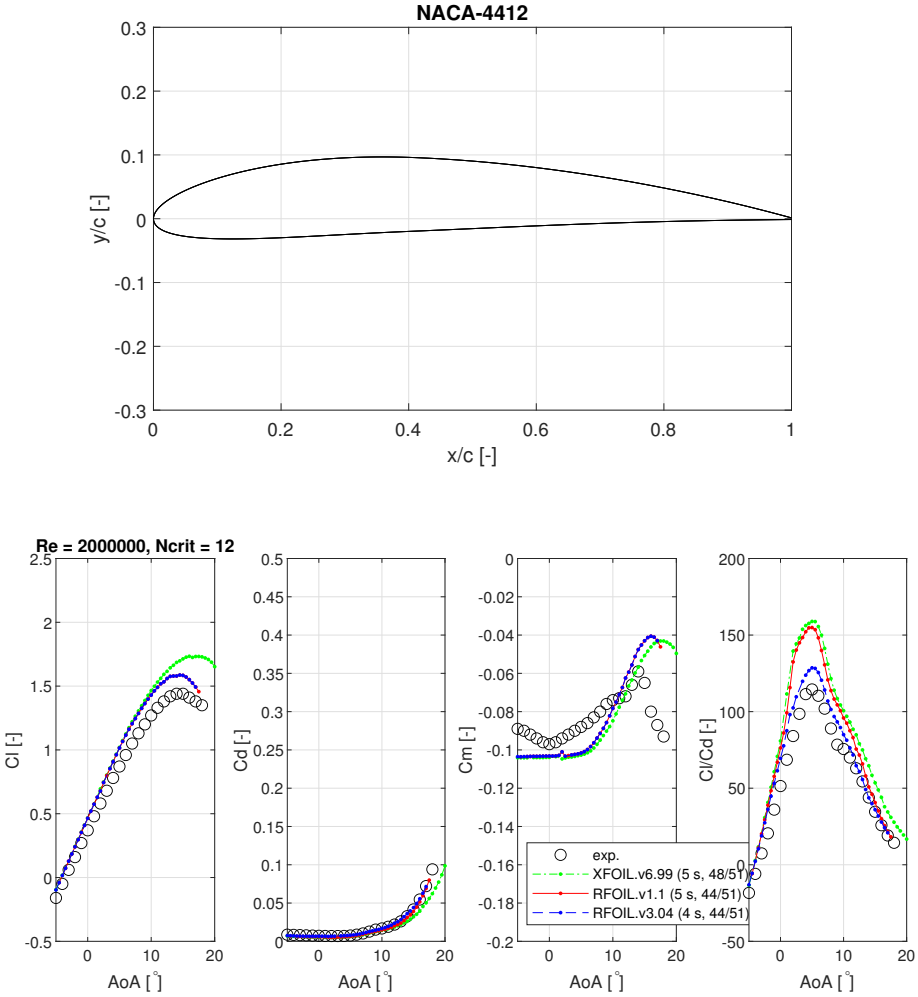

Figure B.257: Differences between experimental and numerical polars for the NACA-4412 airfoil at a Reynolds number of 2000000. Vertical black lines in the middle subplot indicate, from left to right, the angle of attack corresponding to the minimum drag coefficient, maximum lift to drag ratio and maximum lift coefficient, respectively.

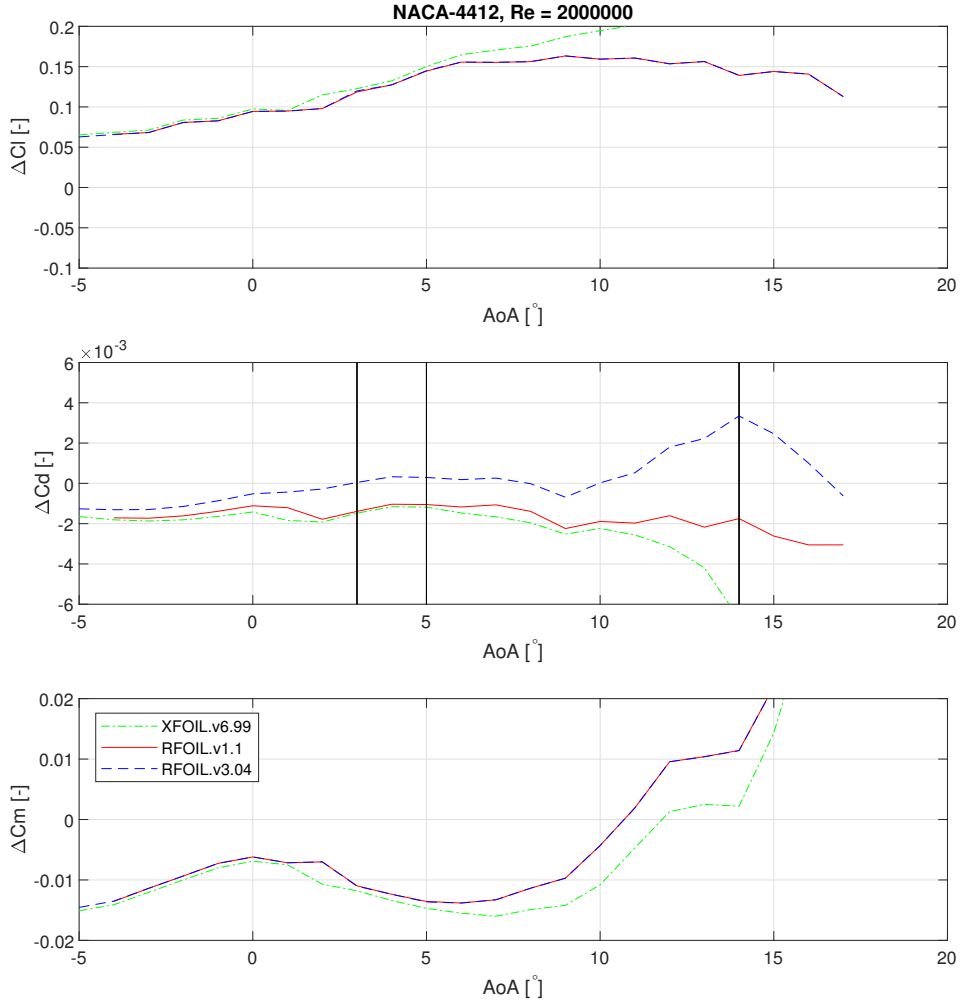

Figure B.258: Comparison between experimental and numerical pressure and skin friction distributions for the NACA-4412 airfoil at a Reynolds number of 2000000 and at the design angle of attack.

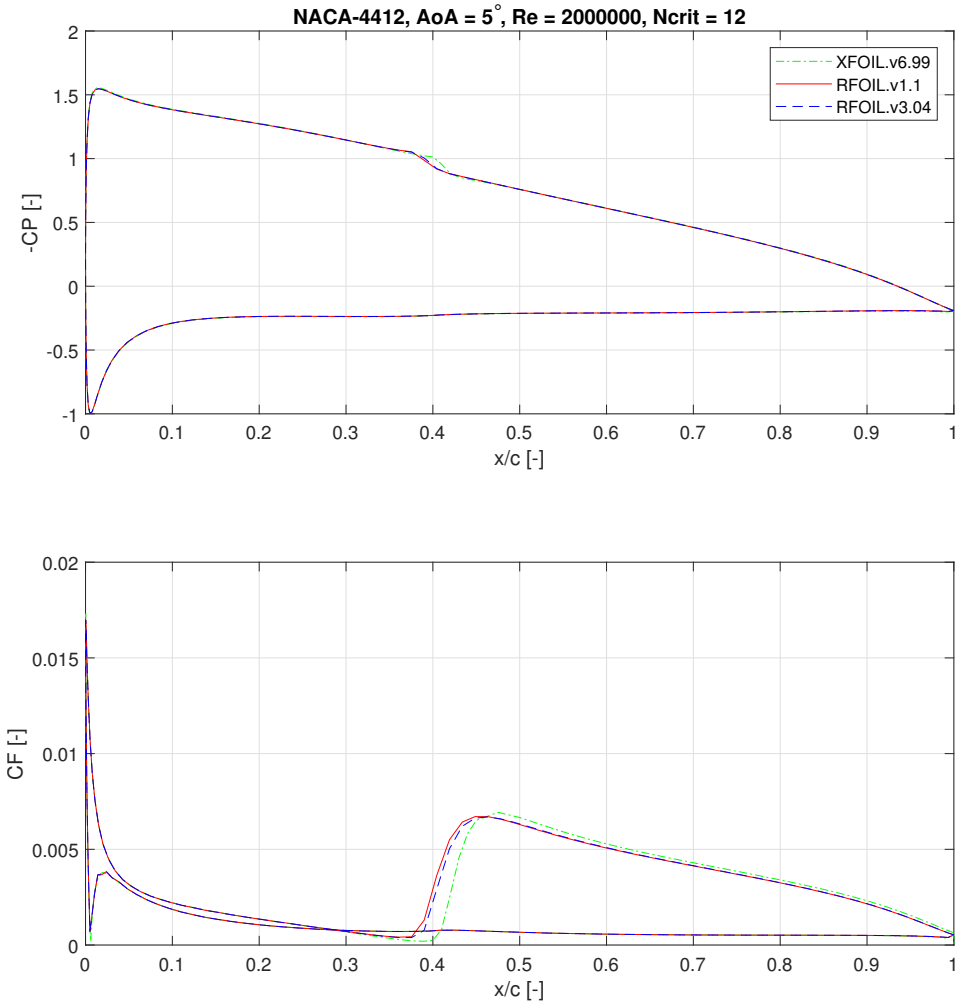

Figure B.259: Comparison between experimental and numerical polars for the NACA-4412 airfoil at a Reynolds number of 3000000. Simulation time to generate the polars by means the different codes and the number of converged polar points are depicted between parentheses.

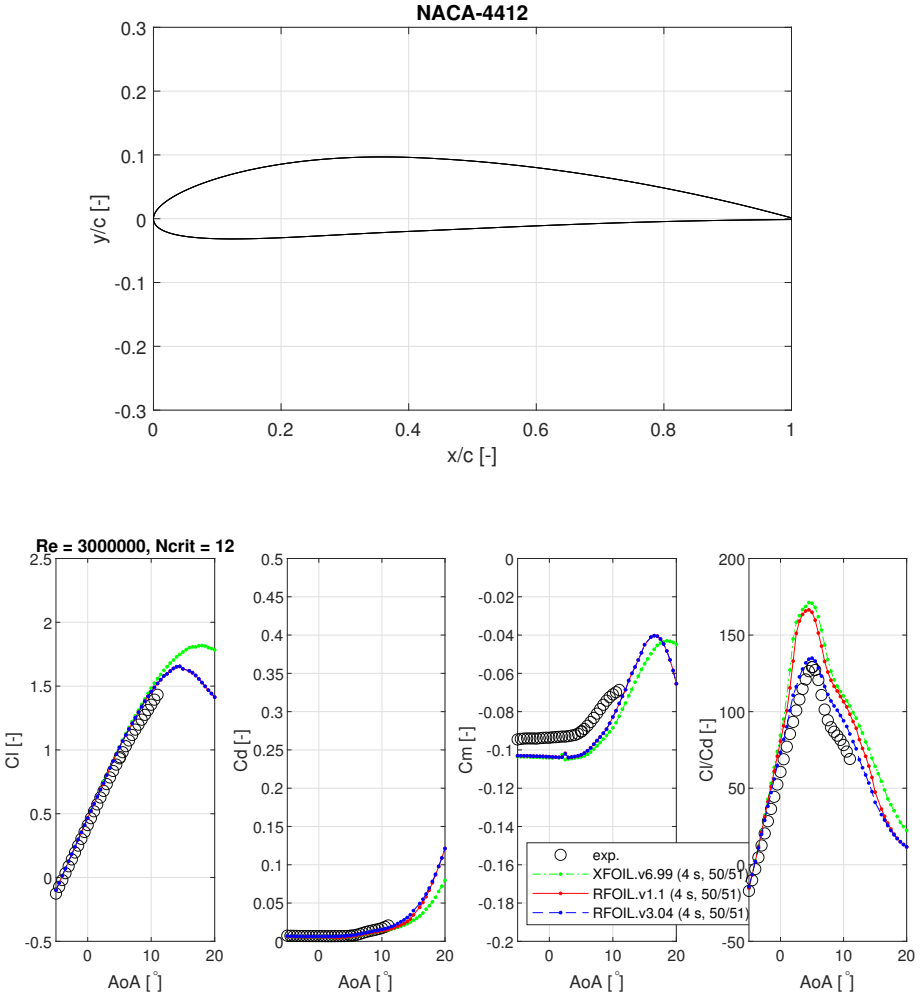

Figure B.260: Differences between experimental and numerical polars for the NACA-4412 airfoil at a Reynolds number of 3000000. Vertical black lines in the middle subplot indicate, from left to right, the angle of attack corresponding to the minimum drag coefficient, maximum lift to drag ratio and maximum lift coefficient, respectively.

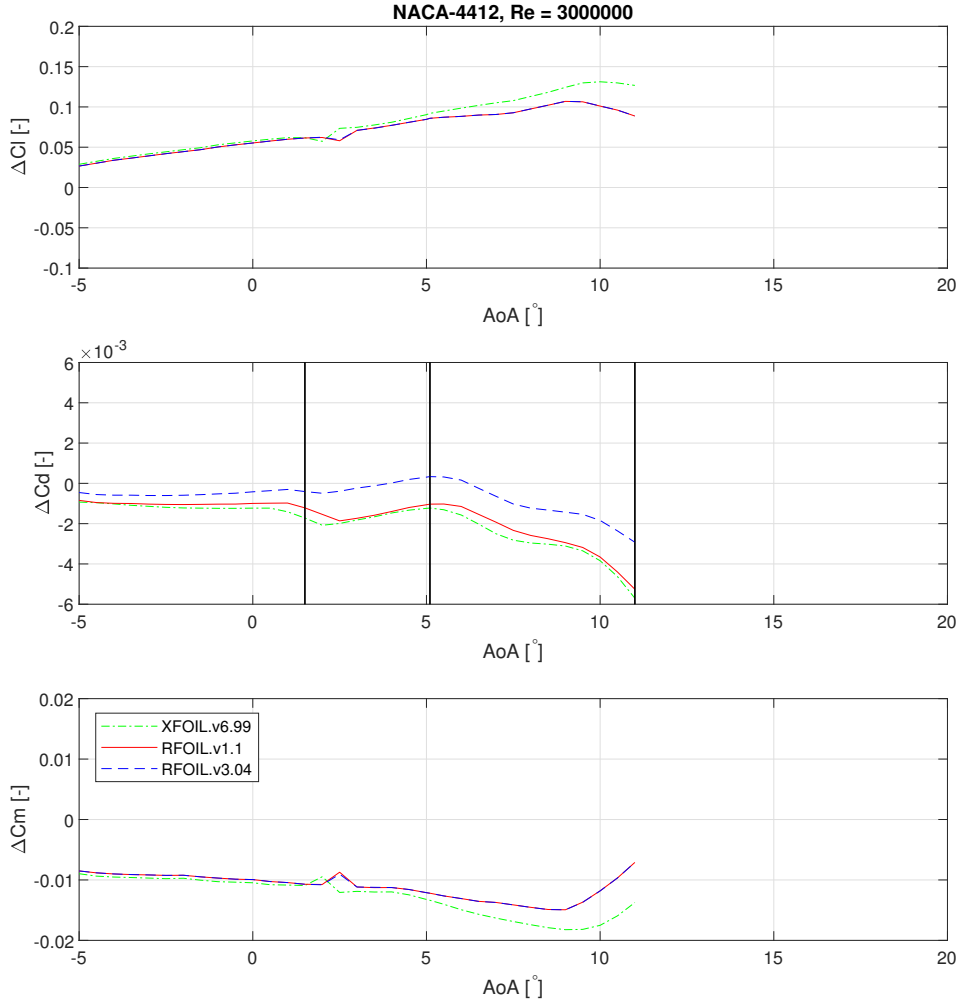

Figure B.261: Comparison between experimental and numerical pressure and skin friction distributions for the NACA-4412 airfoil at a Reynolds number of 3000000 and at the design angle of attack.

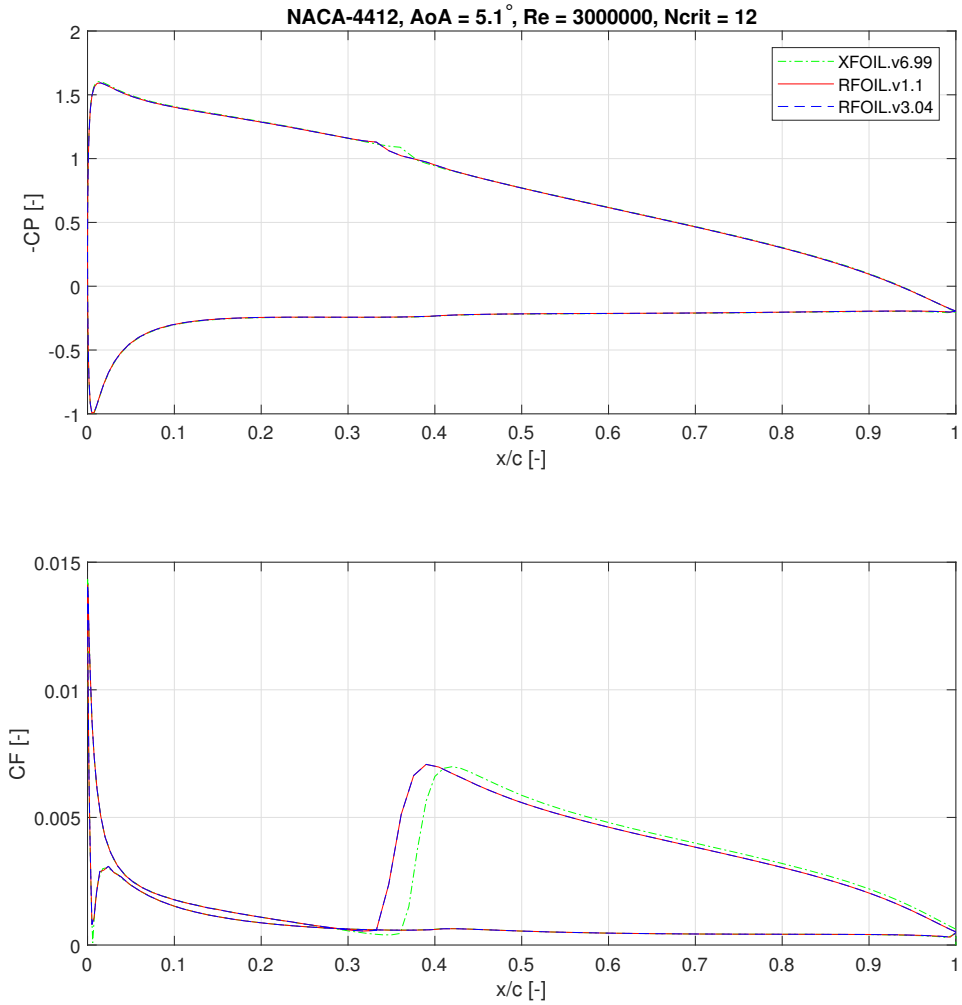

Figure B.262: Comparison between experimental and numerical polars for the NACA-4412 airfoil at a Reynolds number of 6000000. Simulation time to generate the polars by means the different codes and the number of converged polar points are depicted between parentheses.

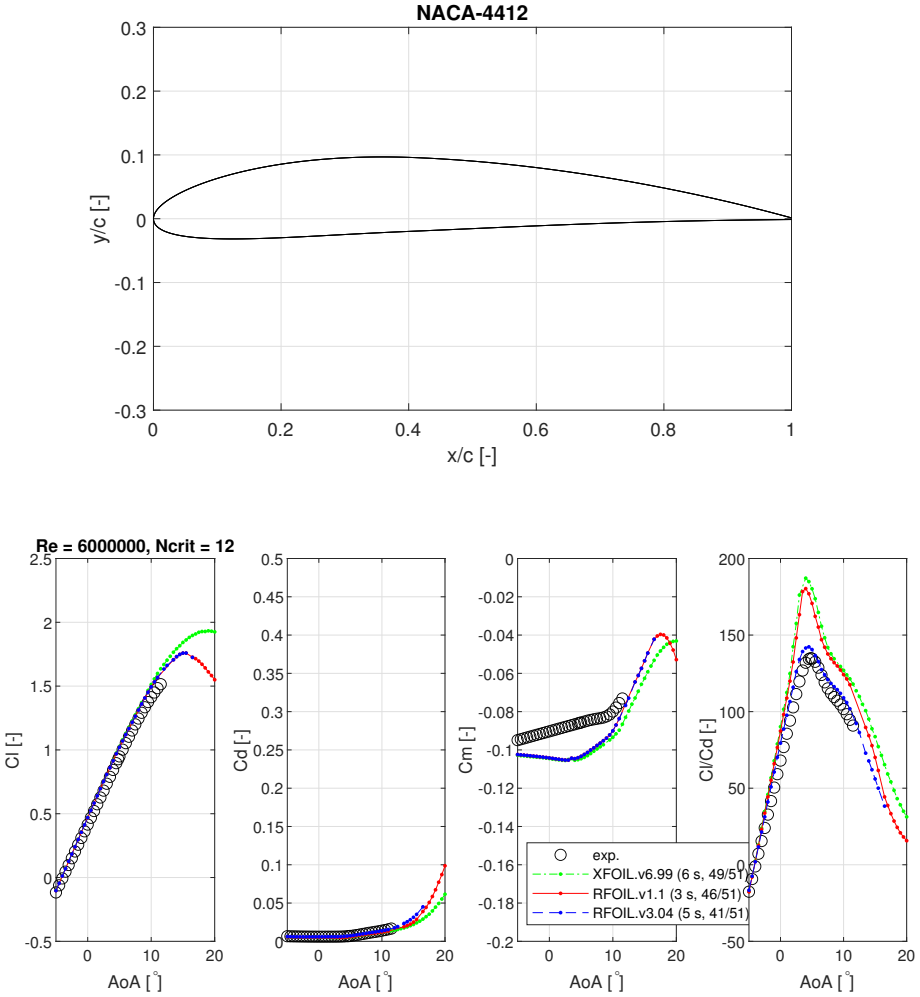

Figure B.263: Differences between experimental and numerical polars for the NACA-4412 airfoil at a Reynolds number of 6000000. Vertical black lines in the middle subplot indicate, from left to right, the angle of attack corresponding to the minimum drag coefficient, maximum lift to drag ratio and maximum lift coefficient, respectively.

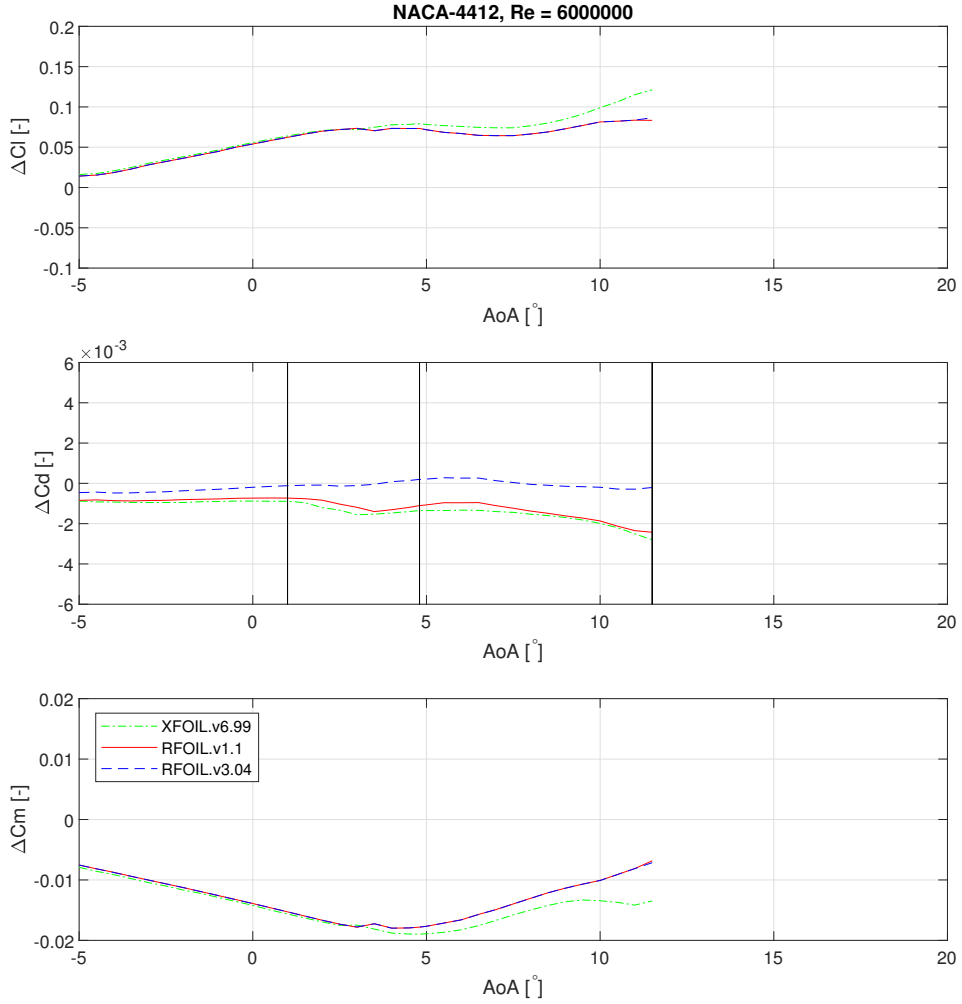

Figure B.264: Comparison between experimental and numerical pressure and skin friction distributions for the NACA-4412 airfoil at a Reynolds number of 6000000 and at the design angle of attack.

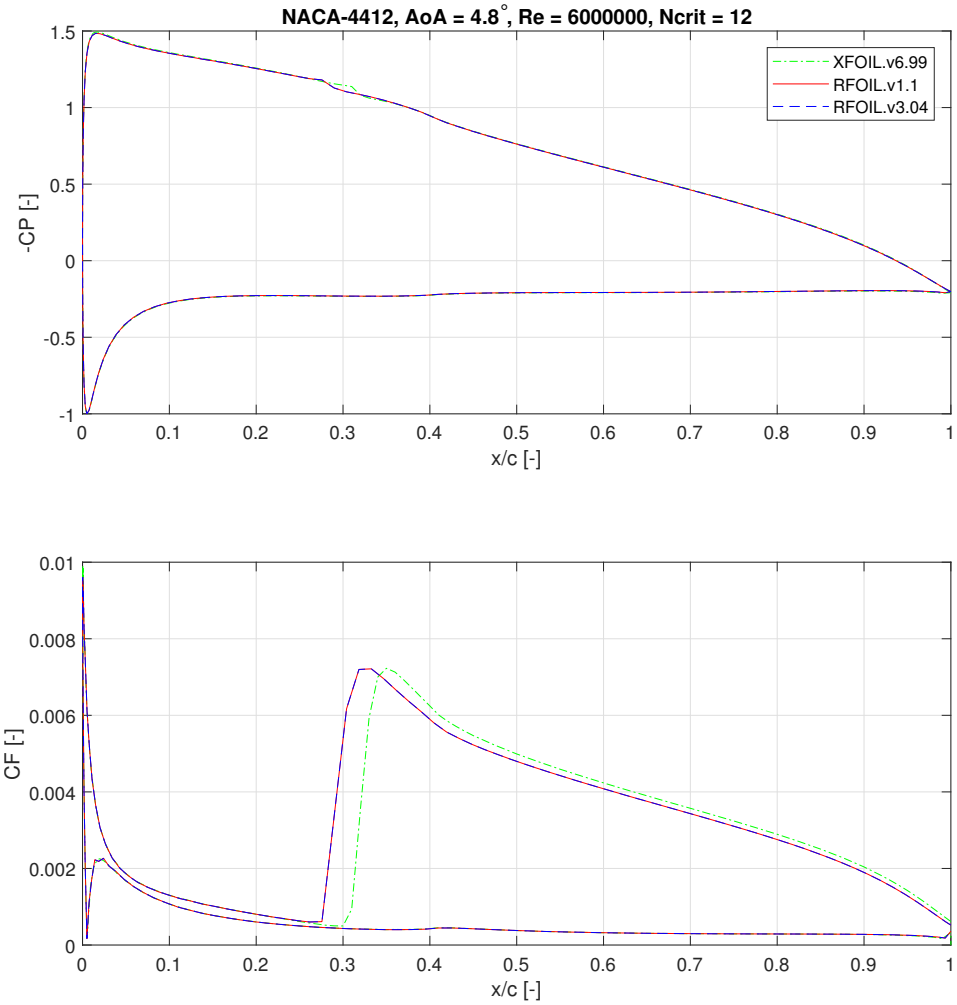

Figure B.265: Comparison between experimental and numerical polars for the NACA-4412 airfoil at a Reynolds number of 700000. Simulation time to generate the polars by means the different codes and the number of converged polar points are depicted between parentheses.

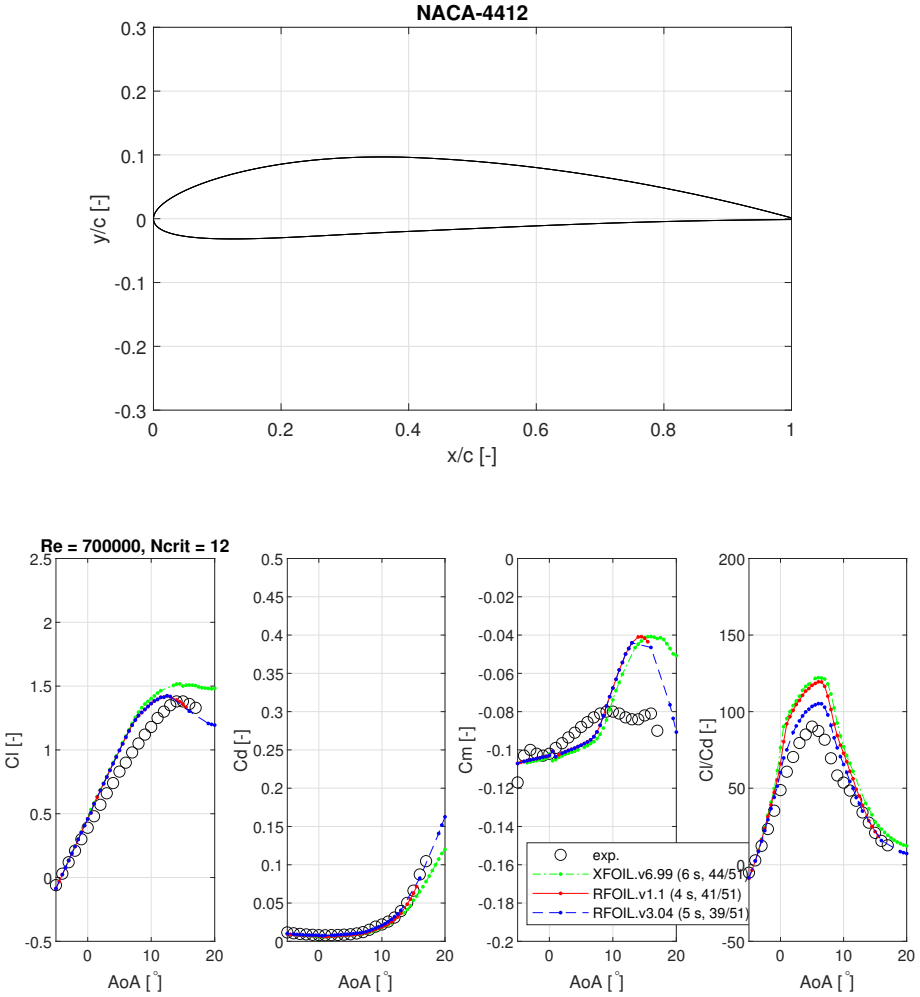

Figure B.266: Differences between experimental and numerical polars for the NACA-4412 airfoil at a Reynolds number of 700000. Vertical black lines in the middle subplot indicate, from left to right, the angle of attack corresponding to the minimum drag coefficient, maximum lift to drag ratio and maximum lift coefficient, respectively.

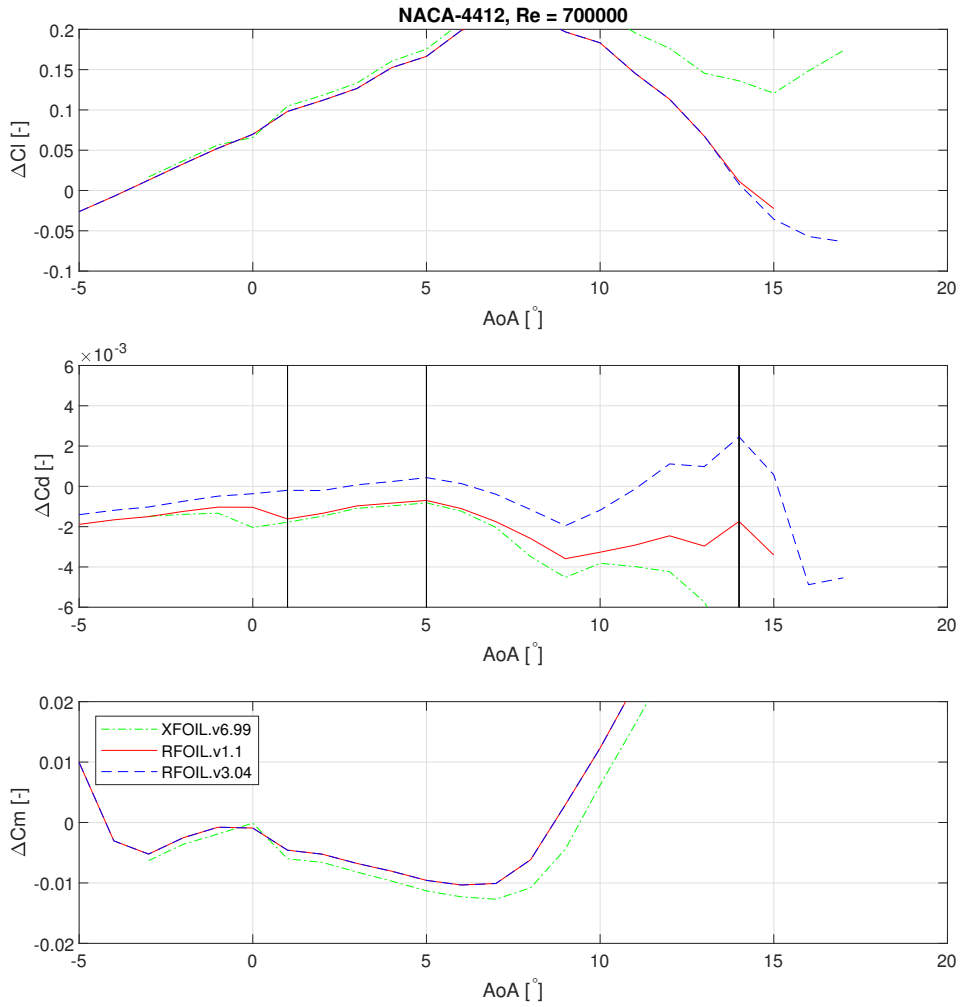

Figure B.267: Comparison between experimental and numerical pressure and skin friction distributions for the NACA-4412 airfoil at a Reynolds number of 700000 and at the design angle of attack.

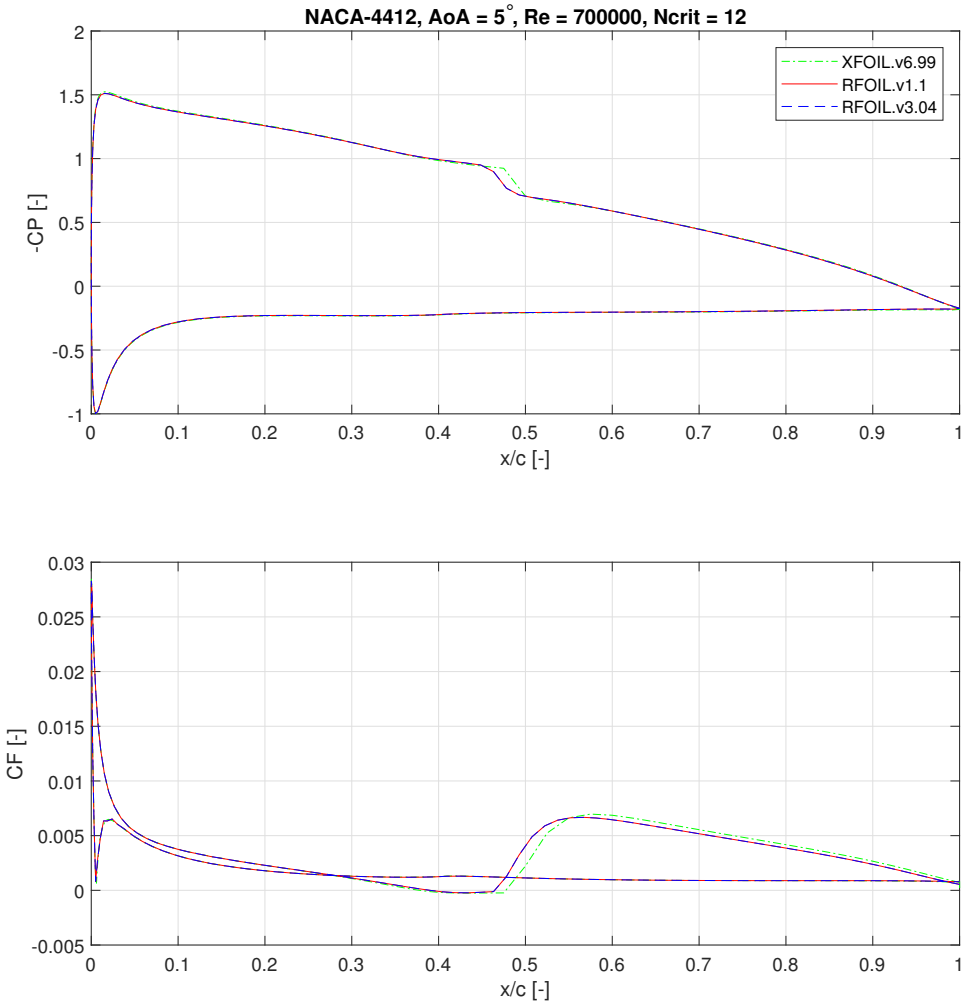

Figure B.268: Comparison between experimental and numerical polars for the NACA-4415 airfoil at a Reynolds number of 1000000. Simulation time to generate the polars by means the different codes and the number of converged polar points are depicted between parentheses.

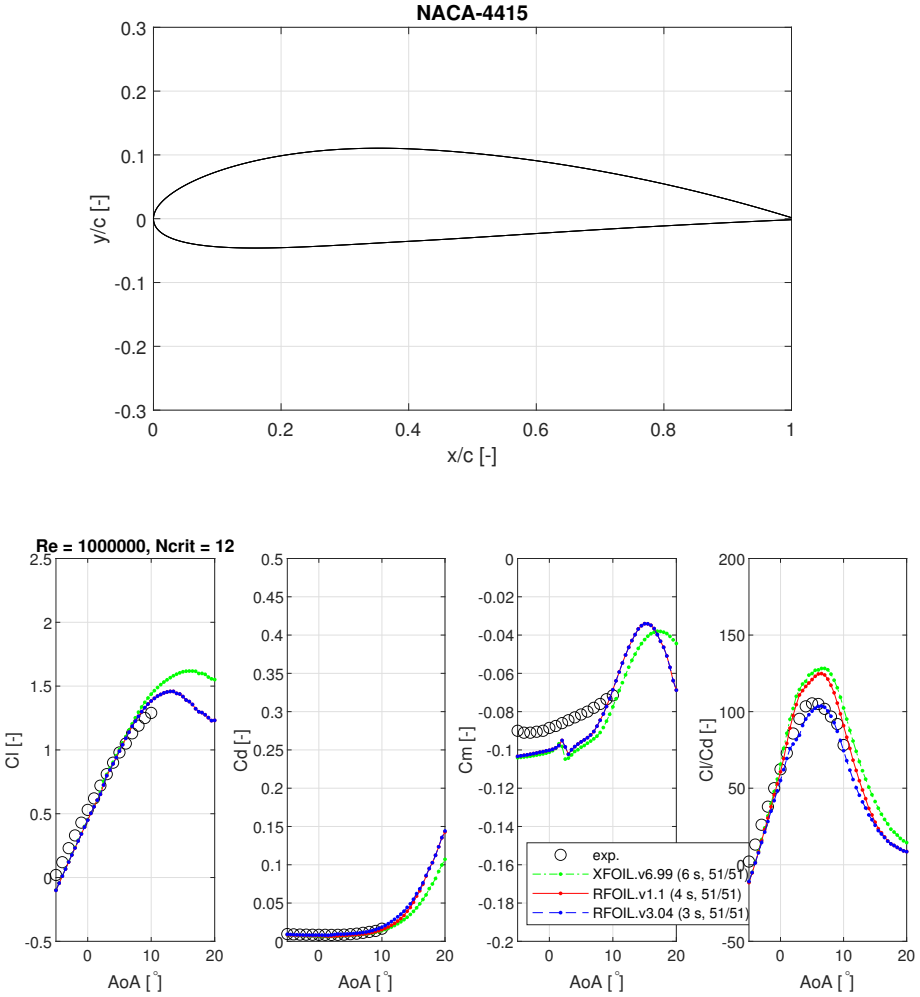

Figure B.269: Differences between experimental and numerical polars for the NACA-4415 airfoil at a Reynolds number of 1000000. Vertical black lines in the middle subplot indicate, from left to right, the angle of attack corresponding to the minimum drag coefficient, maximum lift to drag ratio and maximum lift coefficient, respectively.

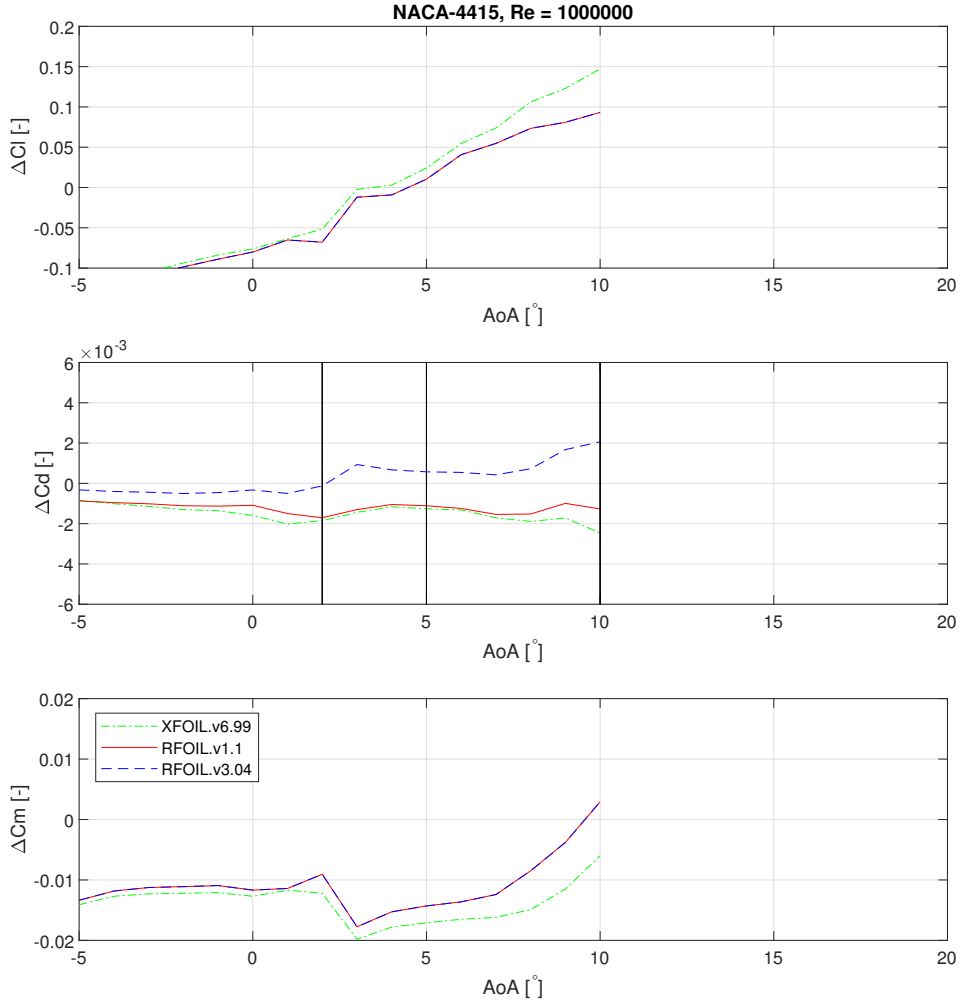

Figure B.270: Comparison between experimental and numerical pressure and skin friction distributions for the NACA-4415 airfoil at a Reynolds number of 1000000 and at the design angle of attack.

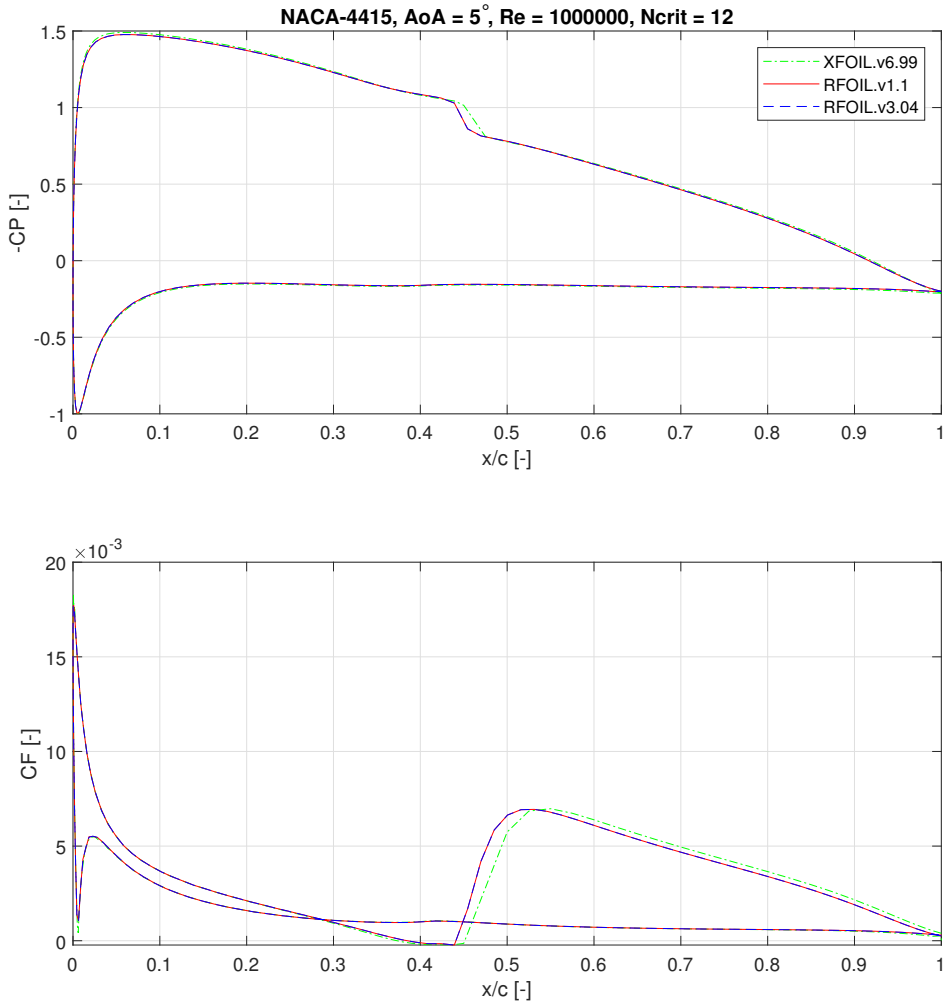

Figure B.271: Comparison between experimental and numerical polars for the NACA-4415 airfoil at a Reynolds number of 1500000. Simulation time to generate the polars by means the different codes and the number of converged polar points are depicted between parentheses.

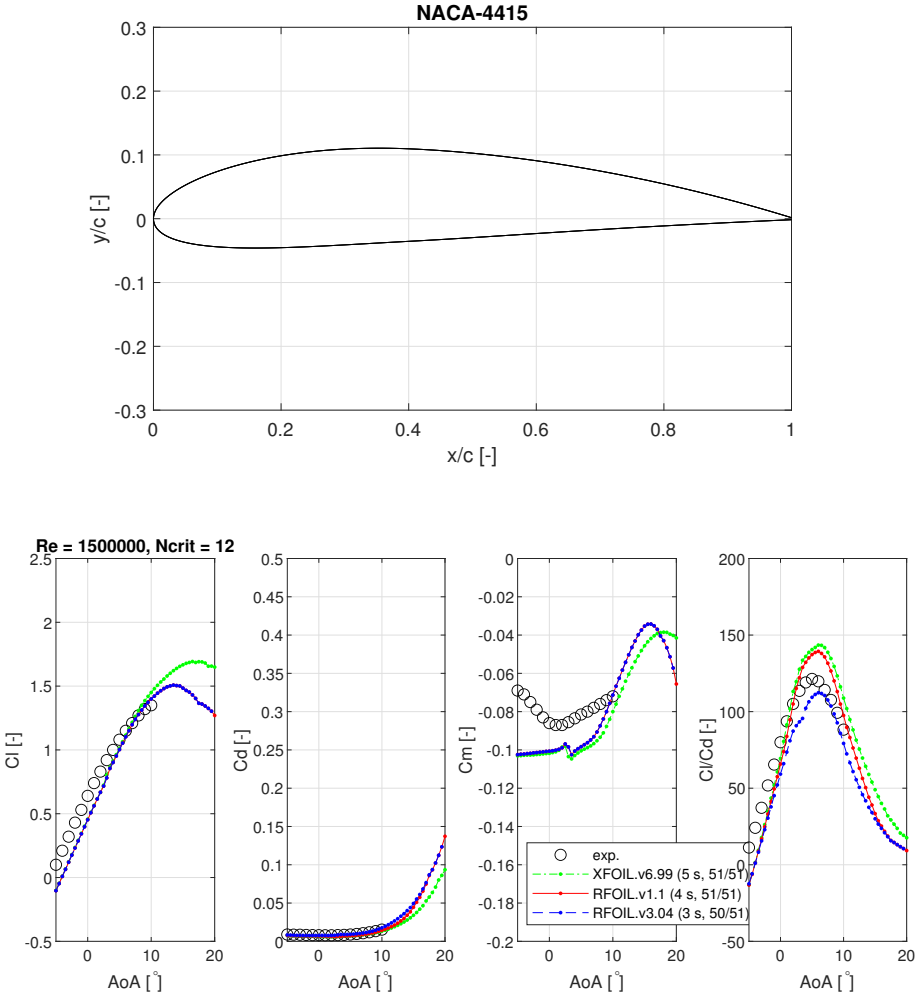

Figure B.272: Differences between experimental and numerical polars for the NACA-4415 airfoil at a Reynolds number of 1500000. Vertical black lines in the middle subplot indicate, from left to right, the angle of attack corresponding to the minimum drag coefficient, maximum lift to drag ratio and maximum lift coefficient, respectively.

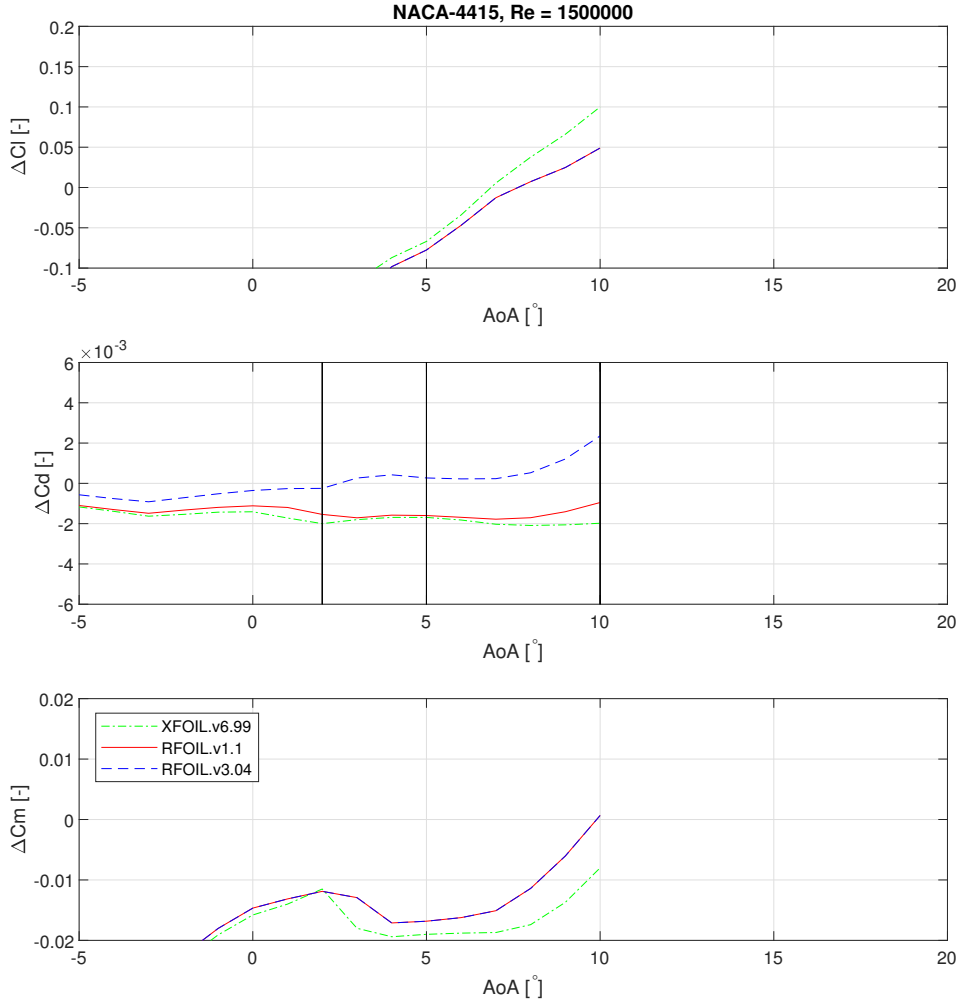

Figure B.273: Comparison between experimental and numerical pressure and skin friction distributions for the NACA-4415 airfoil at a Reynolds number of 1500000 and at the design angle of attack.

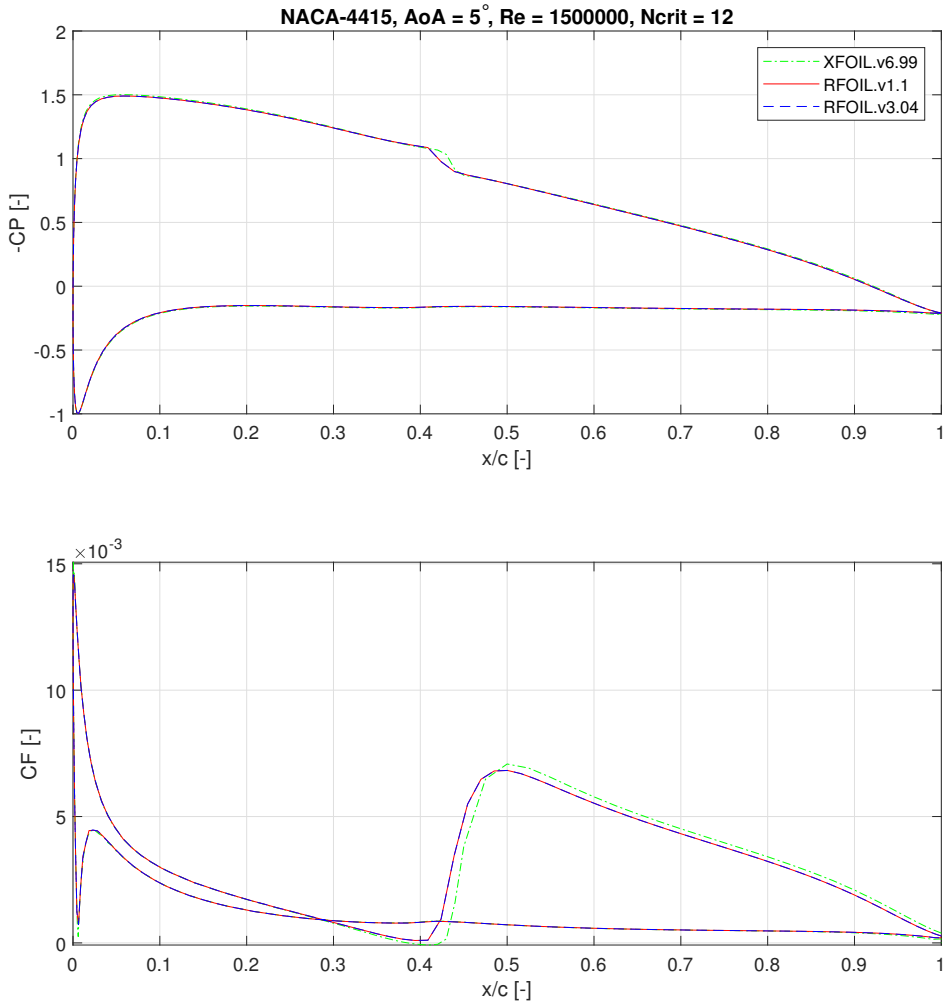

Figure B.274: Comparison between experimental and numerical polars for the NACA-4415 airfoil at a Reynolds number of 2000000. Simulation time to generate the polars by means the different codes and the number of converged polar points are depicted between parentheses.

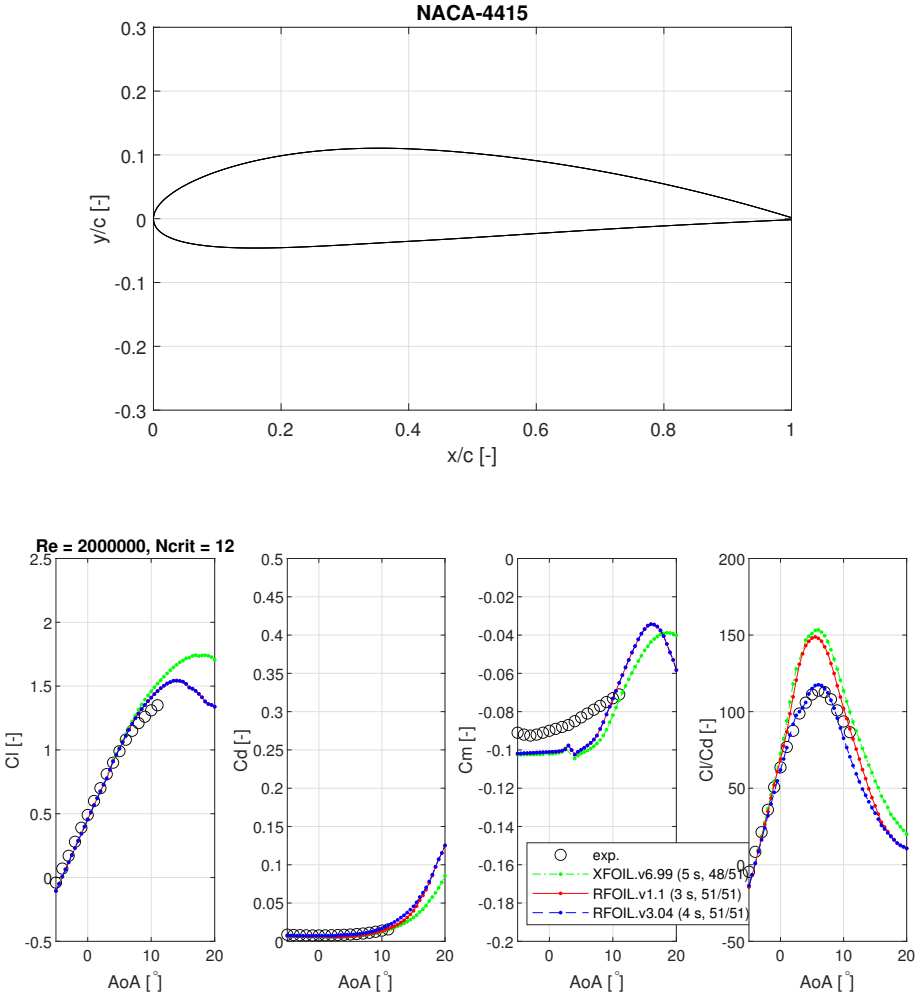

Figure B.275: Differences between experimental and numerical polars for the NACA-4415 airfoil at a Reynolds number of 2000000. Vertical black lines in the middle subplot indicate, from left to right, the angle of attack corresponding to the minimum drag coefficient, maximum lift to drag ratio and maximum lift coefficient, respectively.

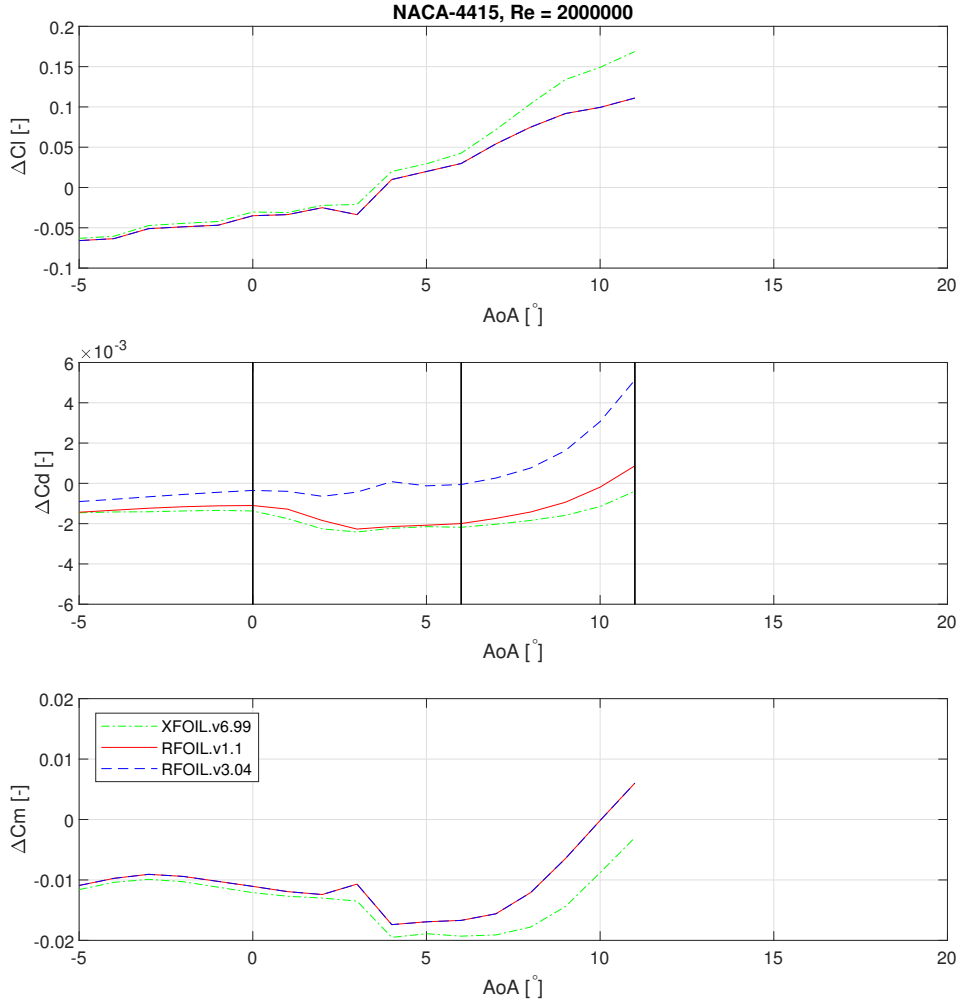

Figure B.276: Comparison between experimental and numerical pressure and skin friction distributions for the NACA-4415 airfoil at a Reynolds number of 2000000 and at the design angle of attack.

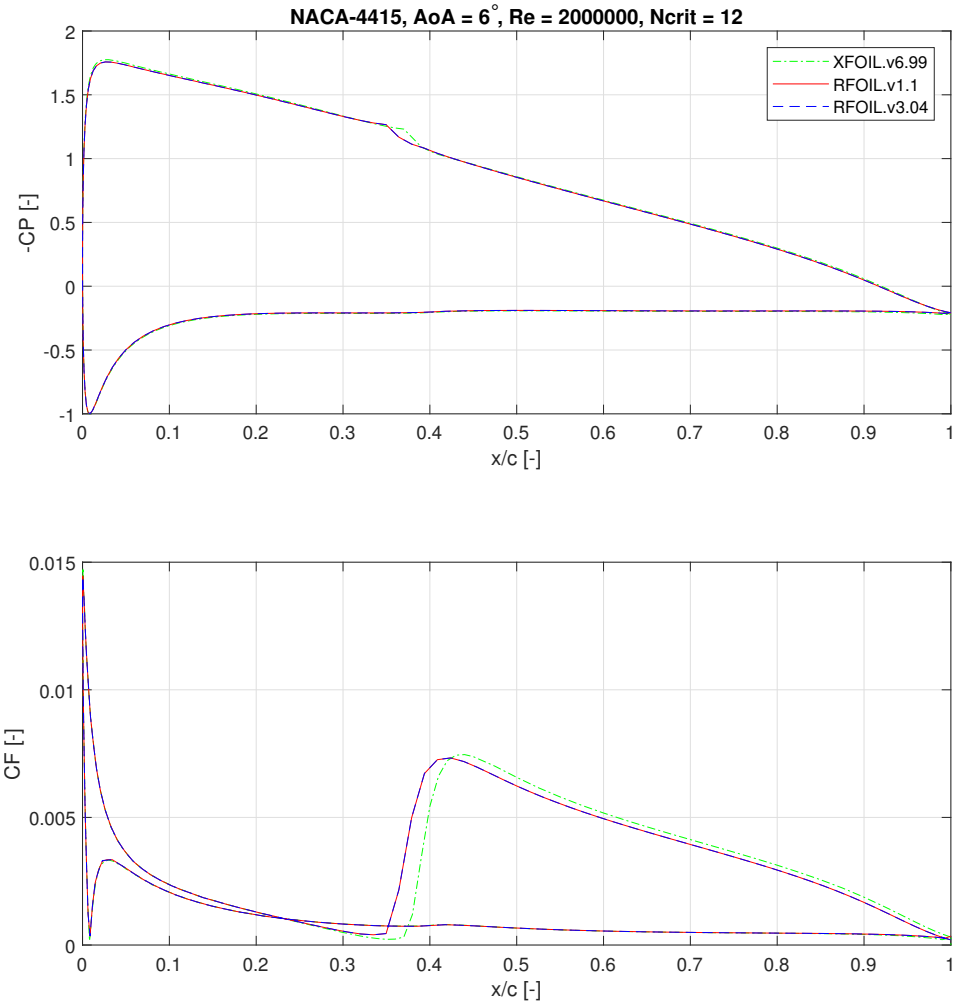

Figure B.277: Comparison between experimental and numerical polars for the NACA-4415 airfoil at a Reynolds number of 3000000. Simulation time to generate the polars by means the different codes and the number of converged polar points are depicted between parentheses.

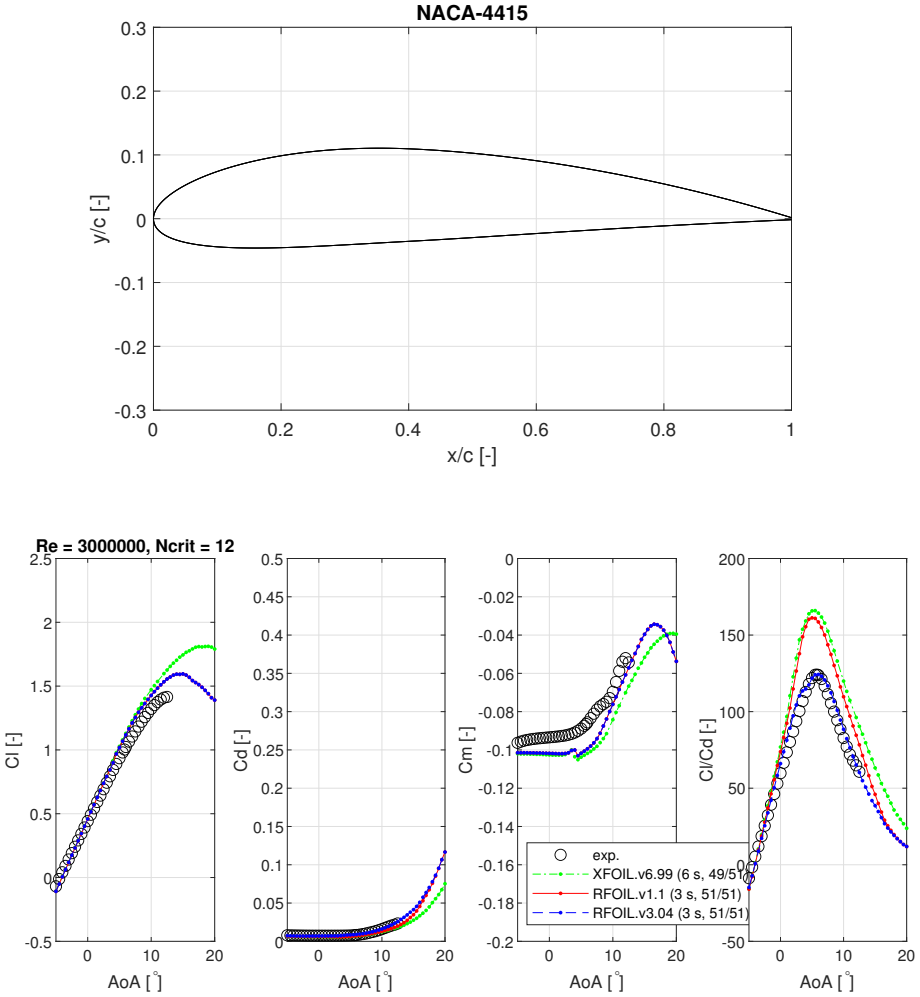

Figure B.278: Differences between experimental and numerical polars for the NACA-4415 airfoil at a Reynolds number of 3000000. Vertical black lines in the middle subplot indicate, from left to right, the angle of attack corresponding to the minimum drag coefficient, maximum lift to drag ratio and maximum lift coefficient, respectively.

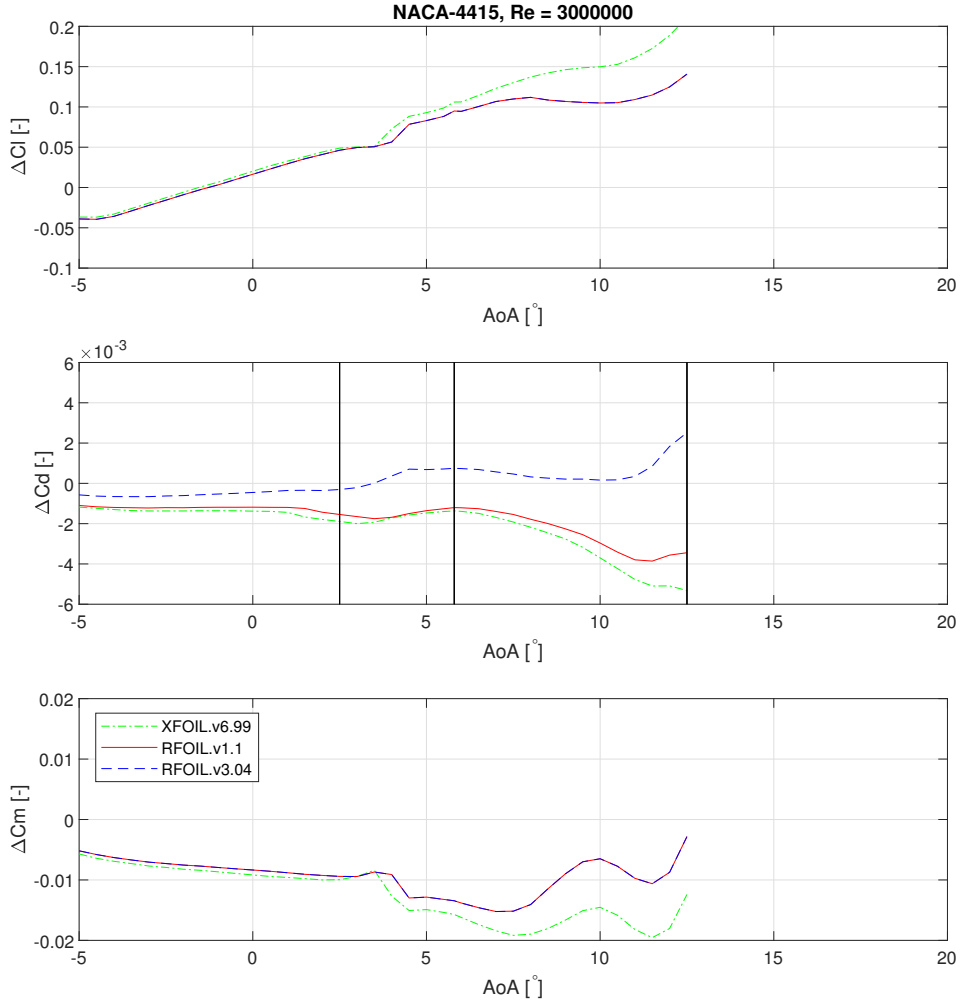

Figure B.279: Comparison between experimental and numerical pressure and skin friction distributions for the NACA-4415 airfoil at a Reynolds number of 3000000 and at the design angle of attack.

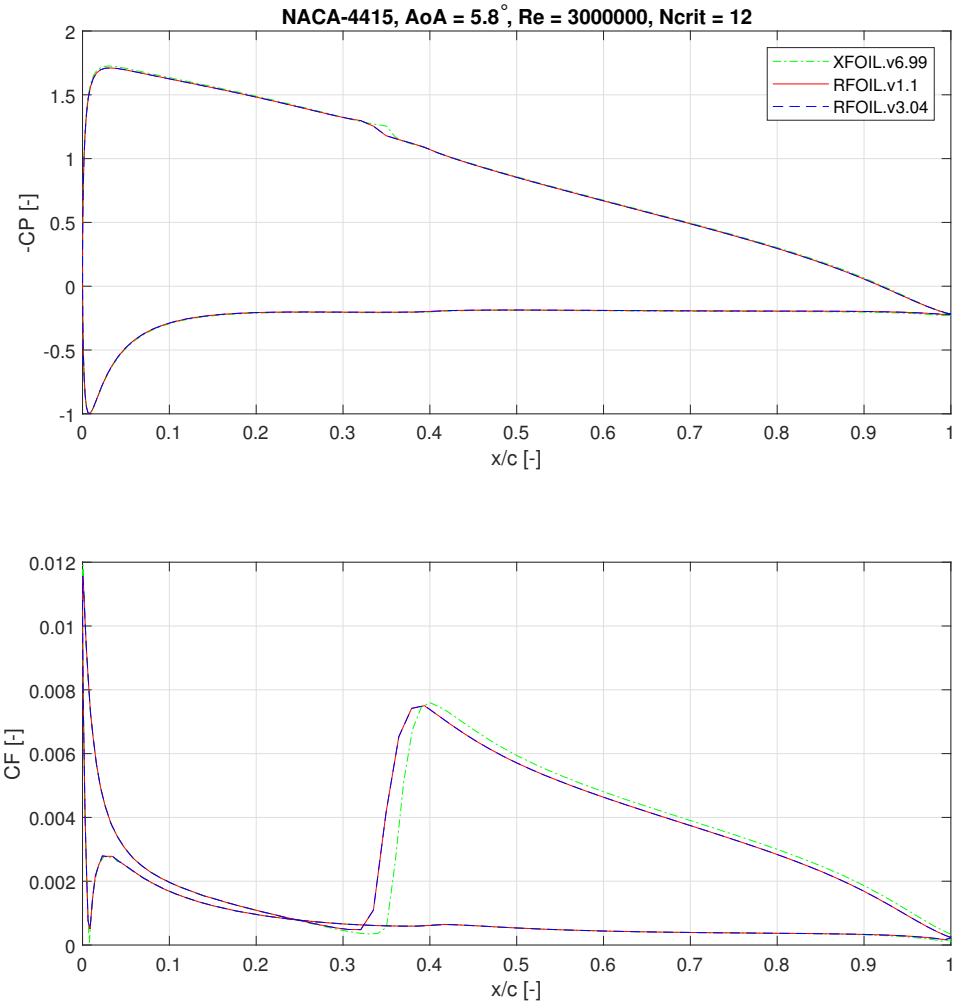

Figure B.280: Comparison between experimental and numerical polars for the NACA-4415 airfoil at a Reynolds number of 6000000. Simulation time to generate the polars by means the different codes and the number of converged polar points are depicted between parentheses.

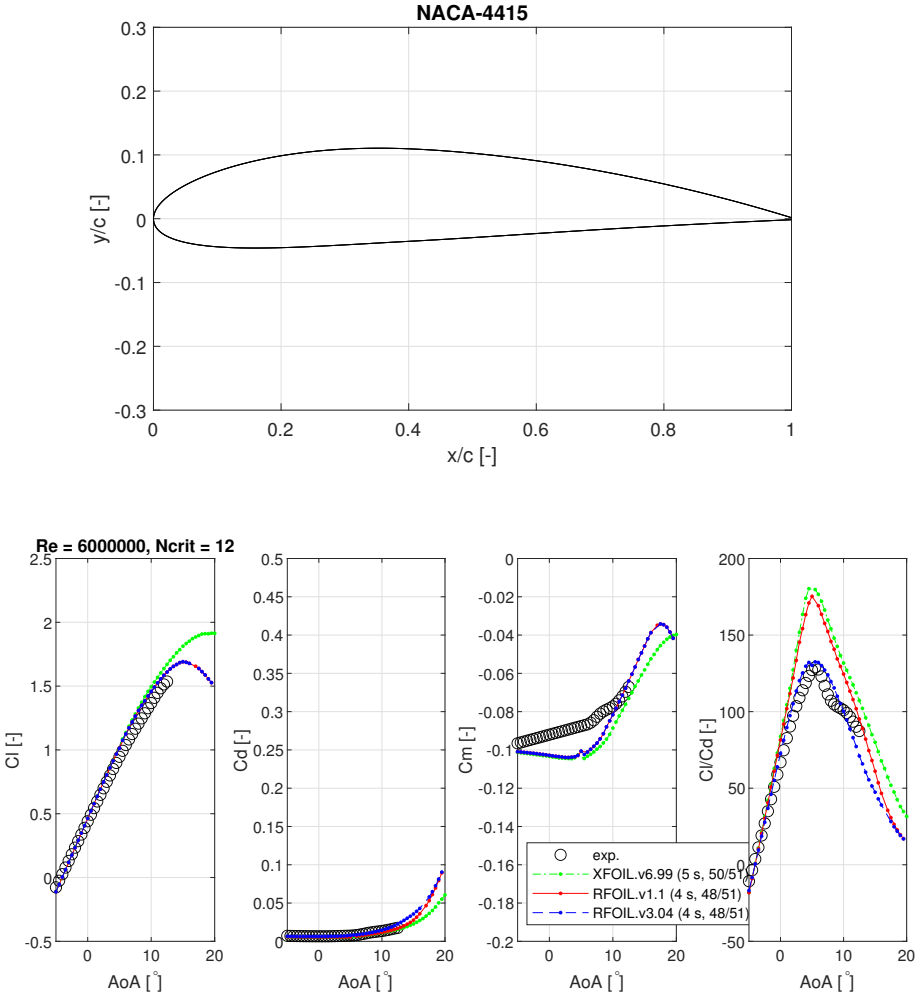

Figure B.281: Differences between experimental and numerical polars for the NACA-4415 airfoil at a Reynolds number of 6000000. Vertical black lines in the middle subplot indicate, from left to right, the angle of attack corresponding to the minimum drag coefficient, maximum lift to drag ratio and maximum lift coefficient, respectively.

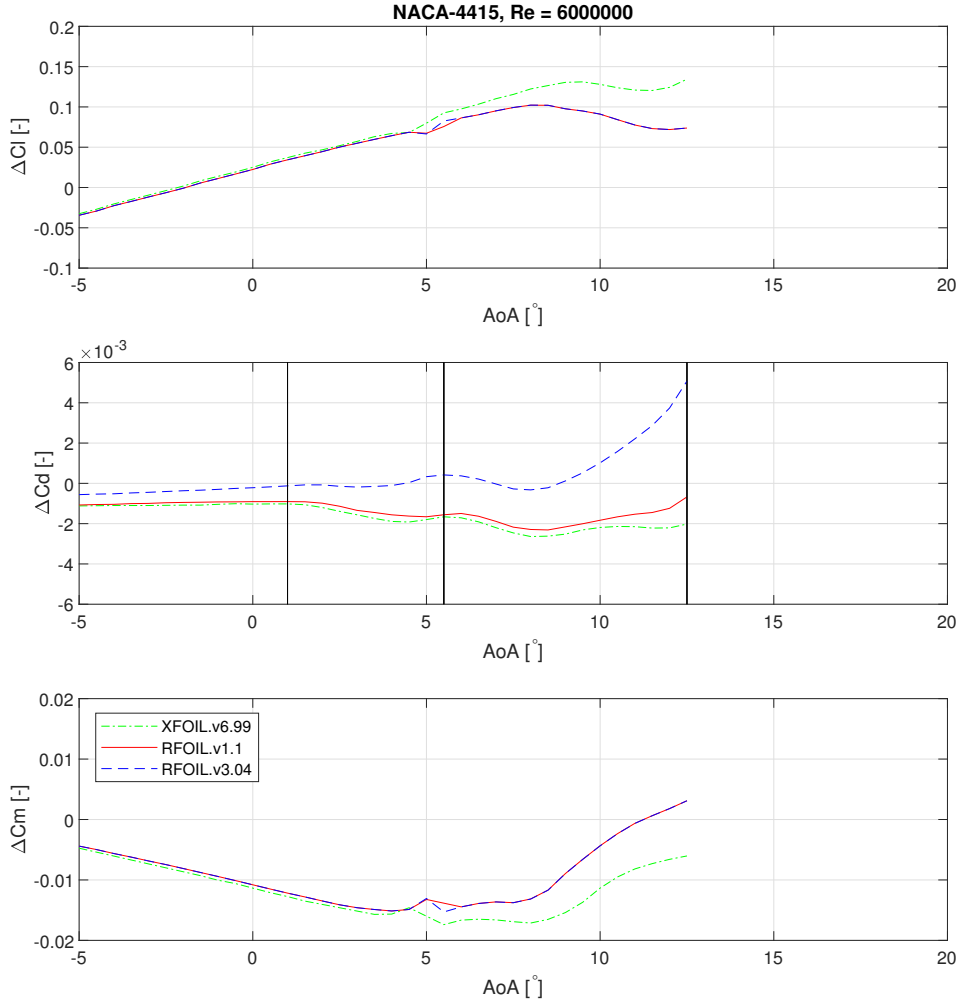

Figure B.282: Comparison between experimental and numerical pressure and skin friction distributions for the NACA-4415 airfoil at a Reynolds number of 6000000 and at the design angle of attack.

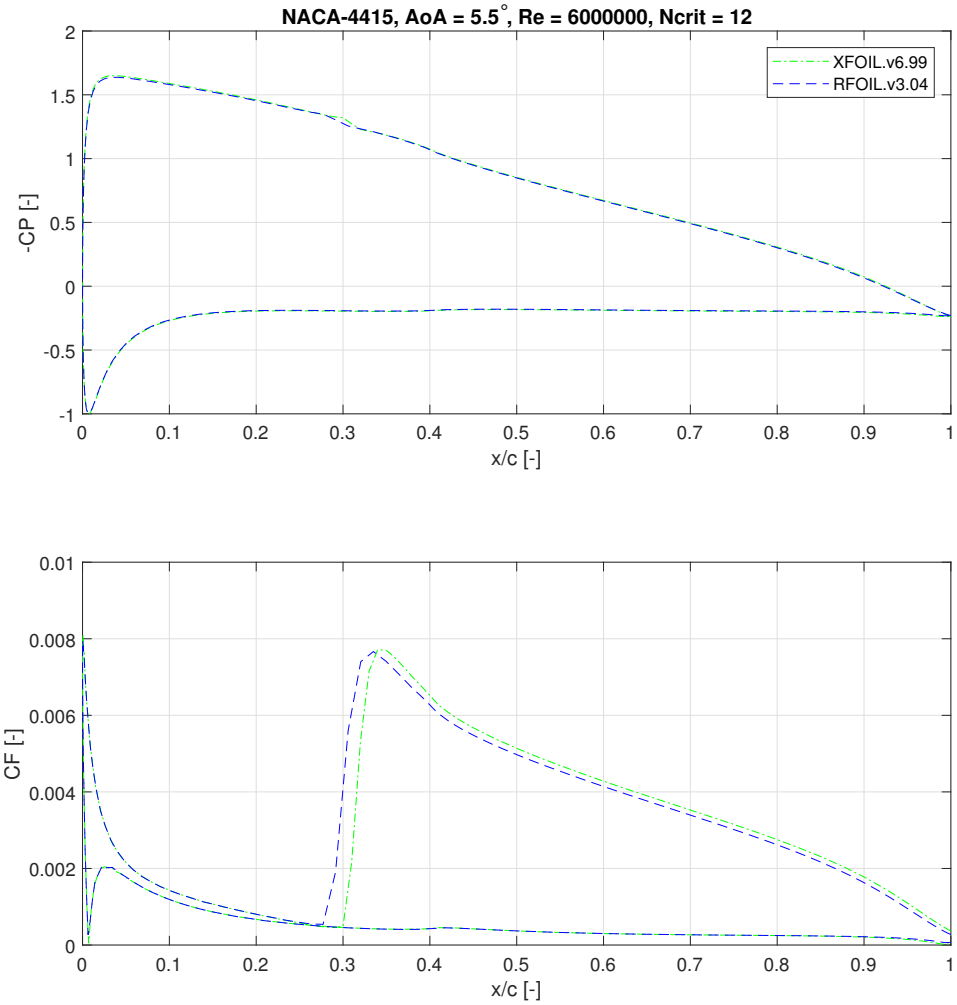

Figure B.283: Comparison between experimental and numerical polars for the NACA-4415 airfoil at a Reynolds number of 700000. Simulation time to generate the polars by means the different codes and the number of converged polar points are depicted between parentheses.

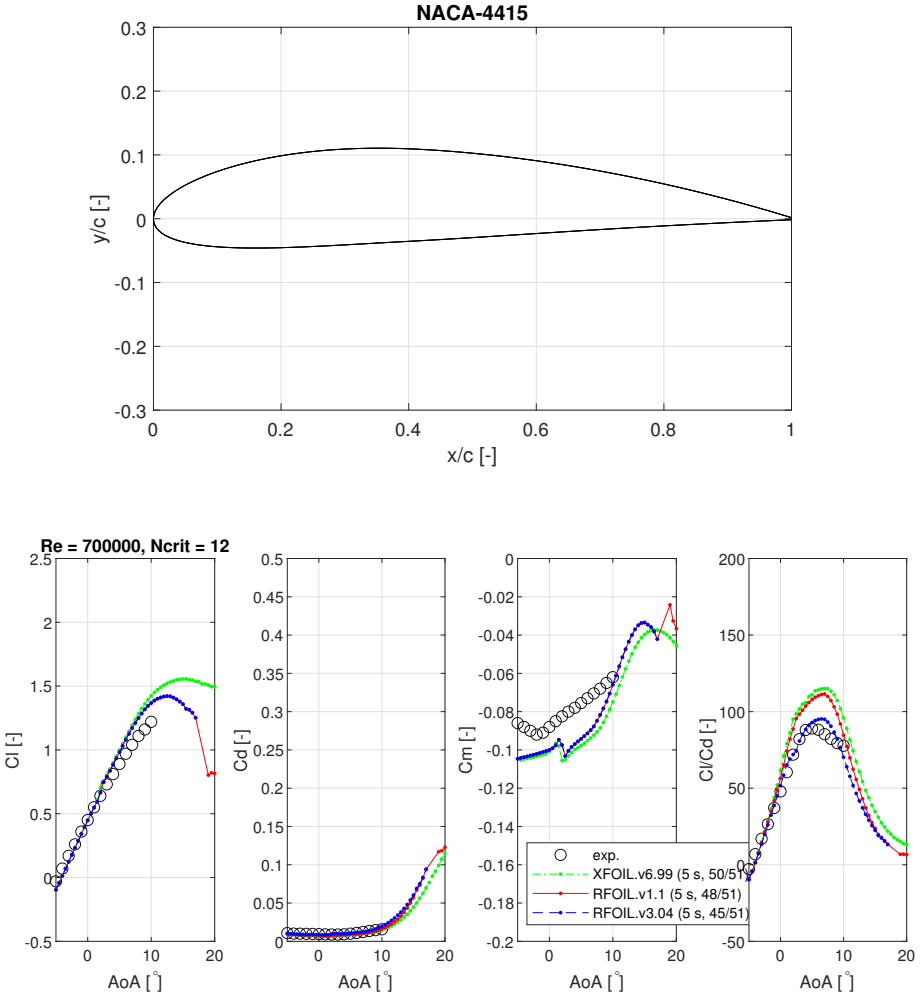

Figure B.284: Differences between experimental and numerical polars for the NACA-4415 airfoil at a Reynolds number of 700000. Vertical black lines in the middle subplot indicate, from left to right, the angle of attack corresponding to the minimum drag coefficient, maximum lift to drag ratio and maximum lift coefficient, respectively.

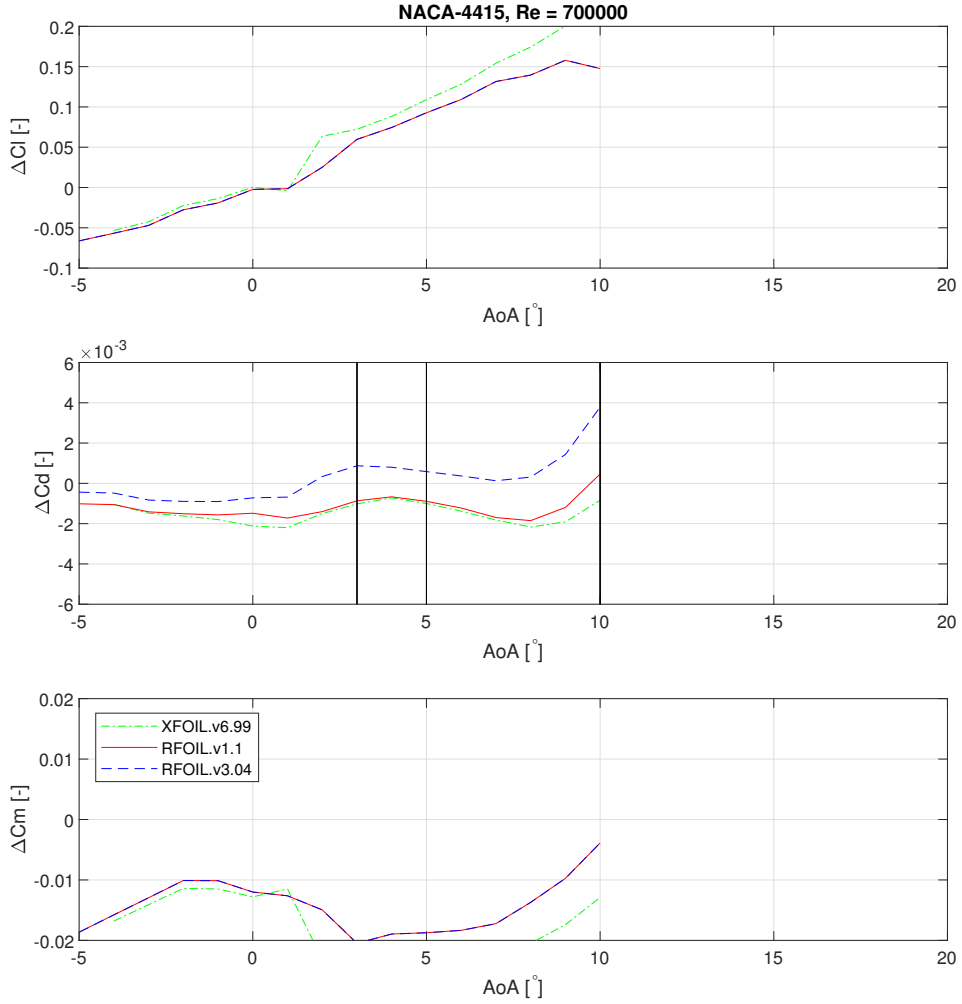

Figure B.285: Comparison between experimental and numerical pressure and skin friction distributions for the NACA-4415 airfoil at a Reynolds number of 700000 and at the design angle of attack.

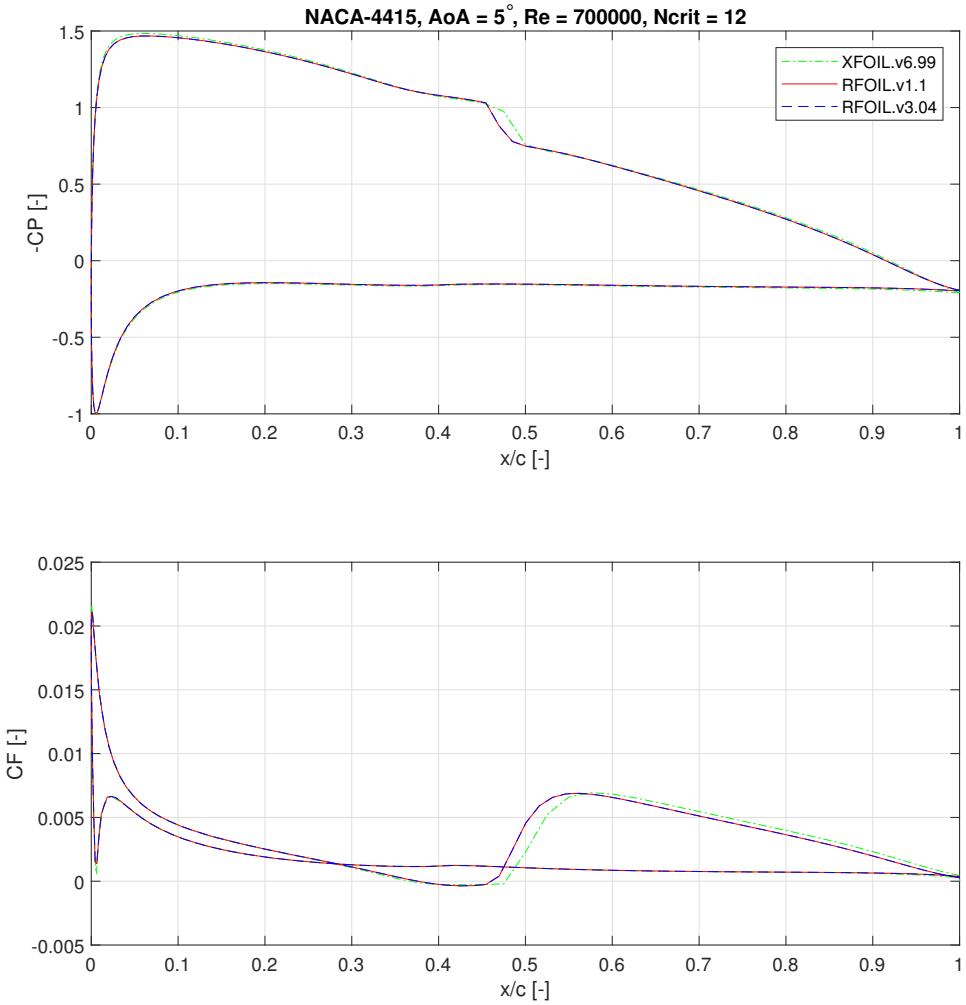

Figure B.286: Comparison between experimental and numerical polars for the NACA-4418 airfoil at a Reynolds number of 3000000. Simulation time to generate the polars by means the different codes and the number of converged polar points are depicted between parentheses.

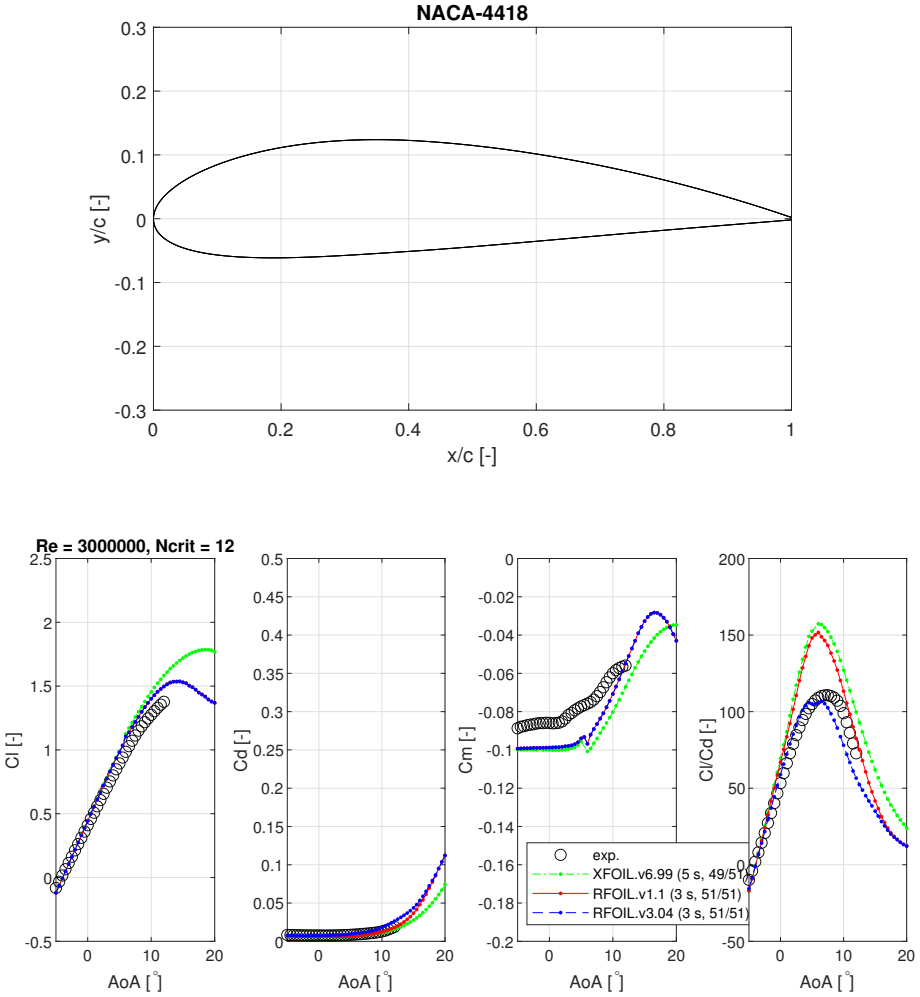

Figure B.287: Differences between experimental and numerical polars for the NACA-4418 airfoil at a Reynolds number of 3000000. Vertical black lines in the middle subplot indicate, from left to right, the angle of attack corresponding to the minimum drag coefficient, maximum lift to drag ratio and maximum lift coefficient, respectively.

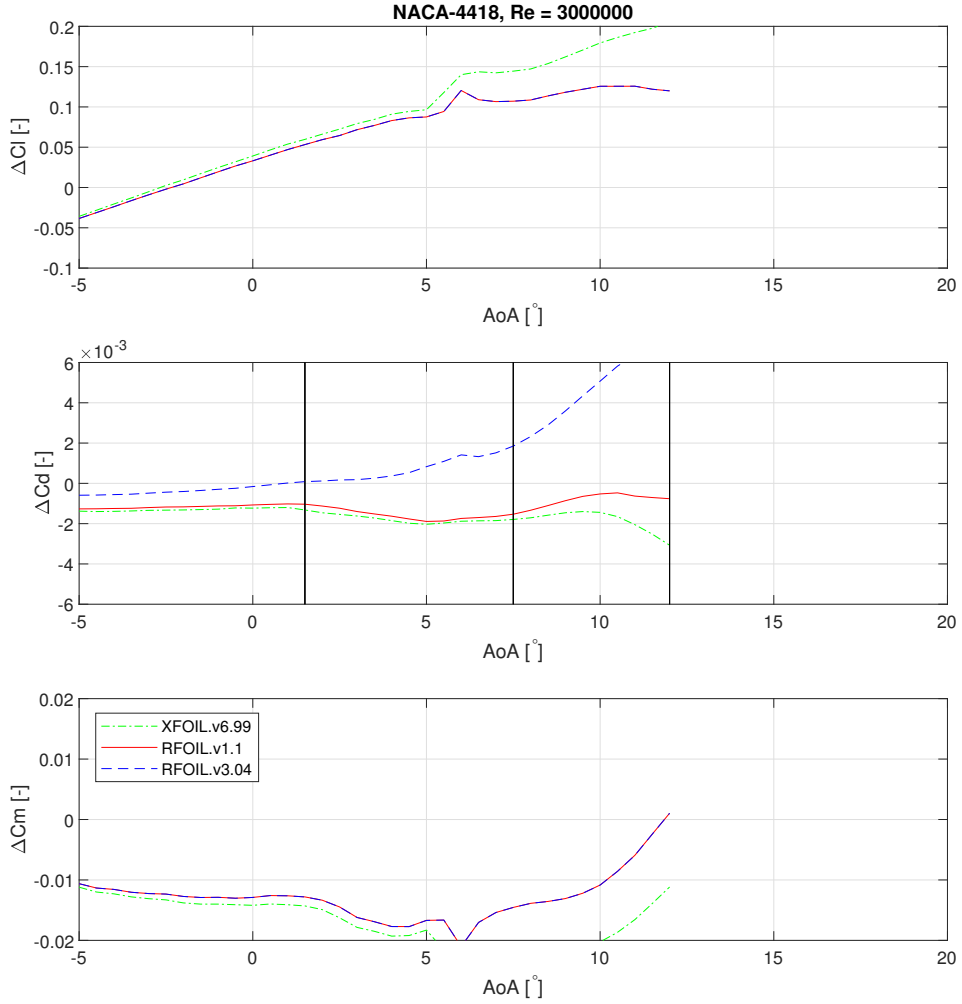

Figure B.288: Comparison between experimental and numerical pressure and skin friction distributions for the NACA-4418 airfoil at a Reynolds number of 3000000 and at the design angle of attack.

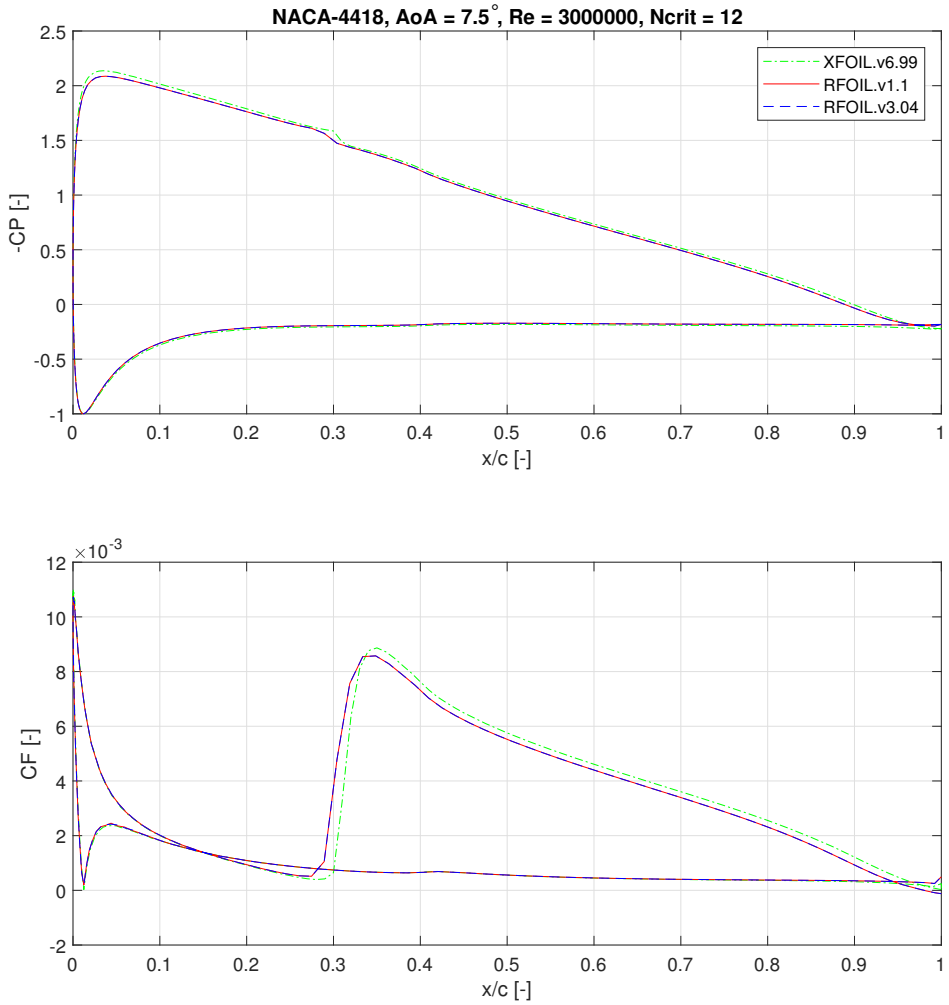

Figure B.289: Comparison between experimental and numerical polars for the NACA-4418 airfoil at a Reynolds number of 6000000. Simulation time to generate the polars by means the different codes and the number of converged polar points are depicted between parentheses.

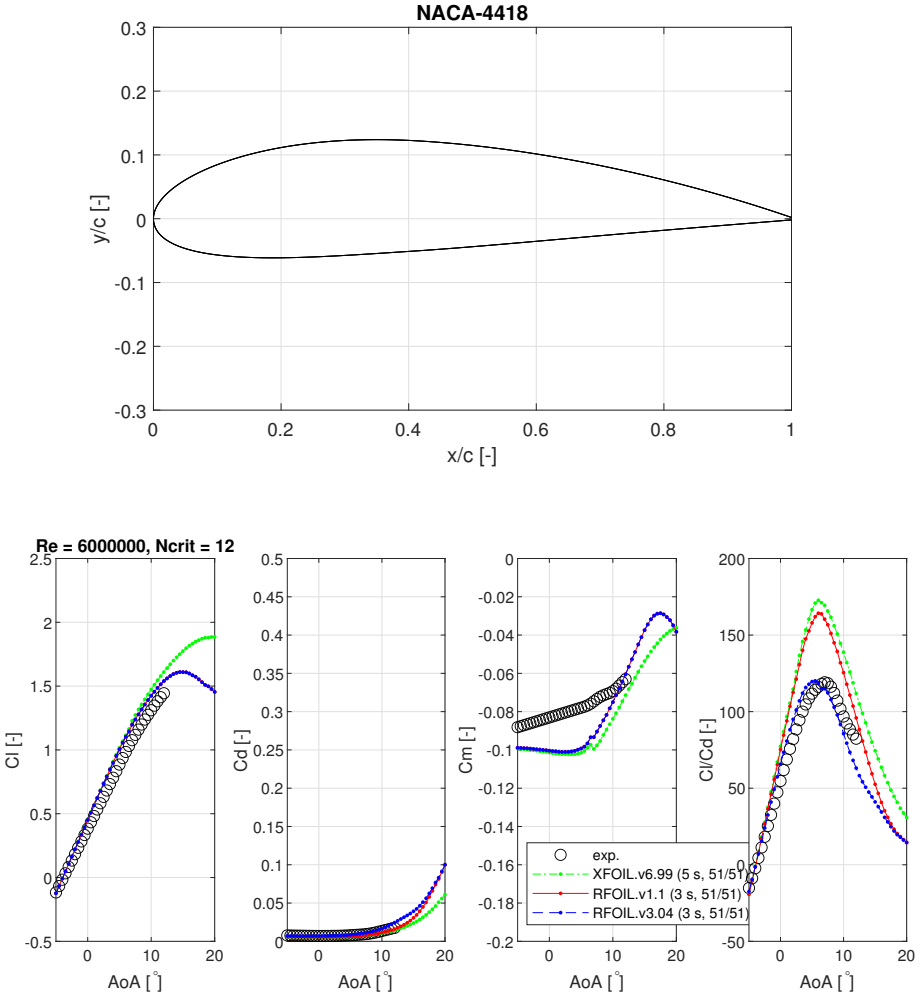

Figure B.290: Differences between experimental and numerical polars for the NACA-4418 airfoil at a Reynolds number of 6000000. Vertical black lines in the middle subplot indicate, from left to right, the angle of attack corresponding to the minimum drag coefficient, maximum lift to drag ratio and maximum lift coefficient, respectively.

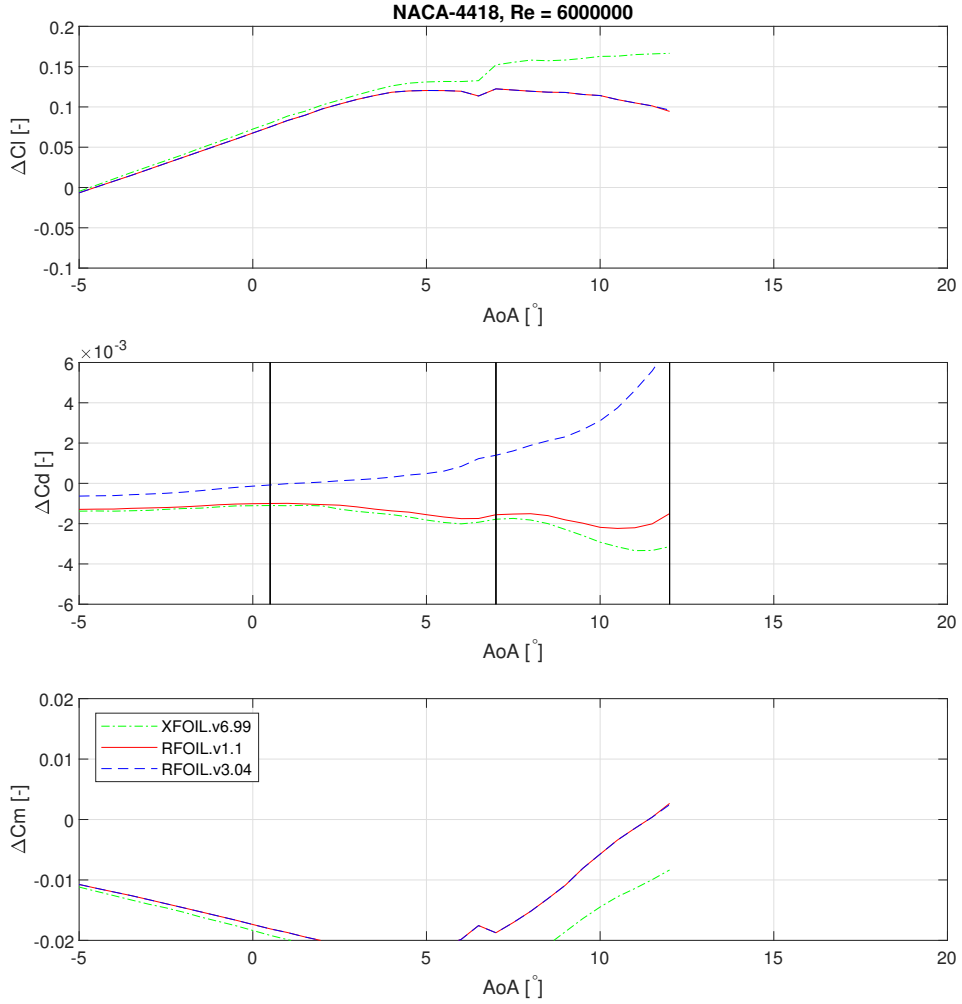

Figure B.291: Comparison between experimental and numerical pressure and skin friction distributions for the NACA-4418 airfoil at a Reynolds number of 6000000 and at the design angle of attack.

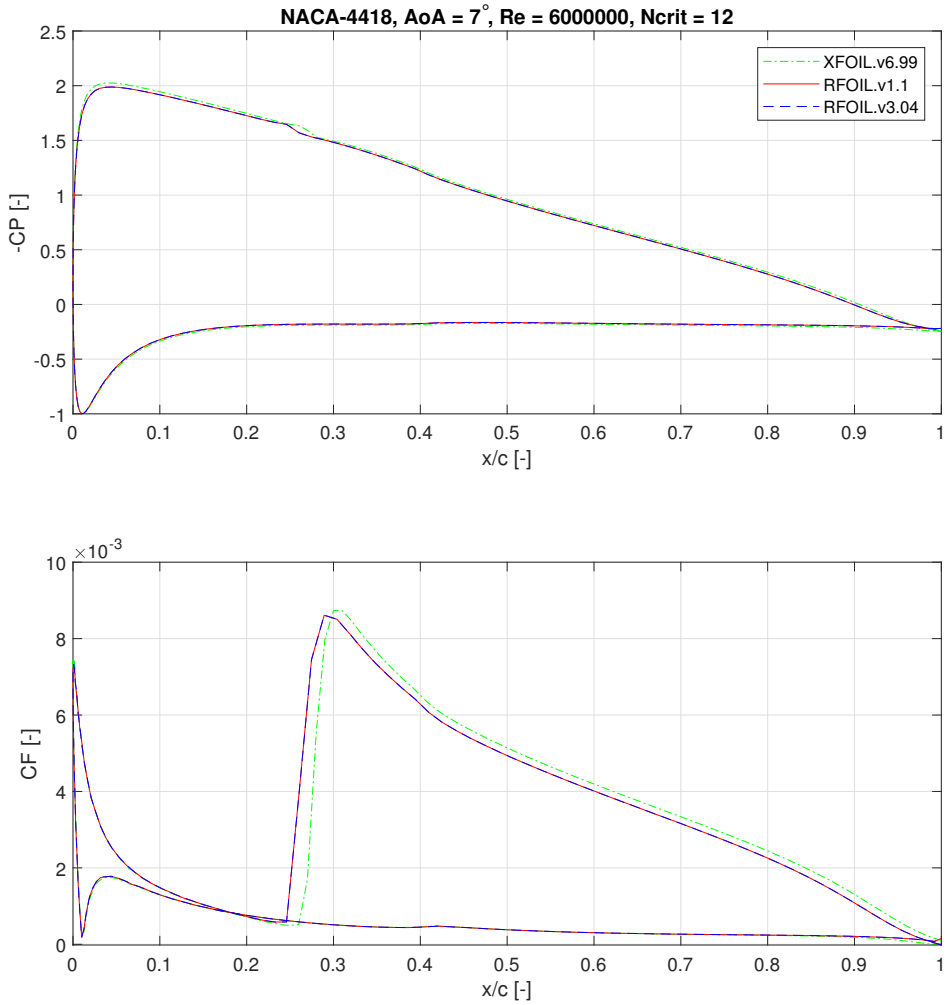

Figure B.292: Comparison between experimental and numerical polars for the NACA-4421 airfoil at a Reynolds number of 3000000. Simulation time to generate the polars by means the different codes and the number of converged polar points are depicted between parentheses.

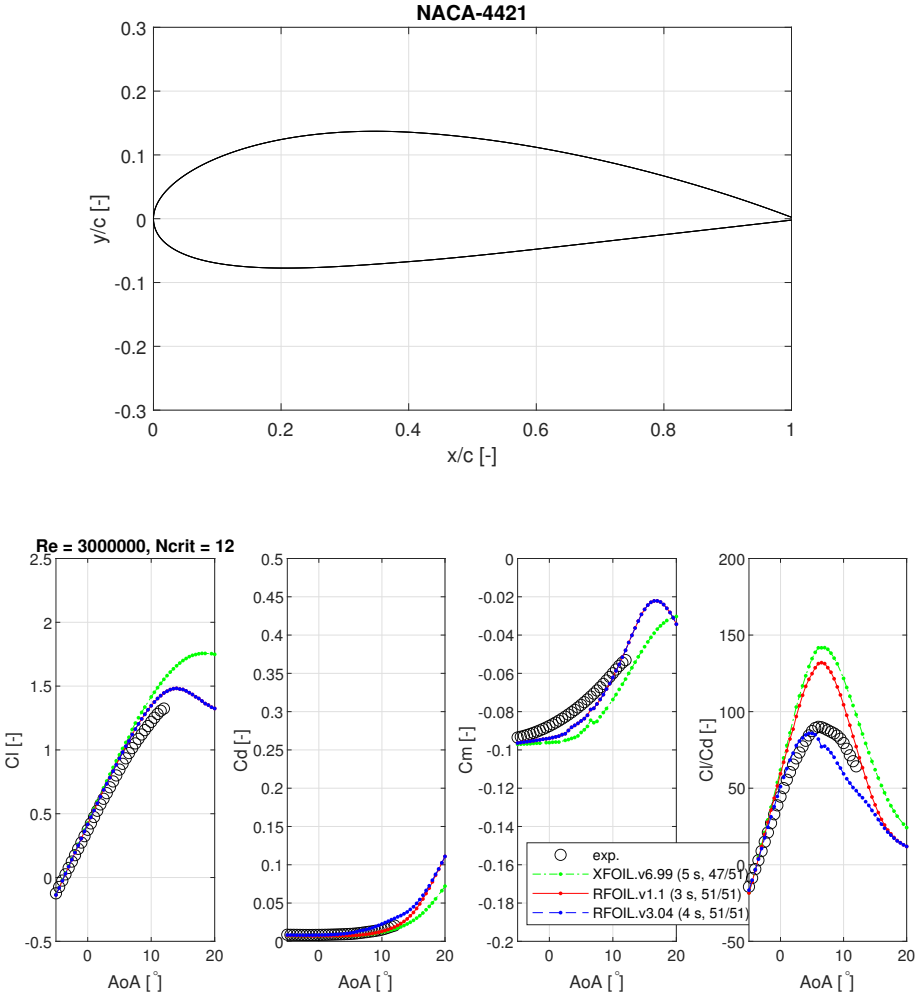

Figure B.293: Differences between experimental and numerical polars for the NACA-4421 airfoil at a Reynolds number of 3000000. Vertical black lines in the middle subplot indicate, from left to right, the angle of attack corresponding to the minimum drag coefficient, maximum lift to drag ratio and maximum lift coefficient, respectively.

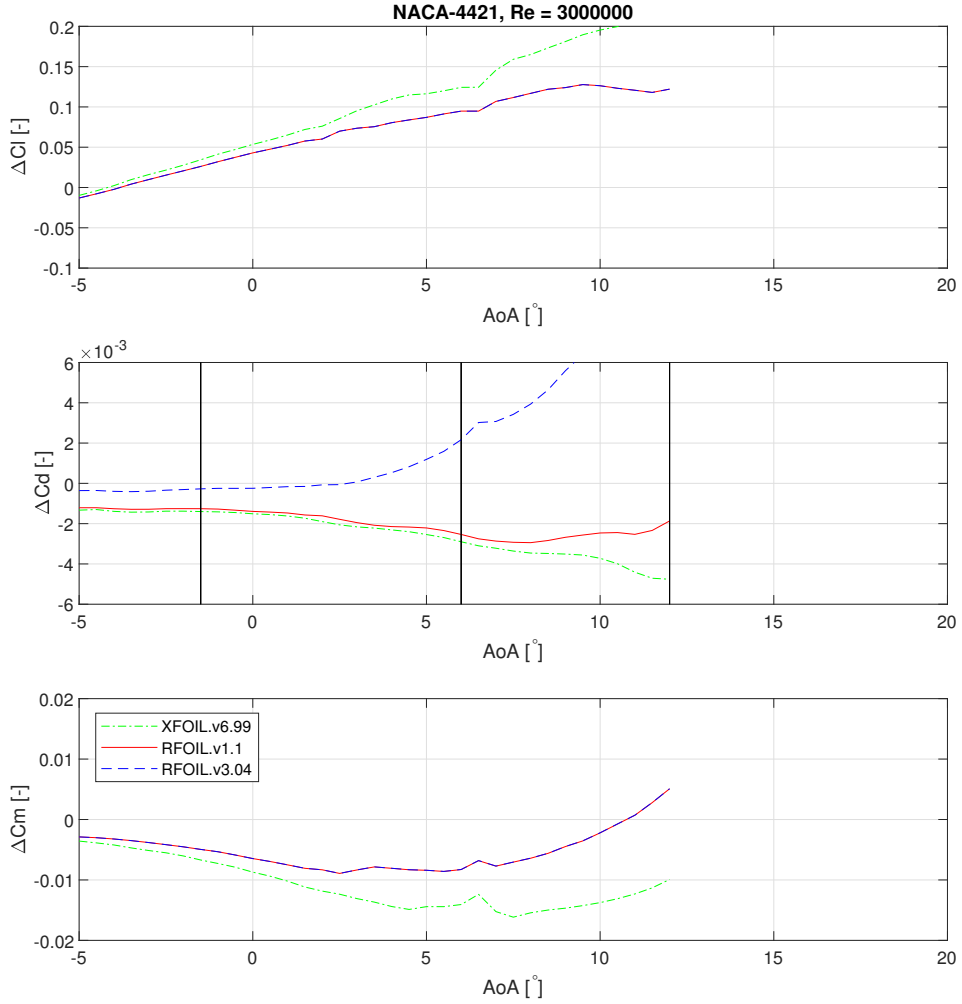

Figure B.294: Comparison between experimental and numerical pressure and skin friction distributions for the NACA-4421 airfoil at a Reynolds number of 3000000 and at the design angle of attack.

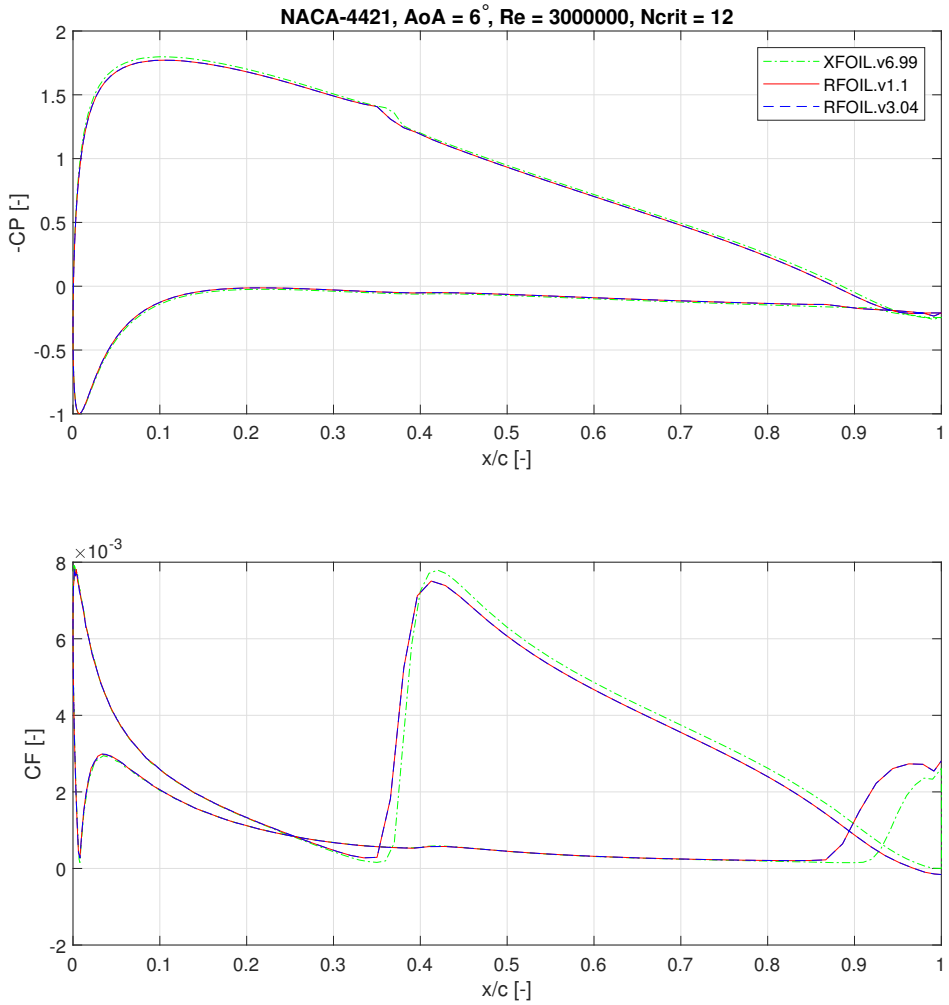

Figure B.295: Comparison between experimental and numerical polars for the NACA-4421 airfoil at a Reynolds number of 6000000. Simulation time to generate the polars by means the different codes and the number of converged polar points are depicted between parentheses.

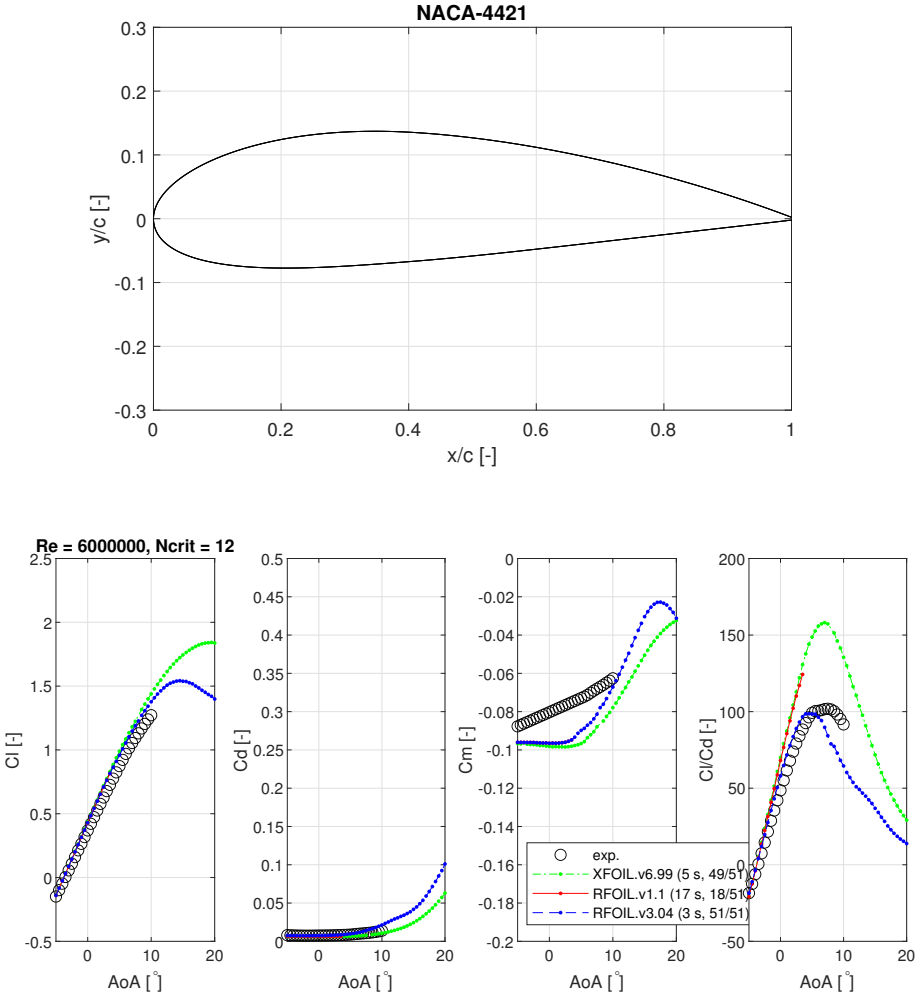

Figure B.296: Differences between experimental and numerical polars for the NACA-4421 airfoil at a Reynolds number of 6000000. Vertical black lines in the middle subplot indicate, from left to right, the angle of attack corresponding to the minimum drag coefficient, maximum lift to drag ratio and maximum lift coefficient, respectively.

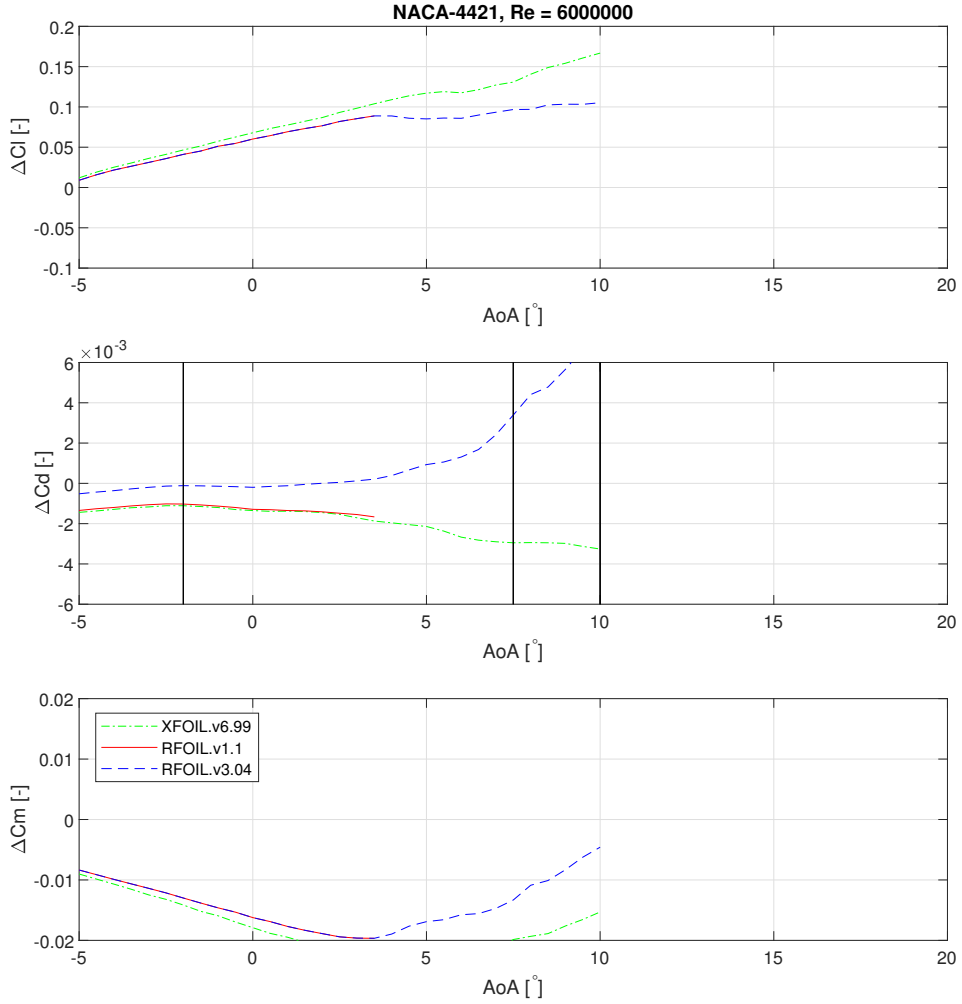

Figure B.297: Comparison between experimental and numerical pressure and skin friction distributions for the NACA-4421 airfoil at a Reynolds number of 6000000 and at the design angle of attack.

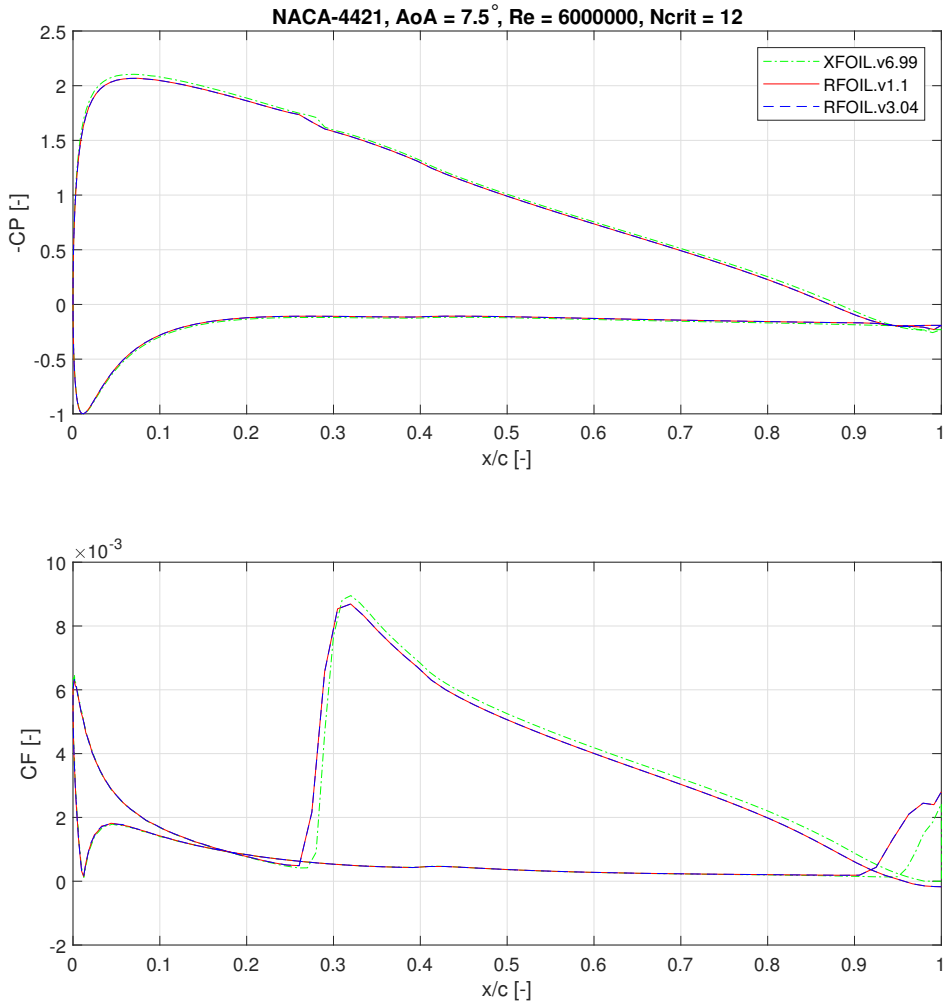

Figure B.298: Comparison between experimental and numerical polars for the NACA-4424 airfoil at a Reynolds number of 3000000. Simulation time to generate the polars by means the different codes and the number of converged polar points are depicted between parentheses.

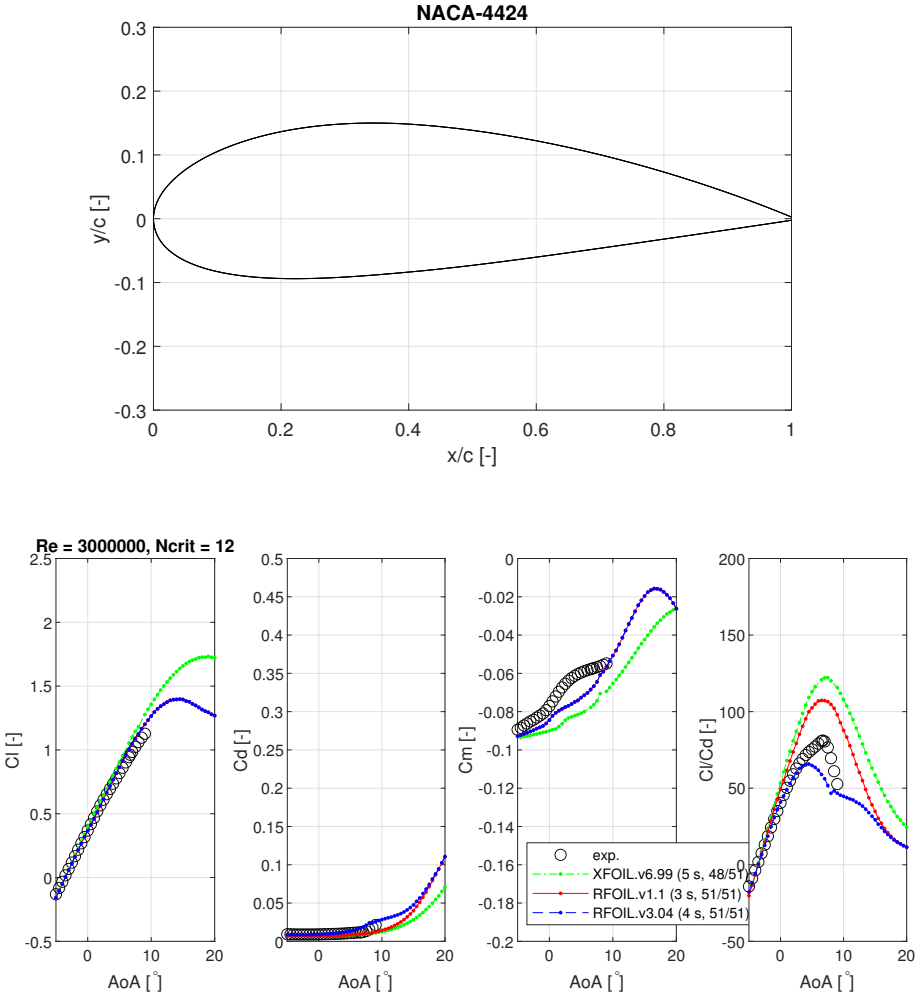

Figure B.299: Differences between experimental and numerical polars for the NACA-4424 airfoil at a Reynolds number of 3000000. Vertical black lines in the middle subplot indicate, from left to right, the angle of attack corresponding to the minimum drag coefficient, maximum lift to drag ratio and maximum lift coefficient, respectively.

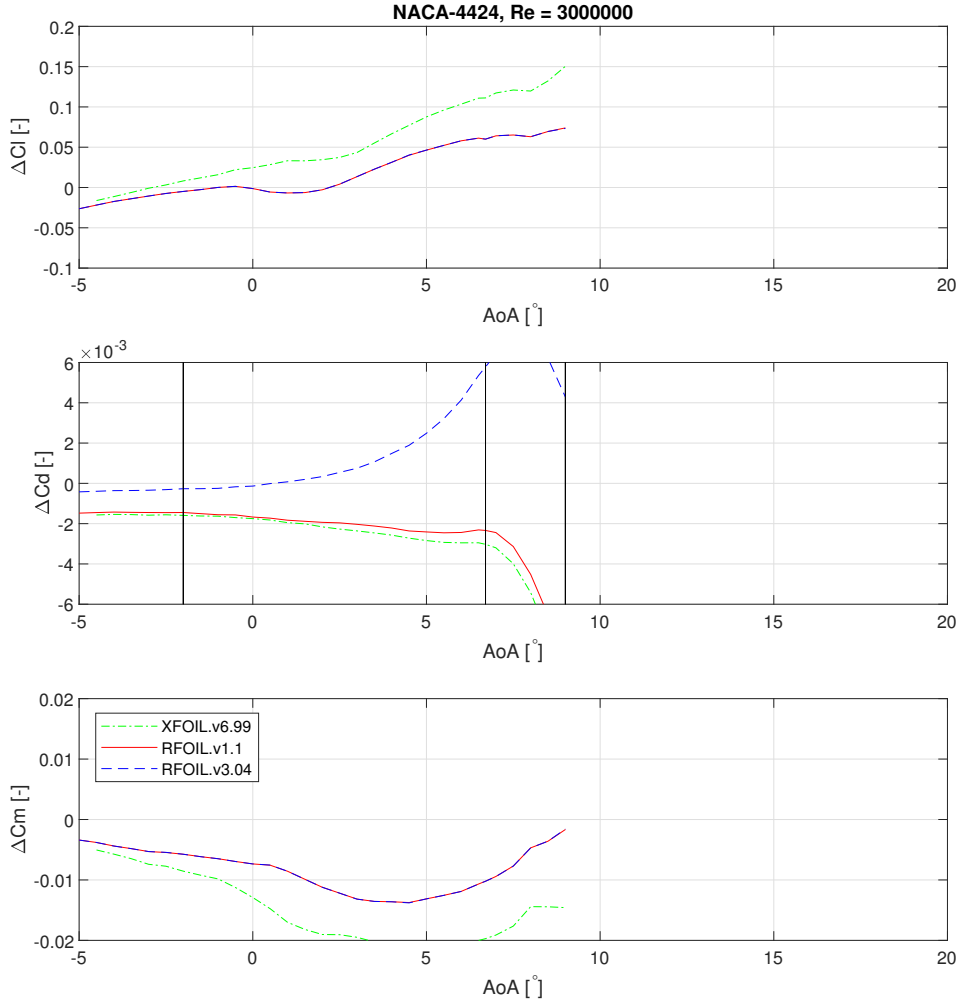

Figure B.300: Comparison between experimental and numerical pressure and skin friction distributions for the NACA-4424 airfoil at a Reynolds number of 3000000 and at the design angle of attack.

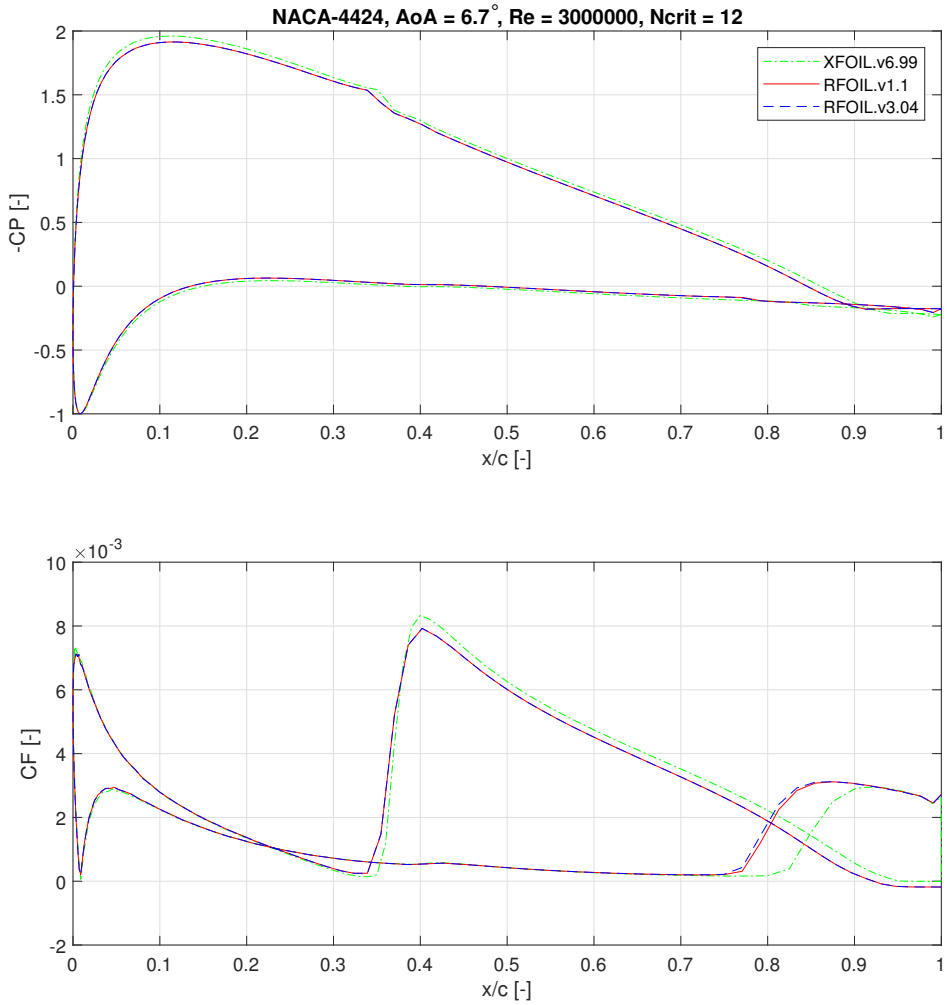

Figure B.301: Comparison between experimental and numerical polars for the NACA-4424 airfoil at a Reynolds number of 6000000. Simulation time to generate the polars by means the different codes and the number of converged polar points are depicted between parentheses.

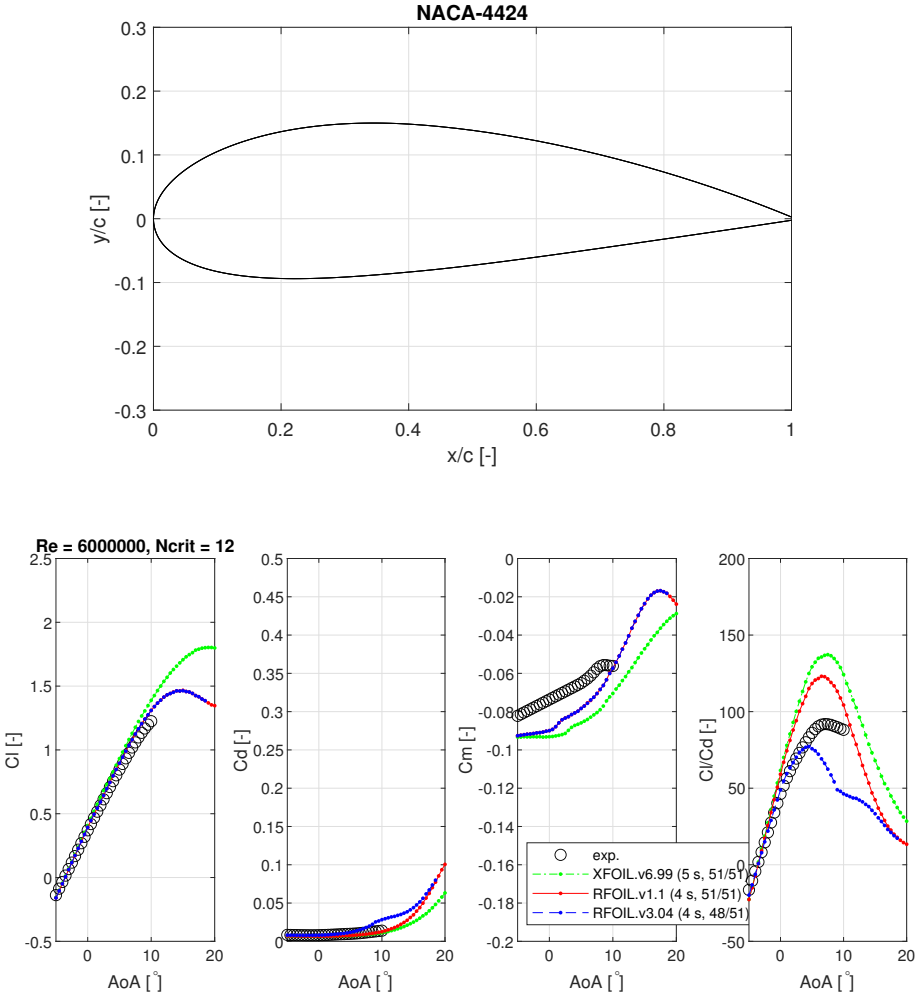

Figure B.302: Differences between experimental and numerical polars for the NACA-4424 airfoil at a Reynolds number of 6000000. Vertical black lines in the middle subplot indicate, from left to right, the angle of attack corresponding to the minimum drag coefficient, maximum lift to drag ratio and maximum lift coefficient, respectively.

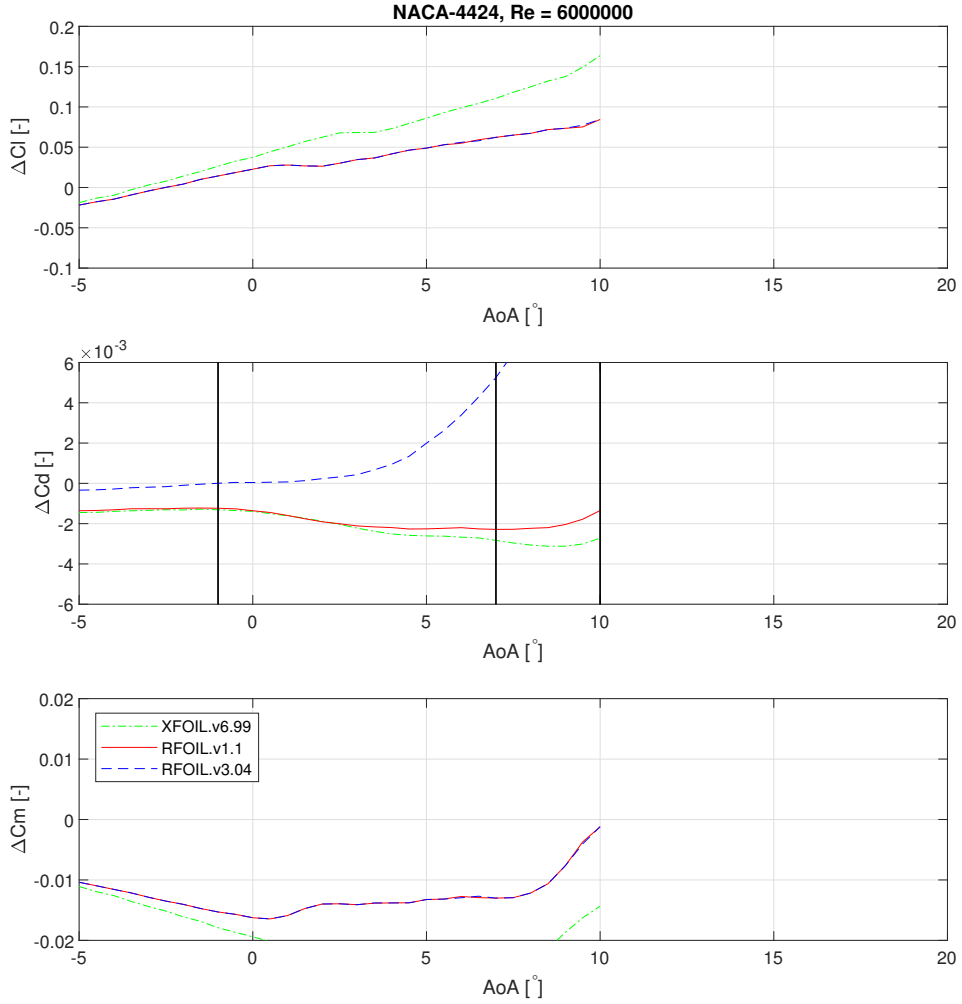

Figure B.303: Comparison between experimental and numerical pressure and skin friction distributions for the NACA-4424 airfoil at a Reynolds number of 6000000 and at the design angle of attack.

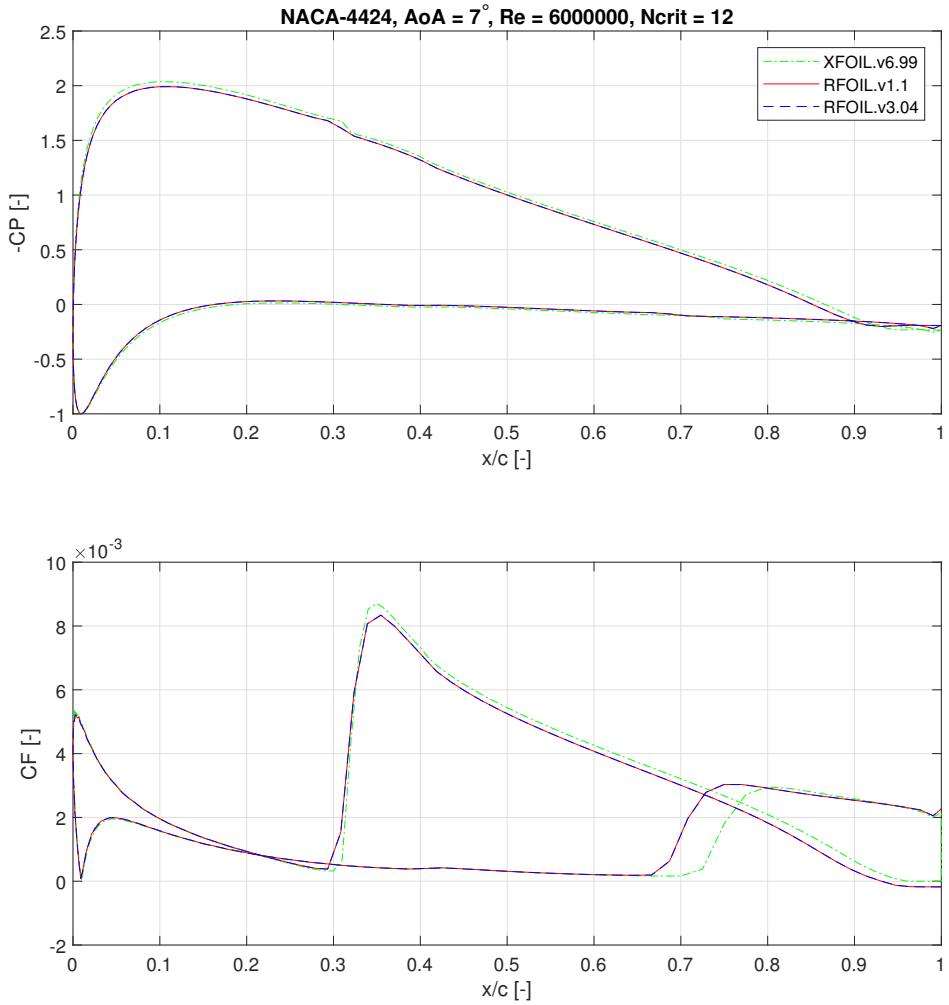

Figure B.304: Comparison between experimental and numerical polars for the NACA-63212 airfoil at a Reynolds number of 3000000. Simulation time to generate the polars by means the different codes and the number of converged polar points are depicted between parentheses.

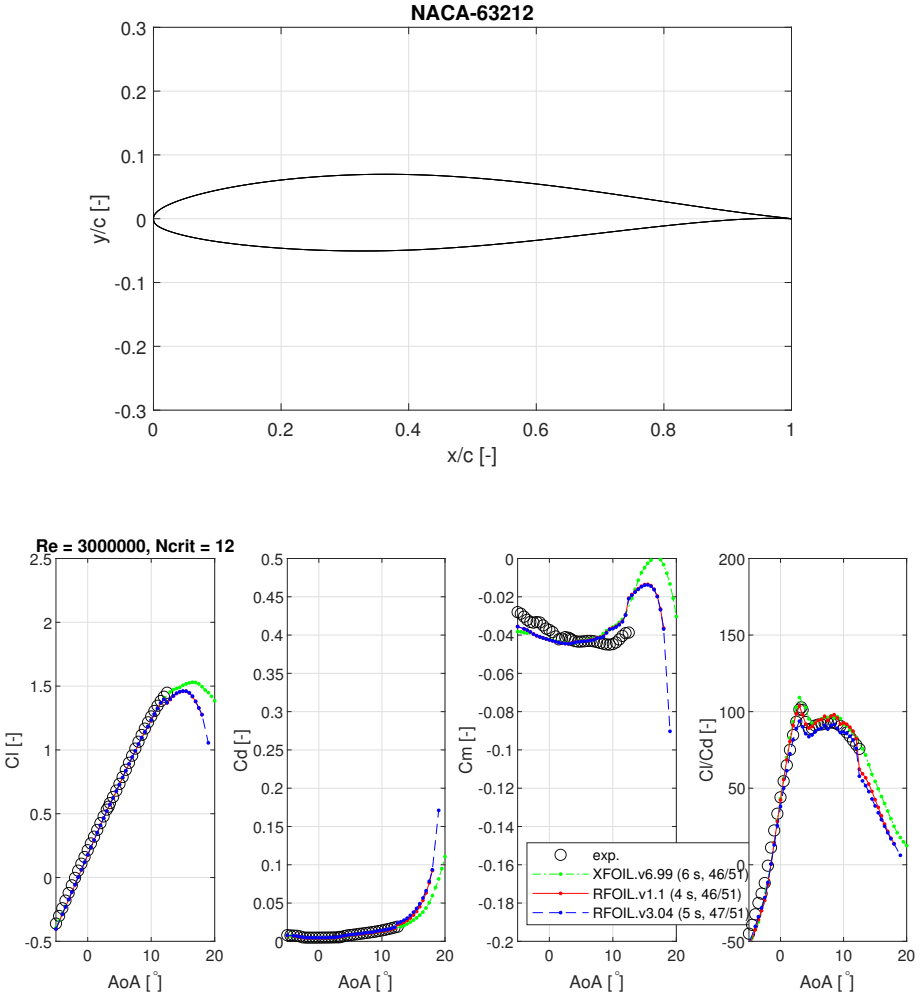

Figure B.305: Differences between experimental and numerical polars for the NACA-63212 airfoil at a Reynolds number of 3000000. Vertical black lines in the middle subplot indicate, from left to right, the angle of attack corresponding to the minimum drag coefficient, maximum lift to drag ratio and maximum lift coefficient, respectively.

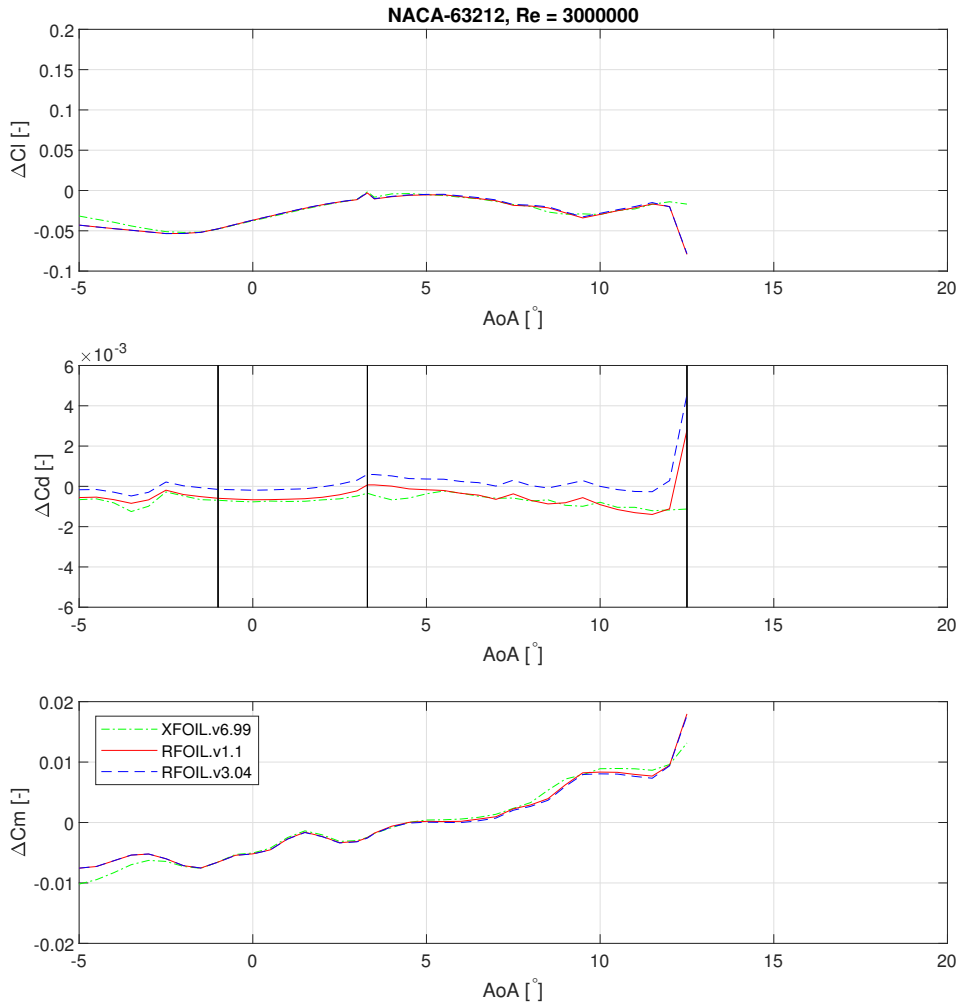

Figure B.306: Comparison between experimental and numerical pressure and skin friction distributions for the NACA-63212 airfoil at a Reynolds number of 3000000 and at the design angle of attack.

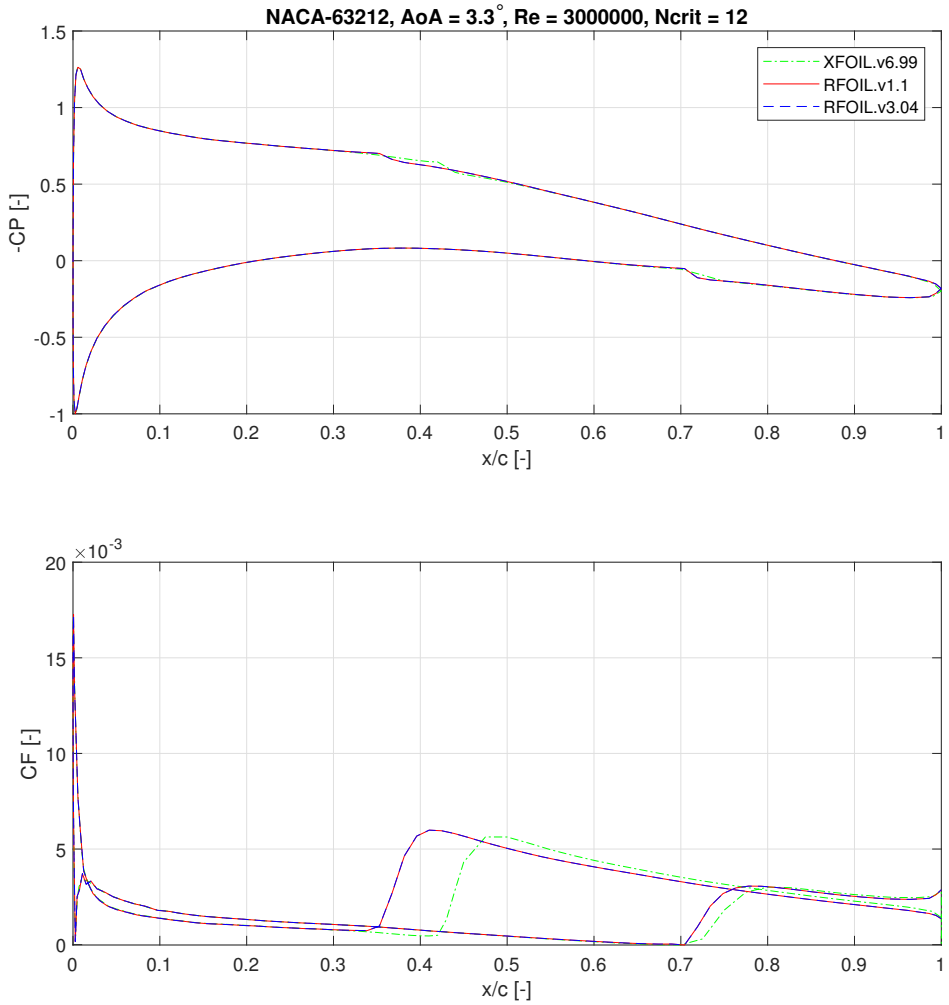

Figure B.307: Comparison between experimental and numerical polars for the NACA-63212 airfoil at a Reynolds number of 6000000. Simulation time to generate the polars by means the different codes and the number of converged polar points are depicted between parentheses.

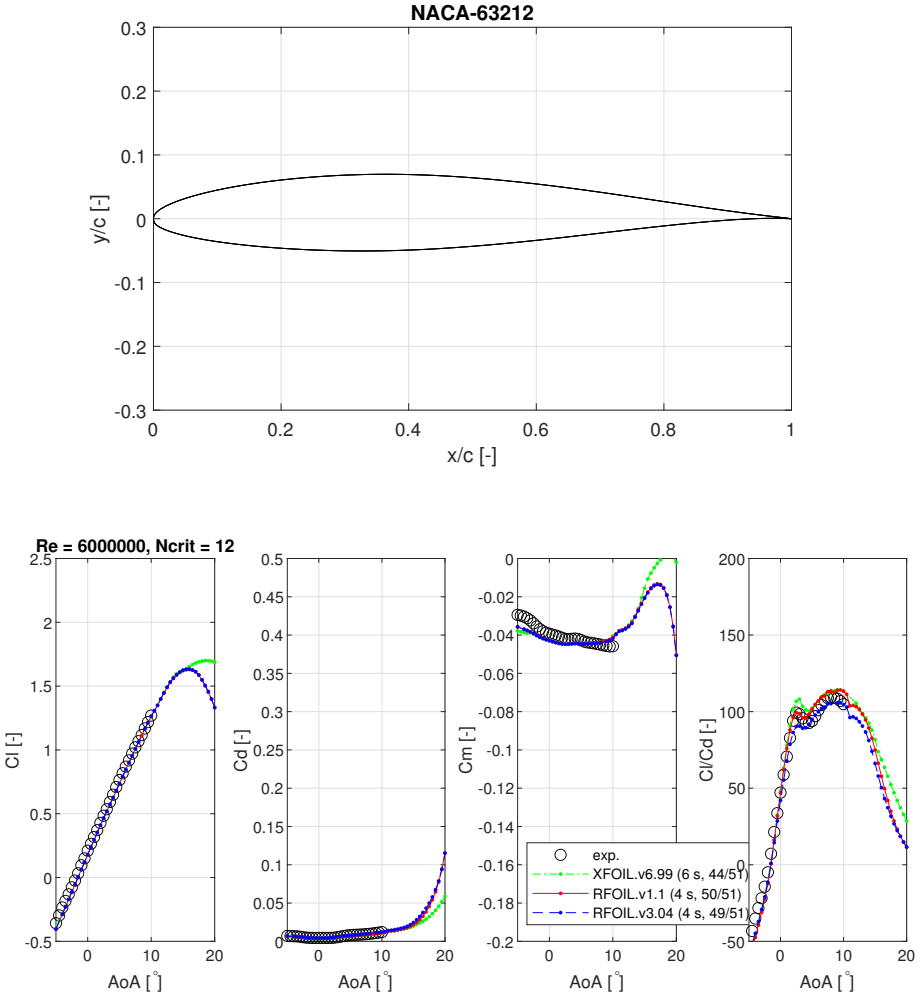

Figure B.308: Differences between experimental and numerical polars for the NACA-63212 airfoil at a Reynolds number of 6000000. Vertical black lines in the middle subplot indicate, from left to right, the angle of attack corresponding to the minimum drag coefficient, maximum lift to drag ratio and maximum lift coefficient, respectively.

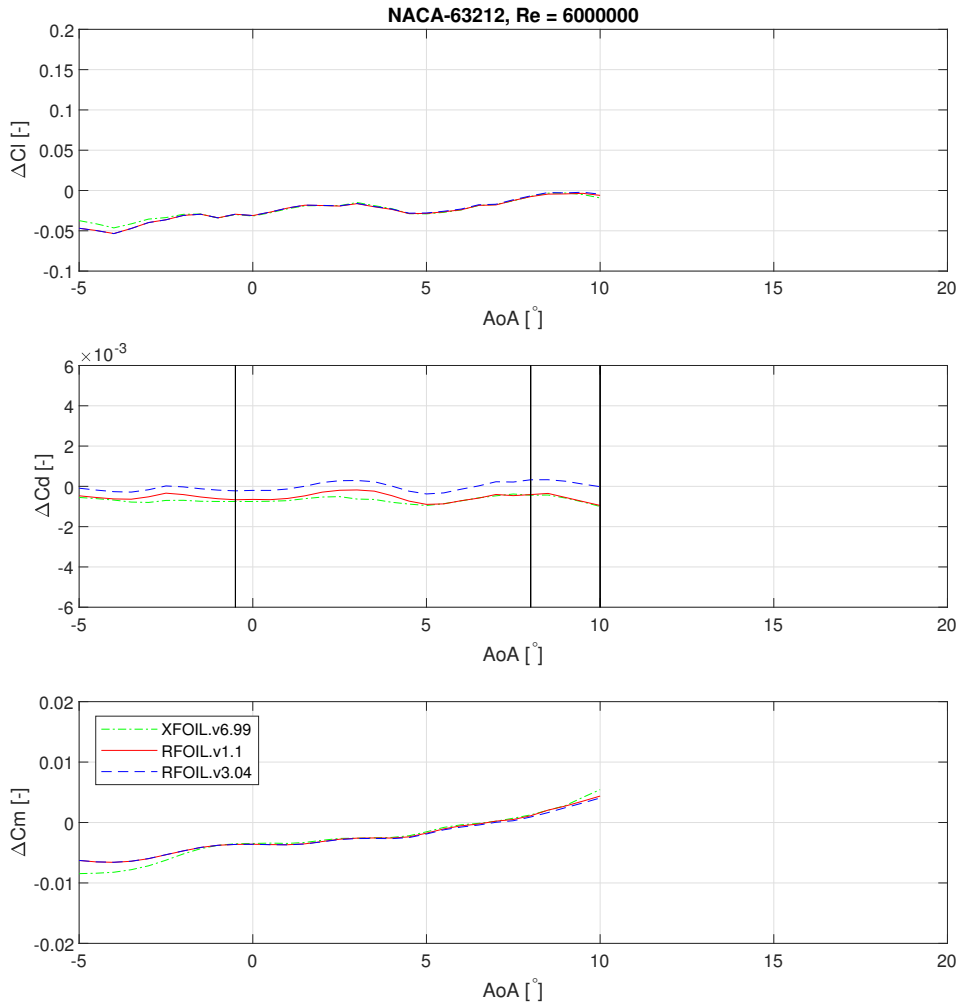

Figure B.309: Comparison between experimental and numerical pressure and skin friction distributions for the NACA-63212 airfoil at a Reynolds number of 6000000 and at the design angle of attack.

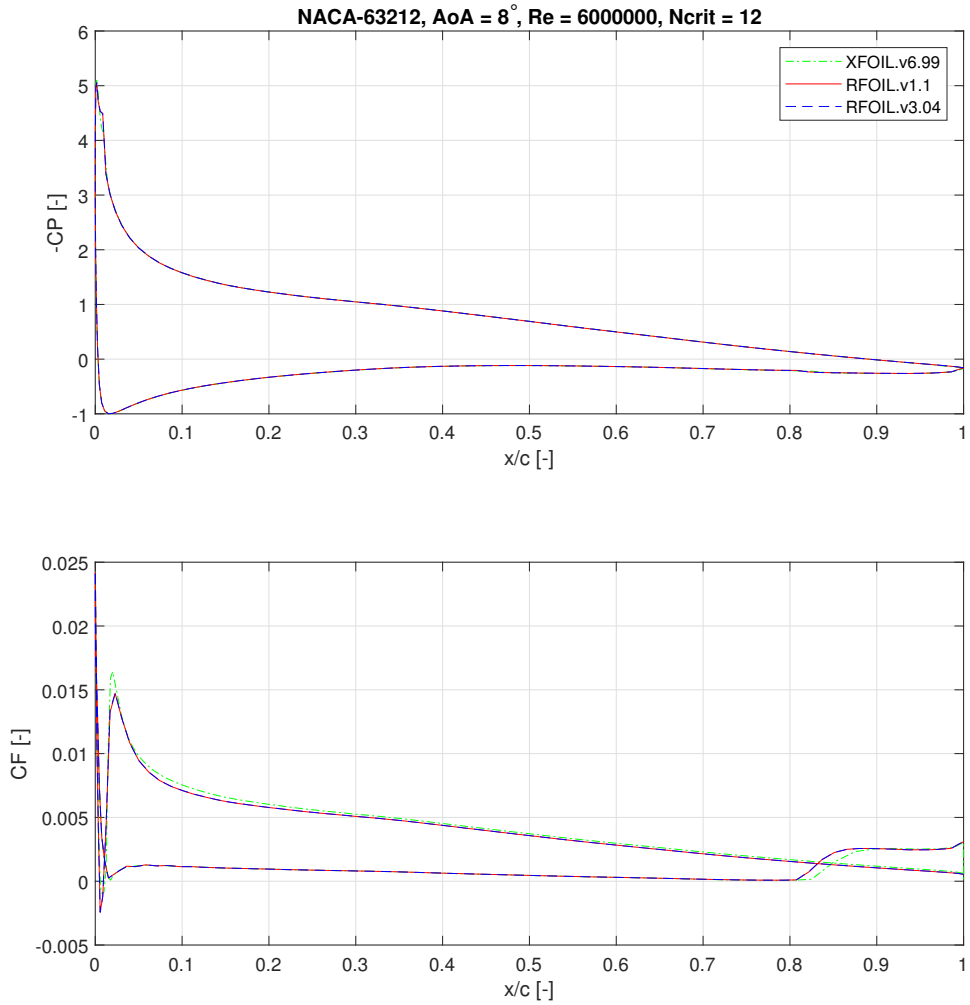

Figure B.310: Comparison between experimental and numerical polars for the NACA-63215 airfoil at a Reynolds number of 3000000. Simulation time to generate the polars by means the different codes and the number of converged polar points are depicted between parentheses.

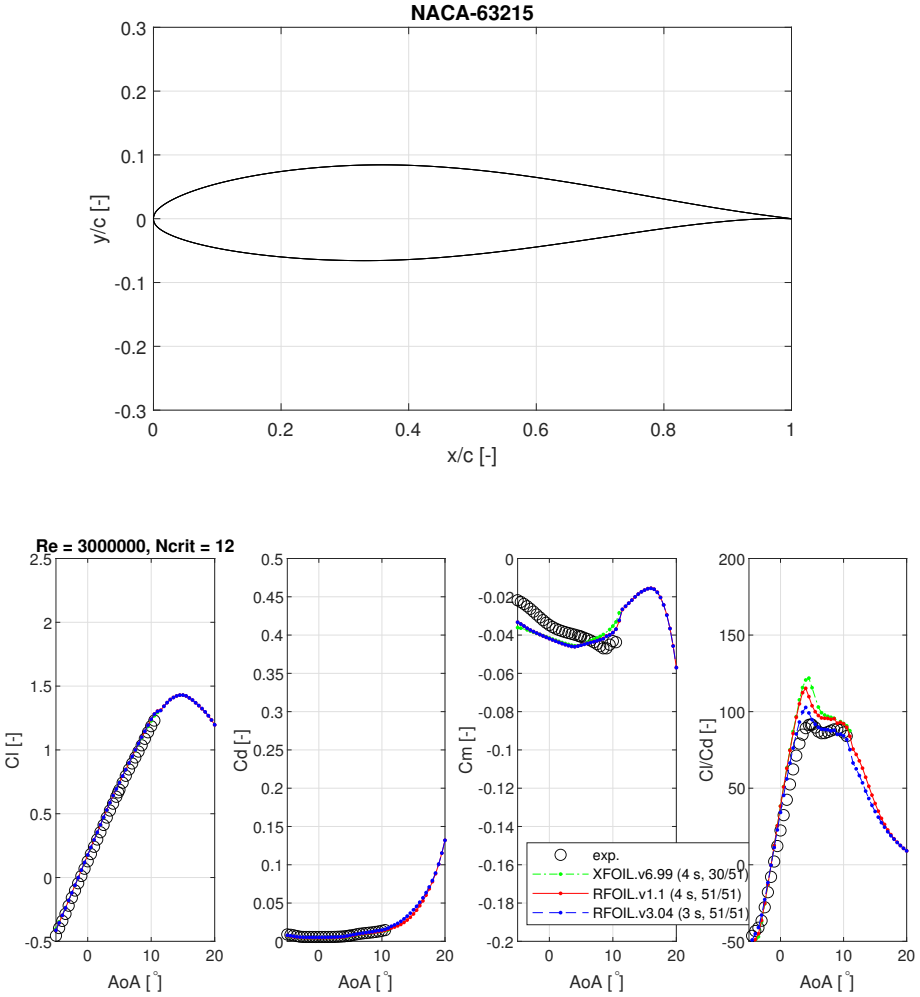

Figure B.311: Differences between experimental and numerical polars for the NACA-63215 airfoil at a Reynolds number of 3000000. Vertical black lines in the middle subplot indicate, from left to right, the angle of attack corresponding to the minimum drag coefficient, maximum lift to drag ratio and maximum lift coefficient, respectively.

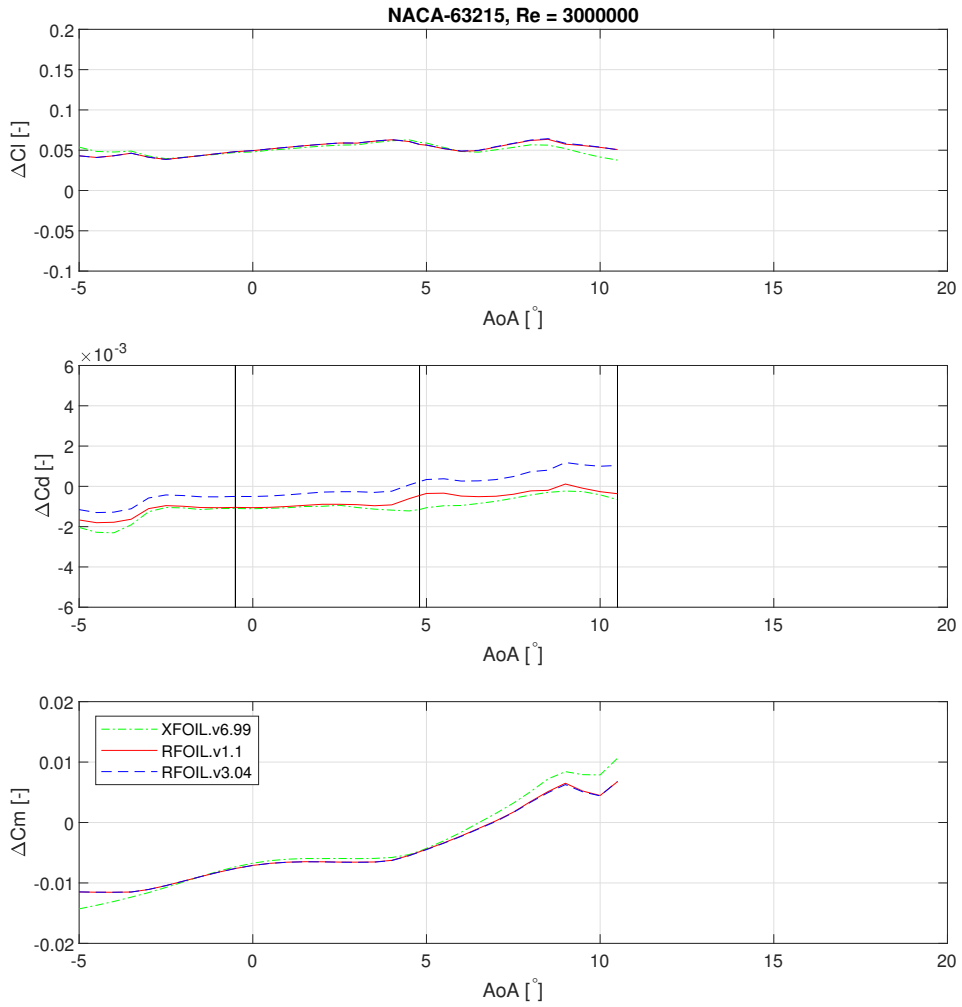

Figure B.312: Comparison between experimental and numerical pressure and skin friction distributions for the NACA-63215 airfoil at a Reynolds number of 3000000 and at the design angle of attack.

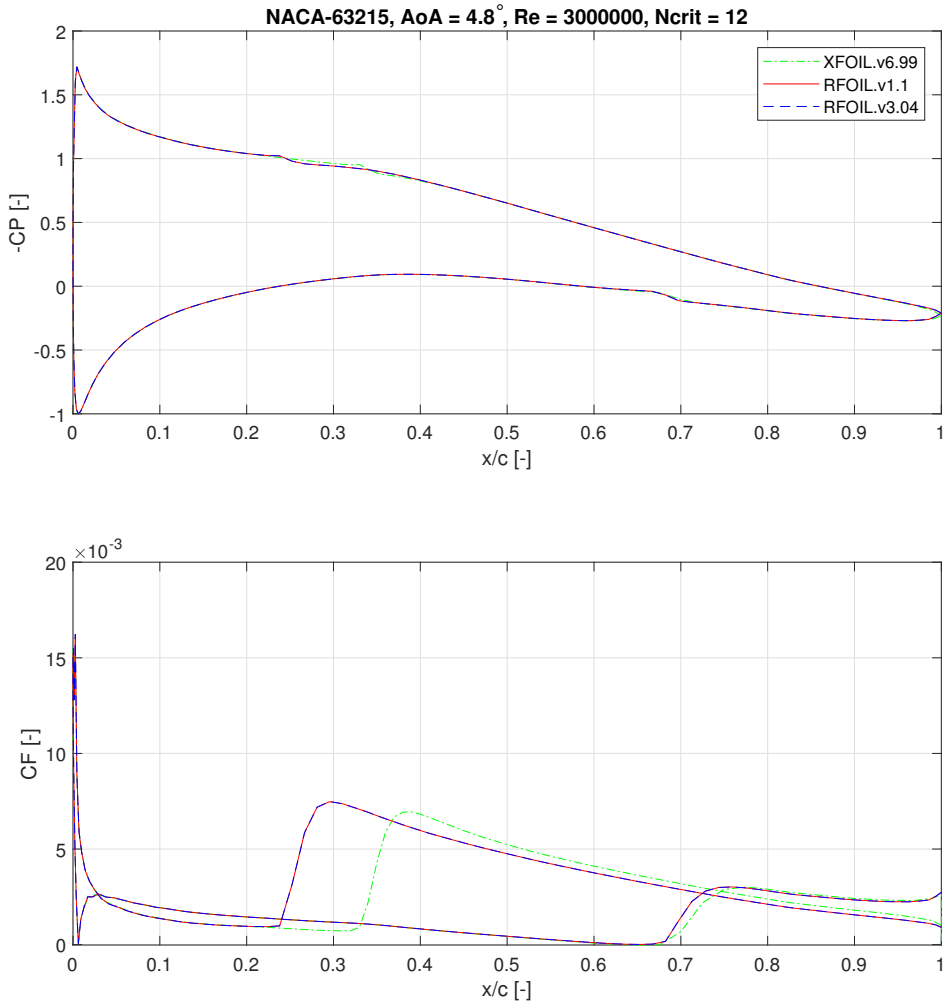

Figure B.313: Comparison between experimental and numerical polars for the NACA-63215 airfoil at a Reynolds number of 6000000. Simulation time to generate the polars by means the different codes and the number of converged polar points are depicted between parentheses.

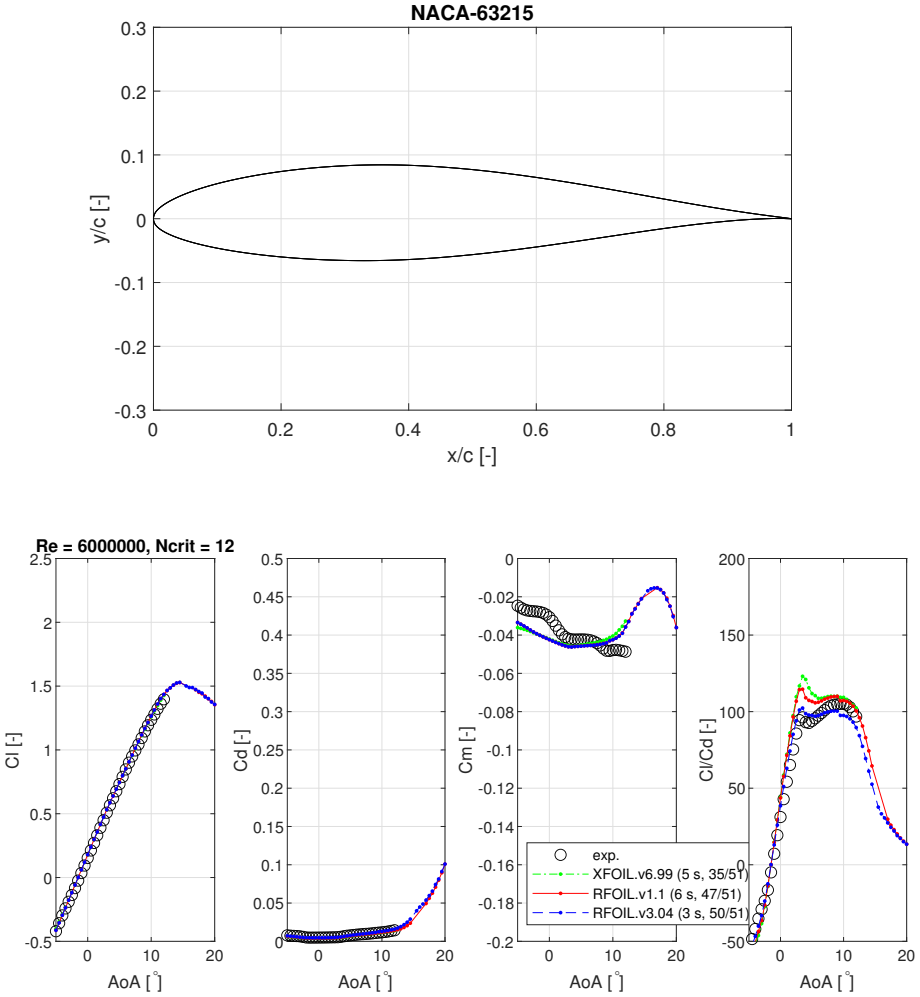

Figure B.314: Differences between experimental and numerical polars for the NACA-63215 airfoil at a Reynolds number of 6000000. Vertical black lines in the middle subplot indicate, from left to right, the angle of attack corresponding to the minimum drag coefficient, maximum lift to drag ratio and maximum lift coefficient, respectively.

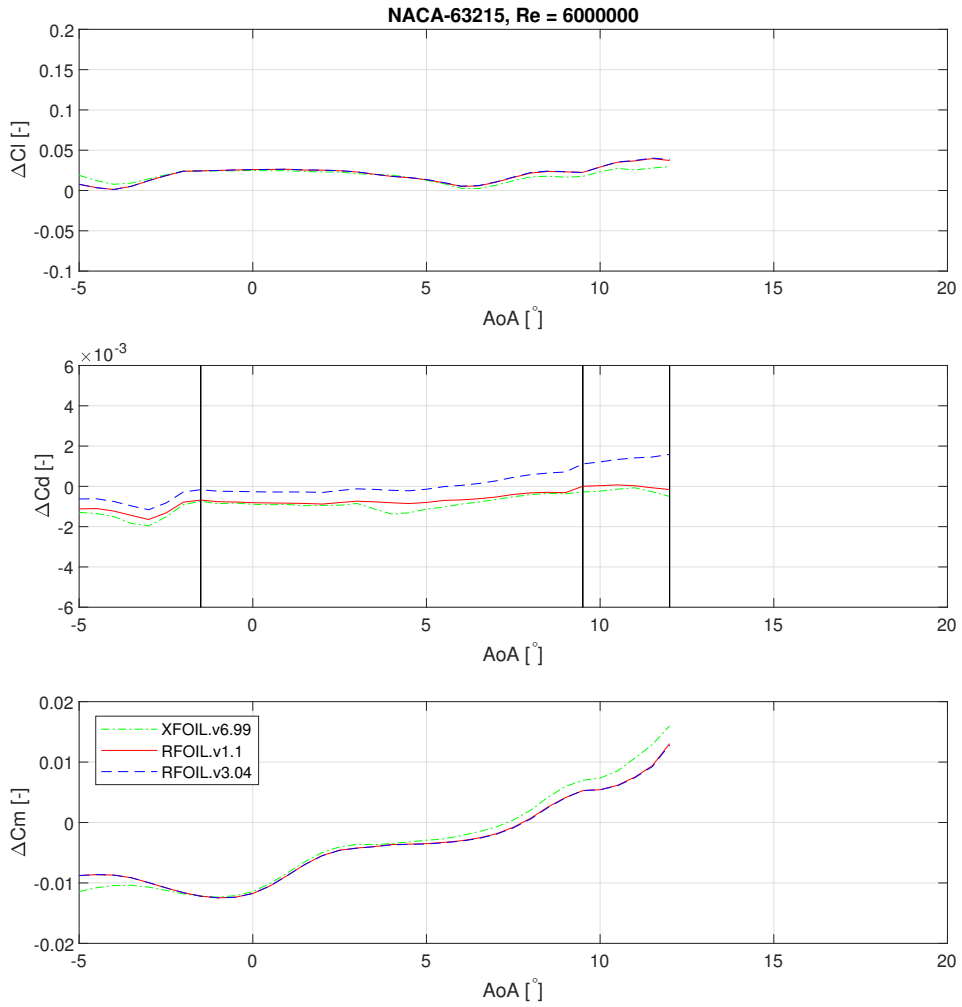

Figure B.315: Comparison between experimental and numerical pressure and skin friction distributions for the NACA-63215 airfoil at a Reynolds number of 6000000 and at the design angle of attack.

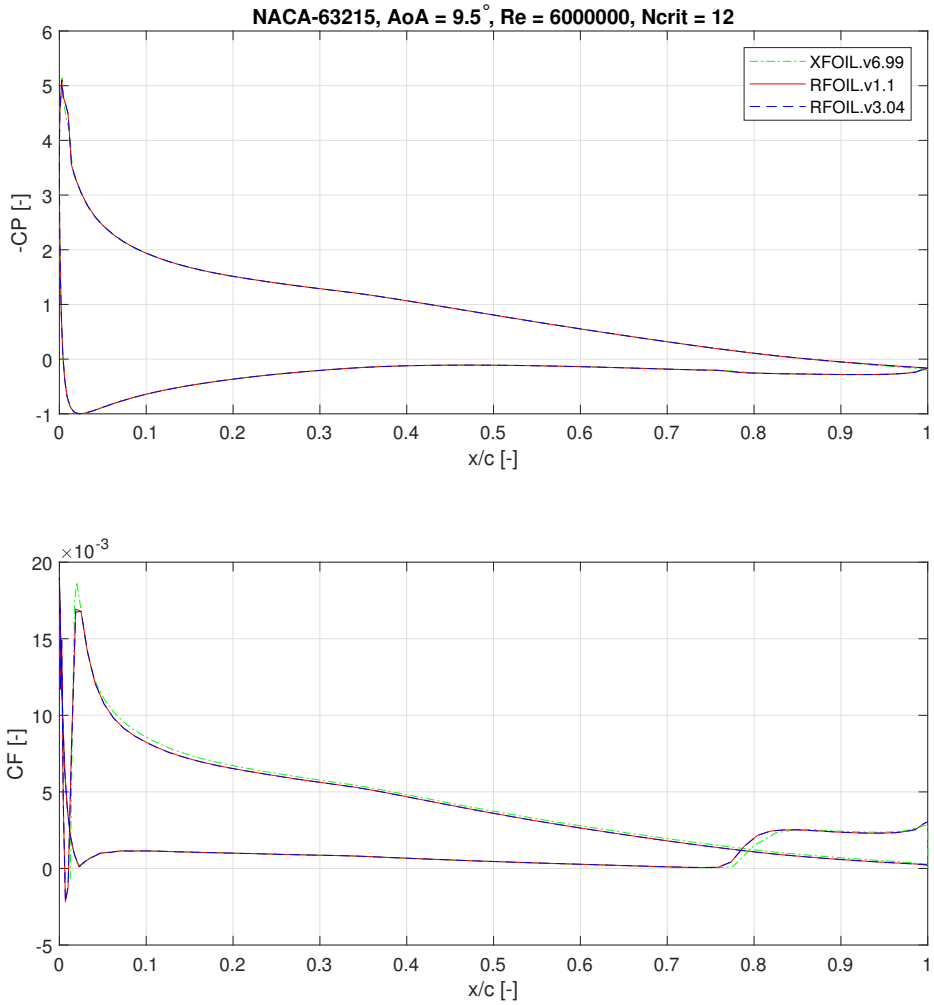

Figure B.316: Comparison between experimental and numerical polars for the NACA-63218 airfoil at a Reynolds number of 3000000. Simulation time to generate the polars by means the different codes and the number of converged polar points are depicted between parentheses.

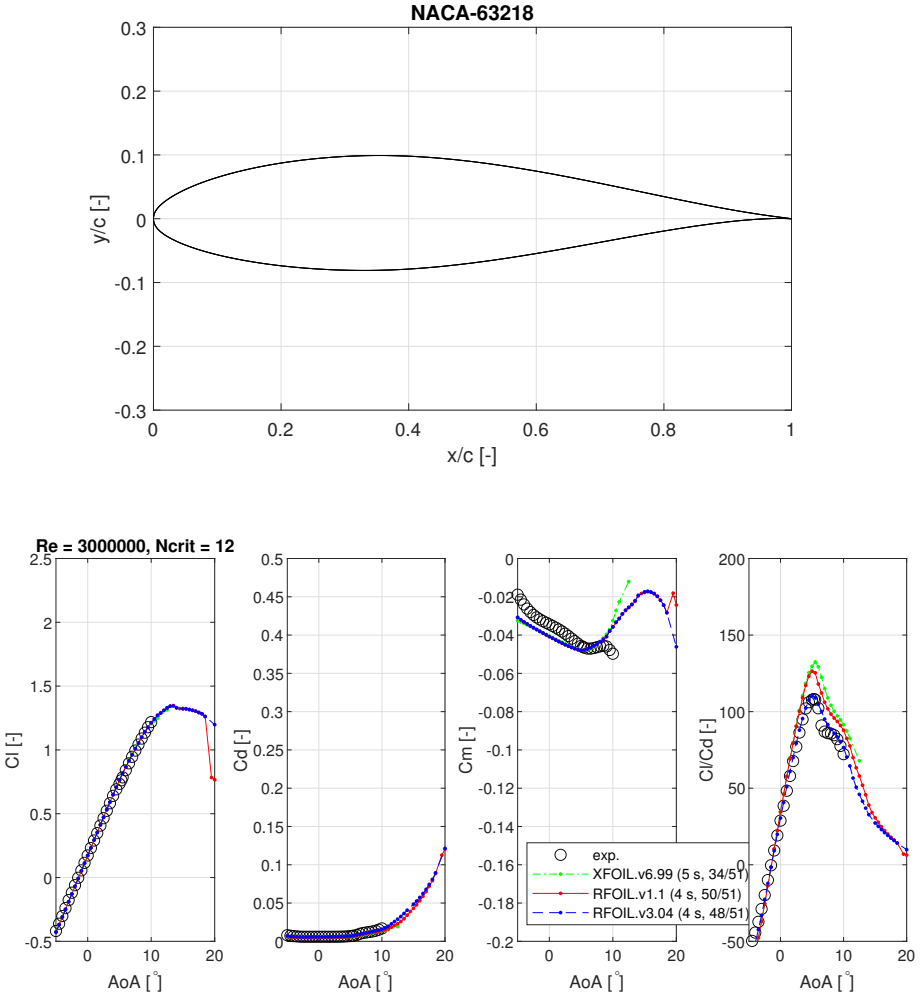

Figure B.317: Differences between experimental and numerical polars for the NACA-63218 airfoil at a Reynolds number of 3000000. Vertical black lines in the middle subplot indicate, from left to right, the angle of attack corresponding to the minimum drag coefficient, maximum lift to drag ratio and maximum lift coefficient, respectively.

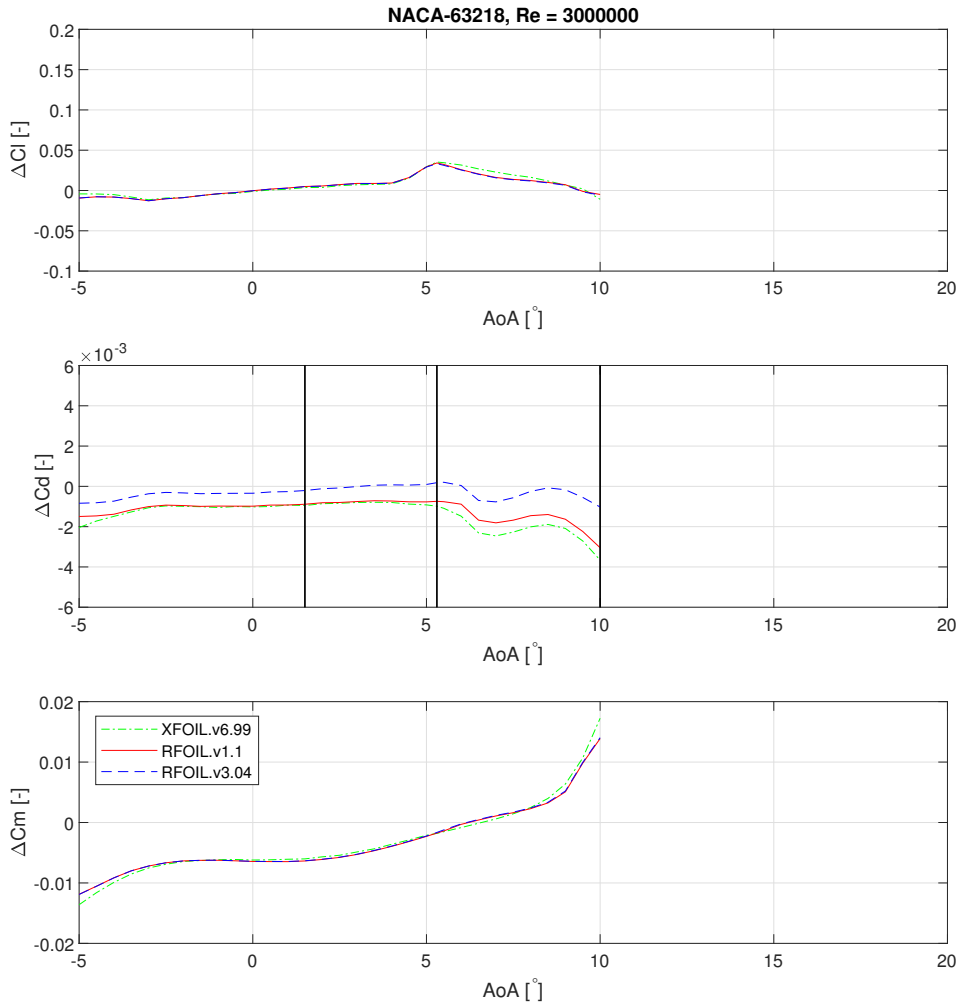

Figure B.318: Comparison between experimental and numerical pressure and skin friction distributions for the NACA-63218 airfoil at a Reynolds number of 3000000 and at the design angle of attack.

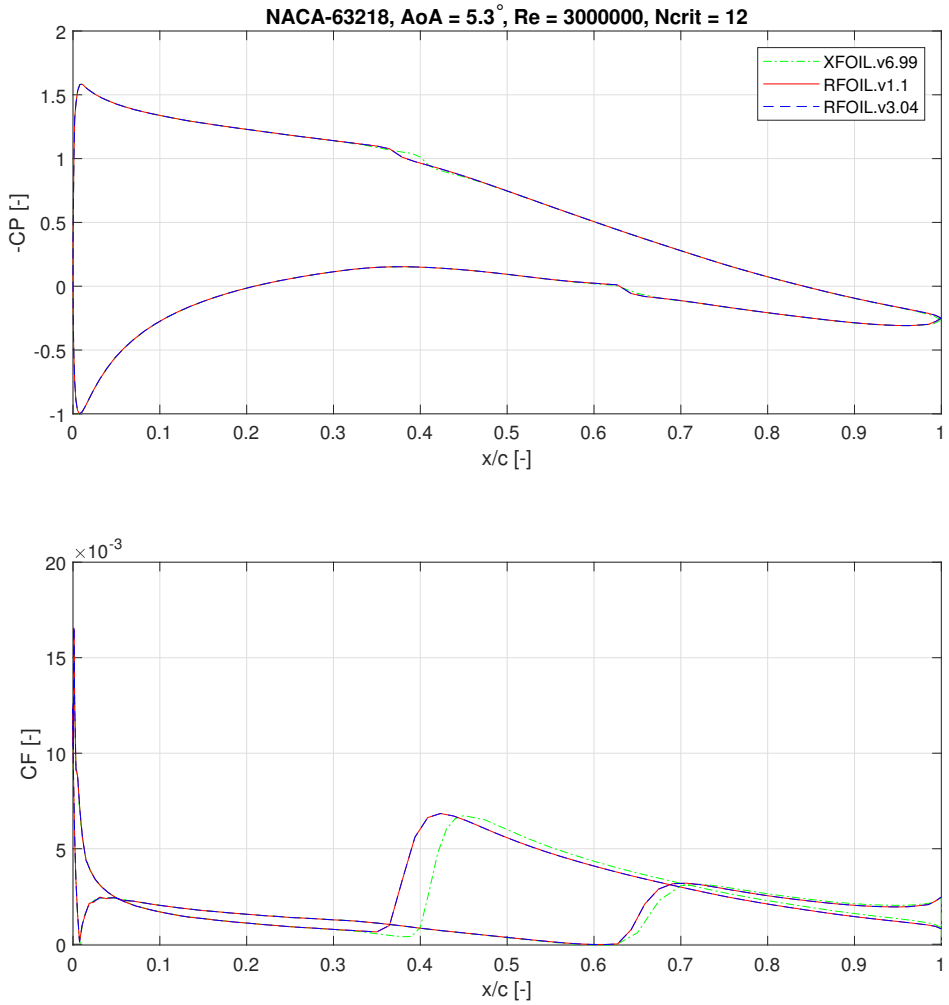

Figure B.319: Comparison between experimental and numerical polars for the NACA-63218 airfoil at a Reynolds number of 6000000. Simulation time to generate the polars by means the different codes and the number of converged polar points are depicted between parentheses.

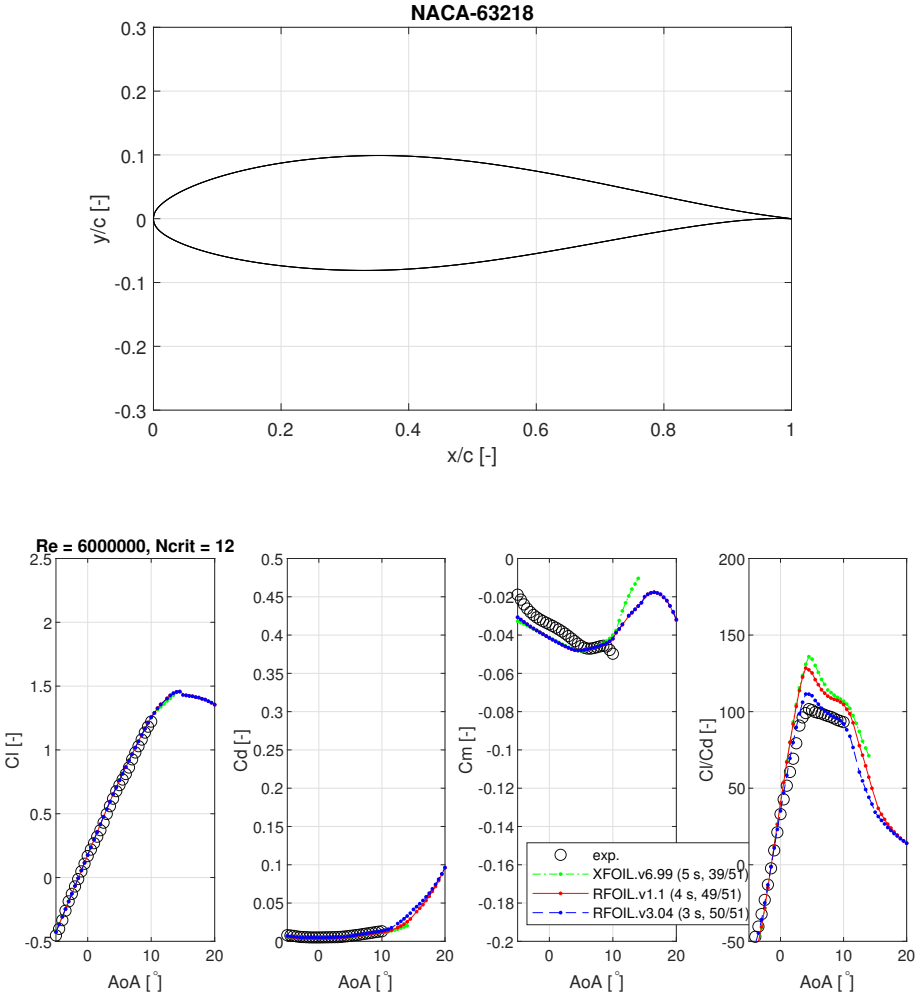

Figure B.320: Differences between experimental and numerical polars for the NACA-63218 airfoil at a Reynolds number of 6000000. Vertical black lines in the middle subplot indicate, from left to right, the angle of attack corresponding to the minimum drag coefficient, maximum lift to drag ratio and maximum lift coefficient, respectively.

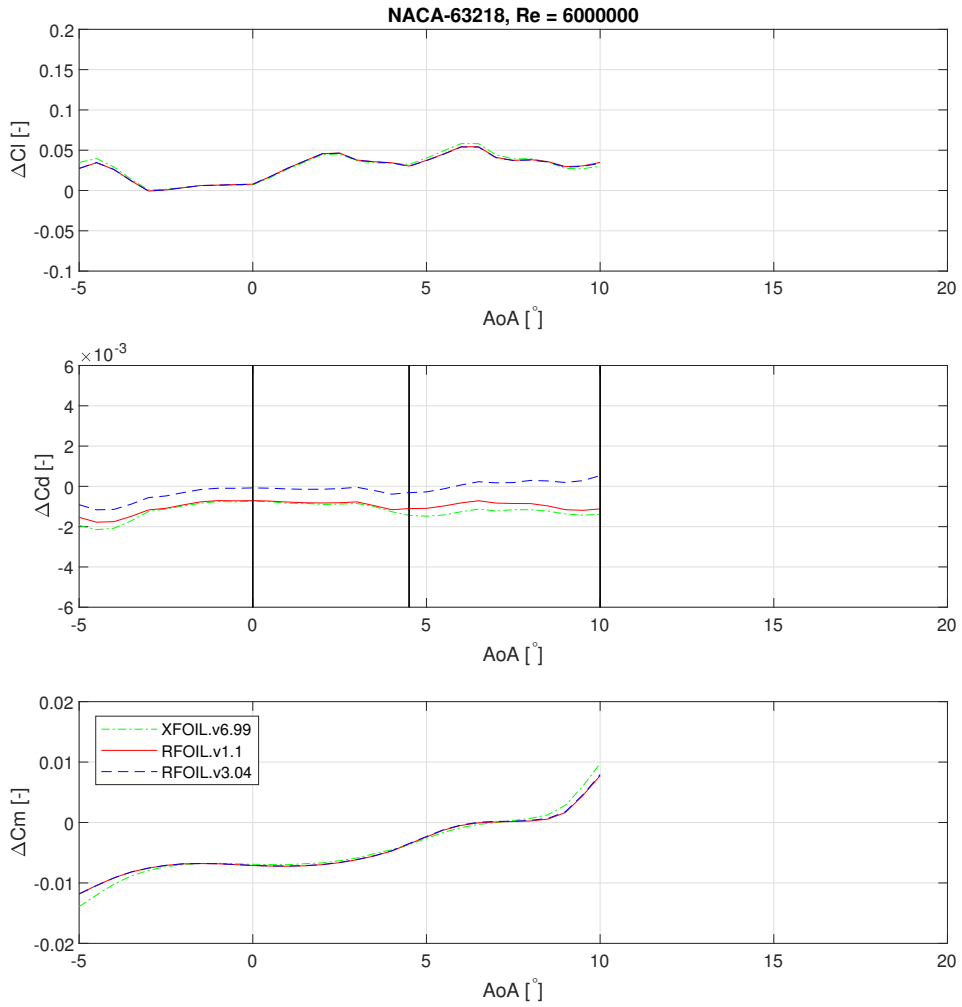

Figure B.321: Comparison between experimental and numerical pressure and skin friction distributions for the NACA-63218 airfoil at a Reynolds number of 6000000 and at the design angle of attack.

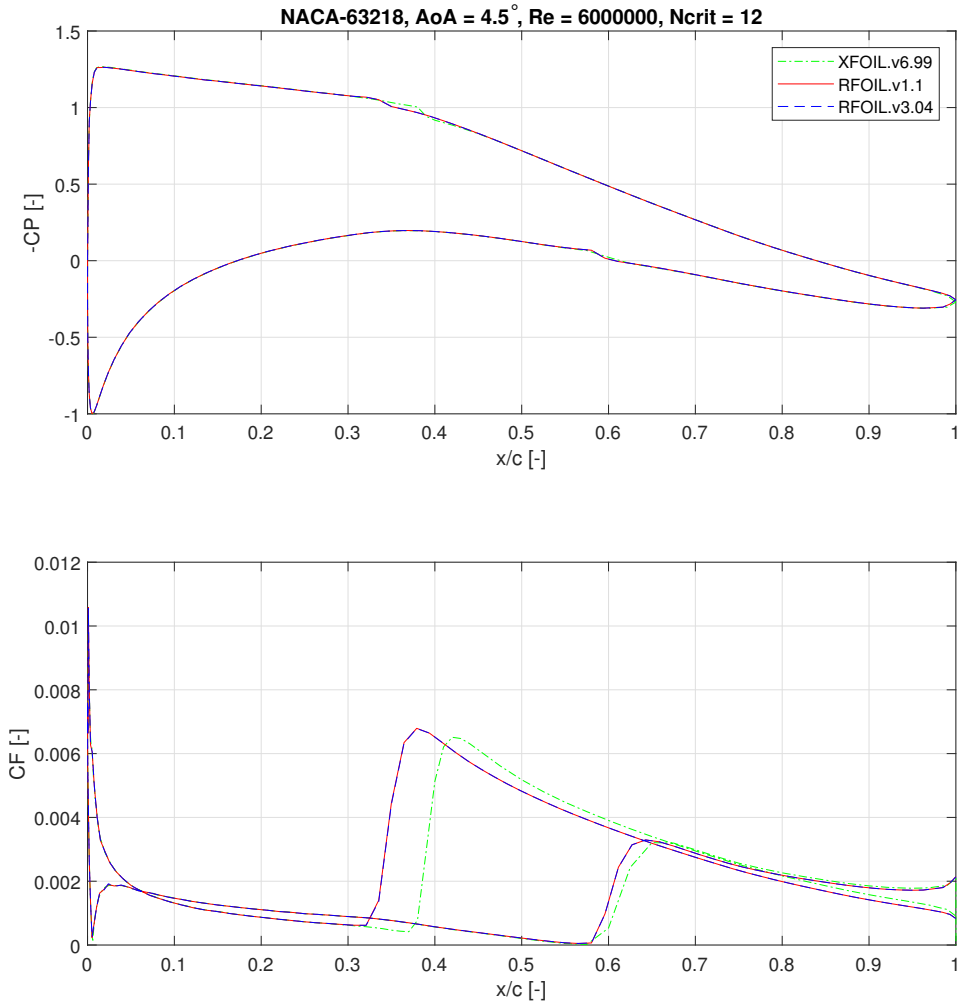

Figure B.322: Comparison between experimental and numerical polars for the NACA-63221 airfoil at a Reynolds number of 3000000. Simulation time to generate the polars by means the different codes and the number of converged polar points are depicted between parentheses.

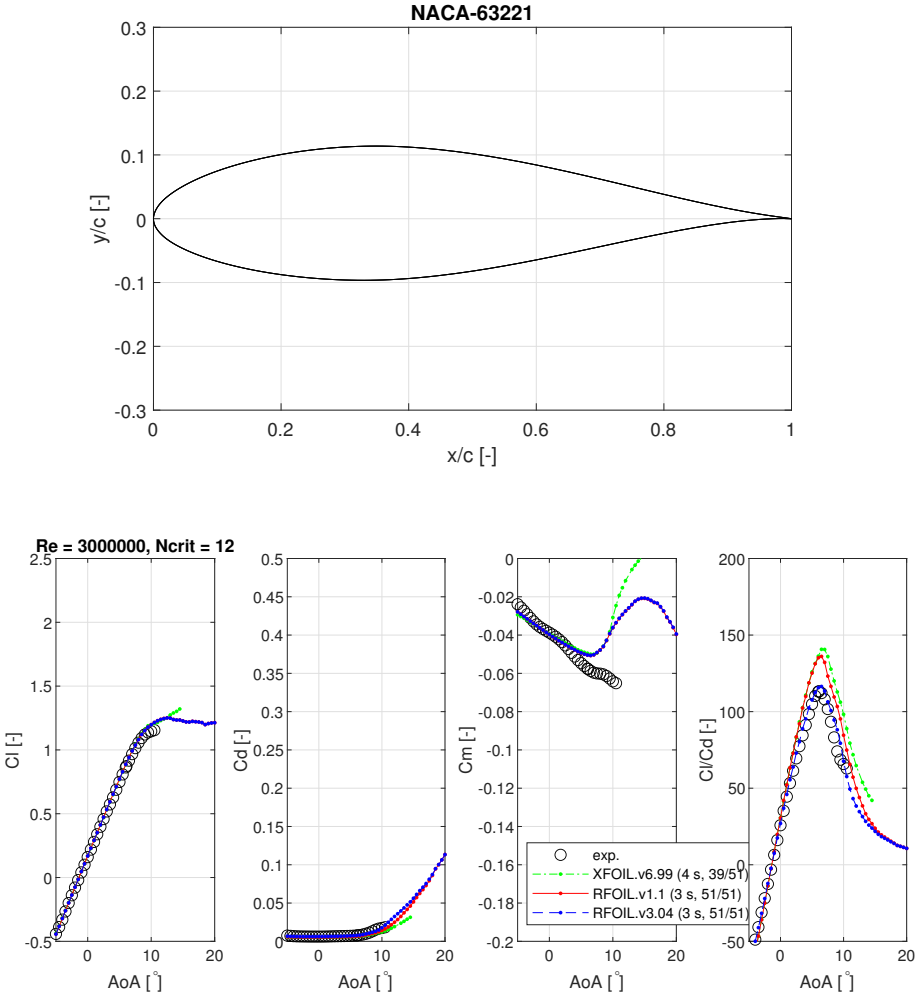

Figure B.323: Differences between experimental and numerical polars for the NACA-63221 airfoil at a Reynolds number of 3000000. Vertical black lines in the middle subplot indicate, from left to right, the angle of attack corresponding to the minimum drag coefficient, maximum lift to drag ratio and maximum lift coefficient, respectively.

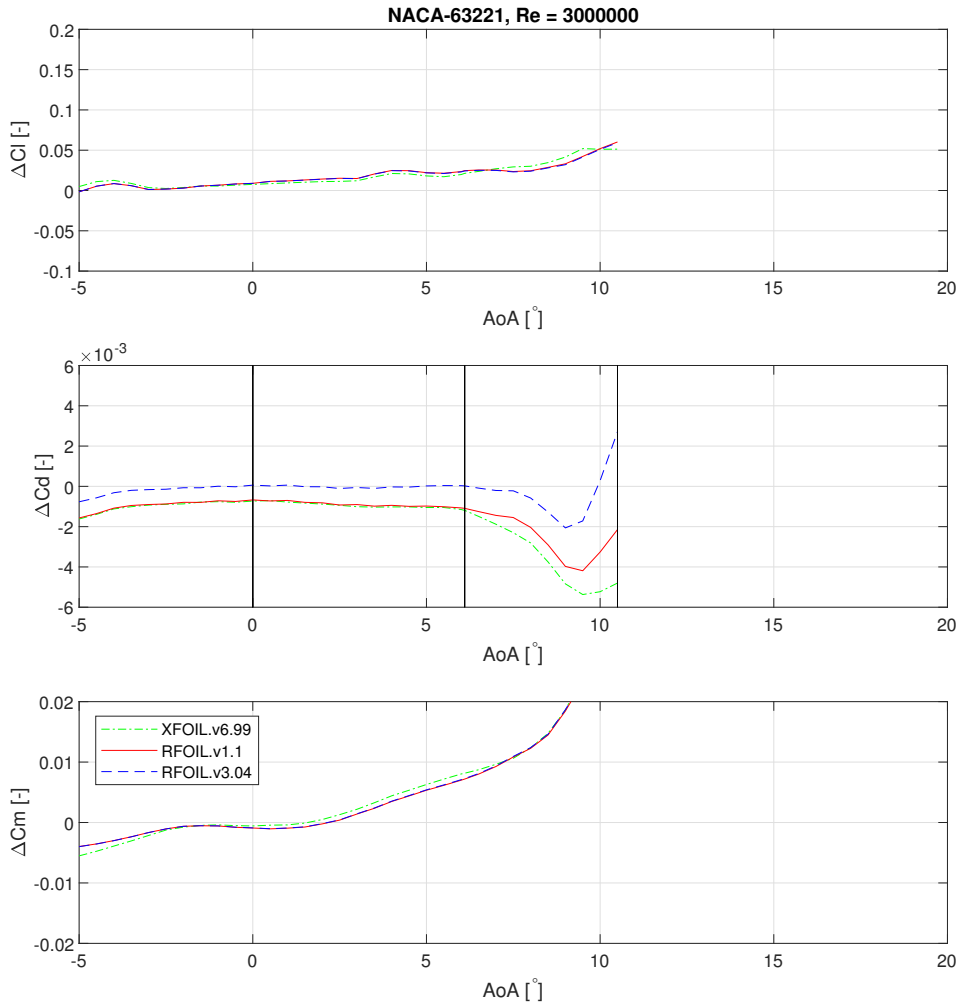

Figure B.324: Comparison between experimental and numerical pressure and skin friction distributions for the NACA-63221 airfoil at a Reynolds number of 3000000 and at the design angle of attack.

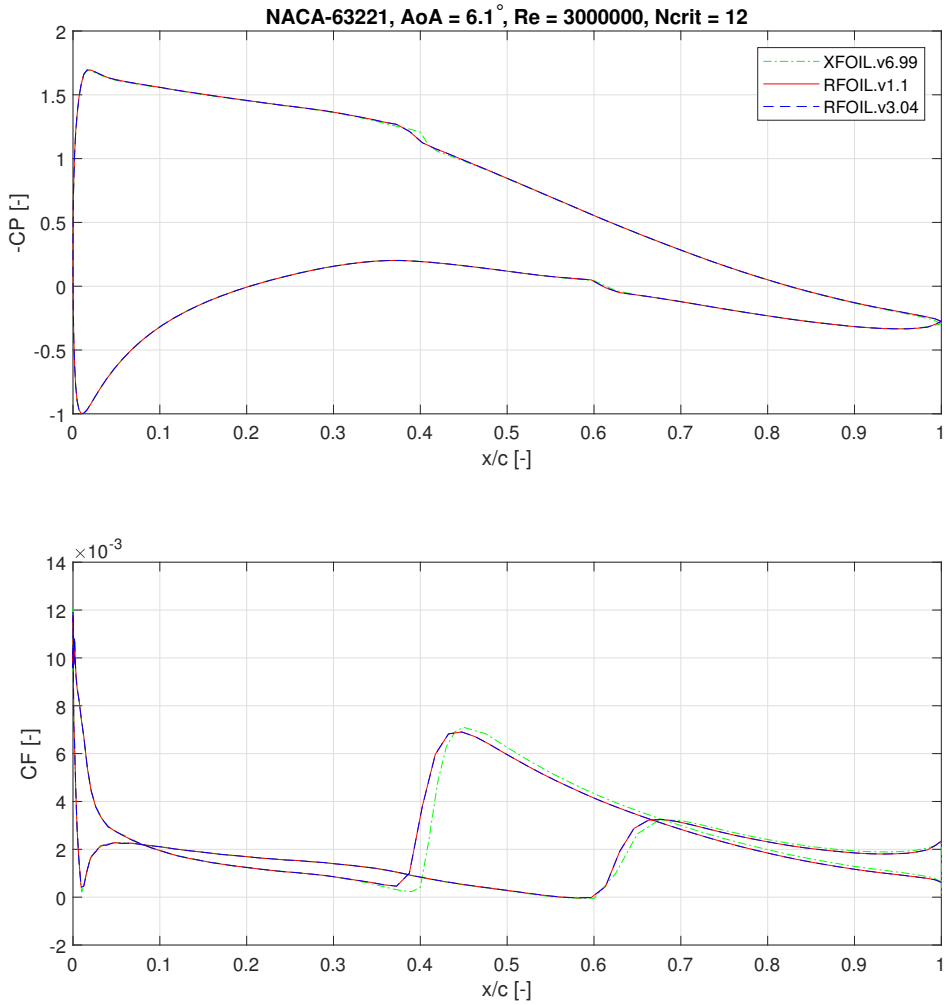

Figure B.325: Comparison between experimental and numerical polars for the NACA-63221 airfoil at a Reynolds number of 6000000. Simulation time to generate the polars by means the different codes and the number of converged polar points are depicted between parentheses.

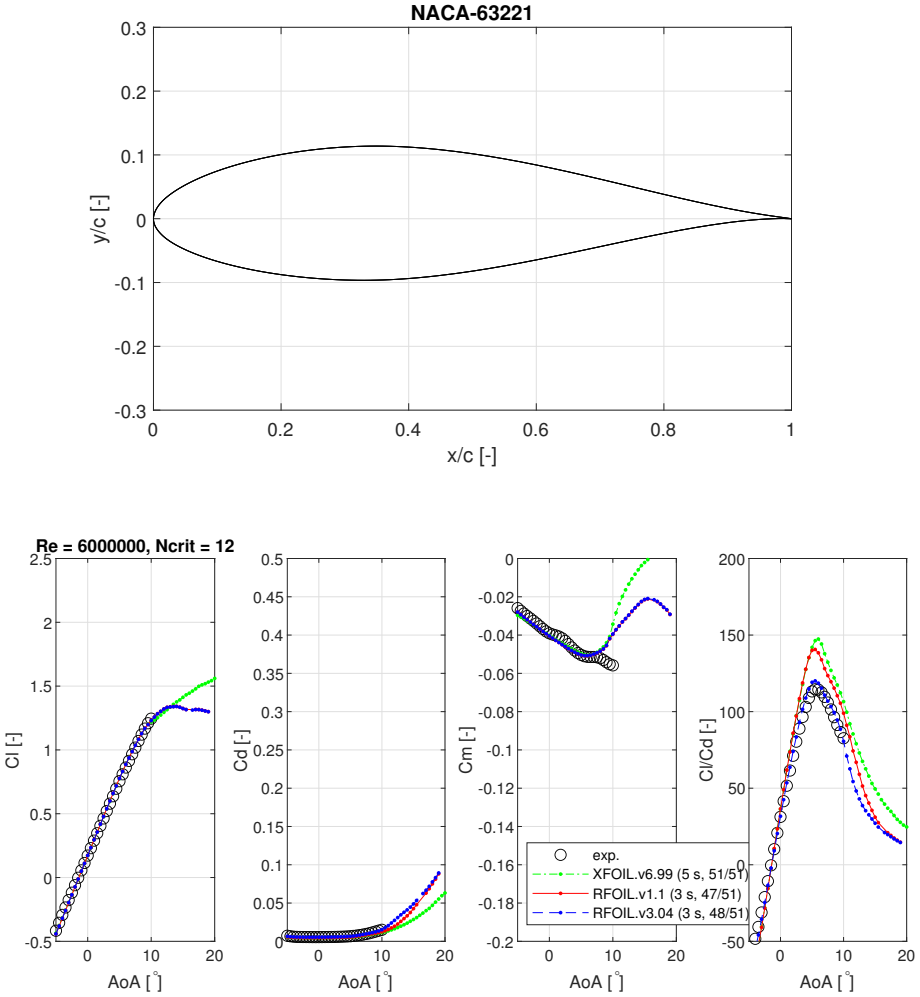

Figure B.326: Differences between experimental and numerical polars for the NACA-63221 airfoil at a Reynolds number of 6000000. Vertical black lines in the middle subplot indicate, from left to right, the angle of attack corresponding to the minimum drag coefficient, maximum lift to drag ratio and maximum lift coefficient, respectively.

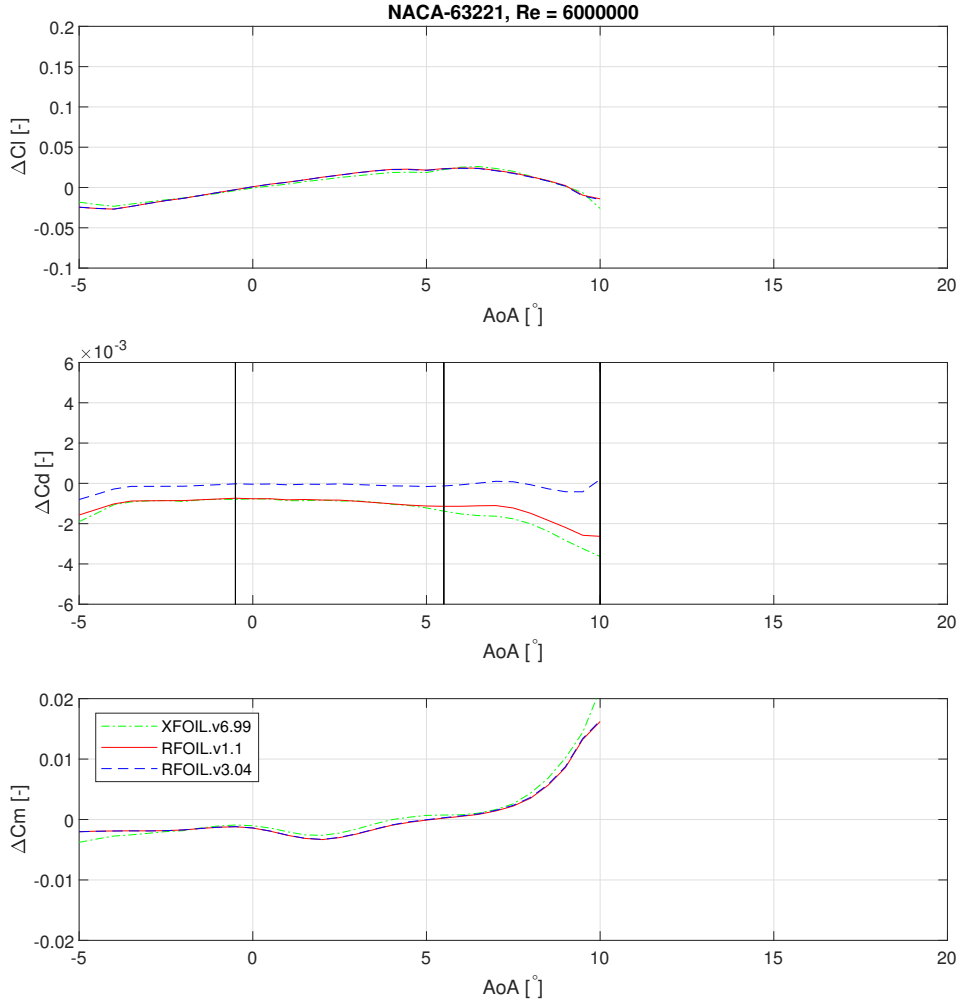

Figure B.327: Comparison between experimental and numerical pressure and skin friction distributions for the NACA-63221 airfoil at a Reynolds number of 6000000 and at the design angle of attack.

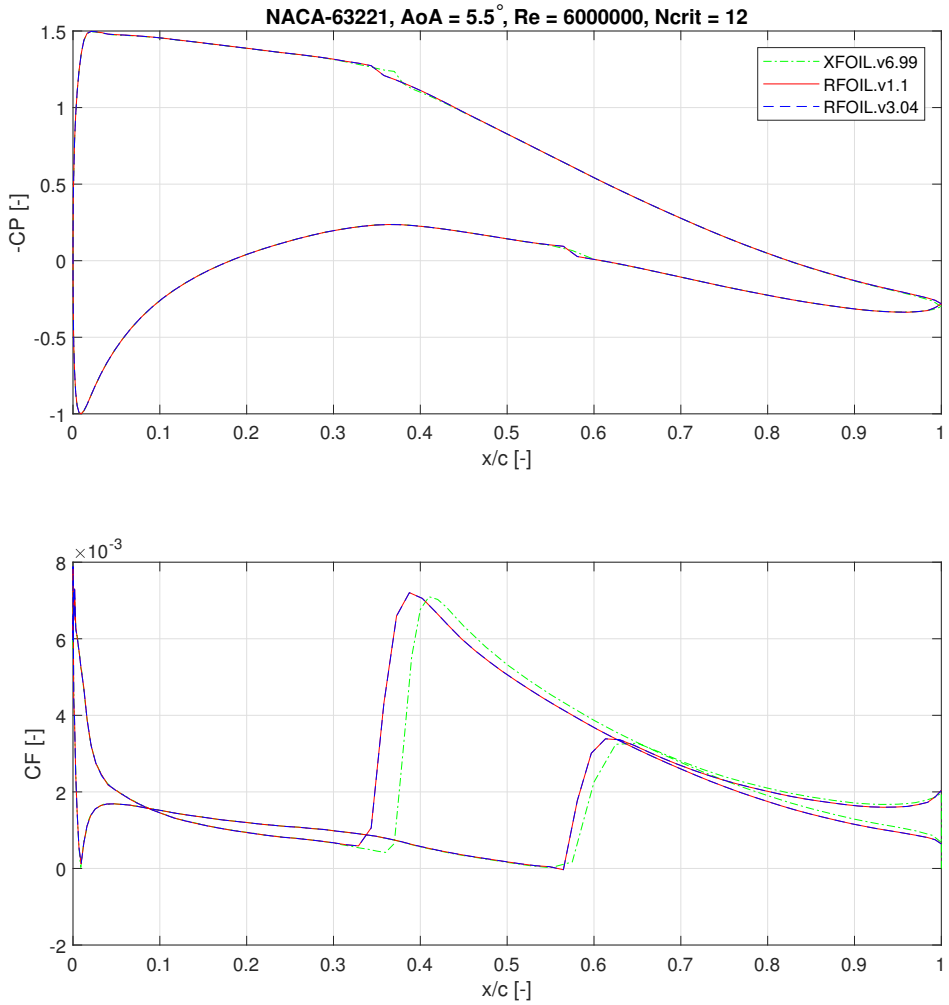

Figure B.328: Comparison between experimental and numerical polars for the NACA-63415 airfoil at a Reynolds number of 1000000. Simulation time to generate the polars by means the different codes and the number of converged polar points are depicted between parentheses.

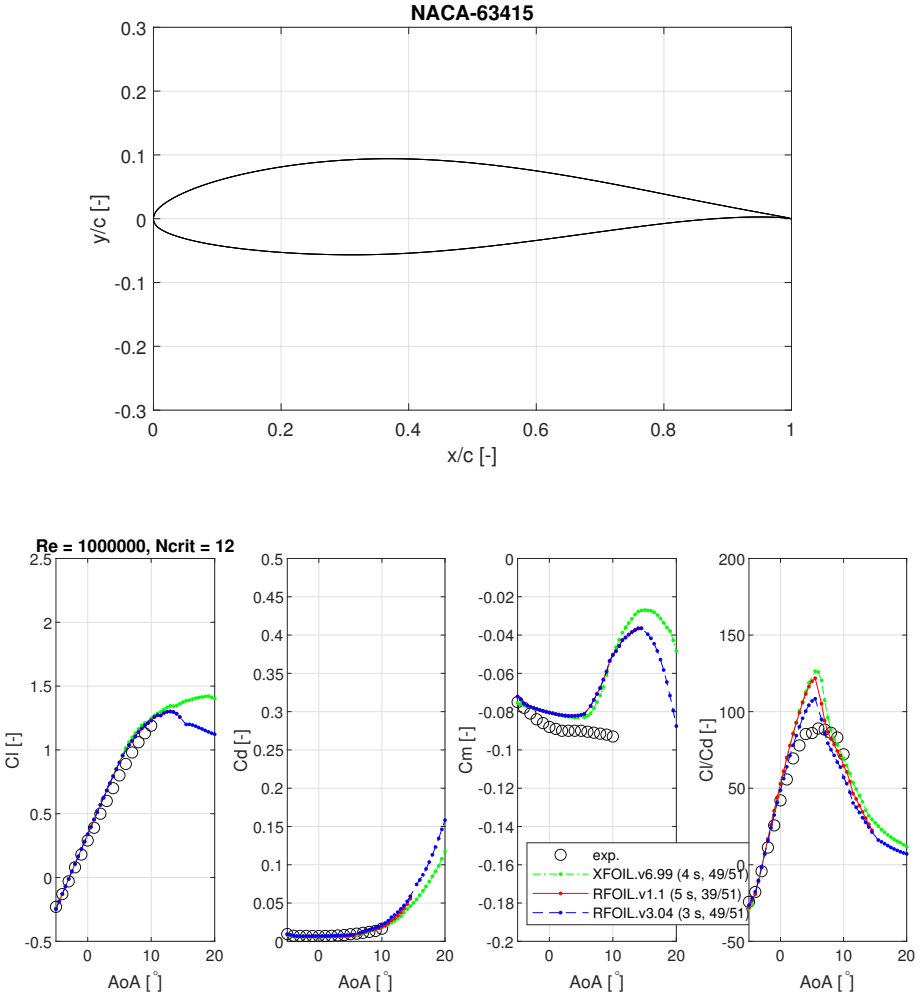

Figure B.329: Differences between experimental and numerical polars for the NACA-63415 airfoil at a Reynolds number of 1000000. Vertical black lines in the middle subplot indicate, from left to right, the angle of attack corresponding to the minimum drag coefficient, maximum lift to drag ratio and maximum lift coefficient, respectively.

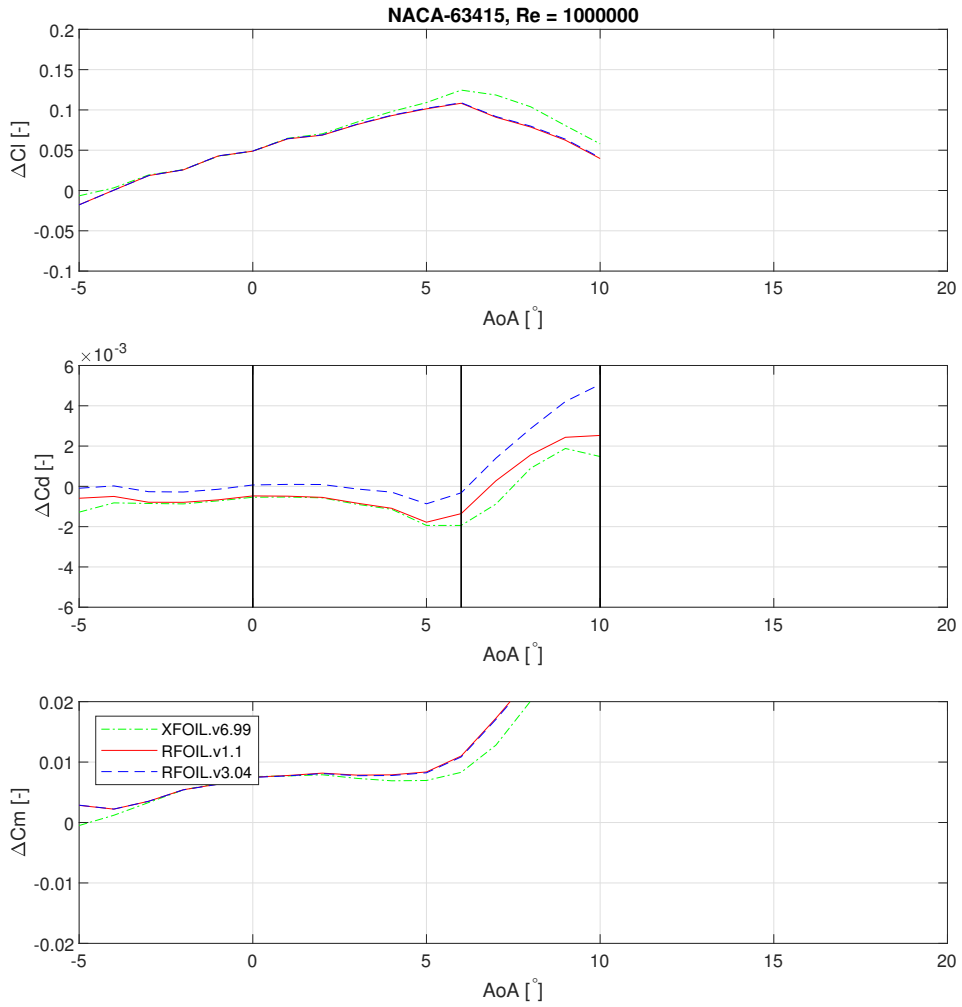

Figure B.330: Comparison between experimental and numerical pressure and skin friction distributions for the NACA-63415 airfoil at a Reynolds number of 1000000 and at the design angle of attack.

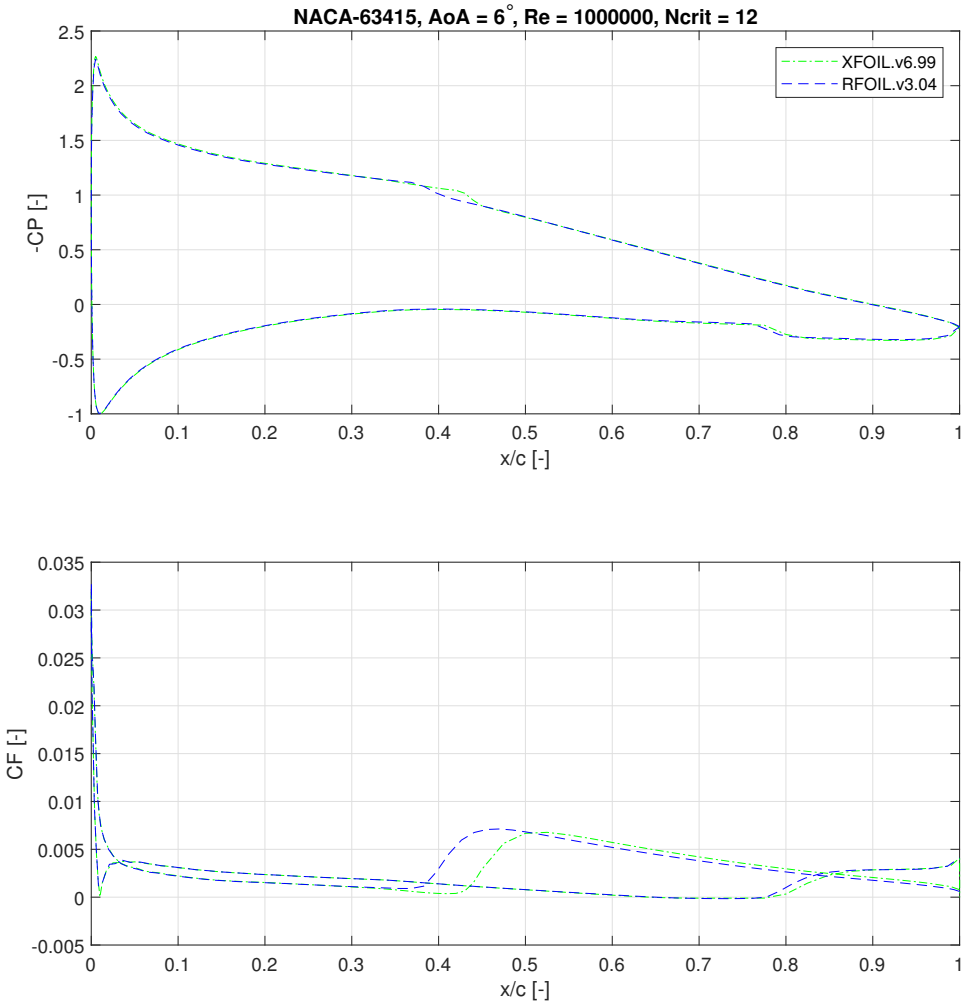

Figure B.331: Comparison between experimental and numerical polars for the NACA-63415 airfoil at a Reynolds number of 1500000. Simulation time to generate the polars by means the different codes and the number of converged polar points are depicted between parentheses.

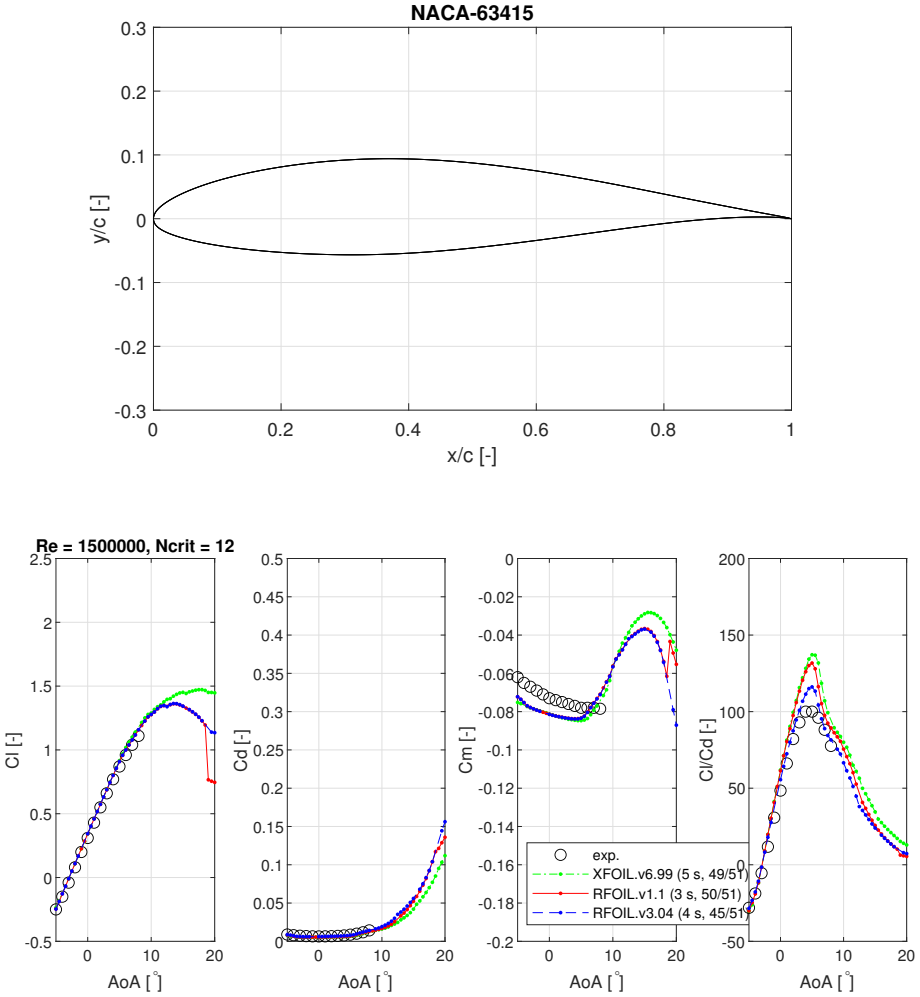

Figure B.332: Differences between experimental and numerical polars for the NACA-63415 airfoil at a Reynolds number of 1500000. Vertical black lines in the middle subplot indicate, from left to right, the angle of attack corresponding to the minimum drag coefficient, maximum lift to drag ratio and maximum lift coefficient, respectively.

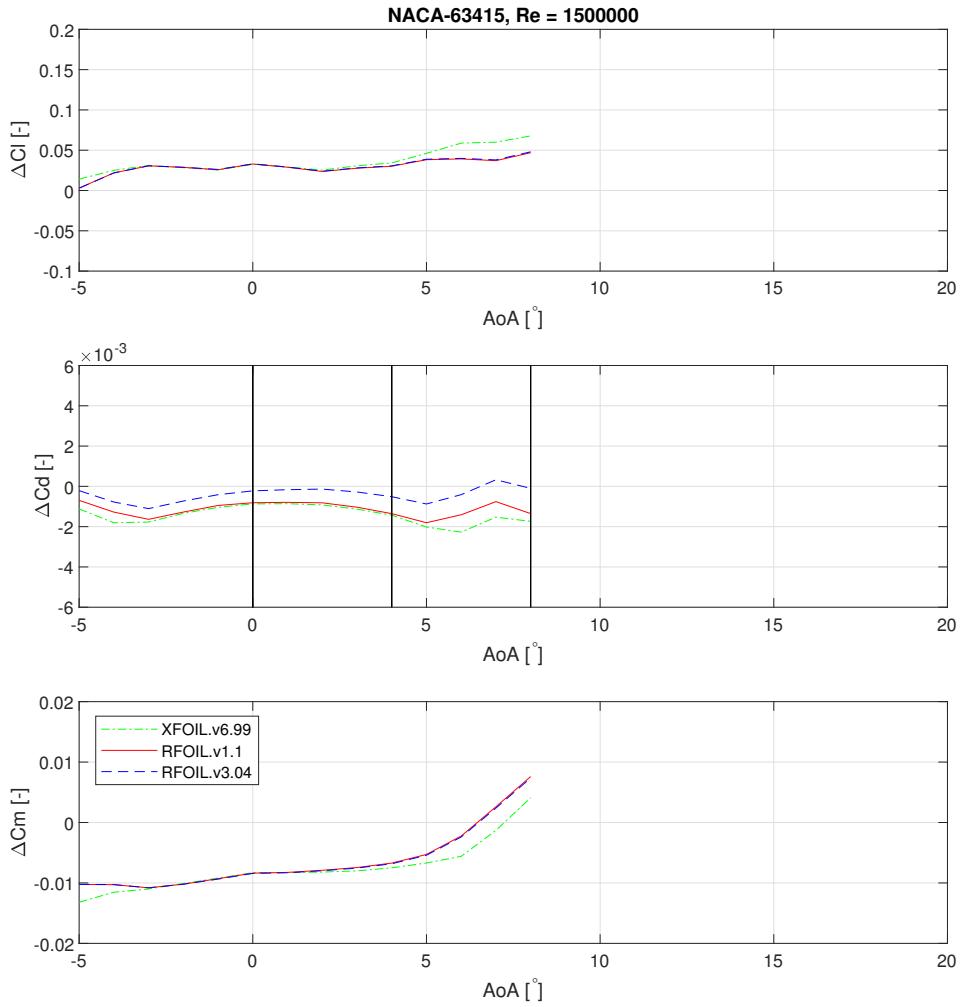

Figure B.333: Comparison between experimental and numerical pressure and skin friction distributions for the NACA-63415 airfoil at a Reynolds number of 1500000 and at the design angle of attack.

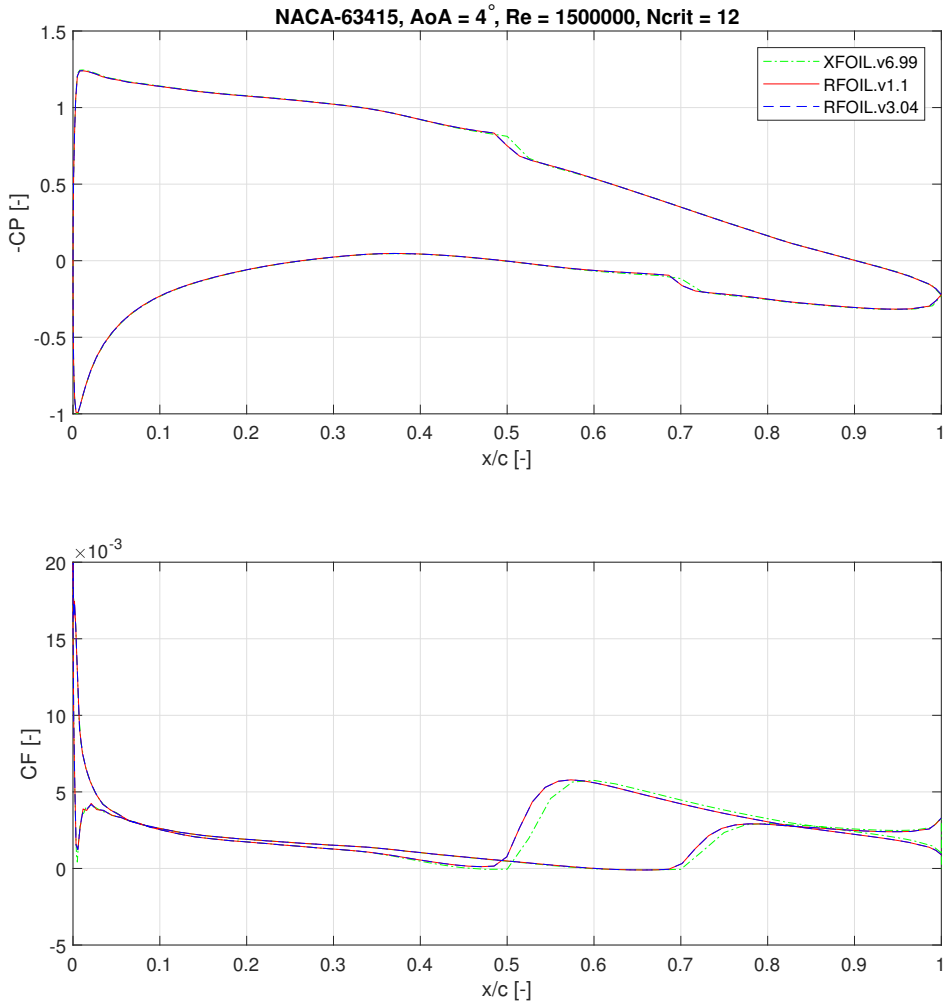

Figure B.334: Comparison between experimental and numerical polars for the NACA-63415 airfoil at a Reynolds number of 2000000. Simulation time to generate the polars by means the different codes and the number of converged polar points are depicted between parentheses.

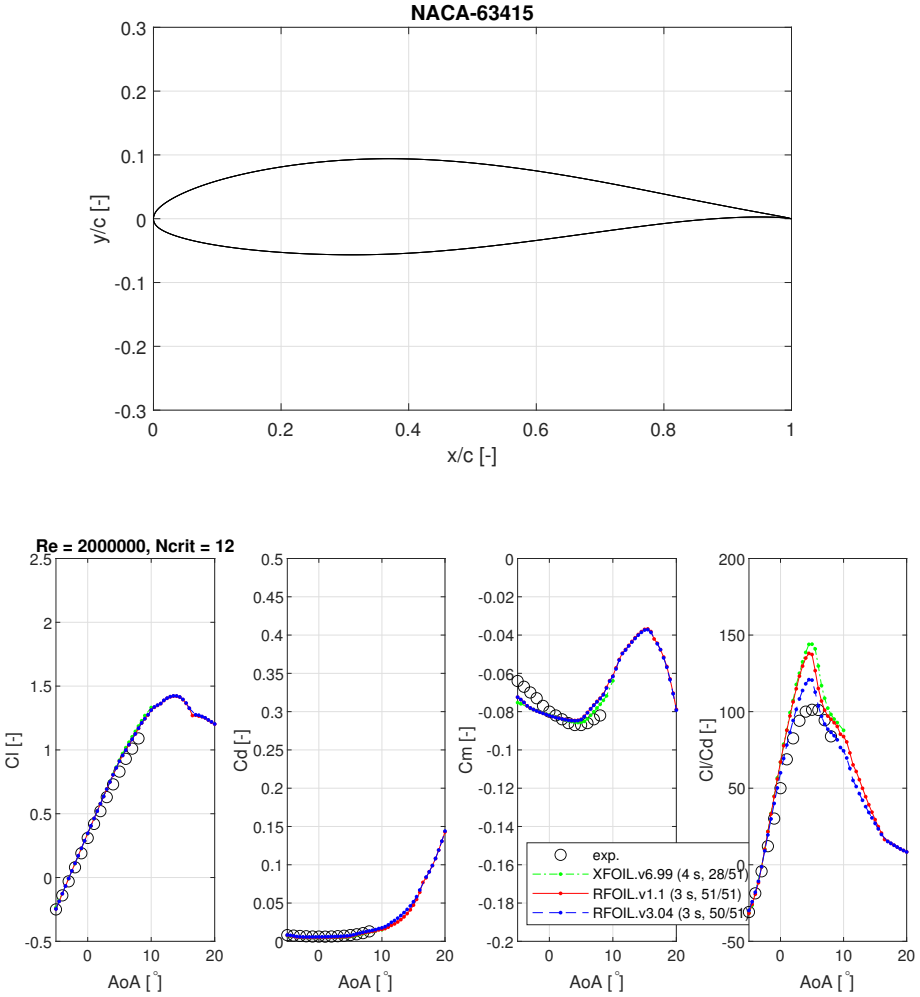

Figure B.335: Differences between experimental and numerical polars for the NACA-63415 airfoil at a Reynolds number of 2000000. Vertical black lines in the middle subplot indicate, from left to right, the angle of attack corresponding to the minimum drag coefficient, maximum lift to drag ratio and maximum lift coefficient, respectively.

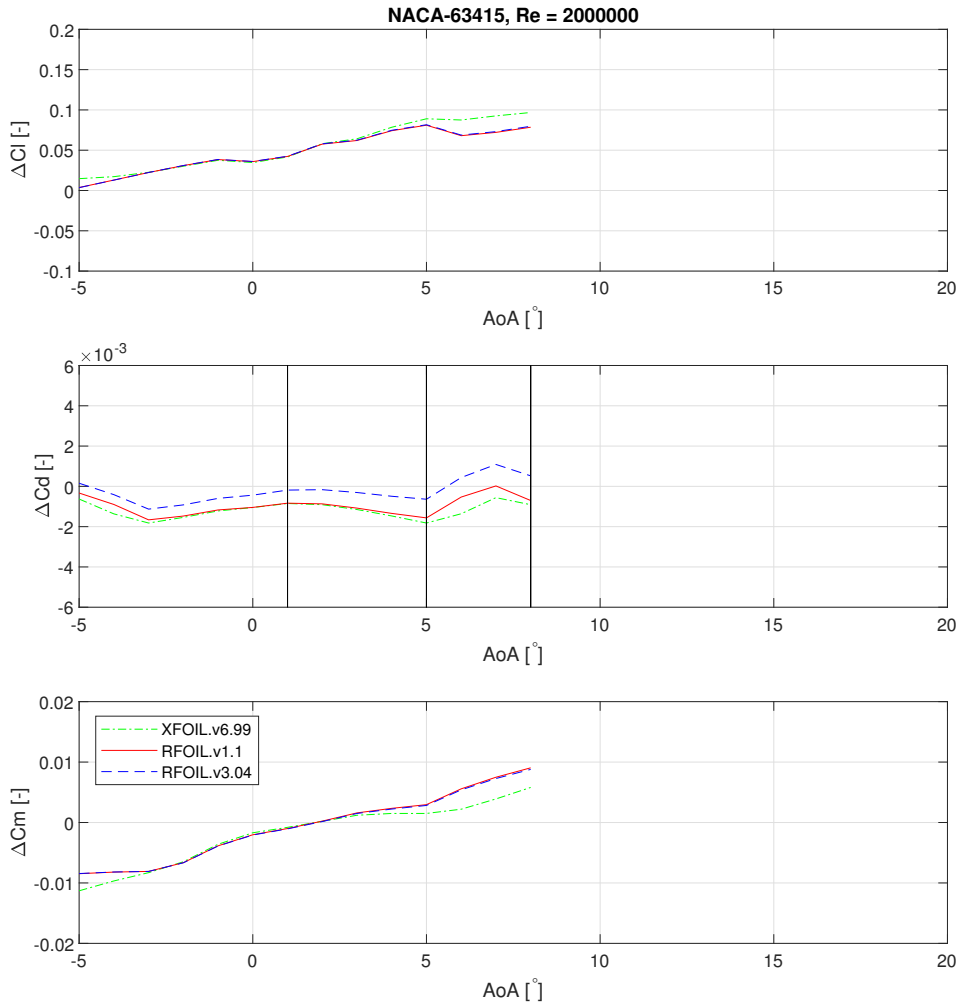

Figure B.336: Comparison between experimental and numerical pressure and skin friction distributions for the NACA-63415 airfoil at a Reynolds number of 2000000 and at the design angle of attack.

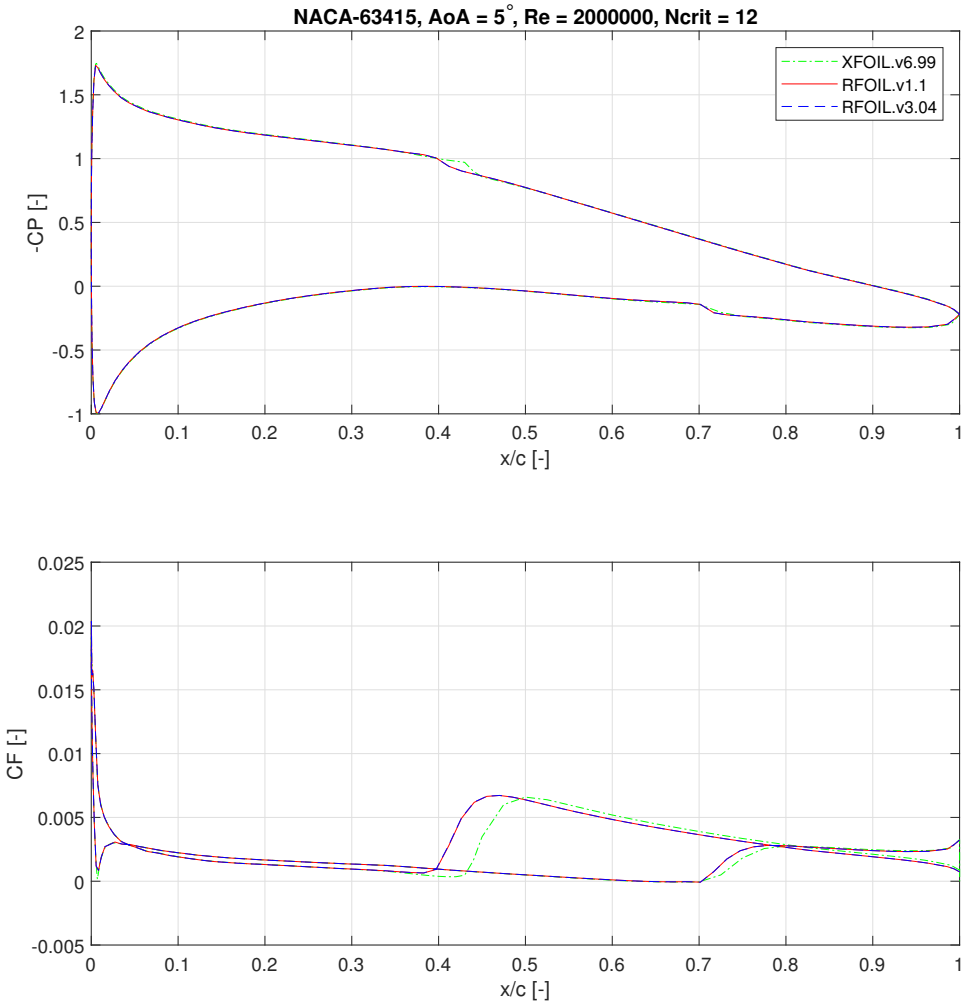

Figure B.337: Comparison between experimental and numerical polars for the NACA-63415 airfoil at a Reynolds number of 3000000. Simulation time to generate the polars by means the different codes and the number of converged polar points are depicted between parentheses.

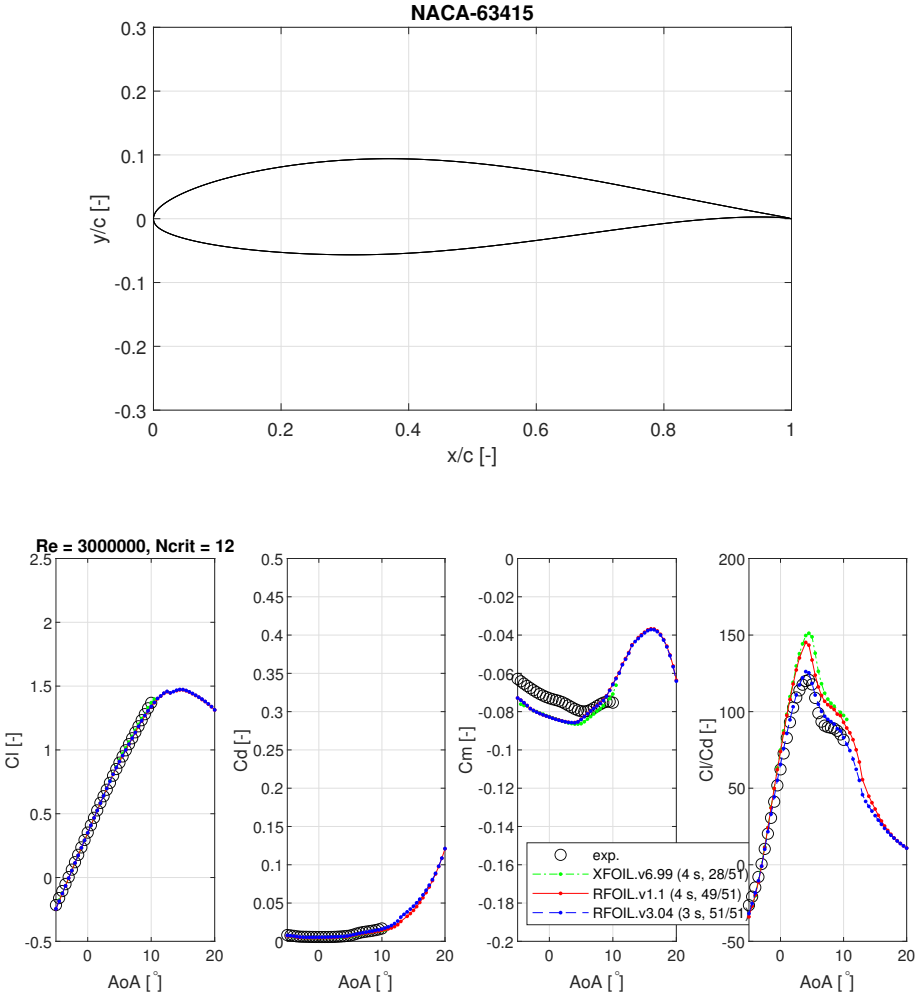

Figure B.338: Differences between experimental and numerical polars for the NACA-63415 airfoil at a Reynolds number of 3000000. Vertical black lines in the middle subplot indicate, from left to right, the angle of attack corresponding to the minimum drag coefficient, maximum lift to drag ratio and maximum lift coefficient, respectively.

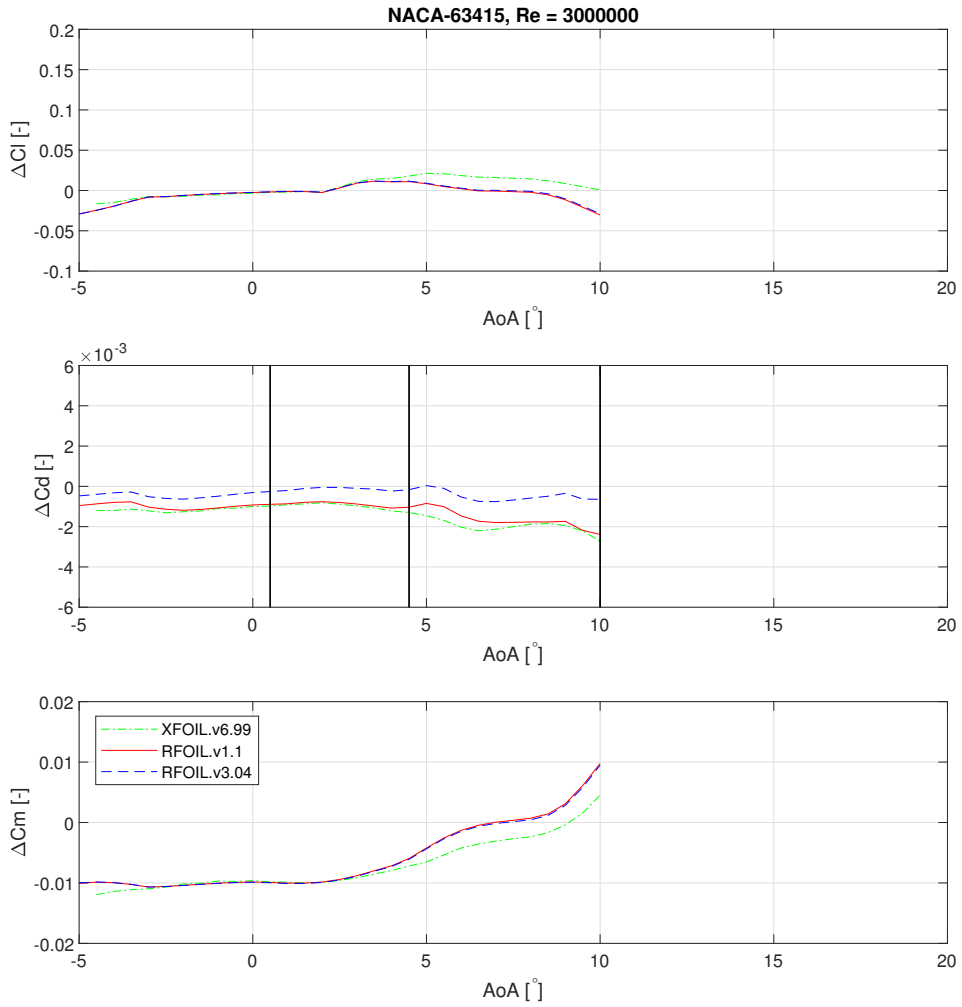

Figure B.339: Comparison between experimental and numerical pressure and skin friction distributions for the NACA-63415 airfoil at a Reynolds number of 3000000 and at the design angle of attack.

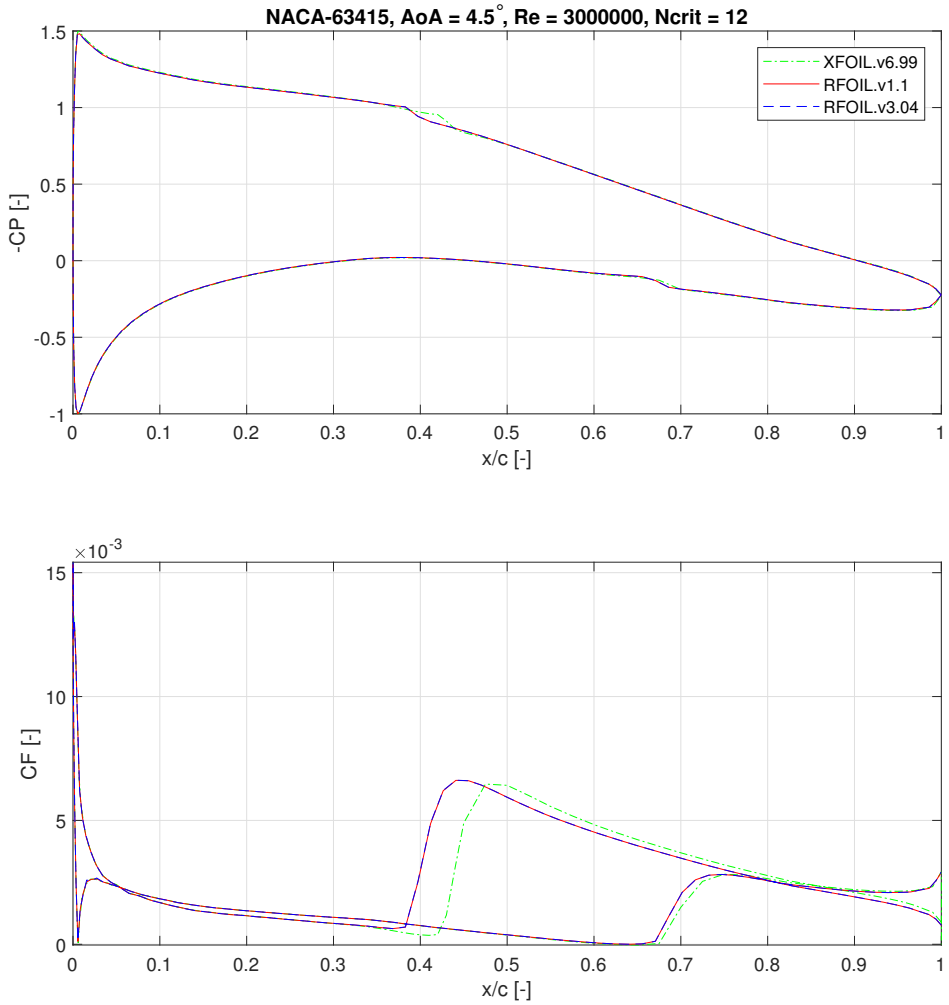

Figure B.340: Comparison between experimental and numerical polars for the NACA-63415 airfoil at a Reynolds number of 6000000. Simulation time to generate the polars by means the different codes and the number of converged polar points are depicted between parentheses.

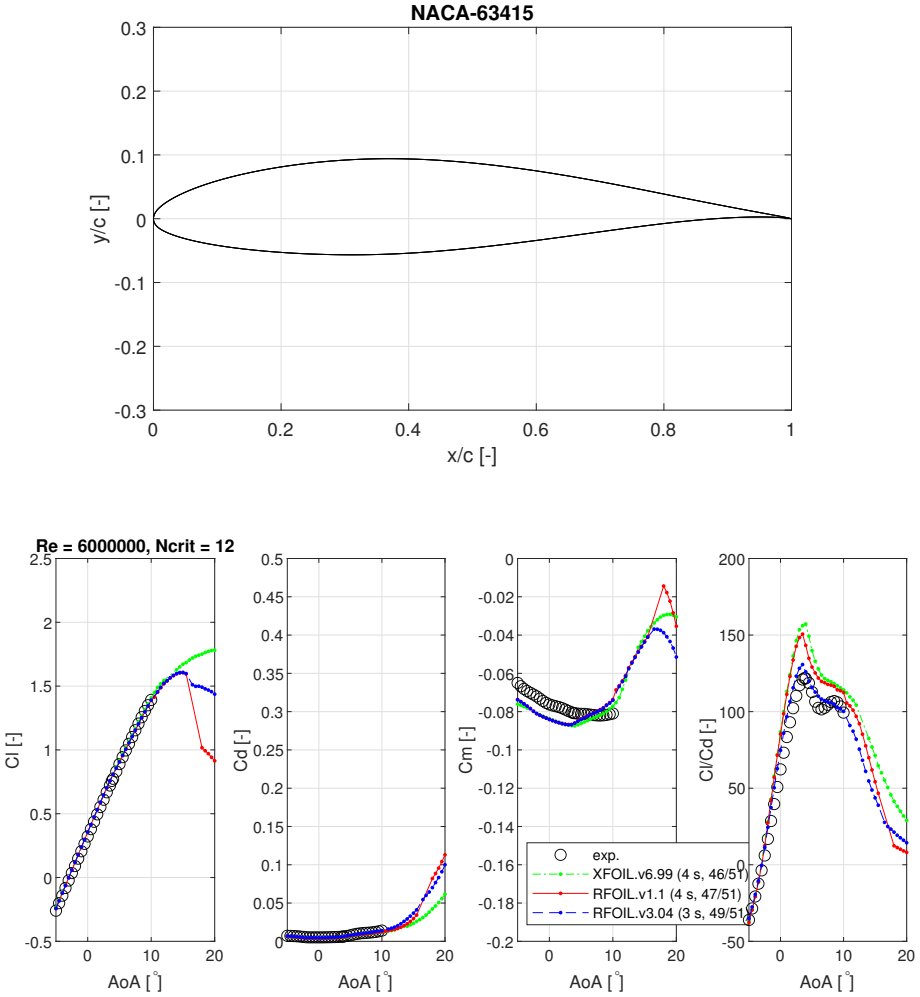

Figure B.341: Differences between experimental and numerical polars for the NACA-63415 airfoil at a Reynolds number of 6000000. Vertical black lines in the middle subplot indicate, from left to right, the angle of attack corresponding to the minimum drag coefficient, maximum lift to drag ratio and maximum lift coefficient, respectively.

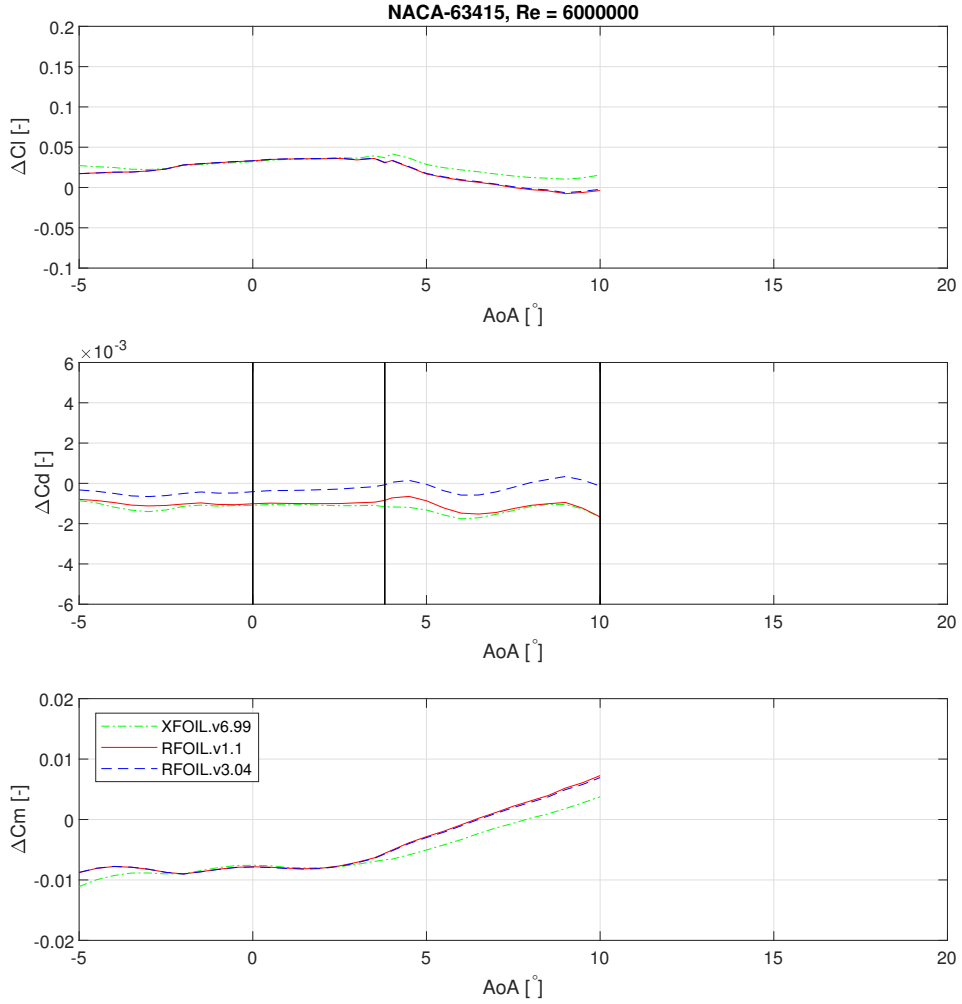

Figure B.342: Comparison between experimental and numerical pressure and skin friction distributions for the NACA-63415 airfoil at a Reynolds number of 6000000 and at the design angle of attack.

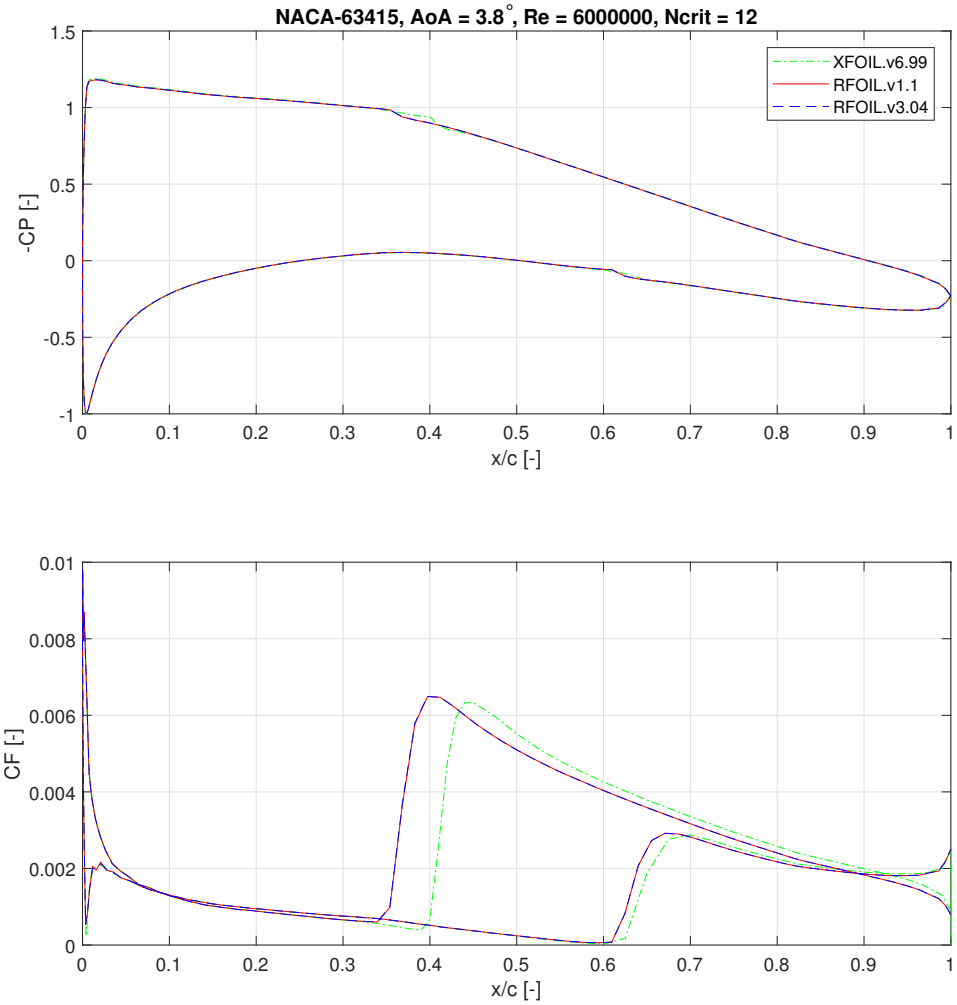

Figure B.343: Comparison between experimental and numerical polars for the NACA-63415 airfoil at a Reynolds number of 700000. Simulation time to generate the polars by means the different codes and the number of converged polar points are depicted between parentheses.

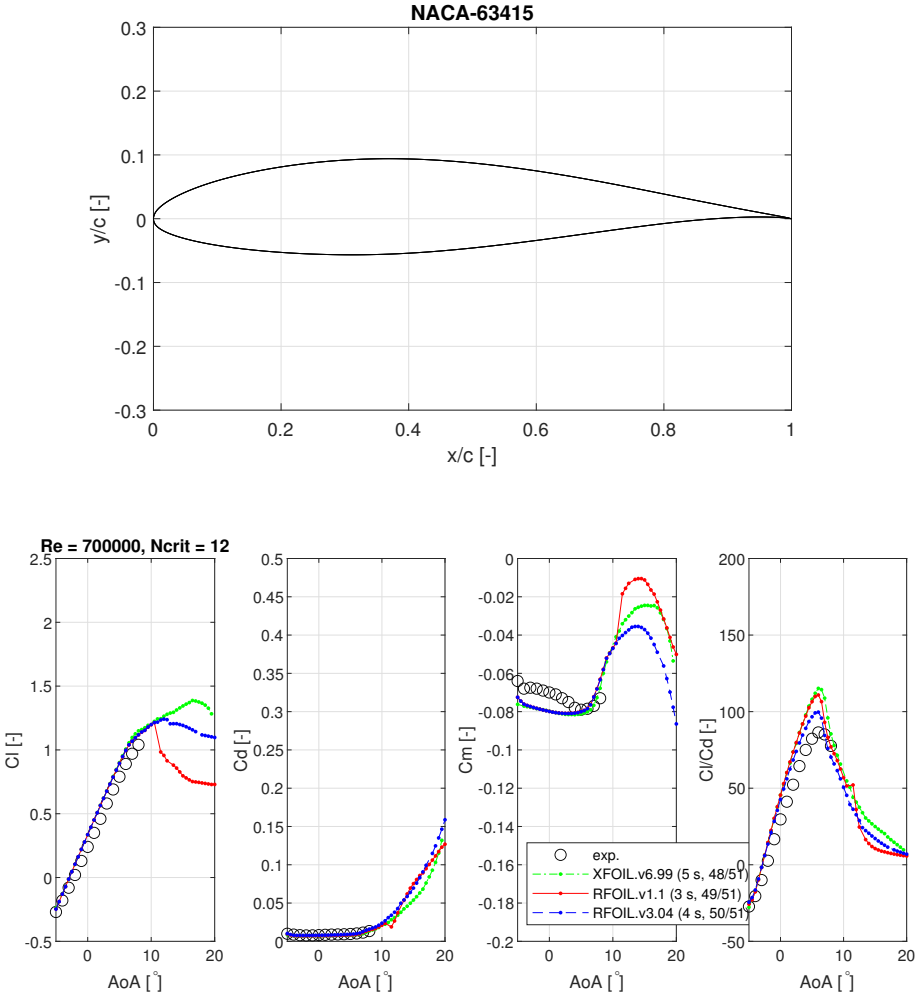

Figure B.344: Differences between experimental and numerical polars for the NACA-63415 airfoil at a Reynolds number of 700000. Vertical black lines in the middle subplot indicate, from left to right, the angle of attack corresponding to the minimum drag coefficient, maximum lift to drag ratio and maximum lift coefficient, respectively.

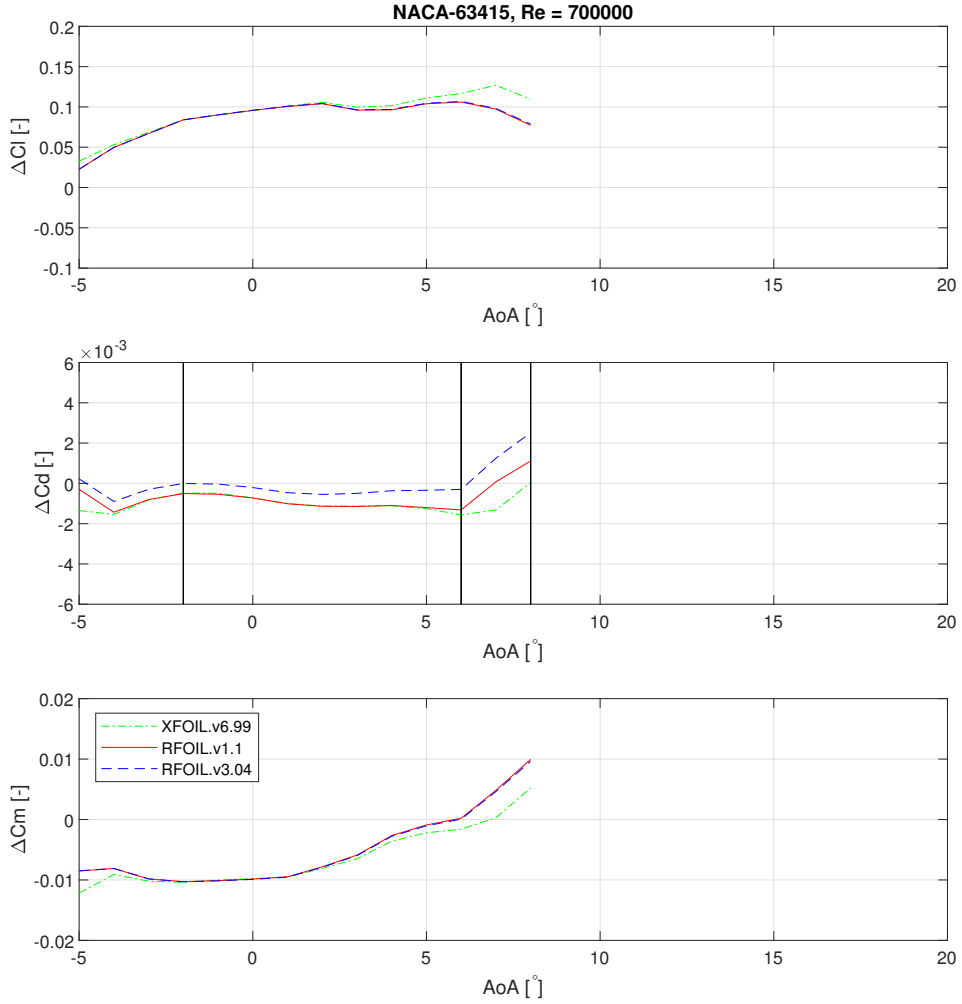

Figure B.345: Comparison between experimental and numerical pressure and skin friction distributions for the NACA-63415 airfoil at a Reynolds number of 700000 and at the design angle of attack.

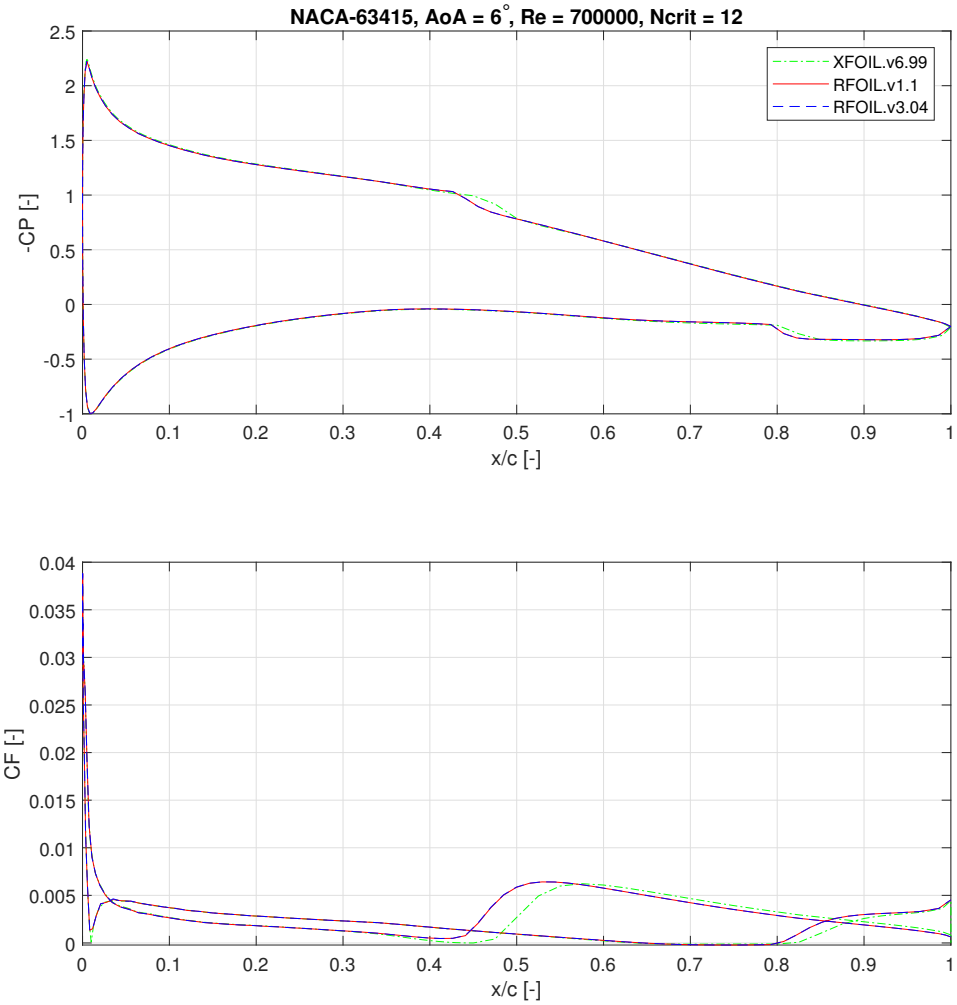

Figure B.346: Comparison between experimental and numerical polars for the NACA-63418 airfoil at a Reynolds number of 3000000. Simulation time to generate the polars by means the different codes and the number of converged polar points are depicted between parentheses.

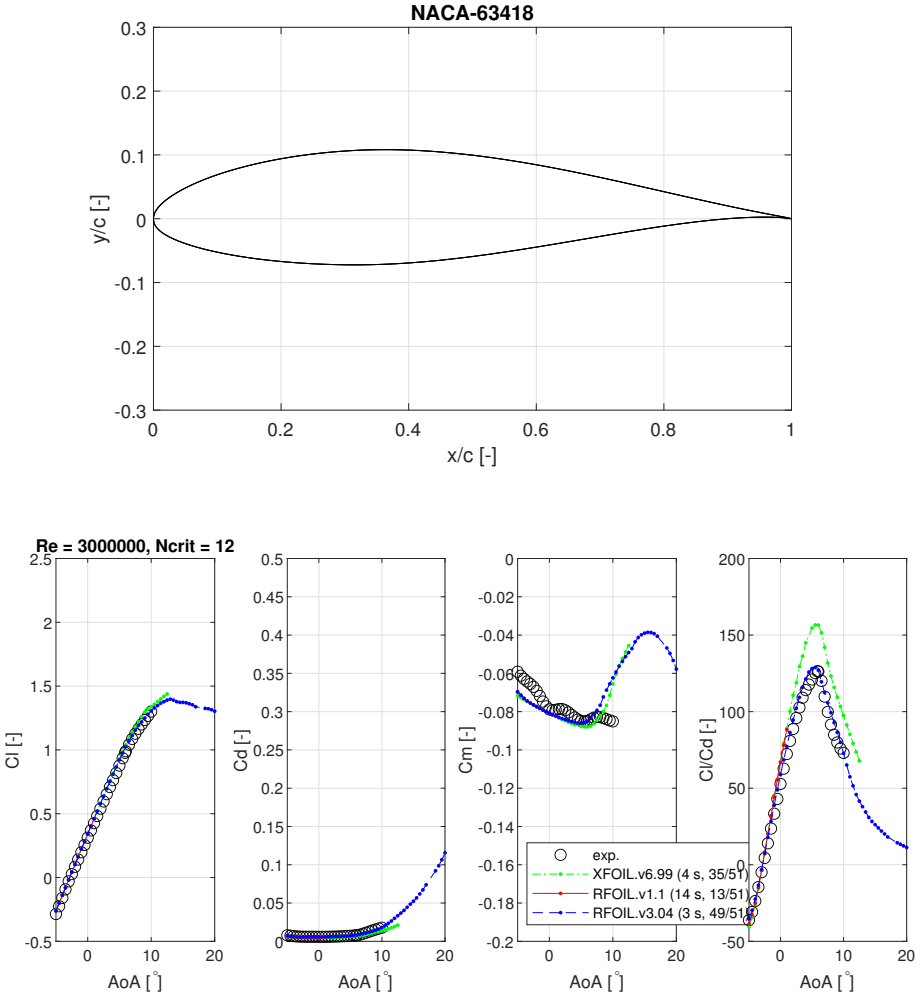

Figure B.347: Differences between experimental and numerical polars for the NACA-63418 airfoil at a Reynolds number of 3000000. Vertical black lines in the middle subplot indicate, from left to right, the angle of attack corresponding to the minimum drag coefficient, maximum lift to drag ratio and maximum lift coefficient, respectively.

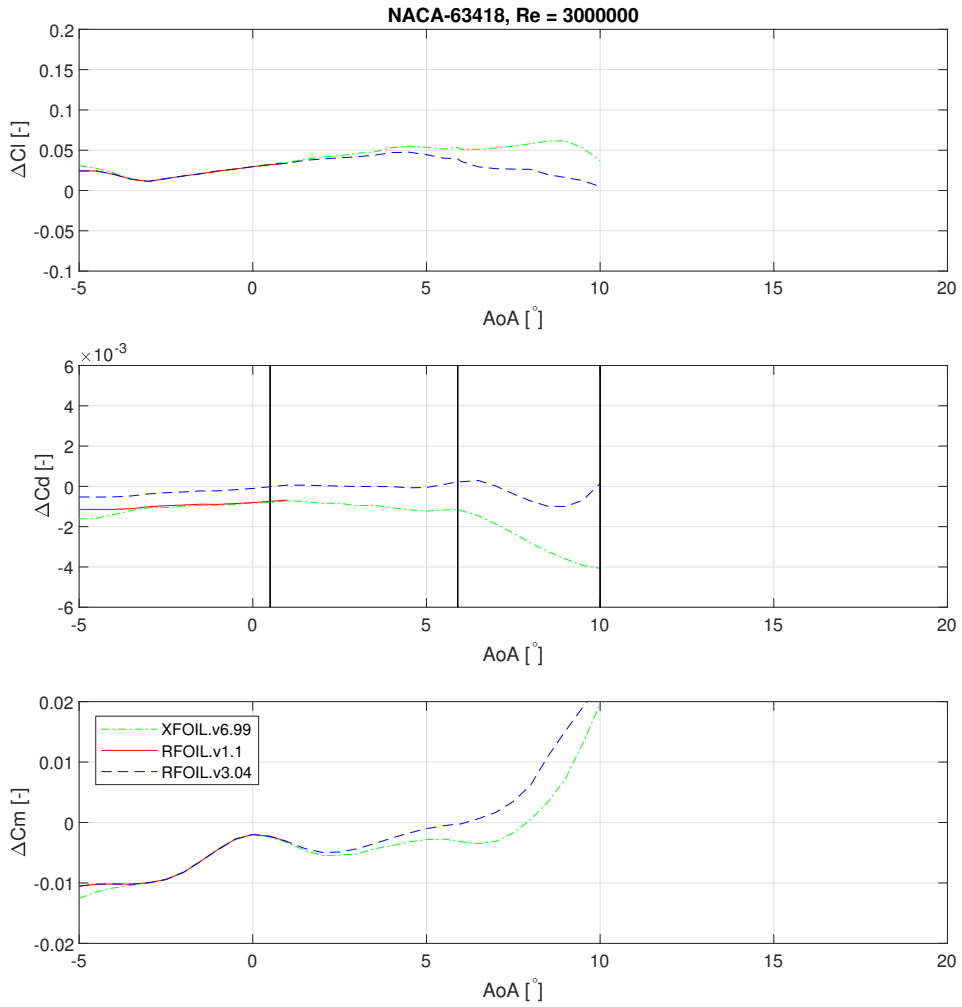

Figure B.348: Comparison between experimental and numerical pressure and skin friction distributions for the NACA-63418 airfoil at a Reynolds number of 3000000 and at the design angle of attack.

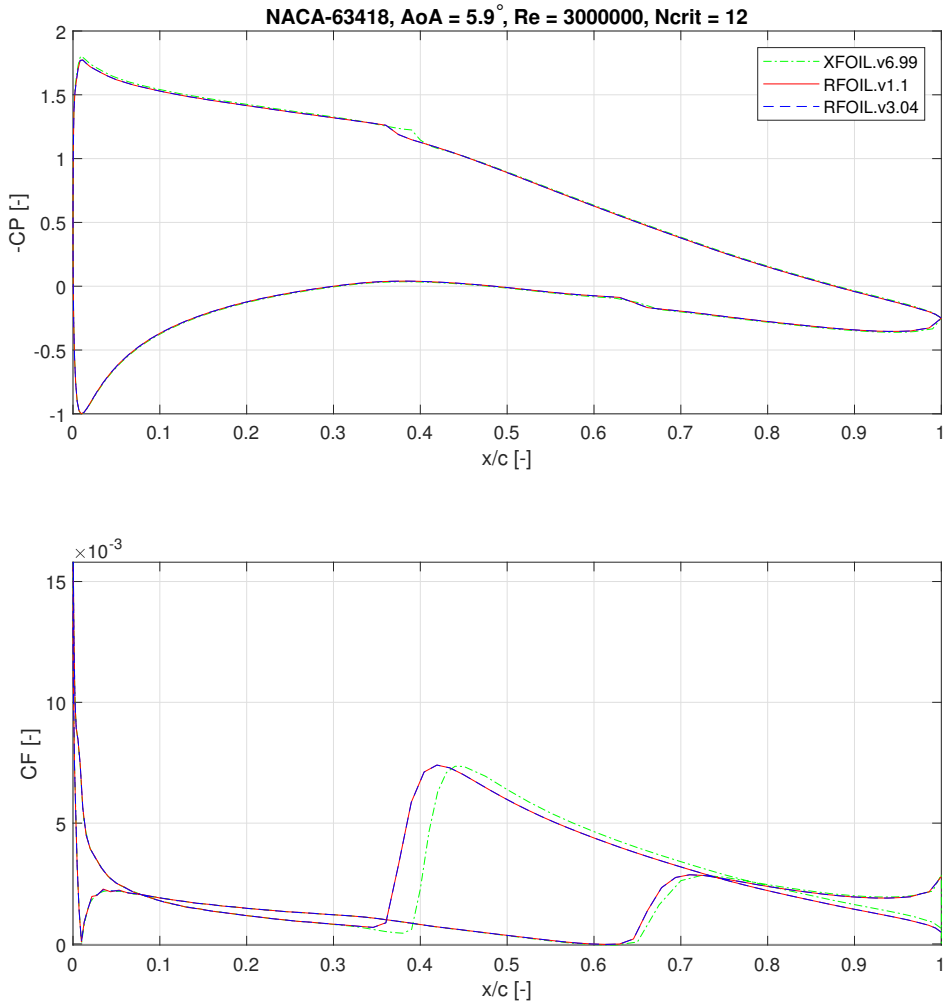

Figure B.349: Comparison between experimental and numerical polars for the NACA-63418 airfoil at a Reynolds number of 6000000. Simulation time to generate the polars by means the different codes and the number of converged polar points are depicted between parentheses.

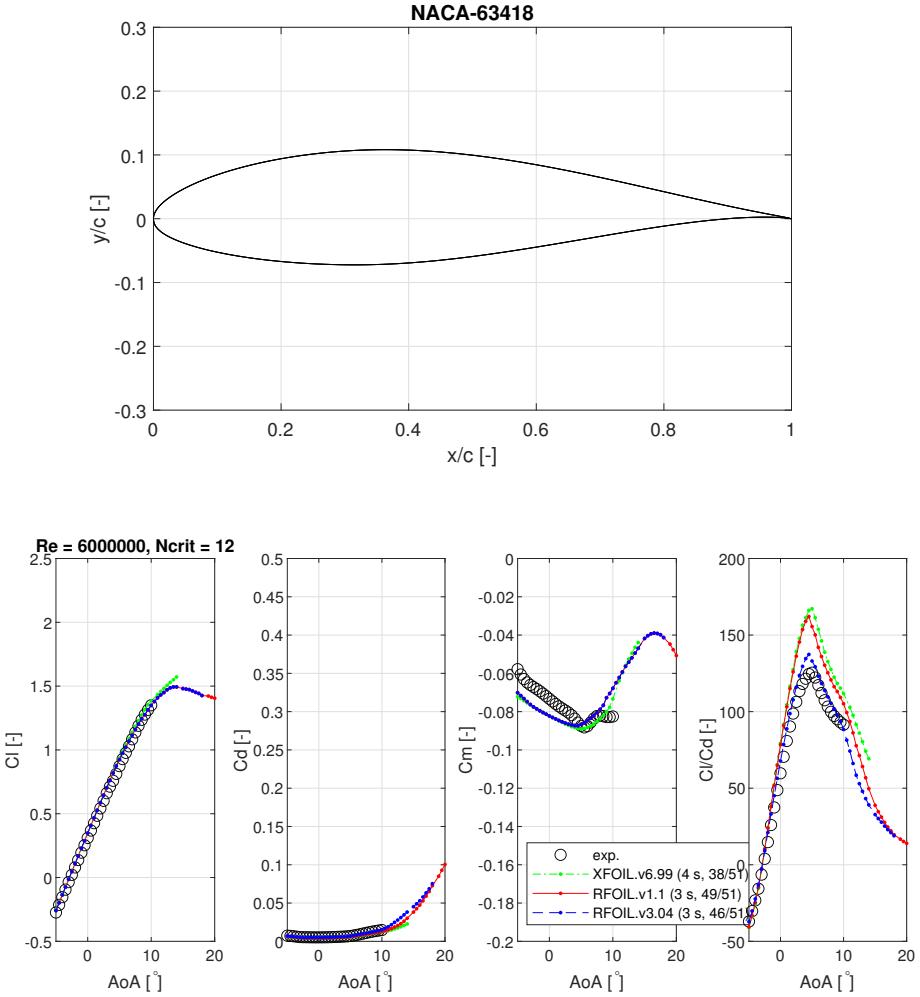

Figure B.350: Differences between experimental and numerical polars for the NACA-63418 airfoil at a Reynolds number of 6000000. Vertical black lines in the middle subplot indicate, from left to right, the angle of attack corresponding to the minimum drag coefficient, maximum lift to drag ratio and maximum lift coefficient, respectively.

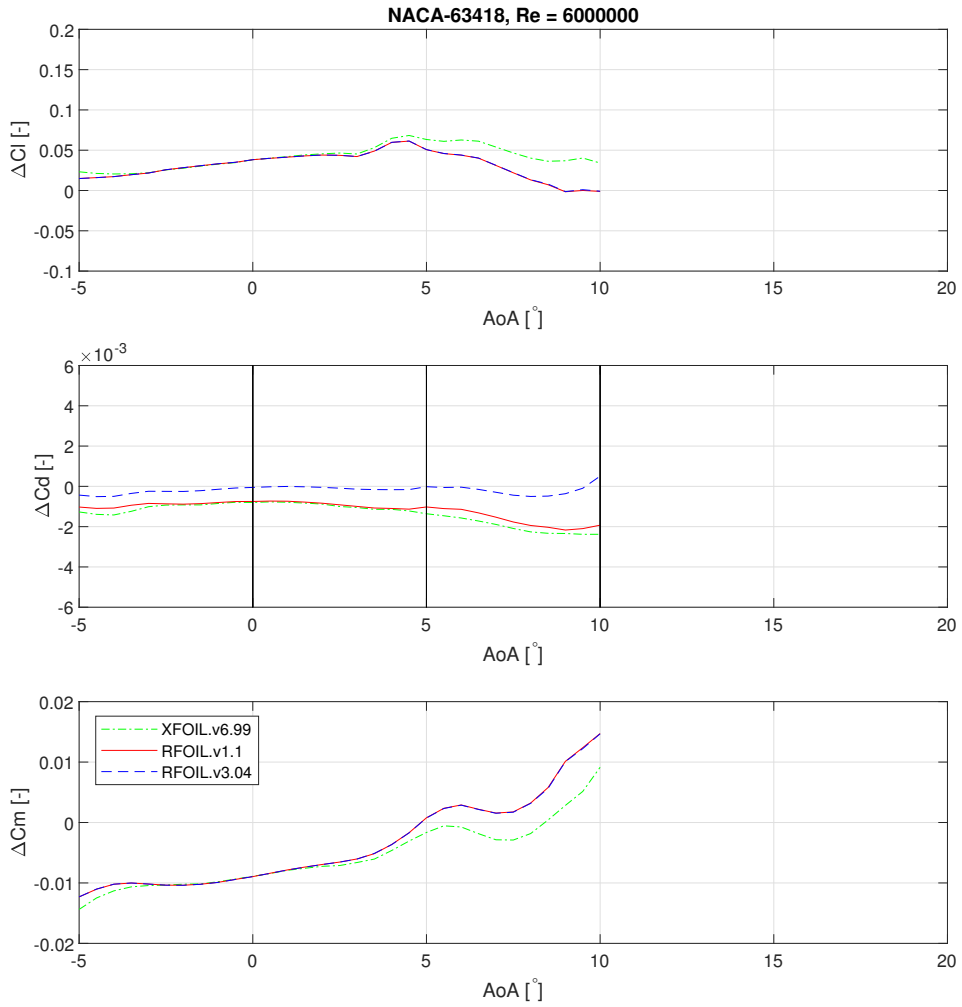

Figure B.351: Comparison between experimental and numerical pressure and skin friction distributions for the NACA-63418 airfoil at a Reynolds number of 6000000 and at the design angle of attack.

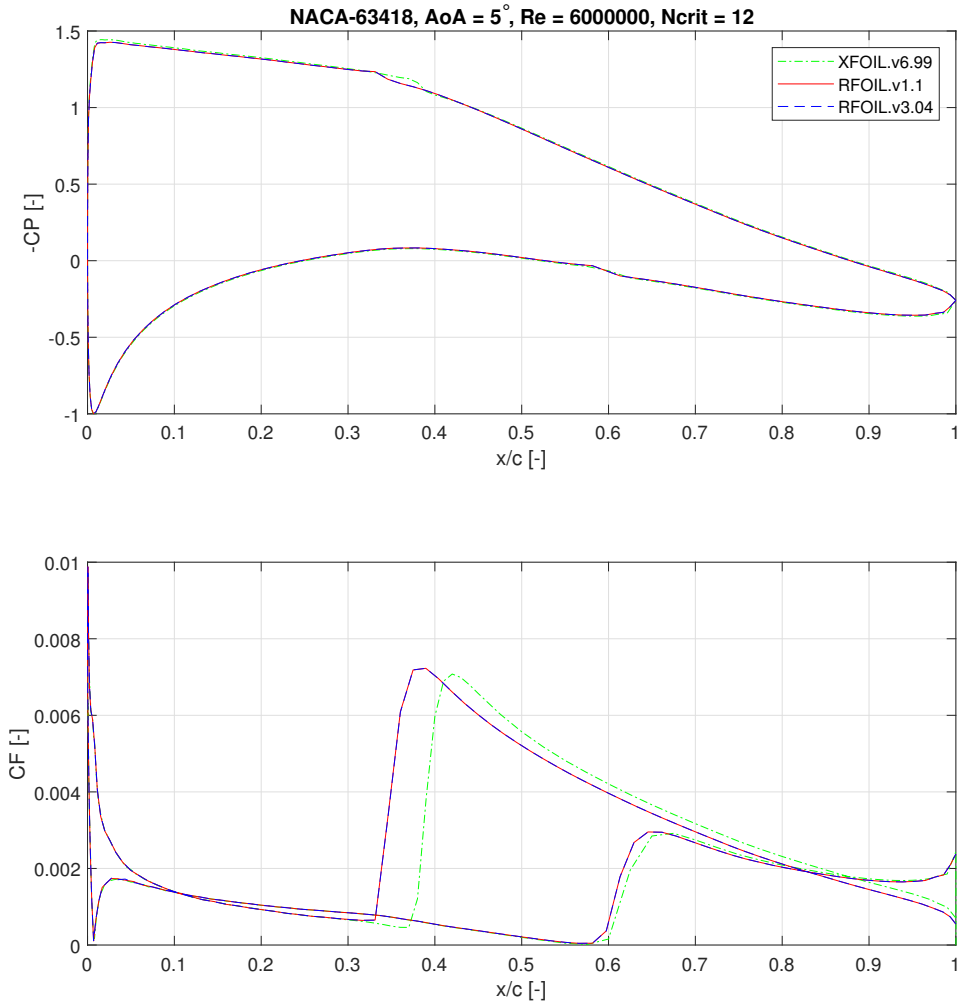

Figure B.352: Comparison between experimental and numerical polars for the NACA-63421 airfoil at a Reynolds number of 3000000. Simulation time to generate the polars by means the different codes and the number of converged polar points are depicted between parentheses.

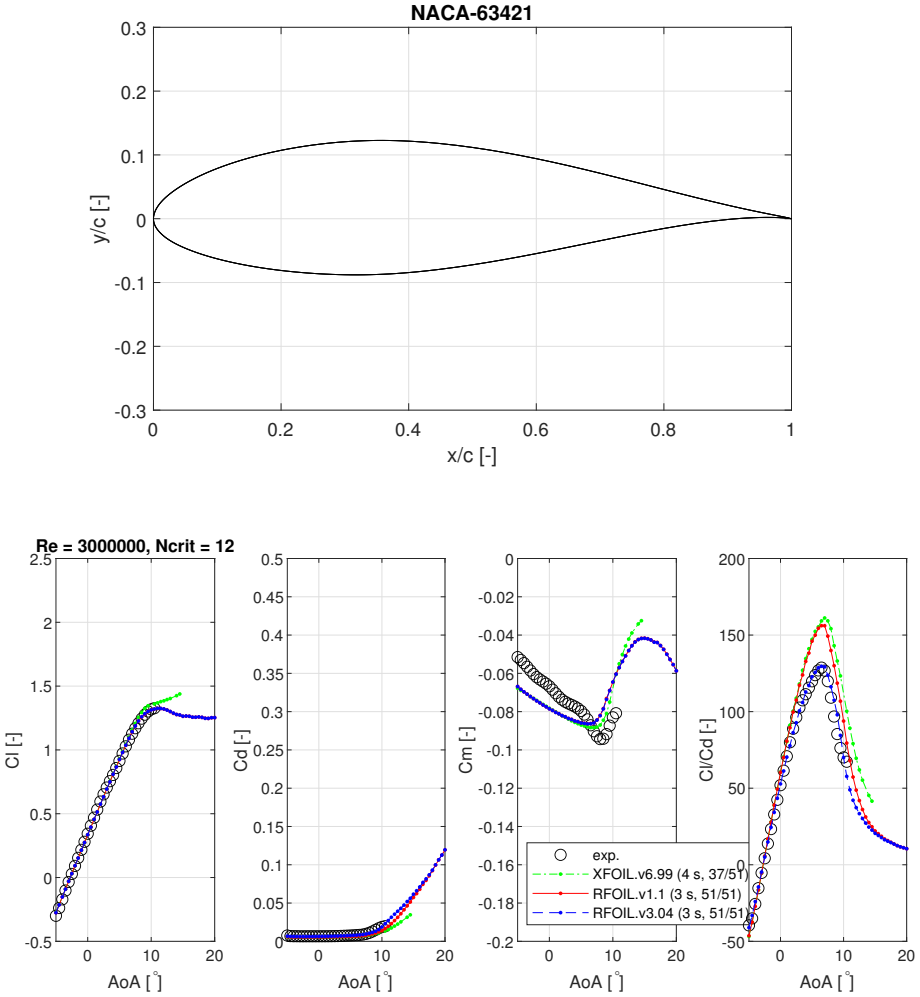

Figure B.353: Differences between experimental and numerical polars for the NACA-63421 airfoil at a Reynolds number of 3000000. Vertical black lines in the middle subplot indicate, from left to right, the angle of attack corresponding to the minimum drag coefficient, maximum lift to drag ratio and maximum lift coefficient, respectively.

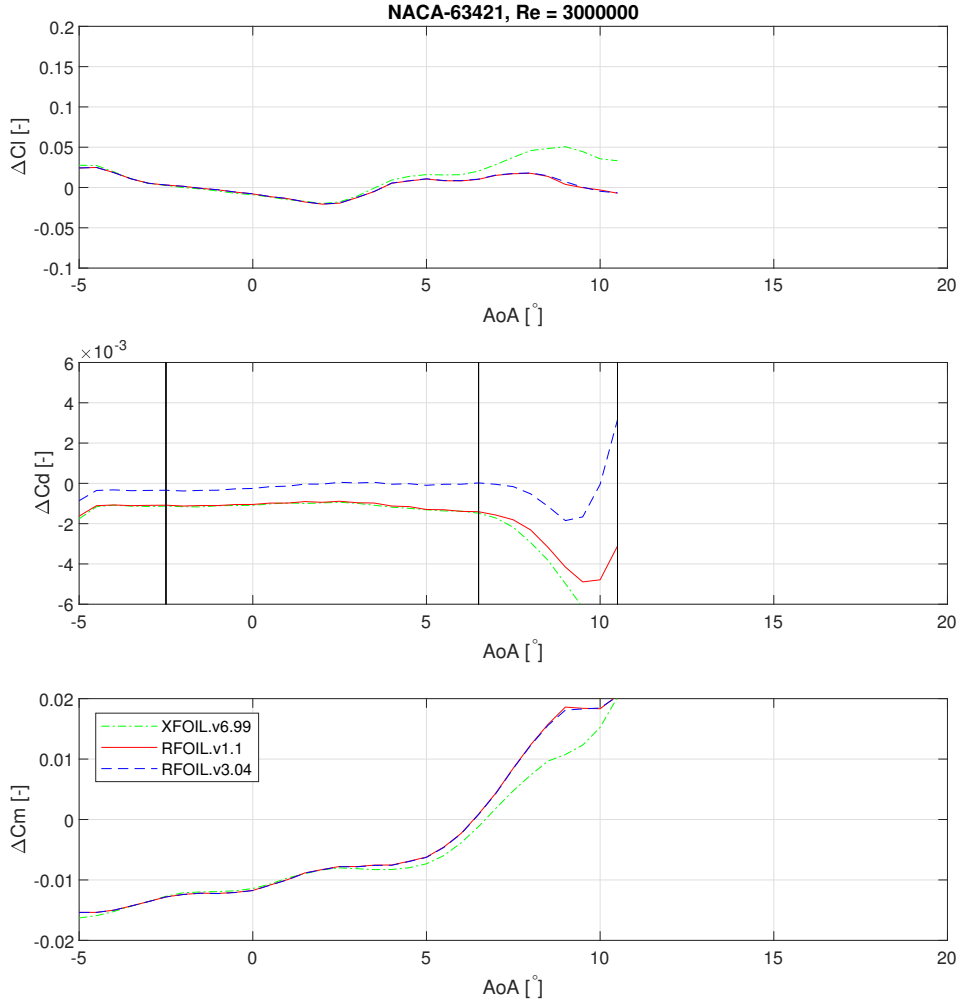

Figure B.354: Comparison between experimental and numerical pressure and skin friction distributions for the NACA-63421 airfoil at a Reynolds number of 3000000 and at the design angle of attack.

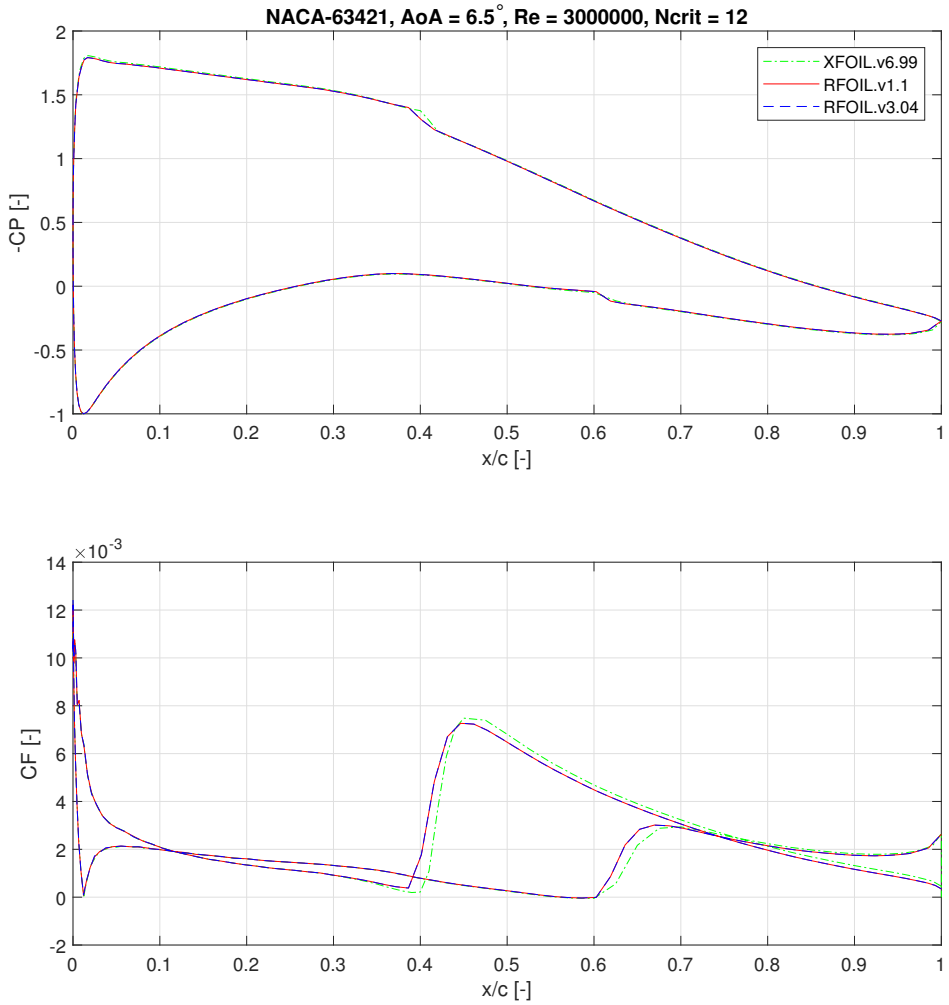

Figure B.355: Comparison between experimental and numerical polars for the NACA-63421 airfoil at a Reynolds number of 6000000. Simulation time to generate the polars by means the different codes and the number of converged polar points are depicted between parentheses.

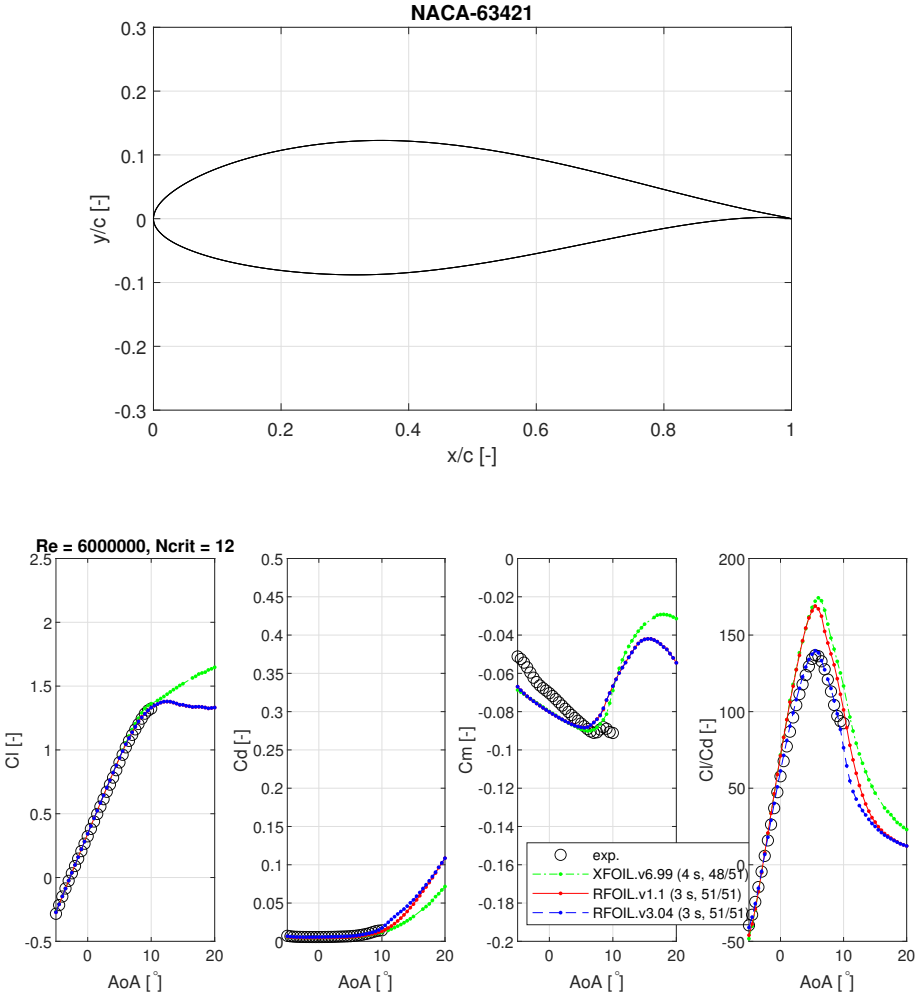

Figure B.356: Differences between experimental and numerical polars for the NACA-63421 airfoil at a Reynolds number of 6000000. Vertical black lines in the middle subplot indicate, from left to right, the angle of attack corresponding to the minimum drag coefficient, maximum lift to drag ratio and maximum lift coefficient, respectively.

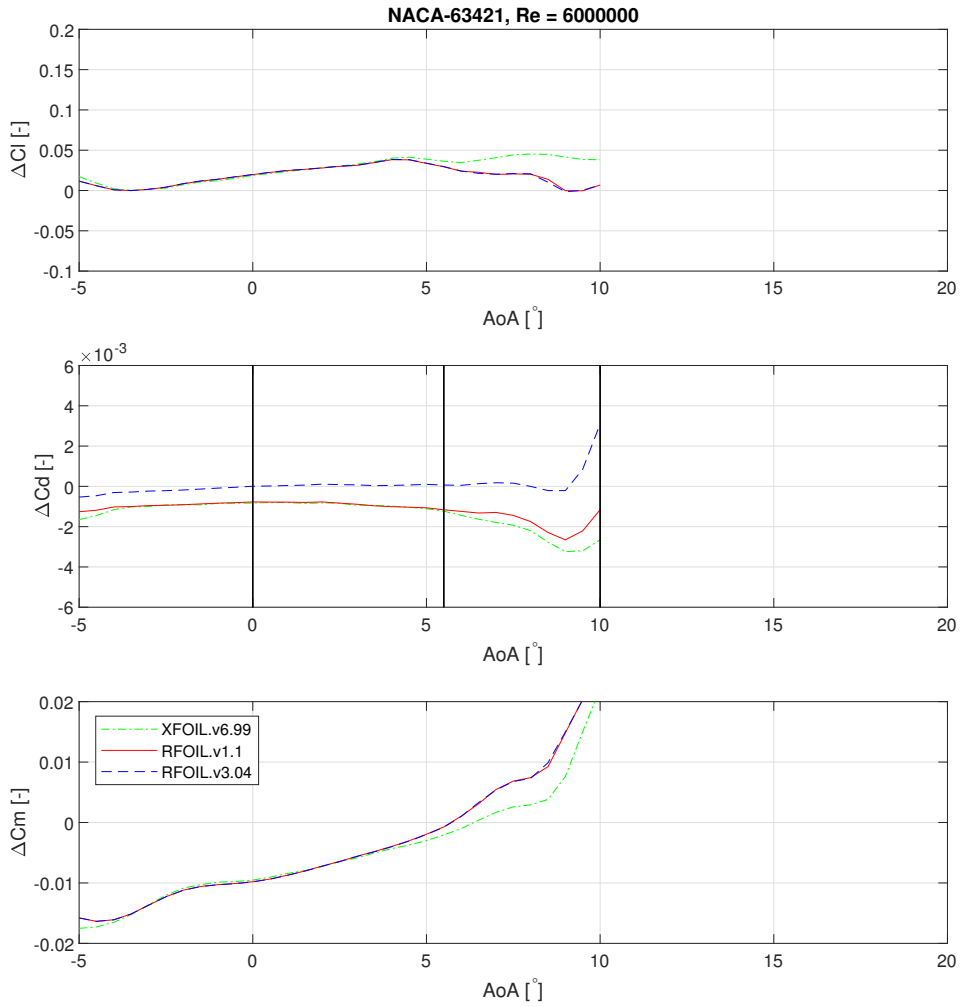

Figure B.357: Comparison between experimental and numerical pressure and skin friction distributions for the NACA-63421 airfoil at a Reynolds number of 6000000 and at the design angle of attack.

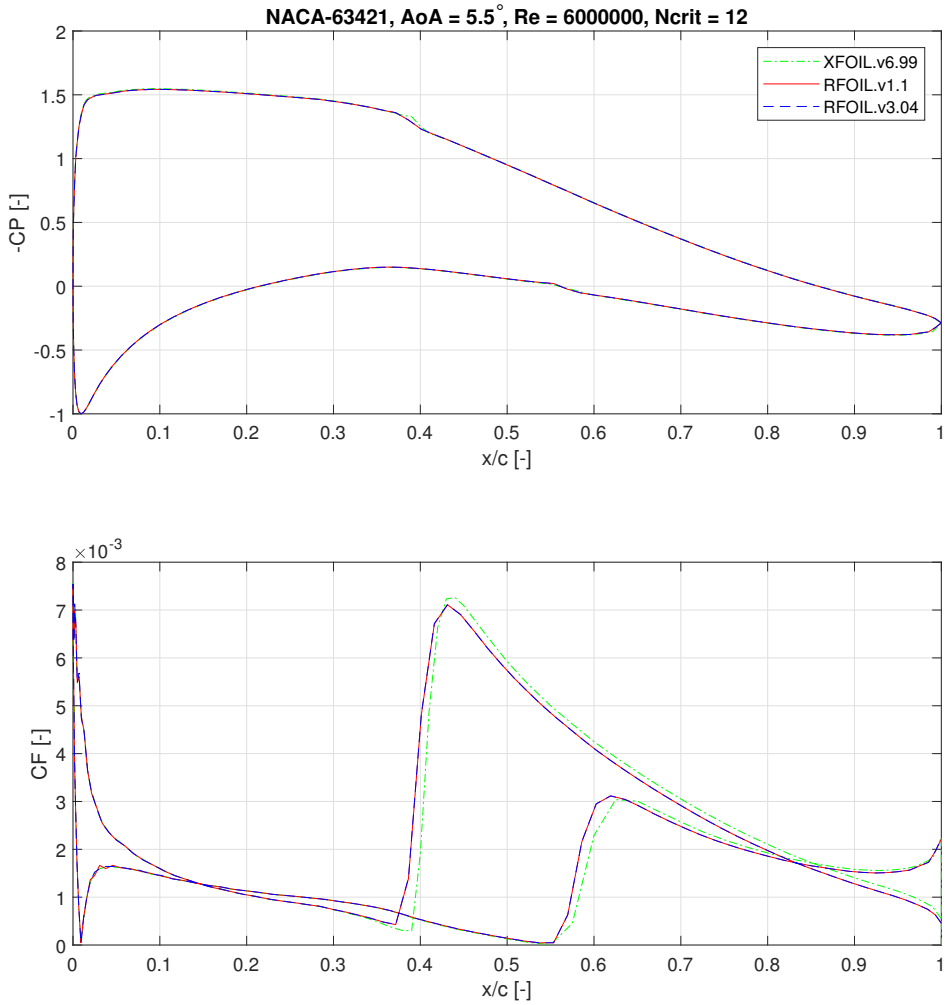

Figure B.358: Comparison between experimental and numerical polars for the NACA-63615 airfoil at a Reynolds number of 3000000. Simulation time to generate the polars by means the different codes and the number of converged polar points are depicted between parentheses.

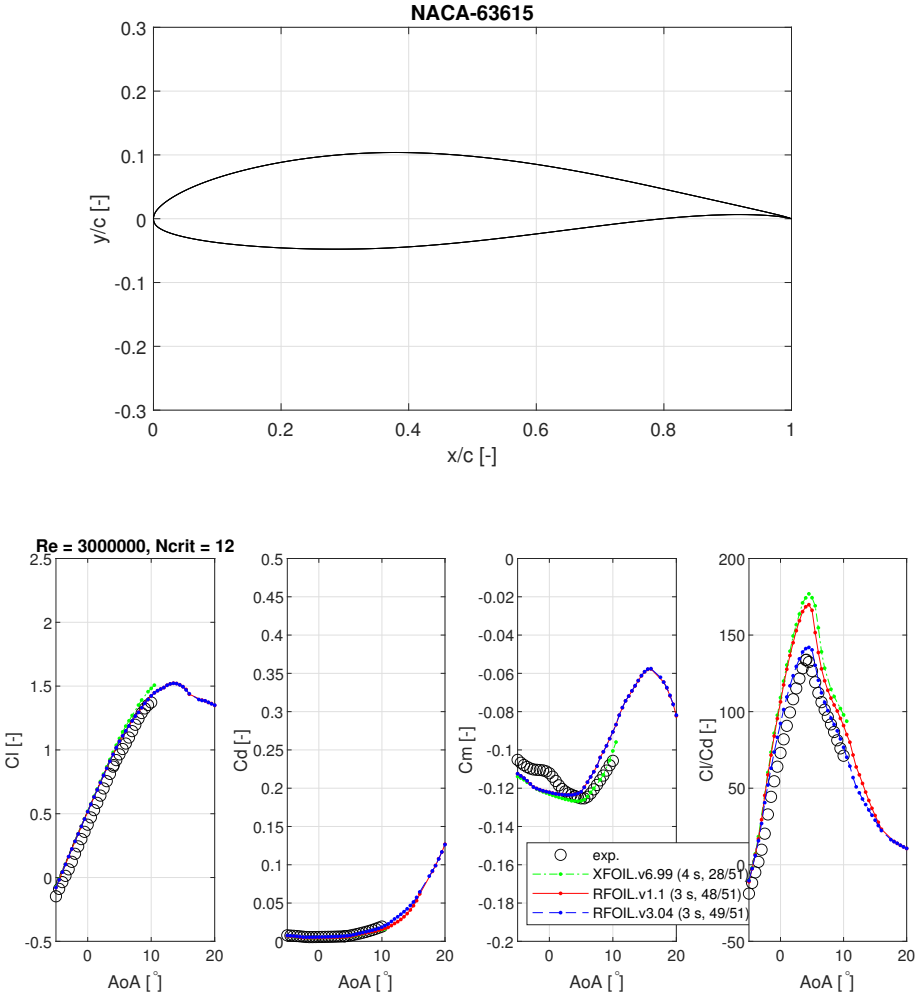

Figure B.359: Differences between experimental and numerical polars for the NACA-63615 airfoil at a Reynolds number of 3000000. Vertical black lines in the middle subplot indicate, from left to right, the angle of attack corresponding to the minimum drag coefficient, maximum lift to drag ratio and maximum lift coefficient, respectively.

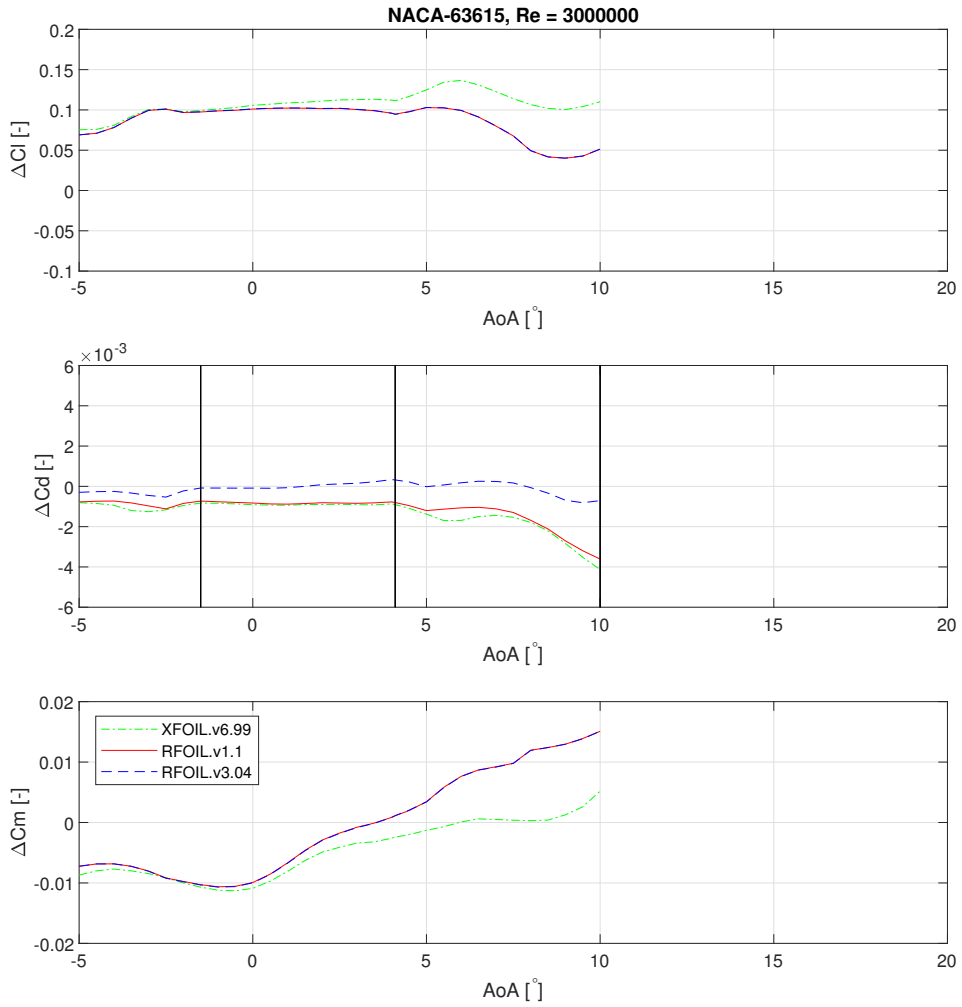

Figure B.360: Comparison between experimental and numerical pressure and skin friction distributions for the NACA-63615 airfoil at a Reynolds number of 3000000 and at the design angle of attack.

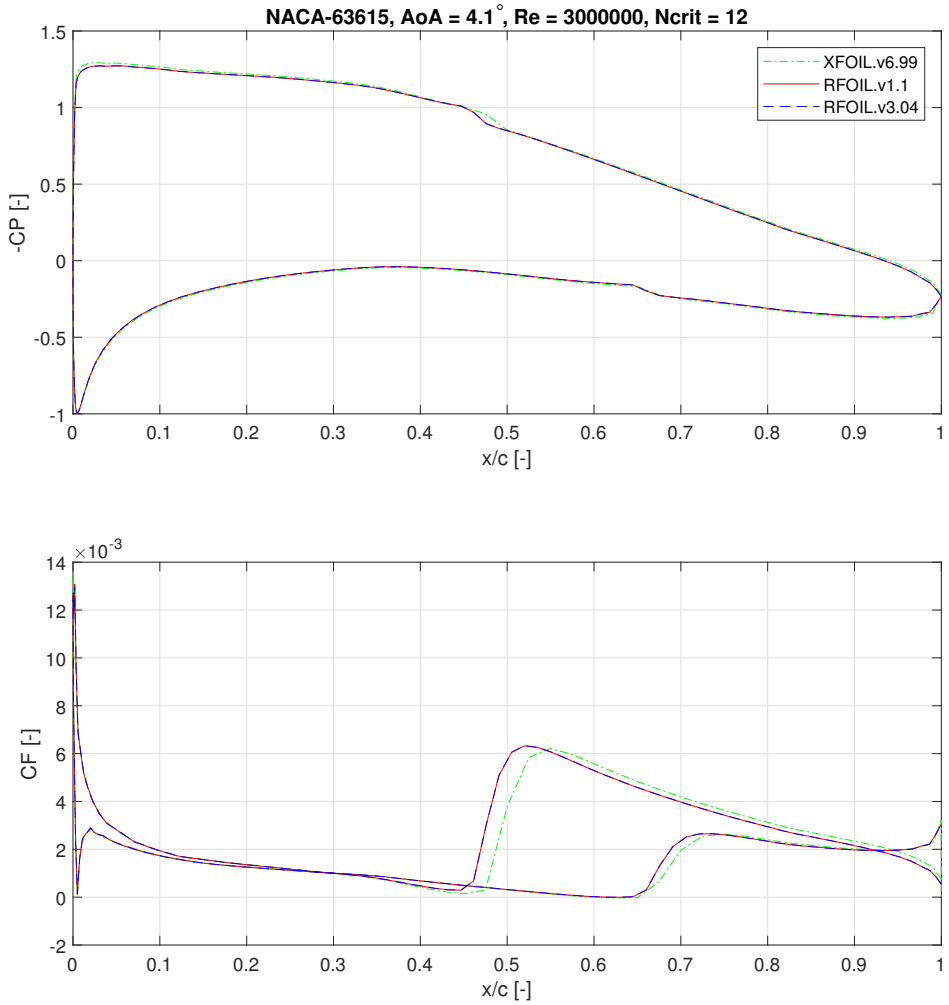

Figure B.361: Comparison between experimental and numerical polars for the NACA-63615 airfoil at a Reynolds number of 6000000. Simulation time to generate the polars by means the different codes and the number of converged polar points are depicted between parentheses.

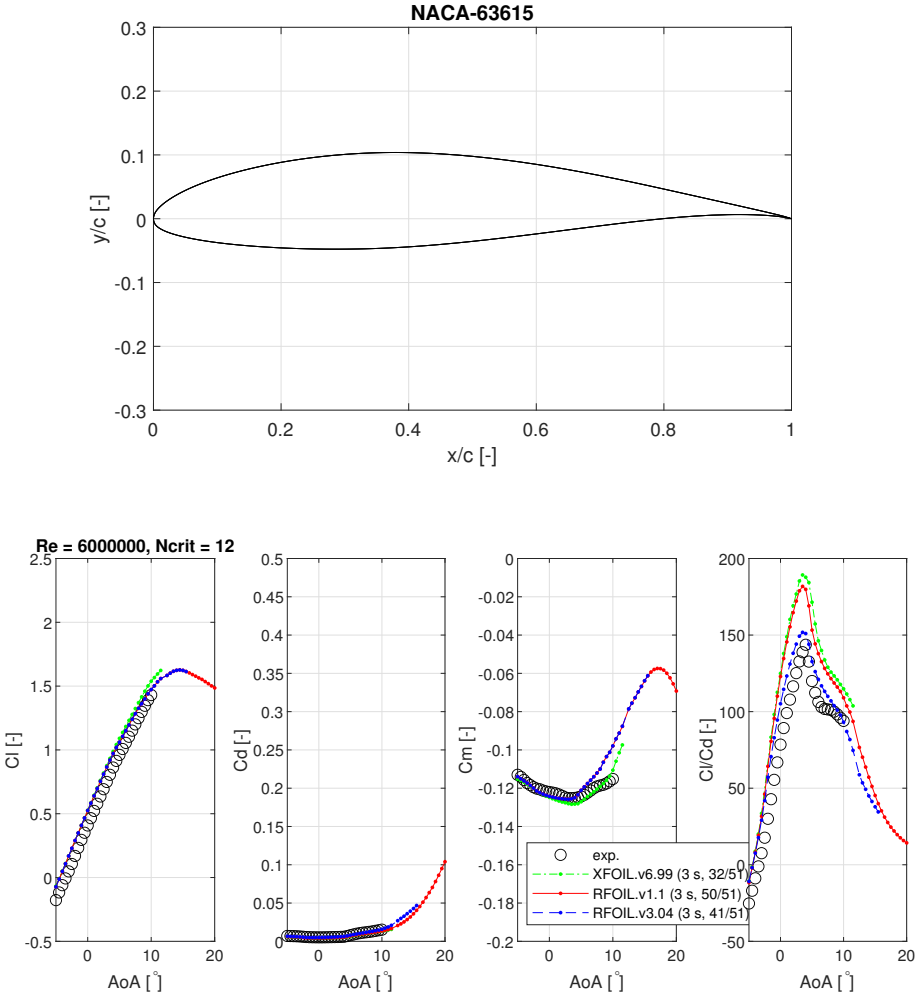

Figure B.362: Differences between experimental and numerical polars for the NACA-63615 airfoil at a Reynolds number of 6000000. Vertical black lines in the middle subplot indicate, from left to right, the angle of attack corresponding to the minimum drag coefficient, maximum lift to drag ratio and maximum lift coefficient, respectively.

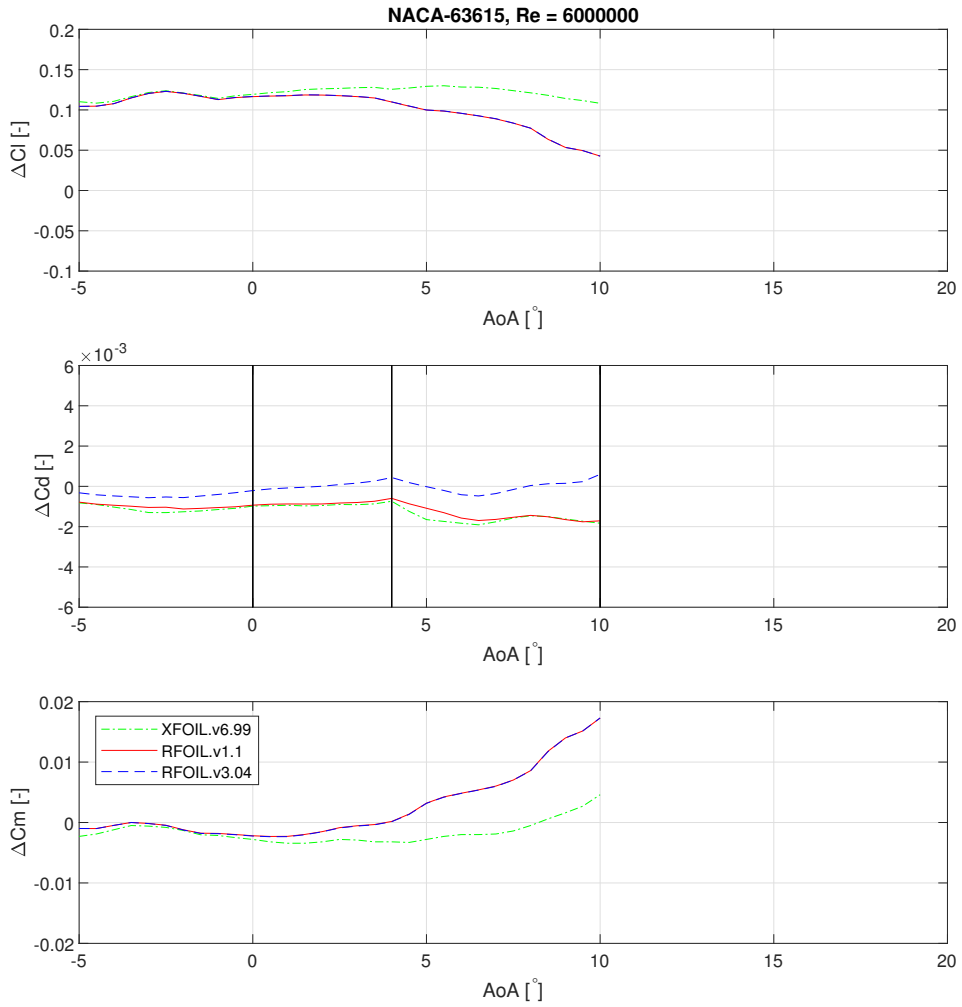

Figure B.363: Comparison between experimental and numerical pressure and skin friction distributions for the NACA-63615 airfoil at a Reynolds number of 6000000 and at the design angle of attack.

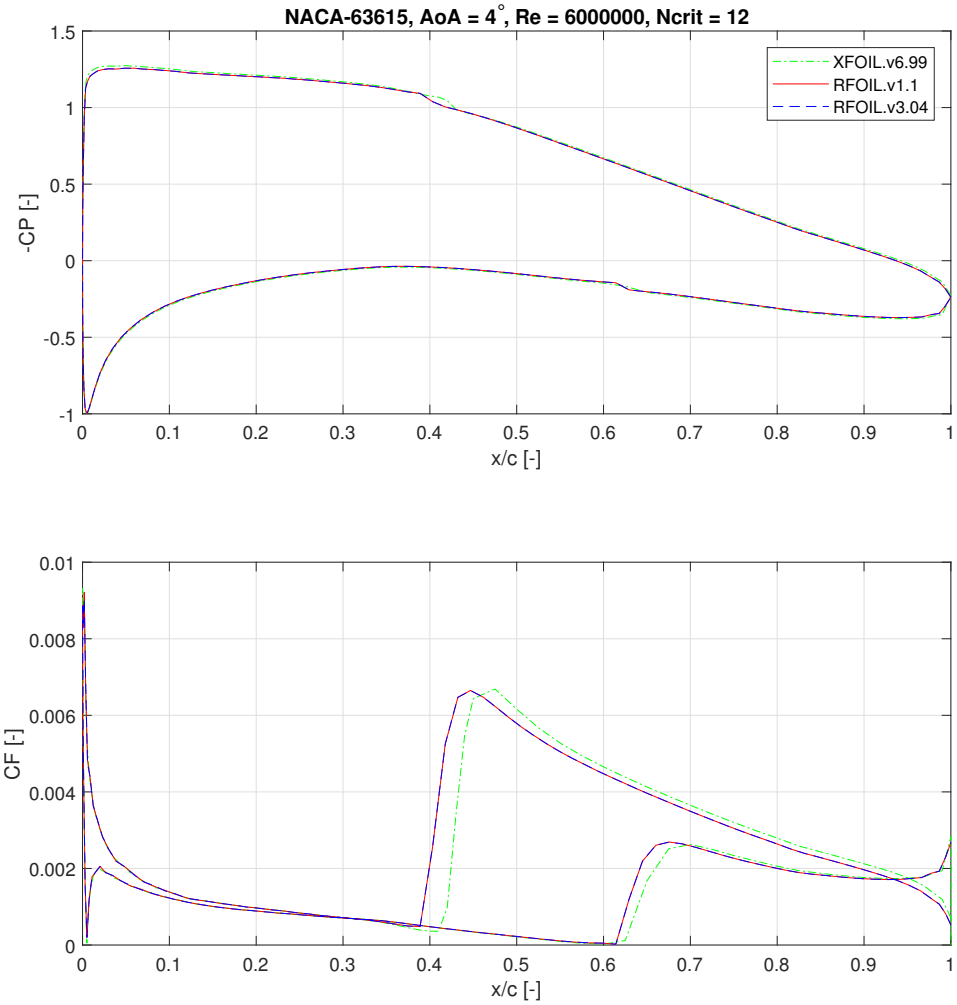

Figure B.364: Comparison between experimental and numerical polars for the NACA-63618 airfoil at a Reynolds number of 3000000. Simulation time to generate the polars by means the different codes and the number of converged polar points are depicted between parentheses.

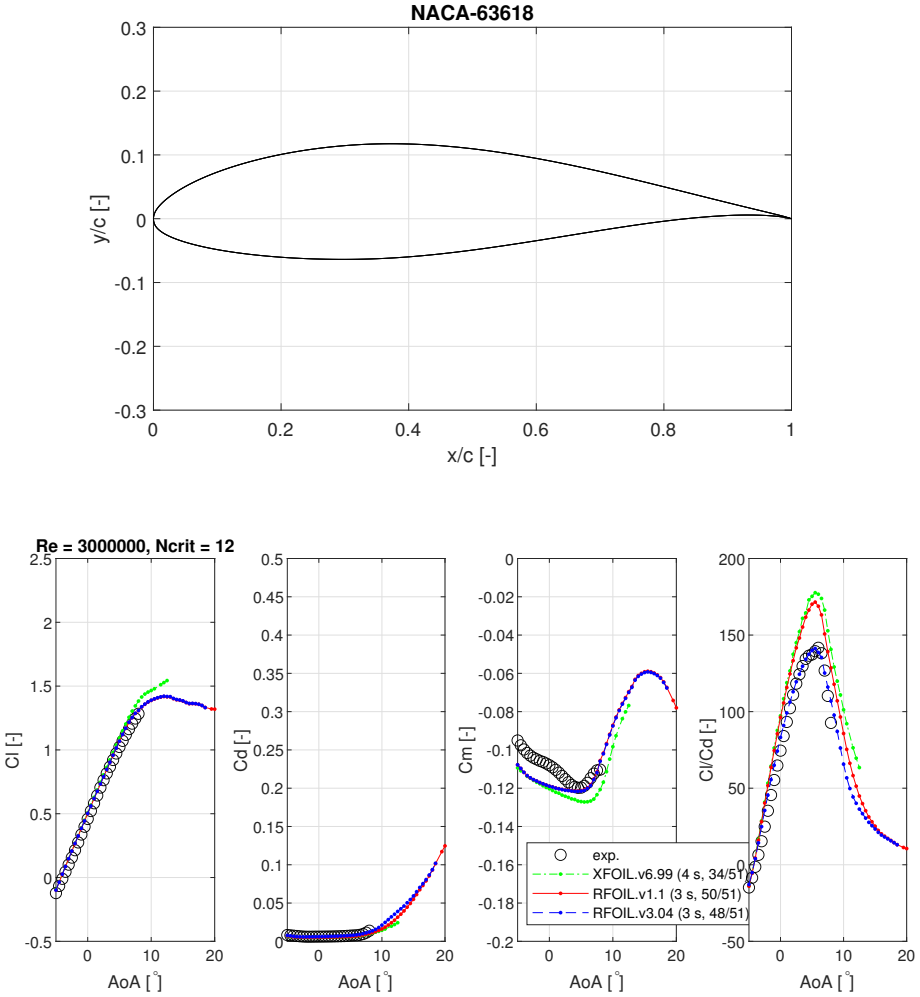

Figure B.365: Differences between experimental and numerical polars for the NACA-63618 airfoil at a Reynolds number of 3000000. Vertical black lines in the middle subplot indicate, from left to right, the angle of attack corresponding to the minimum drag coefficient, maximum lift to drag ratio and maximum lift coefficient, respectively.

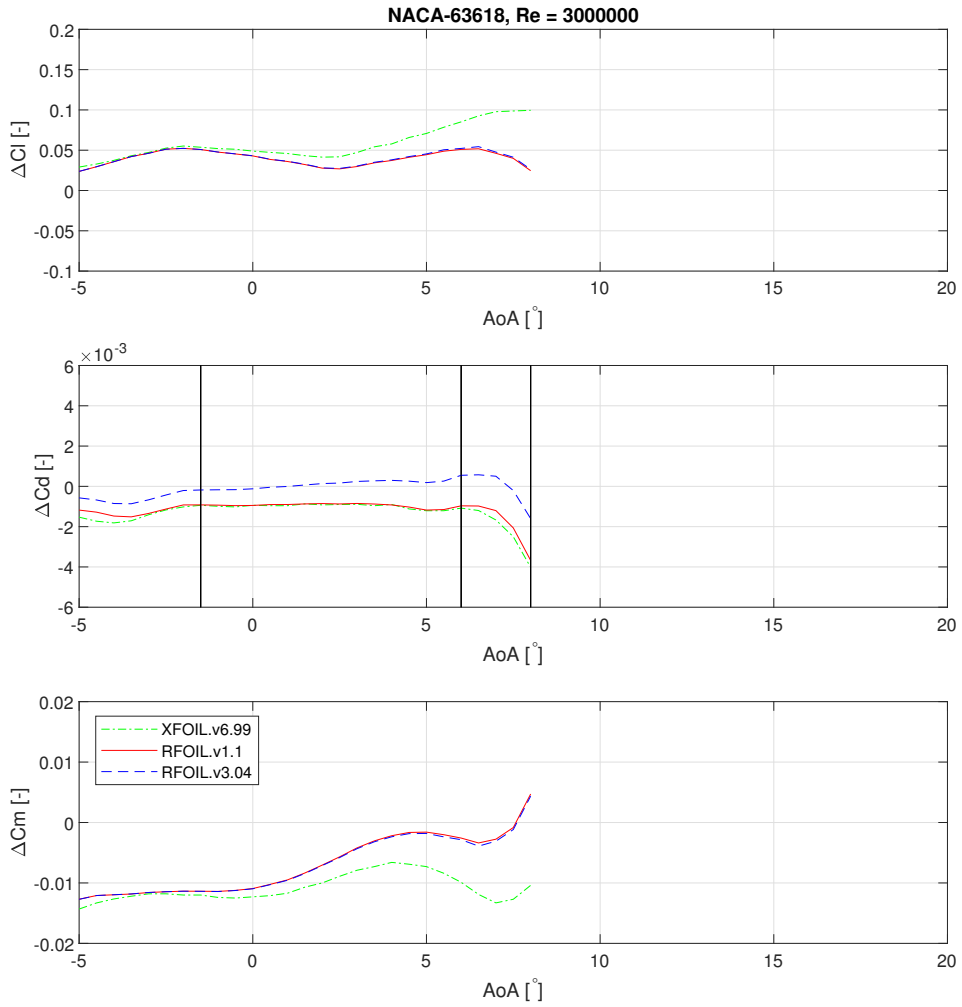

Figure B.366: Comparison between experimental and numerical pressure and skin friction distributions for the NACA-63618 airfoil at a Reynolds number of 3000000 and at the design angle of attack.

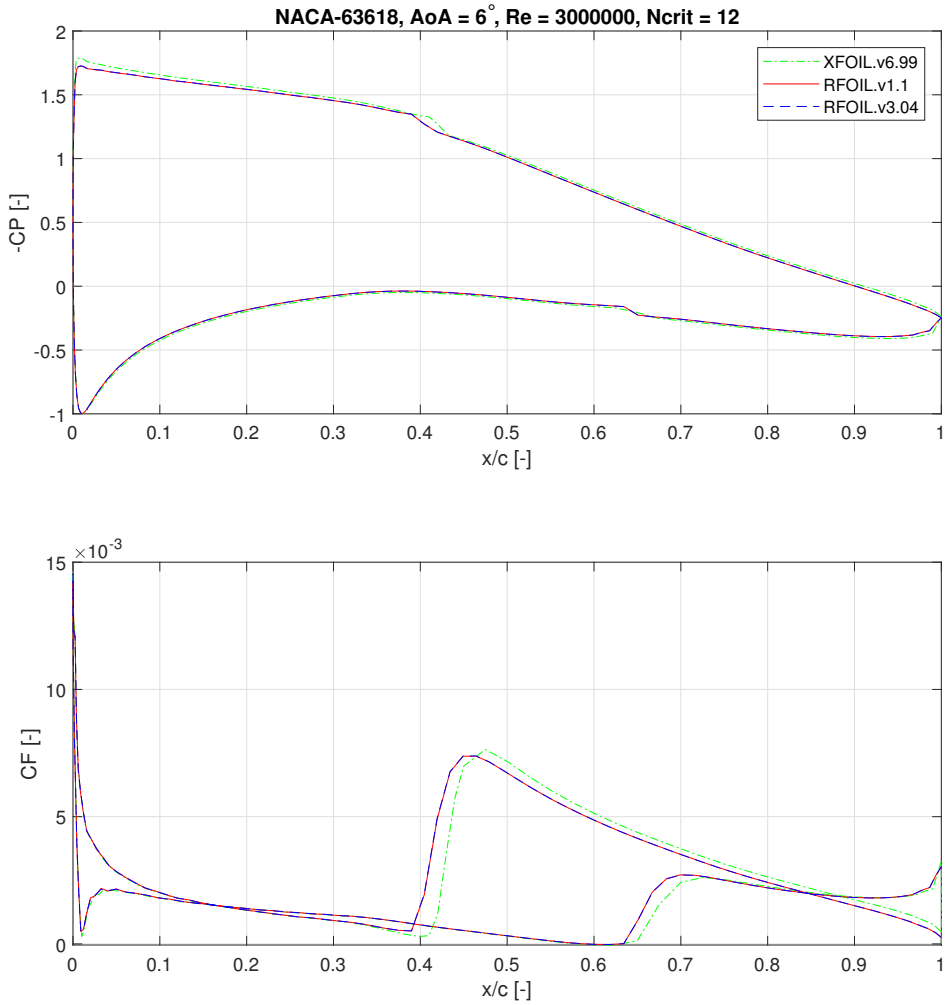

Figure B.367: Comparison between experimental and numerical polars for the NACA-63618 airfoil at a Reynolds number of 6000000. Simulation time to generate the polars by means the different codes and the number of converged polar points are depicted between parentheses.

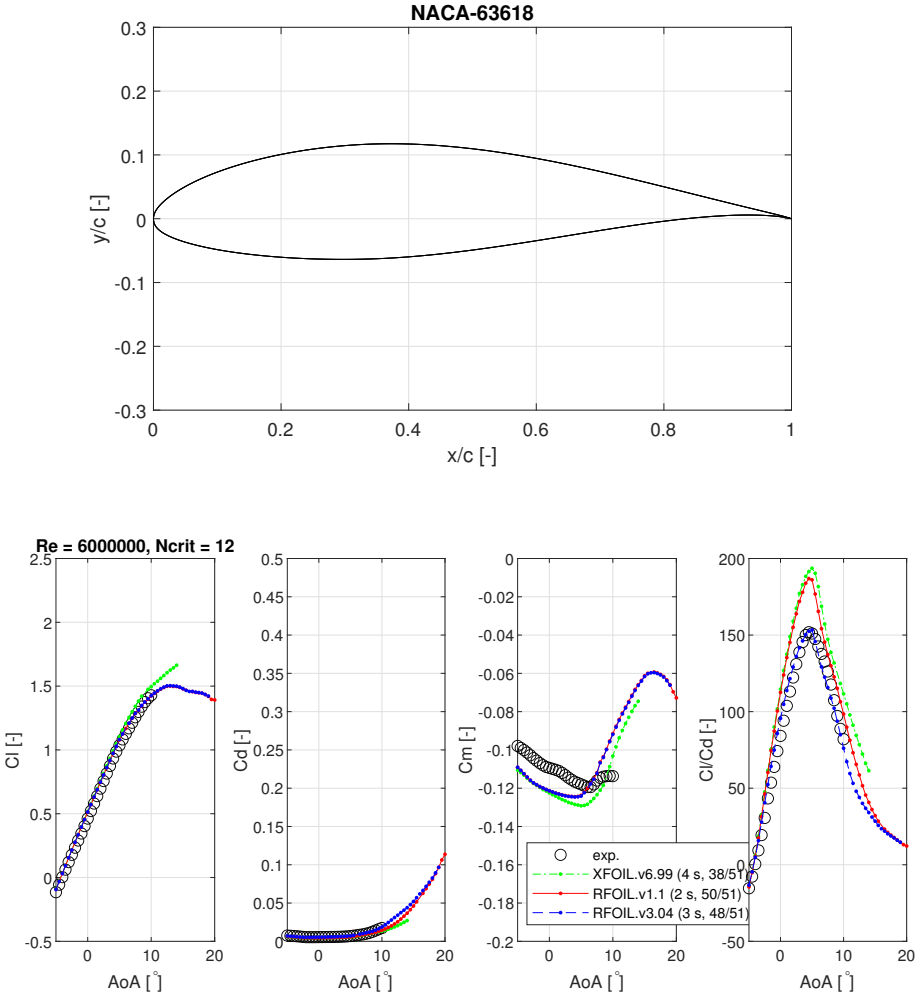

Figure B.368: Differences between experimental and numerical polars for the NACA-63618 airfoil at a Reynolds number of 6000000. Vertical black lines in the middle subplot indicate, from left to right, the angle of attack corresponding to the minimum drag coefficient, maximum lift to drag ratio and maximum lift coefficient, respectively.

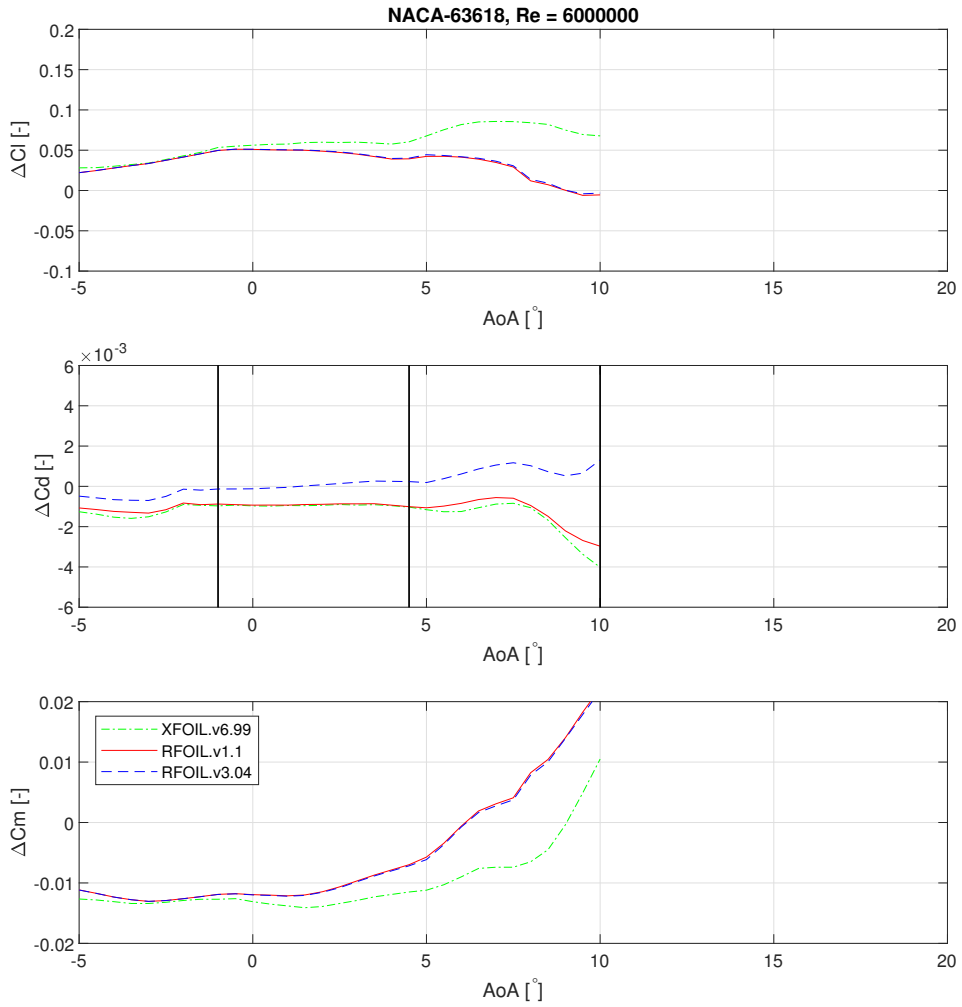

Figure B.369: Comparison between experimental and numerical pressure and skin friction distributions for the NACA-63618 airfoil at a Reynolds number of 6000000 and at the design angle of attack.

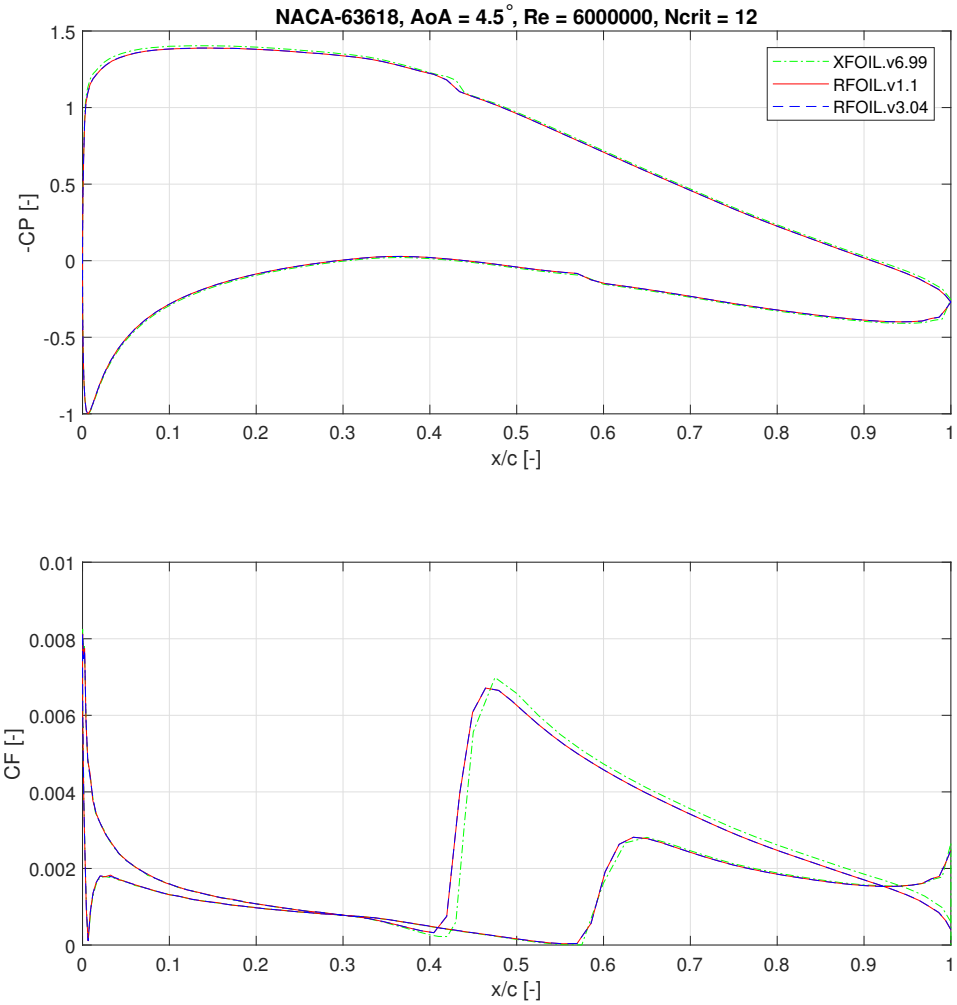

Figure B.370: Comparison between experimental and numerical polars for the NACA-6412 airfoil at a Reynolds number of 1300000. Simulation time to generate the polars by means the different codes and the number of converged polar points are depicted between parentheses.

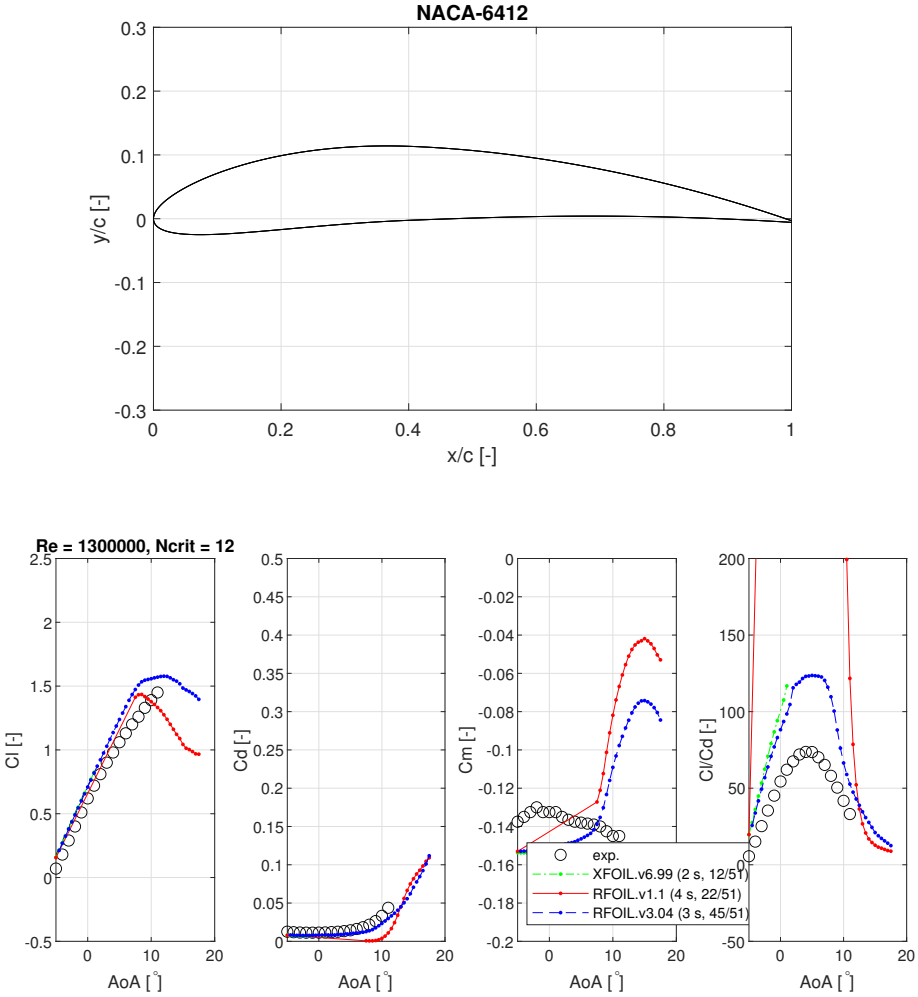

Figure B.371: Differences between experimental and numerical polars for the NACA-6412 airfoil at a Reynolds number of 1300000. Vertical black lines in the middle subplot indicate, from left to right, the angle of attack corresponding to the minimum drag coefficient, maximum lift to drag ratio and maximum lift coefficient, respectively.

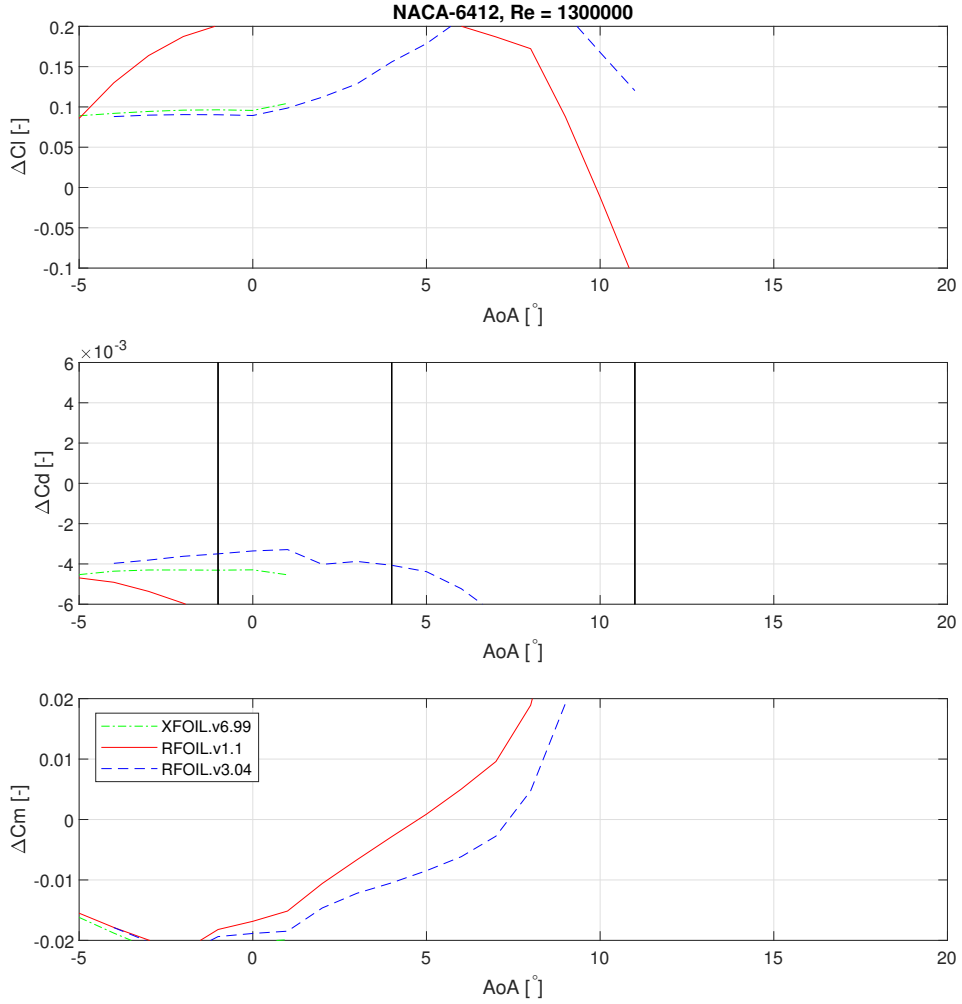

Figure B.372: Comparison between experimental and numerical pressure and skin friction distributions for the NACA-6412 airfoil at a Reynolds number of 1300000 and at the design angle of attack.

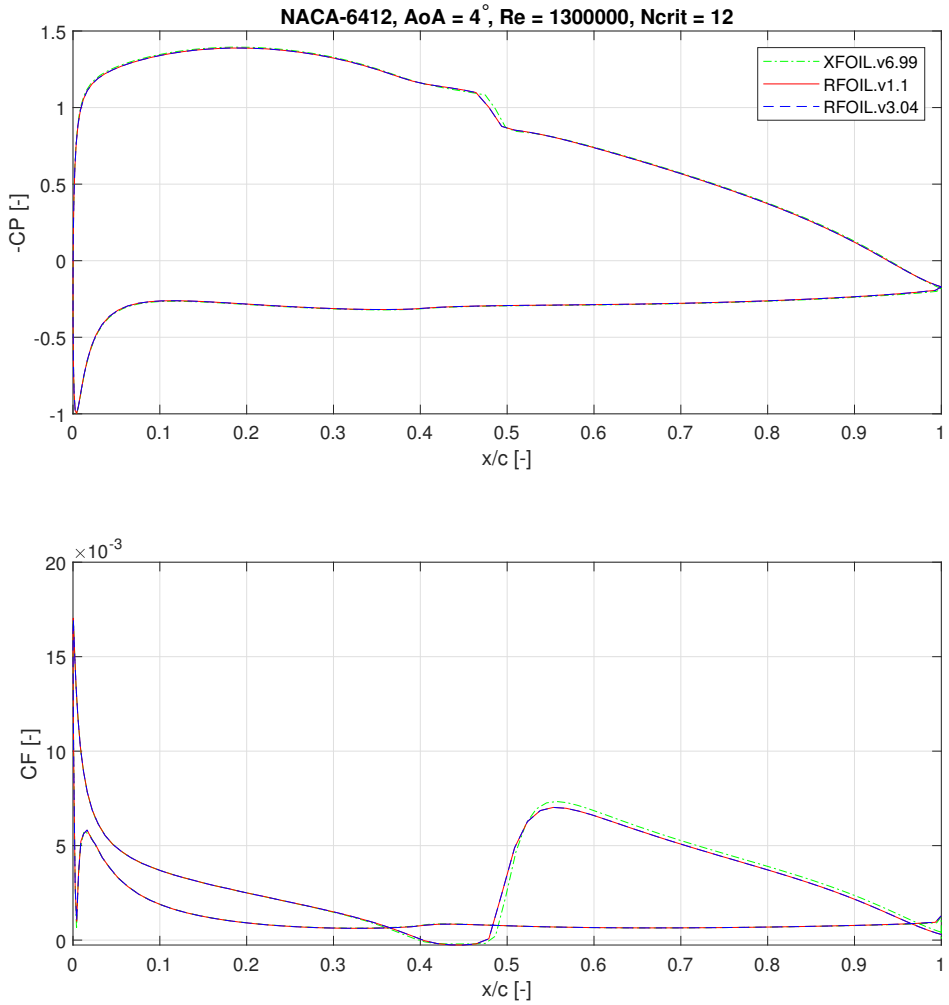

Figure B.373: Comparison between experimental and numerical polars for the NACA-6412 airfoil at a Reynolds number of 2300000. Simulation time to generate the polars by means the different codes and the number of converged polar points are depicted between parentheses.

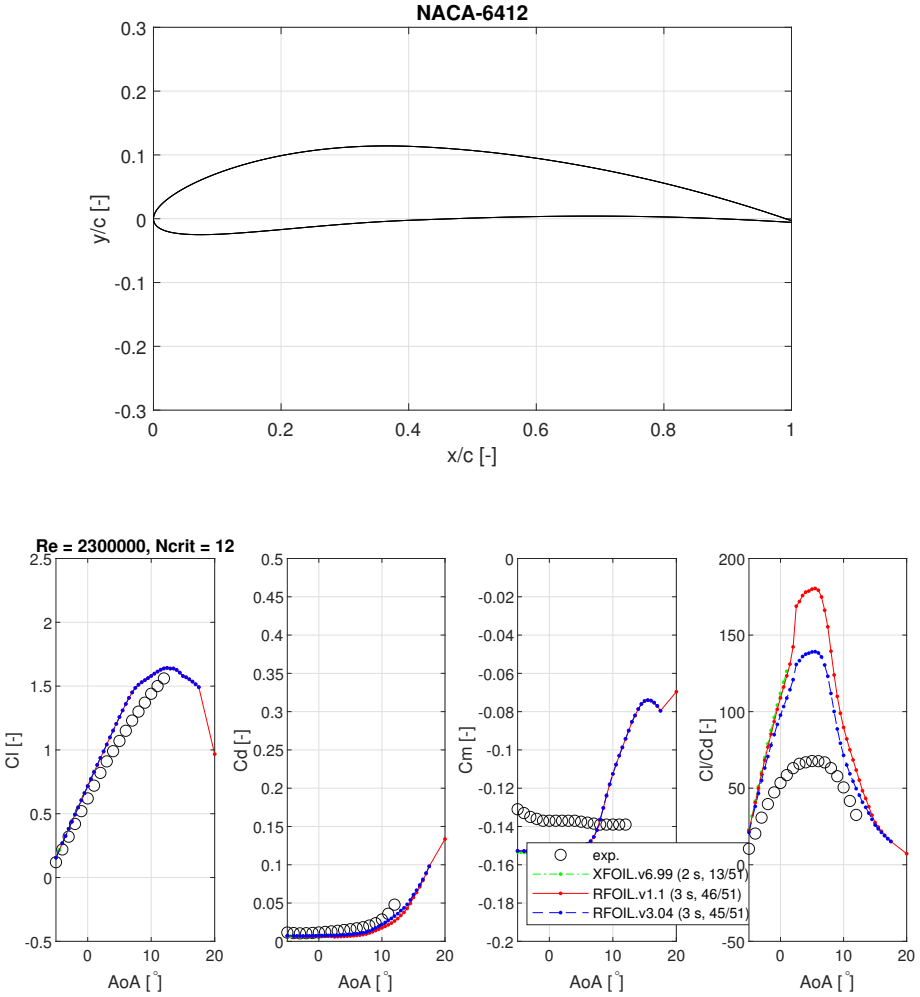

Figure B.374: Differences between experimental and numerical polars for the NACA-6412 airfoil at a Reynolds number of 2300000. Vertical black lines in the middle subplot indicate, from left to right, the angle of attack corresponding to the minimum drag coefficient, maximum lift to drag ratio and maximum lift coefficient, respectively.

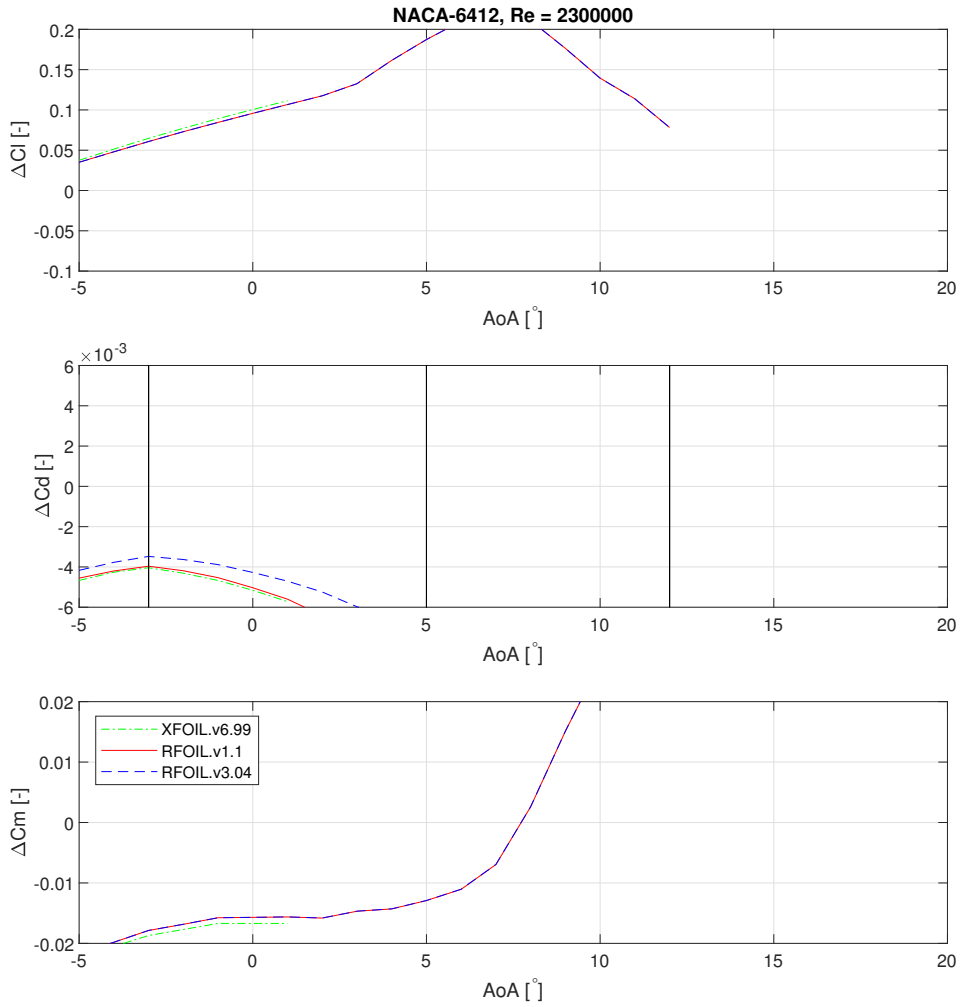

Figure B.375: Comparison between experimental and numerical pressure and skin friction distributions for the NACA-6412 airfoil at a Reynolds number of 2300000 and at the design angle of attack.

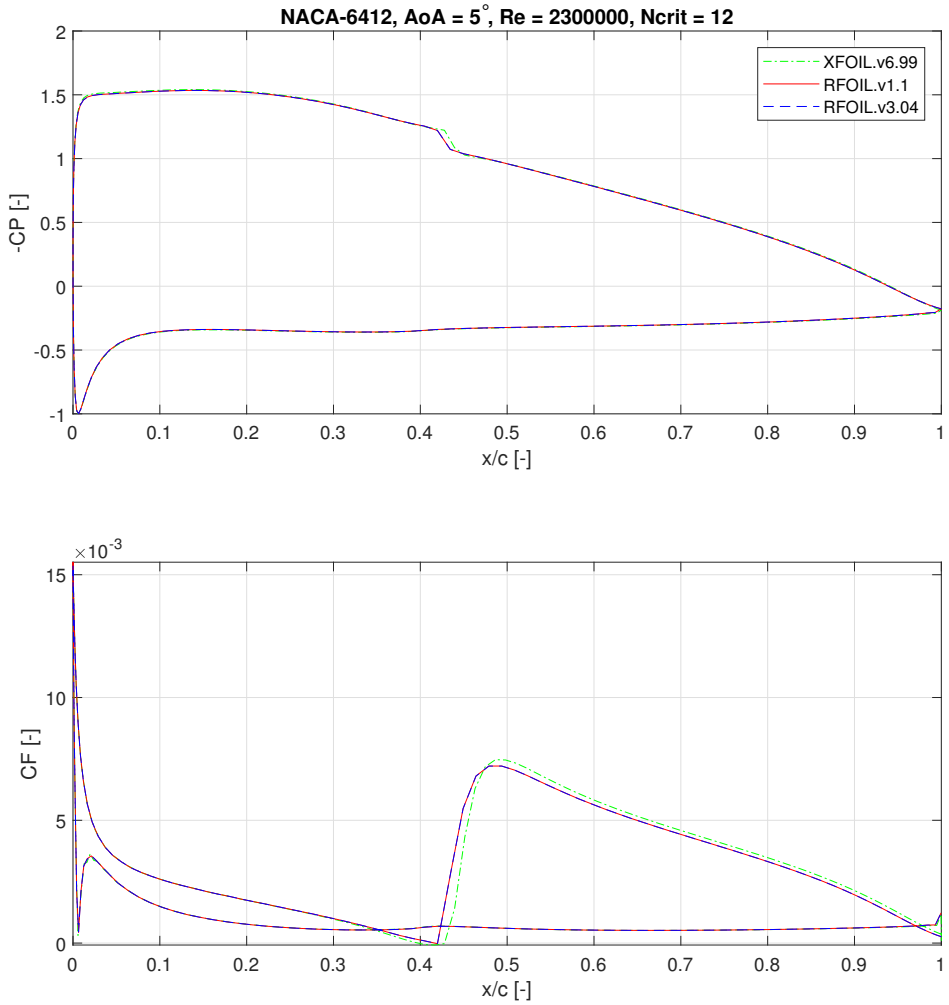

Figure B.376: Comparison between experimental and numerical polars for the NACA-6412 airfoil at a Reynolds number of 3100000. Simulation time to generate the polars by means the different codes and the number of converged polar points are depicted between parentheses.

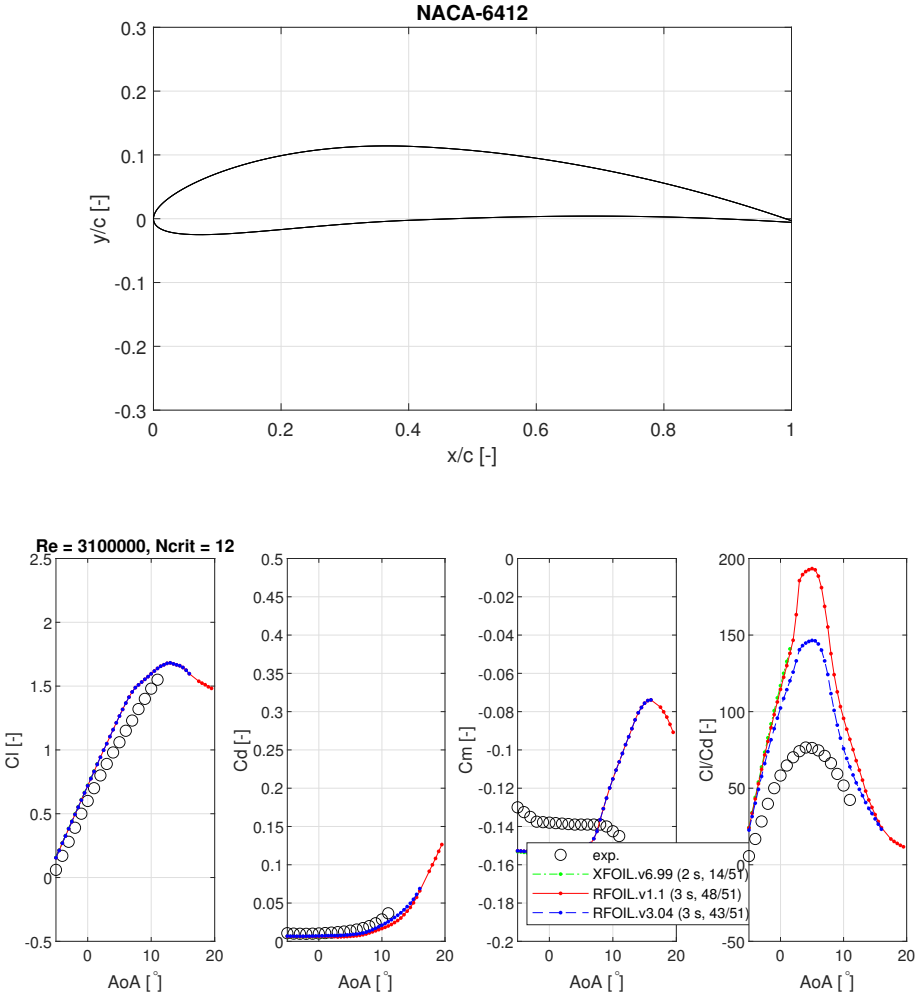

Figure B.377: Differences between experimental and numerical polars for the NACA-6412 airfoil at a Reynolds number of 3100000. Vertical black lines in the middle subplot indicate, from left to right, the angle of attack corresponding to the minimum drag coefficient, maximum lift to drag ratio and maximum lift coefficient, respectively.

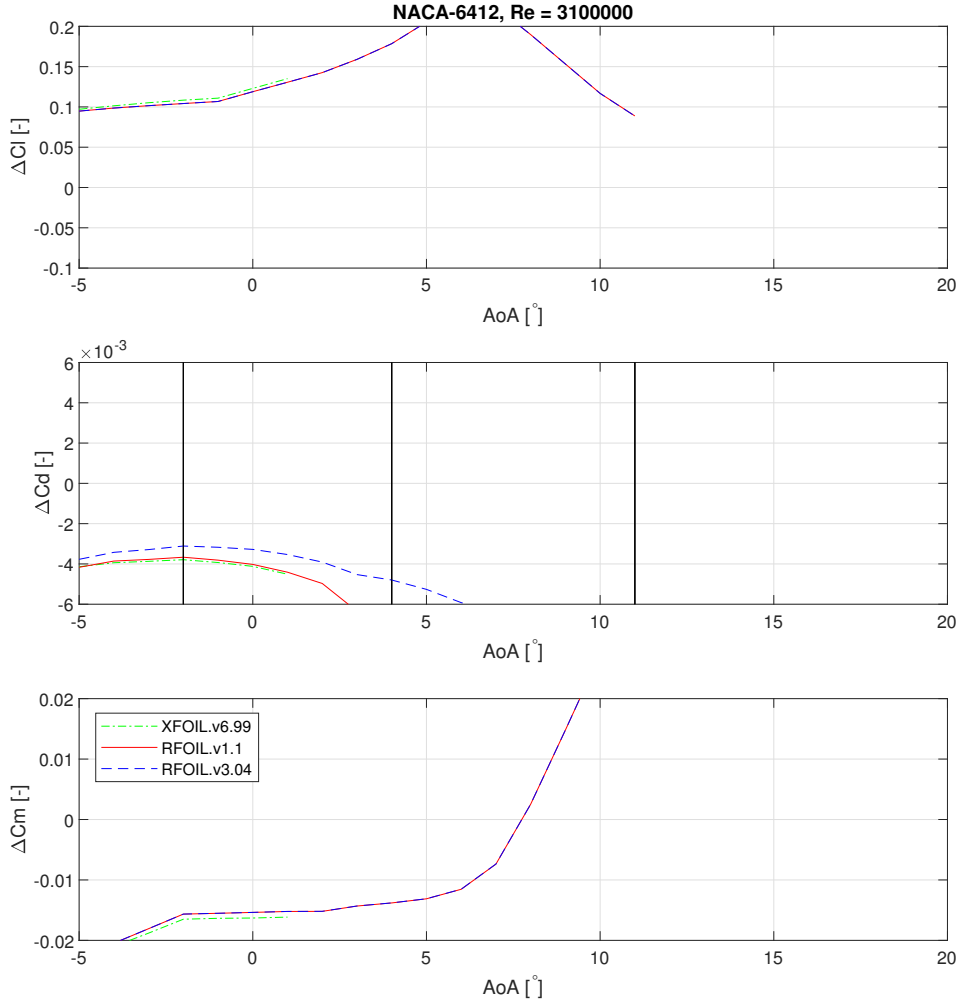

Figure B.378: Comparison between experimental and numerical pressure and skin friction distributions for the NACA-6412 airfoil at a Reynolds number of 3100000 and at the design angle of attack.

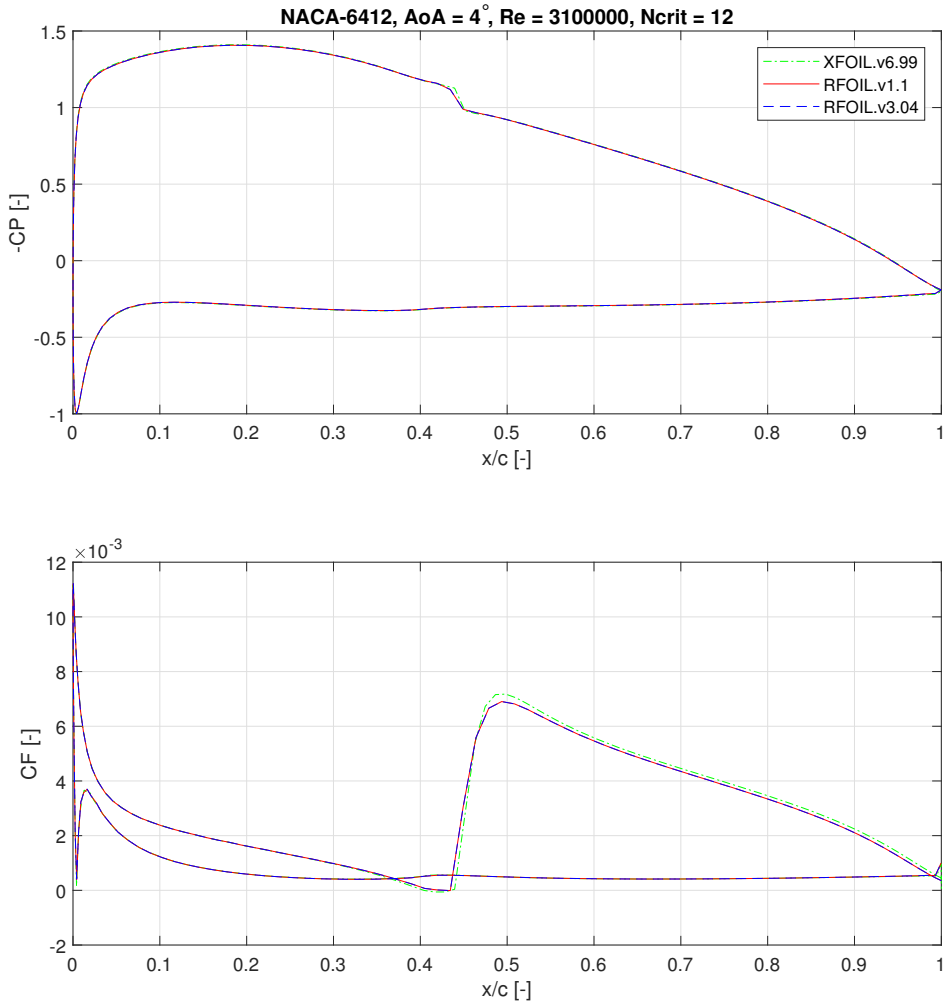

Figure B.379: Comparison between experimental and numerical polars for the NACA-6412 airfoil at a Reynolds number of 600000. Simulation time to generate the polars by means the different codes and the number of converged polar points are depicted between parentheses.

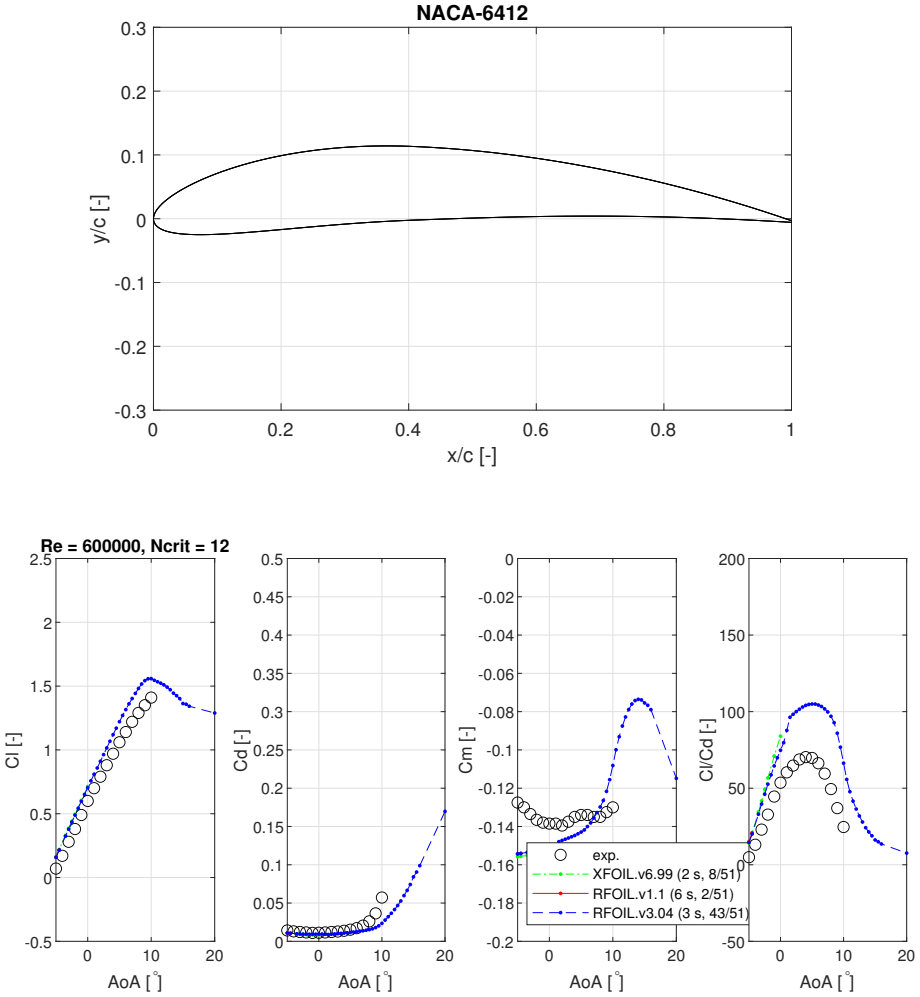

Figure B.380: Differences between experimental and numerical polars for the NACA-6412 airfoil at a Reynolds number of 600000. Vertical black lines in the middle subplot indicate, from left to right, the angle of attack corresponding to the minimum drag coefficient, maximum lift to drag ratio and maximum lift coefficient, respectively.

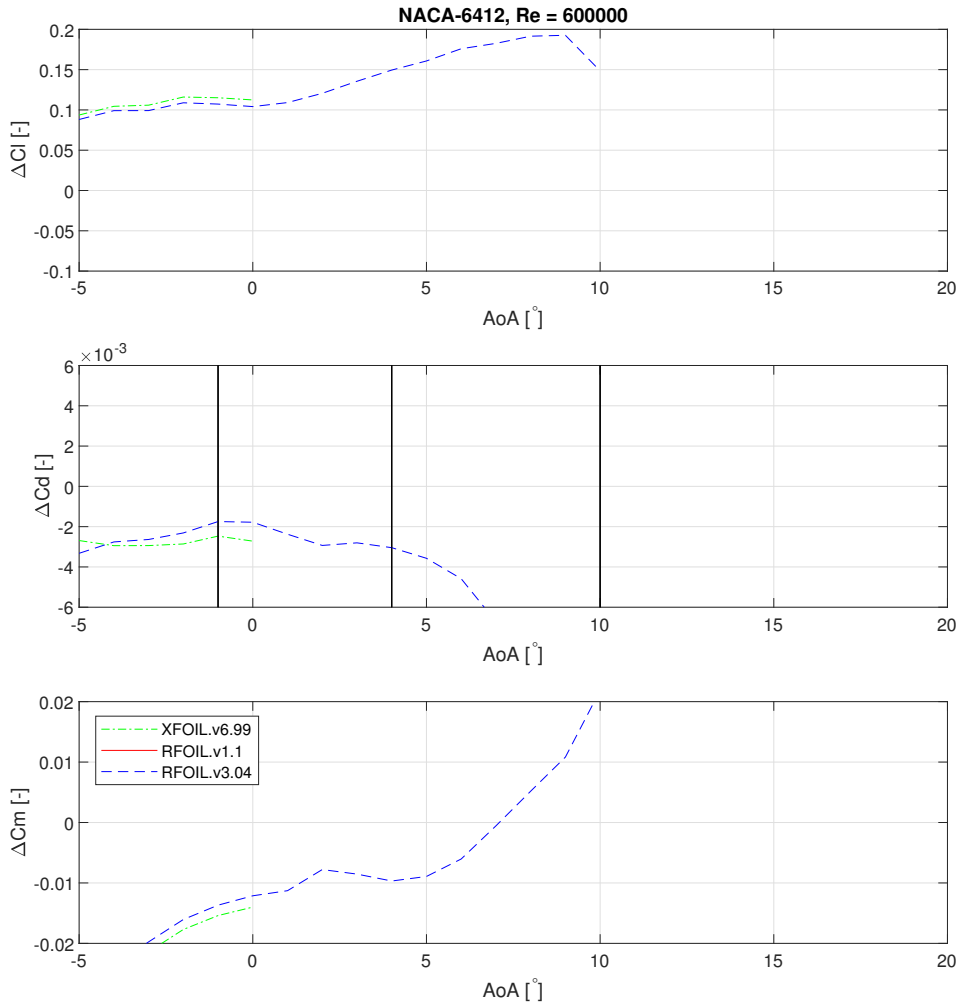

Figure B.381: Comparison between experimental and numerical pressure and skin friction distributions for the NACA-6412 airfoil at a Reynolds number of 600000 and at the design angle of attack.

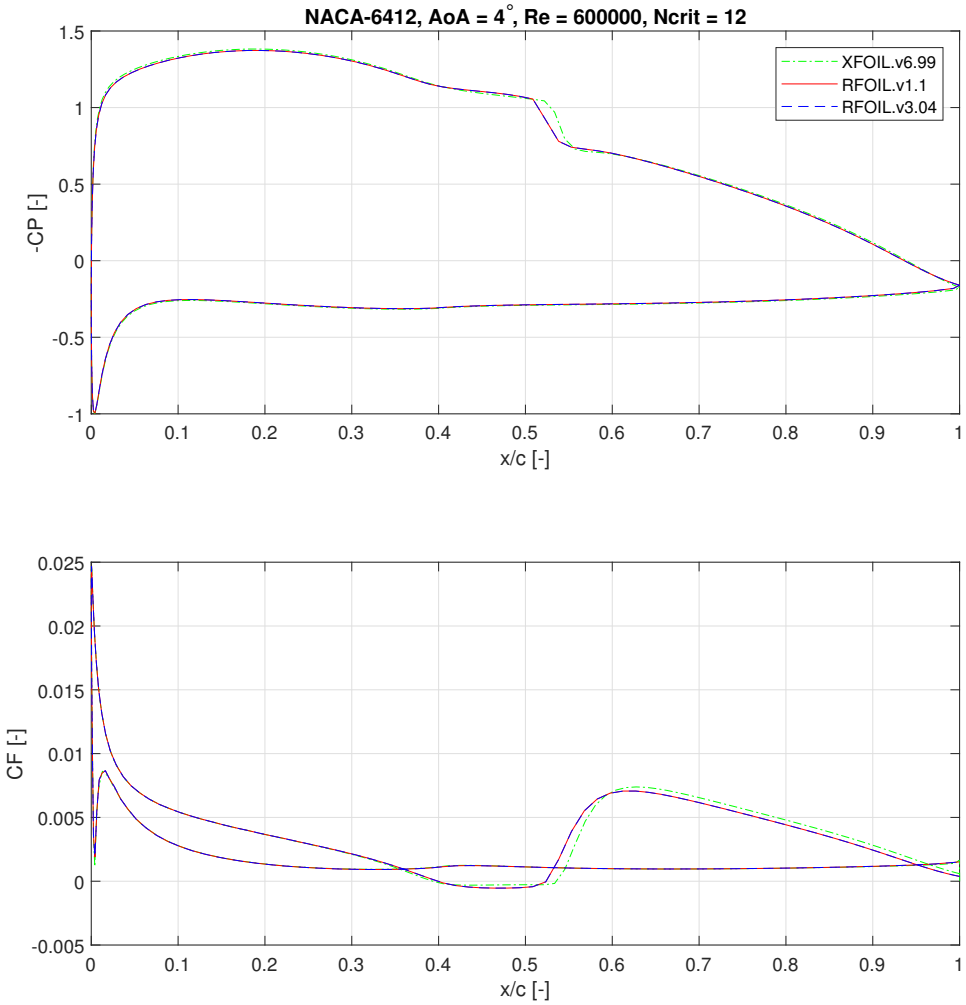

Figure B.382: Comparison between experimental and numerical polars for the NACA-64215 airfoil at a Reynolds number of 3000000. Simulation time to generate the polars by means the different codes and the number of converged polar points are depicted between parentheses.

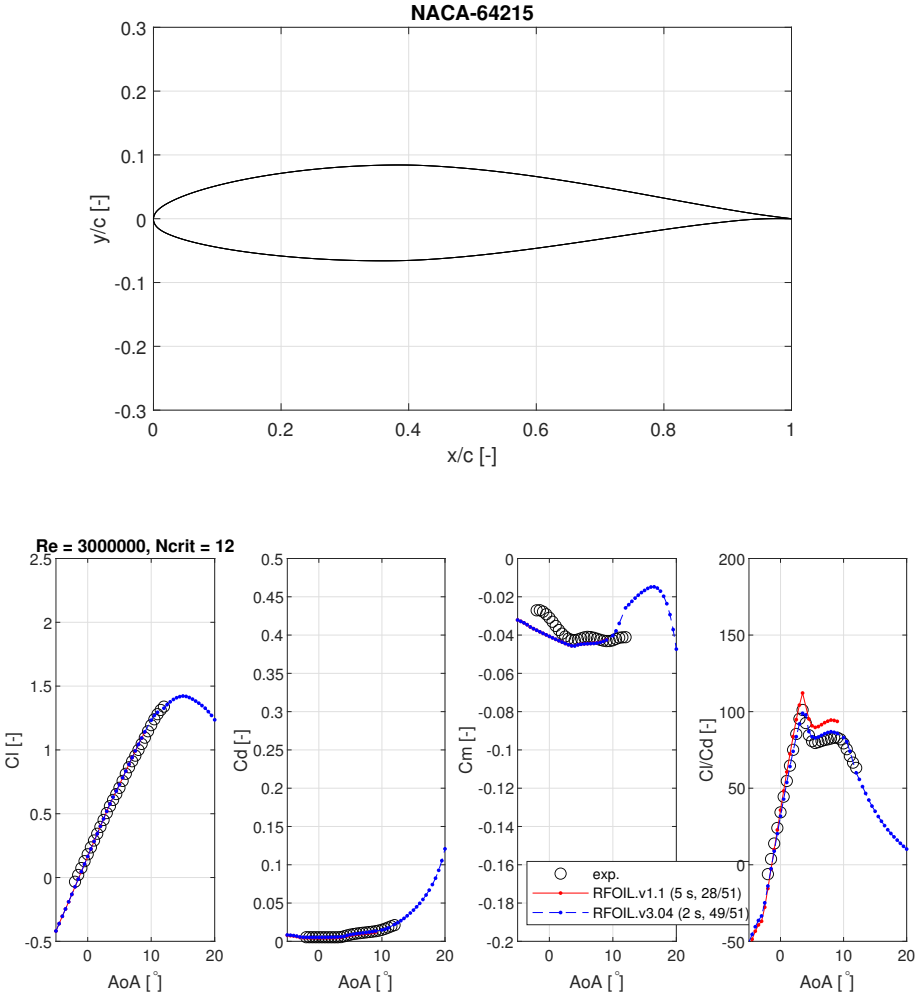

Figure B.383: Differences between experimental and numerical polars for the NACA-64215 airfoil at a Reynolds number of 3000000. Vertical black lines in the middle subplot indicate, from left to right, the angle of attack corresponding to the minimum drag coefficient, maximum lift to drag ratio and maximum lift coefficient, respectively.

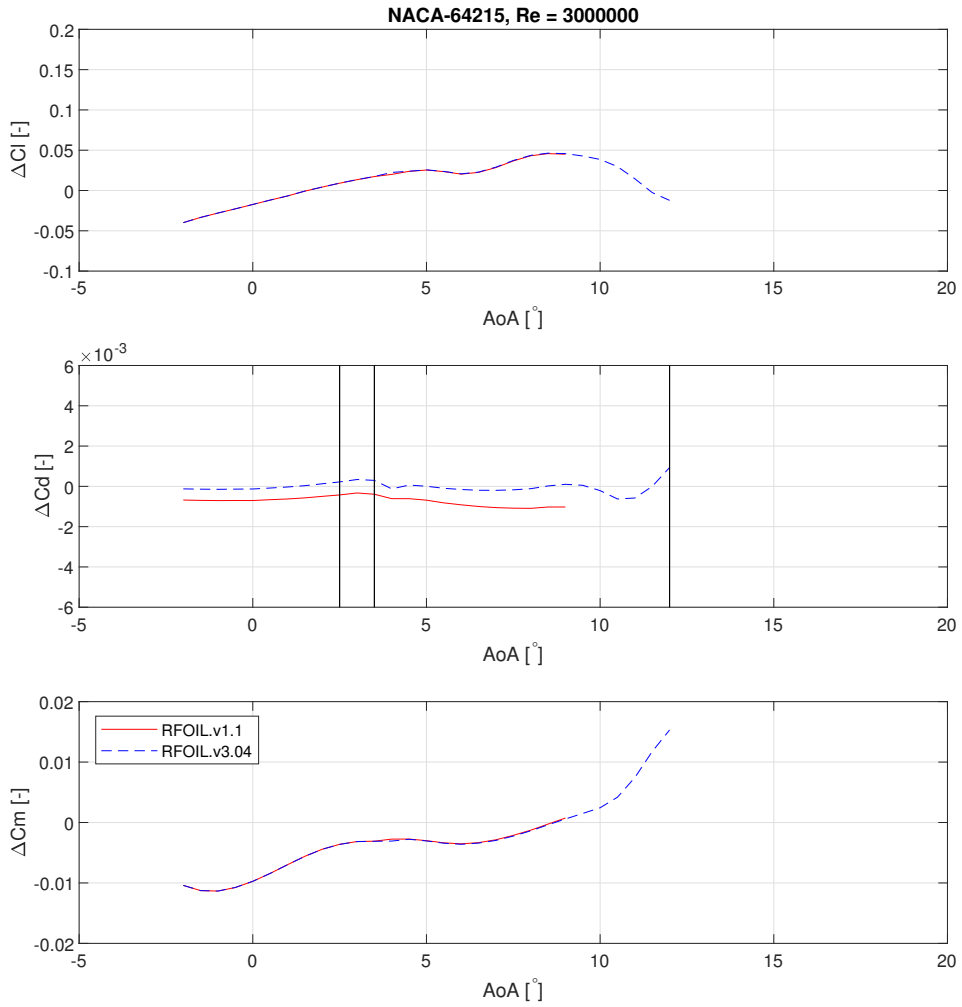

Figure B.384: Comparison between experimental and numerical pressure and skin friction distributions for the NACA-64215 airfoil at a Reynolds number of 3000000 and at the design angle of attack.

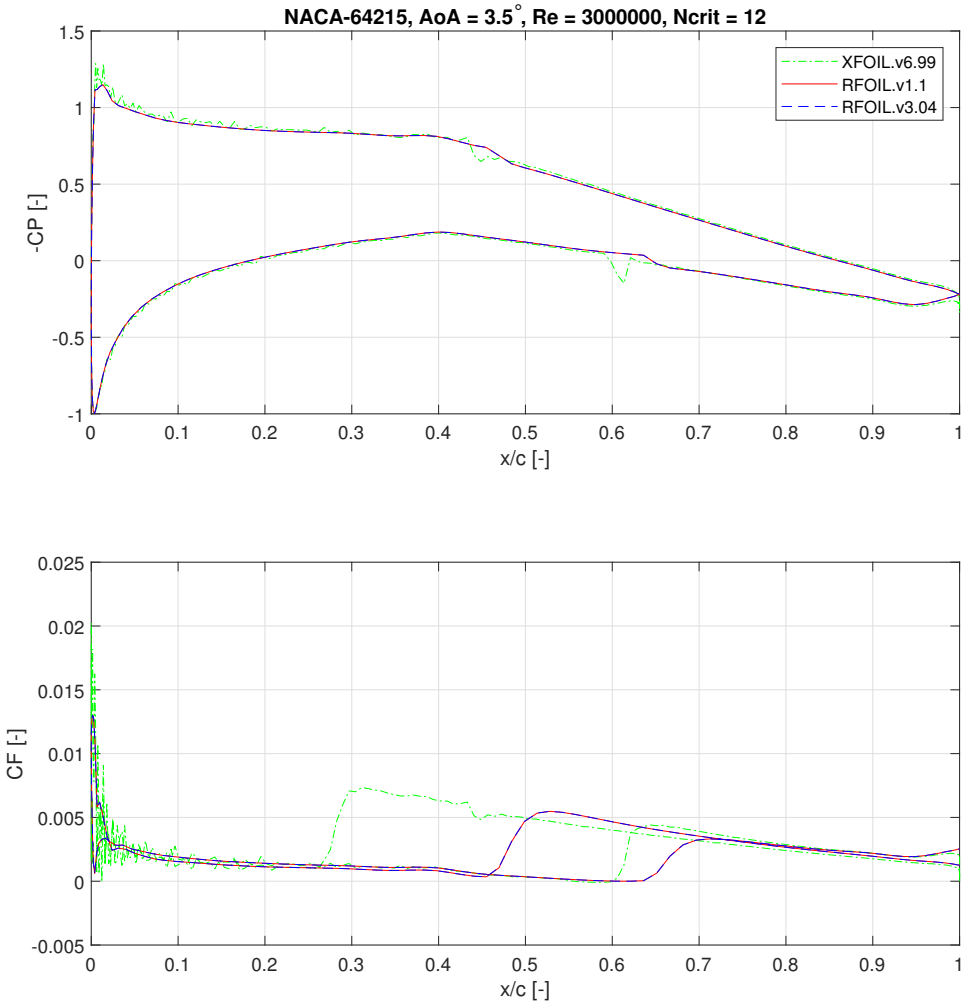

Figure B.385: Comparison between experimental and numerical polars for the NACA-64215 airfoil at a Reynolds number of 6000000. Simulation time to generate the polars by means the different codes and the number of converged polar points are depicted between parentheses.

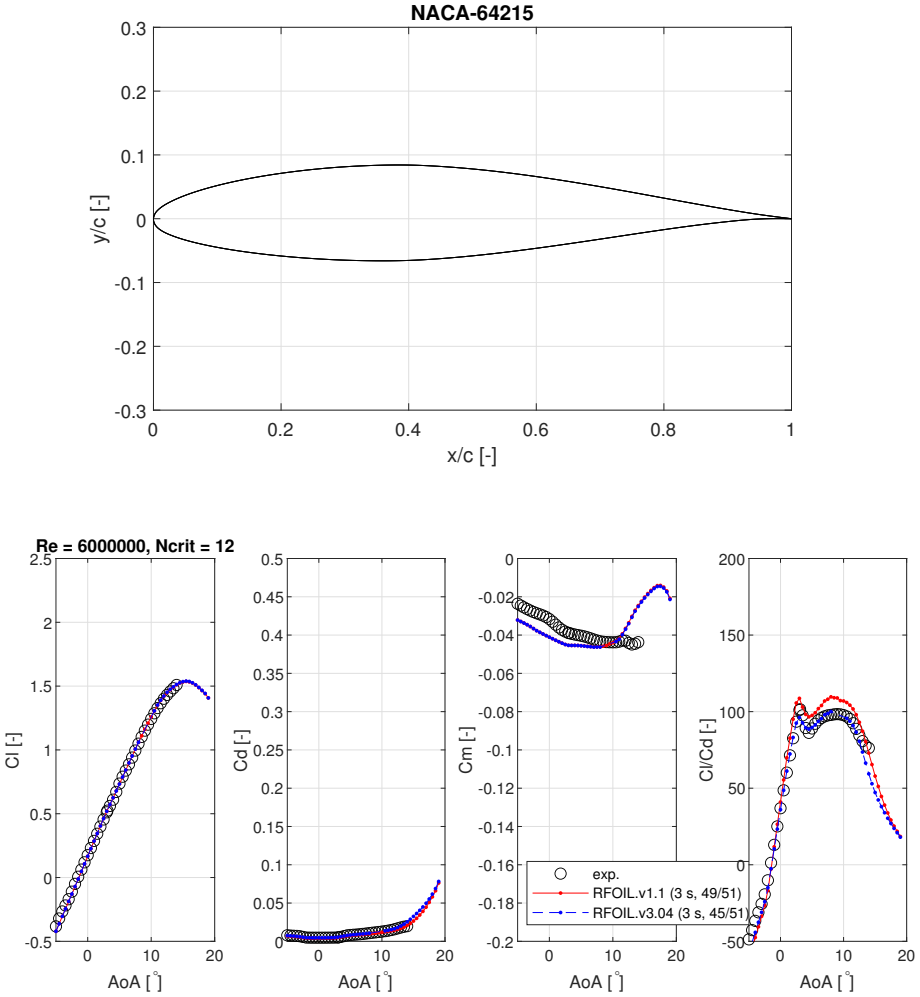

Figure B.386: Differences between experimental and numerical polars for the NACA-64215 airfoil at a Reynolds number of 6000000. Vertical black lines in the middle subplot indicate, from left to right, the angle of attack corresponding to the minimum drag coefficient, maximum lift to drag ratio and maximum lift coefficient, respectively.

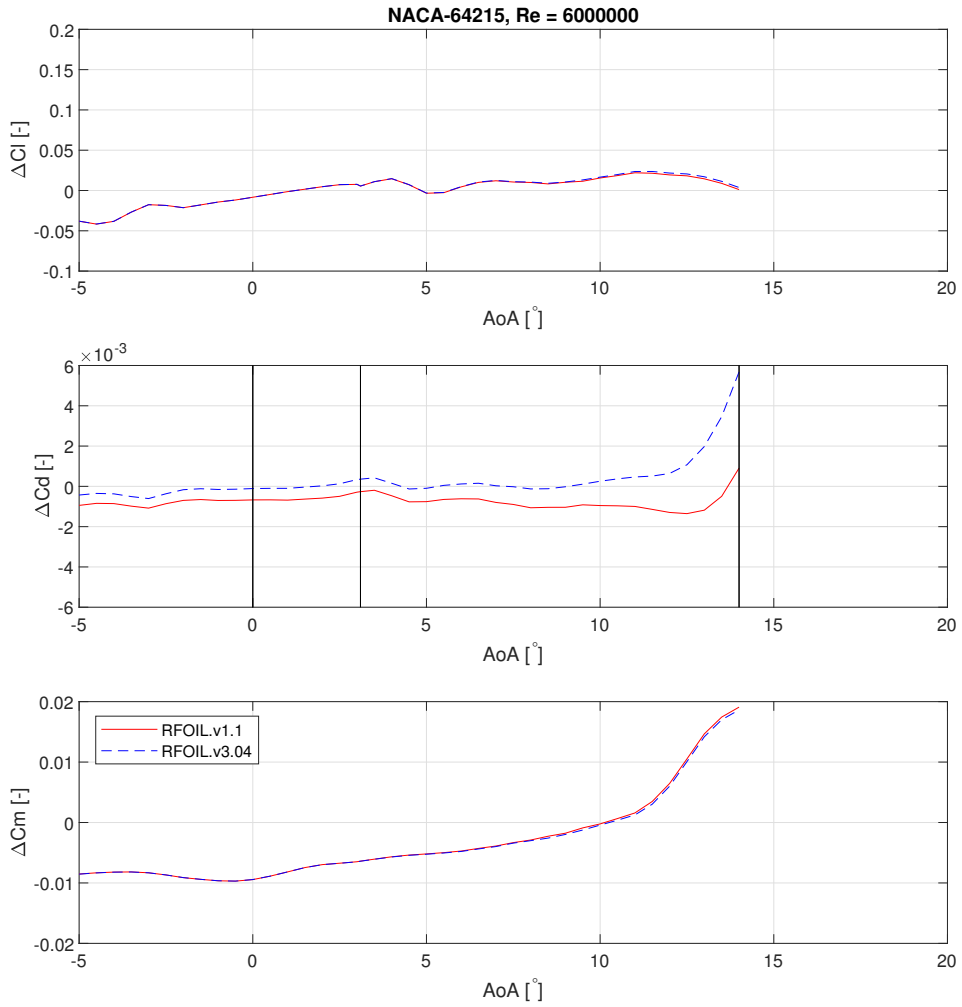

Figure B.387: Comparison between experimental and numerical pressure and skin friction distributions for the NACA-64215 airfoil at a Reynolds number of 6000000 and at the design angle of attack.

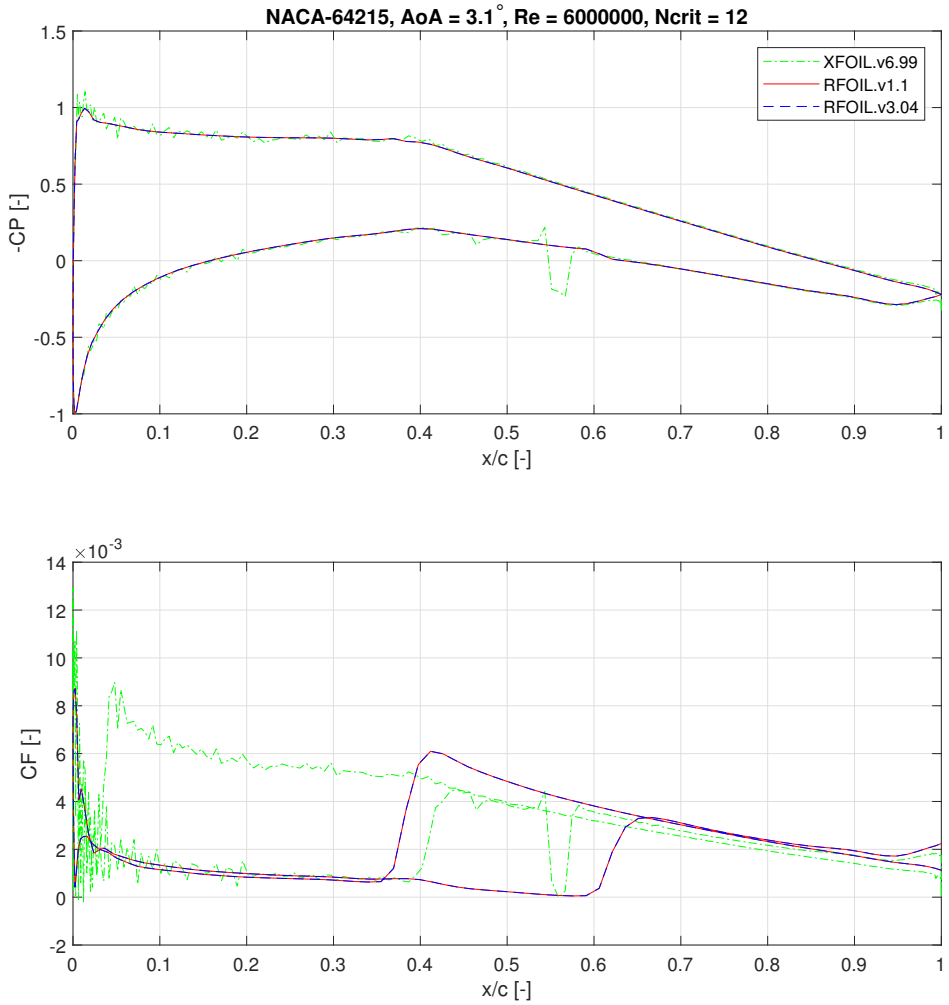

Figure B.388: Comparison between experimental and numerical polars for the NACA-64218 airfoil at a Reynolds number of 3000000. Simulation time to generate the polars by means the different codes and the number of converged polar points are depicted between parentheses.

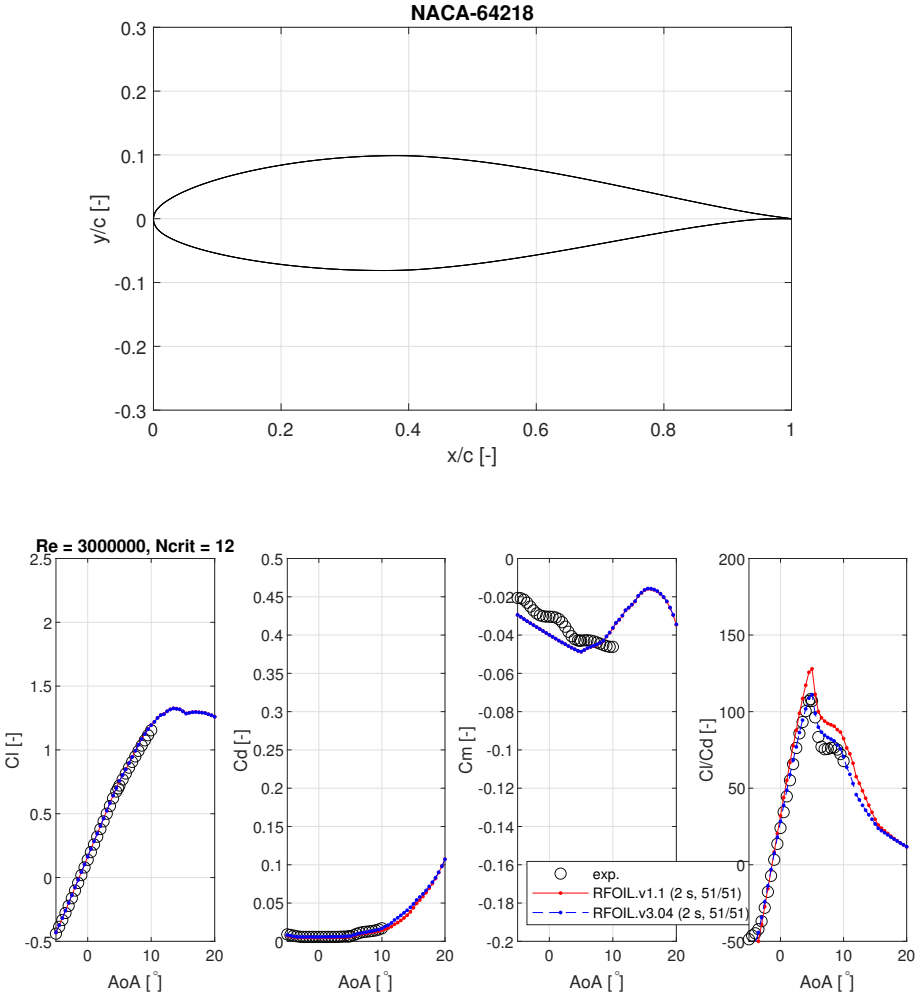

Figure B.389: Differences between experimental and numerical polars for the NACA-64218 airfoil at a Reynolds number of 3000000. Vertical black lines in the middle subplot indicate, from left to right, the angle of attack corresponding to the minimum drag coefficient, maximum lift to drag ratio and maximum lift coefficient, respectively.

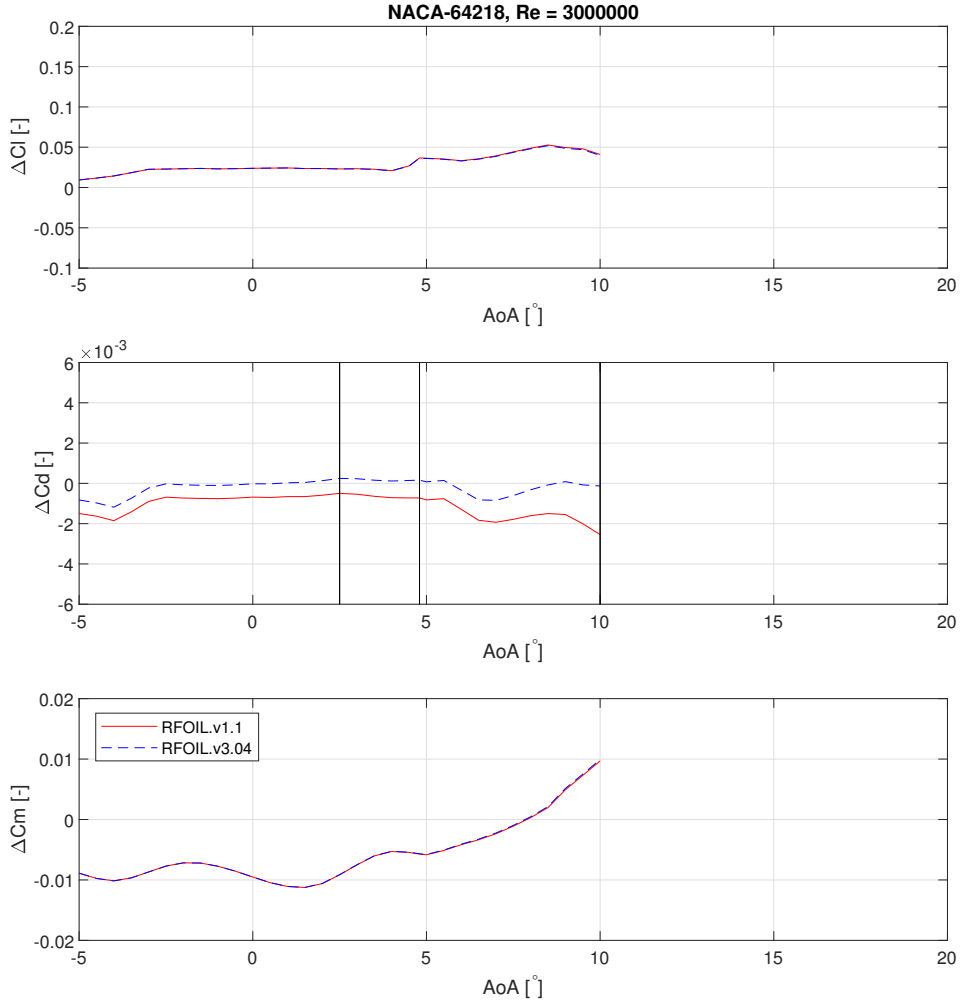

Figure B.390: Comparison between experimental and numerical pressure and skin friction distributions for the NACA-64218 airfoil at a Reynolds number of 3000000 and at the design angle of attack.

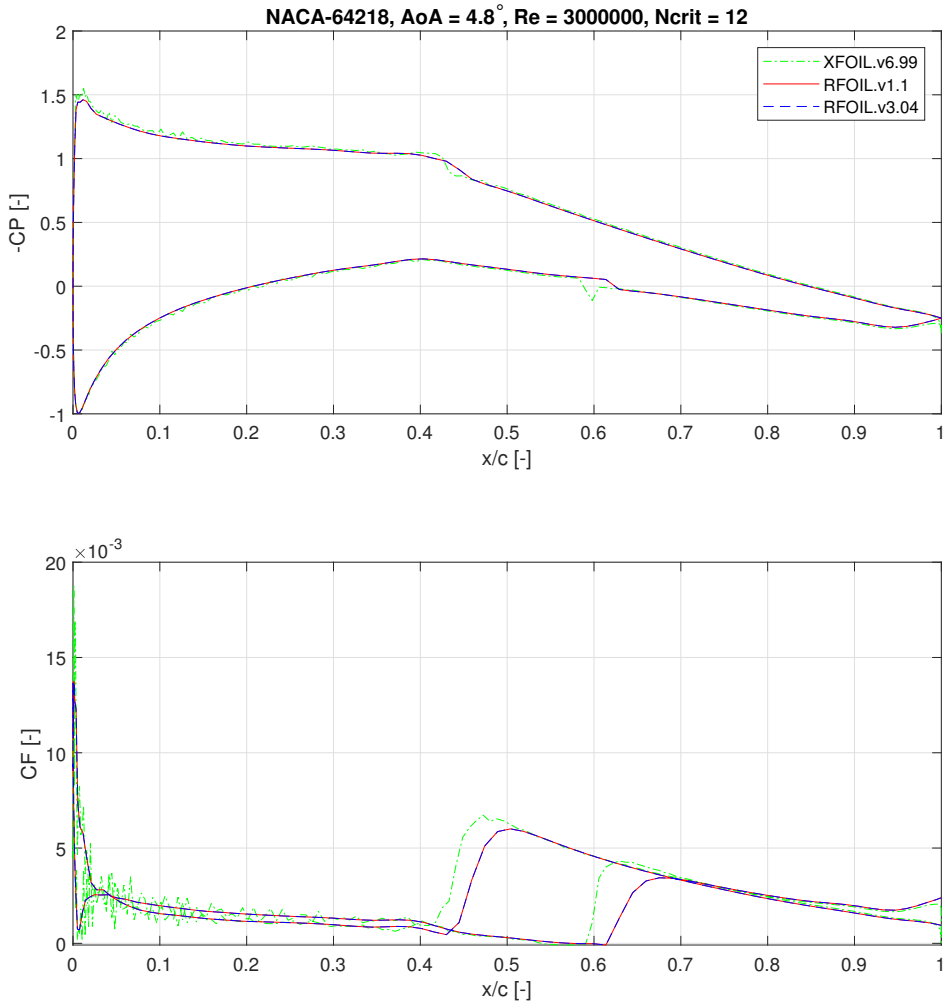

Figure B.391: Comparison between experimental and numerical polars for the NACA-64218 airfoil at a Reynolds number of 6000000. Simulation time to generate the polars by means the different codes and the number of converged polar points are depicted between parentheses.

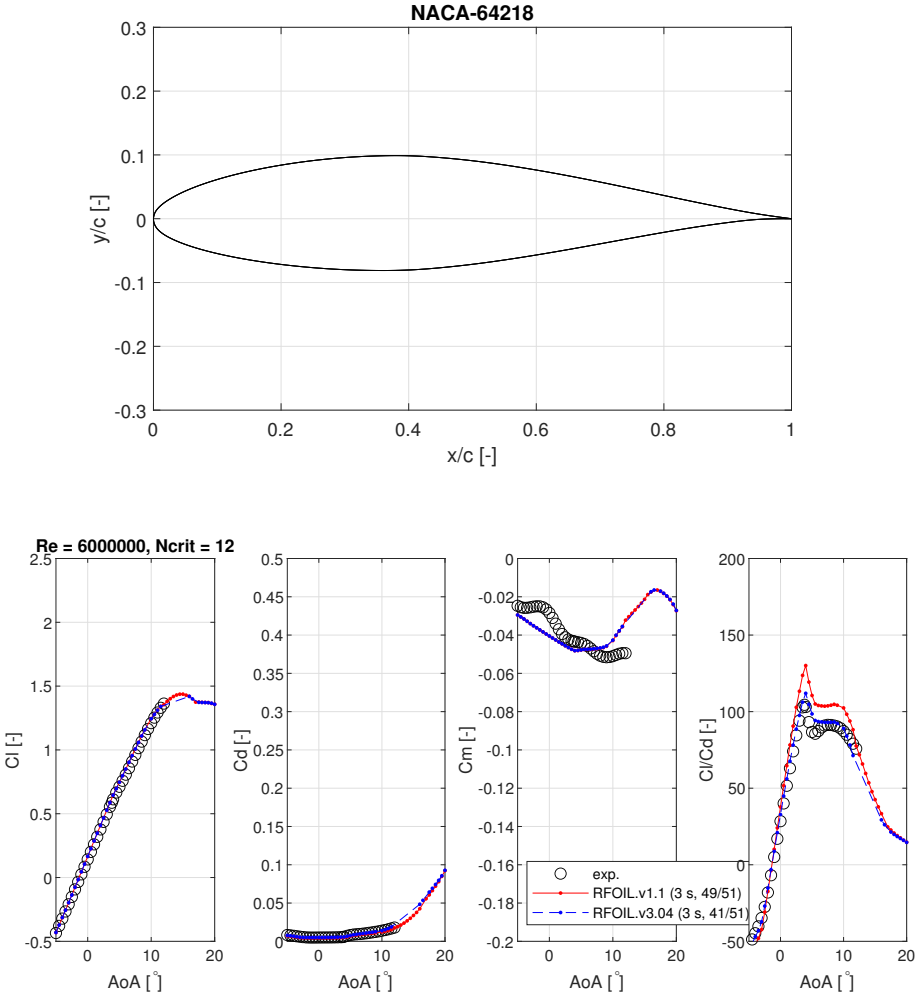

Figure B.392: Differences between experimental and numerical polars for the NACA-64218 airfoil at a Reynolds number of 6000000. Vertical black lines in the middle subplot indicate, from left to right, the angle of attack corresponding to the minimum drag coefficient, maximum lift to drag ratio and maximum lift coefficient, respectively.

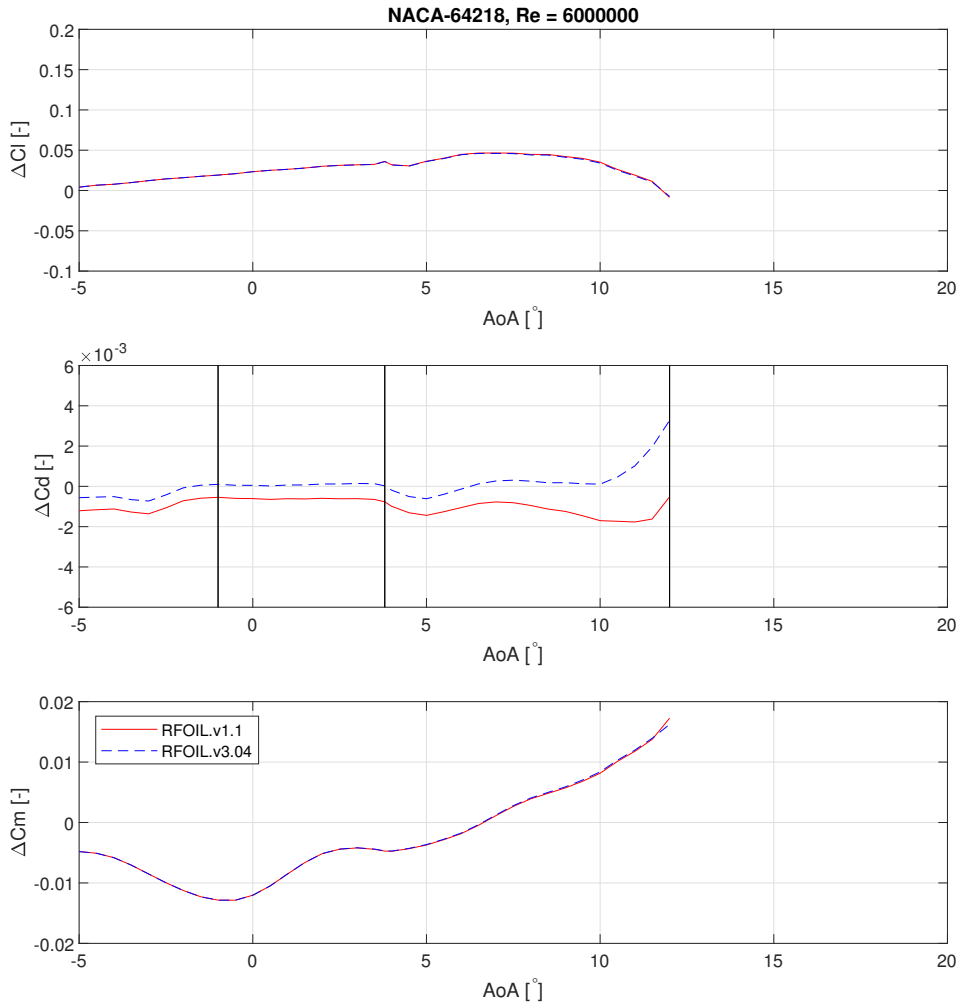

Figure B.393: Comparison between experimental and numerical pressure and skin friction distributions for the NACA-64218 airfoil at a Reynolds number of 6000000 and at the design angle of attack.

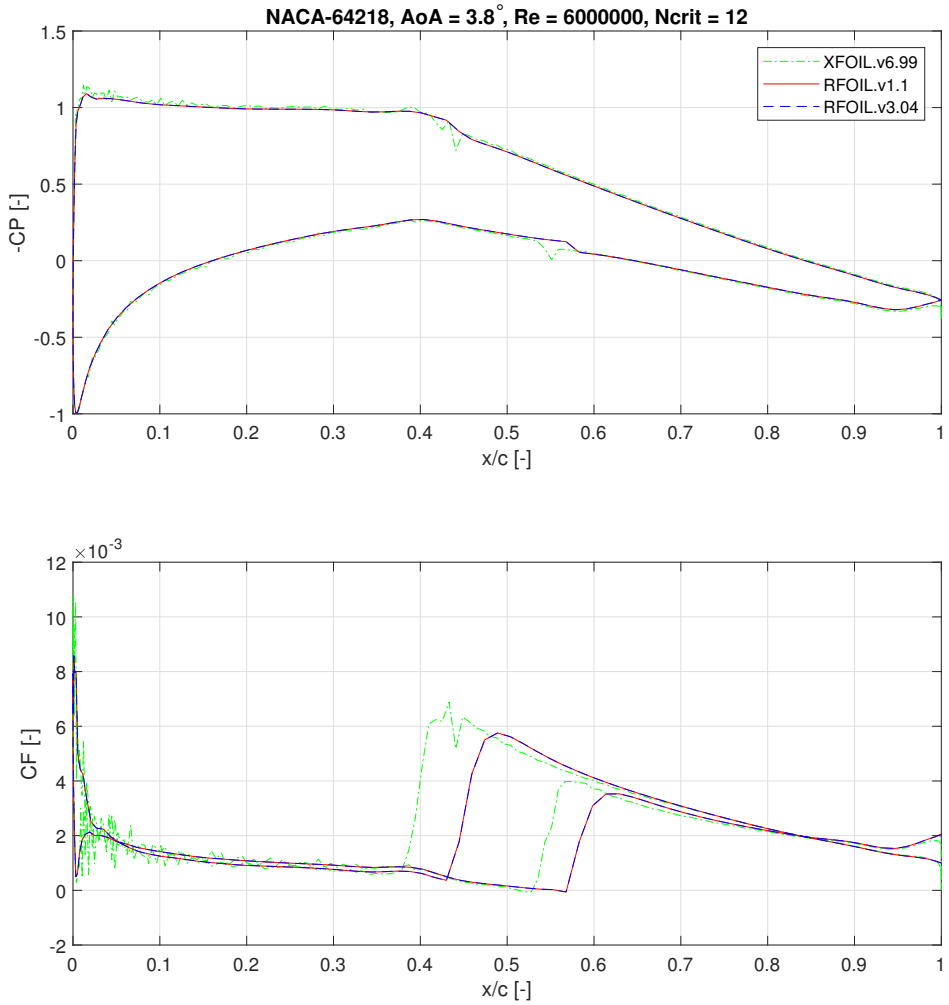

Figure B.394: Comparison between experimental and numerical polars for the NACA-64409 airfoil at a Reynolds number of 1000000. Simulation time to generate the polars by means the different codes and the number of converged polar points are depicted between parentheses.

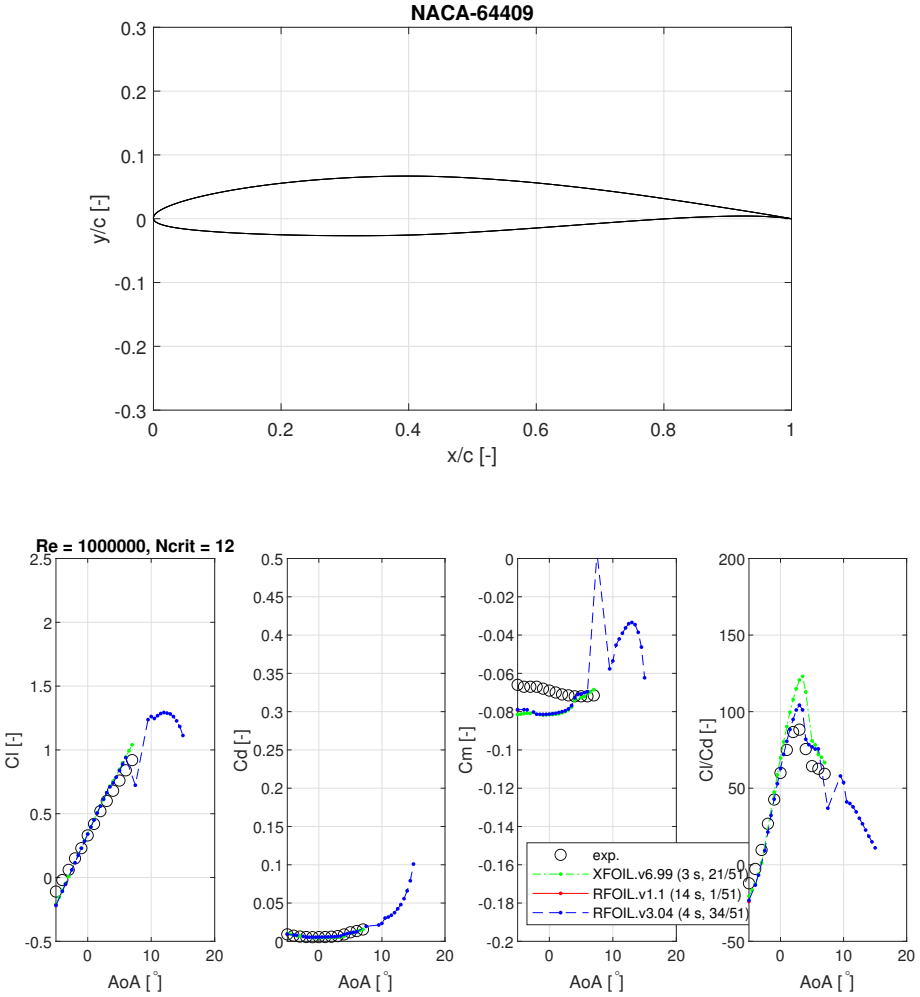

Figure B.395: Differences between experimental and numerical polars for the NACA-64409 airfoil at a Reynolds number of 1000000. Vertical black lines in the middle subplot indicate, from left to right, the angle of attack corresponding to the minimum drag coefficient, maximum lift to drag ratio and maximum lift coefficient, respectively.

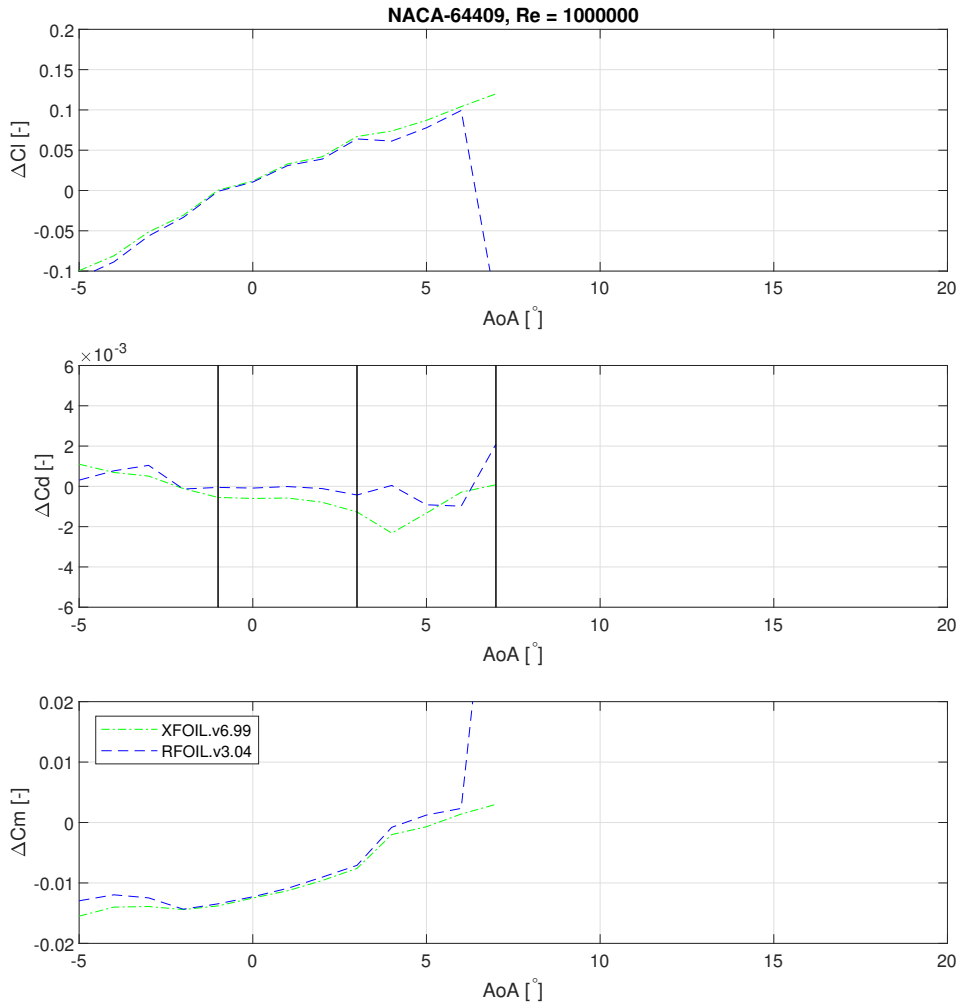

Figure B.396: Comparison between experimental and numerical pressure and skin friction distributions for the NACA-64409 airfoil at a Reynolds number of 1000000 and at the design angle of attack.

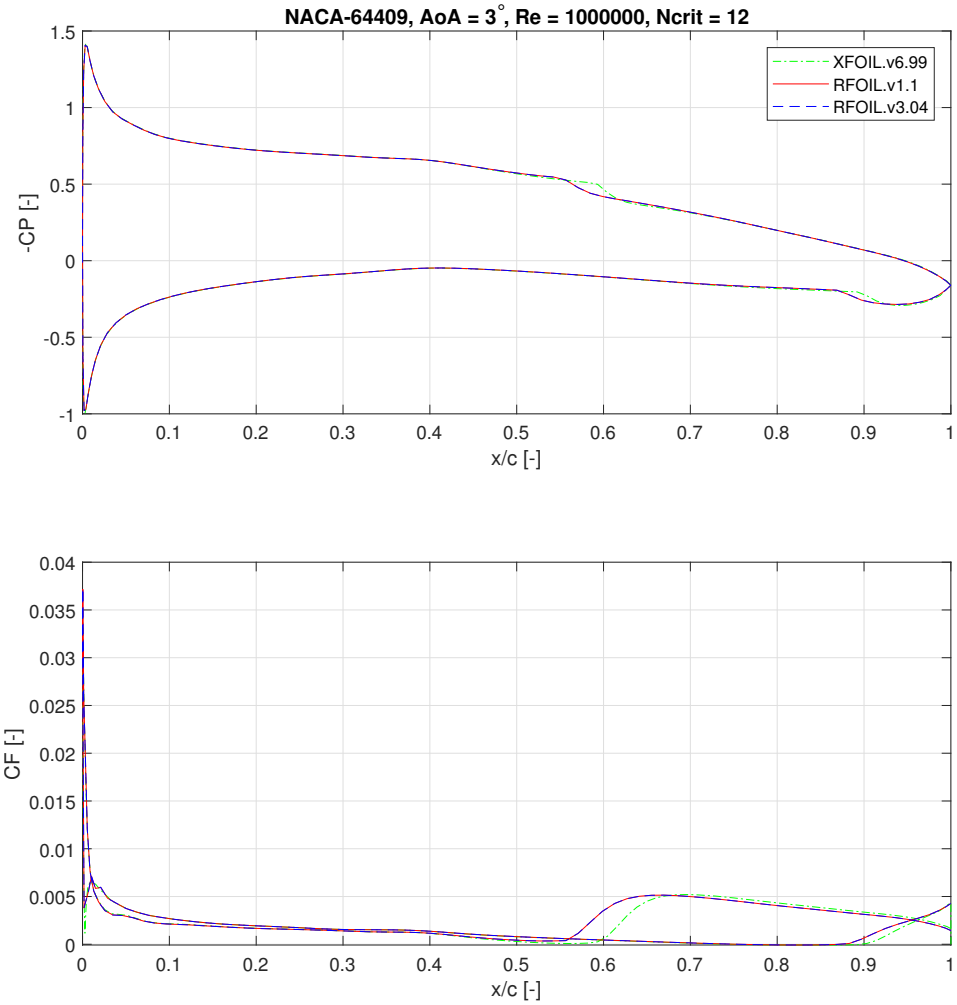

Figure B.397: Comparison between experimental and numerical polars for the NACA-64409 airfoil at a Reynolds number of 1500000. Simulation time to generate the polars by means the different codes and the number of converged polar points are depicted between parentheses.

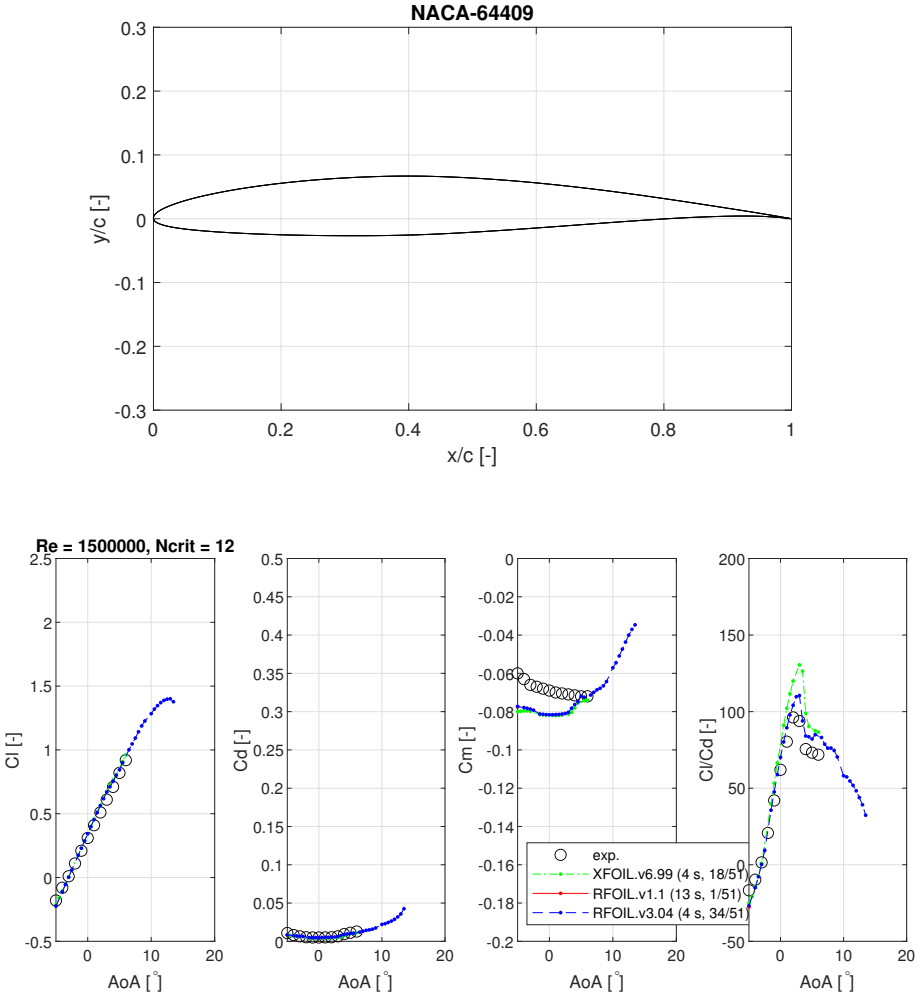

Figure B.398: Differences between experimental and numerical polars for the NACA-64409 airfoil at a Reynolds number of 1500000. Vertical black lines in the middle subplot indicate, from left to right, the angle of attack corresponding to the minimum drag coefficient, maximum lift to drag ratio and maximum lift coefficient, respectively.

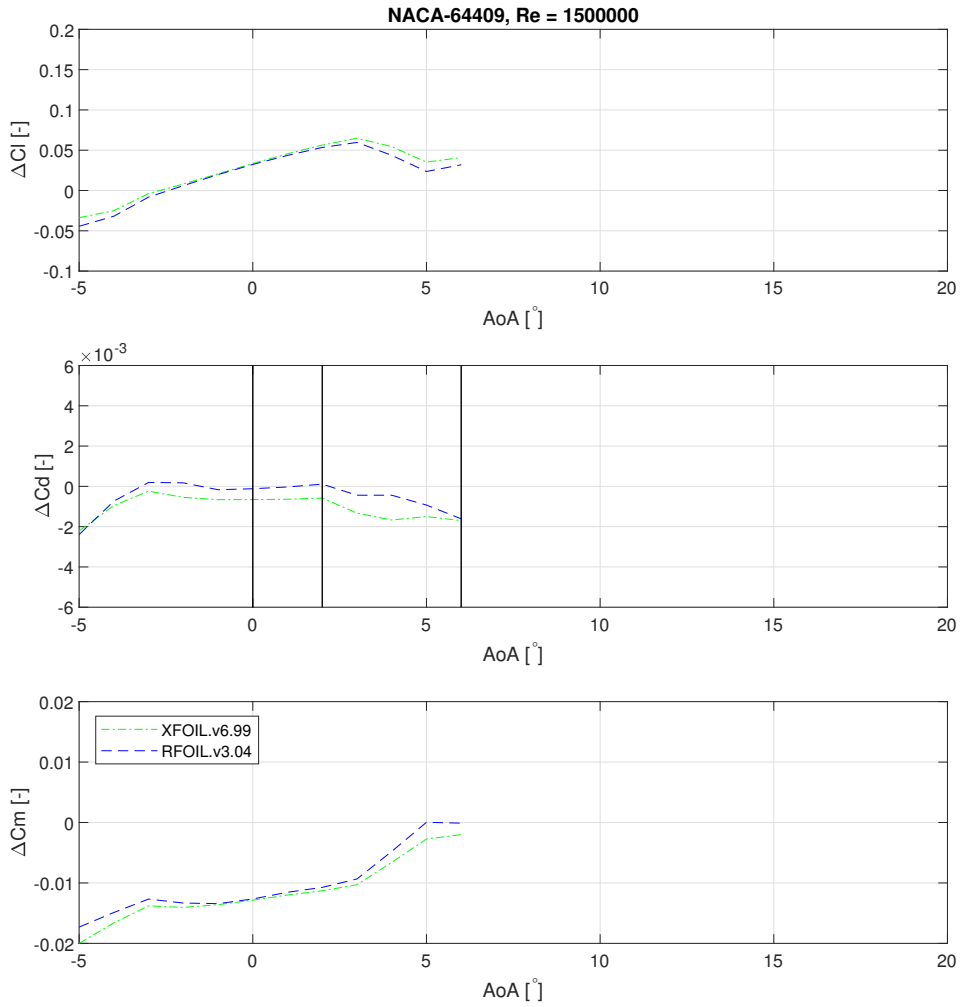

Figure B.399: Comparison between experimental and numerical pressure and skin friction distributions for the NACA-64409 airfoil at a Reynolds number of 1500000 and at the design angle of attack.

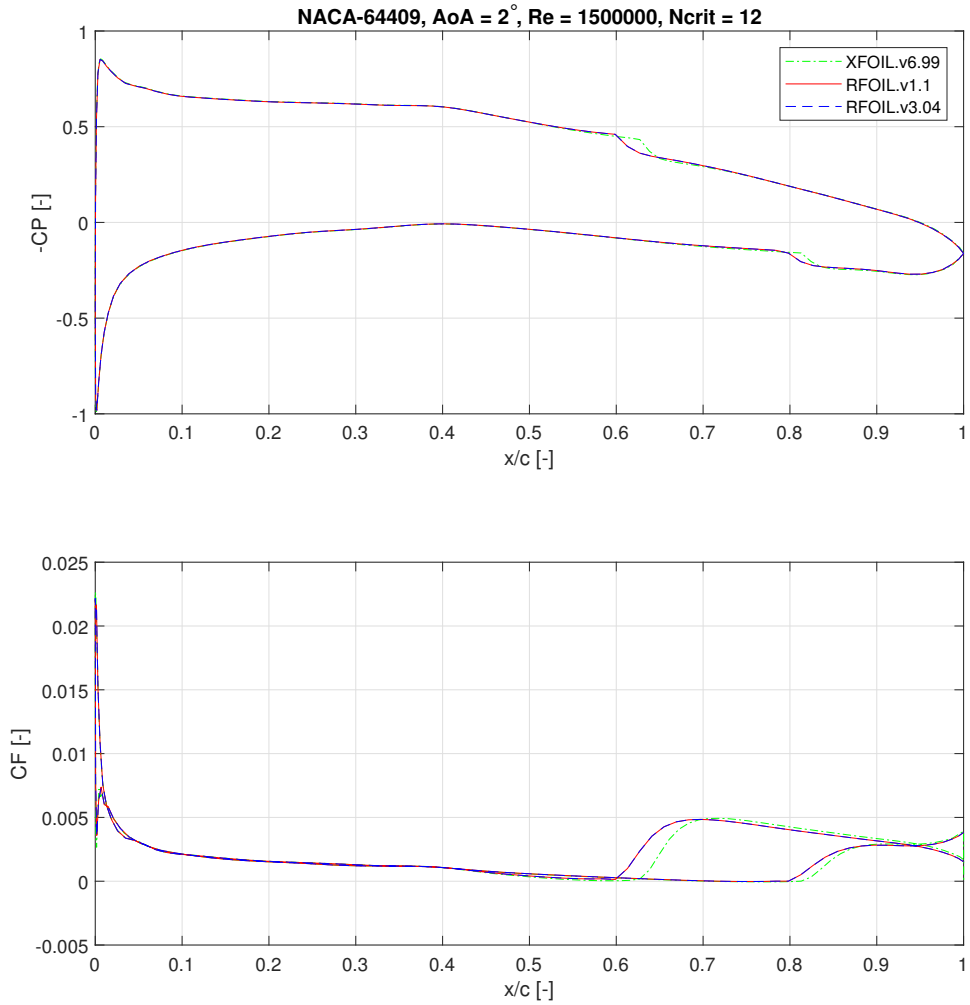

Figure B.400: Comparison between experimental and numerical polars for the NACA-64409 airfoil at a Reynolds number of 2000000. Simulation time to generate the polars by means the different codes and the number of converged polar points are depicted between parentheses.

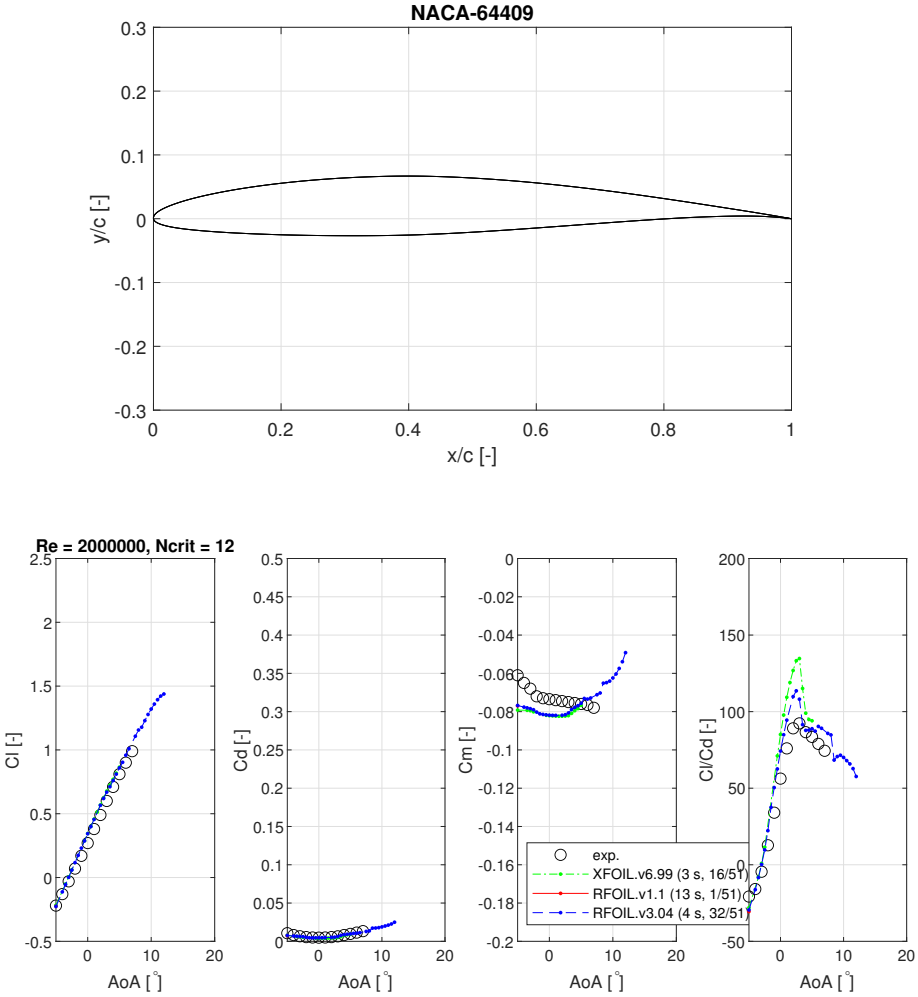

Figure B.401: Differences between experimental and numerical polars for the NACA-64409 airfoil at a Reynolds number of 2000000. Vertical black lines in the middle subplot indicate, from left to right, the angle of attack corresponding to the minimum drag coefficient, maximum lift to drag ratio and maximum lift coefficient, respectively.

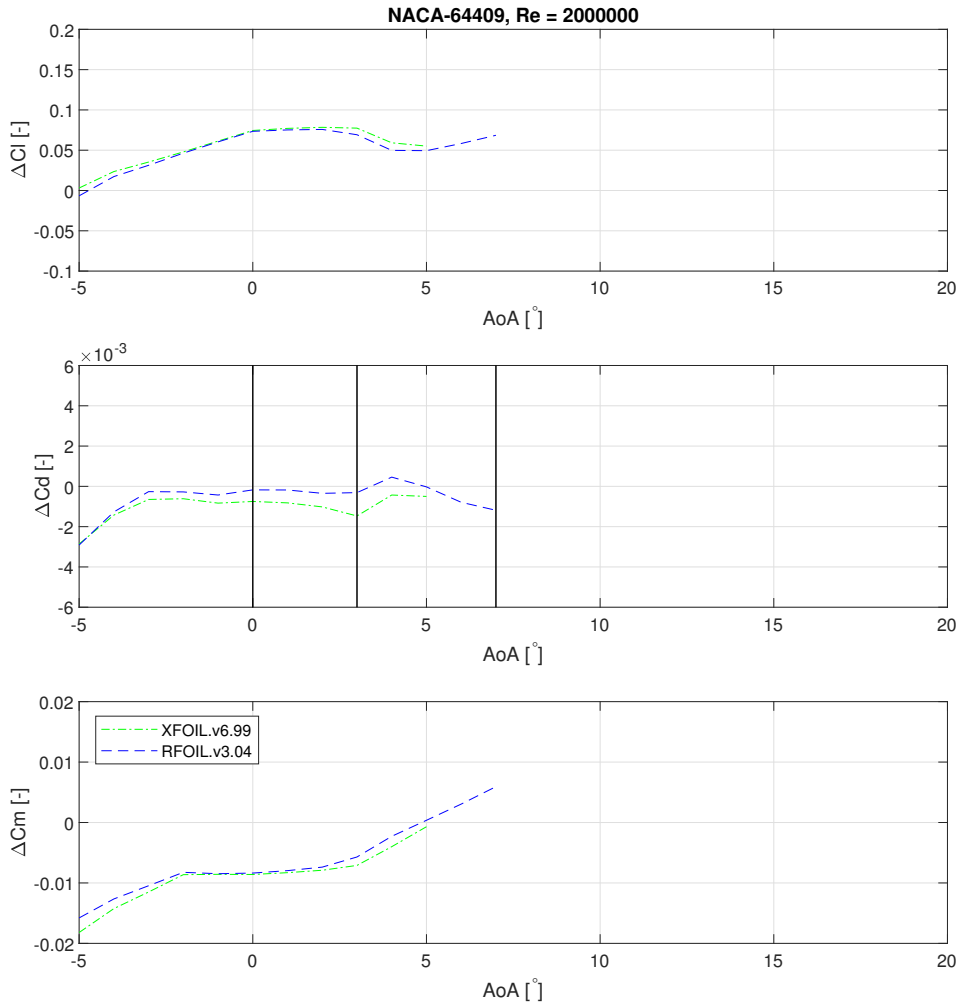

Figure B.402: Comparison between experimental and numerical pressure and skin friction distributions for the NACA-64409 airfoil at a Reynolds number of 2000000 and at the design angle of attack.

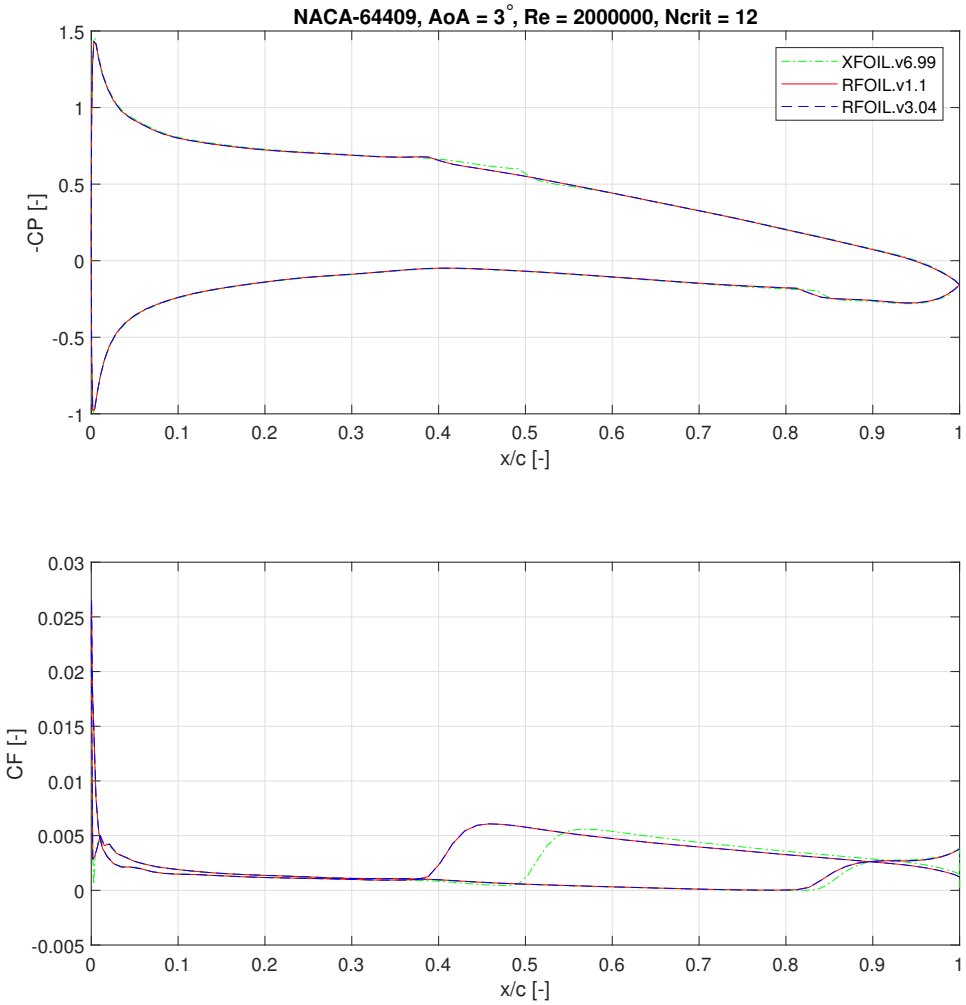

Figure B.403: Comparison between experimental and numerical polars for the NACA-64409 airfoil at a Reynolds number of 3000000. Simulation time to generate the polars by means the different codes and the number of converged polar points are depicted between parentheses.

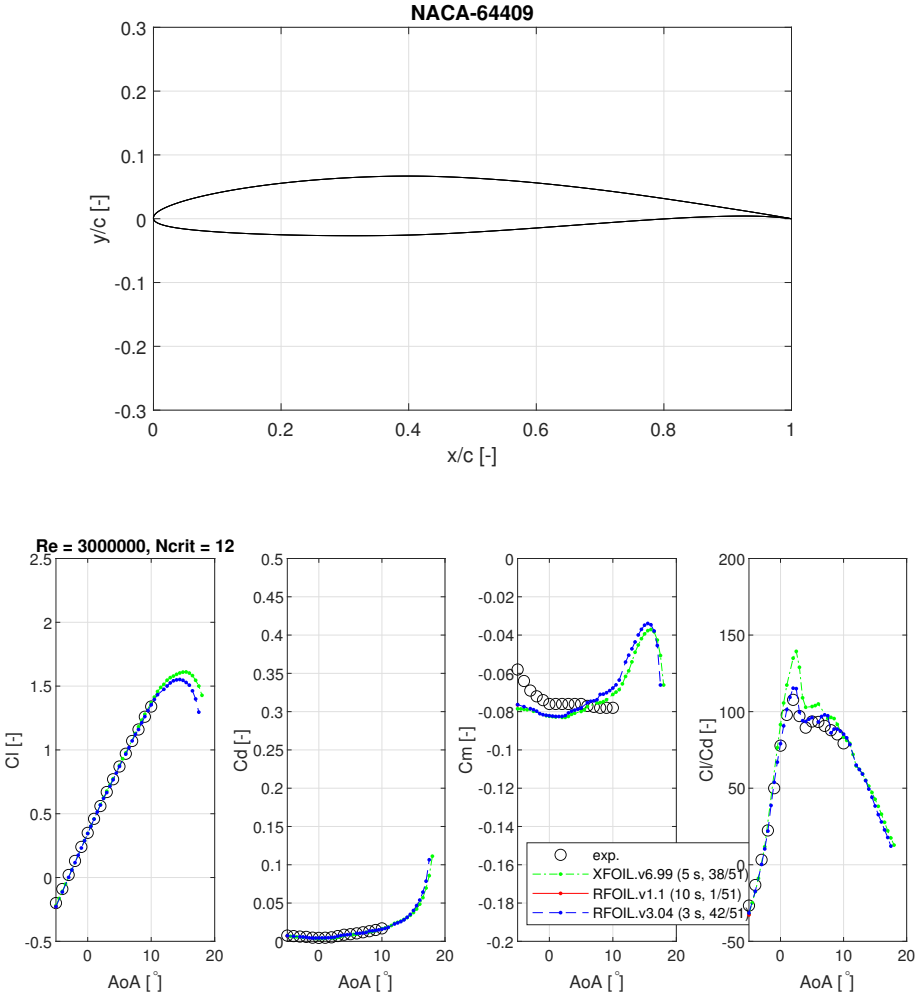

Figure B.404: Differences between experimental and numerical polars for the NACA-64409 airfoil at a Reynolds number of 3000000. Vertical black lines in the middle subplot indicate, from left to right, the angle of attack corresponding to the minimum drag coefficient, maximum lift to drag ratio and maximum lift coefficient, respectively.

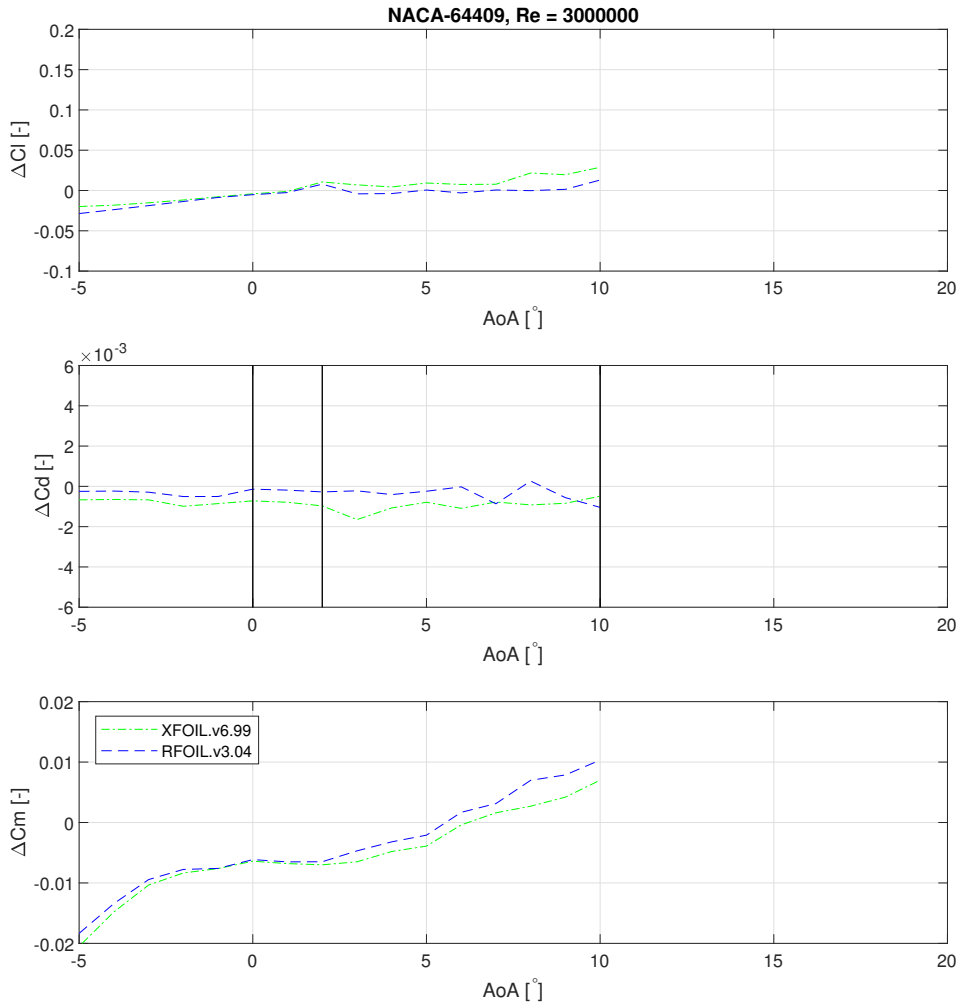

Figure B.405: Comparison between experimental and numerical pressure and skin friction distributions for the NACA-64409 airfoil at a Reynolds number of 3000000 and at the design angle of attack.

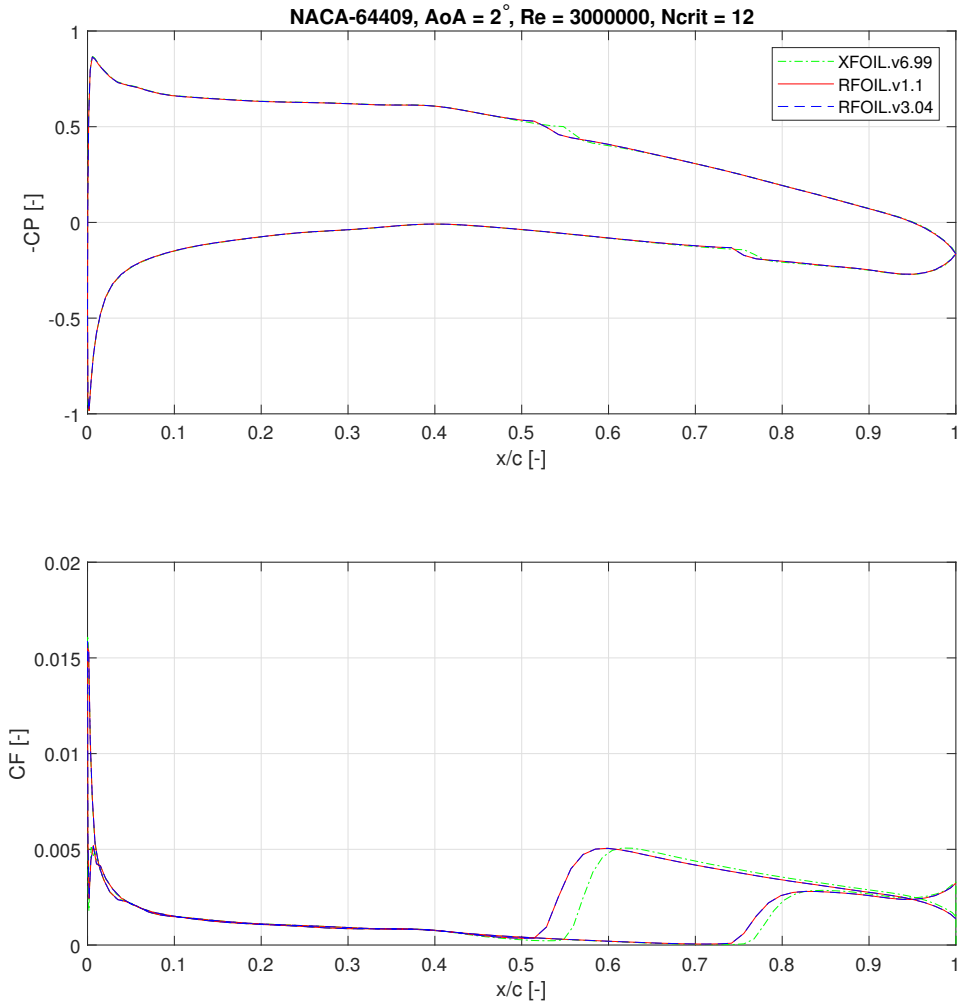

Figure B.406: Comparison between experimental and numerical polars for the NACA-64409 airfoil at a Reynolds number of 700000. Simulation time to generate the polars by means the different codes and the number of converged polar points are depicted between parentheses.

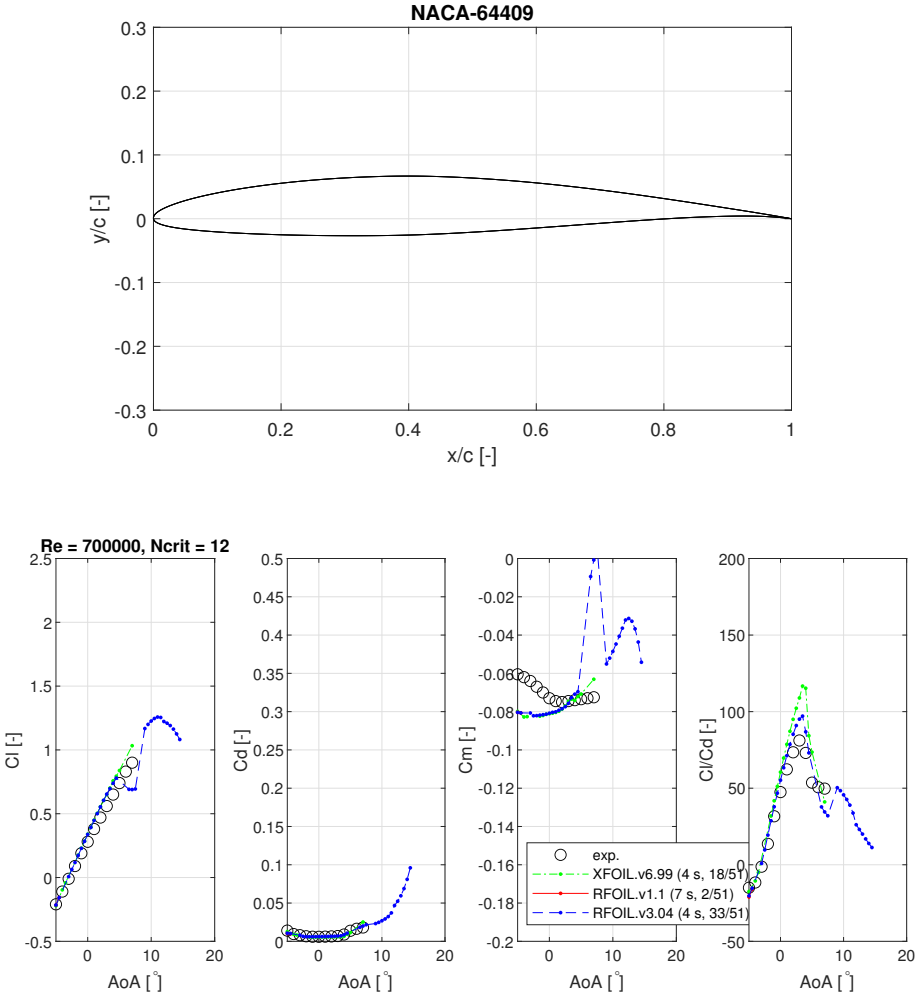

Figure B.407: Differences between experimental and numerical polars for the NACA-64409 airfoil at a Reynolds number of 700000. Vertical black lines in the middle subplot indicate, from left to right, the angle of attack corresponding to the minimum drag coefficient, maximum lift to drag ratio and maximum lift coefficient, respectively.

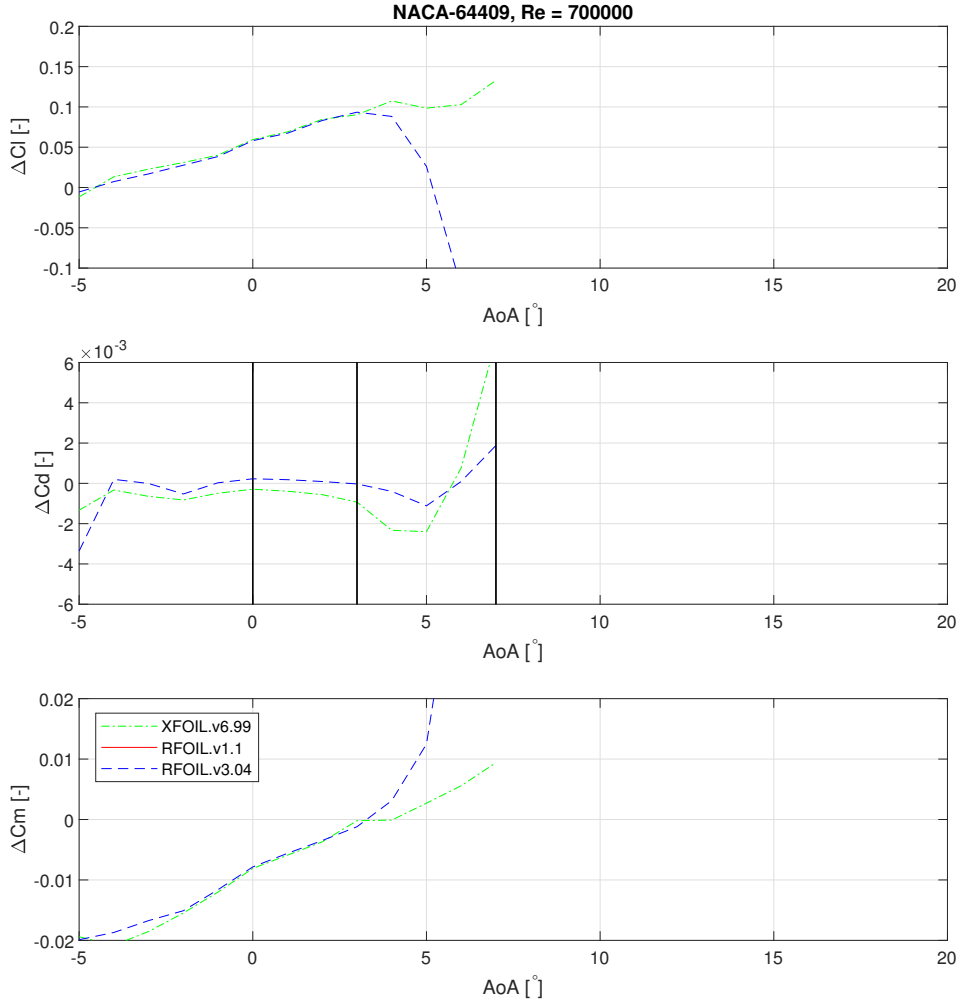

Figure B.408: Comparison between experimental and numerical pressure and skin friction distributions for the NACA-64409 airfoil at a Reynolds number of 700000 and at the design angle of attack.

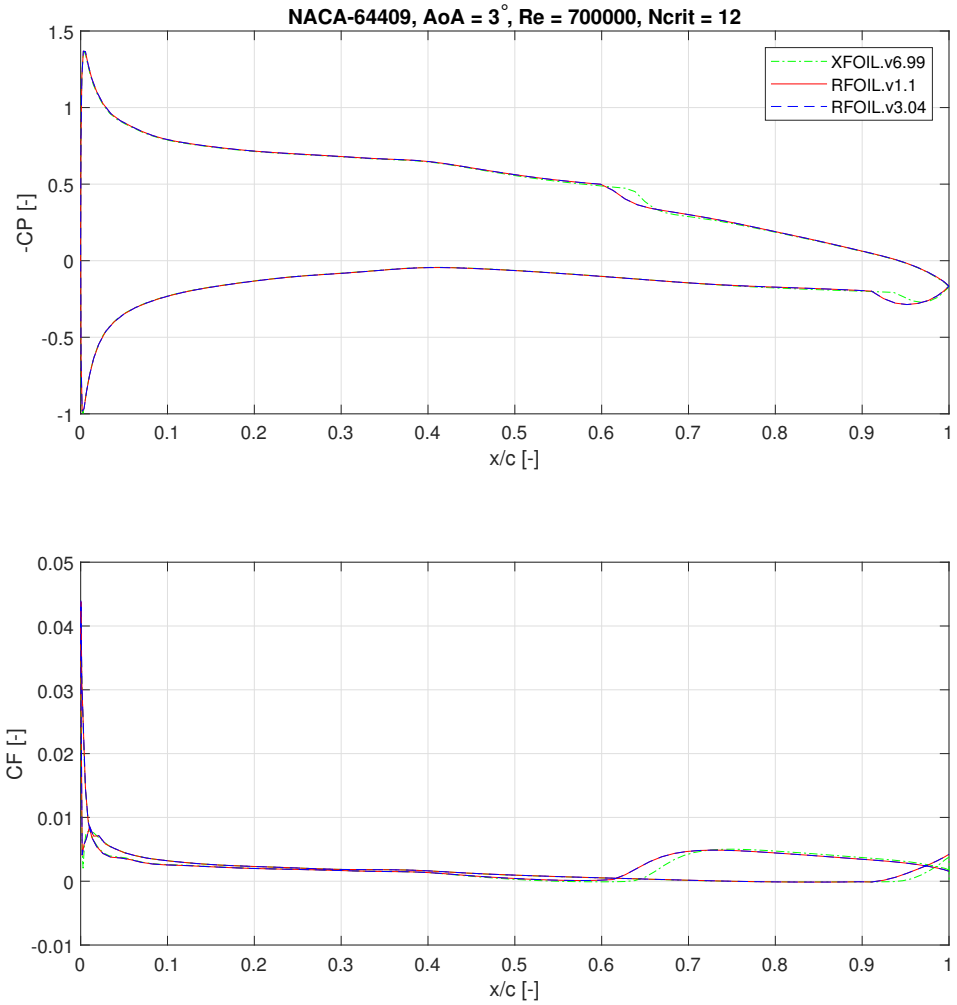

Figure B.409: Comparison between experimental and numerical polars for the NACA-64415 airfoil at a Reynolds number of 1000000. Simulation time to generate the polars by means the different codes and the number of converged polar points are depicted between parentheses.

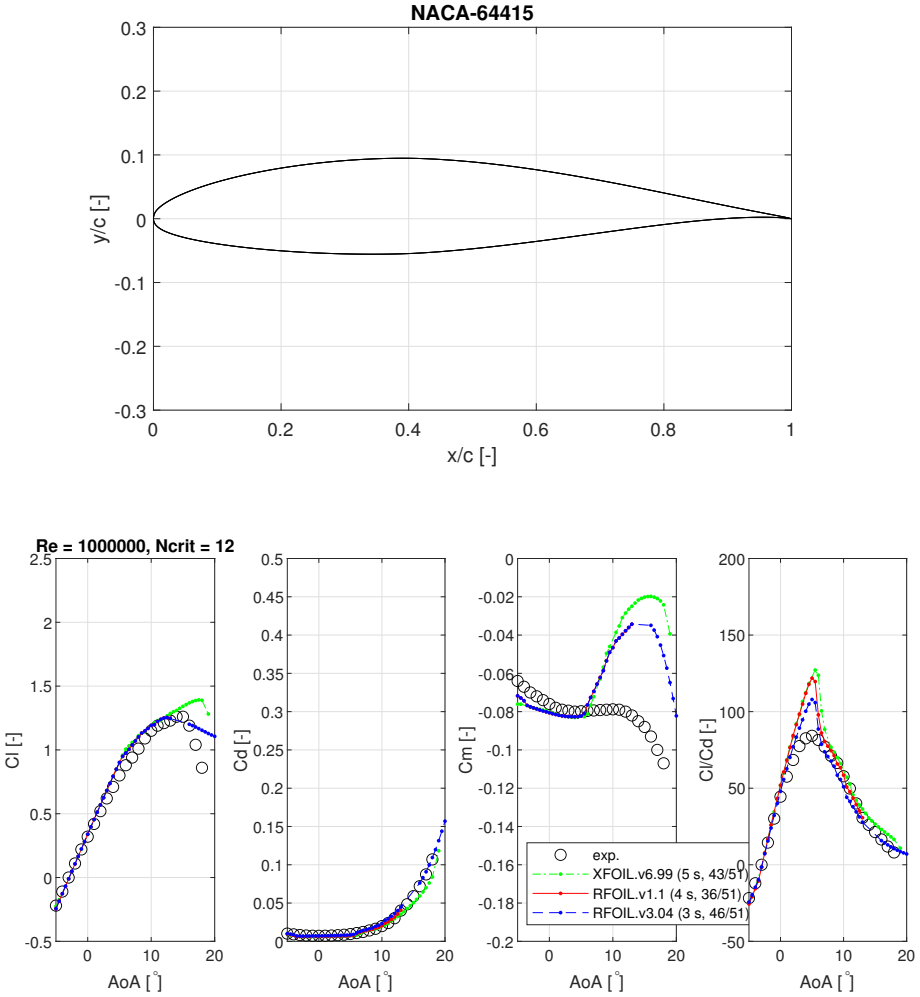

Figure B.410: Differences between experimental and numerical polars for the NACA-64415 airfoil at a Reynolds number of 1000000. Vertical black lines in the middle subplot indicate, from left to right, the angle of attack corresponding to the minimum drag coefficient, maximum lift to drag ratio and maximum lift coefficient, respectively.

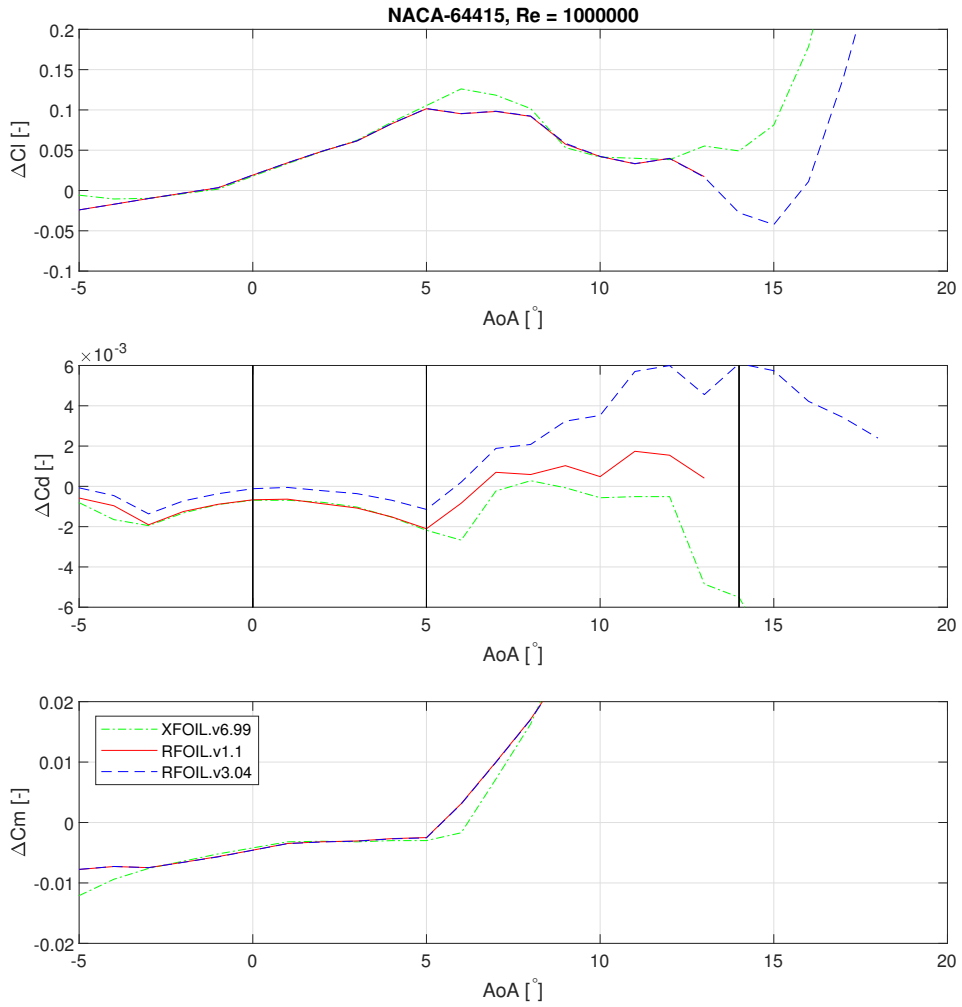

Figure B.411: Comparison between experimental and numerical pressure and skin friction distributions for the NACA-64415 airfoil at a Reynolds number of 1000000 and at the design angle of attack.

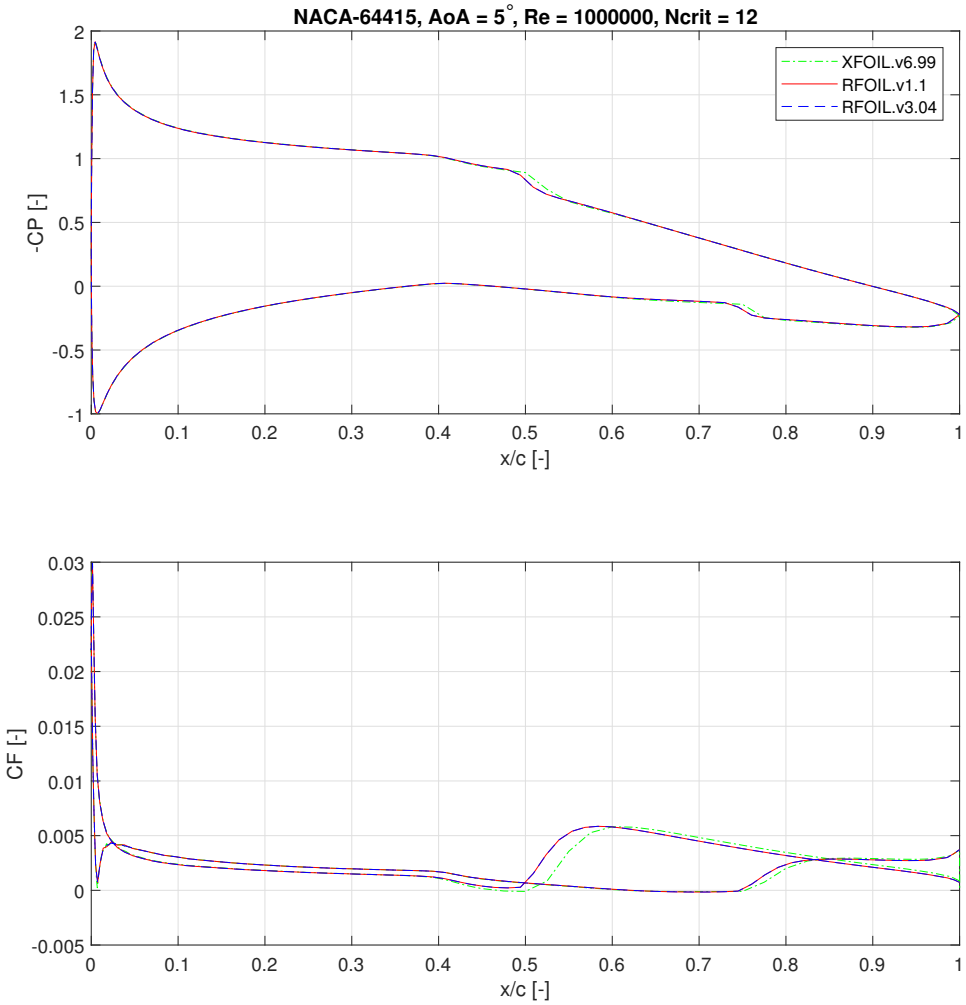

Figure B.412: Comparison between experimental and numerical polars for the NACA-64415 airfoil at a Reynolds number of 1500000. Simulation time to generate the polars by means the different codes and the number of converged polar points are depicted between parentheses.

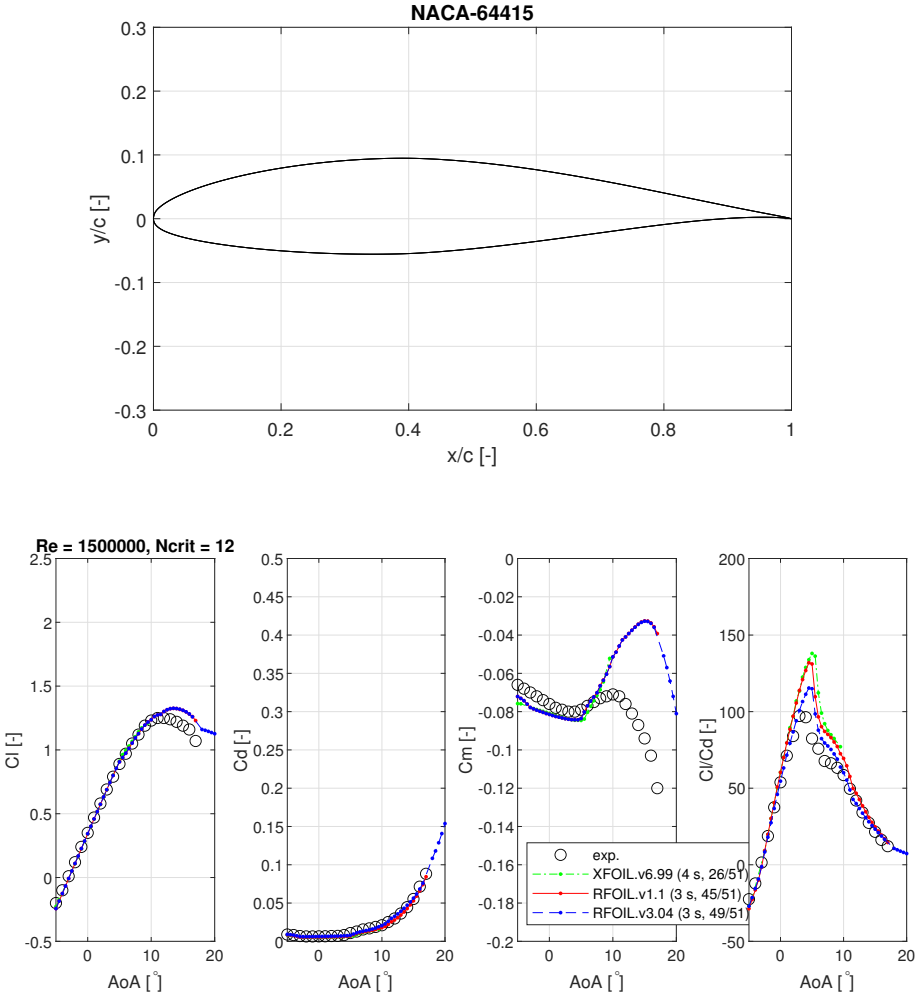

Figure B.413: Differences between experimental and numerical polars for the NACA-64415 airfoil at a Reynolds number of 1500000. Vertical black lines in the middle subplot indicate, from left to right, the angle of attack corresponding to the minimum drag coefficient, maximum lift to drag ratio and maximum lift coefficient, respectively.

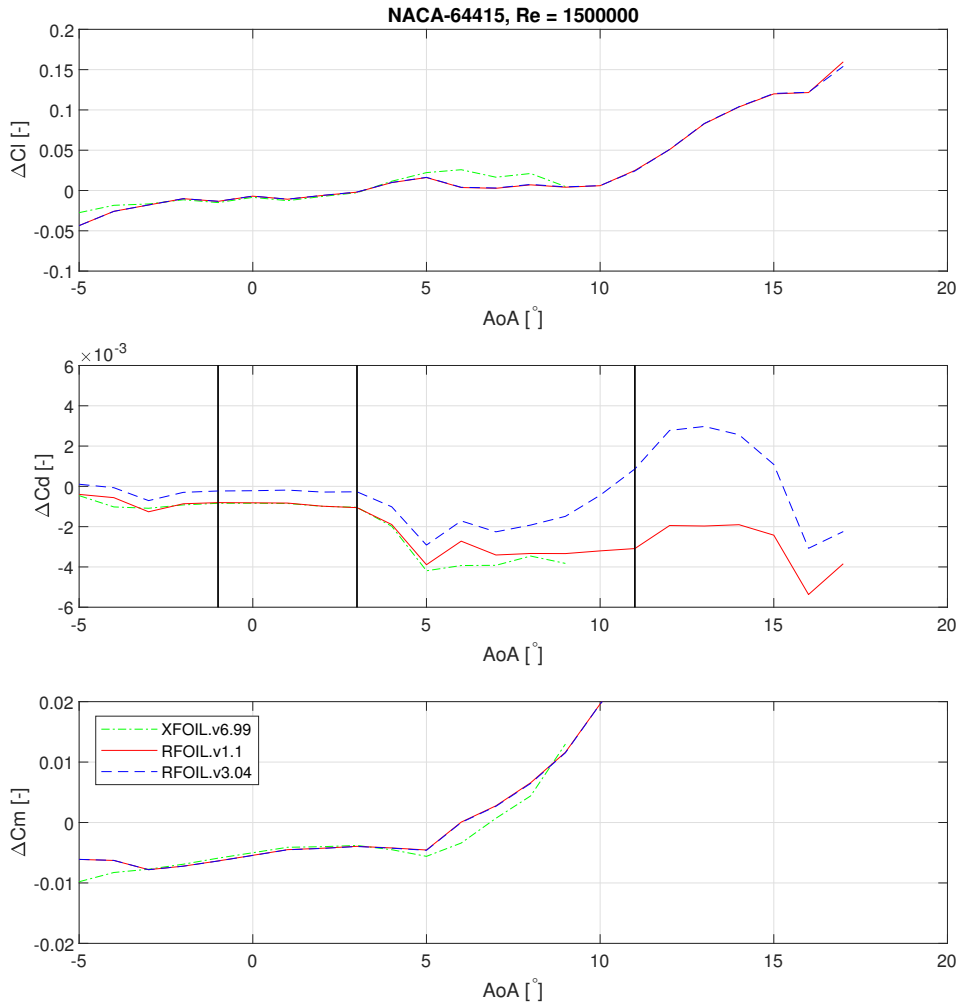

Figure B.414: Comparison between experimental and numerical pressure and skin friction distributions for the NACA-64415 airfoil at a Reynolds number of 1500000 and at the design angle of attack.

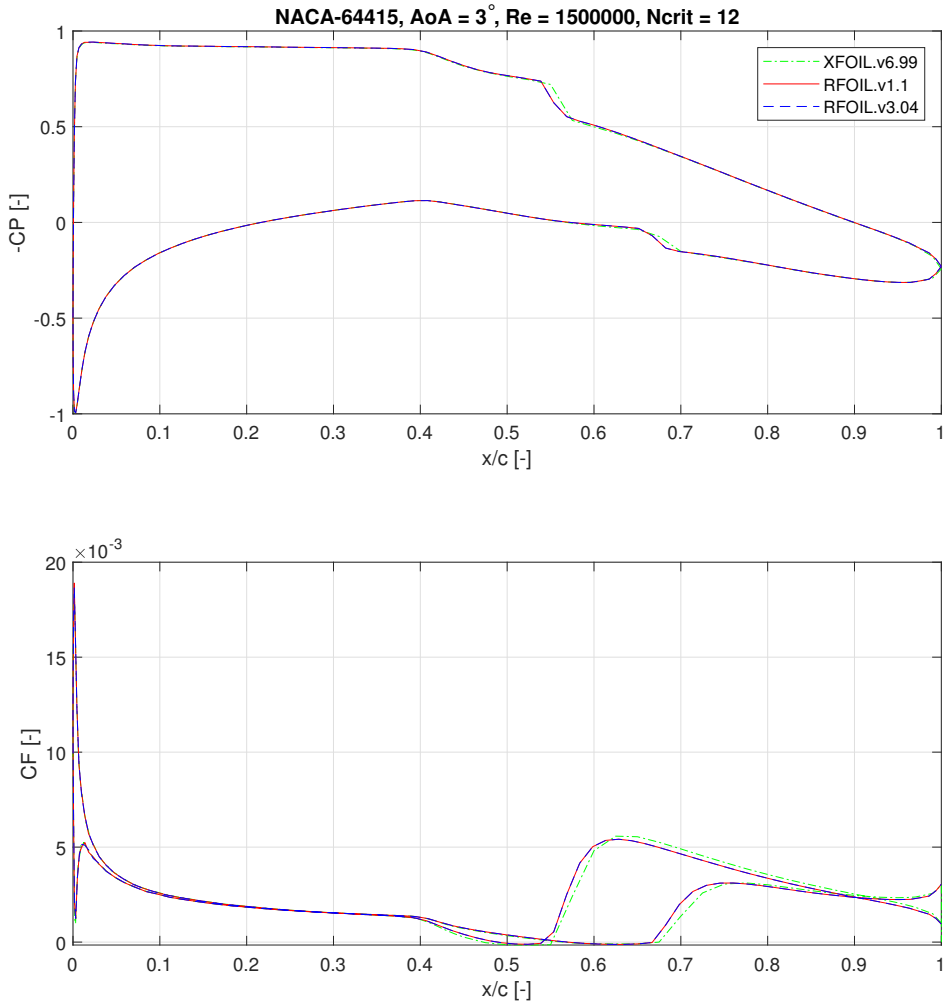

Figure B.415: Comparison between experimental and numerical polars for the NACA-64415 airfoil at a Reynolds number of 2000000. Simulation time to generate the polars by means the different codes and the number of converged polar points are depicted between parentheses.

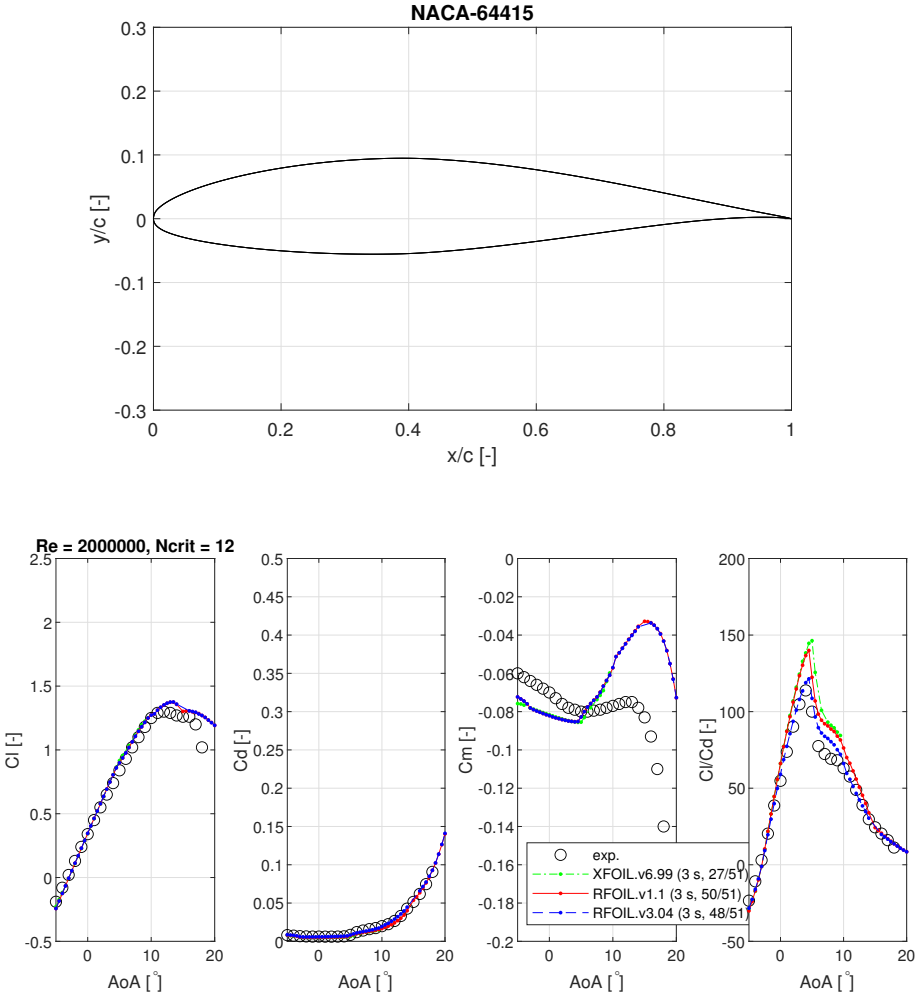

Figure B.416: Differences between experimental and numerical polars for the NACA-64415 airfoil at a Reynolds number of 2000000. Vertical black lines in the middle subplot indicate, from left to right, the angle of attack corresponding to the minimum drag coefficient, maximum lift to drag ratio and maximum lift coefficient, respectively.

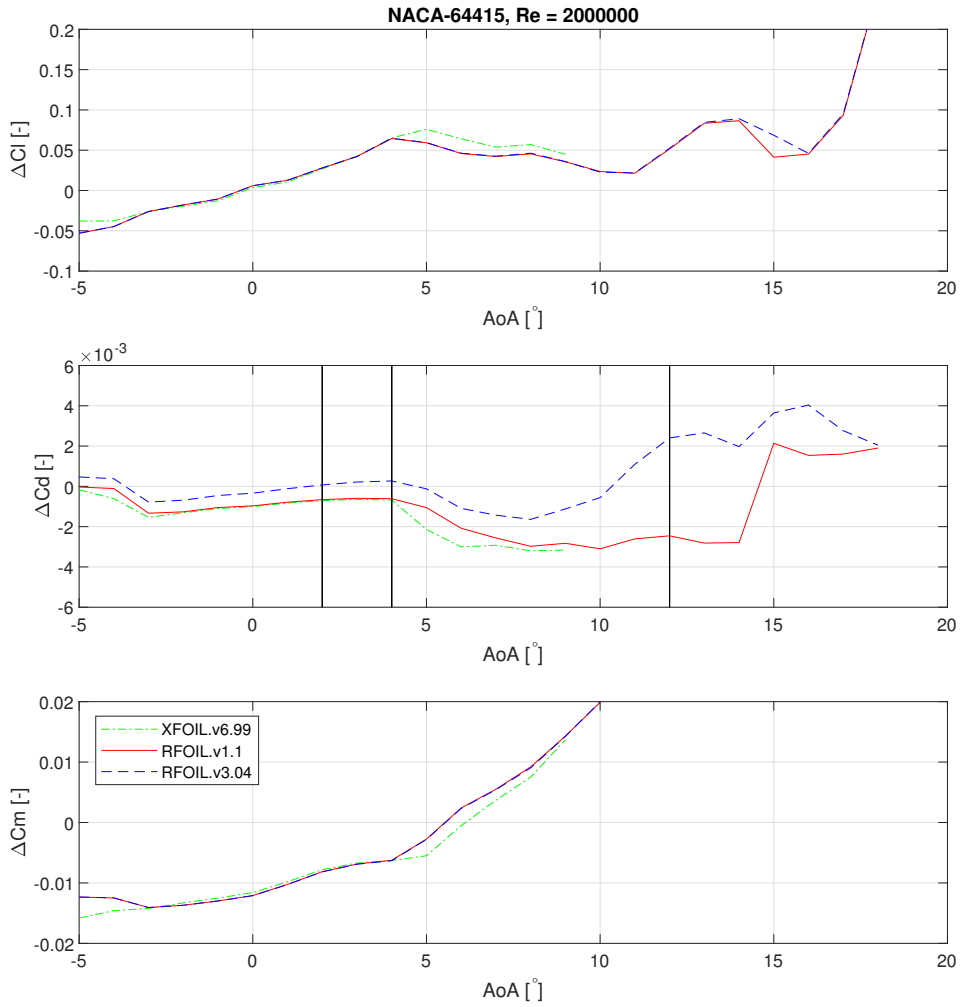

Figure B.417: Comparison between experimental and numerical pressure and skin friction distributions for the NACA-64415 airfoil at a Reynolds number of 2000000 and at the design angle of attack.

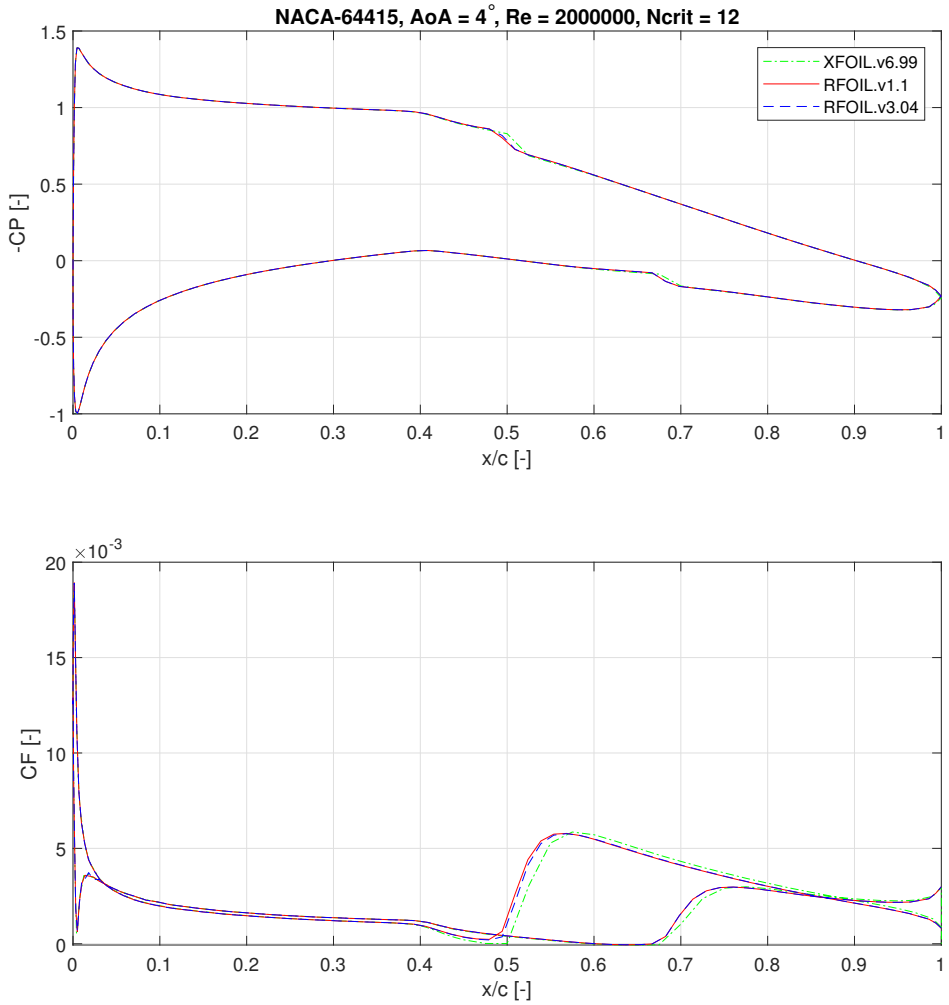

Figure B.418: Comparison between experimental and numerical polars for the NACA-64415 airfoil at a Reynolds number of 3000000. Simulation time to generate the polars by means the different codes and the number of converged polar points are depicted between parentheses.

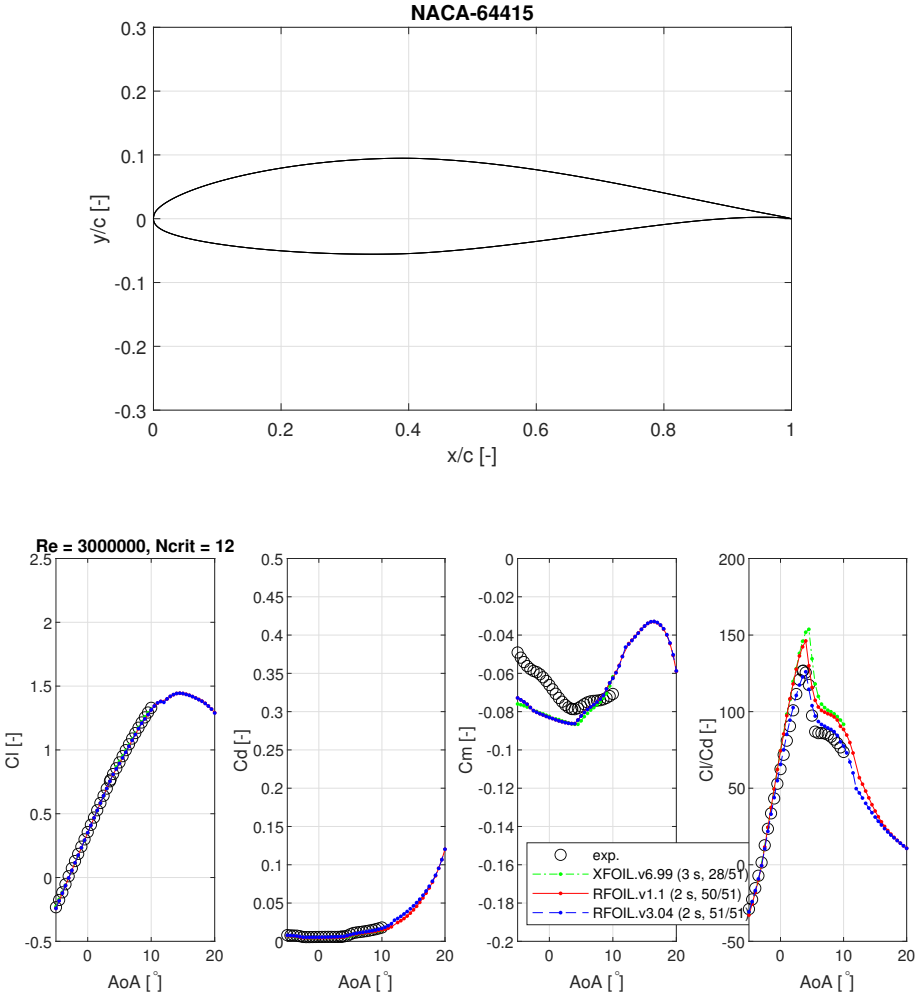

Figure B.419: Differences between experimental and numerical polars for the NACA-64415 airfoil at a Reynolds number of 3000000. Vertical black lines in the middle subplot indicate, from left to right, the angle of attack corresponding to the minimum drag coefficient, maximum lift to drag ratio and maximum lift coefficient, respectively.

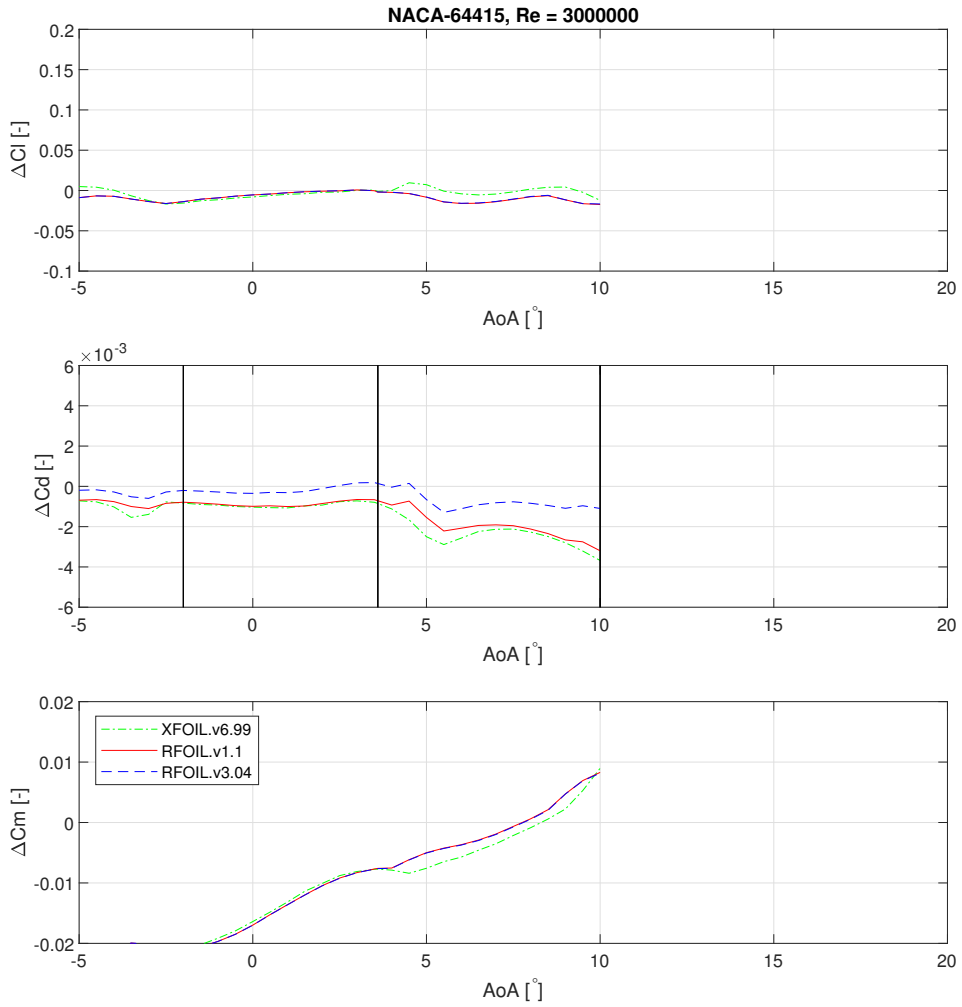

Figure B.420: Comparison between experimental and numerical pressure and skin friction distributions for the NACA-64415 airfoil at a Reynolds number of 3000000 and at the design angle of attack.

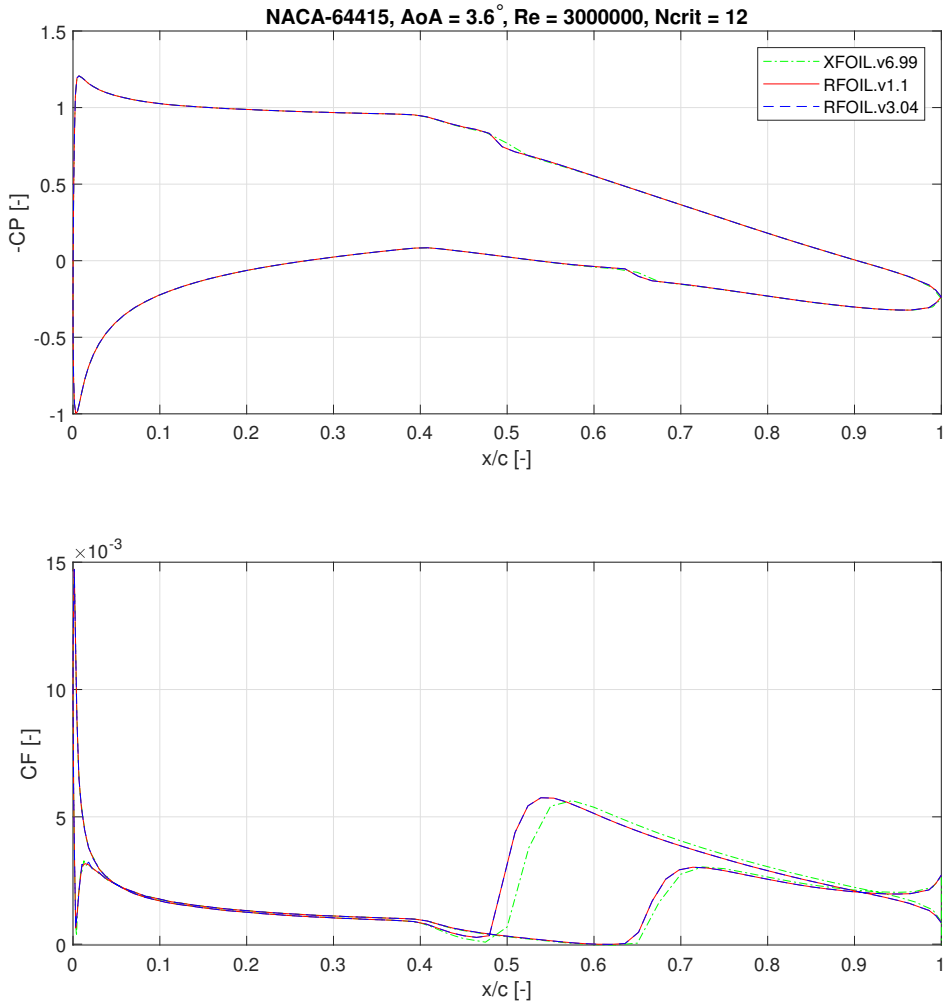

Figure B.421: Comparison between experimental and numerical polars for the NACA-64415 airfoil at a Reynolds number of 6000000. Simulation time to generate the polars by means the different codes and the number of converged polar points are depicted between parentheses.

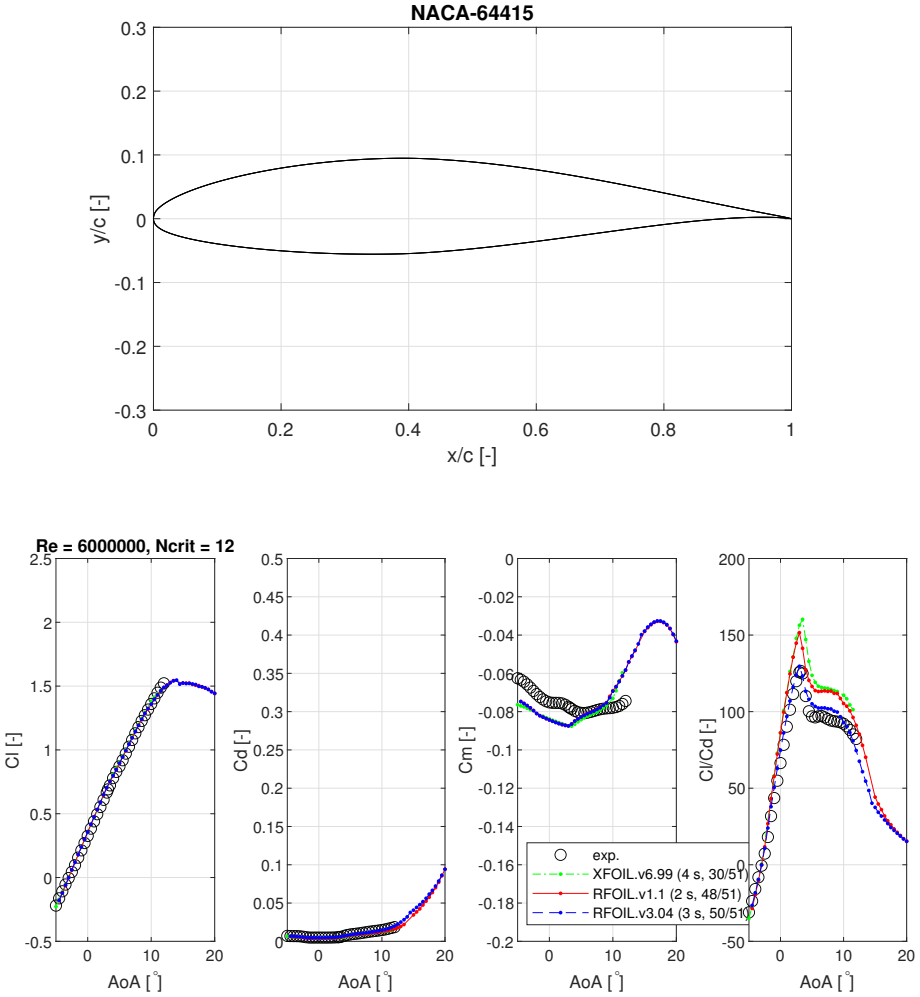

Figure B.422: Differences between experimental and numerical polars for the NACA-64415 airfoil at a Reynolds number of 6000000. Vertical black lines in the middle subplot indicate, from left to right, the angle of attack corresponding to the minimum drag coefficient, maximum lift to drag ratio and maximum lift coefficient, respectively.

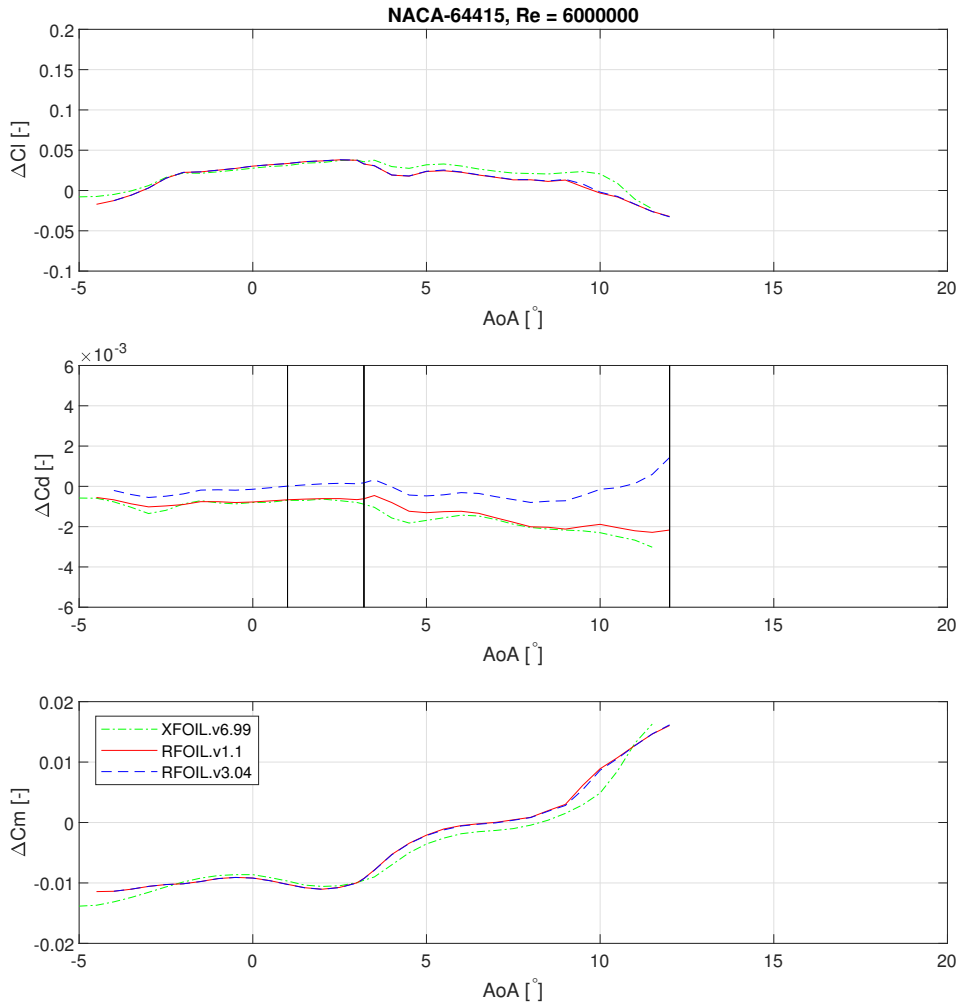

Figure B.423: Comparison between experimental and numerical pressure and skin friction distributions for the NACA-64415 airfoil at a Reynolds number of 6000000 and at the design angle of attack.

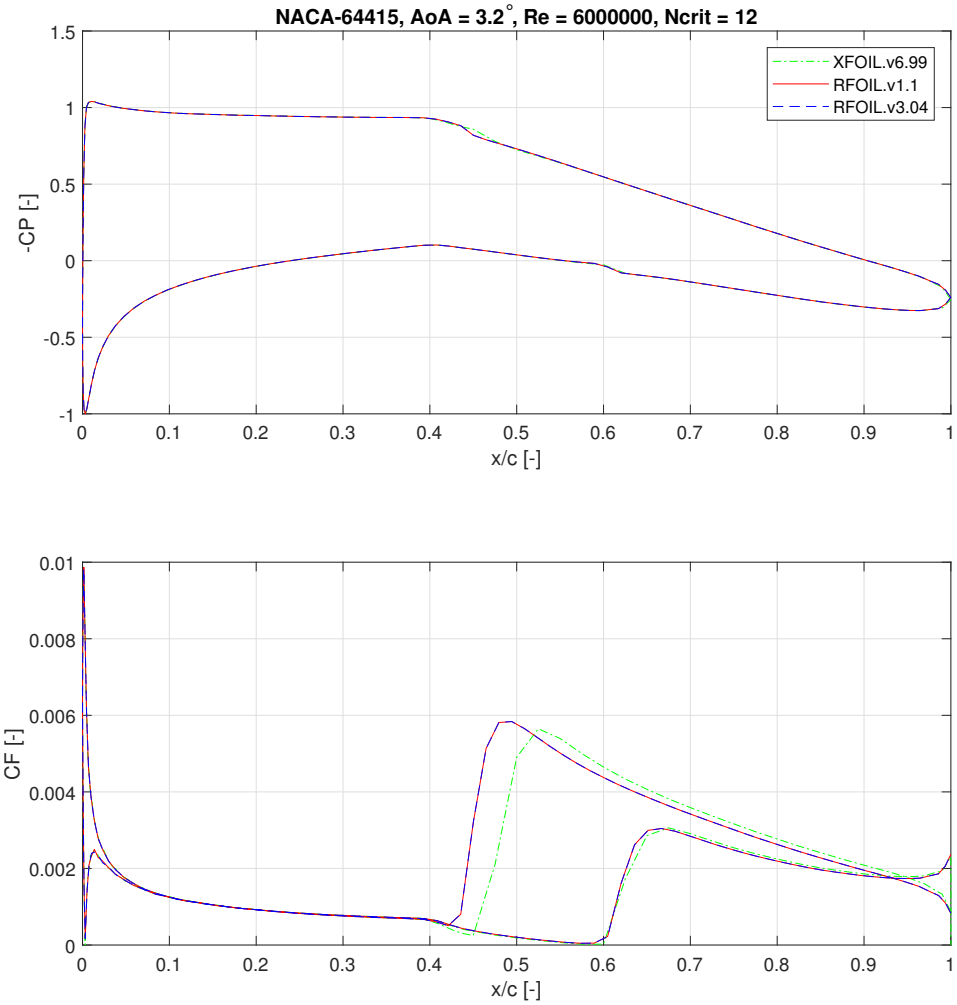

Figure B.424: Comparison between experimental and numerical polars for the NACA-64415 airfoil at a Reynolds number of 700000. Simulation time to generate the polars by means the different codes and the number of converged polar points are depicted between parentheses.

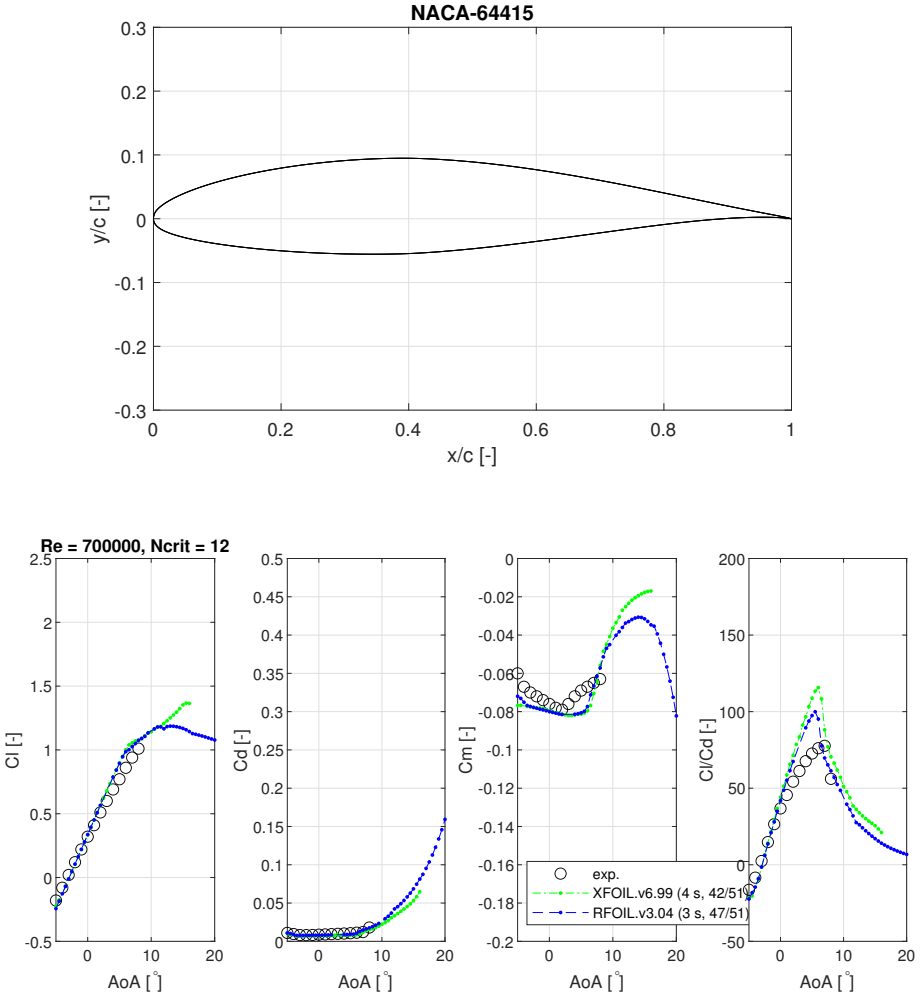

Figure B.425: Differences between experimental and numerical polars for the NACA-64415 airfoil at a Reynolds number of 700000. Vertical black lines in the middle subplot indicate, from left to right, the angle of attack corresponding to the minimum drag coefficient, maximum lift to drag ratio and maximum lift coefficient, respectively.

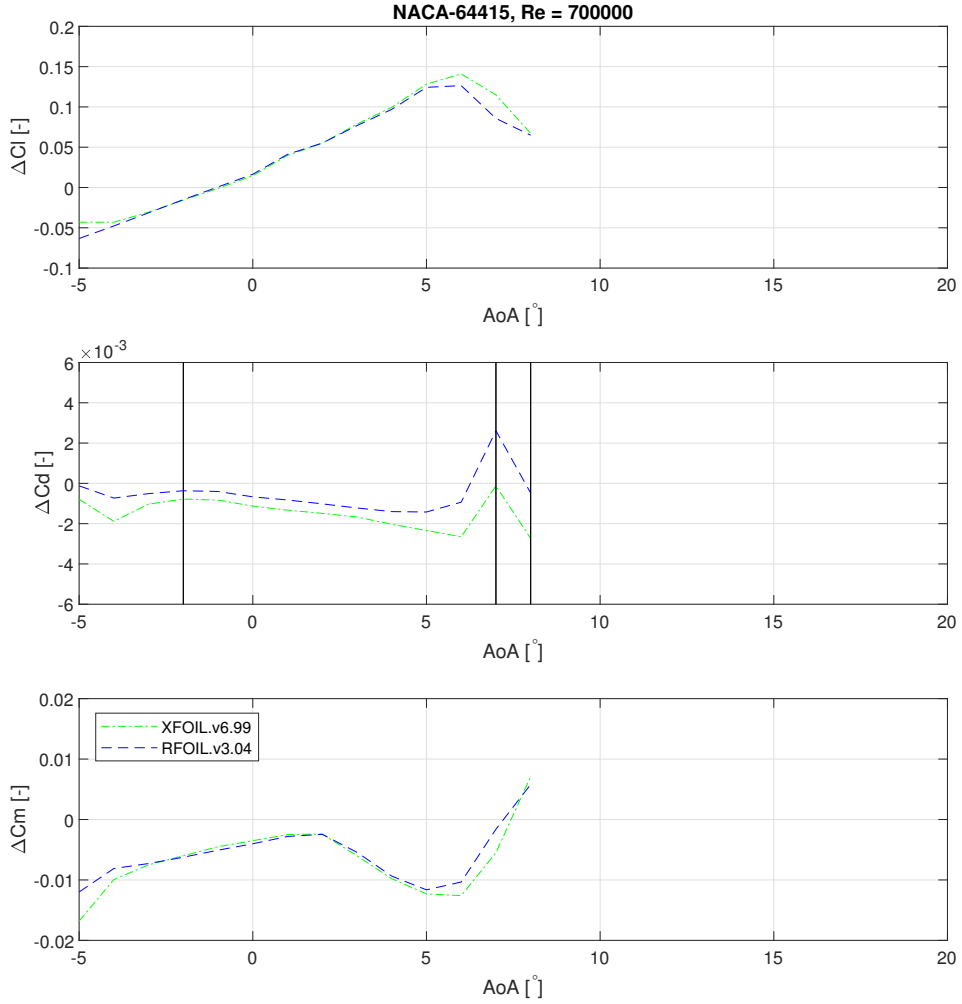

Figure B.426: Comparison between experimental and numerical pressure and skin friction distributions for the NACA-64415 airfoil at a Reynolds number of 700000 and at the design angle of attack.

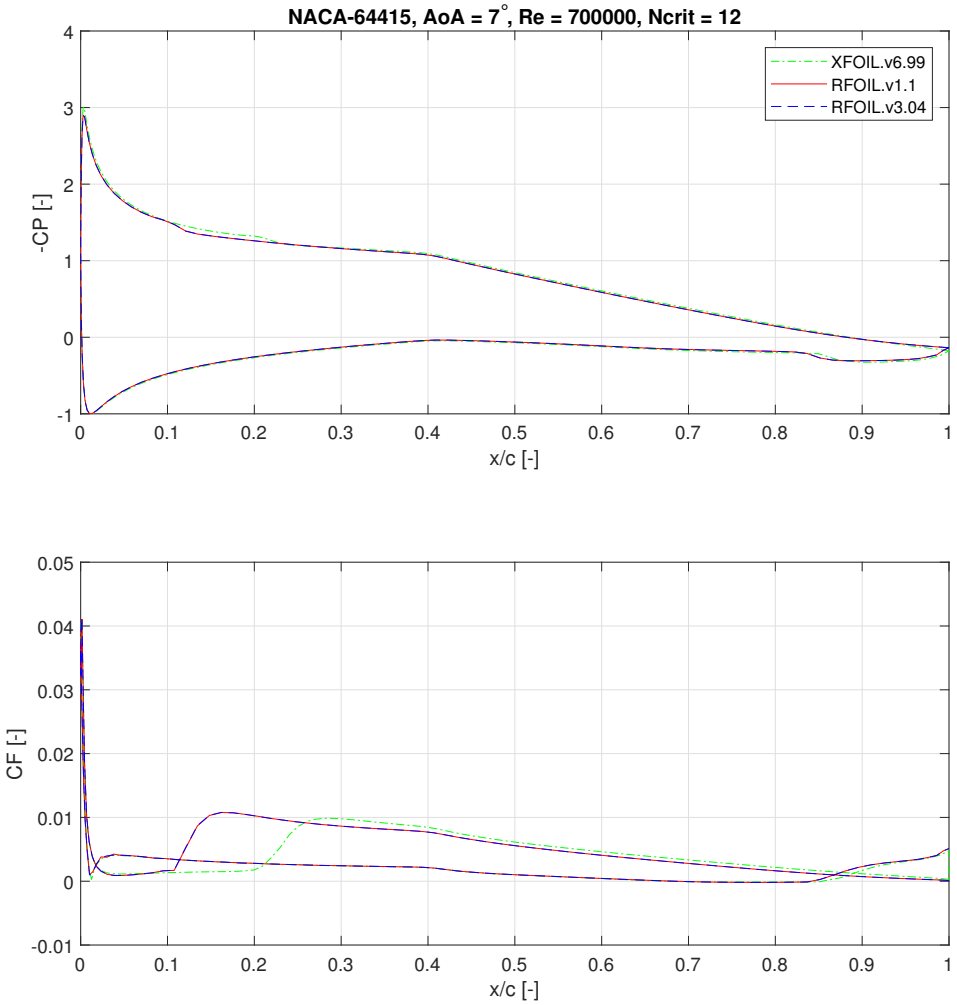

Figure B.427: Comparison between experimental and numerical polars for the NACA-64418 airfoil at a Reynolds number of 1000000. Simulation time to generate the polars by means the different codes and the number of converged polar points are depicted between parentheses.

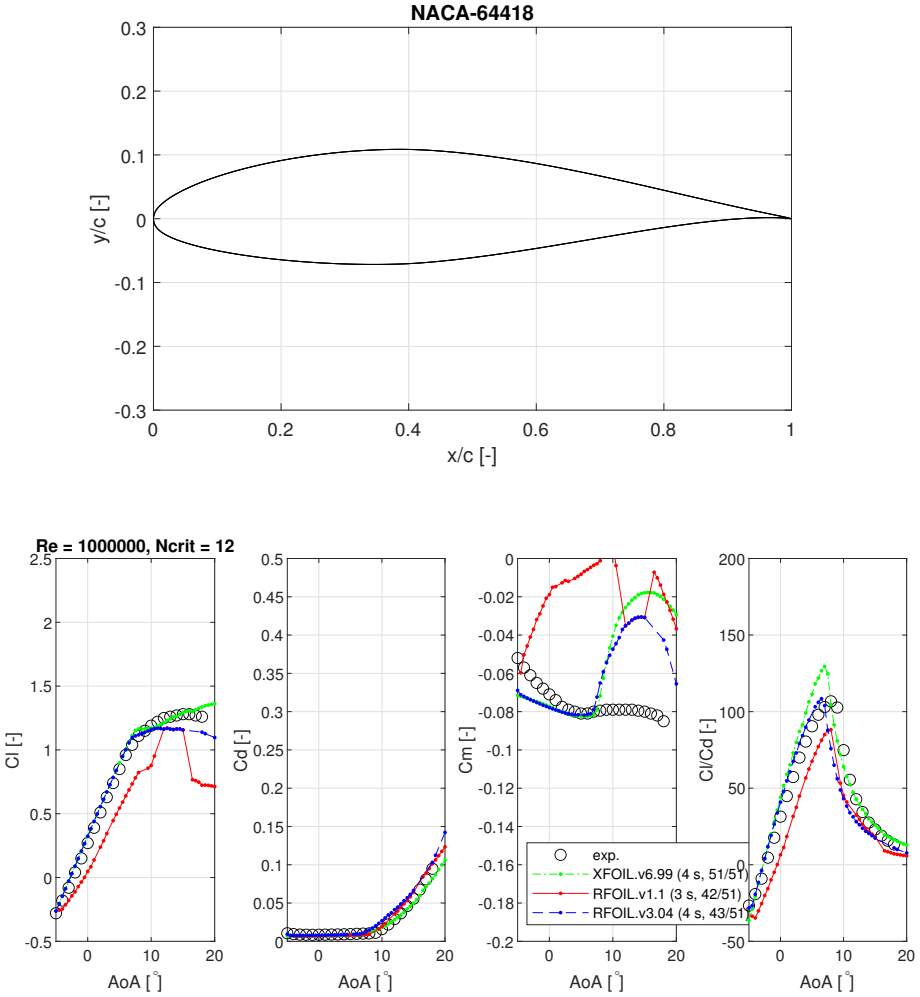

Figure B.428: Differences between experimental and numerical polars for the NACA-64418 airfoil at a Reynolds number of 1000000. Vertical black lines in the middle subplot indicate, from left to right, the angle of attack corresponding to the minimum drag coefficient, maximum lift to drag ratio and maximum lift coefficient, respectively.

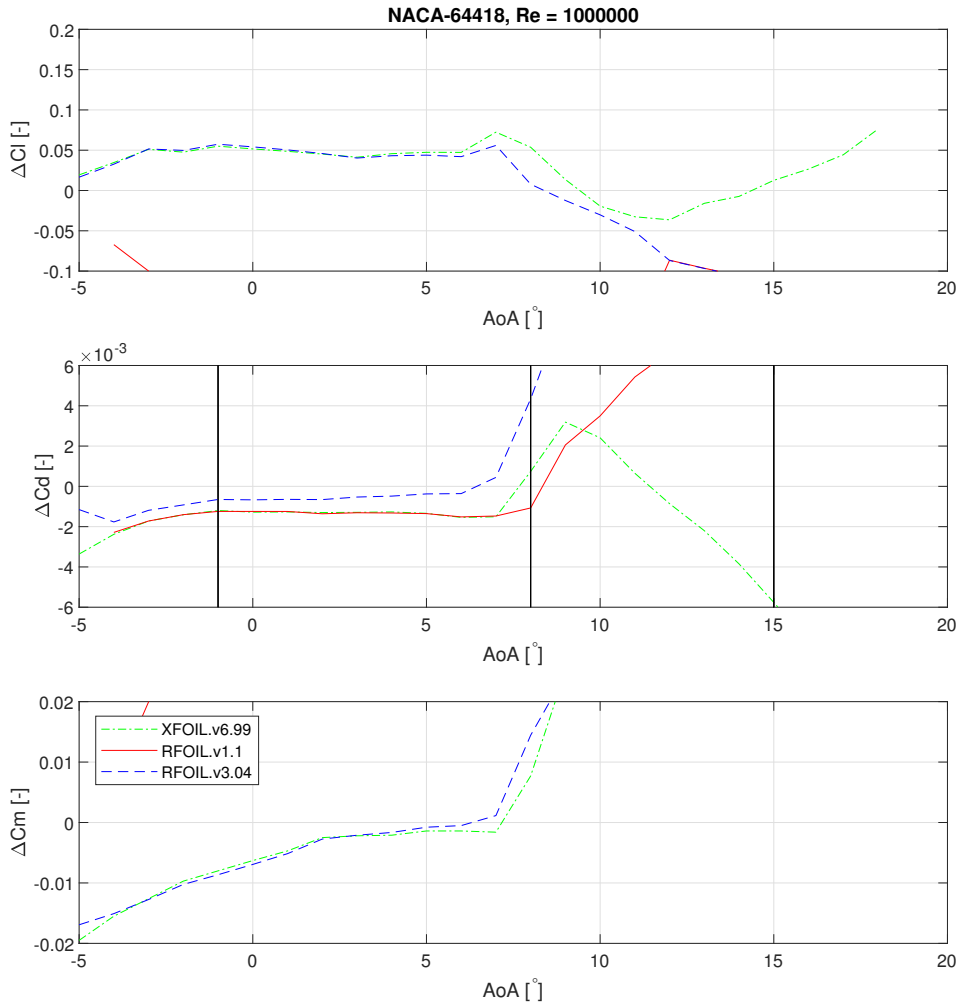

Figure B.429: Comparison between experimental and numerical pressure and skin friction distributions for the NACA-64418 airfoil at a Reynolds number of 1000000 and at the design angle of attack.

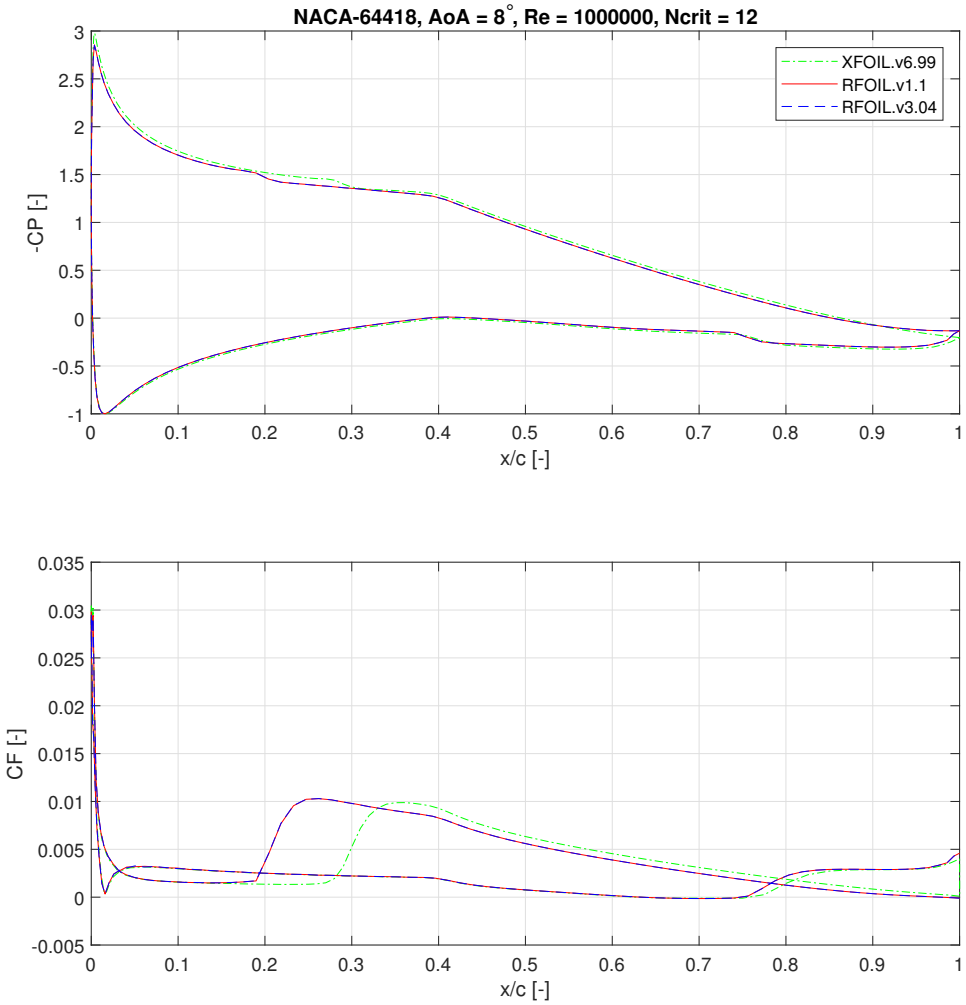

Figure B.430: Comparison between experimental and numerical polars for the NACA-64418 airfoil at a Reynolds number of 1500000. Simulation time to generate the polars by means the different codes and the number of converged polar points are depicted between parentheses.

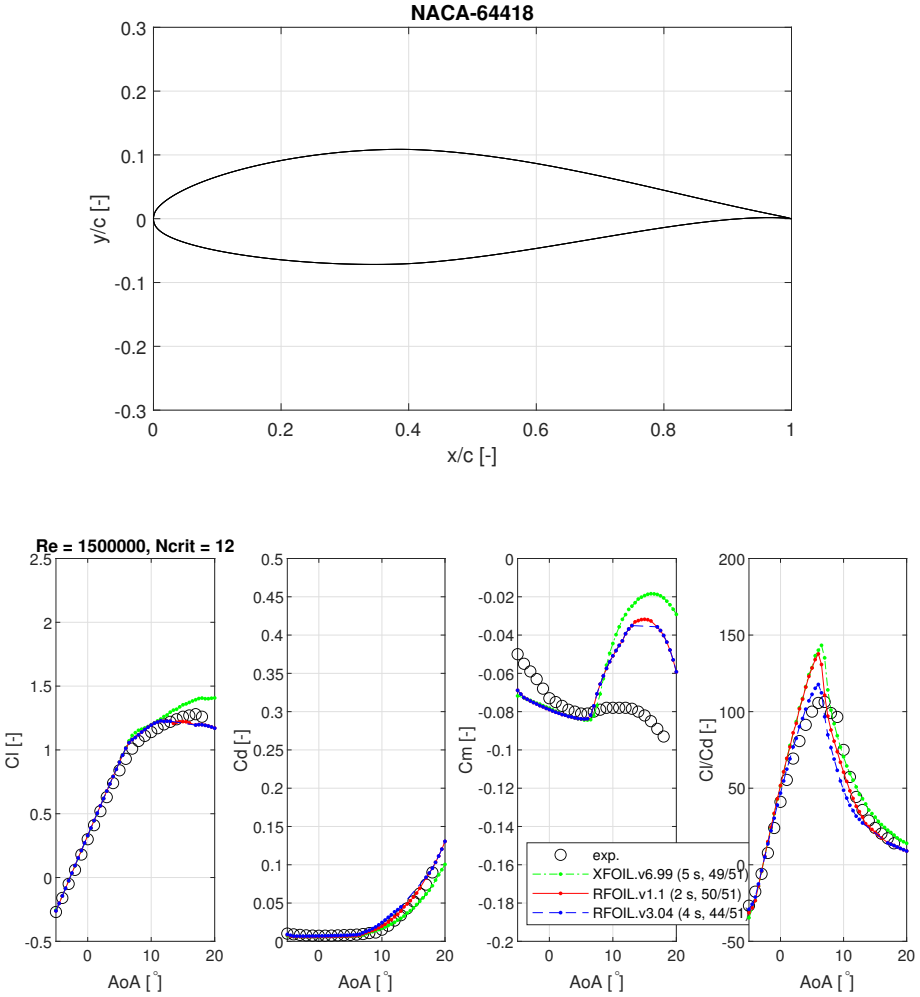

Figure B.431: Differences between experimental and numerical polars for the NACA-64418 airfoil at a Reynolds number of 1500000. Vertical black lines in the middle subplot indicate, from left to right, the angle of attack corresponding to the minimum drag coefficient, maximum lift to drag ratio and maximum lift coefficient, respectively.

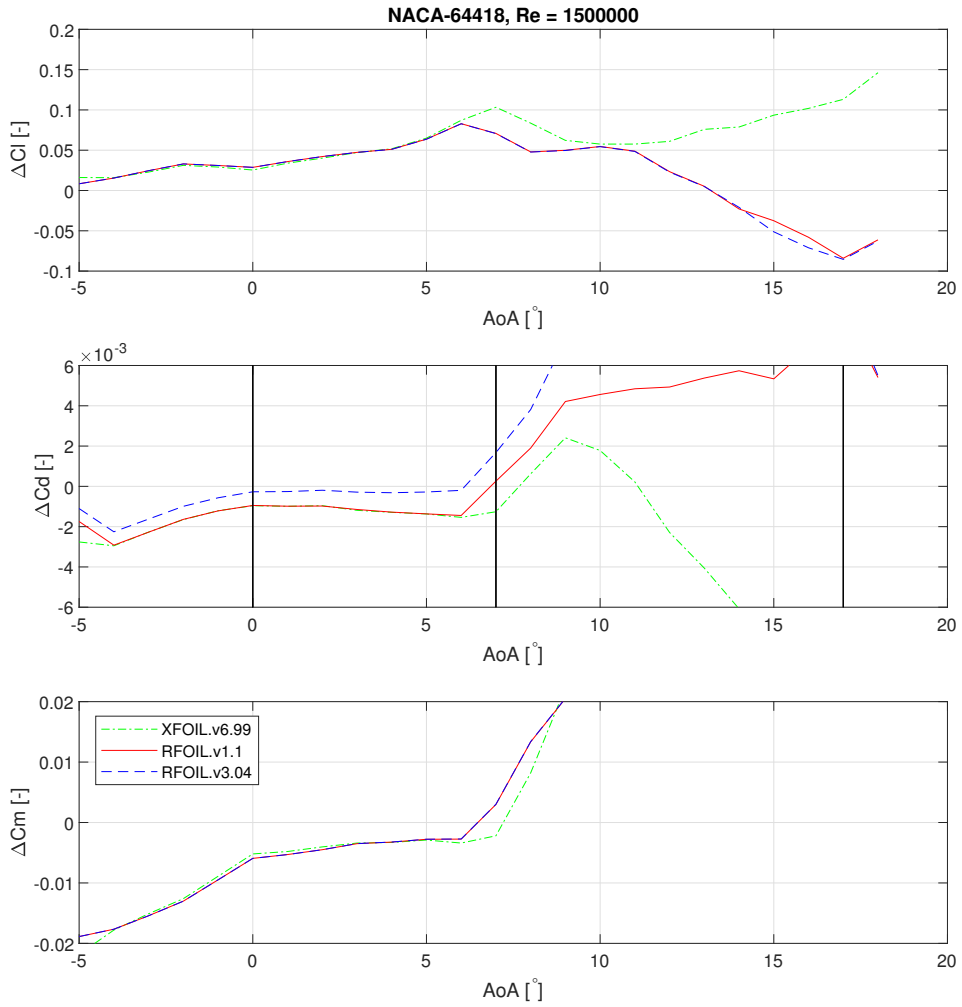

Figure B.432: Comparison between experimental and numerical pressure and skin friction distributions for the NACA-64418 airfoil at a Reynolds number of 1500000 and at the design angle of attack.

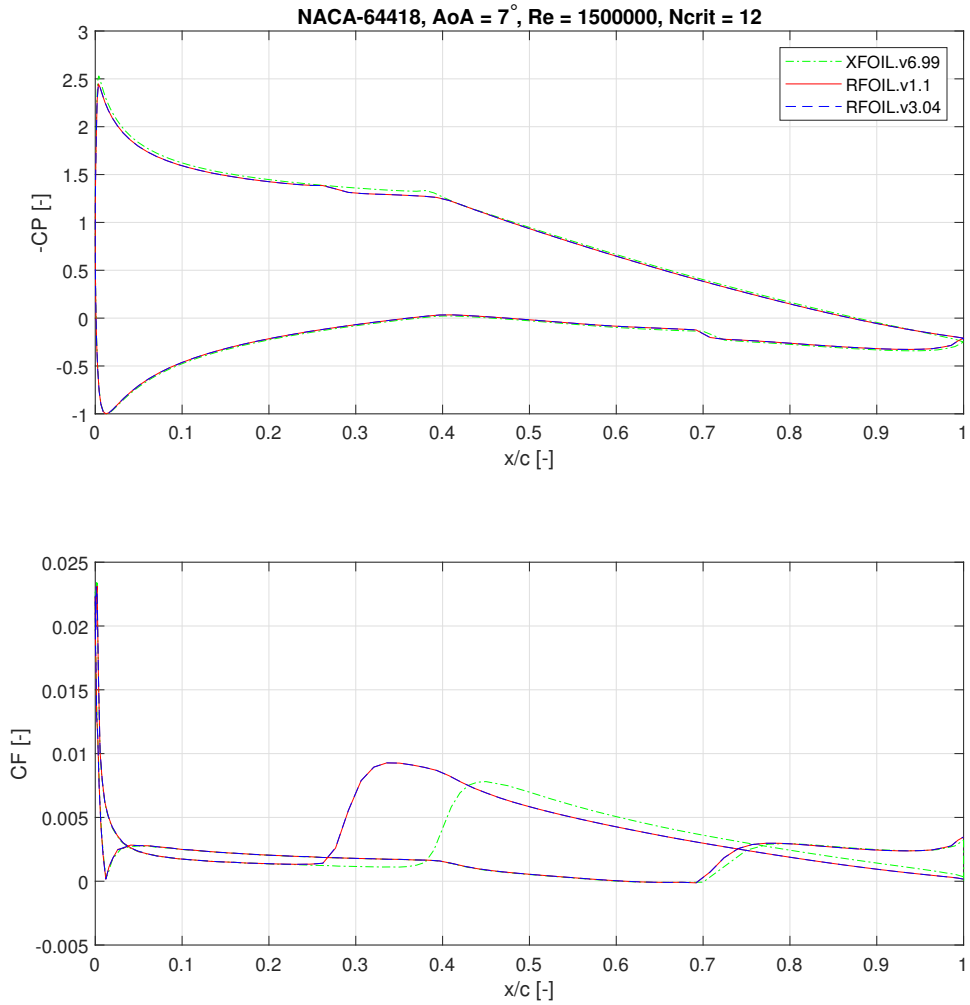

Figure B.433: Comparison between experimental and numerical polars for the NACA-64418 airfoil at a Reynolds number of 2000000. Simulation time to generate the polars by means the different codes and the number of converged polar points are depicted between parentheses.

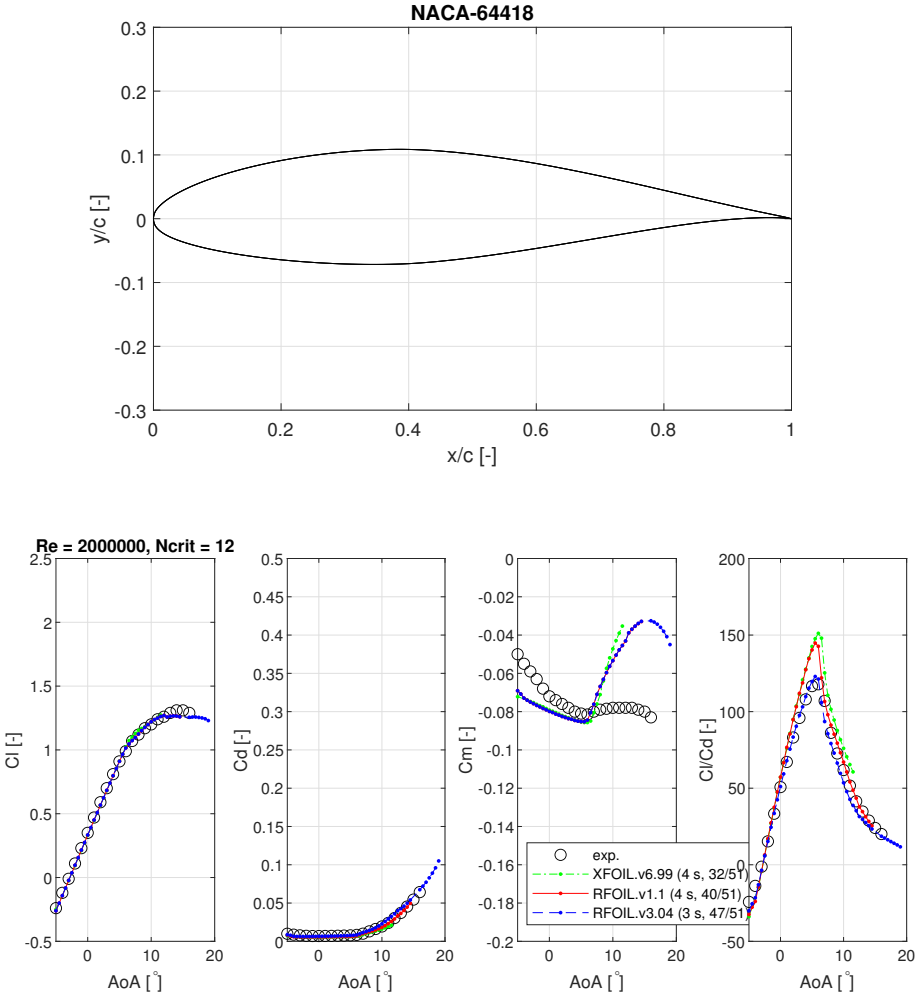

Figure B.434: Differences between experimental and numerical polars for the NACA-64418 airfoil at a Reynolds number of 2000000. Vertical black lines in the middle subplot indicate, from left to right, the angle of attack corresponding to the minimum drag coefficient, maximum lift to drag ratio and maximum lift coefficient, respectively.

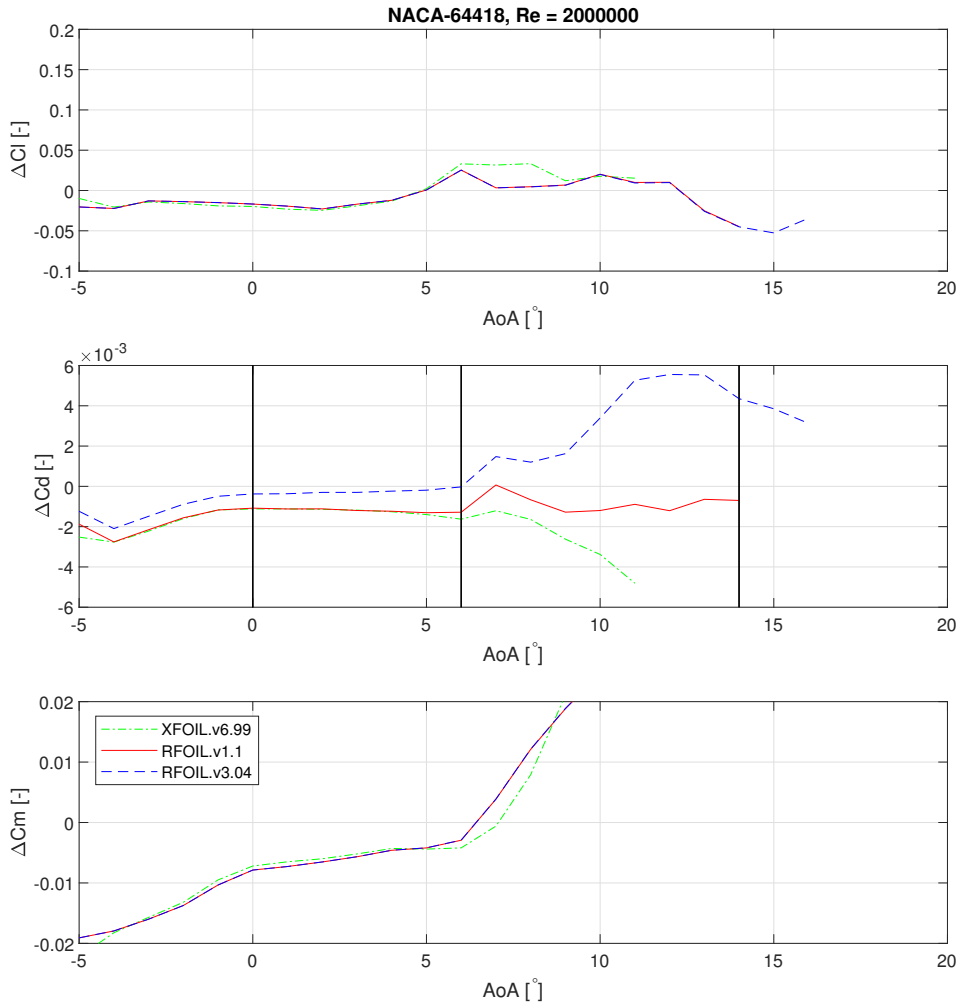

Figure B.435: Comparison between experimental and numerical pressure and skin friction distributions for the NACA-64418 airfoil at a Reynolds number of 2000000 and at the design angle of attack.

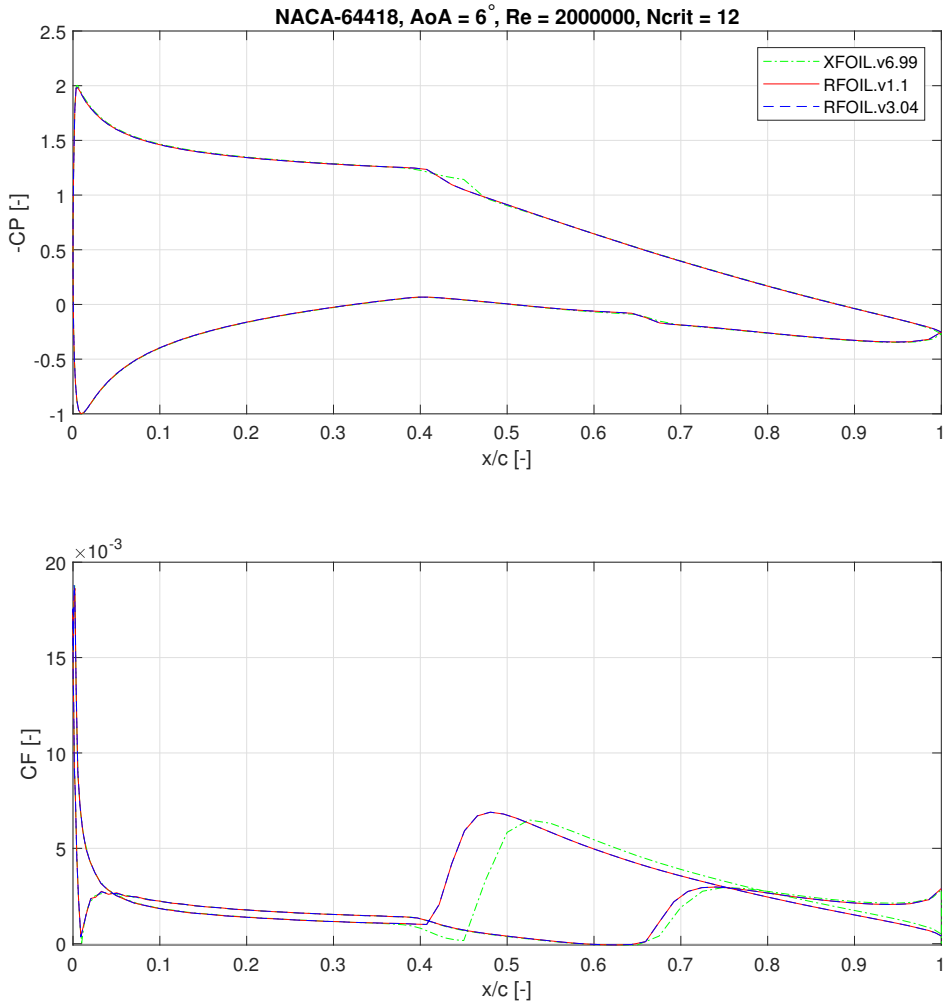

Figure B.436: Comparison between experimental and numerical polars for the NACA-64418 airfoil at a Reynolds number of 3000000. Simulation time to generate the polars by means of the different codes and the number of converged polar points are depicted between parentheses.

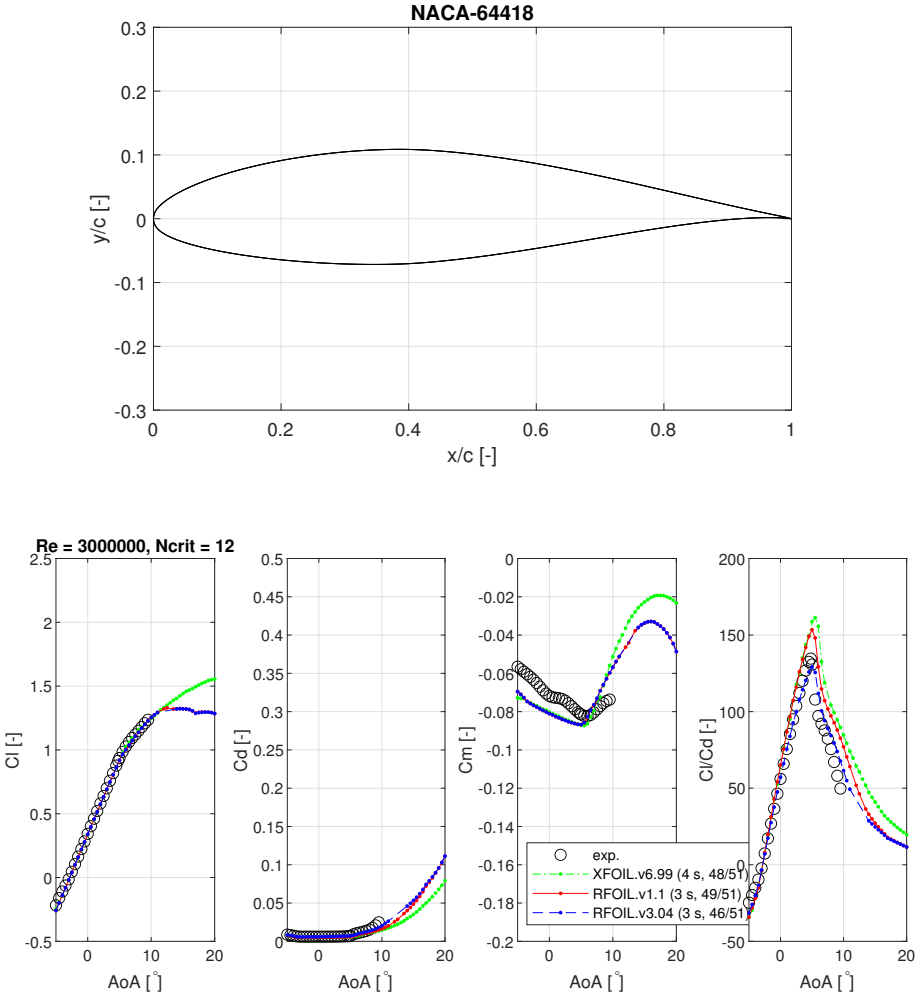

Figure B.437: Differences between experimental and numerical polars for the NACA-64418 airfoil at a Reynolds number of 3000000. Vertical black lines in the middle subplot indicate, from left to right, the angle of attack corresponding to the minimum drag coefficient, maximum lift to drag ratio and maximum lift coefficient, respectively.

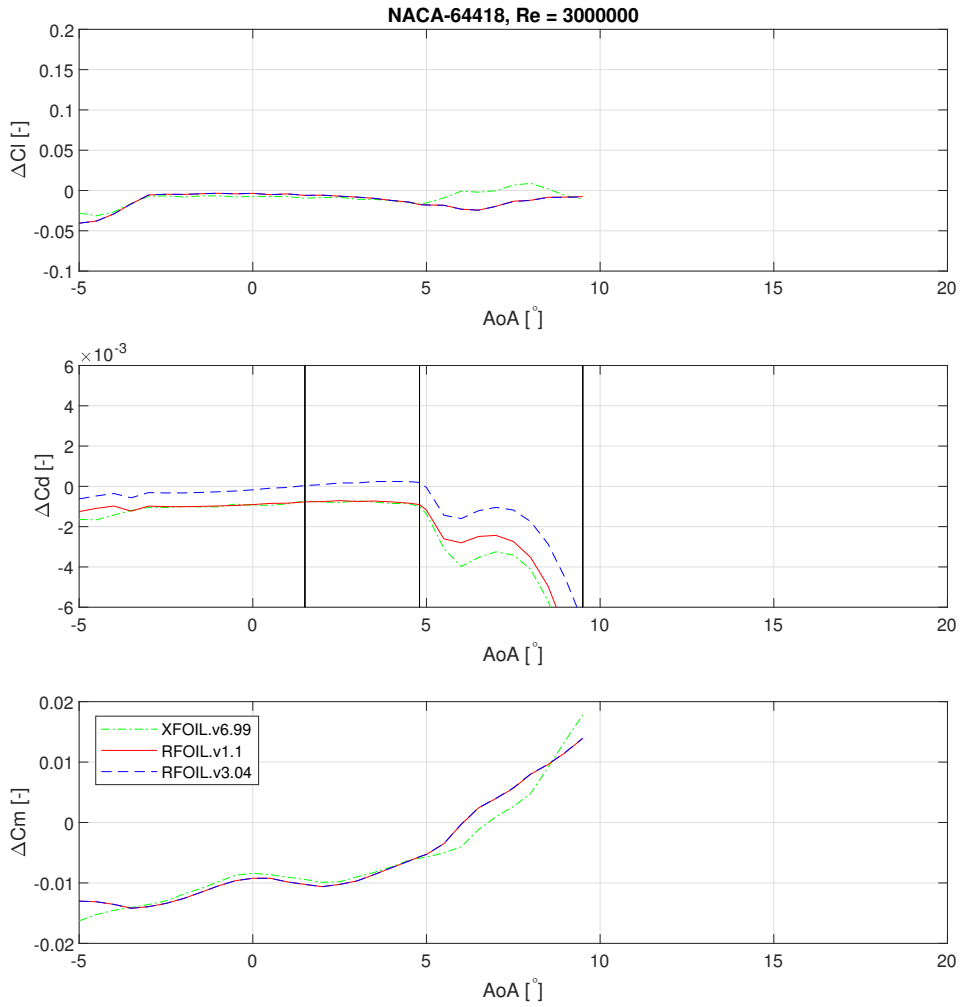

Figure B.438: Comparison between experimental and numerical pressure and skin friction distributions for the NACA-64418 airfoil at a Reynolds number of 3000000 and at the design angle of attack.

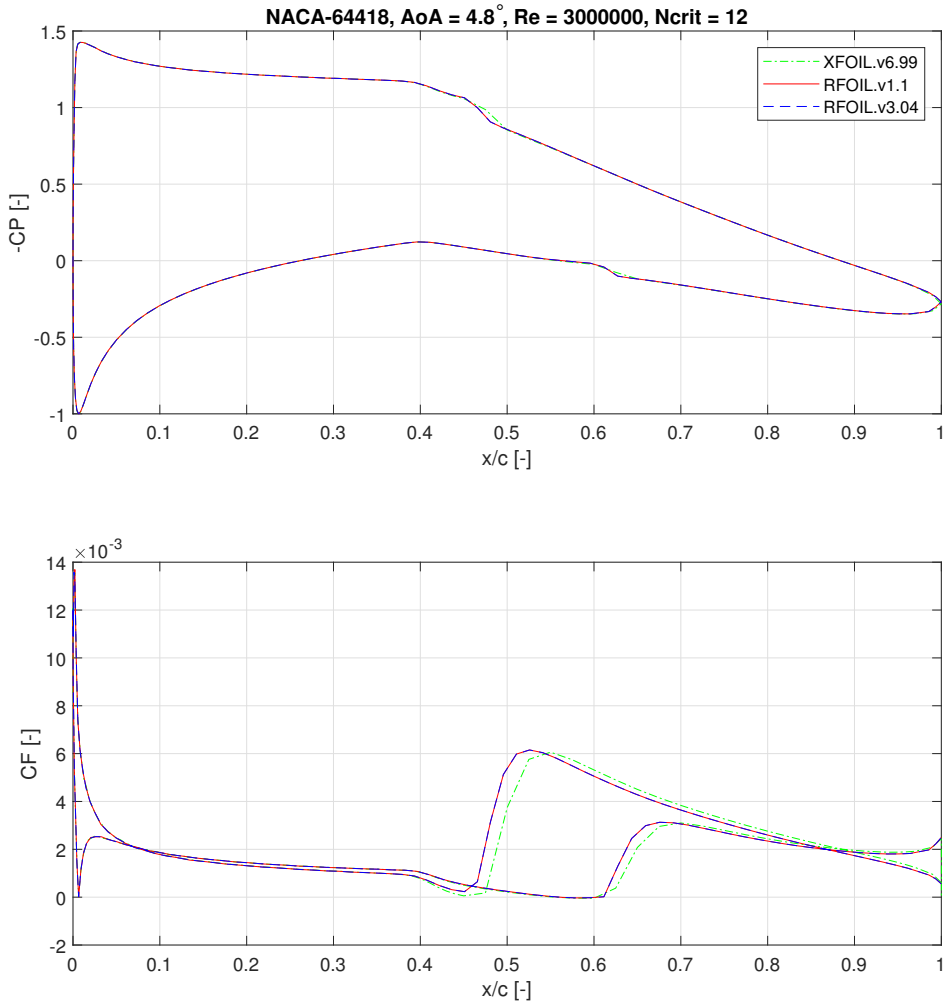

Figure B.439: Comparison between experimental and numerical polars for the NACA-64418 airfoil at a Reynolds number of 6000000. Simulation time to generate the polars by means the different codes and the number of converged polar points are depicted between parentheses.

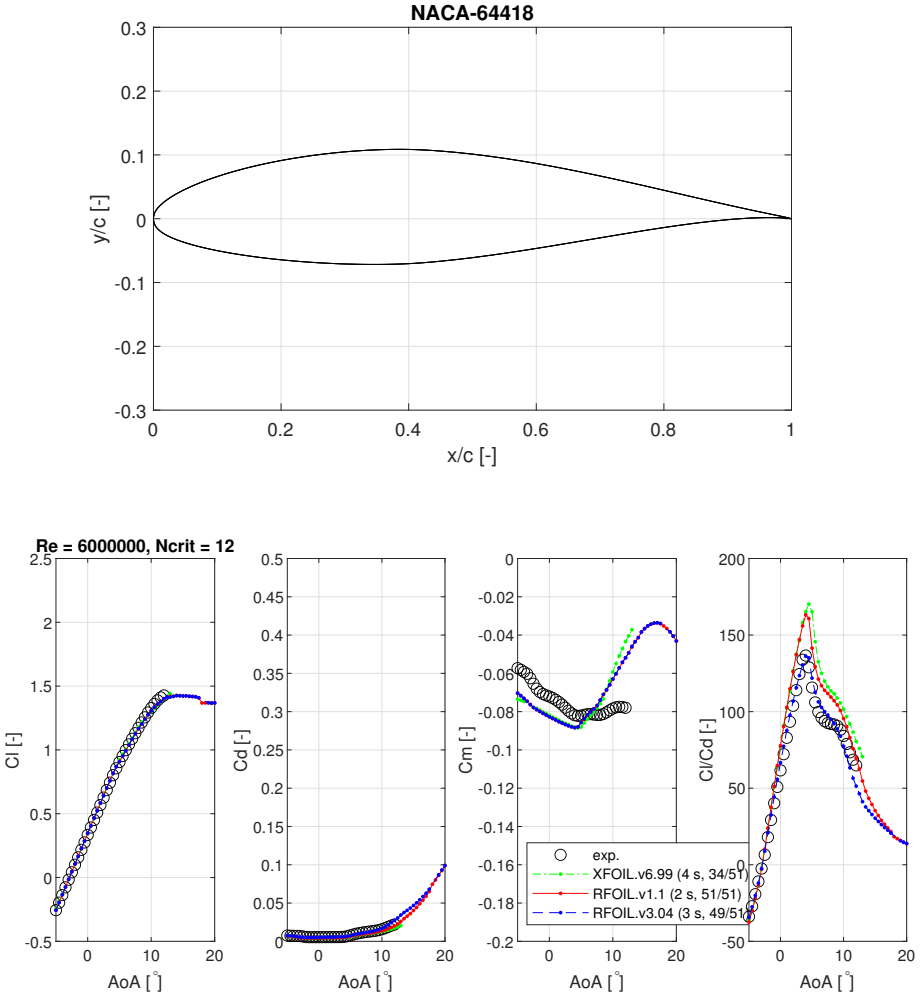

Figure B.440: Differences between experimental and numerical polars for the NACA-64418 airfoil at a Reynolds number of 6000000. Vertical black lines in the middle subplot indicate, from left to right, the angle of attack corresponding to the minimum drag coefficient, maximum lift to drag ratio and maximum lift coefficient, respectively.

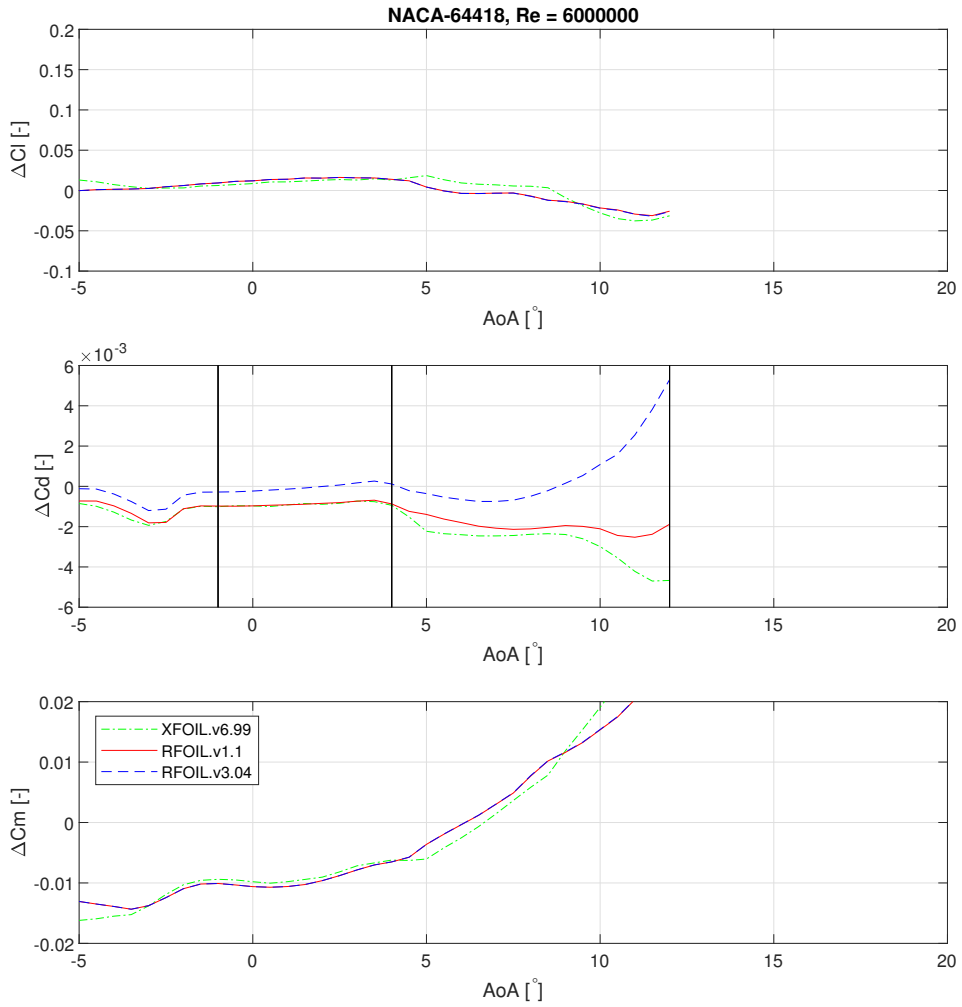

Figure B.441: Comparison between experimental and numerical pressure and skin friction distributions for the NACA-64418 airfoil at a Reynolds number of 6000000 and at the design angle of attack.

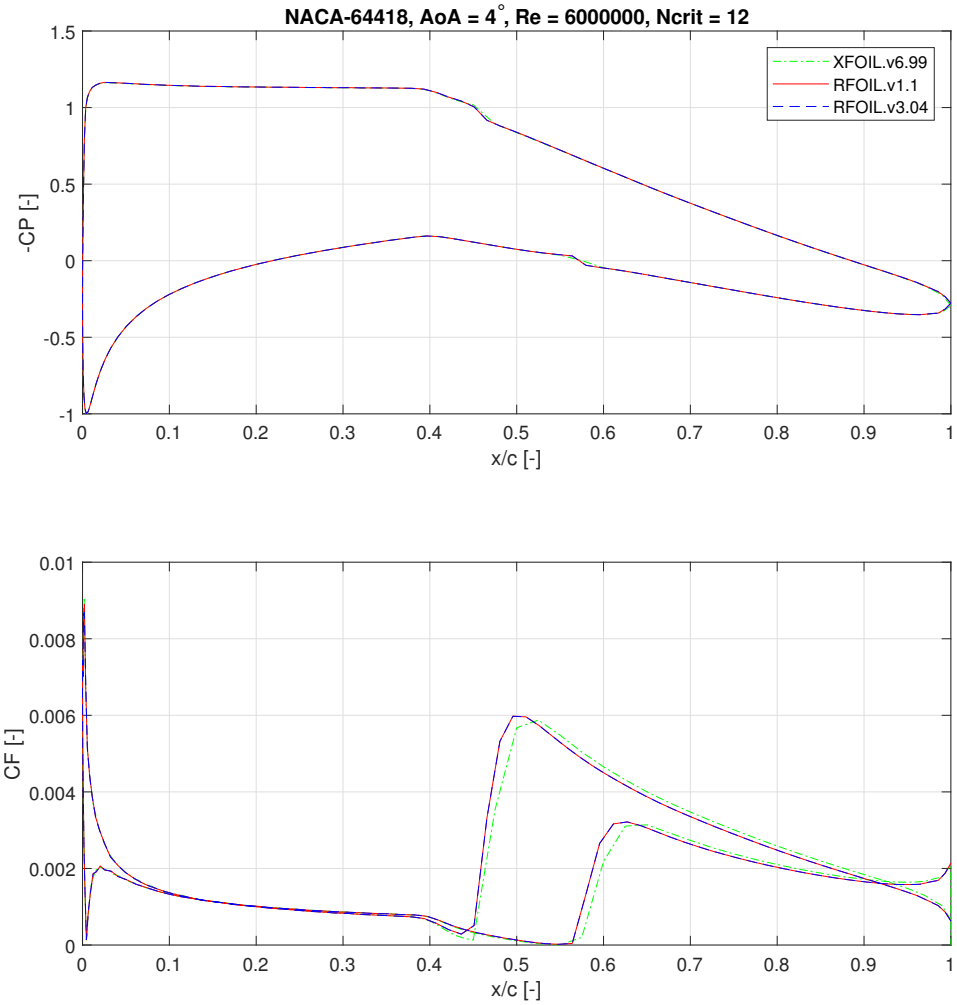

Figure B.442: Comparison between experimental and numerical polars for the NACA-64418 airfoil at a Reynolds number of 700000. Simulation time to generate the polars by means the different codes and the number of converged polar points are depicted between parentheses.

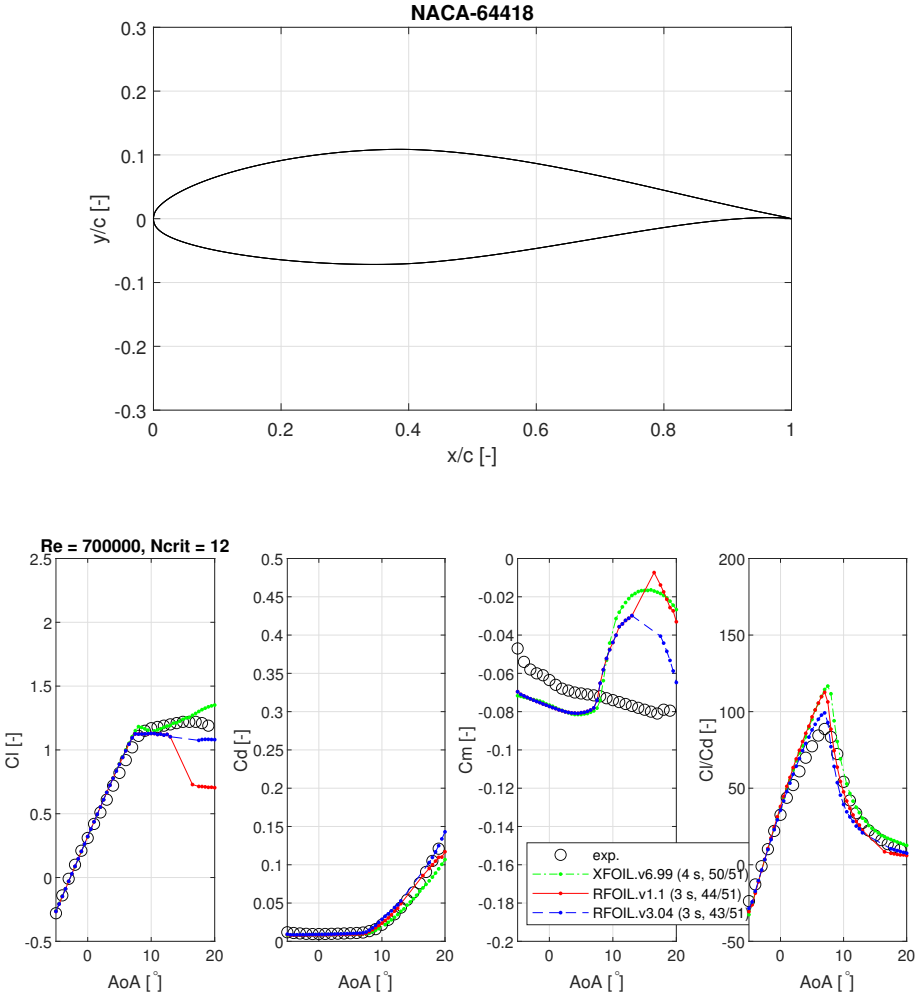

Figure B.443: Differences between experimental and numerical polars for the NACA-64418 airfoil at a Reynolds number of 700000. Vertical black lines in the middle subplot indicate, from left to right, the angle of attack corresponding to the minimum drag coefficient, maximum lift to drag ratio and maximum lift coefficient, respectively.

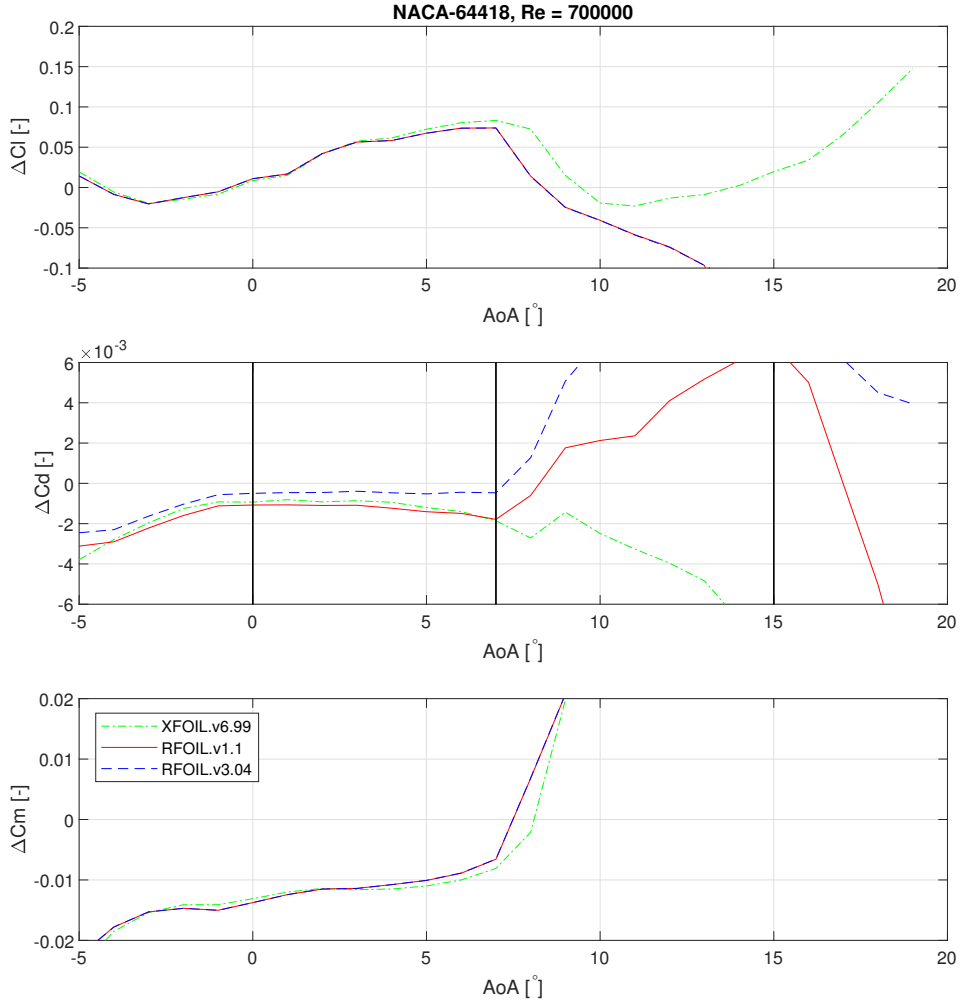

Figure B.444: Comparison between experimental and numerical pressure and skin friction distributions for the NACA-64418 airfoil at a Reynolds number of 700000 and at the design angle of attack.

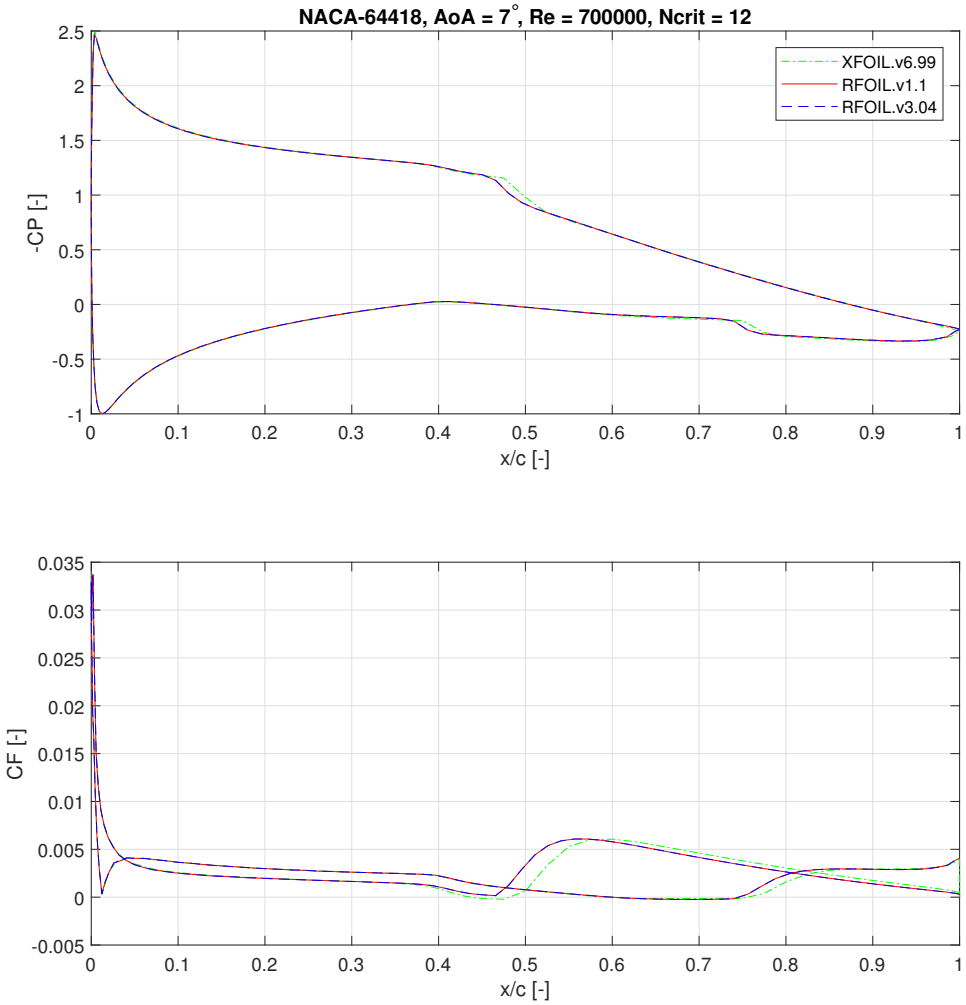

Figure B.445: Comparison between experimental and numerical polars for the NACA-64418 airfoil at a Reynolds number of 9000000. Simulation time to generate the polars by means the different codes and the number of converged polar points are depicted between parentheses.

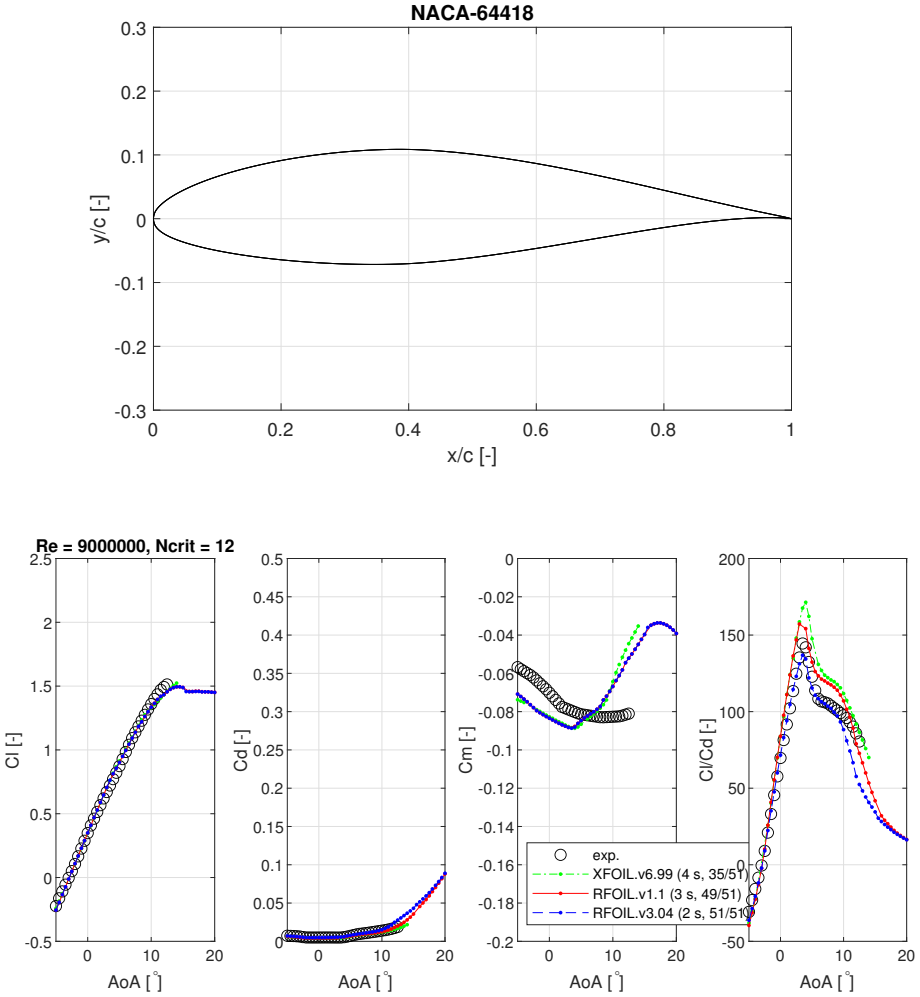

Figure B.446: Differences between experimental and numerical polars for the NACA-64418 airfoil at a Reynolds number of 9000000. Vertical black lines in the middle subplot indicate, from left to right, the angle of attack corresponding to the minimum drag coefficient, maximum lift to drag ratio and maximum lift coefficient, respectively.

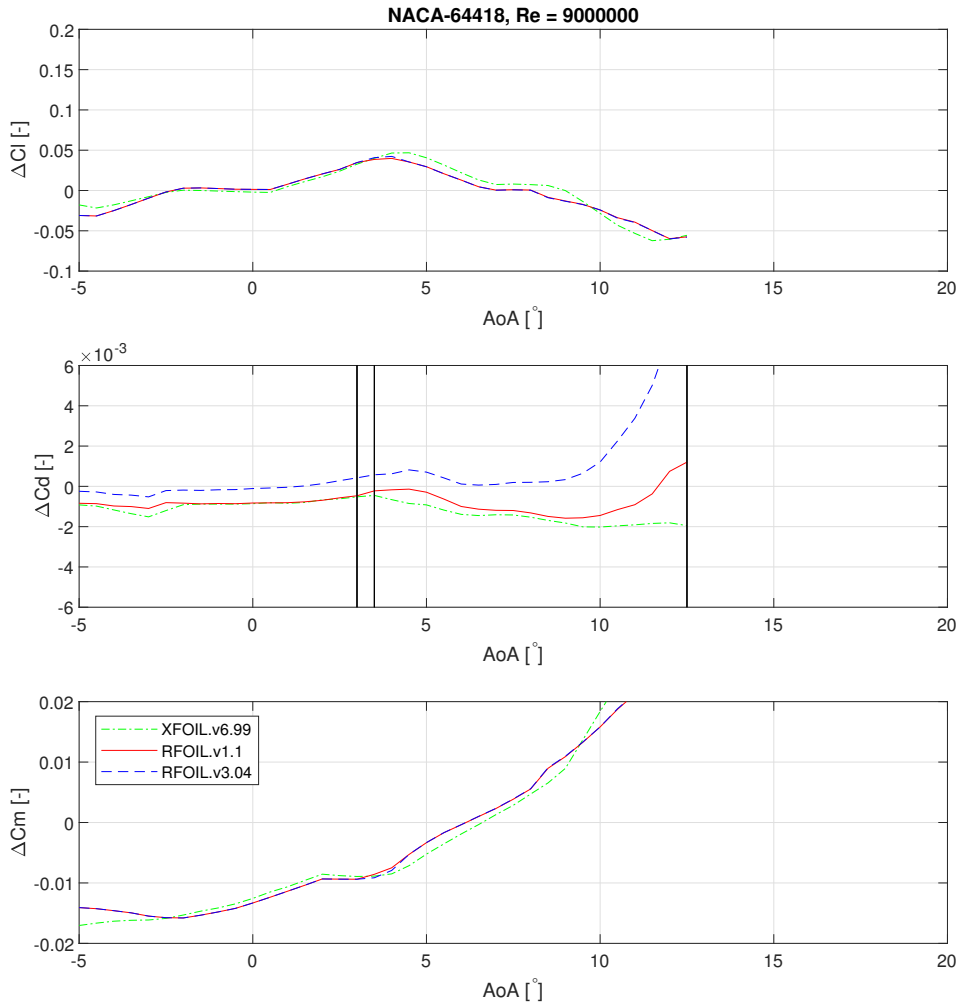

Figure B.447: Comparison between experimental and numerical pressure and skin friction distributions for the NACA-64418 airfoil at a Reynolds number of 9000000 and at the design angle of attack.

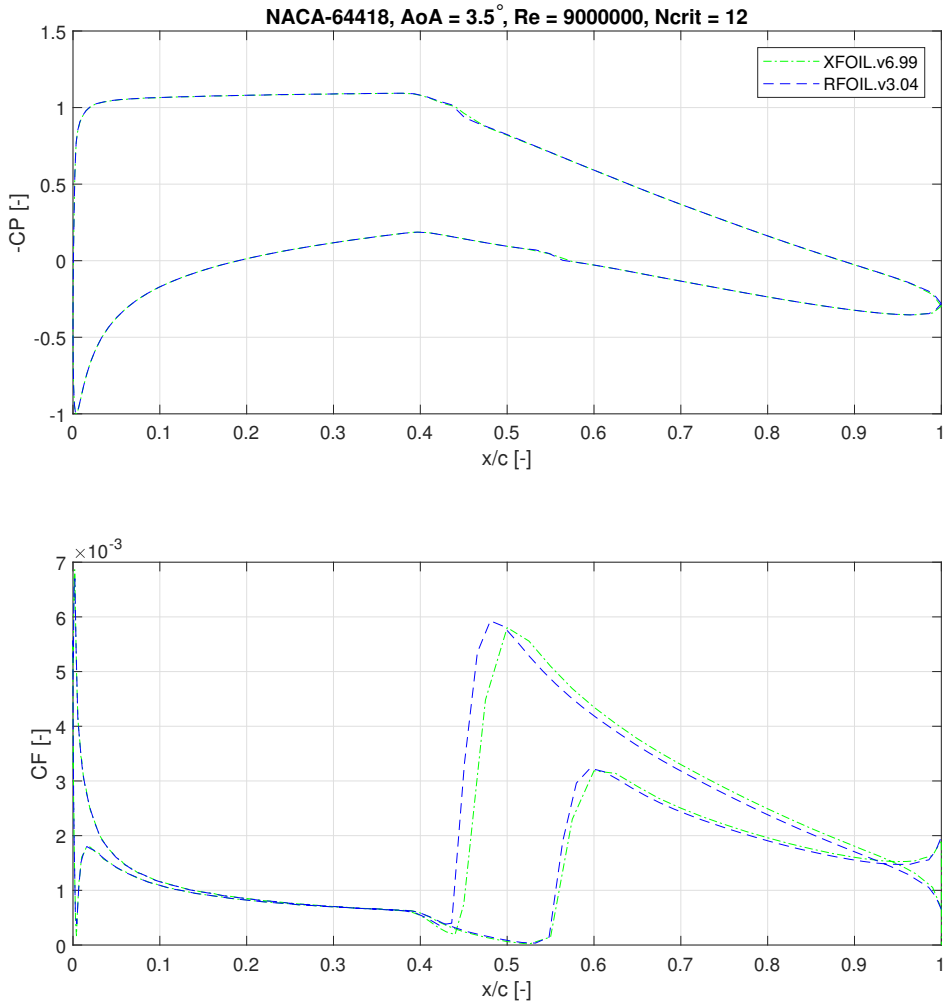

Figure B.448: Comparison between experimental and numerical polars for the NACA-64421 airfoil at a Reynolds number of 3000000. Simulation time to generate the polars by means the different codes and the number of converged polar points are depicted between parentheses.

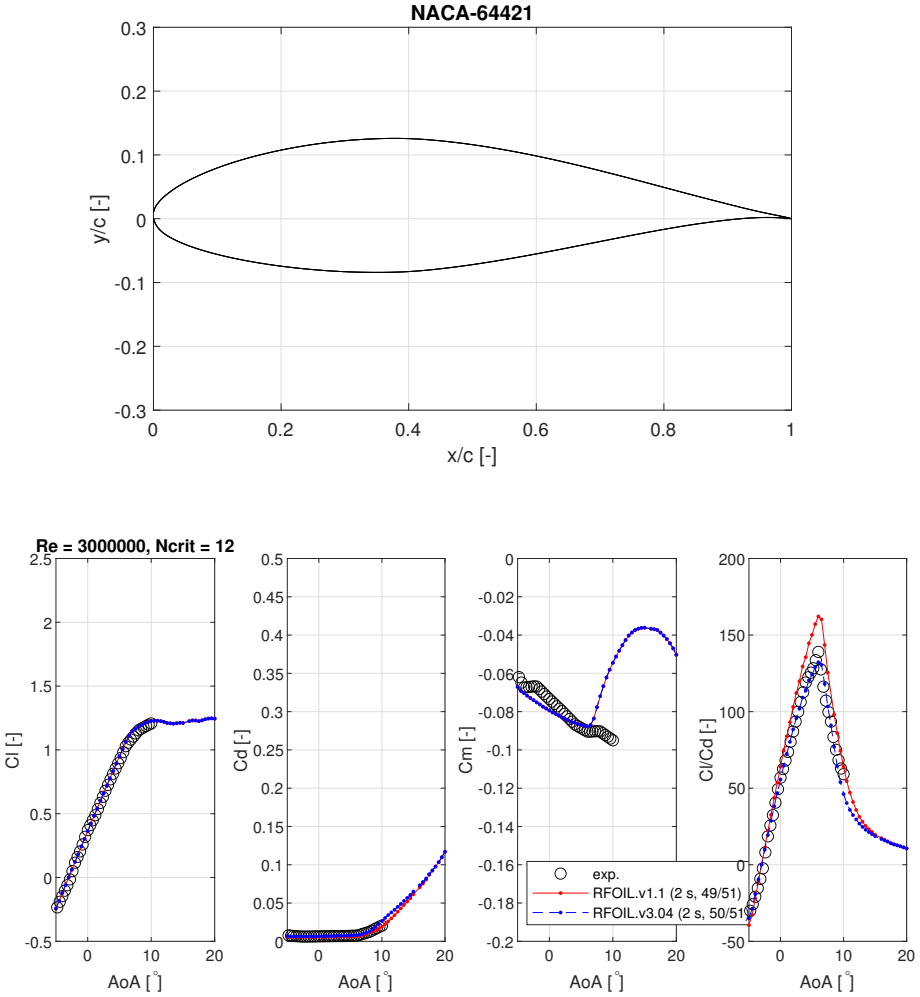

Figure B.449: Differences between experimental and numerical polars for the NACA-64421 airfoil at a Reynolds number of 3000000. Vertical black lines in the middle subplot indicate, from left to right, the angle of attack corresponding to the minimum drag coefficient, maximum lift to drag ratio and maximum lift coefficient, respectively.

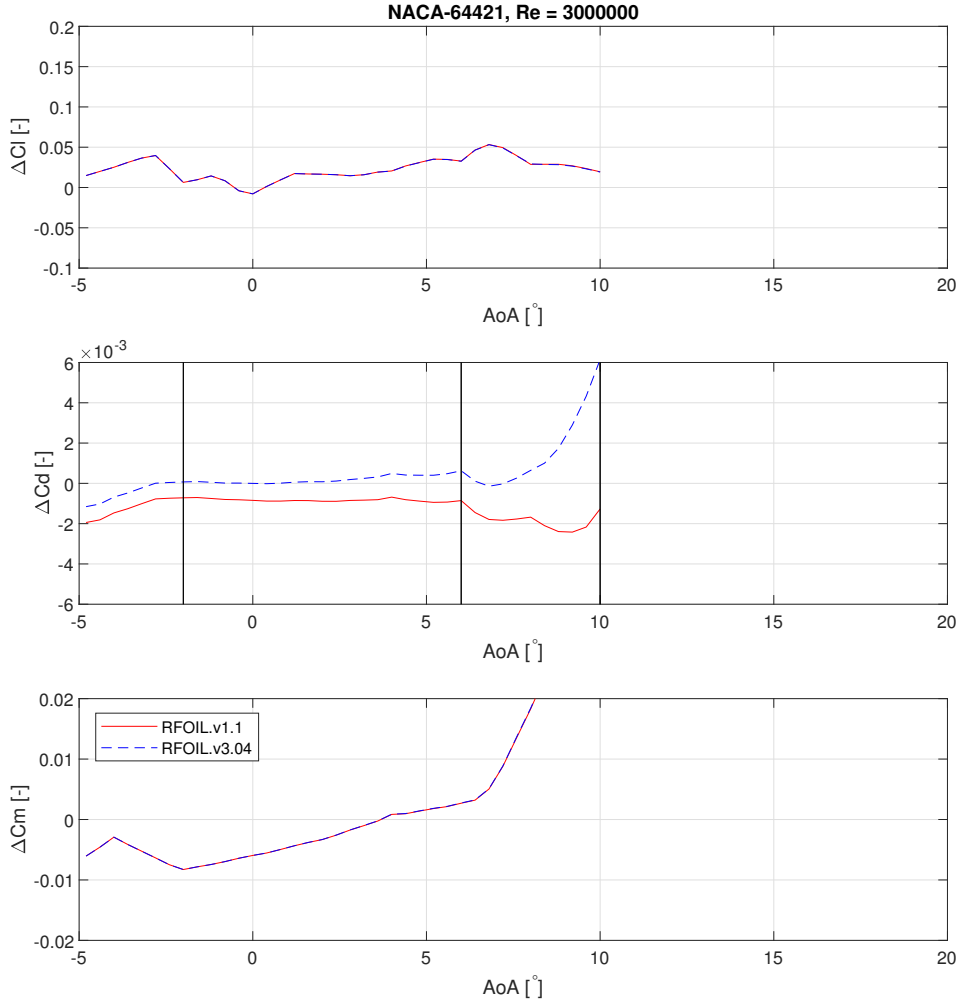

Figure B.450: Comparison between experimental and numerical pressure and skin friction distributions for the NACA-64421 airfoil at a Reynolds number of 3000000 and at the design angle of attack.

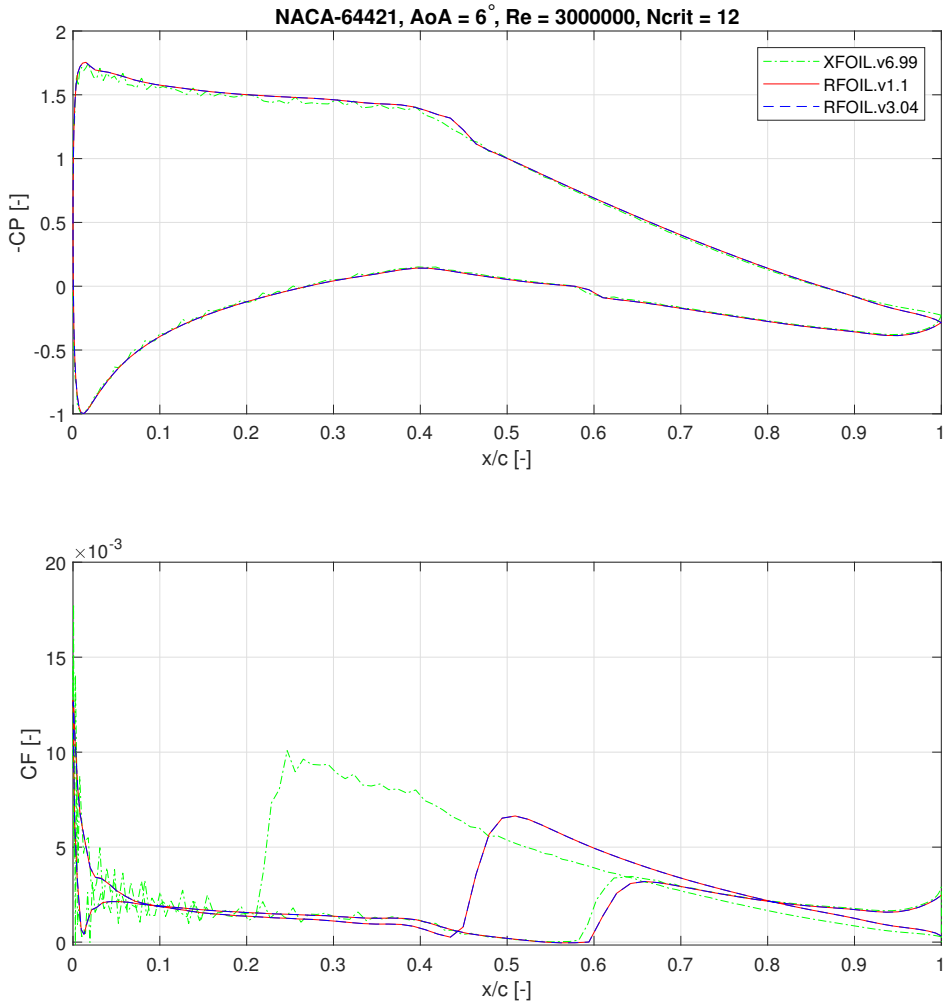

Figure B.451: Comparison between experimental and numerical polars for the NACA-64421 airfoil at a Reynolds number of 6000000. Simulation time to generate the polars by means the different codes and the number of converged polar points are depicted between parentheses.

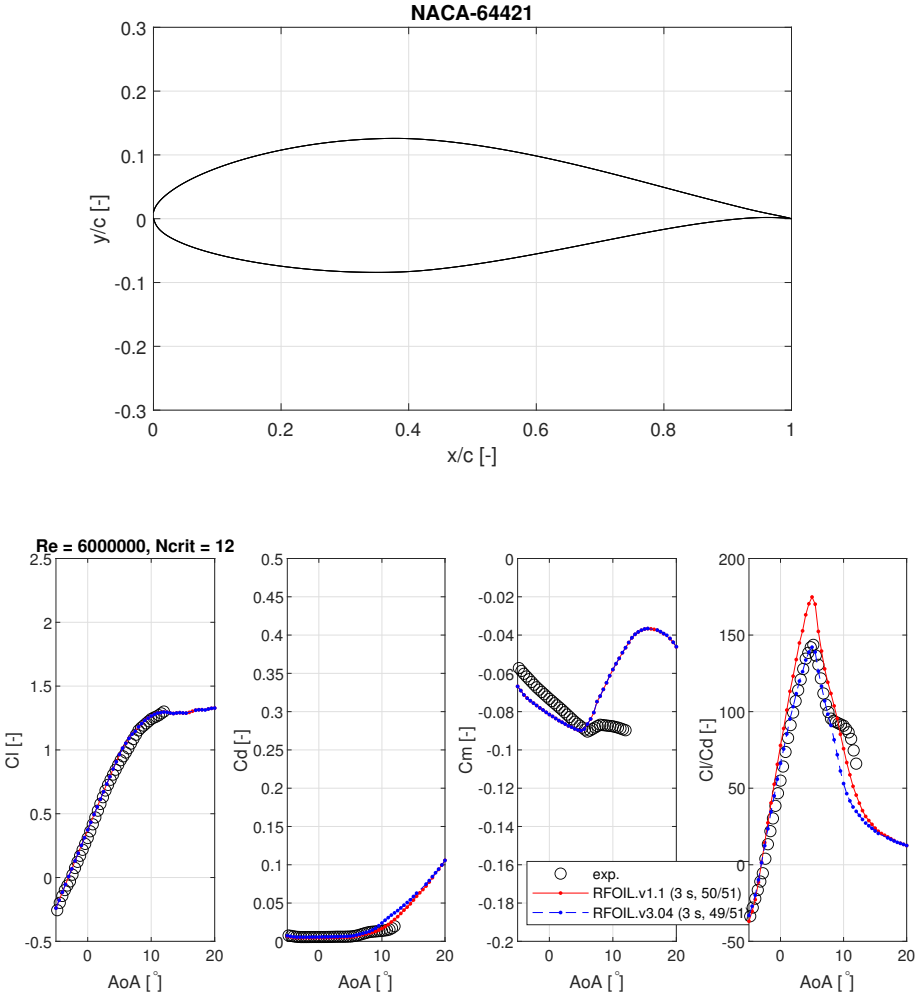

Figure B.452: Differences between experimental and numerical polars for the NACA-64421 airfoil at a Reynolds number of 6000000. Vertical black lines in the middle subplot indicate, from left to right, the angle of attack corresponding to the minimum drag coefficient, maximum lift to drag ratio and maximum lift coefficient, respectively.

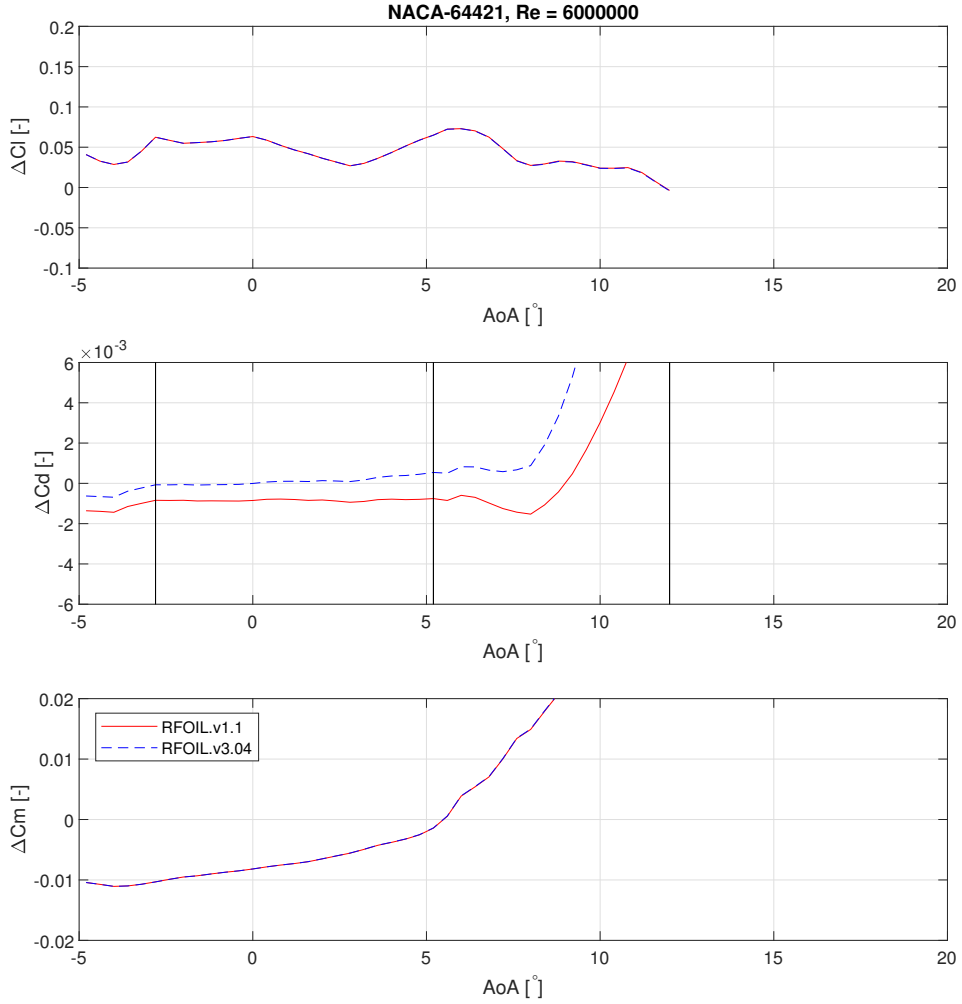

Figure B.453: Comparison between experimental and numerical pressure and skin friction distributions for the NACA-64421 airfoil at a Reynolds number of 6000000 and at the design angle of attack.

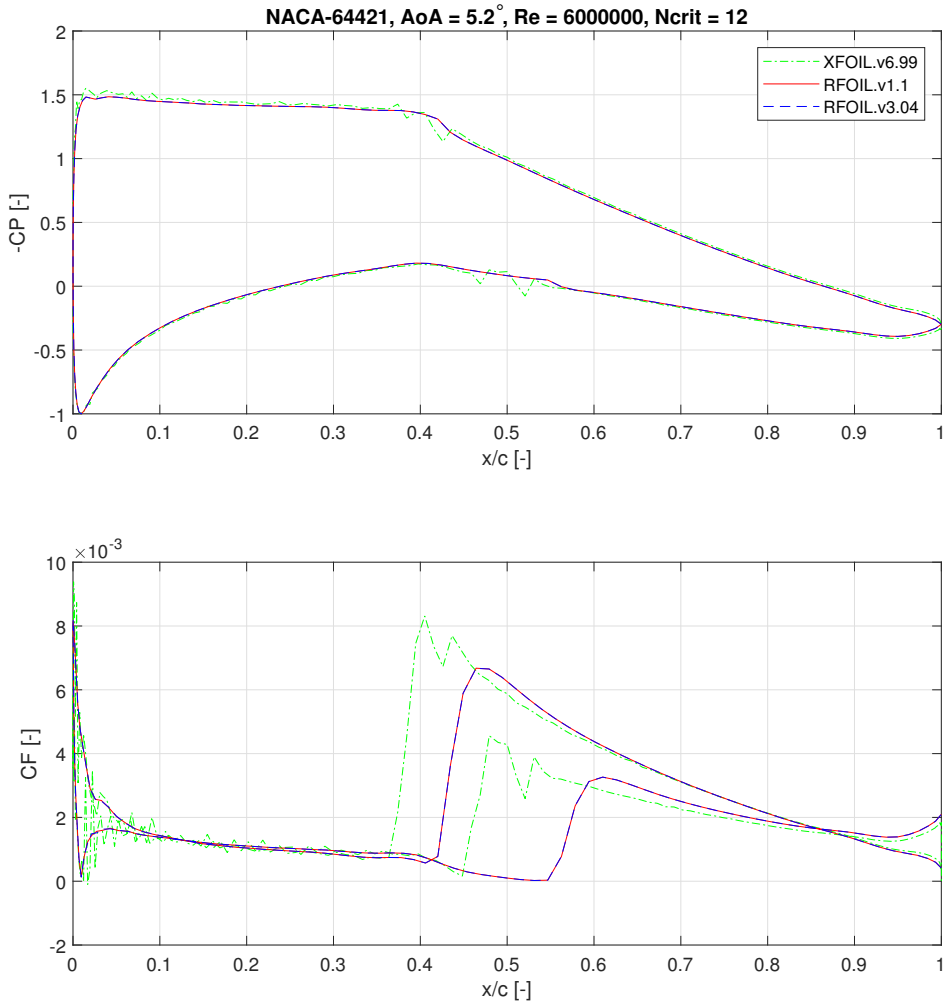

Figure B.454: Comparison between experimental and numerical polars for the NACA-64421 airfoil at a Reynolds number of 9000000. Simulation time to generate the polars by means the different codes and the number of converged polar points are depicted between parentheses.

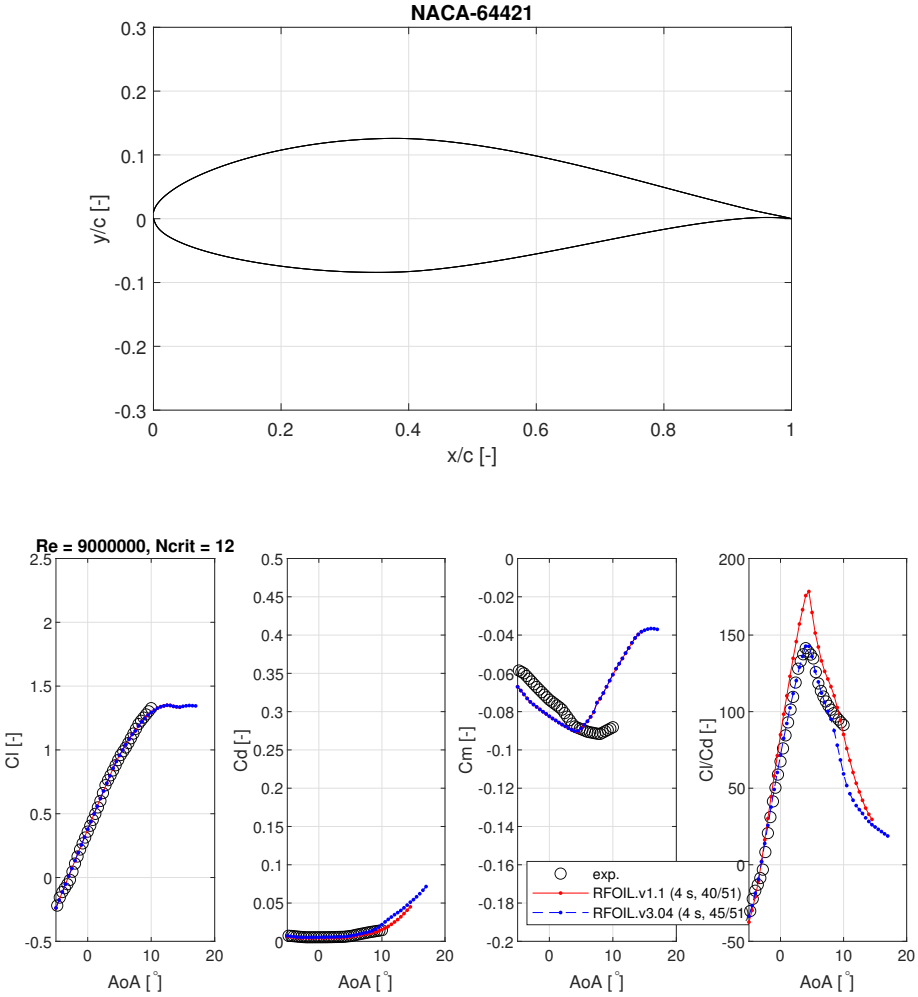

Figure B.455: Differences between experimental and numerical polars for the NACA-64421 airfoil at a Reynolds number of 9000000. Vertical black lines in the middle subplot indicate, from left to right, the angle of attack corresponding to the minimum drag coefficient, maximum lift to drag ratio and maximum lift coefficient, respectively.

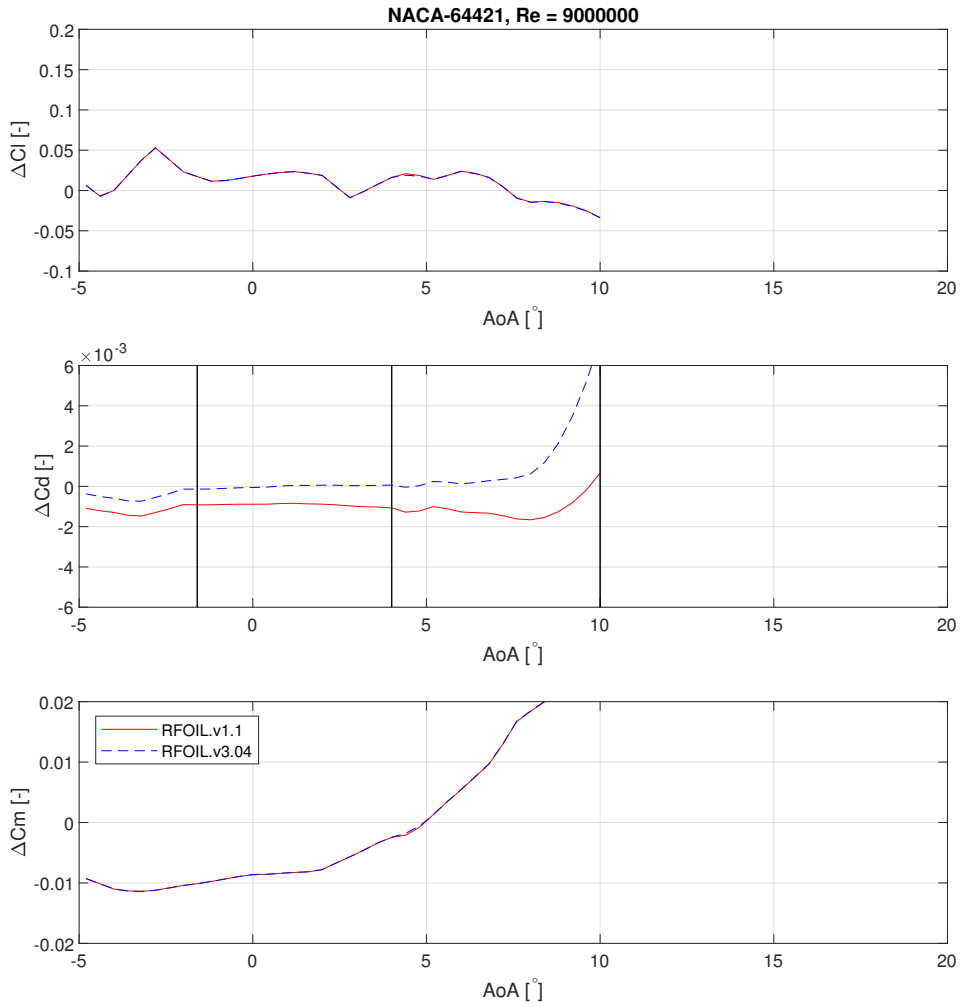

Figure B.456: Comparison between experimental and numerical pressure and skin friction distributions for the NACA-64421 airfoil at a Reynolds number of 9000000 and at the design angle of attack.

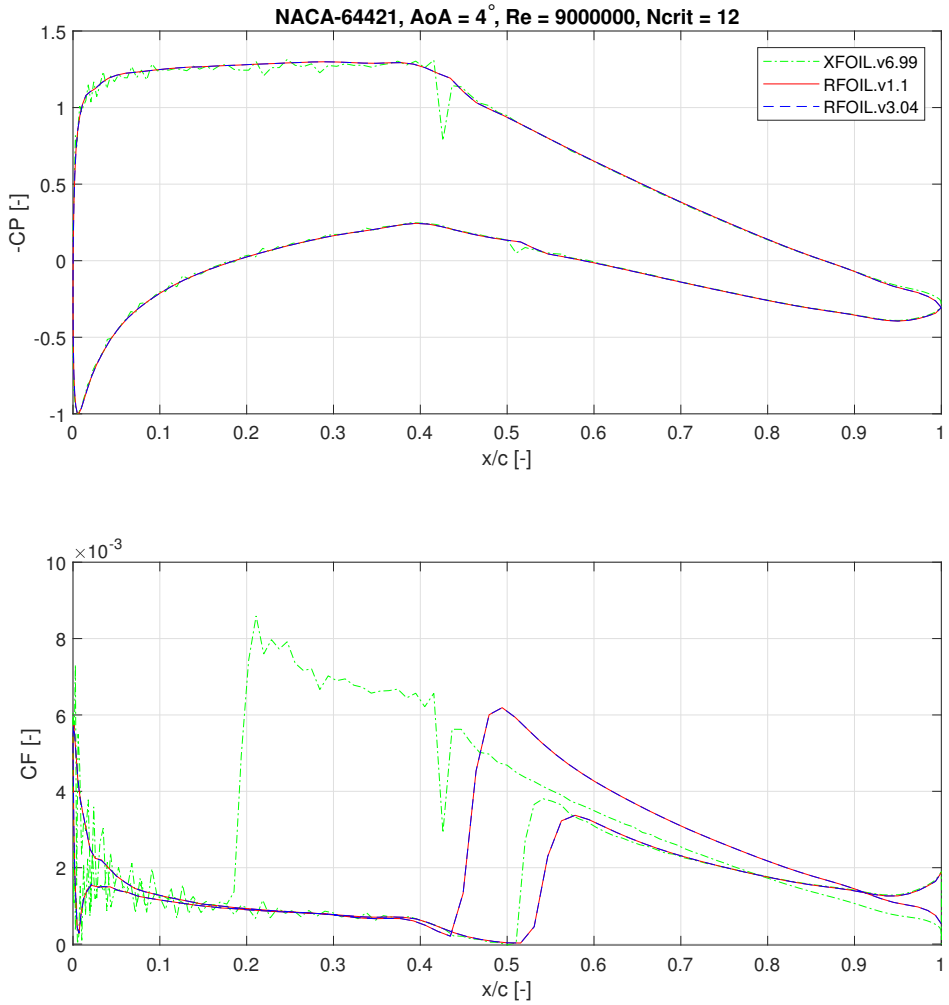

Figure B.457: Comparison between experimental and numerical polars for the NACA-64618 airfoil at a Reynolds number of 3000000. Simulation time to generate the polars by means the different codes and the number of converged polar points are depicted between parentheses.

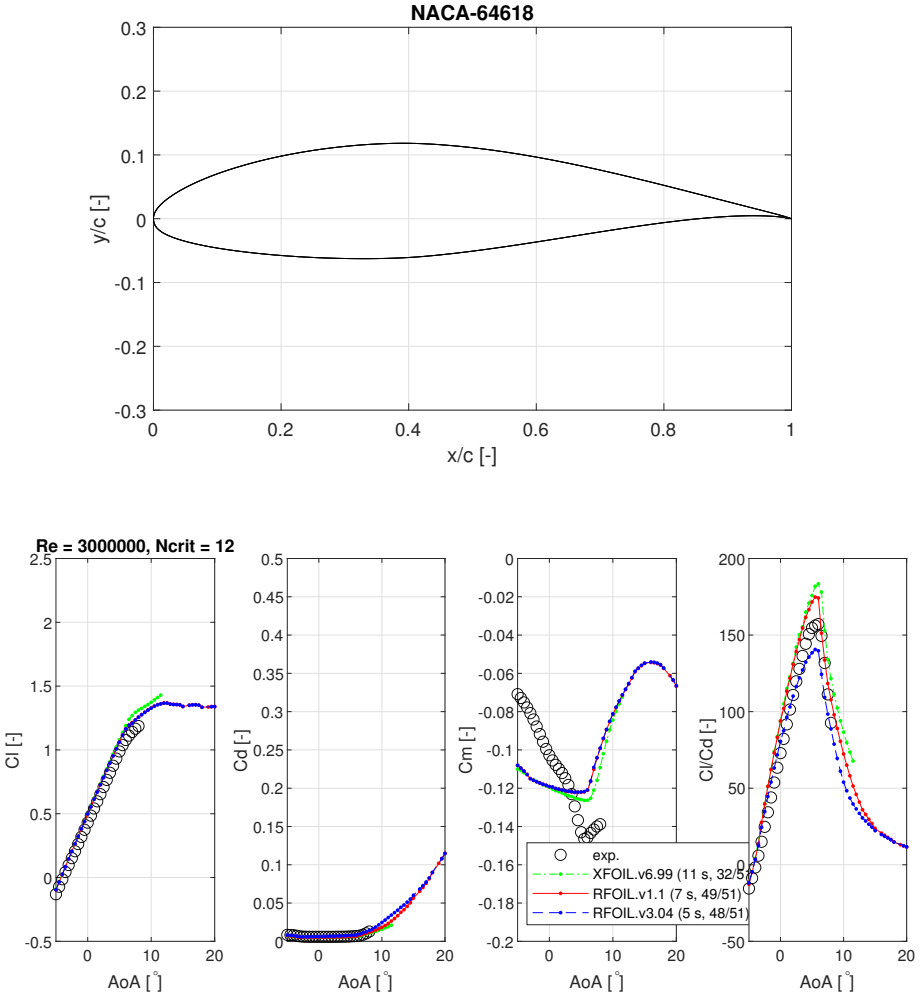

Figure B.458: Differences between experimental and numerical polars for the NACA-64618 airfoil at a Reynolds number of 3000000. Vertical black lines in the middle subplot indicate, from left to right, the angle of attack corresponding to the minimum drag coefficient, maximum lift to drag ratio and maximum lift coefficient, respectively.

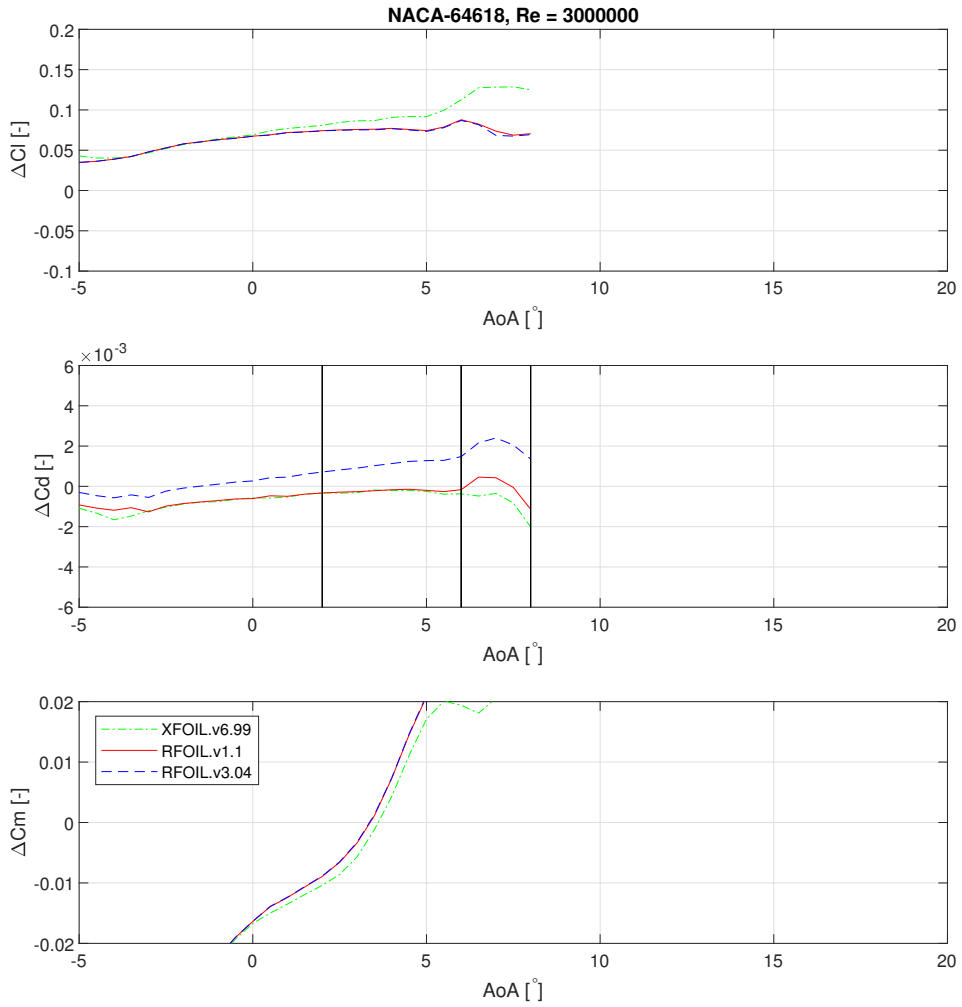

Figure B.459: Comparison between experimental and numerical pressure and skin friction distributions for the NACA-64618 airfoil at a Reynolds number of 3000000 and at the design angle of attack.

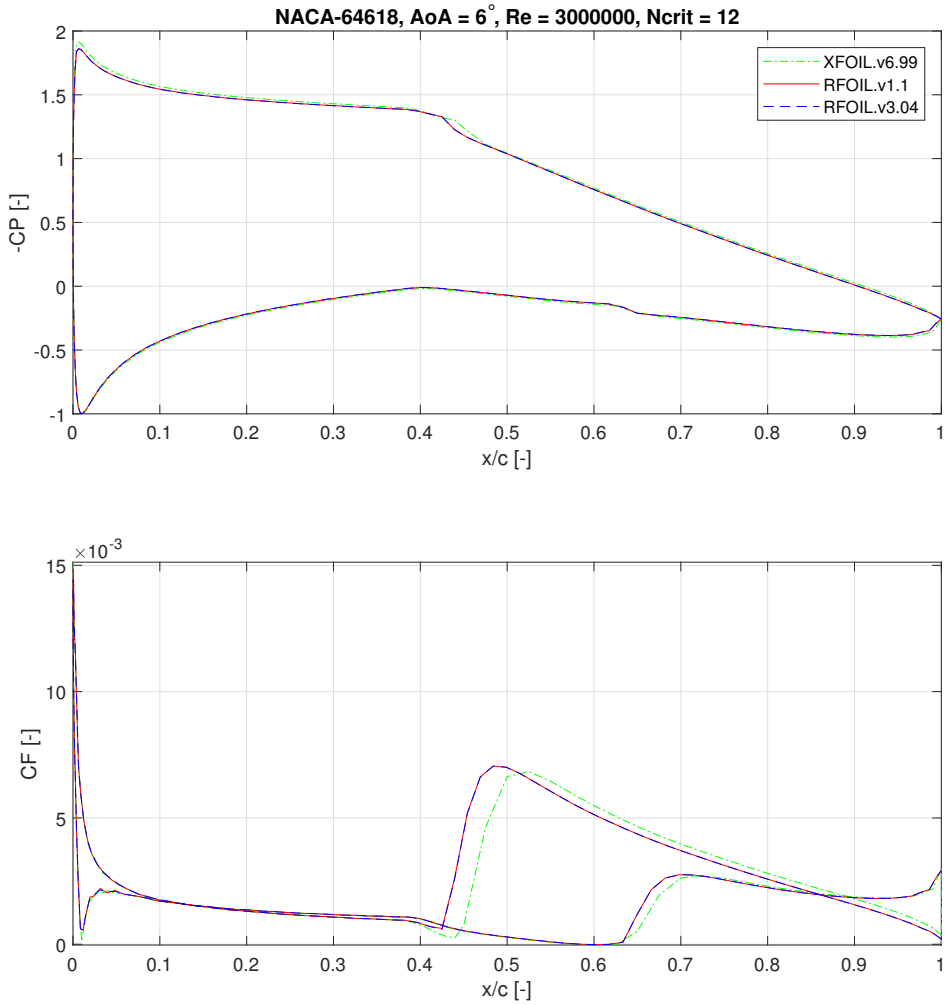

Figure B.460: Comparison between experimental and numerical polars for the NACA-64618 airfoil at a Reynolds number of 6000000. Simulation time to generate the polars by means the different codes and the number of converged polar points are depicted between parentheses.

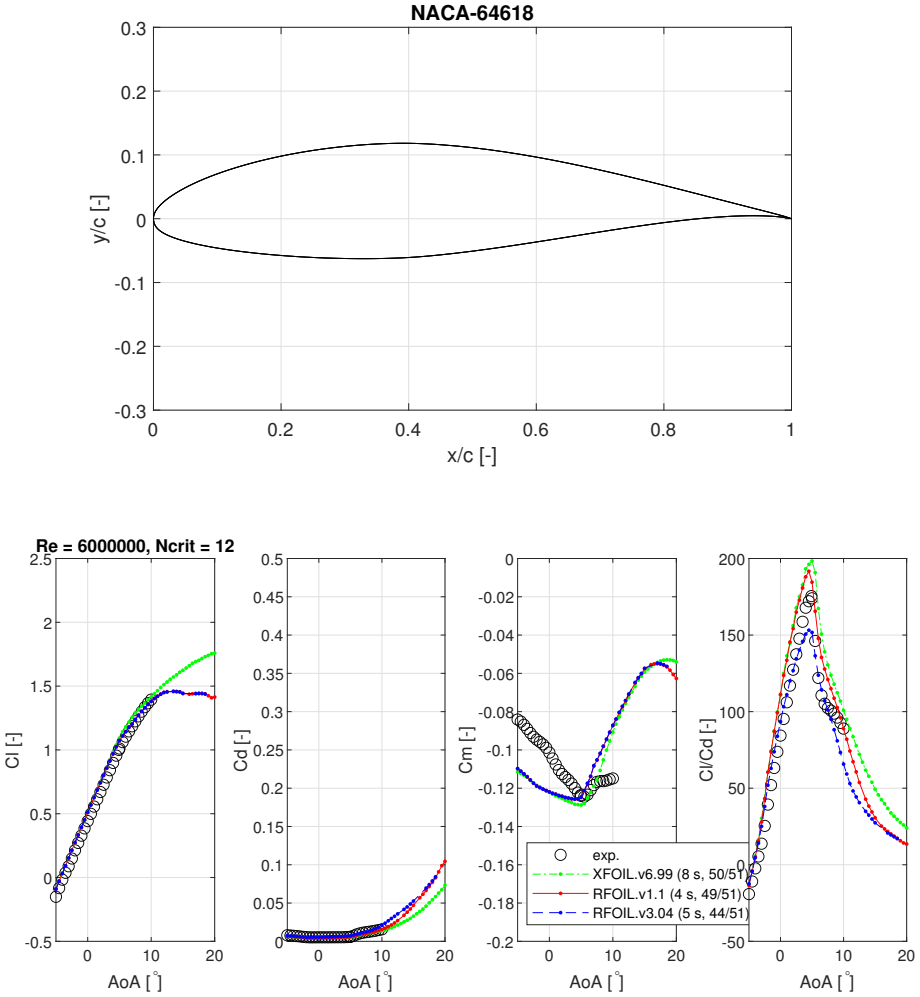

Figure B.461: Differences between experimental and numerical polars for the NACA-64618 airfoil at a Reynolds number of 6000000. Vertical black lines in the middle subplot indicate, from left to right, the angle of attack corresponding to the minimum drag coefficient, maximum lift to drag ratio and maximum lift coefficient, respectively.

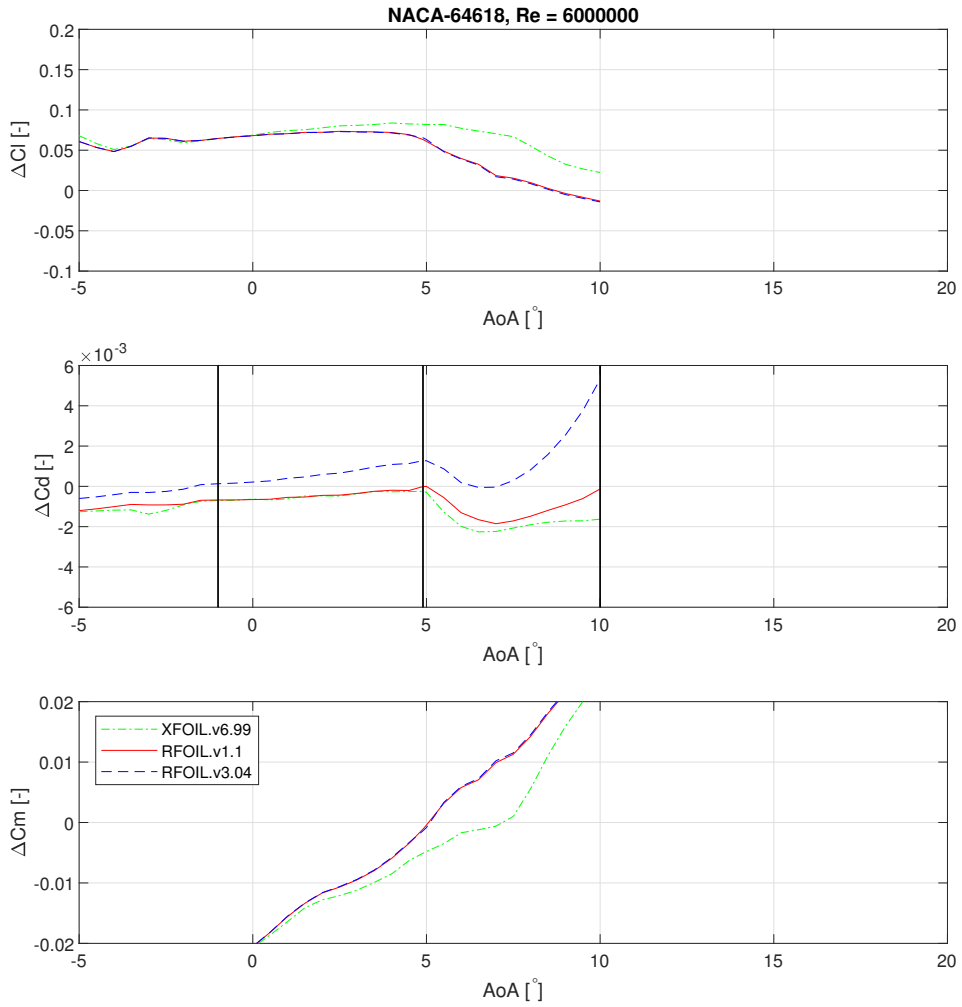

Figure B.462: Comparison between experimental and numerical pressure and skin friction distributions for the NACA-64618 airfoil at a Reynolds number of 6000000 and at the design angle of attack.

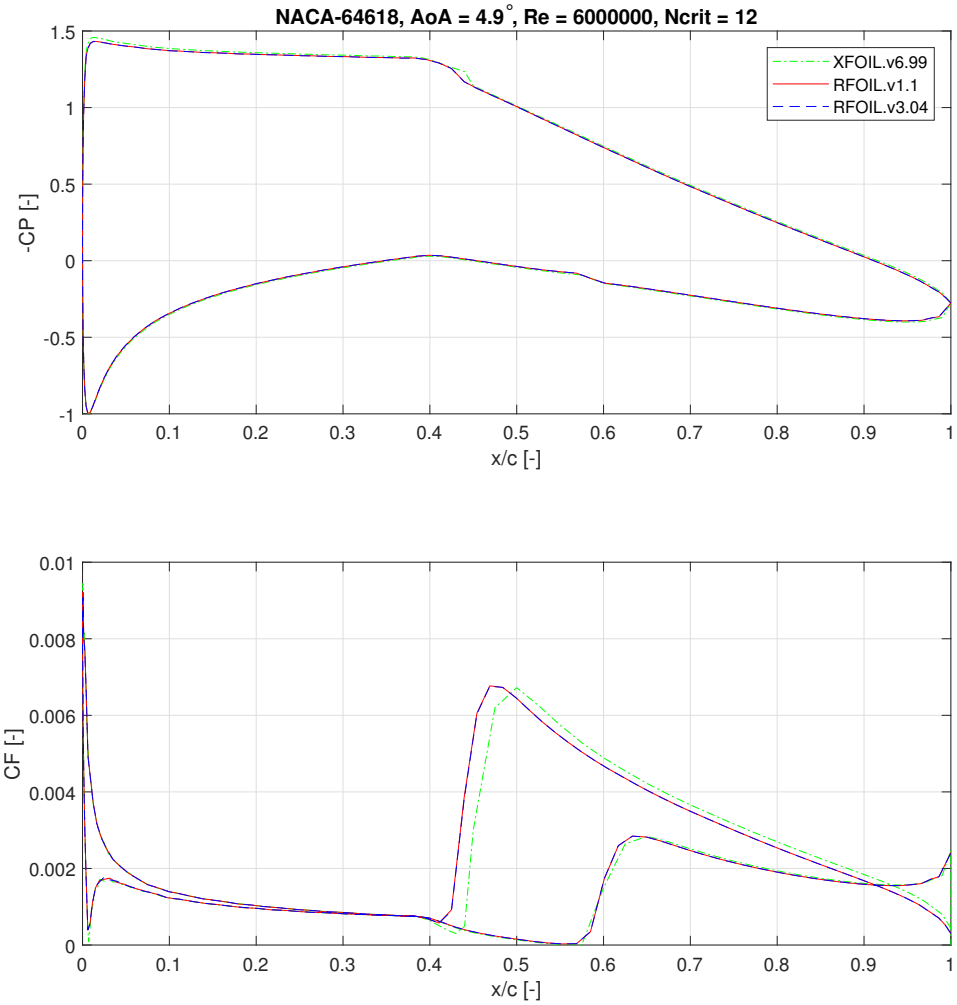

Figure B.463: Comparison between experimental and numerical polars for the NACA-8318 airfoil at a Reynolds number of 1300000. Simulation time to generate the polars by means the different codes and the number of converged polar points are depicted between parentheses.

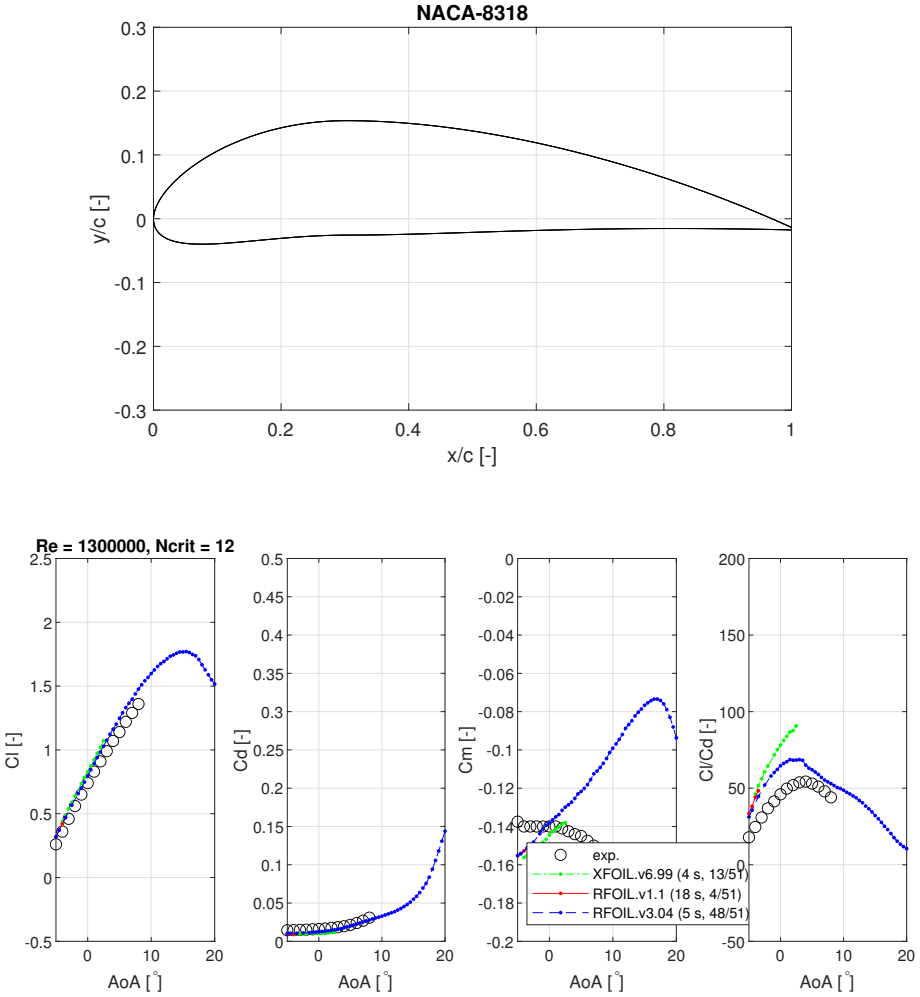

Figure B.464: Differences between experimental and numerical polars for the NACA-8318 airfoil at a Reynolds number of 1300000. Vertical black lines in the middle subplot indicate, from left to right, the angle of attack corresponding to the minimum drag coefficient, maximum lift to drag ratio and maximum lift coefficient, respectively.

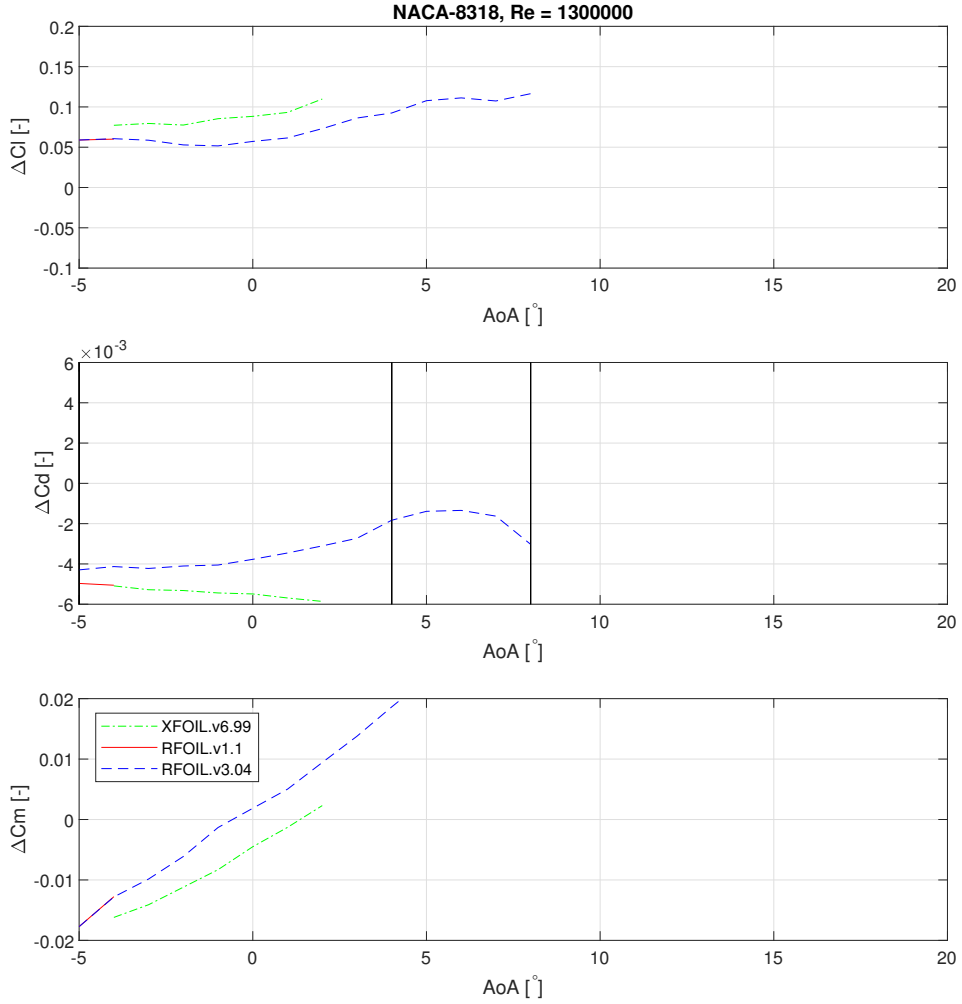

Figure B.465: Comparison between experimental and numerical pressure and skin friction distributions for the NACA-8318 airfoil at a Reynolds number of 1300000 and at the design angle of attack.

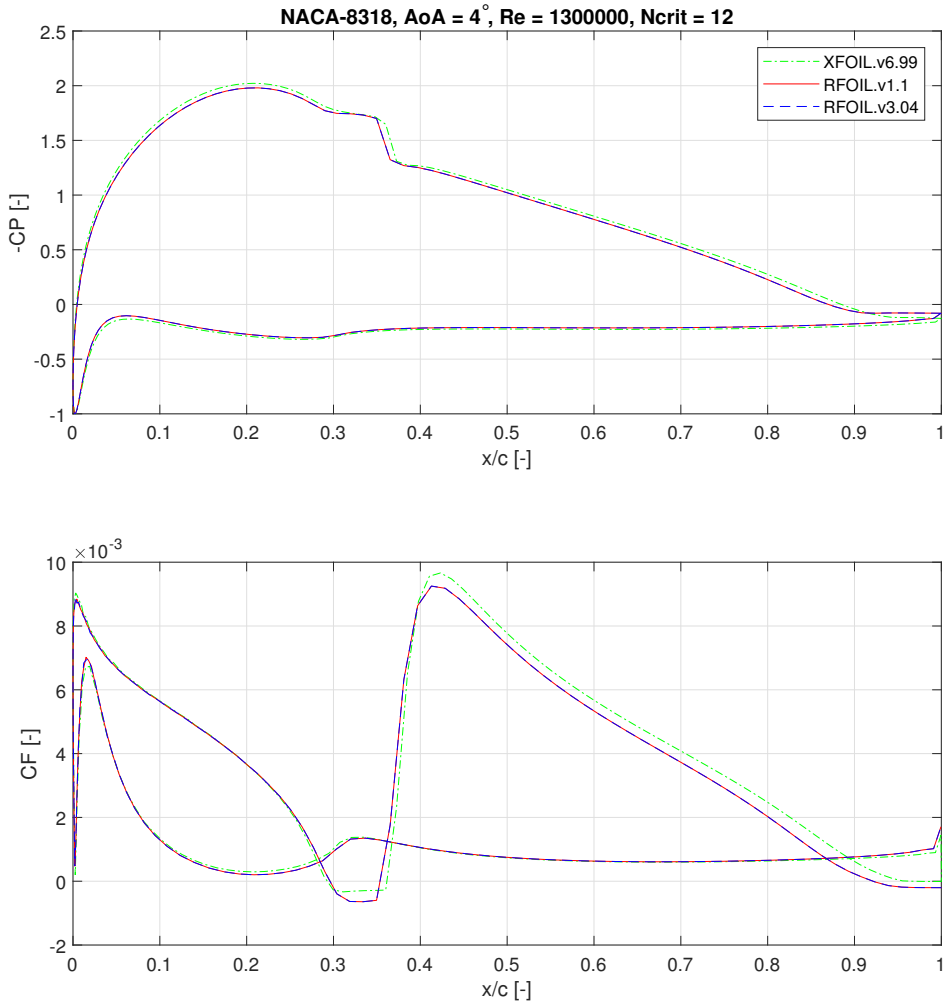

Figure B.466: Comparison between experimental and numerical polars for the NACA-8318 airfoil at a Reynolds number of 2400000. Simulation time to generate the polars by means the different codes and the number of converged polar points are depicted between parentheses.

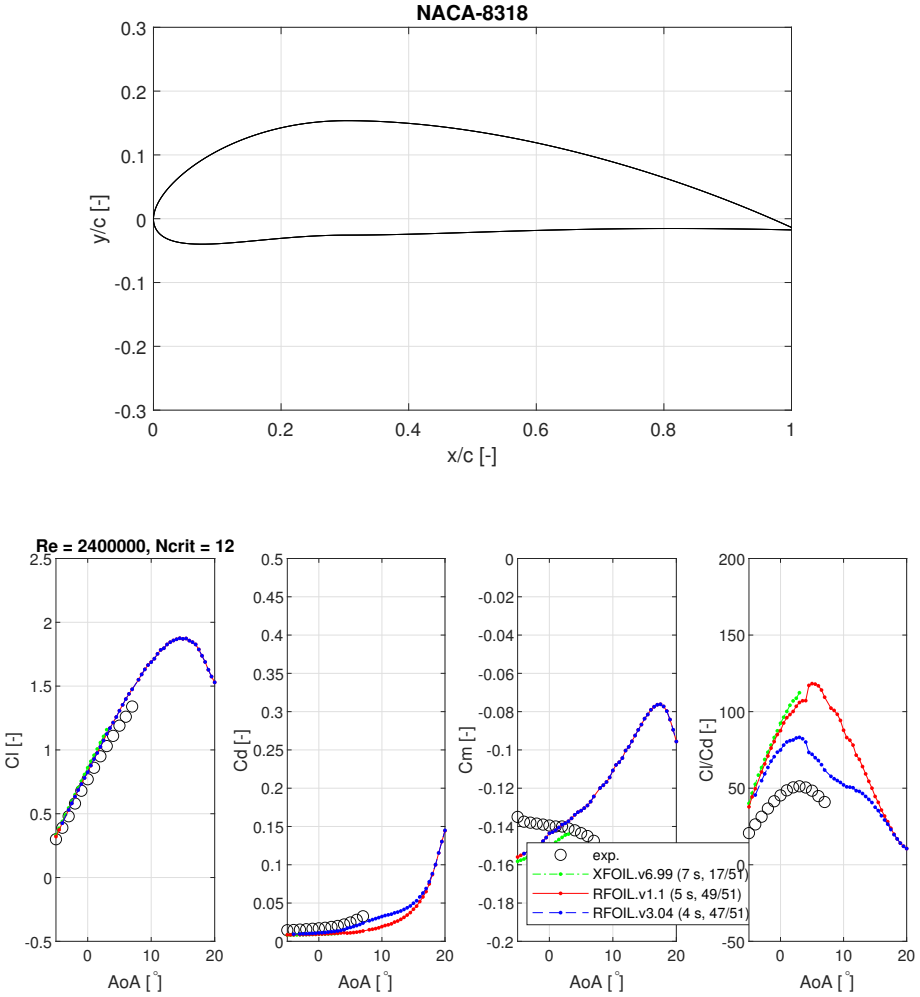

Figure B.467: Differences between experimental and numerical polars for the NACA-8318 airfoil at a Reynolds number of 2400000. Vertical black lines in the middle subplot indicate, from left to right, the angle of attack corresponding to the minimum drag coefficient, maximum lift to drag ratio and maximum lift coefficient, respectively.

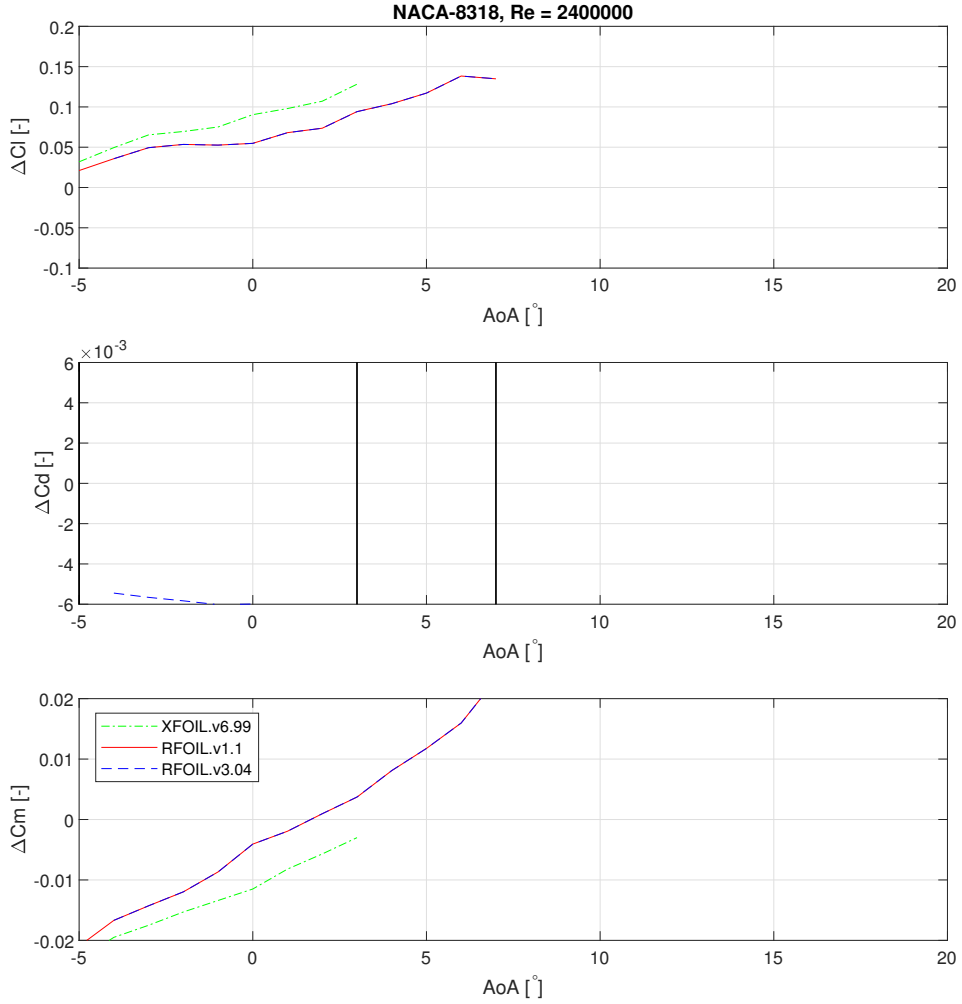

Figure B.468: Comparison between experimental and numerical pressure and skin friction distributions for the NACA-8318 airfoil at a Reynolds number of 2400000 and at the design angle of attack.

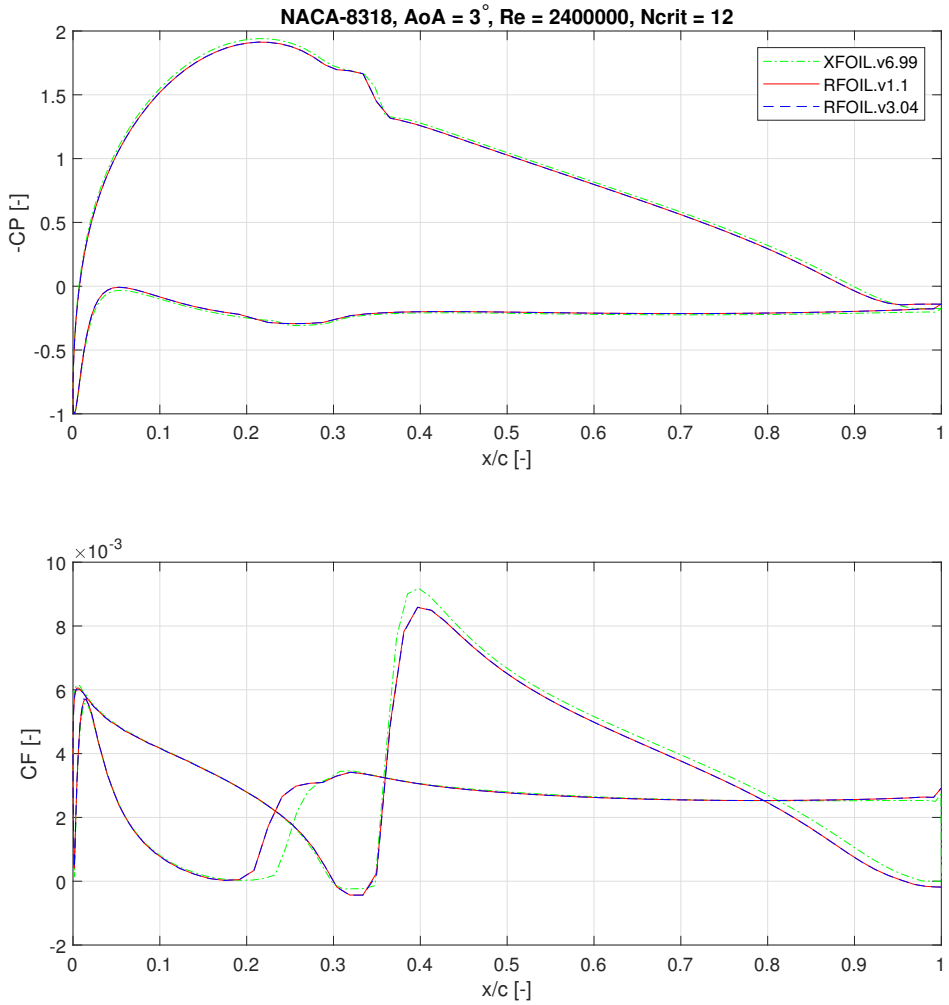

Figure B.469: Comparison between experimental and numerical polars for the NACA-8318 airfoil at a Reynolds number of 3200000. Simulation time to generate the polars by means the different codes and the number of converged polar points are depicted between parentheses.

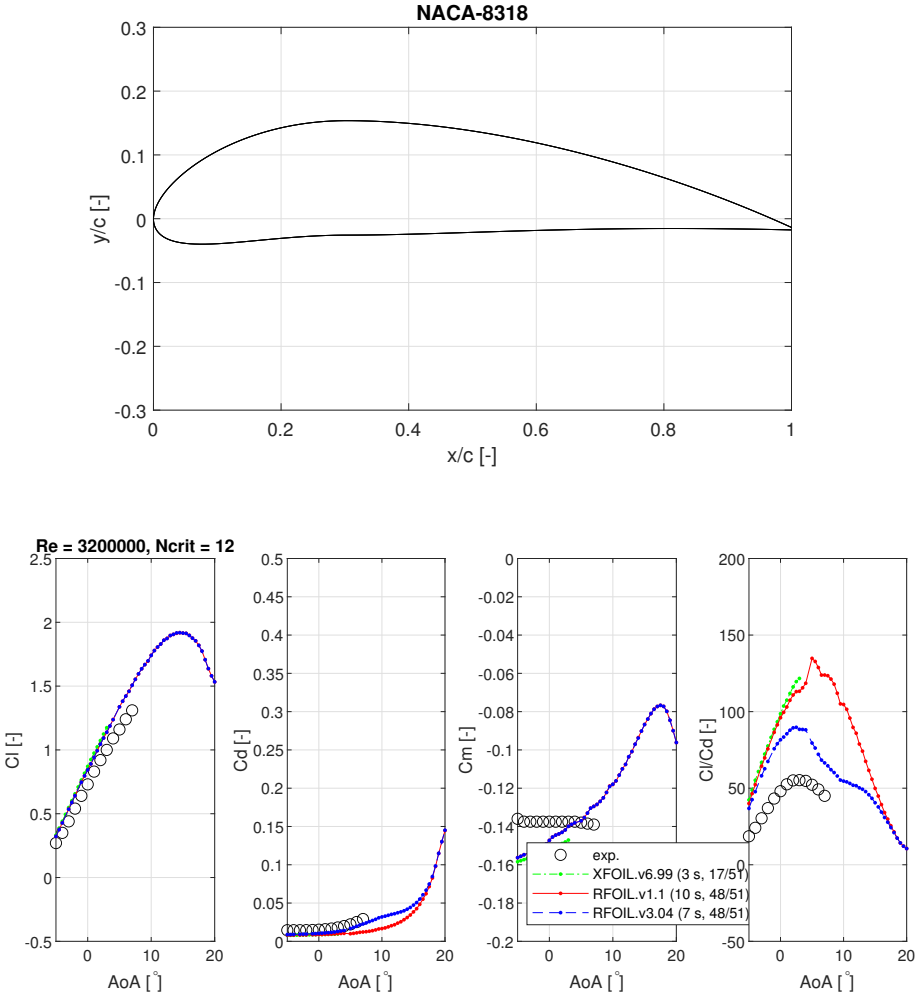

Figure B.470: Differences between experimental and numerical polars for the NACA-8318 airfoil at a Reynolds number of 3200000. Vertical black lines in the middle subplot indicate, from left to right, the angle of attack corresponding to the minimum drag coefficient, maximum lift to drag ratio and maximum lift coefficient, respectively.

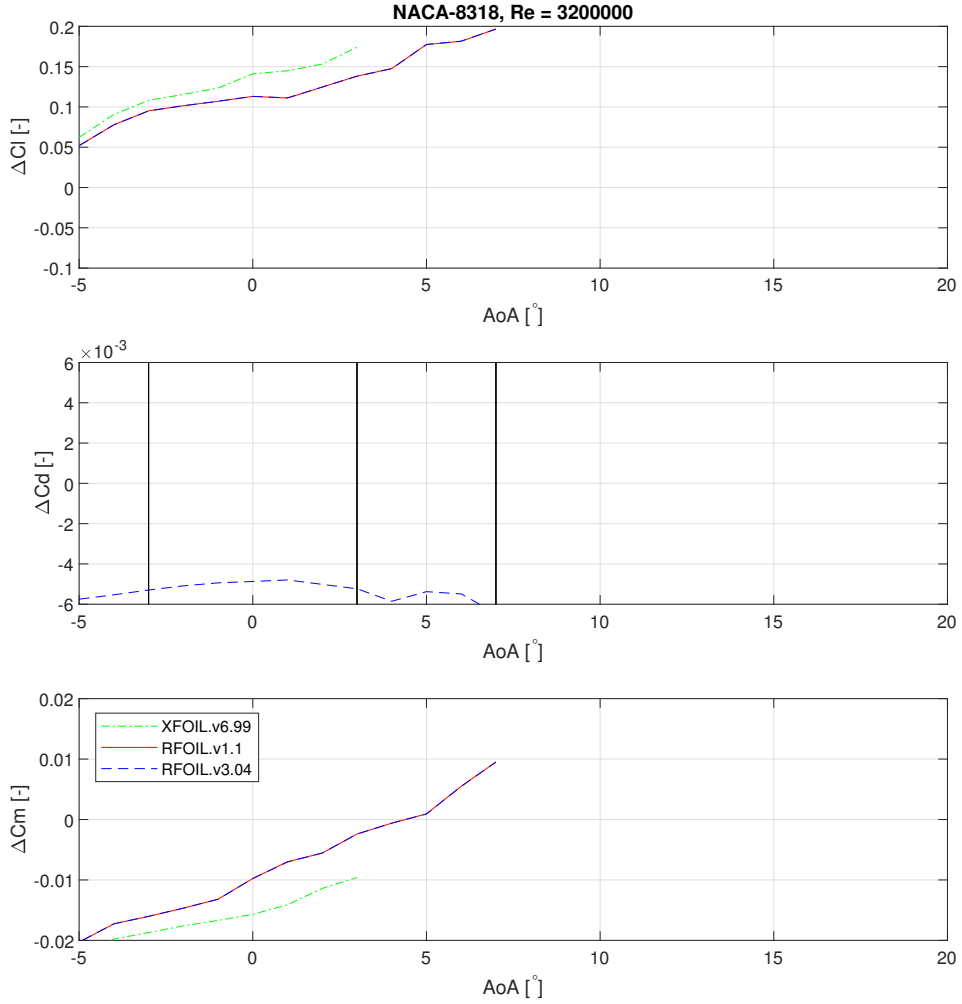

Figure B.471: Comparison between experimental and numerical pressure and skin friction distributions for the NACA-8318 airfoil at a Reynolds number of 3200000 and at the design angle of attack.

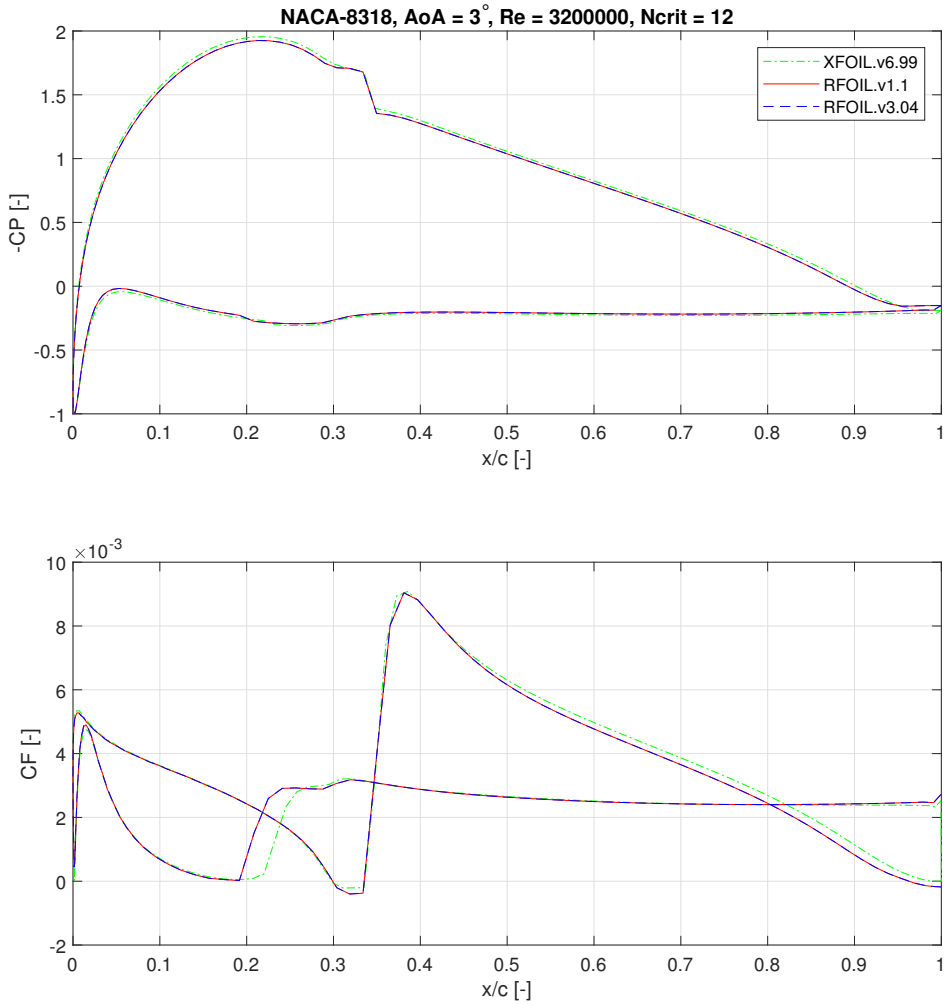

Figure B.472: Comparison between experimental and numerical polars for the NACA-8318 airfoil at a Reynolds number of 600000. Simulation time to generate the polars by means the different codes and the number of converged polar points are depicted between parentheses.

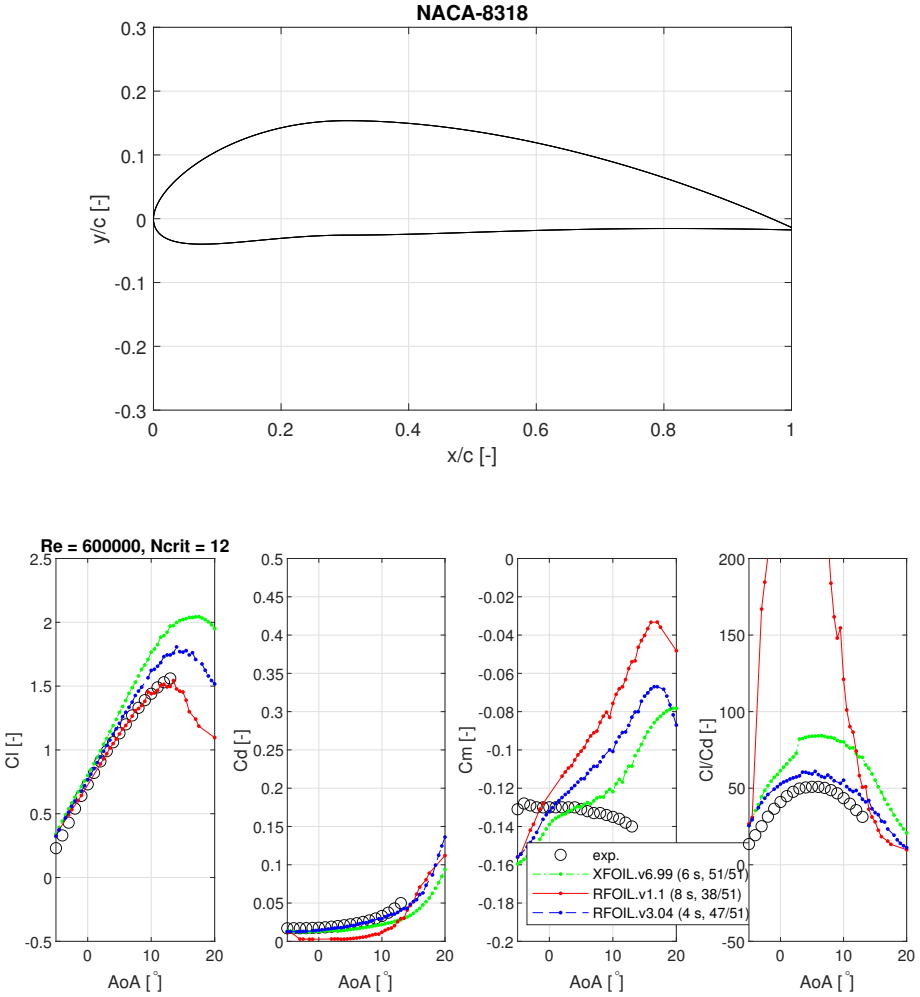

Figure B.473: Differences between experimental and numerical polars for the NACA-8318 airfoil at a Reynolds number of 600000. Vertical black lines in the middle subplot indicate, from left to right, the angle of attack corresponding to the minimum drag coefficient, maximum lift to drag ratio and maximum lift coefficient, respectively.

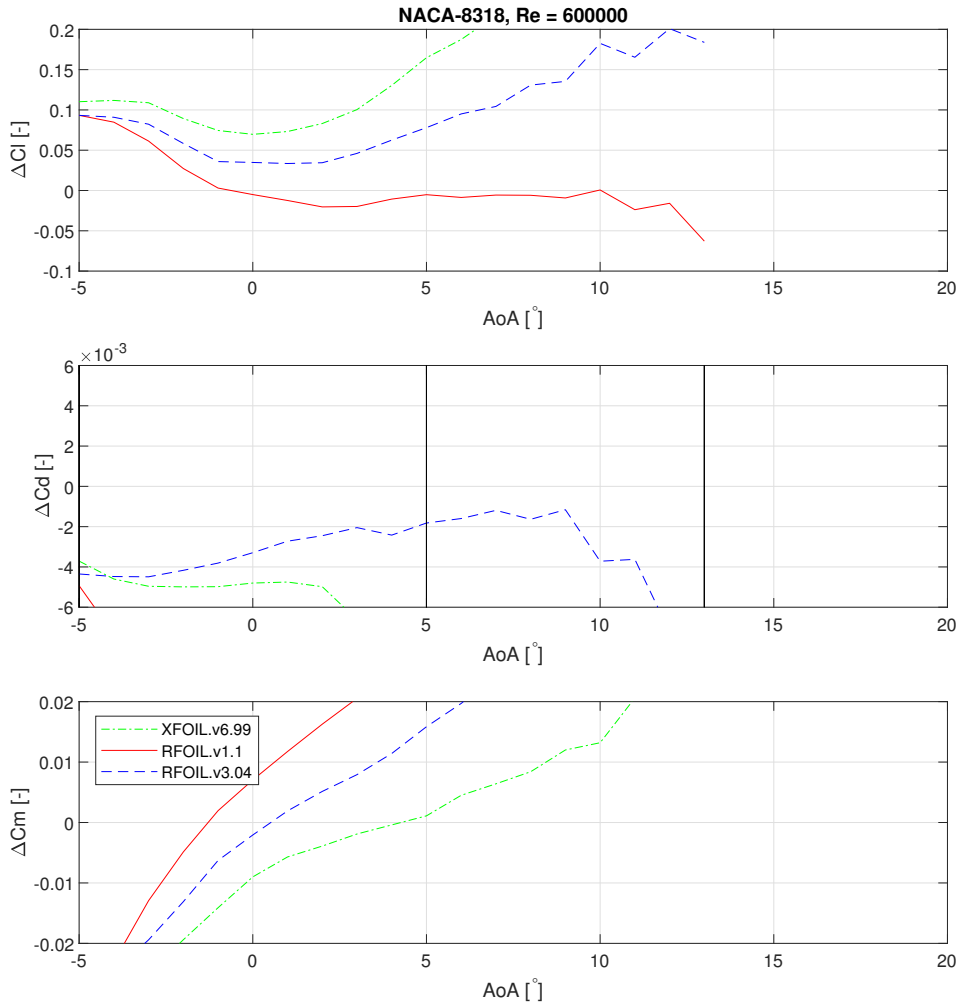

Figure B.474: Comparison between experimental and numerical pressure and skin friction distributions for the NACA-8318 airfoil at a Reynolds number of 600000 and at the design angle of attack.

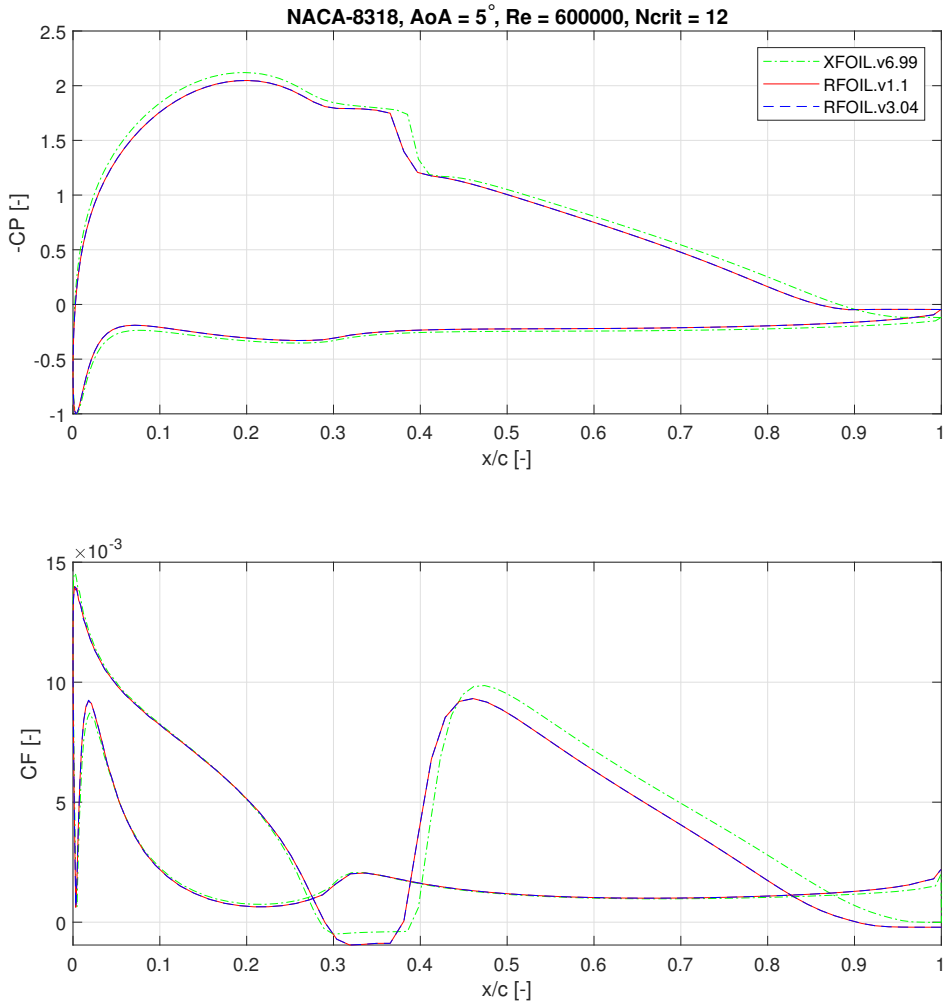

Appendix C

Comparison between experimental and numerical pressure distributions for the AVATAR-DU00-W-212 airfoil

Figure C.1: Comparison between experimental and numerical pressure distributions for the AVATAR-DU00-W-212 airfoil at a Reynolds number of 14990000, and at an angle of attack and a Mach number of -0.001° and 0.081, respectively.

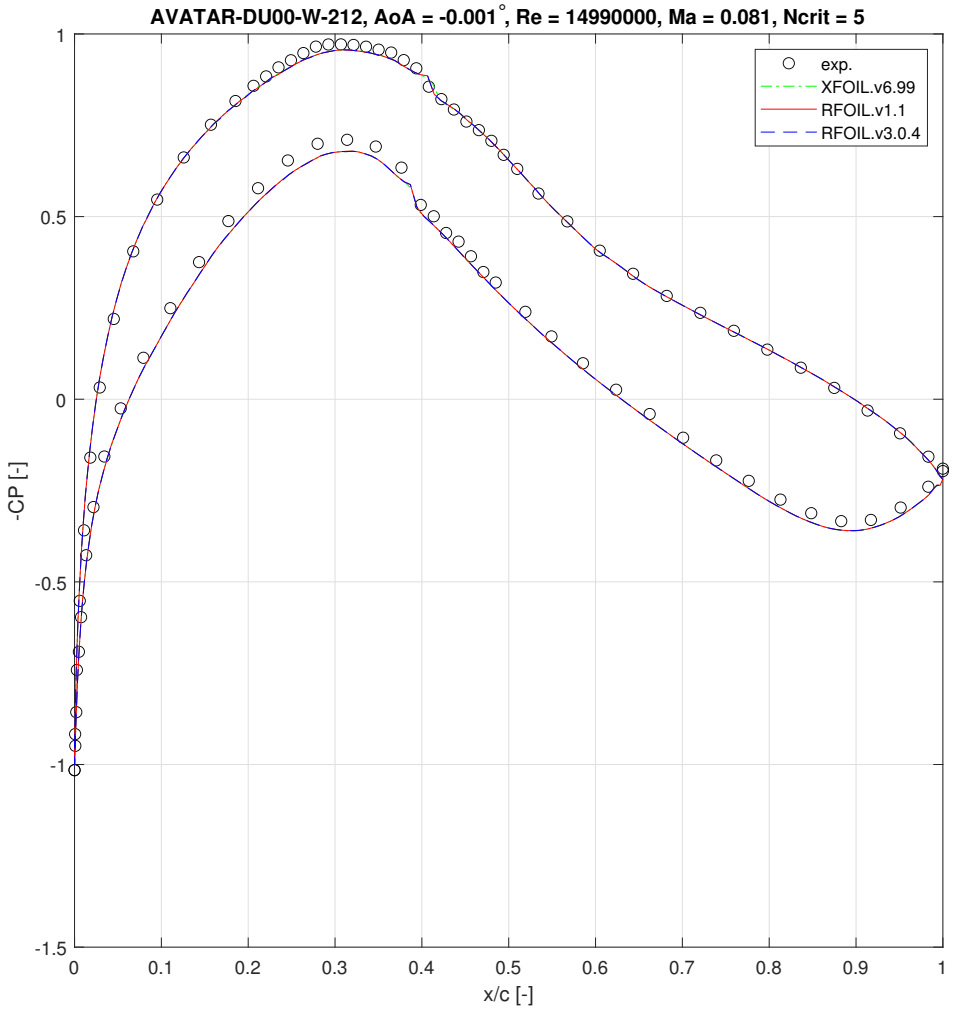

Figure C.2: Comparison between experimental and numerical pressure distributions for the AVATAR-DU00-W-212 airfoil at a Reynolds number of 2980000, and at an angle of attack and a Mach number of -0.001° and 0.074, respectively.

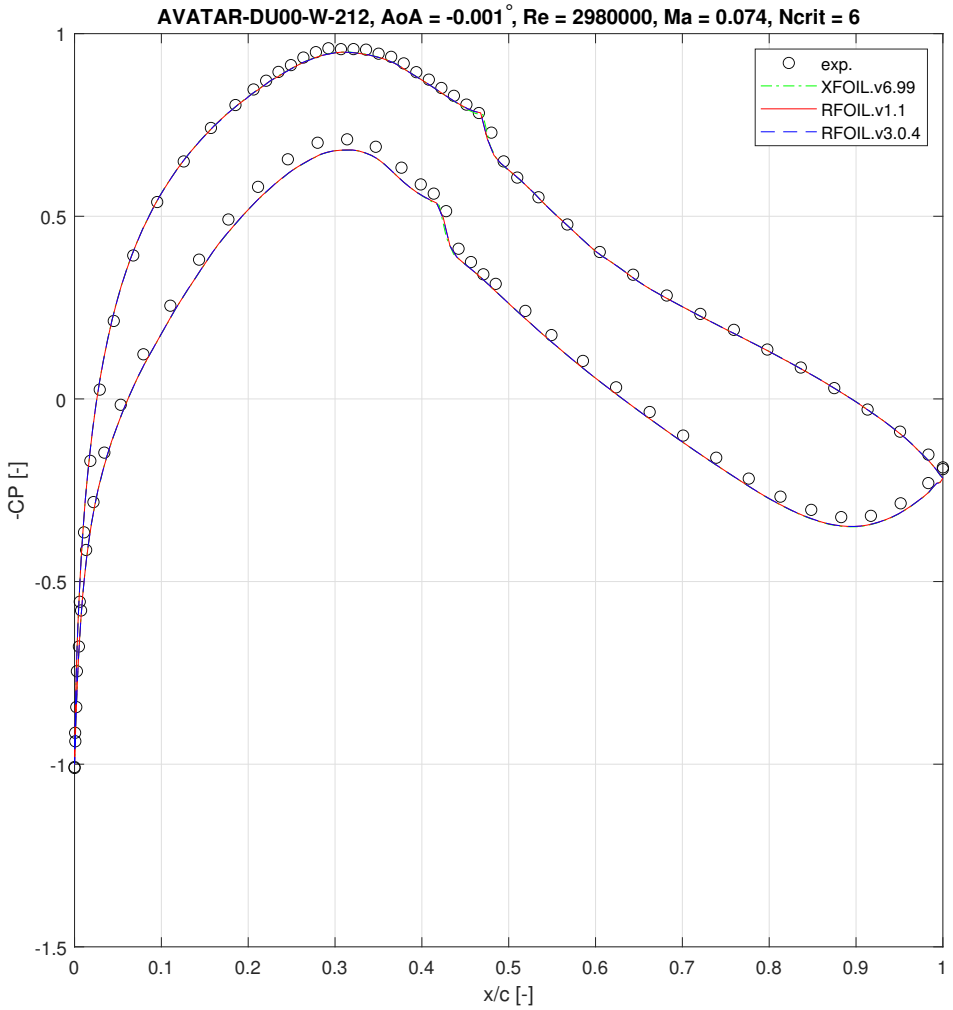

Figure C.3: Comparison between experimental and numerical pressure distributions for the AVATAR-DU00-W-212 airfoil at a Reynolds number of 2990000, and at an angle of attack and a Mach number of -0.001° and 0.074, respectively.

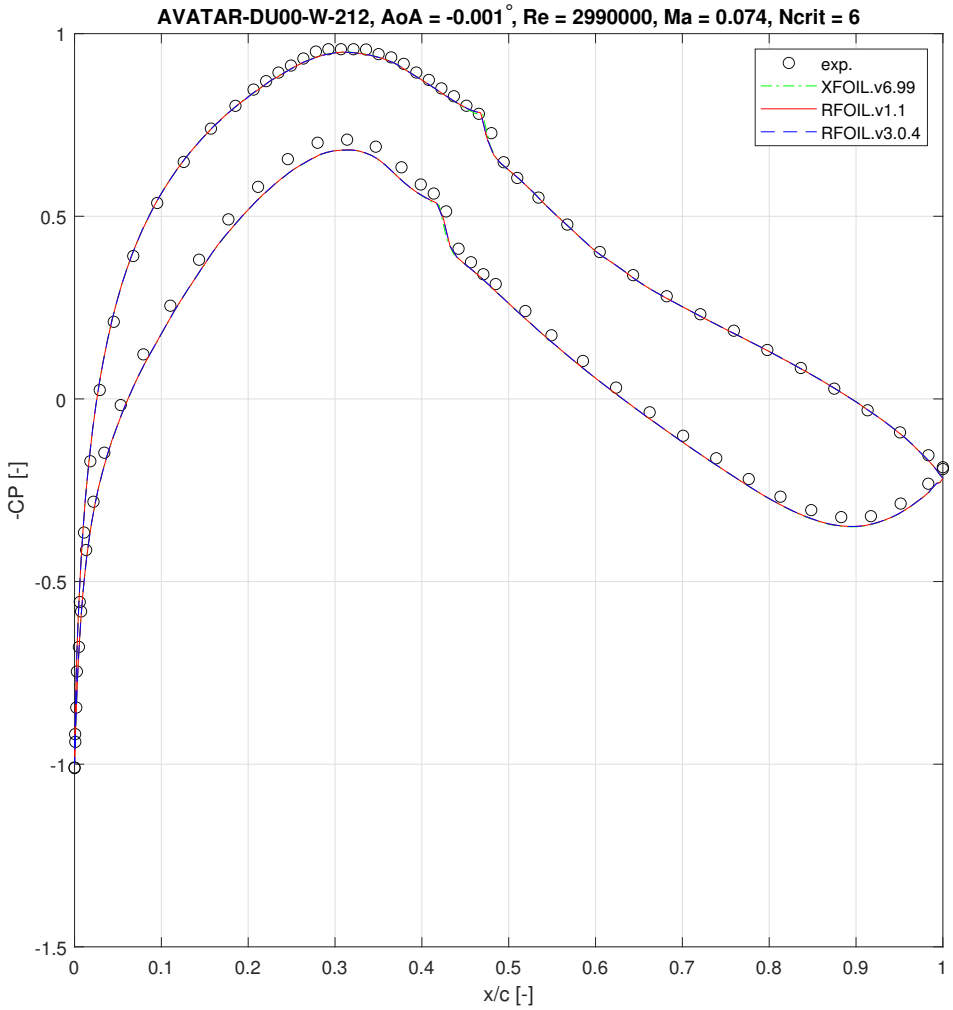

Figure C.4: Comparison between experimental and numerical pressure distributions for the AVATAR-DU00-W-212 airfoil at a Reynolds number of 3000000, and at an angle of attack and a Mach number of -0.001° and 0.074, respectively.

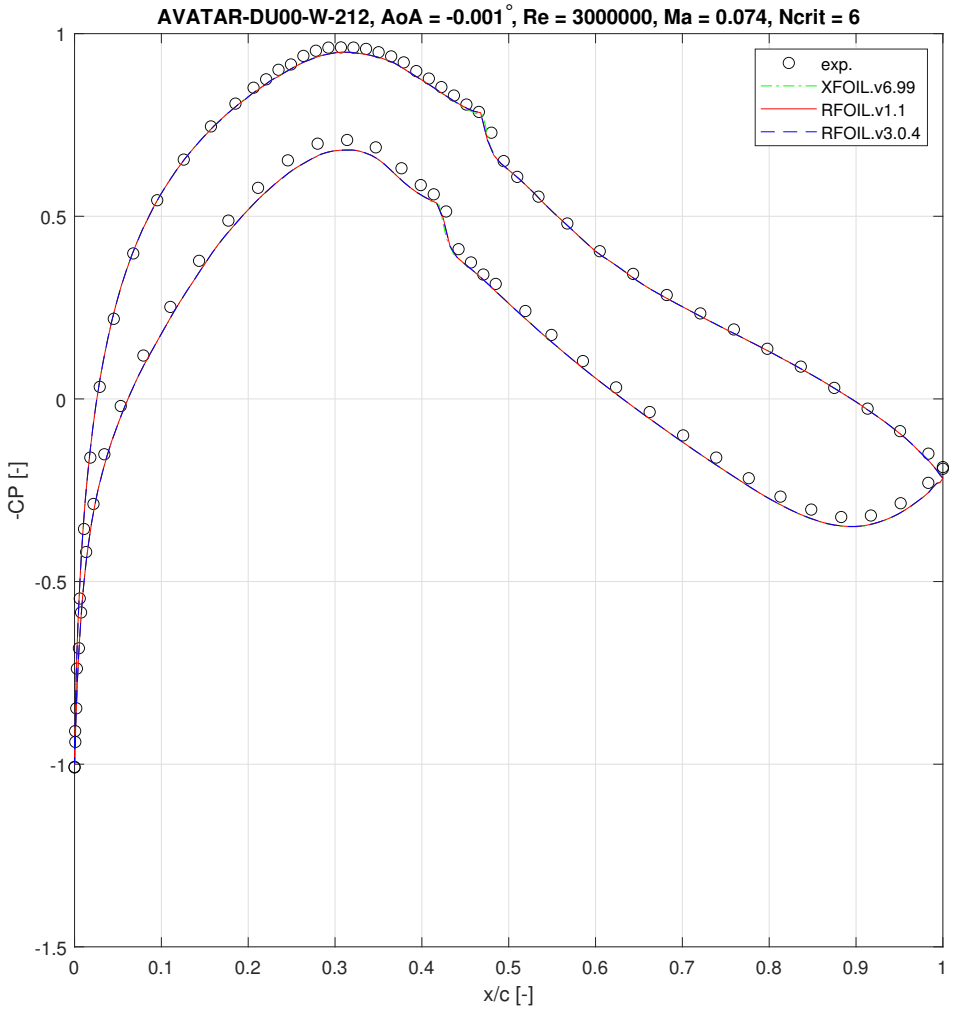

Figure C.5: Comparison between experimental and numerical pressure distributions for the AVATAR-DU00-W-212 airfoil at a Reynolds number of 5970000, and at an angle of attack and a Mach number of -0.001° and 0.055, respectively.

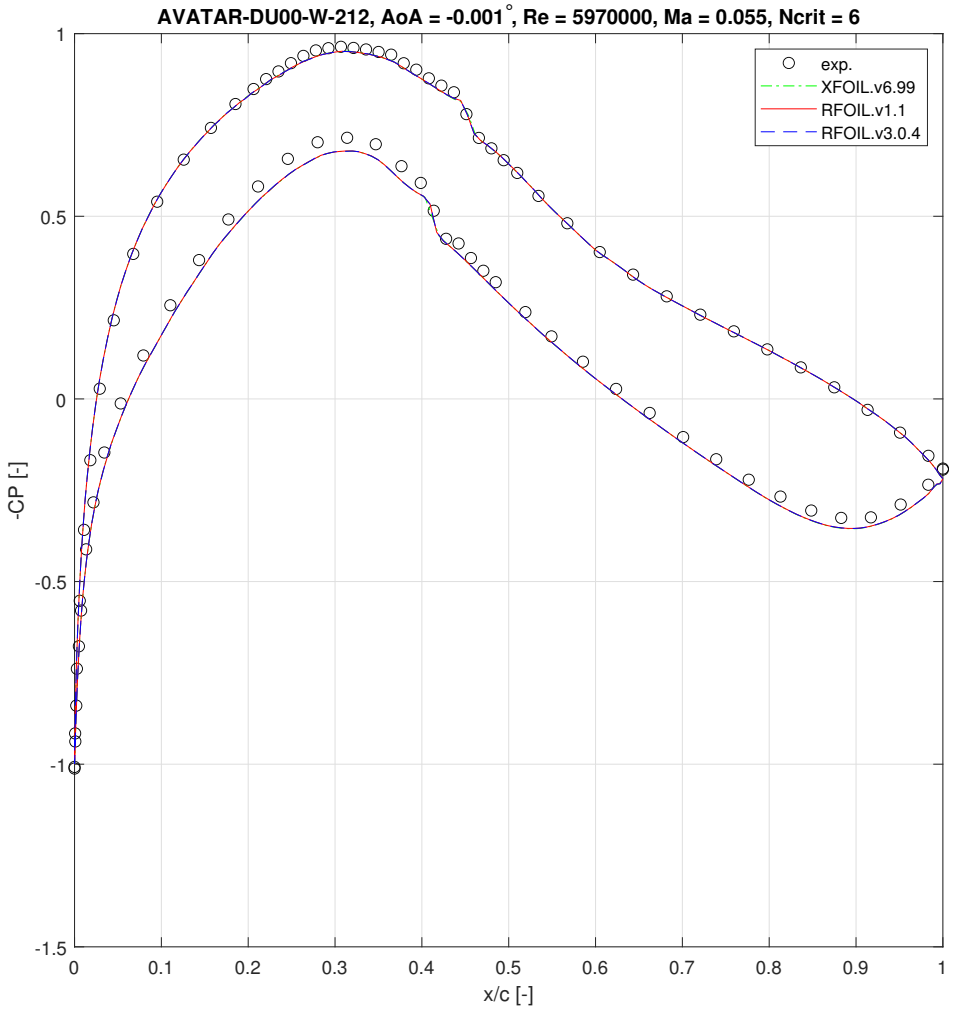

Figure C.6: Comparison between experimental and numerical pressure distributions for the AVATAR-DU00-W-212 airfoil at a Reynolds number of 5990000, and at an angle of attack and a Mach number of -0.002° and 0.055, respectively.

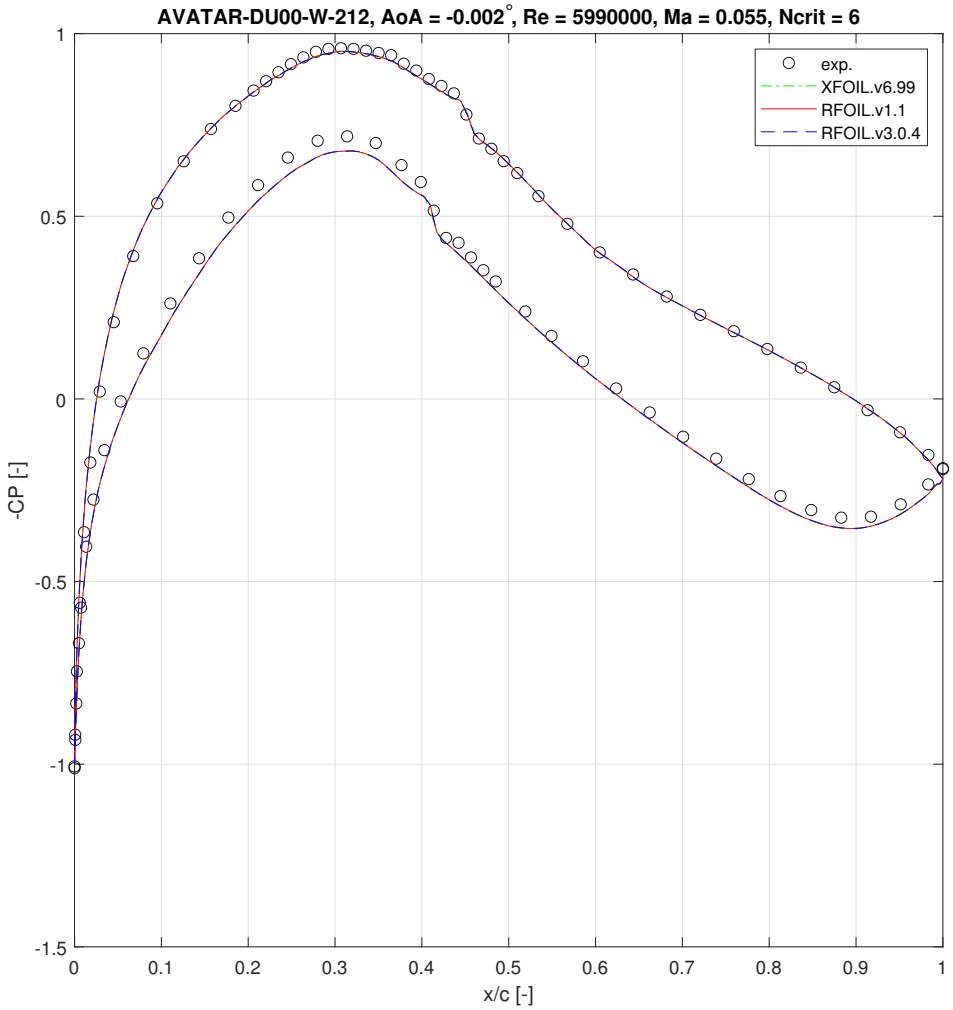

Figure C.7: Comparison between experimental and numerical pressure distributions for the AVATAR-DU00-W-212 airfoil at a Reynolds number of 6000000, and at an angle of attack and a Mach number of -0.002° and 0.055, respectively.

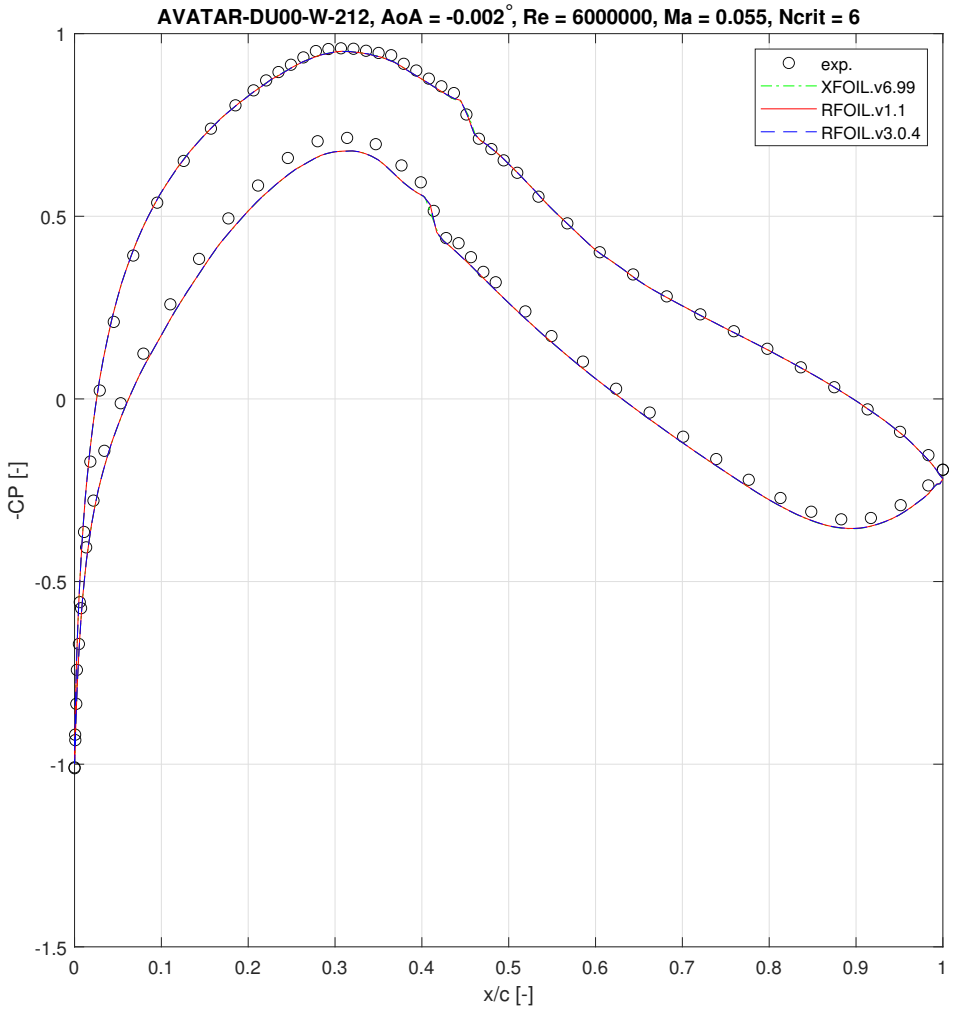

Figure C.8: Comparison between experimental and numerical pressure distributions for the AVATAR-DU00-W-212 airfoil at a Reynolds number of 8990000, and at an angle of attack and a Mach number of -0.002° and 0.083, respectively.

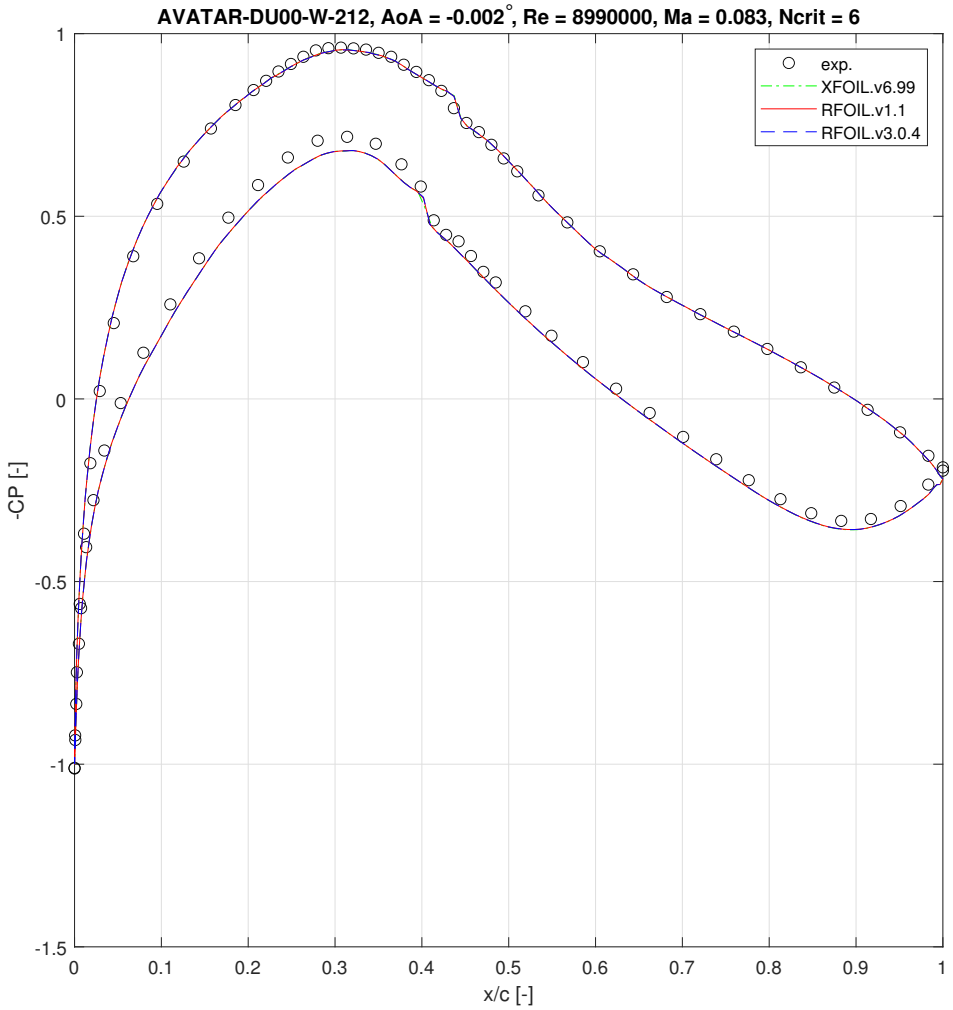

Figure C.9: Comparison between experimental and numerical pressure distributions for the AVATAR-DU00-W-212 airfoil at a Reynolds number of 9000000, and at an angle of attack and a Mach number of -0.002° and 0.083, respectively.

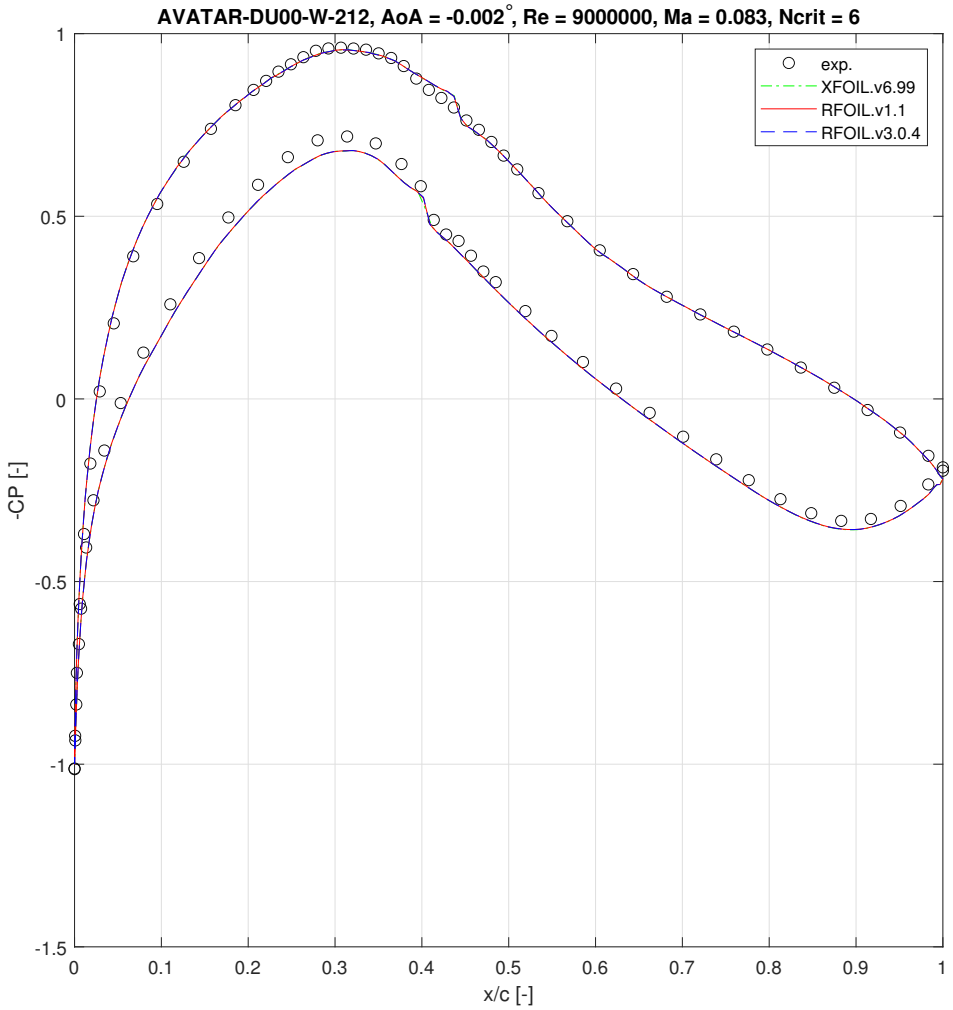

Figure C.10: Comparison between experimental and numerical pressure distributions for the AVATAR-DU00-W-212 airfoil at a Reynolds number of 9020000, and at an angle of attack and a Mach number of -0.002° and 0.083, respectively.

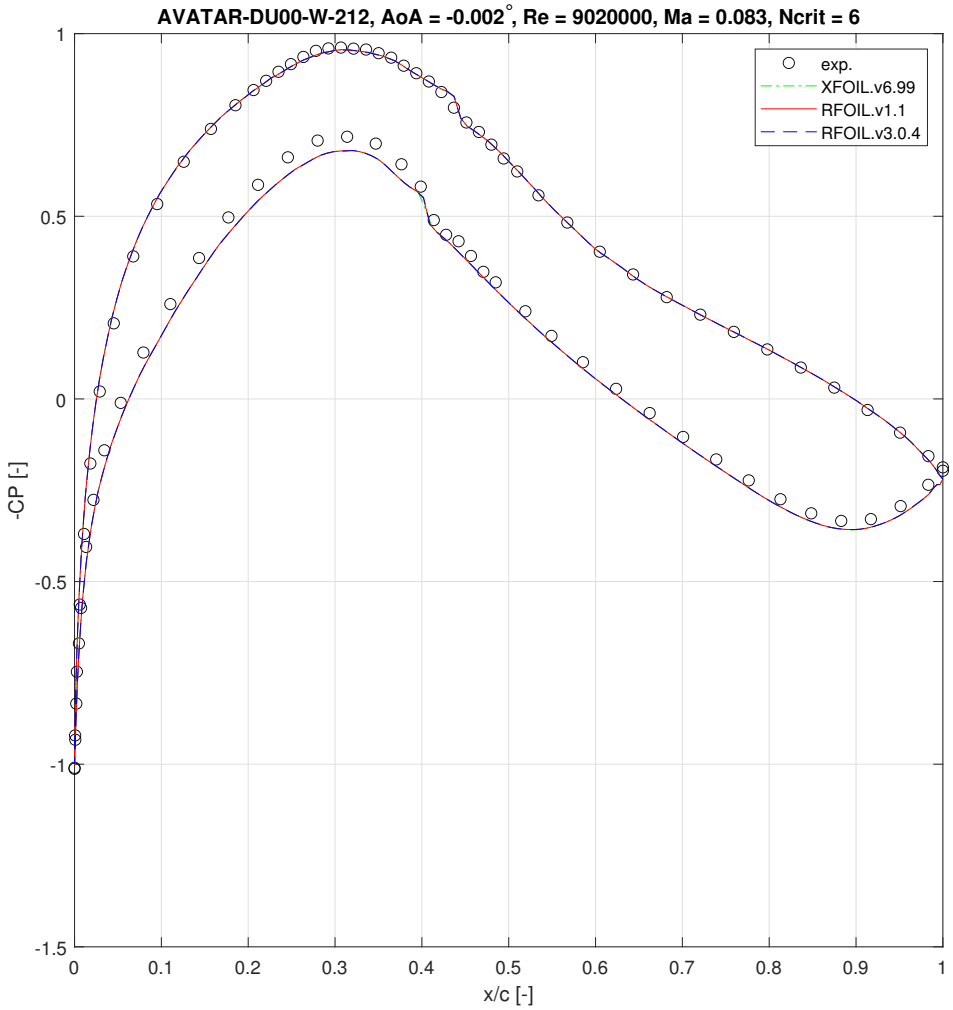

Figure C.11: Comparison between experimental and numerical pressure distributions for the AVATAR-DU00-W-212 airfoil at a Reynolds number of 6000000, and at an angle of attack and a Mach number of -0.003° and 0.029, respectively.

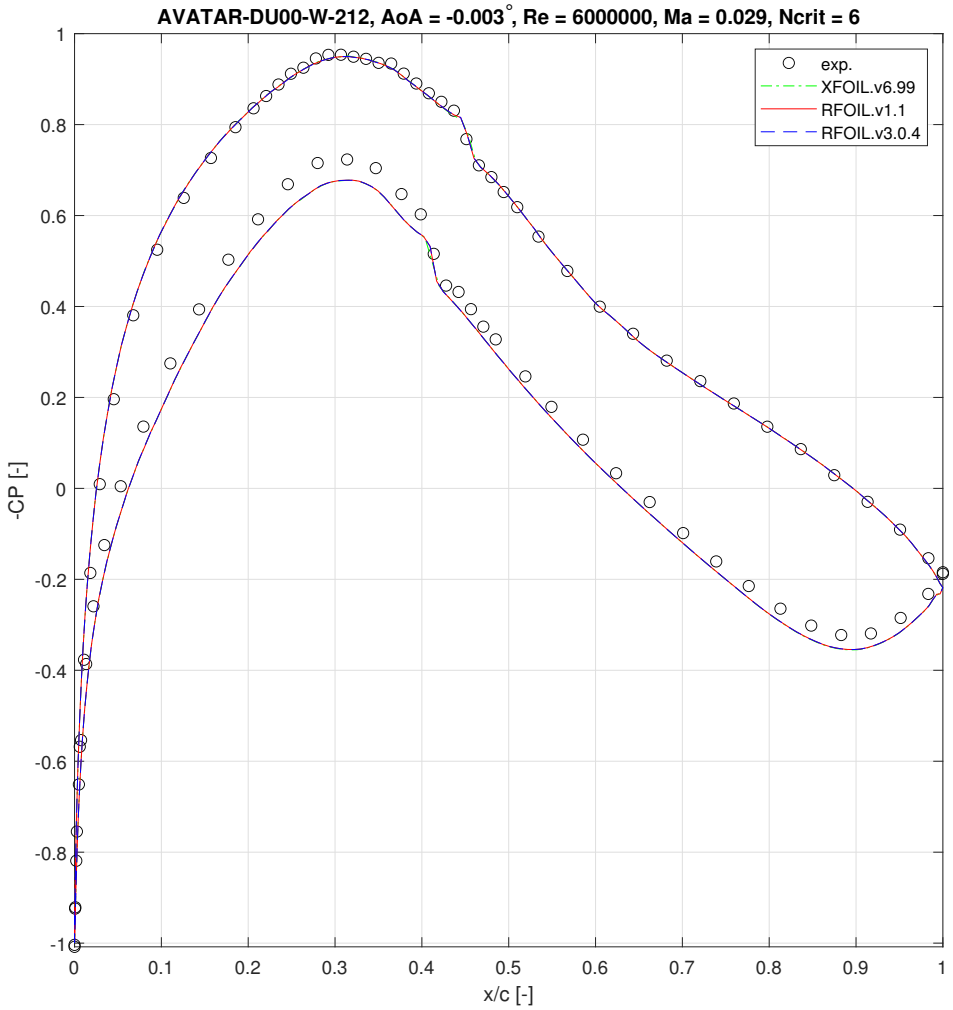

Figure C.12: Comparison between experimental and numerical pressure distributions for the AVATAR-DU00-W-212 airfoil at a Reynolds number of 6010000, and at an angle of attack and a Mach number of -0.003° and 0.029, respectively.

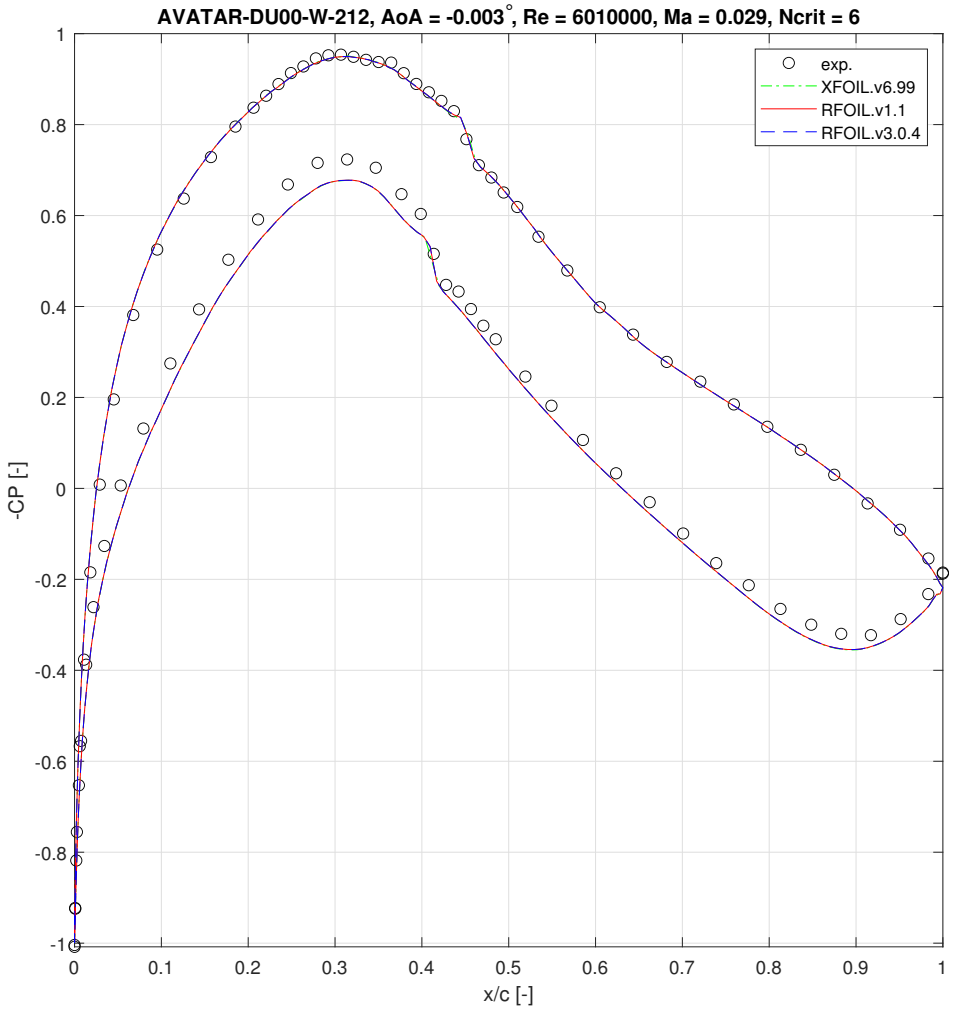

Figure C.13: Comparison between experimental and numerical pressure distributions for the AVATAR-DU00-W-212 airfoil at a Reynolds number of 6020000, and at an angle of attack and a Mach number of -0.003° and 0.029, respectively.

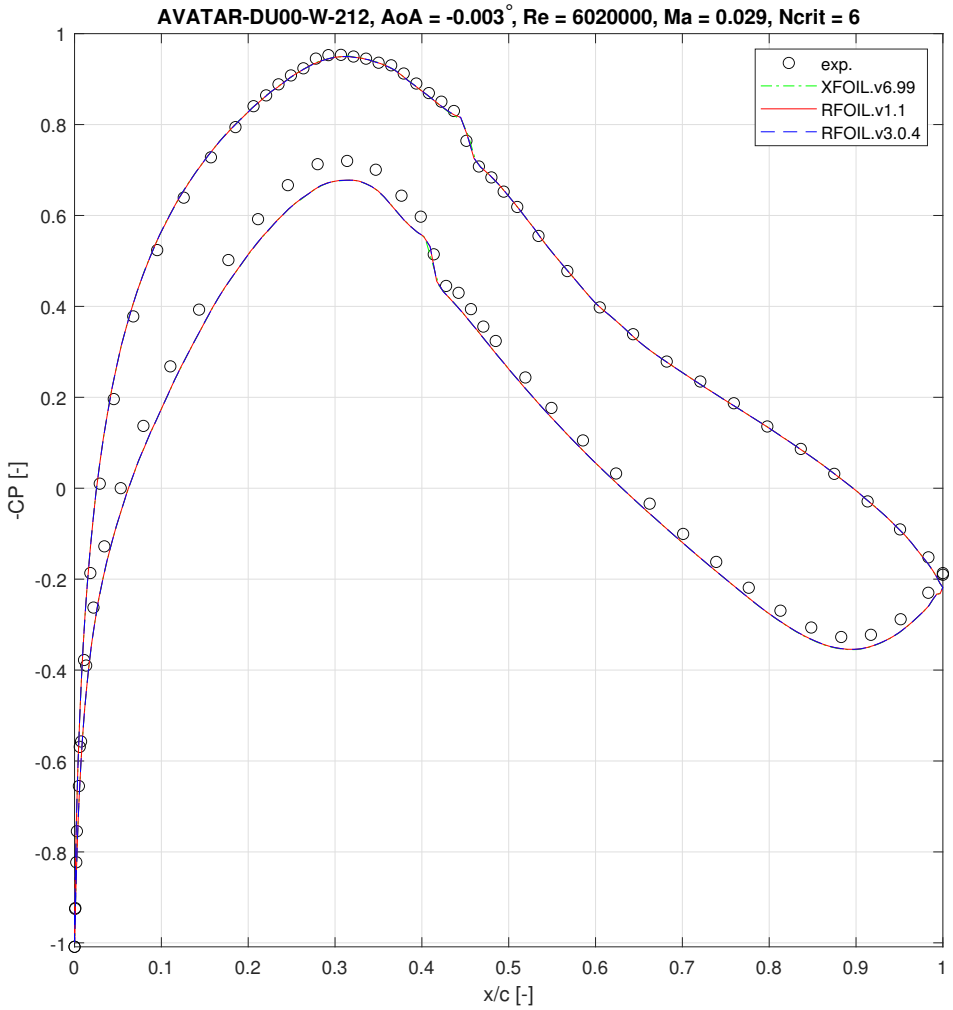

Figure C.14: Comparison between experimental and numerical pressure distributions for the AVATAR-DU00-W-212 airfoil at a Reynolds number of 8990000, and at an angle of attack and a Mach number of -0.003° and 0.043, respectively.

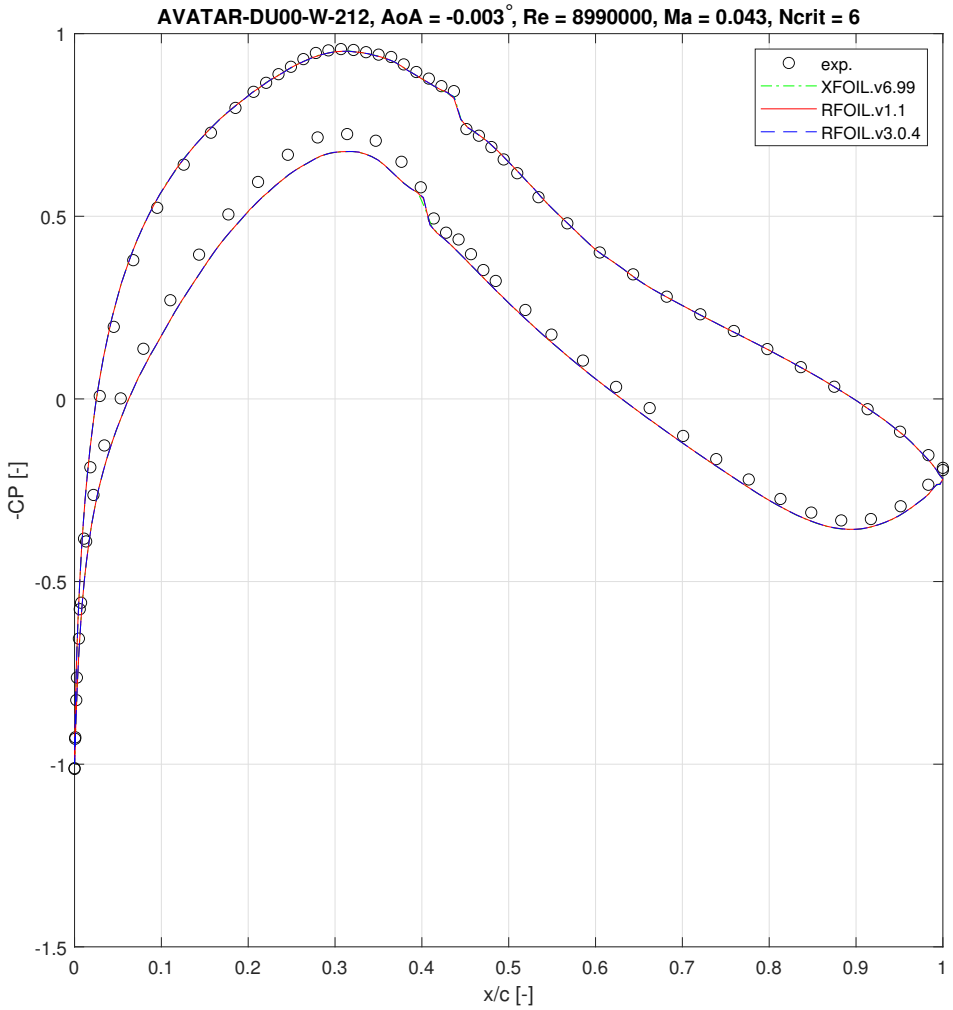

Figure C.15: Comparison between experimental and numerical pressure distributions for the AVATAR-DU00-W-212 airfoil at a Reynolds number of 9000000, and at an angle of attack and a Mach number of -0.003° and 0.043, respectively.

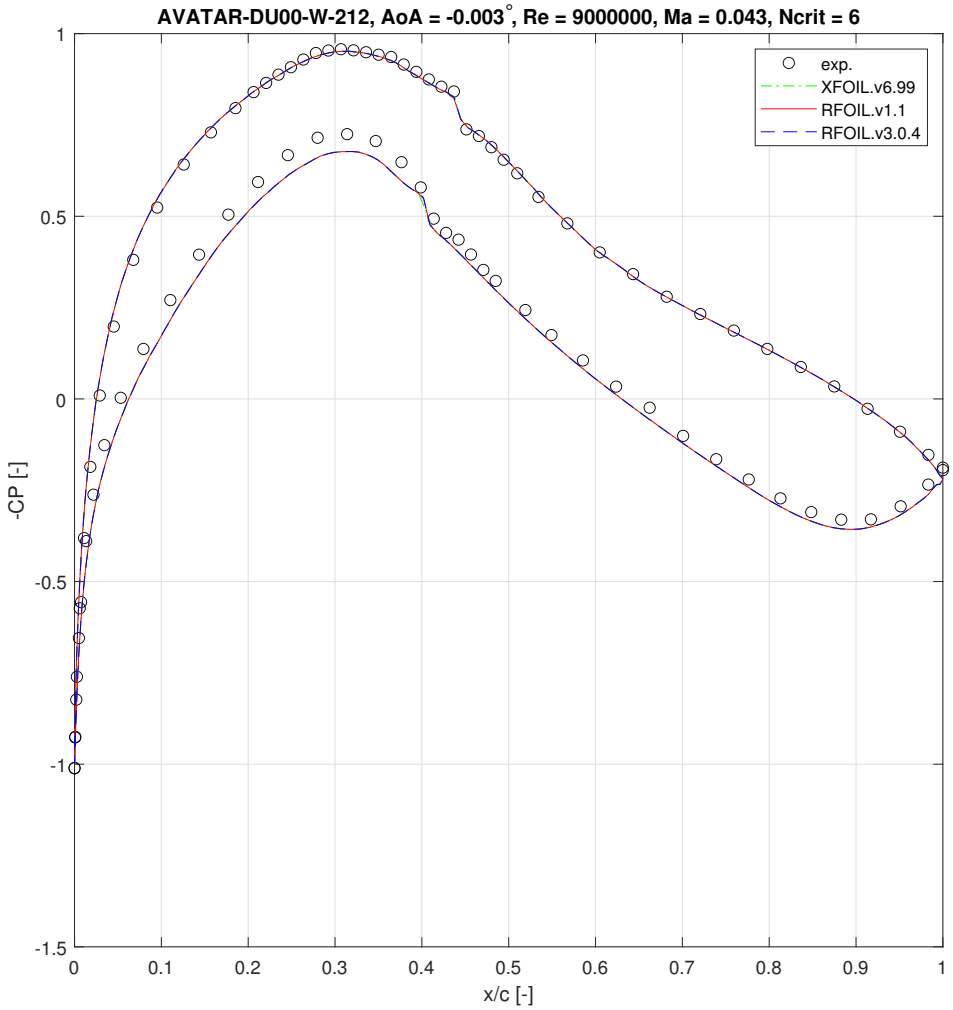

Figure C.16: Comparison between experimental and numerical pressure distributions for the AVATAR-DU00-W-212 airfoil at a Reynolds number of 9040000, and at an angle of attack and a Mach number of -0.003° and 0.044, respectively.

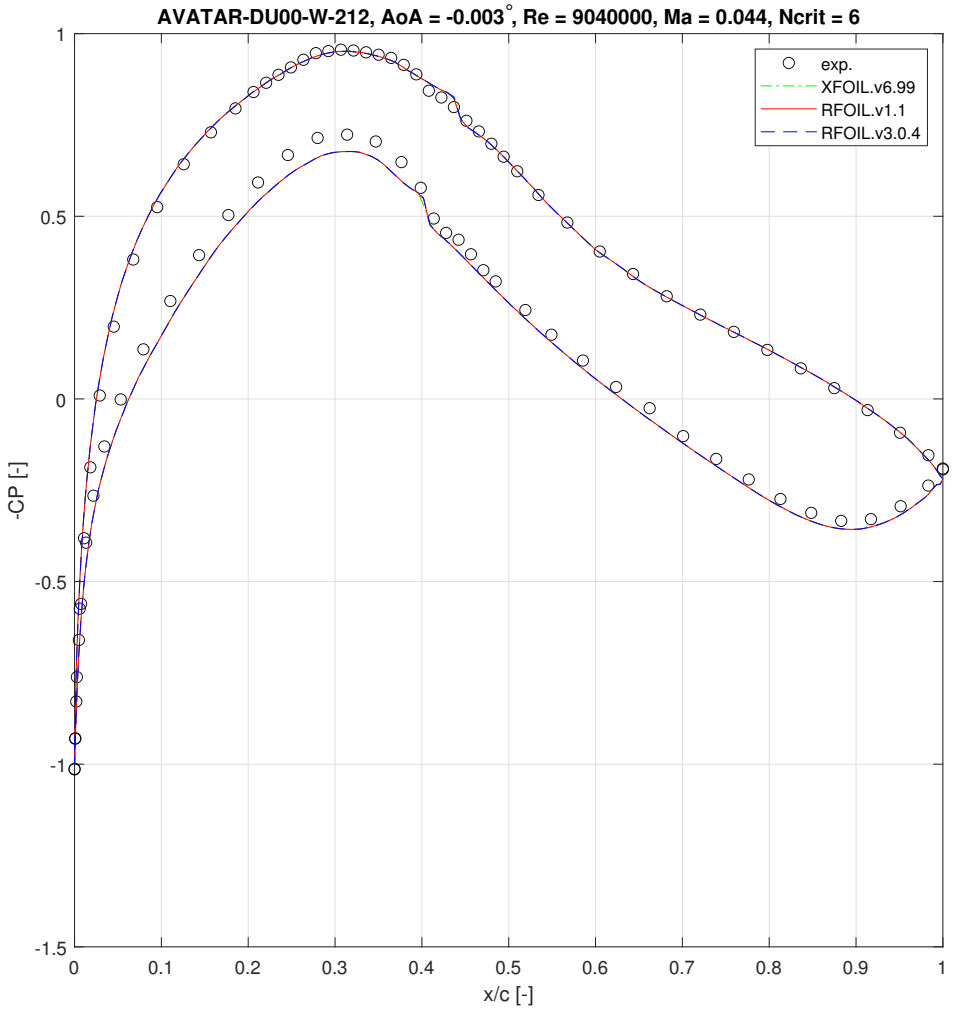

Figure C.17: Comparison between experimental and numerical pressure distributions for the AVATAR-DU00-W-212 airfoil at a Reynolds number of 12010000, and at an angle of attack and a Mach number of -0.958° and 0.058, respectively.

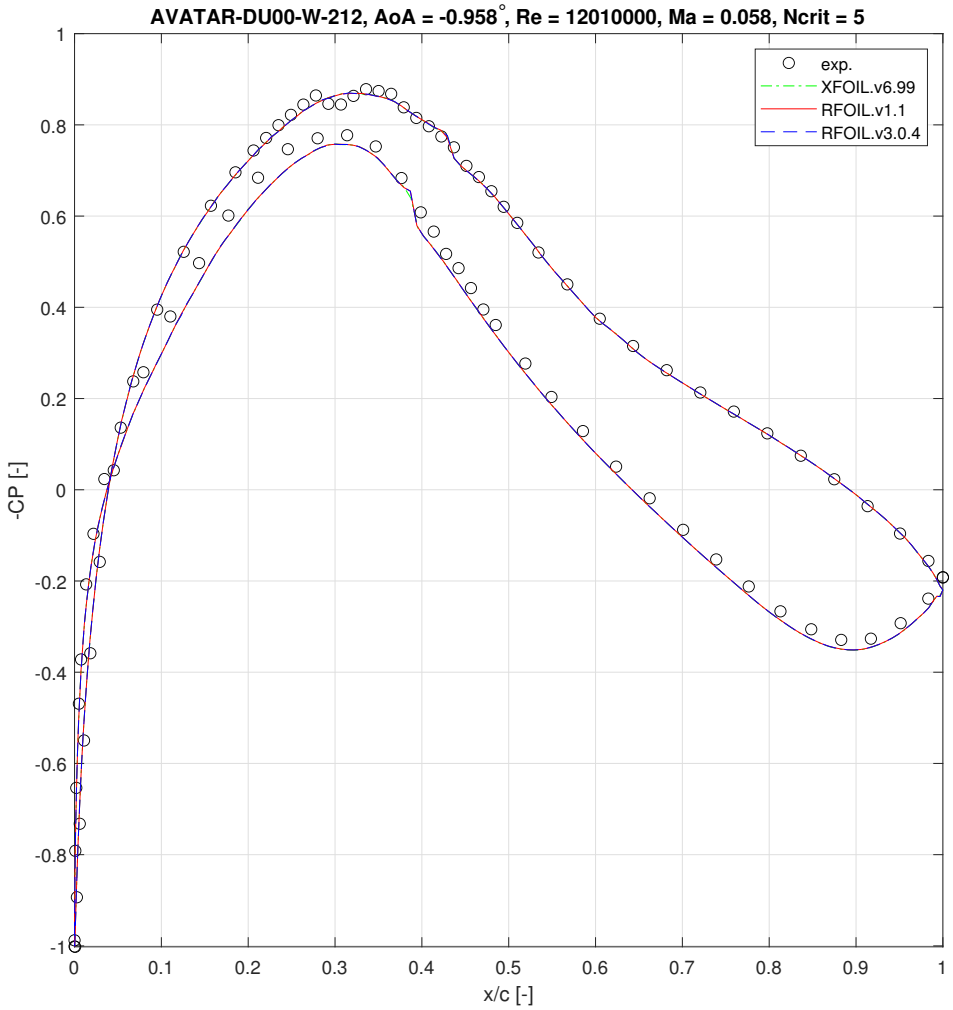

Figure C.18: Comparison between experimental and numerical pressure distributions for the AVATAR-DU00-W-212 airfoil at a Reynolds number of 3000000, and at an angle of attack and a Mach number of -10.088° and 0.074, respectively.

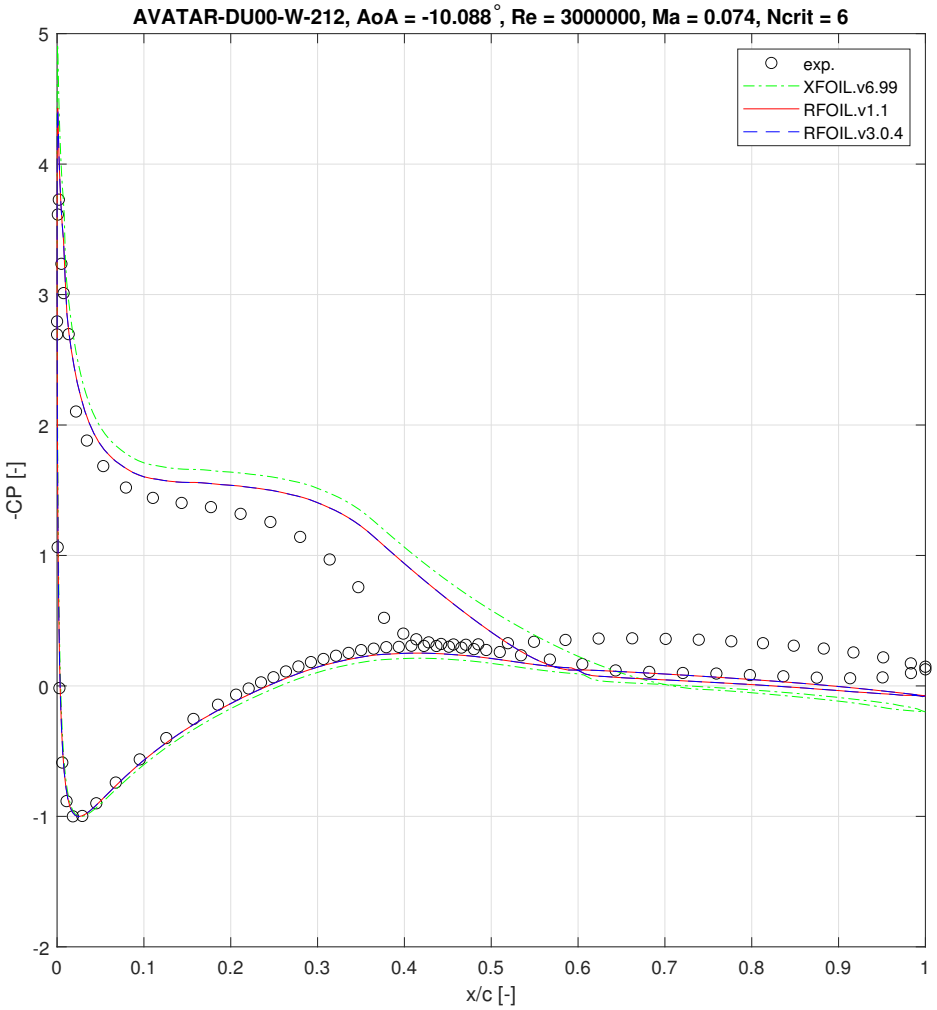

Figure C.19: Comparison between experimental and numerical pressure distributions for the AVATAR-DU00-W-212 airfoil at a Reynolds number of 6010000, and at an angle of attack and a Mach number of -10.122° and 0.029, respectively.

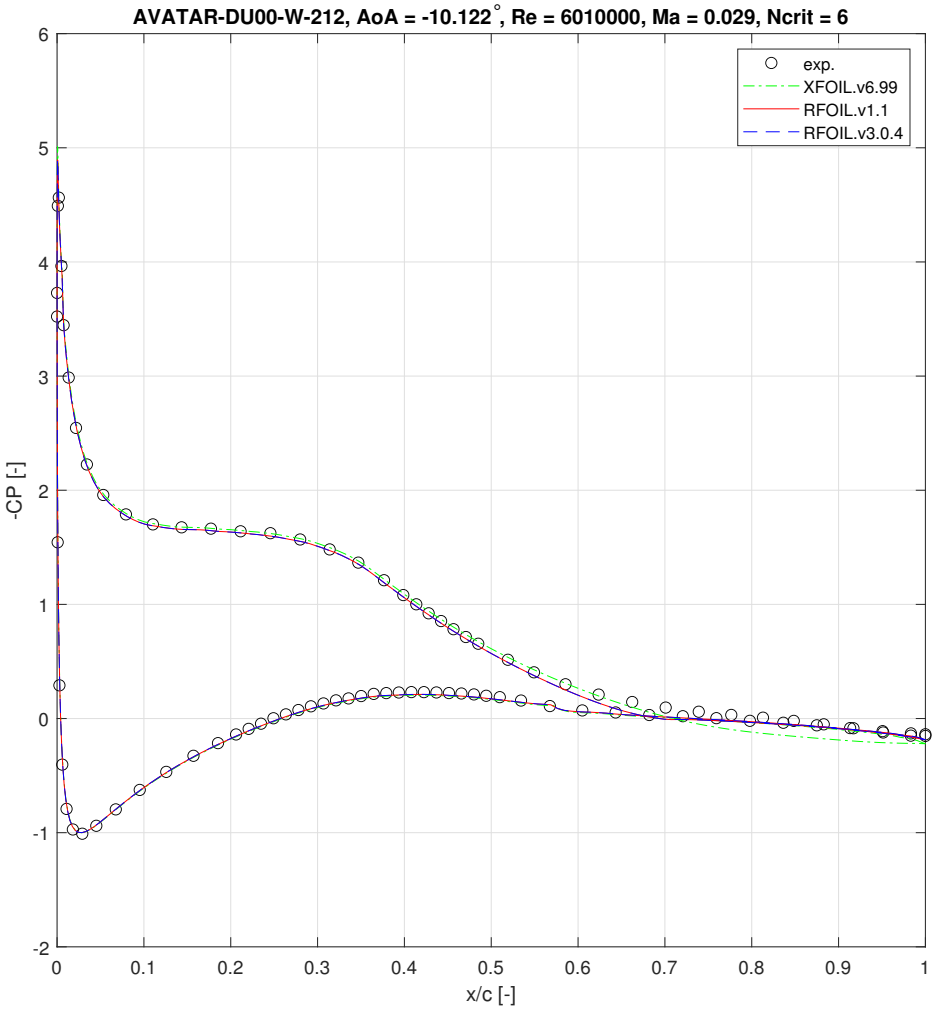

Figure C.20: Comparison between experimental and numerical pressure distributions for the AVATAR-DU00-W-212 airfoil at a Reynolds number of 6020000, and at an angle of attack and a Mach number of -10.122° and 0.055, respectively.

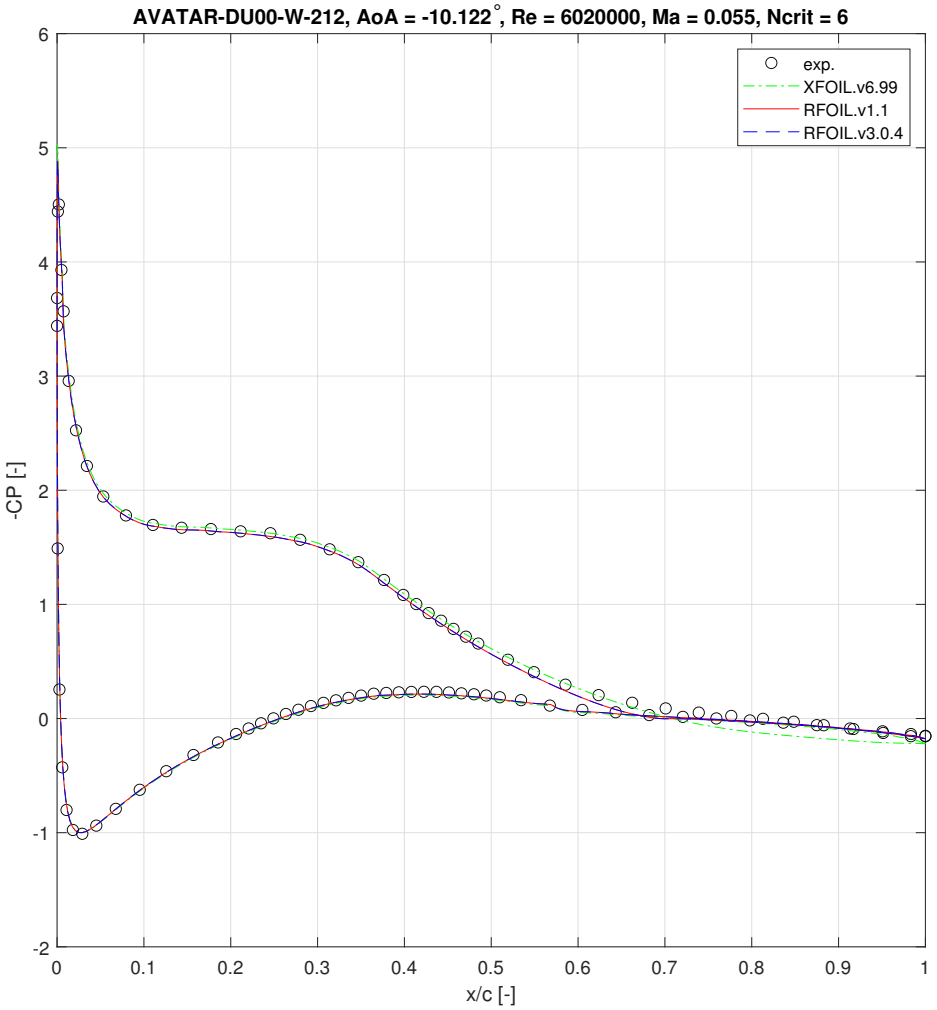

Figure C.21: Comparison between experimental and numerical pressure distributions for the AVATAR-DU00-W-212 airfoil at a Reynolds number of 9000000, and at an angle of attack and a Mach number of -10.127° and 0.043, respectively.

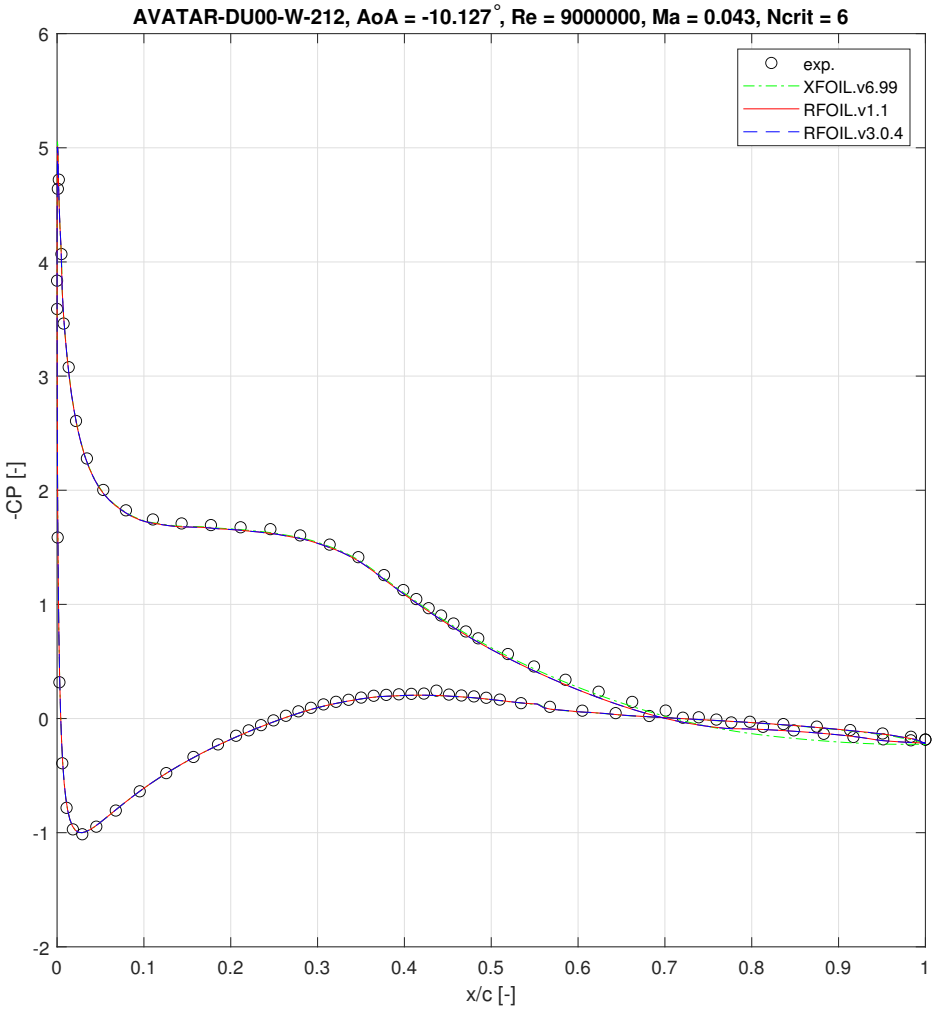

Figure C.22: Comparison between experimental and numerical pressure distributions for the AVATAR-DU00-W-212 airfoil at a Reynolds number of 9020000, and at an angle of attack and a Mach number of -10.127° and 0.083, respectively.

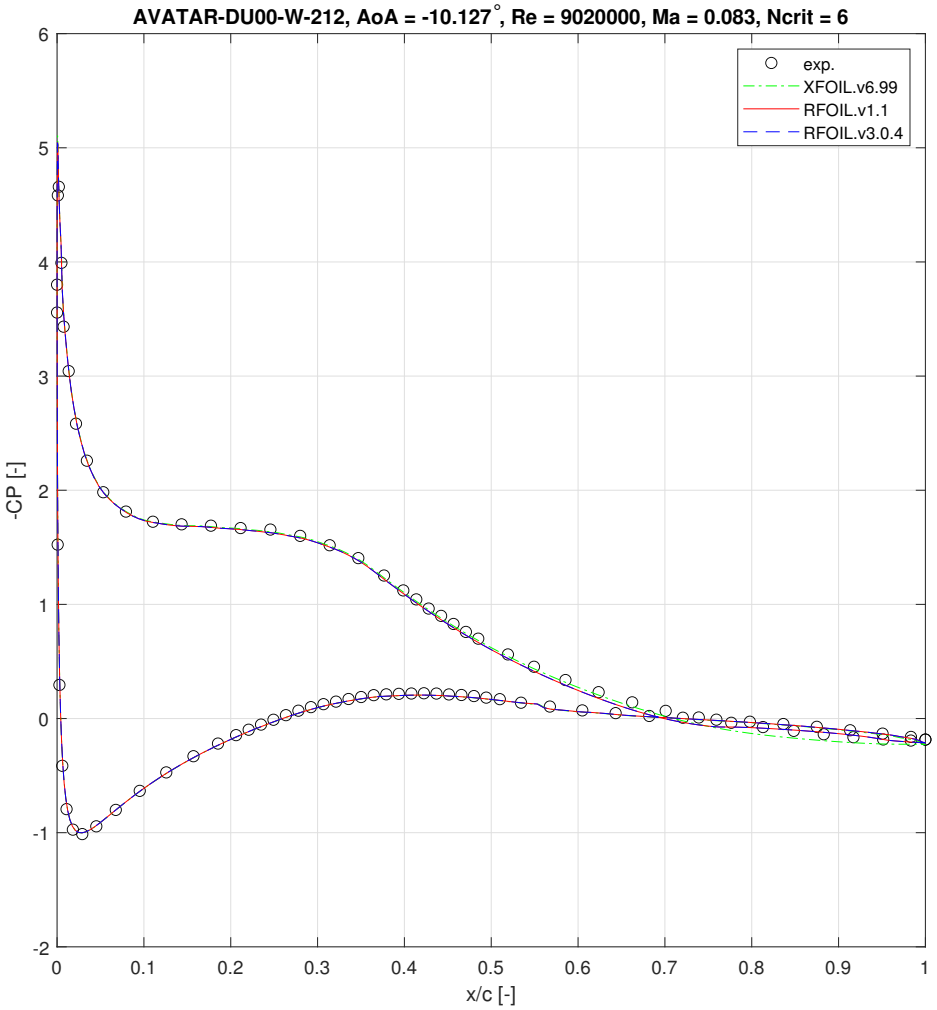

Figure C.23: Comparison between experimental and numerical pressure distributions for the AVATAR-DU00-W-212 airfoil at a Reynolds number of 14990000, and at an angle of attack and a Mach number of -10.129° and 0.081, respectively.

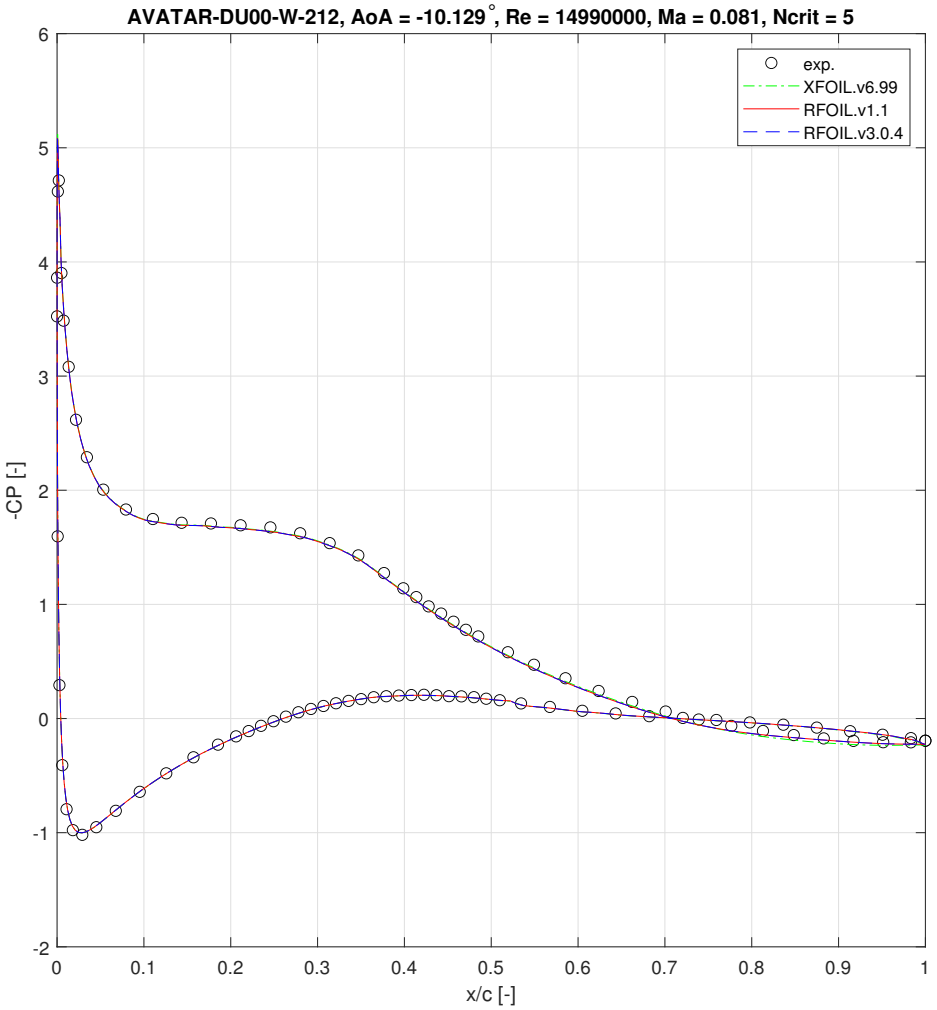

Figure C.24: Comparison between experimental and numerical pressure distributions for the AVATAR-DU00-W-212 airfoil at a Reynolds number of 12010000, and at an angle of attack and a Mach number of -10.953° and 0.058, respectively.

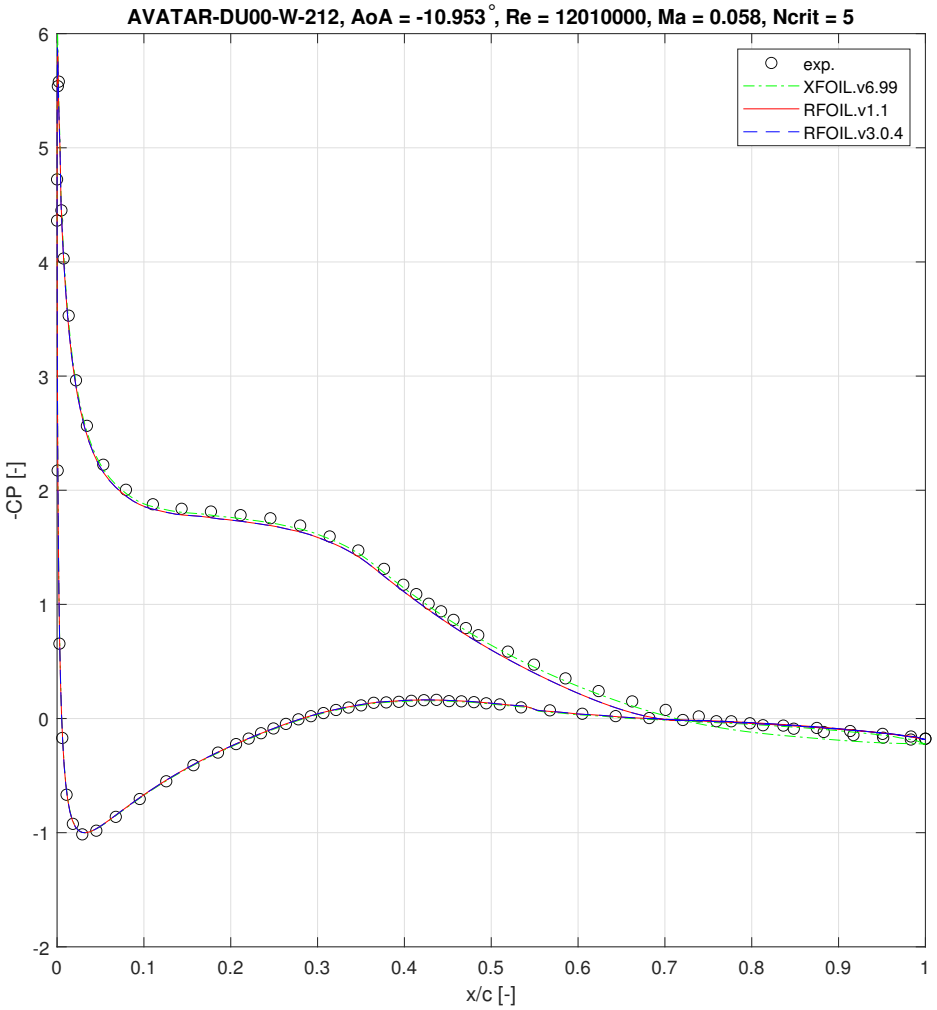

Figure C.25: Comparison between experimental and numerical pressure distributions for the AVATAR-DU00-W-212 airfoil at a Reynolds number of 5970000, and at an angle of attack and a Mach number of -11.098° and 0.029, respectively.

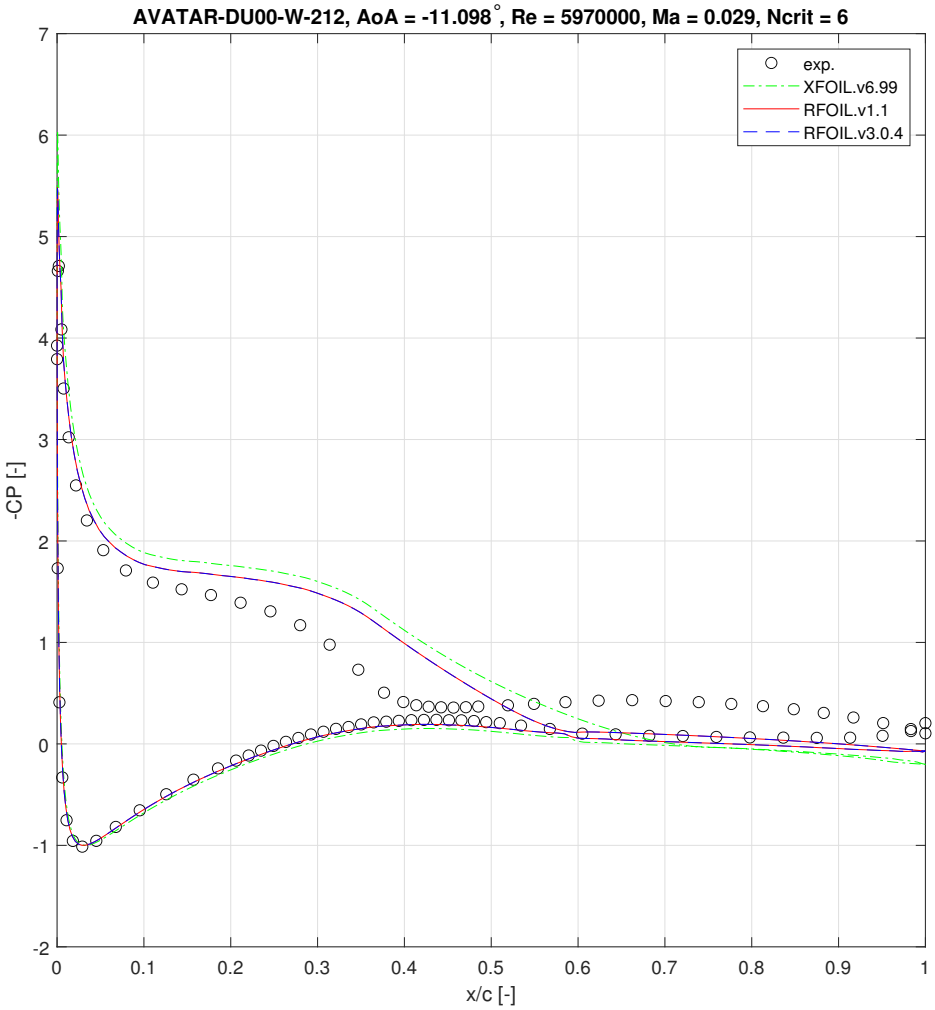

Figure C.26: Comparison between experimental and numerical pressure distributions for the AVATAR-DU00-W-212 airfoil at a Reynolds number of 6000000, and at an angle of attack and a Mach number of -11.098° and 0.055, respectively.

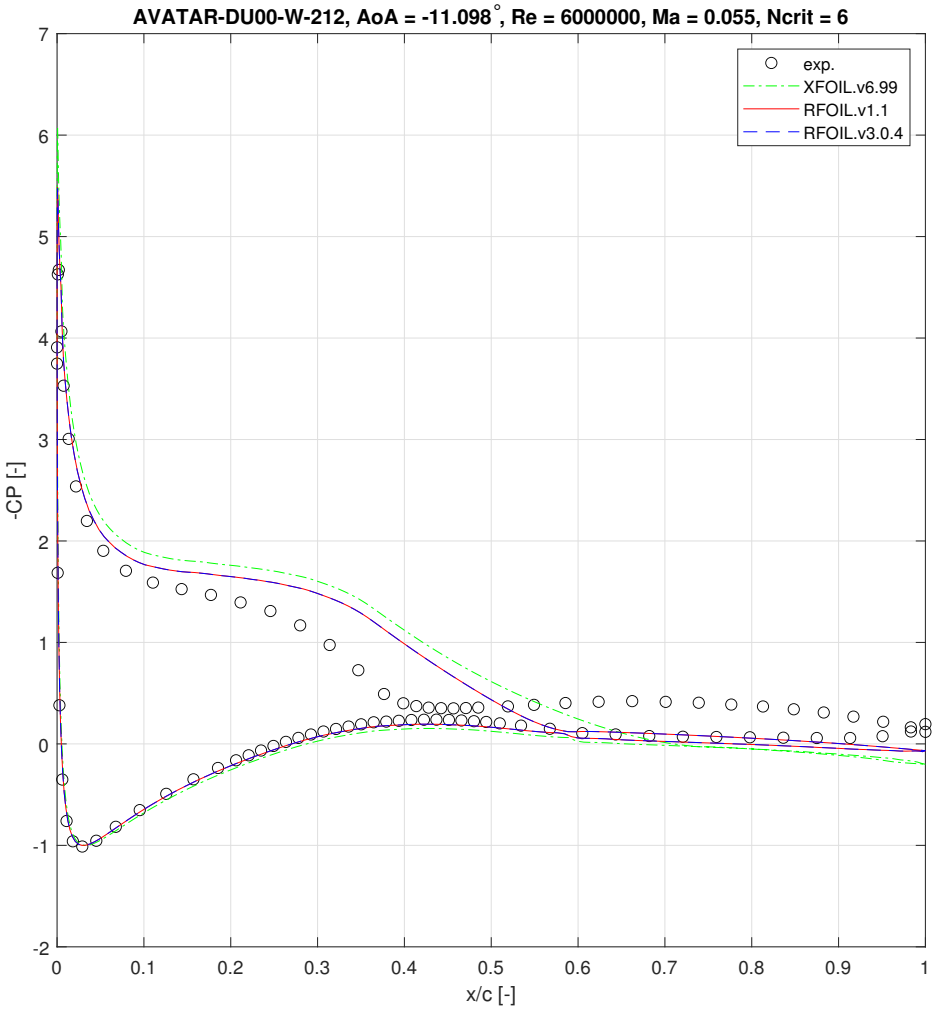

Figure C.27: Comparison between experimental and numerical pressure distributions for the AVATAR-DU00-W-212 airfoil at a Reynolds number of 2990000, and at an angle of attack and a Mach number of -11.090° and 0.074, respectively.

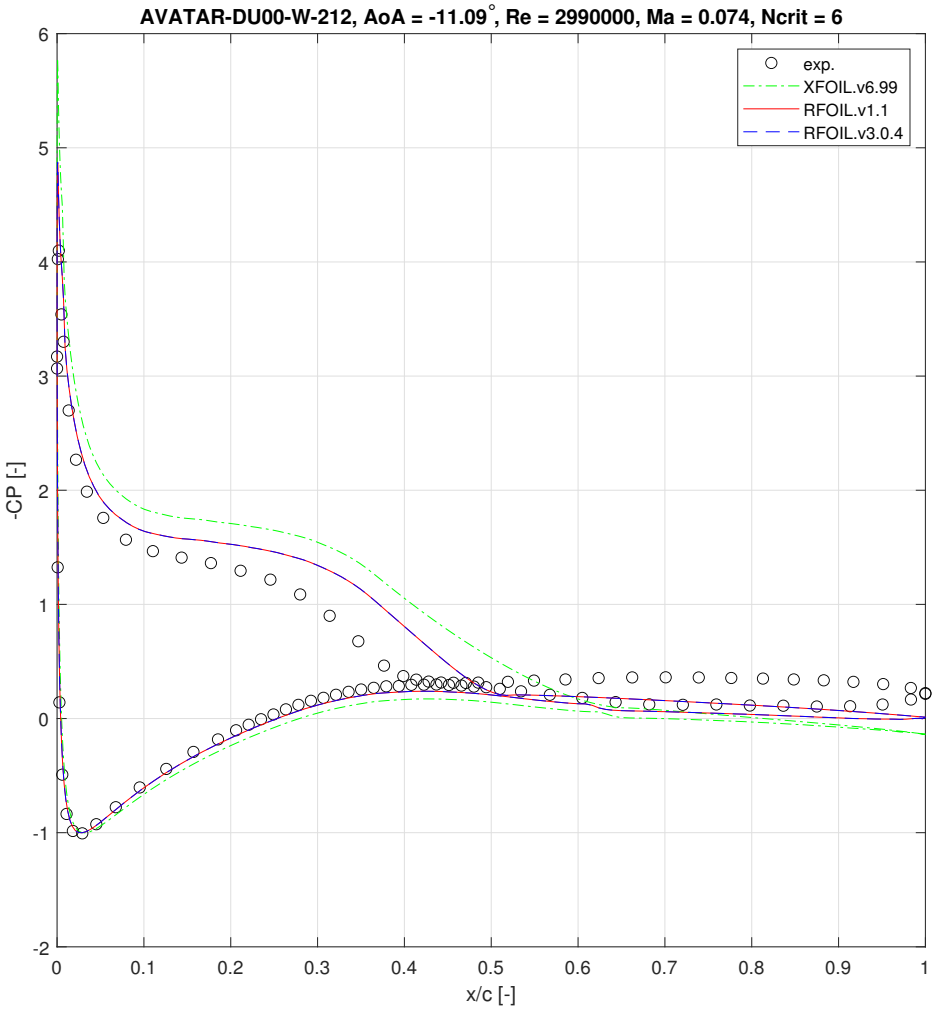

Figure C.28: Comparison between experimental and numerical pressure distributions for the AVATAR-DU00-W-212 airfoil at a Reynolds number of 9010000, and at an angle of attack and a Mach number of -11.135° and 0.083, respectively.

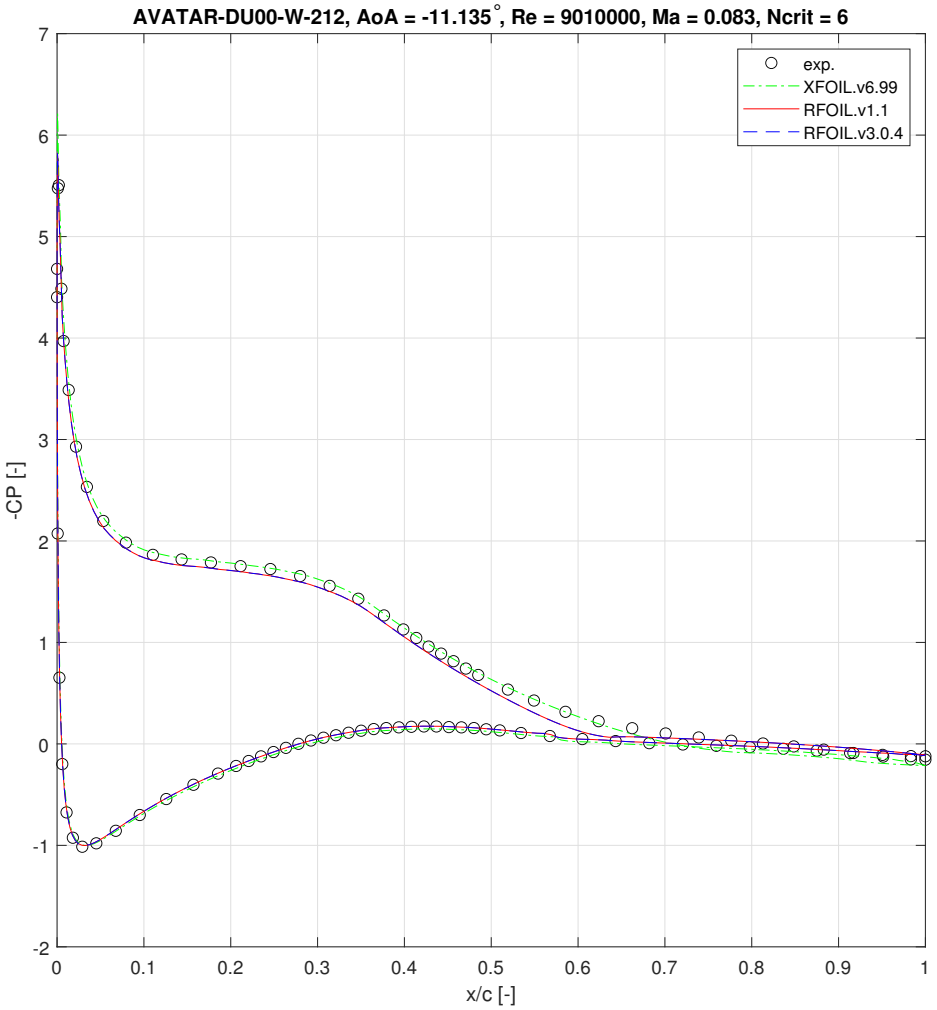

Figure C.29: Comparison between experimental and numerical pressure distributions for the AVATAR-DU00-W-212 airfoil at a Reynolds number of 8990000, and at an angle of attack and a Mach number of -11.136° and 0.043, respectively.

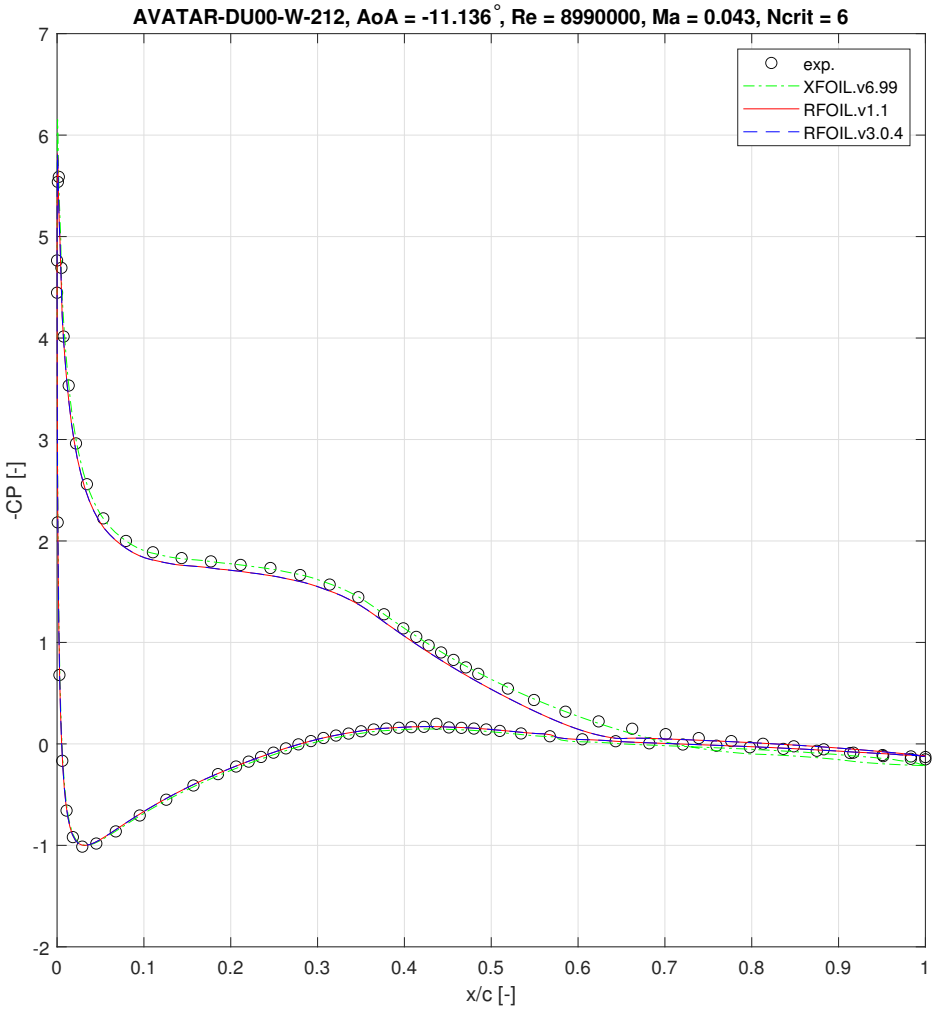

Figure C.30: Comparison between experimental and numerical pressure distributions for the AVATAR-DU00-W-212 airfoil at a Reynolds number of 14990000, and at an angle of attack and a Mach number of -11.141° and 0.081, respectively.

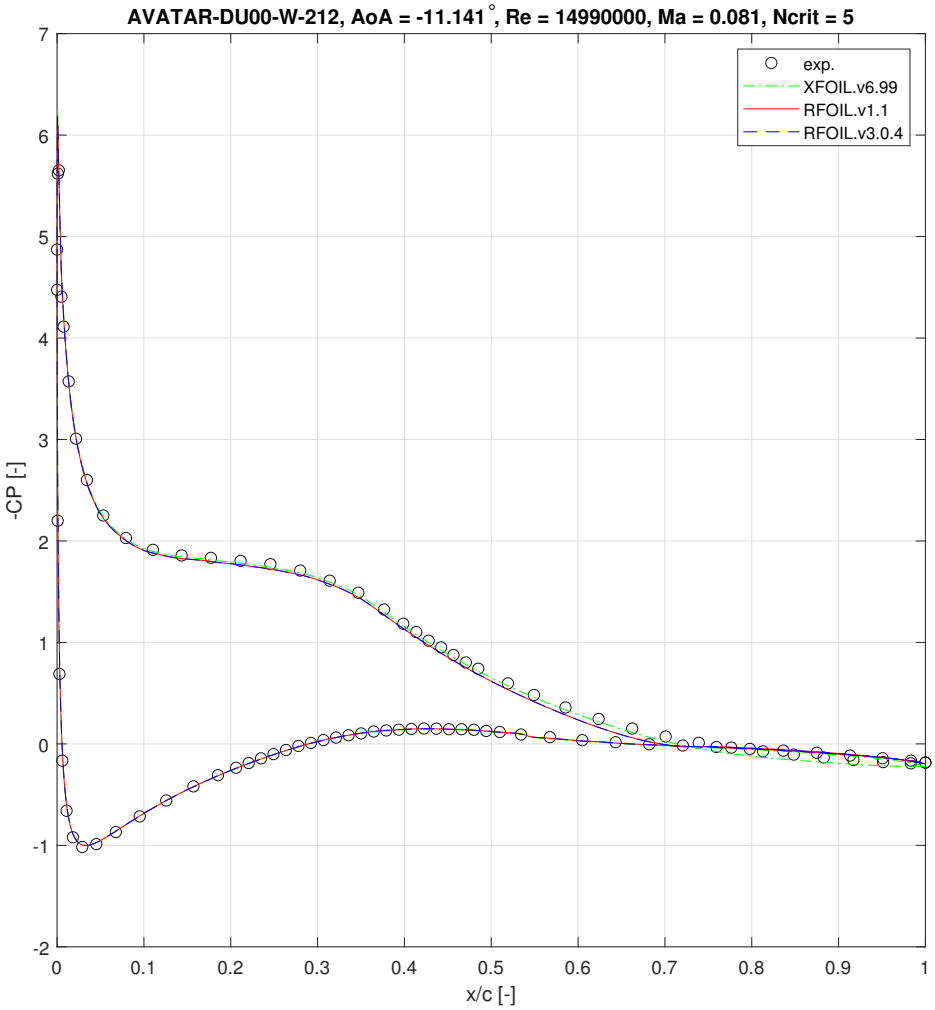

Figure C.31: Comparison between experimental and numerical pressure distributions for the AVATAR-DU00-W-212 airfoil at a Reynolds number of 11980000, and at an angle of attack and a Mach number of -11.956° and 0.058, respectively.

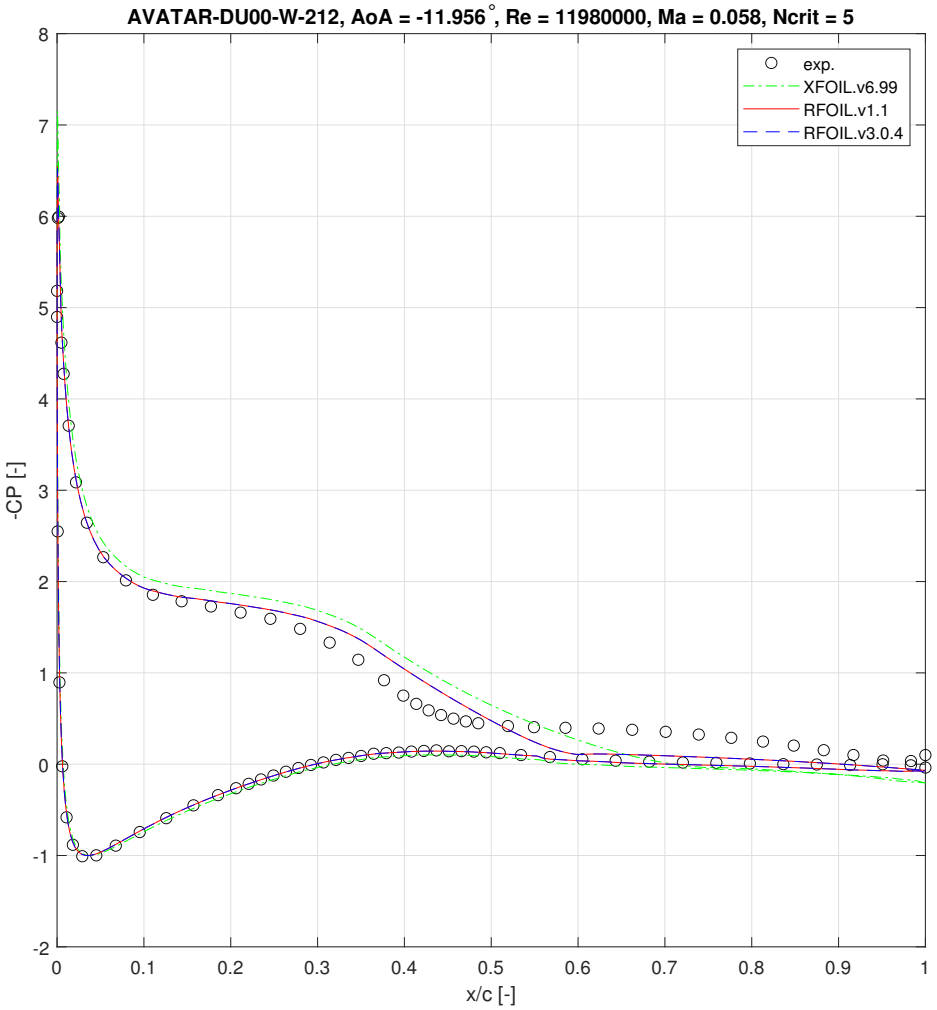

Figure C.32: Comparison between experimental and numerical pressure distributions for the AVATAR-DU00-W-212 airfoil at a Reynolds number of 3000000, and at an angle of attack and a Mach number of -12.093° and 0.074, respectively.

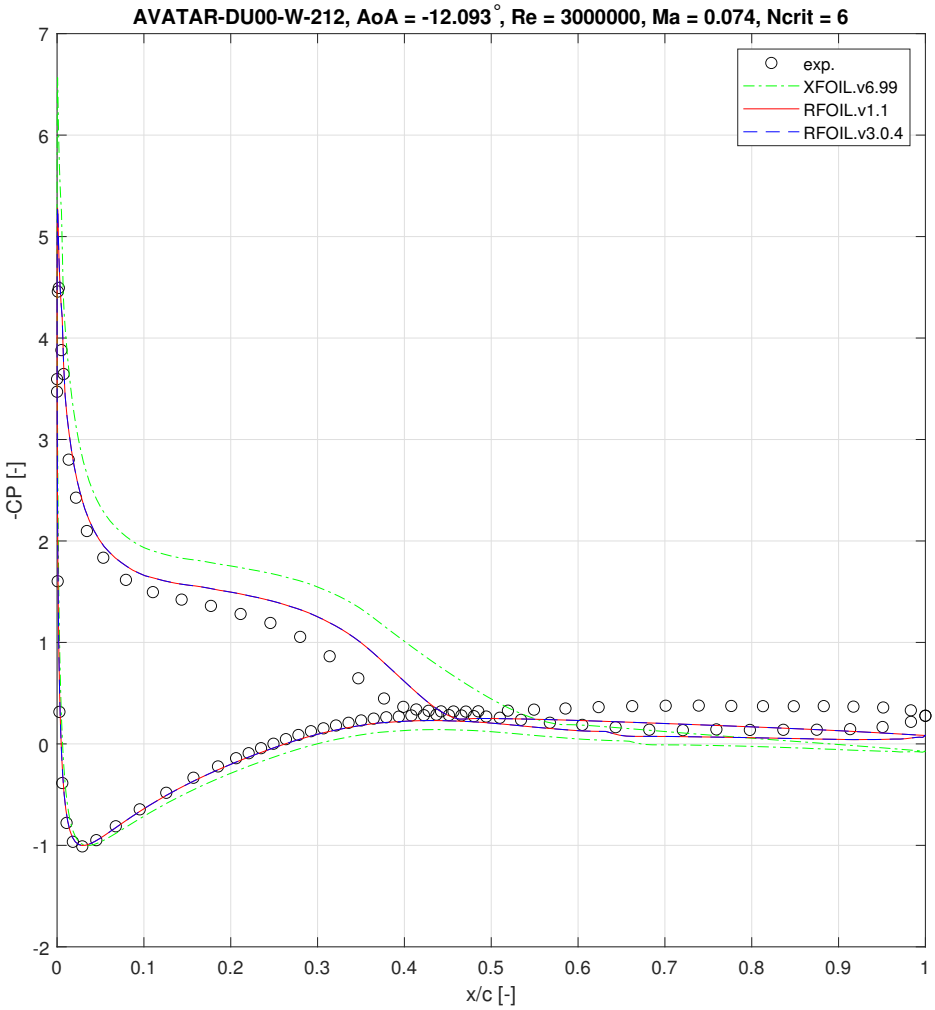

Figure C.33: Comparison between experimental and numerical pressure distributions for the AVATAR-DU00-W-212 airfoil at a Reynolds number of 6000000, and at an angle of attack and a Mach number of -12.098° and 0.055, respectively.

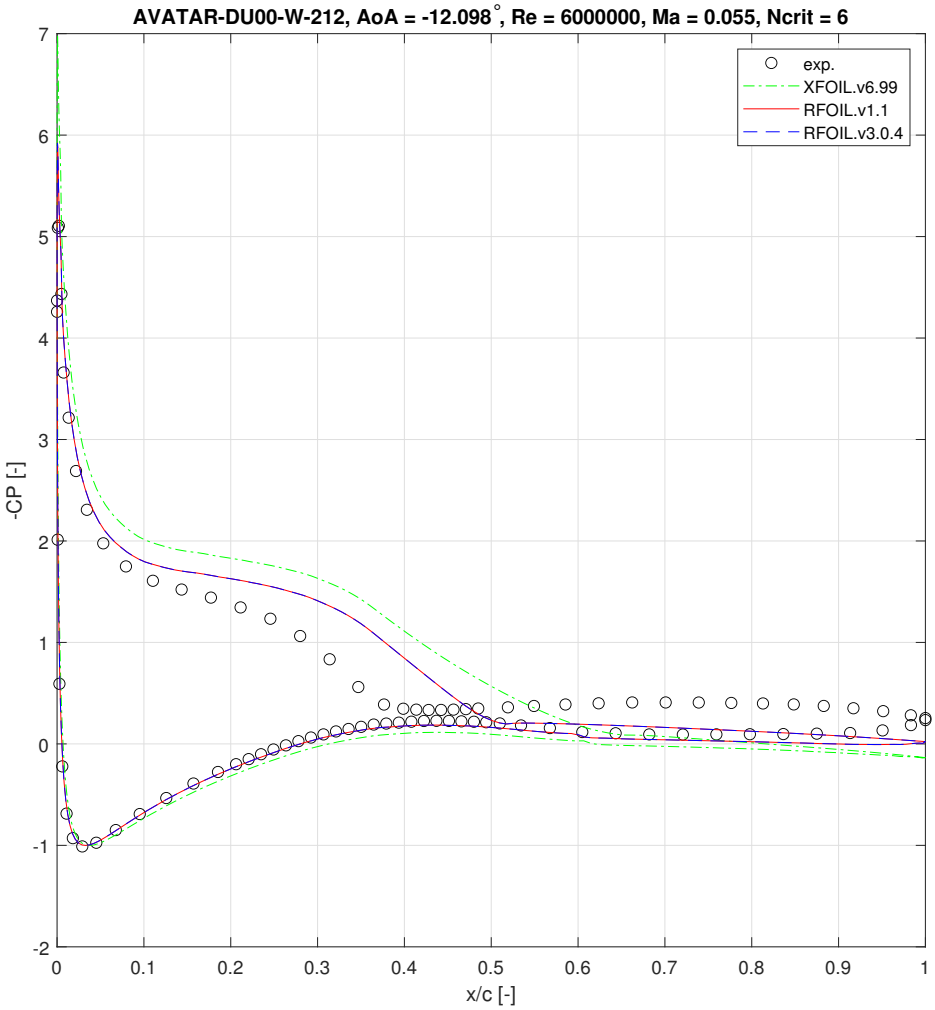

Figure C.34: Comparison between experimental and numerical pressure distributions for the AVATAR-DU00-W-212 airfoil at a Reynolds number of 6030000, and at an angle of attack and a Mach number of -12.098° and 0.029, respectively.

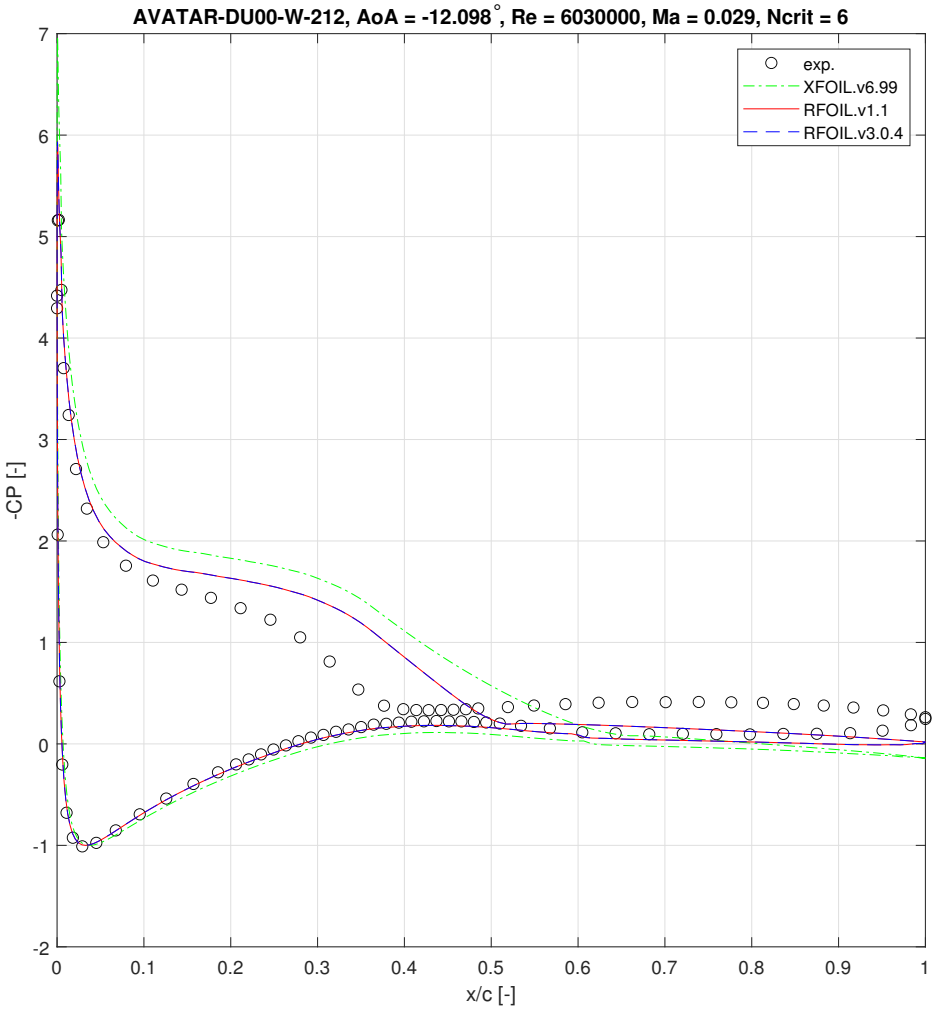

Figure C.35: Comparison between experimental and numerical pressure distributions for the AVATAR-DU00-W-212 airfoil at a Reynolds number of 8960000, and at an angle of attack and a Mach number of -12.109° and 0.043, respectively.

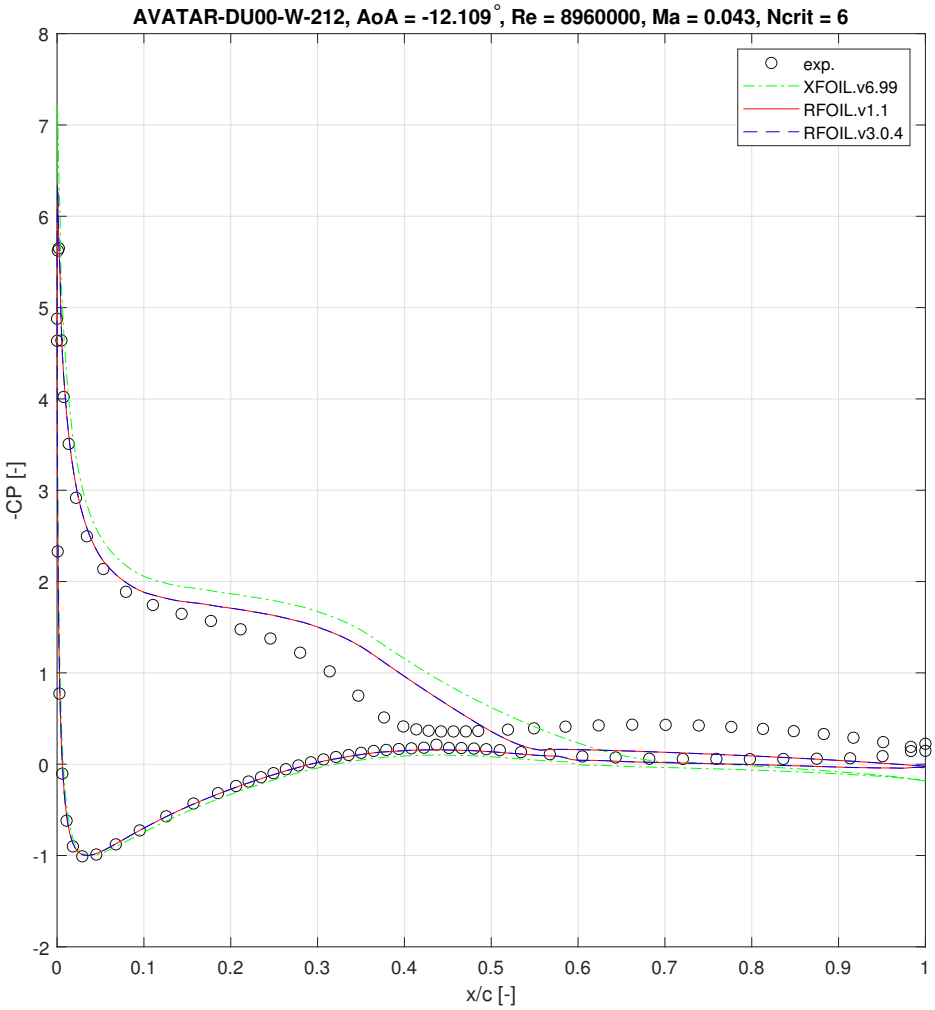

Figure C.36: Comparison between experimental and numerical pressure distributions for the AVATAR-DU00-W-212 airfoil at a Reynolds number of 8970000, and at an angle of attack and a Mach number of -12.109° and 0.082, respectively.

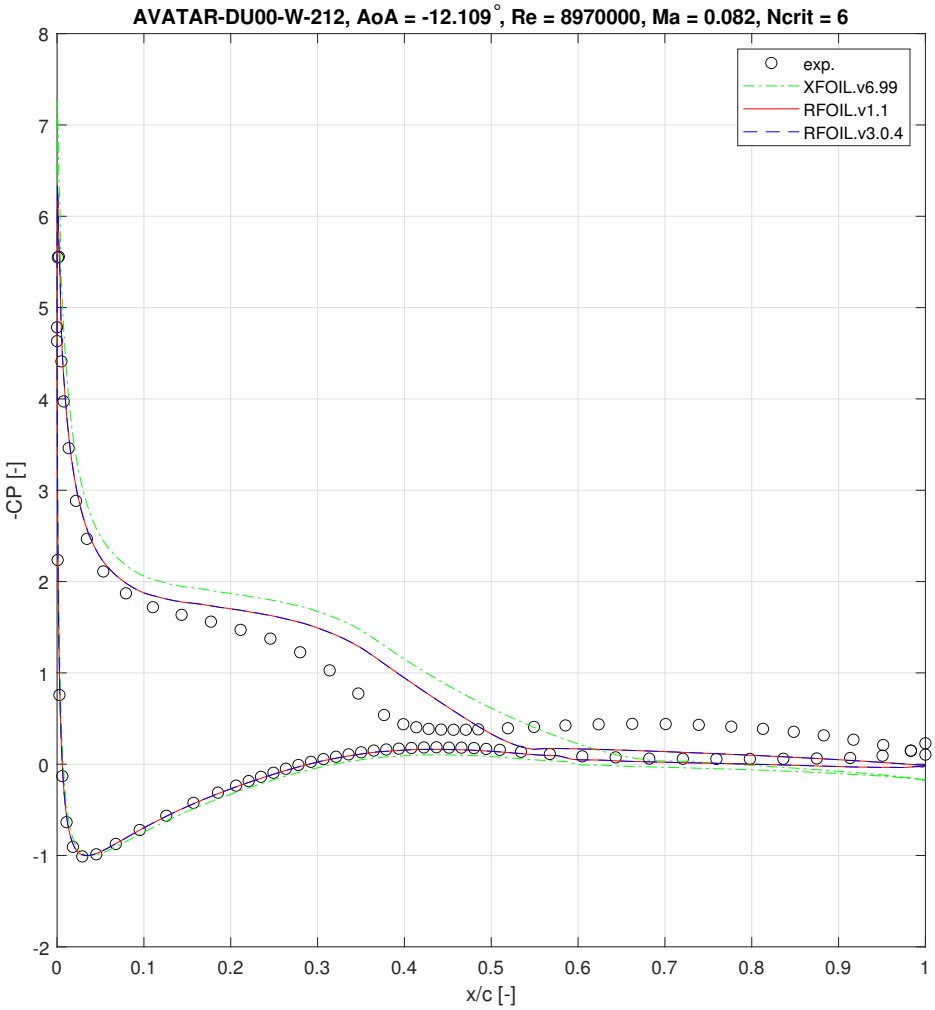

Figure C.37: Comparison between experimental and numerical pressure distributions for the AVATAR-DU00-W-212 airfoil at a Reynolds number of 14980000, and at an angle of attack and a Mach number of -12.150° and 0.081, respectively.

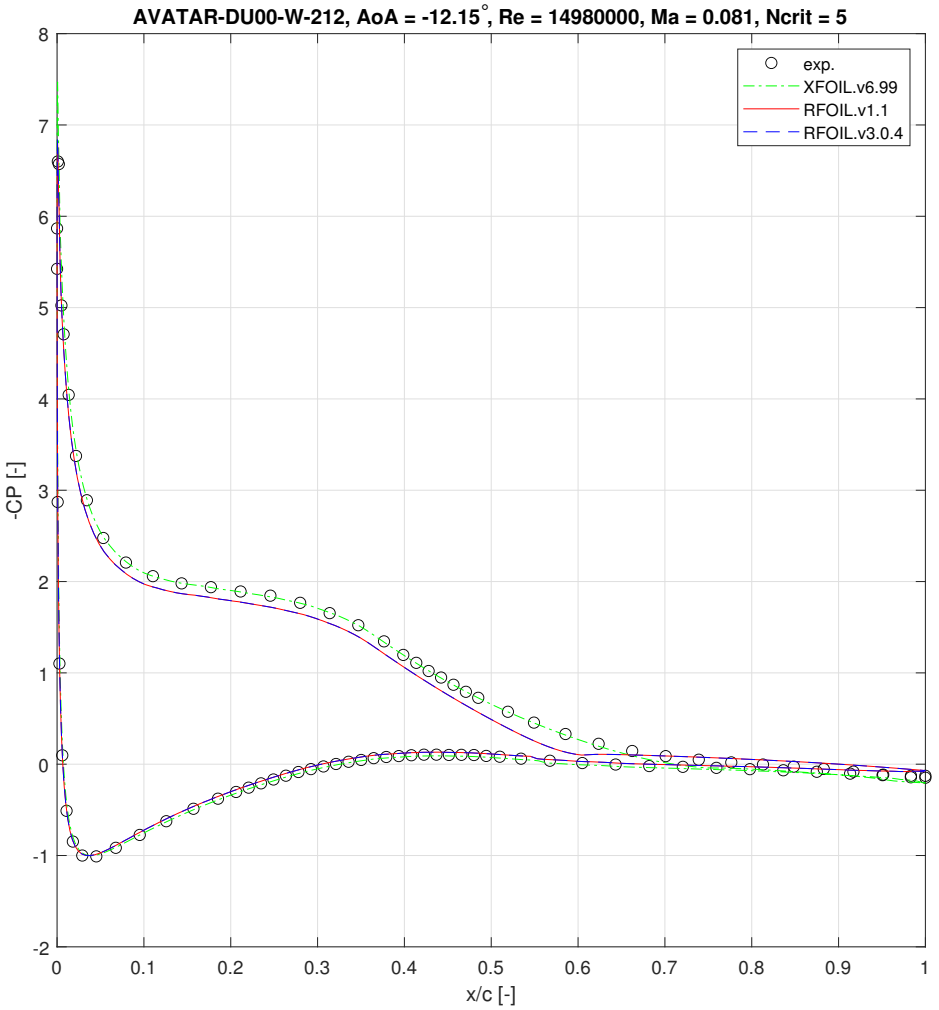

Figure C.38: Comparison between experimental and numerical pressure distributions for the AVATAR-DU00-W-212 airfoil at a Reynolds number of 11970000, and at an angle of attack and a Mach number of -12.954° and 0.058, respectively.

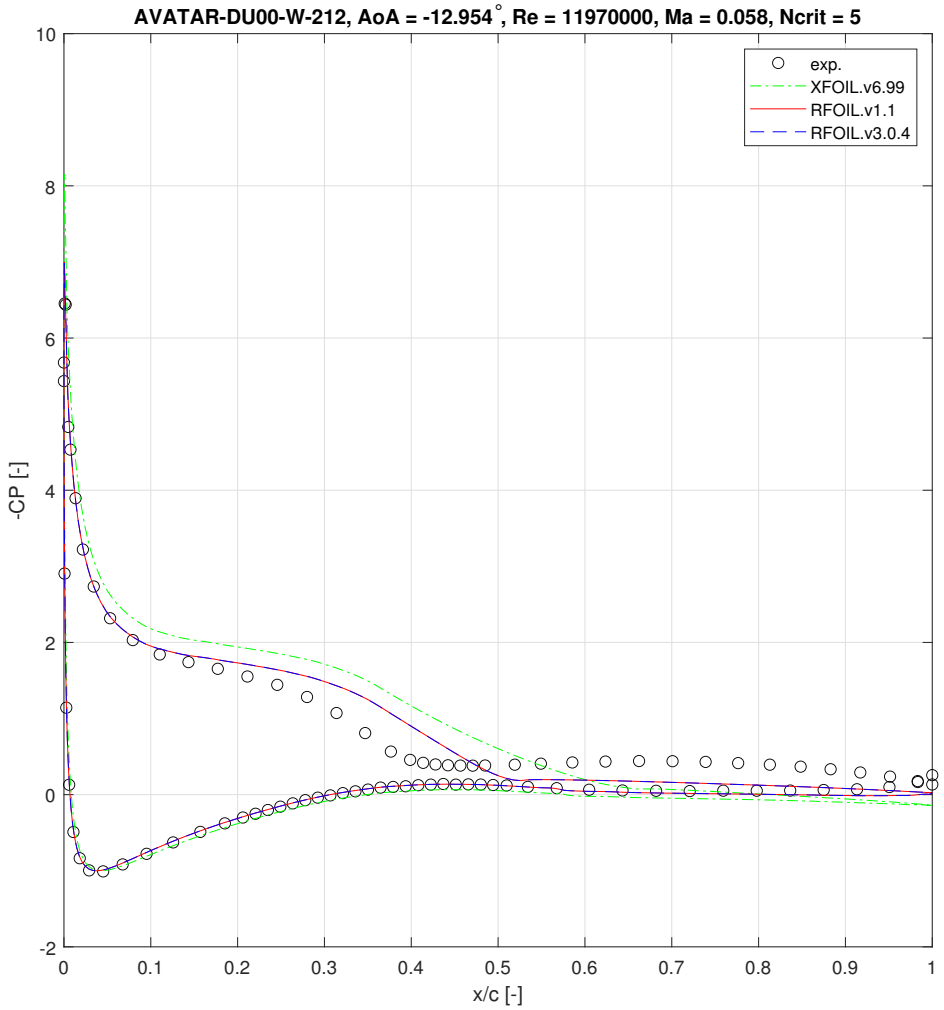

Figure C.39: Comparison between experimental and numerical pressure distributions for the AVATAR-DU00-W-212 airfoil at a Reynolds number of 3000000, and at an angle of attack and a Mach number of -13.098° and 0.074, respectively.

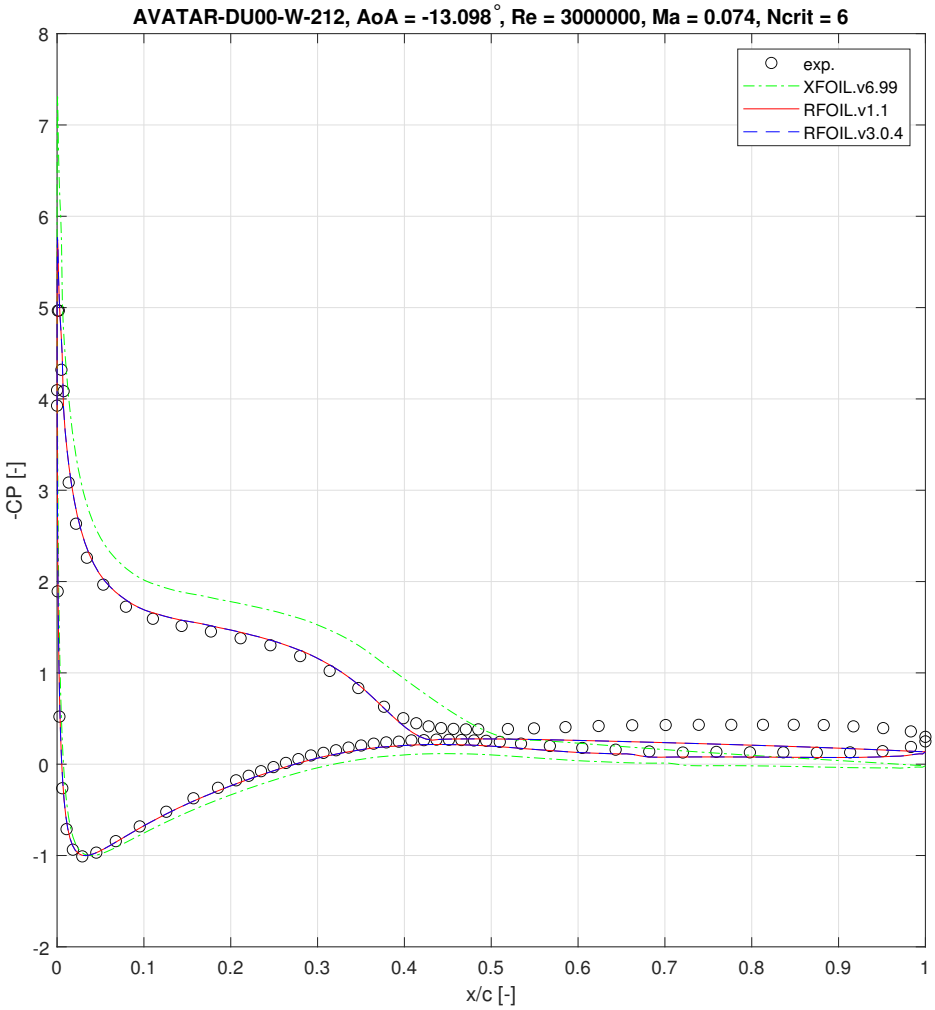

Figure C.40: Comparison between experimental and numerical pressure distributions for the AVATAR-DU00-W-212 airfoil at a Reynolds number of 5990000, and at an angle of attack and a Mach number of -13.103° and 0.055, respectively.

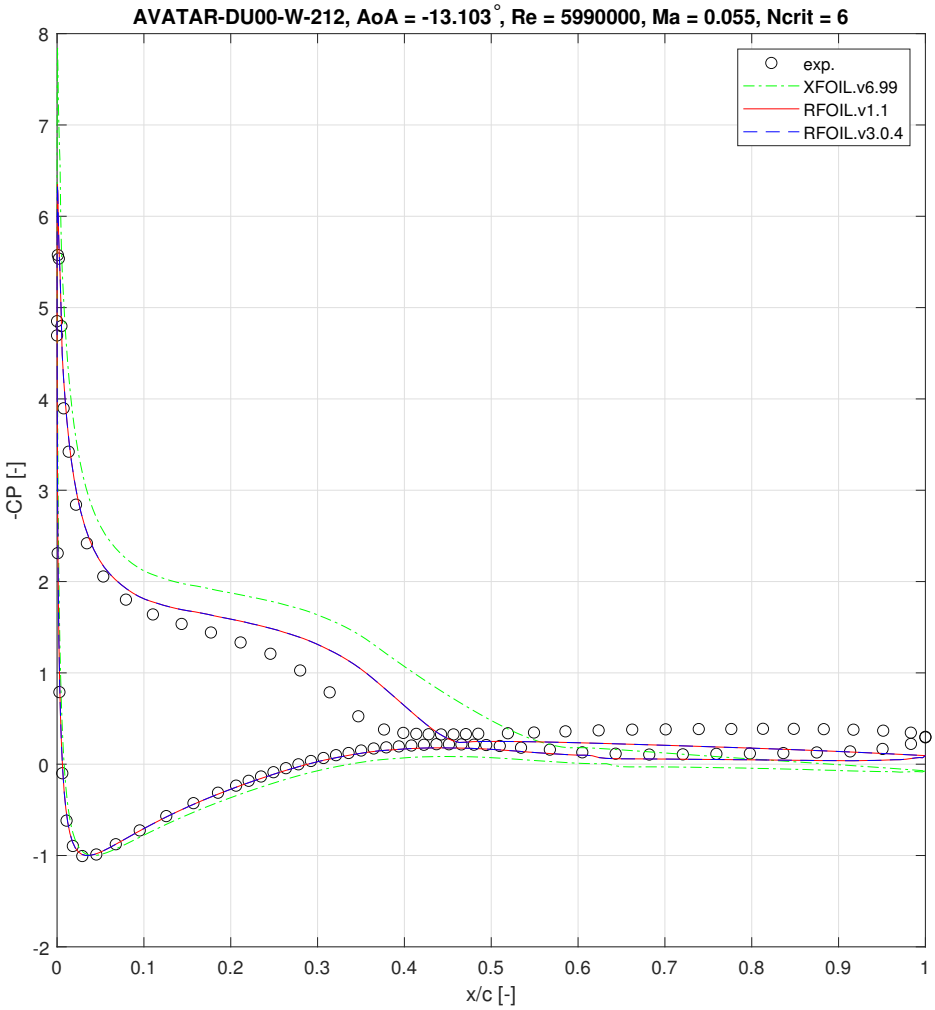

Figure C.41: Comparison between experimental and numerical pressure distributions for the AVATAR-DU00-W-212 airfoil at a Reynolds number of 6030000, and at an angle of attack and a Mach number of -13.103° and 0.029, respectively.

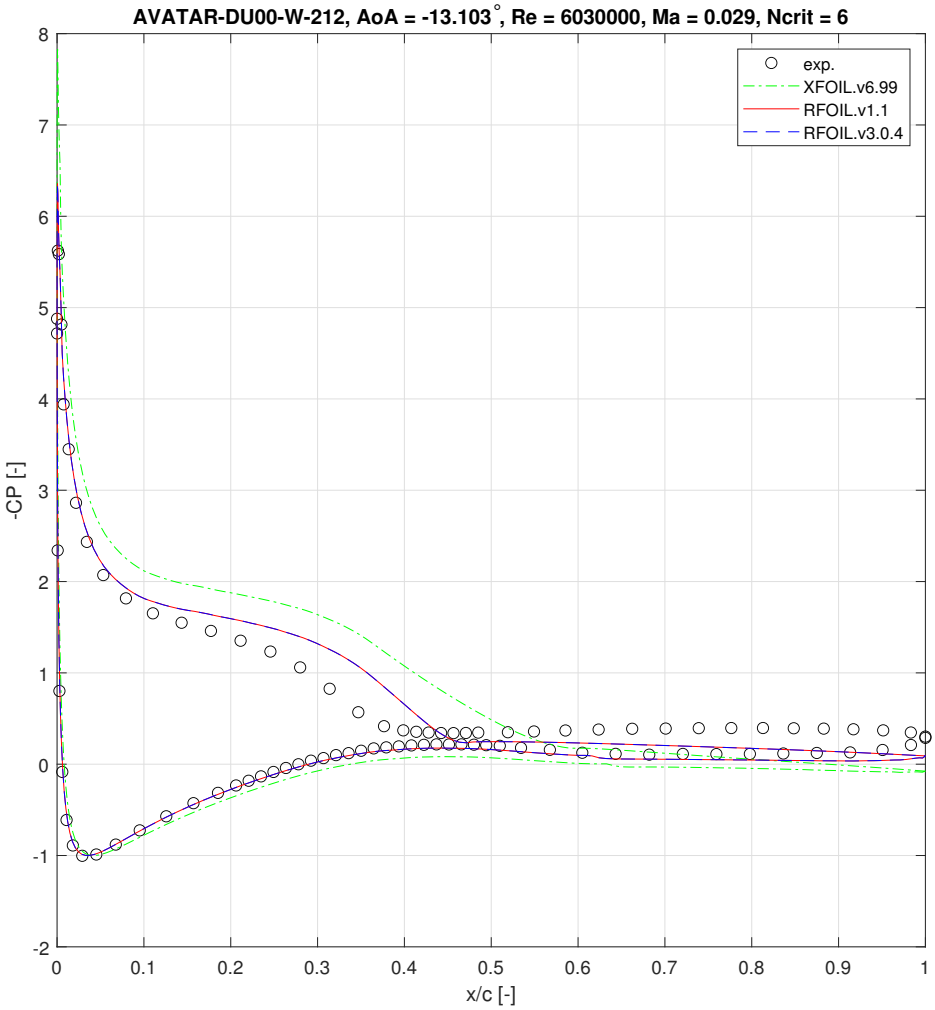

Figure C.42: Comparison between experimental and numerical pressure distributions for the AVATAR-DU00-W-212 airfoil at a Reynolds number of 8990000, and at an angle of attack and a Mach number of -13.110° and 0.083, respectively.

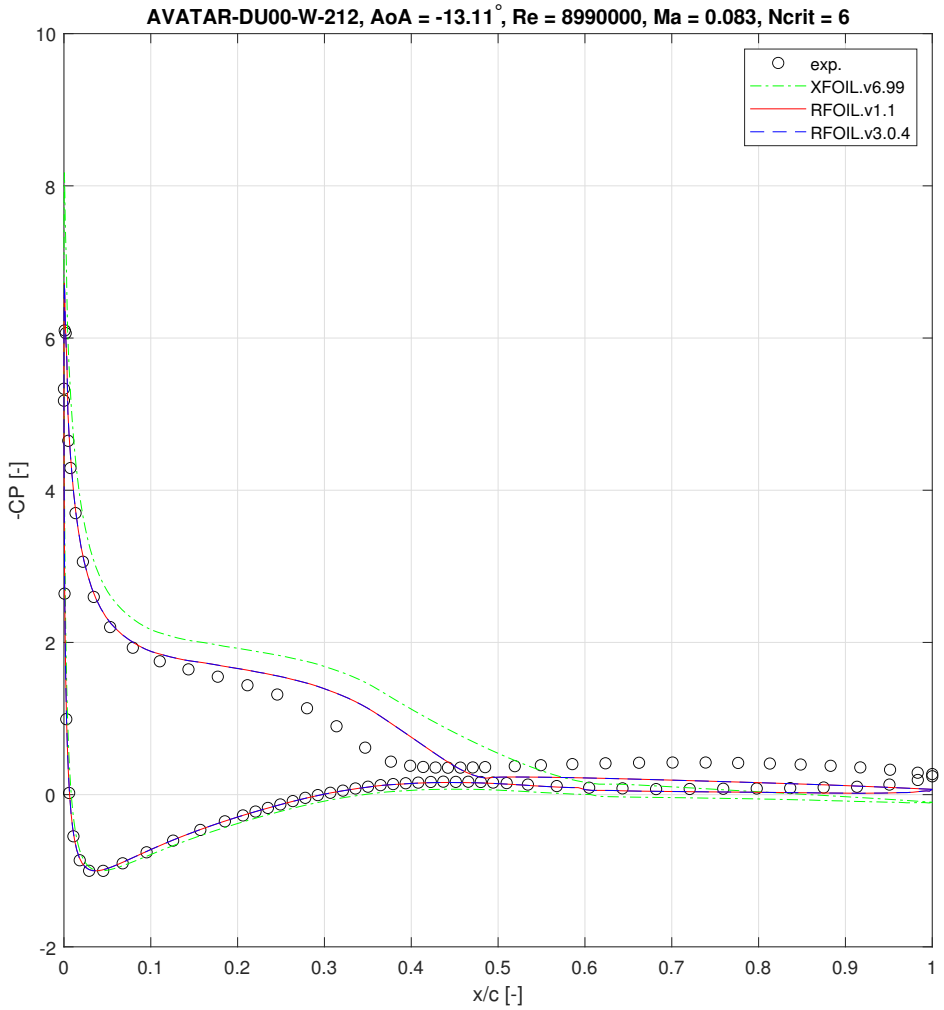

Figure C.43: Comparison between experimental and numerical pressure distributions for the AVATAR-DU00-W-212 airfoil at a Reynolds number of 9020000, and at an angle of attack and a Mach number of -13.110° and 0.044, respectively.

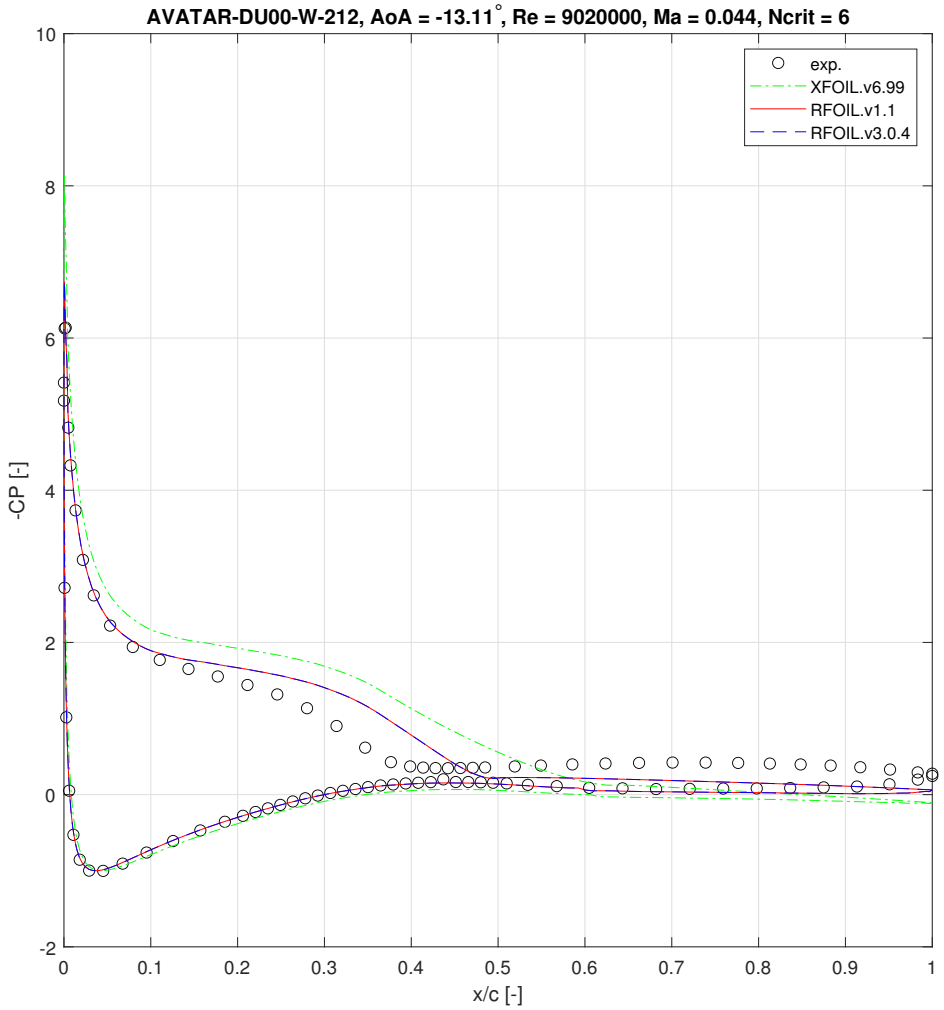

Figure C.44: Comparison between experimental and numerical pressure distributions for the AVATAR-DU00-W-212 airfoil at a Reynolds number of 14960000, and at an angle of attack and a Mach number of -13.125° and 0.081, respectively.

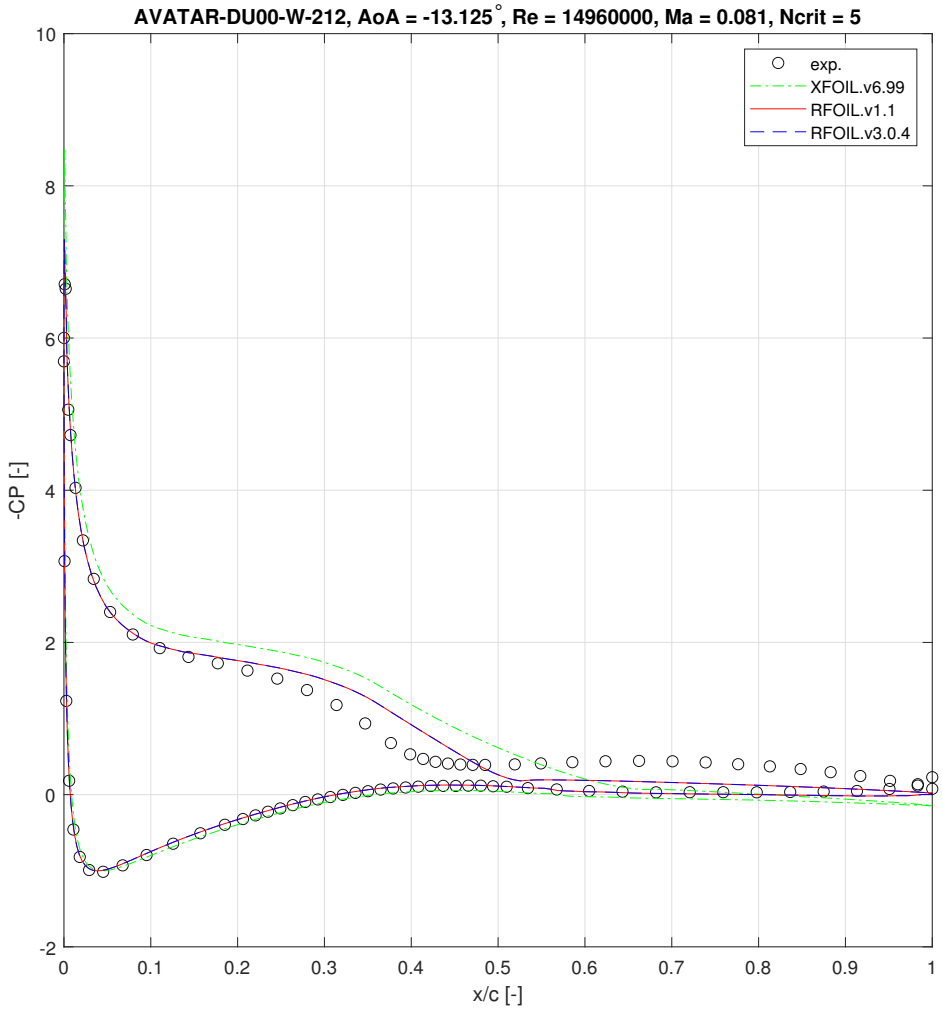

Figure C.45: Comparison between experimental and numerical pressure distributions for the AVATAR-DU00-W-212 airfoil at a Reynolds number of 12010000, and at an angle of attack and a Mach number of -13.952° and 0.058, respectively.

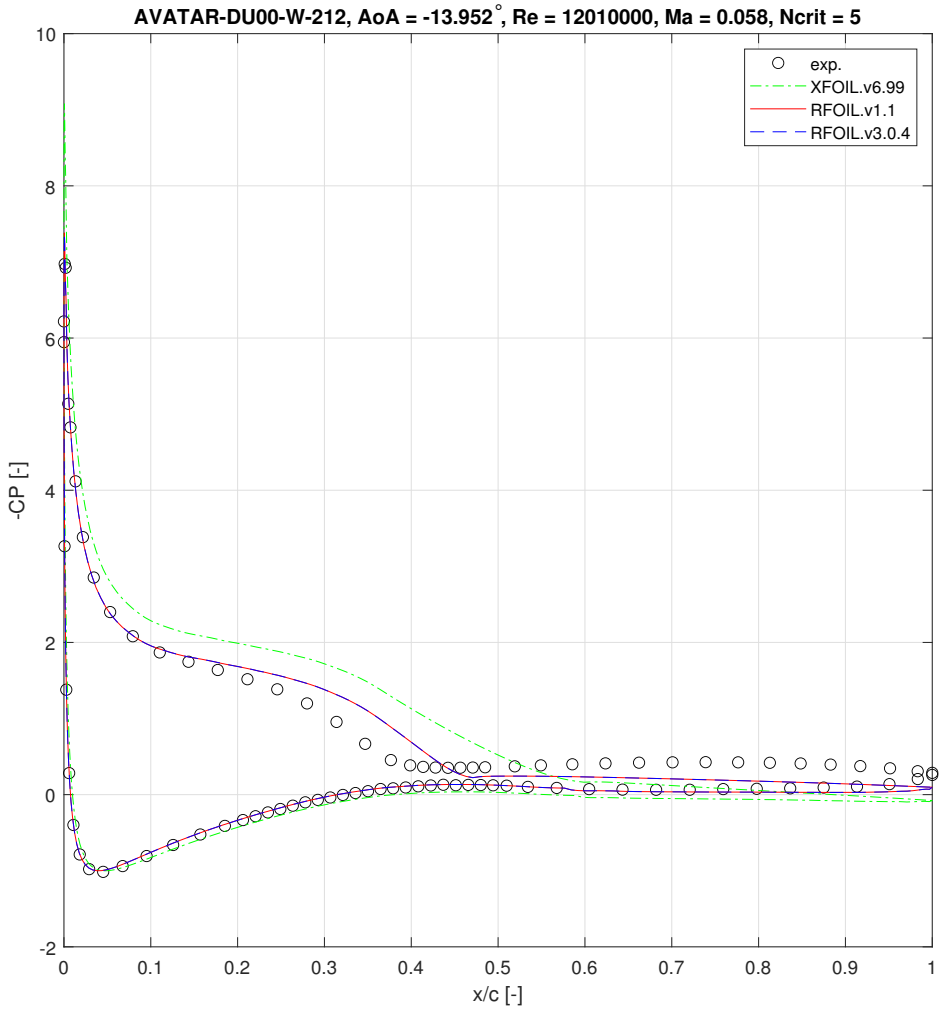

Figure C.46: Comparison between experimental and numerical pressure distributions for the AVATAR-DU00-W-212 airfoil at a Reynolds number of 2960000, and at an angle of attack and a Mach number of -14.102° and 0.073, respectively.

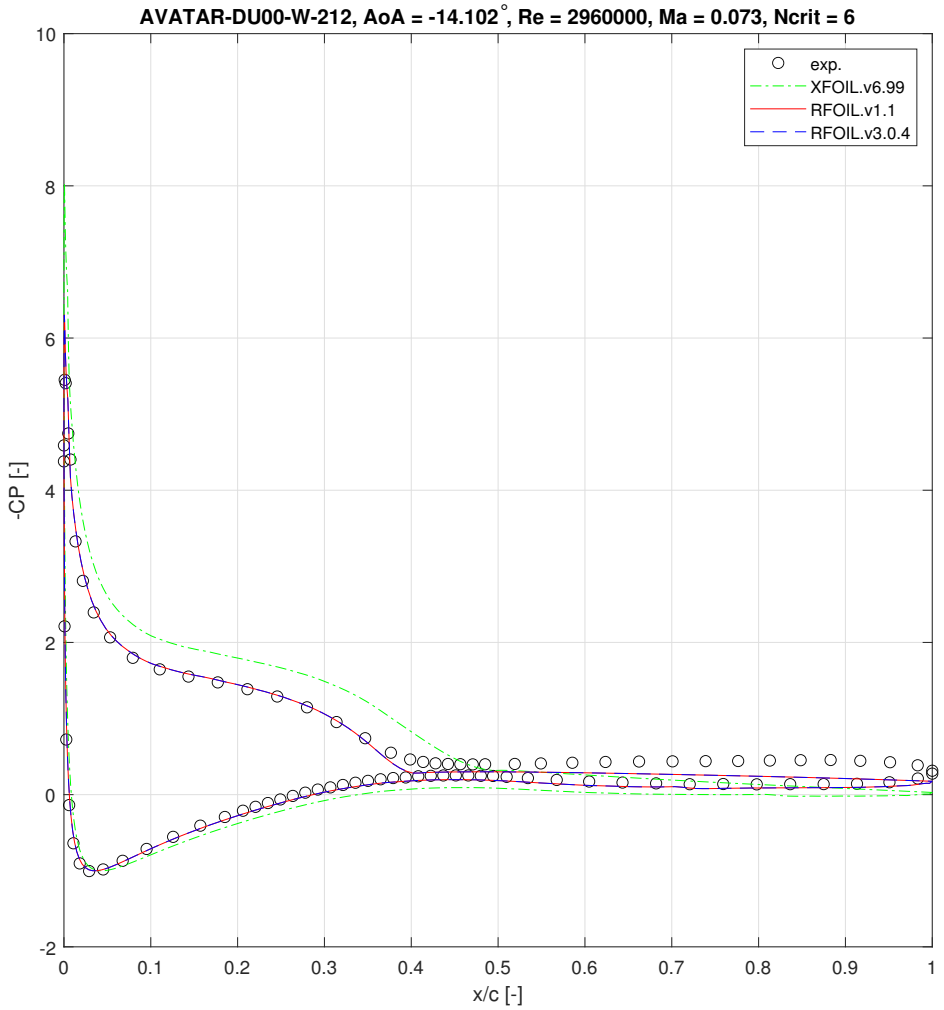

Figure C.47: Comparison between experimental and numerical pressure distributions for the AVATAR-DU00-W-212 airfoil at a Reynolds number of 5990000, and at an angle of attack and a Mach number of -14.108° and 0.055, respectively.

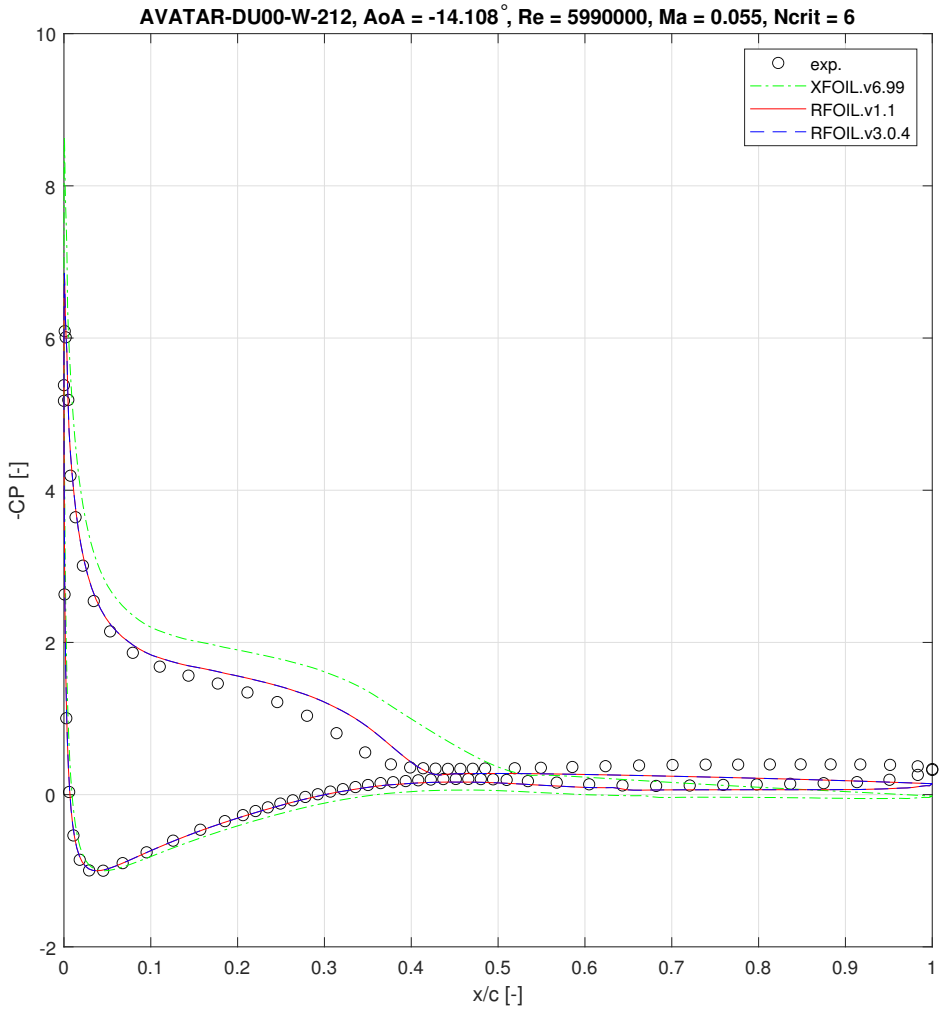

Figure C.48: Comparison between experimental and numerical pressure distributions for the AVATAR-DU00-W-212 airfoil at a Reynolds number of 6020000, and at an angle of attack and a Mach number of -14.108° and 0.029, respectively.

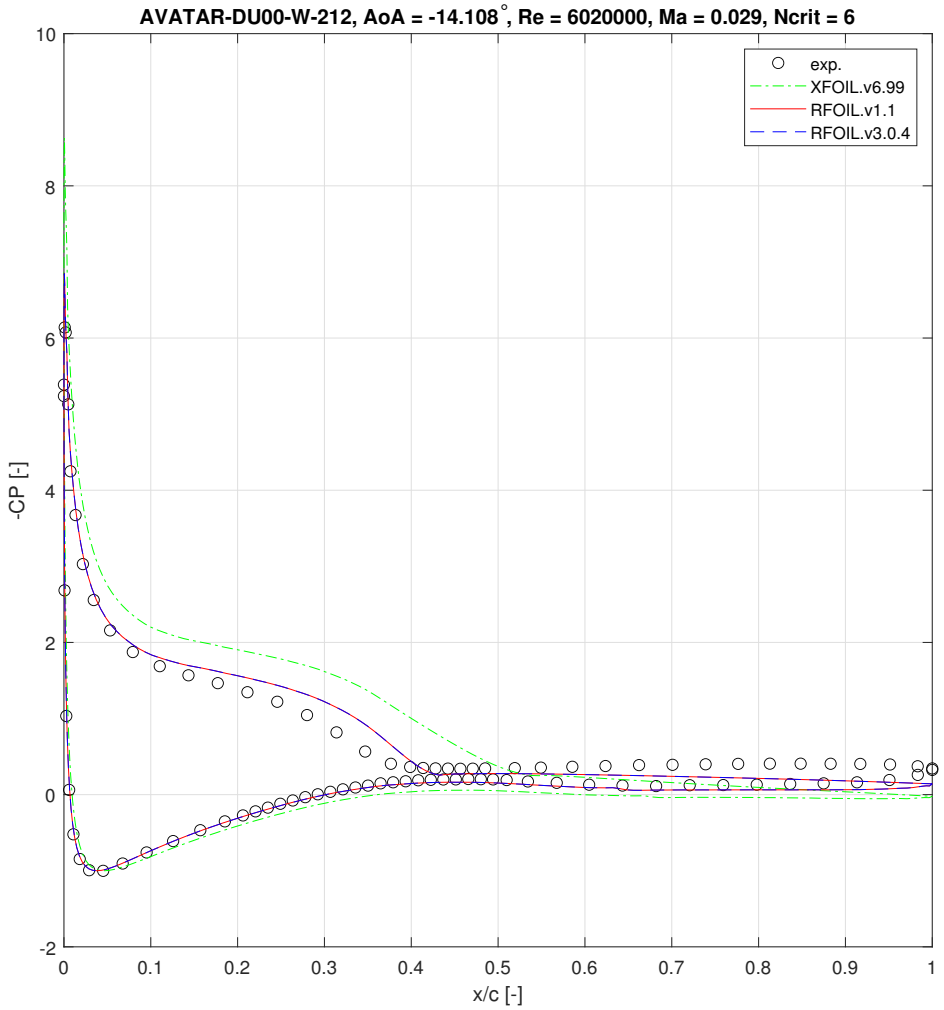

Figure C.49: Comparison between experimental and numerical pressure distributions for the AVATAR-DU00-W-212 airfoil at a Reynolds number of 9020000, and at an angle of attack and a Mach number of -14.113° and 0.083, respectively.

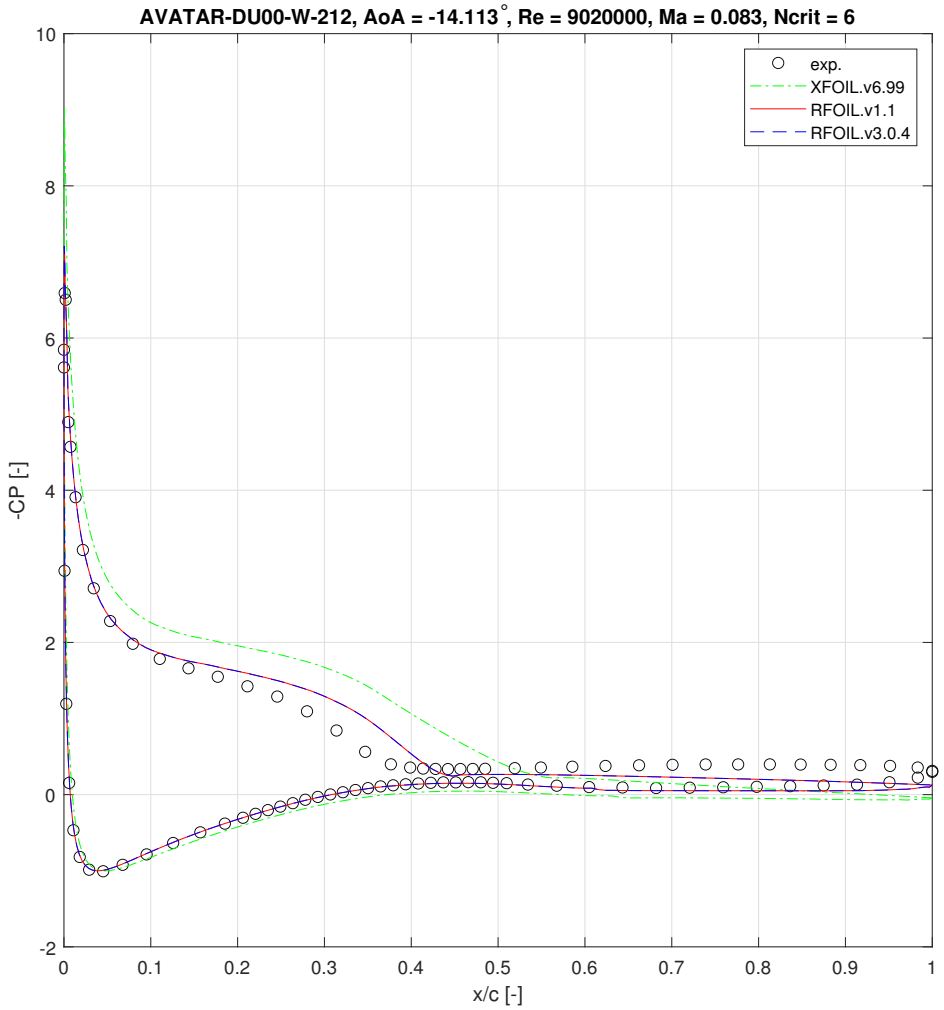

Figure C.50: Comparison between experimental and numerical pressure distributions for the AVATAR-DU00-W-212 airfoil at a Reynolds number of 9010000, and at an angle of attack and a Mach number of -14.114° and 0.043, respectively.

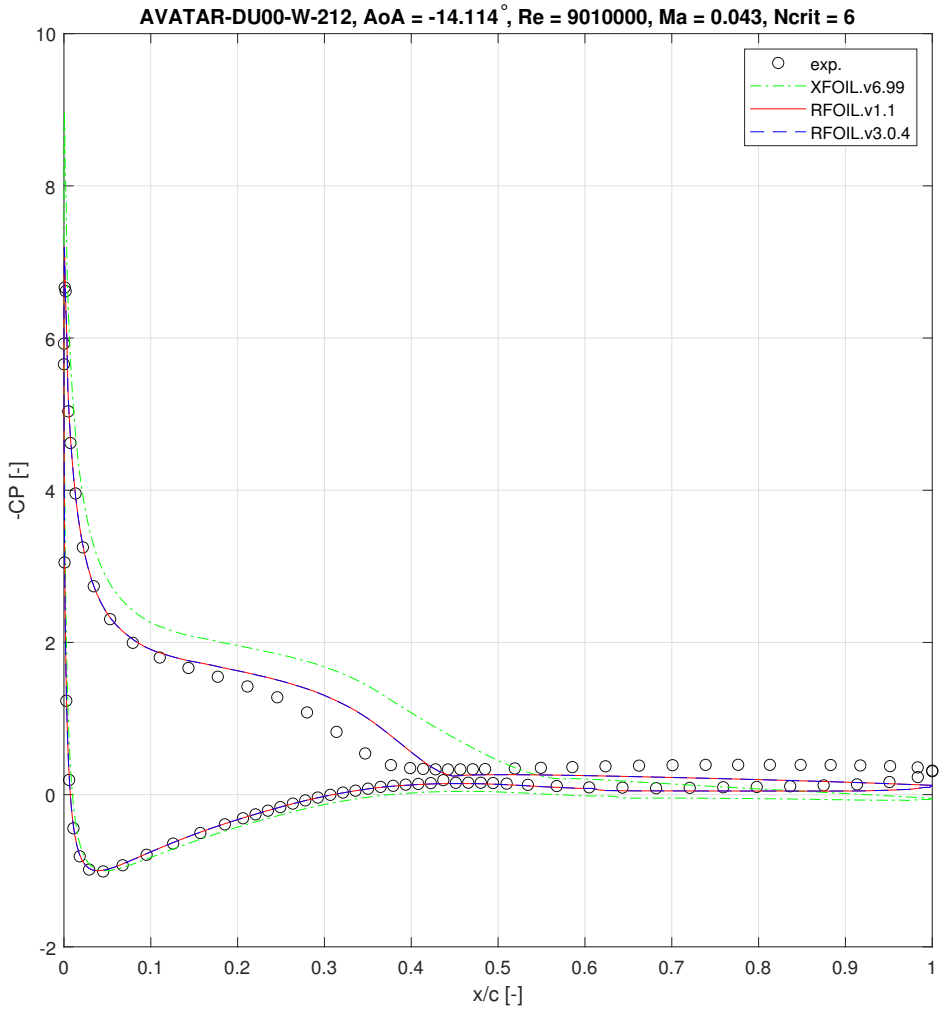

Figure C.51: Comparison between experimental and numerical pressure distributions for the AVATAR-DU00-W-212 airfoil at a Reynolds number of 14990000, and at an angle of attack and a Mach number of -14.123° and 0.081, respectively.

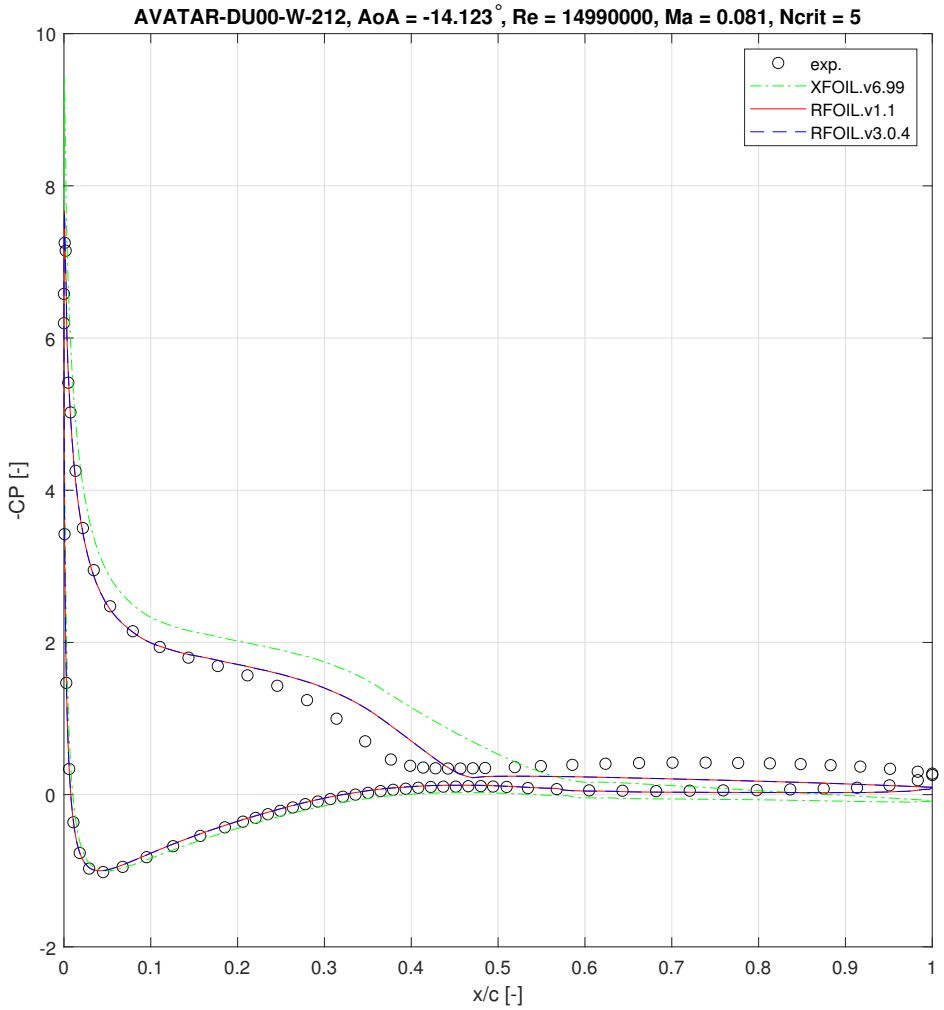

Figure C.52: Comparison between experimental and numerical pressure distributions for the AVATAR-DU00-W-212 airfoil at a Reynolds number of 15070000, and at an angle of attack and a Mach number of -14.124° and 0.082, respectively.

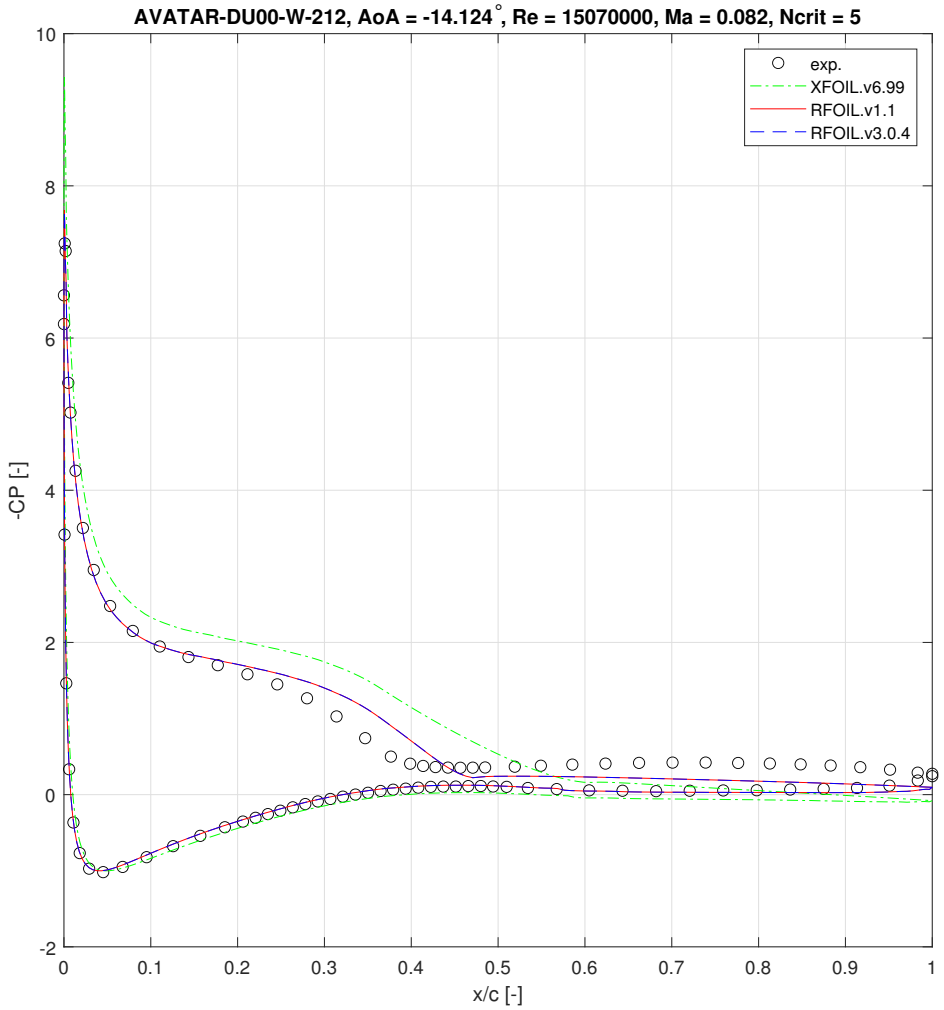

Figure C.53: Comparison between experimental and numerical pressure distributions for the AVATAR-DU00-W-212 airfoil at a Reynolds number of 12050000, and at an angle of attack and a Mach number of -14.949° and 0.058, respectively.

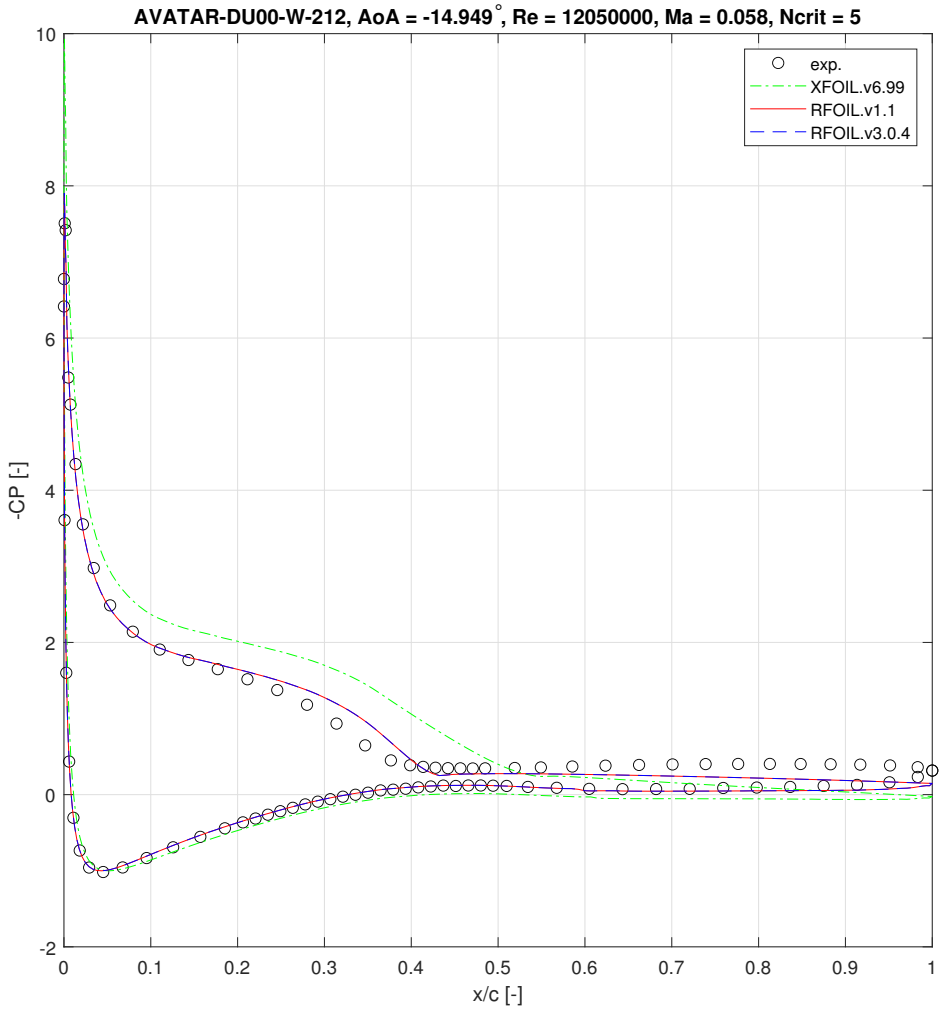

Figure C.54: Comparison between experimental and numerical pressure distributions for the AVATAR-DU00-W-212 airfoil at a Reynolds number of 2960000, and at an angle of attack and a Mach number of -15.101° and 0.073, respectively.

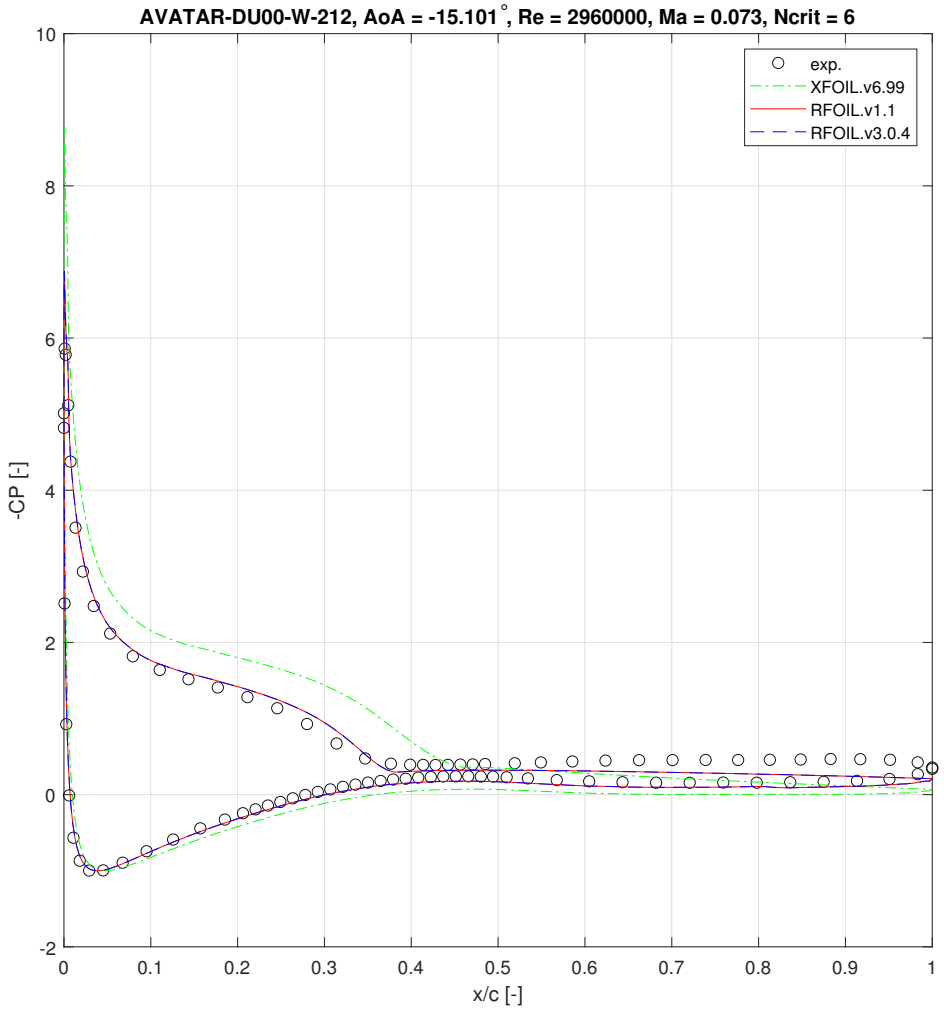

Figure C.55: Comparison between experimental and numerical pressure distributions for the AVATAR-DU00-W-212 airfoil at a Reynolds number of 6000000, and at an angle of attack and a Mach number of -15.113° and 0.055, respectively.

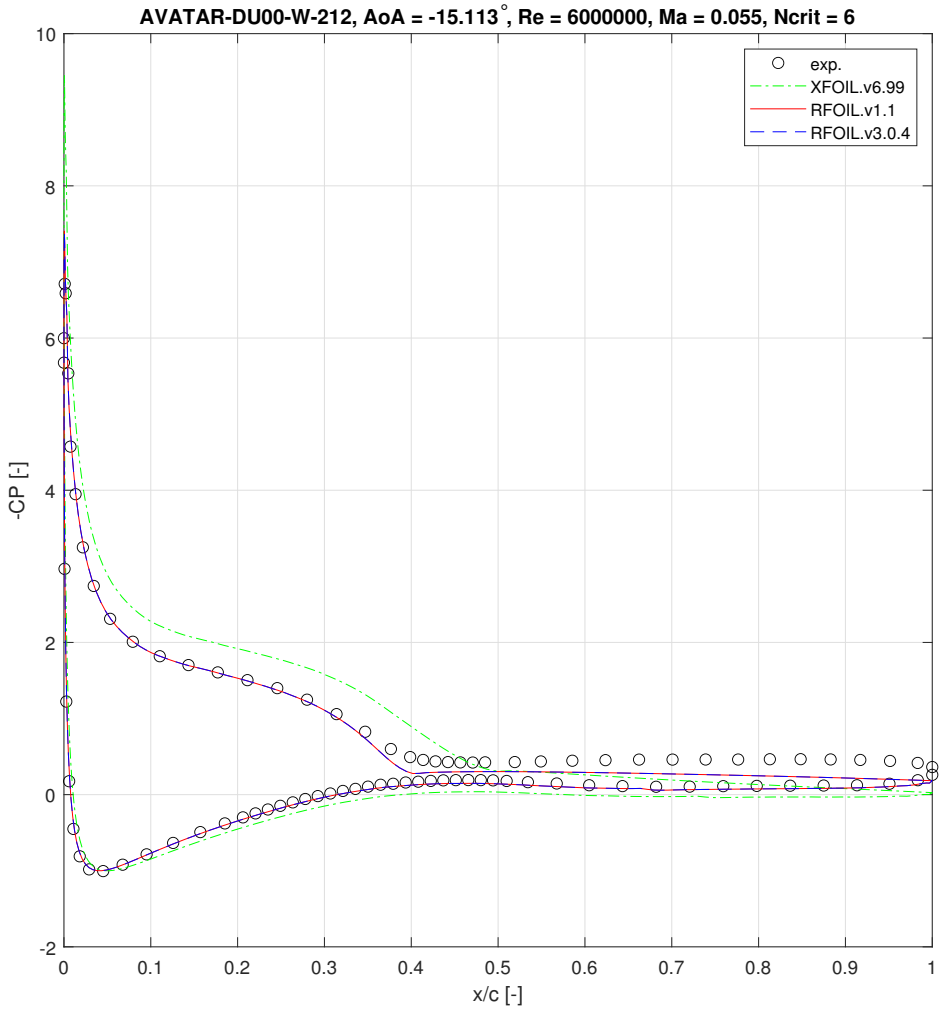

Figure C.56: Comparison between experimental and numerical pressure distributions for the AVATAR-DU00-W-212 airfoil at a Reynolds number of 6020000, and at an angle of attack and a Mach number of -15.113° and 0.029, respectively.

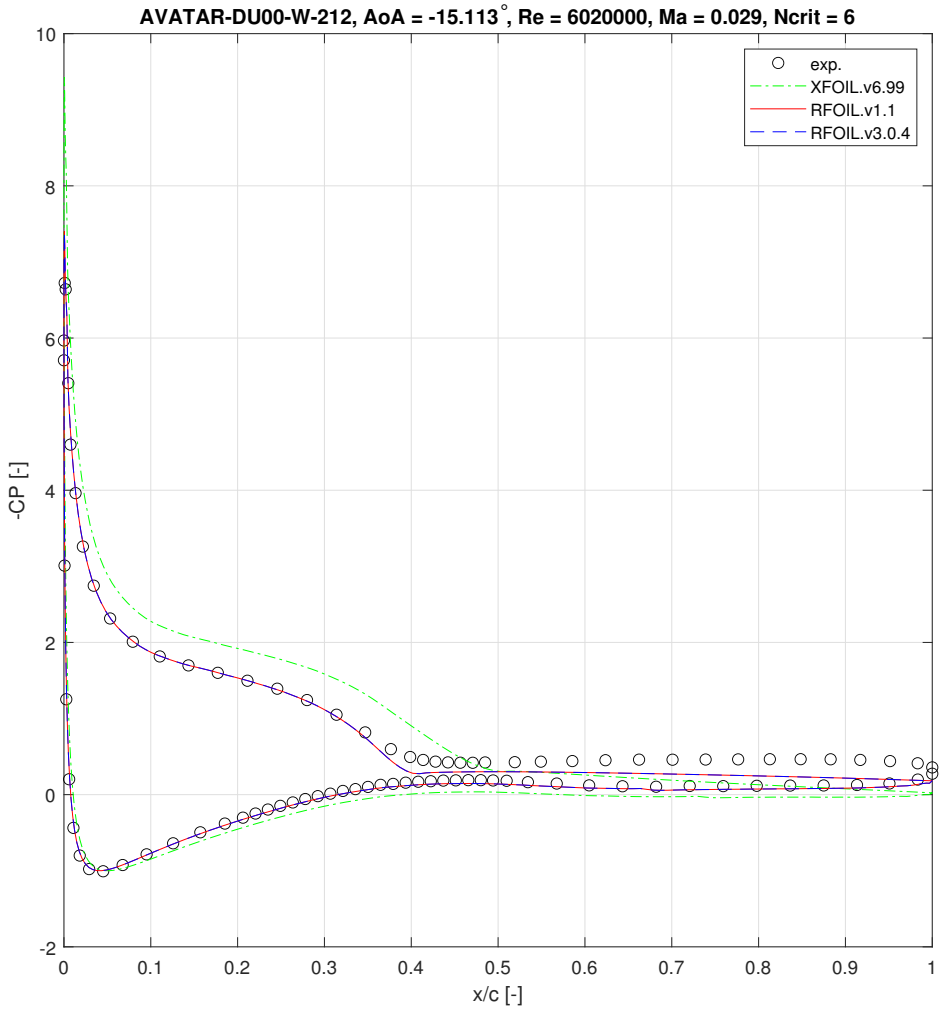

Figure C.57: Comparison between experimental and numerical pressure distributions for the AVATAR-DU00-W-212 airfoil at a Reynolds number of 9010000, and at an angle of attack and a Mach number of -15.118° and 0.083, respectively.

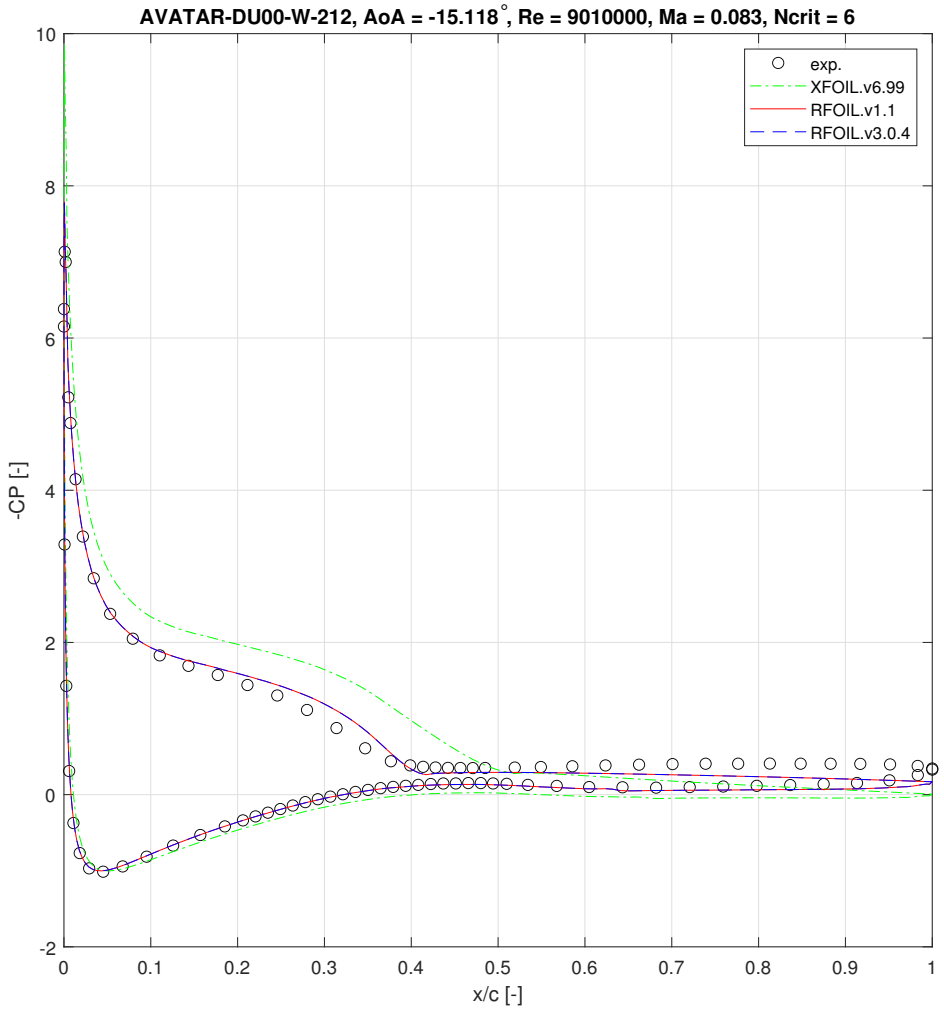

Figure C.58: Comparison between experimental and numerical pressure distributions for the AVATAR-DU00-W-212 airfoil at a Reynolds number of 9020000, and at an angle of attack and a Mach number of -15.119° and 0.044, respectively.

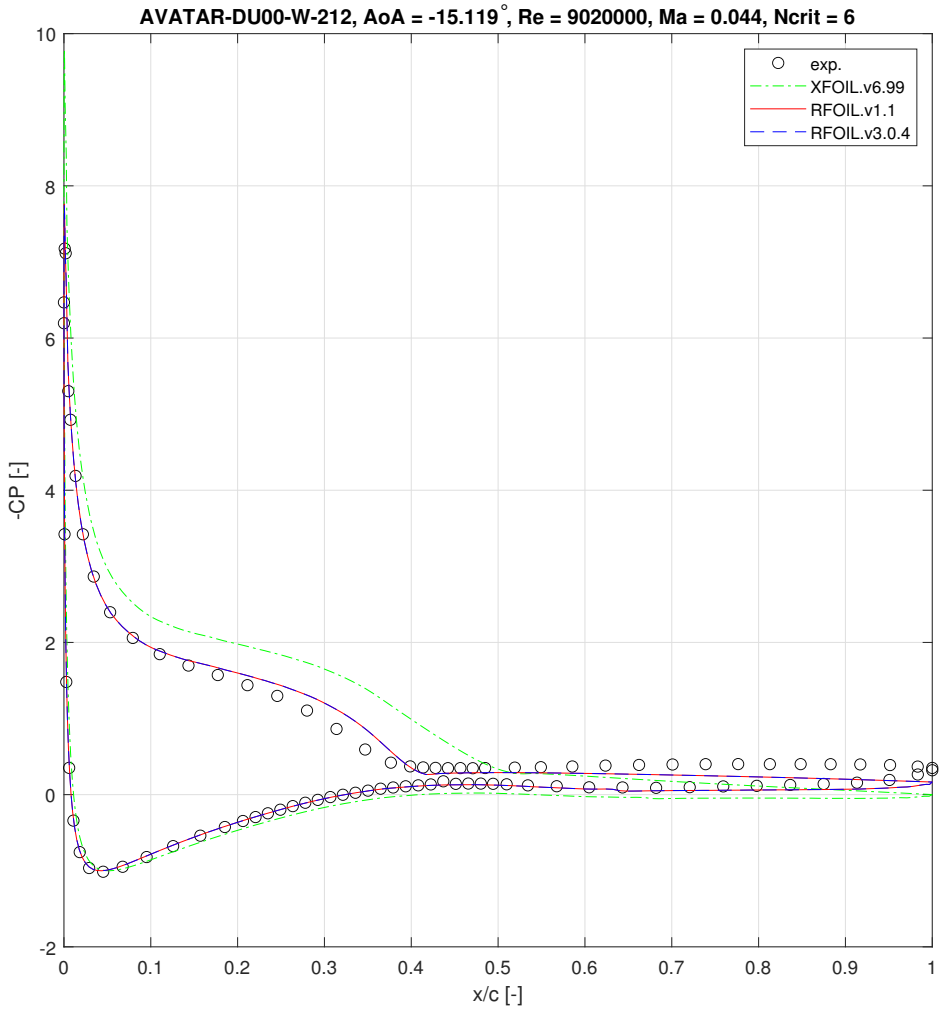

Figure C.59: Comparison between experimental and numerical pressure distributions for the AVATAR-DU00-W-212 airfoil at a Reynolds number of 15040000, and at an angle of attack and a Mach number of -15.127° and 0.082, respectively.

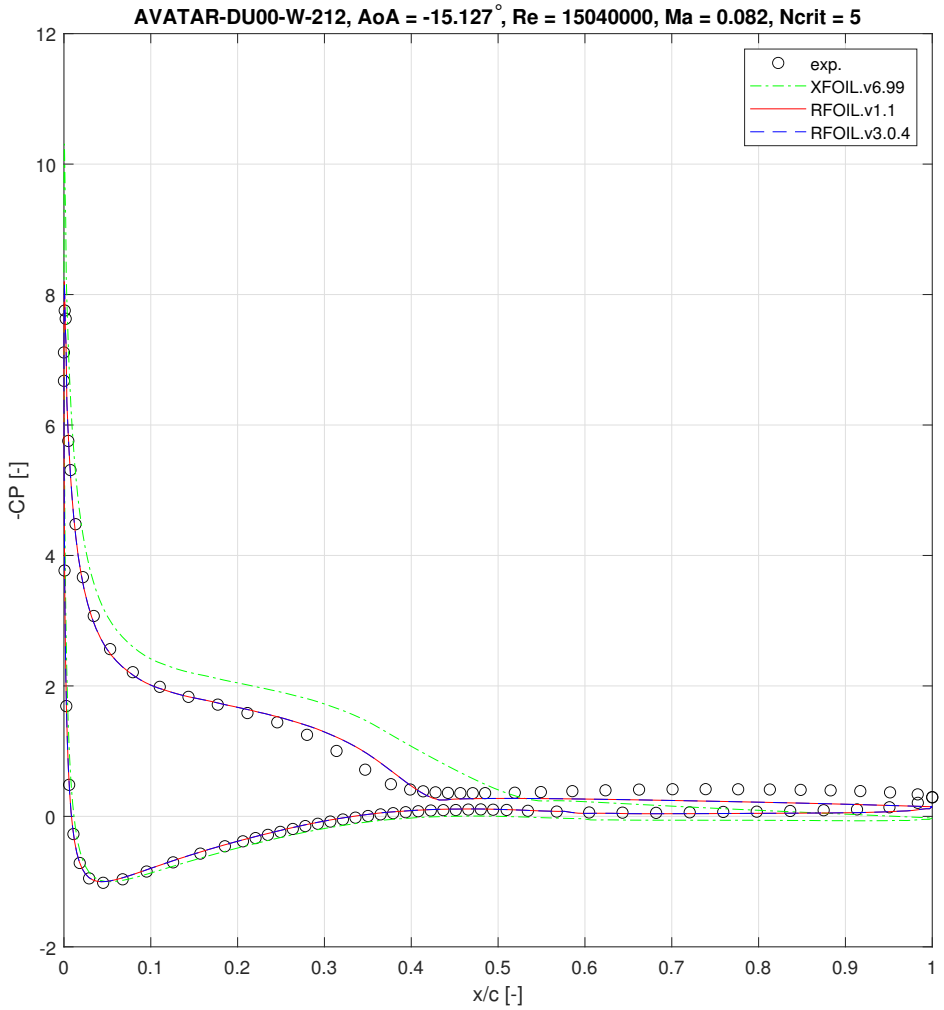

Figure C.60: Comparison between experimental and numerical pressure distributions for the AVATAR-DU00-W-212 airfoil at a Reynolds number of 12030000, and at an angle of attack and a Mach number of -15.948° and 0.058, respectively.

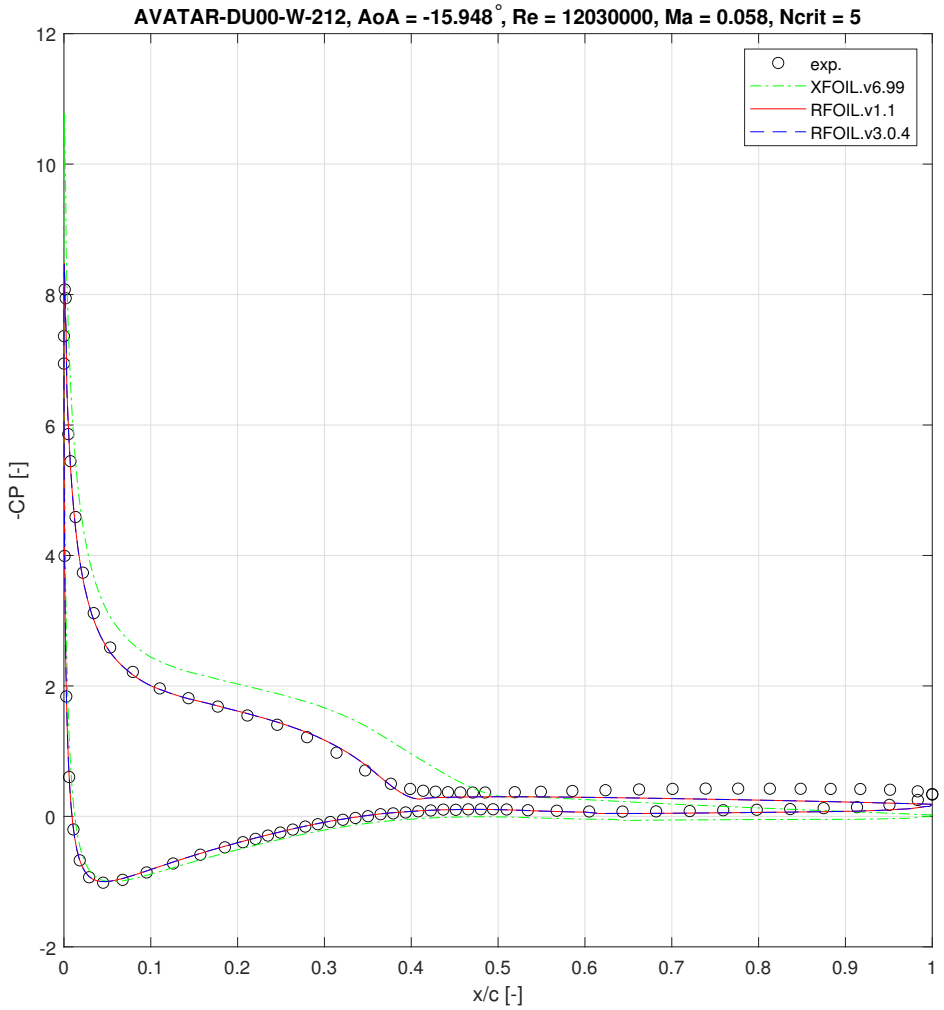

Figure C.61: Comparison between experimental and numerical pressure distributions for the AVATAR-DU00-W-212 airfoil at a Reynolds number of 2960000, and at an angle of attack and a Mach number of -16.102° and 0.073, respectively.

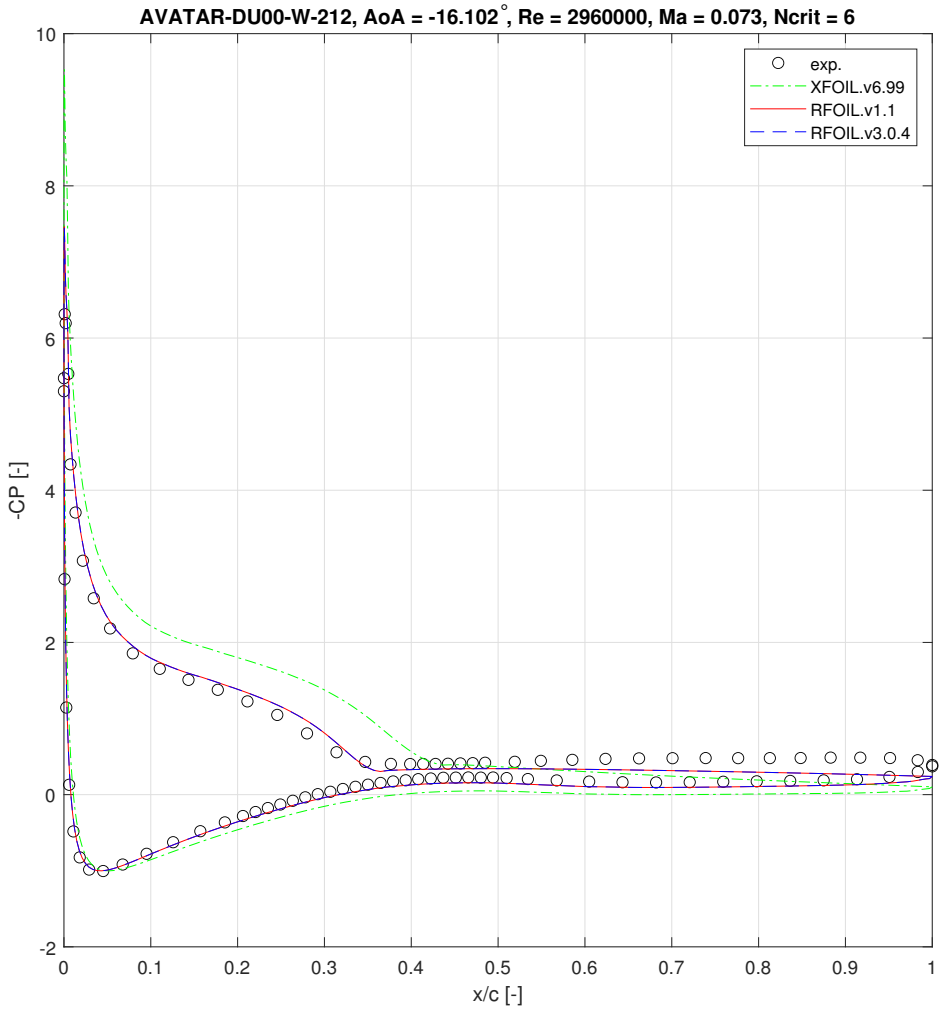

Figure C.62: Comparison between experimental and numerical pressure distributions for the AVATAR-DU00-W-212 airfoil at a Reynolds number of 5950000, and at an angle of attack and a Mach number of -16.116° and 0.054, respectively.

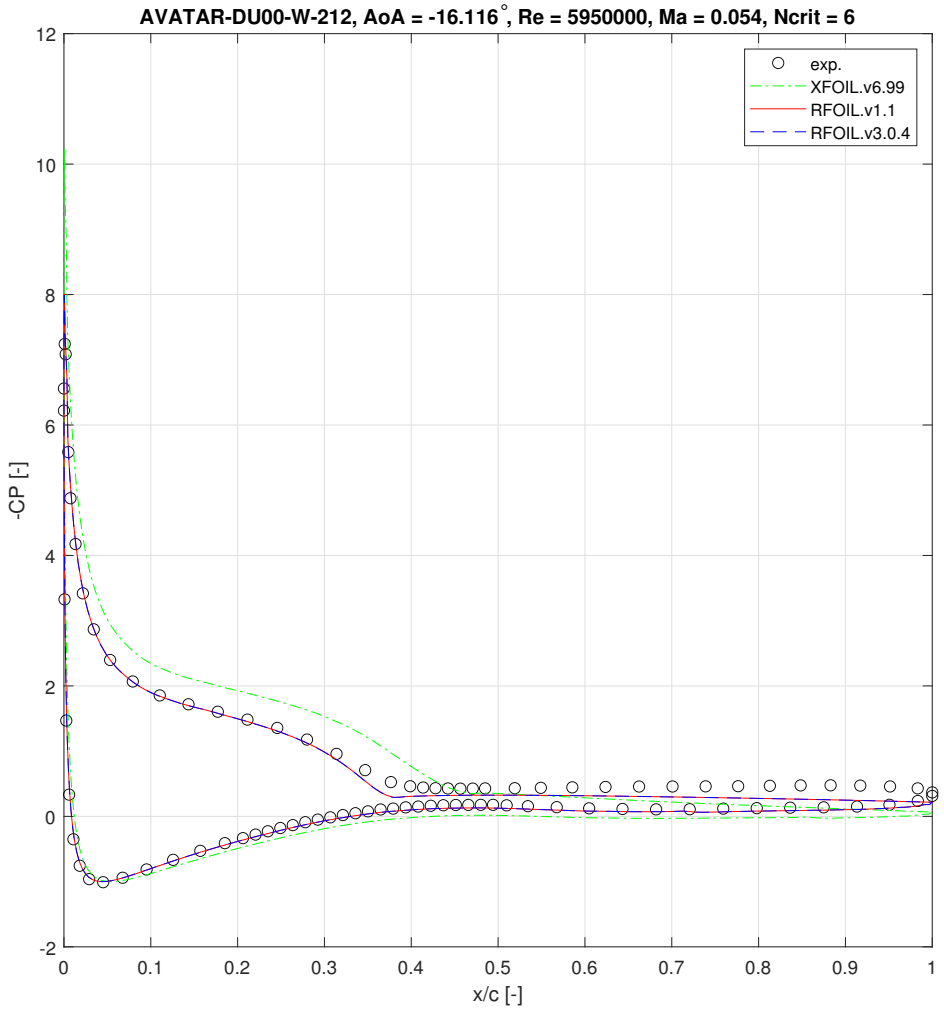

Figure C.63: Comparison between experimental and numerical pressure distributions for the AVATAR-DU00-W-212 airfoil at a Reynolds number of 5960000, and at an angle of attack and a Mach number of -16.116° and 0.029, respectively.

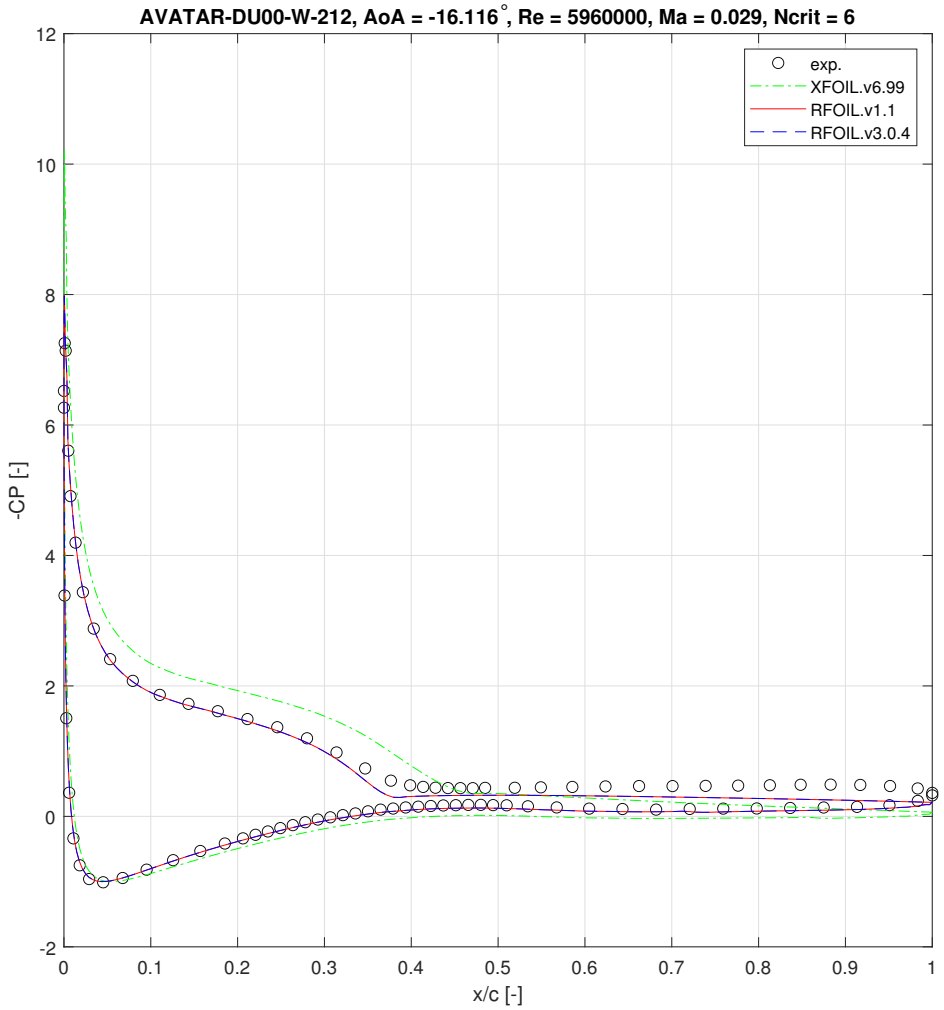

Figure C.64: Comparison between experimental and numerical pressure distributions for the AVATAR-DU00-W-212 airfoil at a Reynolds number of 9030000, and at an angle of attack and a Mach number of -16.124° and 0.083, respectively.

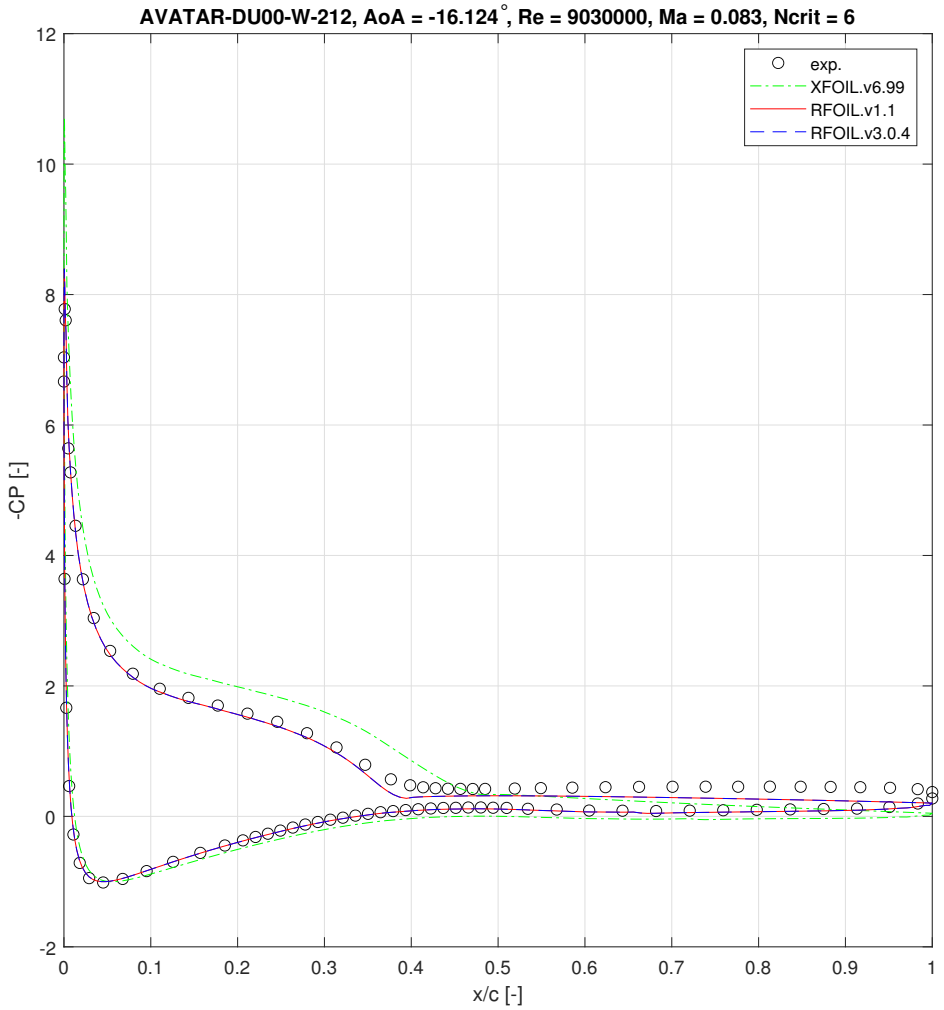

Figure C.65: Comparison between experimental and numerical pressure distributions for the AVATAR-DU00-W-212 airfoil at a Reynolds number of 9010000, and at an angle of attack and a Mach number of -16.125° and 0.043, respectively.

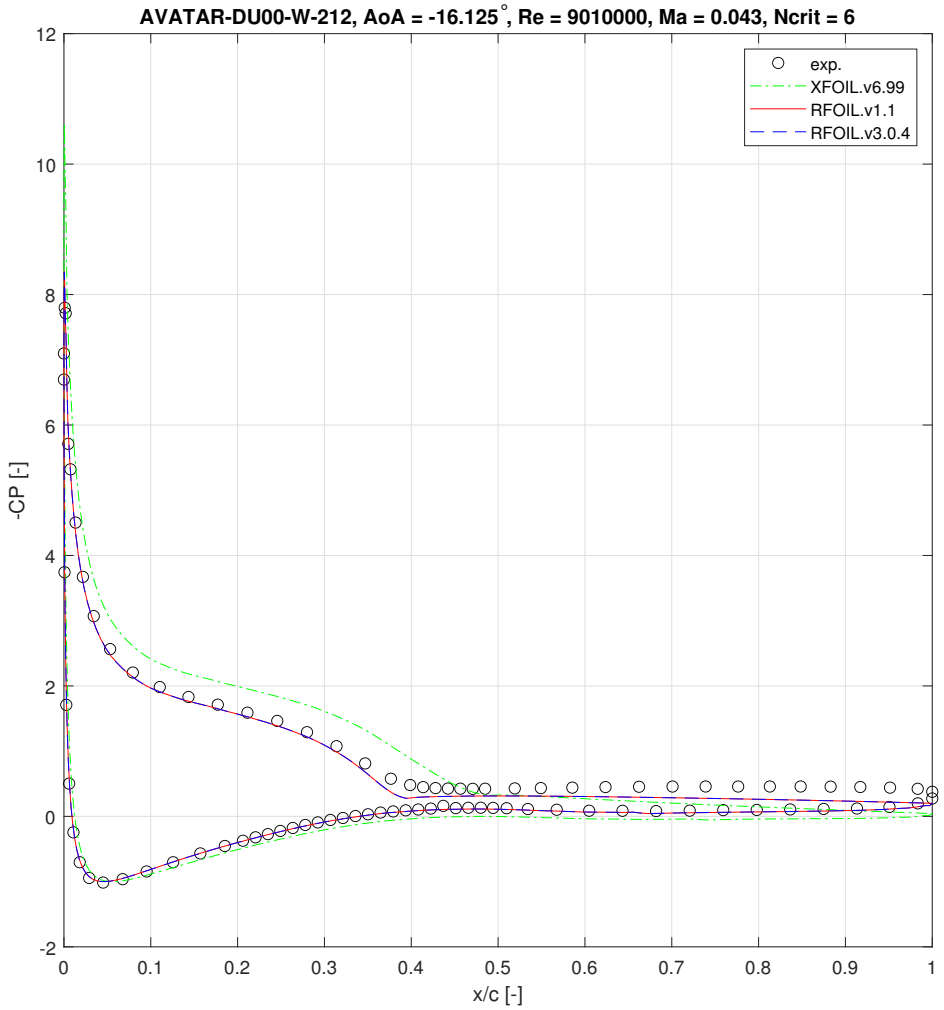

Figure C.66: Comparison between experimental and numerical pressure distributions for the AVATAR-DU00-W-212 airfoil at a Reynolds number of 15000000, and at an angle of attack and a Mach number of -16.132° and 0.081, respectively.

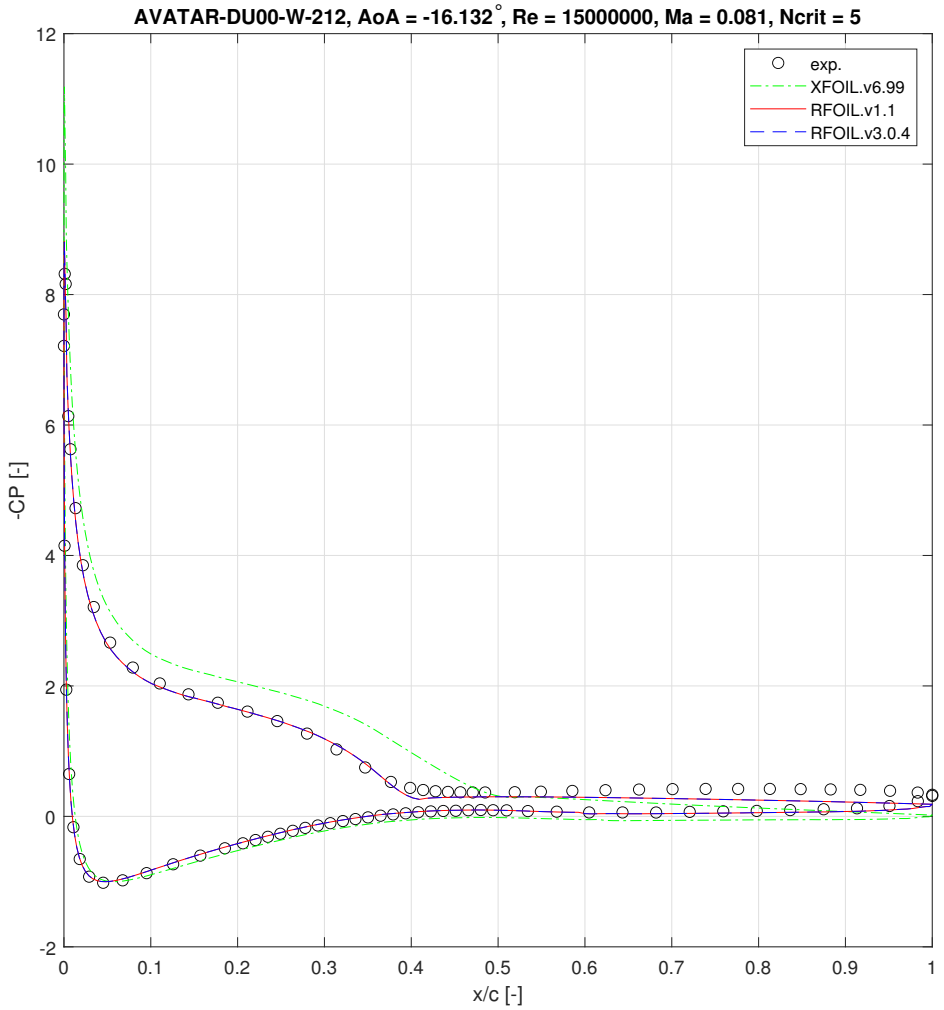

Figure C.67: Comparison between experimental and numerical pressure distributions for the AVATAR-DU00-W-212 airfoil at a Reynolds number of 12040000, and at an angle of attack and a Mach number of -16.951° and 0.058, respectively.

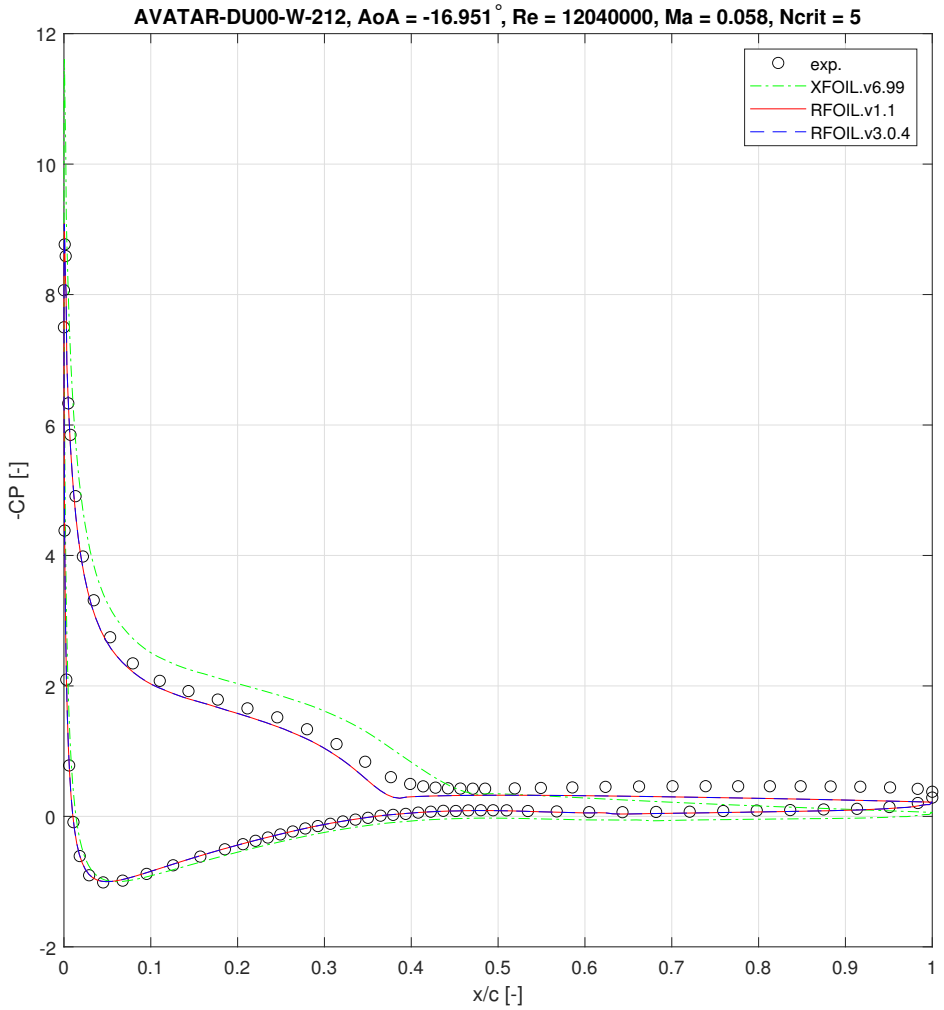

Figure C.68: Comparison between experimental and numerical pressure distributions for the AVATAR-DU00-W-212 airfoil at a Reynolds number of 2940000, and at an angle of attack and a Mach number of -17.104° and 0.073, respectively.

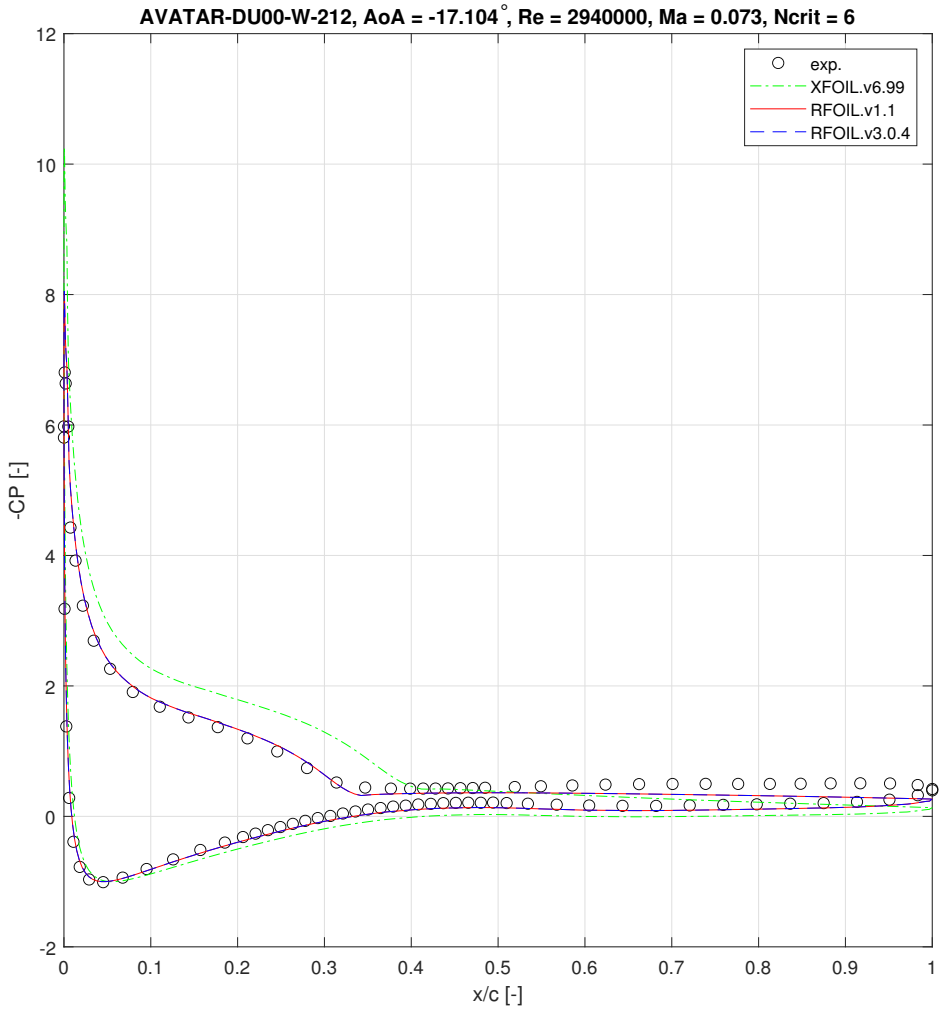

Figure C.69: Comparison between experimental and numerical pressure distributions for the AVATAR-DU00-W-212 airfoil at a Reynolds number of 5960000, and at an angle of attack and a Mach number of -17.116° and 0.054, respectively.

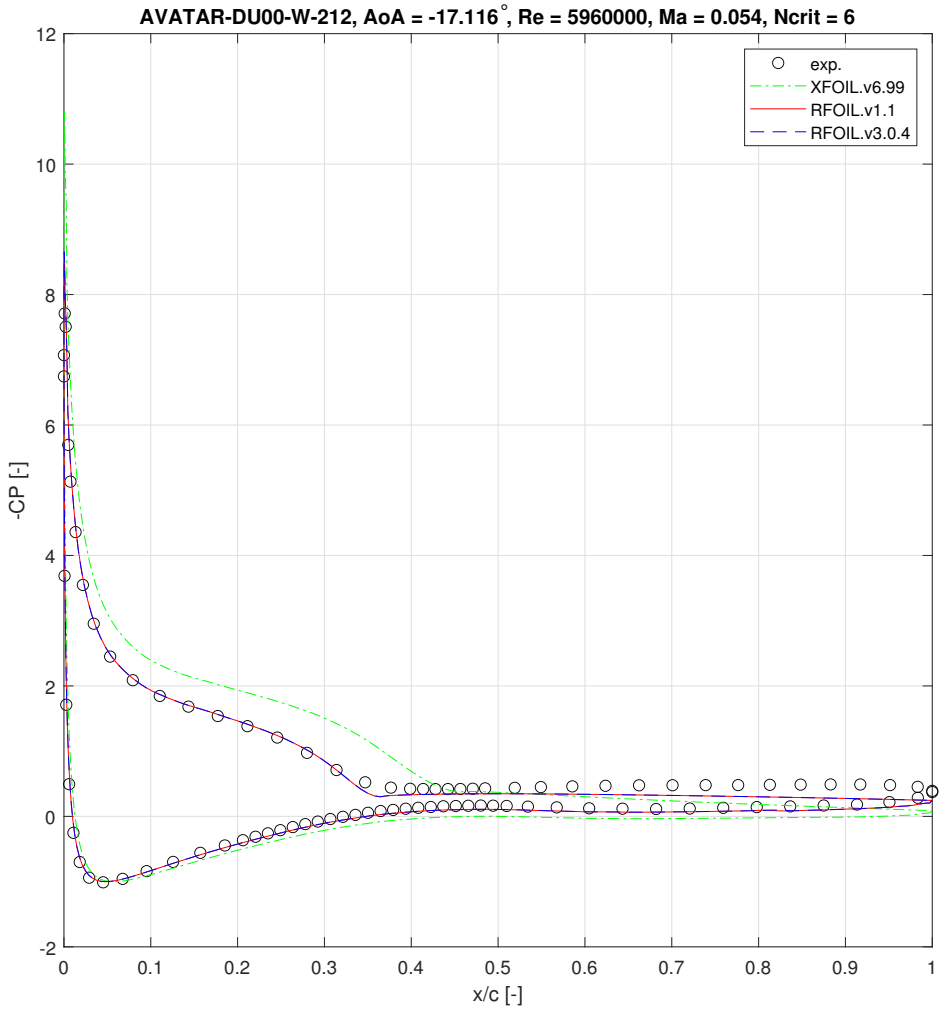

Figure C.70: Comparison between experimental and numerical pressure distributions for the AVATAR-DU00-W-212 airfoil at a Reynolds number of 5980000, and at an angle of attack and a Mach number of -17.116° and 0.029, respectively.

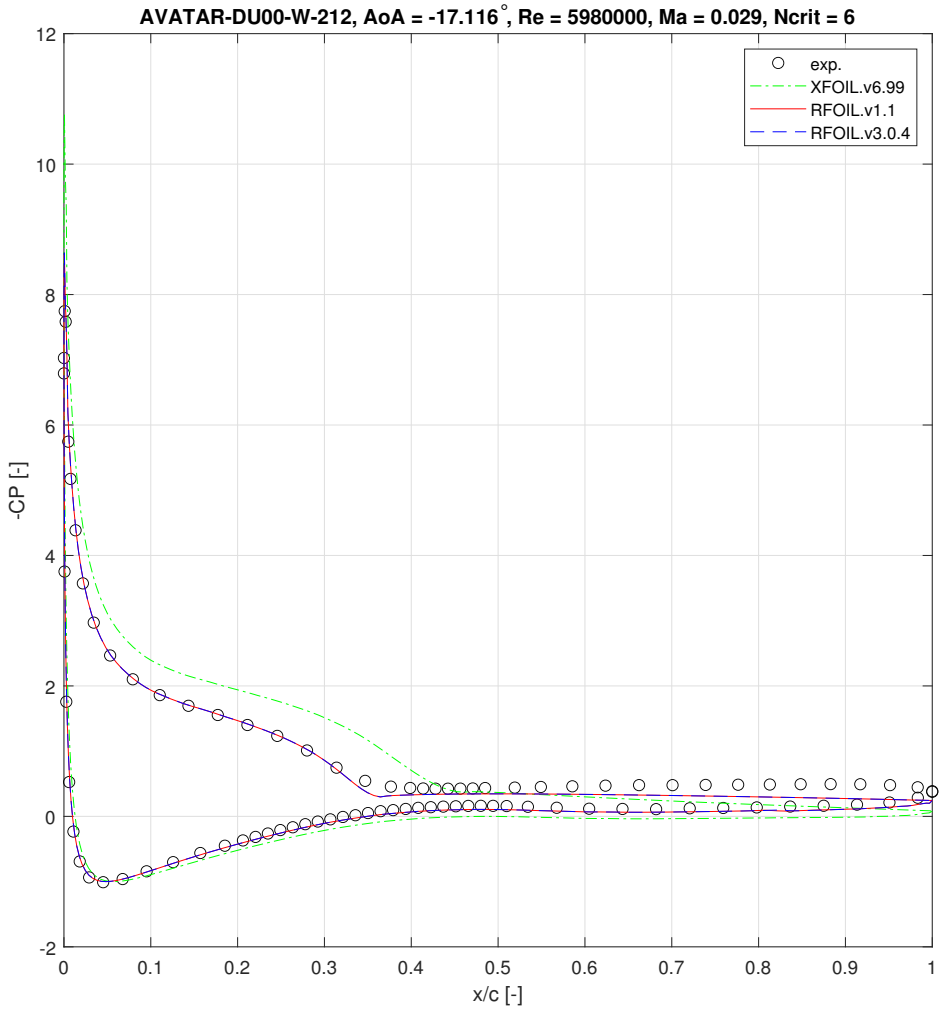

Figure C.71: Comparison between experimental and numerical pressure distributions for the AVATAR-DU00-W-212 airfoil at a Reynolds number of 8960000, and at an angle of attack and a Mach number of -17.128° and 0.082, respectively.

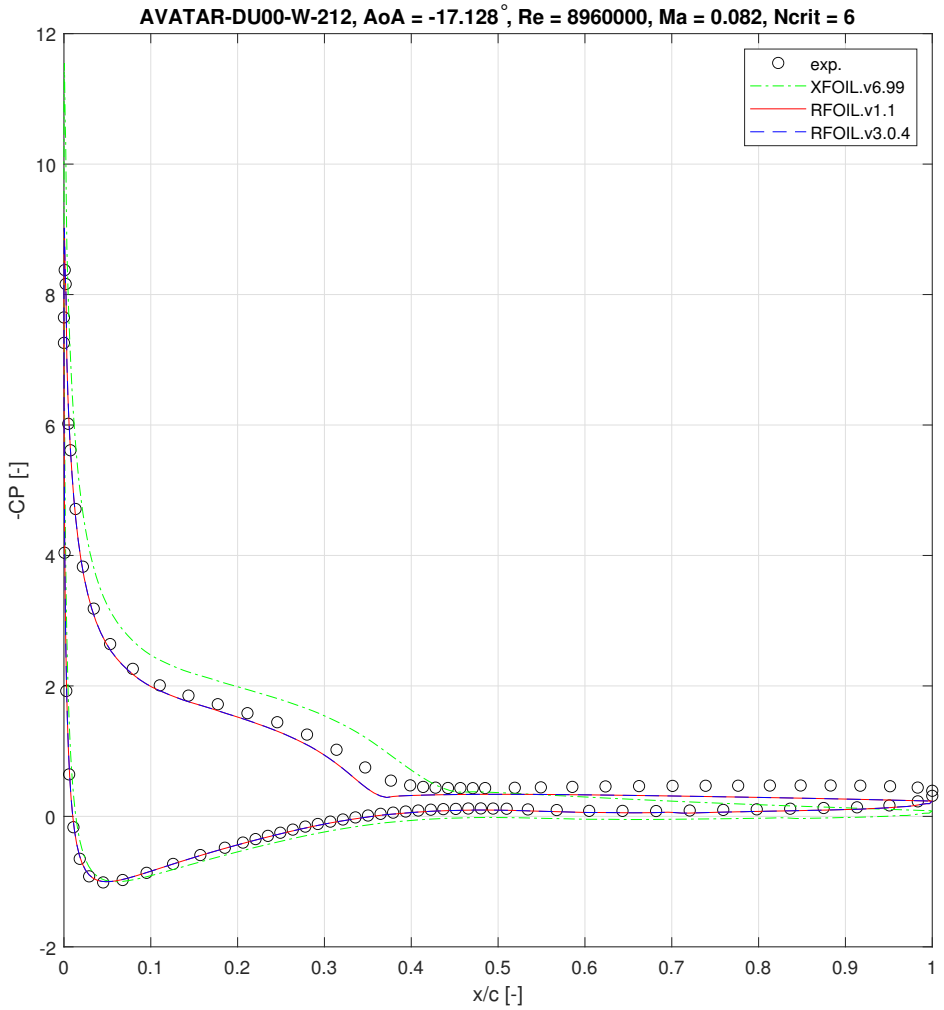

Figure C.72: Comparison between experimental and numerical pressure distributions for the AVATAR-DU00-W-212 airfoil at a Reynolds number of 8970000, and at an angle of attack and a Mach number of -17.129° and 0.043, respectively.

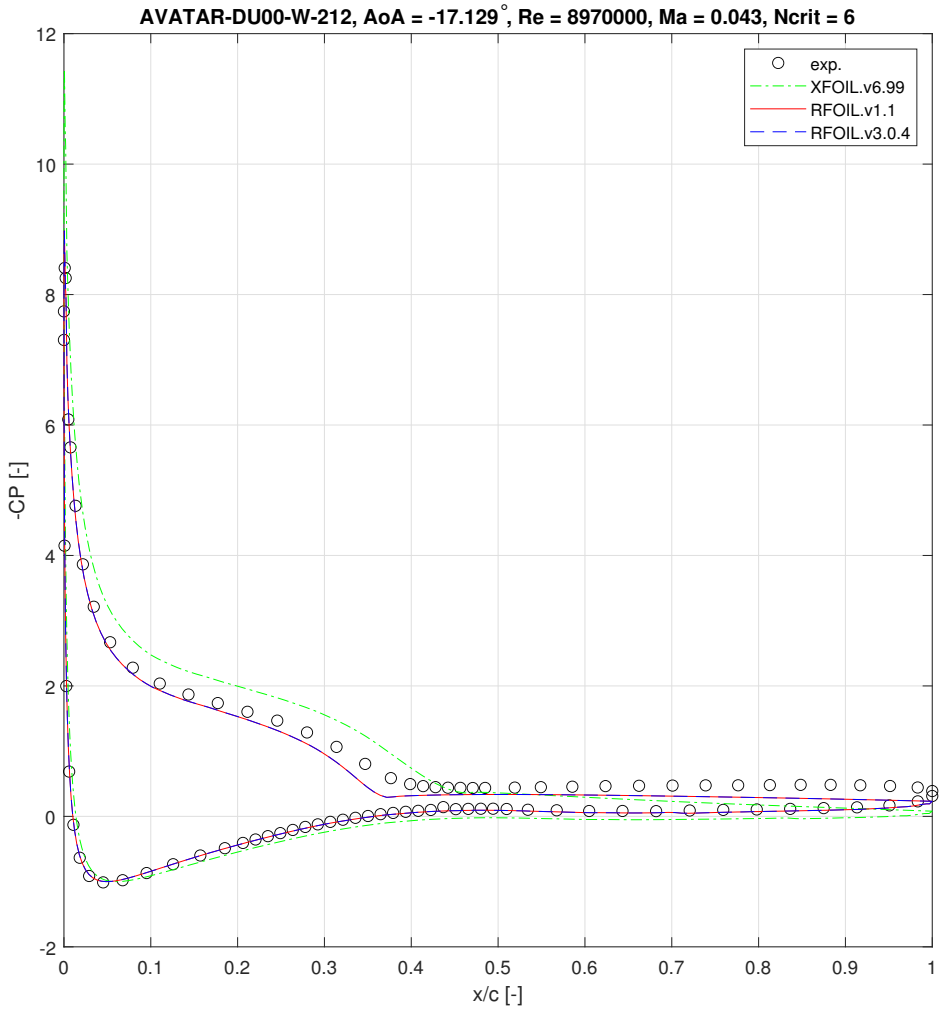

Figure C.73: Comparison between experimental and numerical pressure distributions for the AVATAR-DU00-W-212 airfoil at a Reynolds number of 11990000, and at an angle of attack and a Mach number of -17.951° and 0.058, respectively.

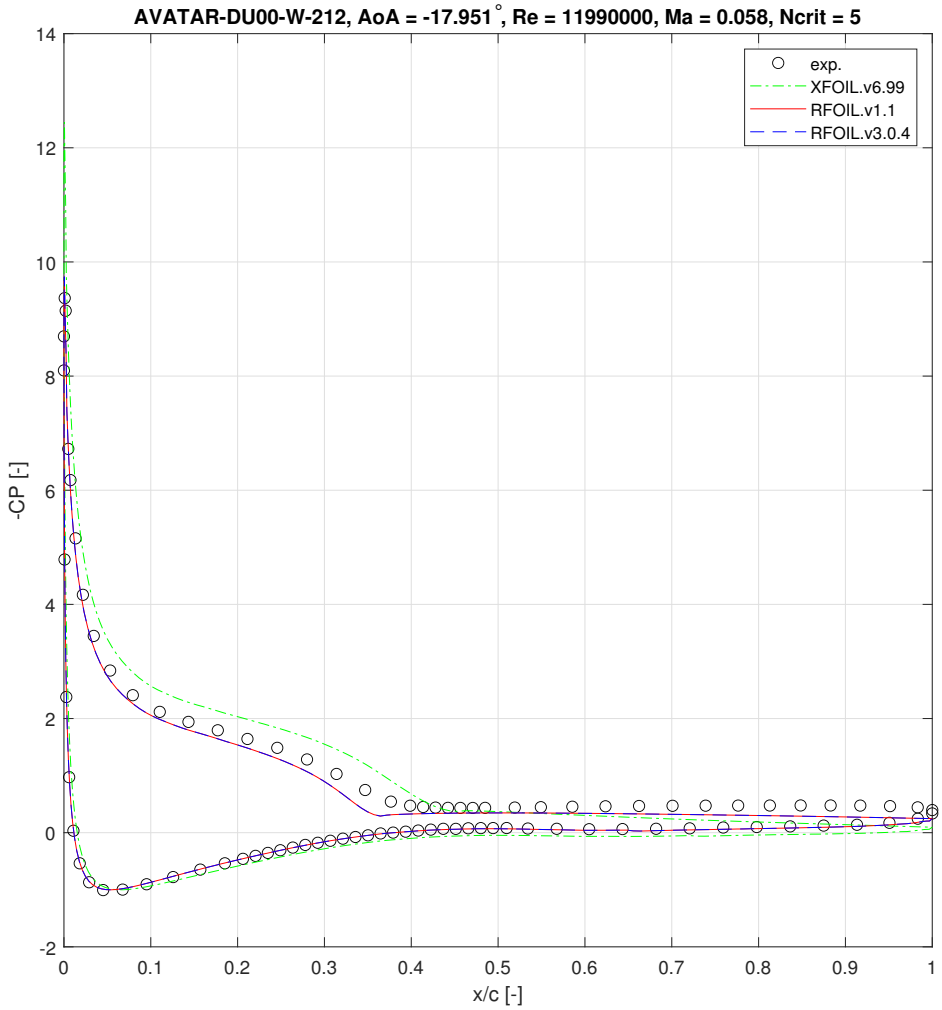

Figure C.74: Comparison between experimental and numerical pressure distributions for the AVATAR-DU00-W-212 airfoil at a Reynolds number of 2950000, and at an angle of attack and a Mach number of -18.107° and 0.073, respectively.

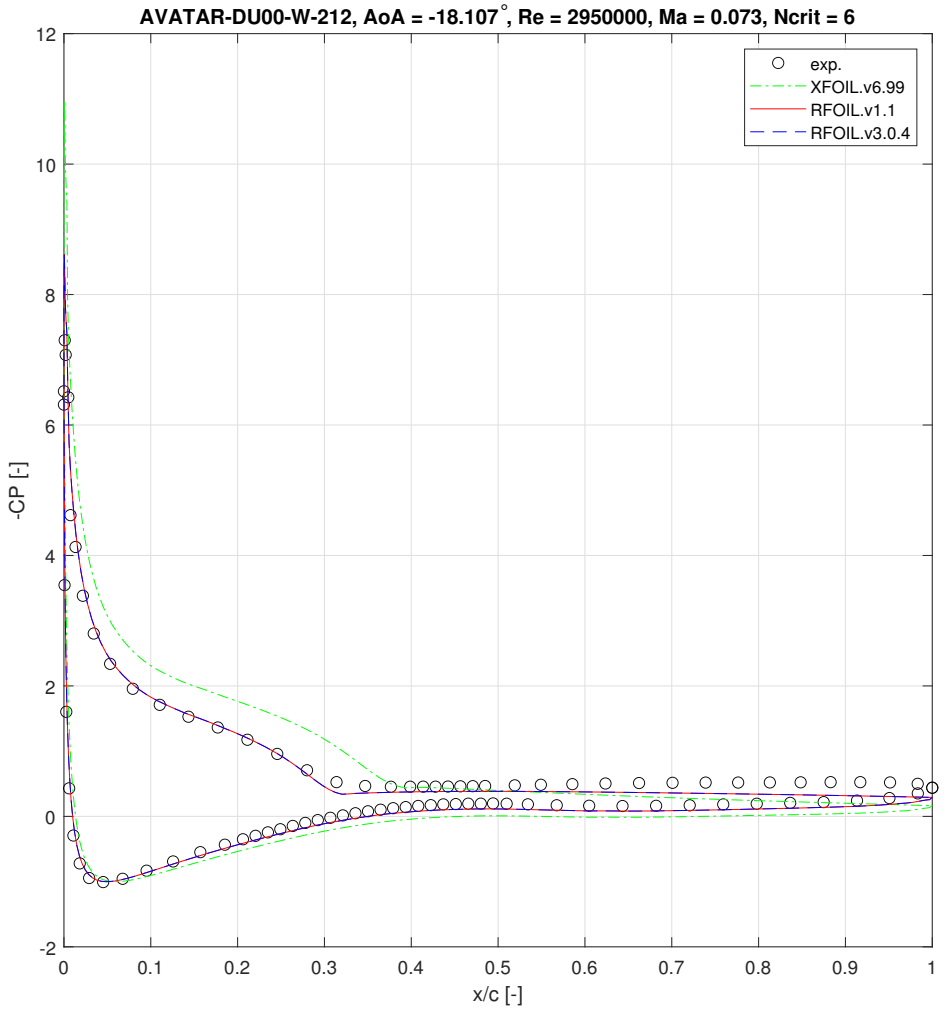

Figure C.75: Comparison between experimental and numerical pressure distributions for the AVATAR-DU00-W-212 airfoil at a Reynolds number of 5920000, and at an angle of attack and a Mach number of -18.117° and 0.054, respectively.

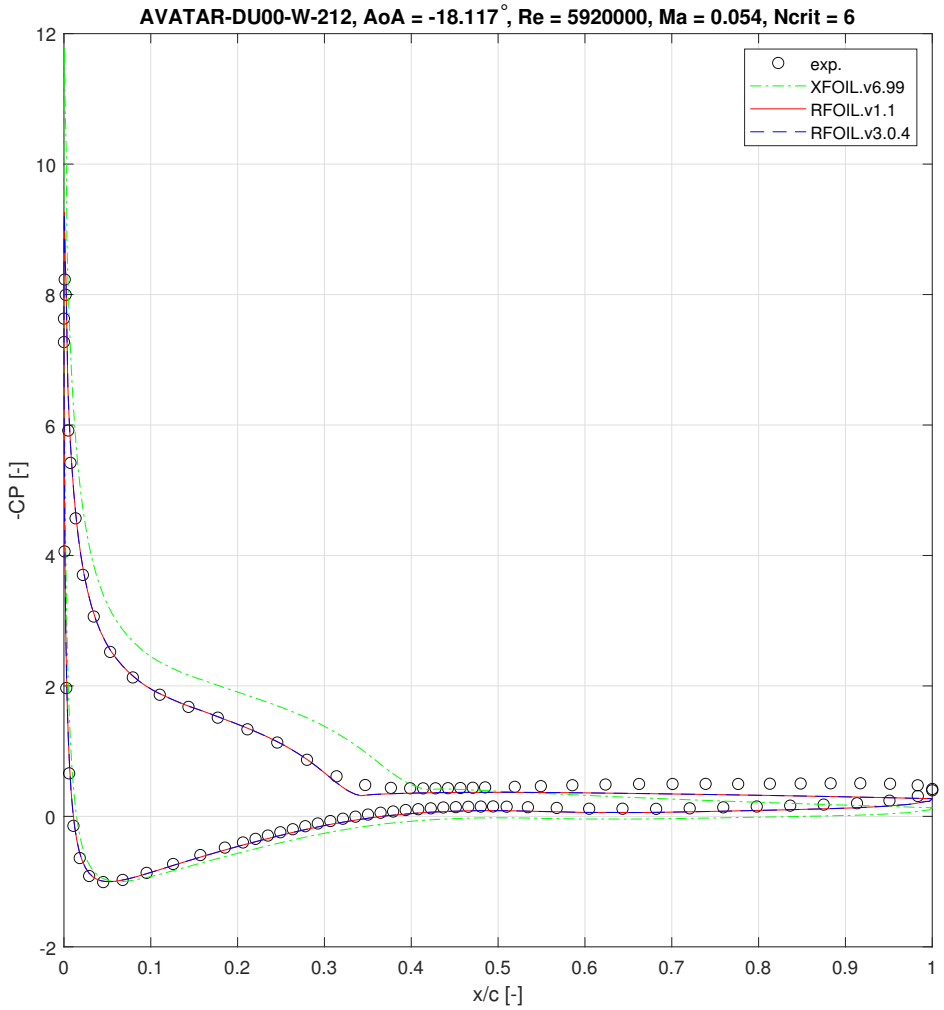

Figure C.76: Comparison between experimental and numerical pressure distributions for the AVATAR-DU00-W-212 airfoil at a Reynolds number of 5970000, and at an angle of attack and a Mach number of -18.117° and 0.054, respectively.

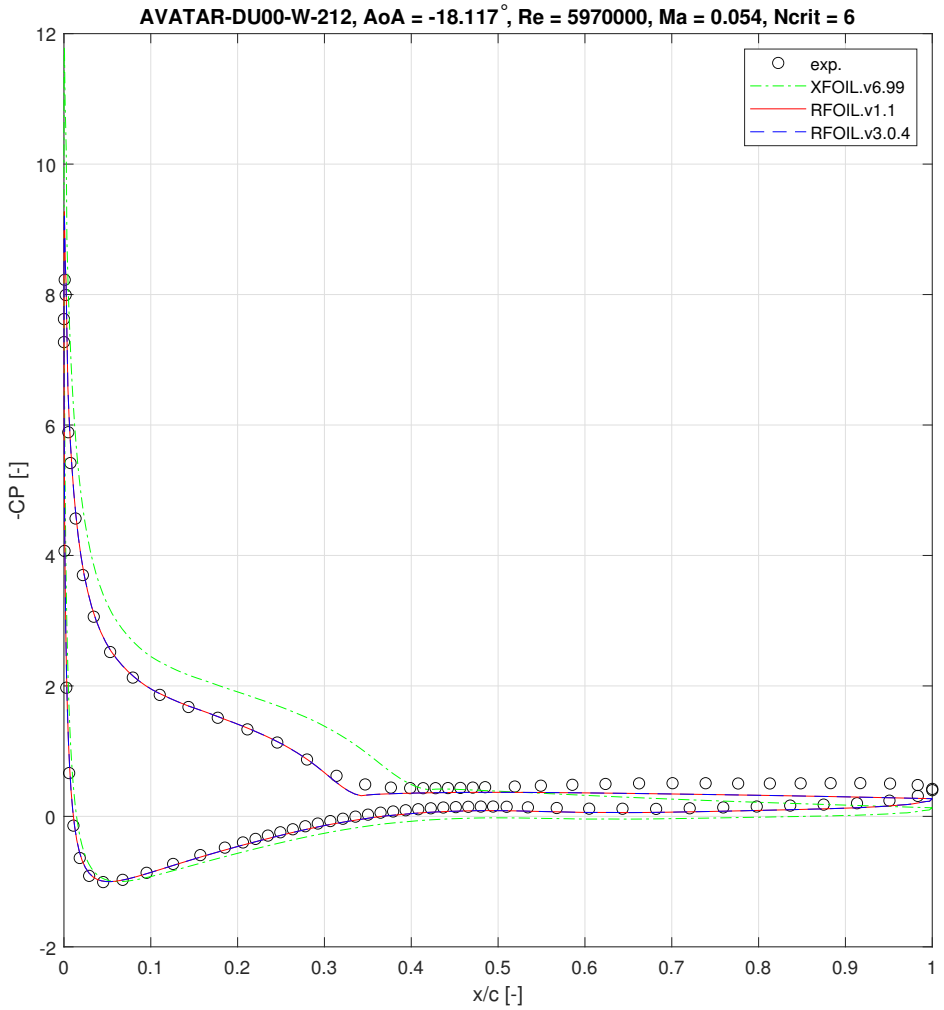

Figure C.77: Comparison between experimental and numerical pressure distributions for the AVATAR-DU00-W-212 airfoil at a Reynolds number of 5980000, and at an angle of attack and a Mach number of -18.119° and 0.029, respectively.

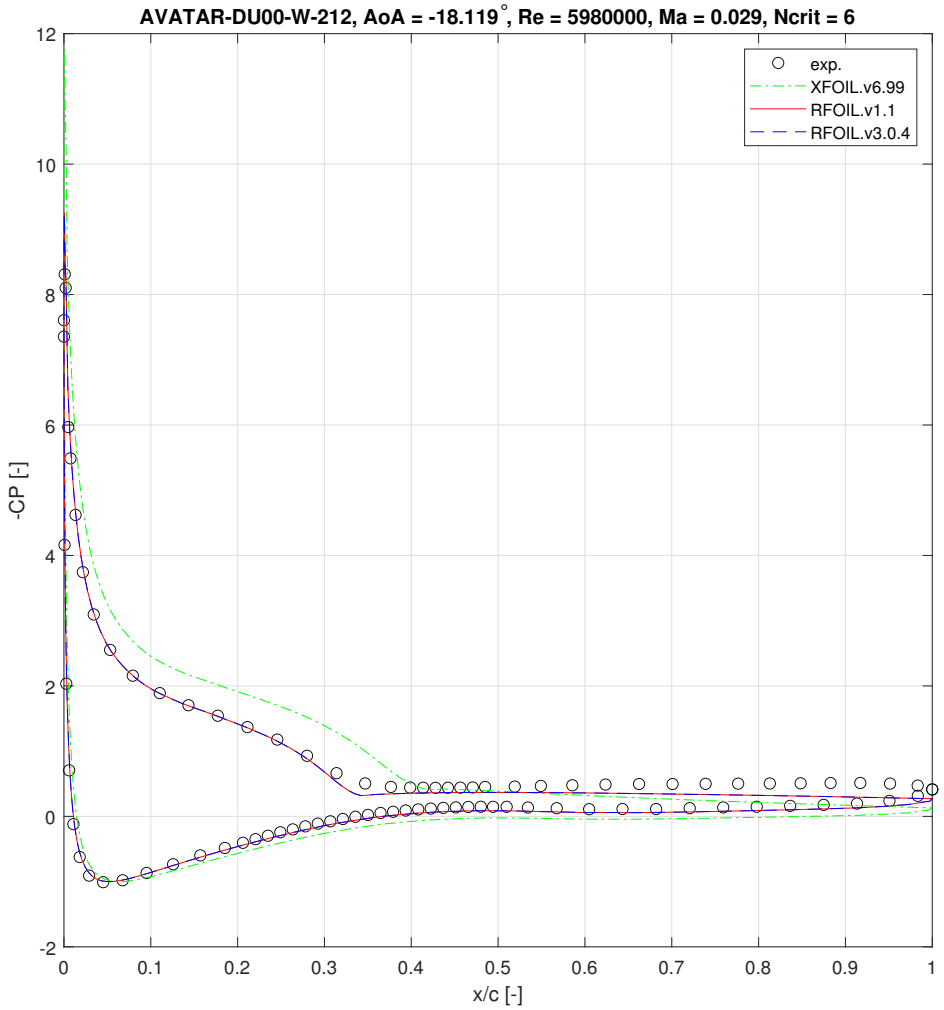

Figure C.78: Comparison between experimental and numerical pressure distributions for the AVATAR-DU00-W-212 airfoil at a Reynolds number of 8950000, and at an angle of attack and a Mach number of -18.131° and 0.043, respectively.

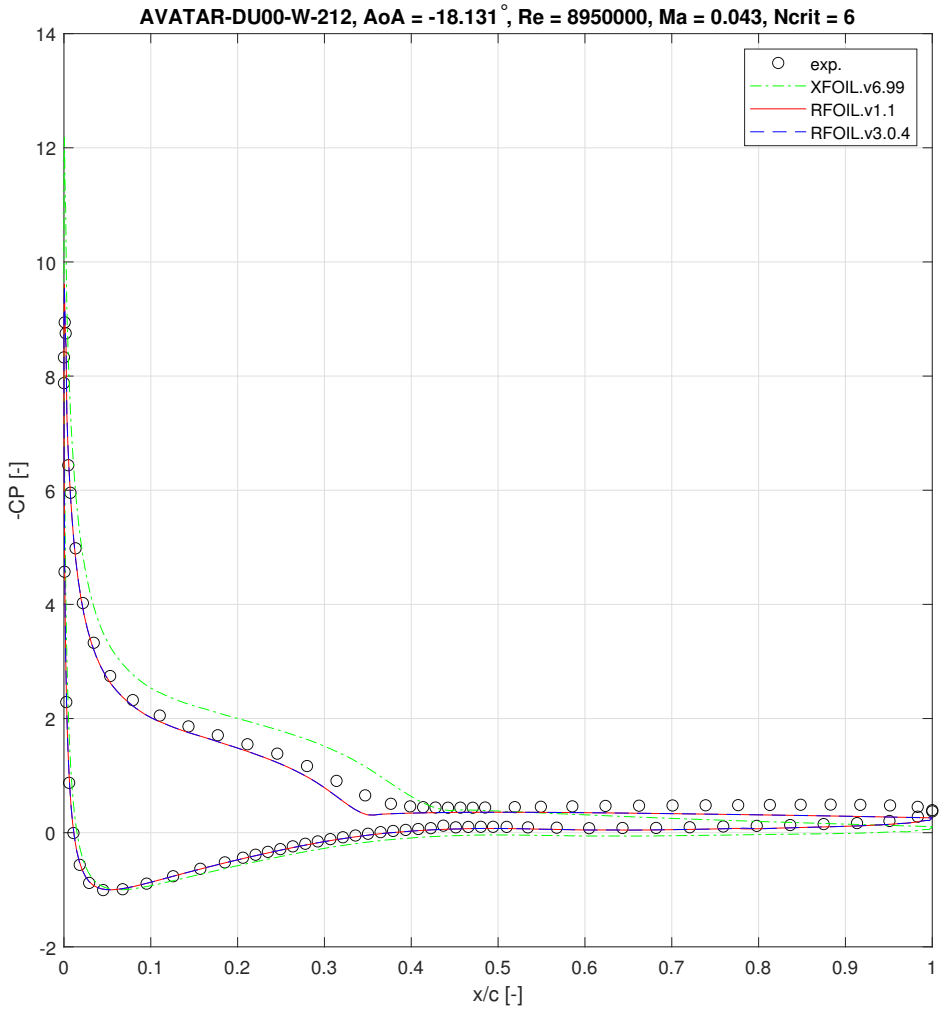

Figure C.79: Comparison between experimental and numerical pressure distributions for the AVATAR-DU00-W-212 airfoil at a Reynolds number of 8950000, and at an angle of attack and a Mach number of -18.130° and 0.082, respectively.

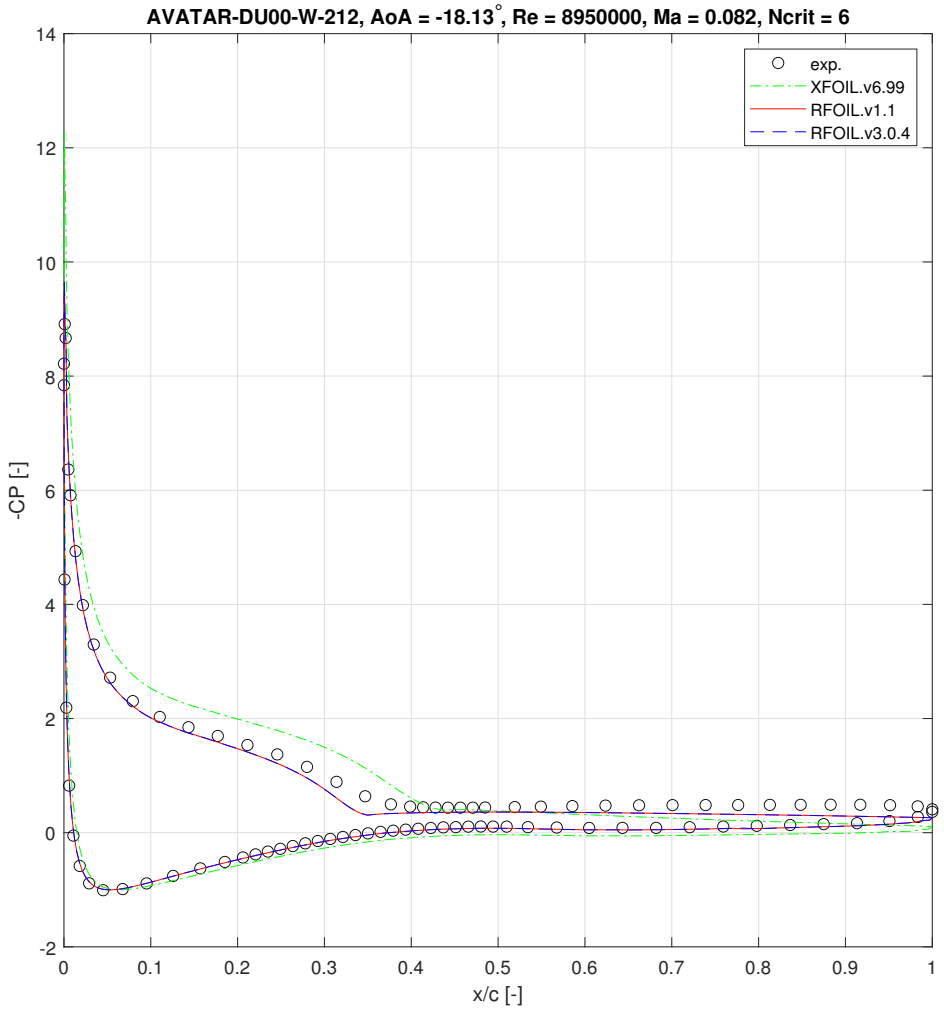

Figure C.80: Comparison between experimental and numerical pressure distributions for the AVATAR-DU00-W-212 airfoil at a Reynolds number of 11880000, and at an angle of attack and a Mach number of -18.952° and 0.057, respectively.

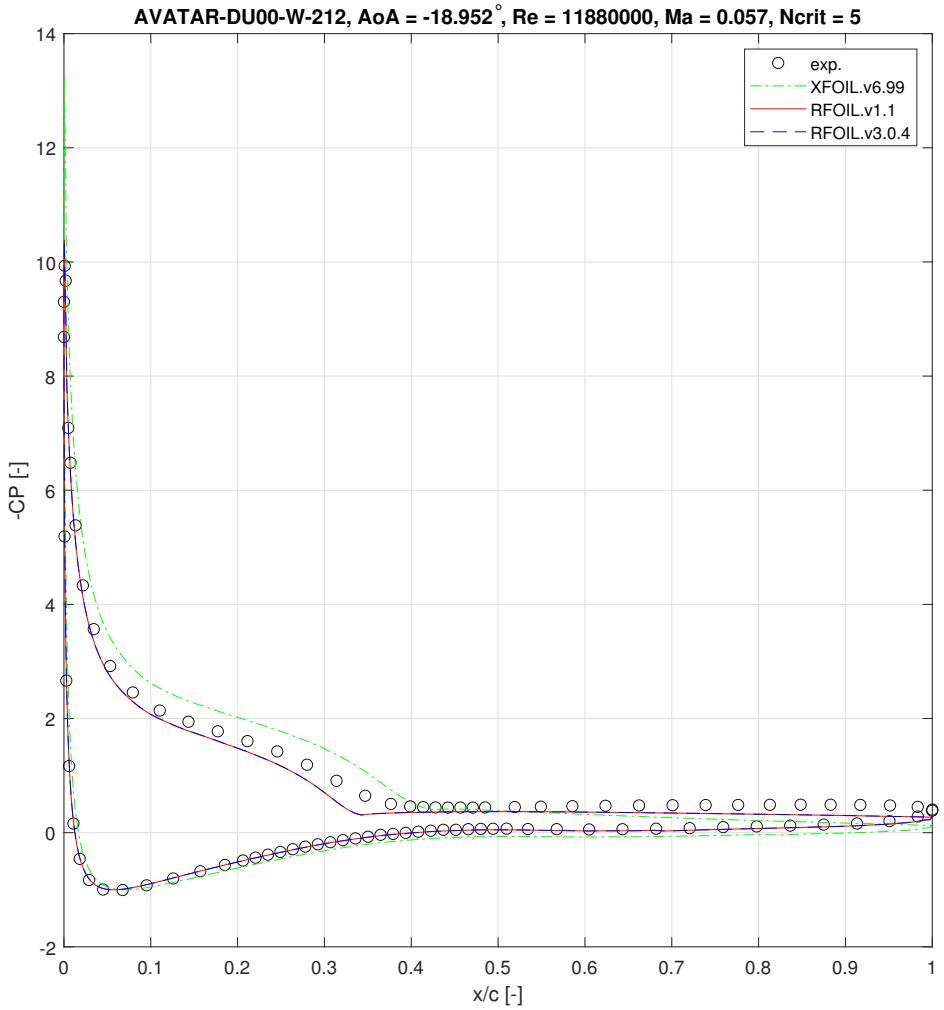

Figure C.81: Comparison between experimental and numerical pressure distributions for the AVATAR-DU00-W-212 airfoil at a Reynolds number of 2970000, and at an angle of attack and a Mach number of -19.109° and 0.073, respectively.

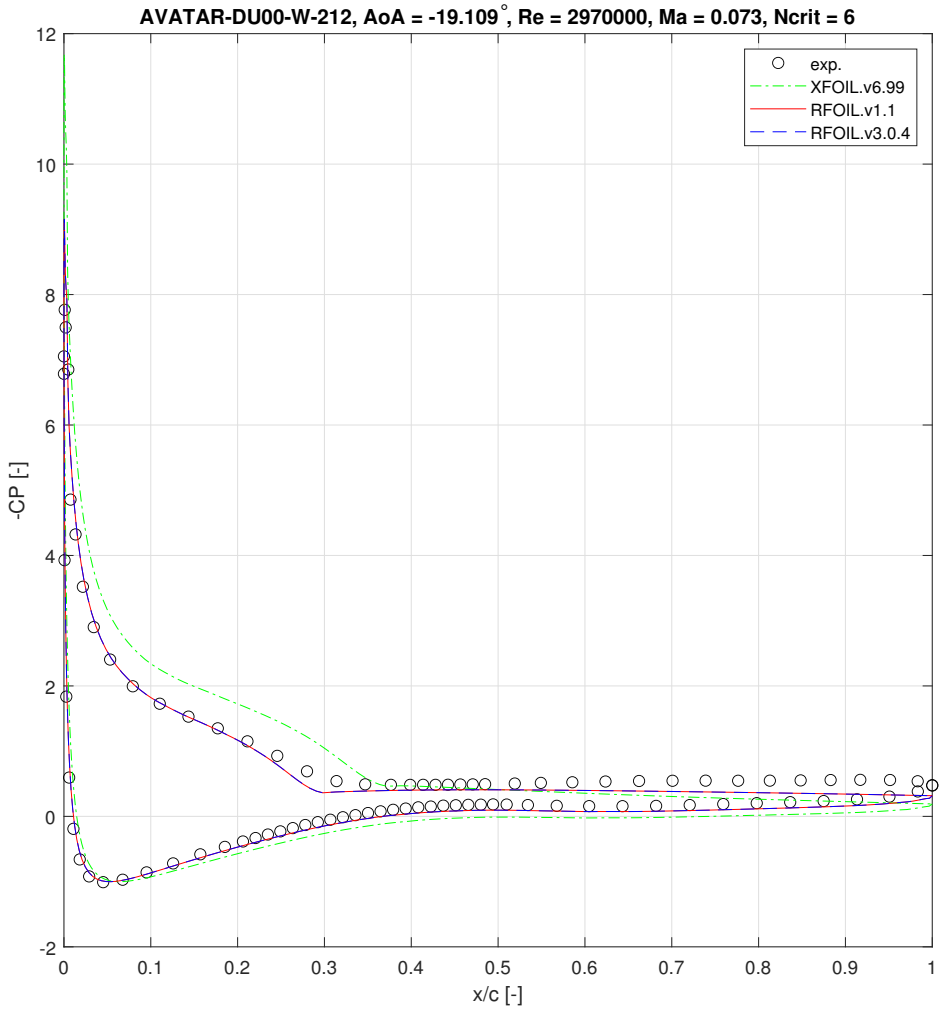

Figure C.82: Comparison between experimental and numerical pressure distributions for the AVATAR-DU00-W-212 airfoil at a Reynolds number of 8910000, and at an angle of attack and a Mach number of -19.129° and 0.082, respectively.

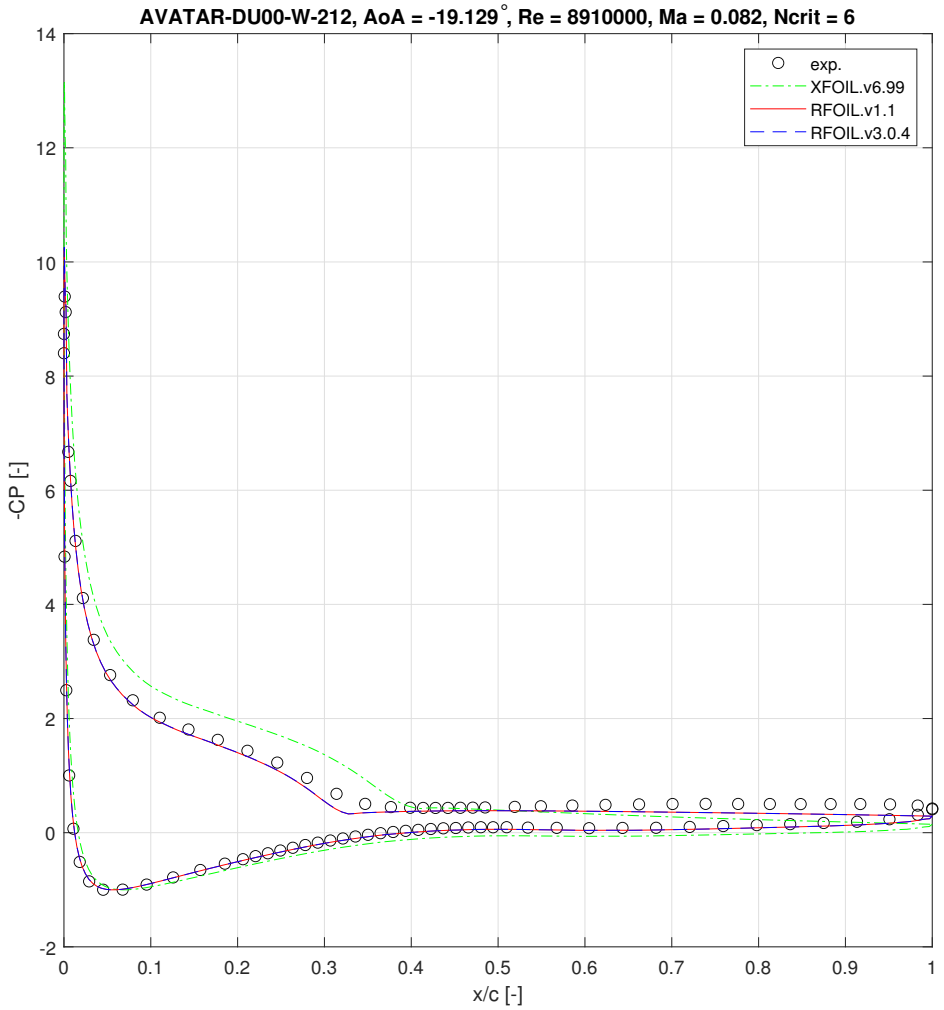

Figure C.83: Comparison between experimental and numerical pressure distributions for the AVATAR-DU00-W-212 airfoil at a Reynolds number of 5980000, and at an angle of attack and a Mach number of -19.120° and 0.055, respectively.

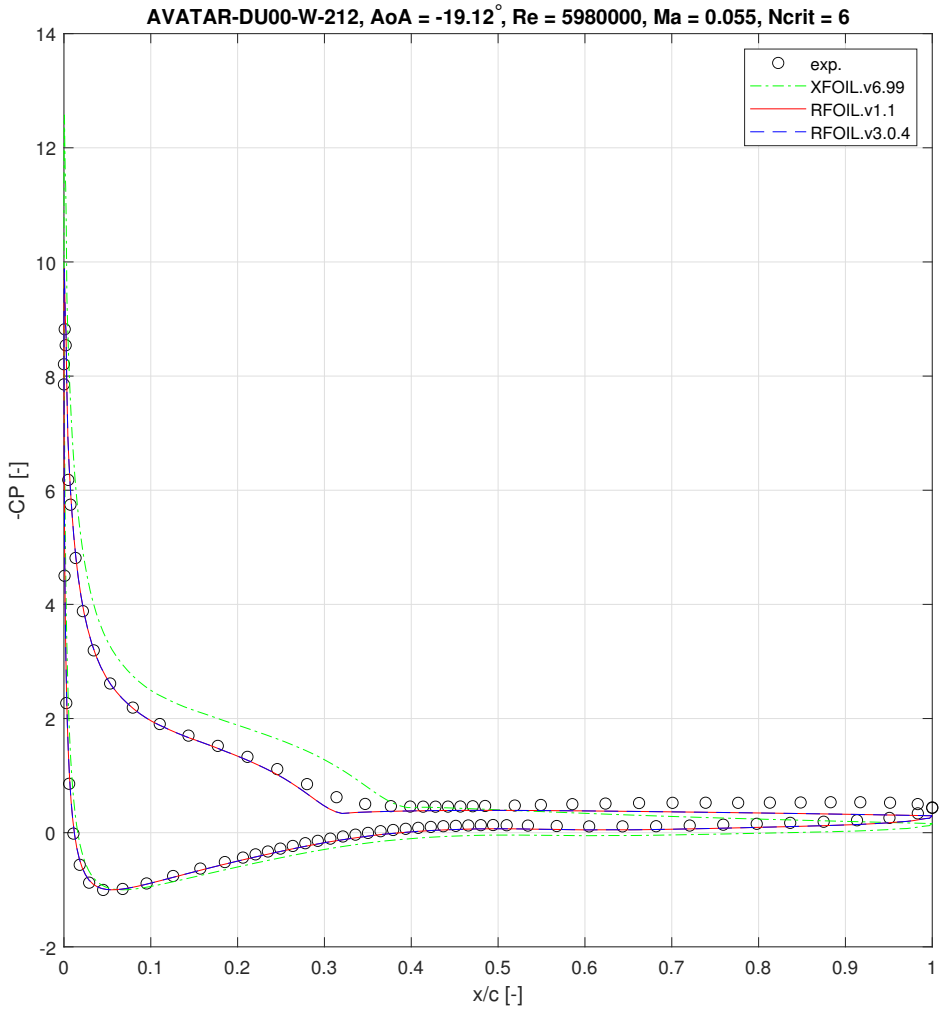

Figure C.84: Comparison between experimental and numerical pressure distributions for the AVATAR-DU00-W-212 airfoil at a Reynolds number of 6010000, and at an angle of attack and a Mach number of -19.120° and 0.029, respectively.

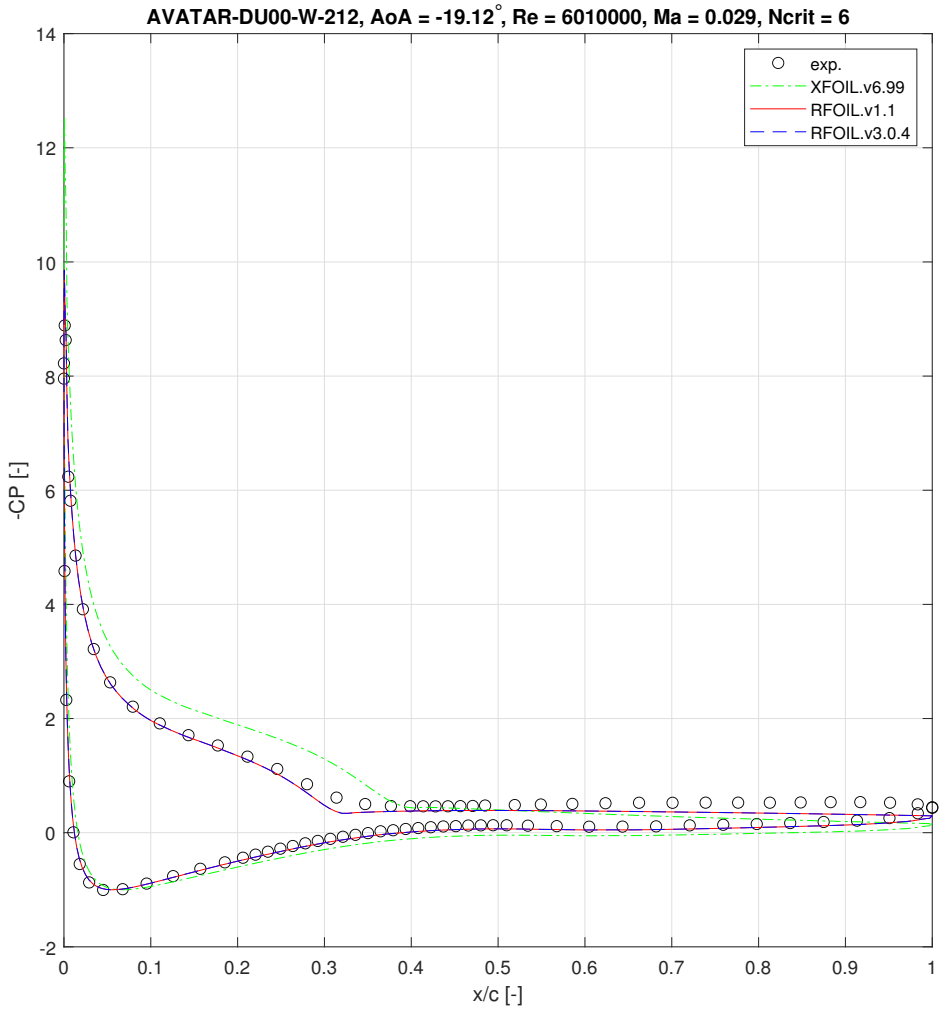

Figure C.85: Comparison between experimental and numerical pressure distributions for the AVATAR-DU00-W-212 airfoil at a Reynolds number of 8920000, and at an angle of attack and a Mach number of -19.130° and 0.043, respectively.

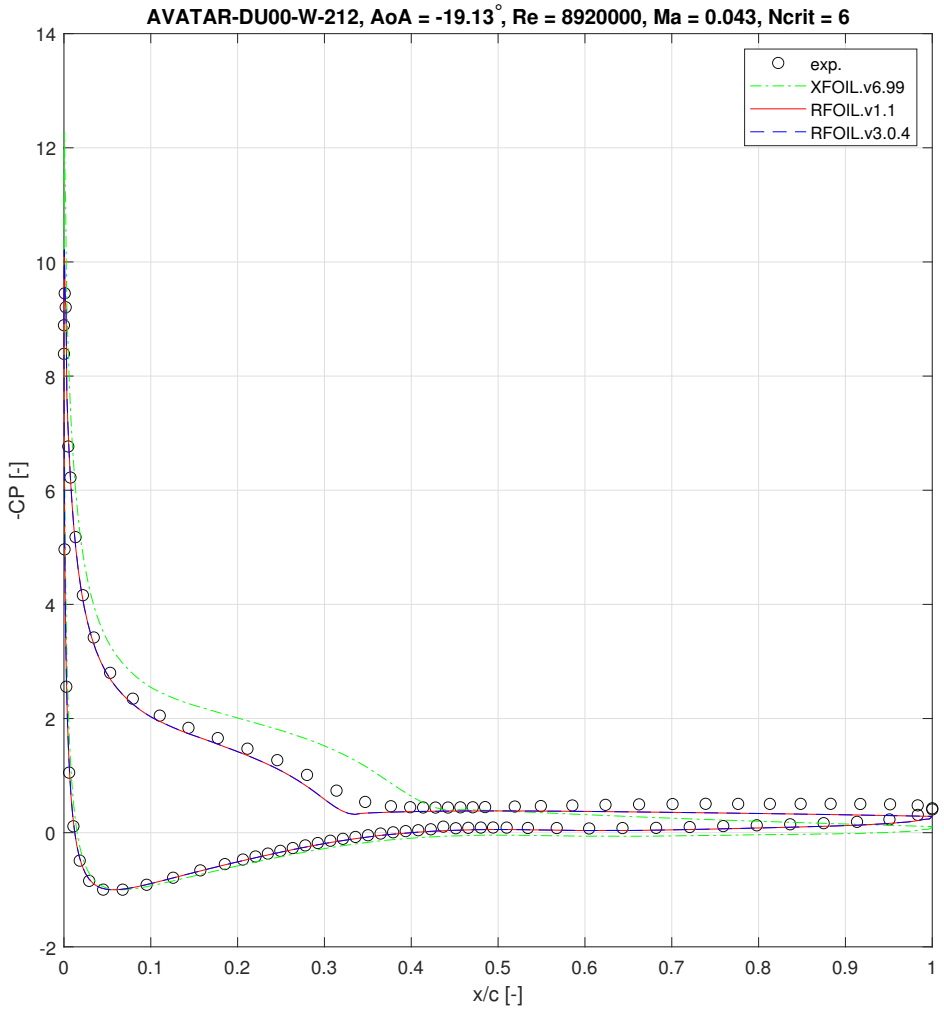

Figure C.86: Comparison between experimental and numerical pressure distributions for the AVATAR-DU00-W-212 airfoil at a Reynolds number of 12010000, and at an angle of attack and a Mach number of -19.950° and 0.058, respectively.

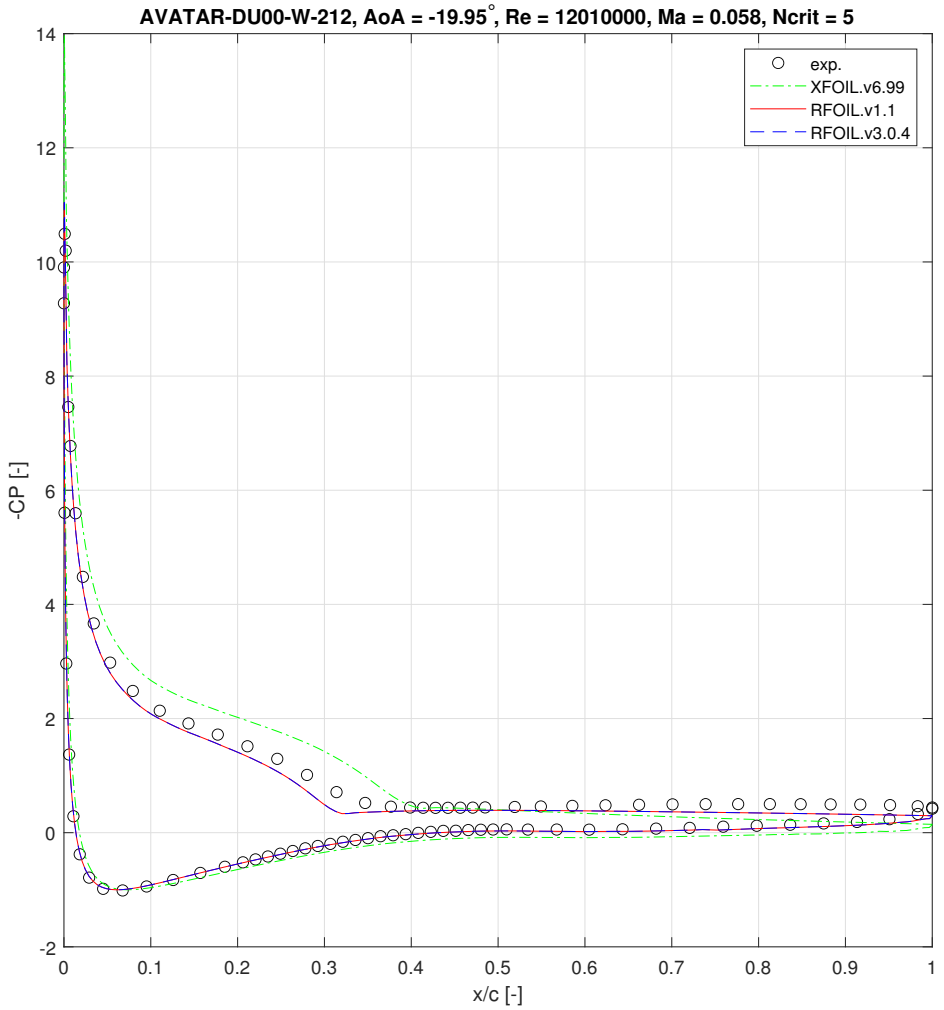

Figure C.87: Comparison between experimental and numerical pressure distributions for the AVATAR-DU00-W-212 airfoil at a Reynolds number of 15030000, and at an angle of attack and a Mach number of -1.014° and 0.081, respectively.

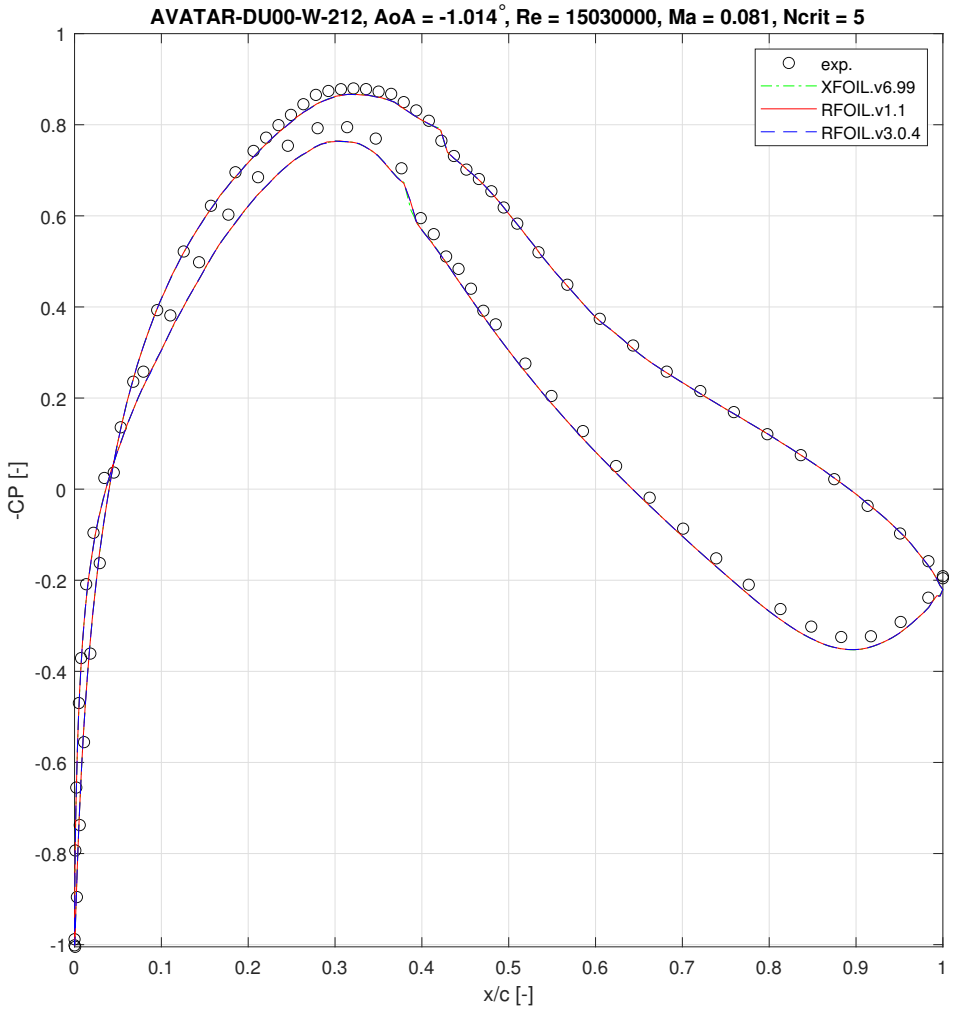

Figure C.88: Comparison between experimental and numerical pressure distributions for the AVATAR-DU00-W-212 airfoil at a Reynolds number of 3020000, and at an angle of attack and a Mach number of -1.014° and 0.074, respectively.

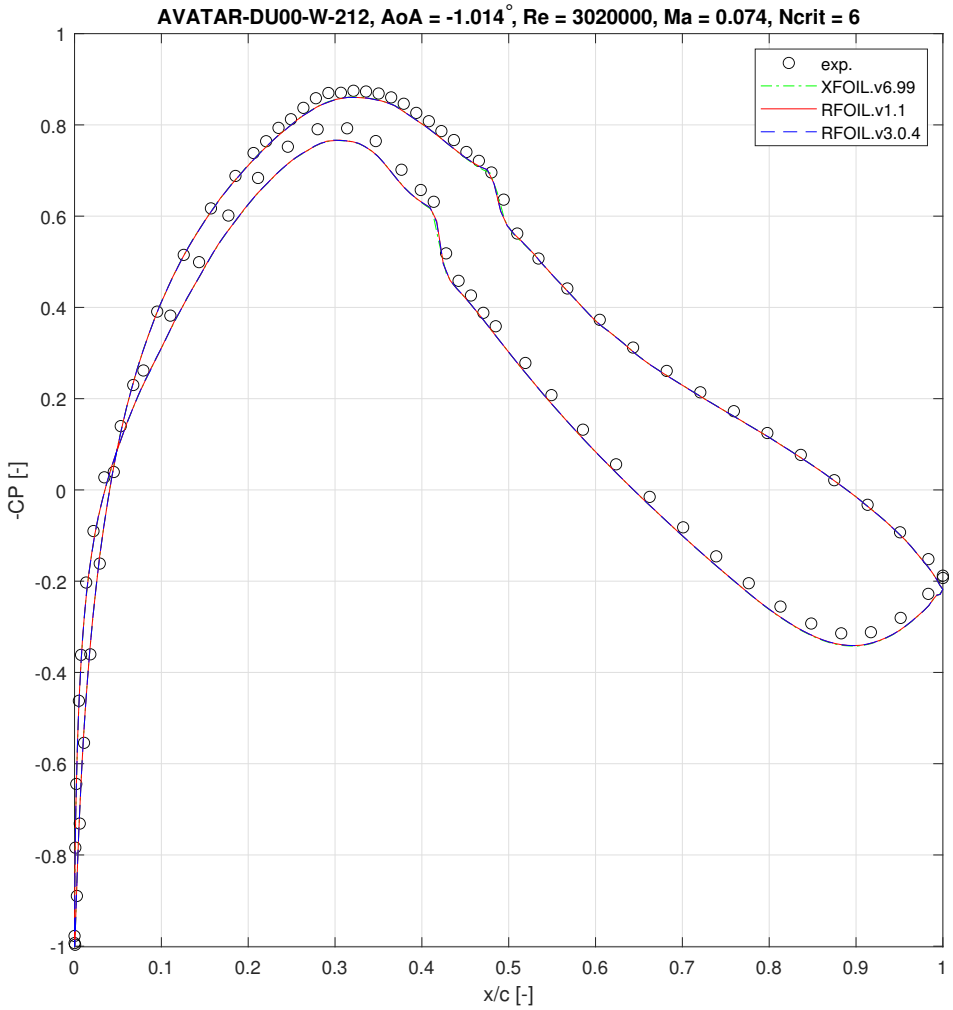

Figure C.89: Comparison between experimental and numerical pressure distributions for the AVATAR-DU00-W-212 airfoil at a Reynolds number of 9020000, and at an angle of attack and a Mach number of -1.014° and 0.083, respectively.

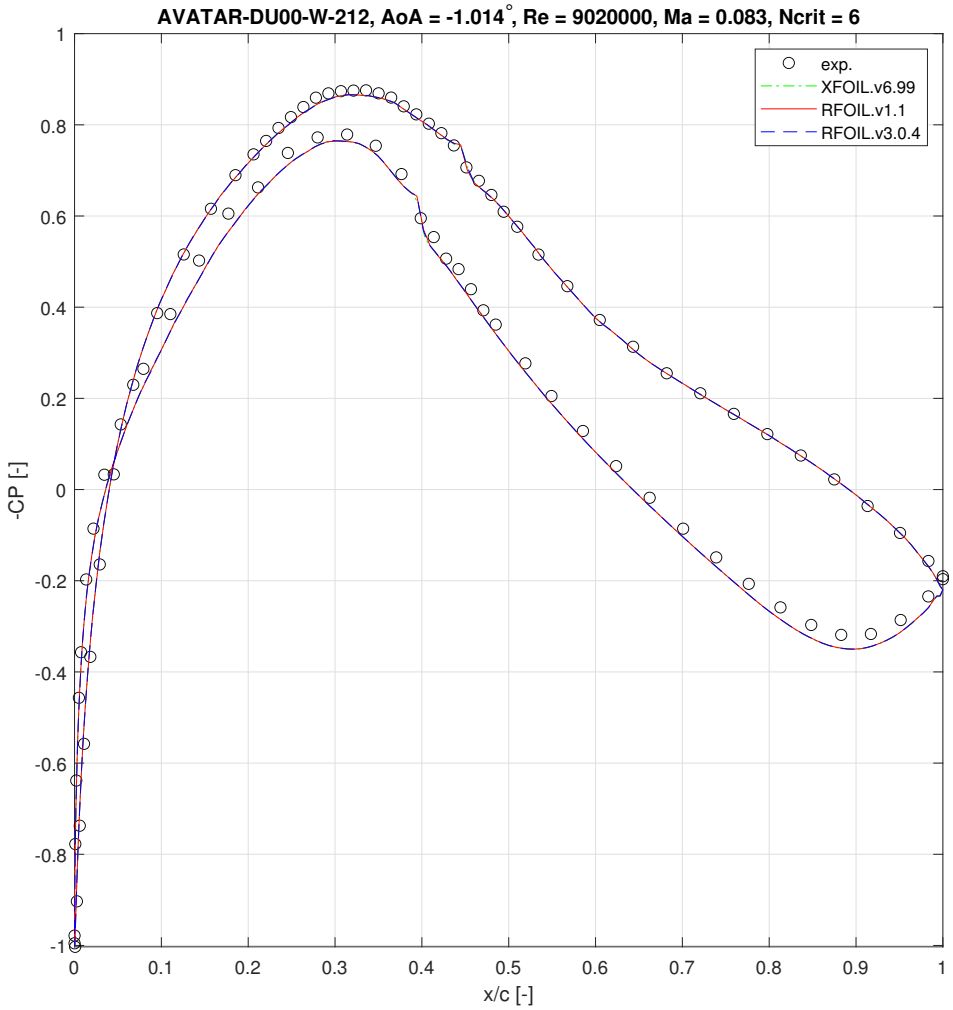

Figure C.90: Comparison between experimental and numerical pressure distributions for the AVATAR-DU00-W-212 airfoil at a Reynolds number of 6020000, and at an angle of attack and a Mach number of -1.015° and 0.055, respectively.

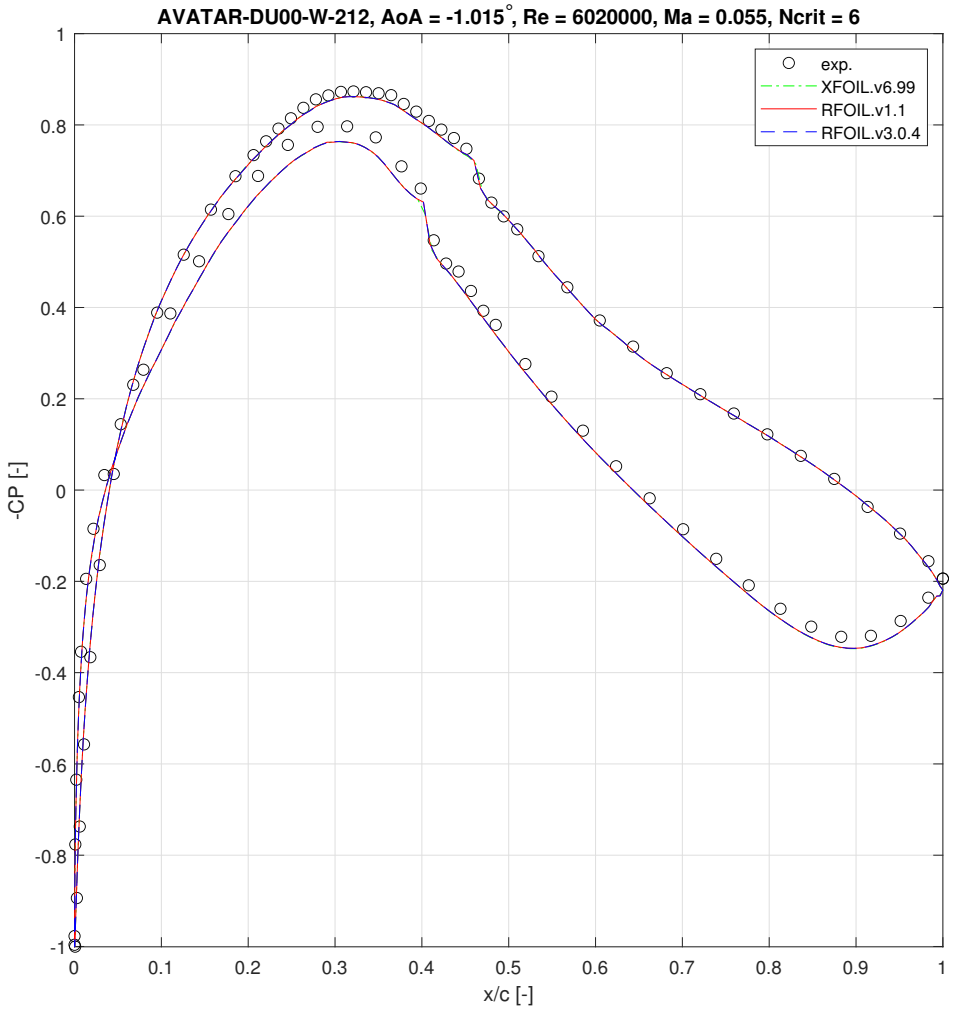

Figure C.91: Comparison between experimental and numerical pressure distributions for the AVATAR-DU00-W-212 airfoil at a Reynolds number of 6020000, and at an angle of attack and a Mach number of -1.016° and 0.029, respectively.

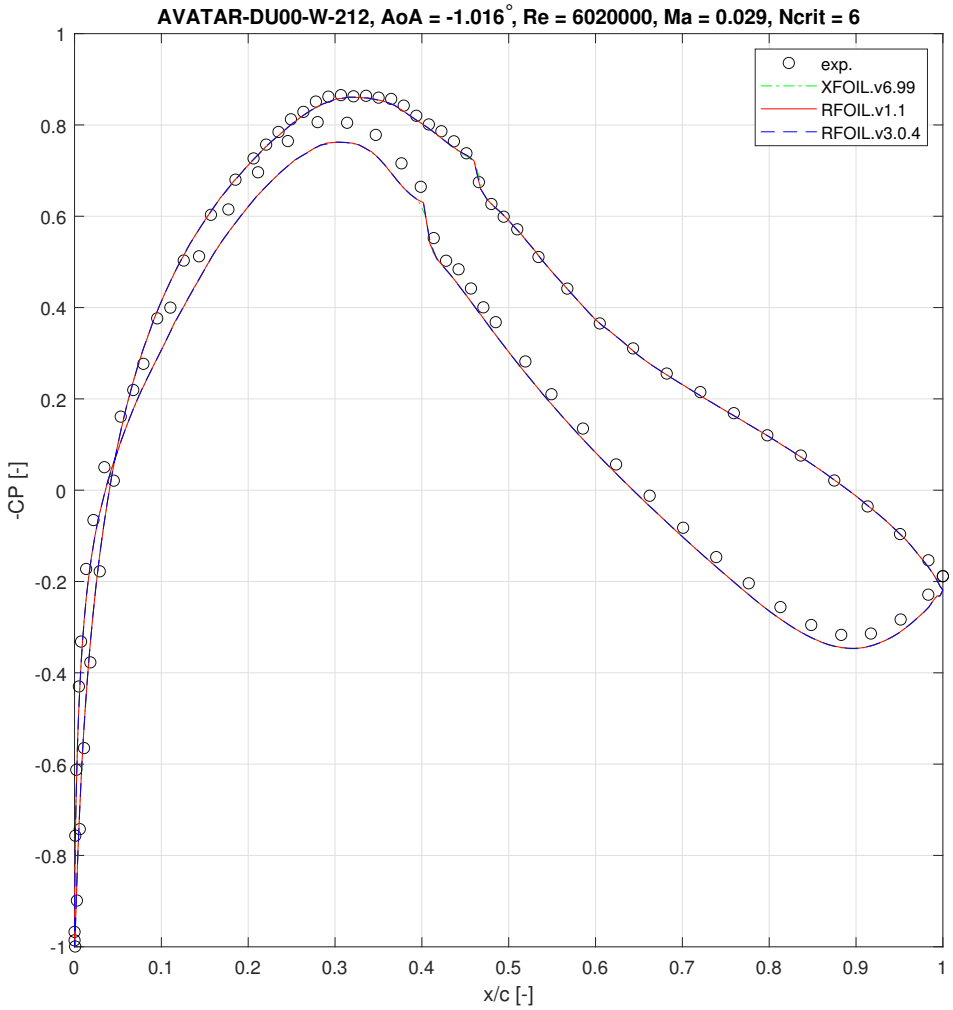

Figure C.92: Comparison between experimental and numerical pressure distributions for the AVATAR-DU00-W-212 airfoil at a Reynolds number of 9030000, and at an angle of attack and a Mach number of -1.016° and 0.044, respectively.

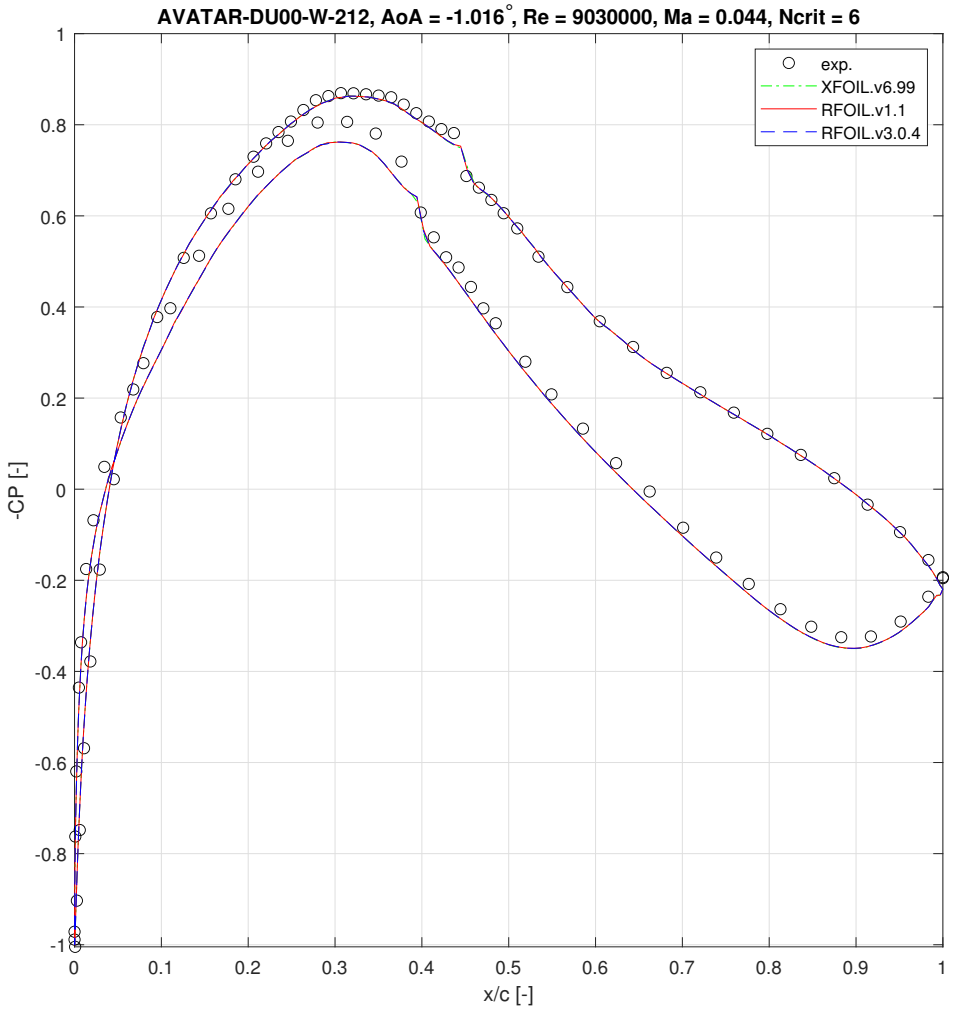

Figure C.93: Comparison between experimental and numerical pressure distributions for the AVATAR-DU00-W-212 airfoil at a Reynolds number of 12010000, and at an angle of attack and a Mach number of -1.955° and 0.058, respectively.

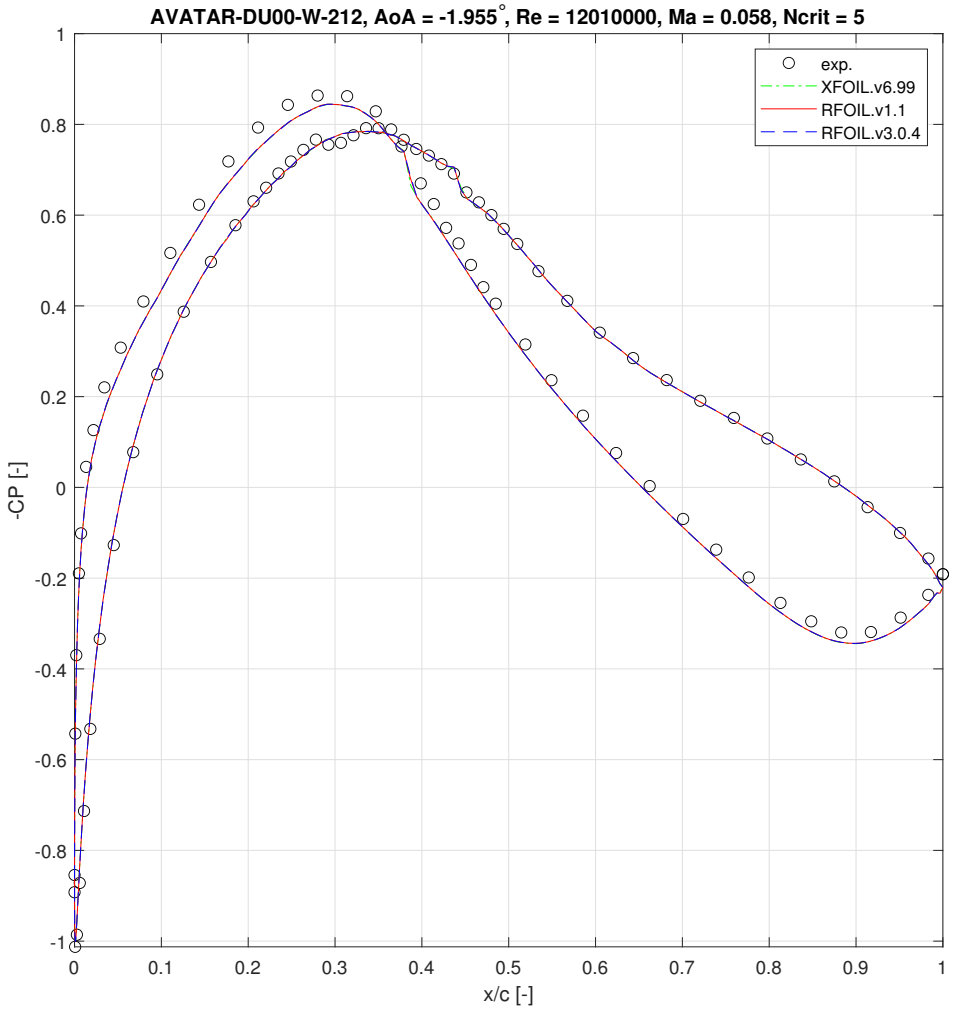

Figure C.94: Comparison between experimental and numerical pressure distributions for the AVATAR-DU00-W-212 airfoil at a Reynolds number of 2980000, and at an angle of attack and a Mach number of -20.108° and 0.074, respectively.

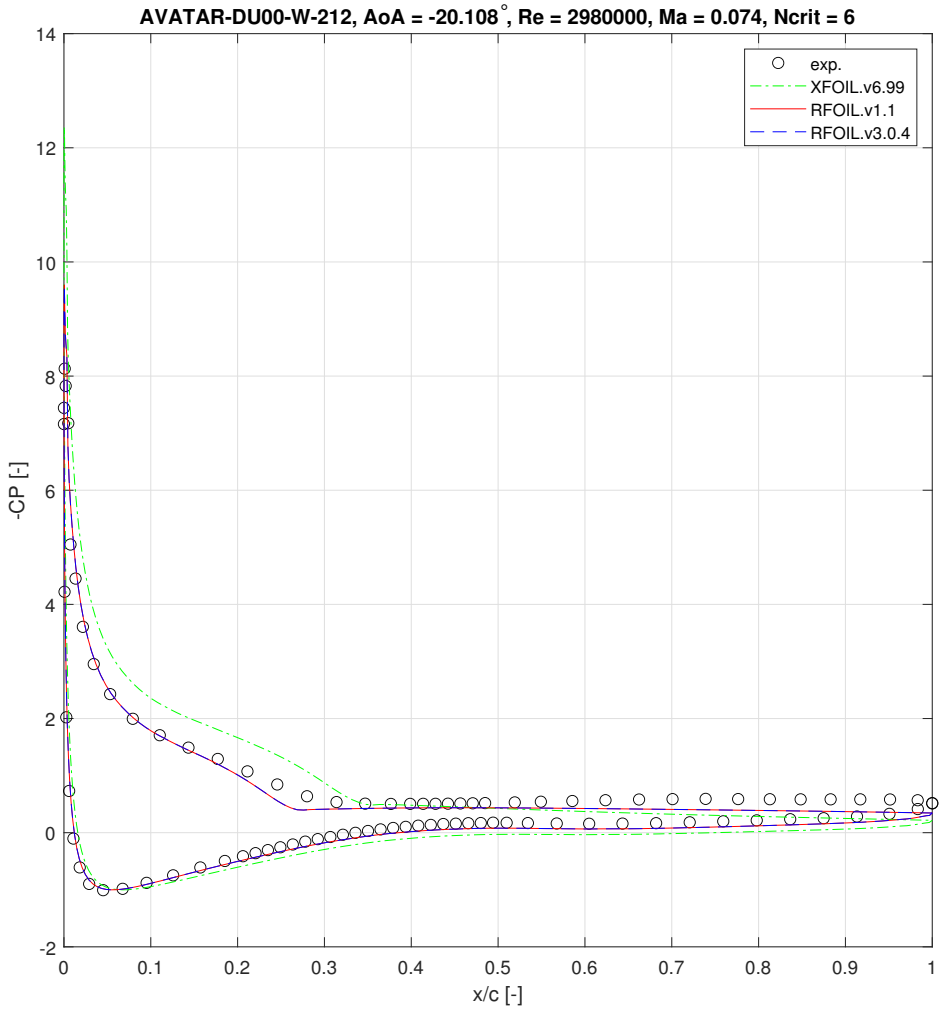

Figure C.95: Comparison between experimental and numerical pressure distributions for the AVATAR-DU00-W-212 airfoil at a Reynolds number of 5930000, and at an angle of attack and a Mach number of -20.122° and 0.054, respectively.

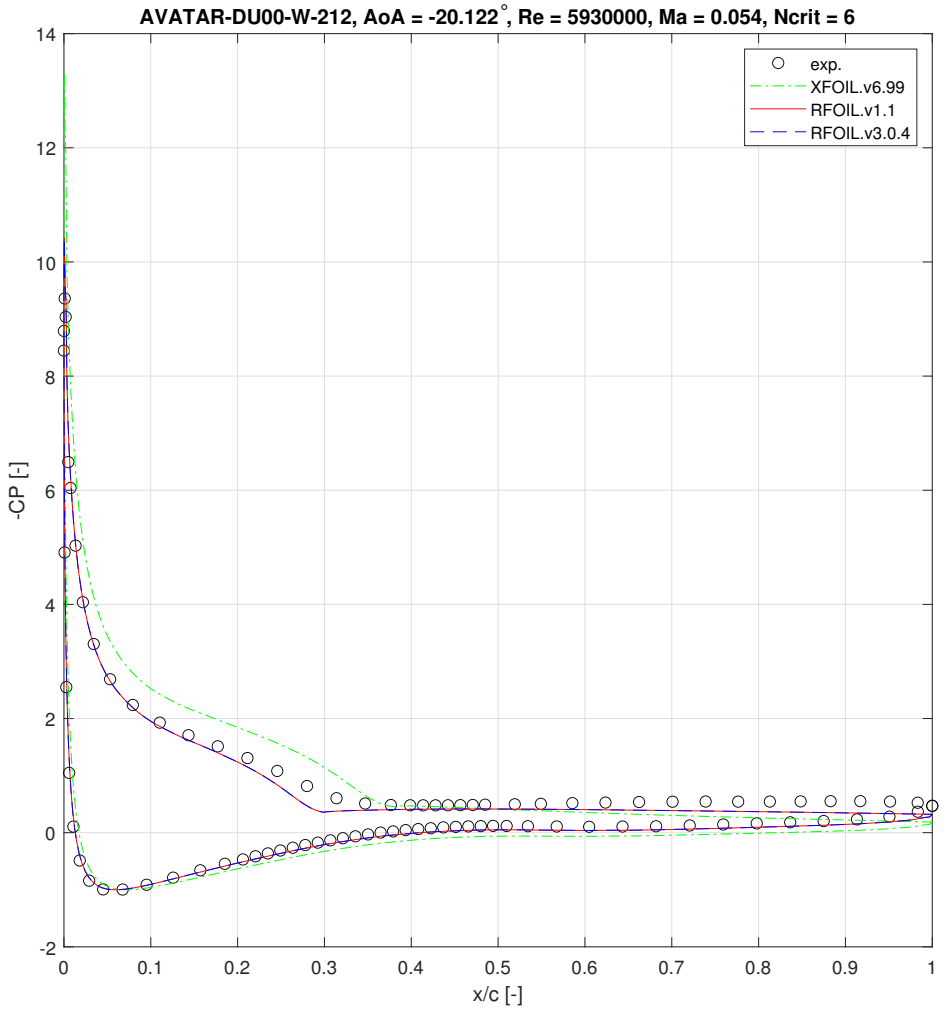

Figure C.96: Comparison between experimental and numerical pressure distributions for the AVATAR-DU00-W-212 airfoil at a Reynolds number of 5990000, and at an angle of attack and a Mach number of -20.123° and 0.029, respectively.

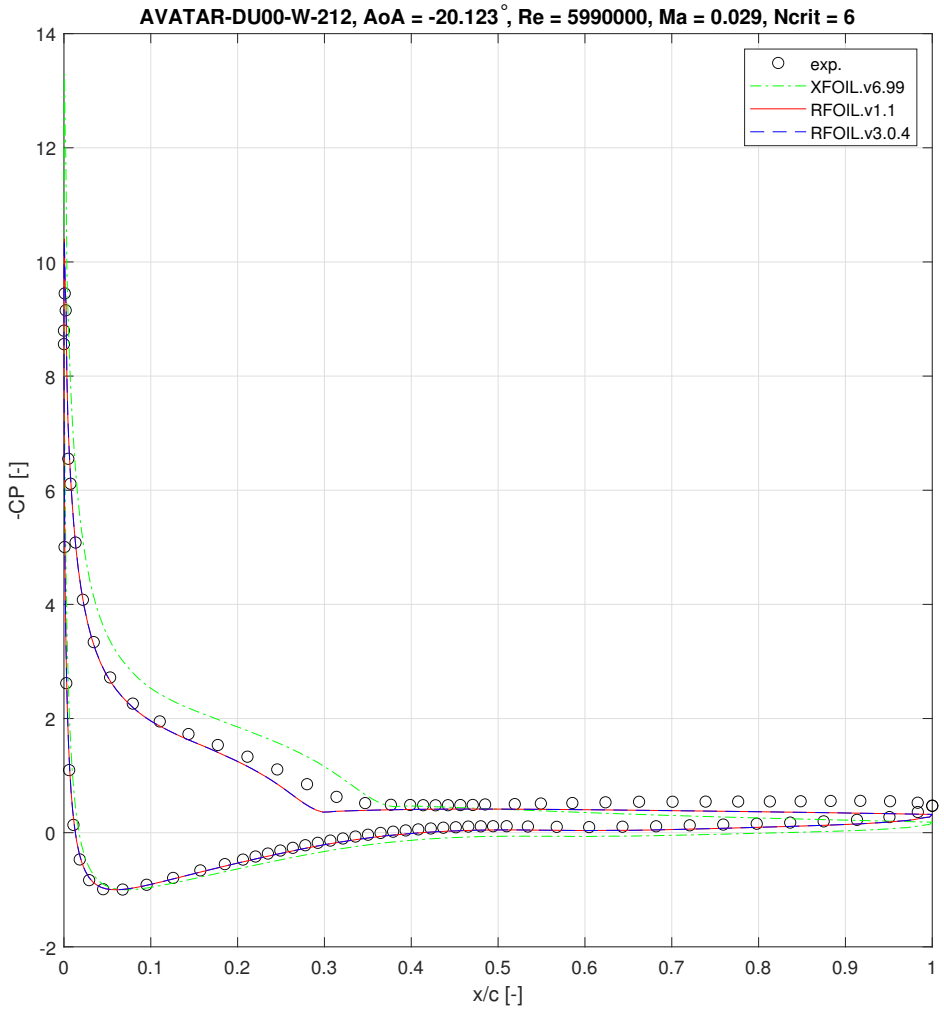

Figure C.97: Comparison between experimental and numerical pressure distributions for the AVATAR-DU00-W-212 airfoil at a Reynolds number of 9040000, and at an angle of attack and a Mach number of -20.133° and 0.044, respectively.

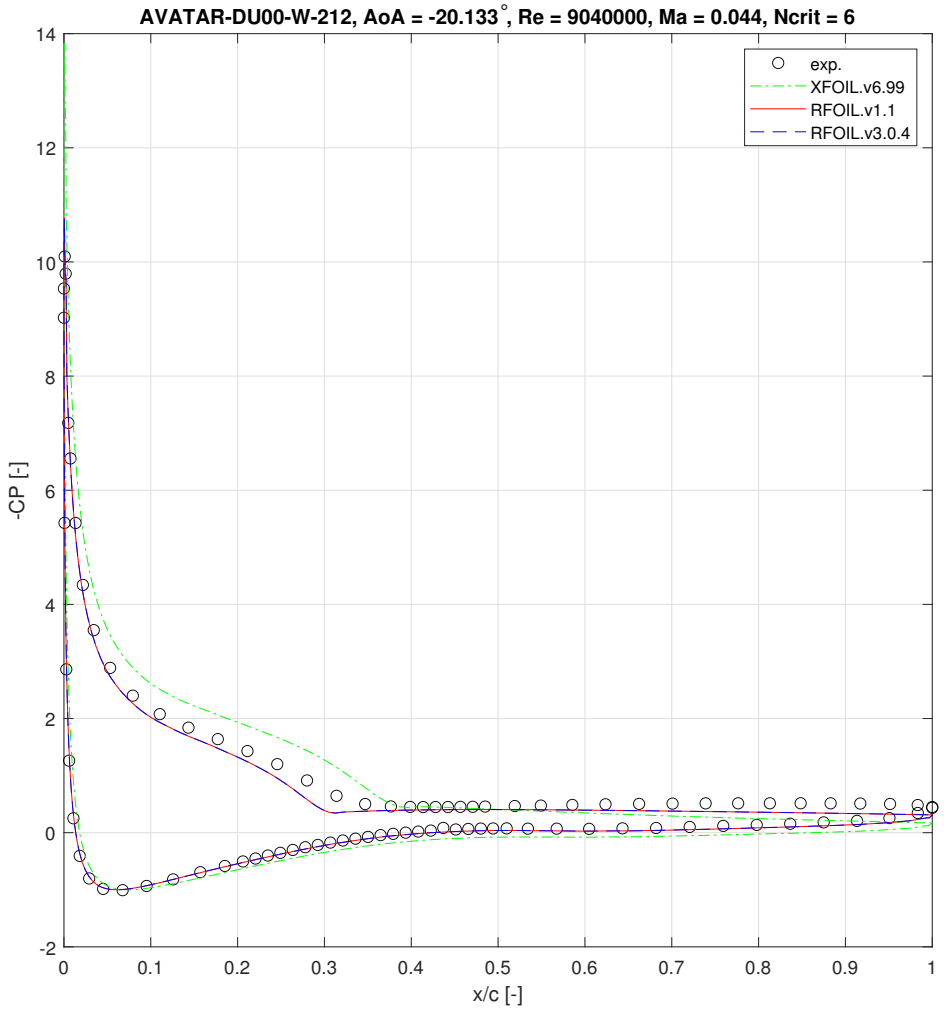

Figure C.98: Comparison between experimental and numerical pressure distributions for the AVATAR-DU00-W-212 airfoil at a Reynolds number of 9100000, and at an angle of attack and a Mach number of -20.133° and 0.084, respectively.

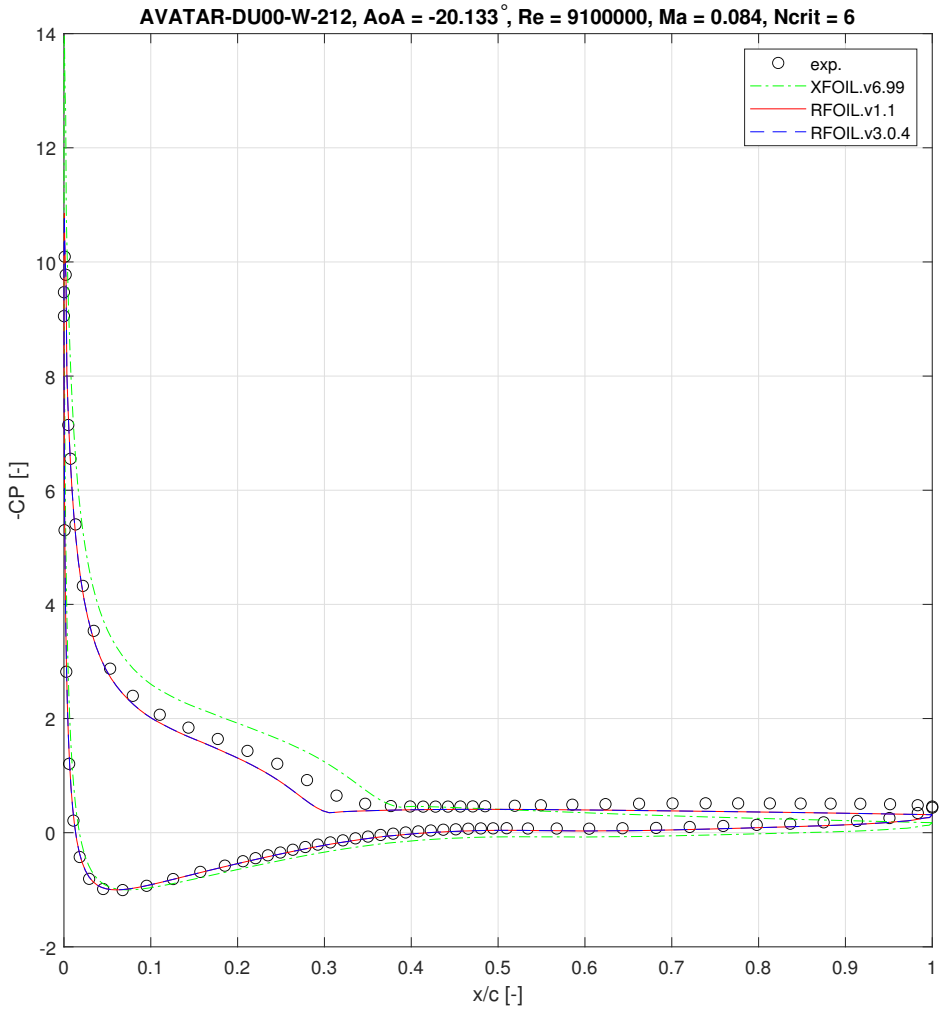

Figure C.99: Comparison between experimental and numerical pressure distributions for the AVATAR-DU00-W-212 airfoil at a Reynolds number of 3010000, and at an angle of attack and a Mach number of -2.027° and 0.074, respectively.

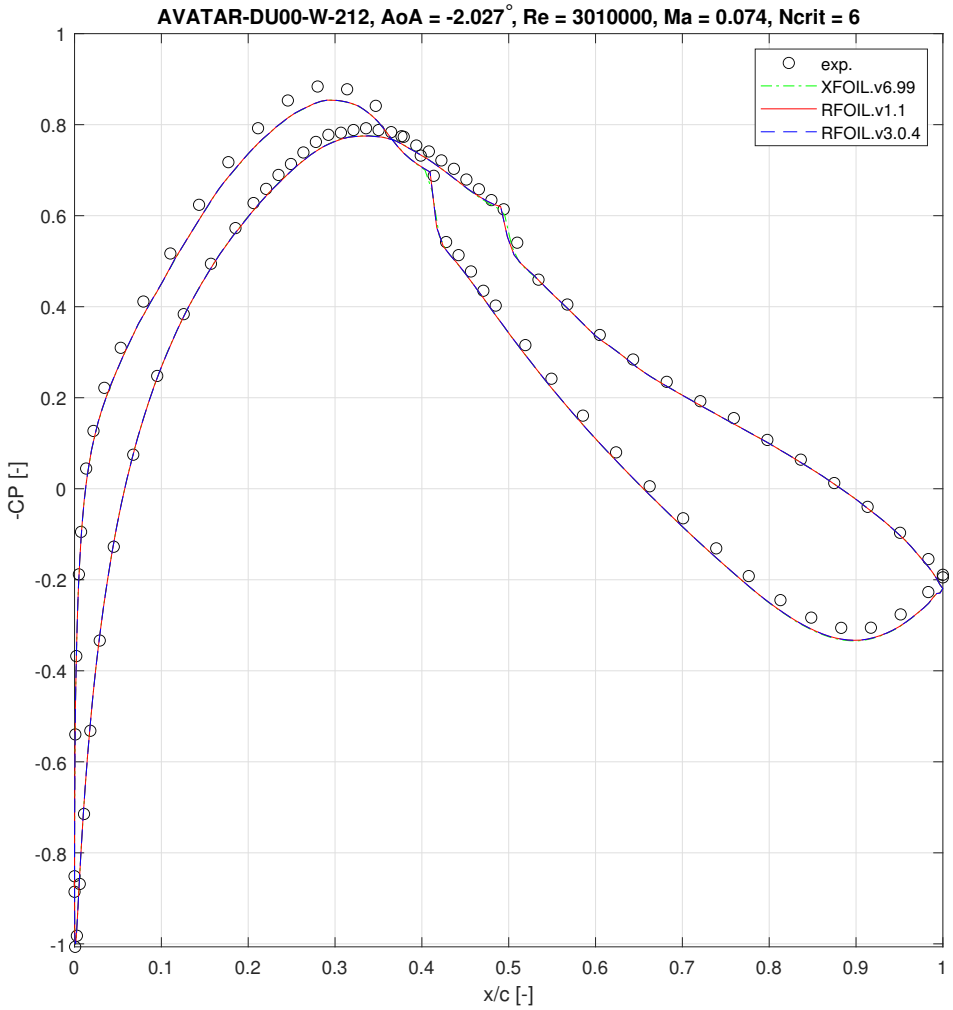

Figure C.100: Comparison between experimental and numerical pressure distributions for the AVATAR-DU00-W-212 airfoil at a Reynolds number of 15050000, and at an angle of attack and a Mach number of -2.028° and 0.082, respectively.

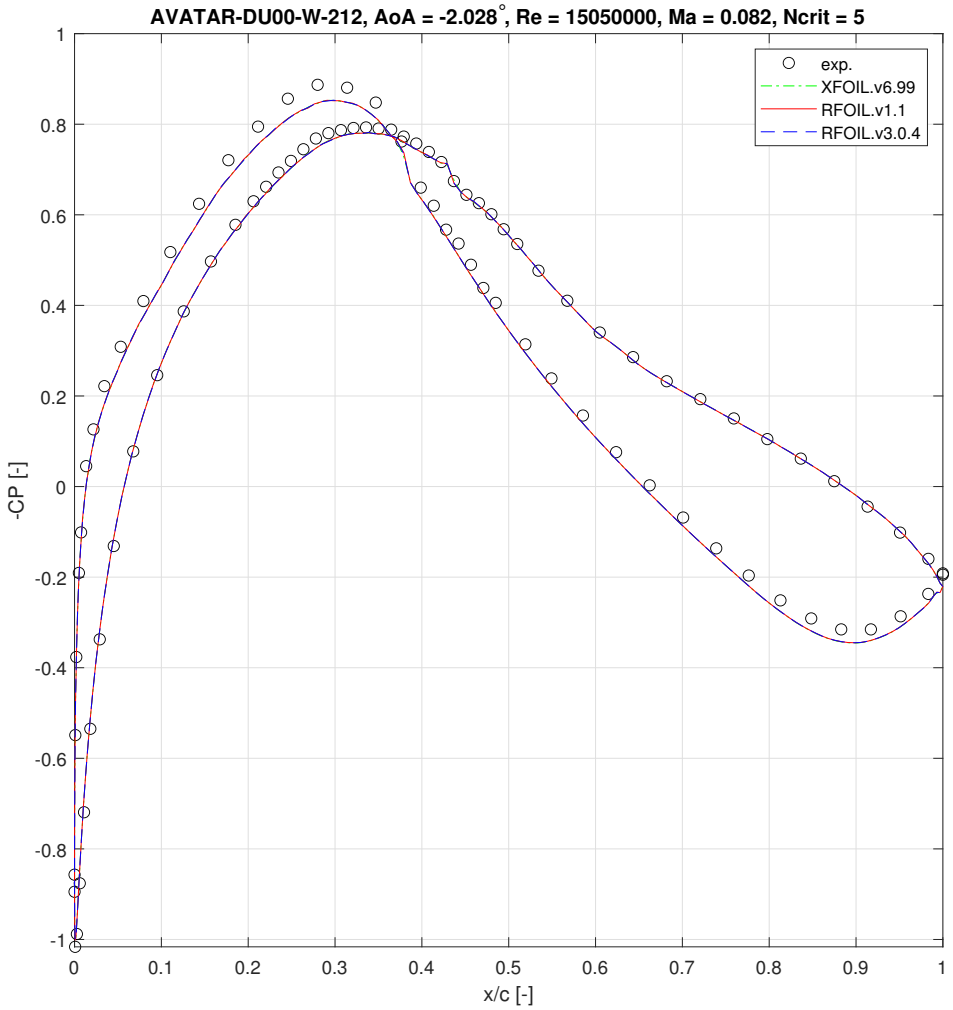

Figure C.101: Comparison between experimental and numerical pressure distributions for the AVATAR-DU00-W-212 airfoil at a Reynolds number of 6030000, and at an angle of attack and a Mach number of -2.028° and 0.055, respectively.

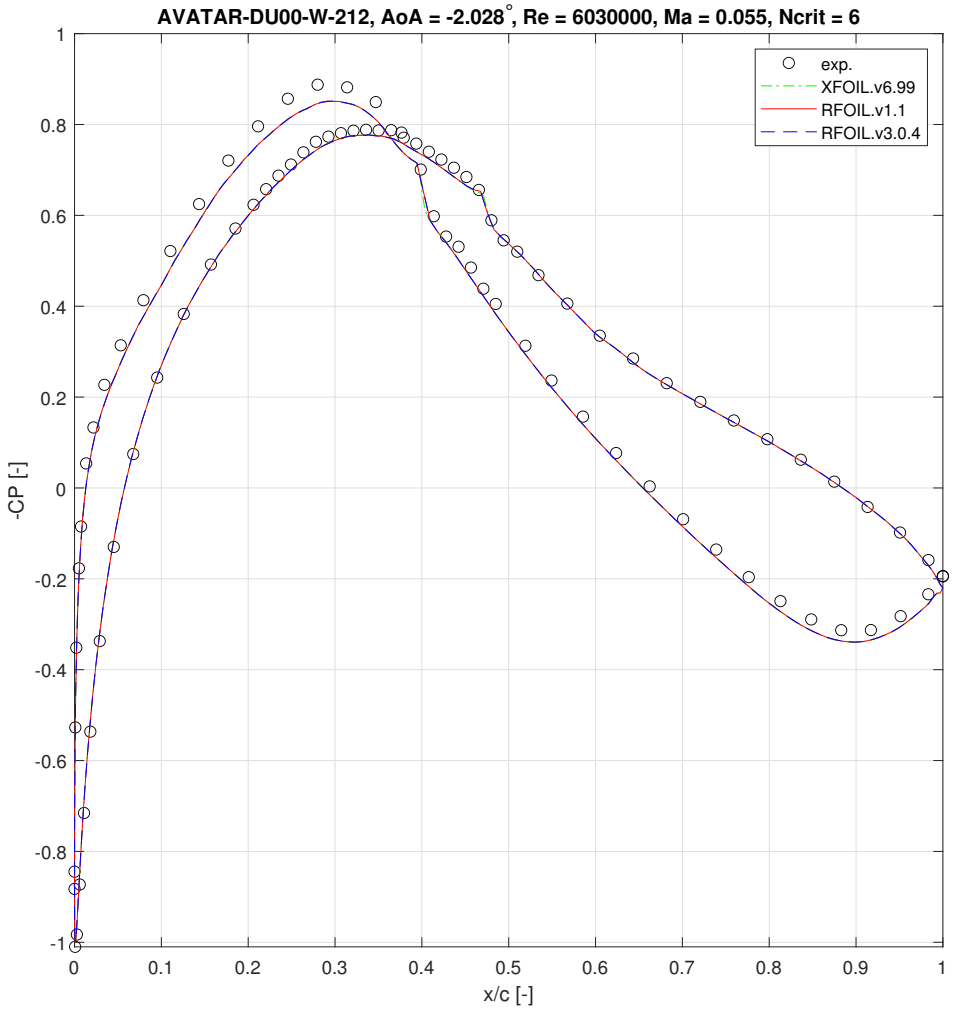

Figure C.102: Comparison between experimental and numerical pressure distributions for the AVATAR-DU00-W-212 airfoil at a Reynolds number of 9010000, and at an angle of attack and a Mach number of -2.028° and 0.083, respectively.

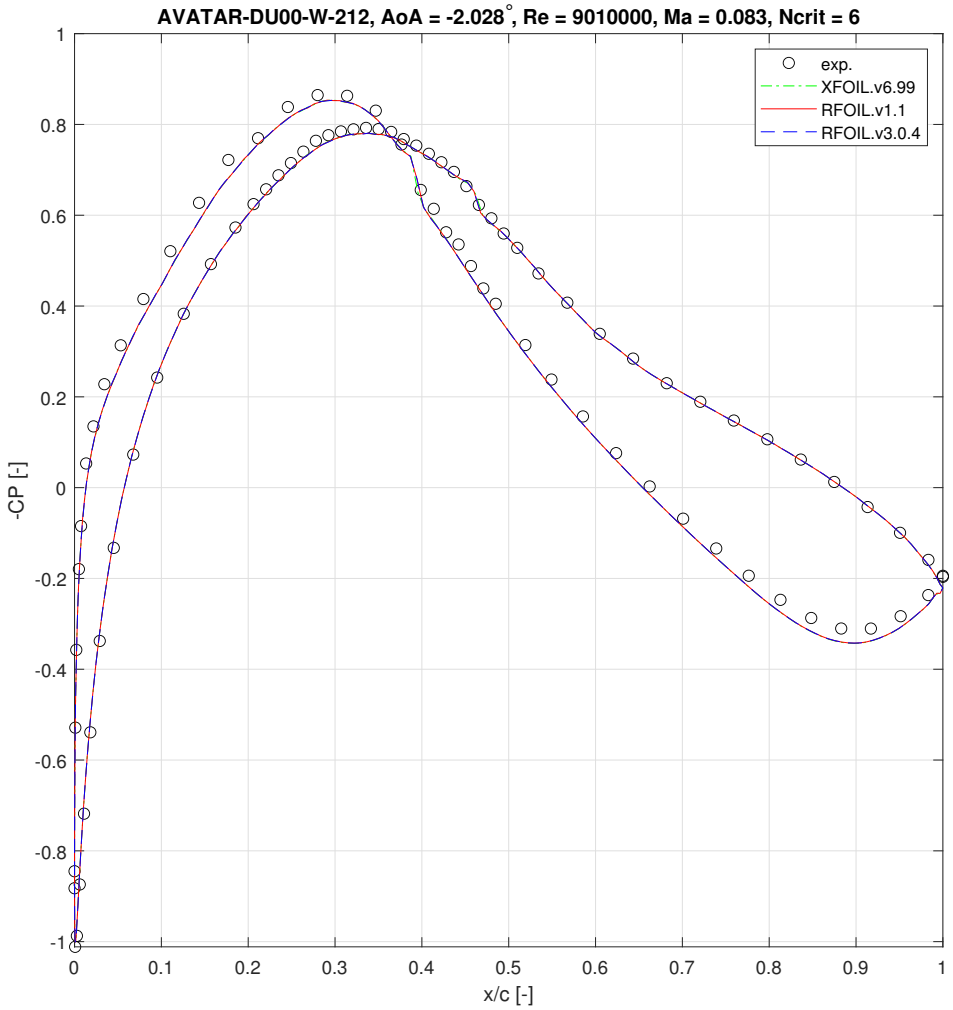

Figure C.103: Comparison between experimental and numerical pressure distributions for the AVATAR-DU00-W-212 airfoil at a Reynolds number of 6030000, and at an angle of attack and a Mach number of -2.029° and 0.029, respectively.

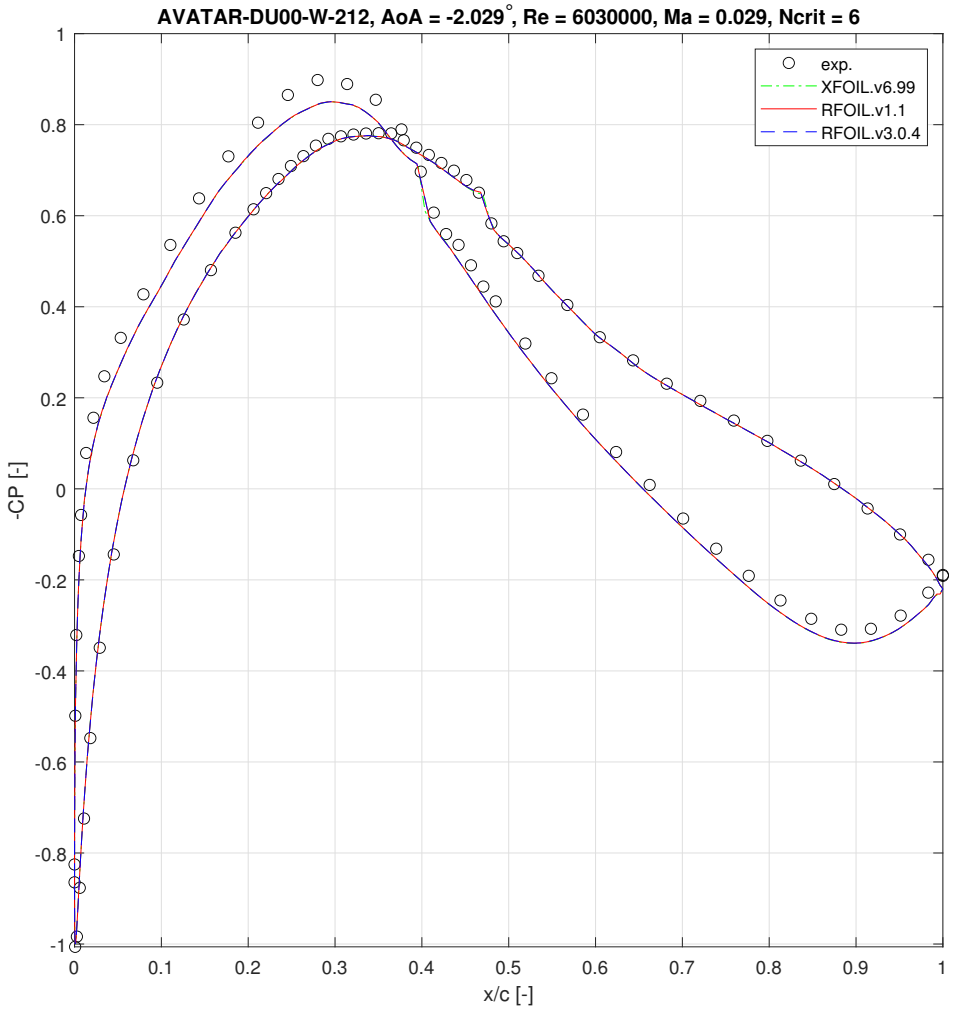

Figure C.104: Comparison between experimental and numerical pressure distributions for the AVATAR-DU00-W-212 airfoil at a Reynolds number of 9050000, and at an angle of attack and a Mach number of -2.029° and 0.044, respectively.

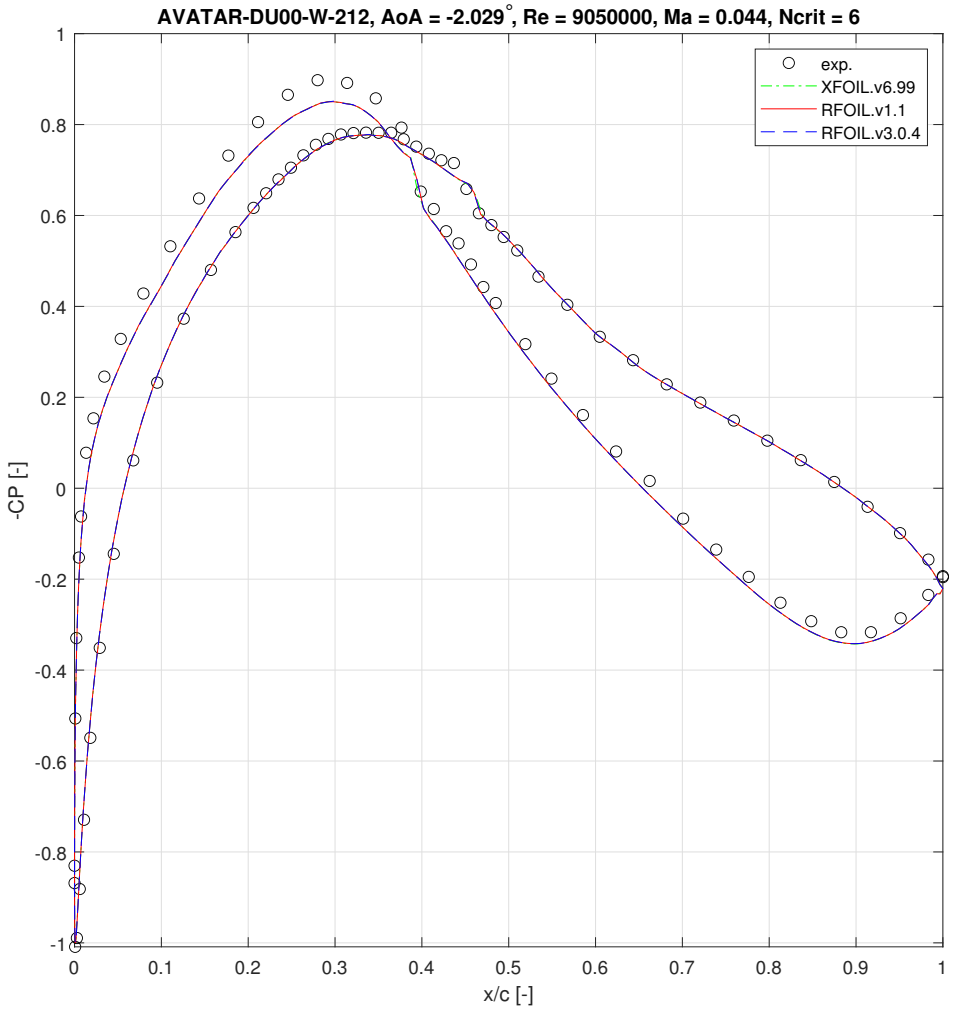

Figure C.105: Comparison between experimental and numerical pressure distributions for the AVATAR-DU00-W-212 airfoil at a Reynolds number of 15030000, and at an angle of attack and a Mach number of -2.535° and 0.082, respectively.

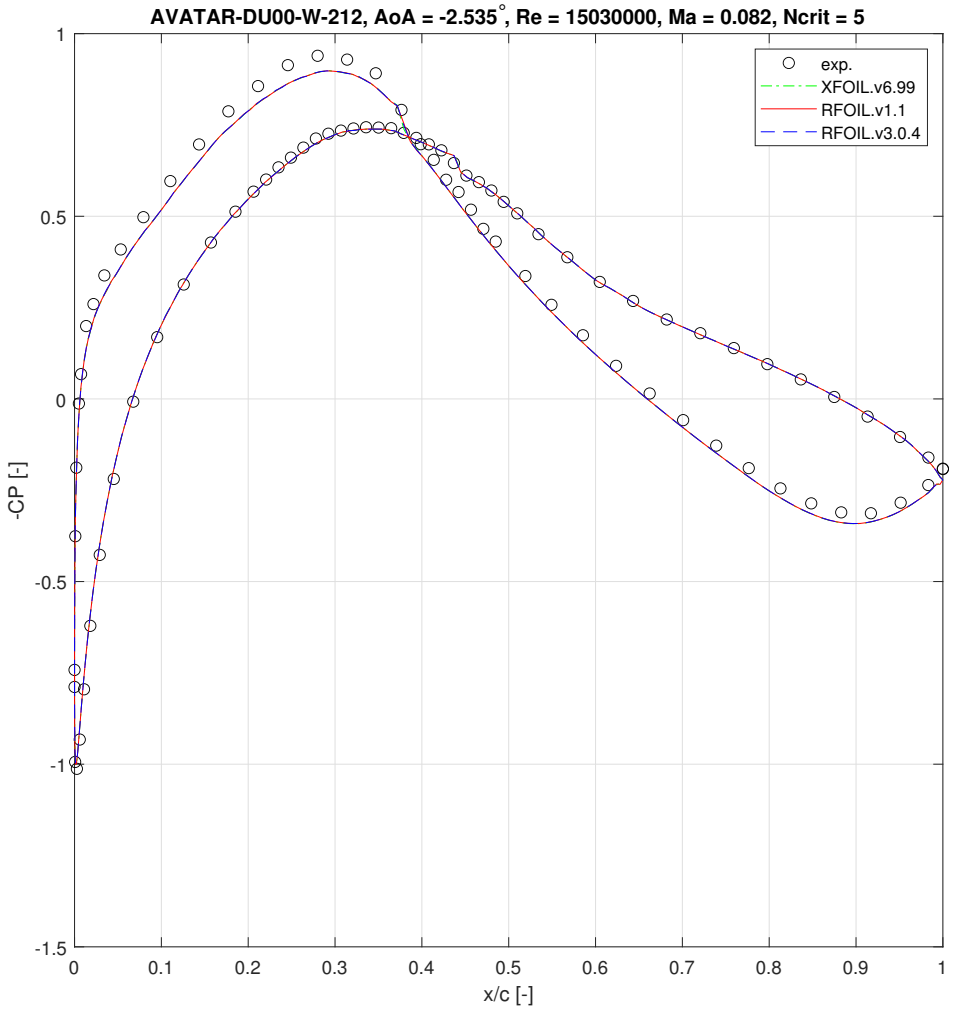

Figure C.106: Comparison between experimental and numerical pressure distributions for the AVATAR-DU00-W-212 airfoil at a Reynolds number of 12090000, and at an angle of attack and a Mach number of -2.956° and 0.058, respectively.

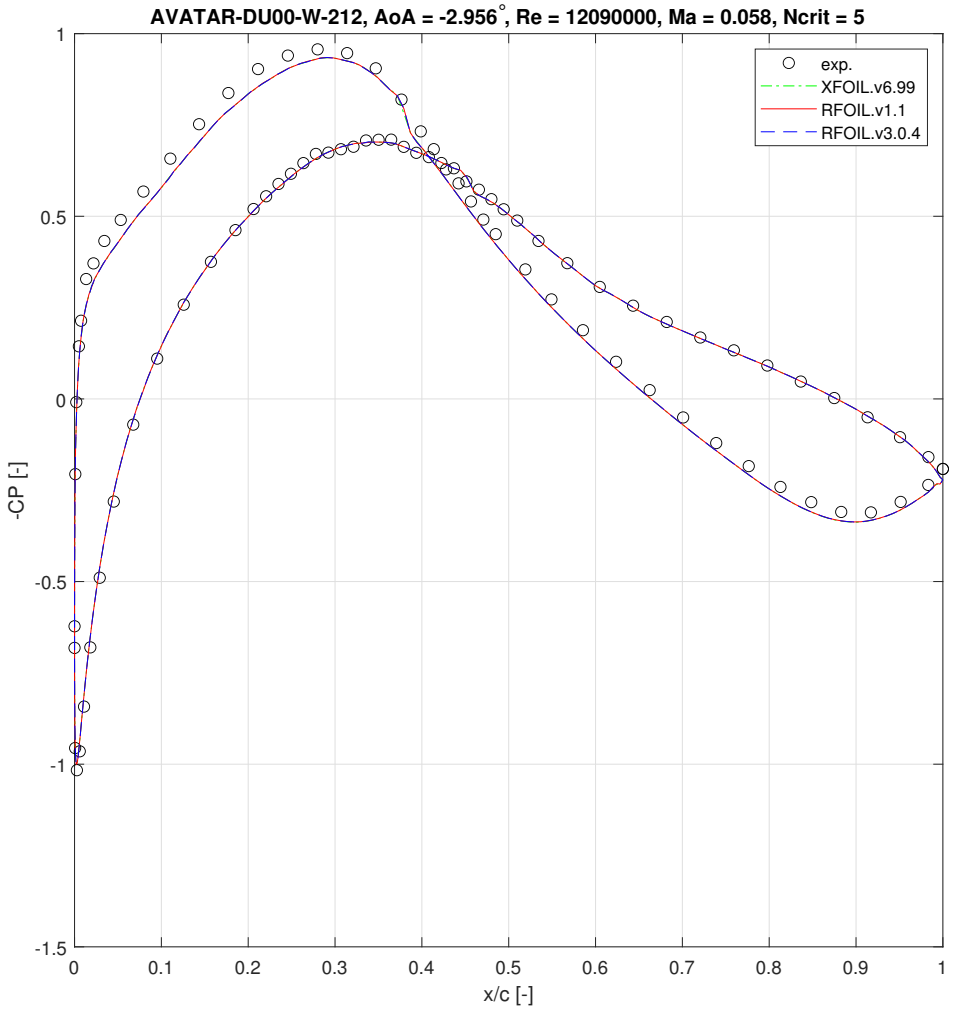

Figure C.107: Comparison between experimental and numerical pressure distributions for the AVATAR-DU00-W-212 airfoil at a Reynolds number of 3020000, and at an angle of attack and a Mach number of -3.041° and 0.075, respectively.

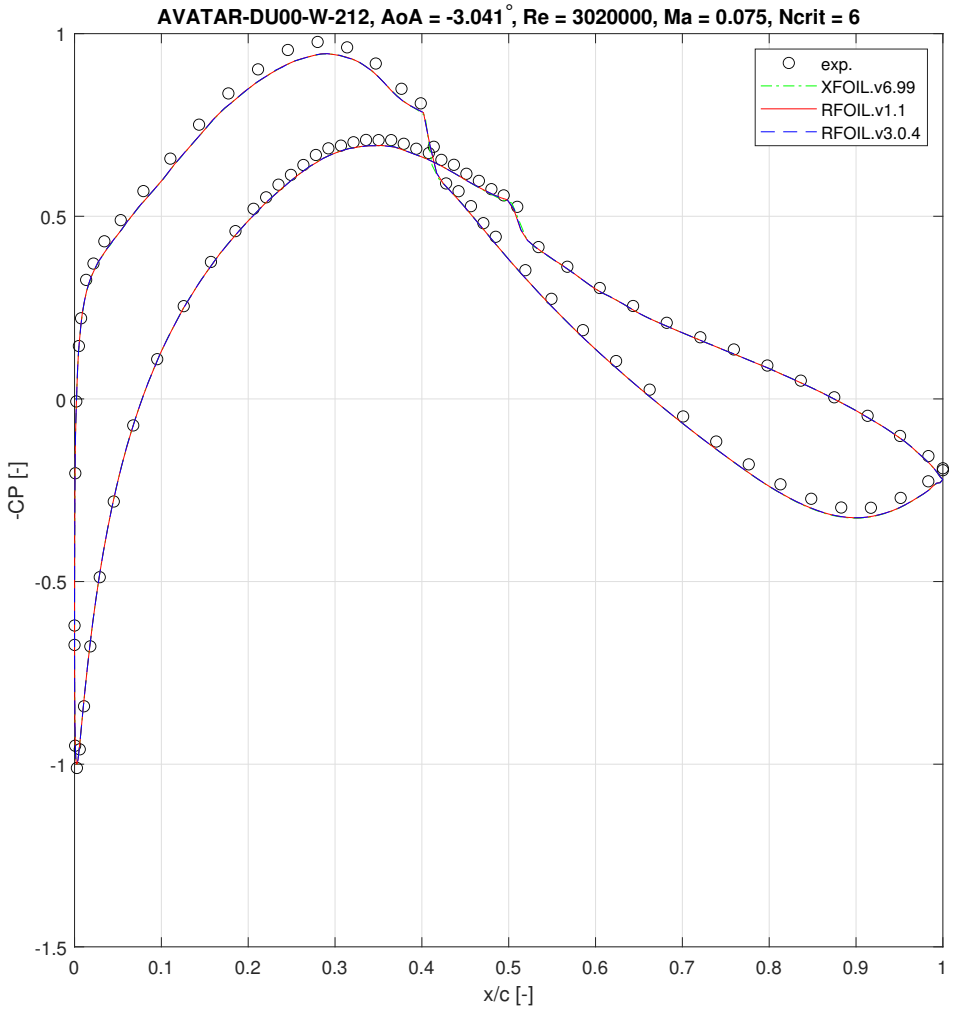

Figure C.108: Comparison between experimental and numerical pressure distributions for the AVATAR-DU00-W-212 airfoil at a Reynolds number of 6020000, and at an angle of attack and a Mach number of -3.041° and 0.055, respectively.

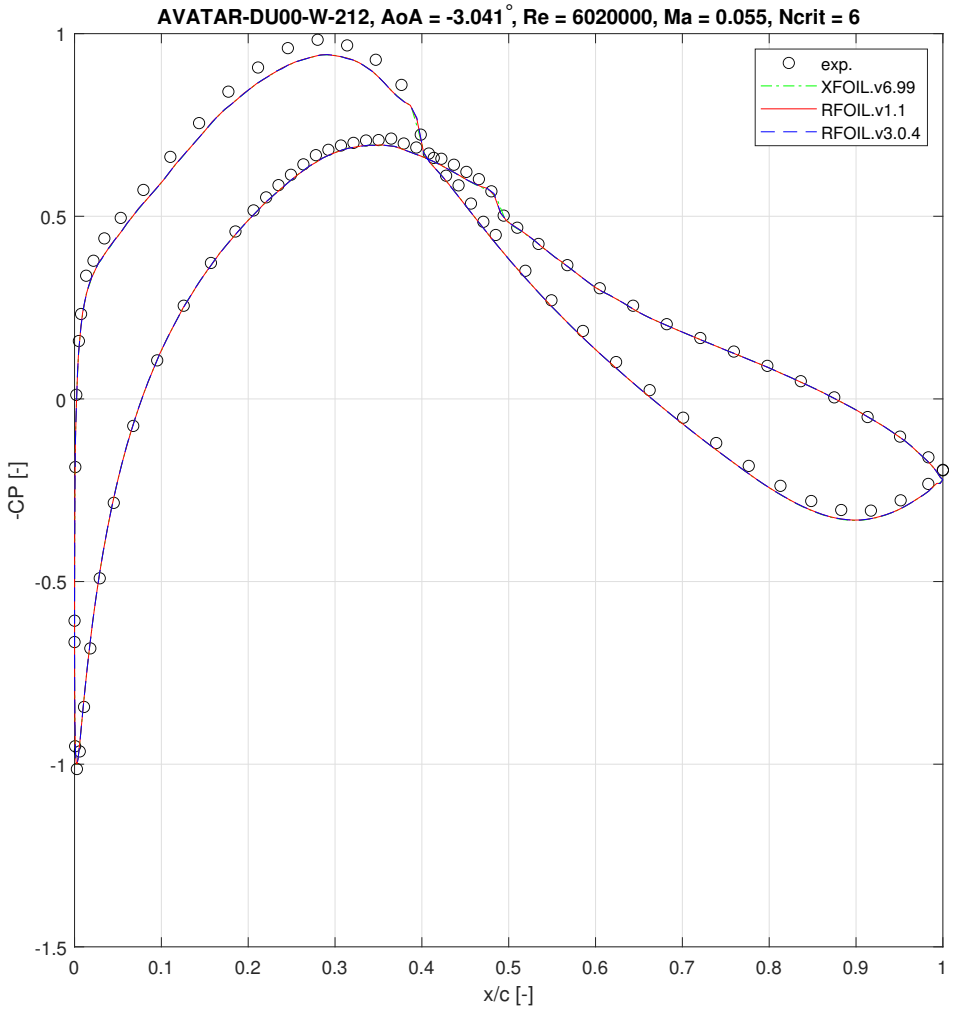

Figure C.109: Comparison between experimental and numerical pressure distributions for the AVATAR-DU00-W-212 airfoil at a Reynolds number of 9020000, and at an angle of attack and a Mach number of -3.041° and 0.083, respectively.

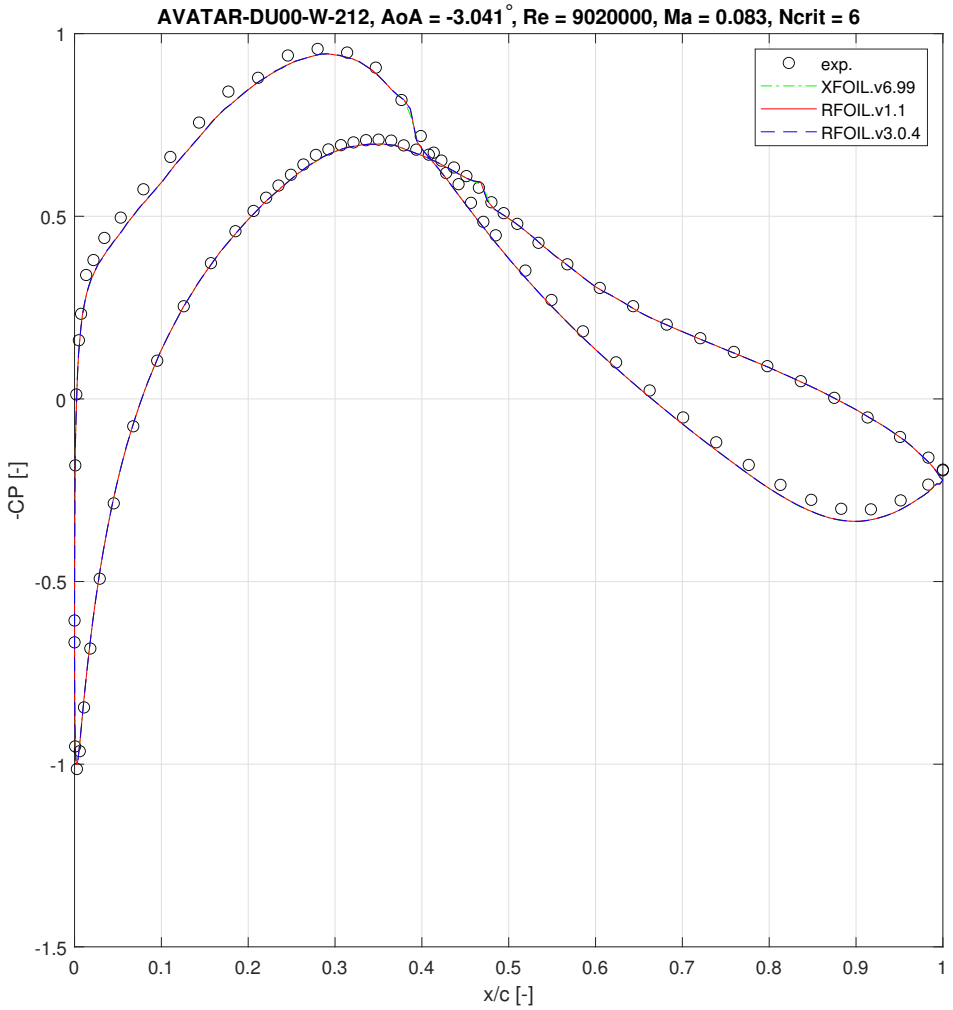

Figure C.110: Comparison between experimental and numerical pressure distributions for the AVATAR-DU00-W-212 airfoil at a Reynolds number of 15040000, and at an angle of attack and a Mach number of -3.042° and 0.082, respectively.

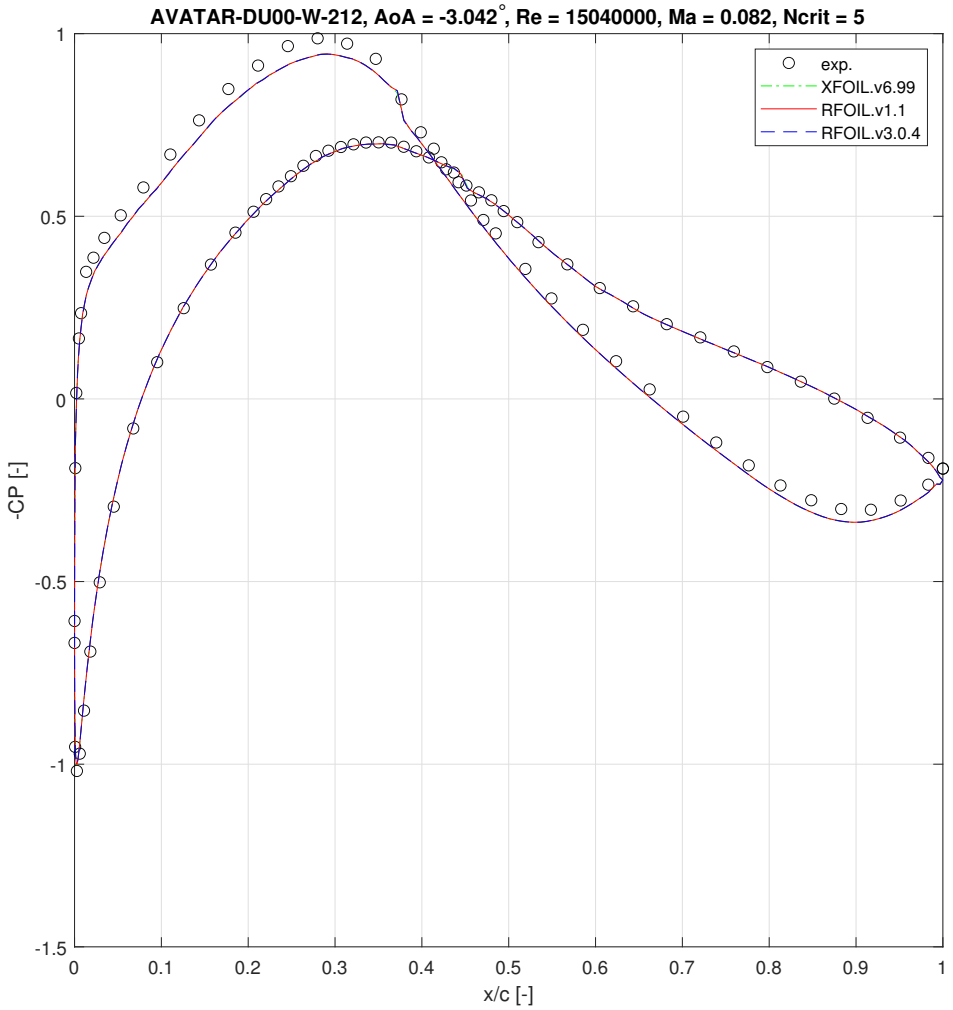

Figure C.111: Comparison between experimental and numerical pressure distributions for the AVATAR-DU00-W-212 airfoil at a Reynolds number of 6000000, and at an angle of attack and a Mach number of -3.042° and 0.029, respectively.

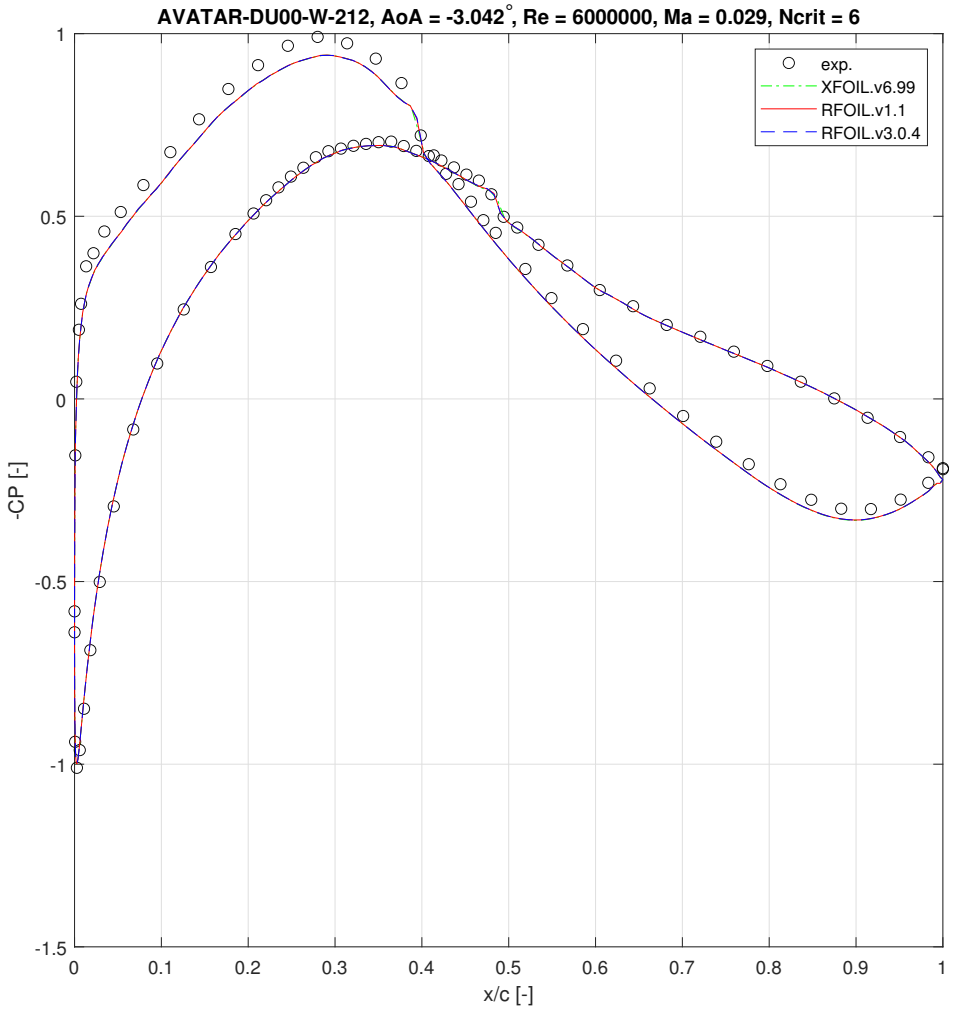

Figure C.112: Comparison between experimental and numerical pressure distributions for the AVATAR-DU00-W-212 airfoil at a Reynolds number of 8980000, and at an angle of attack and a Mach number of -3.042° and 0.043, respectively.

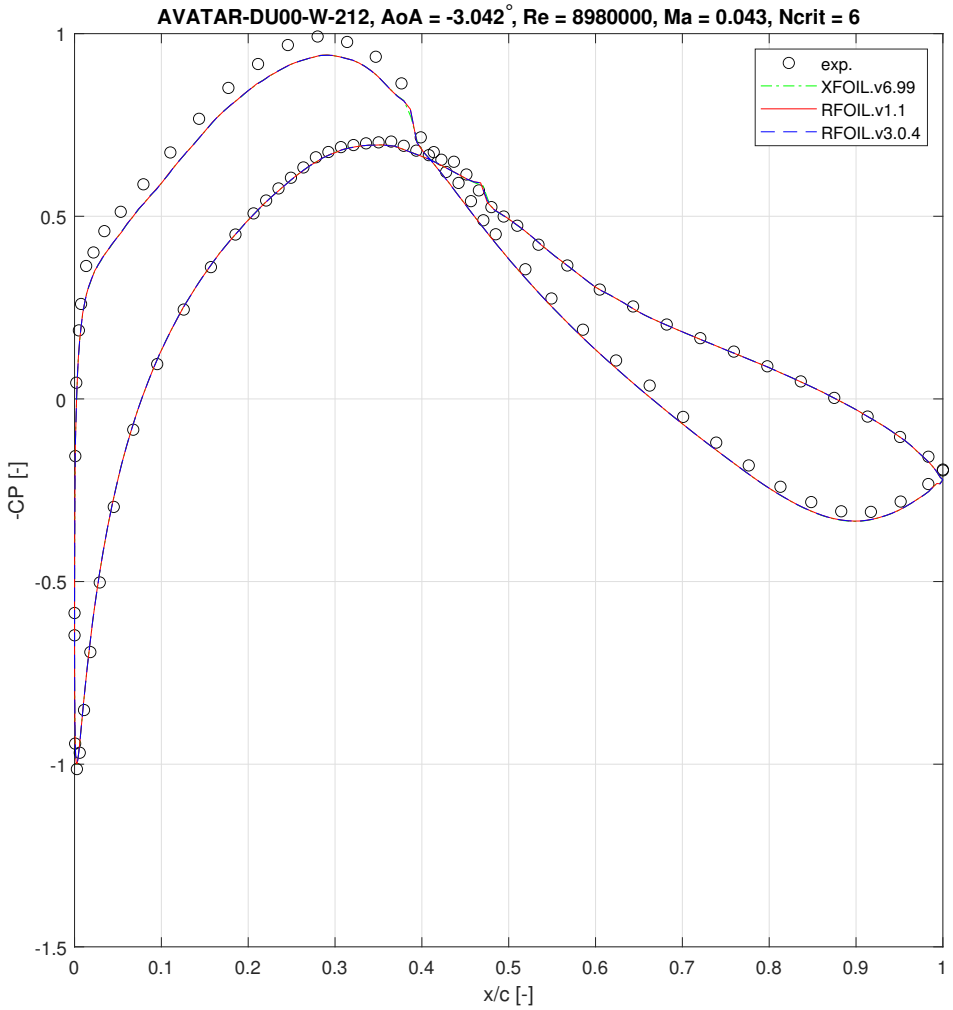

Figure C.113: Comparison between experimental and numerical pressure distributions for the AVATAR-DU00-W-212 airfoil at a Reynolds number of 12000000, and at an angle of attack and a Mach number of -3.154° and 0.058, respectively.

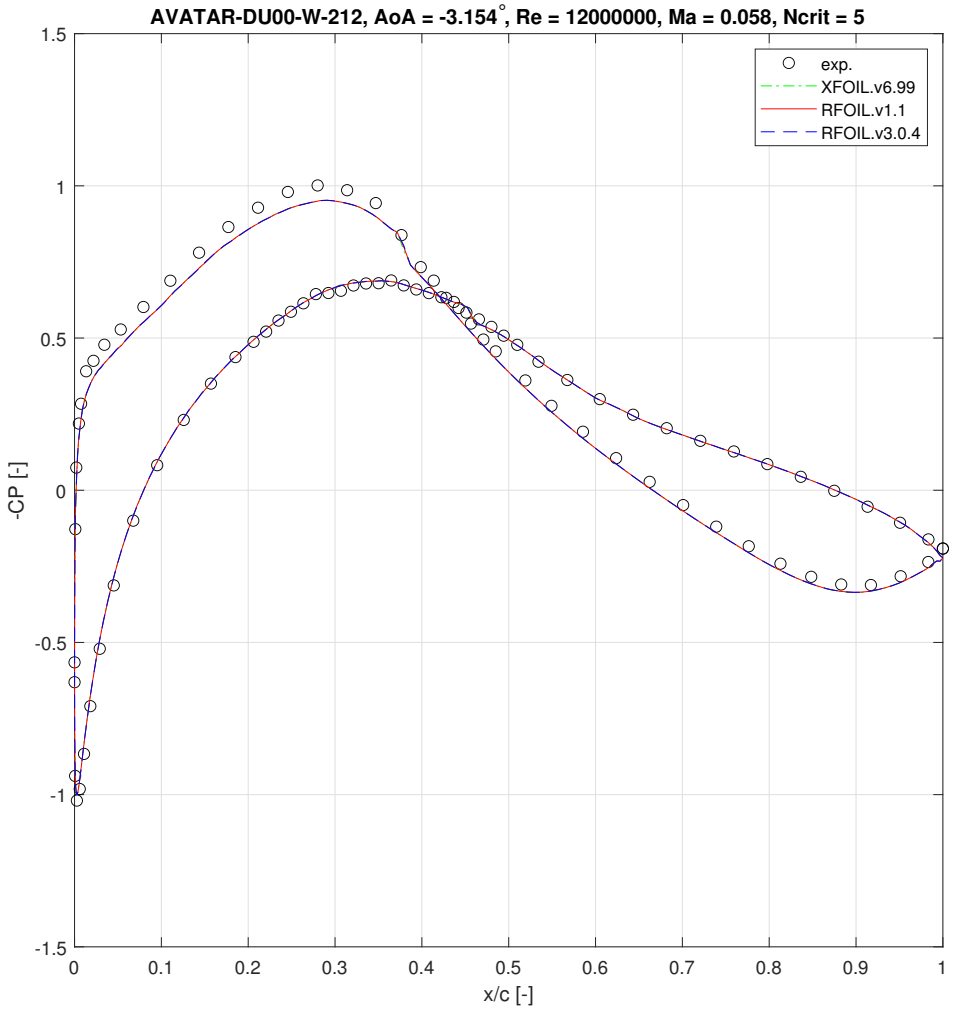

Figure C.114: Comparison between experimental and numerical pressure distributions for the AVATAR-DU00-W-212 airfoil at a Reynolds number of 14980000, and at an angle of attack and a Mach number of -3.244° and 0.081, respectively.

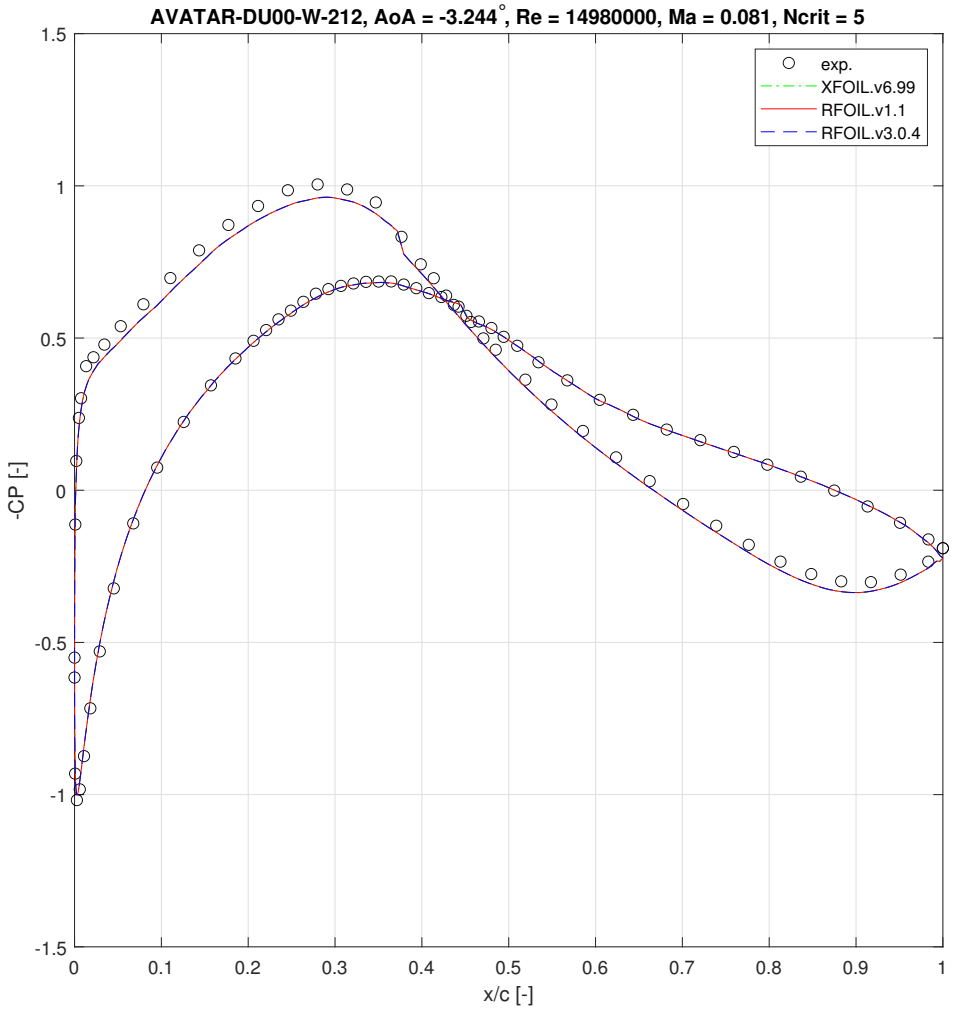

Figure C.115: Comparison between experimental and numerical pressure distributions for the AVATAR-DU00-W-212 airfoil at a Reynolds number of 15030000, and at an angle of attack and a Mach number of -3.447° and 0.082, respectively.

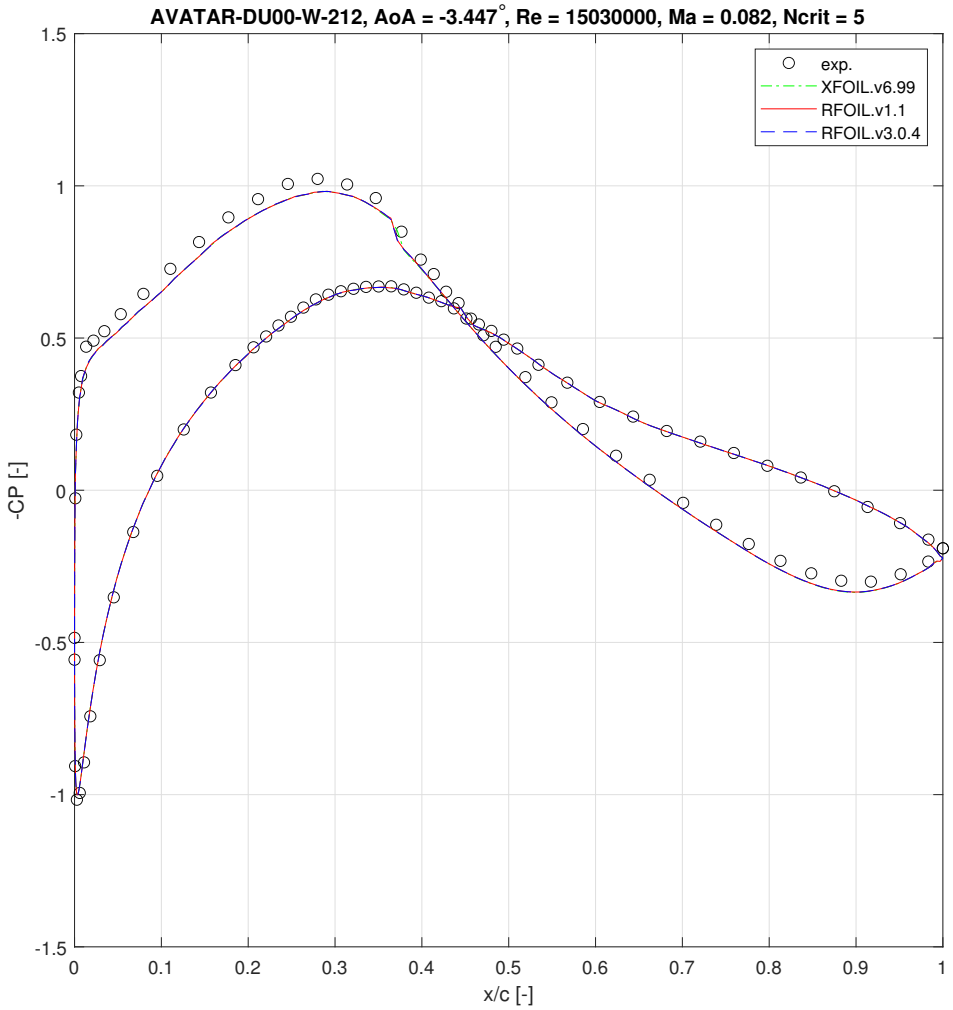

Figure C.116: Comparison between experimental and numerical pressure distributions for the AVATAR-DU00-W-212 airfoil at a Reynolds number of 12040000, and at an angle of attack and a Mach number of -3.553° and 0.058, respectively.

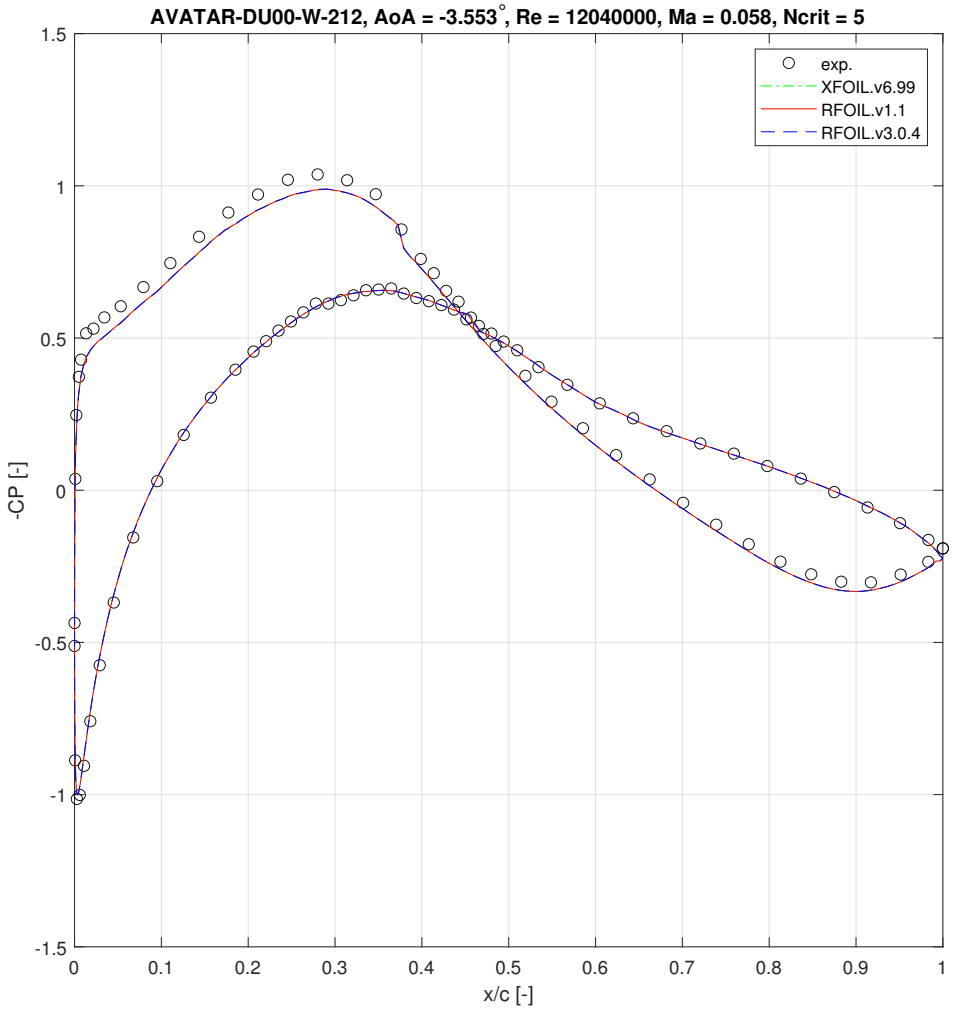

Figure C.117: Comparison between experimental and numerical pressure distributions for the AVATAR-DU00-W-212 airfoil at a Reynolds number of 15000000, and at an angle of attack and a Mach number of -3.650° and 0.081, respectively.

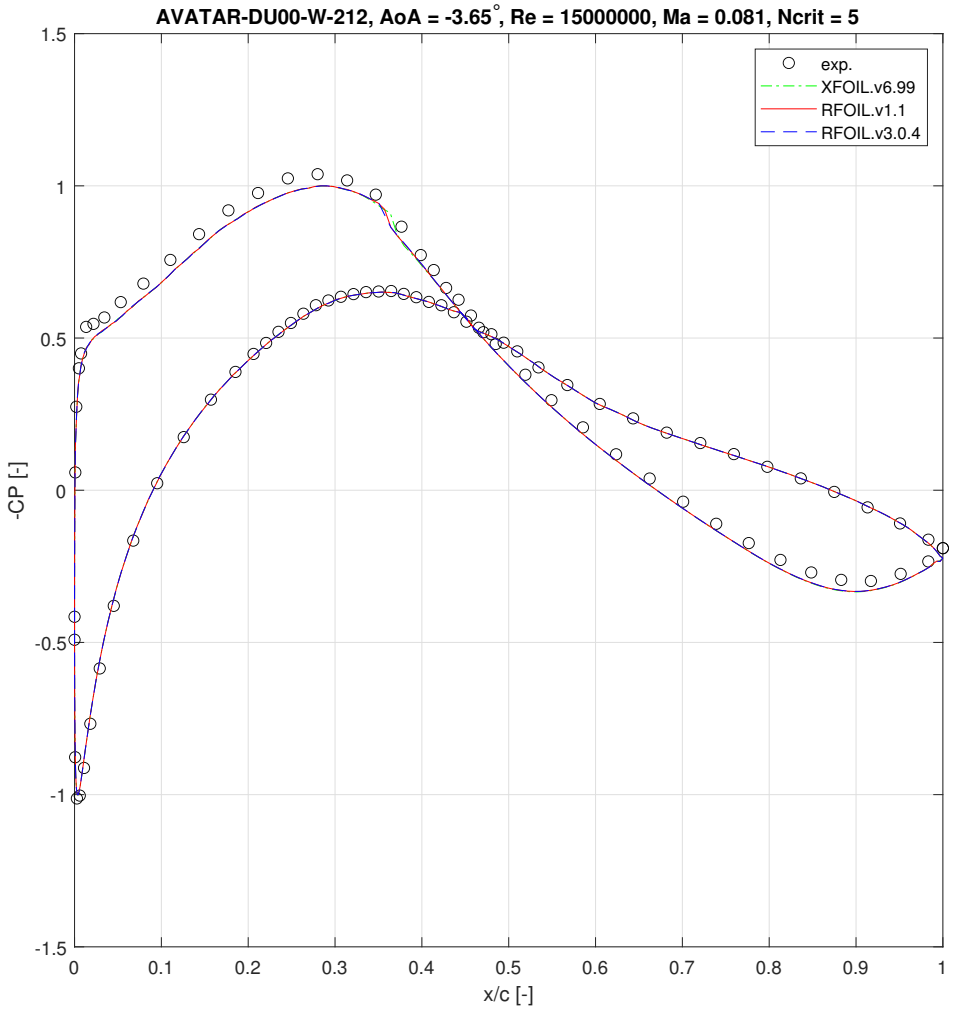

Figure C.118: Comparison between experimental and numerical pressure distributions for the AVATAR-DU00-W-212 airfoil at a Reynolds number of 12050000, and at an angle of attack and a Mach number of -3.755° and 0.058, respectively.

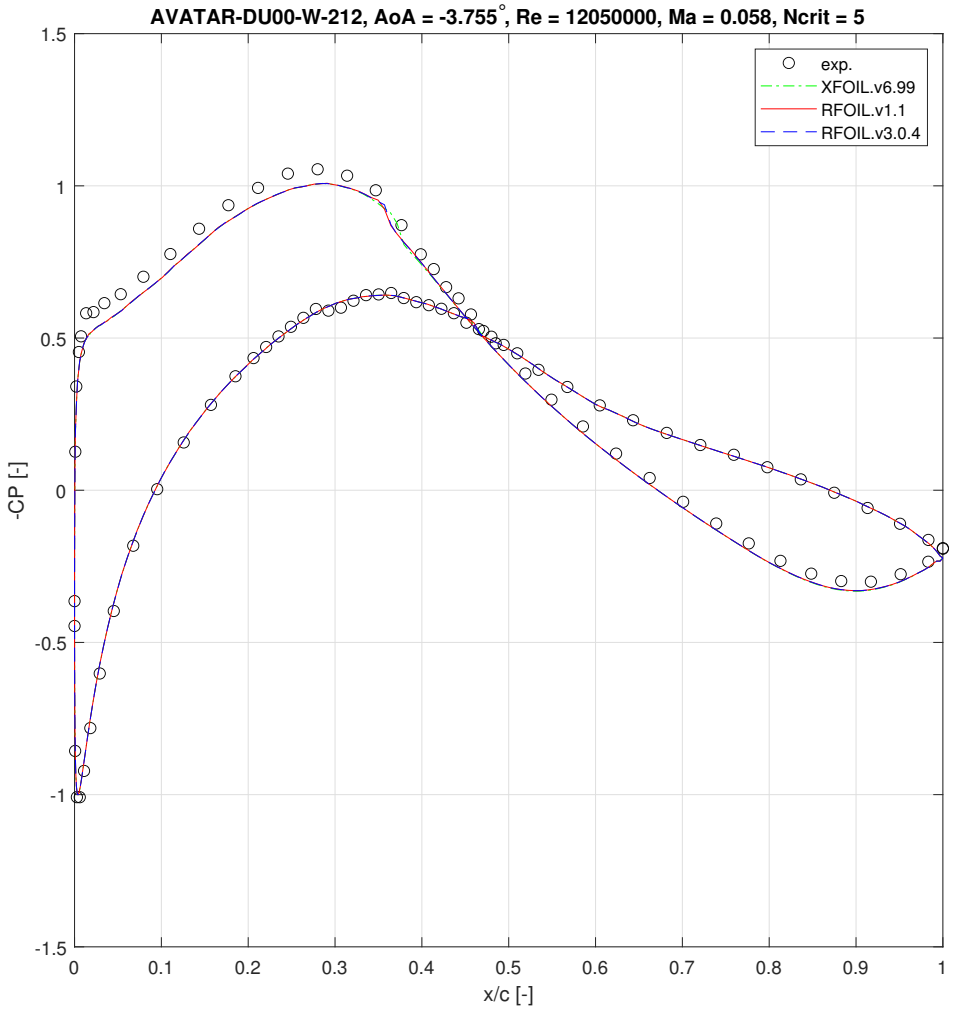

Figure C.119: Comparison between experimental and numerical pressure distributions for the AVATAR-DU00-W-212 airfoil at a Reynolds number of 14980000, and at an angle of attack and a Mach number of -3.852° and 0.081, respectively.

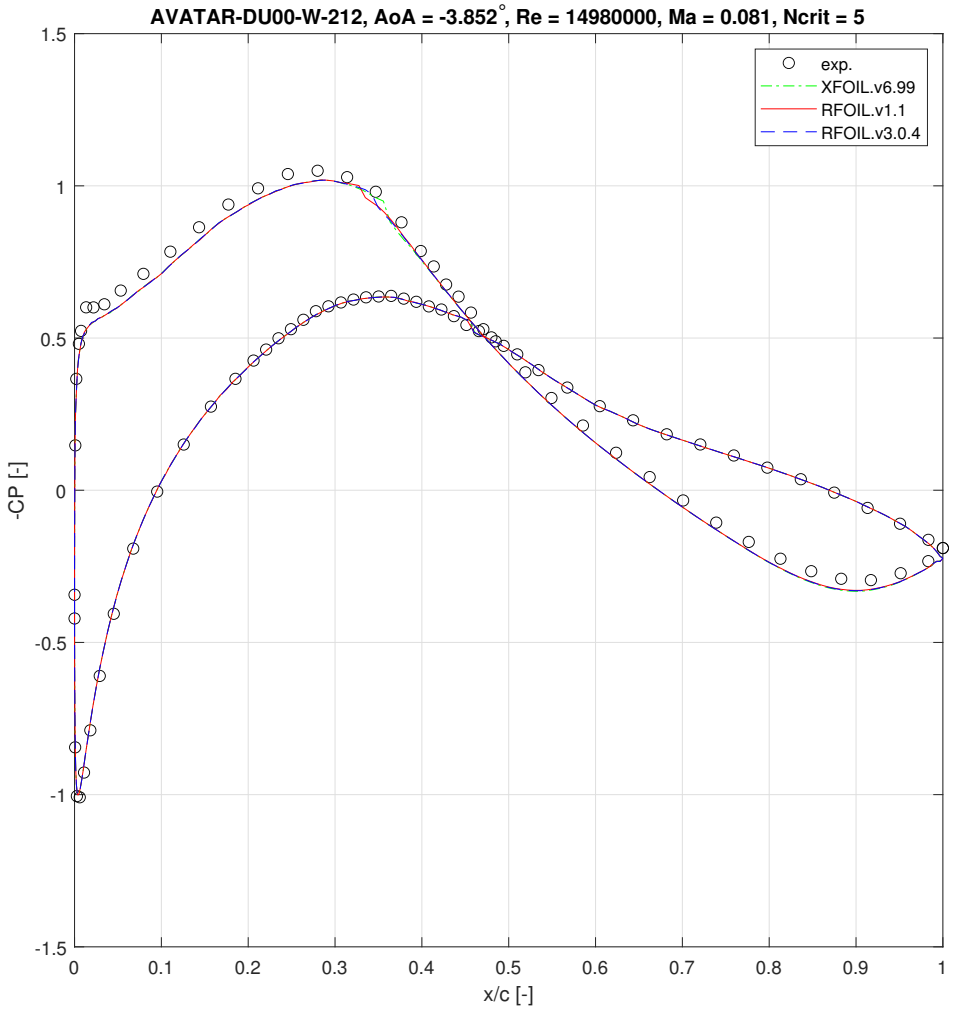

Figure C.120: Comparison between experimental and numerical pressure distributions for the AVATAR-DU00-W-212 airfoil at a Reynolds number of 9030000, and at an angle of attack and a Mach number of -3.852° and 0.083, respectively.

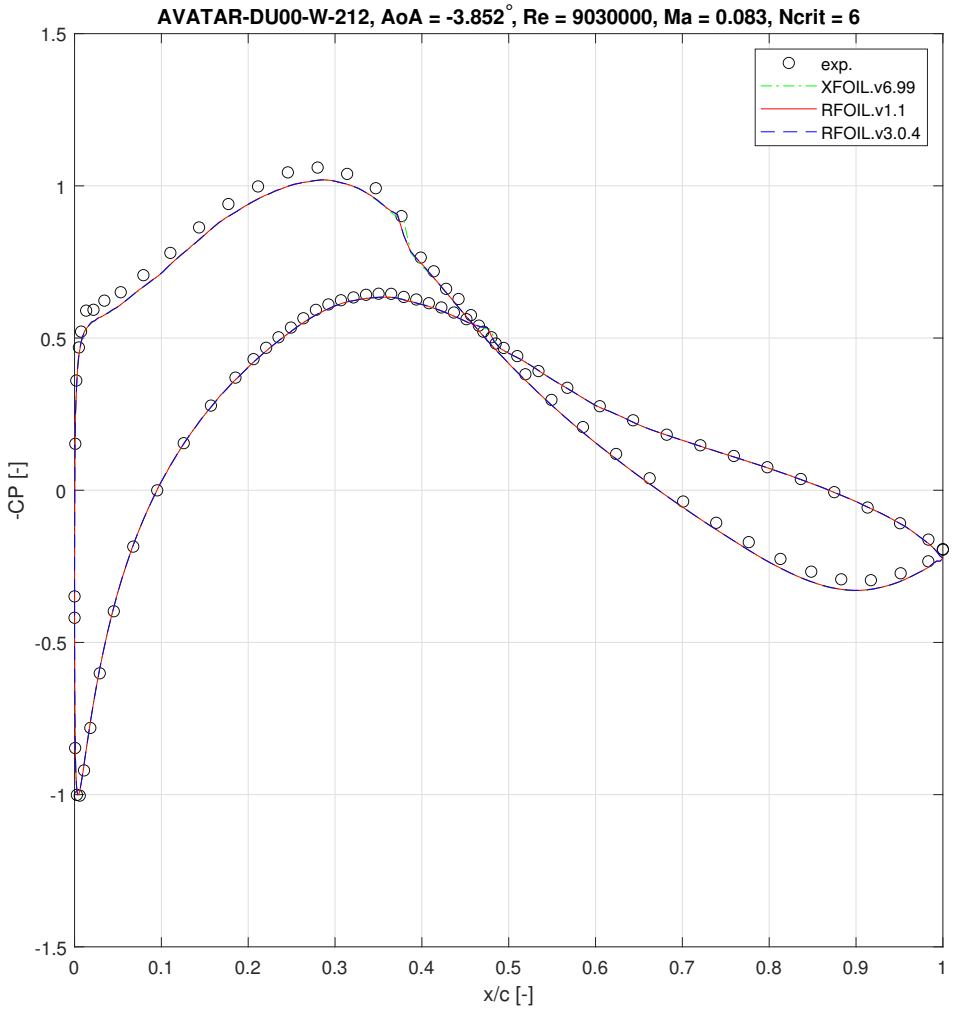

Figure C.121: Comparison between experimental and numerical pressure distributions for the AVATAR-DU00-W-212 airfoil at a Reynolds number of 9010000, and at an angle of attack and a Mach number of -3.853° and 0.043, respectively.

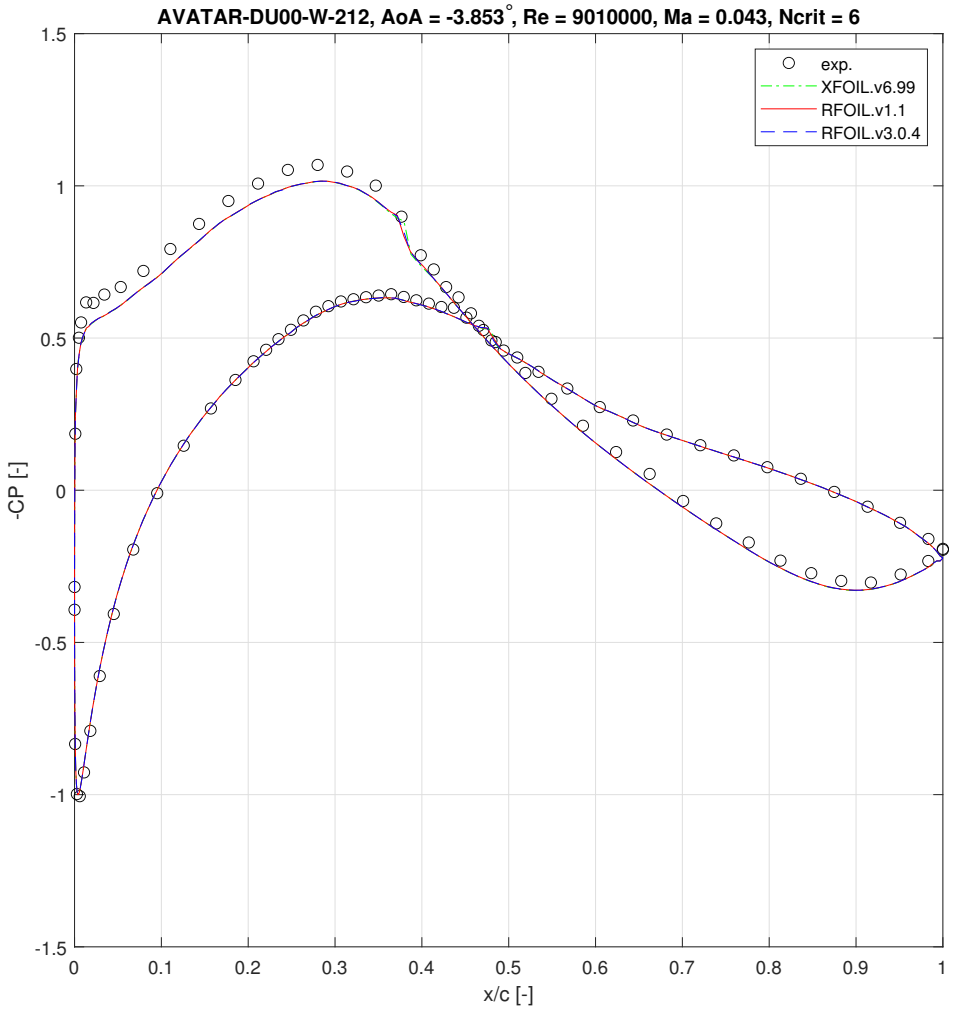

Figure C.122: Comparison between experimental and numerical pressure distributions for the AVATAR-DU00-W-212 airfoil at a Reynolds number of 12020000, and at an angle of attack and a Mach number of -3.954° and 0.058, respectively.

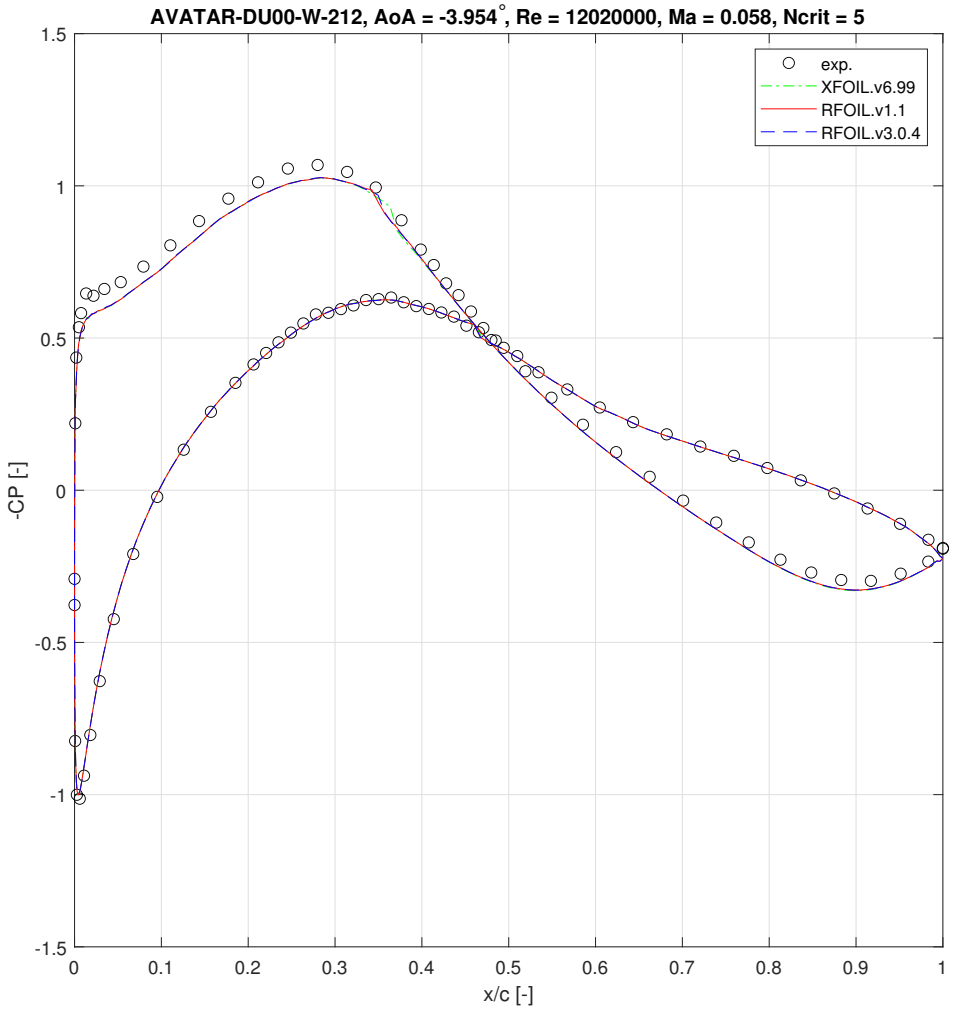

Figure C.123: Comparison between experimental and numerical pressure distributions for the AVATAR-DU00-W-212 airfoil at a Reynolds number of 15020000, and at an angle of attack and a Mach number of -4.054° and 0.082, respectively.

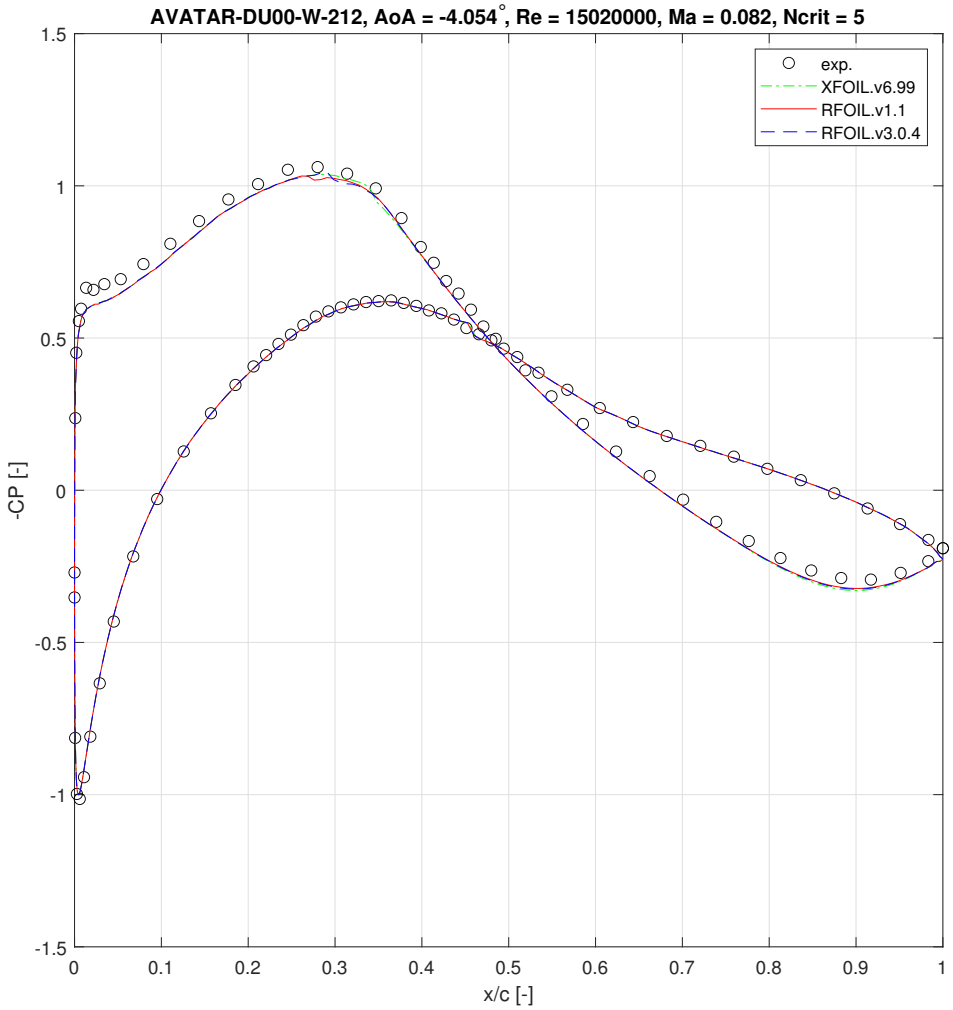

Figure C.124: Comparison between experimental and numerical pressure distributions for the AVATAR-DU00-W-212 airfoil at a Reynolds number of 3030000, and at an angle of attack and a Mach number of -4.054° and 0.075, respectively.

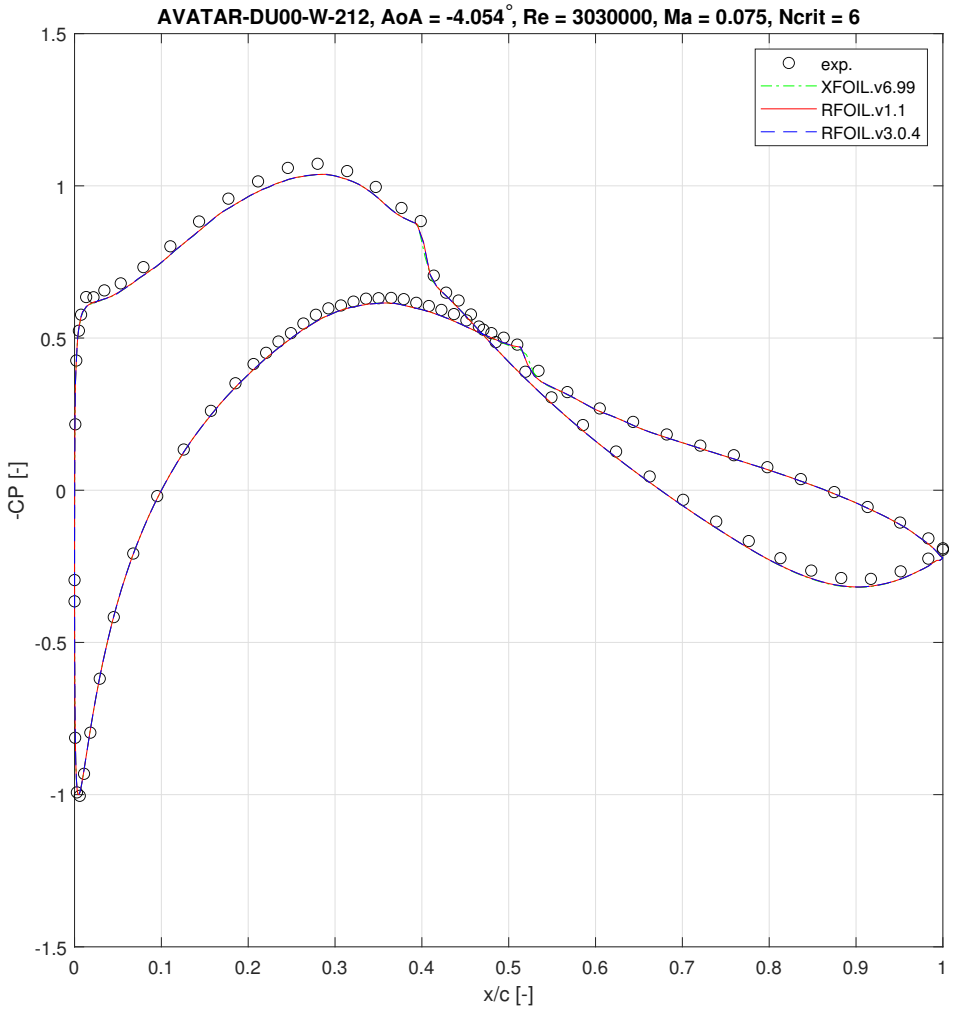

Figure C.125: Comparison between experimental and numerical pressure distributions for the AVATAR-DU00-W-212 airfoil at a Reynolds number of 6060000, and at an angle of attack and a Mach number of -4.054° and 0.055, respectively.

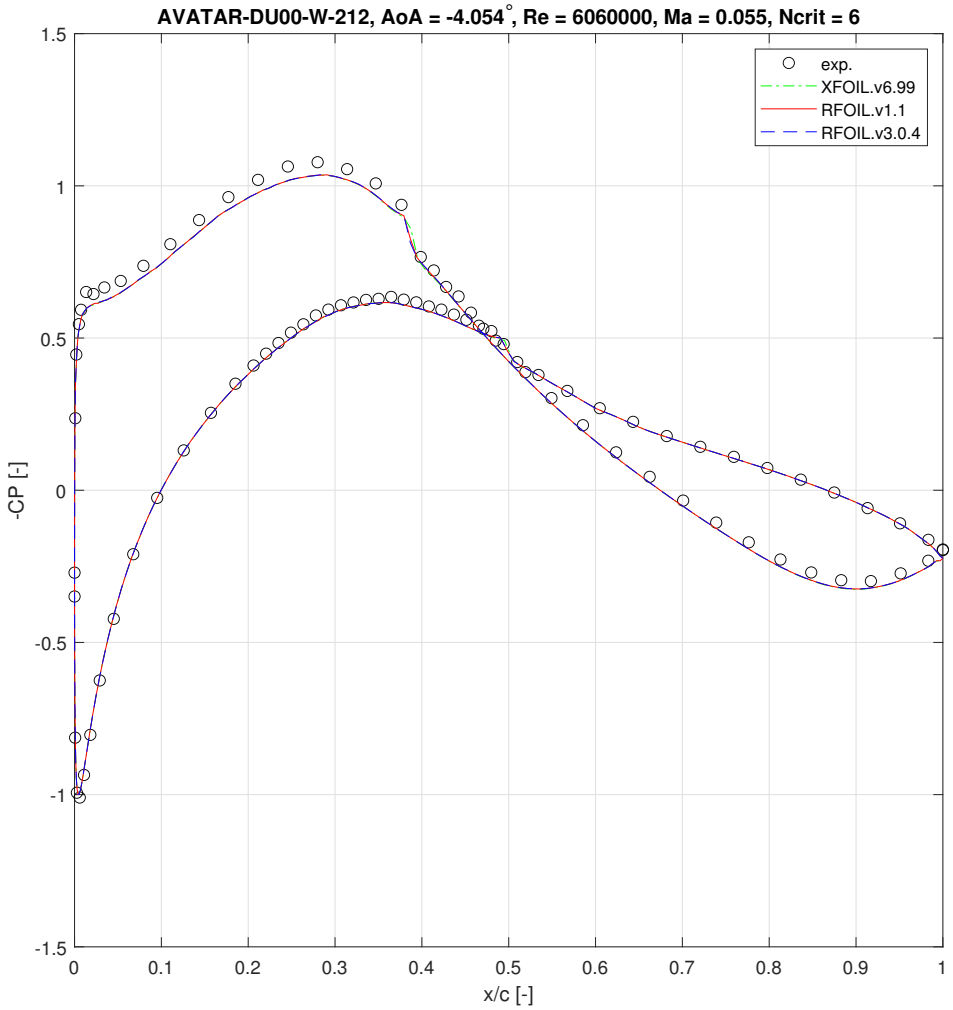

Figure C.126: Comparison between experimental and numerical pressure distributions for the AVATAR-DU00-W-212 airfoil at a Reynolds number of 9040000, and at an angle of attack and a Mach number of -4.054° and 0.083, respectively.

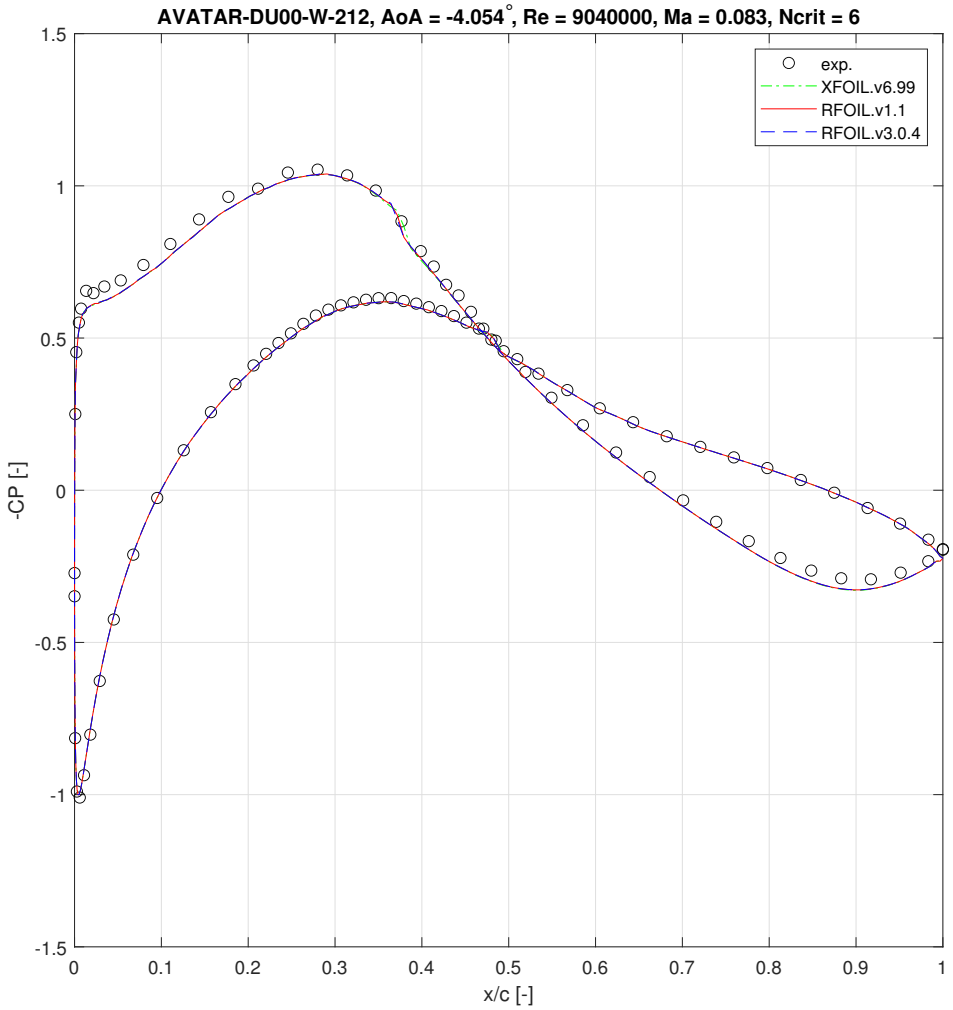

Figure C.127: Comparison between experimental and numerical pressure distributions for the AVATAR-DU00-W-212 airfoil at a Reynolds number of 6020000, and at an angle of attack and a Mach number of -4.055° and 0.029, respectively.

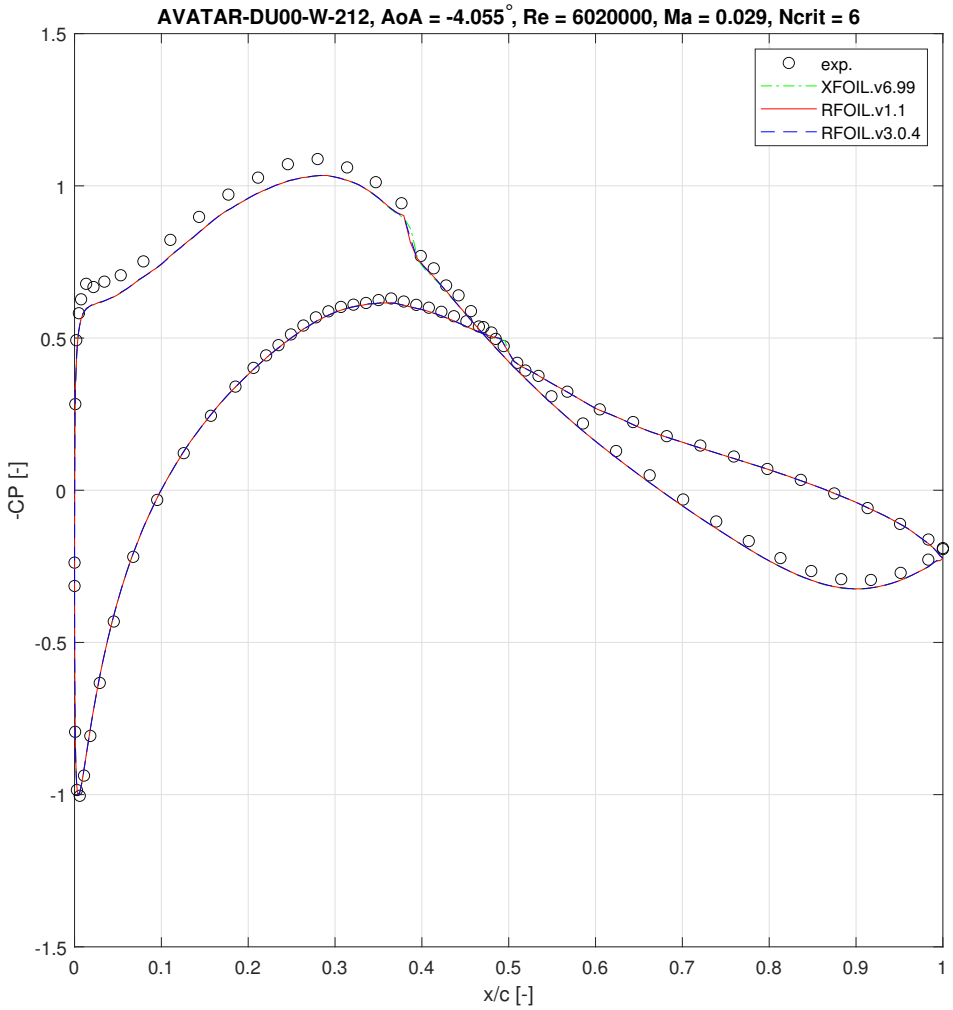

Figure C.128: Comparison between experimental and numerical pressure distributions for the AVATAR-DU00-W-212 airfoil at a Reynolds number of 9010000, and at an angle of attack and a Mach number of -4.055° and 0.083, respectively.

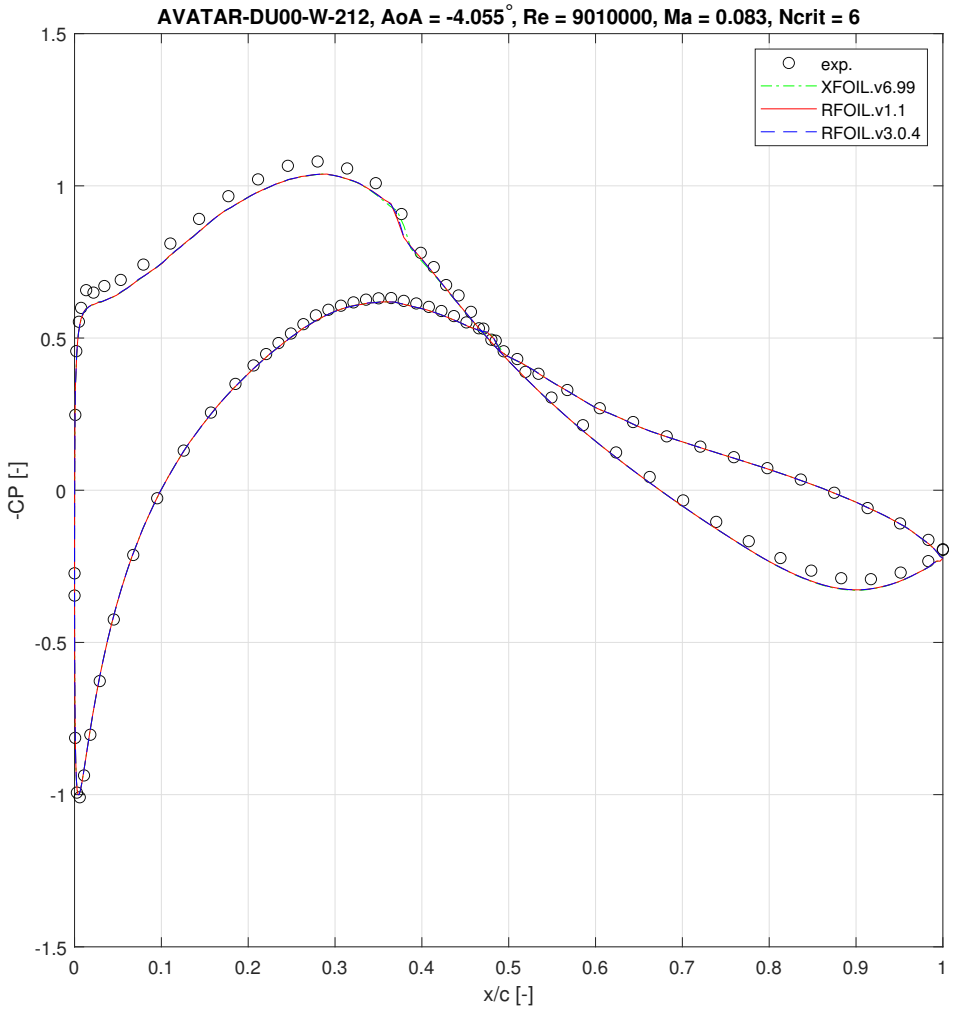

Figure C.129: Comparison between experimental and numerical pressure distributions for the AVATAR-DU00-W-212 airfoil at a Reynolds number of 9020000, and at an angle of attack and a Mach number of -4.055° and 0.044, respectively.

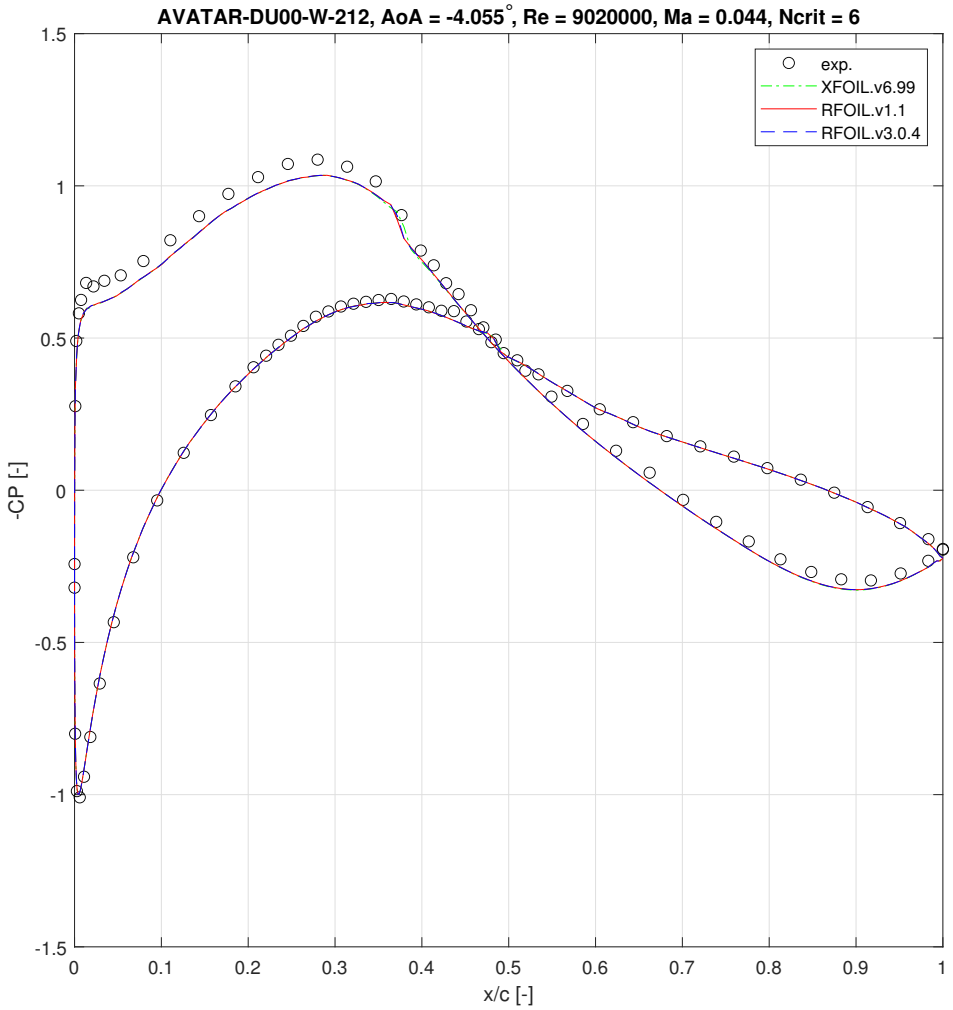

Figure C.130: Comparison between experimental and numerical pressure distributions for the AVATAR-DU00-W-212 airfoil at a Reynolds number of 12010000, and at an angle of attack and a Mach number of -4.153° and 0.058, respectively.

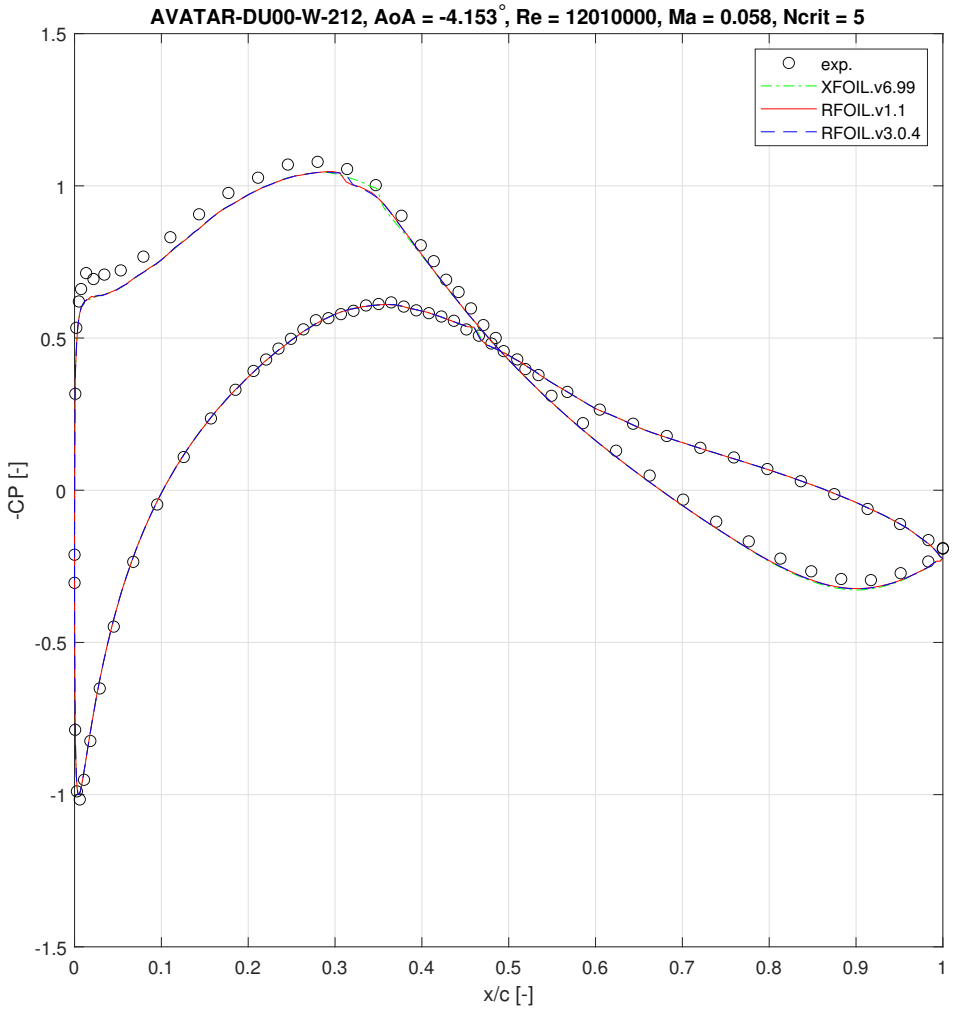

Figure C.131: Comparison between experimental and numerical pressure distributions for the AVATAR-DU00-W-212 airfoil at a Reynolds number of 15010000, and at an angle of attack and a Mach number of -4.257° and 0.082, respectively.

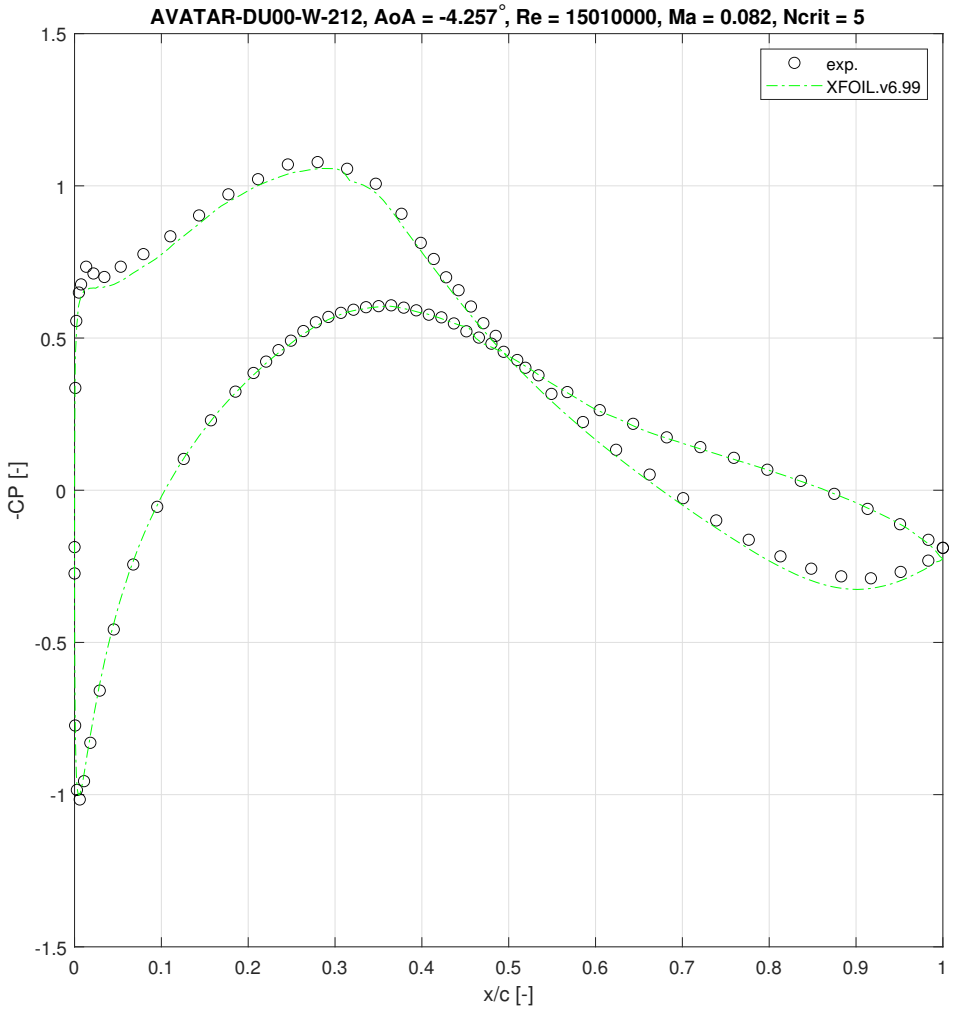

Figure C.132: Comparison between experimental and numerical pressure distributions for the AVATAR-DU00-W-212 airfoil at a Reynolds number of 9030000, and at an angle of attack and a Mach number of -4.257° and 0.083, respectively.

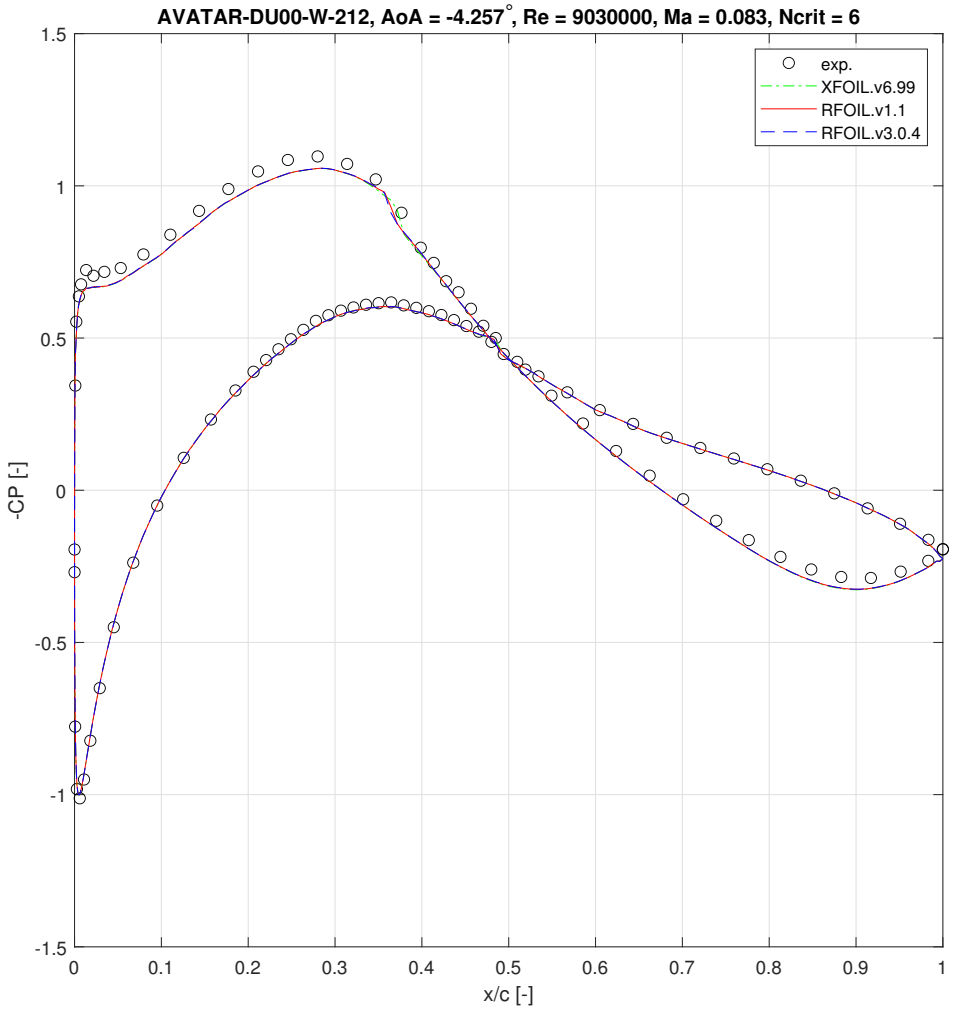

Figure C.133: Comparison between experimental and numerical pressure distributions for the AVATAR-DU00-W-212 airfoil at a Reynolds number of 8960000, and at an angle of attack and a Mach number of -4.258° and 0.043, respectively.

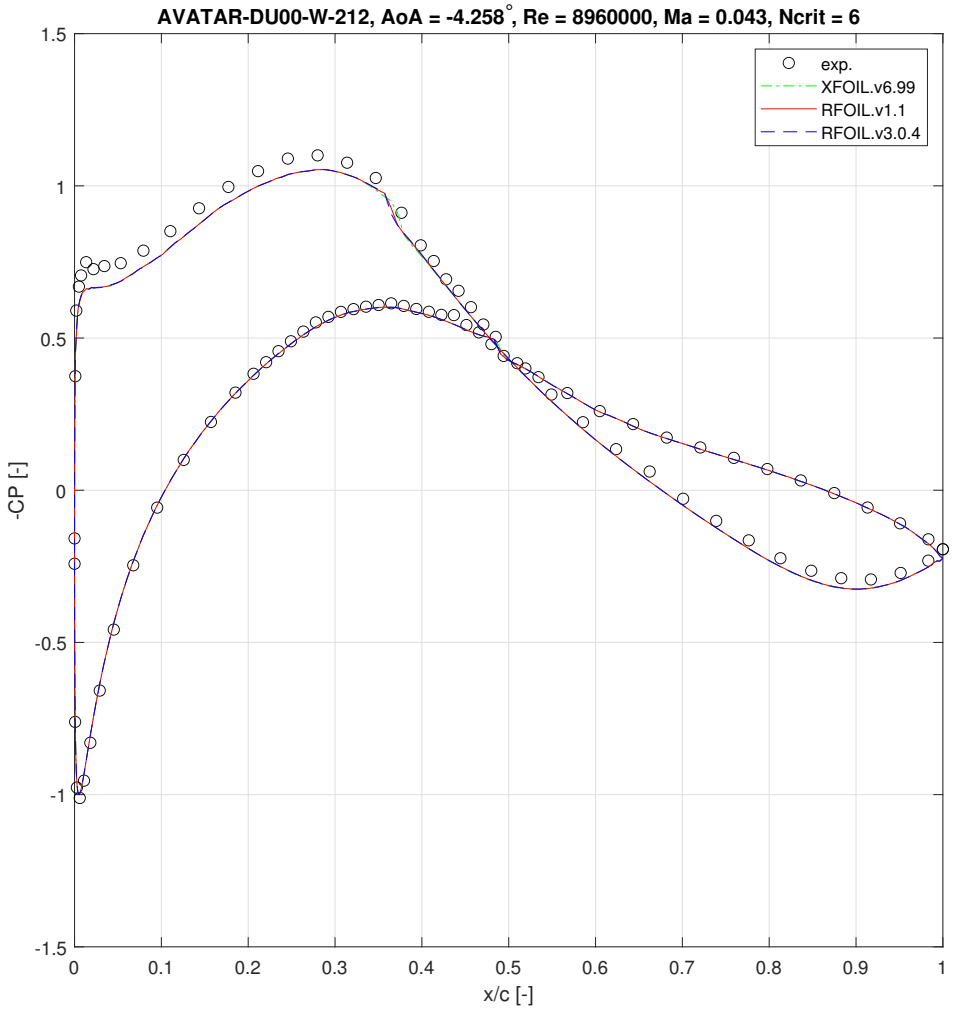

Figure C.134: Comparison between experimental and numerical pressure distributions for the AVATAR-DU00-W-212 airfoil at a Reynolds number of 11960000, and at an angle of attack and a Mach number of -4.354° and 0.057, respectively.

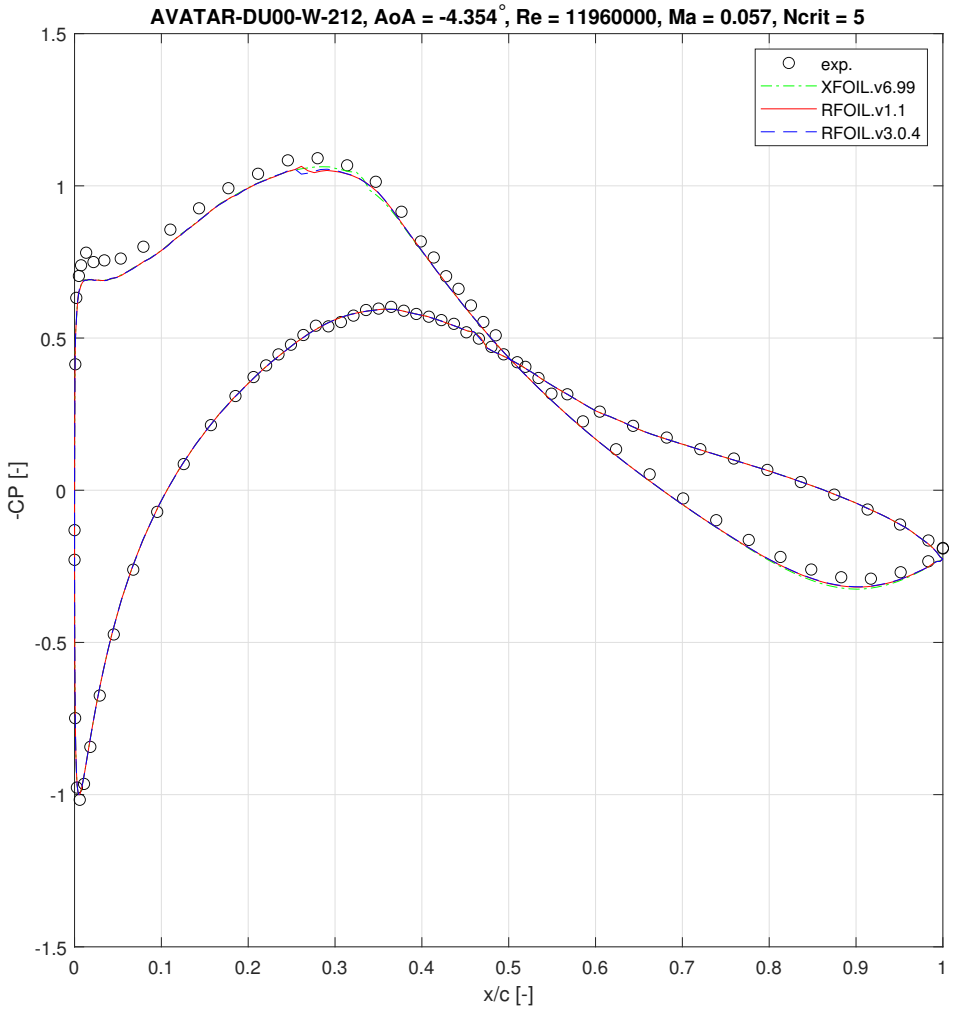

Figure C.135: Comparison between experimental and numerical pressure distributions for the AVATAR-DU00-W-212 airfoil at a Reynolds number of 15010000, and at an angle of attack and a Mach number of -4.459° and 0.082, respectively.

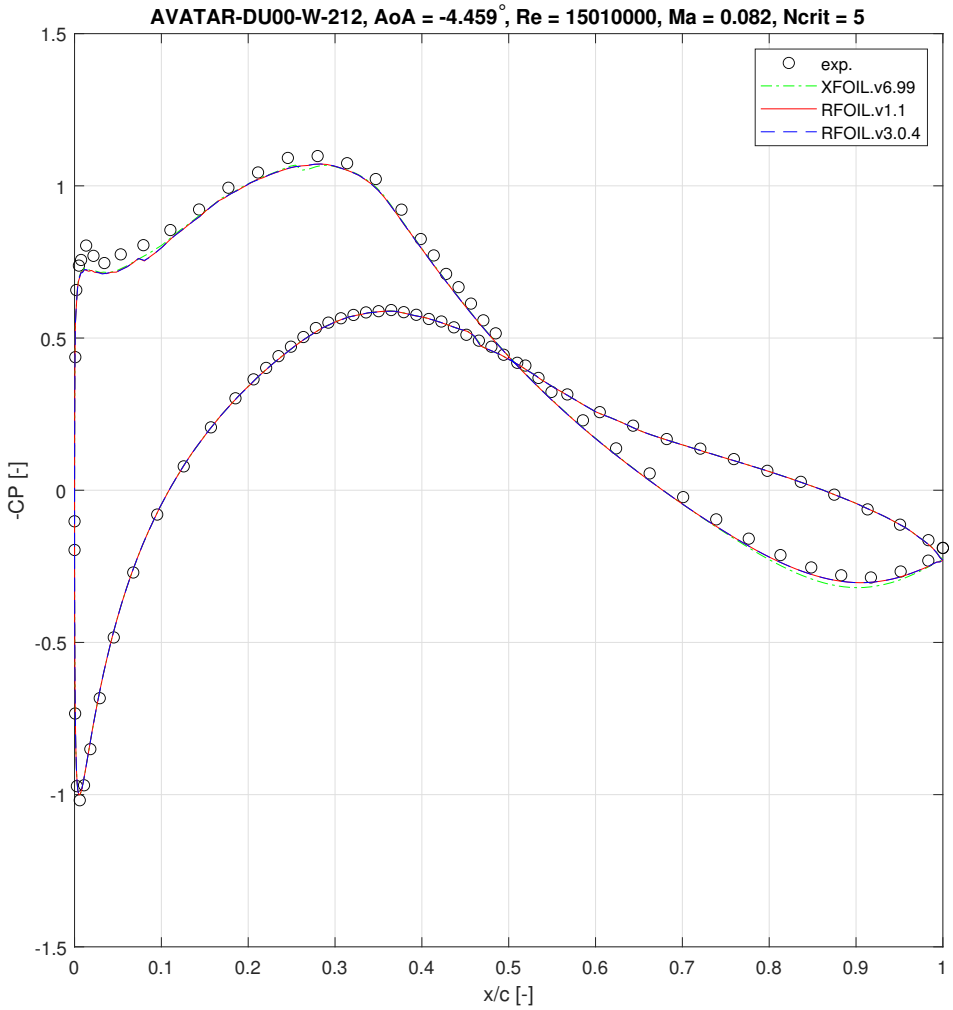

Figure C.136: Comparison between experimental and numerical pressure distributions for the AVATAR-DU00-W-212 airfoil at a Reynolds number of 9000000, and at an angle of attack and a Mach number of -4.460° and 0.083, respectively.

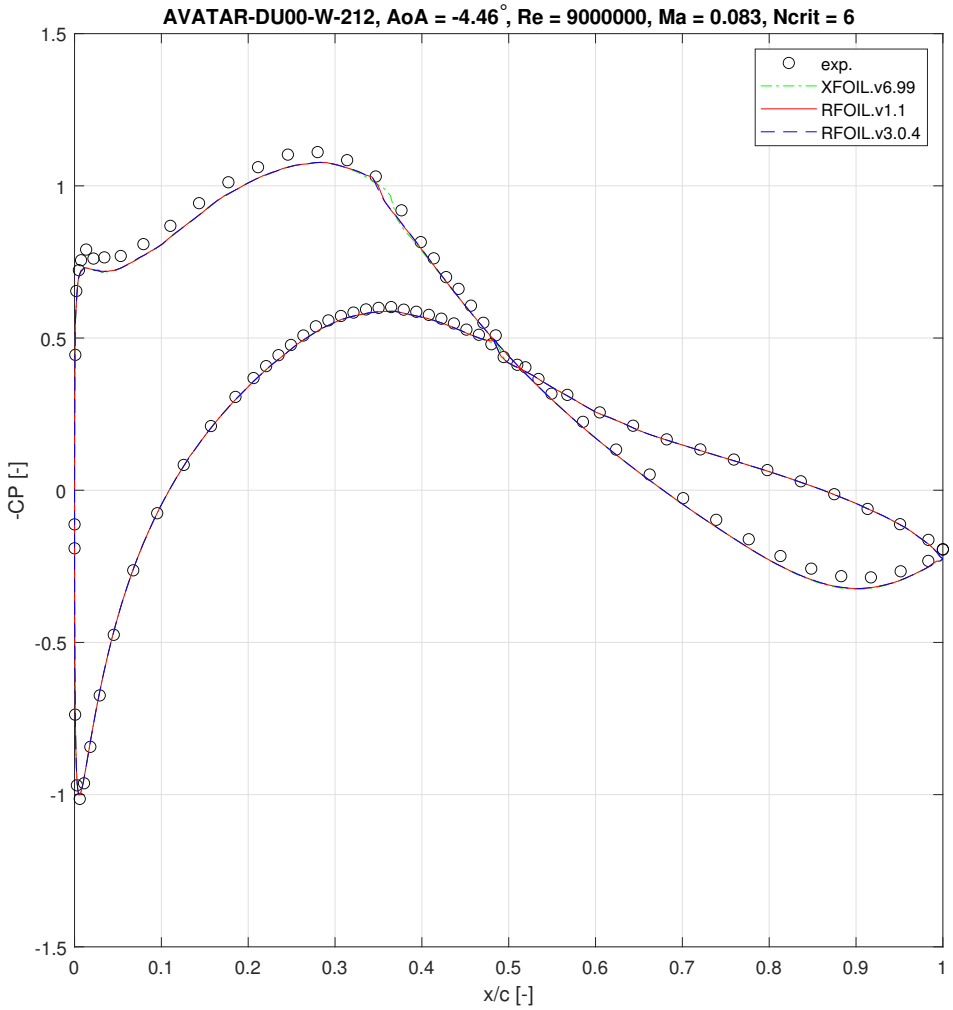

Figure C.137: Comparison between experimental and numerical pressure distributions for the AVATAR-DU00-W-212 airfoil at a Reynolds number of 9010000, and at an angle of attack and a Mach number of -4.460° and 0.044, respectively.

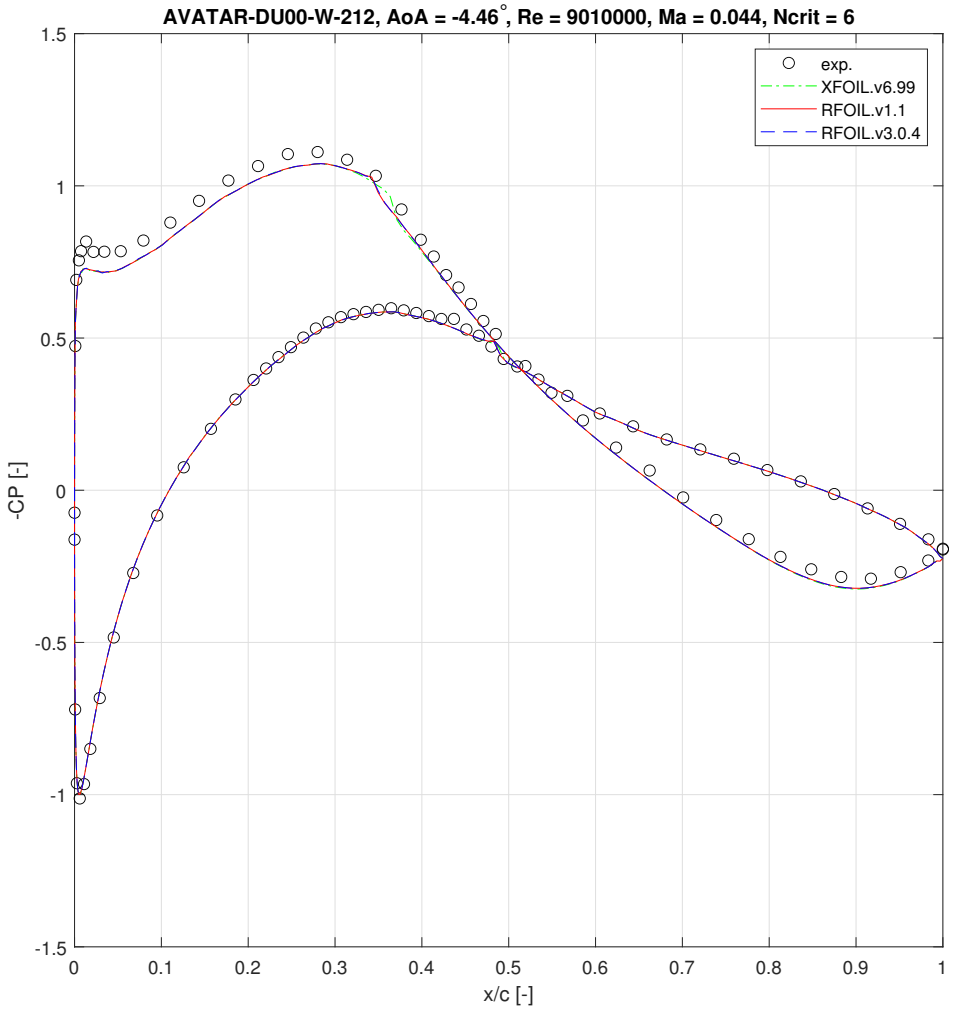

Figure C.138: Comparison between experimental and numerical pressure distributions for the AVATAR-DU00-W-212 airfoil at a Reynolds number of 11970000, and at an angle of attack and a Mach number of -4.553° and 0.058, respectively.

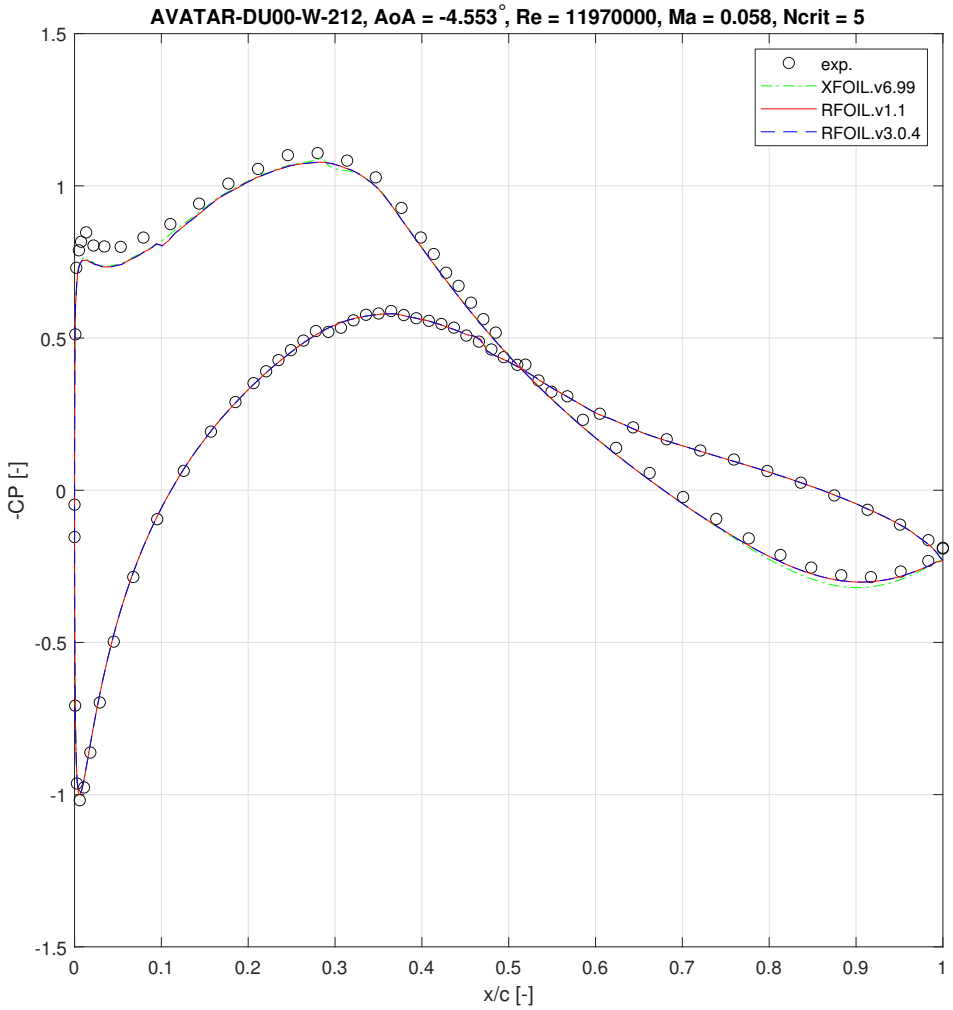

Figure C.139: Comparison between experimental and numerical pressure distributions for the AVATAR-DU00-W-212 airfoil at a Reynolds number of 15010000, and at an angle of attack and a Mach number of -4.662° and 0.082, respectively.

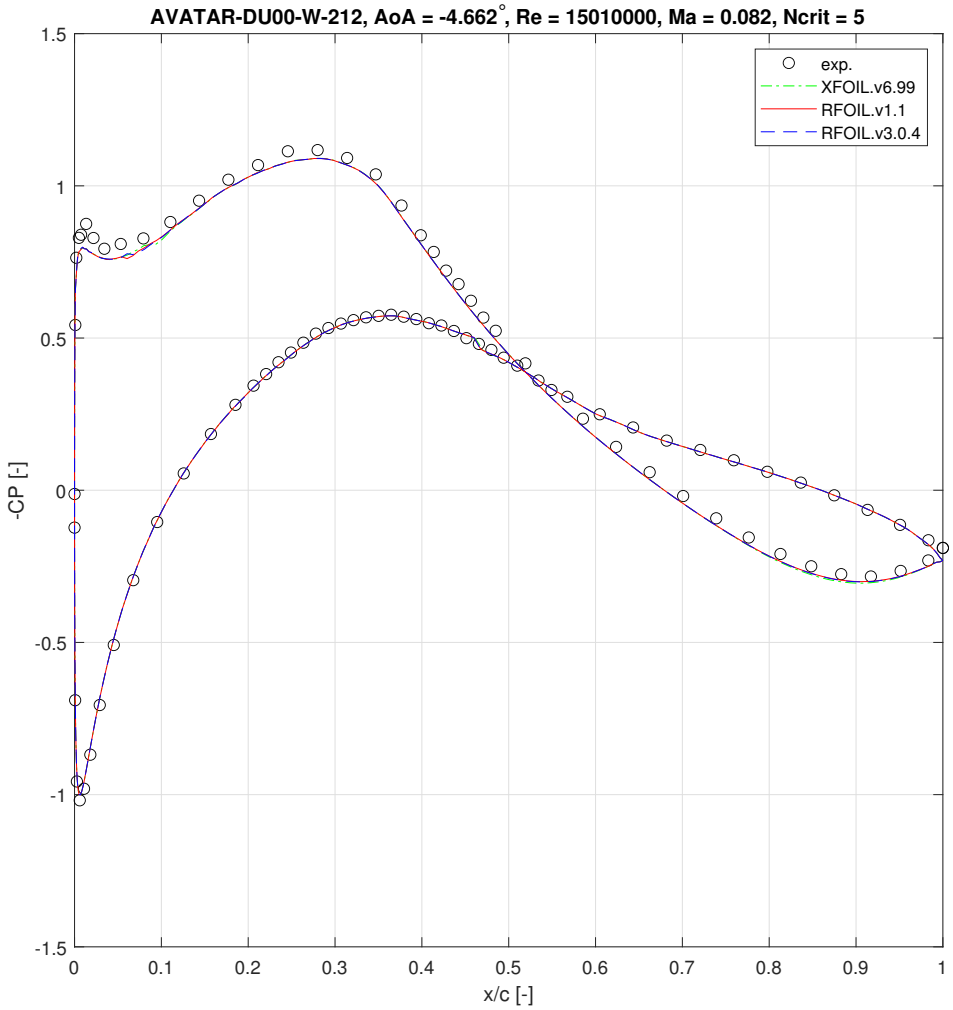

Figure C.140: Comparison between experimental and numerical pressure distributions for the AVATAR-DU00-W-212 airfoil at a Reynolds number of 9000000, and at an angle of attack and a Mach number of -4.662° and 0.083, respectively.

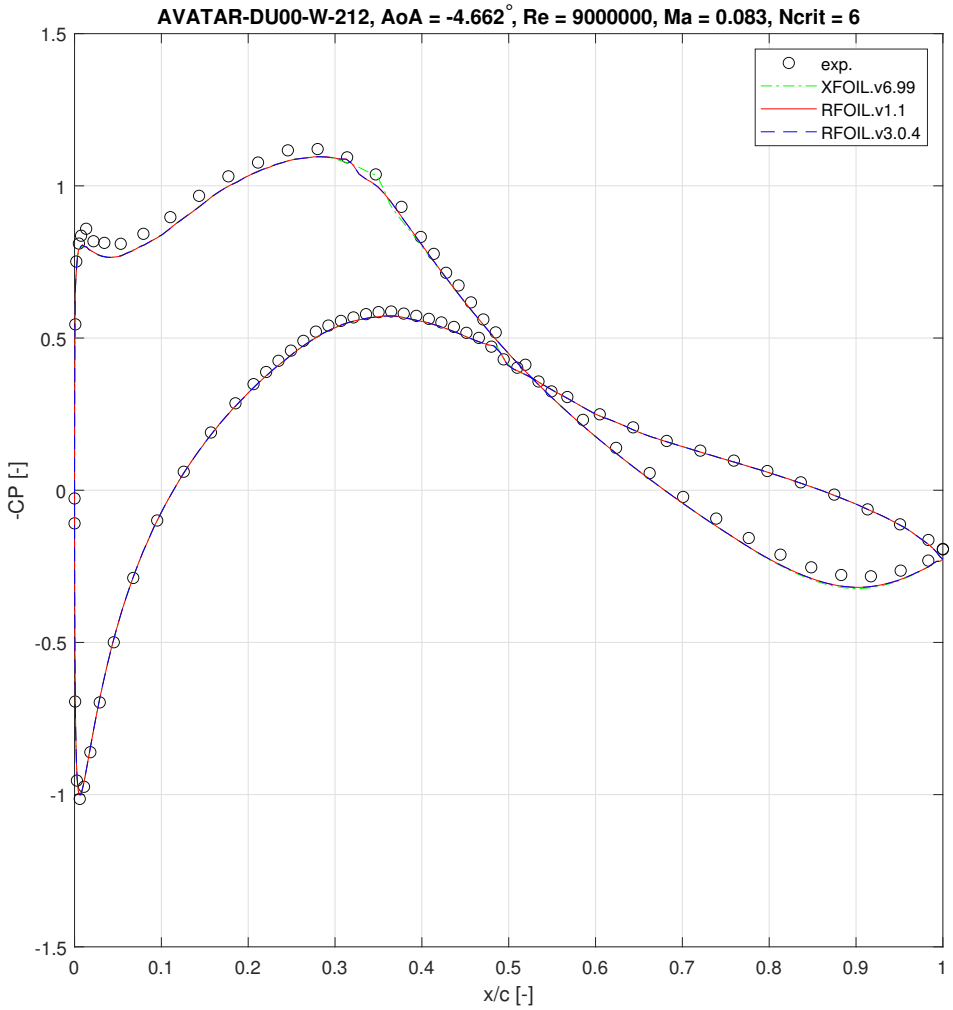

Figure C.141: Comparison between experimental and numerical pressure distributions for the AVATAR-DU00-W-212 airfoil at a Reynolds number of 9000000, and at an angle of attack and a Mach number of -4.663° and 0.043, respectively.

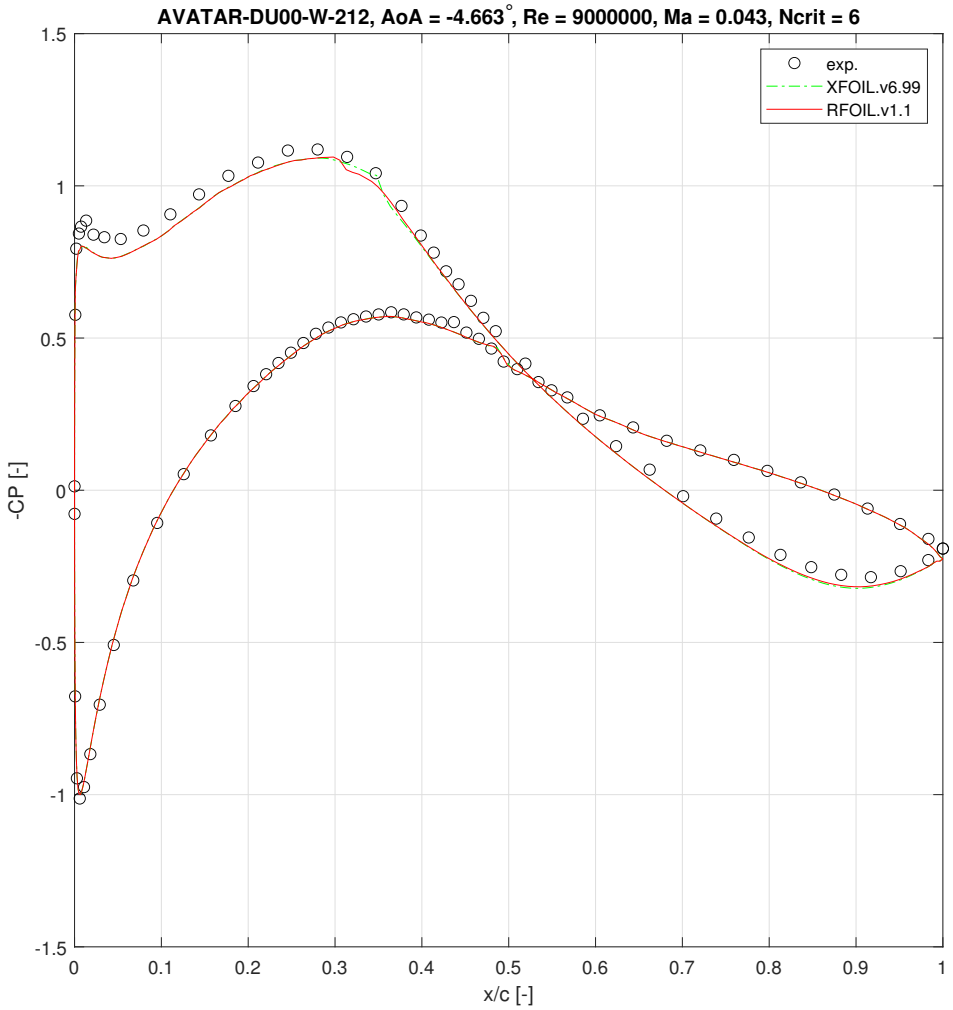

Figure C.142: Comparison between experimental and numerical pressure distributions for the AVATAR-DU00-W-212 airfoil at a Reynolds number of 11960000, and at an angle of attack and a Mach number of -4.753° and 0.058, respectively.

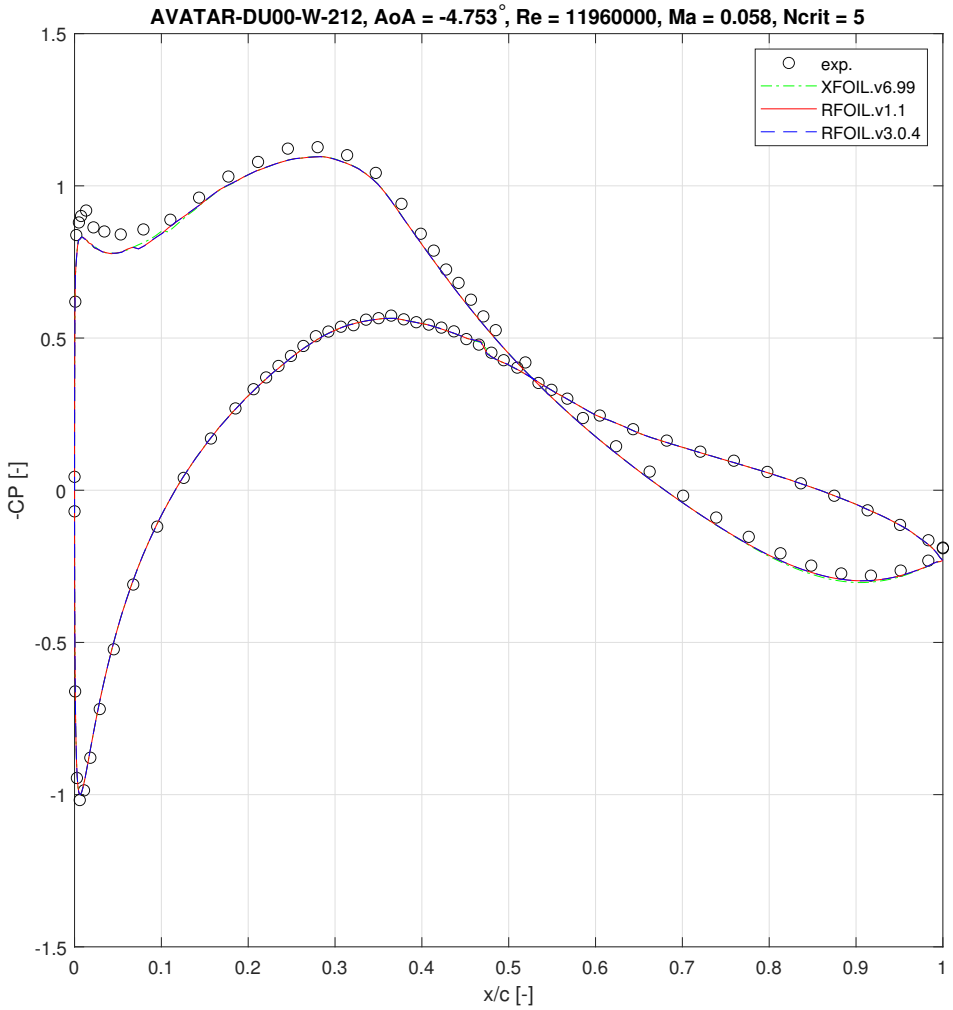

Figure C.143: Comparison between experimental and numerical pressure distributions for the AVATAR-DU00-W-212 airfoil at a Reynolds number of 15030000, and at an angle of attack and a Mach number of -4.864° and 0.082, respectively.

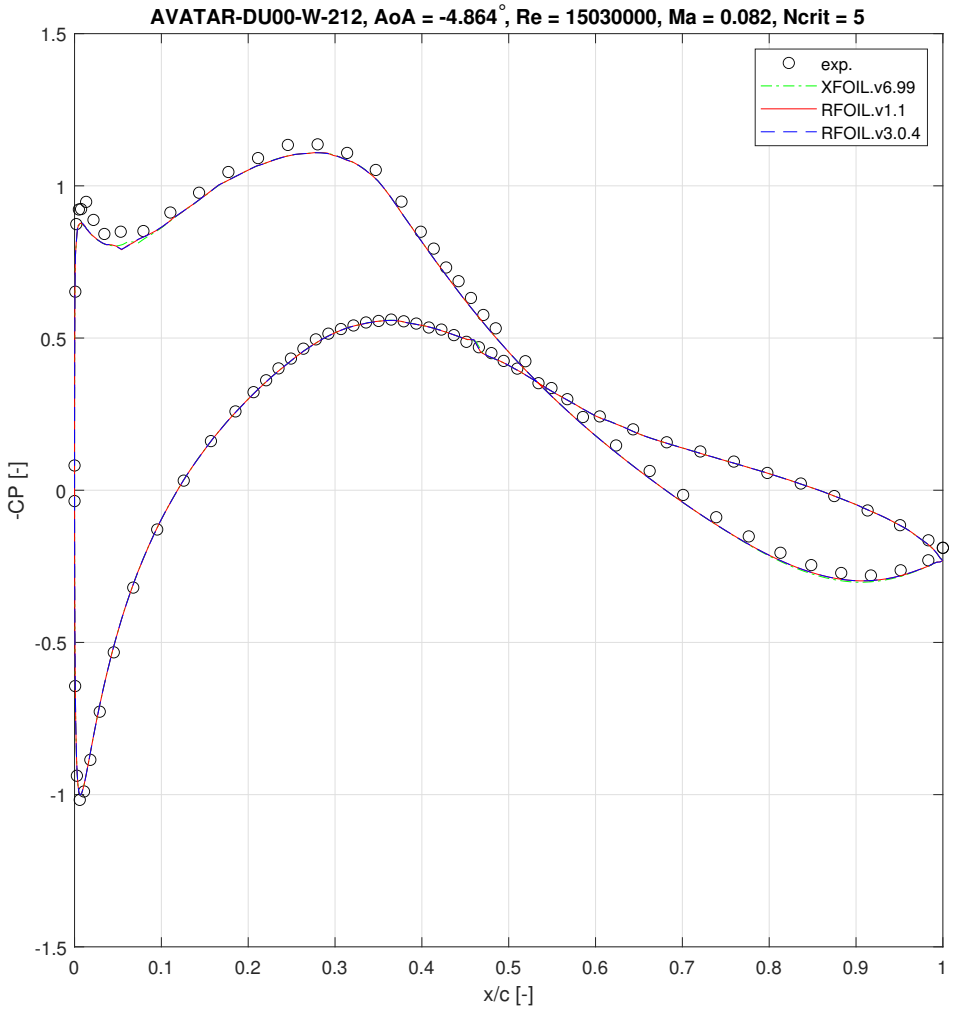

Figure C.144: Comparison between experimental and numerical pressure distributions for the AVATAR-DU00-W-212 airfoil at a Reynolds number of 9000000, and at an angle of attack and a Mach number of -4.864° and 0.083, respectively.

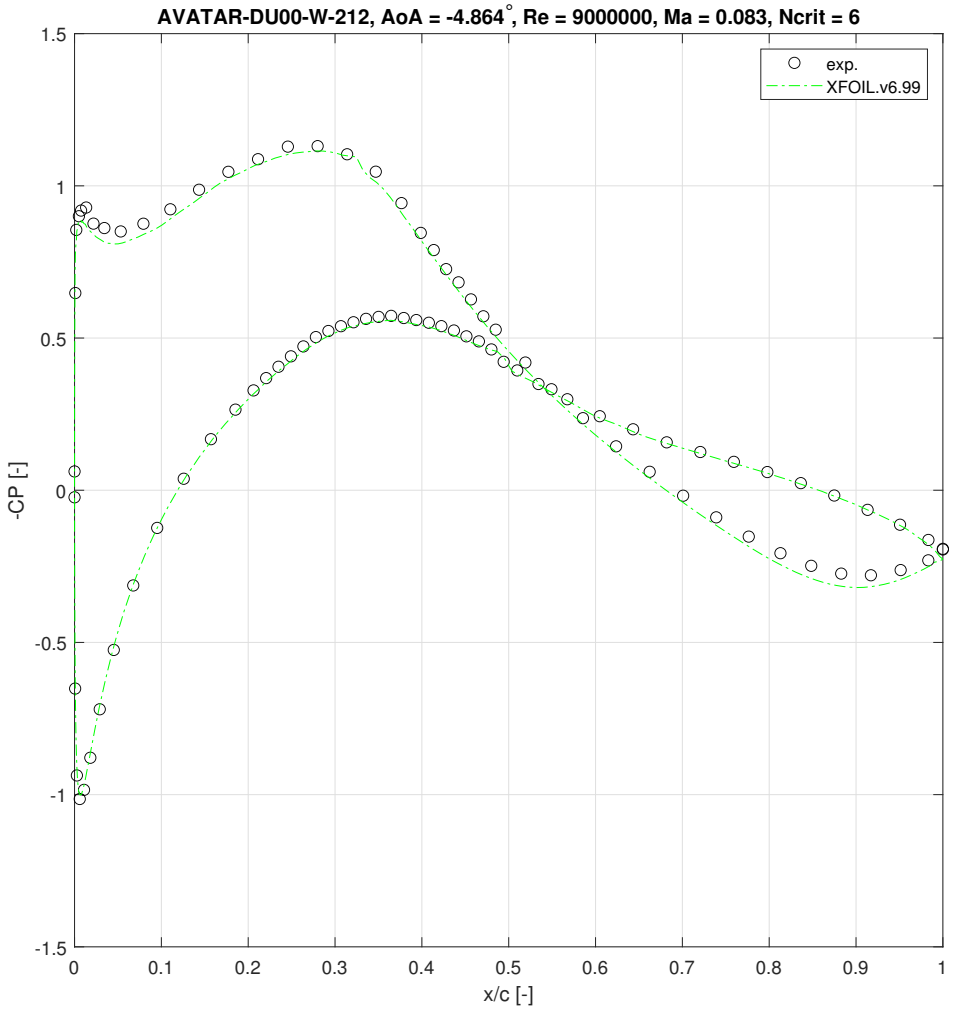

Figure C.145: Comparison between experimental and numerical pressure distributions for the AVATAR-DU00-W-212 airfoil at a Reynolds number of 6020000, and at an angle of attack and a Mach number of -4.865° and 0.029, respectively.

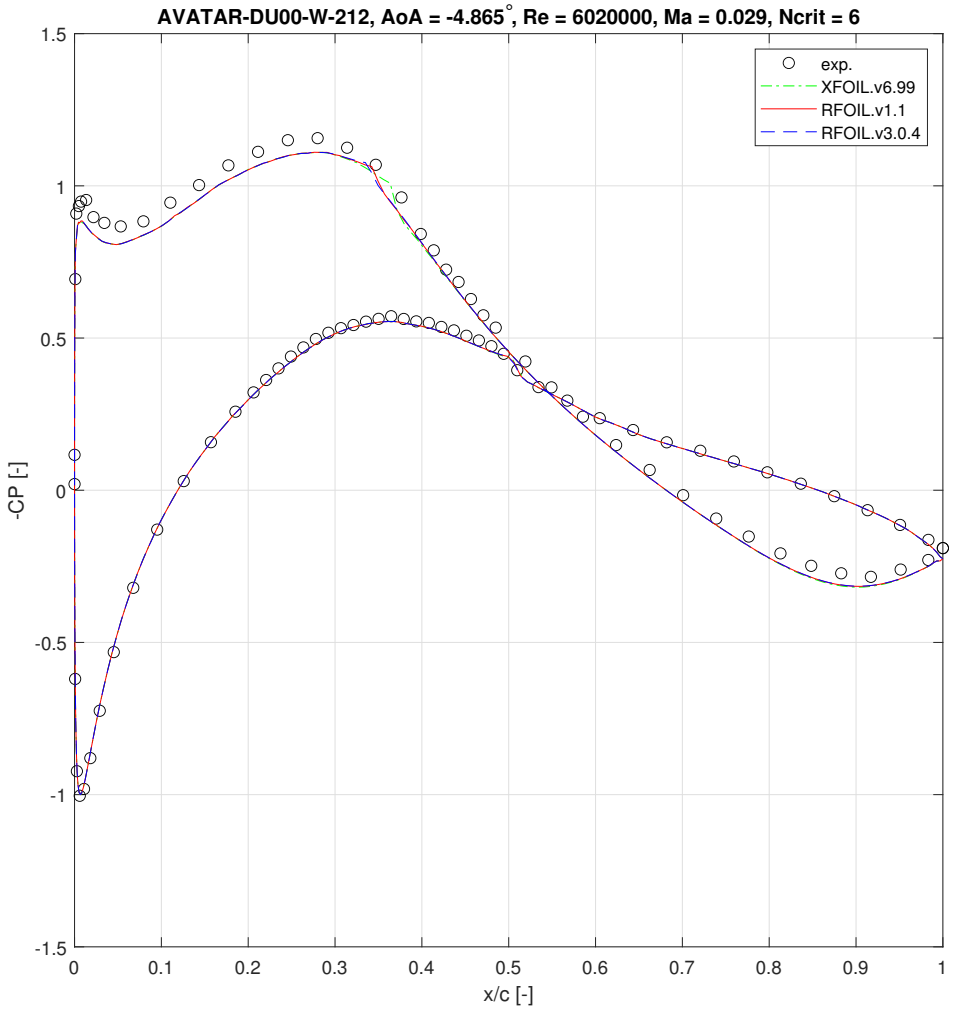

Figure C.146: Comparison between experimental and numerical pressure distributions for the AVATAR-DU00-W-212 airfoil at a Reynolds number of 6090000, and at an angle of attack and a Mach number of -4.865° and 0.056, respectively.

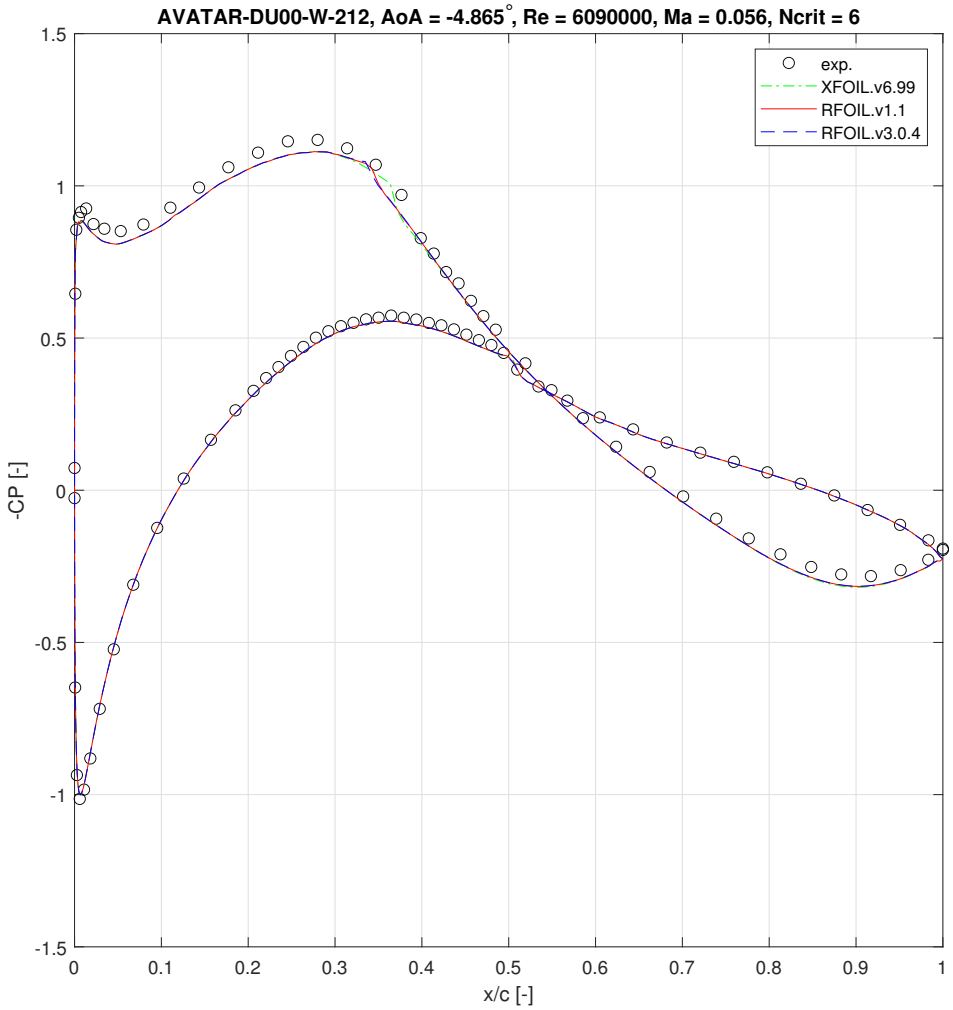

Figure C.147: Comparison between experimental and numerical pressure distributions for the AVATAR-DU00-W-212 airfoil at a Reynolds number of 8990000, and at an angle of attack and a Mach number of -4.865° and 0.043, respectively.

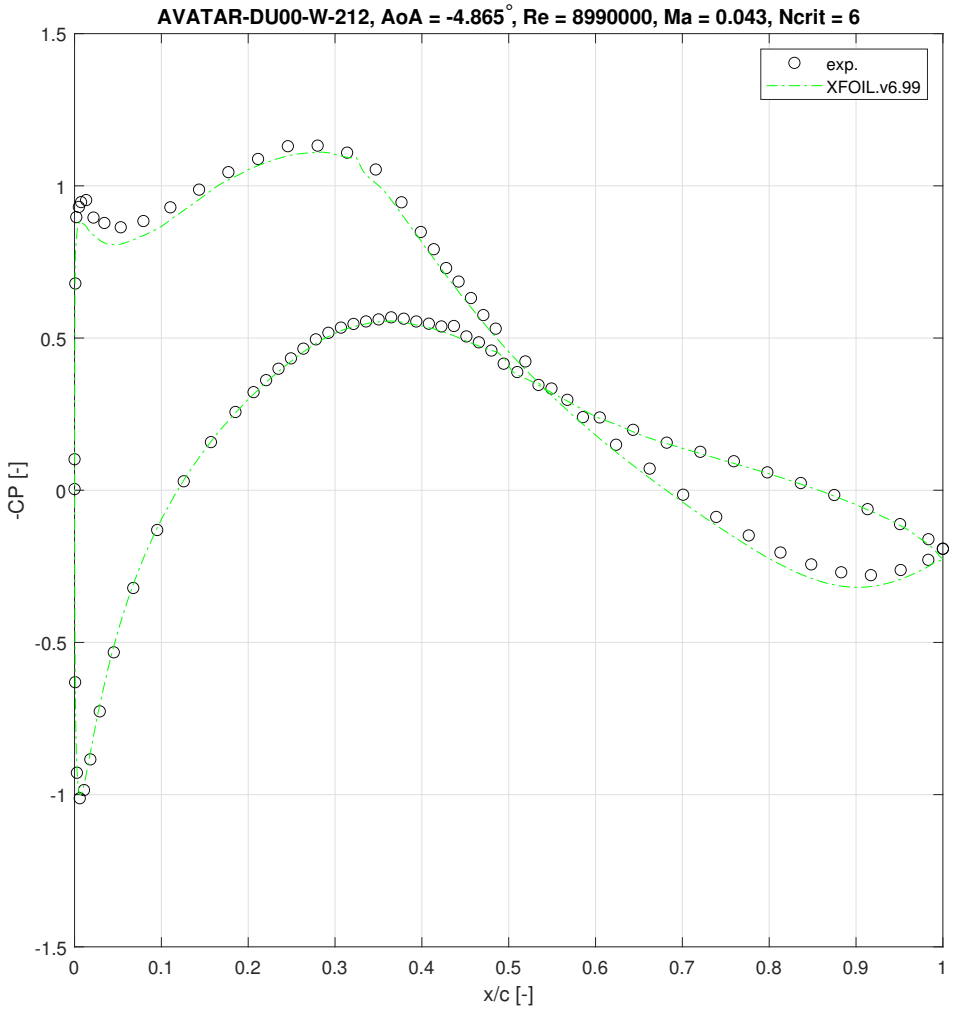

Figure C.148: Comparison between experimental and numerical pressure distributions for the AVATAR-DU00-W-212 airfoil at a Reynolds number of 12060000, and at an angle of attack and a Mach number of -4.954° and 0.058, respectively.

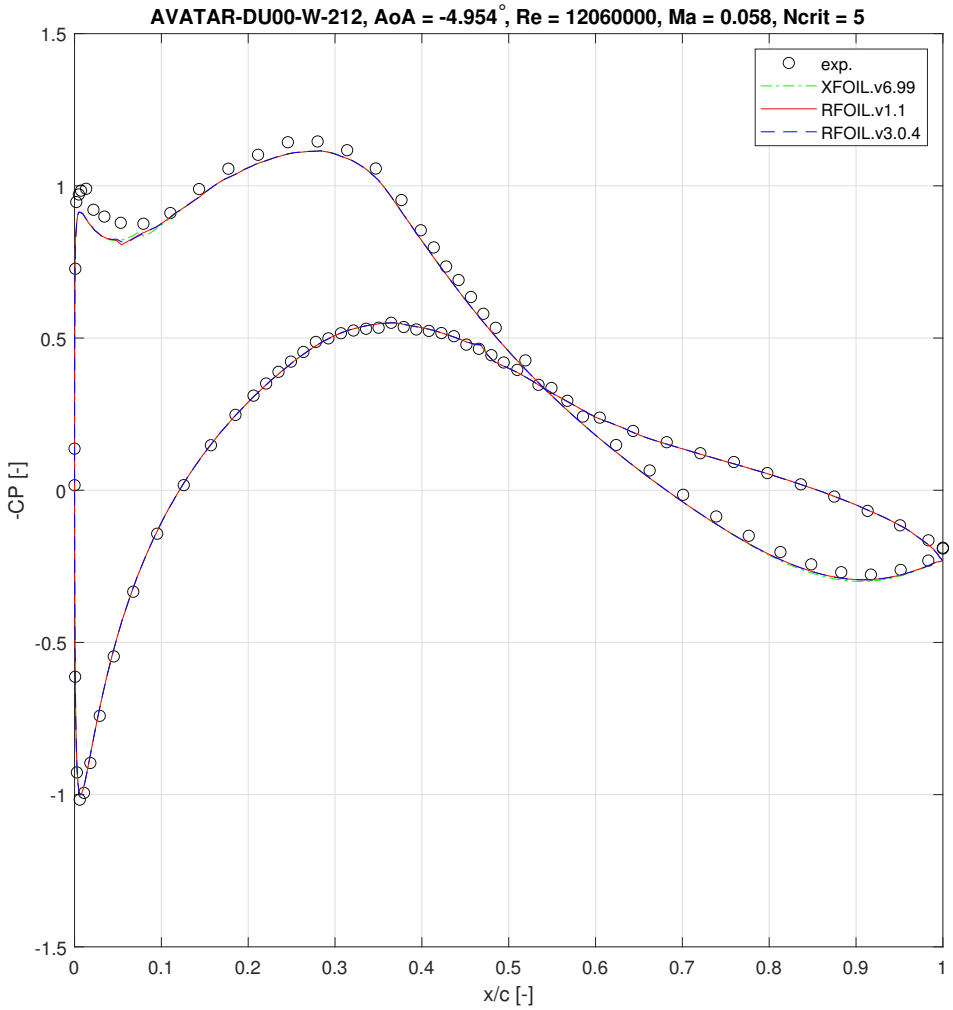

Figure C.149: Comparison between experimental and numerical pressure distributions for the AVATAR-DU00-W-212 airfoil at a Reynolds number of 8980000, and at an angle of attack and a Mach number of -5.066° and 0.083, respectively.

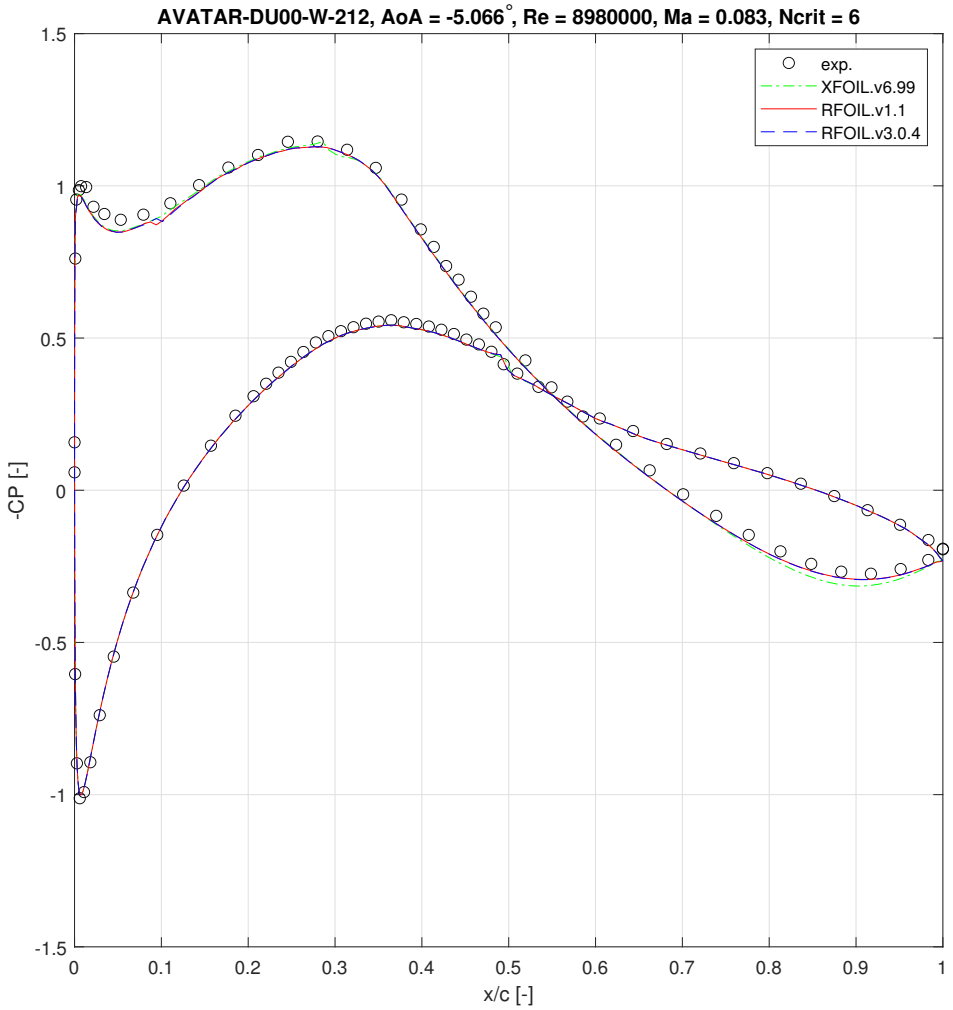

Figure C.150: Comparison between experimental and numerical pressure distributions for the AVATAR-DU00-W-212 airfoil at a Reynolds number of 9000000, and at an angle of attack and a Mach number of -5.066° and 0.083, respectively.

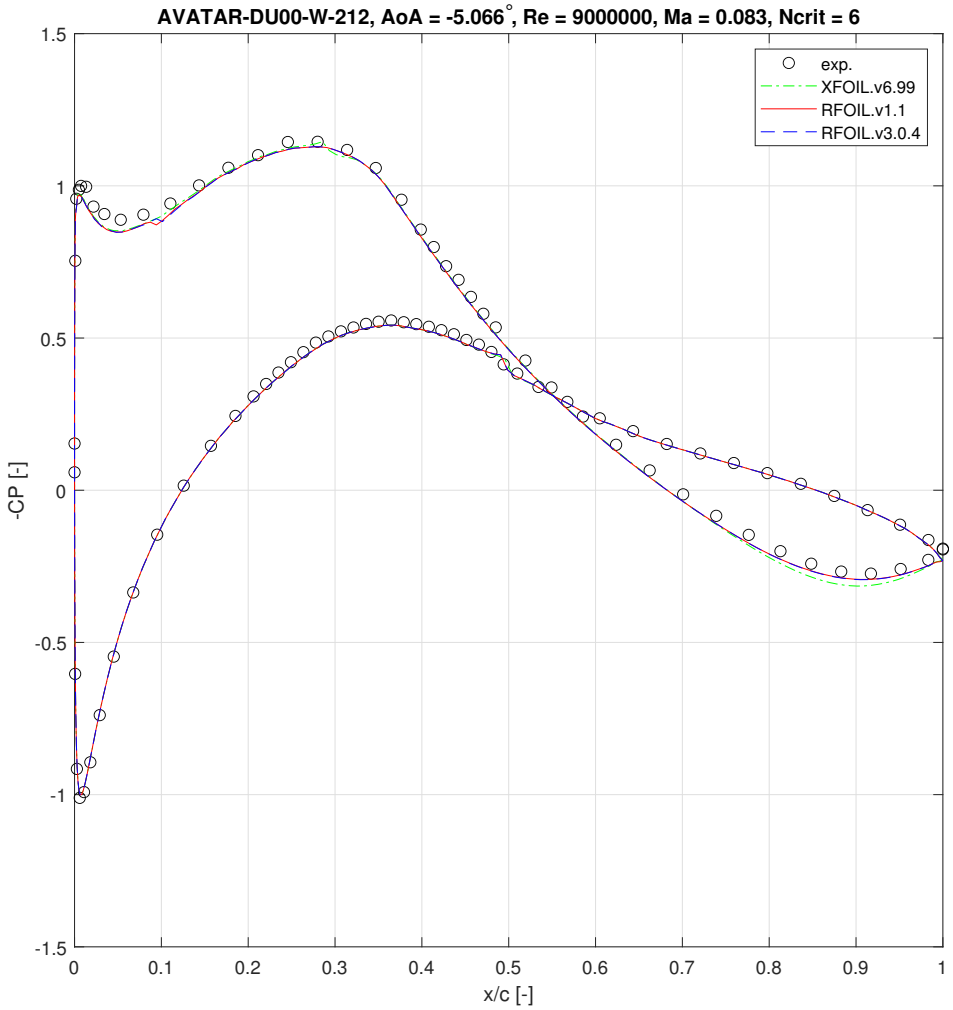

Figure C.151: Comparison between experimental and numerical pressure distributions for the AVATAR-DU00-W-212 airfoil at a Reynolds number of 15040000, and at an angle of attack and a Mach number of -5.067° and 0.082, respectively.

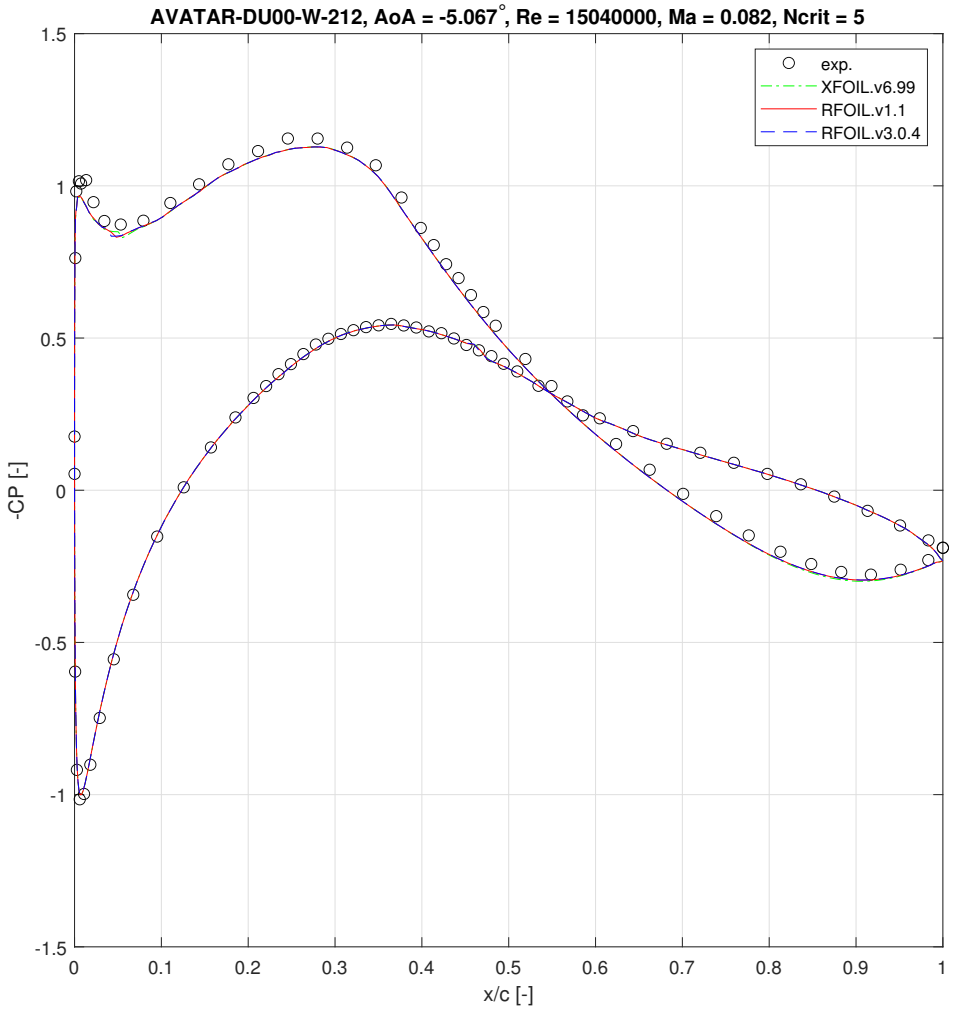

Figure C.152: Comparison between experimental and numerical pressure distributions for the AVATAR-DU00-W-212 airfoil at a Reynolds number of 3010000, and at an angle of attack and a Mach number of -5.067° and 0.074, respectively.

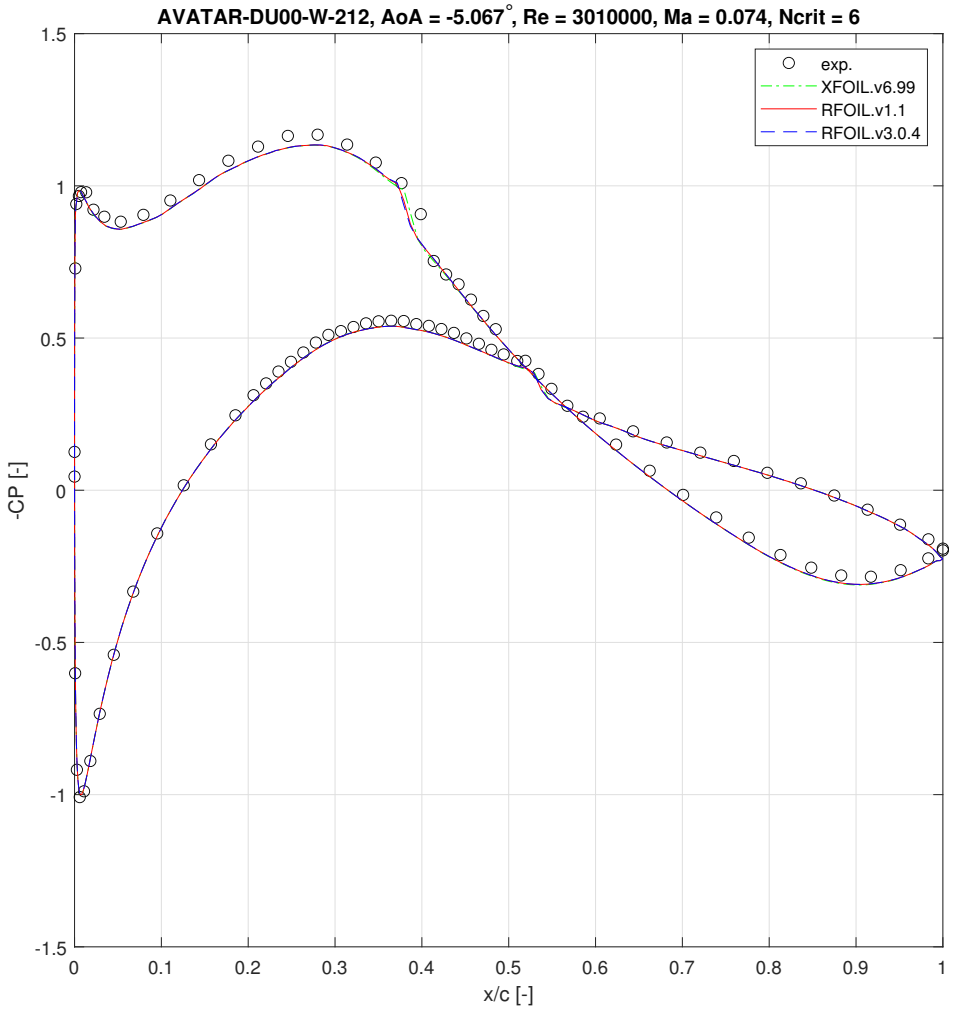

Figure C.153: Comparison between experimental and numerical pressure distributions for the AVATAR-DU00-W-212 airfoil at a Reynolds number of 3020000, and at an angle of attack and a Mach number of -5.067° and 0.075, respectively.

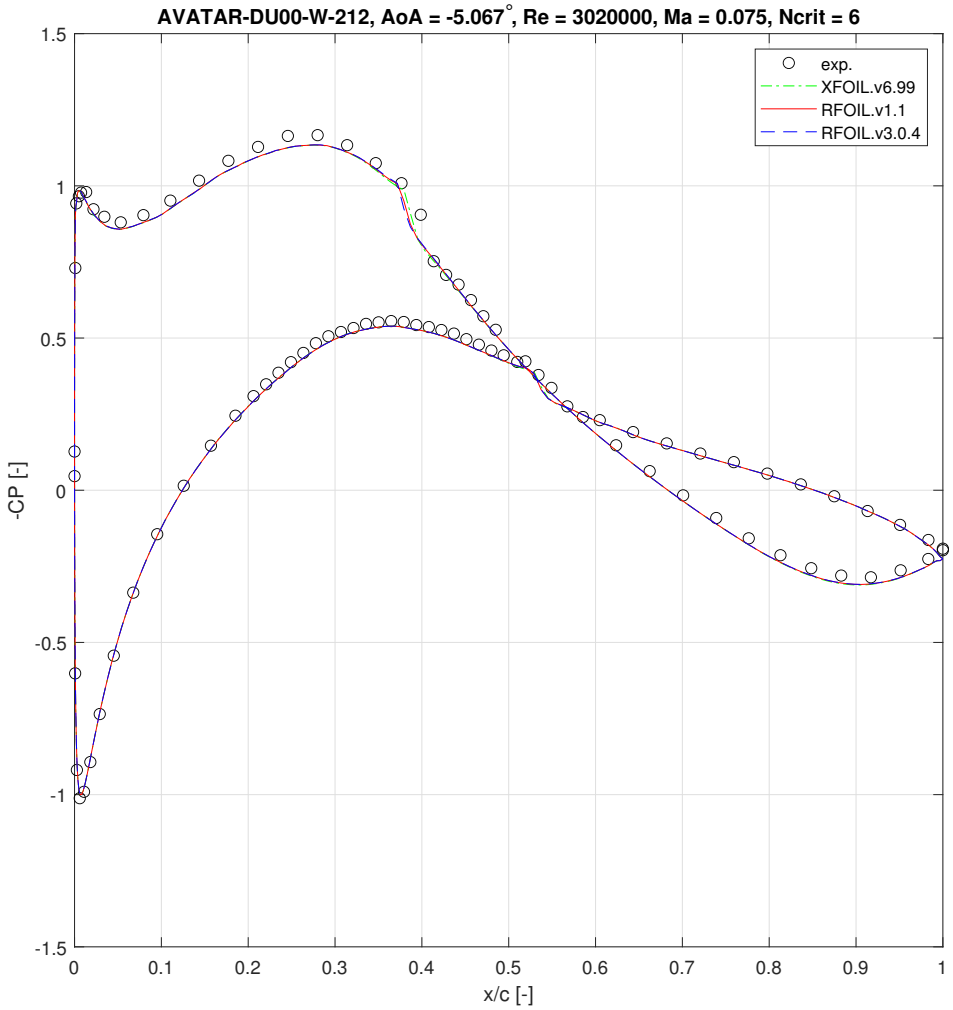

Figure C.154: Comparison between experimental and numerical pressure distributions for the AVATAR-DU00-W-212 airfoil at a Reynolds number of 6010000, and at an angle of attack and a Mach number of -5.067° and 0.055, respectively.

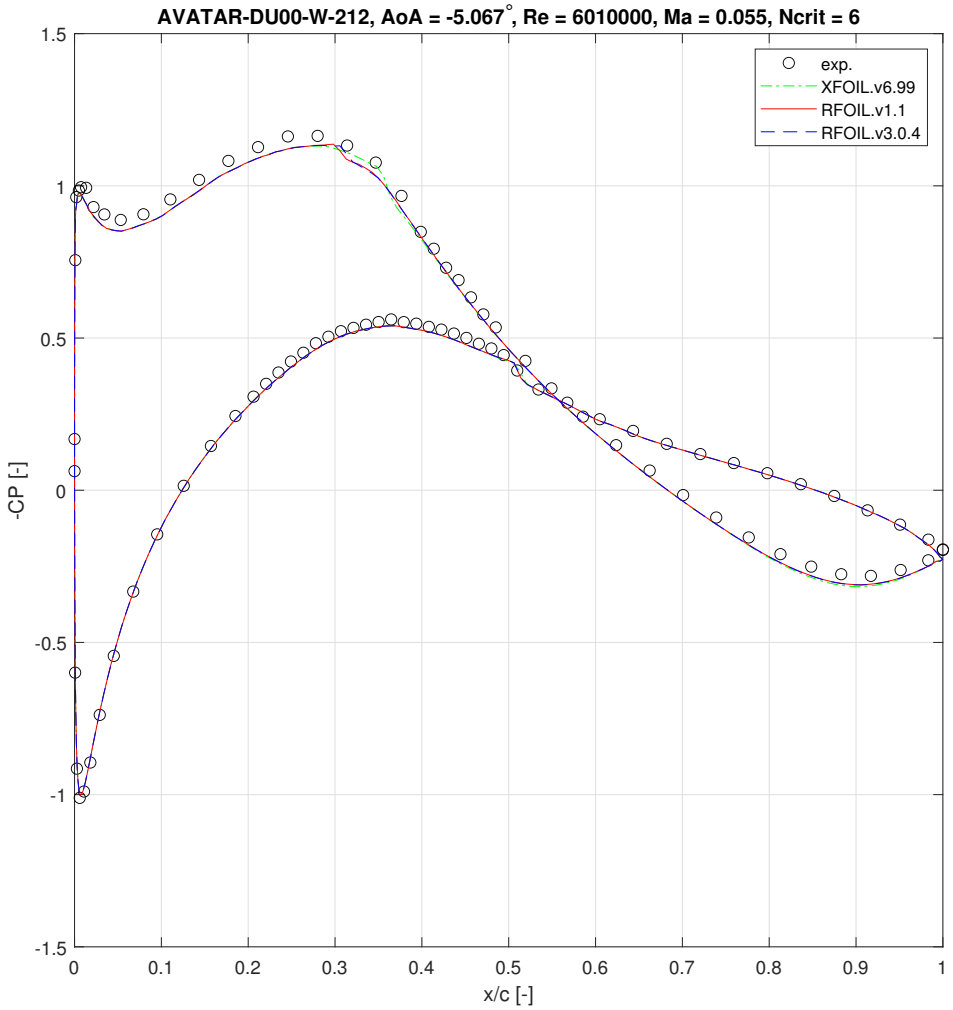

Figure C.155: Comparison between experimental and numerical pressure distributions for the AVATAR-DU00-W-212 airfoil at a Reynolds number of 8990000, and at an angle of attack and a Mach number of -5.067° and 0.043, respectively.

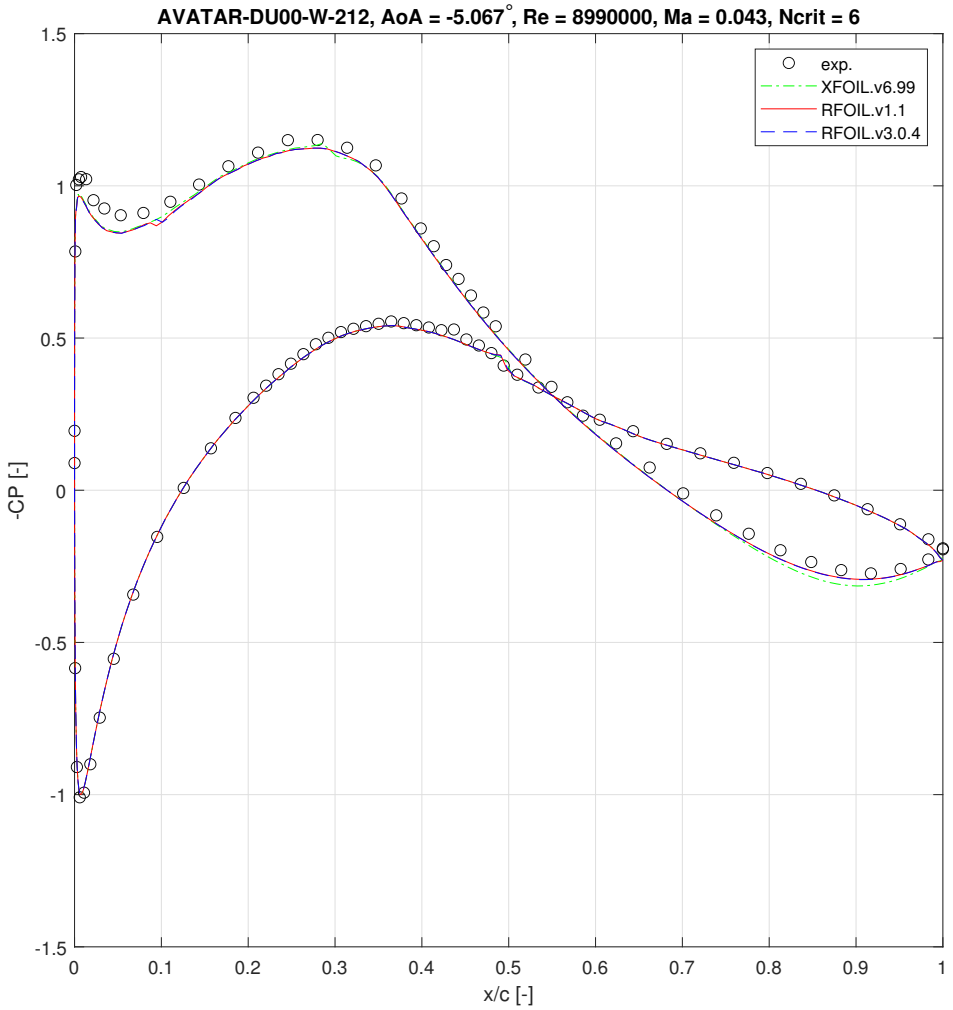

Figure C.156: Comparison between experimental and numerical pressure distributions for the AVATAR-DU00-W-212 airfoil at a Reynolds number of 6020000, and at an angle of attack and a Mach number of -5.068° and 0.029, respectively.

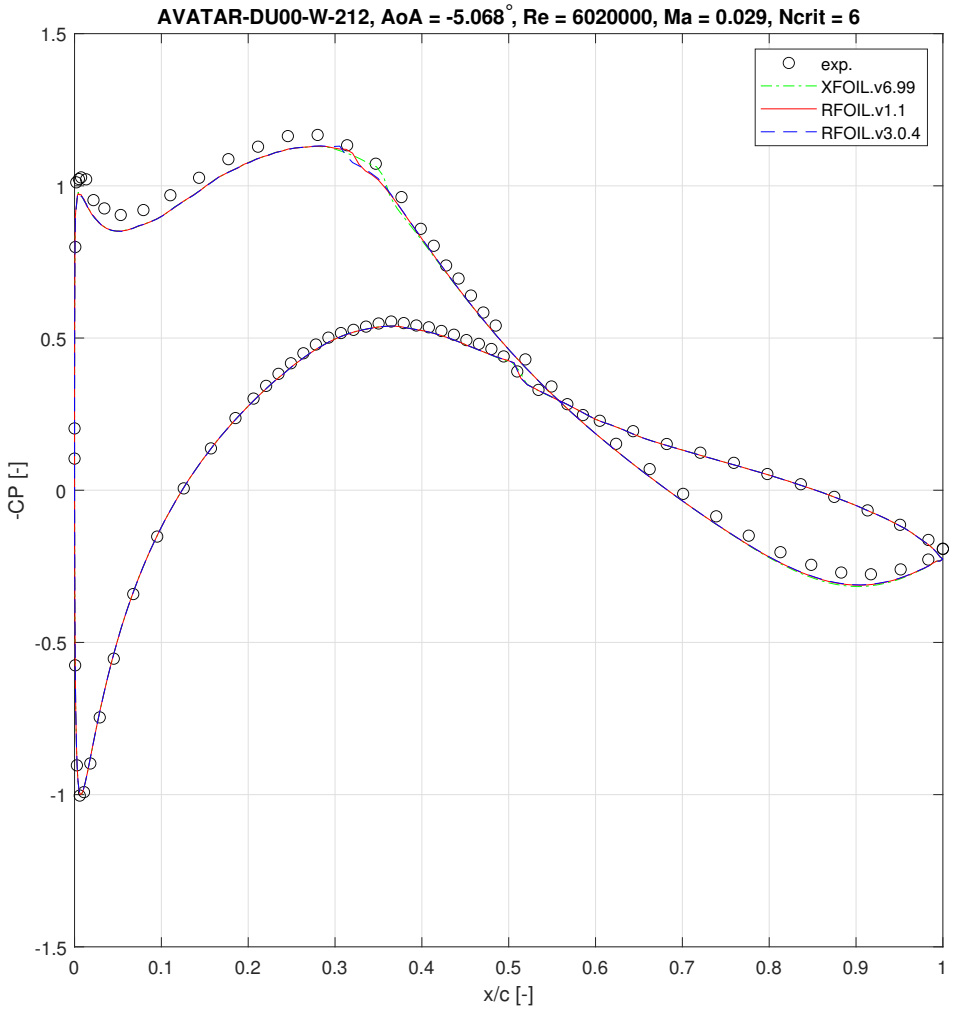

Figure C.157: Comparison between experimental and numerical pressure distributions for the AVATAR-DU00-W-212 airfoil at a Reynolds number of 12010000, and at an angle of attack and a Mach number of -5.154° and 0.058, respectively.

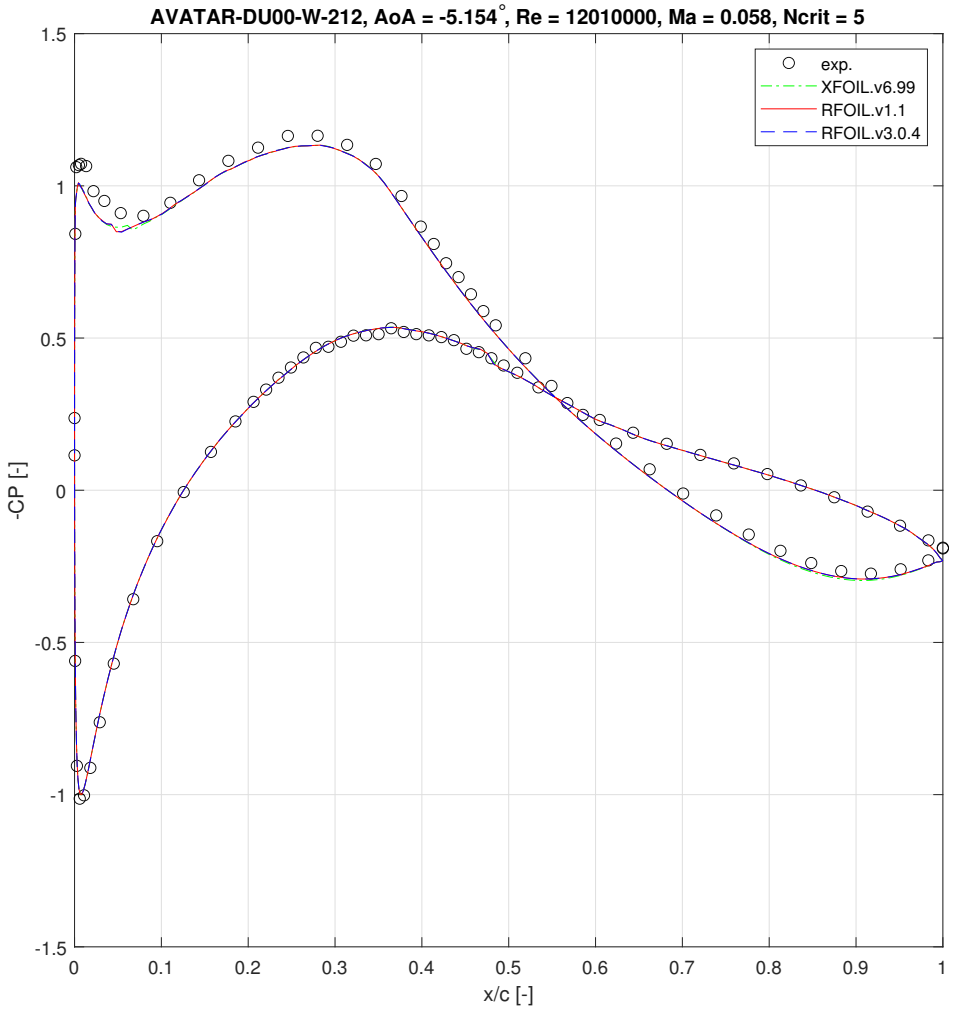

Figure C.158: Comparison between experimental and numerical pressure distributions for the AVATAR-DU00-W-212 airfoil at a Reynolds number of 15020000, and at an angle of attack and a Mach number of -5.269° and 0.082, respectively.

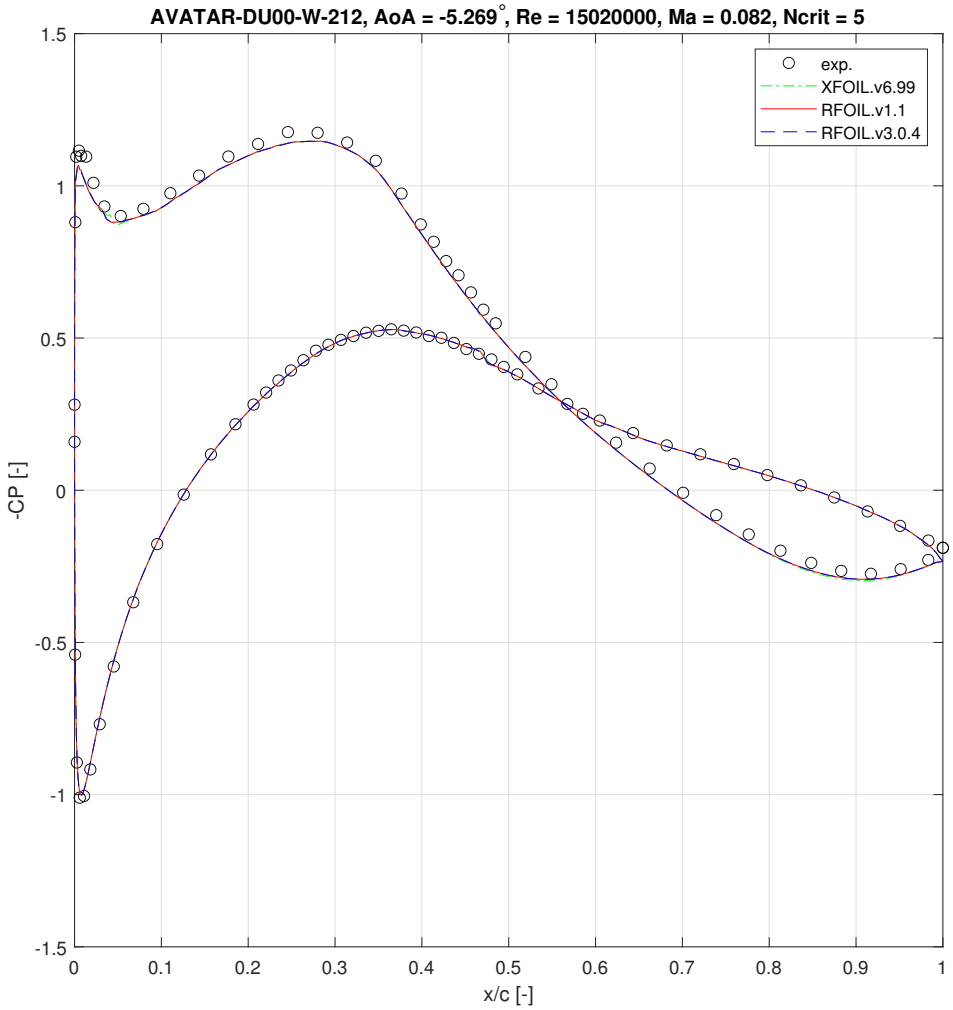

Figure C.159: Comparison between experimental and numerical pressure distributions for the AVATAR-DU00-W-212 airfoil at a Reynolds number of 5960000, and at an angle of attack and a Mach number of -5.269° and 0.054, respectively.

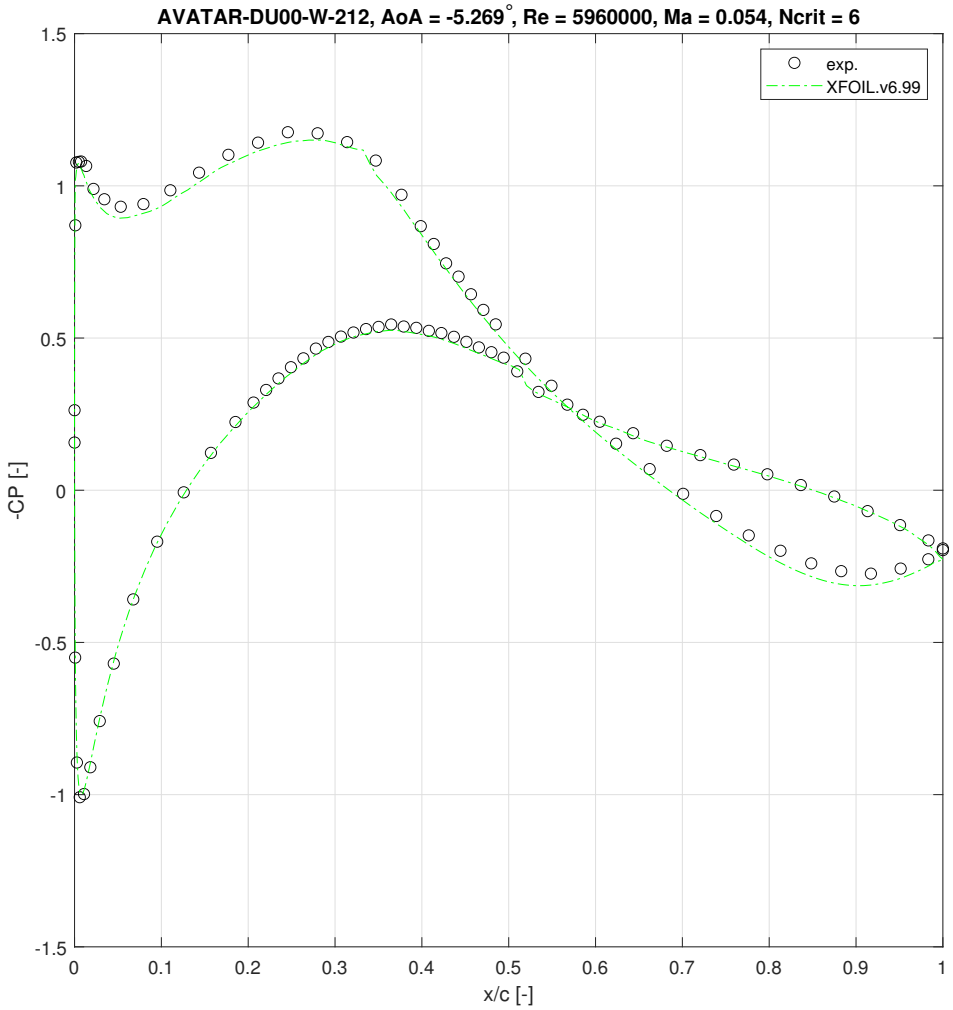

Figure C.160: Comparison between experimental and numerical pressure distributions for the AVATAR-DU00-W-212 airfoil at a Reynolds number of 6020000, and at an angle of attack and a Mach number of -5.269° and 0.029, respectively.

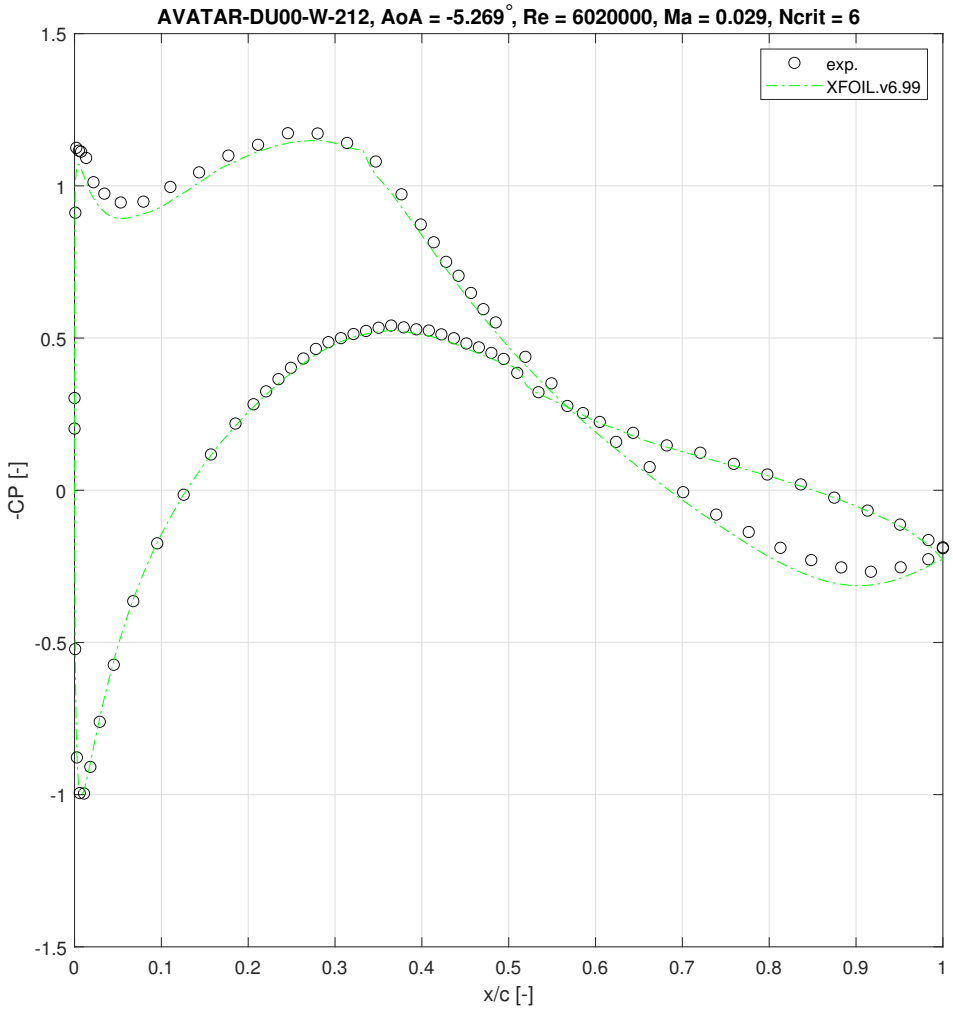

Figure C.161: Comparison between experimental and numerical pressure distributions for the AVATAR-DU00-W-212 airfoil at a Reynolds number of 9000000, and at an angle of attack and a Mach number of -5.269° and 0.043, respectively.

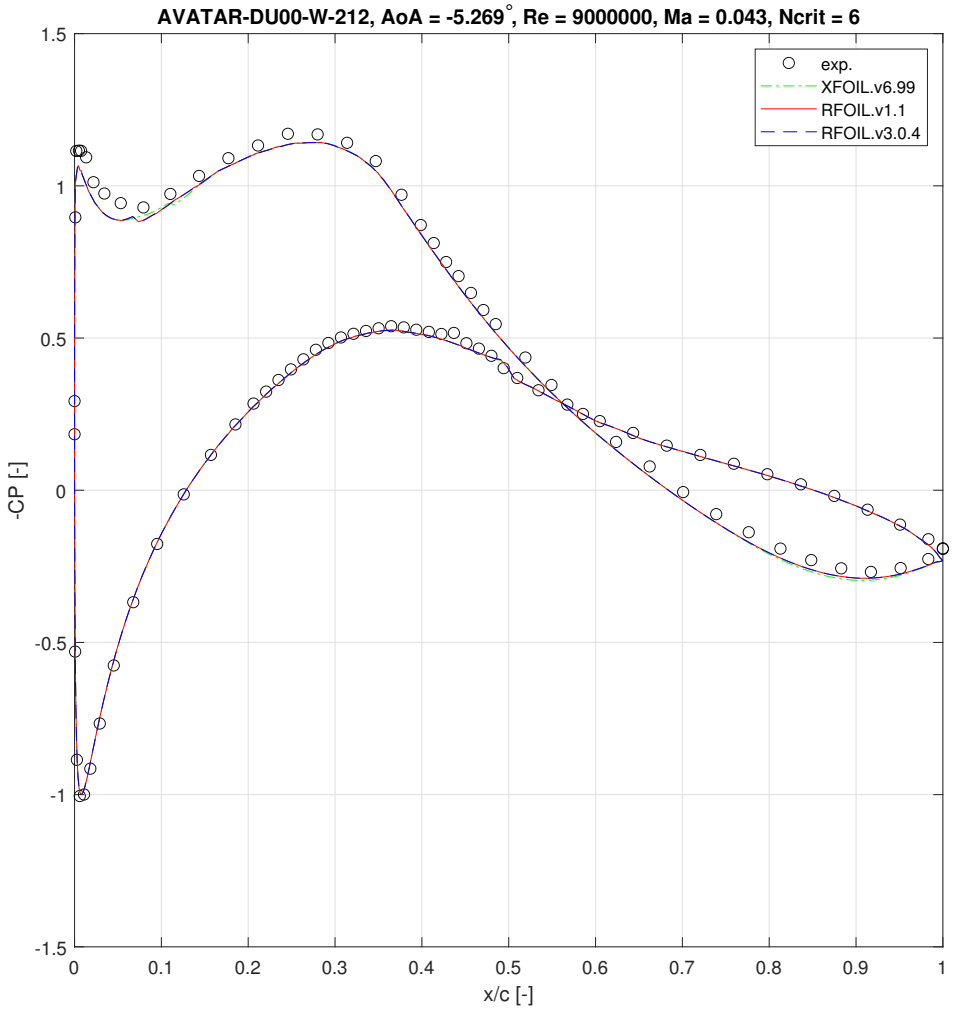

Figure C.162: Comparison between experimental and numerical pressure distributions for the AVATAR-DU00-W-212 airfoil at a Reynolds number of 12010000, and at an angle of attack and a Mach number of -5.354° and 0.058, respectively.

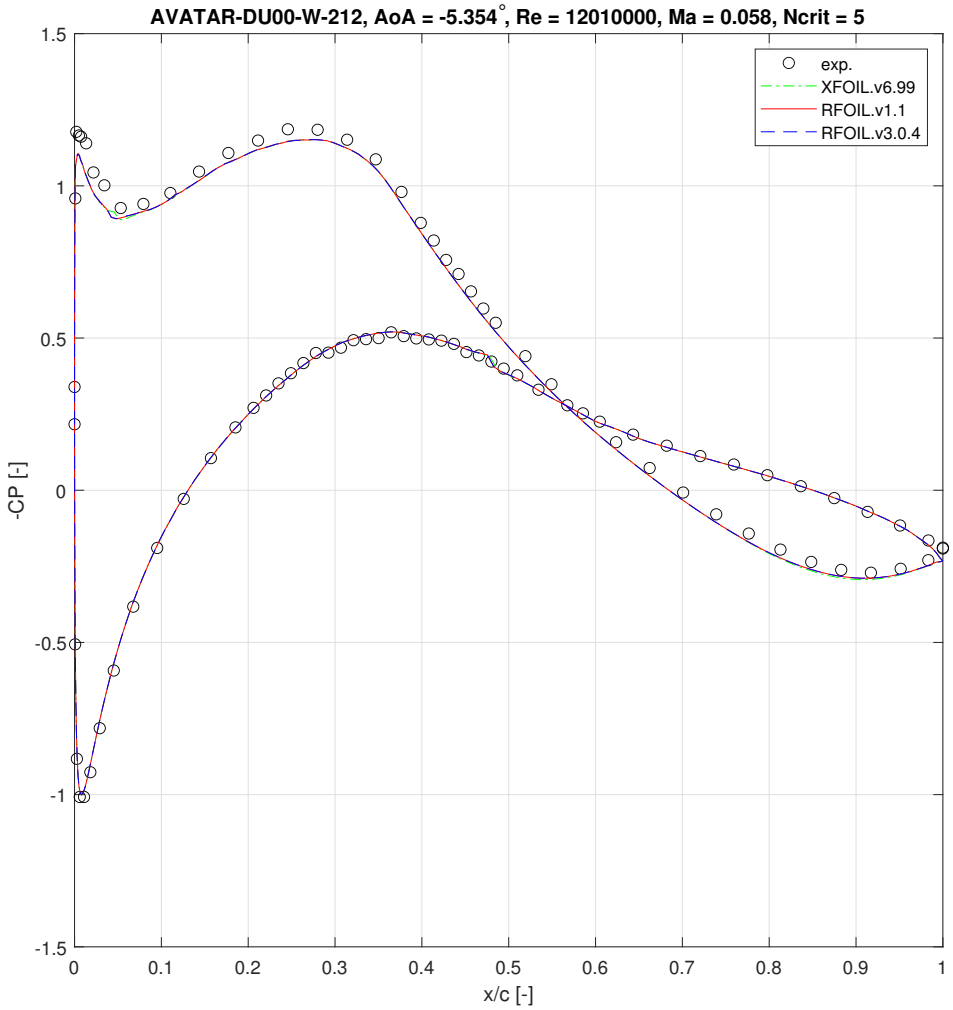

Figure C.163: Comparison between experimental and numerical pressure distributions for the AVATAR-DU00-W-212 airfoil at a Reynolds number of 6020000, and at an angle of attack and a Mach number of -5.471° and 0.029, respectively.

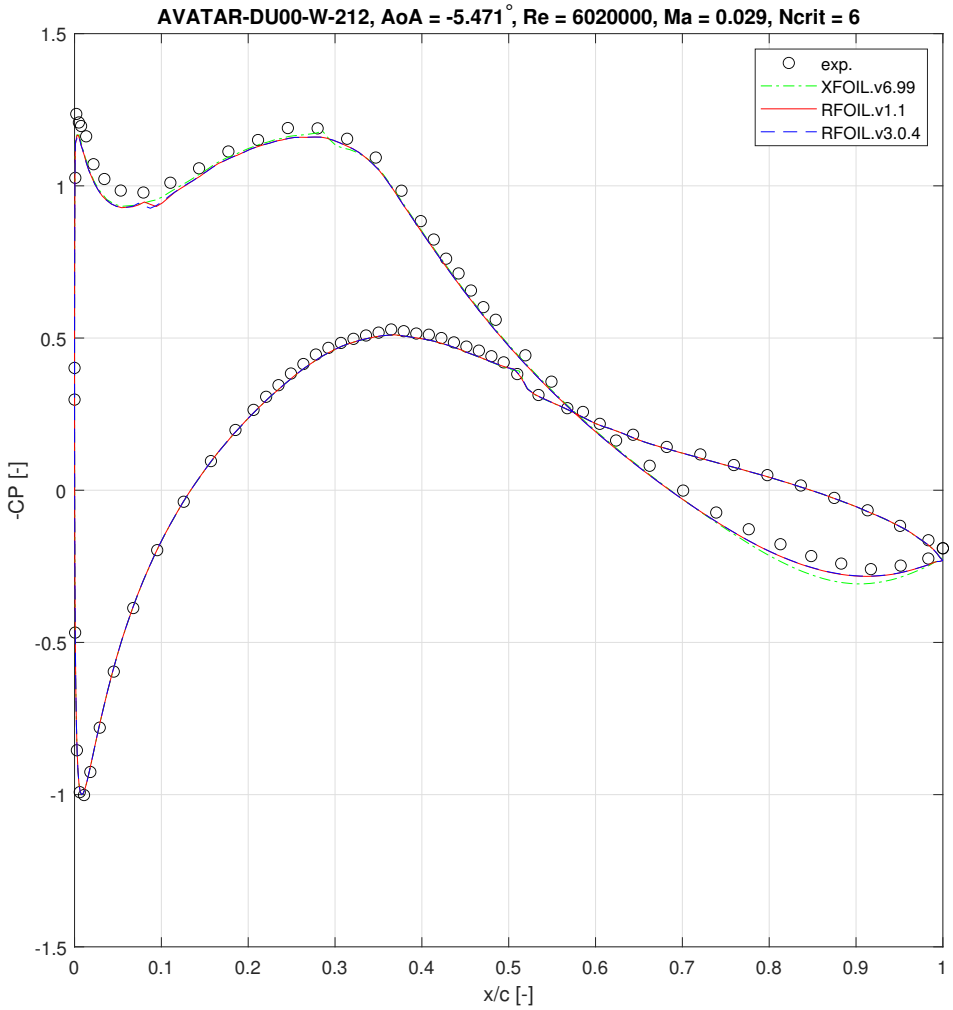

Figure C.164: Comparison between experimental and numerical pressure distributions for the AVATAR-DU00-W-212 airfoil at a Reynolds number of 6030000, and at an angle of attack and a Mach number of -5.471° and 0.055, respectively.

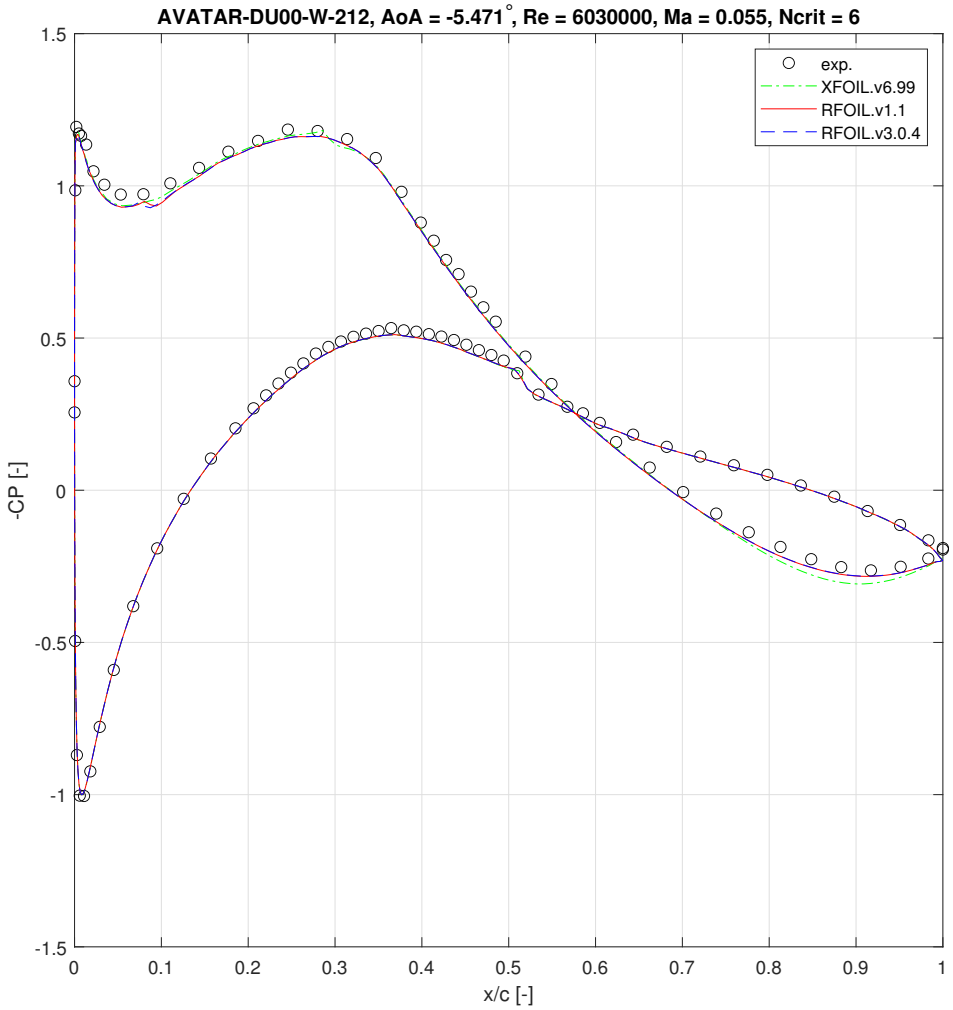

Figure C.165: Comparison between experimental and numerical pressure distributions for the AVATAR-DU00-W-212 airfoil at a Reynolds number of 12000000, and at an angle of attack and a Mach number of -5.554° and 0.058, respectively.

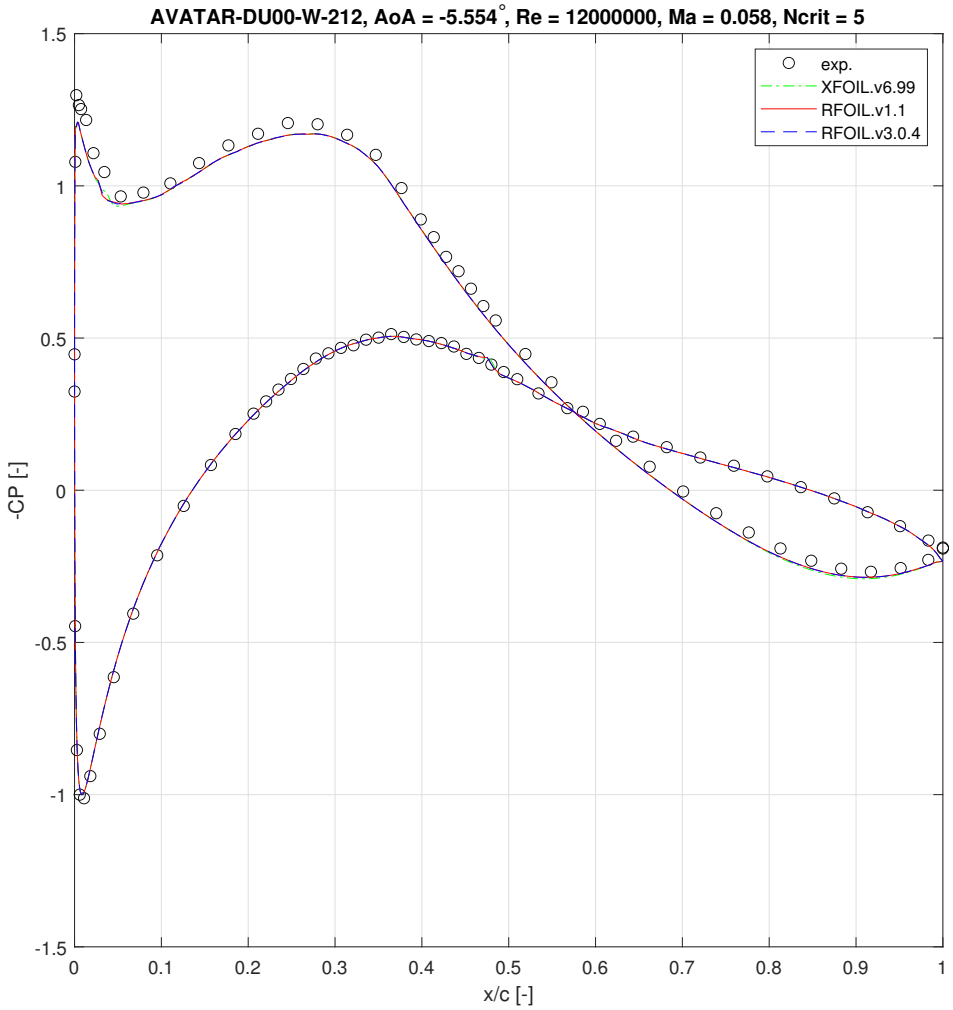

Figure C.166: Comparison between experimental and numerical pressure distributions for the AVATAR-DU00-W-212 airfoil at a Reynolds number of 15070000, and at an angle of attack and a Mach number of -5.573° and 0.082, respectively.

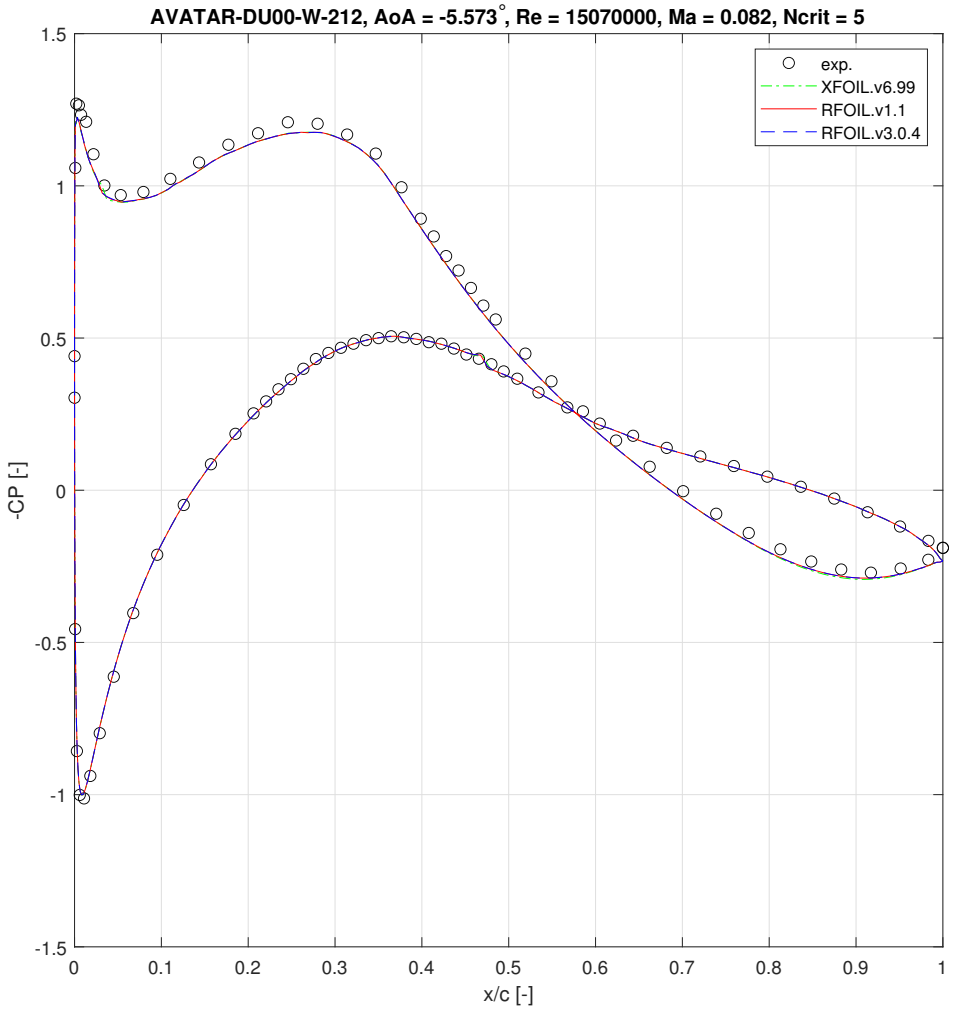

Figure C.167: Comparison between experimental and numerical pressure distributions for the AVATAR-DU00-W-212 airfoil at a Reynolds number of 3020000, and at an angle of attack and a Mach number of -5.574° and 0.075, respectively.

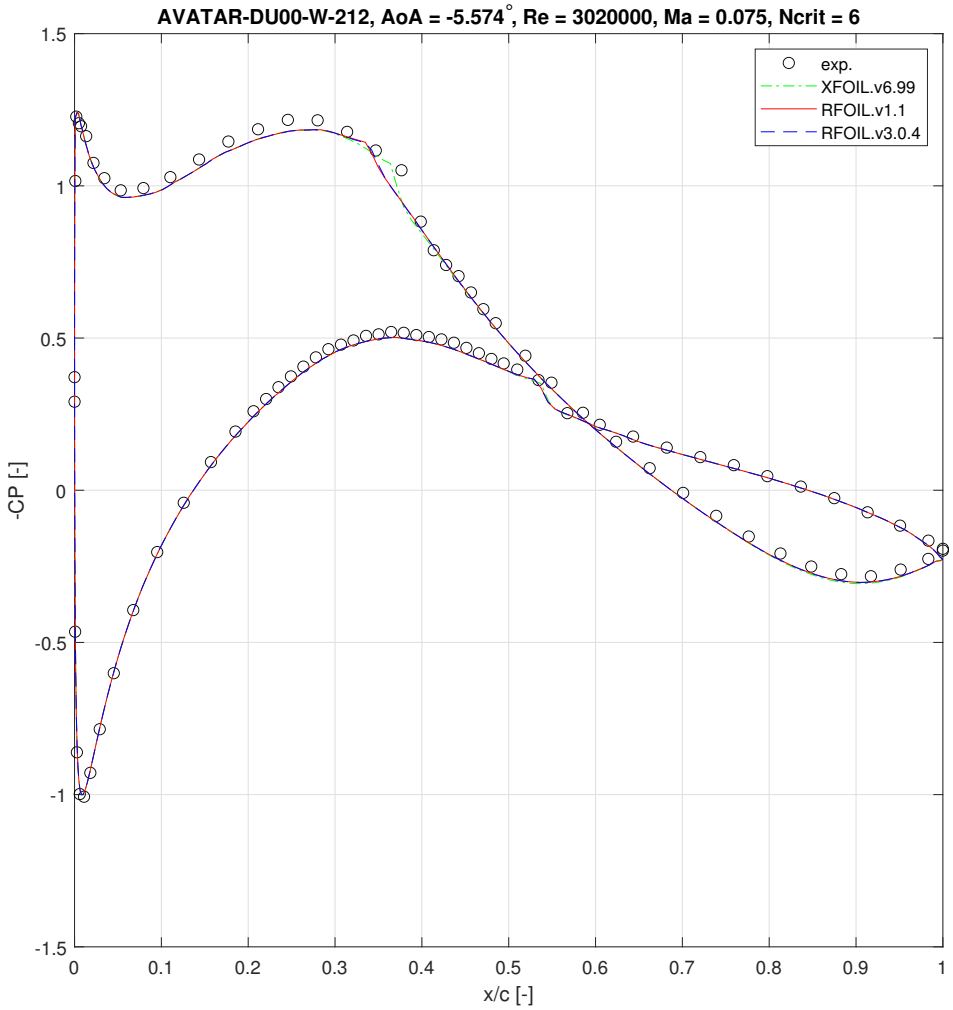

Figure C.168: Comparison between experimental and numerical pressure distributions for the AVATAR-DU00-W-212 airfoil at a Reynolds number of 6030000, and at an angle of attack and a Mach number of -5.673° and 0.029, respectively.

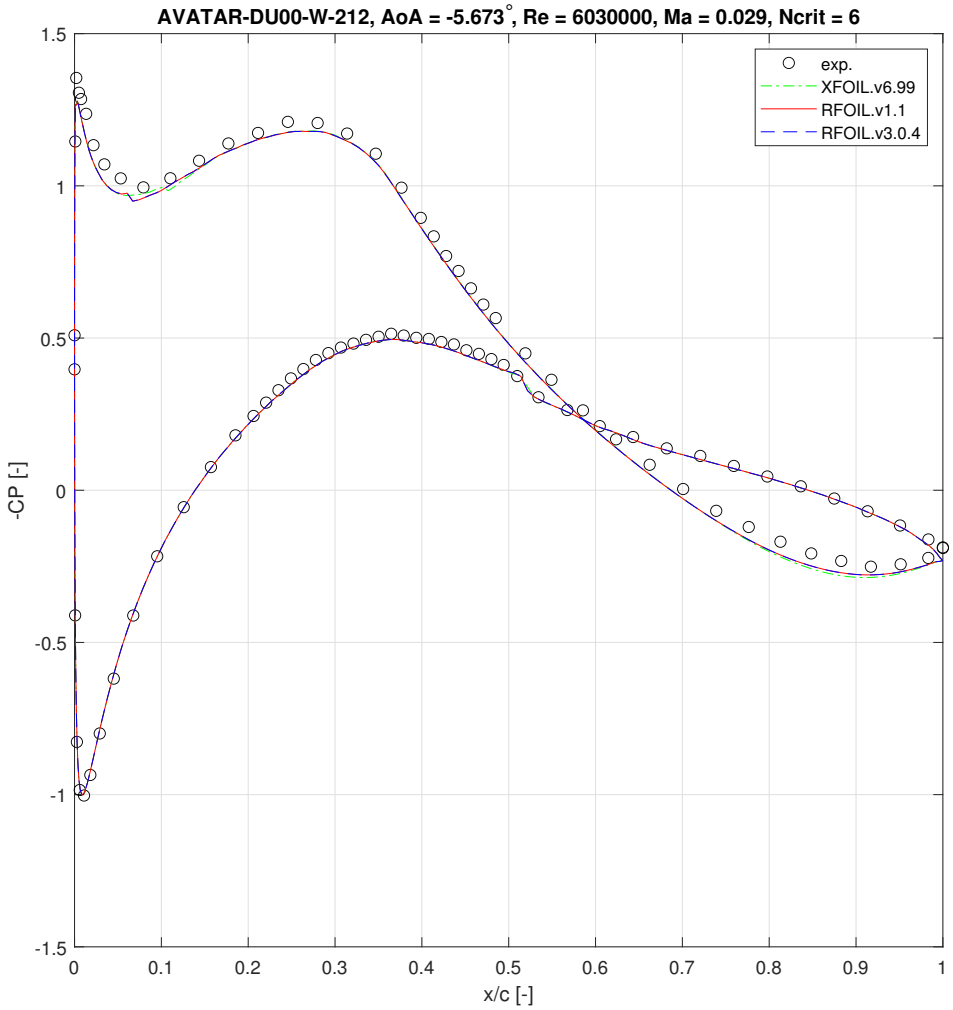

Figure C.169: Comparison between experimental and numerical pressure distributions for the AVATAR-DU00-W-212 airfoil at a Reynolds number of 6070000, and at an angle of attack and a Mach number of -5.673° and 0.055, respectively.

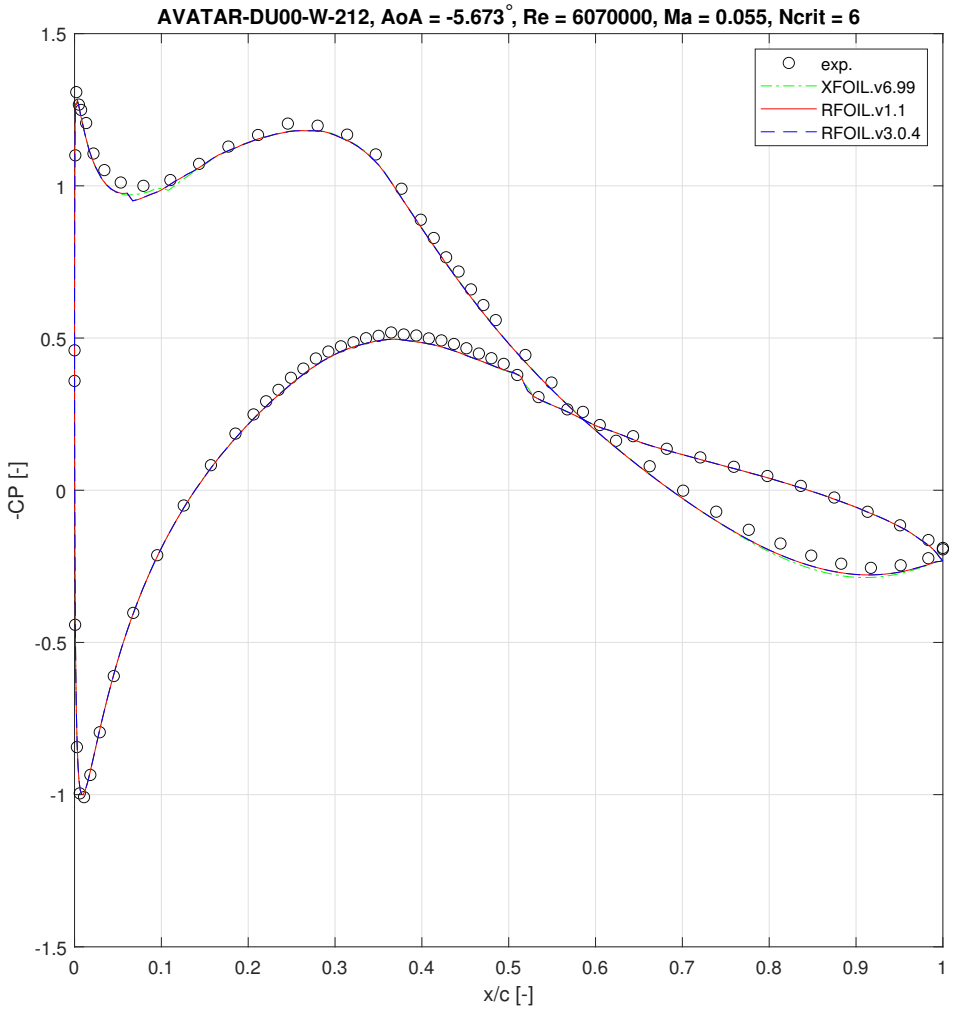

Figure C.170: Comparison between experimental and numerical pressure distributions for the AVATAR-DU00-W-212 airfoil at a Reynolds number of 6030000, and at an angle of attack and a Mach number of -5.876° and 0.029, respectively.

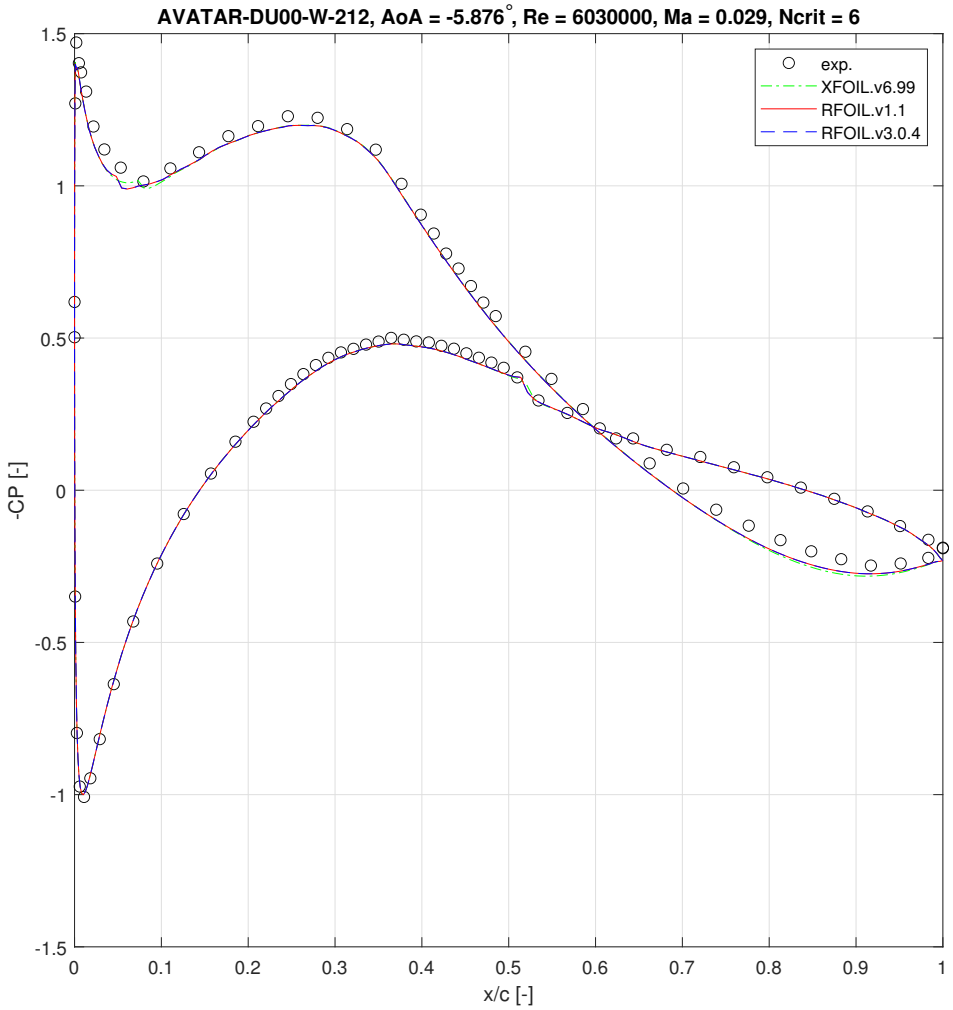

Figure C.171: Comparison between experimental and numerical pressure distributions for the AVATAR-DU00-W-212 airfoil at a Reynolds number of 11980000, and at an angle of attack and a Mach number of -5.955° and 0.058, respectively.

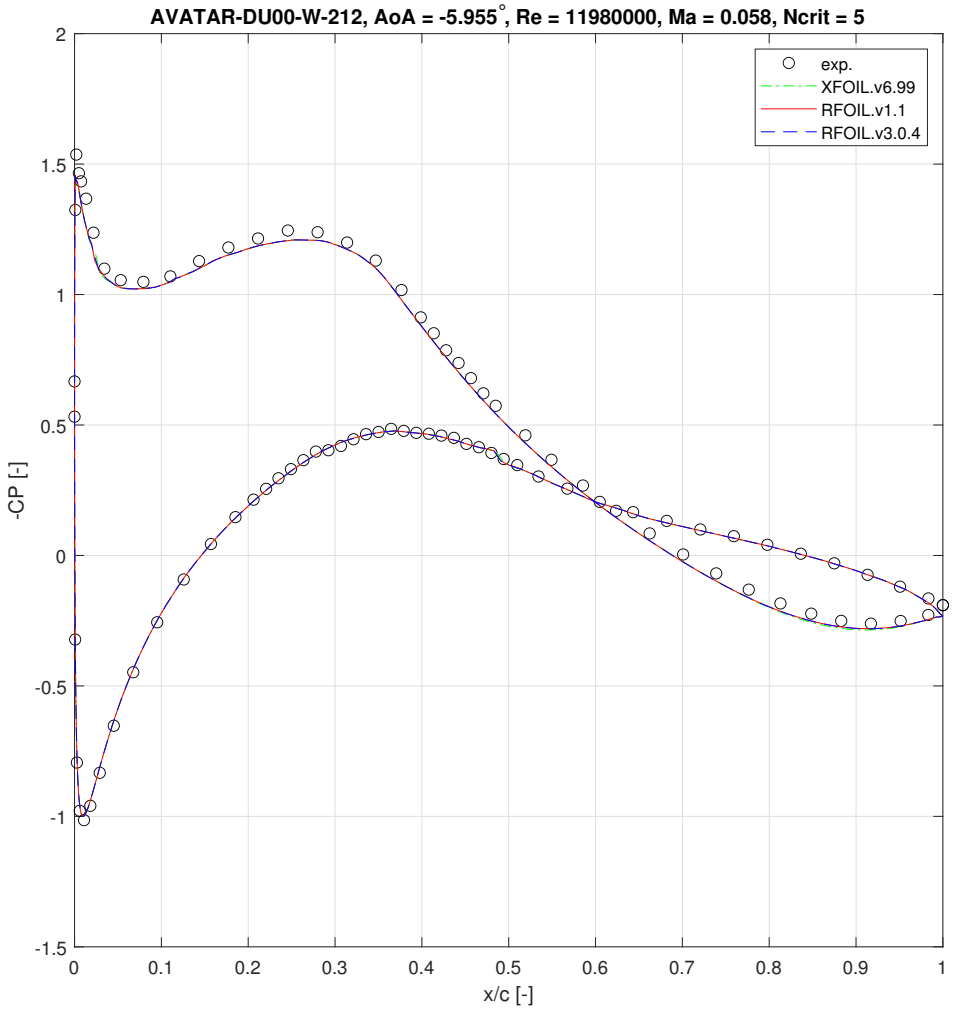

Figure C.172: Comparison between experimental and numerical pressure distributions for the AVATAR-DU00-W-212 airfoil at a Reynolds number of 6050000, and at an angle of attack and a Mach number of -6.077° and 0.055, respectively.

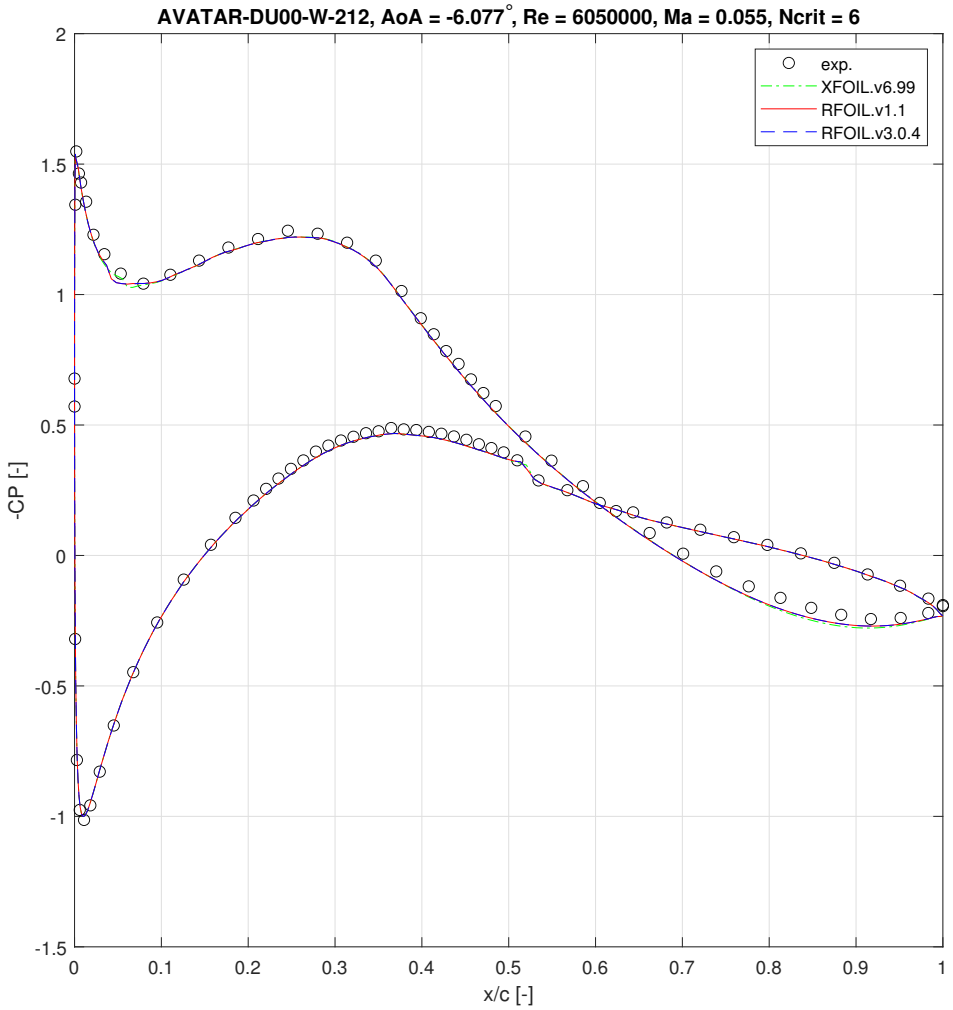

Figure C.173: Comparison between experimental and numerical pressure distributions for the AVATAR-DU00-W-212 airfoil at a Reynolds number of 6010000, and at an angle of attack and a Mach number of -6.078° and 0.029, respectively.

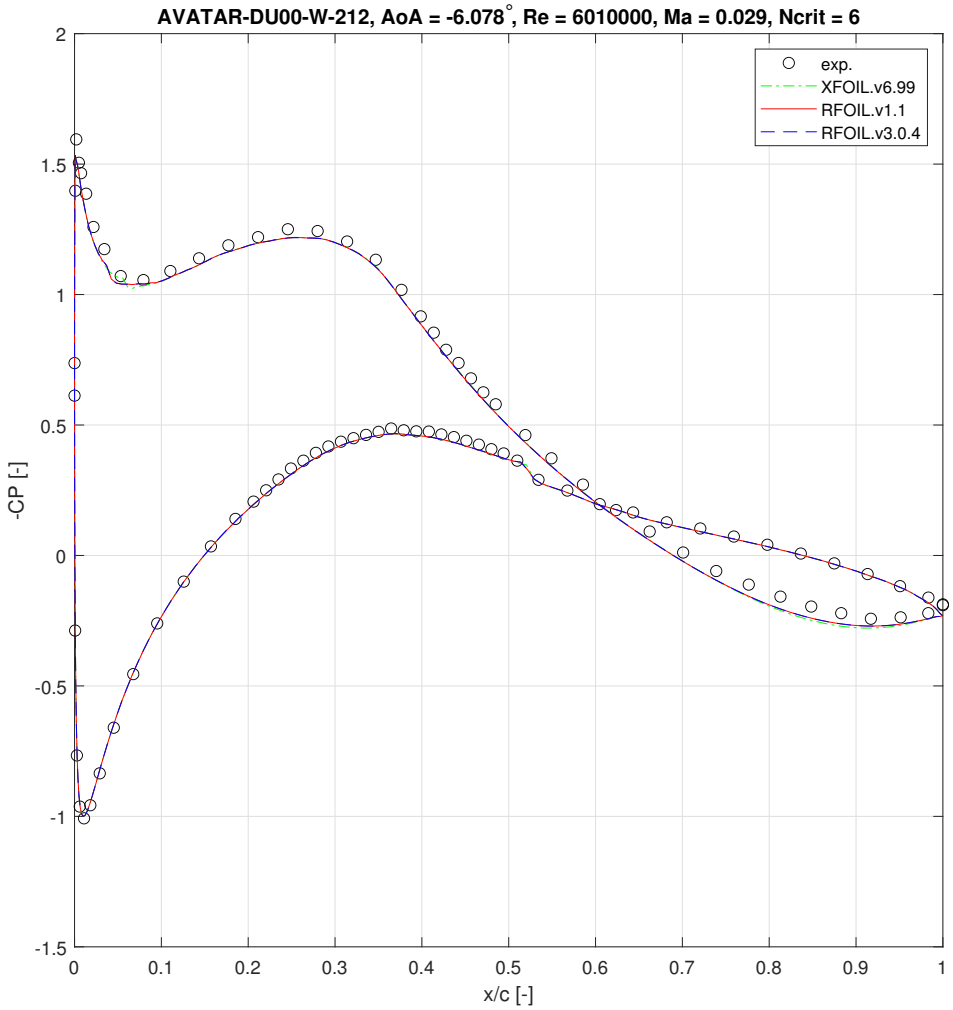

Figure C.174: Comparison between experimental and numerical pressure distributions for the AVATAR-DU00-W-212 airfoil at a Reynolds number of 6010000, and at an angle of attack and a Mach number of -6.078° and 0.055, respectively.

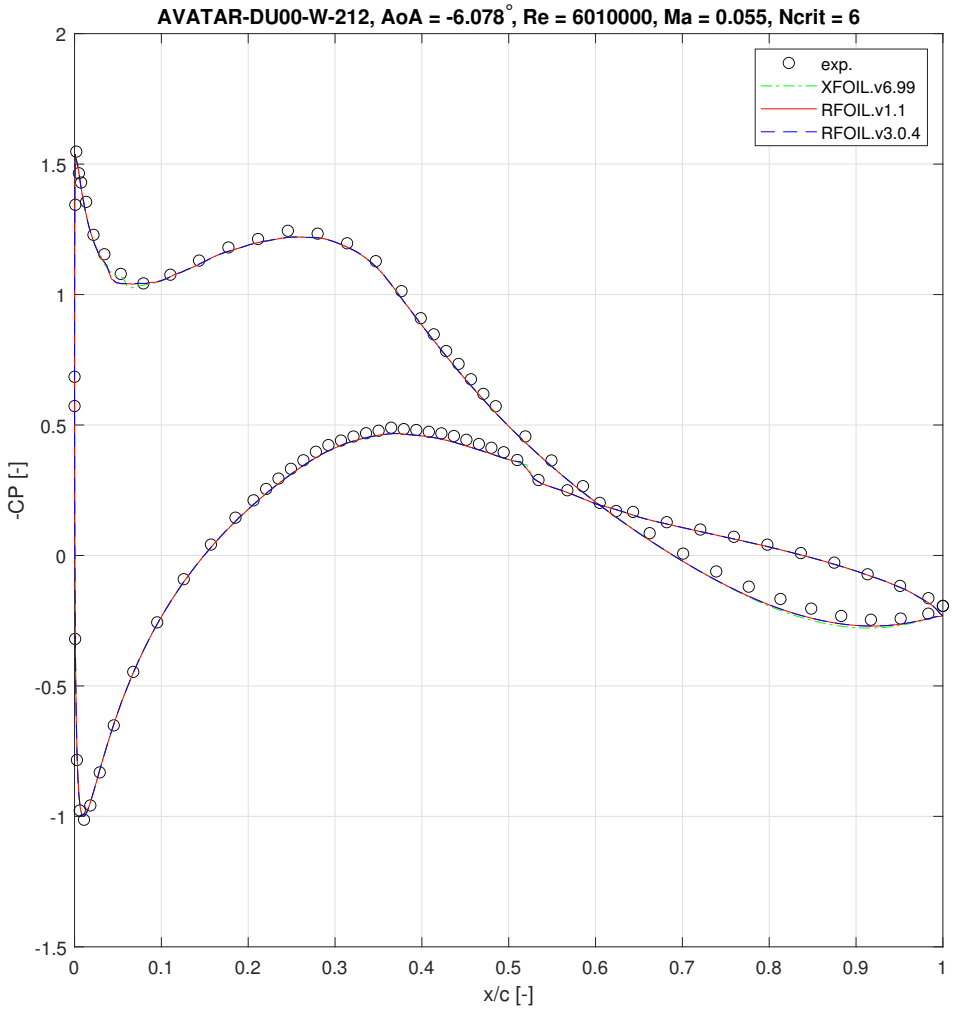

Figure C.175: Comparison between experimental and numerical pressure distributions for the AVATAR-DU00-W-212 airfoil at a Reynolds number of 9010000, and at an angle of attack and a Mach number of -6.078° and 0.083, respectively.

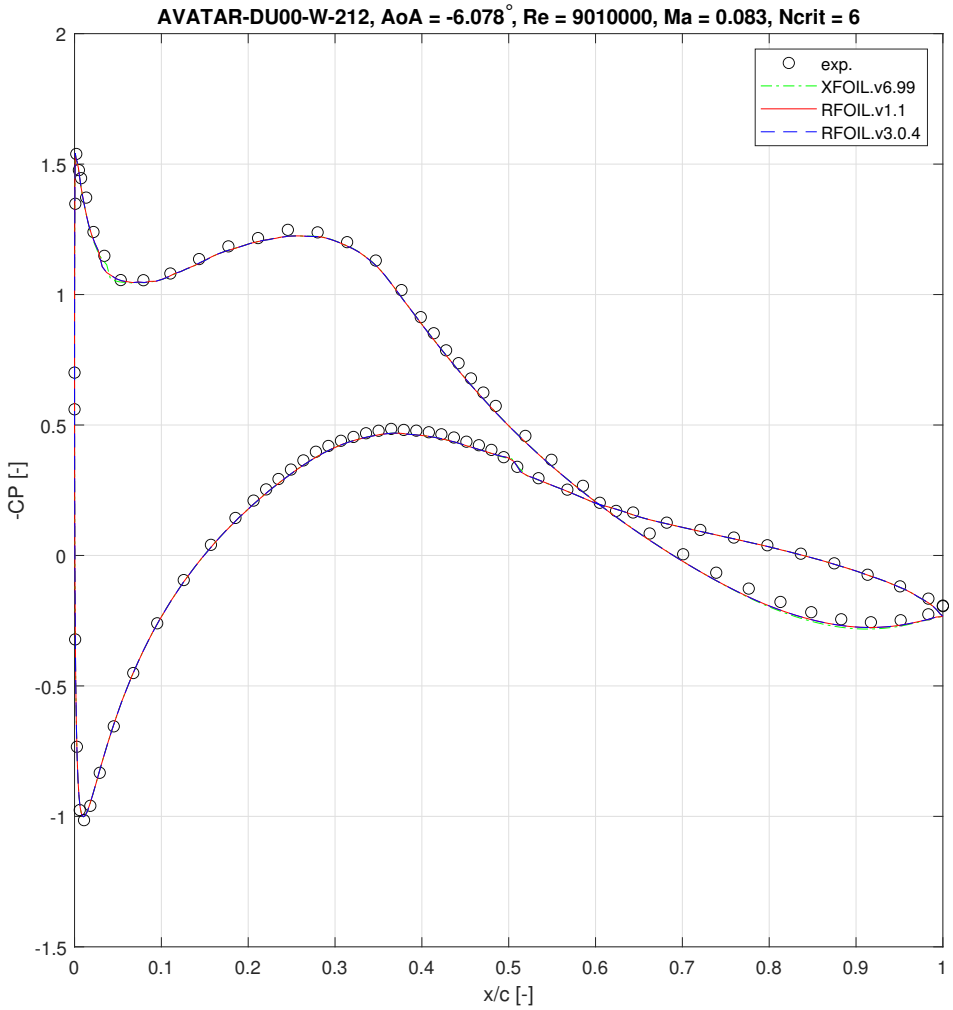

Figure C.176: Comparison between experimental and numerical pressure distributions for the AVATAR-DU00-W-212 airfoil at a Reynolds number of 15000000, and at an angle of attack and a Mach number of -6.079° and 0.081, respectively.

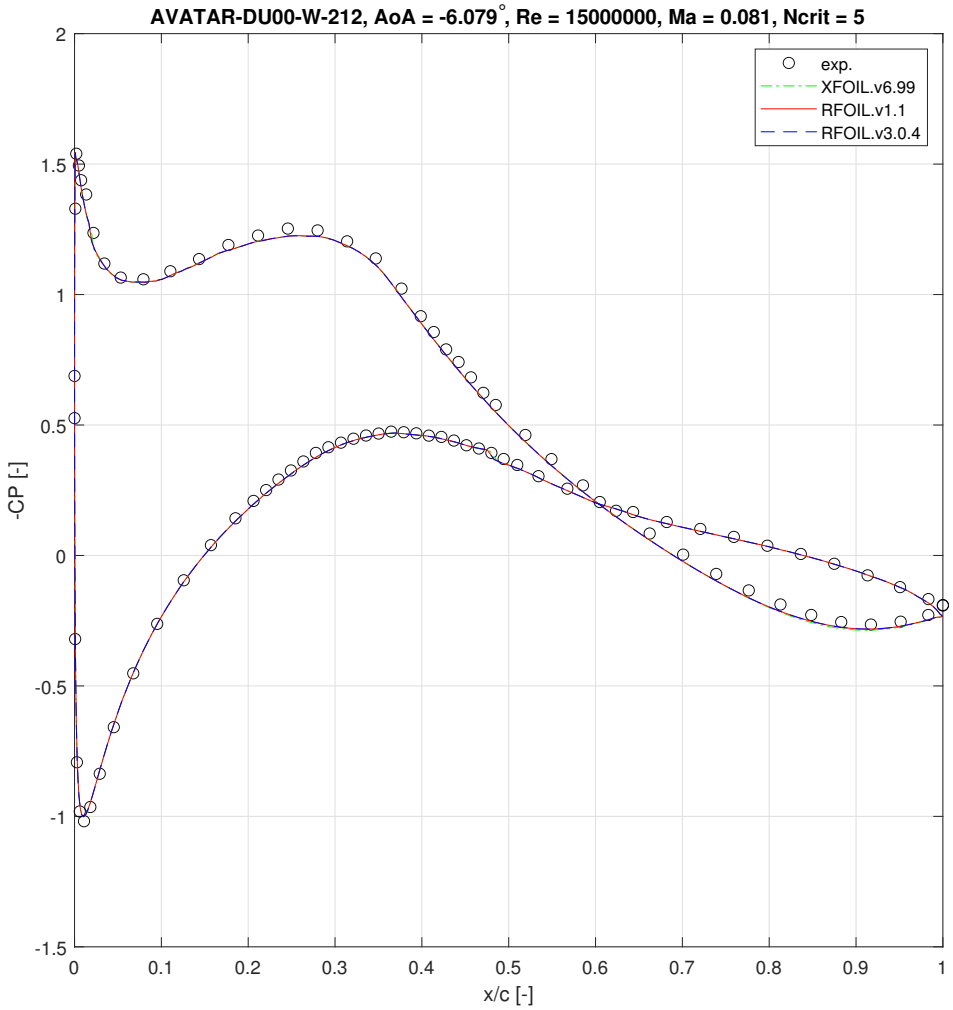

Figure C.177: Comparison between experimental and numerical pressure distributions for the AVATAR-DU00-W-212 airfoil at a Reynolds number of 9020000, and at an angle of attack and a Mach number of -6.079° and 0.044, respectively.

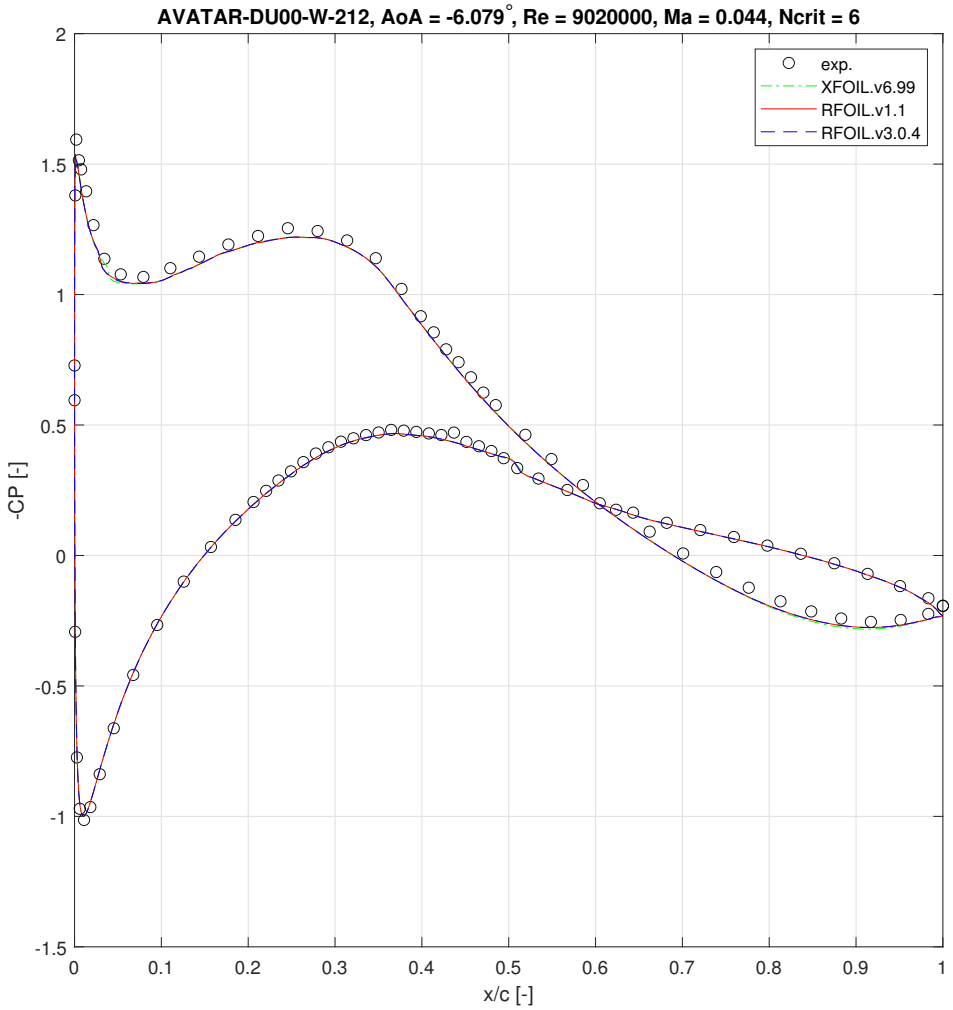

Figure C.178: Comparison between experimental and numerical pressure distributions for the AVATAR-DU00-W-212 airfoil at a Reynolds number of 3010000, and at an angle of attack and a Mach number of -6.080° and 0.074, respectively.

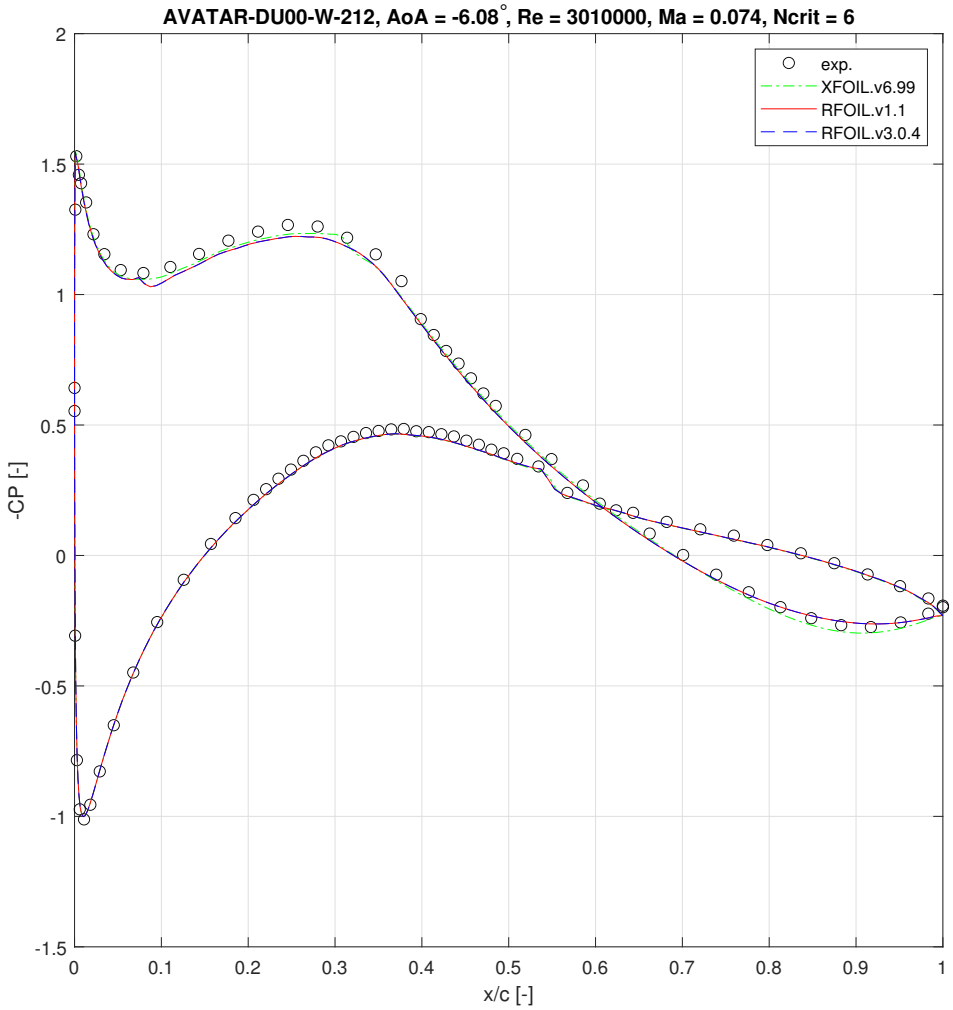

Figure C.179: Comparison between experimental and numerical pressure distributions for the AVATAR-DU00-W-212 airfoil at a Reynolds number of 3010000, and at an angle of attack and a Mach number of -6.281° and 0.074, respectively.

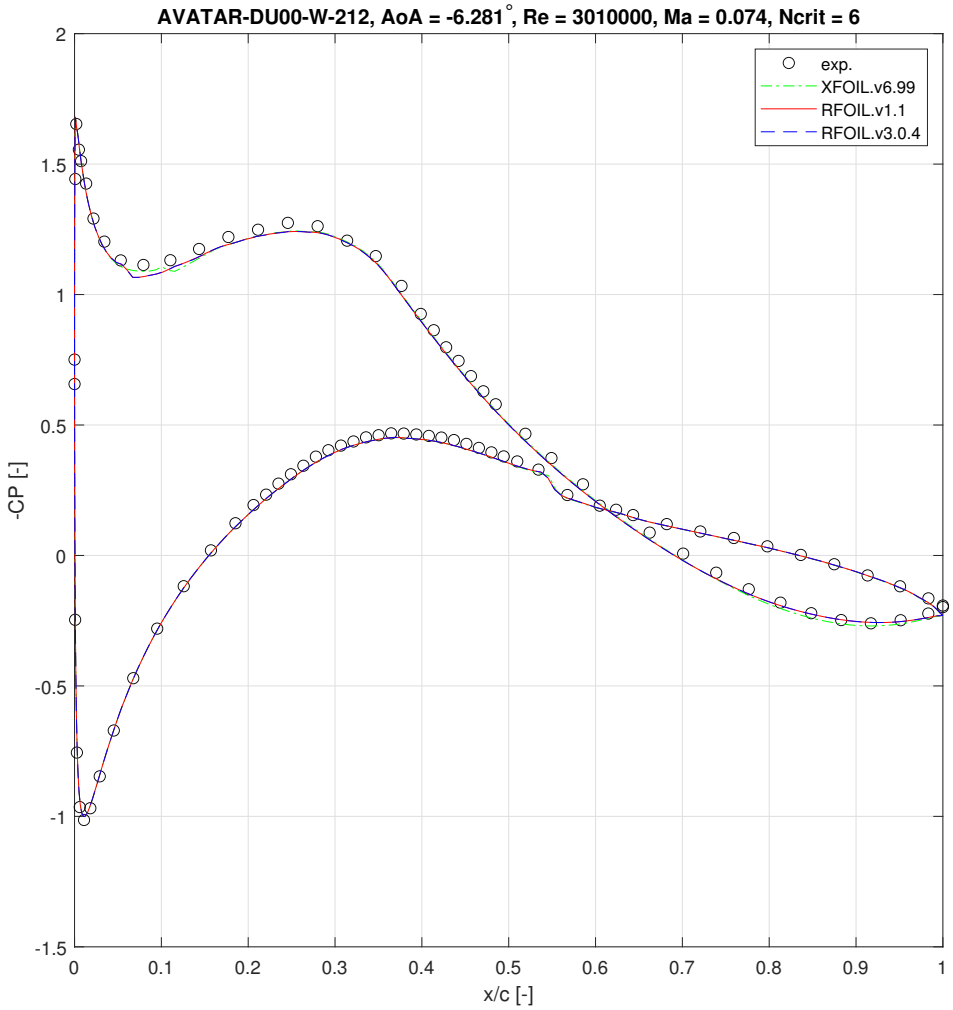

Figure C.180: Comparison between experimental and numerical pressure distributions for the AVATAR-DU00-W-212 airfoil at a Reynolds number of 6010000, and at an angle of attack and a Mach number of -6.280° and 0.029, respectively.

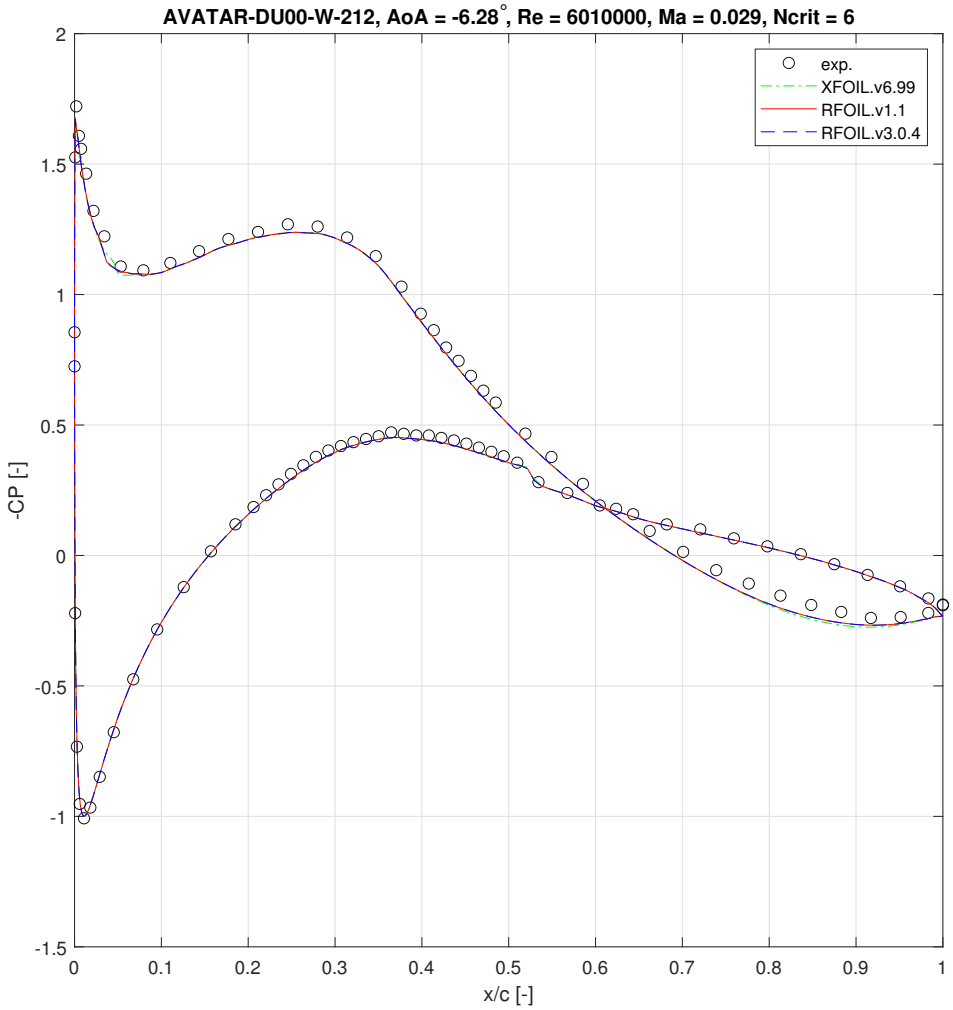

Figure C.181: Comparison between experimental and numerical pressure distributions for the AVATAR-DU00-W-212 airfoil at a Reynolds number of 3010000, and at an angle of attack and a Mach number of -6.482° and 0.074, respectively.

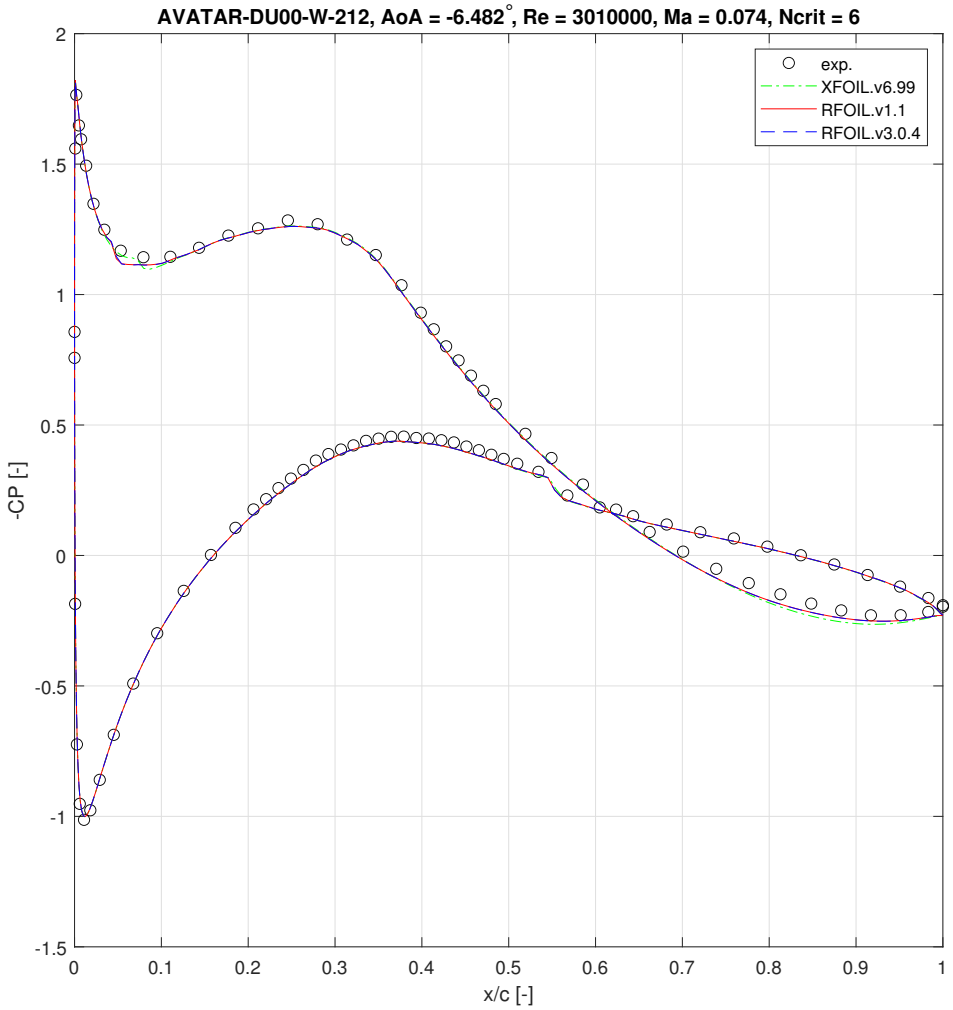

Figure C.182: Comparison between experimental and numerical pressure distributions for the AVATAR-DU00-W-212 airfoil at a Reynolds number of 6020000, and at an angle of attack and a Mach number of -6.483° and 0.029, respectively.

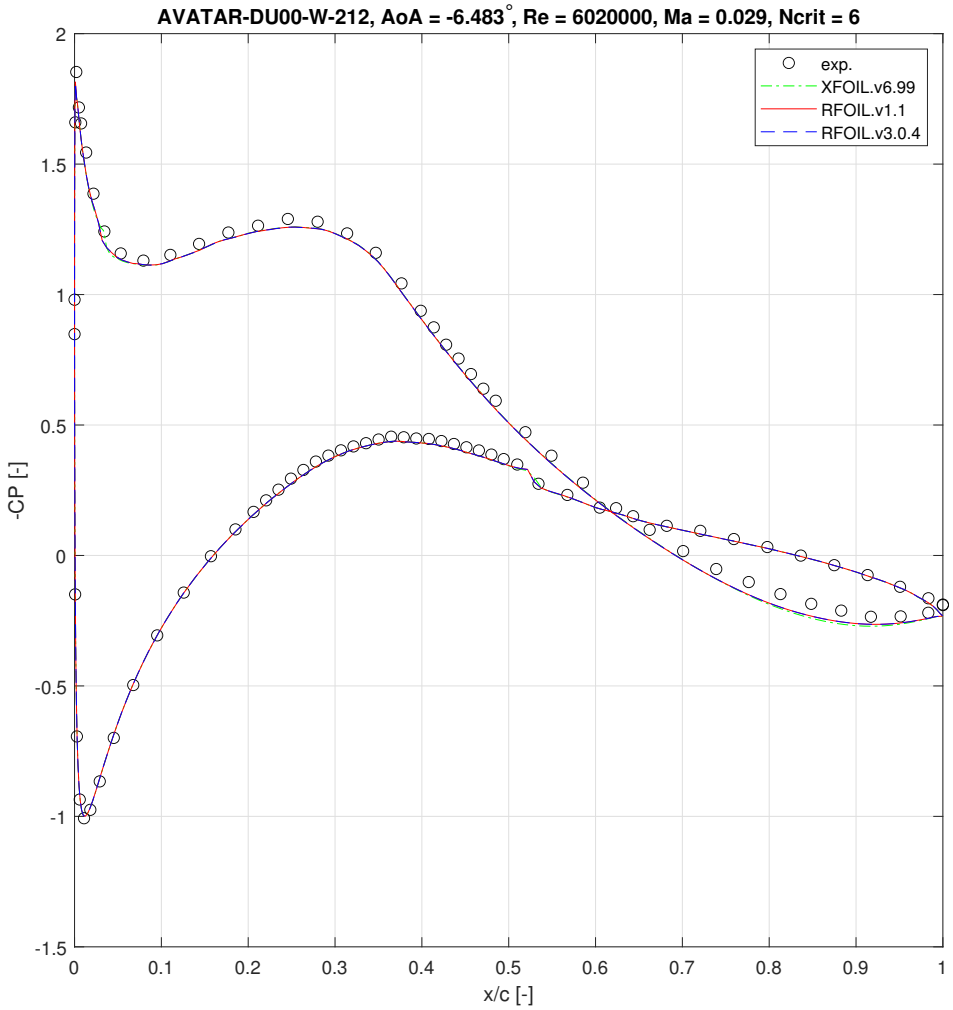

Figure C.183: Comparison between experimental and numerical pressure distributions for the AVATAR-DU00-W-212 airfoil at a Reynolds number of 3010000, and at an angle of attack and a Mach number of -6.684° and 0.074, respectively.

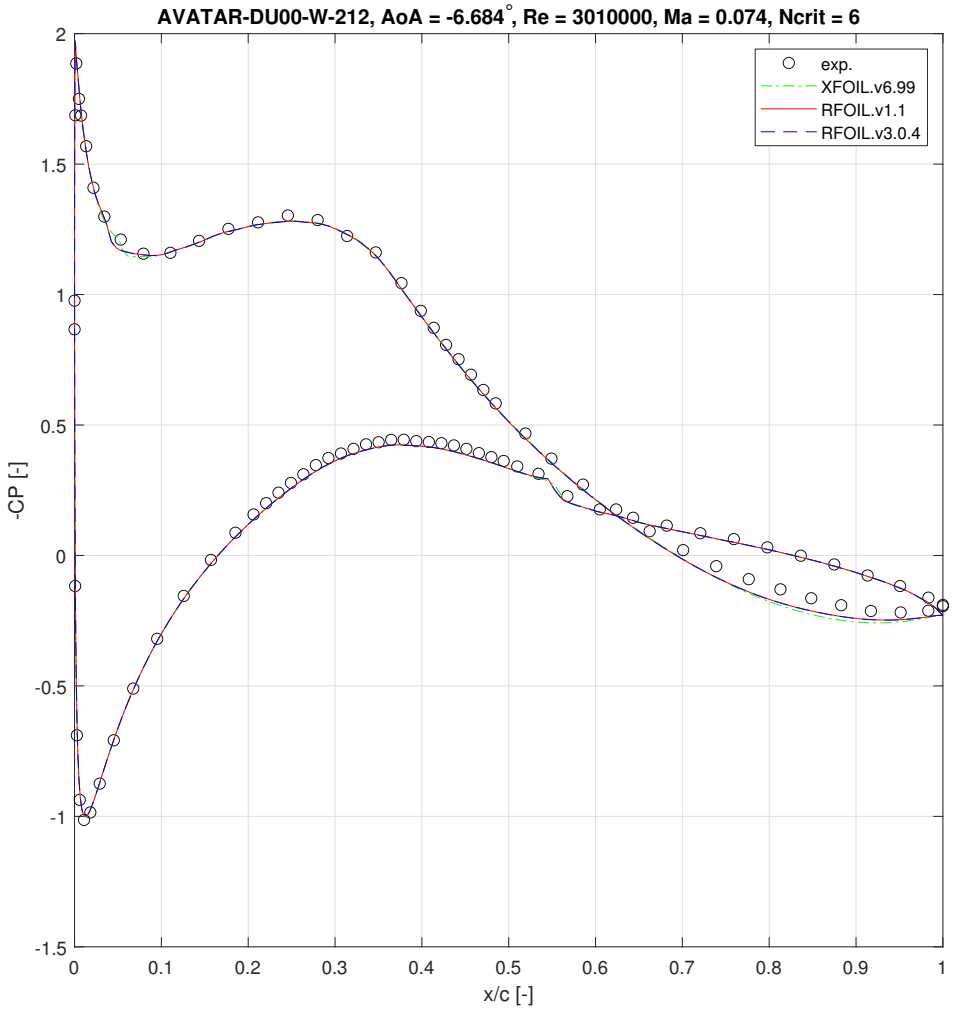

Figure C.184: Comparison between experimental and numerical pressure distributions for the AVATAR-DU00-W-212 airfoil at a Reynolds number of 3010000, and at an angle of attack and a Mach number of -6.886° and 0.074, respectively.

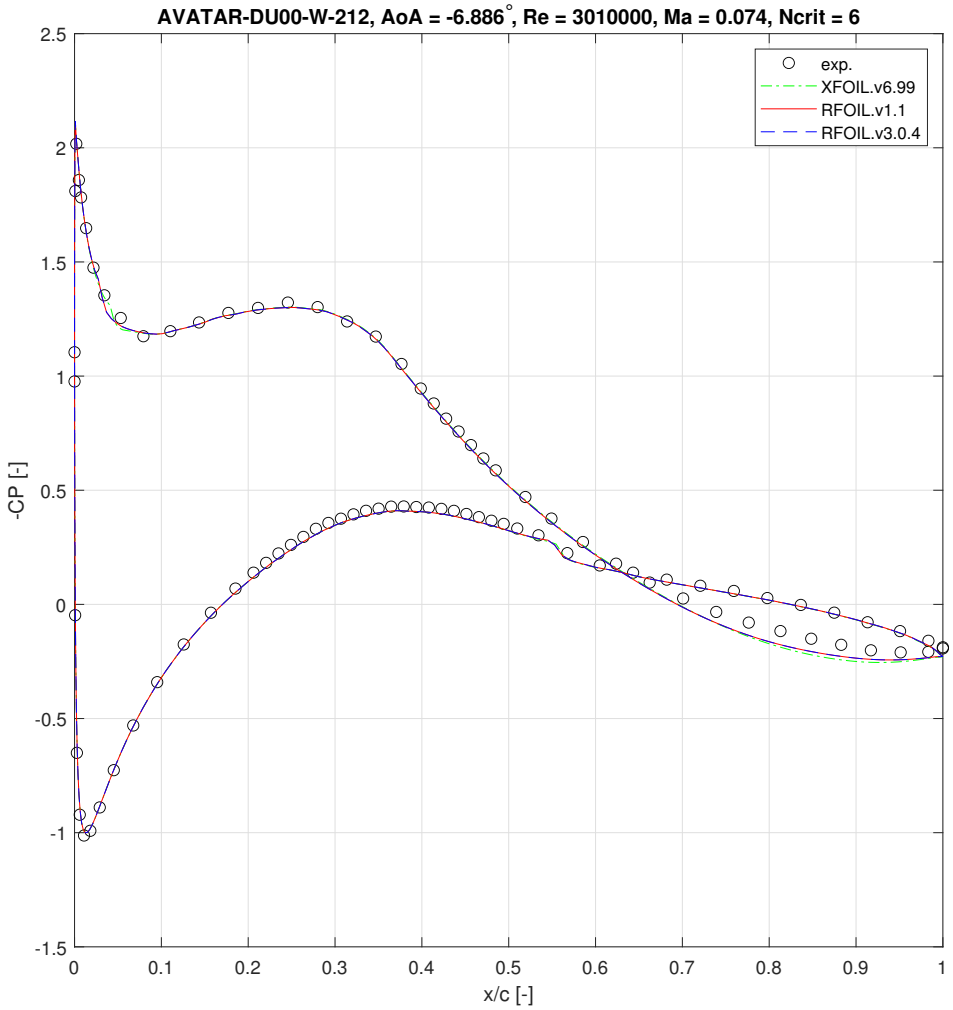

Figure C.185: Comparison between experimental and numerical pressure distributions for the AVATAR-DU00-W-212 airfoil at a Reynolds number of 11980000, and at an angle of attack and a Mach number of -6.951° and 0.058, respectively.

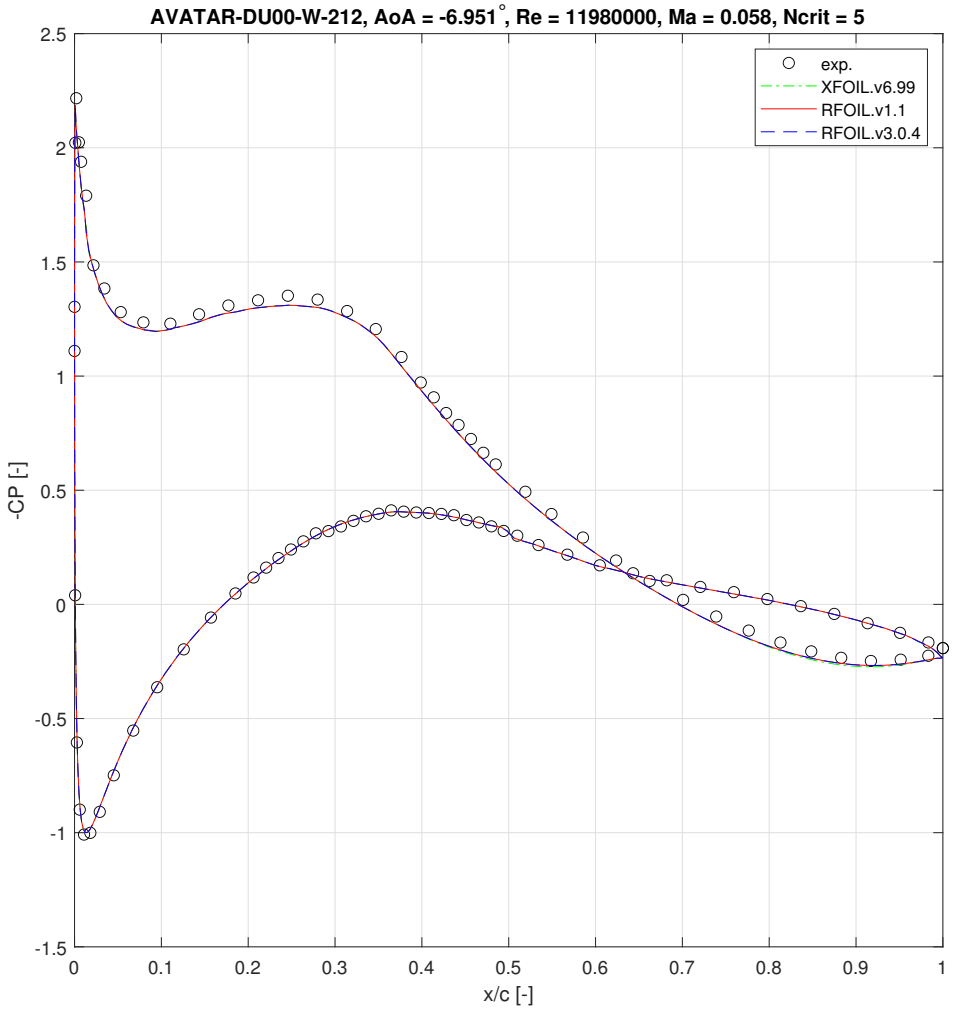

Figure C.186: Comparison between experimental and numerical pressure distributions for the AVATAR-DU00-W-212 airfoil at a Reynolds number of 3010000, and at an angle of attack and a Mach number of -7.088° and 0.074, respectively.

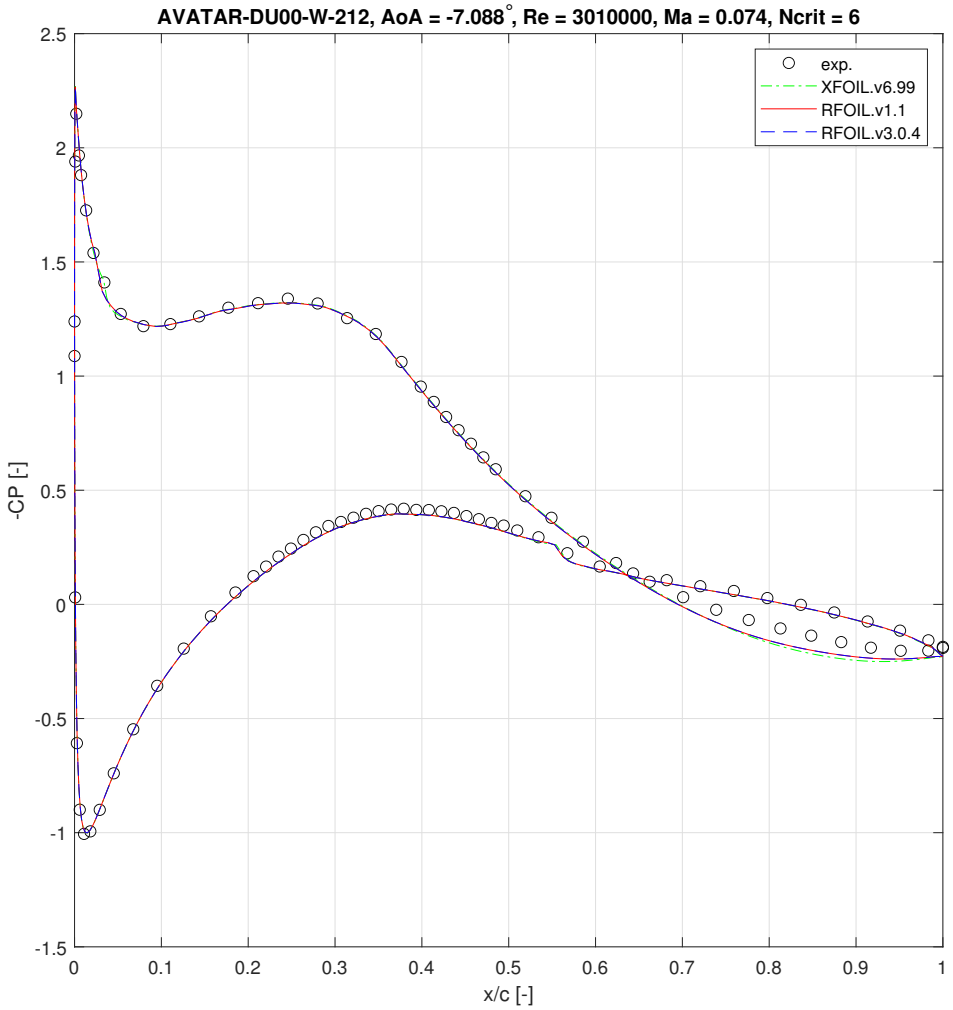

Figure C.187: Comparison between experimental and numerical pressure distributions for the AVATAR-DU00-W-212 airfoil at a Reynolds number of 9000000, and at an angle of attack and a Mach number of -7.091° and 0.083, respectively.

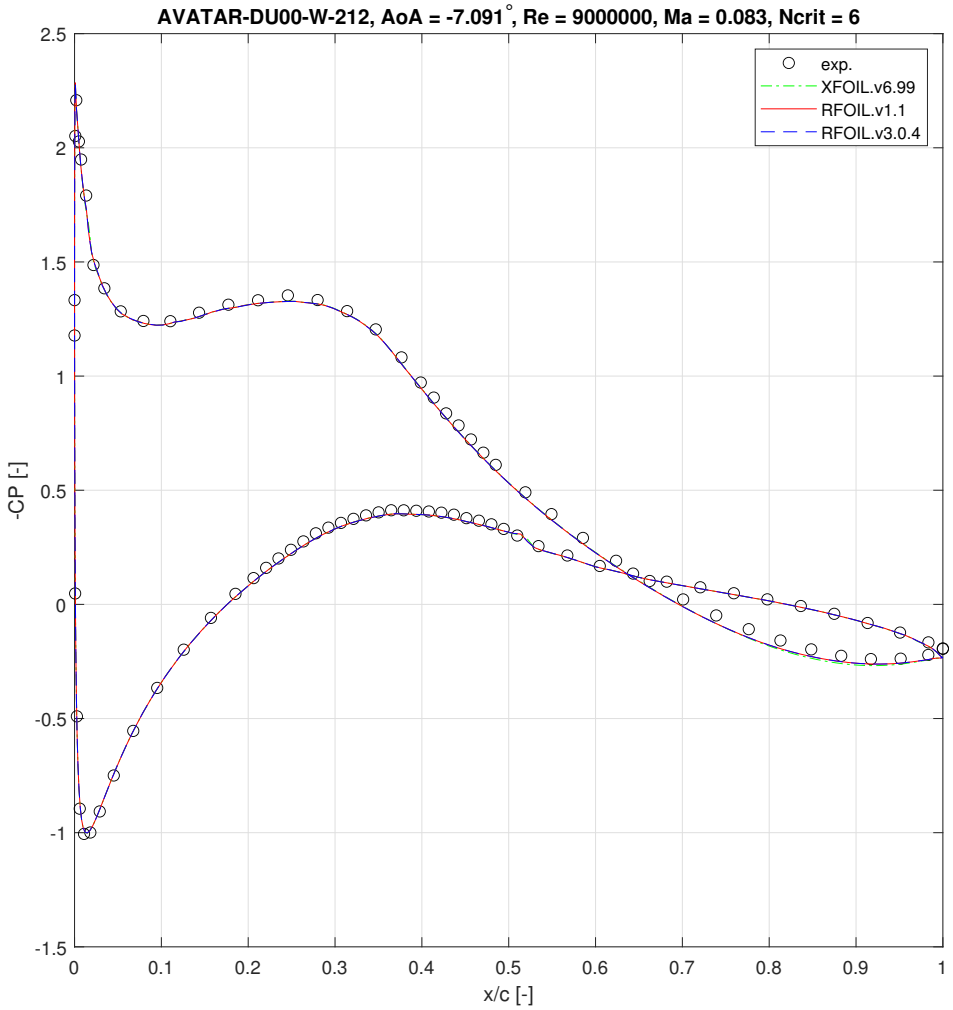

Figure C.188: Comparison between experimental and numerical pressure distributions for the AVATAR-DU00-W-212 airfoil at a Reynolds number of 14990000, and at an angle of attack and a Mach number of -7.092° and 0.081, respectively.

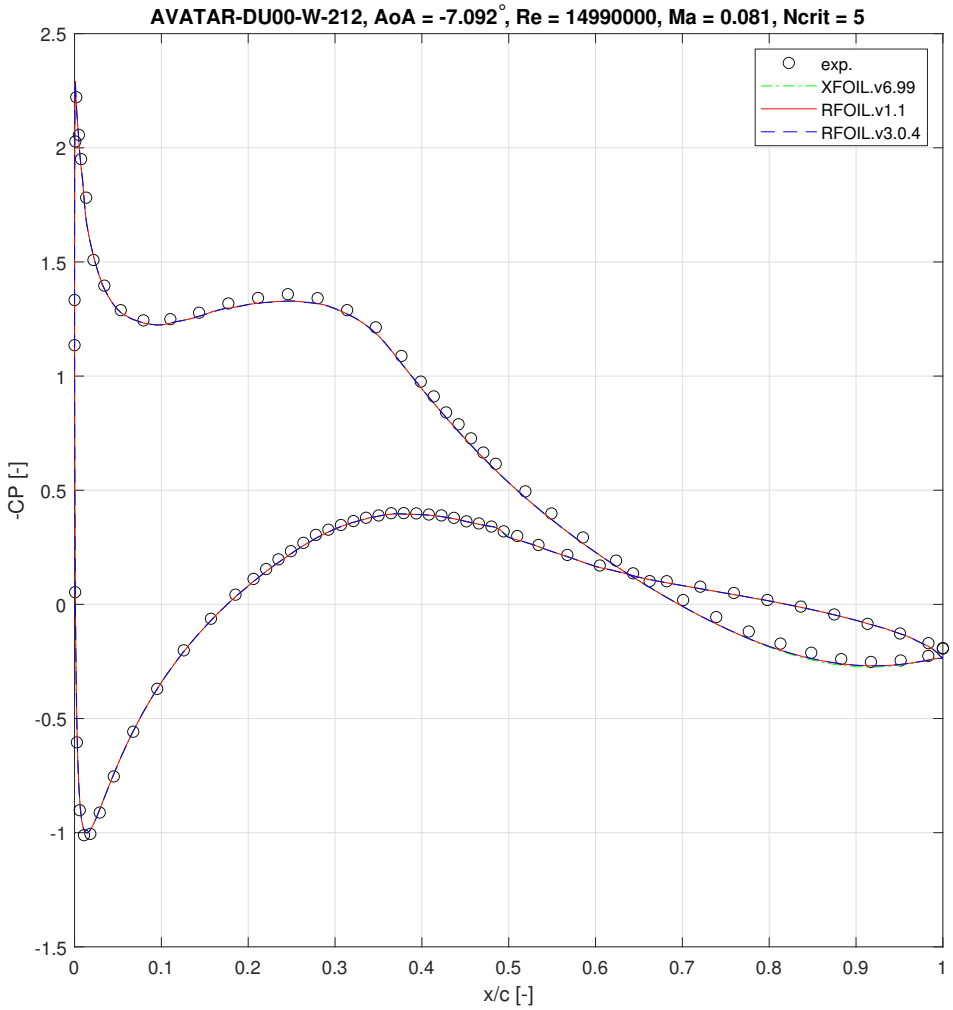

Figure C.189: Comparison between experimental and numerical pressure distributions for the AVATAR-DU00-W-212 airfoil at a Reynolds number of 9020000, and at an angle of attack and a Mach number of -7.092° and 0.044, respectively.

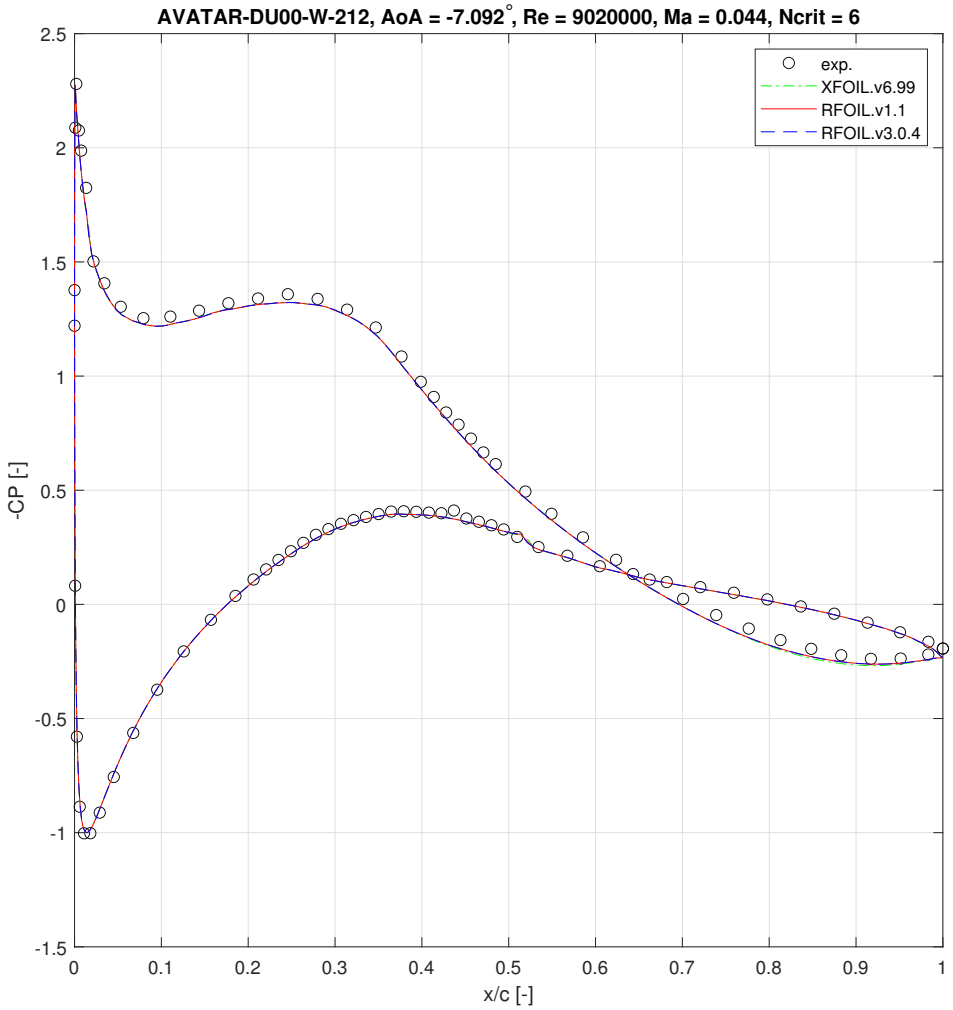

Figure C.190: Comparison between experimental and numerical pressure distributions for the AVATAR-DU00-W-212 airfoil at a Reynolds number of 6010000, and at an angle of attack and a Mach number of -7.090° and 0.029, respectively.

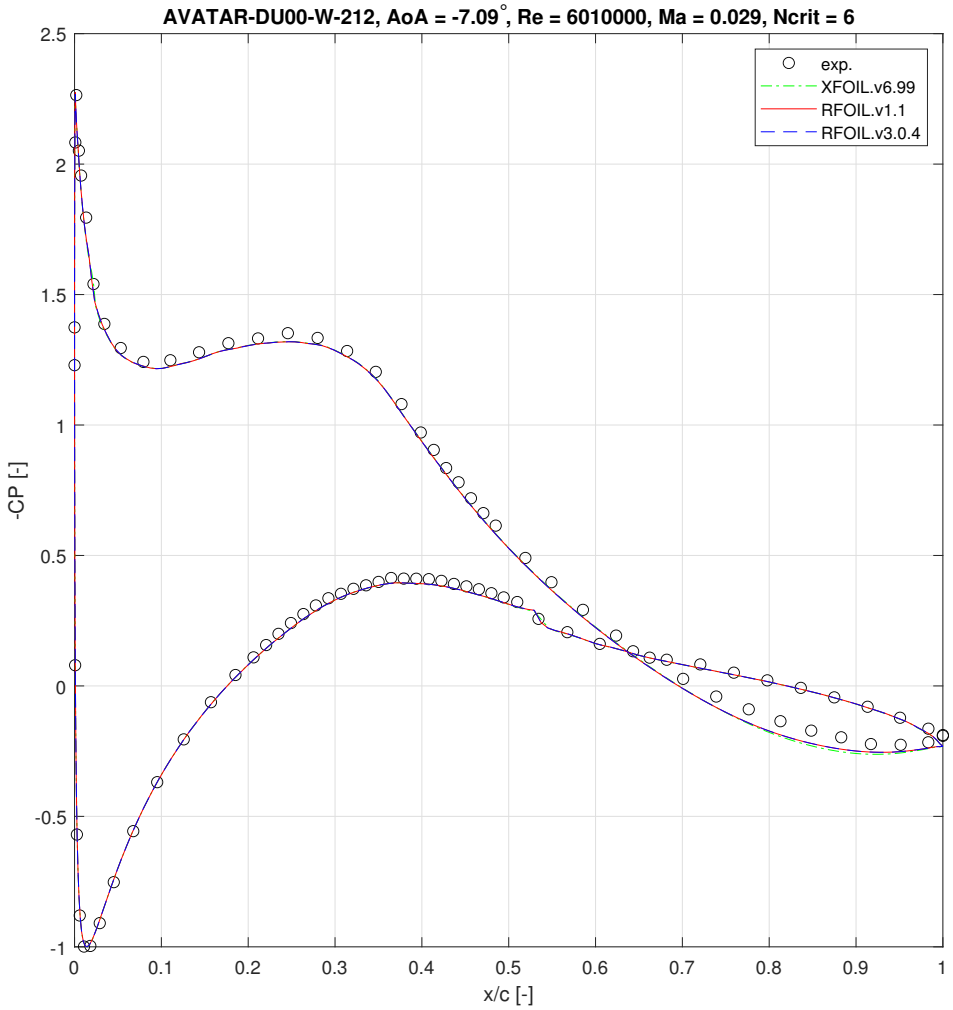

Figure C.191: Comparison between experimental and numerical pressure distributions for the AVATAR-DU00-W-212 airfoil at a Reynolds number of 6010000, and at an angle of attack and a Mach number of -7.090° and 0.055, respectively.

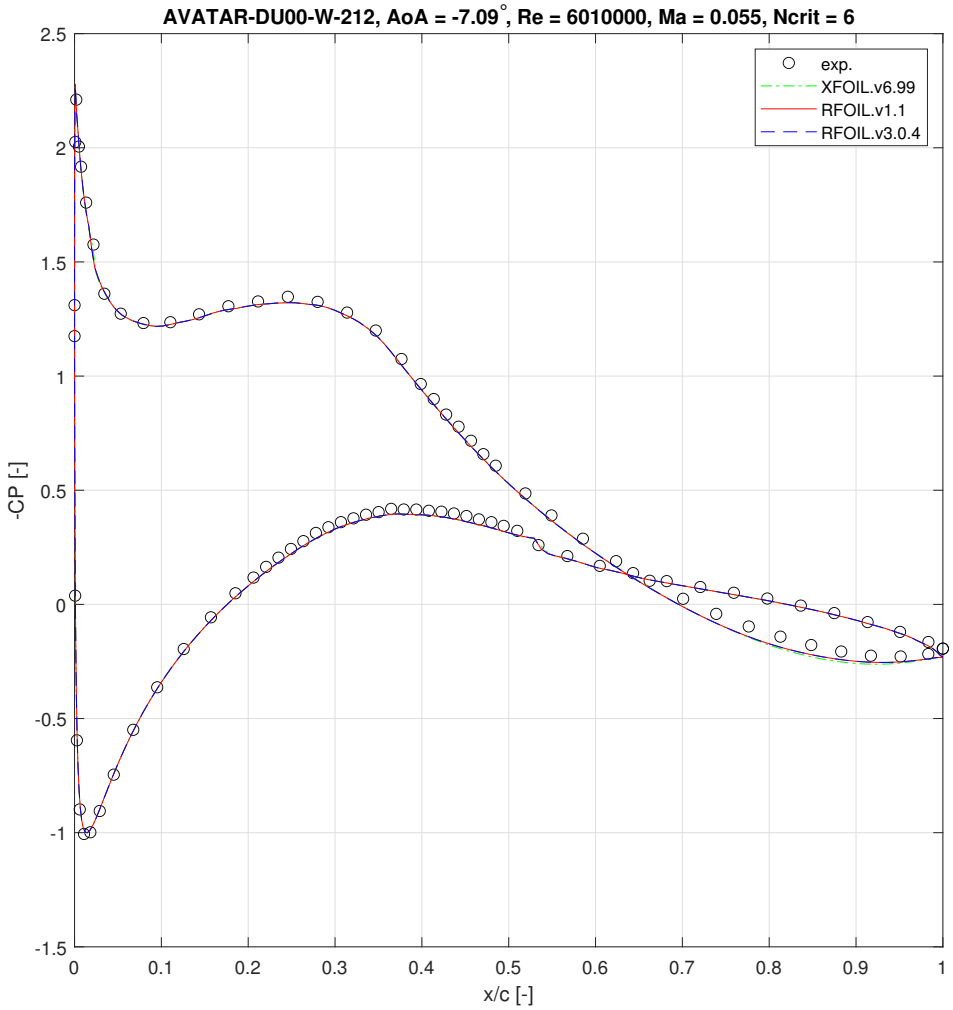

Figure C.192: Comparison between experimental and numerical pressure distributions for the AVATAR-DU00-W-212 airfoil at a Reynolds number of 3010000, and at an angle of attack and a Mach number of -7.593° and 0.074, respectively.

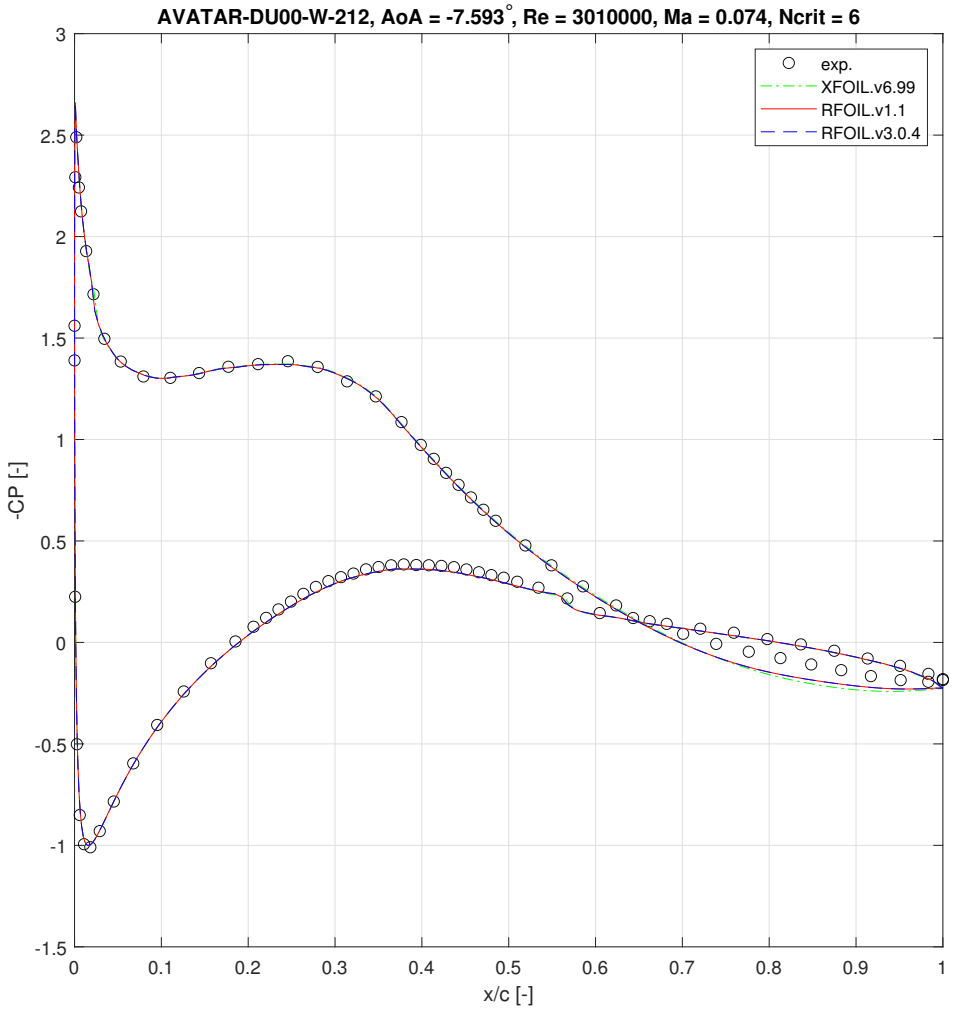

Figure C.193: Comparison between experimental and numerical pressure distributions for the AVATAR-DU00-W-212 airfoil at a Reynolds number of 12010000, and at an angle of attack and a Mach number of -7.953° and 0.058, respectively.

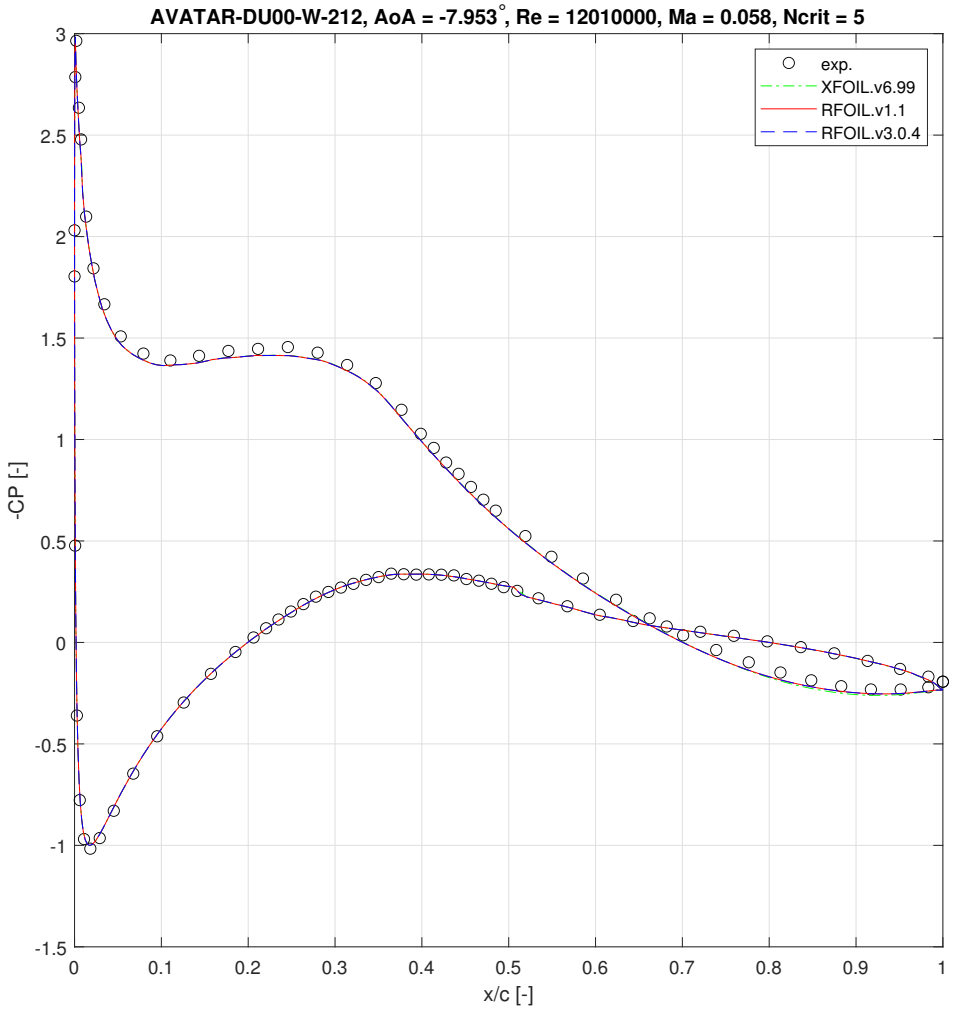

Figure C.194: Comparison between experimental and numerical pressure distributions for the AVATAR-DU00-W-212 airfoil at a Reynolds number of 3010000, and at an angle of attack and a Mach number of -8.098° and 0.074, respectively.

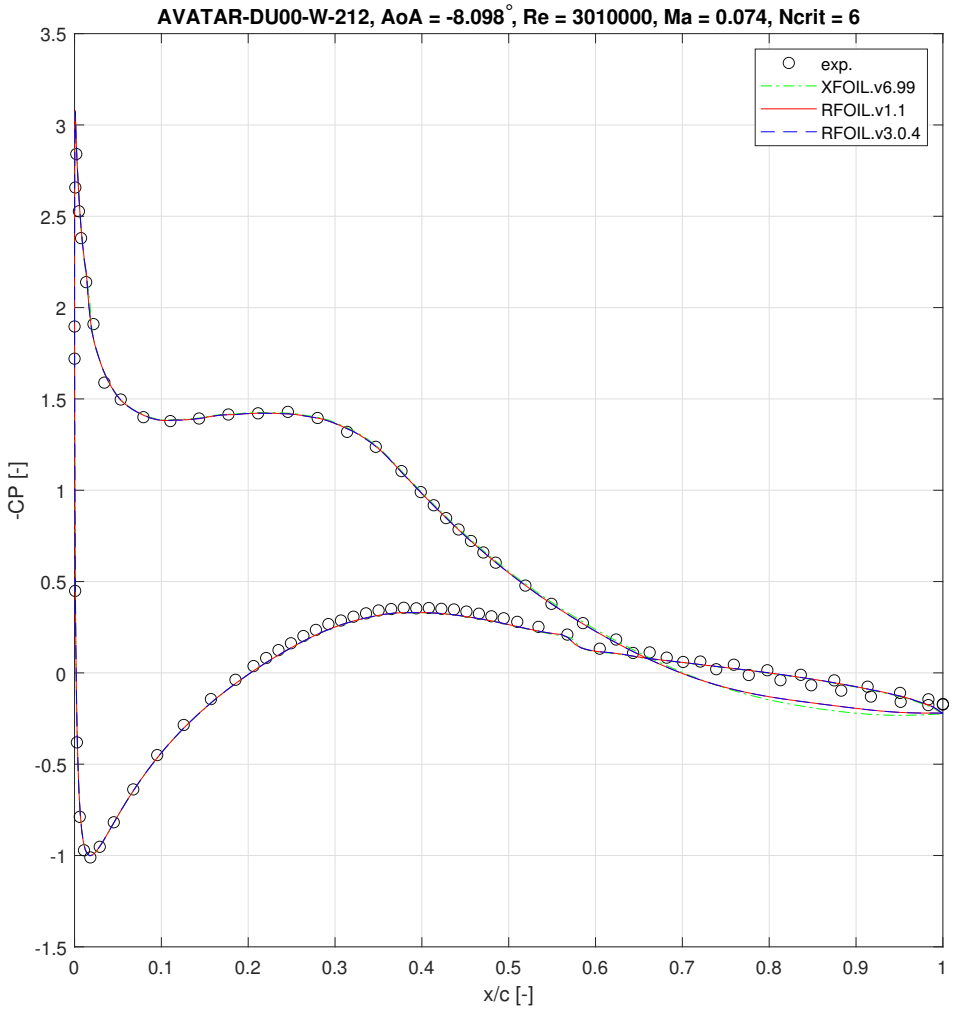

Figure C.195: Comparison between experimental and numerical pressure distributions for the AVATAR-DU00-W-212 airfoil at a Reynolds number of 6010000, and at an angle of attack and a Mach number of -8.102° and 0.029, respectively.

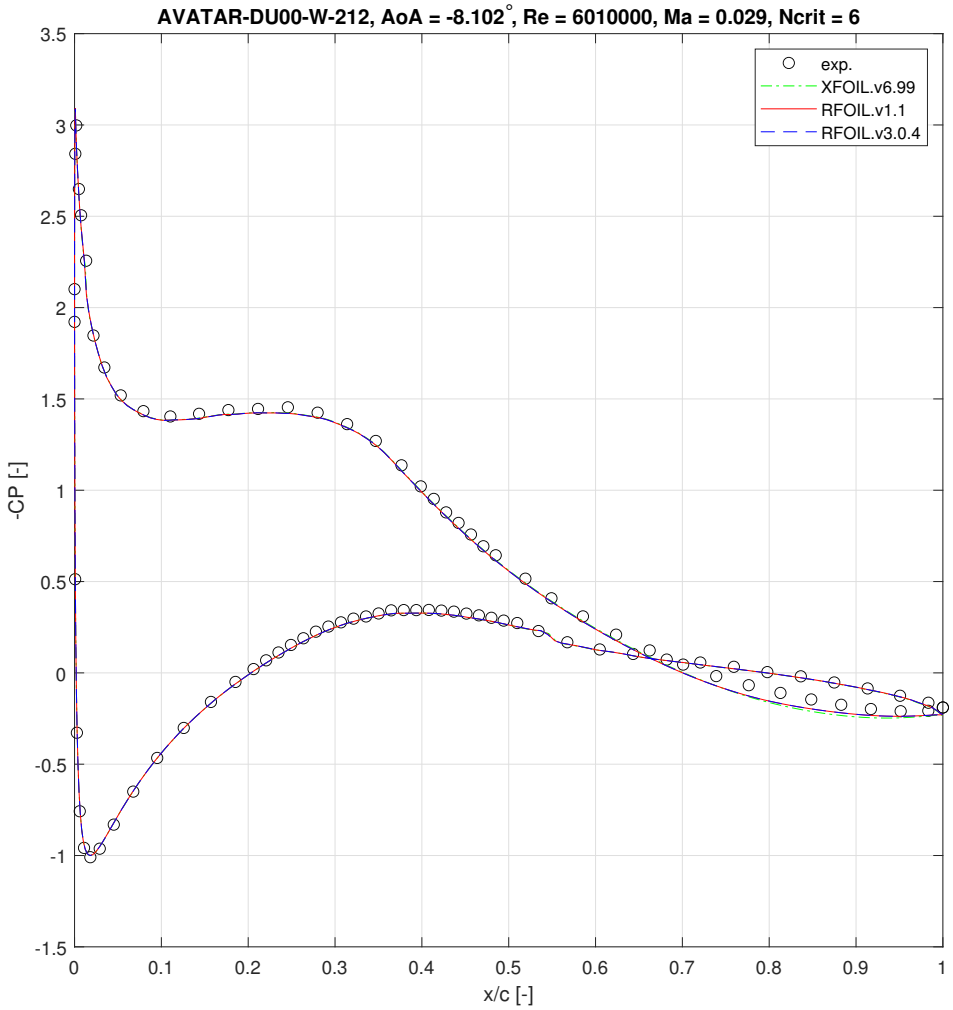

Figure C.196: Comparison between experimental and numerical pressure distributions for the AVATAR-DU00-W-212 airfoil at a Reynolds number of 6020000, and at an angle of attack and a Mach number of -8.102° and 0.055, respectively.

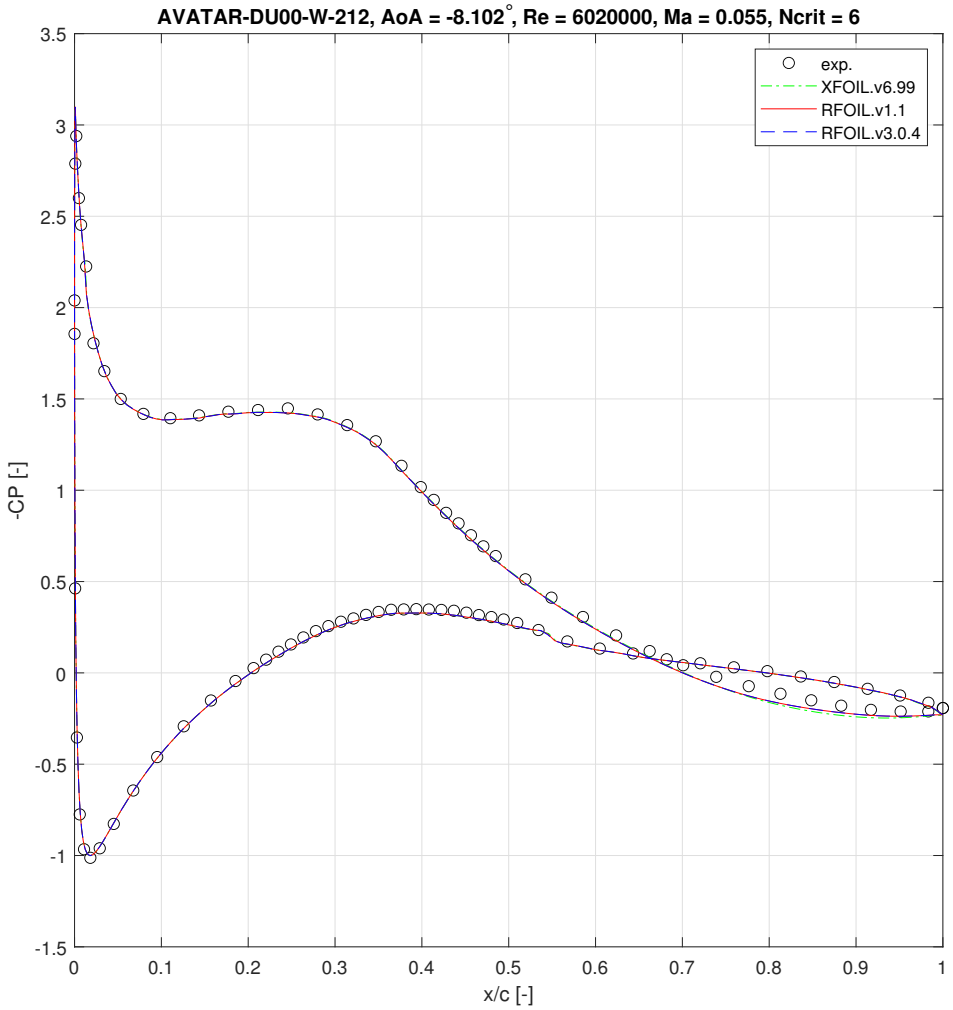

Figure C.197: Comparison between experimental and numerical pressure distributions for the AVATAR-DU00-W-212 airfoil at a Reynolds number of 9020000, and at an angle of attack and a Mach number of -8.103° and 0.083, respectively.

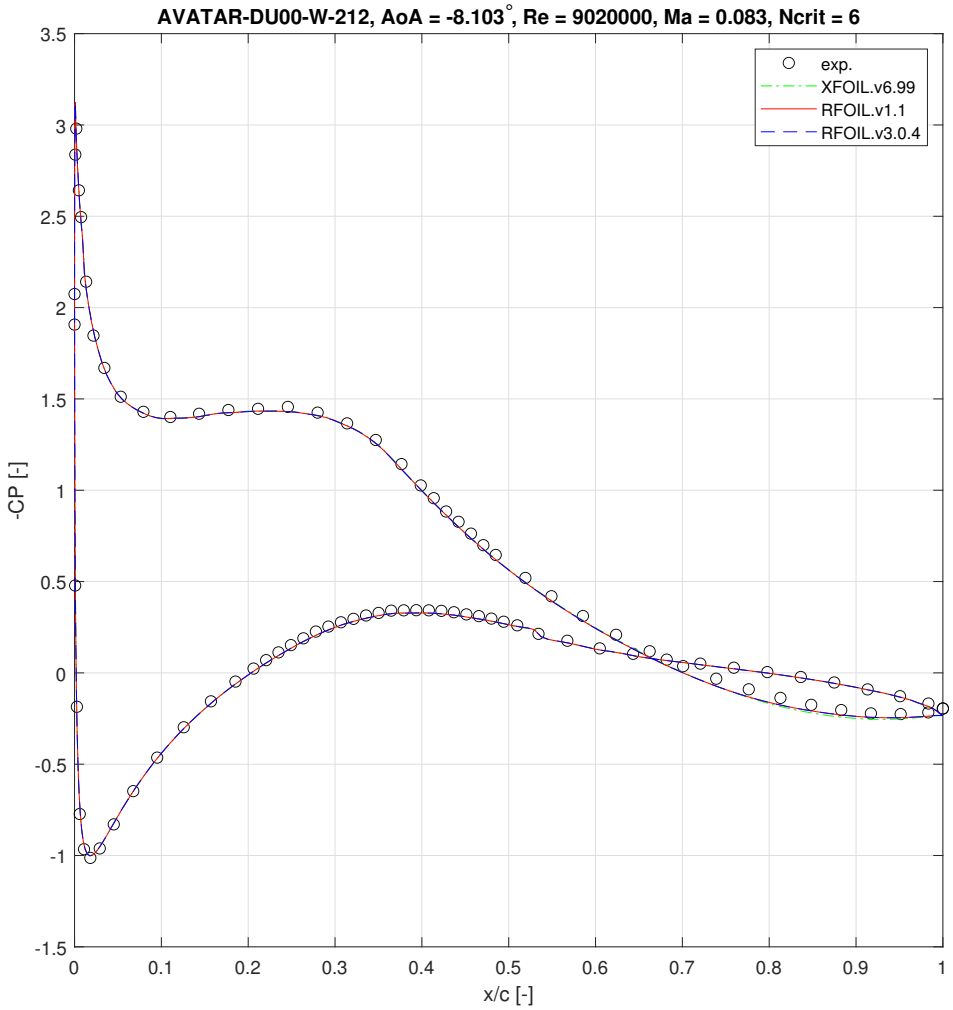

Figure C.198: Comparison between experimental and numerical pressure distributions for the AVATAR-DU00-W-212 airfoil at a Reynolds number of 9030000, and at an angle of attack and a Mach number of -8.104° and 0.044, respectively.

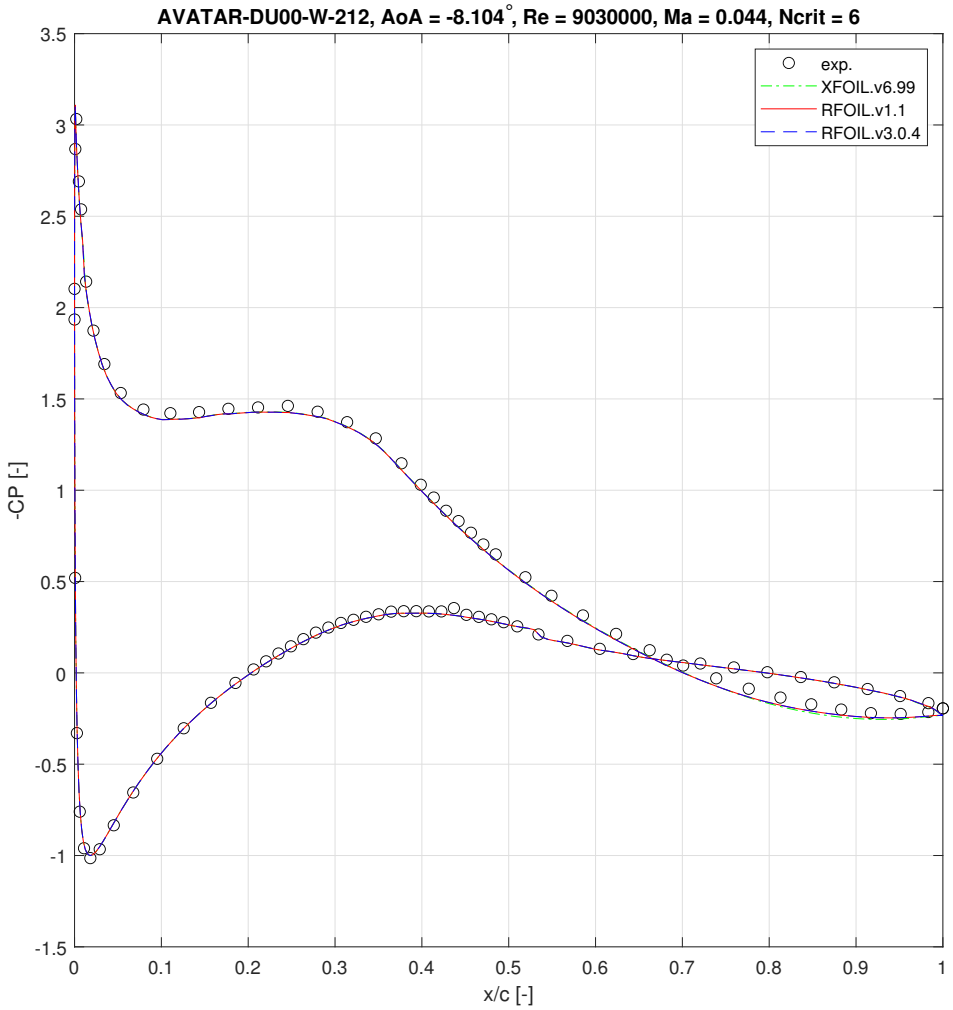

Figure C.199: Comparison between experimental and numerical pressure distributions for the AVATAR-DU00-W-212 airfoil at a Reynolds number of 15040000, and at an angle of attack and a Mach number of -8.105° and 0.082, respectively.

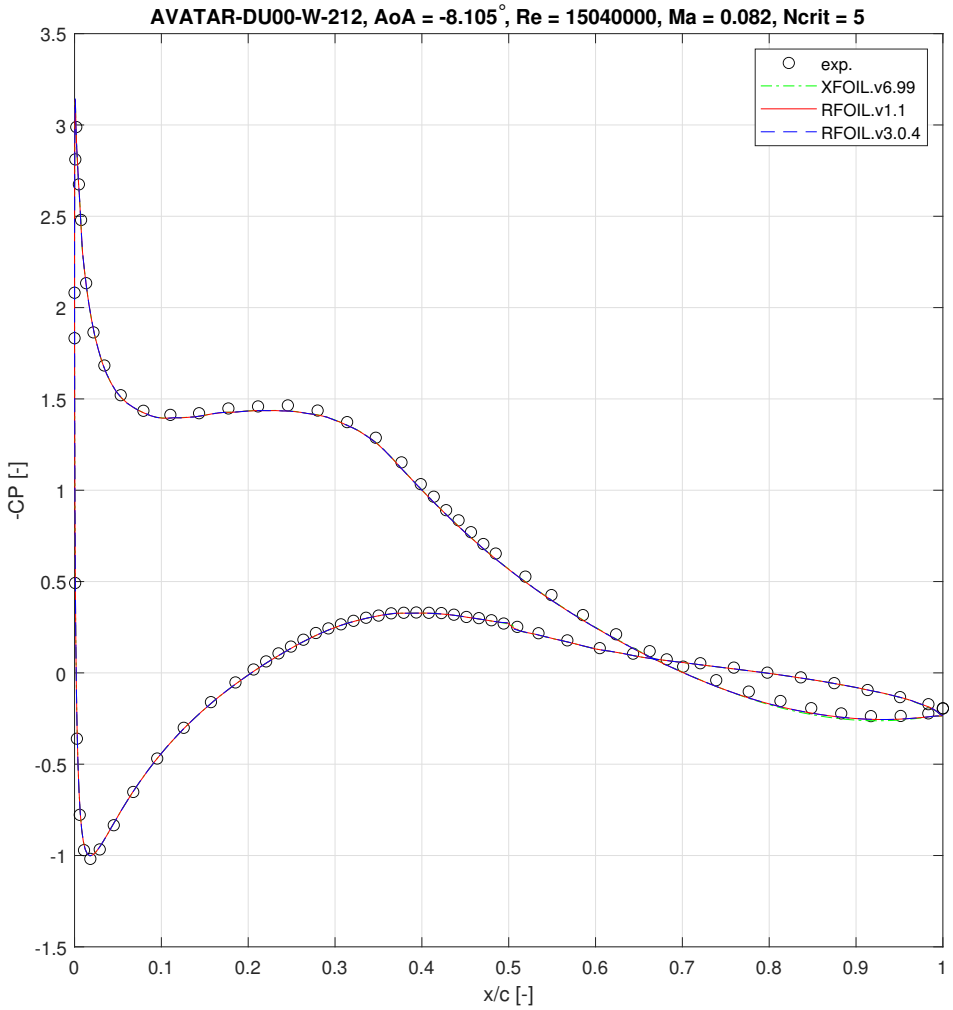

Figure C.200: Comparison between experimental and numerical pressure distributions for the AVATAR-DU00-W-212 airfoil at a Reynolds number of 12010000, and at an angle of attack and a Mach number of -8.953° and 0.058, respectively.

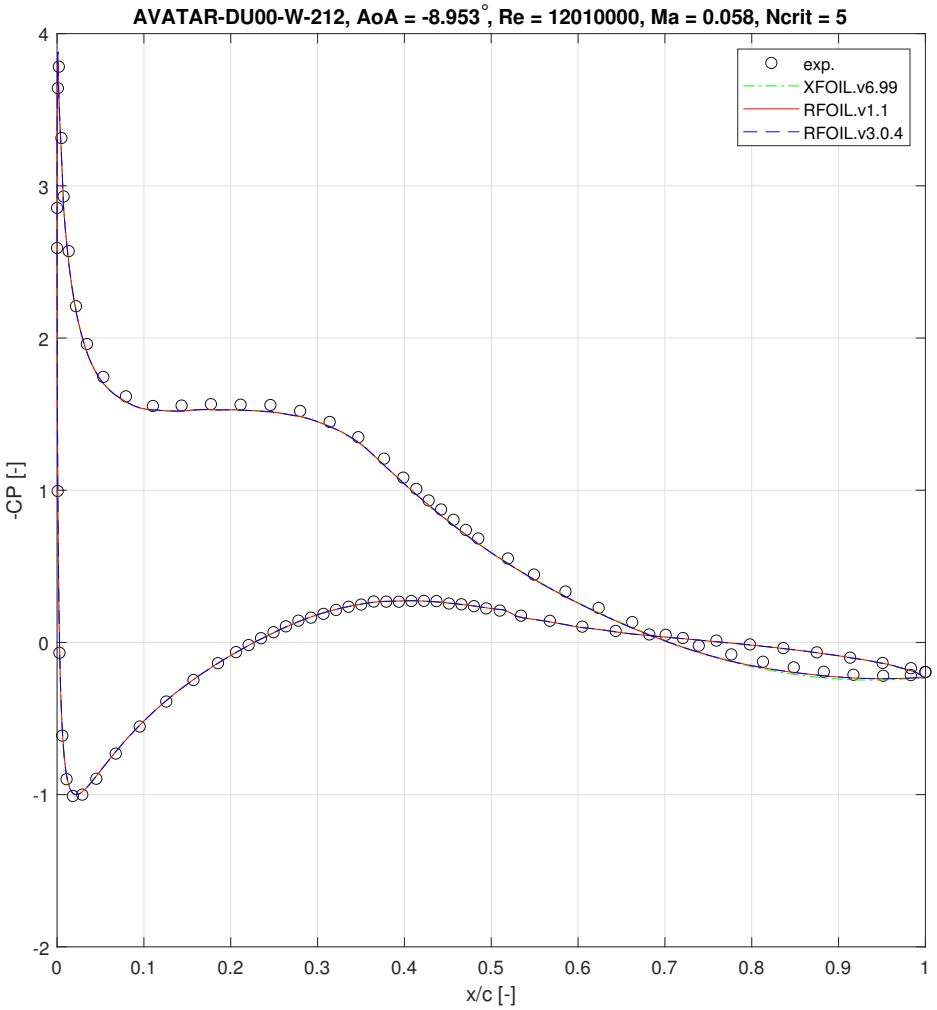

Figure C.201: Comparison between experimental and numerical pressure distributions for the AVATAR-DU00-W-212 airfoil at a Reynolds number of 3010000, and at an angle of attack and a Mach number of -9.095° and 0.074, respectively.

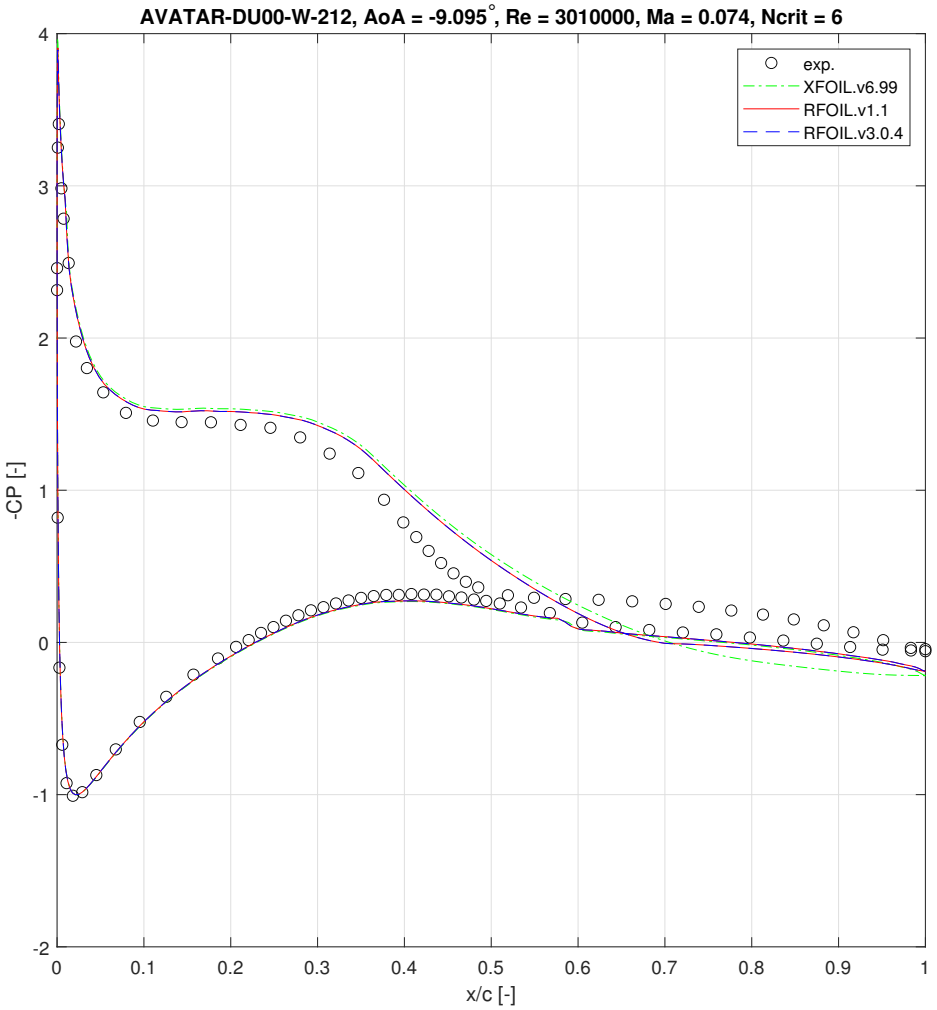

Figure C.202: Comparison between experimental and numerical pressure distributions for the AVATAR-DU00-W-212 airfoil at a Reynolds number of 5980000, and at an angle of attack and a Mach number of -9.113° and 0.055, respectively.

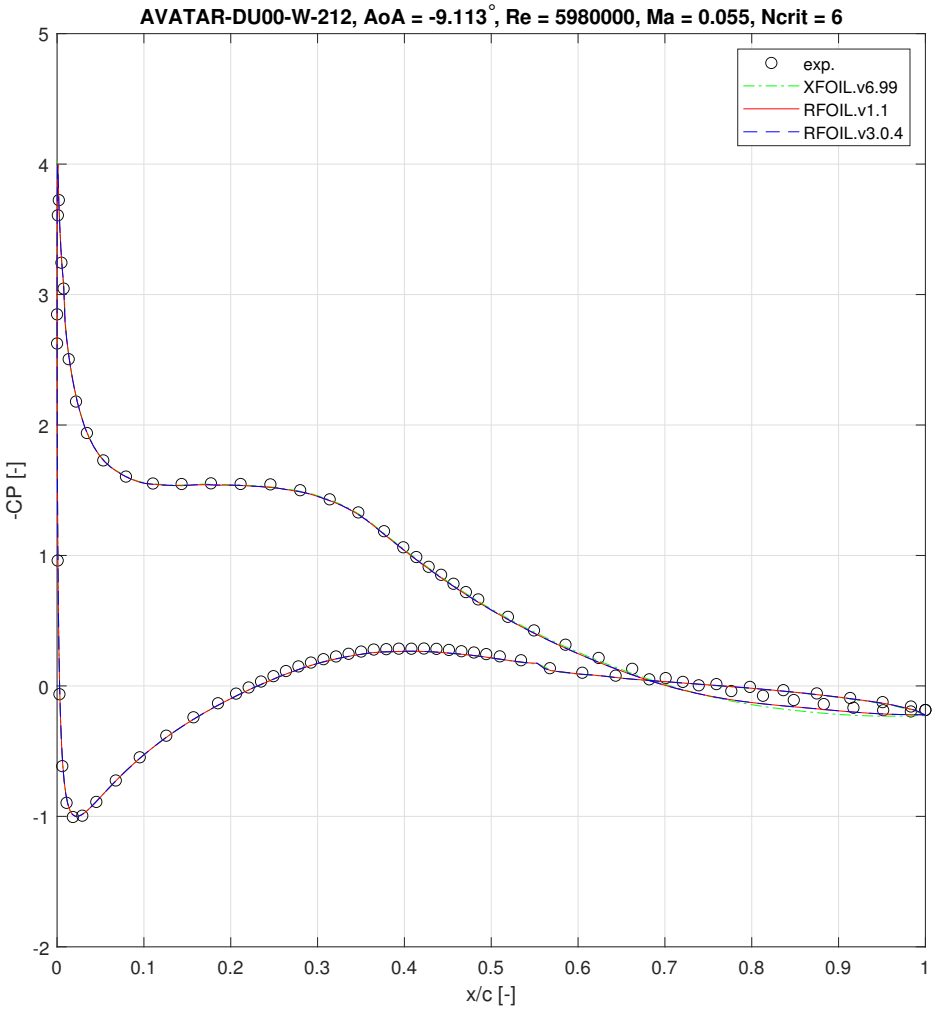

Figure C.203: Comparison between experimental and numerical pressure distributions for the AVATAR-DU00-W-212 airfoil at a Reynolds number of 6010000, and at an angle of attack and a Mach number of -9.113° and 0.029, respectively.

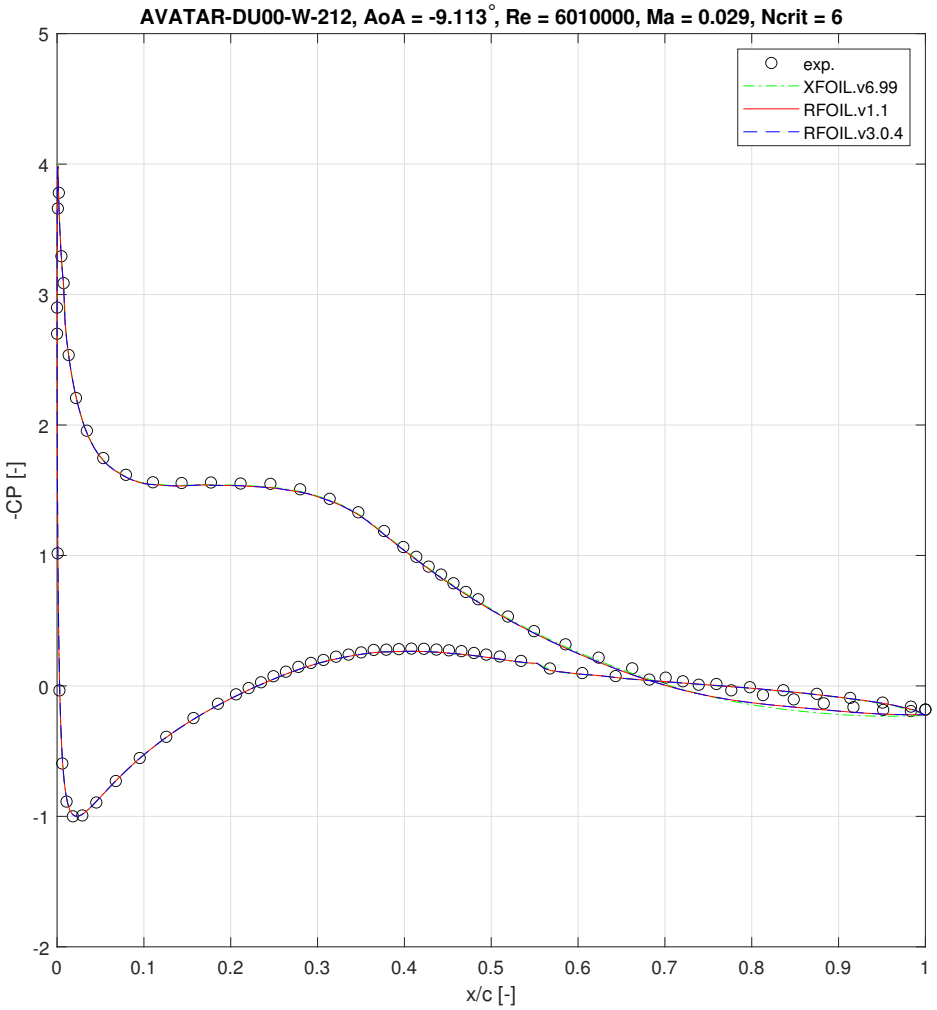

Figure C.204: Comparison between experimental and numerical pressure distributions for the AVATAR-DU00-W-212 airfoil at a Reynolds number of 9020000, and at an angle of attack and a Mach number of -9.115° and 0.083, respectively.

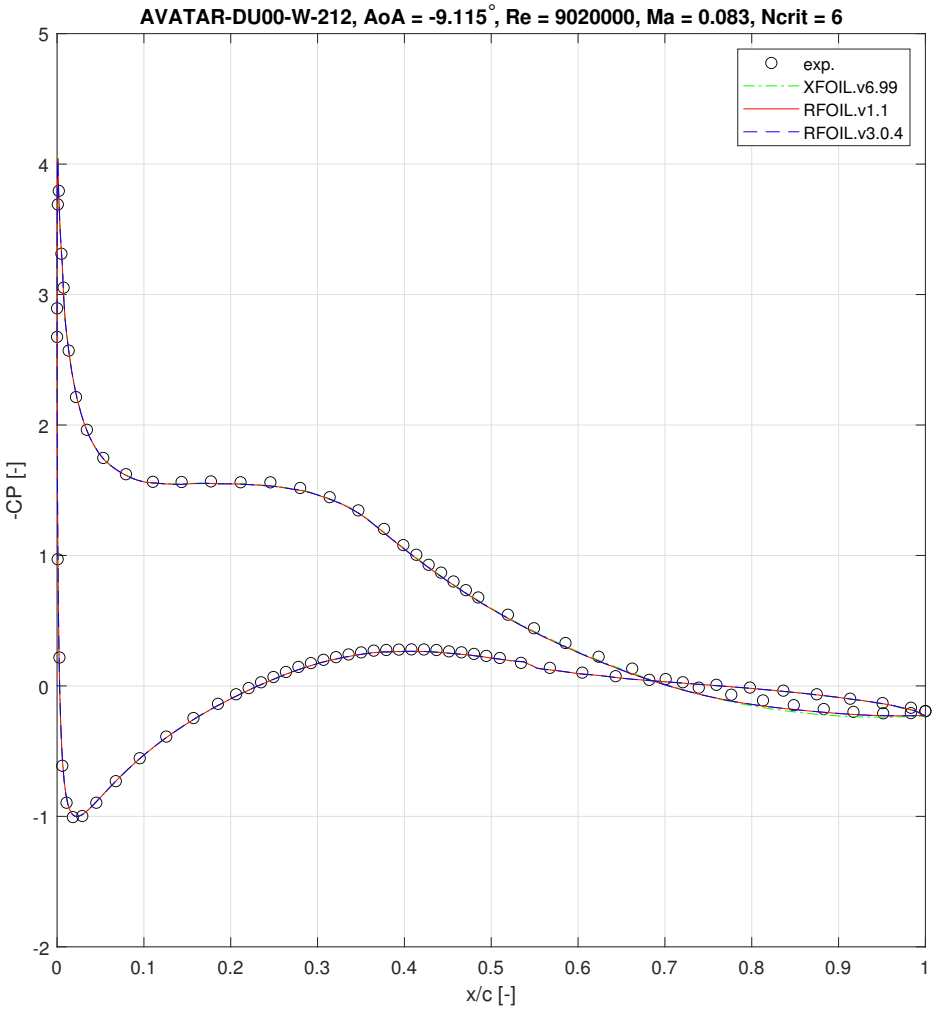

Figure C.205: Comparison between experimental and numerical pressure distributions for the AVATAR-DU00-W-212 airfoil at a Reynolds number of 9010000, and at an angle of attack and a Mach number of -9.116° and 0.043, respectively.

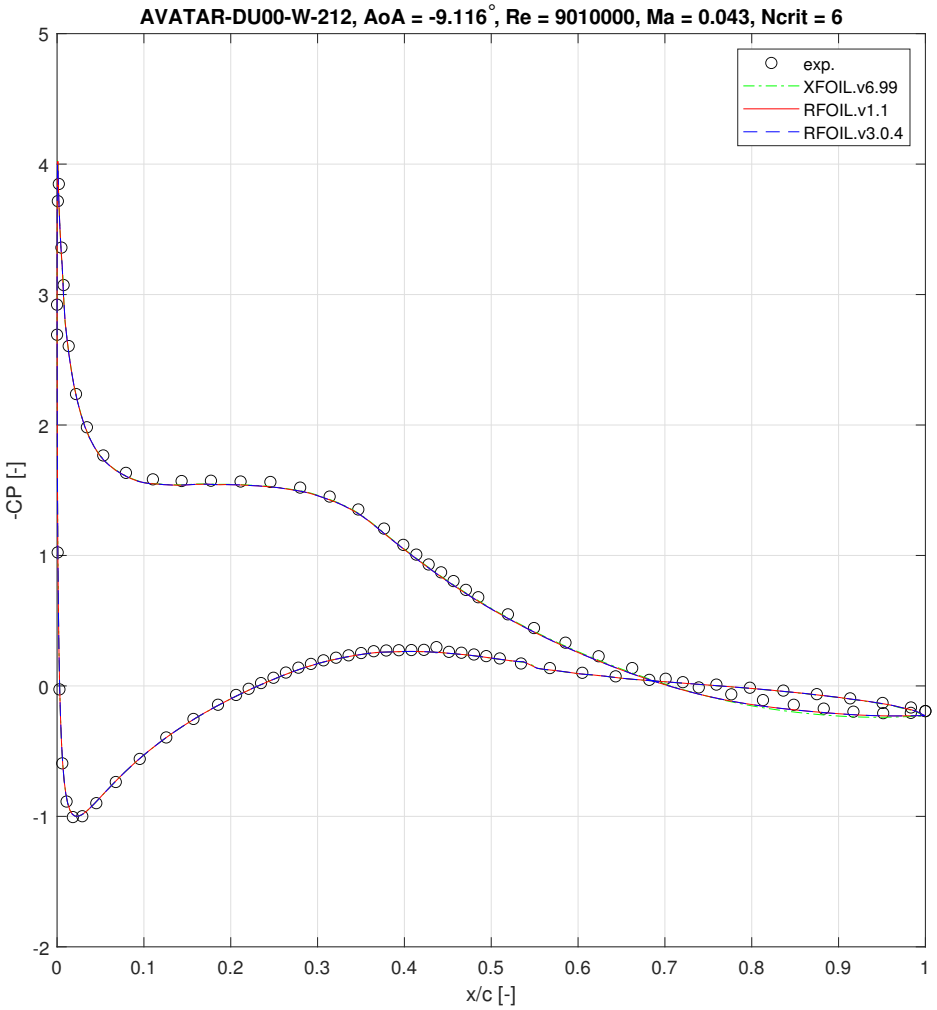

Figure C.206: Comparison between experimental and numerical pressure distributions for the AVATAR-DU00-W-212 airfoil at a Reynolds number of 15010000, and at an angle of attack and a Mach number of -9.117° and 0.081, respectively.

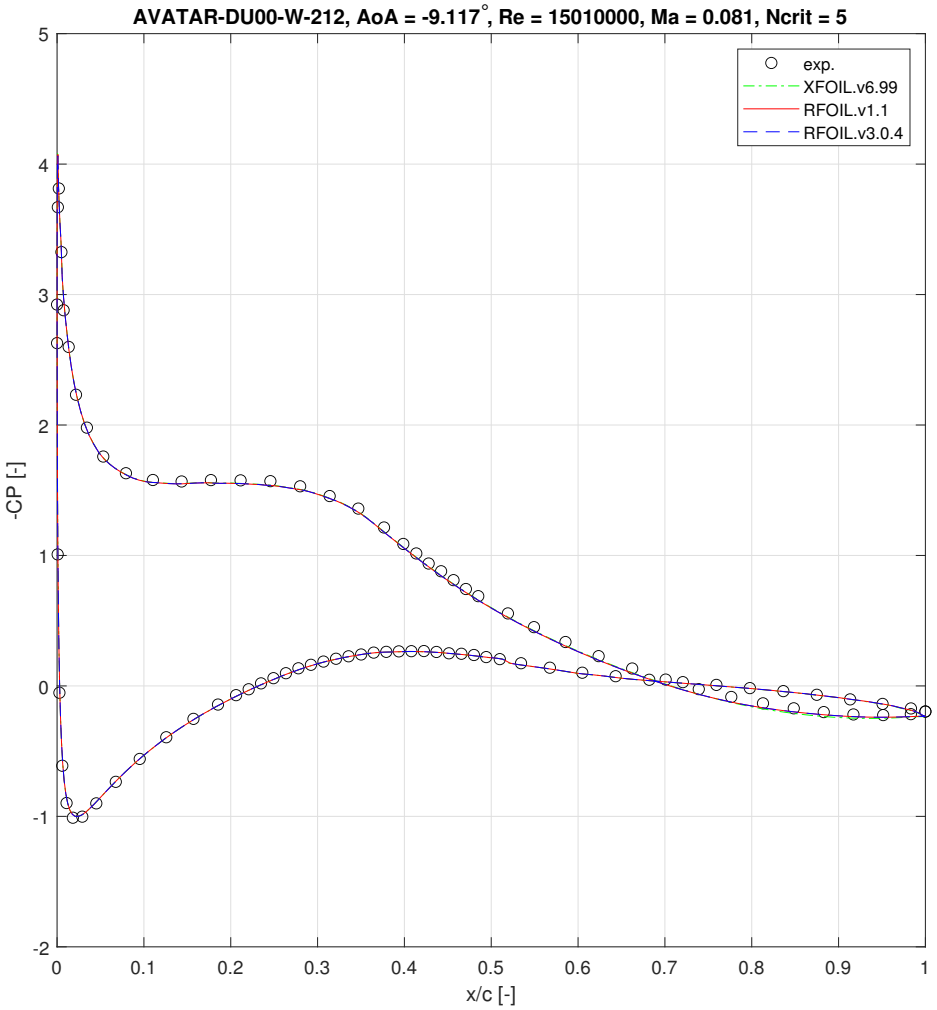

Figure C.207: Comparison between experimental and numerical pressure distributions for the AVATAR-DU00-W-212 airfoil at a Reynolds number of 11990000, and at an angle of attack and a Mach number of -9.953° and 0.058, respectively.

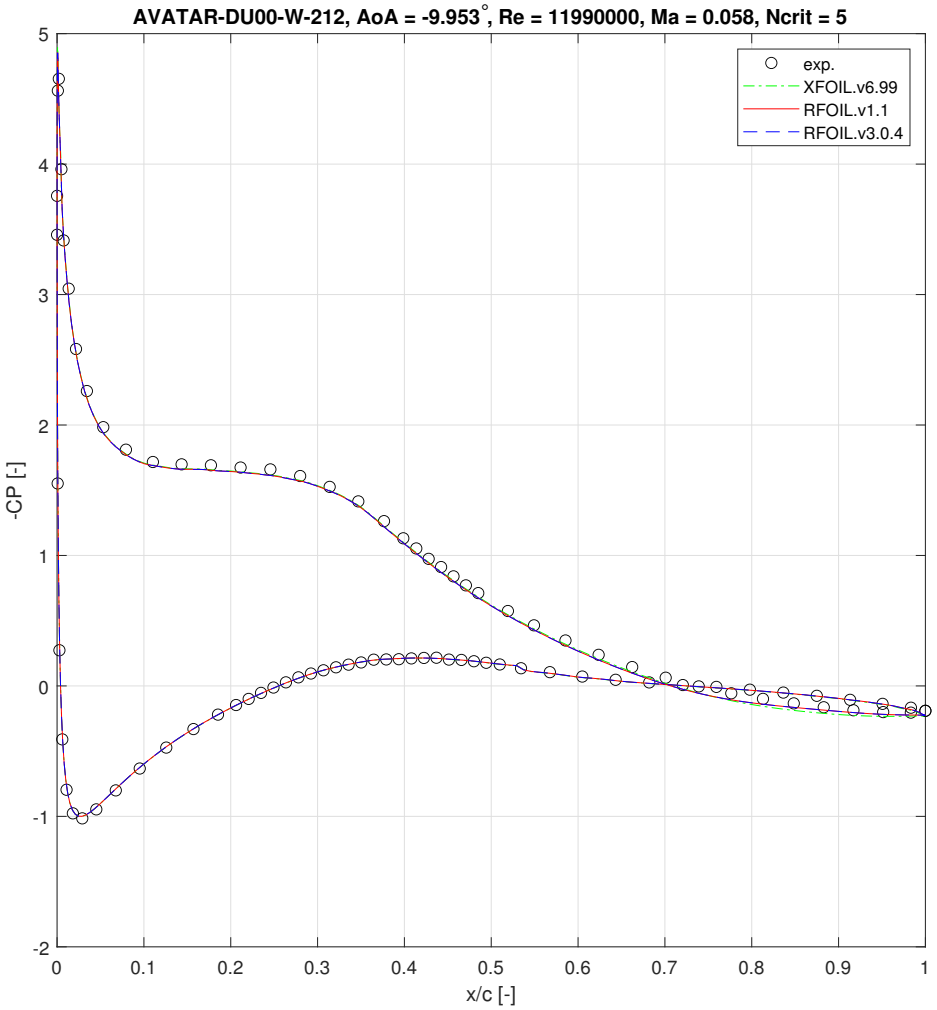

Figure C.208: Comparison between experimental and numerical pressure distributions for the AVATAR-DU00-W-212 airfoil at a Reynolds number of 11920000, and at an angle of attack and a Mach number of 0.044° and 0.057, respectively.

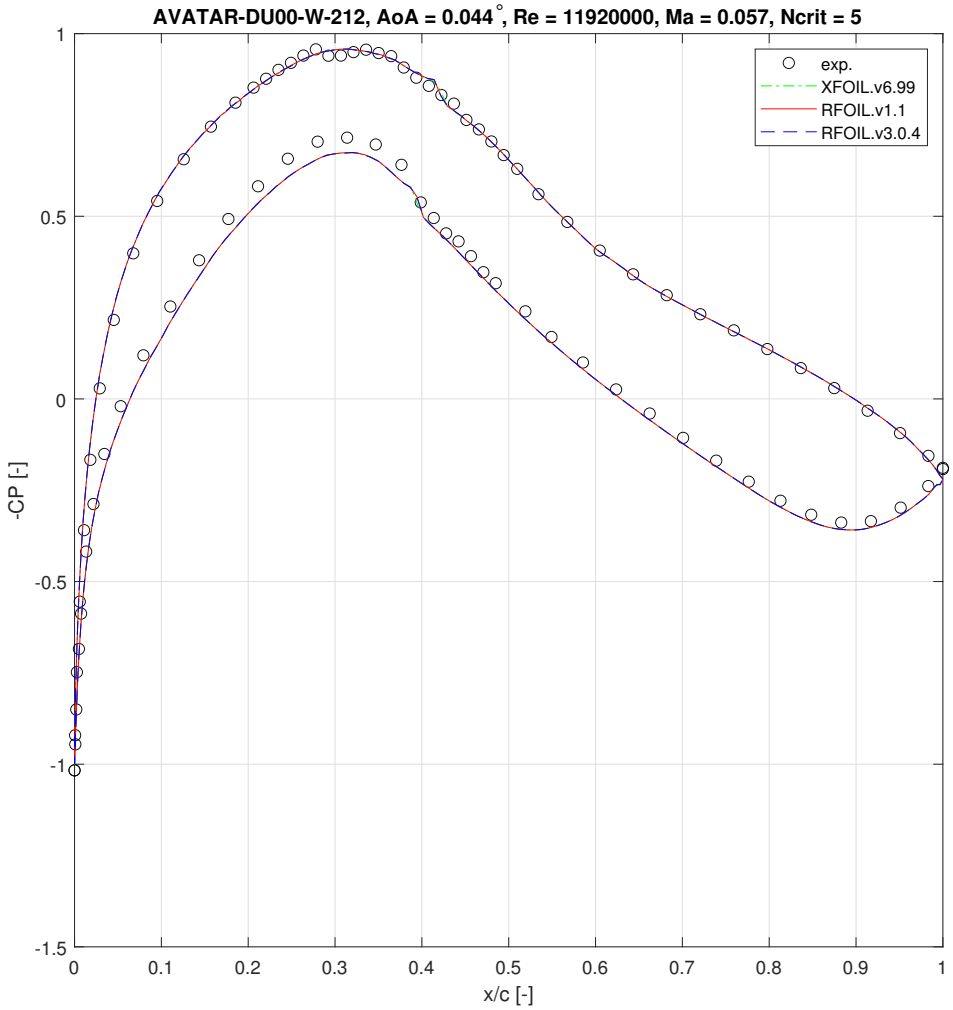

Figure C.209: Comparison between experimental and numerical pressure distributions for the AVATAR-DU00-W-212 airfoil at a Reynolds number of 12010000, and at an angle of attack and a Mach number of 10.025° and 0.058, respectively.

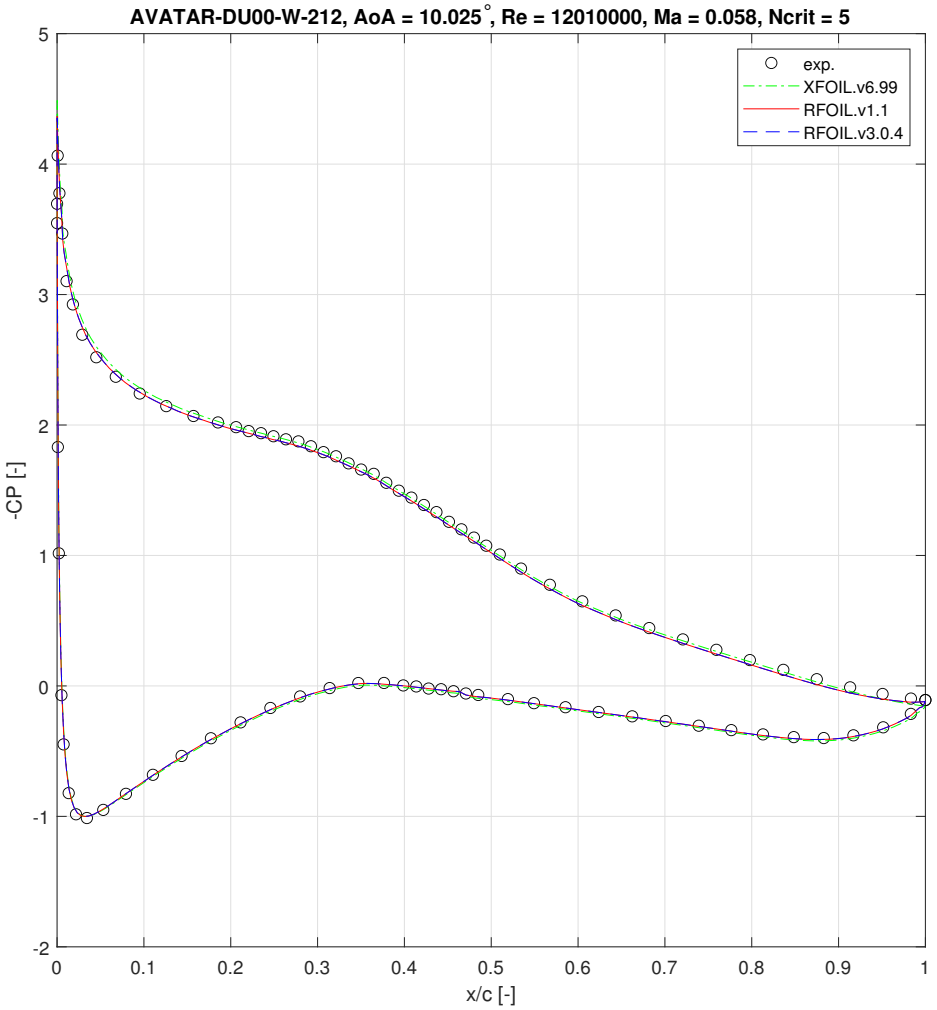

Figure C.210: Comparison between experimental and numerical pressure distributions for the AVATAR-DU00-W-212 airfoil at a Reynolds number of 3010000, and at an angle of attack and a Mach number of 10.116° and 0.074, respectively.

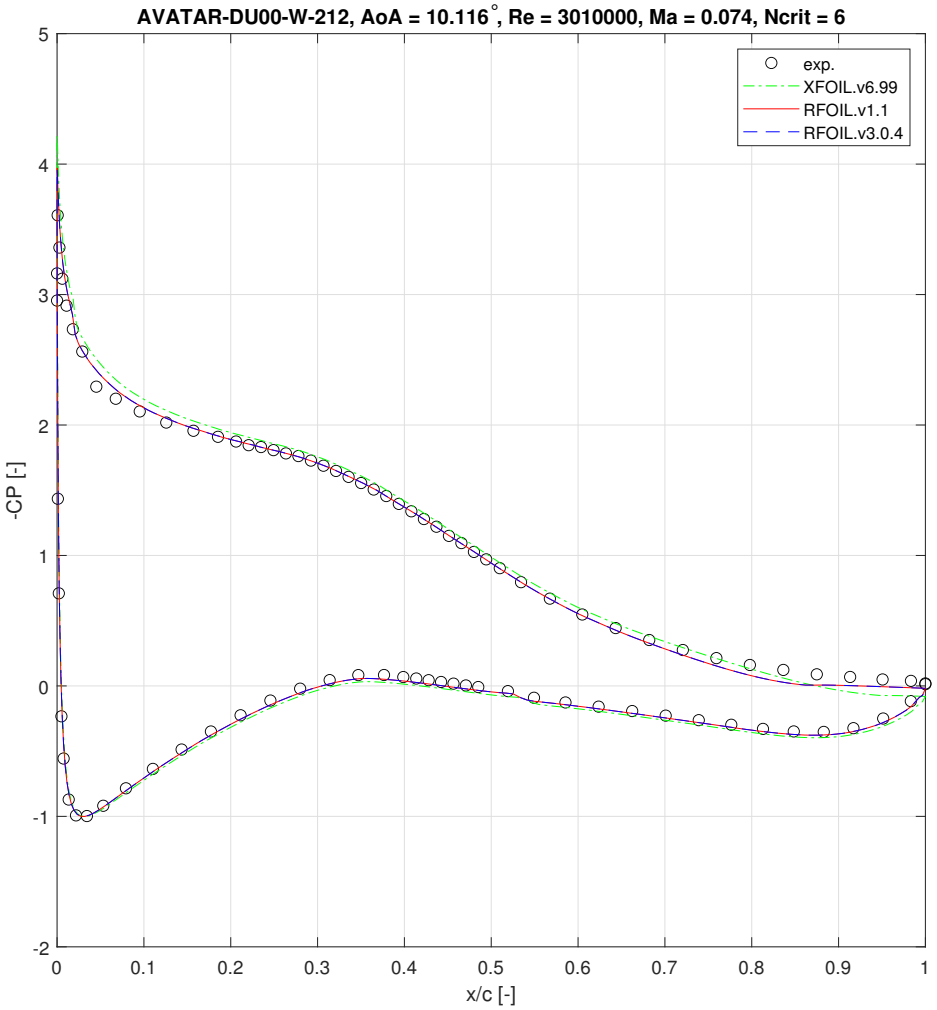

Figure C.211: Comparison between experimental and numerical pressure distributions for the AVATAR-DU00-W-212 airfoil at a Reynolds number of 6010000, and at an angle of attack and a Mach number of 10.119° and 0.029, respectively.

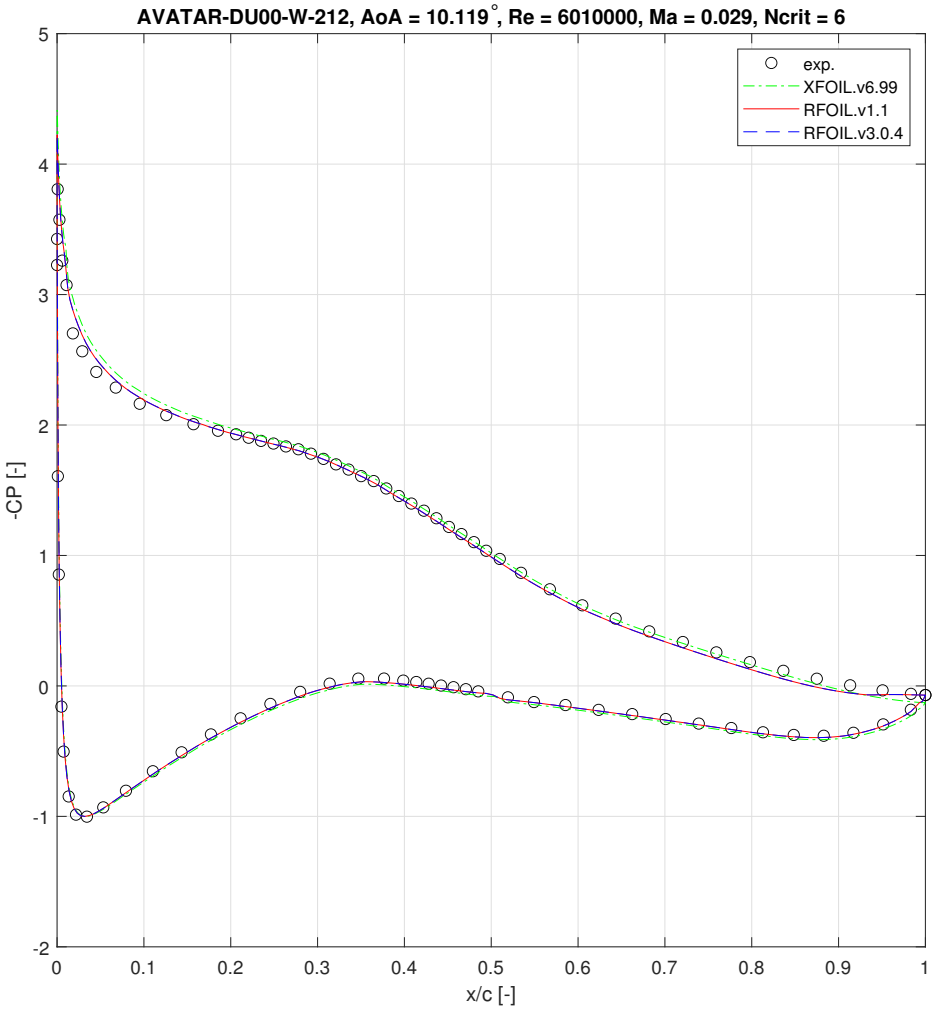

Figure C.212: Comparison between experimental and numerical pressure distributions for the AVATAR-DU00-W-212 airfoil at a Reynolds number of 9010000, and at an angle of attack and a Mach number of 10.121° and 0.043, respectively.

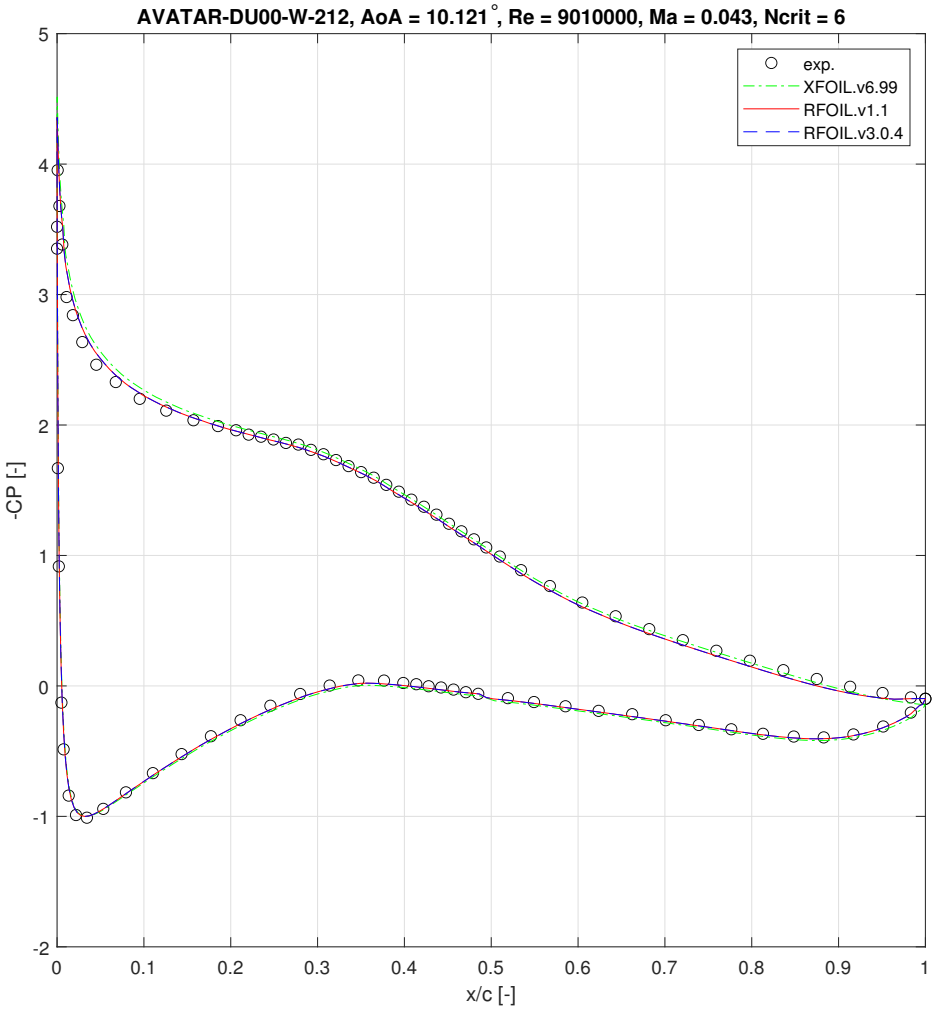

Figure C.213: Comparison between experimental and numerical pressure distributions for the AVATAR-DU00-W-212 airfoil at a Reynolds number of 9010000, and at an angle of attack and a Mach number of 10.122° and 0.083, respectively.

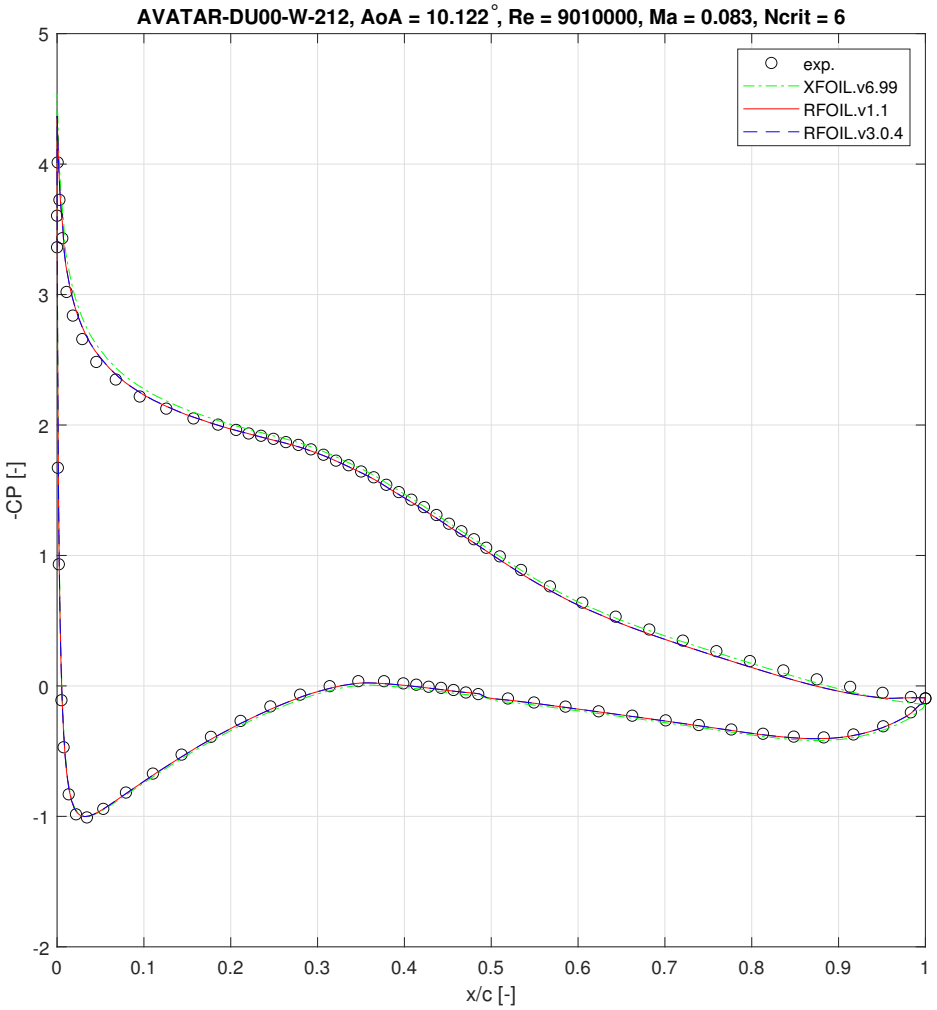

Figure C.214: Comparison between experimental and numerical pressure distributions for the AVATAR-DU00-W-212 airfoil at a Reynolds number of 14990000, and at an angle of attack and a Mach number of 10.125° and 0.081, respectively.

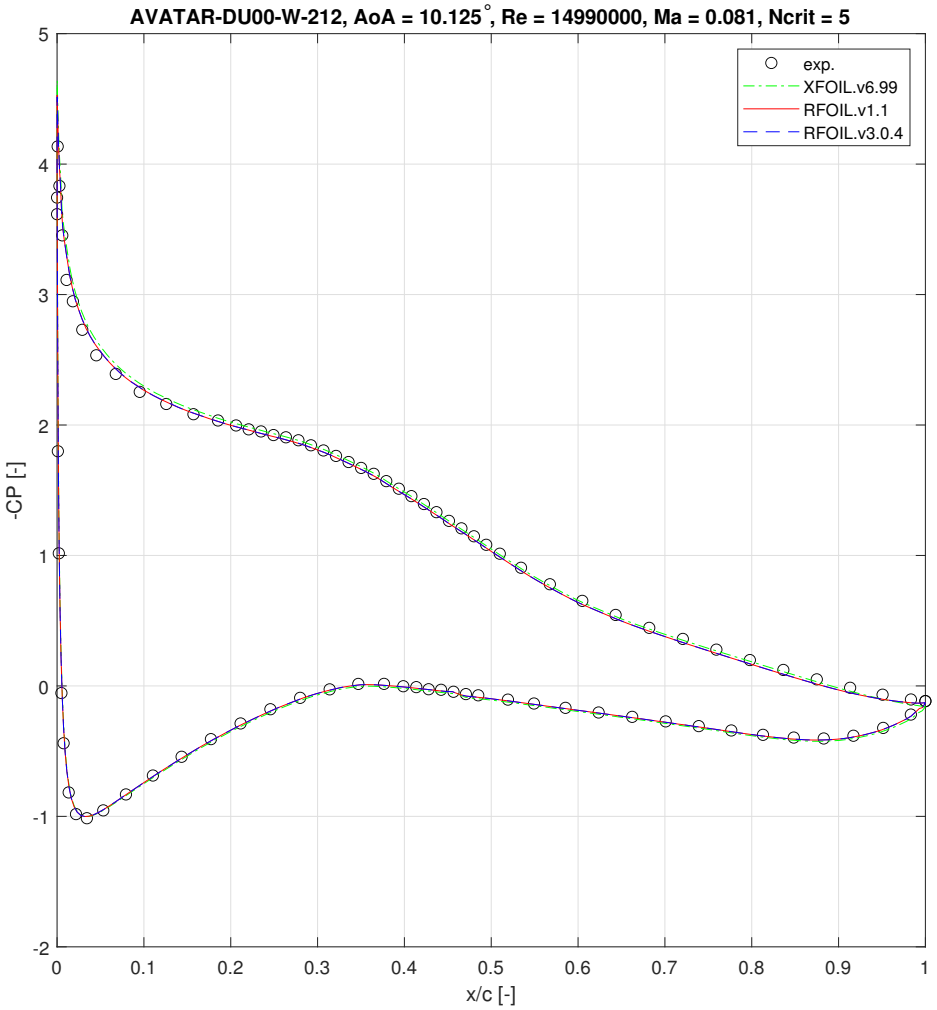

Figure C.215: Comparison between experimental and numerical pressure distributions for the AVATAR-DU00-W-212 airfoil at a Reynolds number of 6000000, and at an angle of attack and a Mach number of 10.120° and 0.055, respectively.

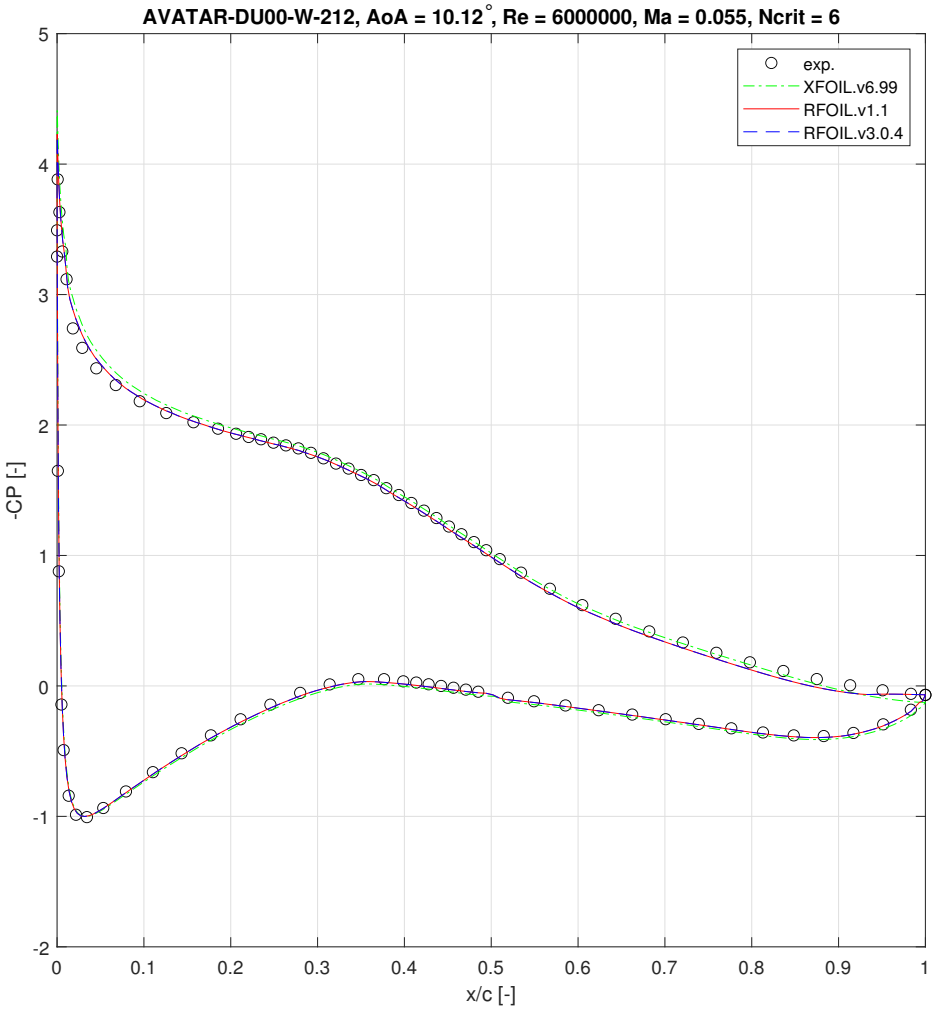

Figure C.216: Comparison between experimental and numerical pressure distributions for the AVATAR-DU00-W-212 airfoil at a Reynolds number of 3010000, and at an angle of attack and a Mach number of 10.317° and 0.074, respectively.

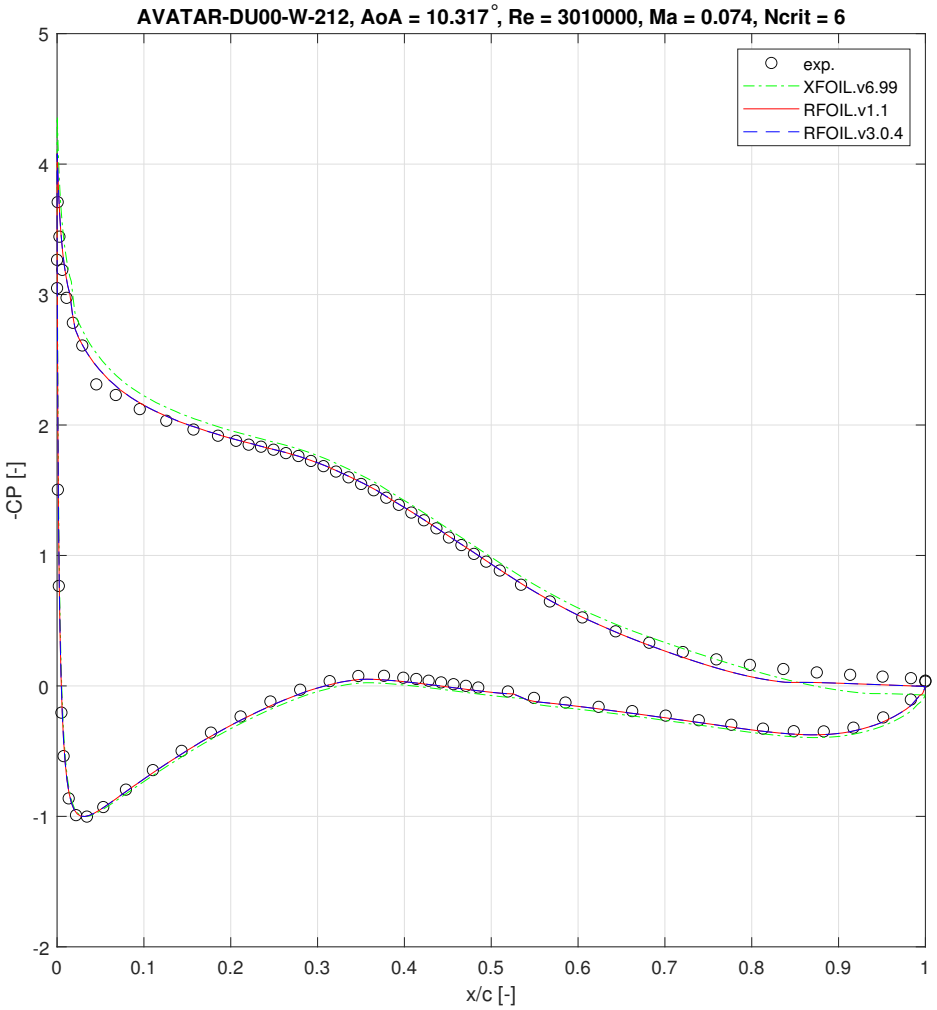

Figure C.217: Comparison between experimental and numerical pressure distributions for the AVATAR-DU00-W-212 airfoil at a Reynolds number of 3000000, and at an angle of attack and a Mach number of 10.512° and 0.074, respectively.

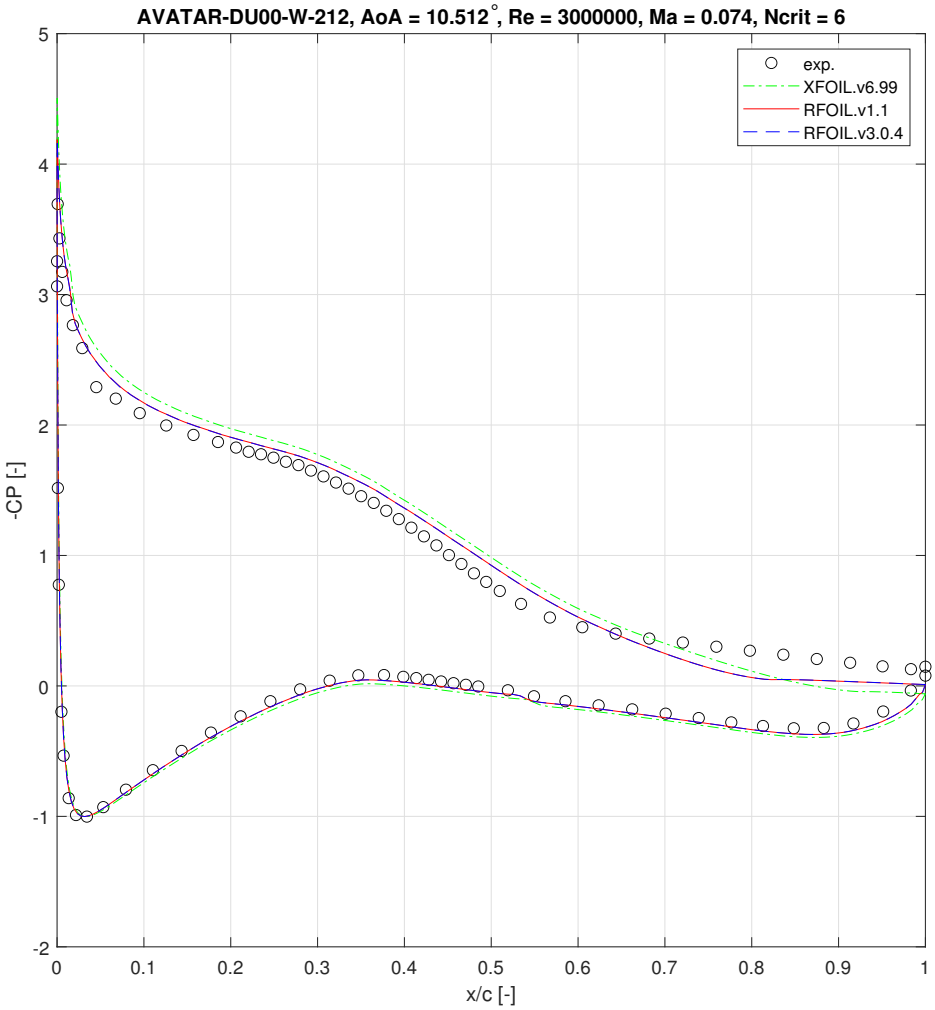

Figure C.218: Comparison between experimental and numerical pressure distributions for the AVATAR-DU00-W-212 airfoil at a Reynolds number of 5980000, and at an angle of attack and a Mach number of 10.624° and 0.029, respectively.

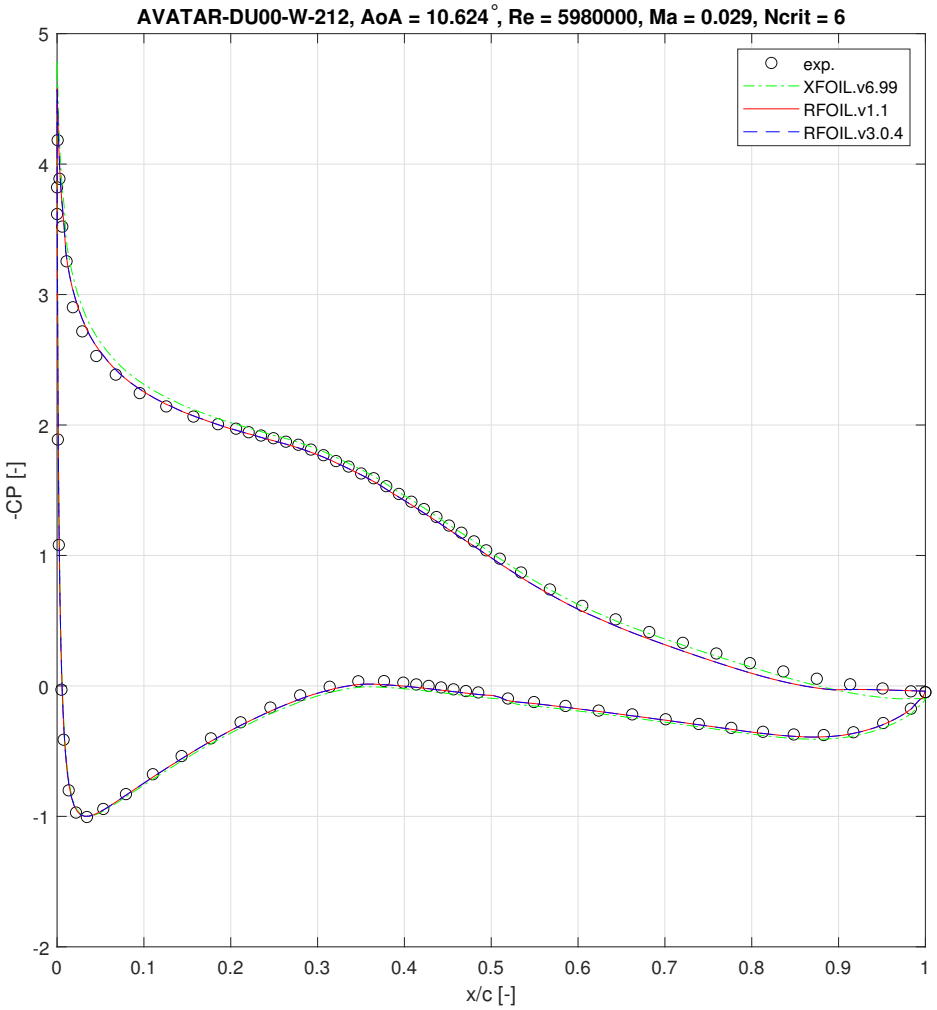

Figure C.219: Comparison between experimental and numerical pressure distributions for the AVATAR-DU00-W-212 airfoil at a Reynolds number of 6010000, and at an angle of attack and a Mach number of 10.625° and 0.055, respectively.

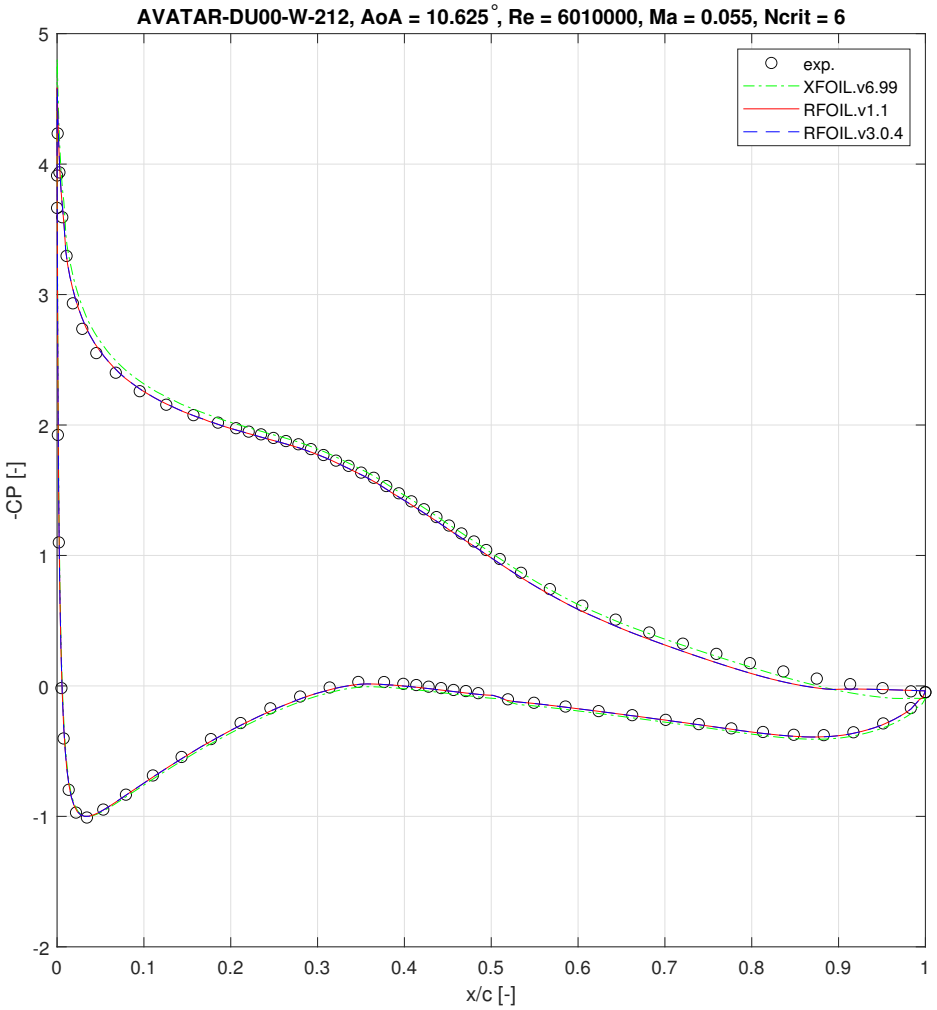

Figure C.220: Comparison between experimental and numerical pressure distributions for the AVATAR-DU00-W-212 airfoil at a Reynolds number of 3000000, and at an angle of attack and a Mach number of 10.704° and 0.074, respectively.

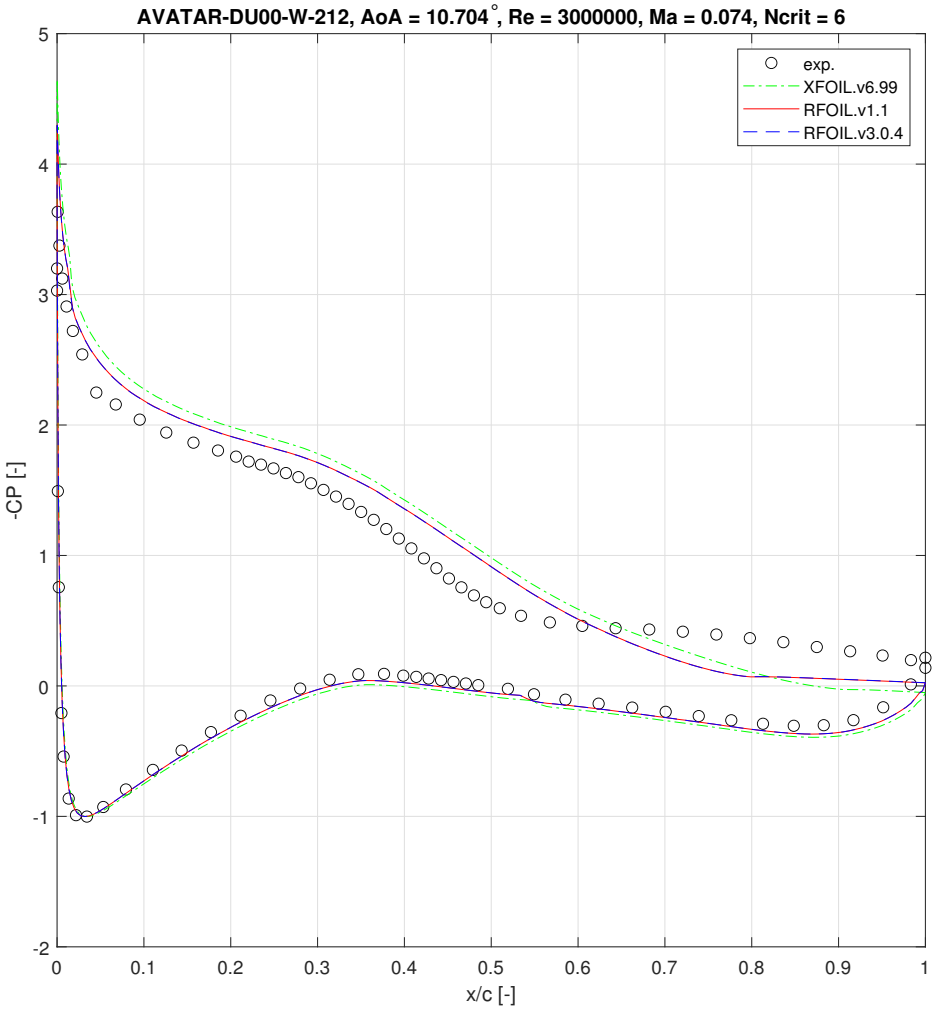

Figure C.221: Comparison between experimental and numerical pressure distributions for the AVATAR-DU00-W-212 airfoil at a Reynolds number of 3000000, and at an angle of attack and a Mach number of 10.903° and 0.074, respectively.

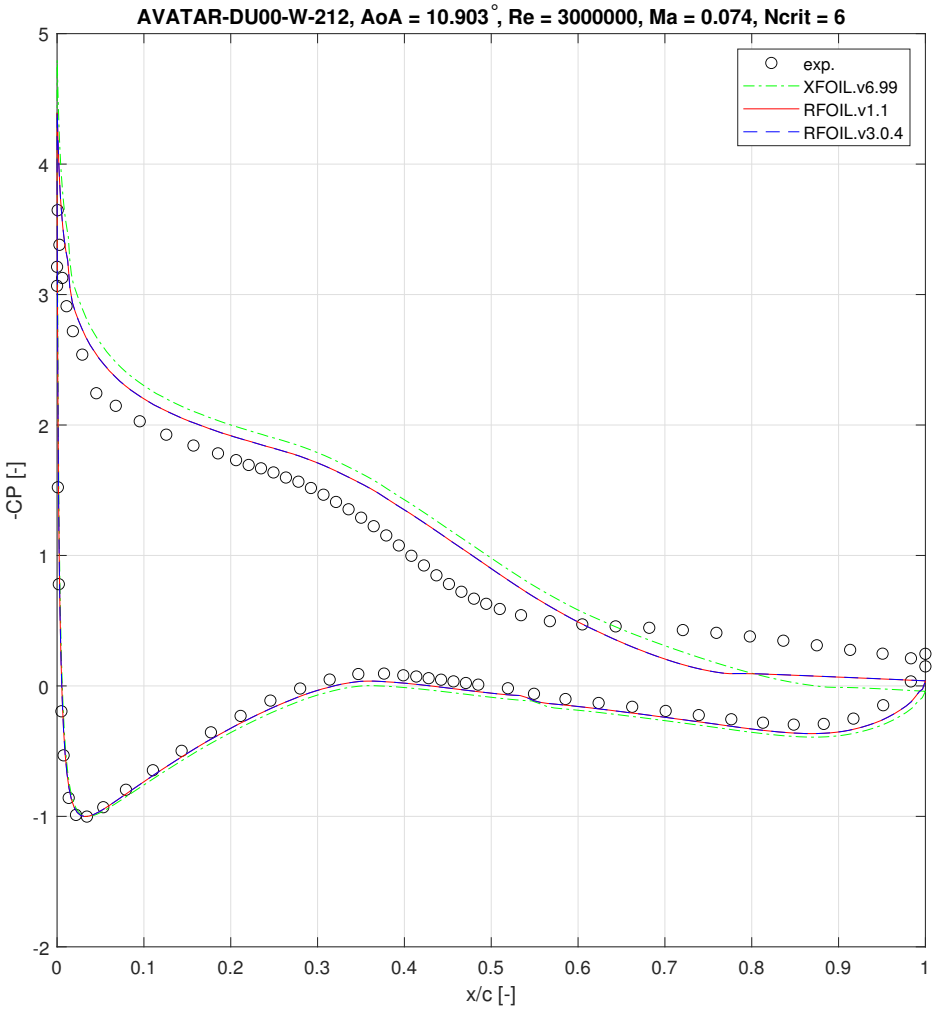

Figure C.222: Comparison between experimental and numerical pressure distributions for the AVATAR-DU00-W-212 airfoil at a Reynolds number of 6030000, and at an angle of attack and a Mach number of 10.927° and 0.029, respectively.

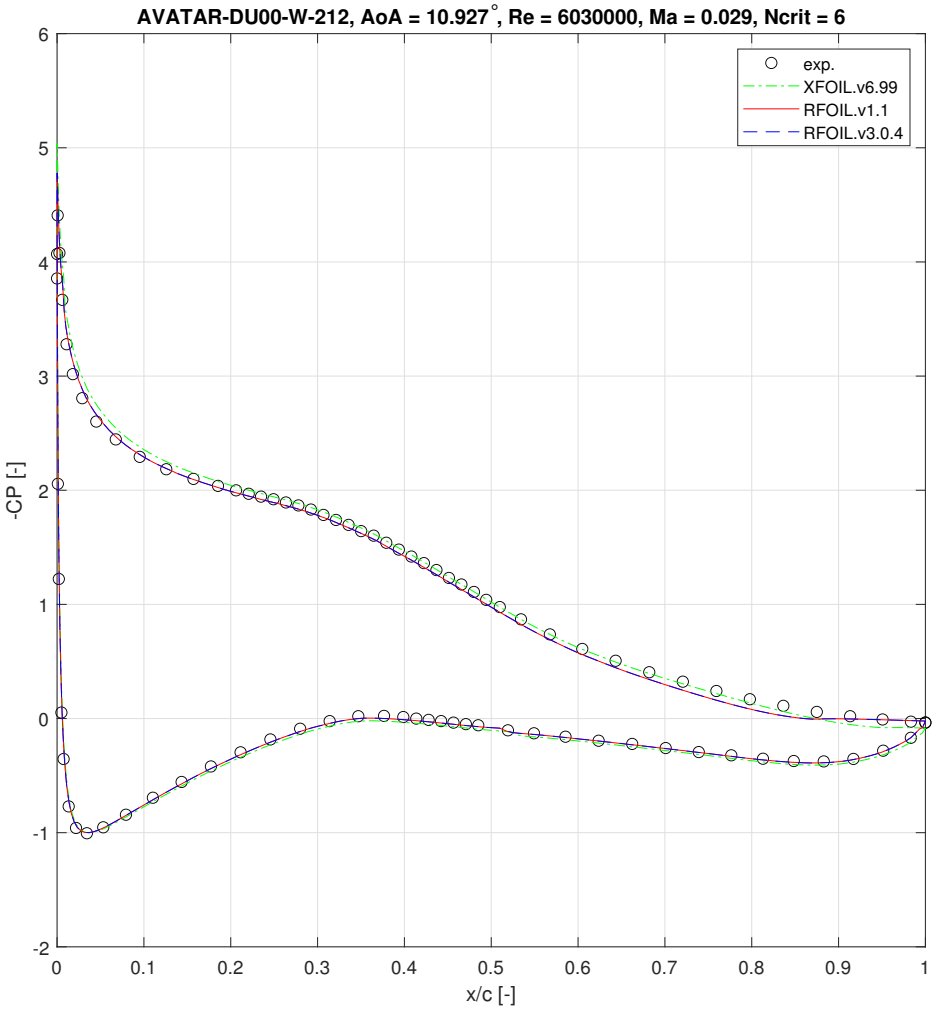

Figure C.223: Comparison between experimental and numerical pressure distributions for the AVATAR-DU00-W-212 airfoil at a Reynolds number of 6020000, and at an angle of attack and a Mach number of 10.928° and 0.055, respectively.

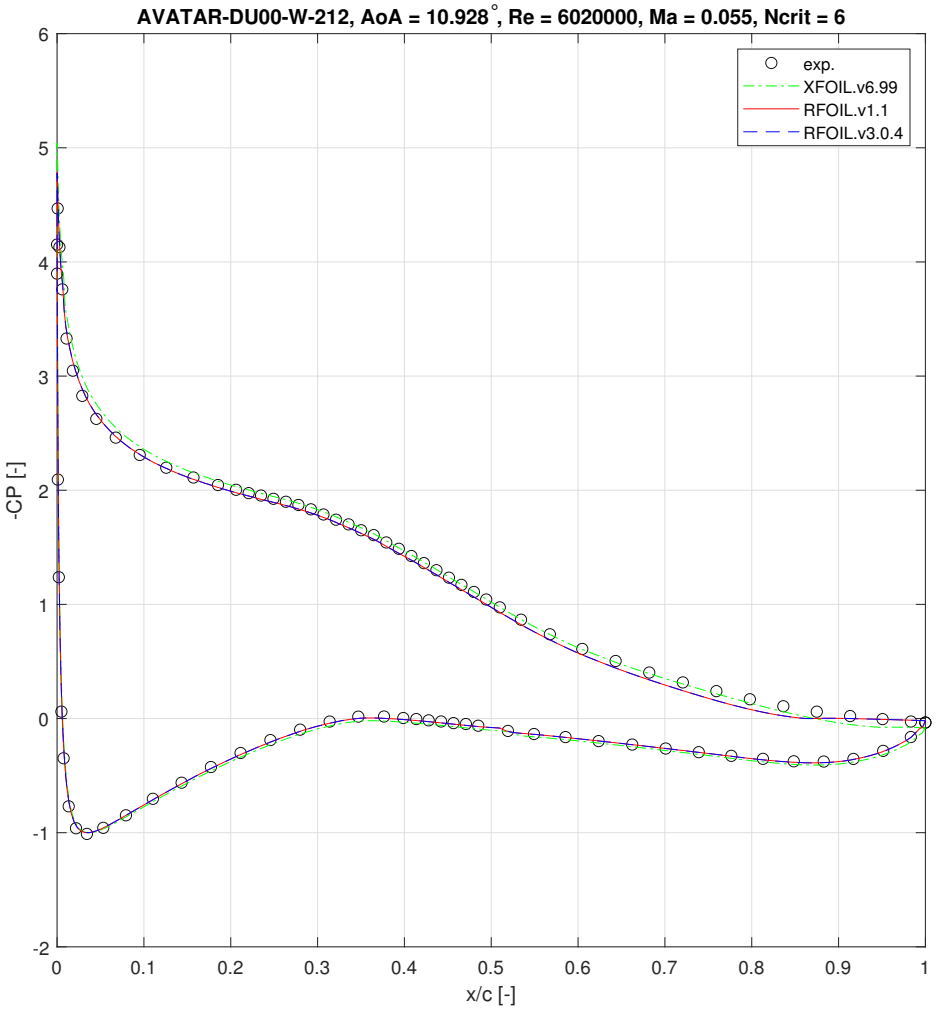

Figure C.224: Comparison between experimental and numerical pressure distributions for the AVATAR-DU00-W-212 airfoil at a Reynolds number of 11980000, and at an angle of attack and a Mach number of 11.026° and 0.058, respectively.

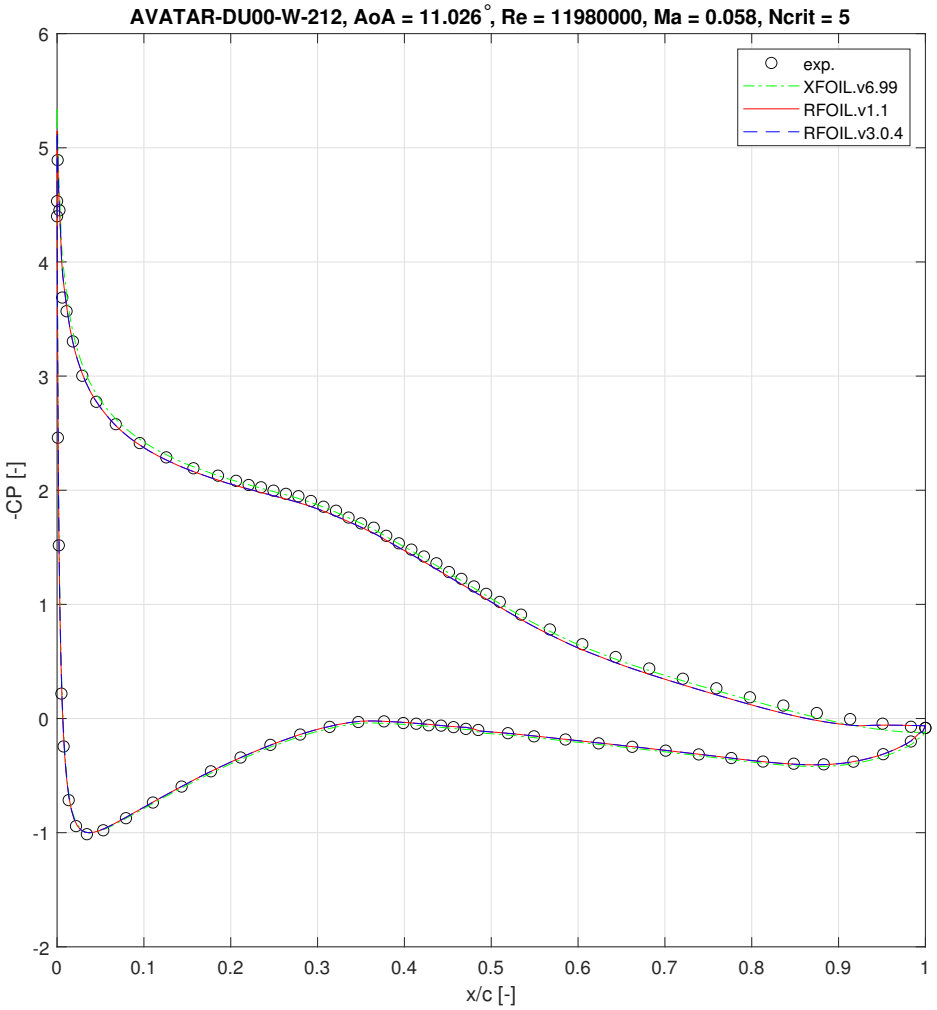

Figure C.225: Comparison between experimental and numerical pressure distributions for the AVATAR-DU00-W-212 airfoil at a Reynolds number of 5980000, and at an angle of attack and a Mach number of 11.129° and 0.029, respectively.

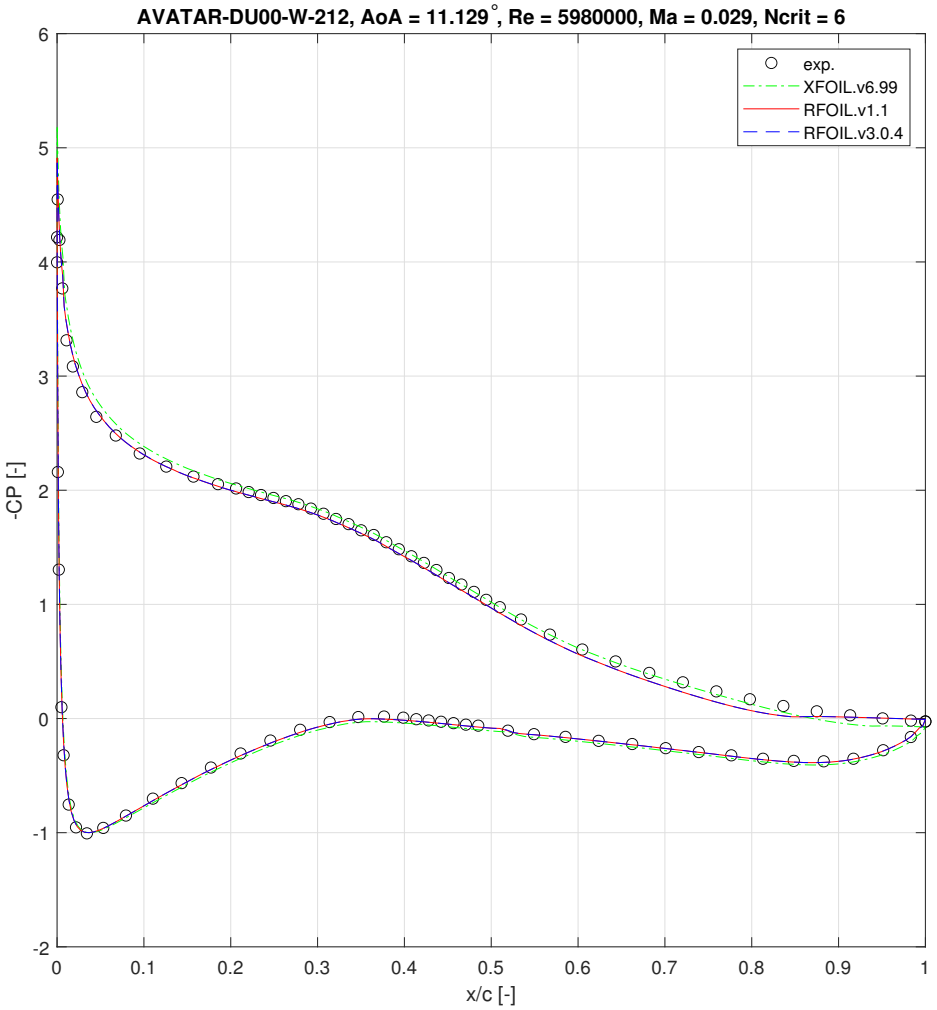

Figure C.226: Comparison between experimental and numerical pressure distributions for the AVATAR-DU00-W-212 airfoil at a Reynolds number of 9000000, and at an angle of attack and a Mach number of 11.132° and 0.044, respectively.

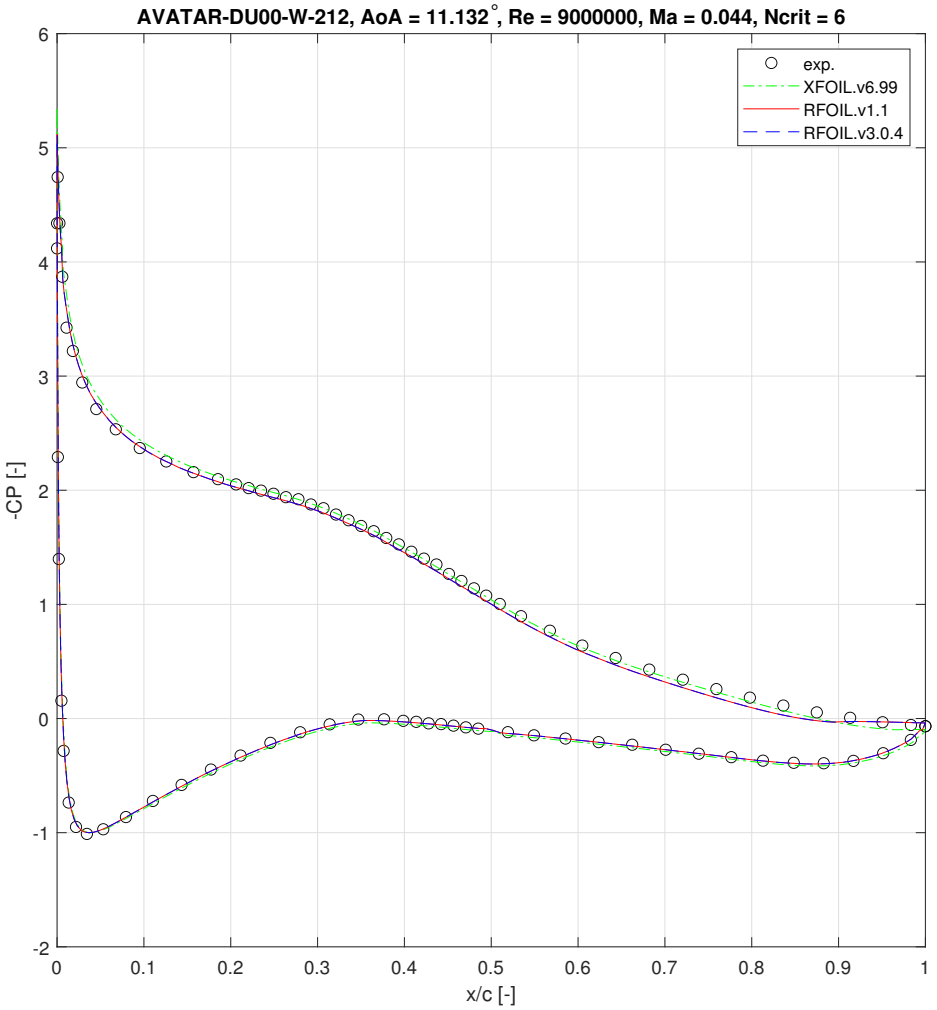

Figure C.227: Comparison between experimental and numerical pressure distributions for the AVATAR-DU00-W-212 airfoil at a Reynolds number of 9010000, and at an angle of attack and a Mach number of 11.132° and 0.043, respectively.

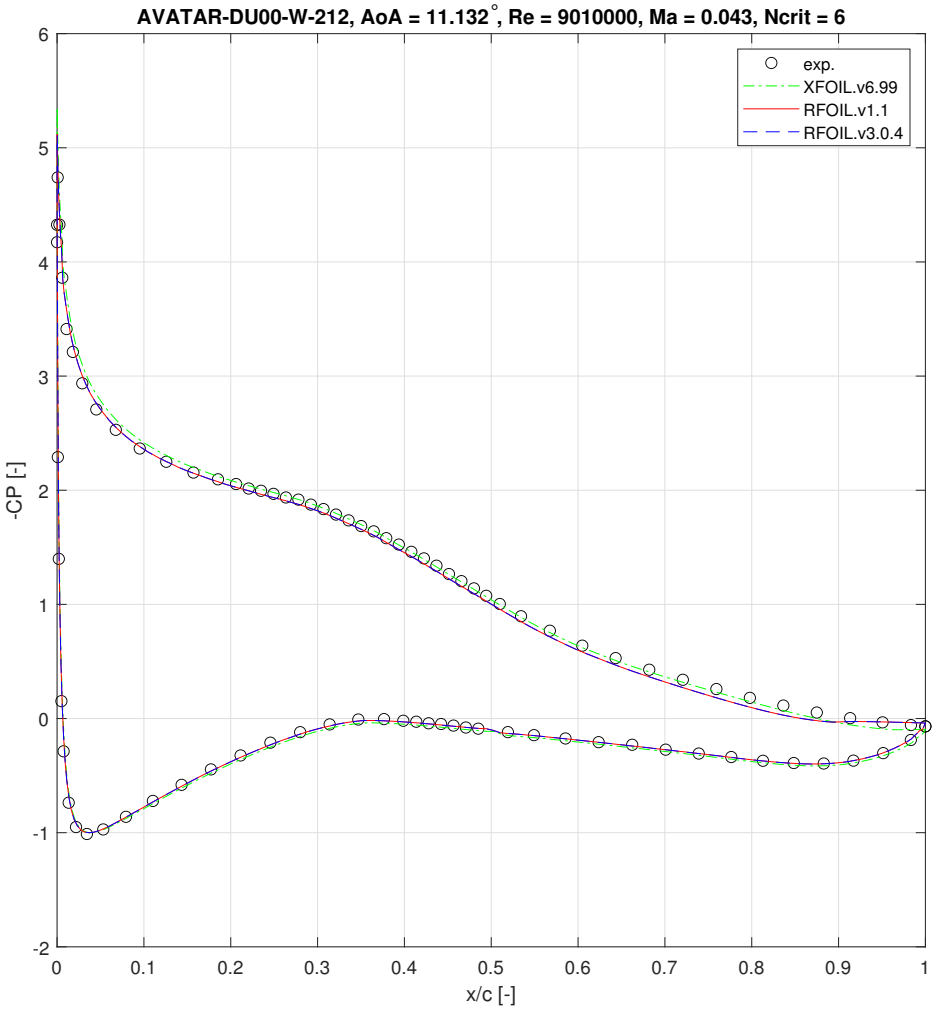

Figure C.228: Comparison between experimental and numerical pressure distributions for the AVATAR-DU00-W-212 airfoil at a Reynolds number of 8990000, and at an angle of attack and a Mach number of 11.133° and 0.083, respectively.

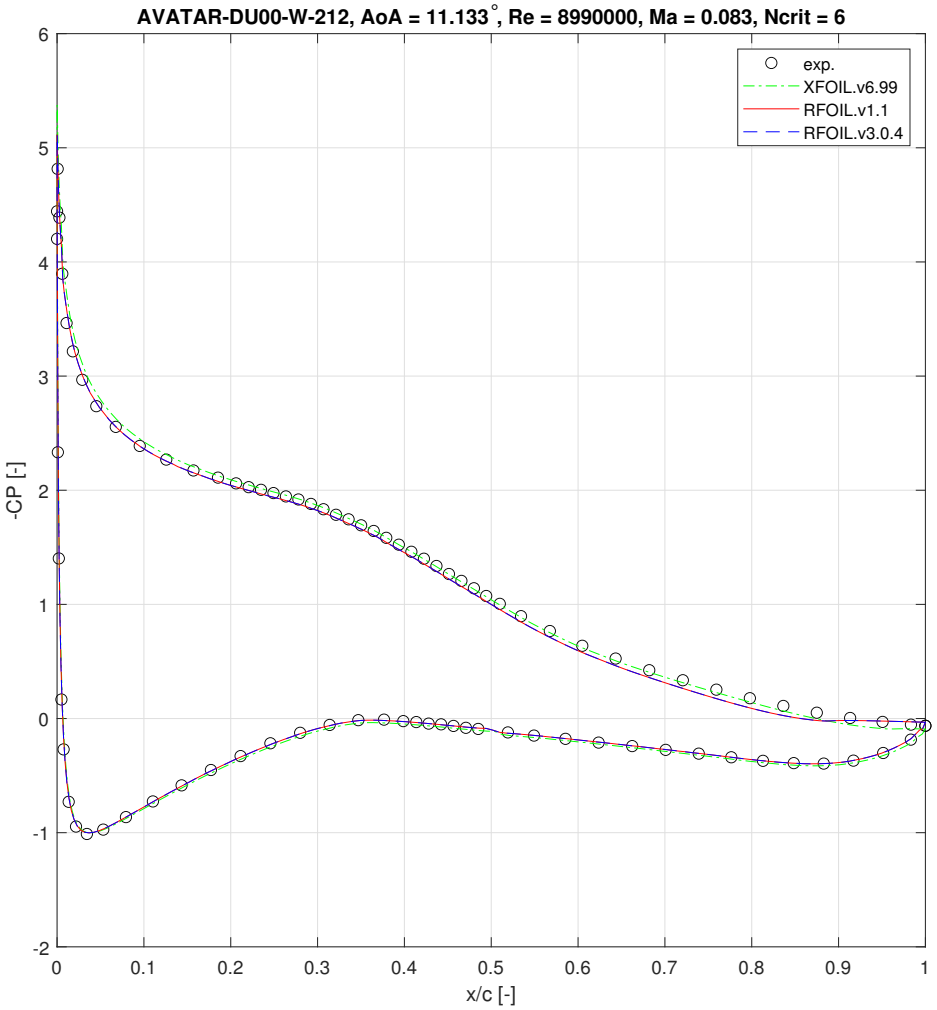

Figure C.229: Comparison between experimental and numerical pressure distributions for the AVATAR-DU00-W-212 airfoil at a Reynolds number of 15010000, and at an angle of attack and a Mach number of 11.136° and 0.081, respectively.

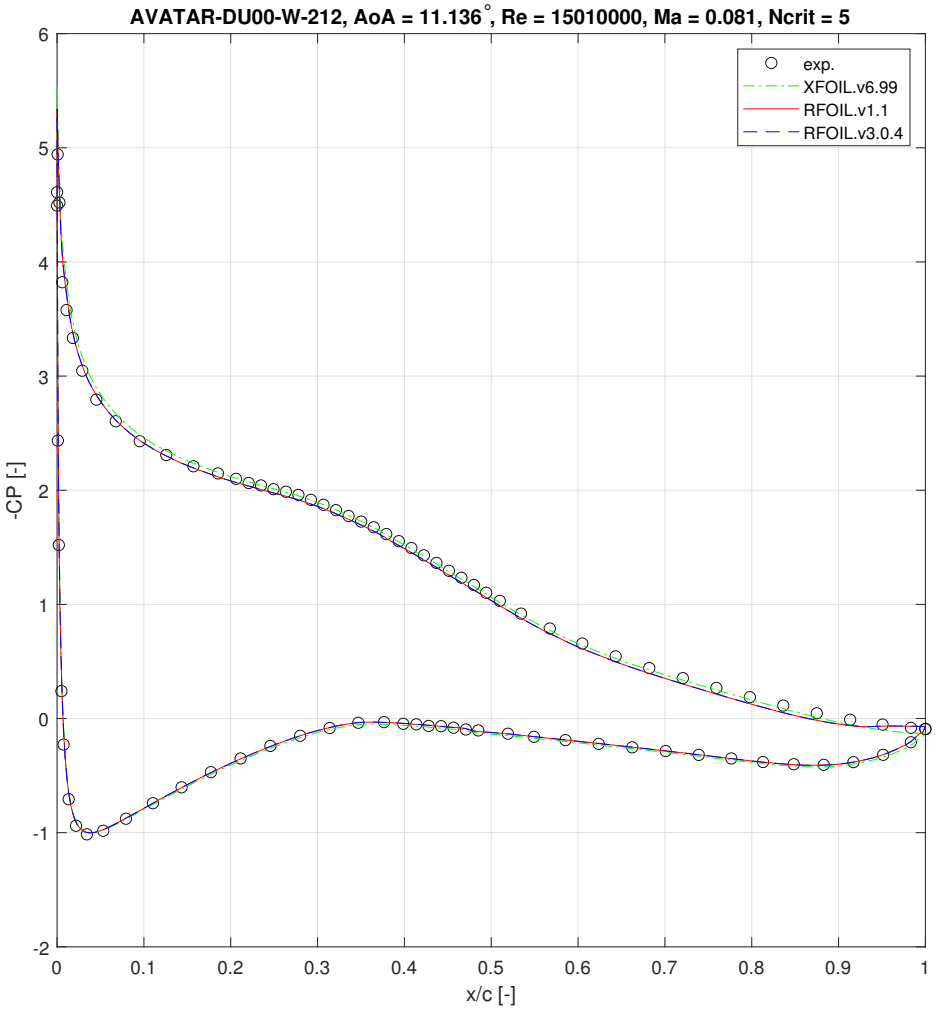

Figure C.230: Comparison between experimental and numerical pressure distributions for the AVATAR-DU00-W-212 airfoil at a Reynolds number of 6000000, and at an angle of attack and a Mach number of 11.130° and 0.055, respectively.

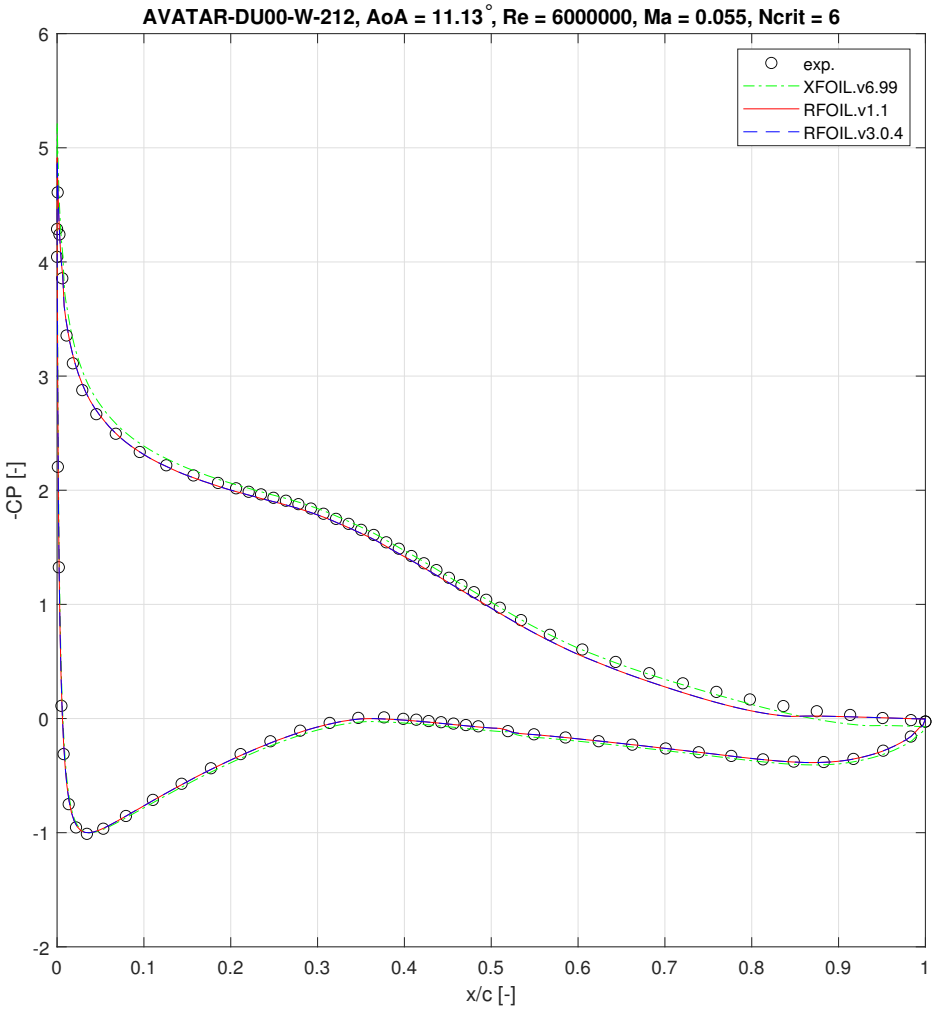

Figure C.231: Comparison between experimental and numerical pressure distributions for the AVATAR-DU00-W-212 airfoil at a Reynolds number of 3000000, and at an angle of attack and a Mach number of 11.100° and 0.074, respectively.

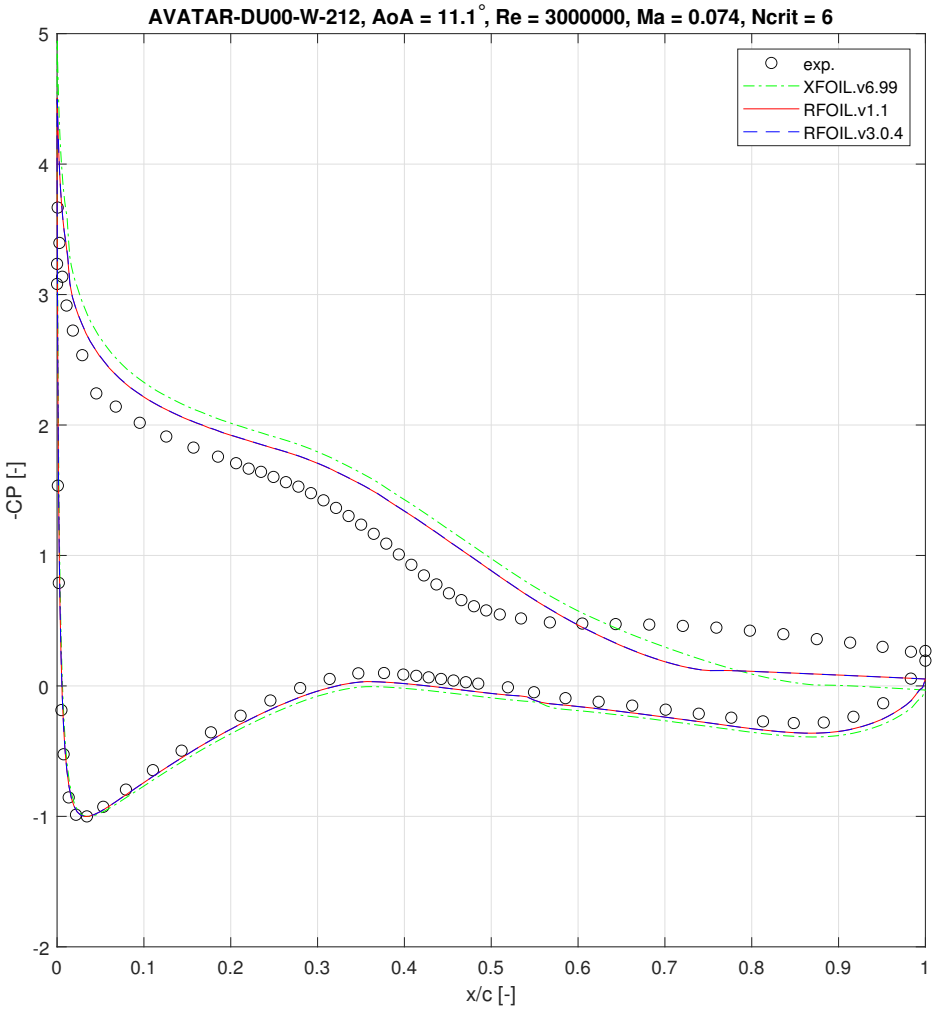

Figure C.232: Comparison between experimental and numerical pressure distributions for the AVATAR-DU00-W-212 airfoil at a Reynolds number of 6000000, and at an angle of attack and a Mach number of 11.331° and 0.029, respectively.

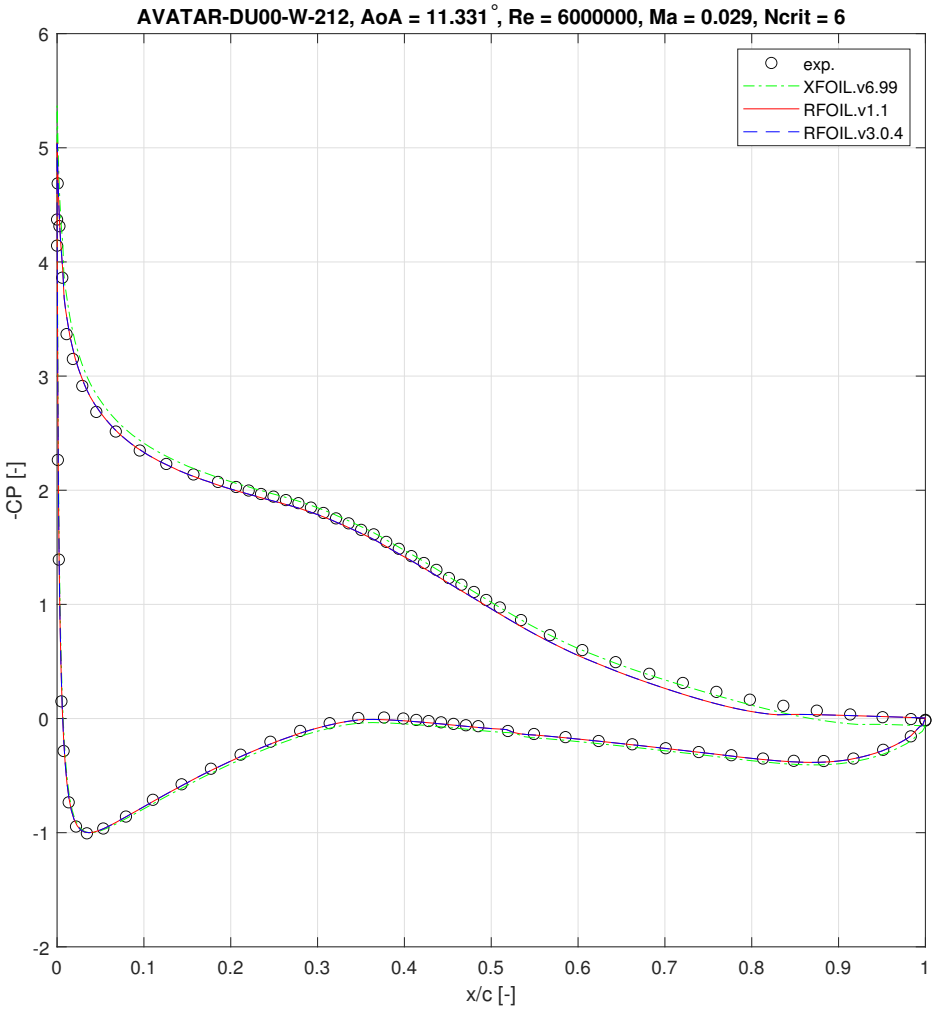

Figure C.233: Comparison between experimental and numerical pressure distributions for the AVATAR-DU00-W-212 airfoil at a Reynolds number of 6010000, and at an angle of attack and a Mach number of 11.332° and 0.055, respectively.

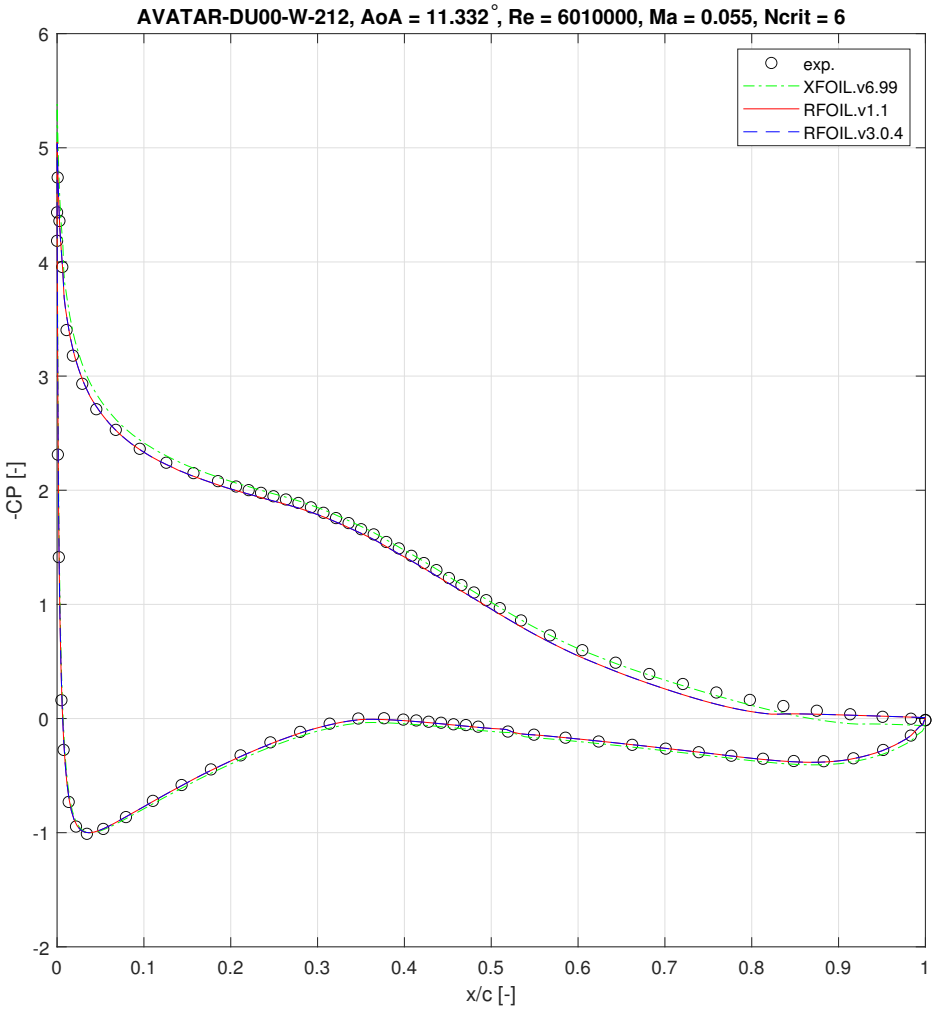

Figure C.234: Comparison between experimental and numerical pressure distributions for the AVATAR-DU00-W-212 airfoil at a Reynolds number of 6010000, and at an angle of attack and a Mach number of 11.633° and 0.029, respectively.

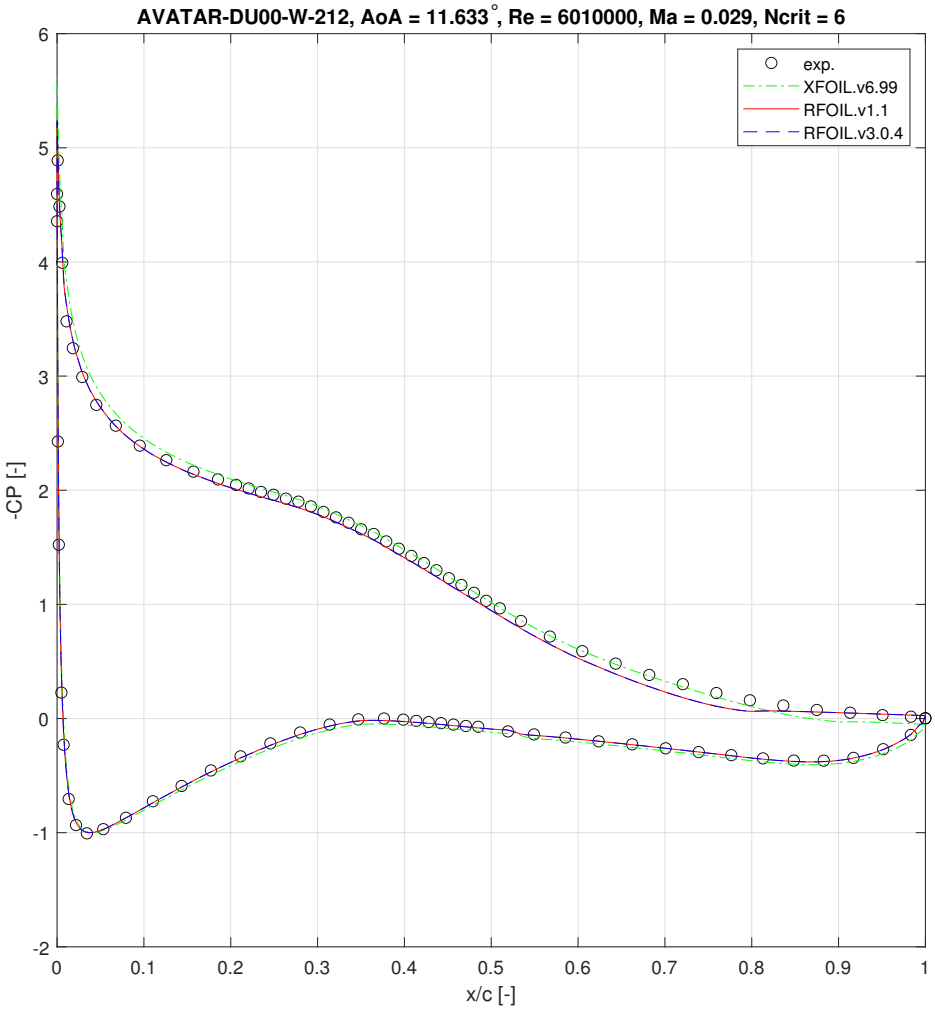

Figure C.235: Comparison between experimental and numerical pressure distributions for the AVATAR-DU00-W-212 airfoil at a Reynolds number of 6000000, and at an angle of attack and a Mach number of 11.634° and 0.055, respectively.

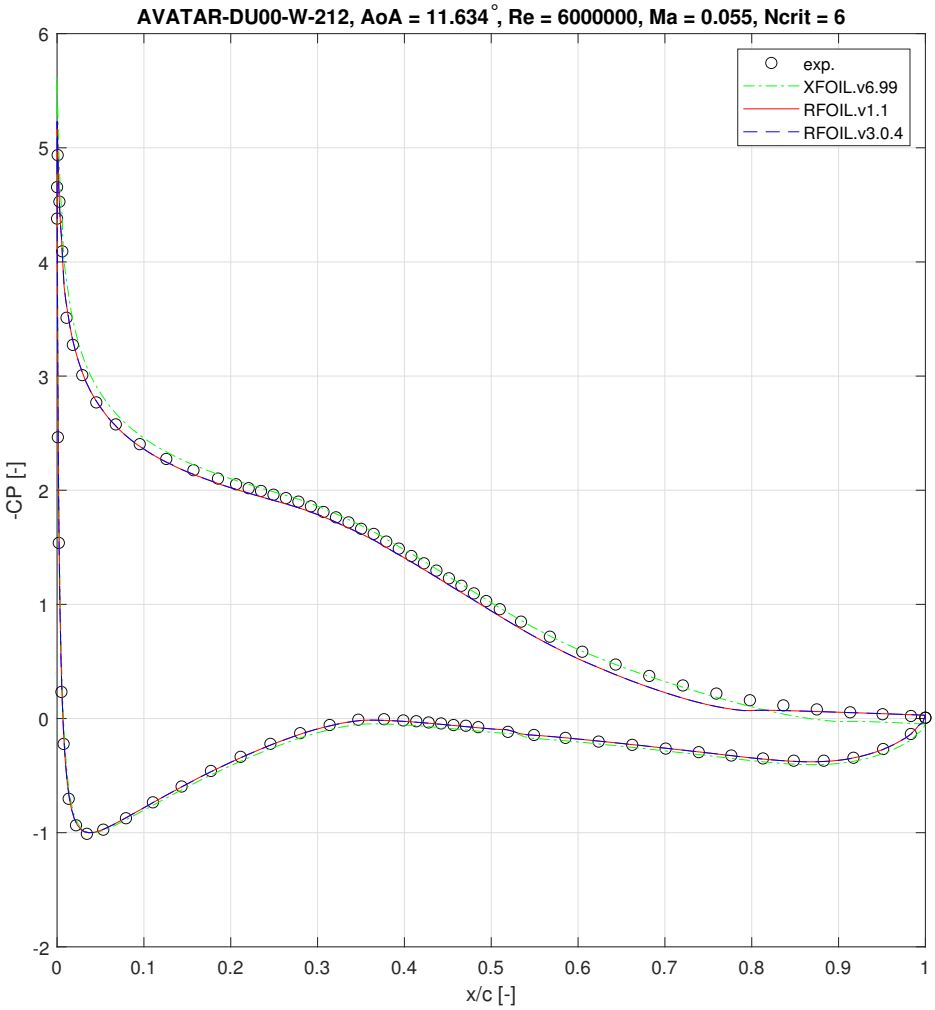

Figure C.236: Comparison between experimental and numerical pressure distributions for the AVATAR-DU00-W-212 airfoil at a Reynolds number of 8990000, and at an angle of attack and a Mach number of 11.637° and 0.043, respectively.

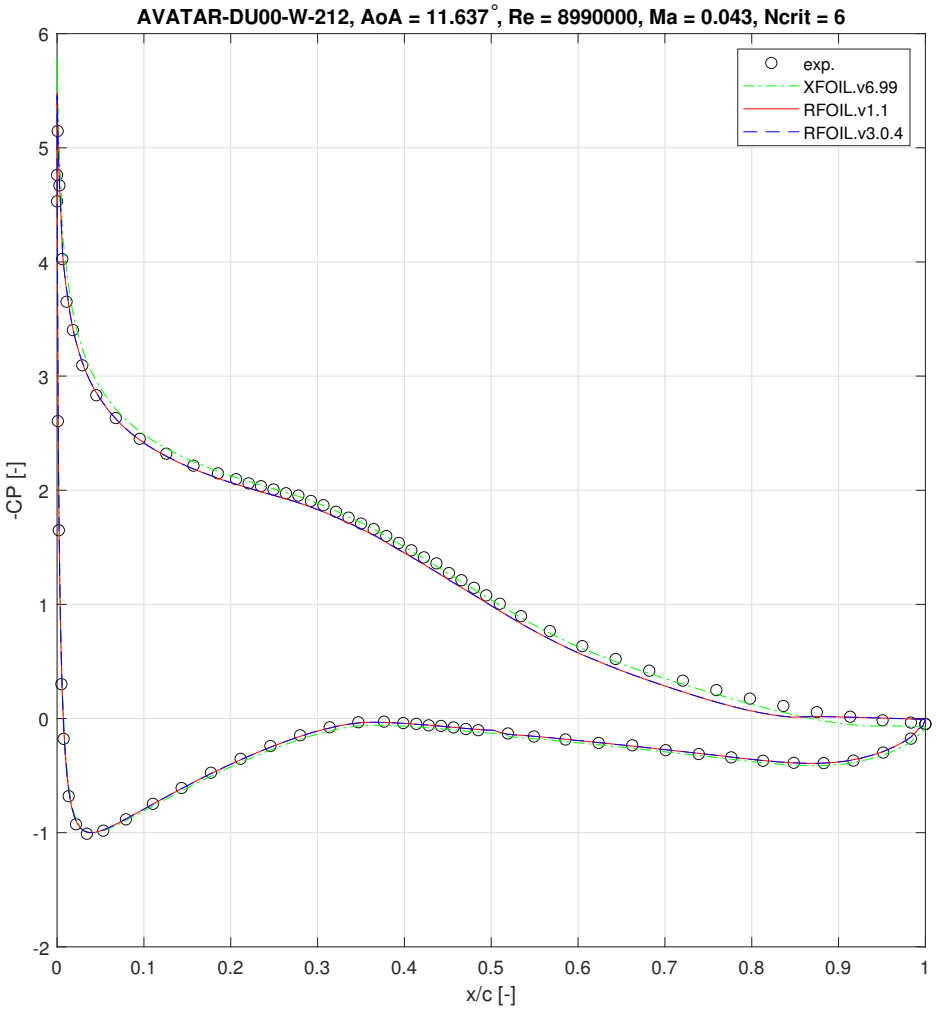

Figure C.237: Comparison between experimental and numerical pressure distributions for the AVATAR-DU00-W-212 airfoil at a Reynolds number of 8990000, and at an angle of attack and a Mach number of 11.638° and 0.083, respectively.

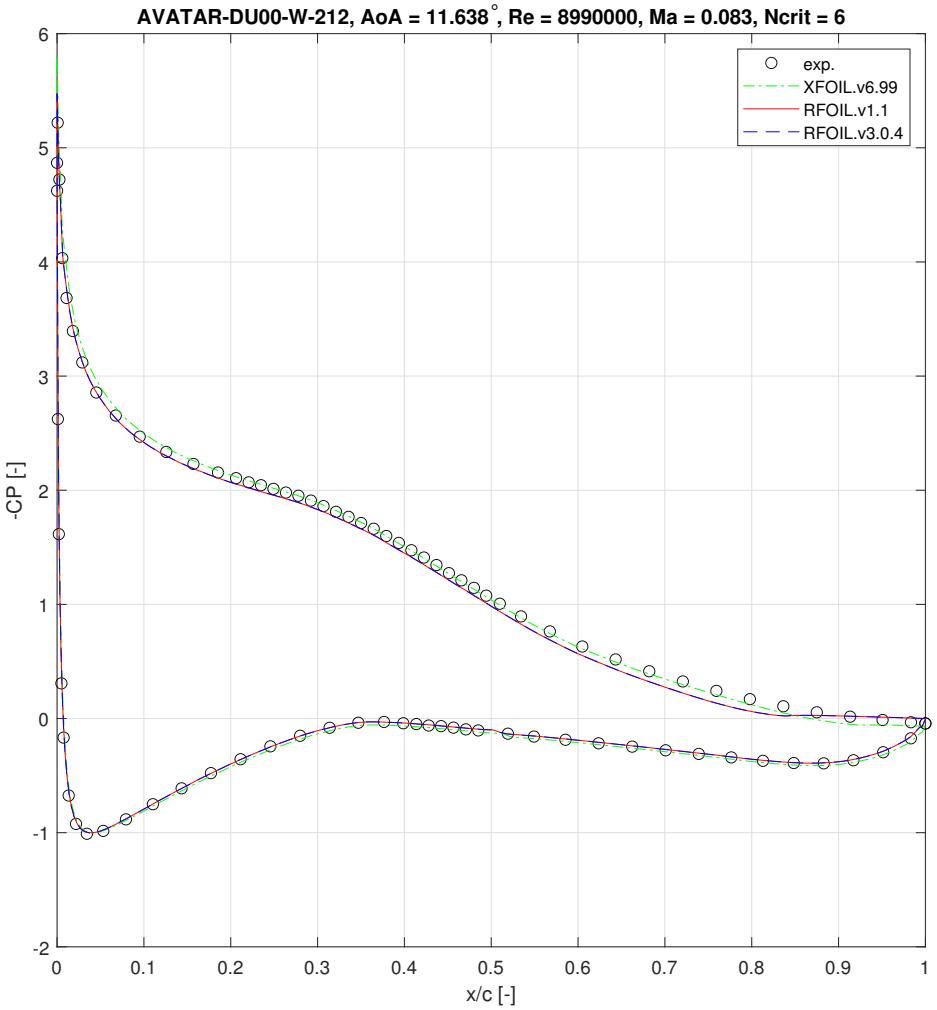

Figure C.238: Comparison between experimental and numerical pressure distributions for the AVATAR-DU00-W-212 airfoil at a Reynolds number of 3010000, and at an angle of attack and a Mach number of 11.600° and 0.075, respectively.

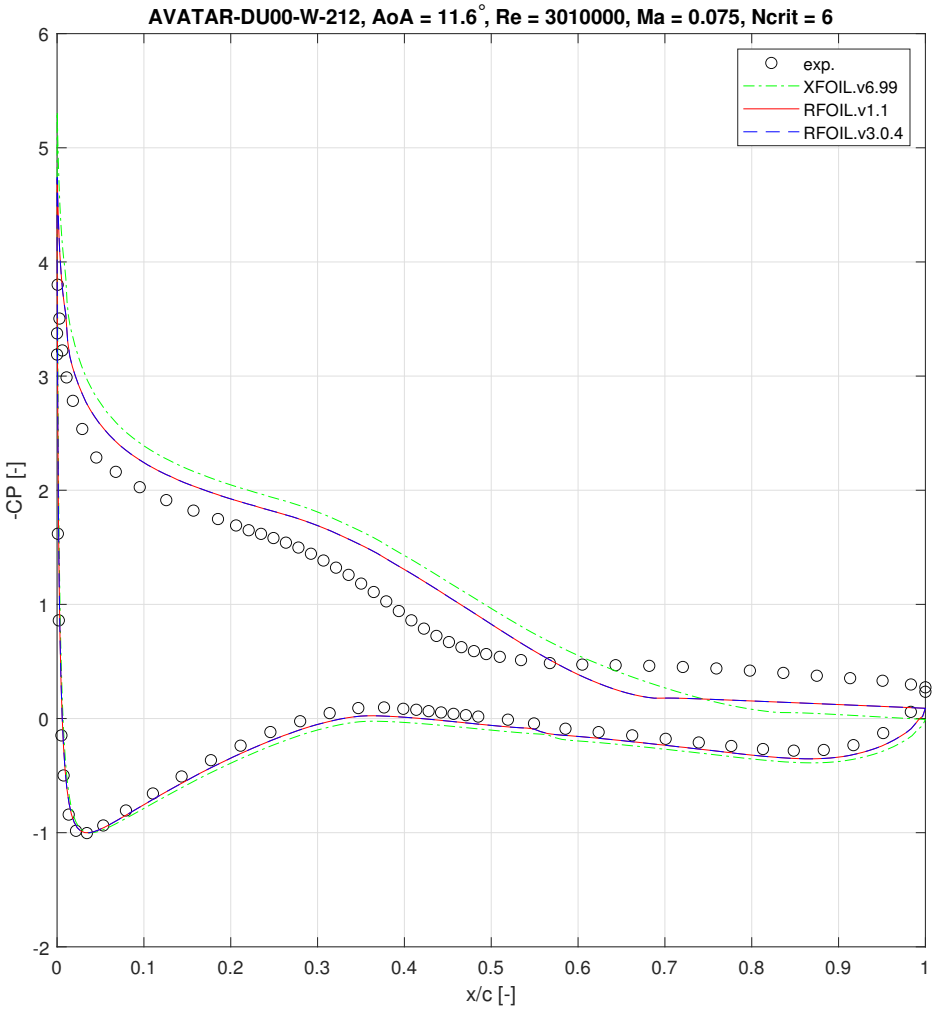

Figure C.239: Comparison between experimental and numerical pressure distributions for the AVATAR-DU00-W-212 airfoil at a Reynolds number of 5990000, and at an angle of attack and a Mach number of 11.834° and 0.029, respectively.

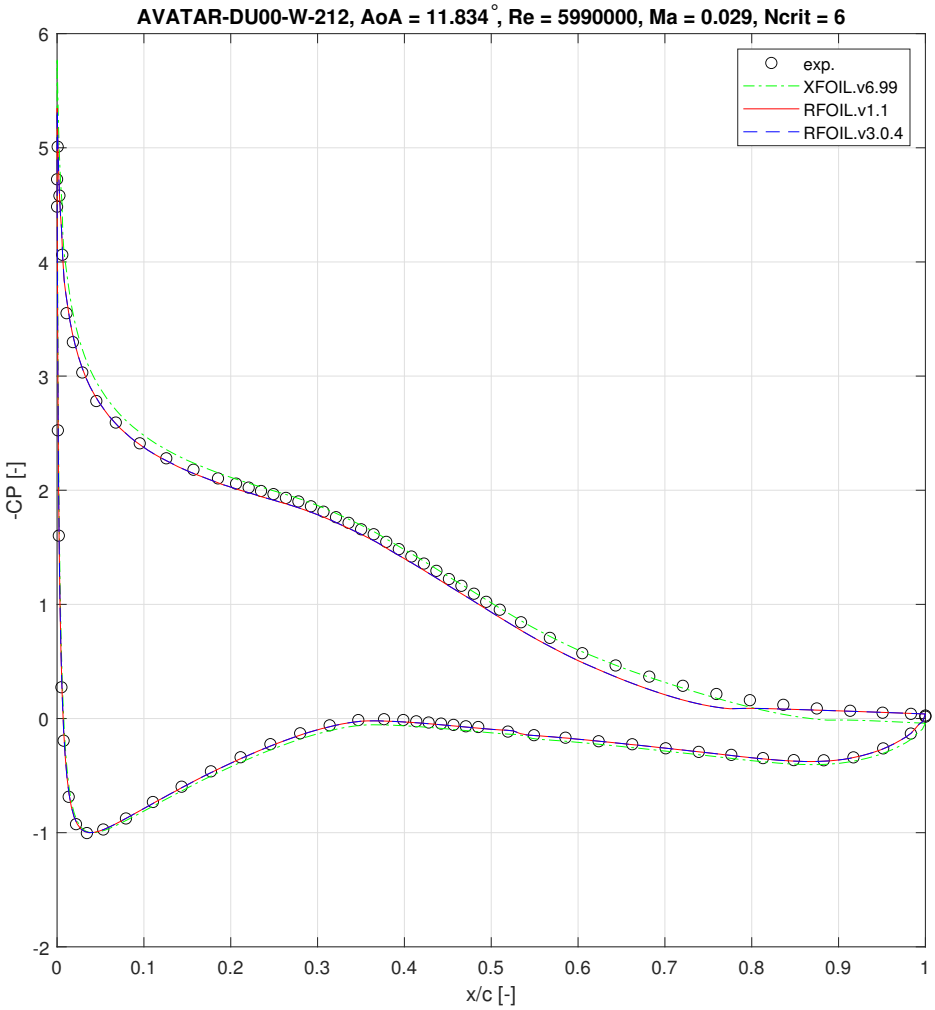

Figure C.240: Comparison between experimental and numerical pressure distributions for the AVATAR-DU00-W-212 airfoil at a Reynolds number of 6010000, and at an angle of attack and a Mach number of 11.836° and 0.055, respectively.

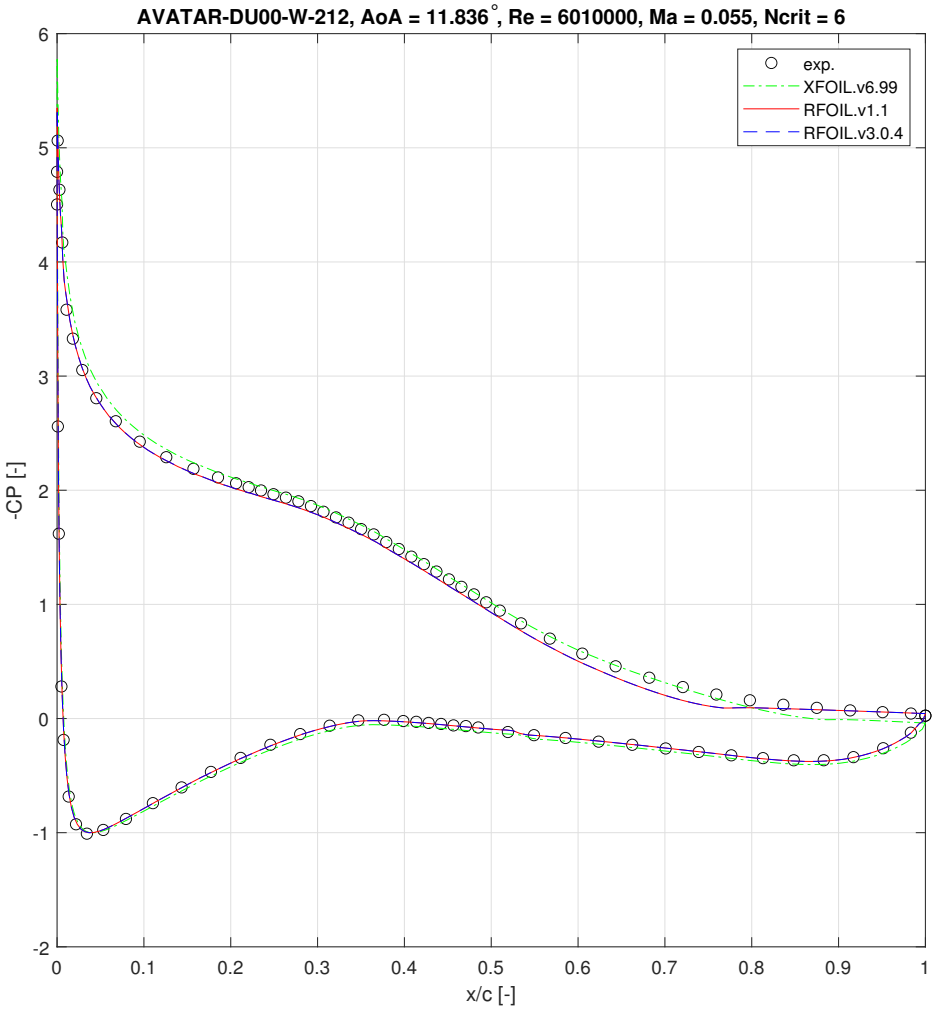

Figure C.241: Comparison between experimental and numerical pressure distributions for the AVATAR-DU00-W-212 airfoil at a Reynolds number of 6000000, and at an angle of attack and a Mach number of 11.935° and 0.029, respectively.

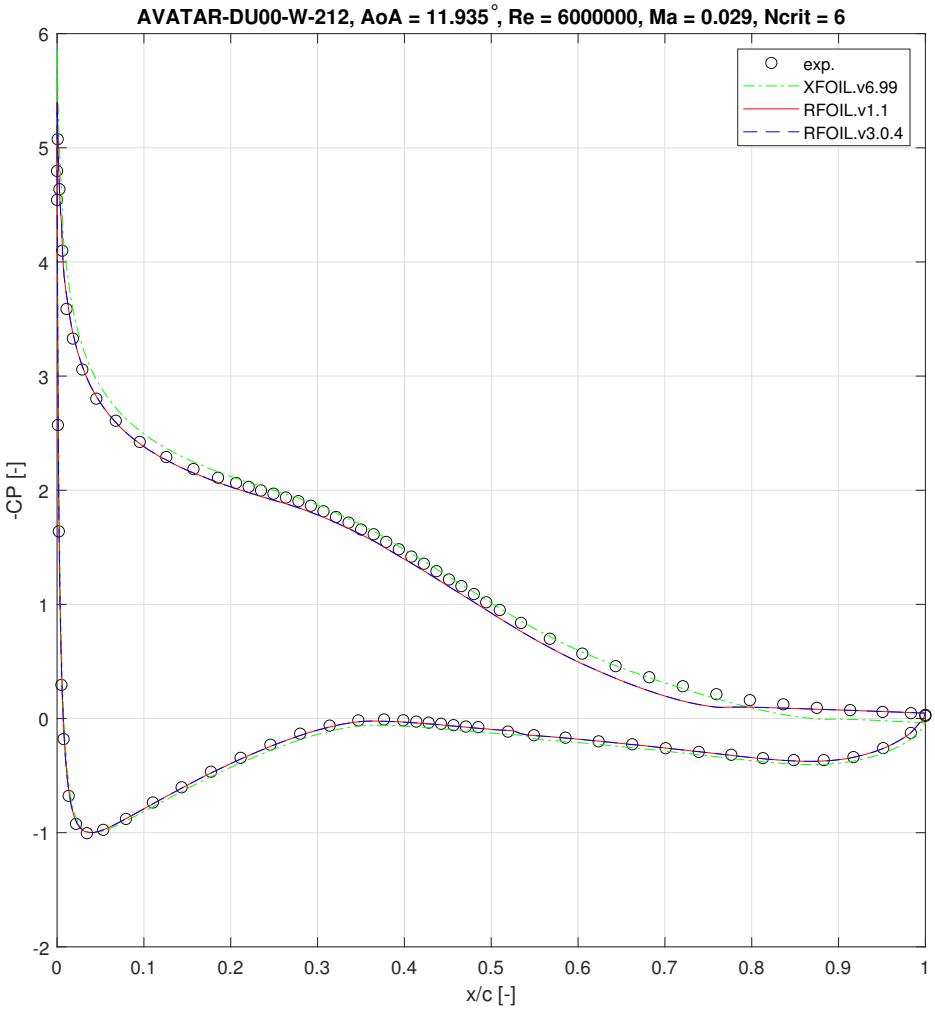

Figure C.242: Comparison between experimental and numerical pressure distributions for the AVATAR-DU00-W-212 airfoil at a Reynolds number of 6010000, and at an angle of attack and a Mach number of 11.936° and 0.055, respectively.

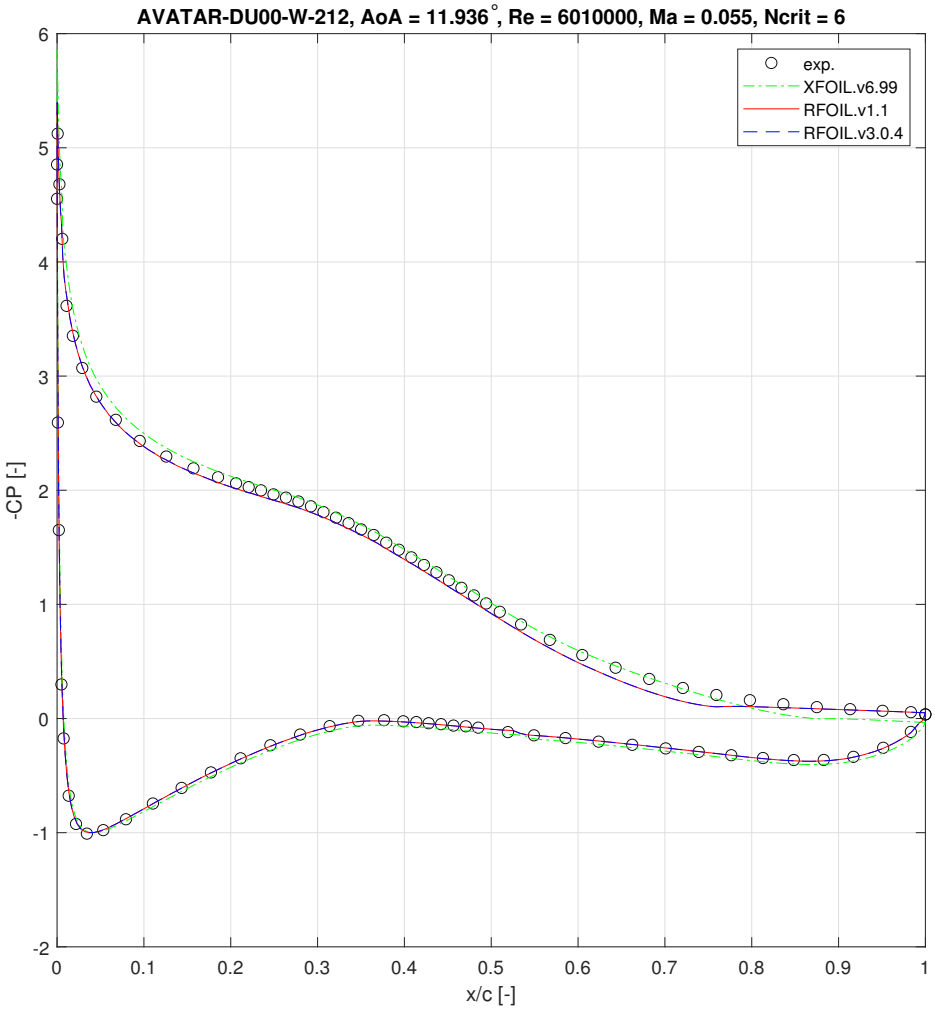

Figure C.243: Comparison between experimental and numerical pressure distributions for the AVATAR-DU00-W-212 airfoil at a Reynolds number of 6000000, and at an angle of attack and a Mach number of 12.007° and 0.055, respectively.

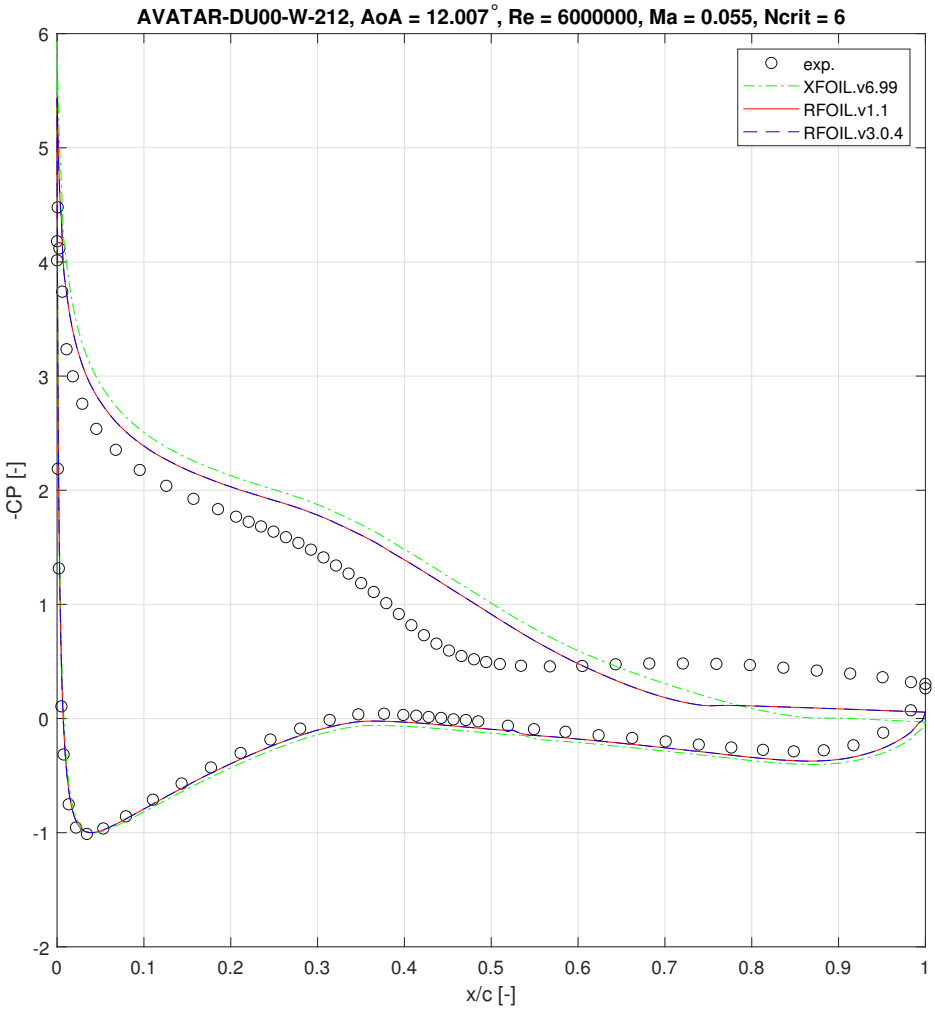

Figure C.244: Comparison between experimental and numerical pressure distributions for the AVATAR-DU00-W-212 airfoil at a Reynolds number of 12050000, and at an angle of attack and a Mach number of 12.023° and 0.058, respectively.

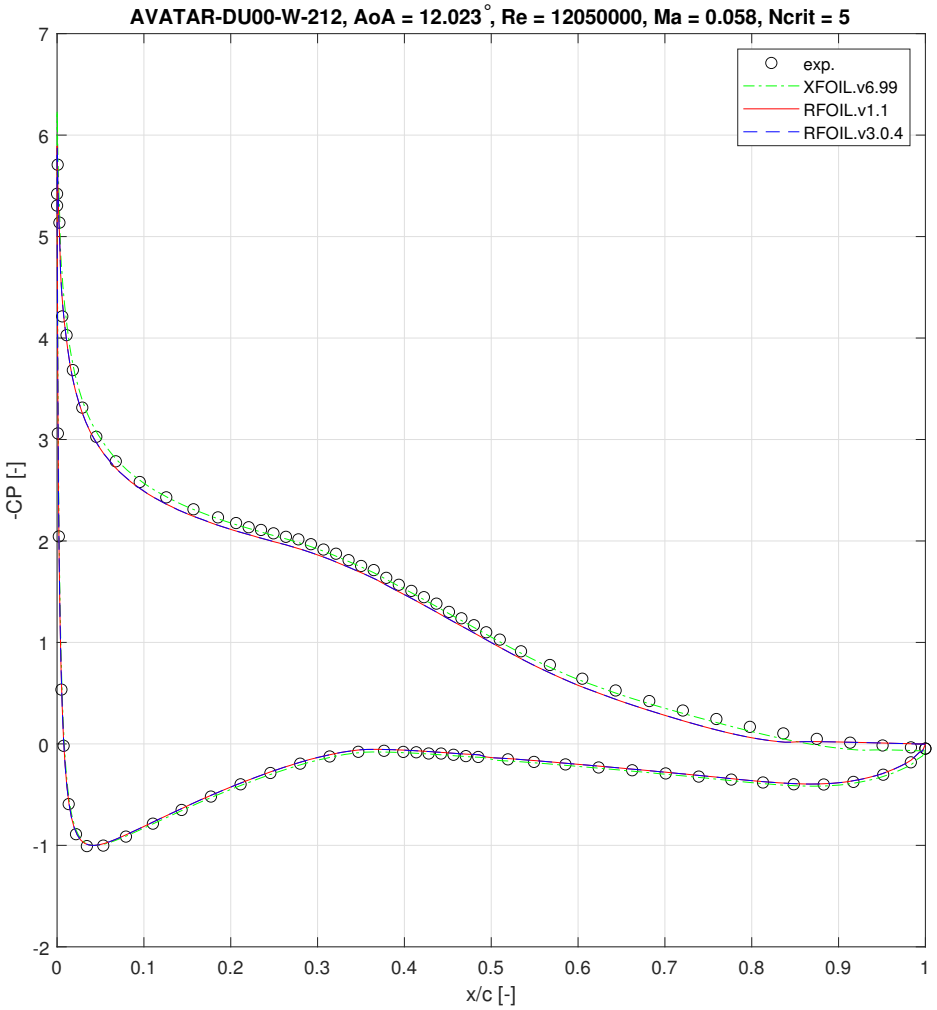

Figure C.245: Comparison between experimental and numerical pressure distributions for the AVATAR-DU00-W-212 airfoil at a Reynolds number of 3030000, and at an angle of attack and a Mach number of 12.101° and 0.075, respectively.

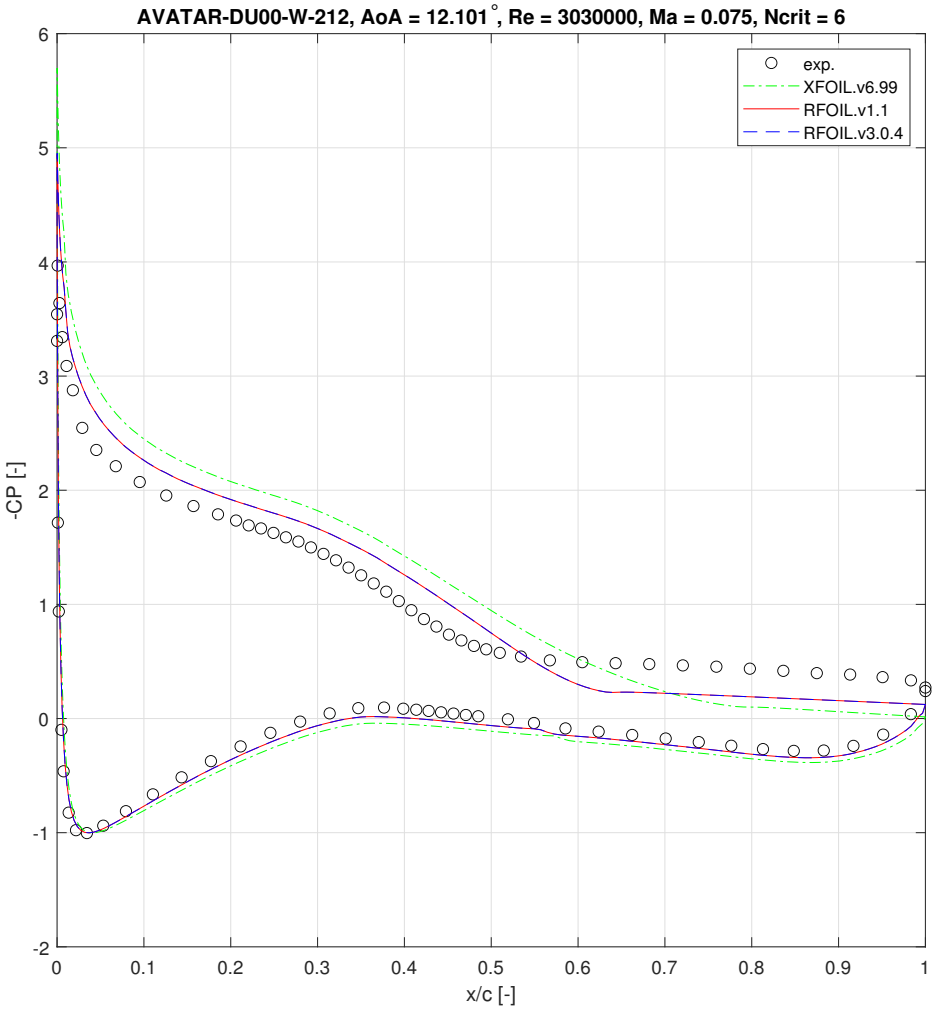

Figure C.246: Comparison between experimental and numerical pressure distributions for the AVATAR-DU00-W-212 airfoil at a Reynolds number of 3030000, and at an angle of attack and a Mach number of 12.103° and 0.075, respectively.

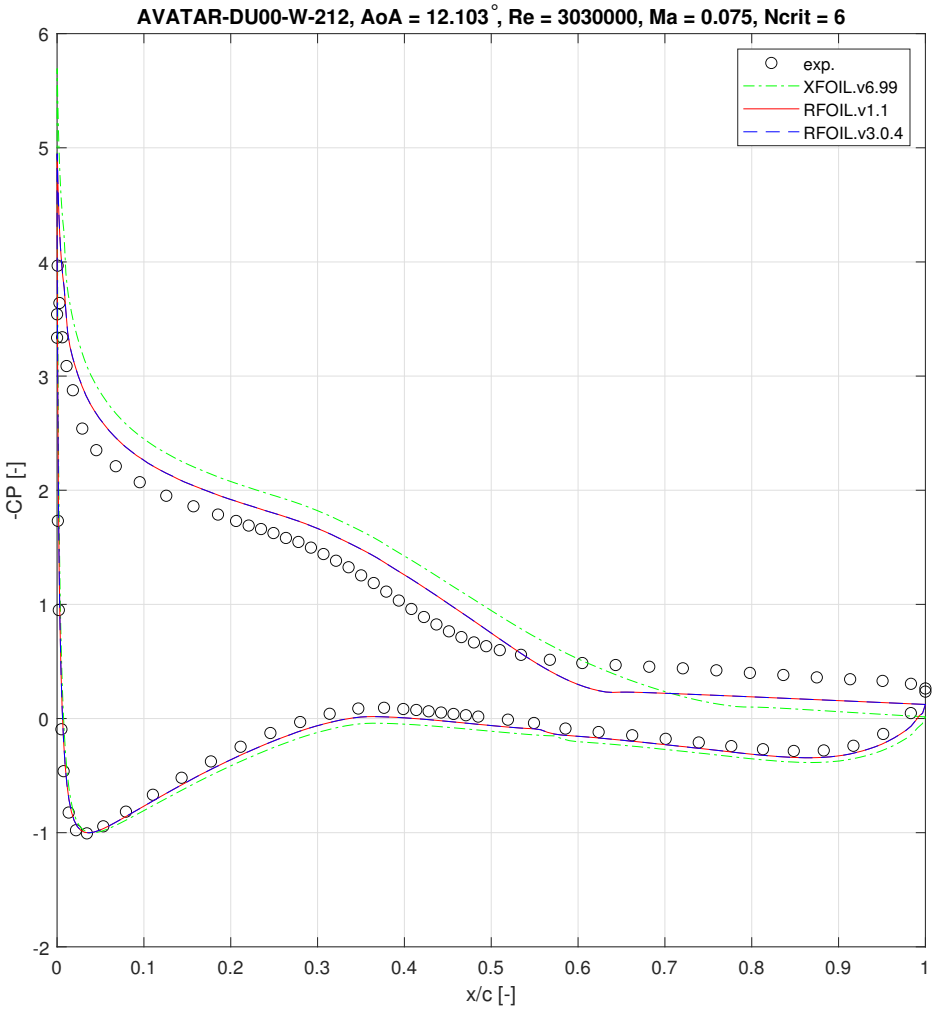

Figure C.247: Comparison between experimental and numerical pressure distributions for the AVATAR-DU00-W-212 airfoil at a Reynolds number of 5980000, and at an angle of attack and a Mach number of 12.106° and 0.055, respectively.

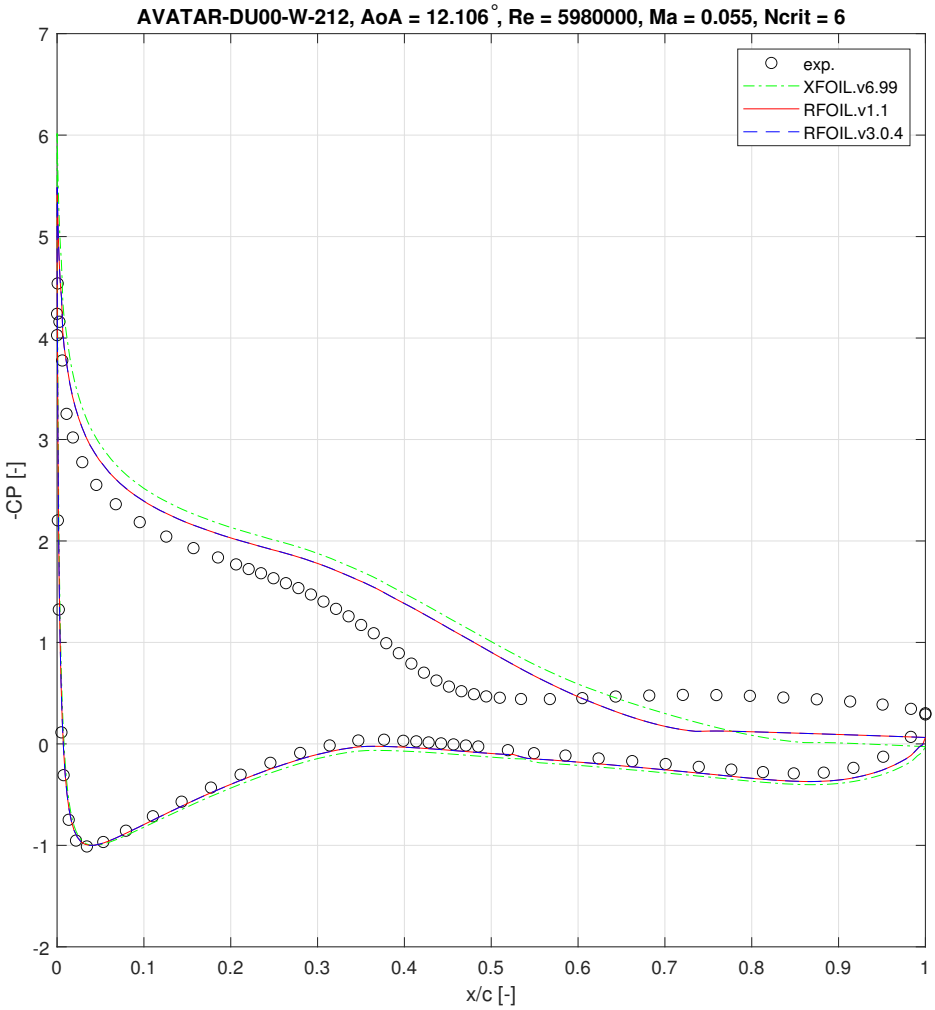

Figure C.248: Comparison between experimental and numerical pressure distributions for the AVATAR-DU00-W-212 airfoil at a Reynolds number of 5990000, and at an angle of attack and a Mach number of 12.111° and 0.029, respectively.

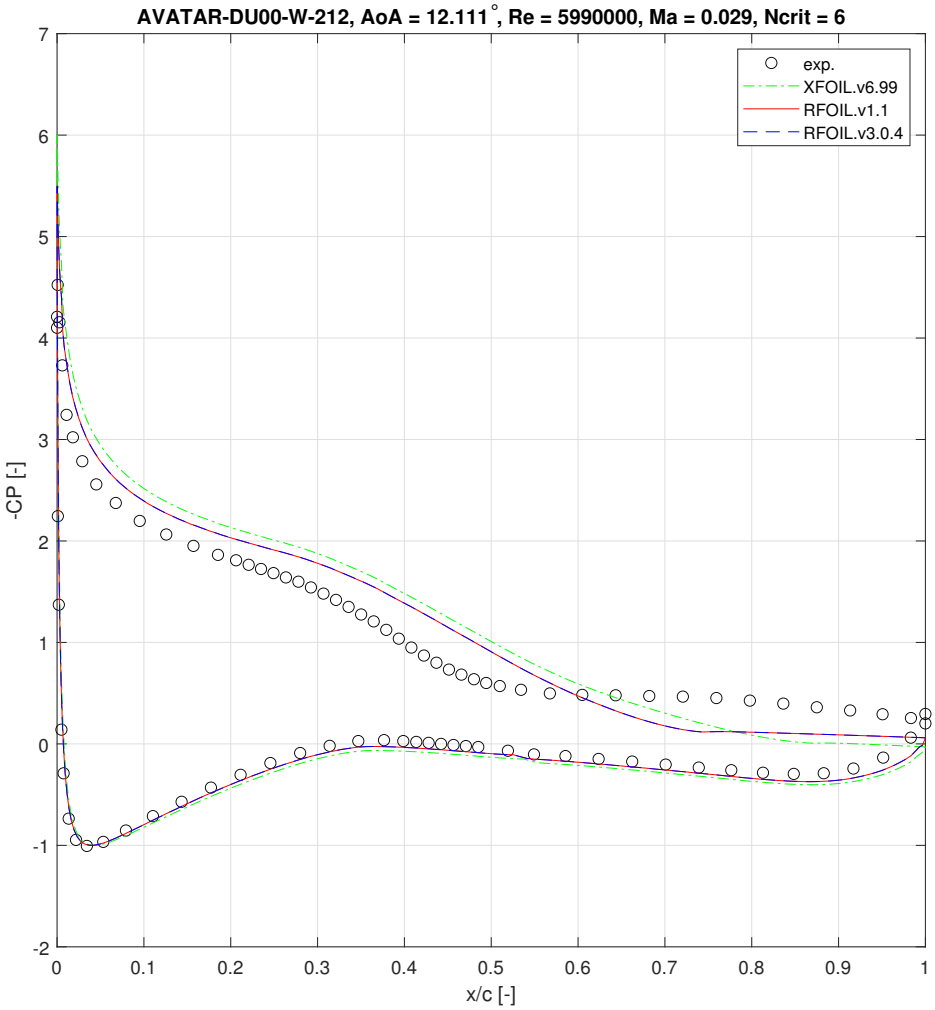

Figure C.249: Comparison between experimental and numerical pressure distributions for the AVATAR-DU00-W-212 airfoil at a Reynolds number of 9020000, and at an angle of attack and a Mach number of 12.142° and 0.044, respectively.

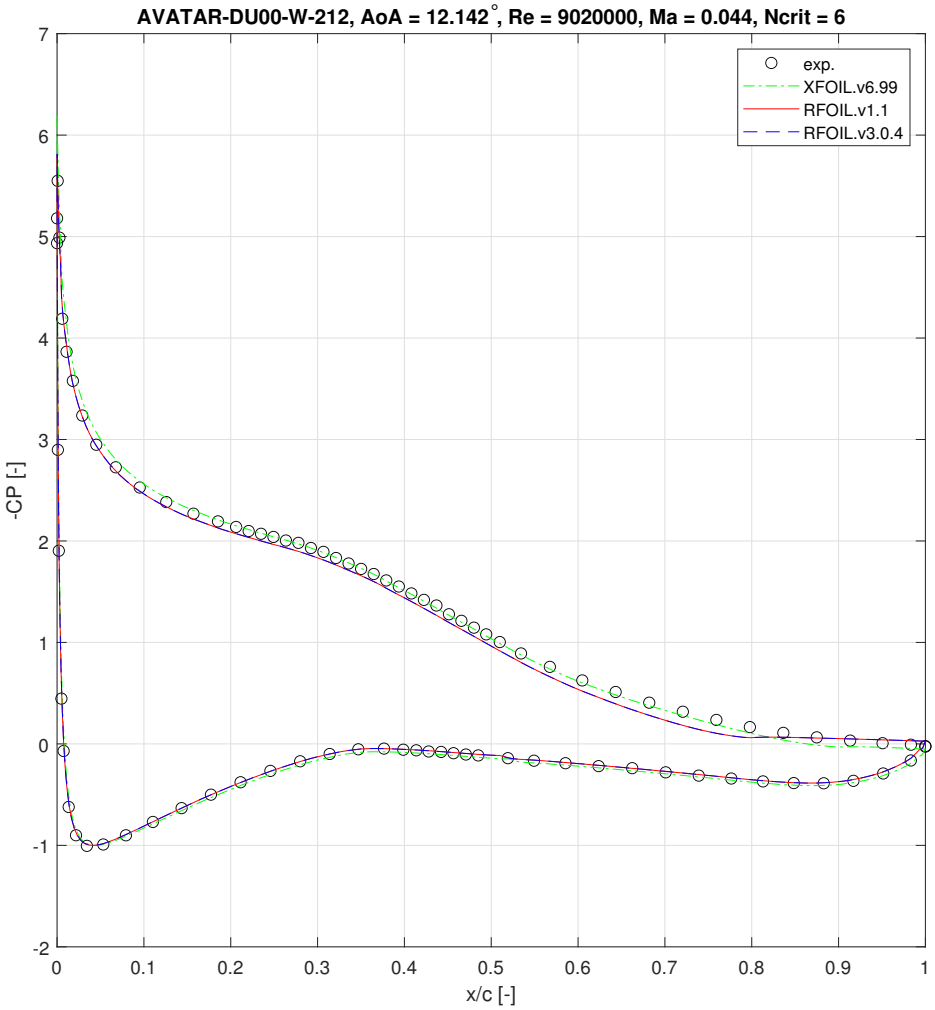

Figure C.250: Comparison between experimental and numerical pressure distributions for the AVATAR-DU00-W-212 airfoil at a Reynolds number of 9000000, and at an angle of attack and a Mach number of 12.143° and 0.083, respectively.

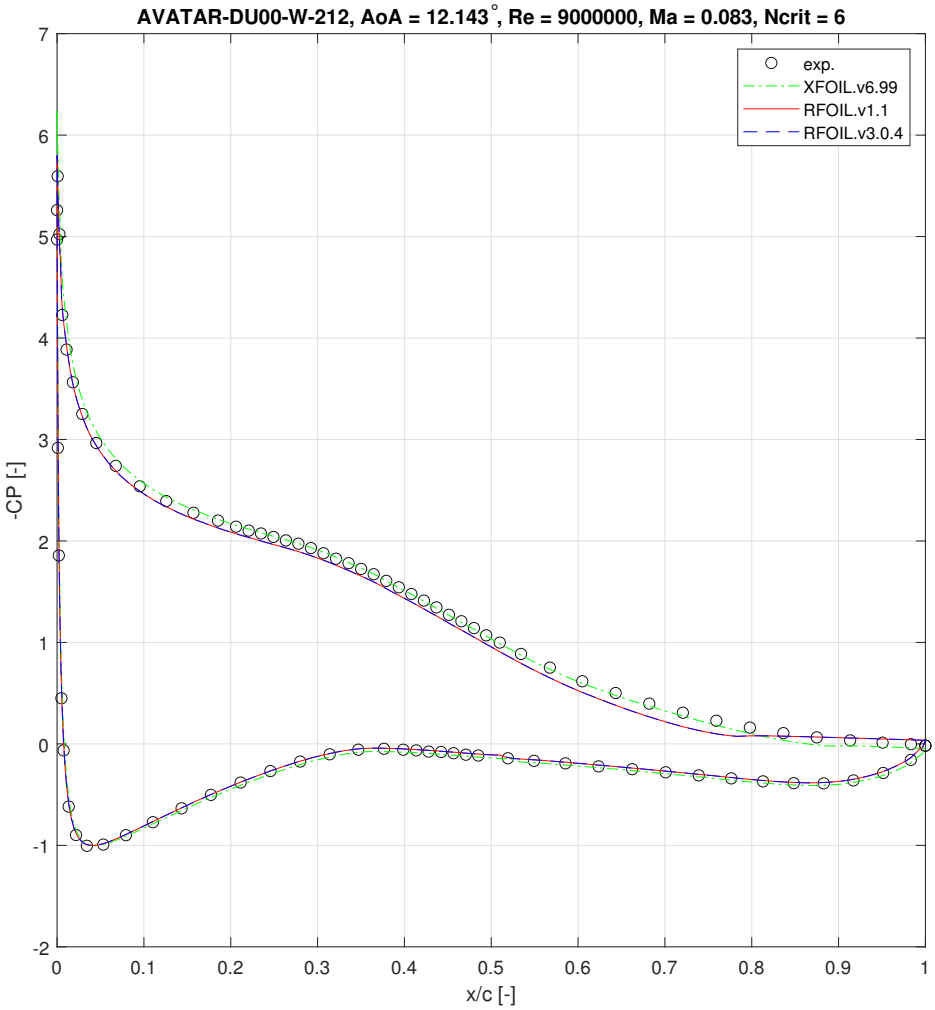

Figure C.251: Comparison between experimental and numerical pressure distributions for the AVATAR-DU00-W-212 airfoil at a Reynolds number of 14970000, and at an angle of attack and a Mach number of 12.147° and 0.081, respectively.

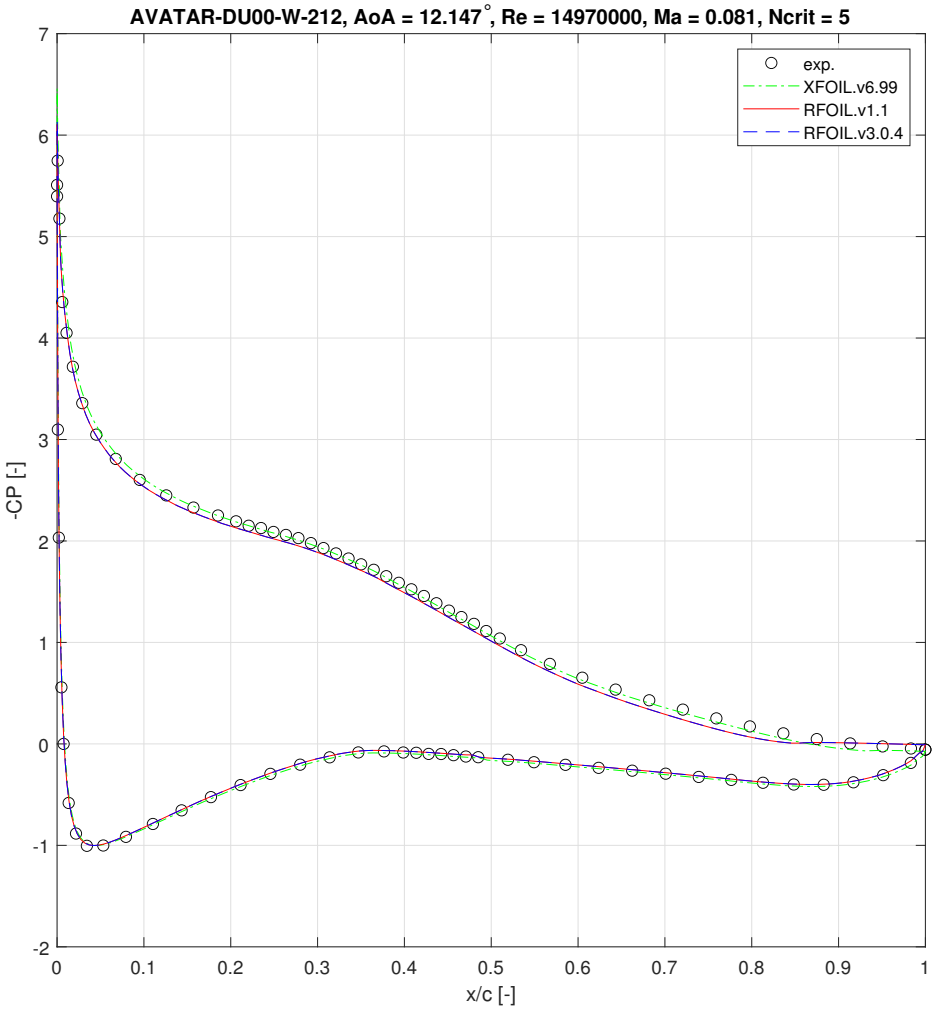

Figure C.252: Comparison between experimental and numerical pressure distributions for the AVATAR-DU00-W-212 airfoil at a Reynolds number of 9000000, and at an angle of attack and a Mach number of 12.344° and 0.044, respectively.

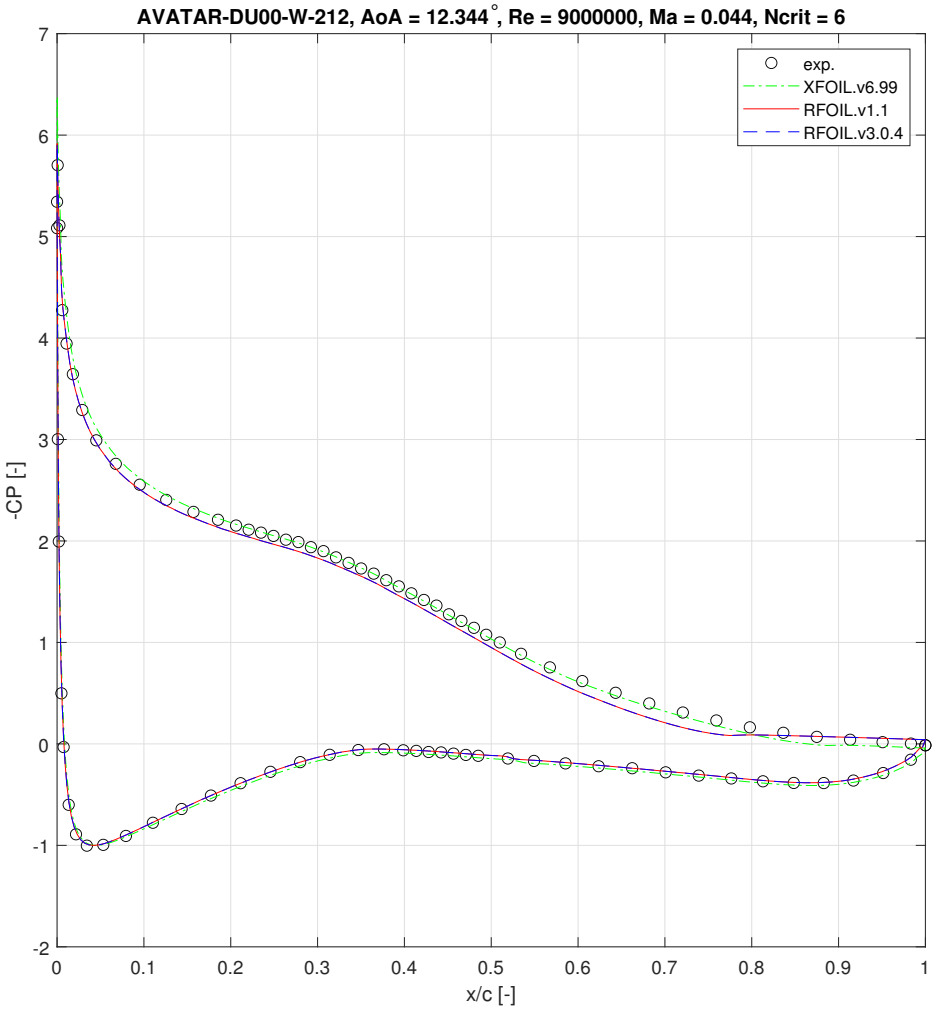

Figure C.253: Comparison between experimental and numerical pressure distributions for the AVATAR-DU00-W-212 airfoil at a Reynolds number of 9010000, and at an angle of attack and a Mach number of 12.345° and 0.083, respectively.

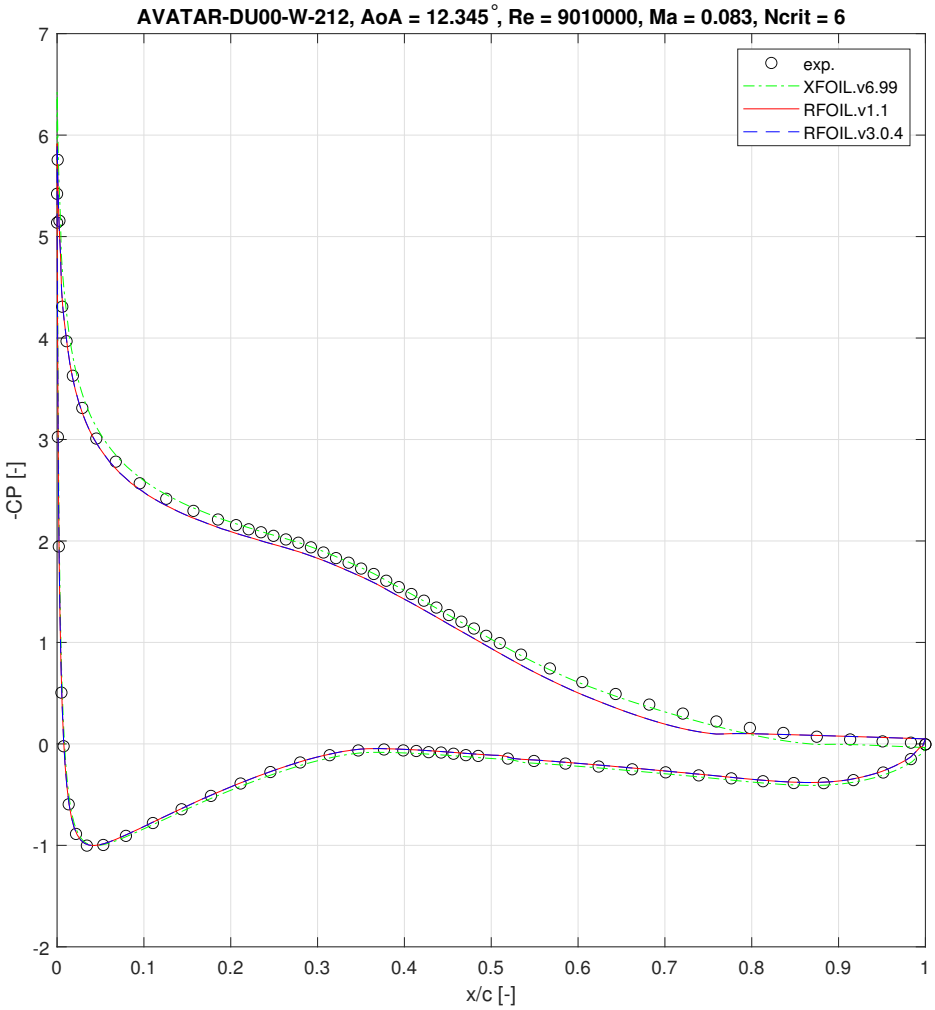

Figure C.254: Comparison between experimental and numerical pressure distributions for the AVATAR-DU00-W-212 airfoil at a Reynolds number of 11970000, and at an angle of attack and a Mach number of 12.525° and 0.058, respectively.

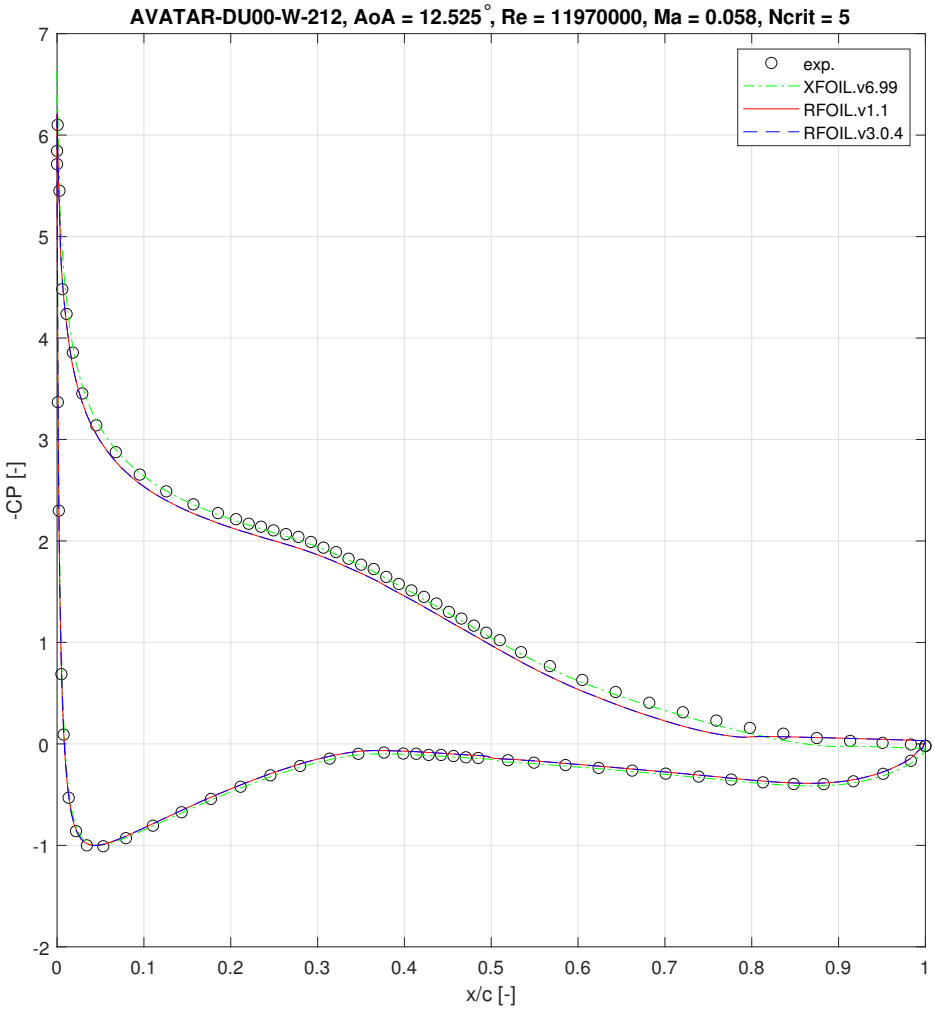

Figure C.255: Comparison between experimental and numerical pressure distributions for the AVATAR-DU00-W-212 airfoil at a Reynolds number of 9010000, and at an angle of attack and a Mach number of 12.646° and 0.044, respectively.

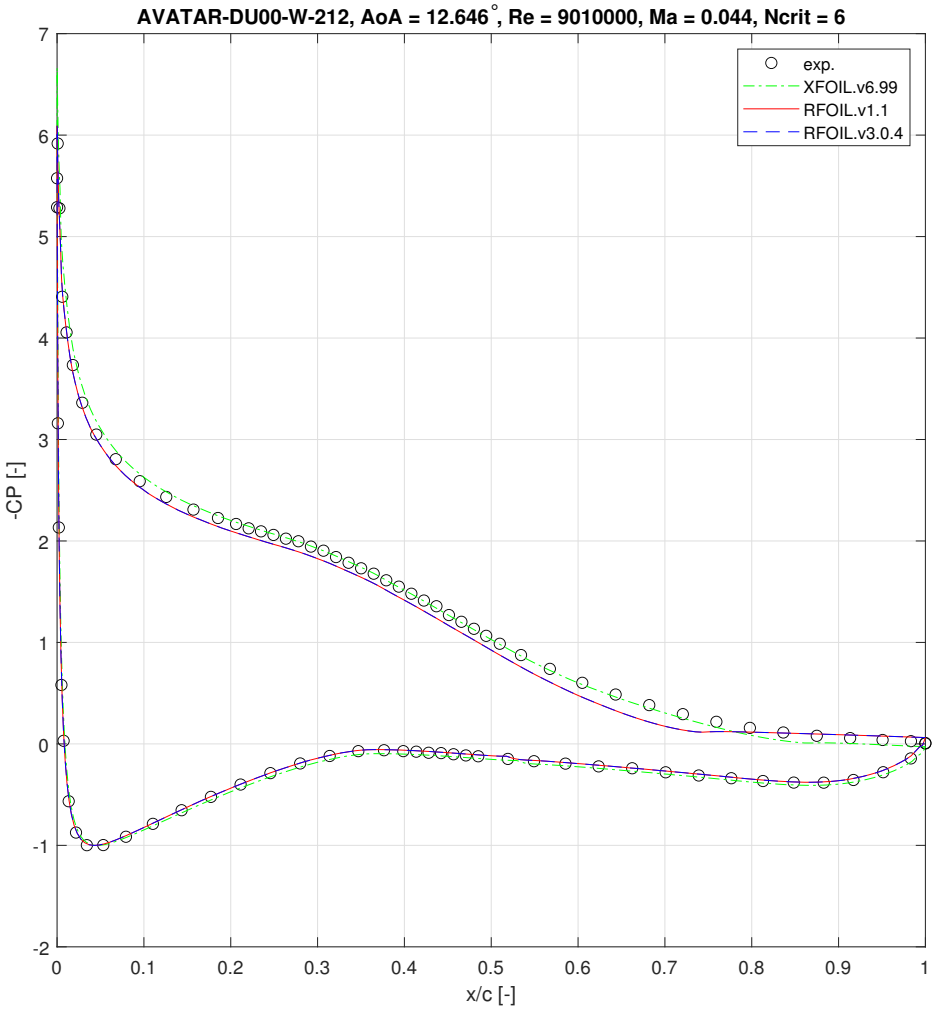

Figure C.256: Comparison between experimental and numerical pressure distributions for the AVATAR-DU00-W-212 airfoil at a Reynolds number of 9010000, and at an angle of attack and a Mach number of 12.647° and 0.083, respectively.

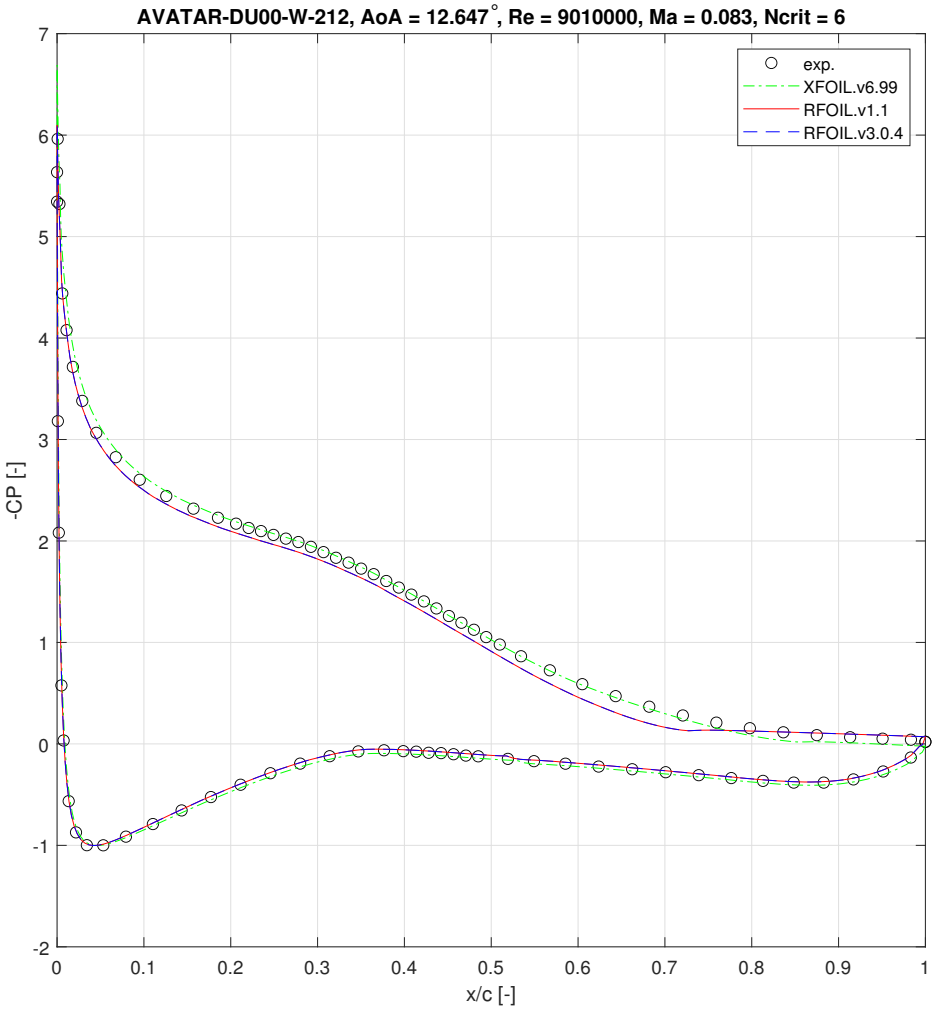

Figure C.257: Comparison between experimental and numerical pressure distributions for the AVATAR-DU00-W-212 airfoil at a Reynolds number of 14970000, and at an angle of attack and a Mach number of 12.652° and 0.081, respectively.

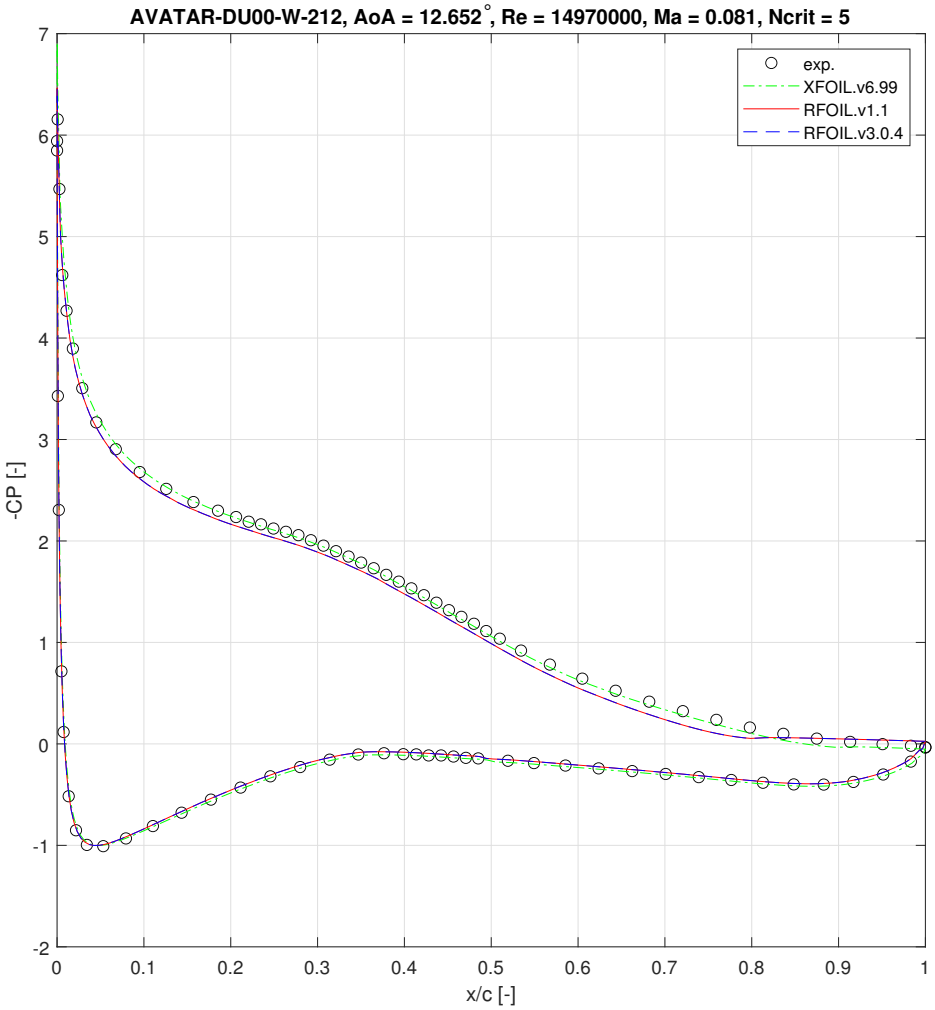

Figure C.258: Comparison between experimental and numerical pressure distributions for the AVATAR-DU00-W-212 airfoil at a Reynolds number of 9020000, and at an angle of attack and a Mach number of 12.746° and 0.044, respectively.

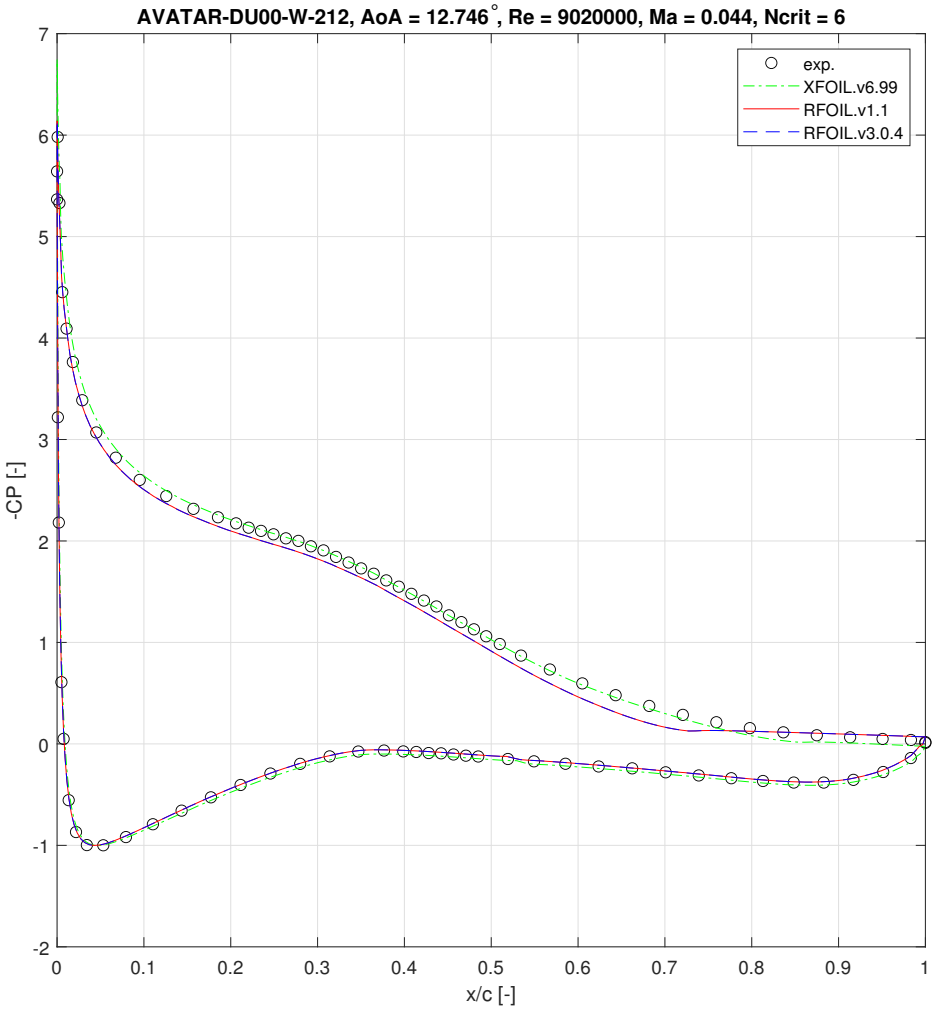

Figure C.259: Comparison between experimental and numerical pressure distributions for the AVATAR-DU00-W-212 airfoil at a Reynolds number of 11990000, and at an angle of attack and a Mach number of 12.821° and 0.058, respectively.

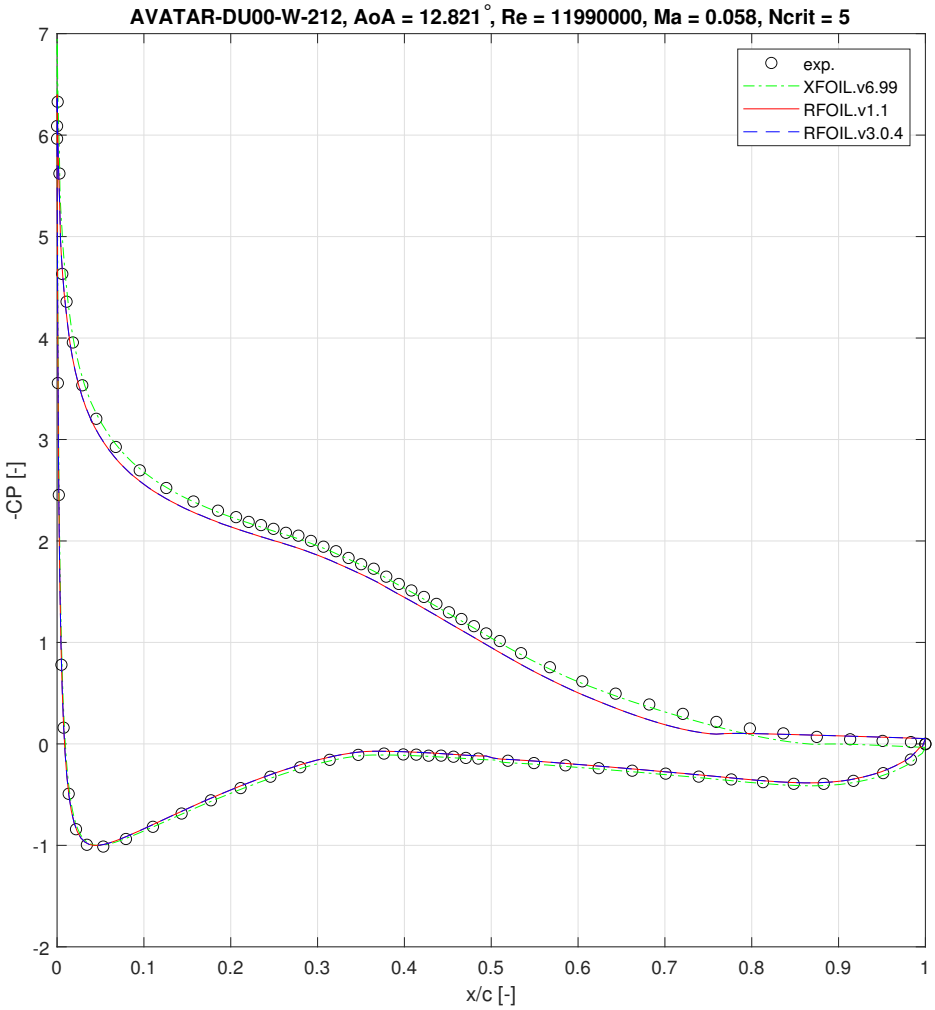

Figure C.260: Comparison between experimental and numerical pressure distributions for the AVATAR-DU00-W-212 airfoil at a Reynolds number of 8990000, and at an angle of attack and a Mach number of 12.826° and 0.083, respectively.

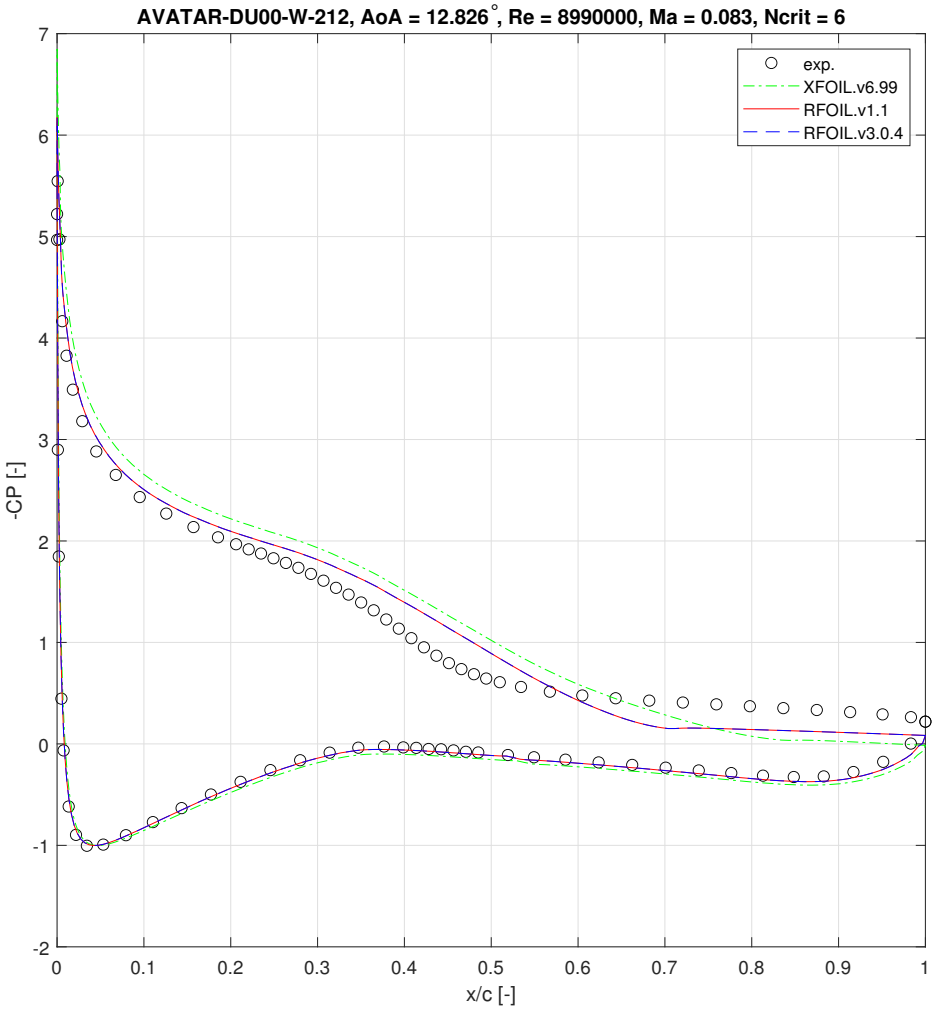

Figure C.261: Comparison between experimental and numerical pressure distributions for the AVATAR-DU00-W-212 airfoil at a Reynolds number of 9010000, and at an angle of attack and a Mach number of 12.847° and 0.044, respectively.

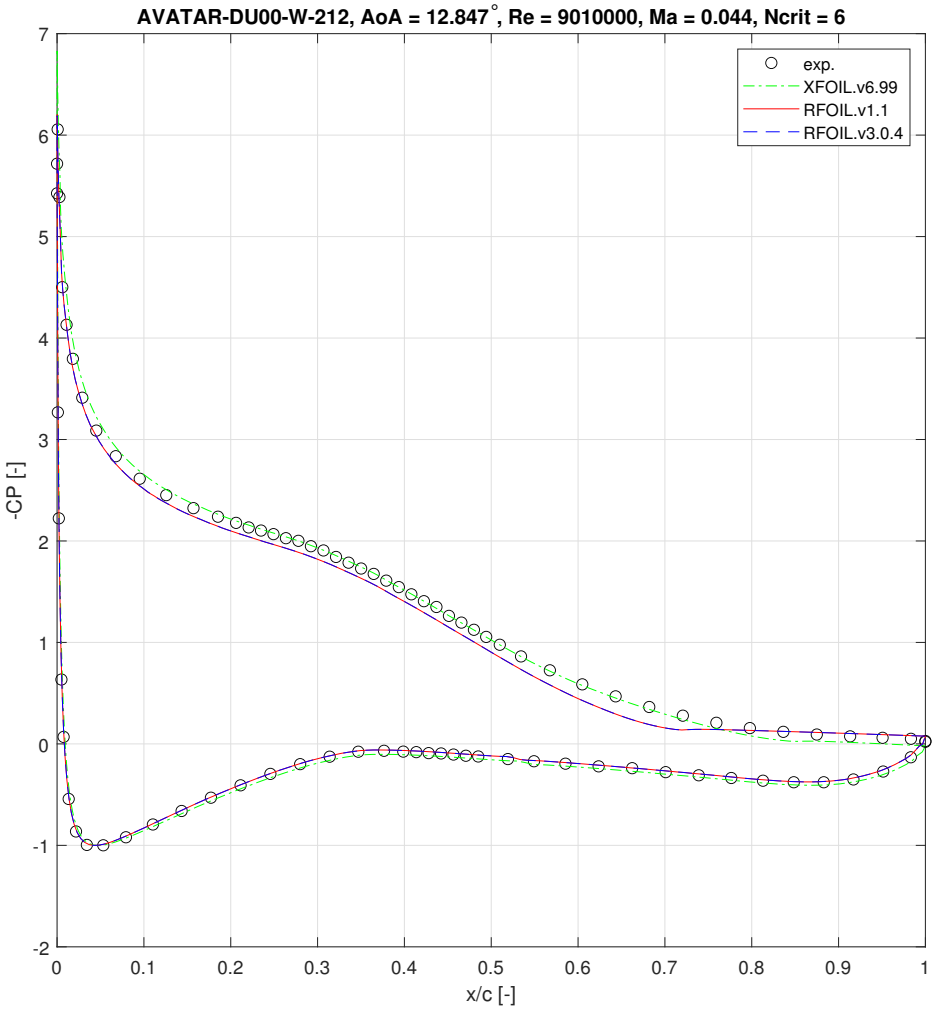

Figure C.262: Comparison between experimental and numerical pressure distributions for the AVATAR-DU00-W-212 airfoil at a Reynolds number of 15030000, and at an angle of attack and a Mach number of 12.954° and 0.082, respectively.

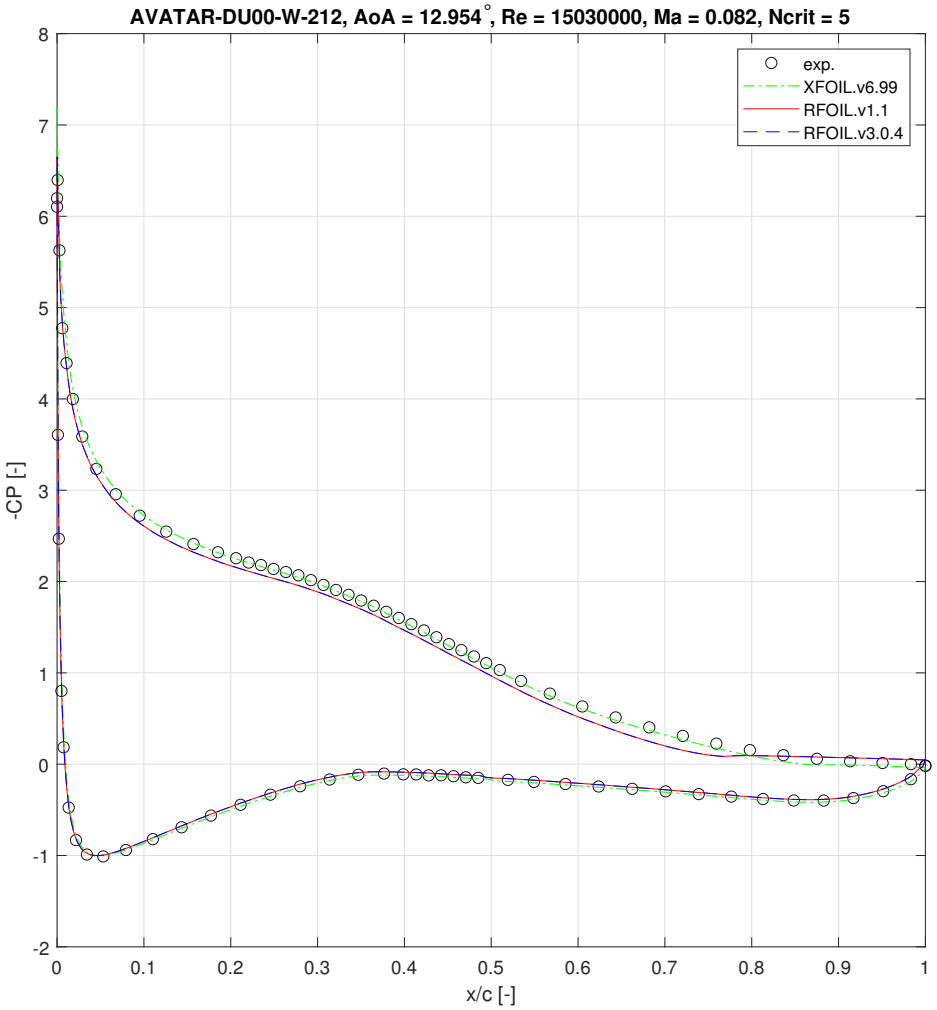

Figure C.263: Comparison between experimental and numerical pressure distributions for the AVATAR-DU00-W-212 airfoil at a Reynolds number of 12010000, and at an angle of attack and a Mach number of 13.022° and 0.058, respectively.

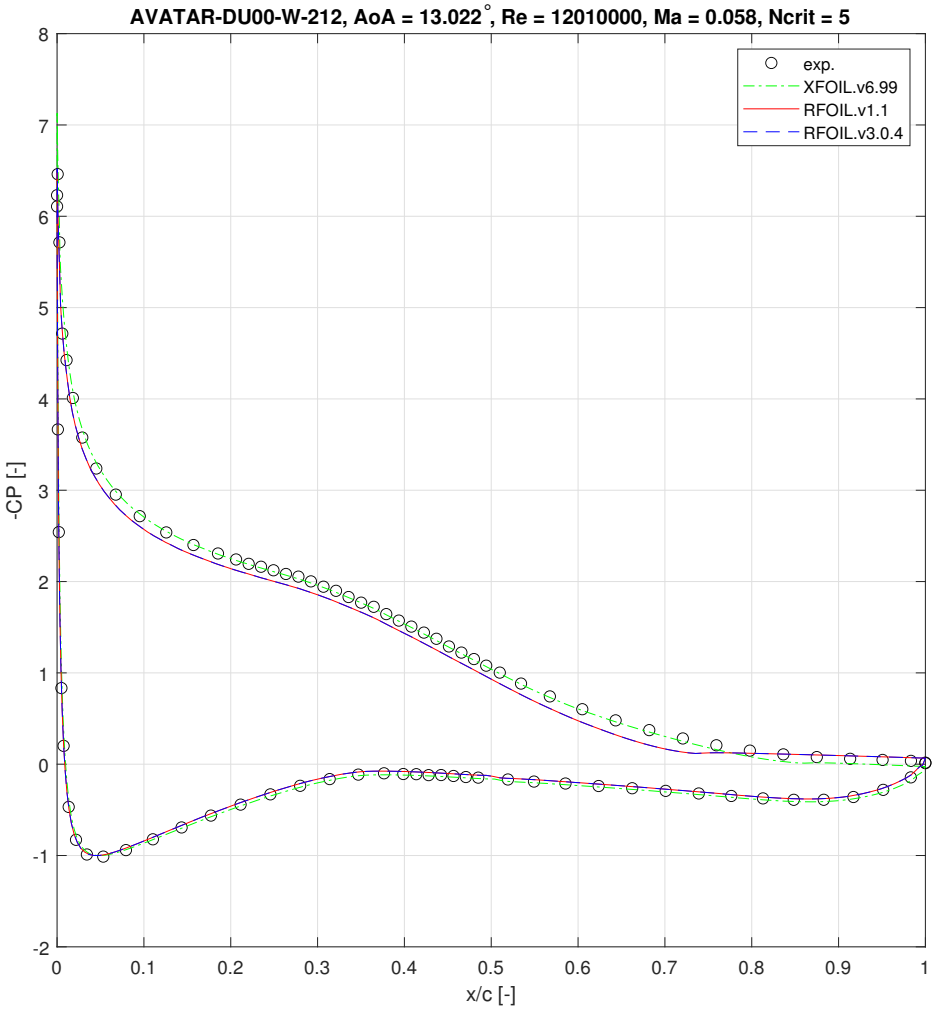

Figure C.264: Comparison between experimental and numerical pressure distributions for the AVATAR-DU00-W-212 airfoil at a Reynolds number of 6030000, and at an angle of attack and a Mach number of 13.112° and 0.055, respectively.

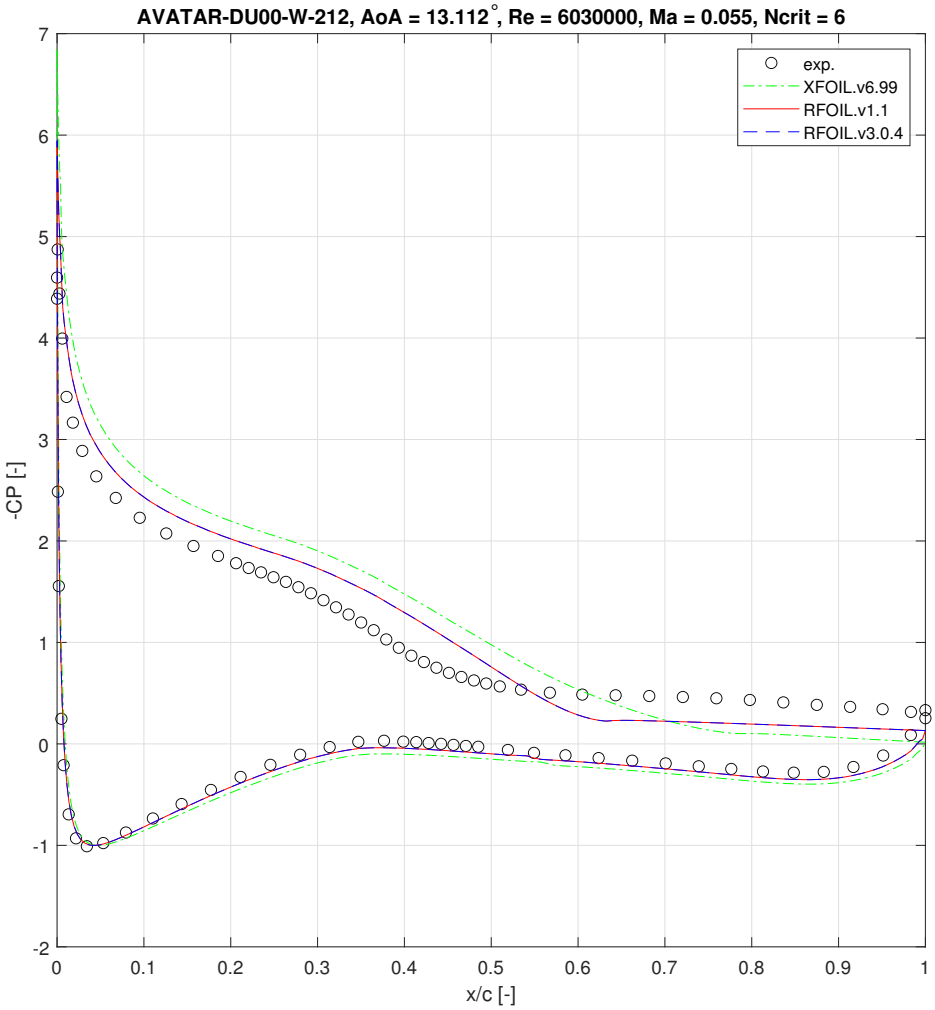

Figure C.265: Comparison between experimental and numerical pressure distributions for the AVATAR-DU00-W-212 airfoil at a Reynolds number of 6010000, and at an angle of attack and a Mach number of 13.115° and 0.029, respectively.

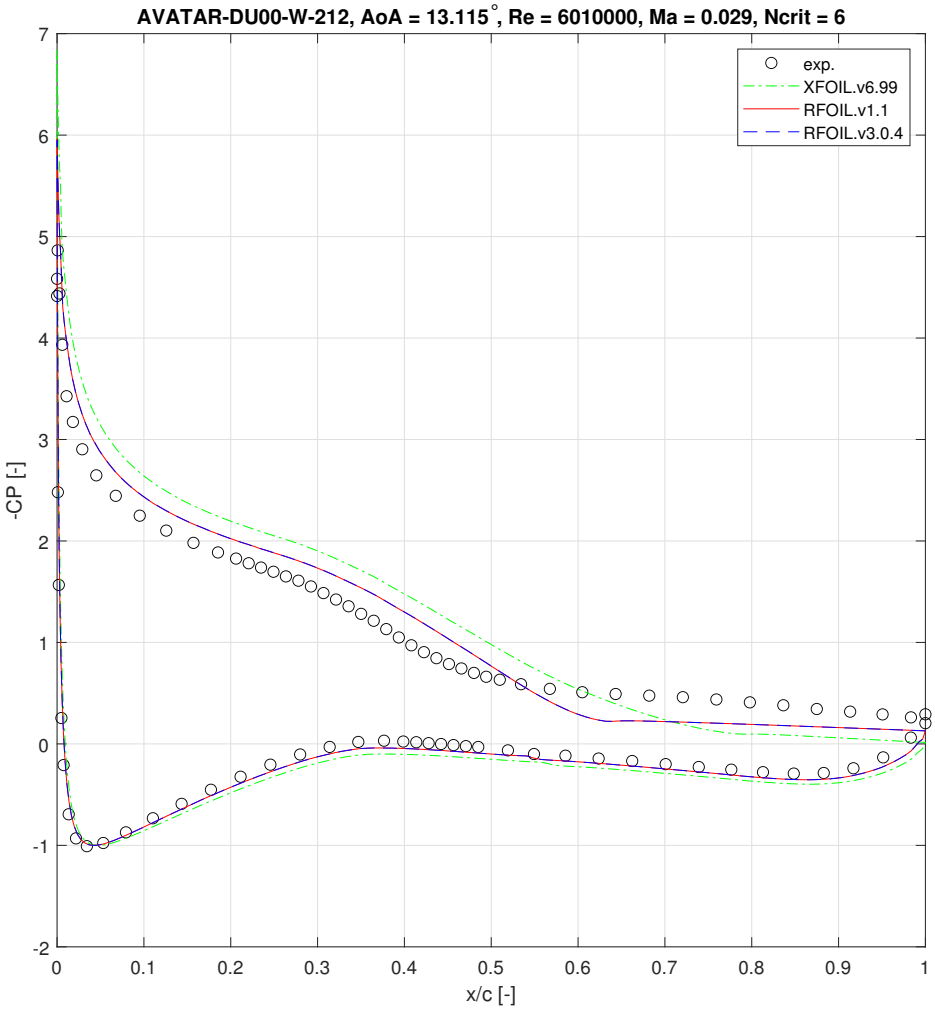

Figure C.266: Comparison between experimental and numerical pressure distributions for the AVATAR-DU00-W-212 airfoil at a Reynolds number of 8960000, and at an angle of attack and a Mach number of 13.117° and 0.082, respectively.

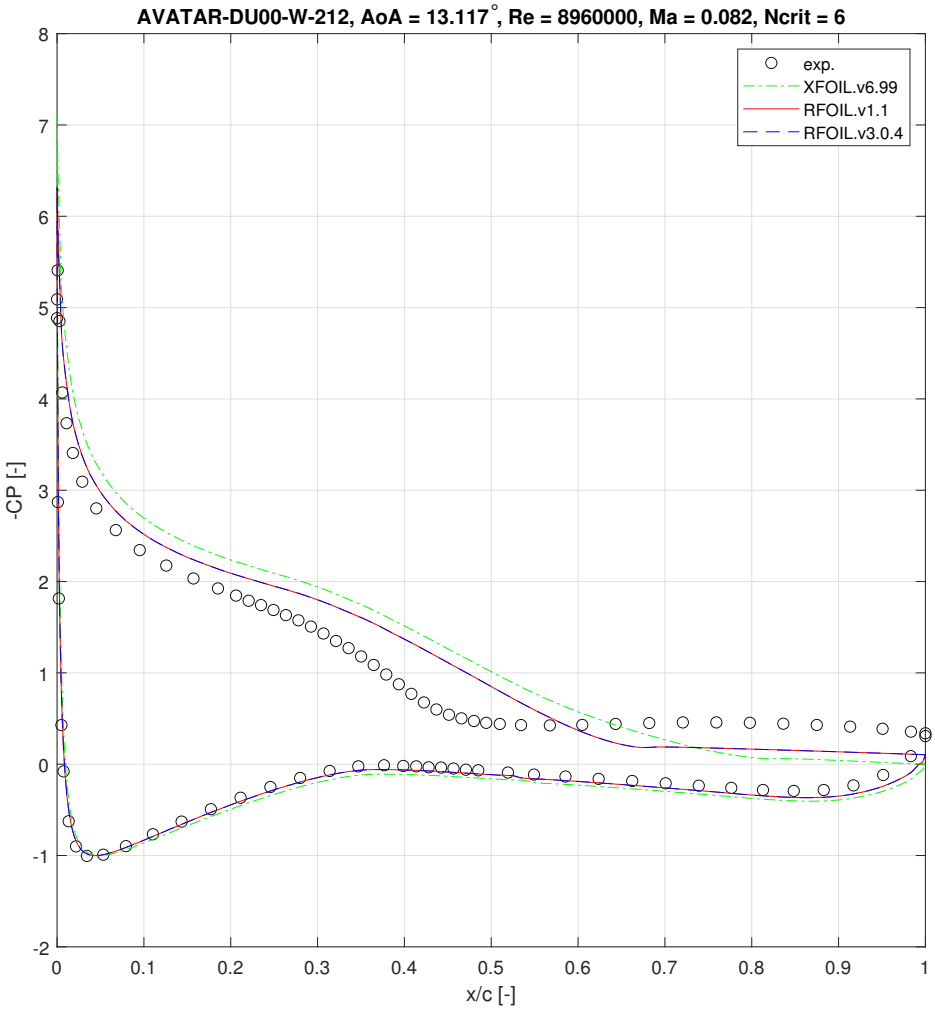

Figure C.267: Comparison between experimental and numerical pressure distributions for the AVATAR-DU00-W-212 airfoil at a Reynolds number of 8960000, and at an angle of attack and a Mach number of 13.119° and 0.043, respectively.

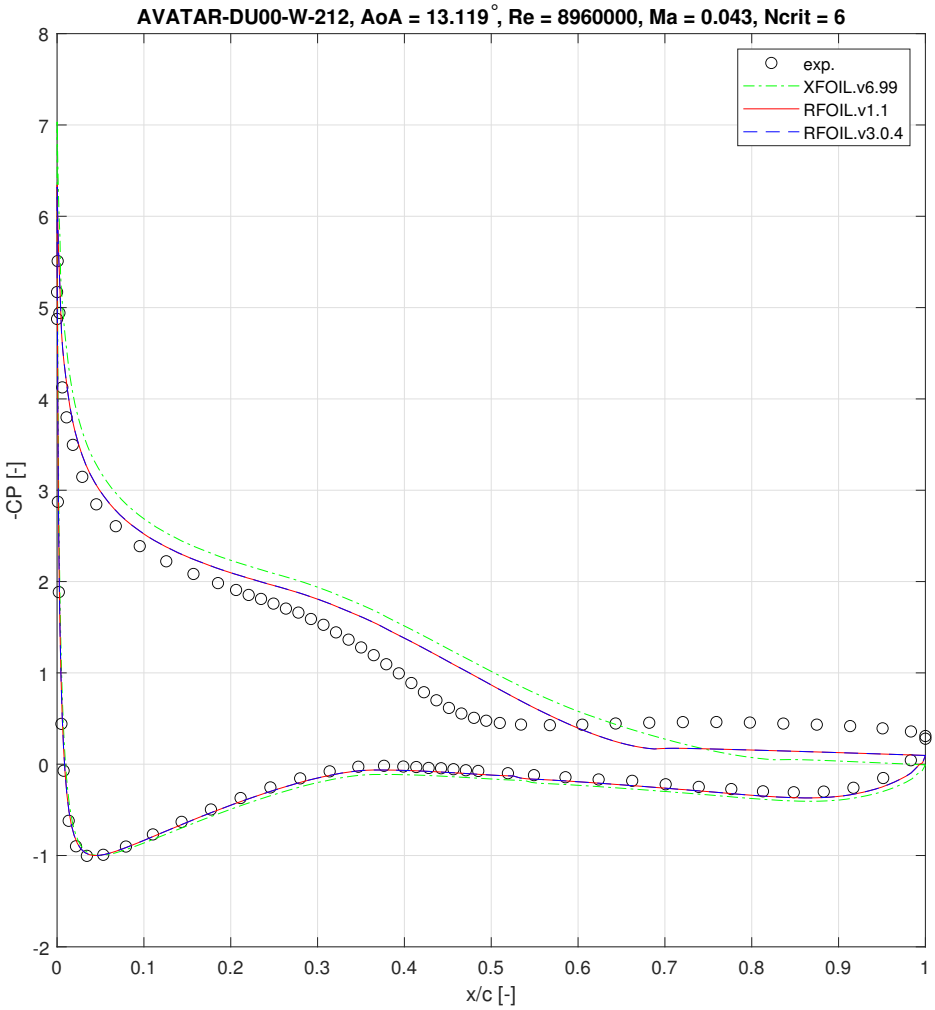

Figure C.268: Comparison between experimental and numerical pressure distributions for the AVATAR-DU00-W-212 airfoil at a Reynolds number of 3030000, and at an angle of attack and a Mach number of 13.110° and 0.075, respectively.

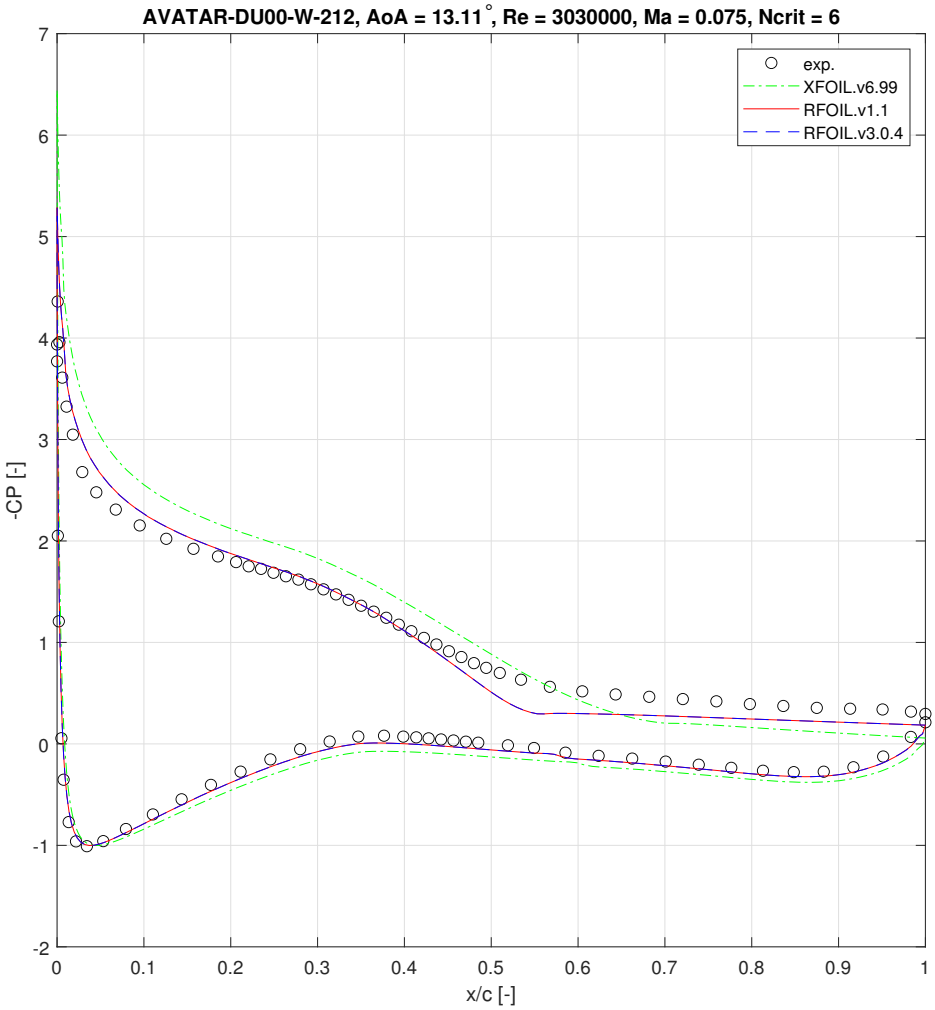

Figure C.269: Comparison between experimental and numerical pressure distributions for the AVATAR-DU00-W-212 airfoil at a Reynolds number of 15020000, and at an angle of attack and a Mach number of 13.156° and 0.082, respectively.

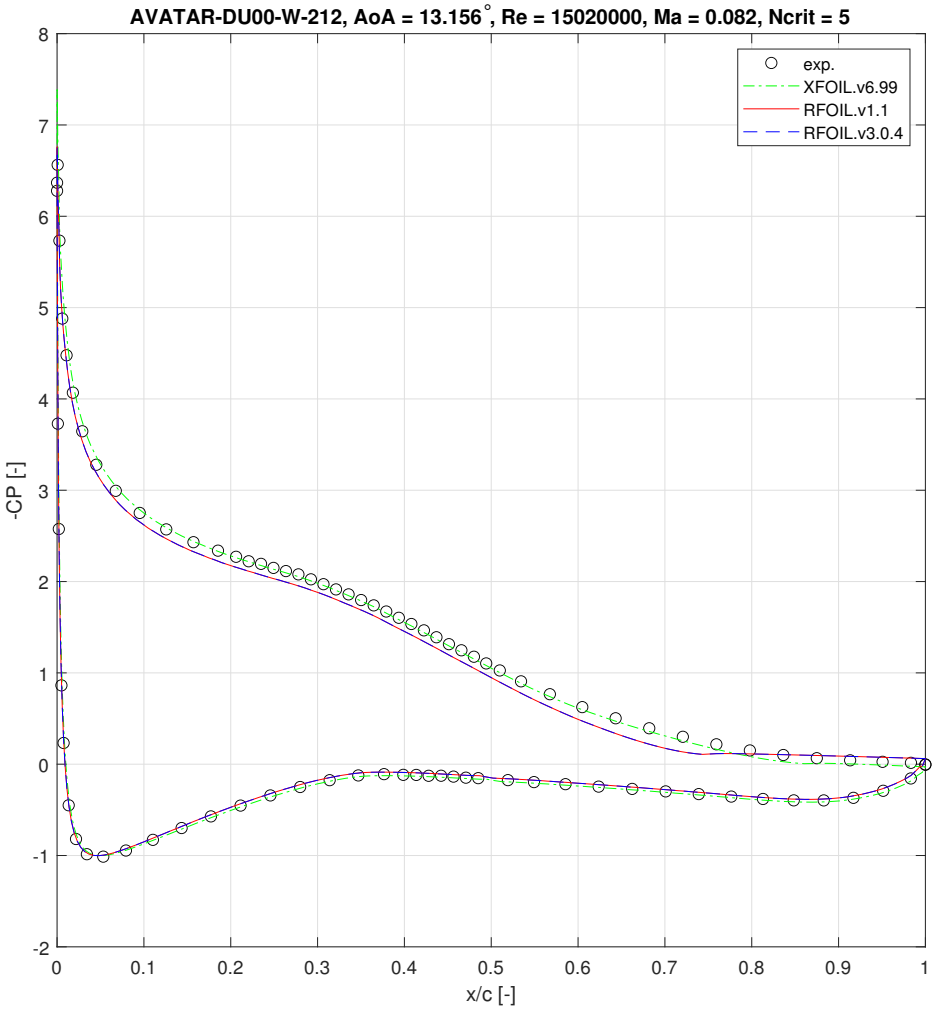

Figure C.270: Comparison between experimental and numerical pressure distributions for the AVATAR-DU00-W-212 airfoil at a Reynolds number of 12030000, and at an angle of attack and a Mach number of 13.221° and 0.058, respectively.

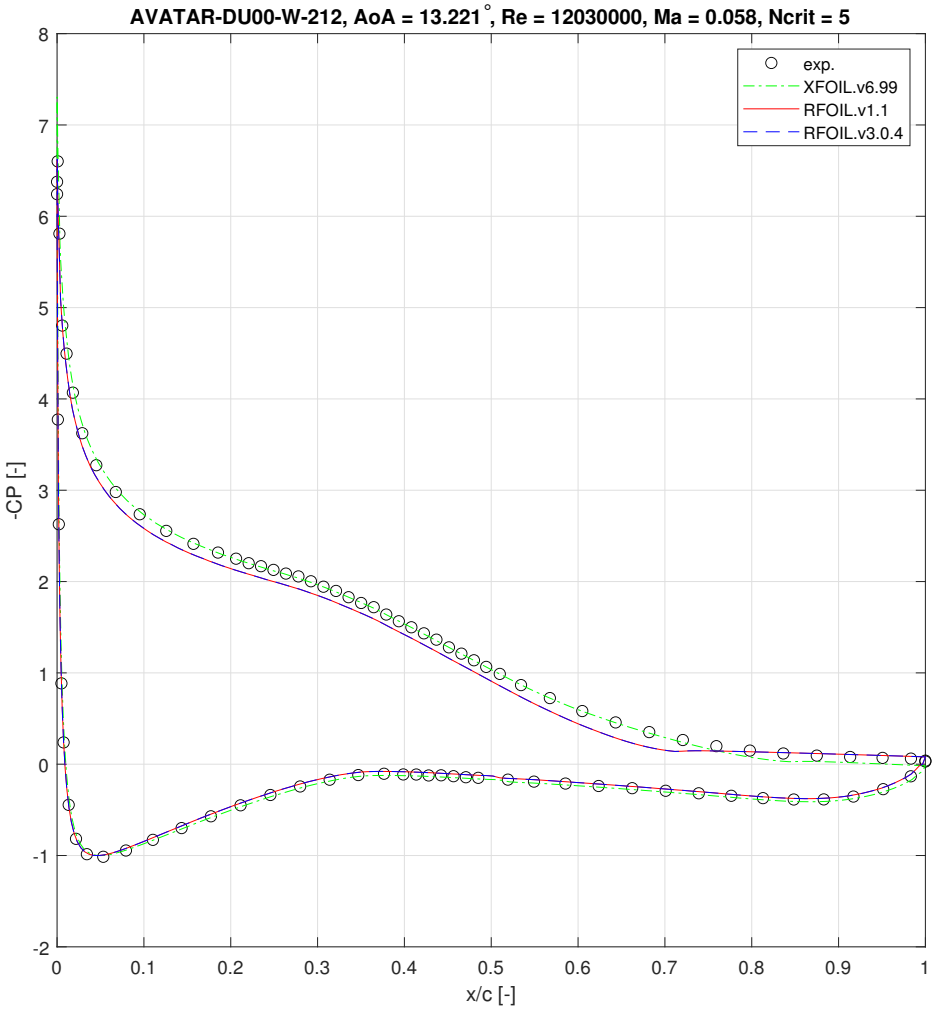

Figure C.271: Comparison between experimental and numerical pressure distributions for the AVATAR-DU00-W-212 airfoil at a Reynolds number of 12020000, and at an angle of attack and a Mach number of 13.318° and 0.058, respectively.

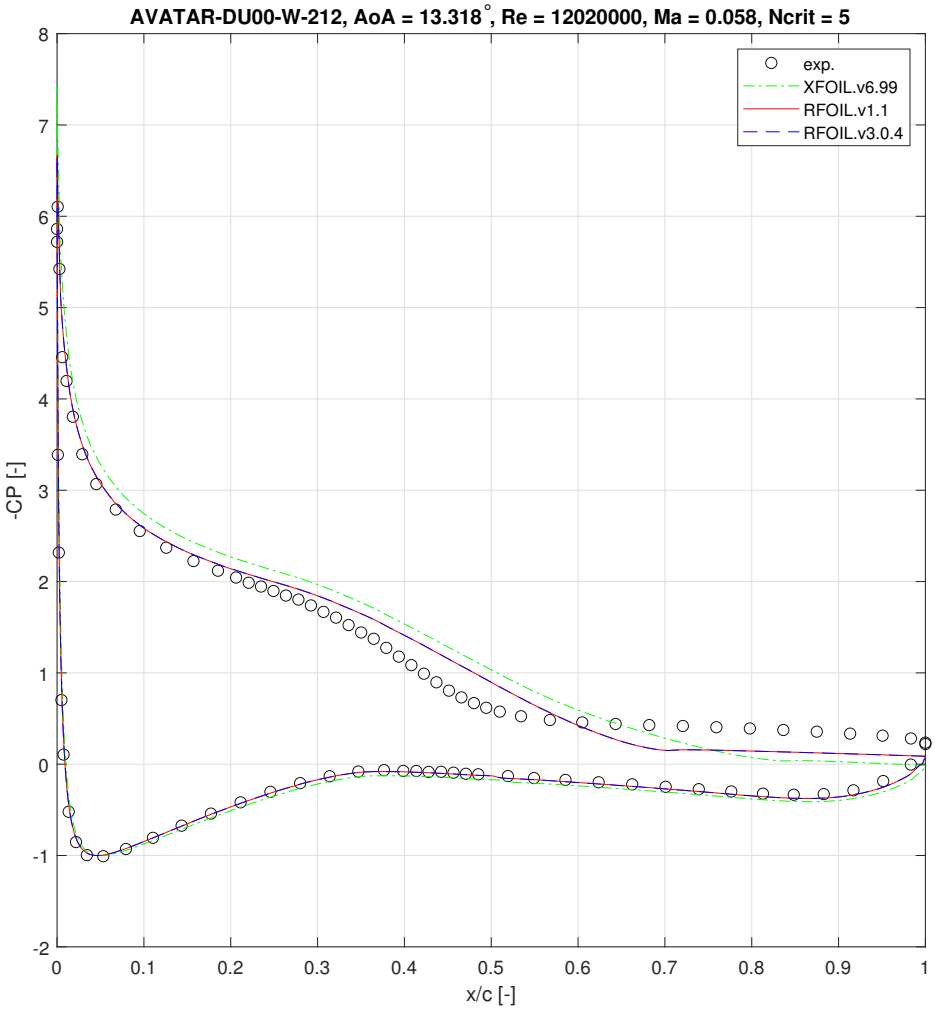

Figure C.272: Comparison between experimental and numerical pressure distributions for the AVATAR-DU00-W-212 airfoil at a Reynolds number of 14980000, and at an angle of attack and a Mach number of 13.357° and 0.082, respectively.

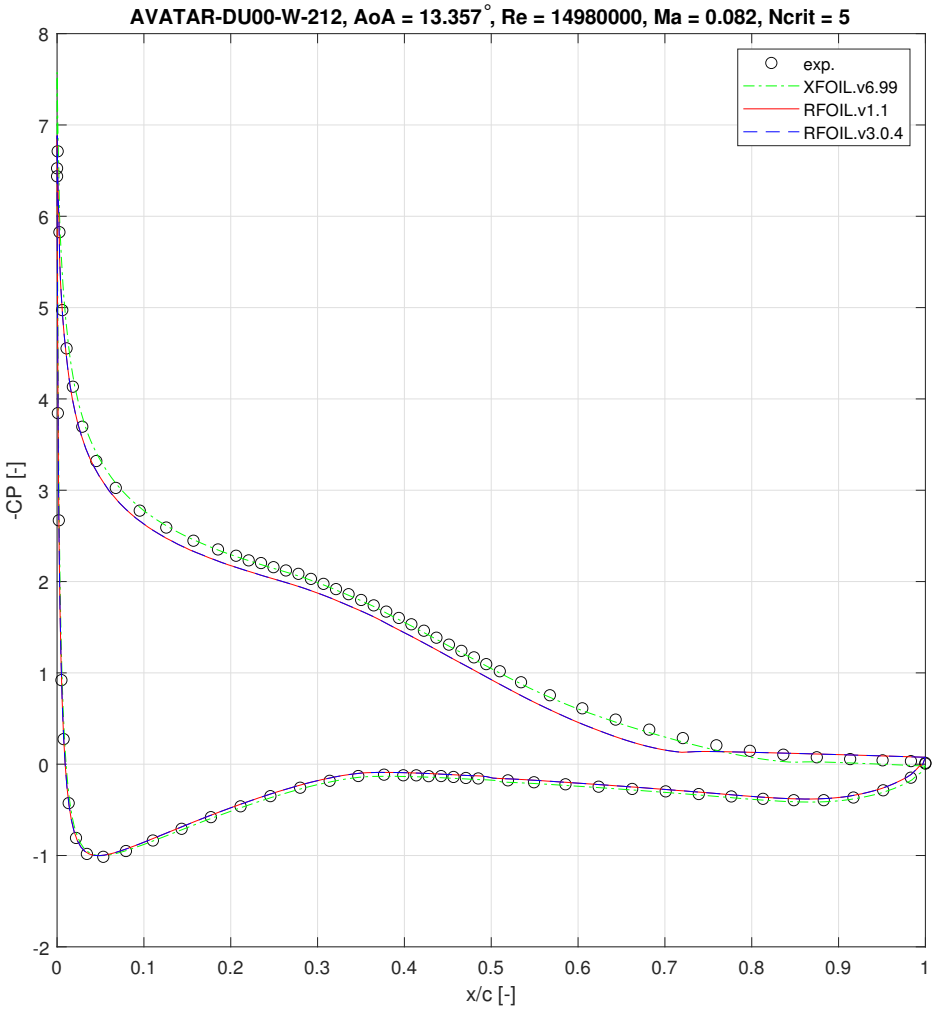

Figure C.273: Comparison between experimental and numerical pressure distributions for the AVATAR-DU00-W-212 airfoil at a Reynolds number of 11960000, and at an angle of attack and a Mach number of 13.418° and 0.058, respectively.

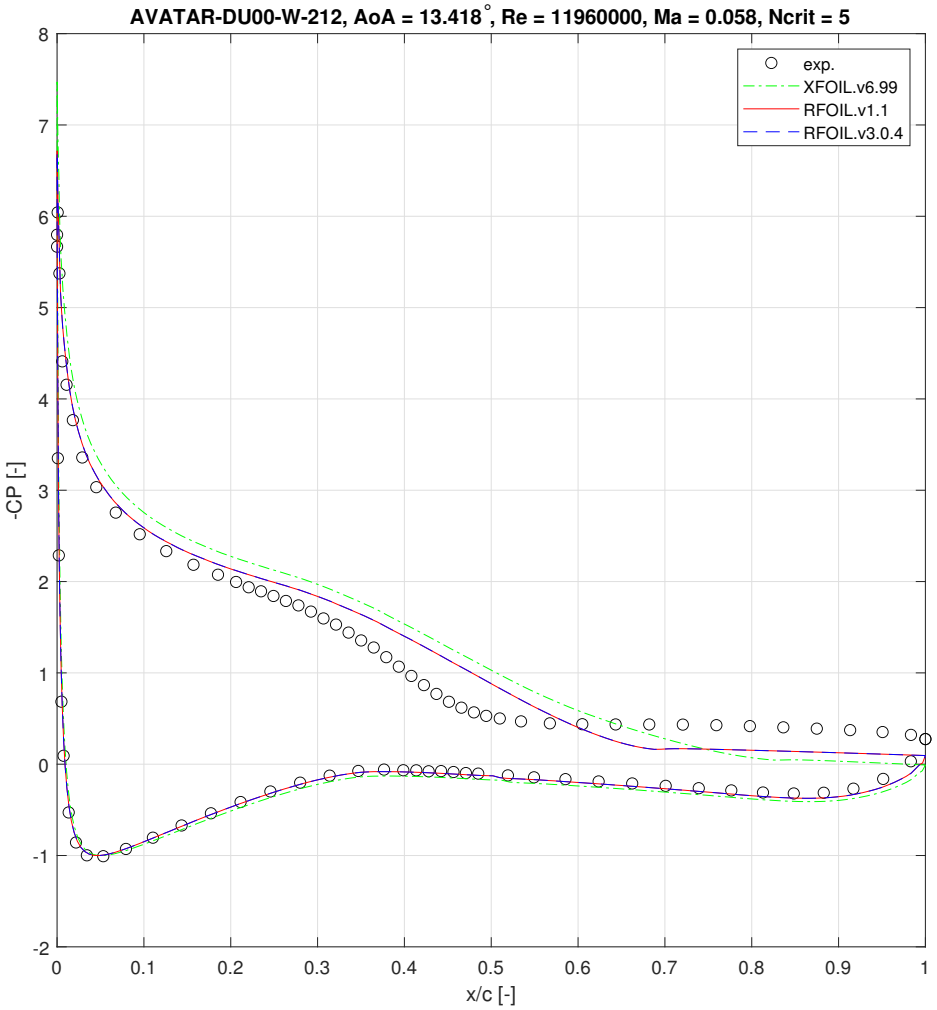

Figure C.274: Comparison between experimental and numerical pressure distributions for the AVATAR-DU00-W-212 airfoil at a Reynolds number of 15030000, and at an angle of attack and a Mach number of 13.458° and 0.082, respectively.

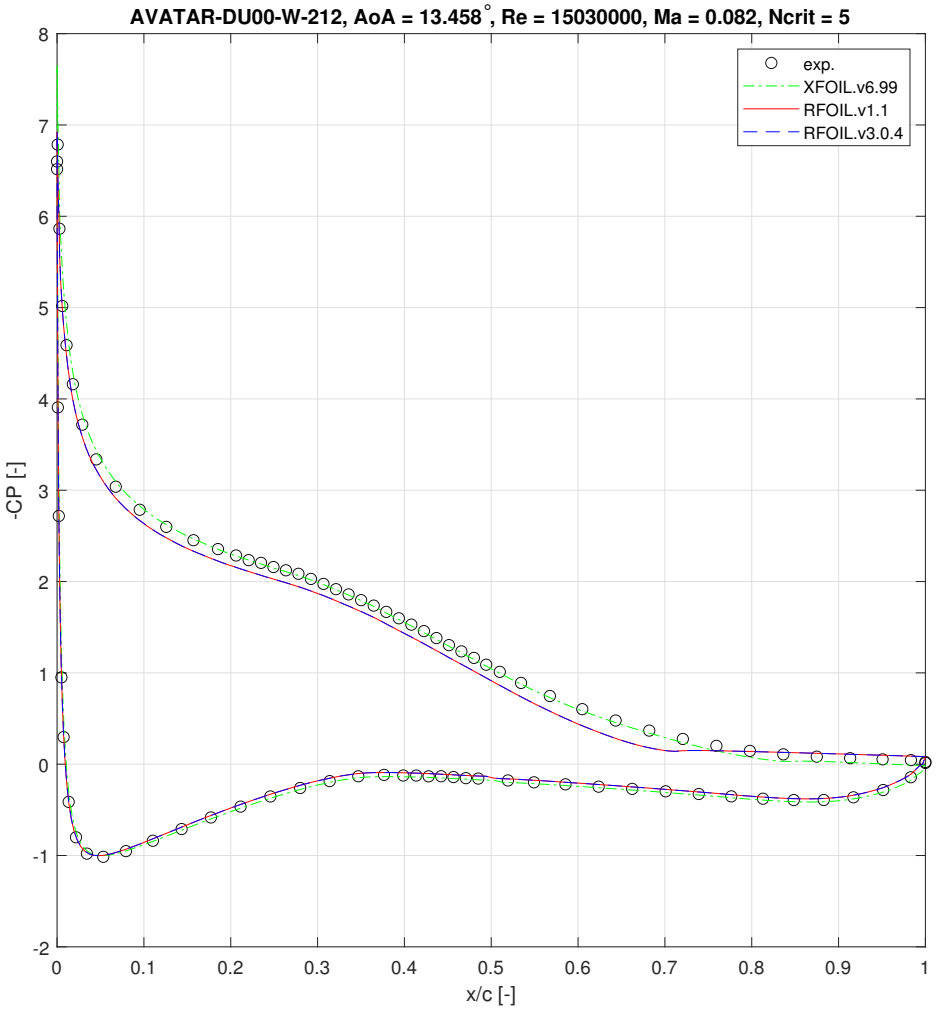

Figure C.275: Comparison between experimental and numerical pressure distributions for the AVATAR-DU00-W-212 airfoil at a Reynolds number of 15020000, and at an angle of attack and a Mach number of 13.558° and 0.082, respectively.

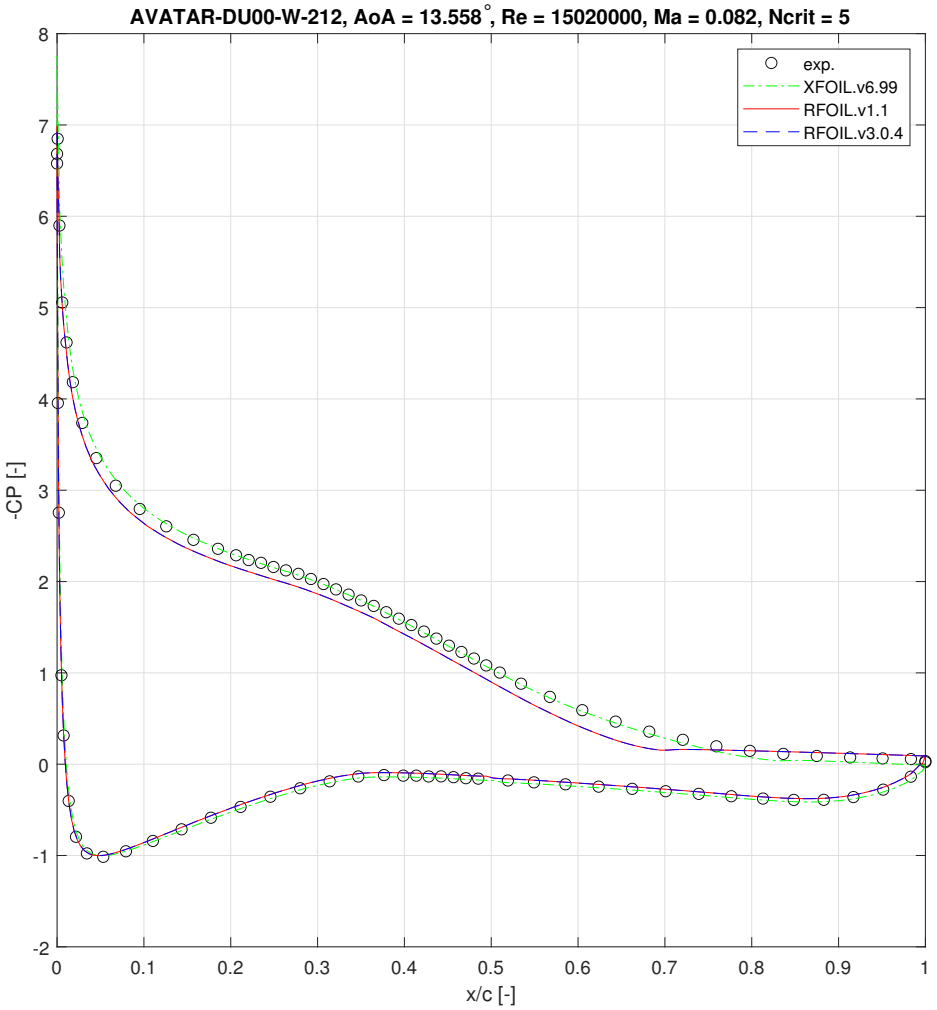

Figure C.276: Comparison between experimental and numerical pressure distributions for the AVATAR-DU00-W-212 airfoil at a Reynolds number of 15030000, and at an angle of attack and a Mach number of 13.659° and 0.082, respectively.

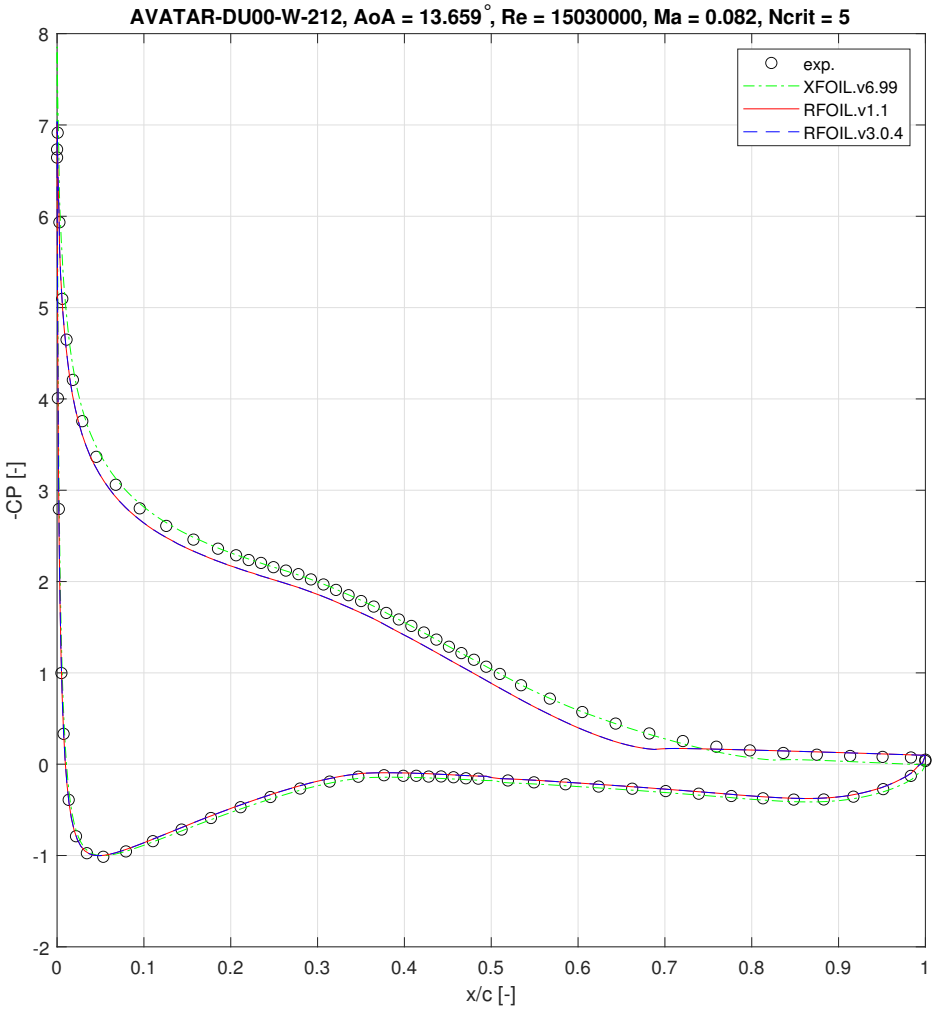

Figure C.277: Comparison between experimental and numerical pressure distributions for the AVATAR-DU00-W-212 airfoil at a Reynolds number of 11980000, and at an angle of attack and a Mach number of 14.014° and 0.058, respectively.

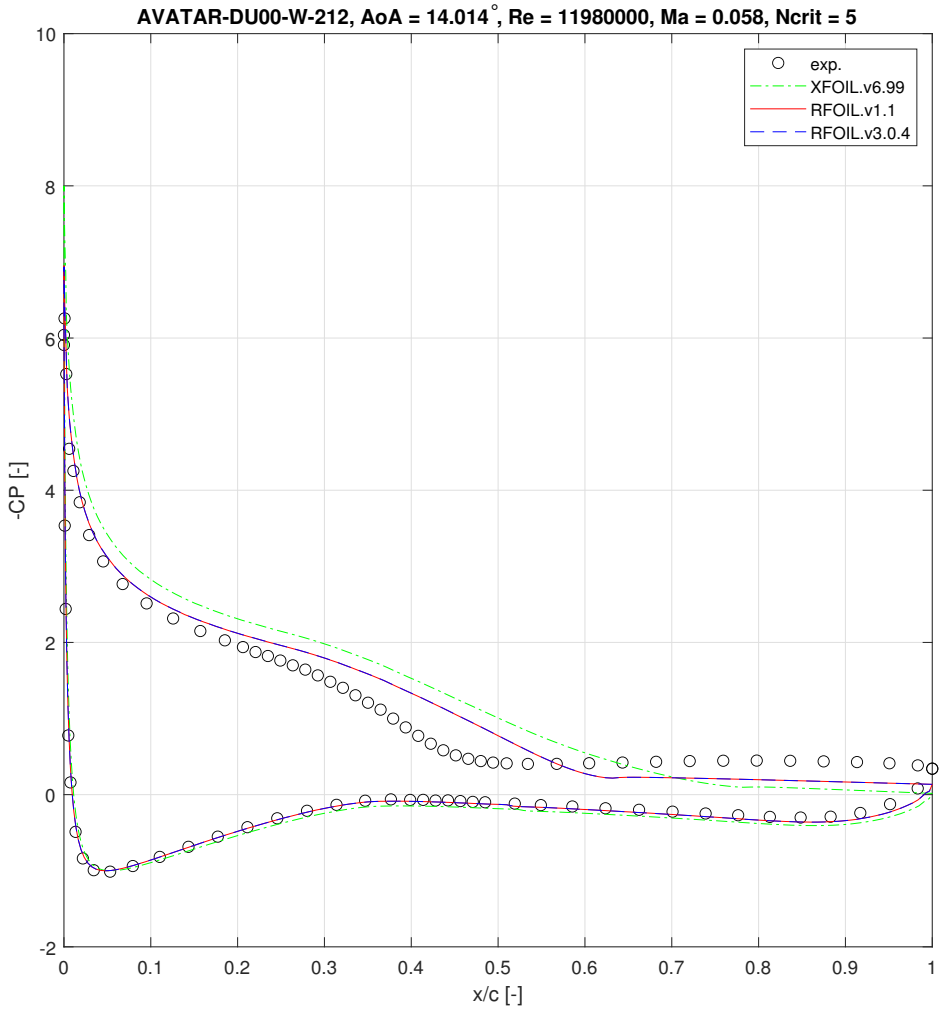

Figure C.278: Comparison between experimental and numerical pressure distributions for the AVATAR-DU00-W-212 airfoil at a Reynolds number of 6070000, and at an angle of attack and a Mach number of 14.116° and 0.055, respectively.

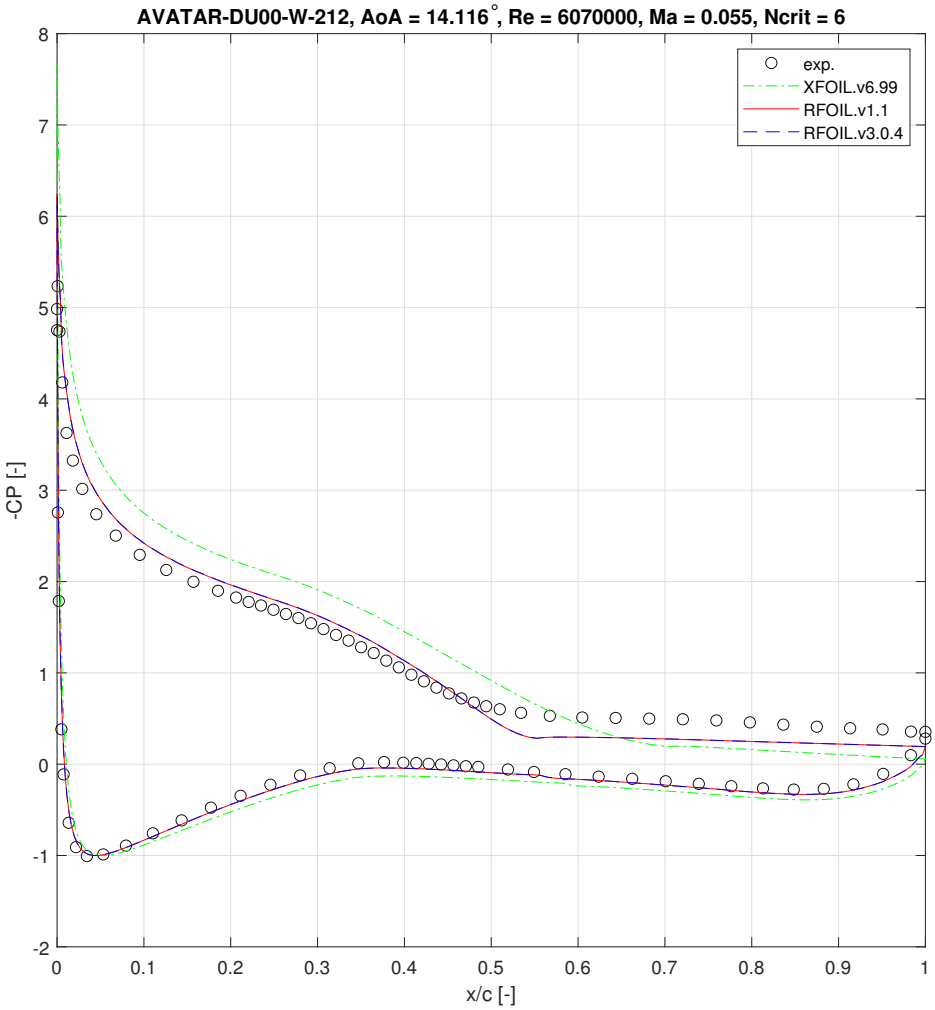

Figure C.279: Comparison between experimental and numerical pressure distributions for the AVATAR-DU00-W-212 airfoil at a Reynolds number of 6040000, and at an angle of attack and a Mach number of 14.118° and 0.055, respectively.

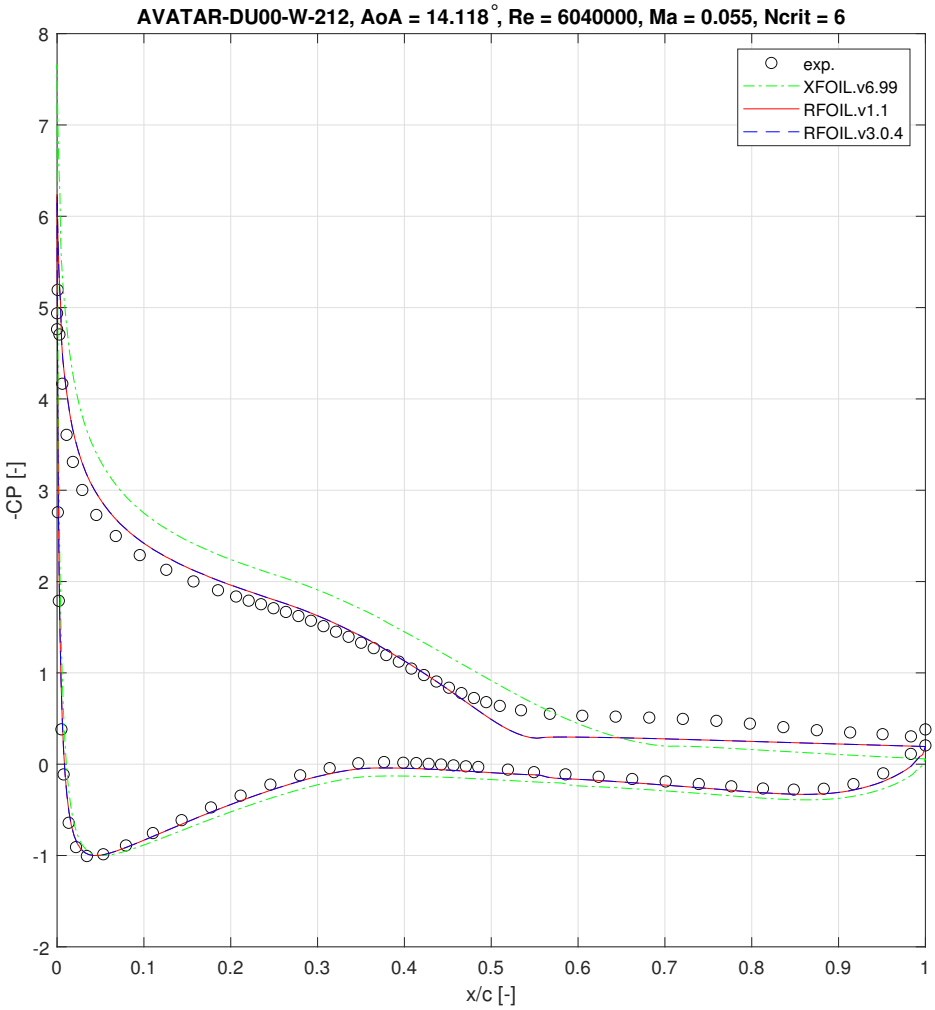

Figure C.280: Comparison between experimental and numerical pressure distributions for the AVATAR-DU00-W-212 airfoil at a Reynolds number of 6070000, and at an angle of attack and a Mach number of 14.119° and 0.029, respectively.

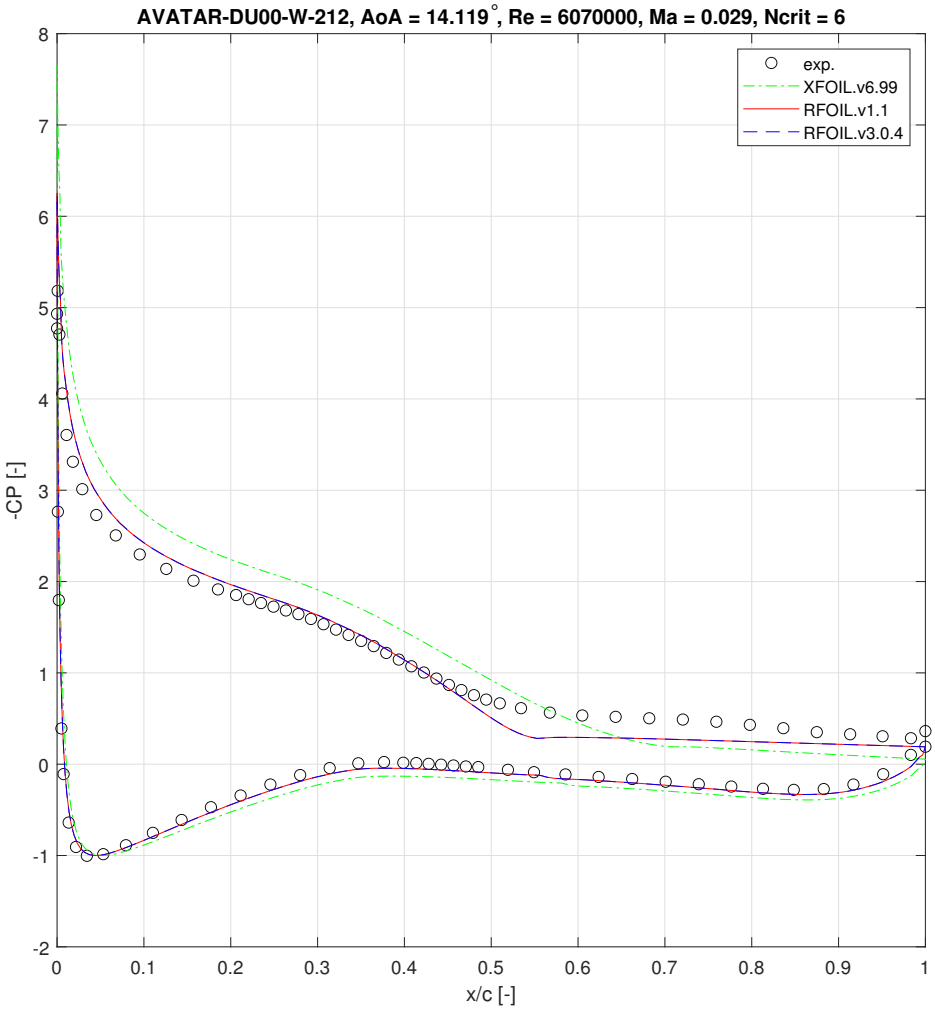

Figure C.281: Comparison between experimental and numerical pressure distributions for the AVATAR-DU00-W-212 airfoil at a Reynolds number of 3020000, and at an angle of attack and a Mach number of 14.110° and 0.074, respectively.

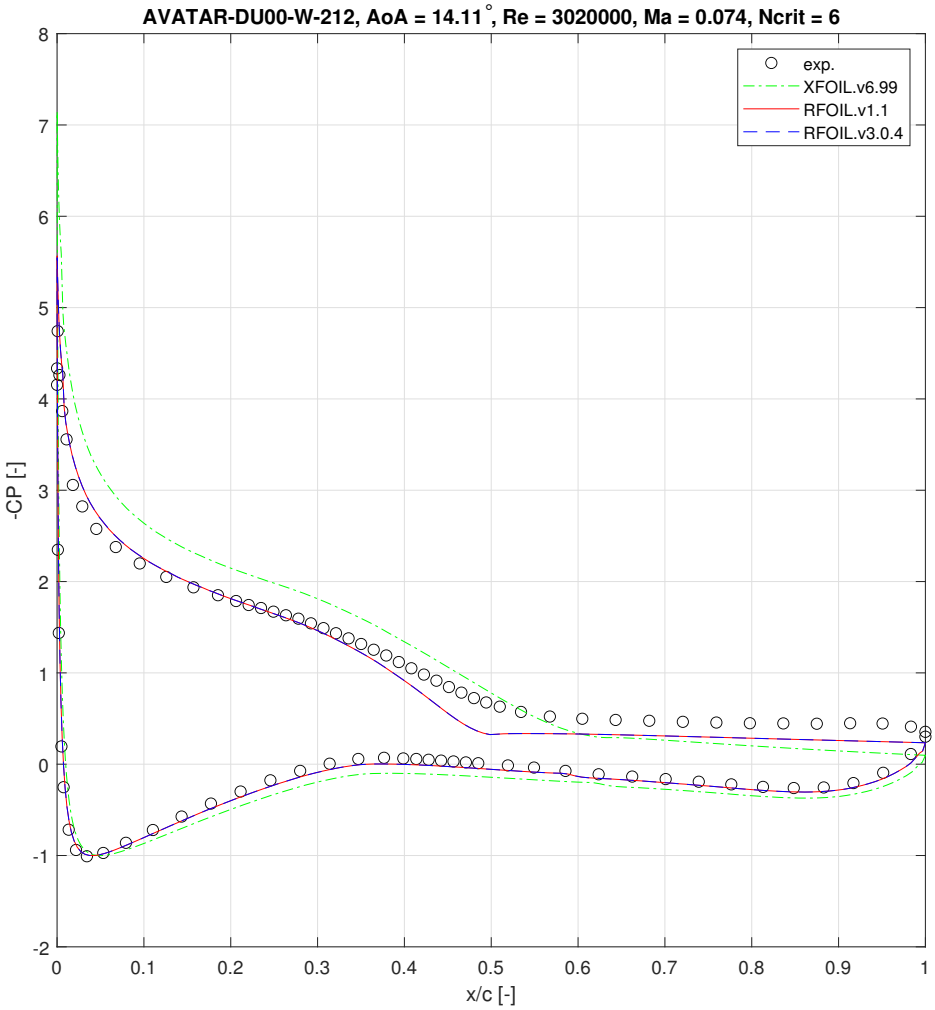

Figure C.282: Comparison between experimental and numerical pressure distributions for the AVATAR-DU00-W-212 airfoil at a Reynolds number of 8950000, and at an angle of attack and a Mach number of 14.124° and 0.082, respectively.

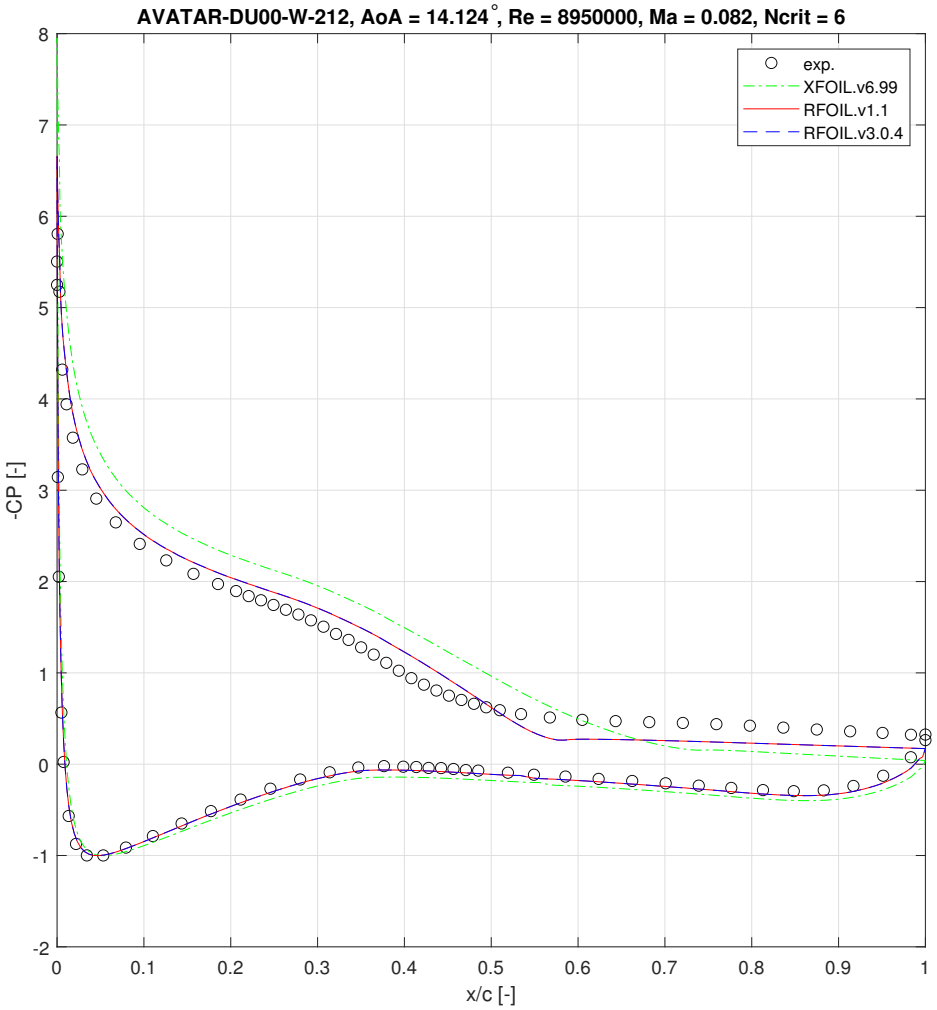

Figure C.283: Comparison between experimental and numerical pressure distributions for the AVATAR-DU00-W-212 airfoil at a Reynolds number of 9030000, and at an angle of attack and a Mach number of 14.127° and 0.044, respectively.

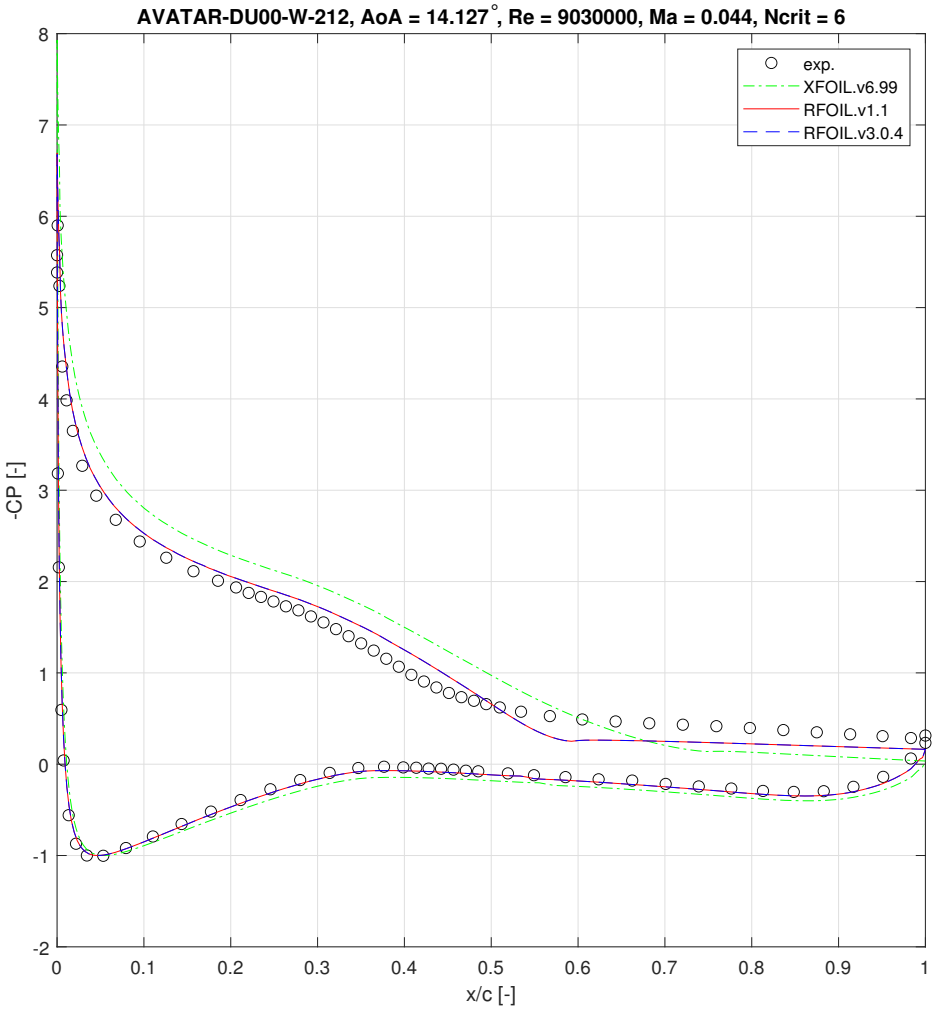

Figure C.284: Comparison between experimental and numerical pressure distributions for the AVATAR-DU00-W-212 airfoil at a Reynolds number of 14950000, and at an angle of attack and a Mach number of 14.134° and 0.081, respectively.

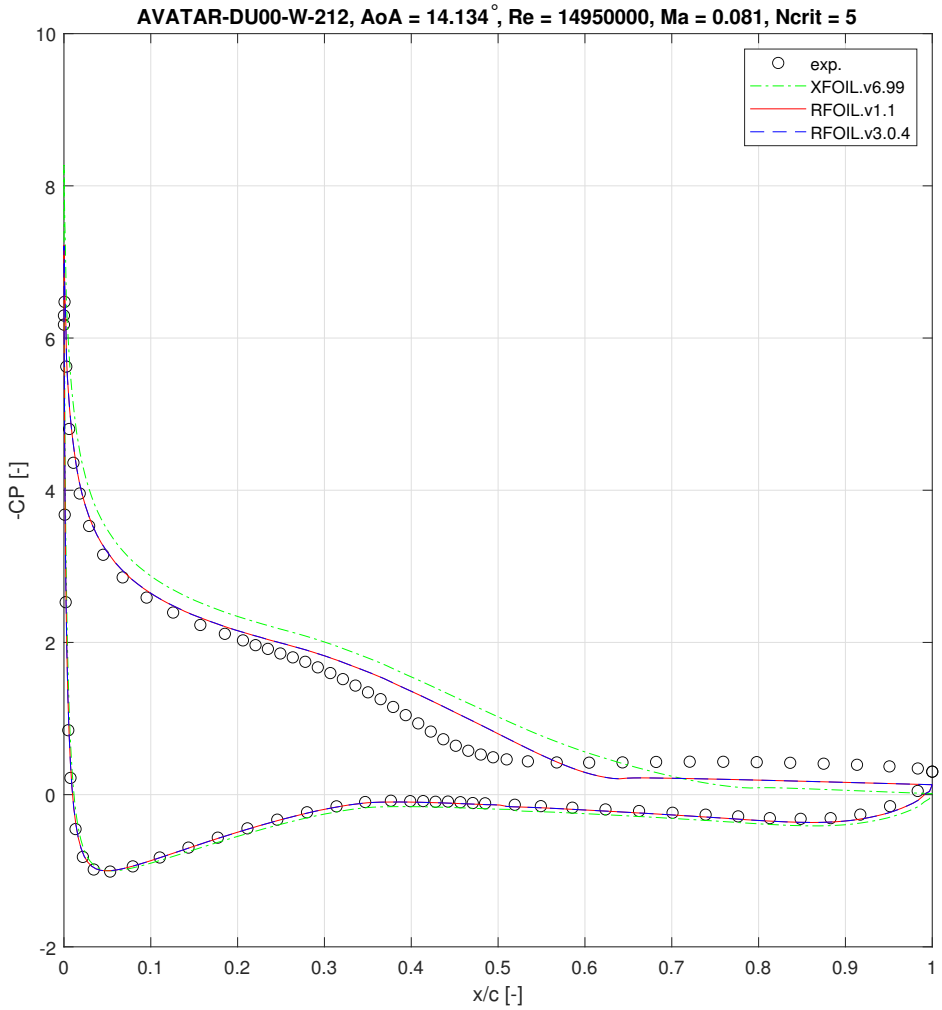

Figure C.285: Comparison between experimental and numerical pressure distributions for the AVATAR-DU00-W-212 airfoil at a Reynolds number of 12130000, and at an angle of attack and a Mach number of 15.013° and 0.058, respectively.

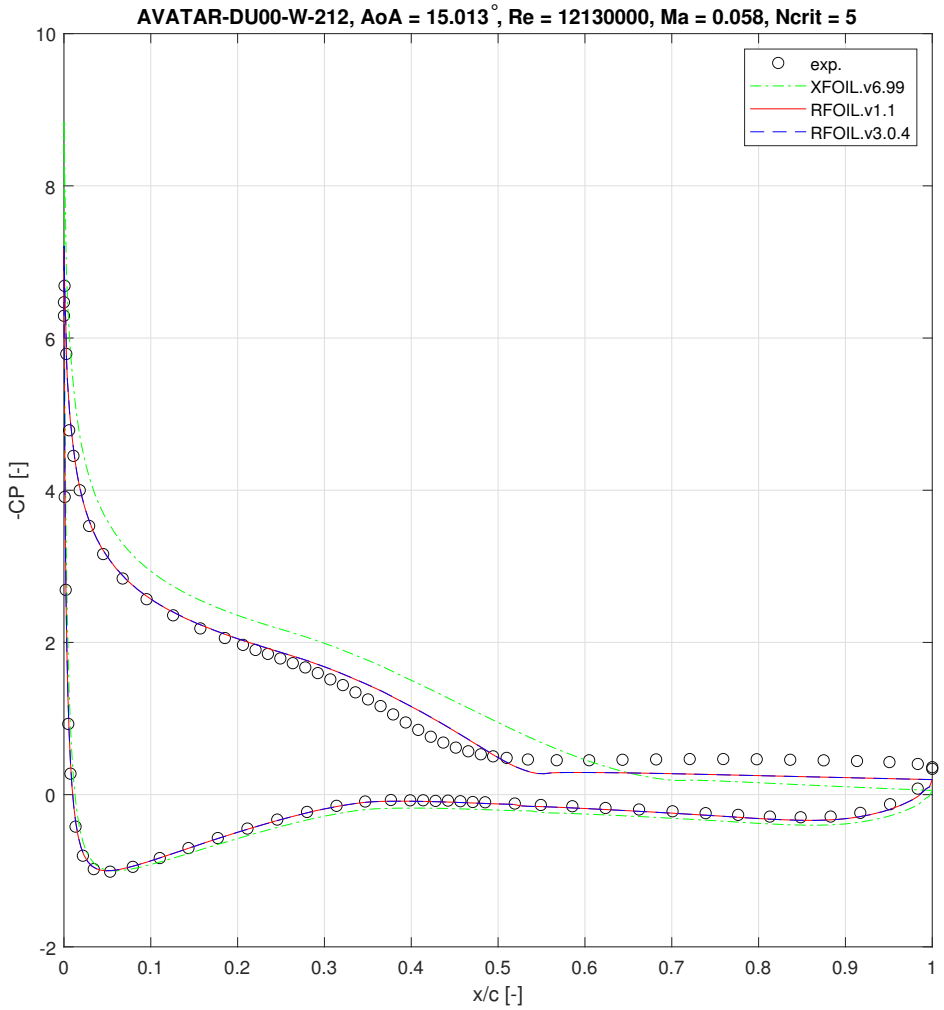

Figure C.286: Comparison between experimental and numerical pressure distributions for the AVATAR-DU00-W-212 airfoil at a Reynolds number of 3000000, and at an angle of attack and a Mach number of 15.108° and 0.074, respectively.

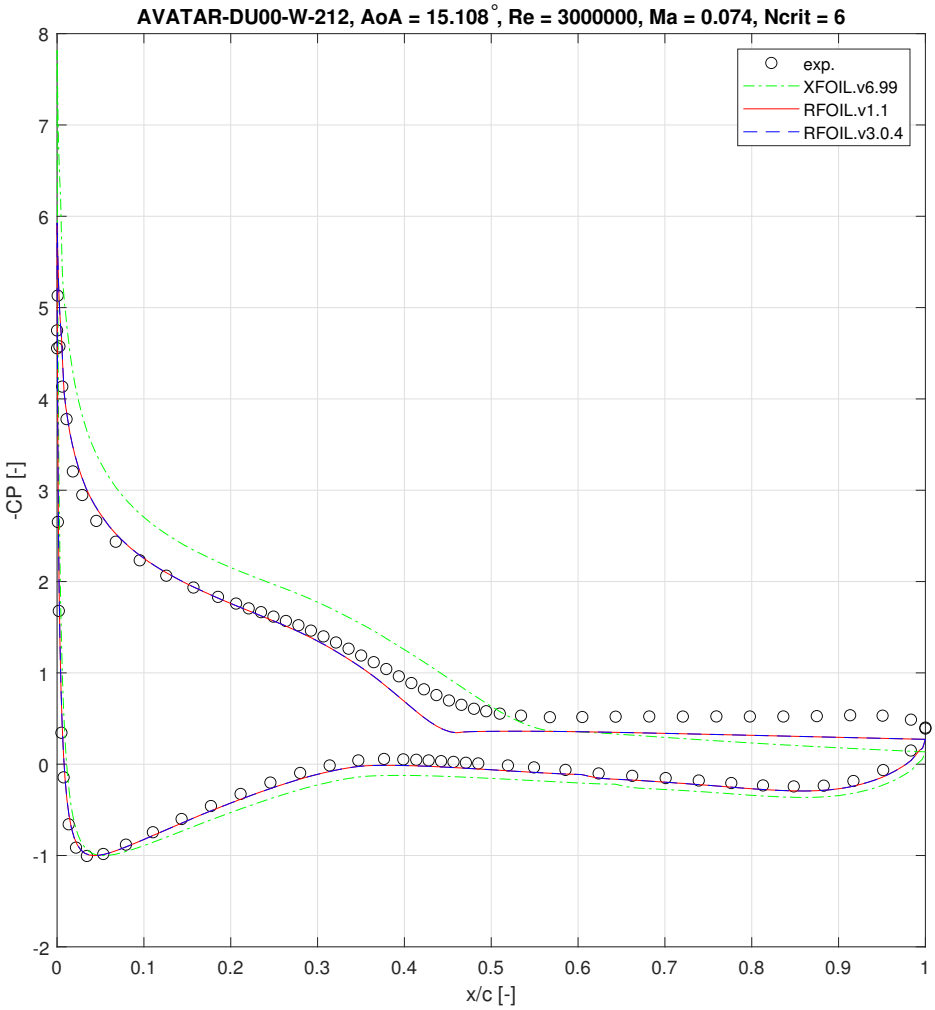

Figure C.287: Comparison between experimental and numerical pressure distributions for the AVATAR-DU00-W-212 airfoil at a Reynolds number of 3010000, and at an angle of attack and a Mach number of 15.108° and 0.074, respectively.

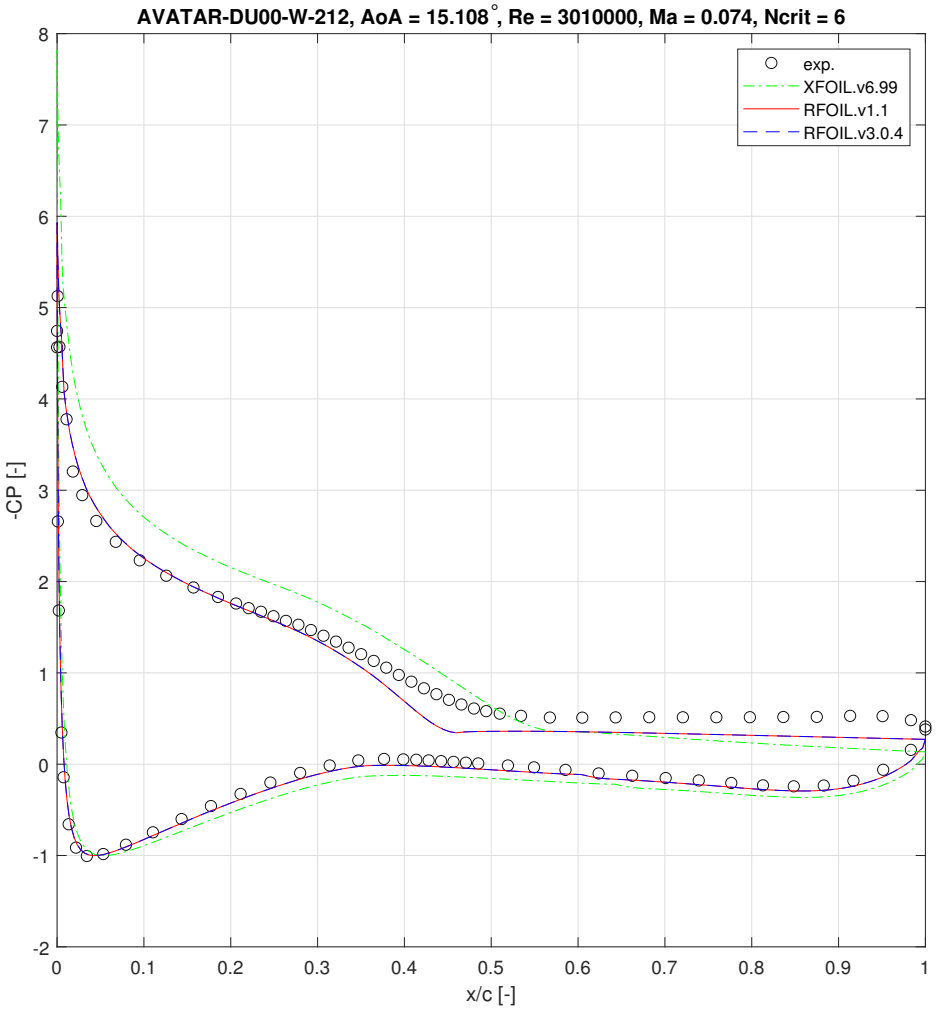

Figure C.288: Comparison between experimental and numerical pressure distributions for the AVATAR-DU00-W-212 airfoil at a Reynolds number of 6030000, and at an angle of attack and a Mach number of 15.116° and 0.029, respectively.

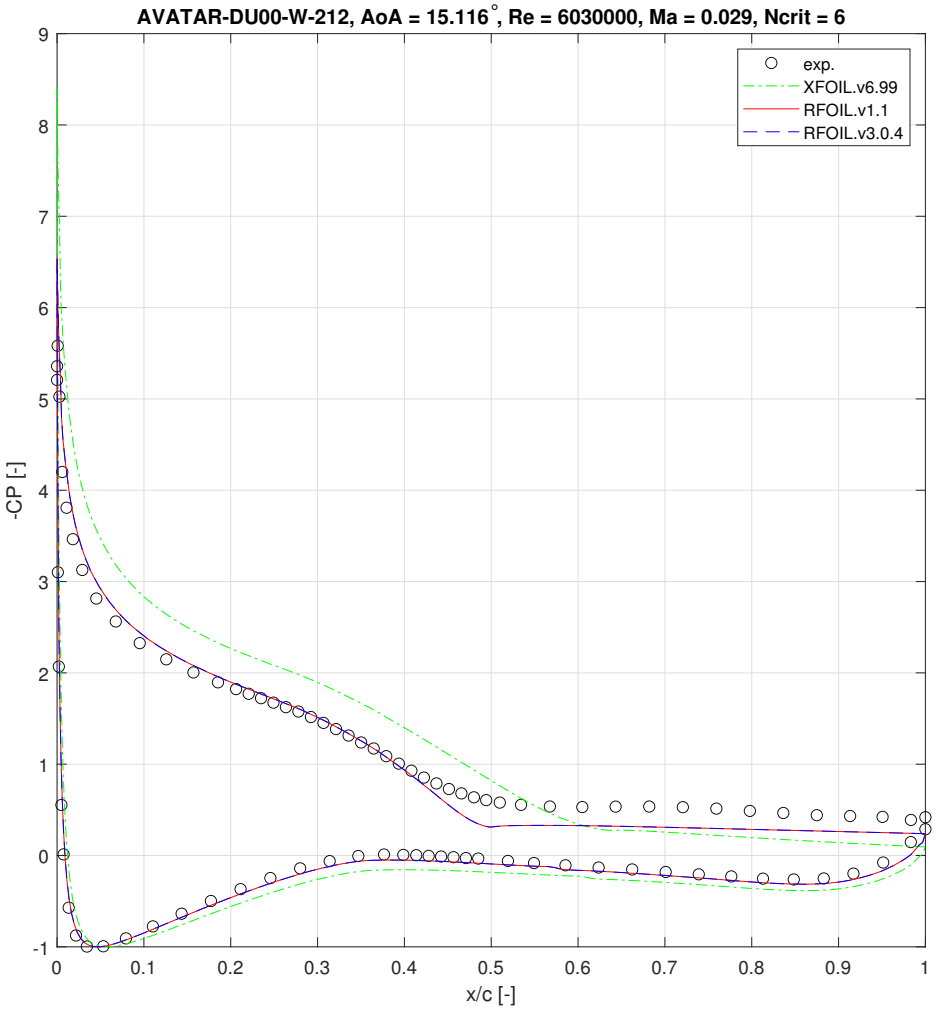

Figure C.289: Comparison between experimental and numerical pressure distributions for the AVATAR-DU00-W-212 airfoil at a Reynolds number of 6080000, and at an angle of attack and a Mach number of 15.119° and 0.055, respectively.

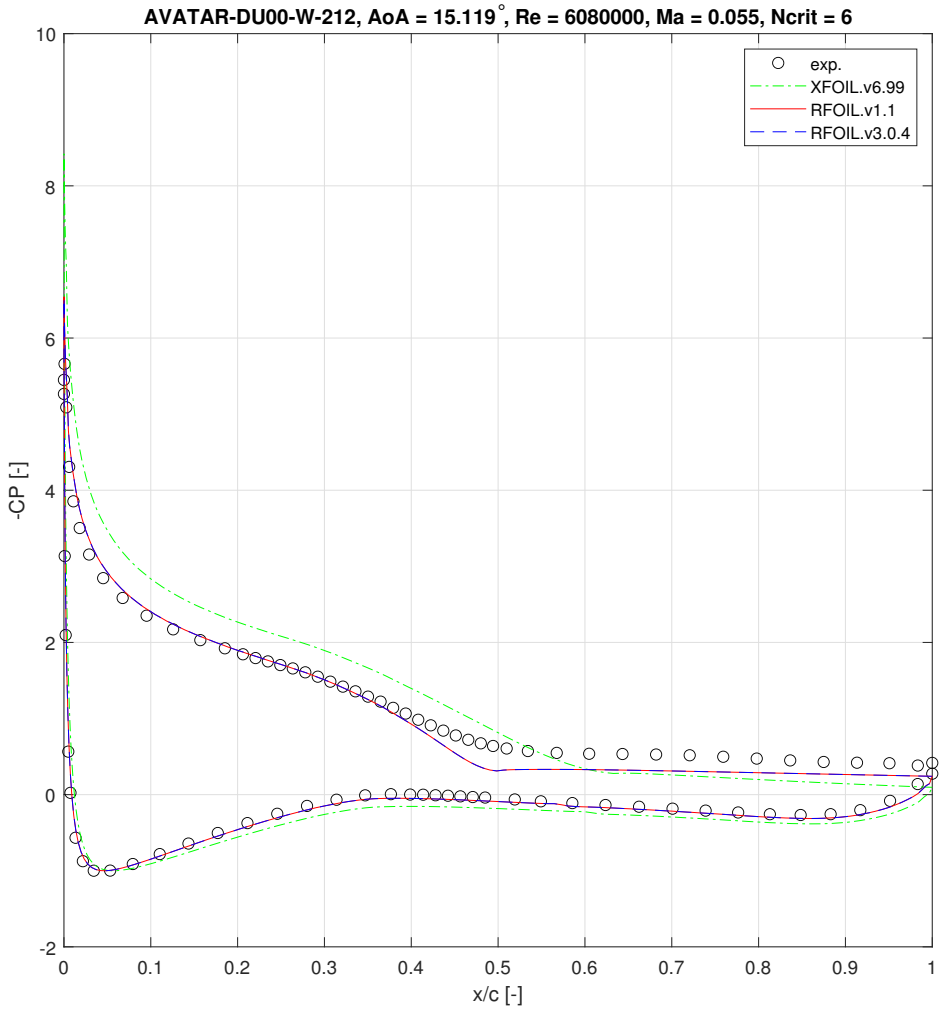

Figure C.290: Comparison between experimental and numerical pressure distributions for the AVATAR-DU00-W-212 airfoil at a Reynolds number of 6010000, and at an angle of attack and a Mach number of 15.120° and 0.055, respectively.

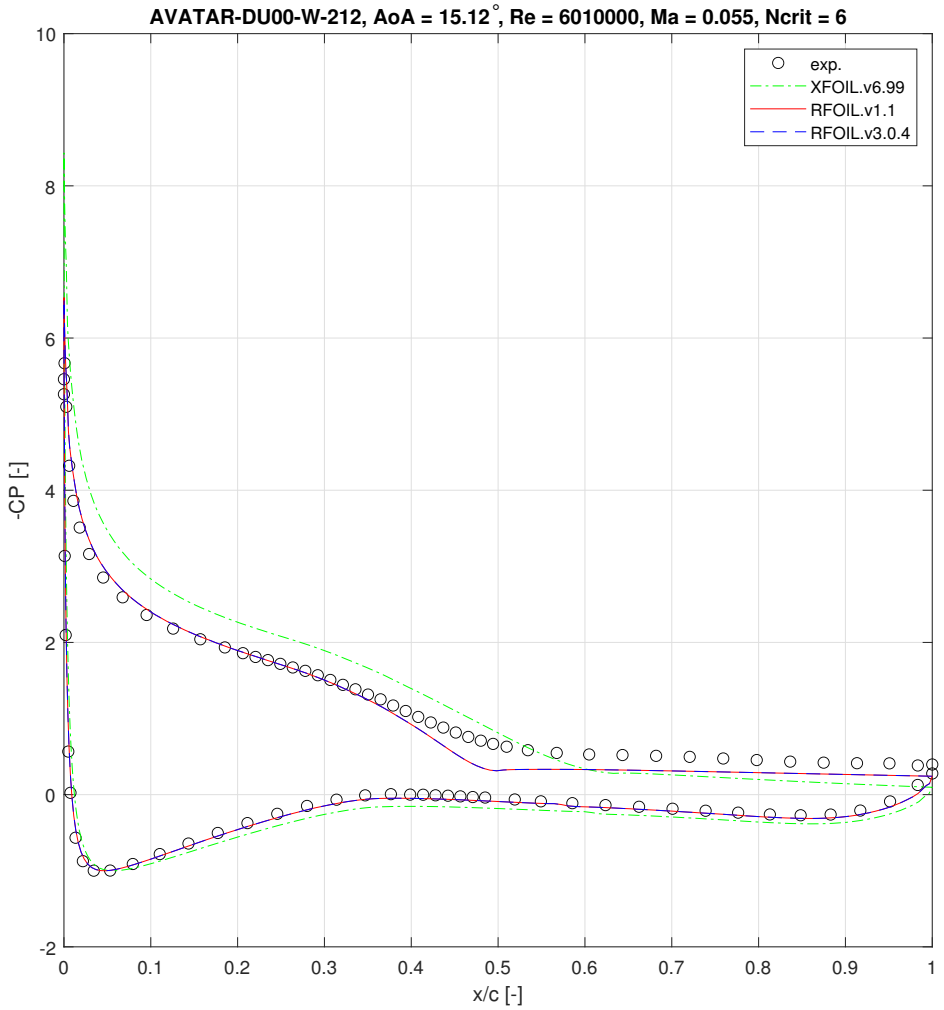

Figure C.291: Comparison between experimental and numerical pressure distributions for the AVATAR-DU00-W-212 airfoil at a Reynolds number of 9060000, and at an angle of attack and a Mach number of 15.131° and 0.083, respectively.

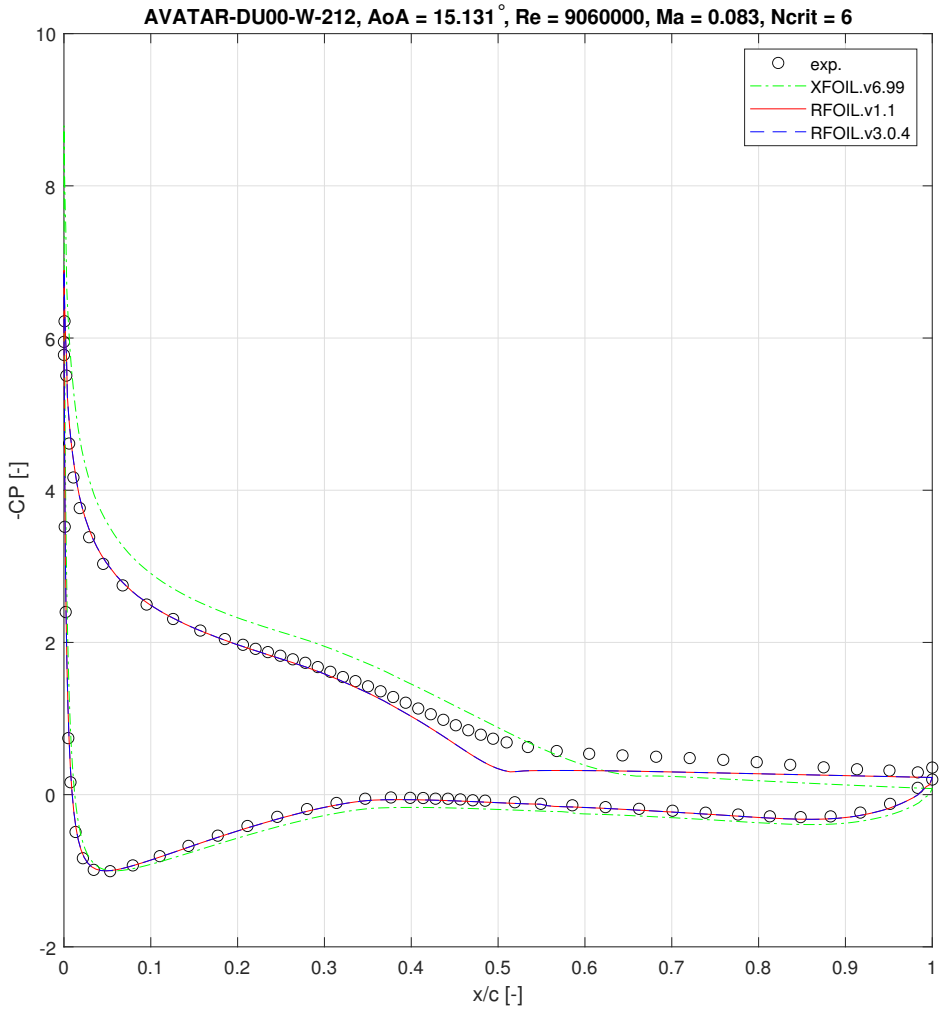

Figure C.292: Comparison between experimental and numerical pressure distributions for the AVATAR-DU00-W-212 airfoil at a Reynolds number of 9040000, and at an angle of attack and a Mach number of 15.132° and 0.083, respectively.

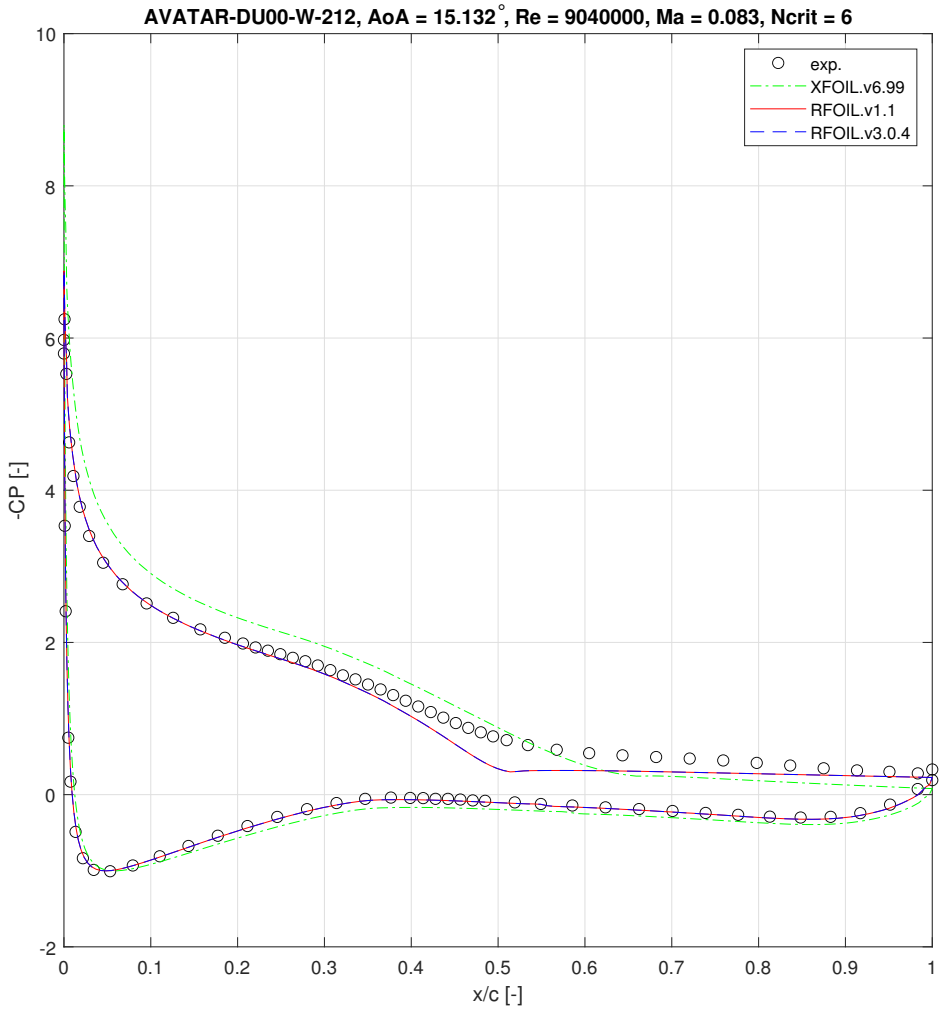

Figure C.293: Comparison between experimental and numerical pressure distributions for the AVATAR-DU00-W-212 airfoil at a Reynolds number of 9080000, and at an angle of attack and a Mach number of 15.132° and 0.083, respectively.

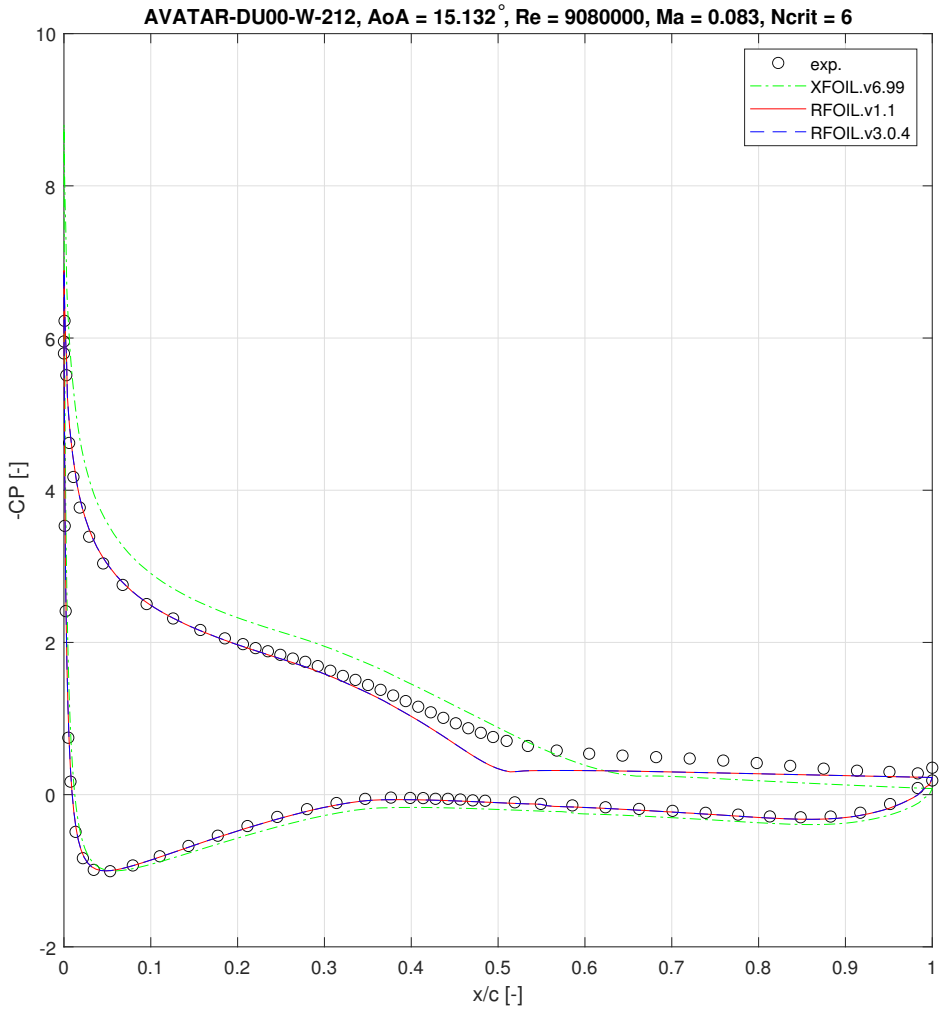

Figure C.294: Comparison between experimental and numerical pressure distributions for the AVATAR-DU00-W-212 airfoil at a Reynolds number of 9080000, and at an angle of attack and a Mach number of 15.130° and 0.044, respectively.

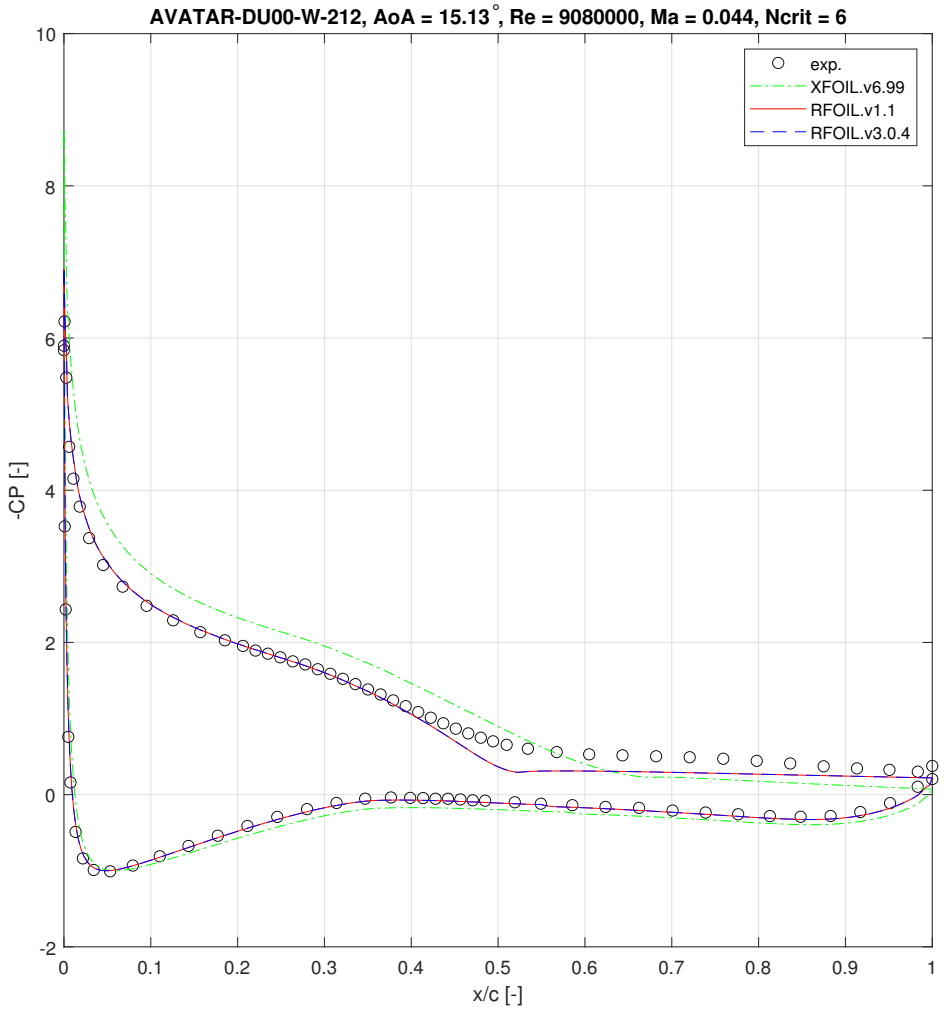

Figure C.295: Comparison between experimental and numerical pressure distributions for the AVATAR-DU00-W-212 airfoil at a Reynolds number of 15060000, and at an angle of attack and a Mach number of 15.140° and 0.082, respectively.

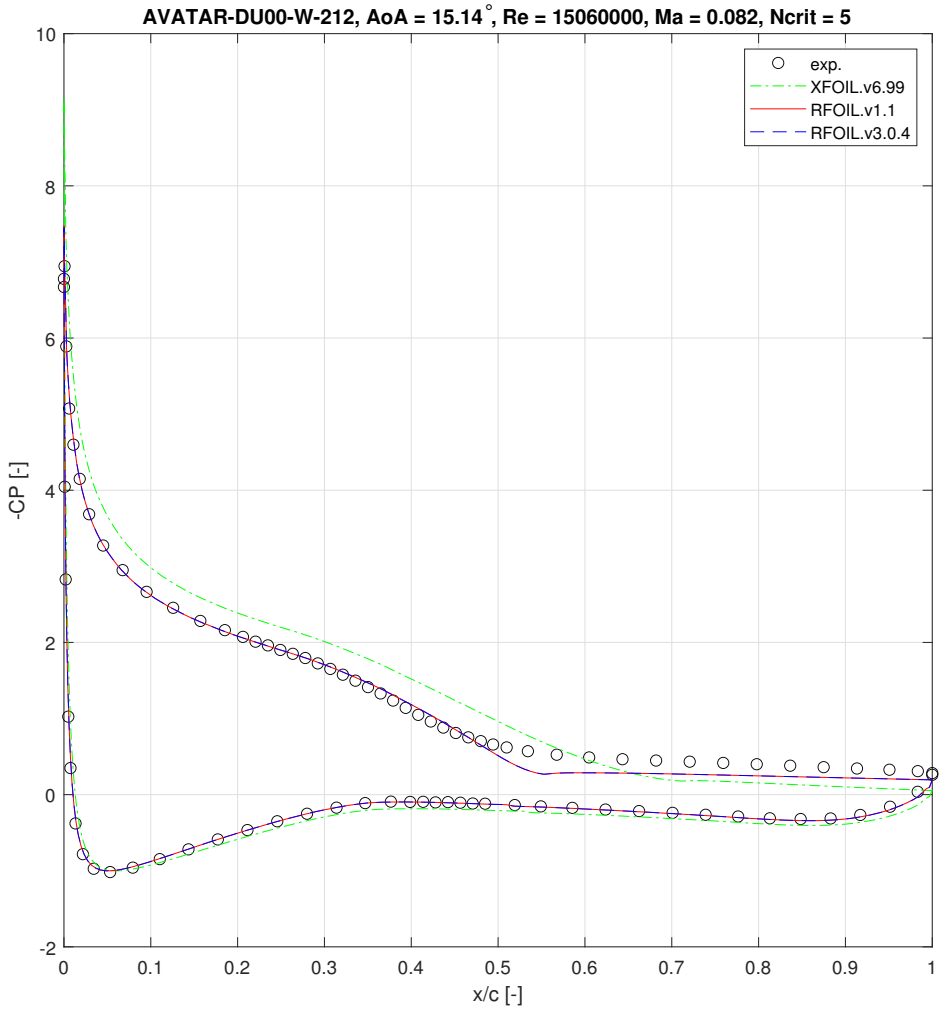

Figure C.296: Comparison between experimental and numerical pressure distributions for the AVATAR-DU00-W-212 airfoil at a Reynolds number of 11980000, and at an angle of attack and a Mach number of 16.014° and 0.058, respectively.

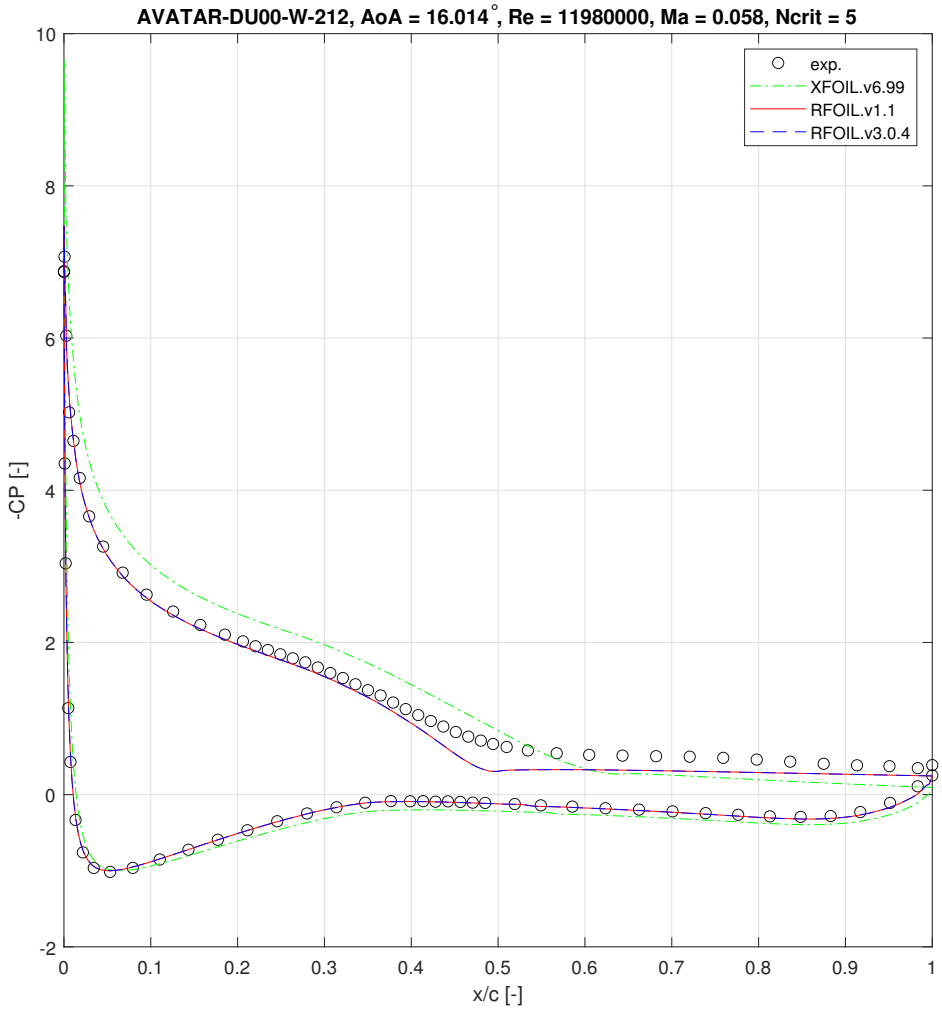

Figure C.297: Comparison between experimental and numerical pressure distributions for the AVATAR-DU00-W-212 airfoil at a Reynolds number of 2990000, and at an angle of attack and a Mach number of 16.107° and 0.073, respectively.

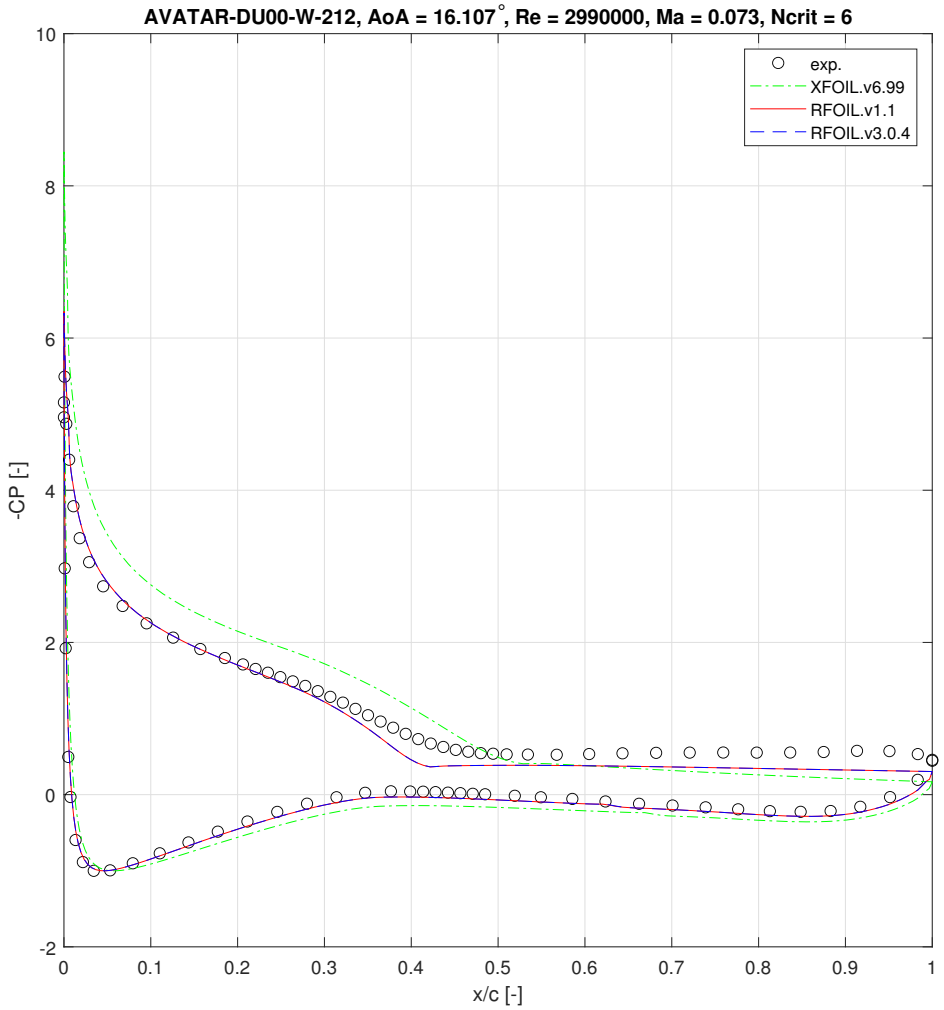

Figure C.298: Comparison between experimental and numerical pressure distributions for the AVATAR-DU00-W-212 airfoil at a Reynolds number of 6010000, and at an angle of attack and a Mach number of 16.120° and 0.055, respectively.

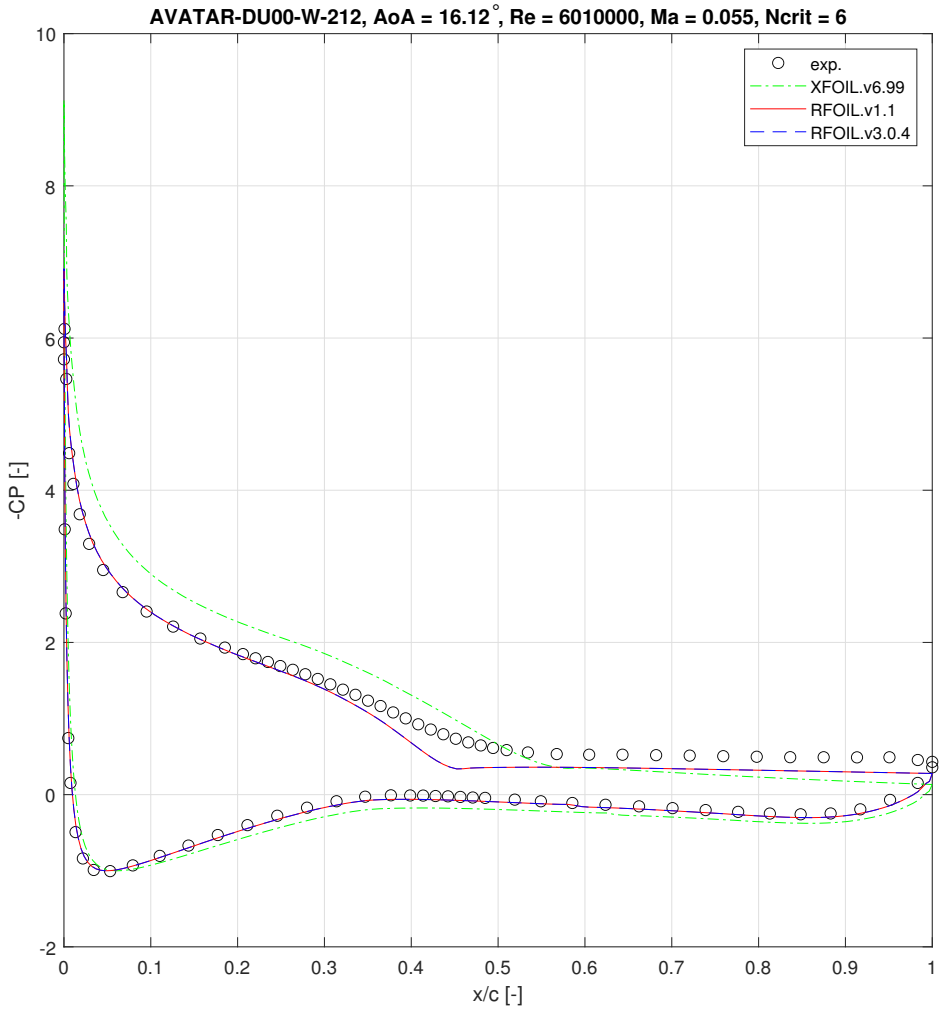

Figure C.299: Comparison between experimental and numerical pressure distributions for the AVATAR-DU00-W-212 airfoil at a Reynolds number of 6030000, and at an angle of attack and a Mach number of 16.120° and 0.029, respectively.

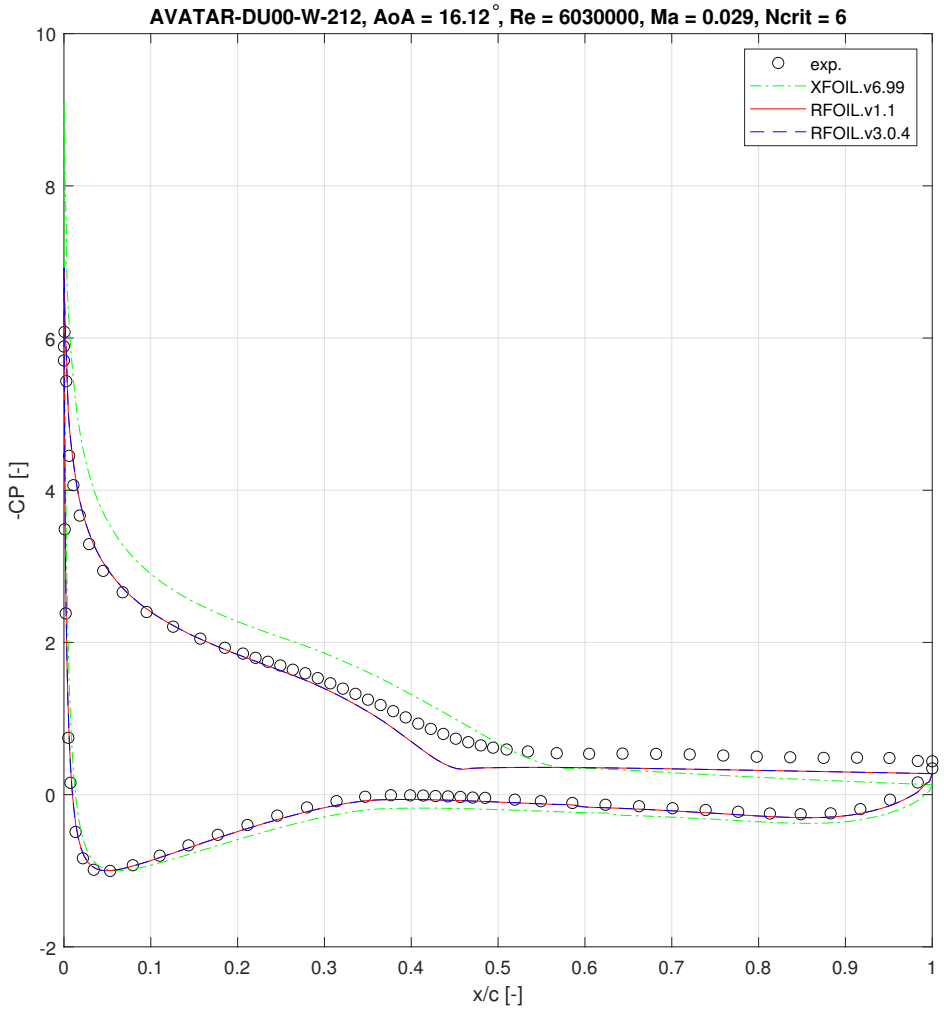

Figure C.300: Comparison between experimental and numerical pressure distributions for the AVATAR-DU00-W-212 airfoil at a Reynolds number of 9060000, and at an angle of attack and a Mach number of 16.134° and 0.083, respectively.

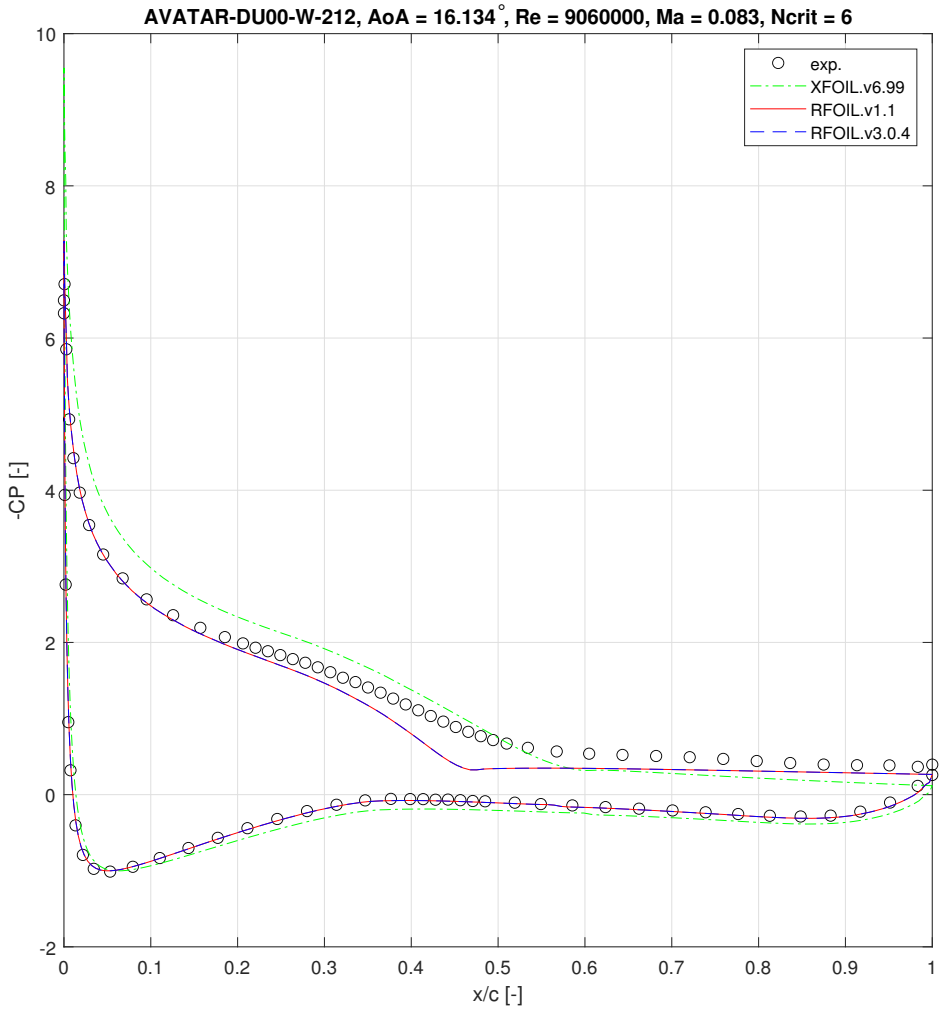

Figure C.301: Comparison between experimental and numerical pressure distributions for the AVATAR-DU00-W-212 airfoil at a Reynolds number of 9090000, and at an angle of attack and a Mach number of 16.130° and 0.044, respectively.

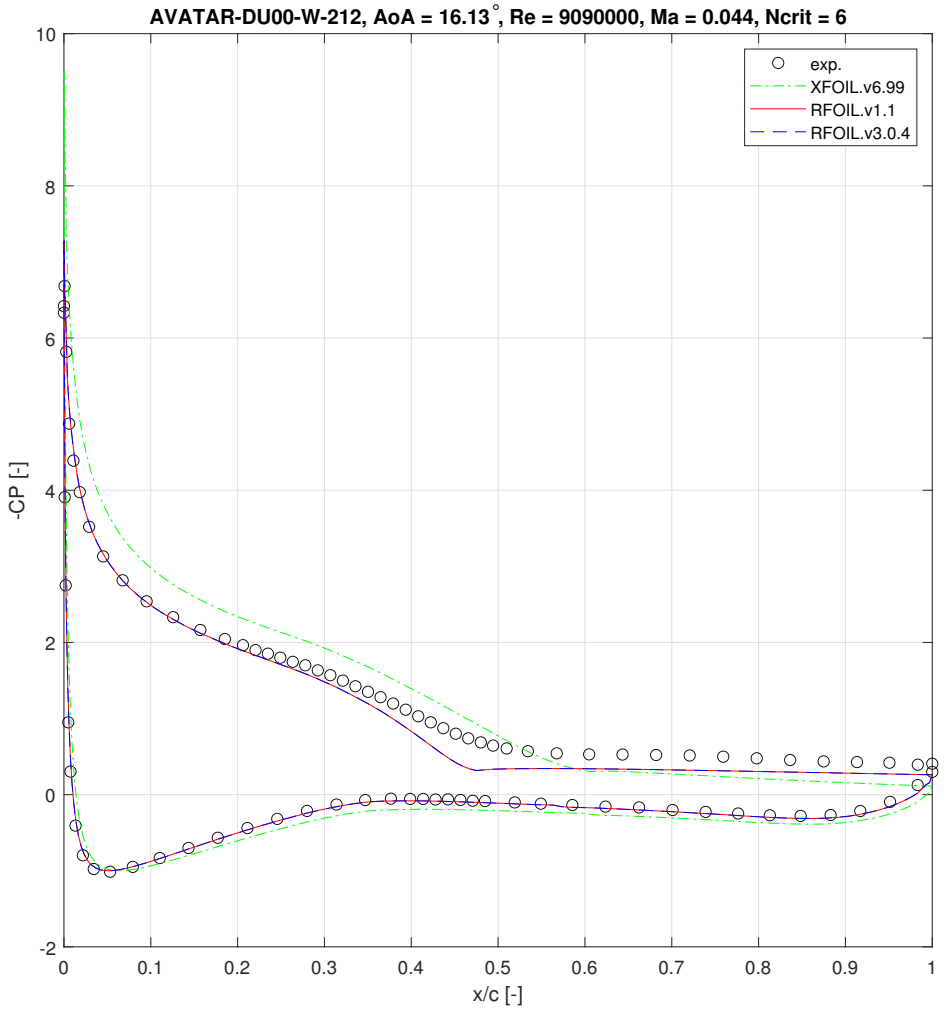

Figure C.302: Comparison between experimental and numerical pressure distributions for the AVATAR-DU00-W-212 airfoil at a Reynolds number of 15030000, and at an angle of attack and a Mach number of 16.142° and 0.081, respectively.

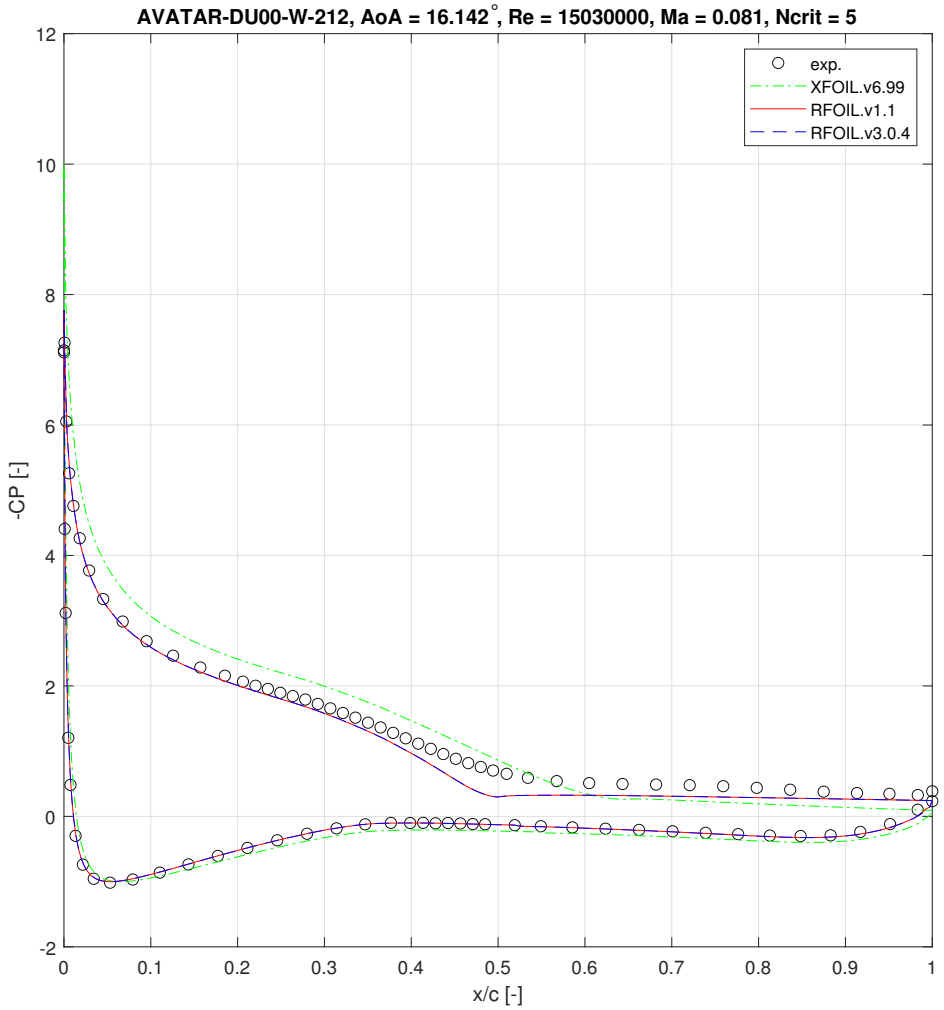

Figure C.303: Comparison between experimental and numerical pressure distributions for the AVATAR-DU00-W-212 airfoil at a Reynolds number of 11990000, and at an angle of attack and a Mach number of 17.013° and 0.058, respectively.

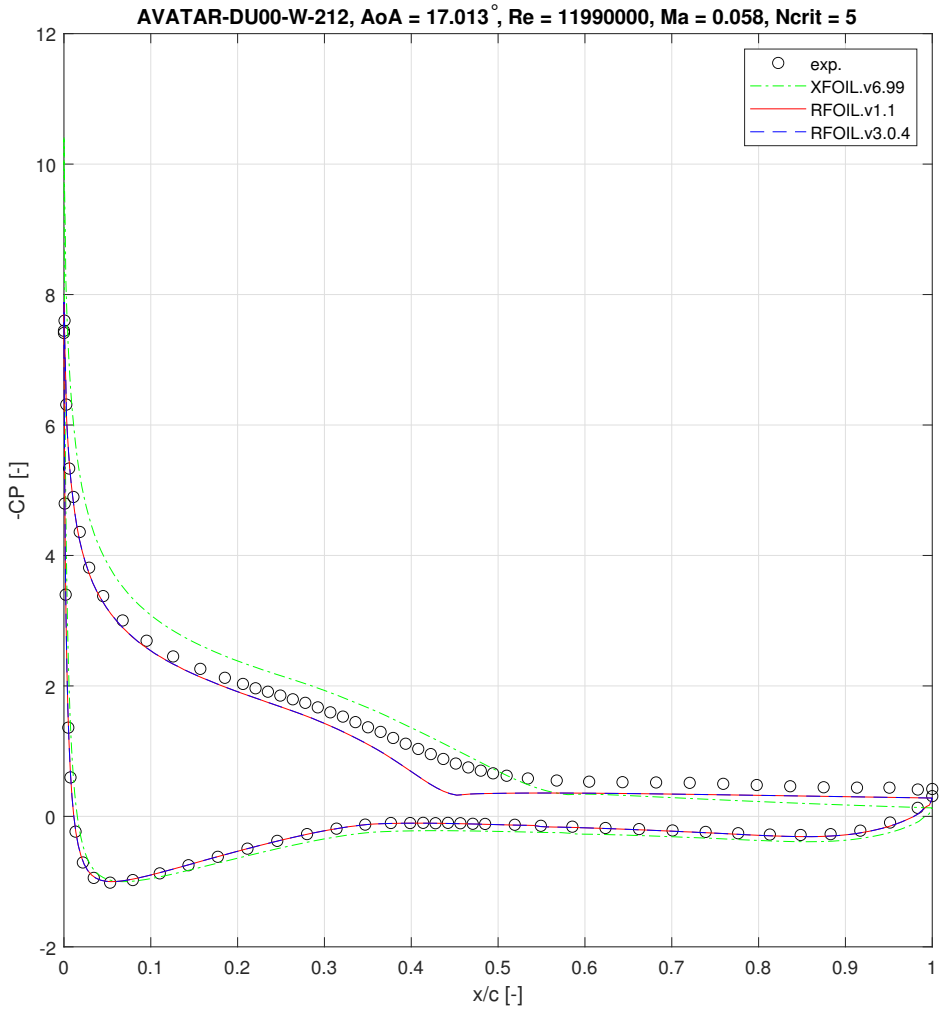

Figure C.304: Comparison between experimental and numerical pressure distributions for the AVATAR-DU00-W-212 airfoil at a Reynolds number of 2980000, and at an angle of attack and a Mach number of 17.107° and 0.073, respectively.

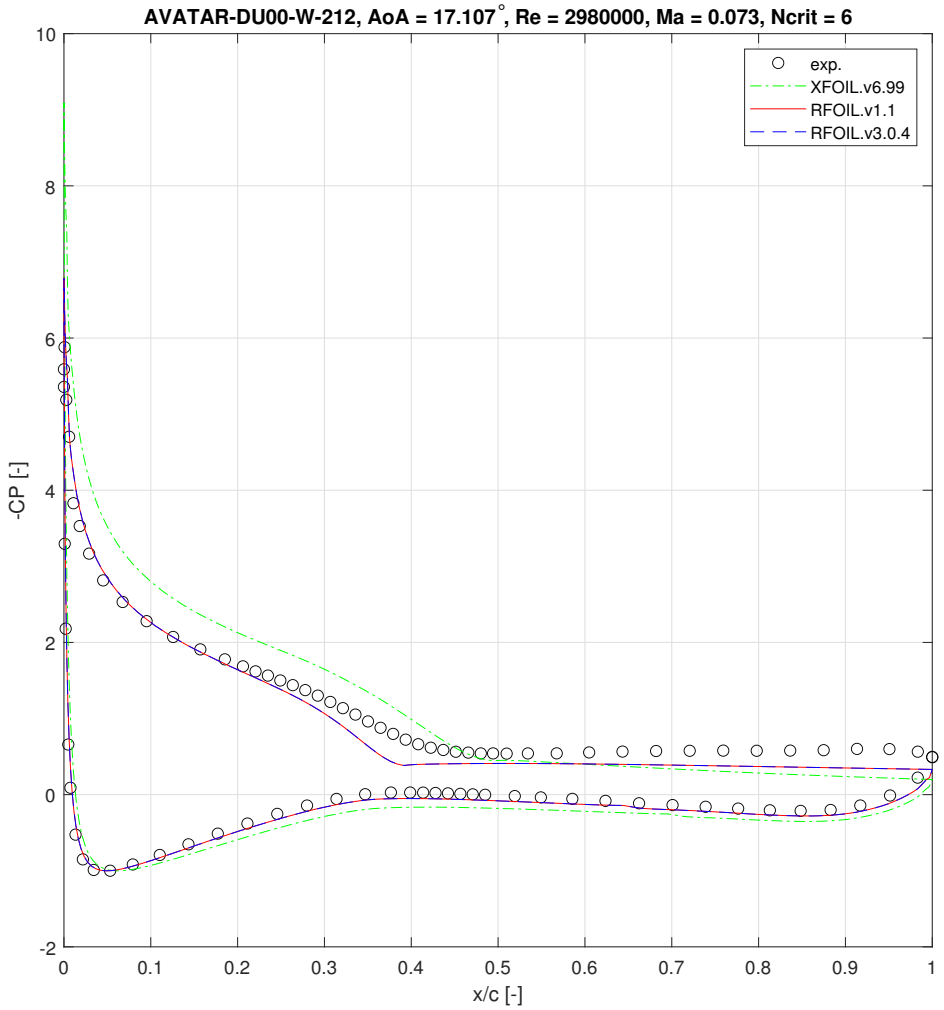

Figure C.305: Comparison between experimental and numerical pressure distributions for the AVATAR-DU00-W-212 airfoil at a Reynolds number of 5990000, and at an angle of attack and a Mach number of 17.118° and 0.055, respectively.

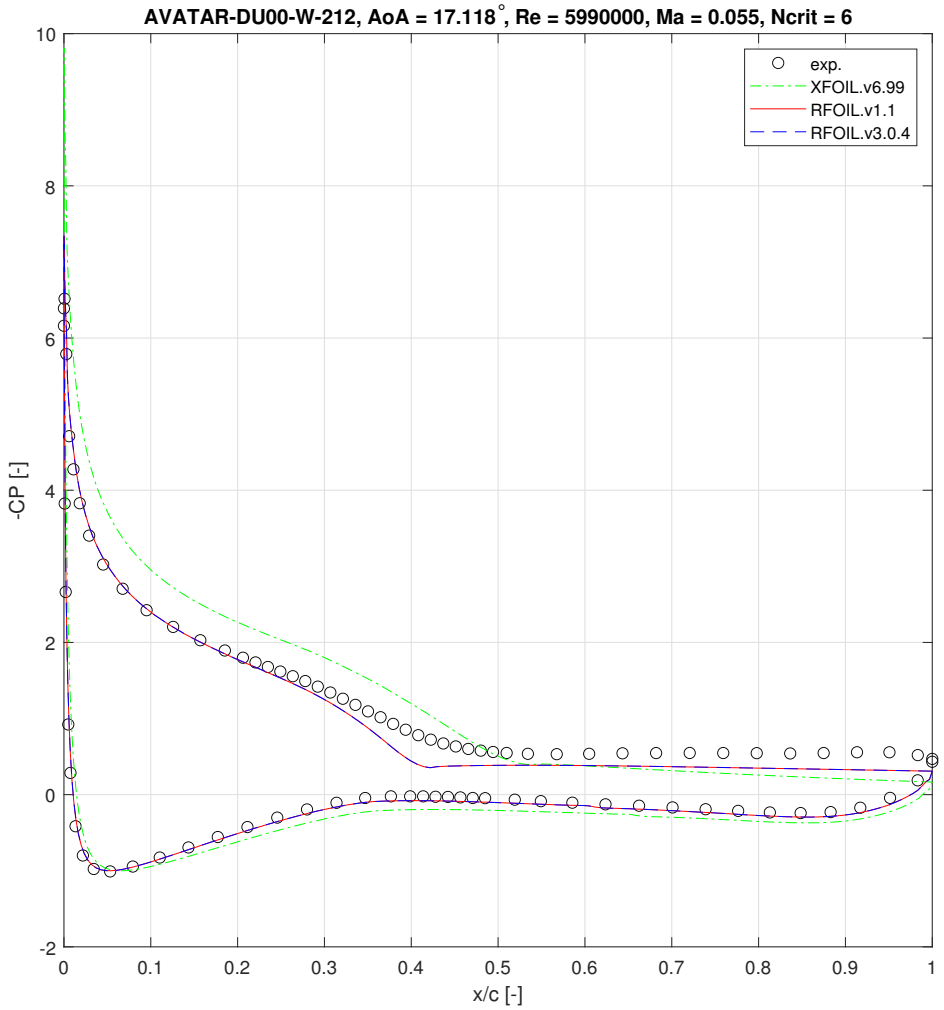

Figure C.306: Comparison between experimental and numerical pressure distributions for the AVATAR-DU00-W-212 airfoil at a Reynolds number of 5980000, and at an angle of attack and a Mach number of 17.121° and 0.029, respectively.

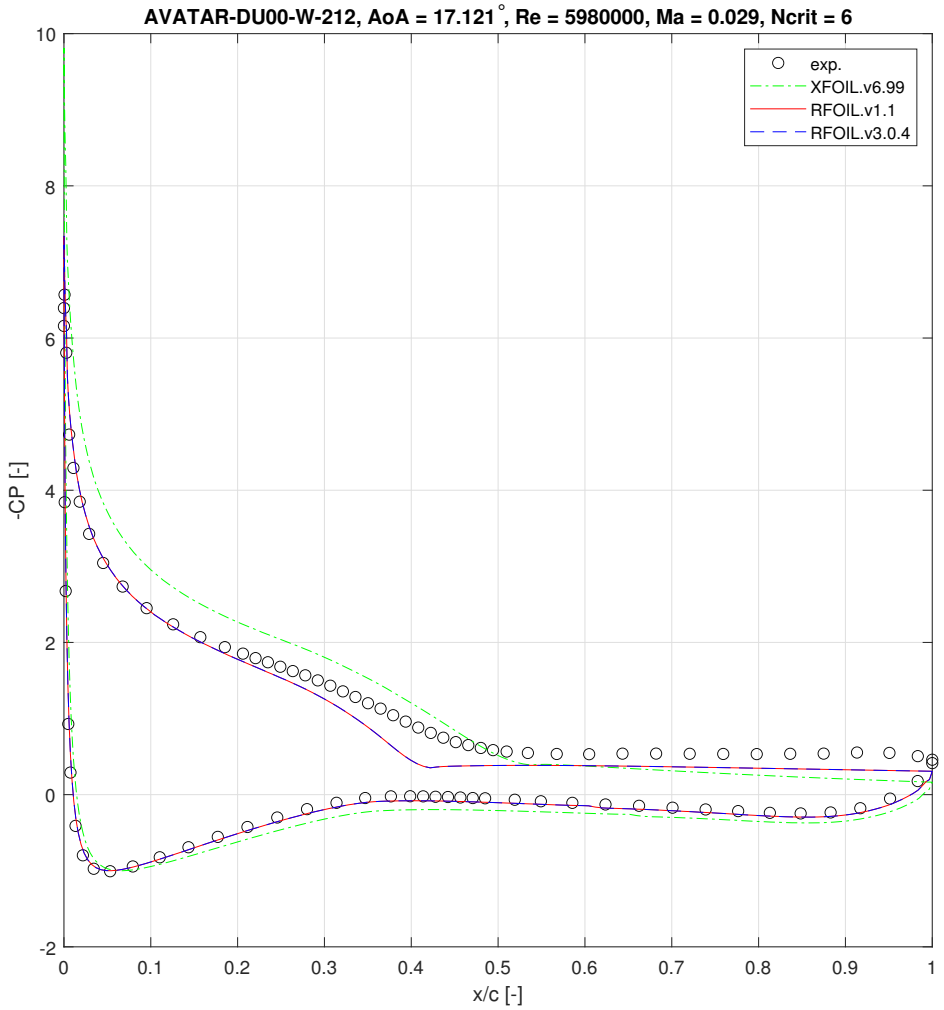

Figure C.307: Comparison between experimental and numerical pressure distributions for the AVATAR-DU00-W-212 airfoil at a Reynolds number of 9060000, and at an angle of attack and a Mach number of 17.131° and 0.044, respectively.

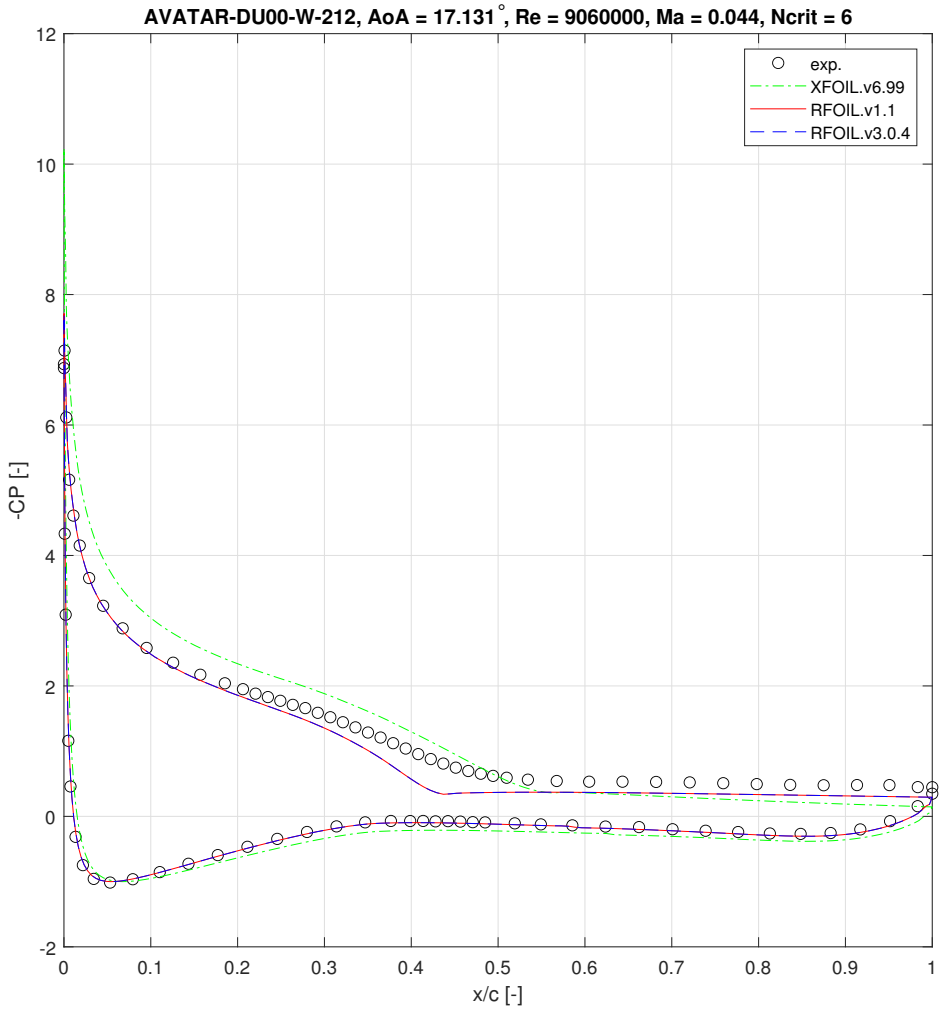

Figure C.308: Comparison between experimental and numerical pressure distributions for the AVATAR-DU00-W-212 airfoil at a Reynolds number of 9000000, and at an angle of attack and a Mach number of 17.132° and 0.083, respectively.

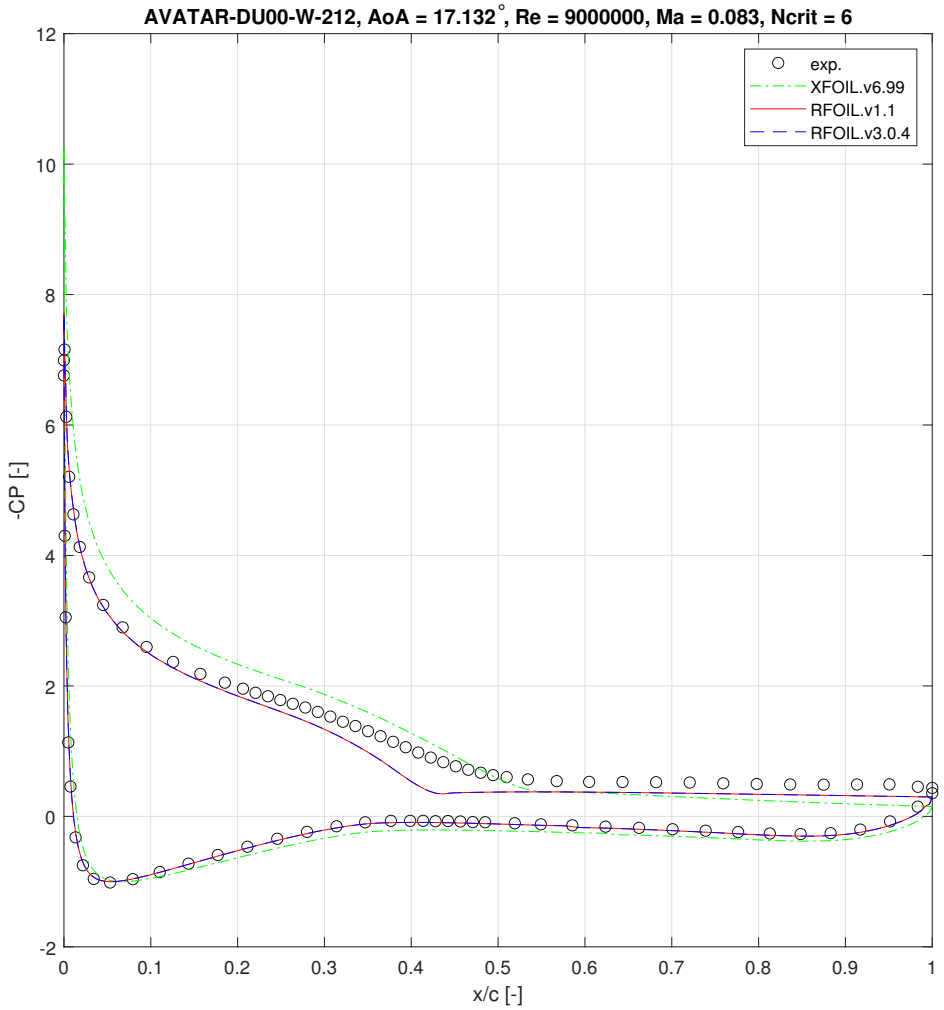

Figure C.309: Comparison between experimental and numerical pressure distributions for the AVATAR-DU00-W-212 airfoil at a Reynolds number of 15130000, and at an angle of attack and a Mach number of 17.145° and 0.082, respectively.

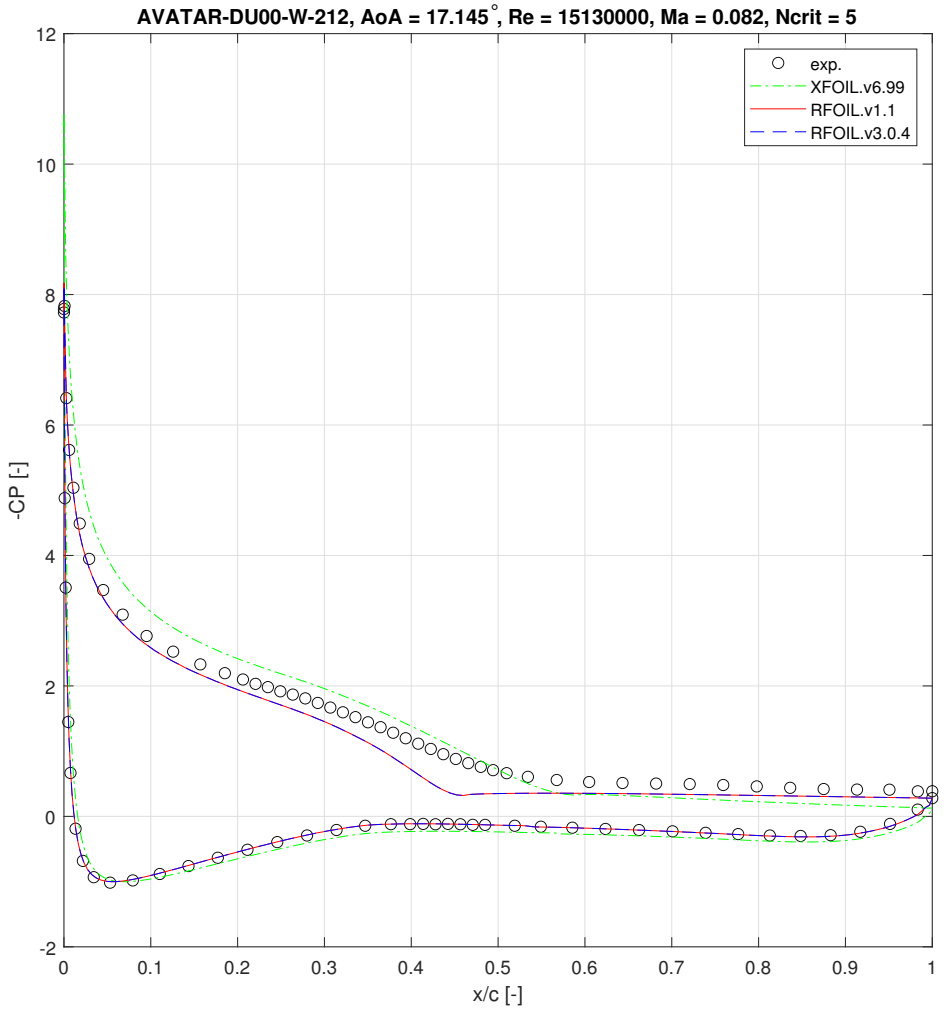

Figure C.310: Comparison between experimental and numerical pressure distributions for the AVATAR-DU00-W-212 airfoil at a Reynolds number of 12040000, and at an angle of attack and a Mach number of 18.012° and 0.058, respectively.

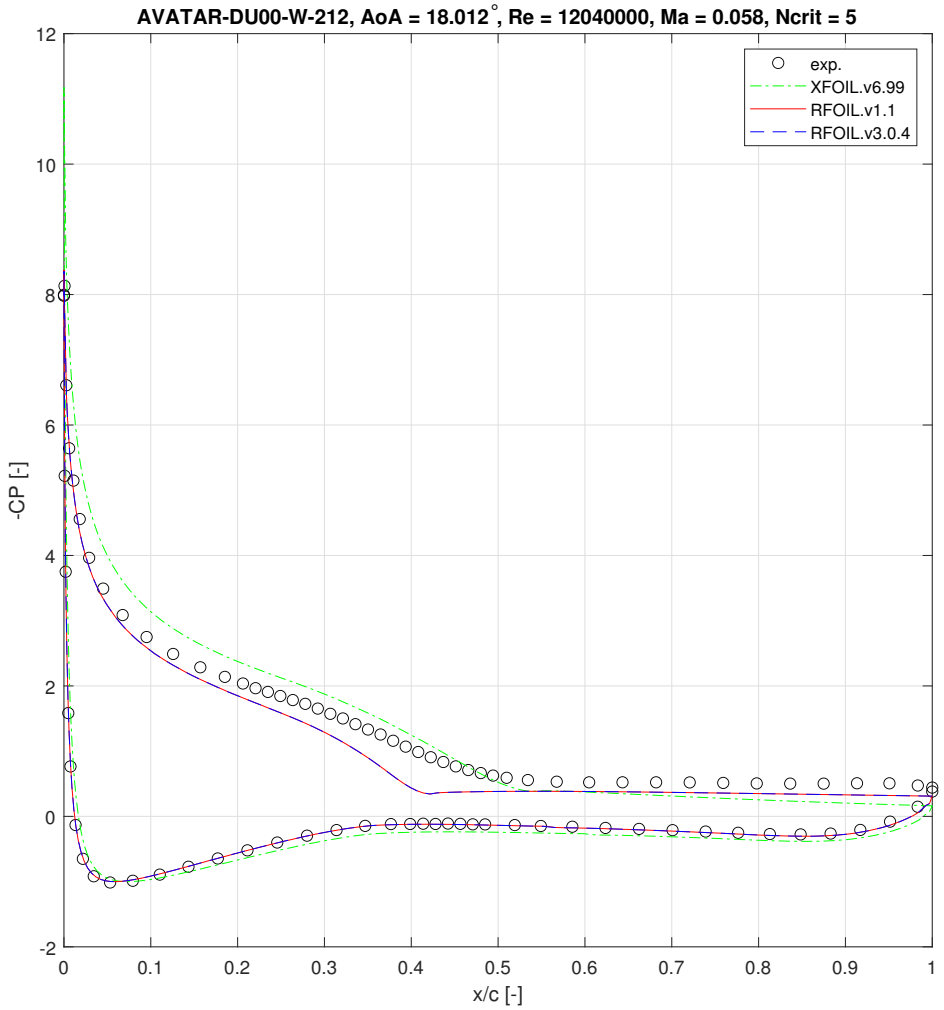

Figure C.311: Comparison between experimental and numerical pressure distributions for the AVATAR-DU00-W-212 airfoil at a Reynolds number of 2980000, and at an angle of attack and a Mach number of 18.107° and 0.073, respectively.

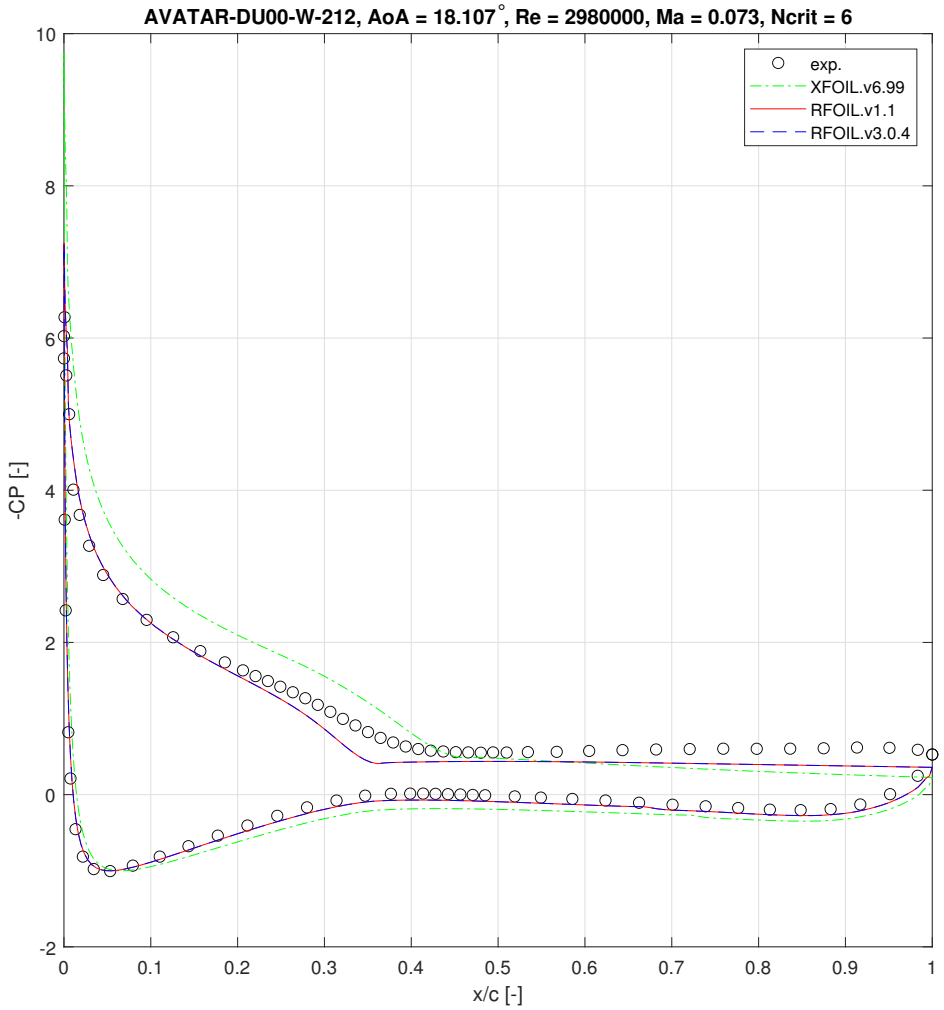

Figure C.312: Comparison between experimental and numerical pressure distributions for the AVATAR-DU00-W-212 airfoil at a Reynolds number of 5950000, and at an angle of attack and a Mach number of 18.119° and 0.054, respectively.

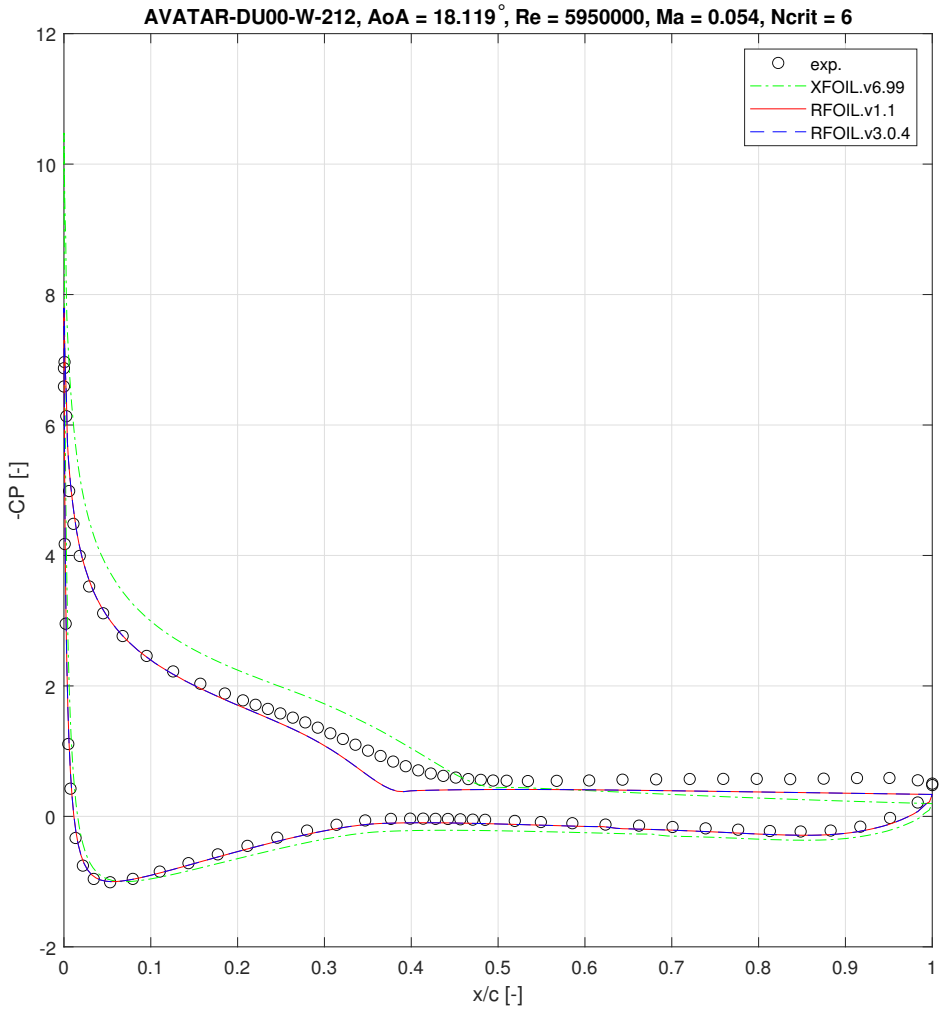

Figure C.313: Comparison between experimental and numerical pressure distributions for the AVATAR-DU00-W-212 airfoil at a Reynolds number of 5980000, and at an angle of attack and a Mach number of 18.119° and 0.029, respectively.

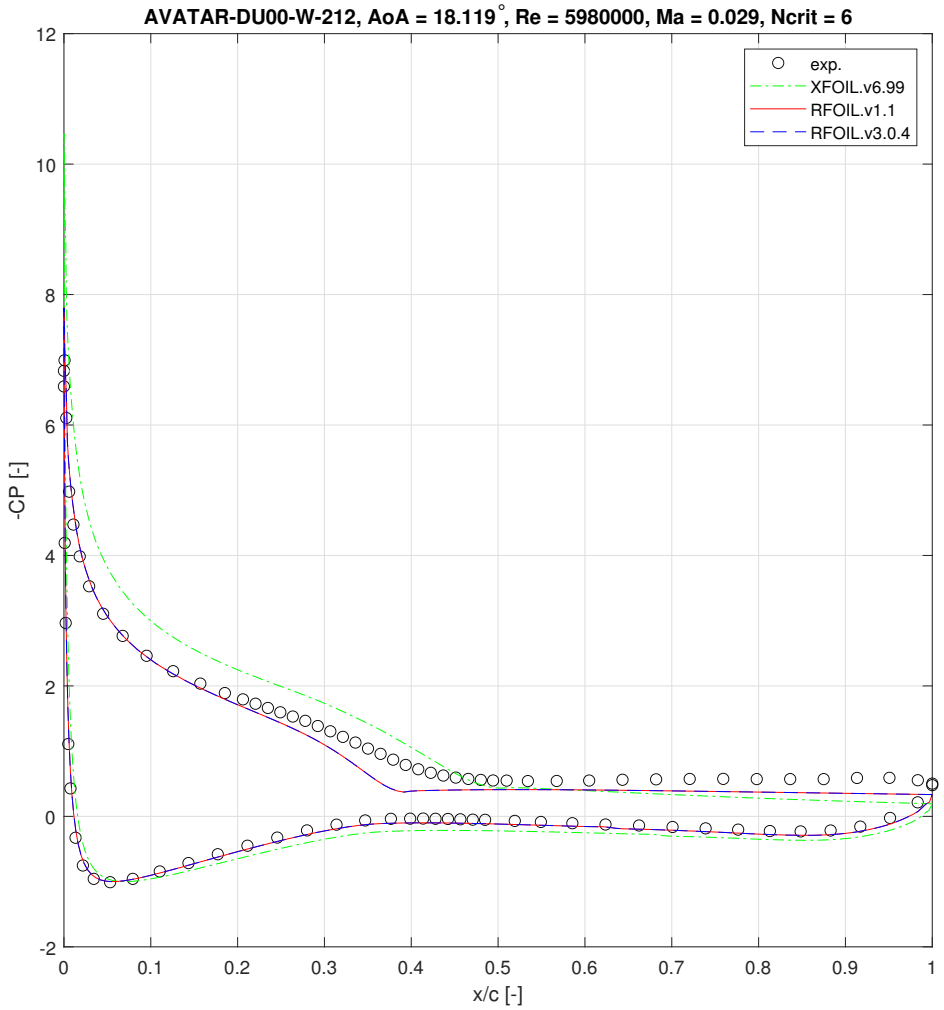

Figure C.314: Comparison between experimental and numerical pressure distributions for the AVATAR-DU00-W-212 airfoil at a Reynolds number of 8990000, and at an angle of attack and a Mach number of 18.128° and 0.043, respectively.

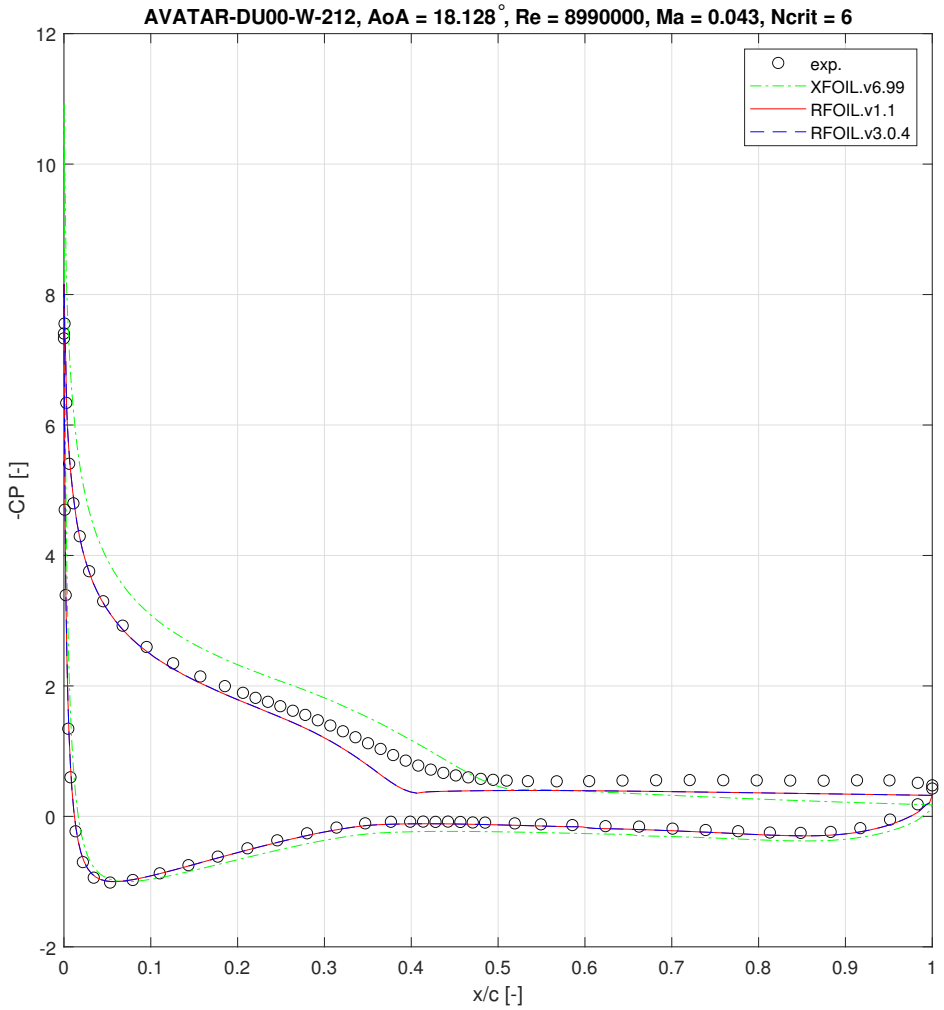

Figure C.315: Comparison between experimental and numerical pressure distributions for the AVATAR-DU00-W-212 airfoil at a Reynolds number of 8970000, and at an angle of attack and a Mach number of 18.130° and 0.082, respectively.

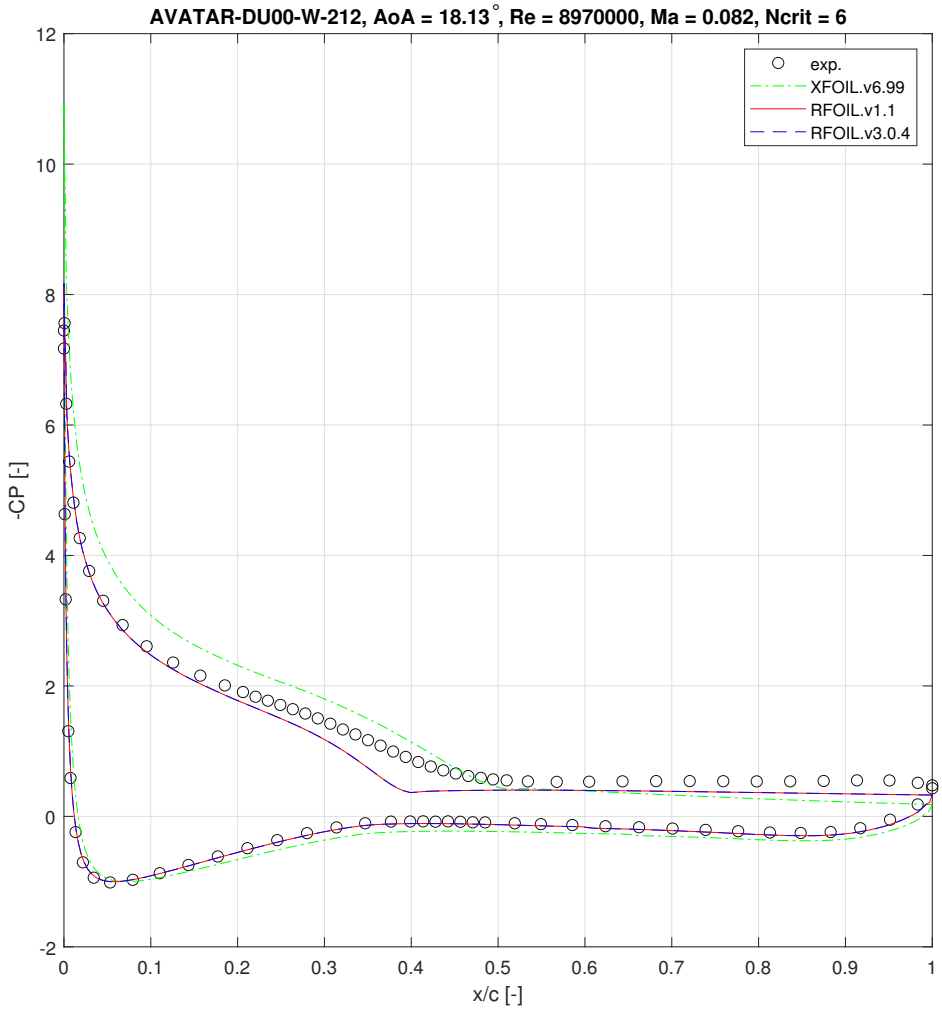

Figure C.316: Comparison between experimental and numerical pressure distributions for the AVATAR-DU00-W-212 airfoil at a Reynolds number of 15060000, and at an angle of attack and a Mach number of 18.147° and 0.082, respectively.

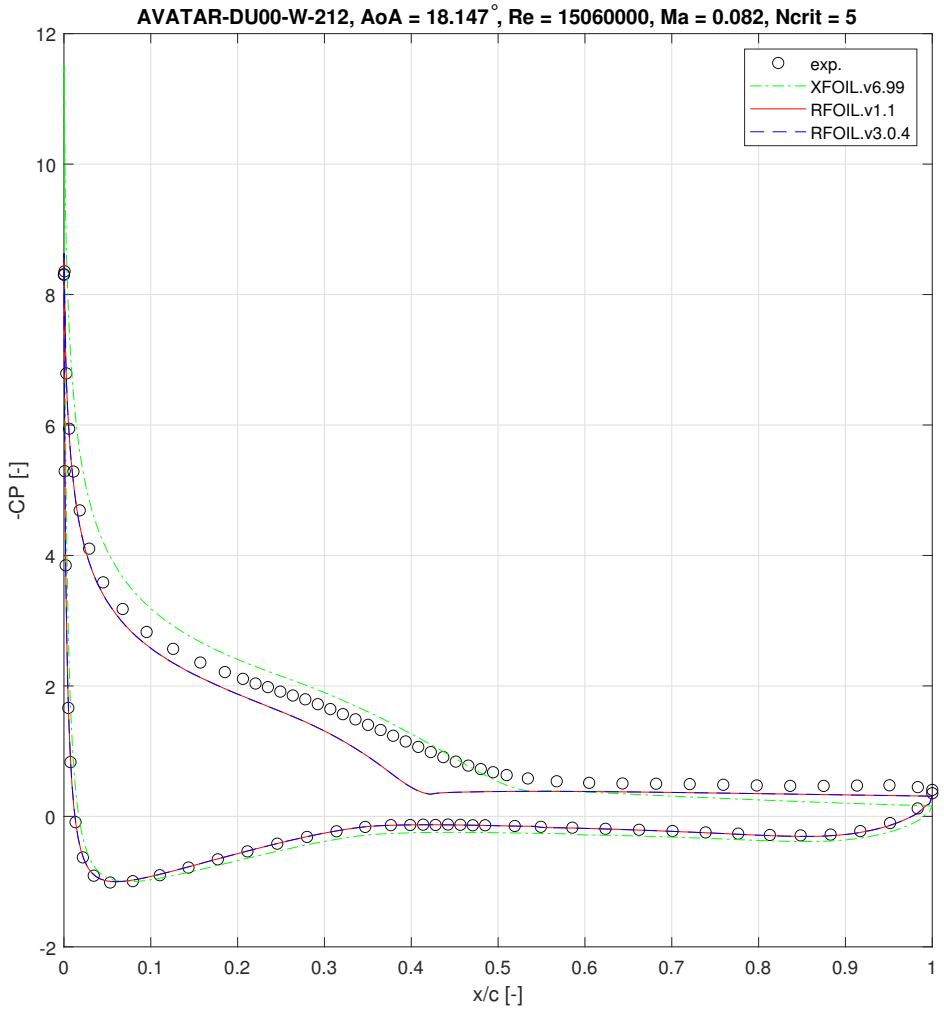

Figure C.317: Comparison between experimental and numerical pressure distributions for the AVATAR-DU00-W-212 airfoil at a Reynolds number of 11950000, and at an angle of attack and a Mach number of 19.010° and 0.057, respectively.

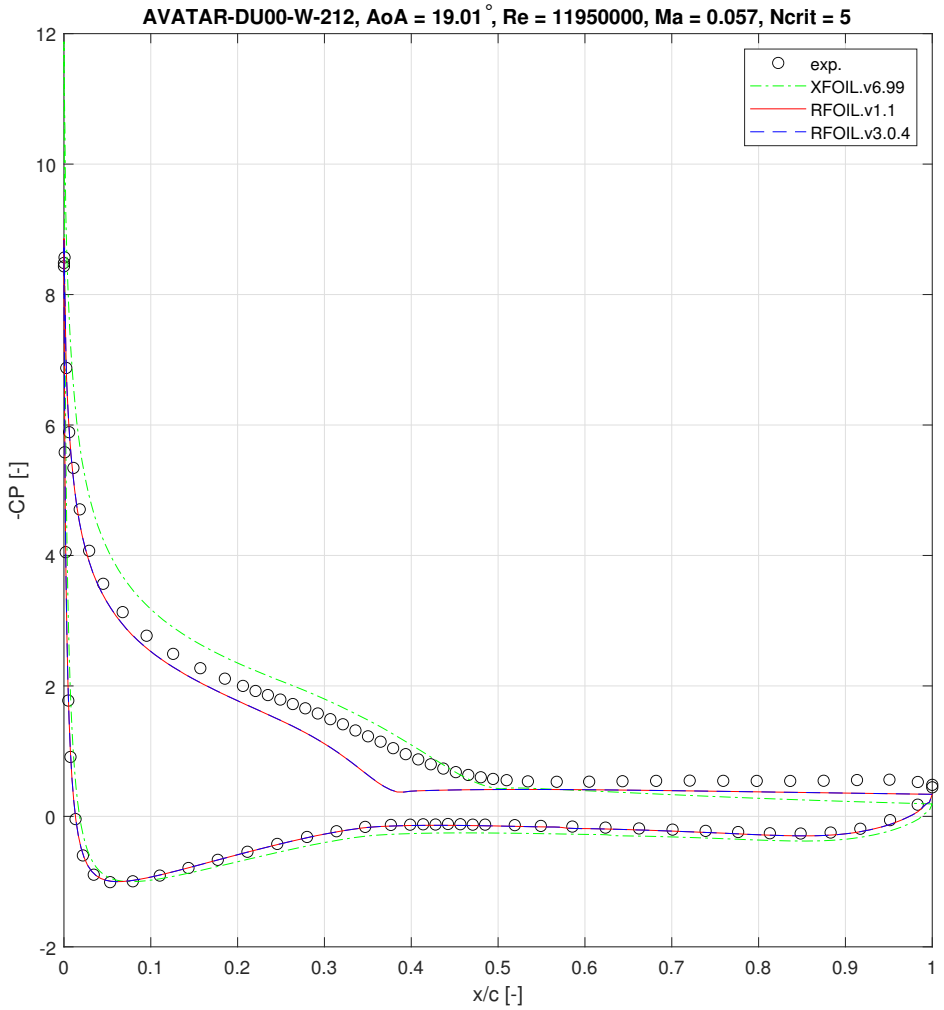

Figure C.318: Comparison between experimental and numerical pressure distributions for the AVATAR-DU00-W-212 airfoil at a Reynolds number of 3000000, and at an angle of attack and a Mach number of 19.105° and 0.074, respectively.

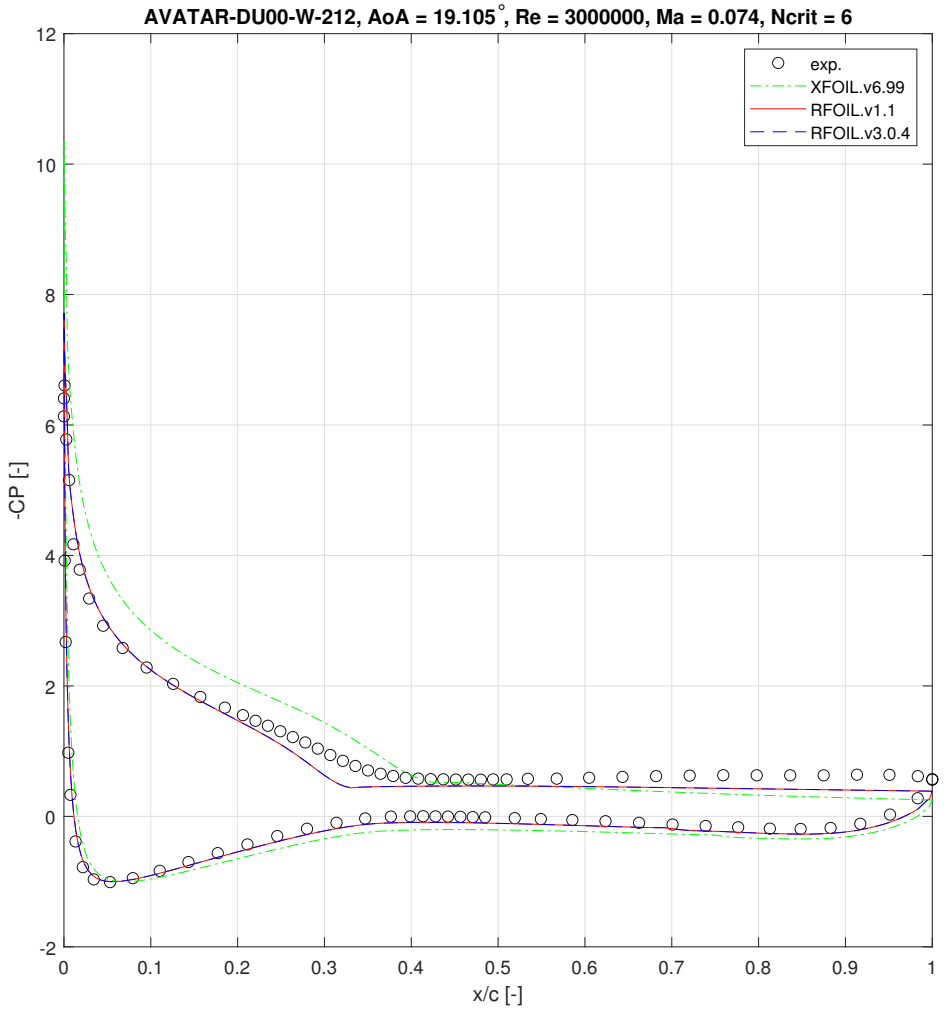

Figure C.319: Comparison between experimental and numerical pressure distributions for the AVATAR-DU00-W-212 airfoil at a Reynolds number of 5980000, and at an angle of attack and a Mach number of 19.118° and 0.029, respectively.

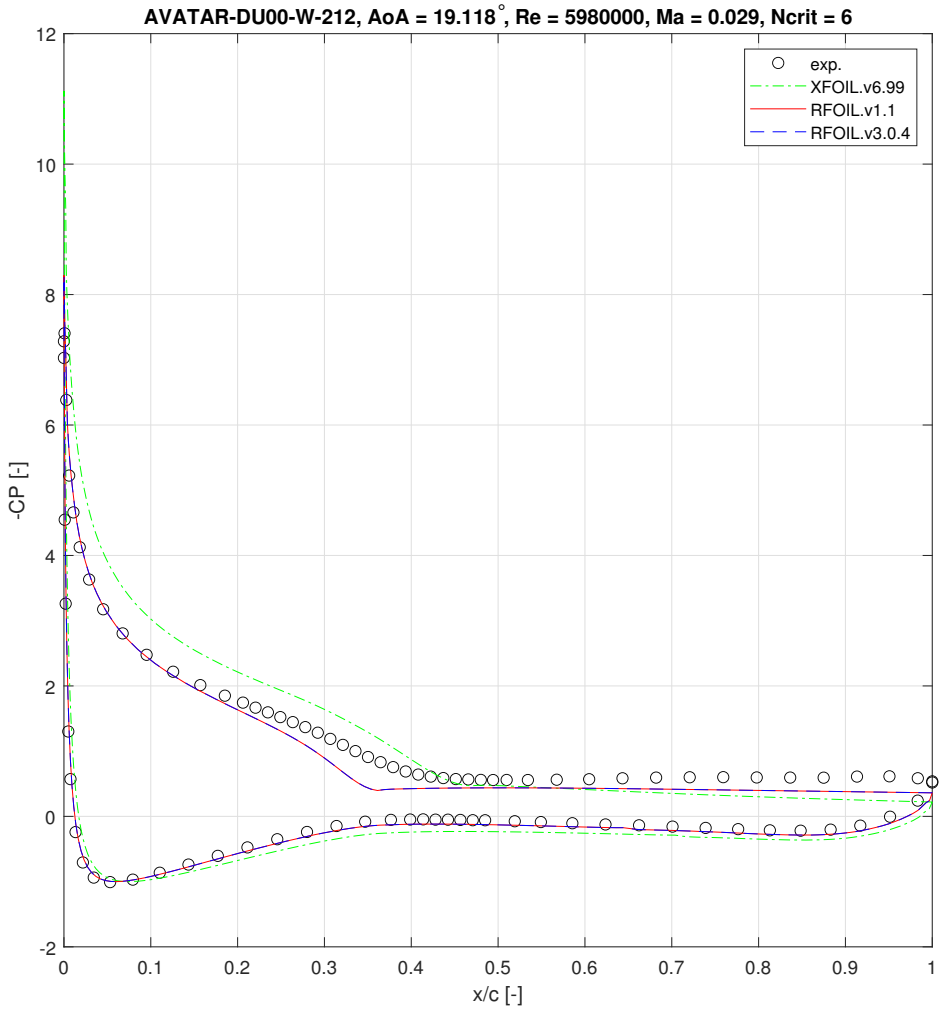

Figure C.320: Comparison between experimental and numerical pressure distributions for the AVATAR-DU00-W-212 airfoil at a Reynolds number of 5980000, and at an angle of attack and a Mach number of 19.119° and 0.055, respectively.

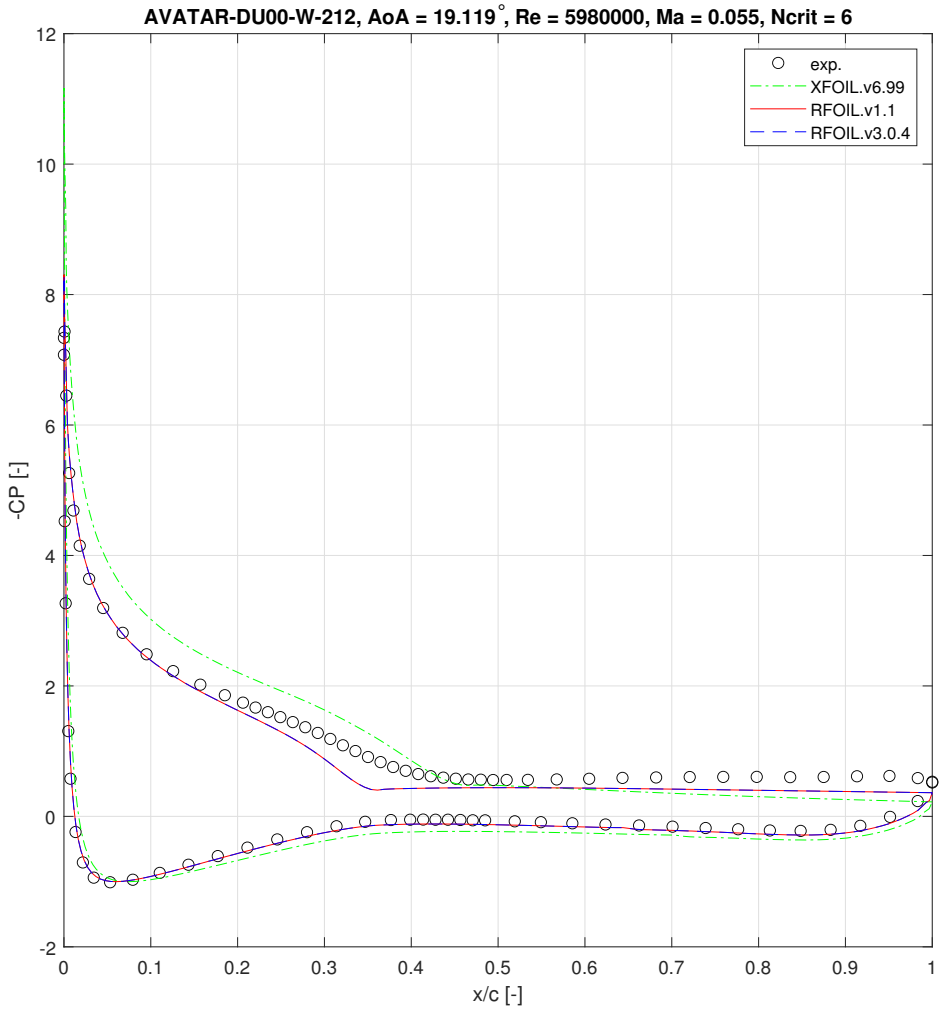

Figure C.321: Comparison between experimental and numerical pressure distributions for the AVATAR-DU00-W-212 airfoil at a Reynolds number of 8940000, and at an angle of attack and a Mach number of 19.132° and 0.082, respectively.

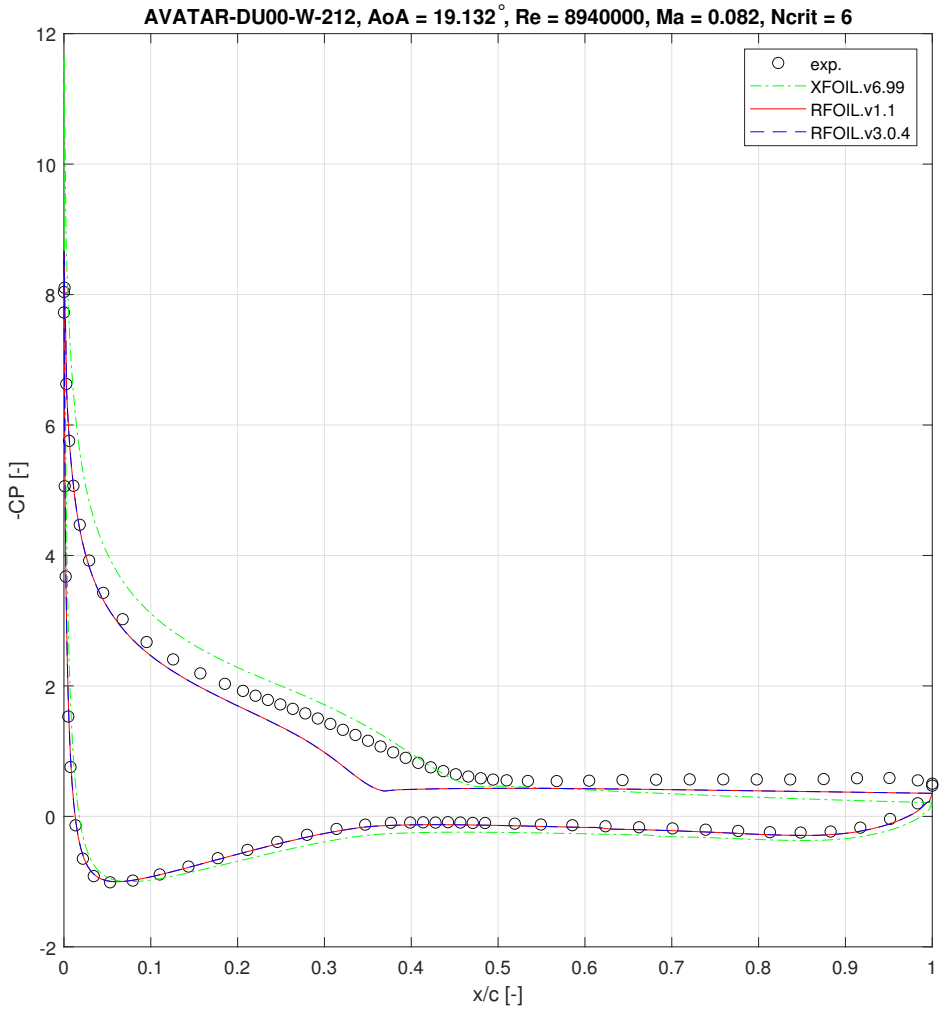

Figure C.322: Comparison between experimental and numerical pressure distributions for the AVATAR-DU00-W-212 airfoil at a Reynolds number of 8980000, and at an angle of attack and a Mach number of 19.133° and 0.043, respectively.

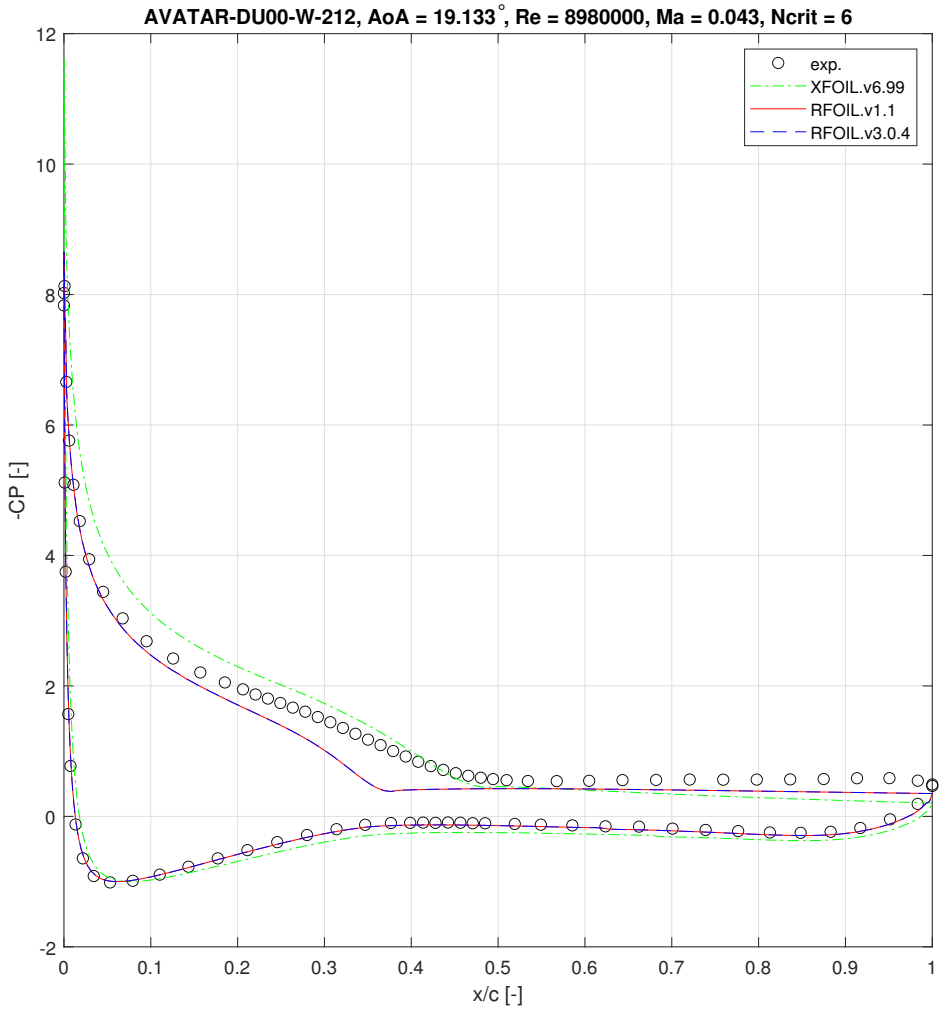

Figure C.323: Comparison between experimental and numerical pressure distributions for the AVATAR-DU00-W-212 airfoil at a Reynolds number of 14990000, and at an angle of attack and a Mach number of 19.145° and 0.081, respectively.

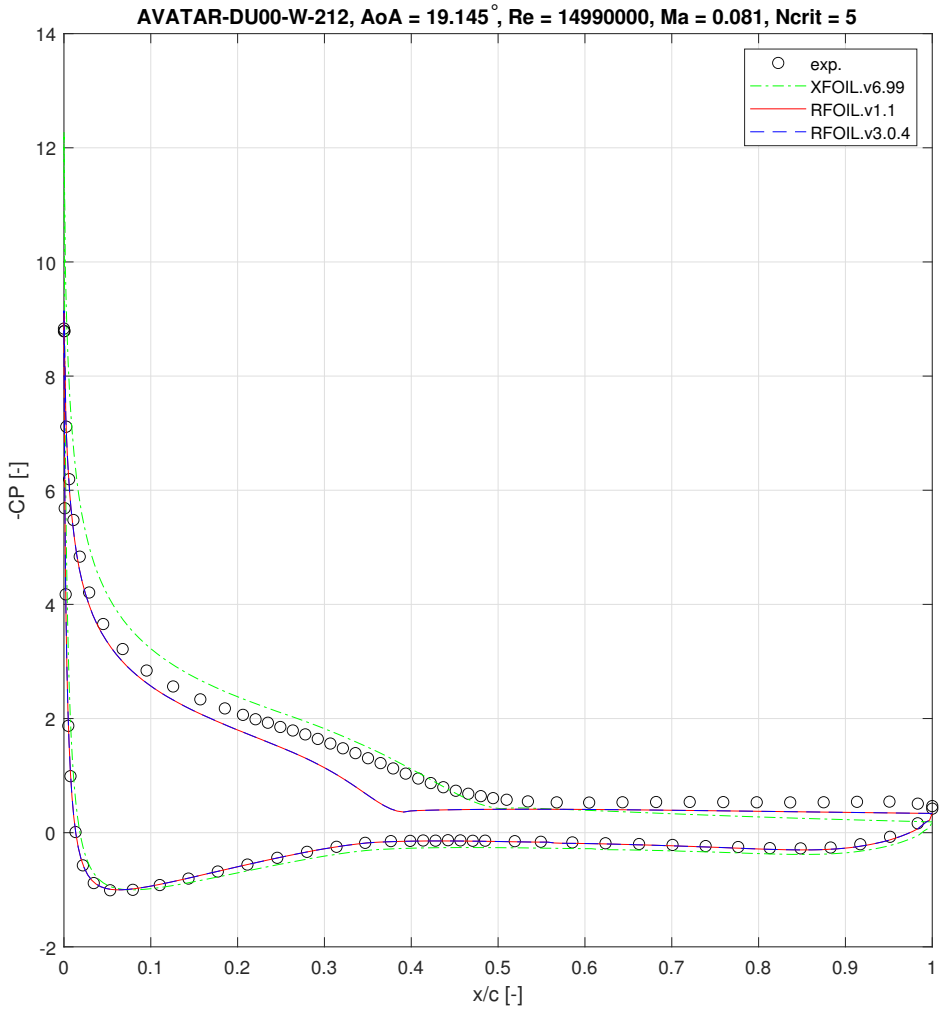

Figure C.324: Comparison between experimental and numerical pressure distributions for the AVATAR-DU00-W-212 airfoil at a Reynolds number of 14970000, and at an angle of attack and a Mach number of 1.011° and 0.081, respectively.

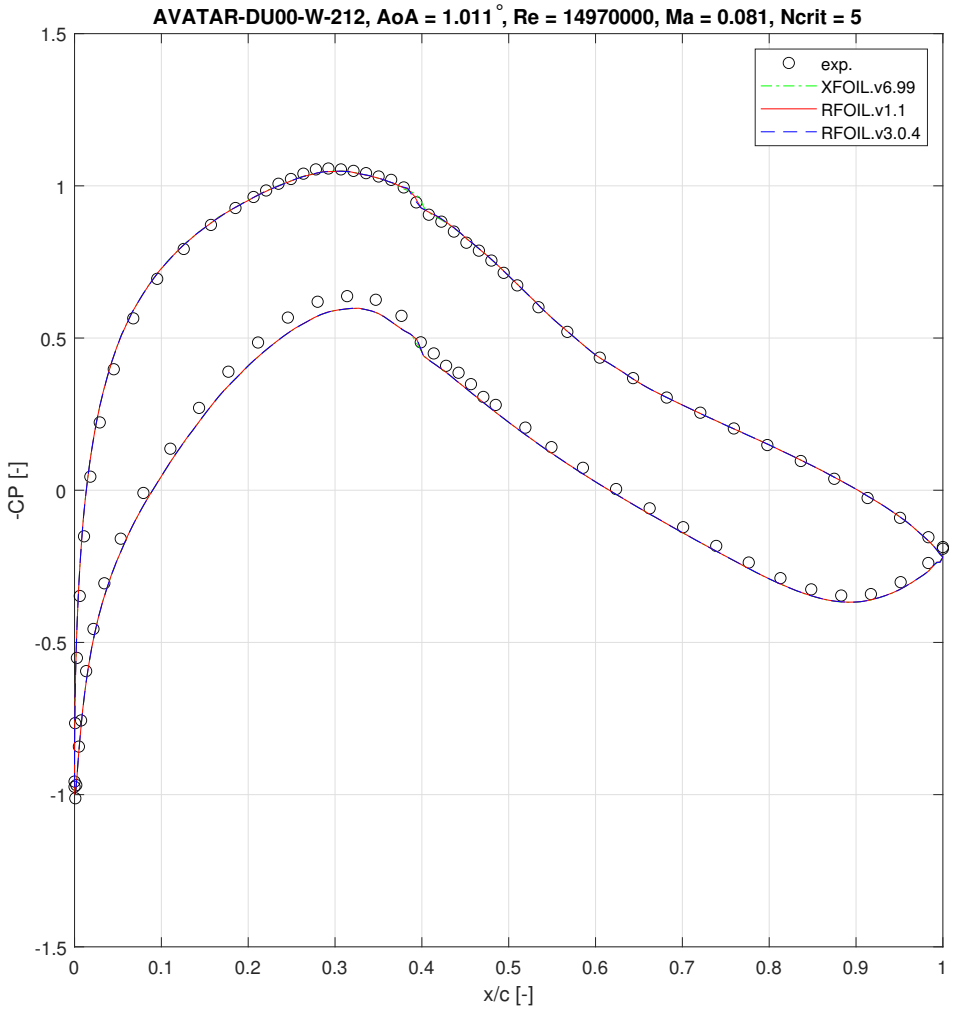

Figure C.325: Comparison between experimental and numerical pressure distributions for the AVATAR-DU00-W-212 airfoil at a Reynolds number of 5980000, and at an angle of attack and a Mach number of 1.011° and 0.055, respectively.

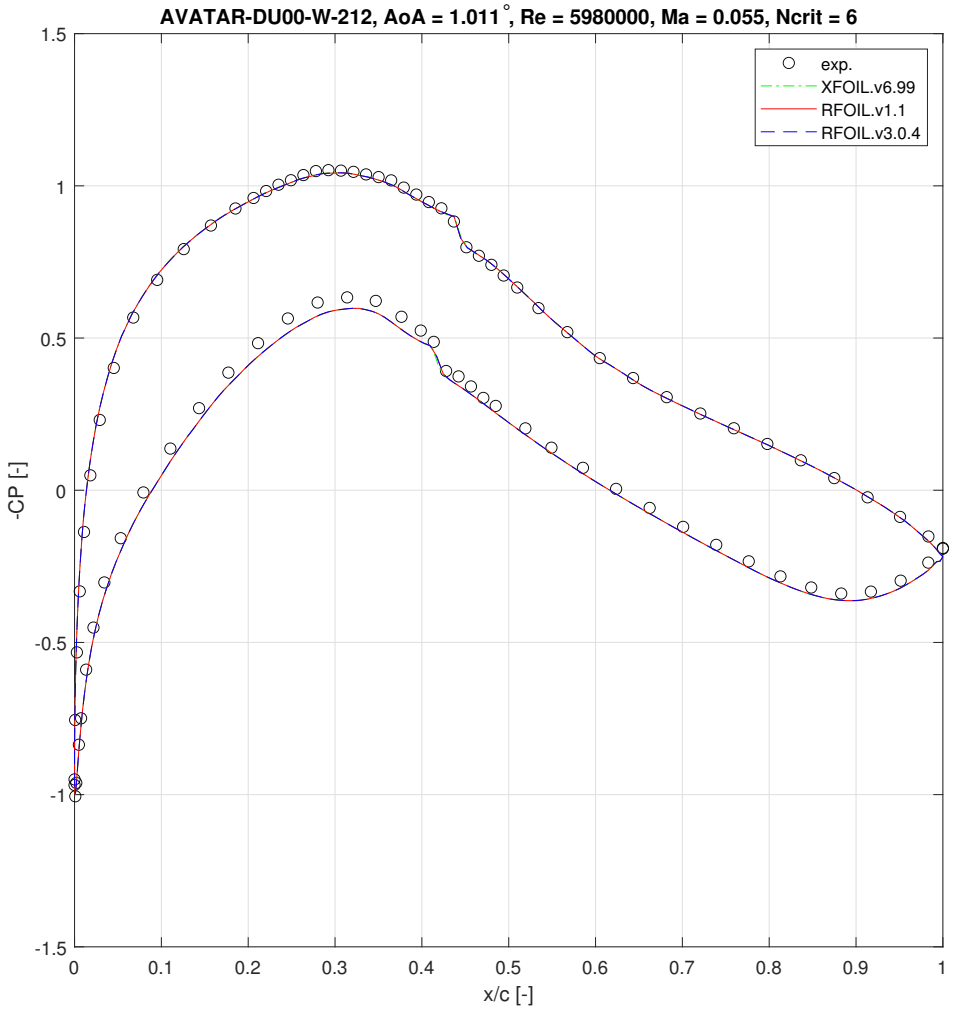

Figure C.326: Comparison between experimental and numerical pressure distributions for the AVATAR-DU00-W-212 airfoil at a Reynolds number of 9000000, and at an angle of attack and a Mach number of 1.011° and 0.083, respectively.

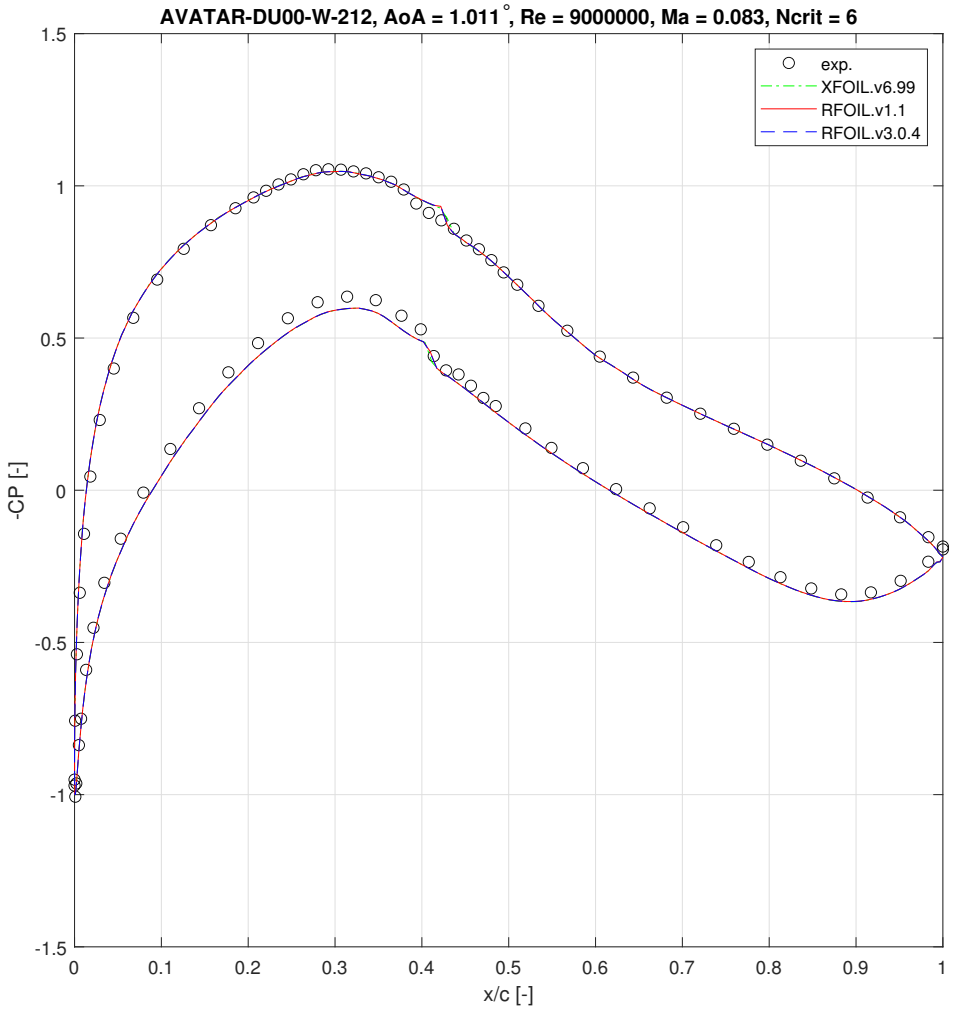

Figure C.327: Comparison between experimental and numerical pressure distributions for the AVATAR-DU00-W-212 airfoil at a Reynolds number of 3000000, and at an angle of attack and a Mach number of 1.012° and 0.074, respectively.

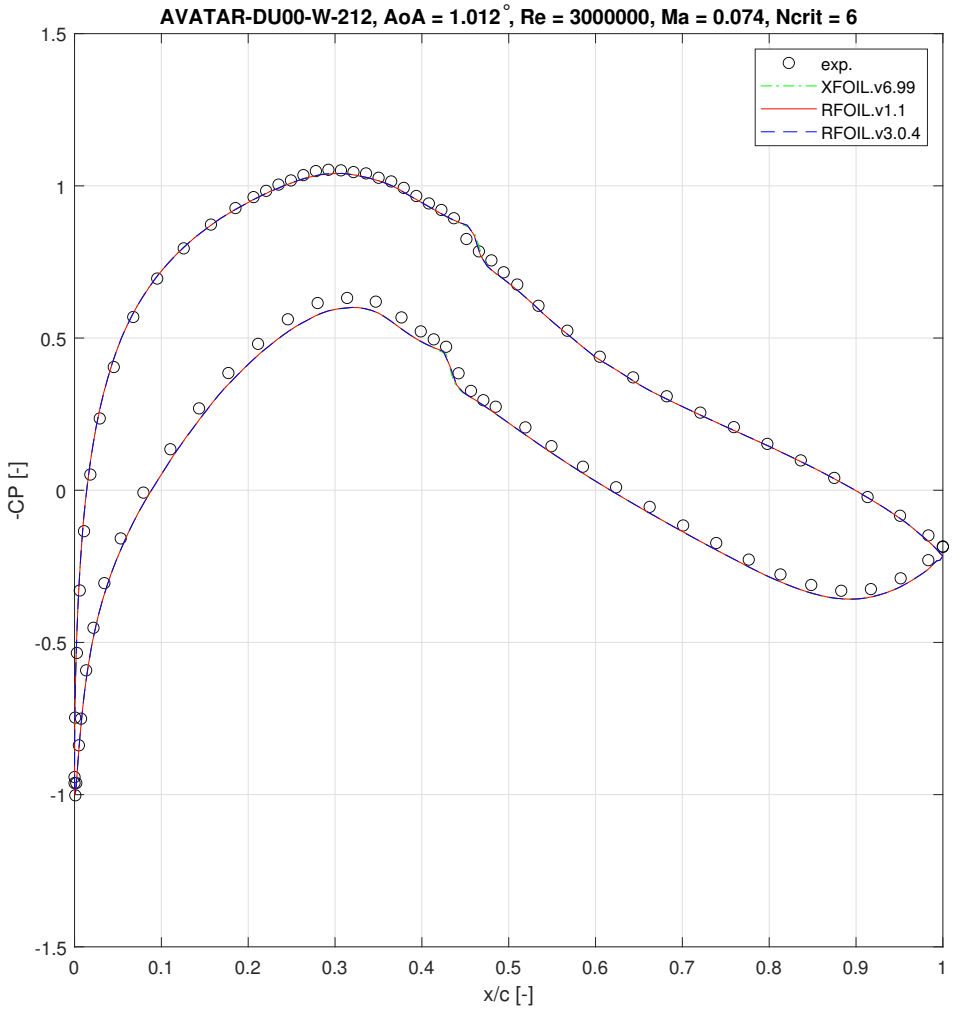

Figure C.328: Comparison between experimental and numerical pressure distributions for the AVATAR-DU00-W-212 airfoil at a Reynolds number of 5990000, and at an angle of attack and a Mach number of 1.010° and 0.029, respectively.

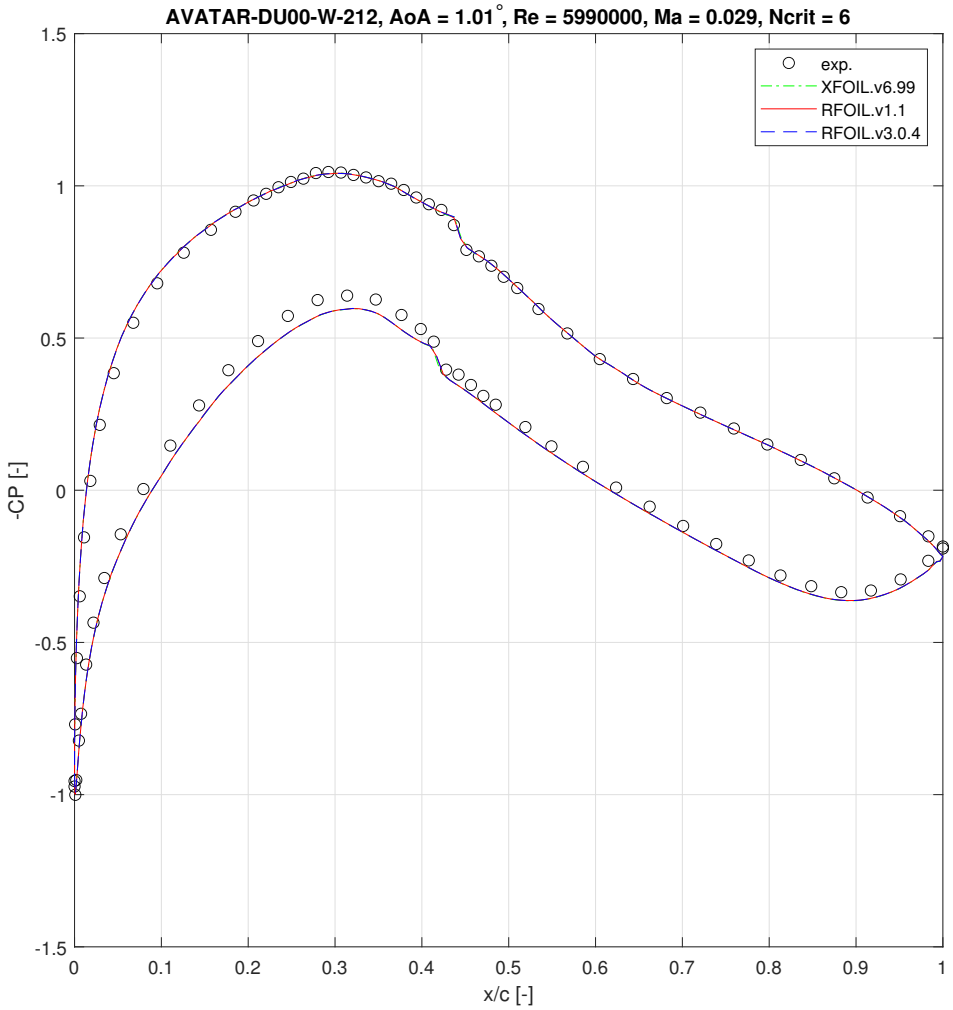

Figure C.329: Comparison between experimental and numerical pressure distributions for the AVATAR-DU00-W-212 airfoil at a Reynolds number of 8960000, and at an angle of attack and a Mach number of 1.010° and 0.043, respectively.

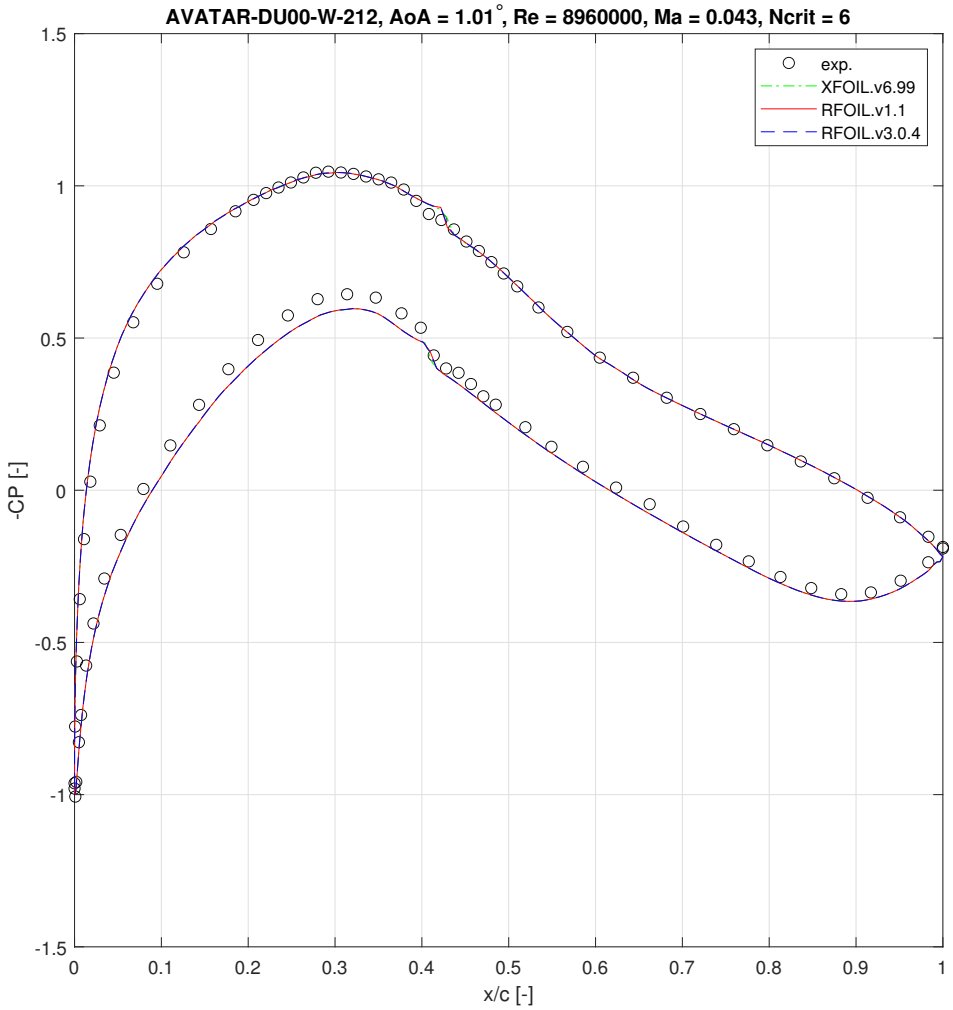

Figure C.330: Comparison between experimental and numerical pressure distributions for the AVATAR-DU00-W-212 airfoil at a Reynolds number of 11920000, and at an angle of attack and a Mach number of 1.040° and 0.057, respectively.

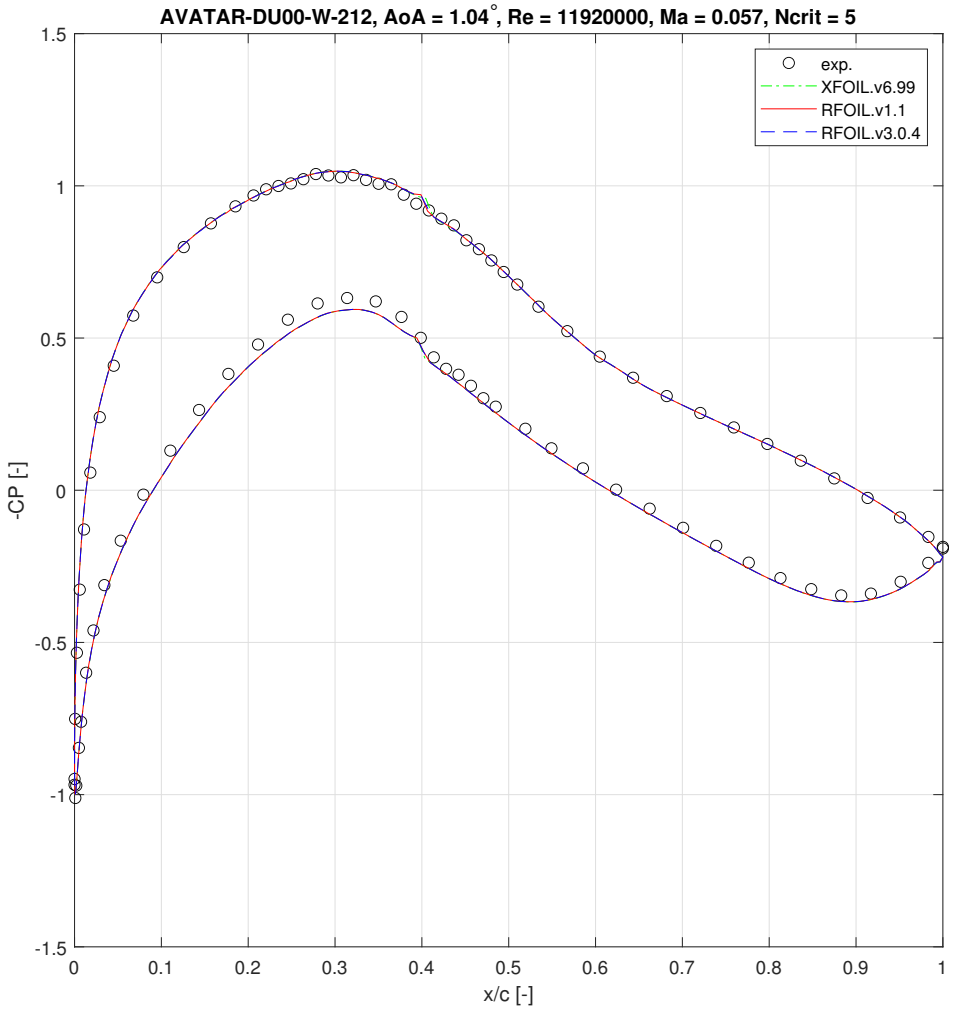

Figure C.331: Comparison between experimental and numerical pressure distributions for the AVATAR-DU00-W-212 airfoil at a Reynolds number of 14990000, and at an angle of attack and a Mach number of 1.518° and 0.081, respectively.

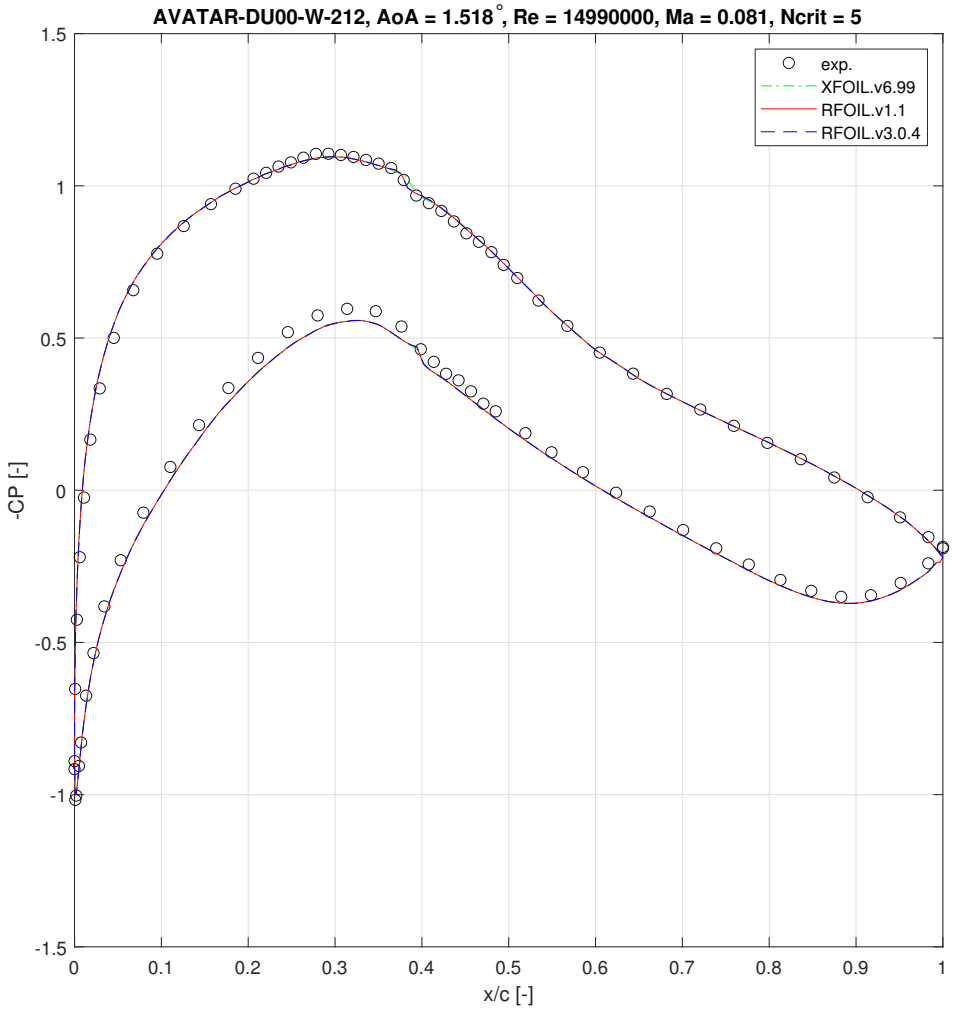

Figure C.332: Comparison between experimental and numerical pressure distributions for the AVATAR-DU00-W-212 airfoil at a Reynolds number of 11980000, and at an angle of attack and a Mach number of 1.542° and 0.058, respectively.

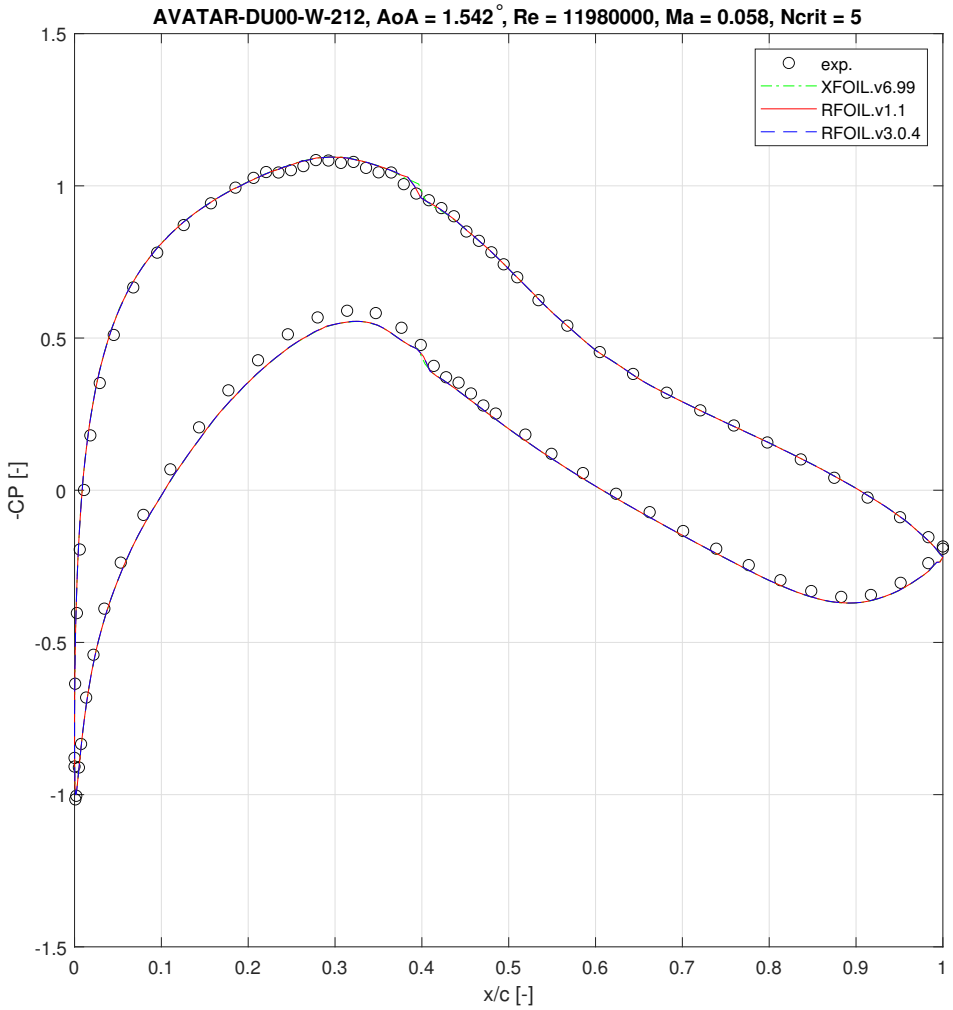

Figure C.333: Comparison between experimental and numerical pressure distributions for the AVATAR-DU00-W-212 airfoil at a Reynolds number of 6020000, and at an angle of attack and a Mach number of 2.023° and 0.029, respectively.

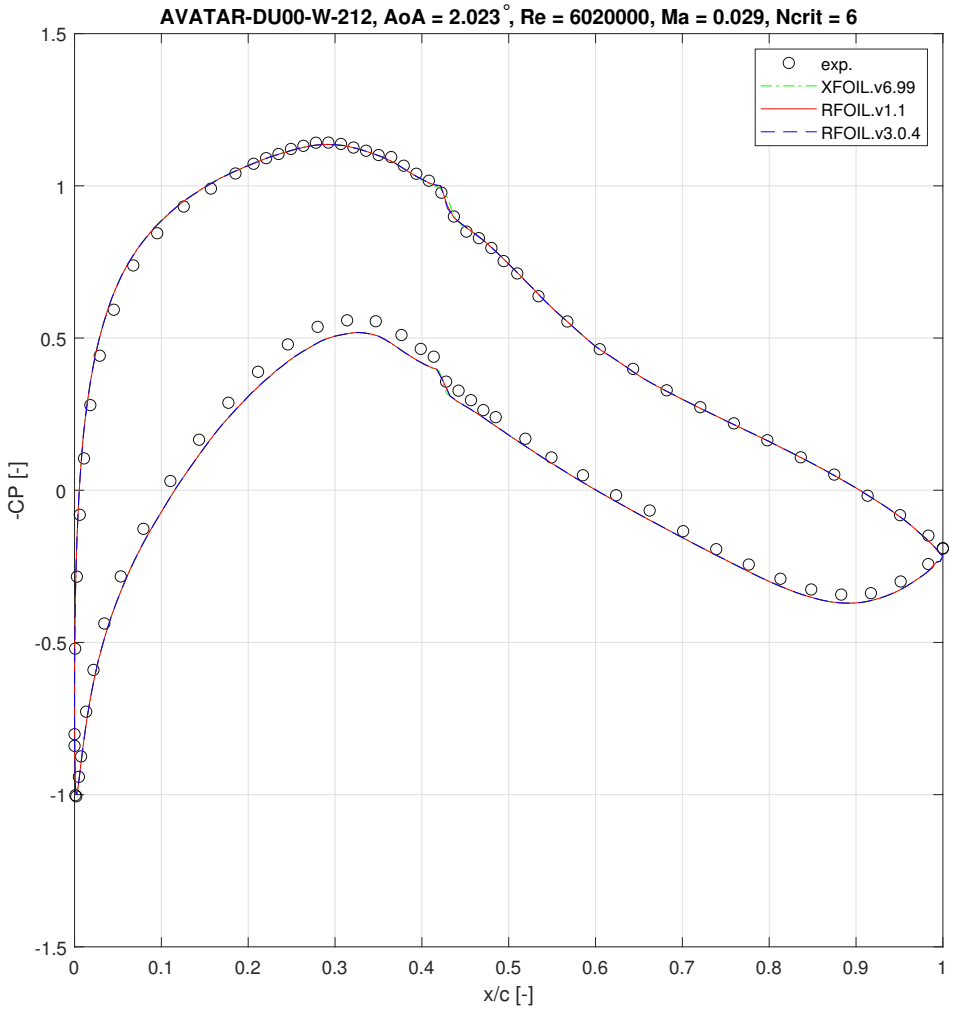

Figure C.334: Comparison between experimental and numerical pressure distributions for the AVATAR-DU00-W-212 airfoil at a Reynolds number of 8990000, and at an angle of attack and a Mach number of 2.023° and 0.043, respectively.

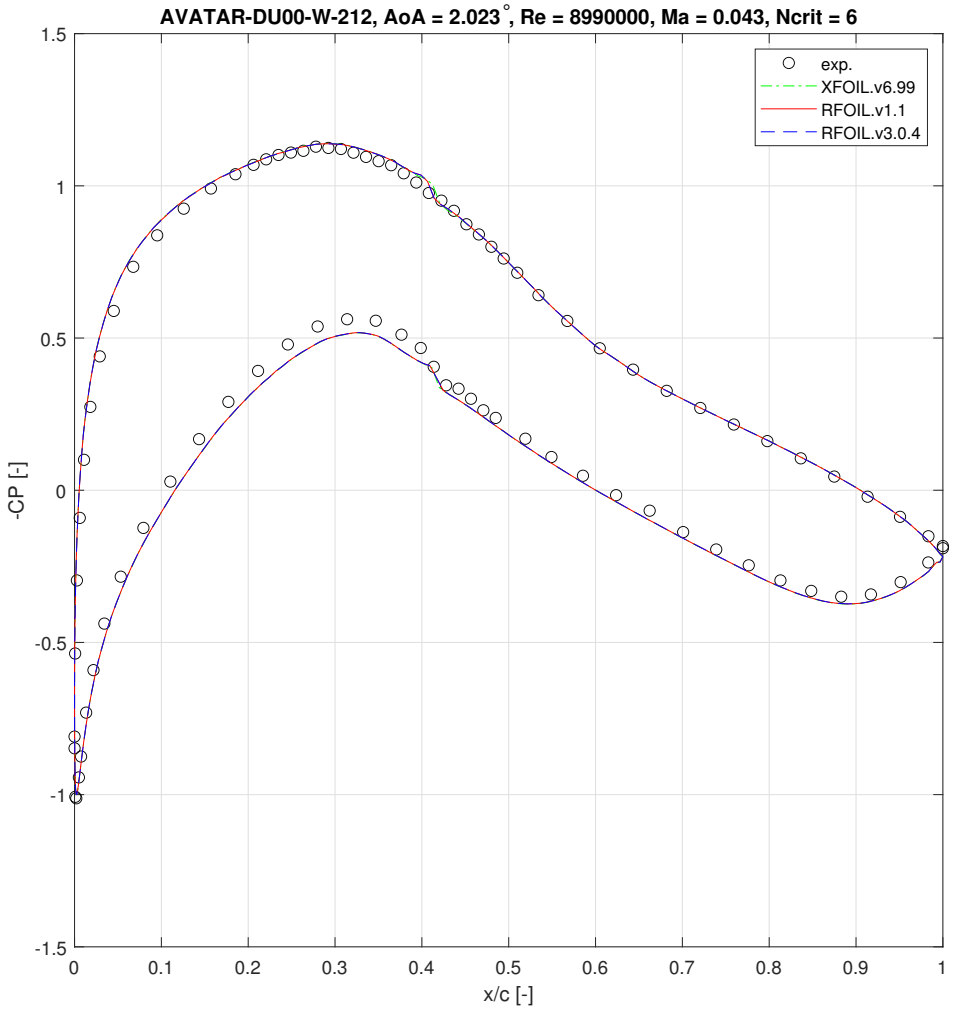

Figure C.335: Comparison between experimental and numerical pressure distributions for the AVATAR-DU00-W-212 airfoil at a Reynolds number of 14990000, and at an angle of attack and a Mach number of 2.024° and 0.081, respectively.

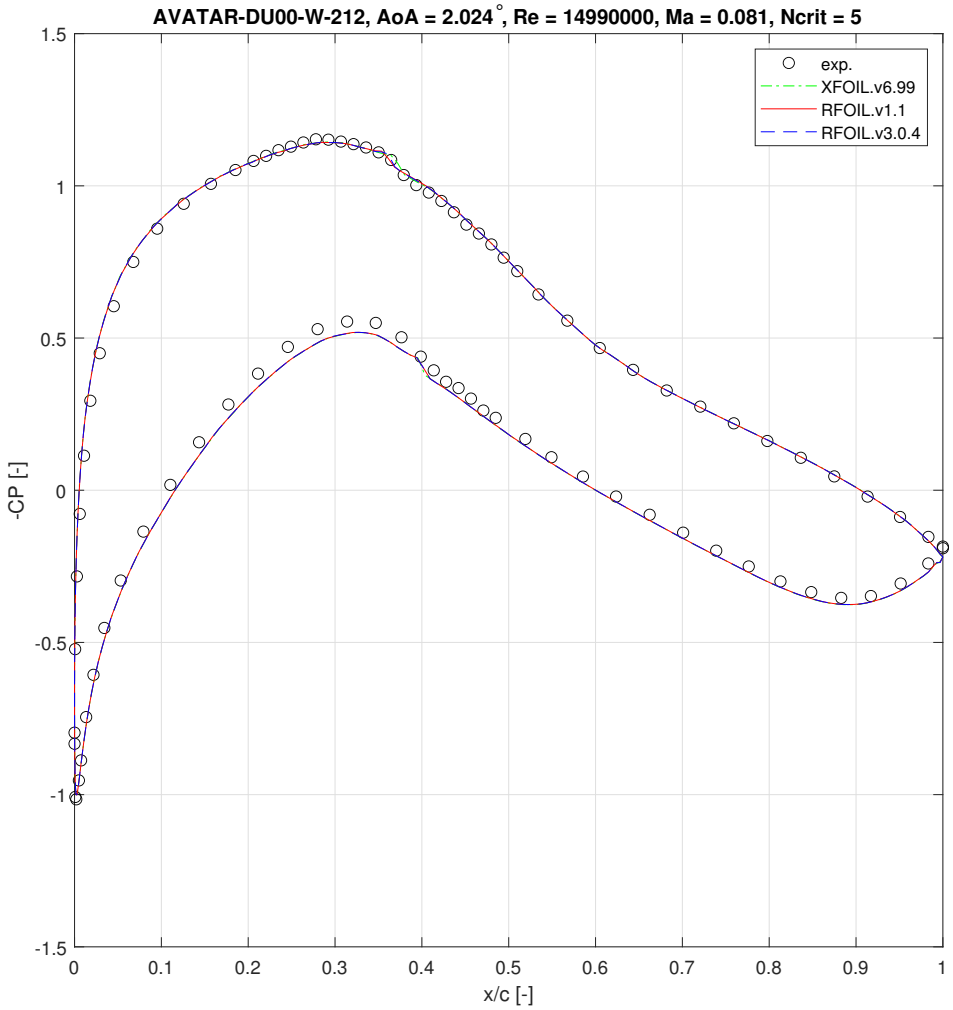

Figure C.336: Comparison between experimental and numerical pressure distributions for the AVATAR-DU00-W-212 airfoil at a Reynolds number of 6000000, and at an angle of attack and a Mach number of 2.024° and 0.055, respectively.

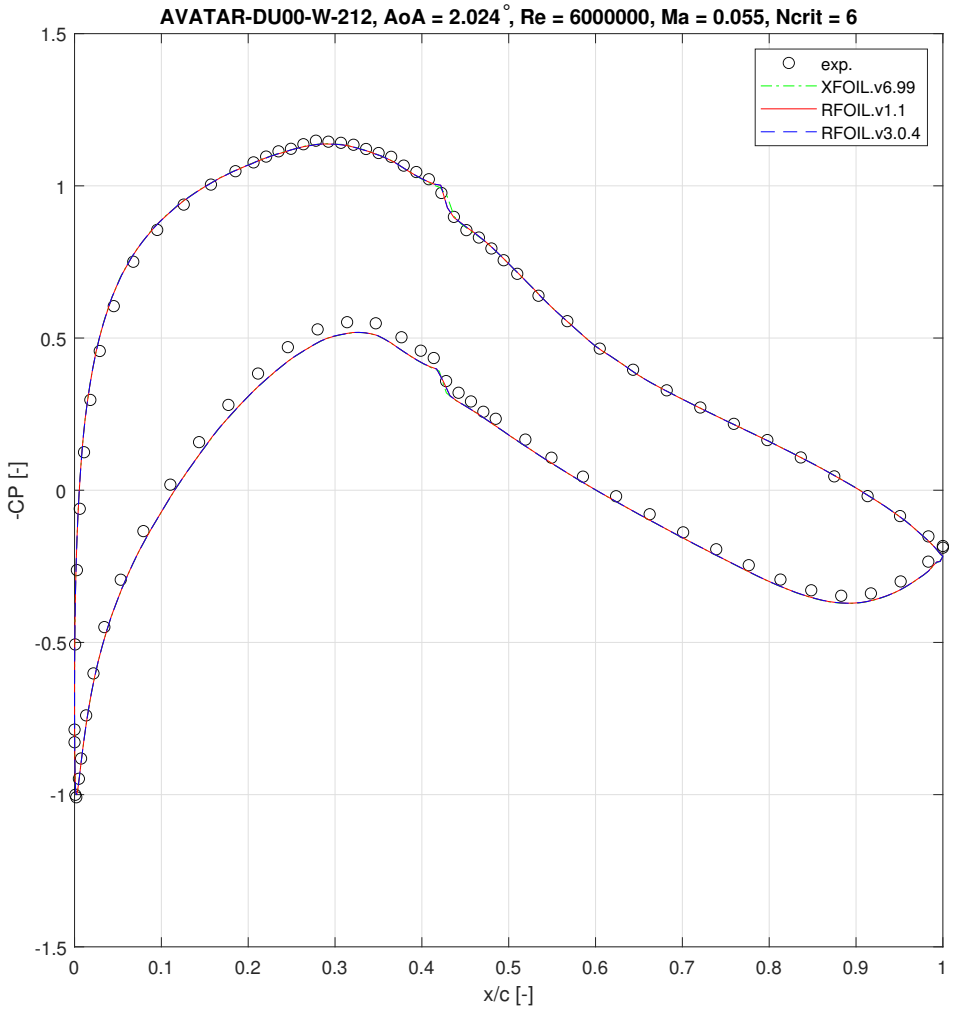

Figure C.337: Comparison between experimental and numerical pressure distributions for the AVATAR-DU00-W-212 airfoil at a Reynolds number of 8970000, and at an angle of attack and a Mach number of 2.024° and 0.082, respectively.

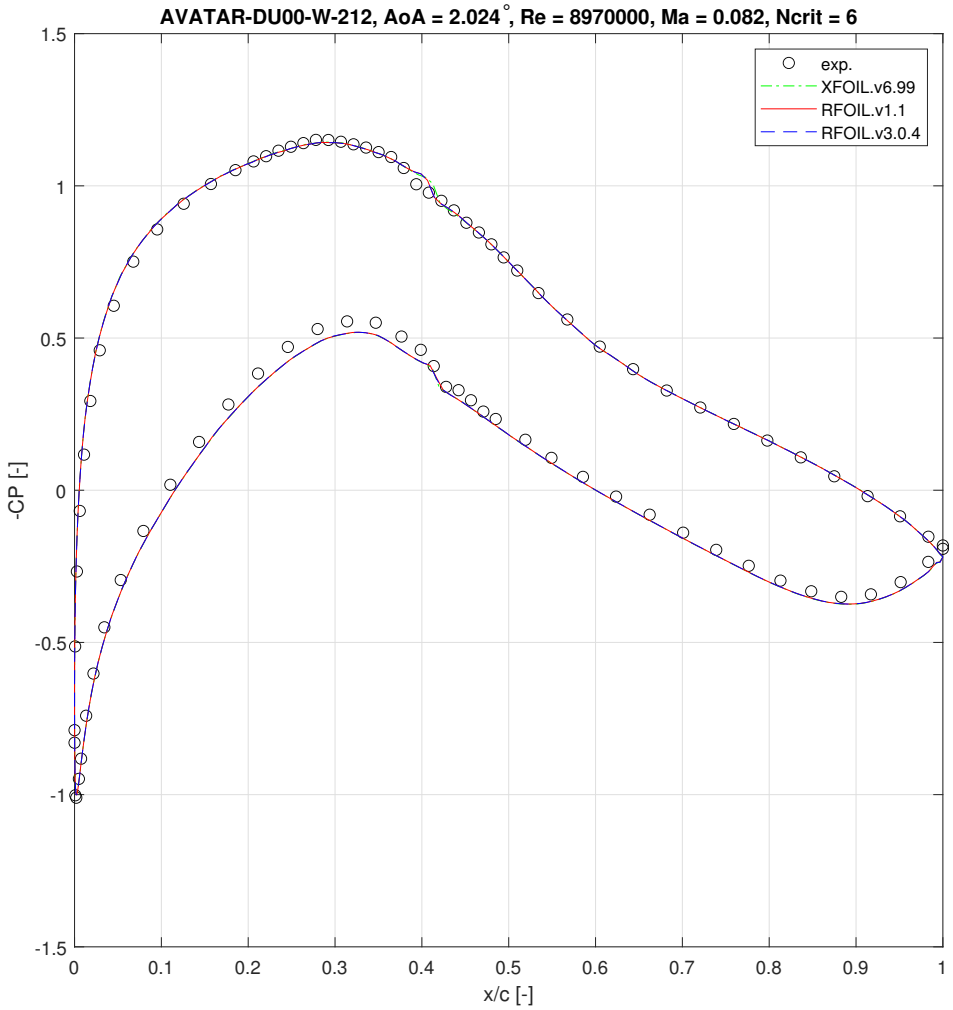

Figure C.338: Comparison between experimental and numerical pressure distributions for the AVATAR-DU00-W-212 airfoil at a Reynolds number of 2990000, and at an angle of attack and a Mach number of 2.025° and 0.074, respectively.

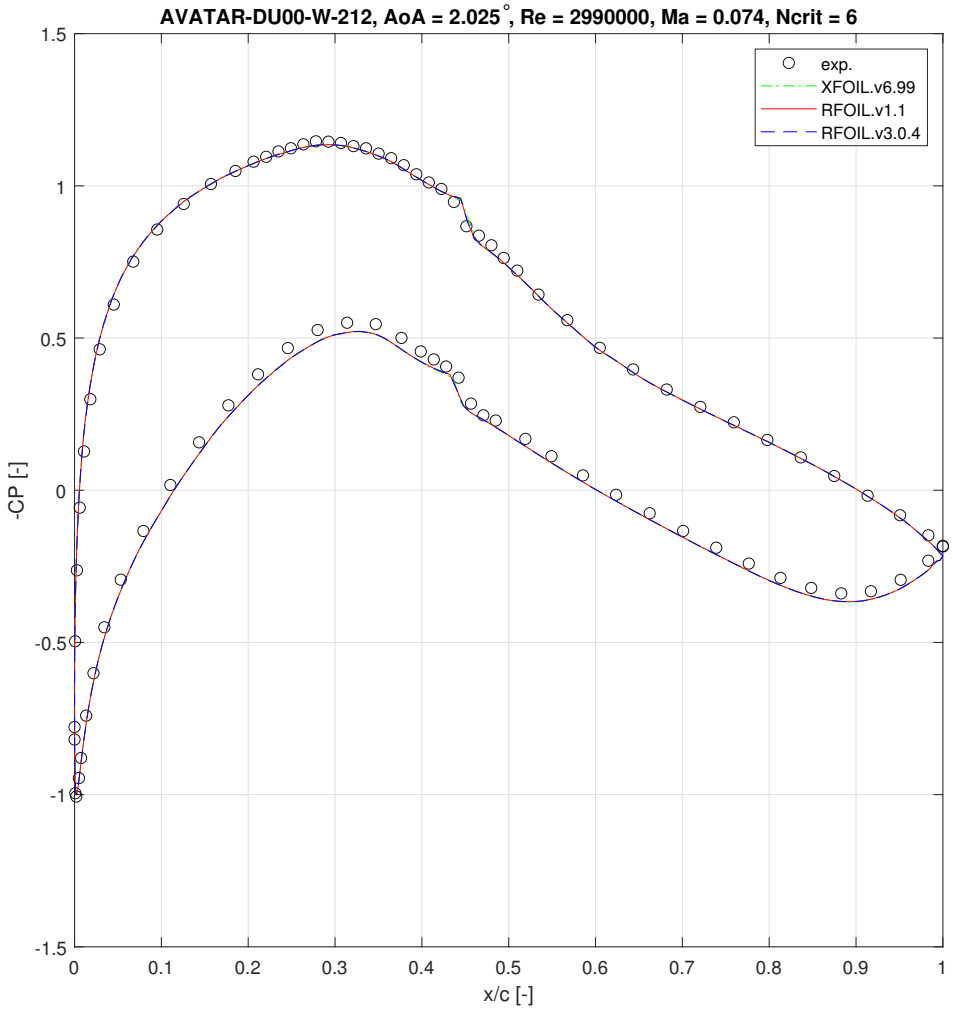

Figure C.339: Comparison between experimental and numerical pressure distributions for the AVATAR-DU00-W-212 airfoil at a Reynolds number of 12010000, and at an angle of attack and a Mach number of 2.039° and 0.058, respectively.

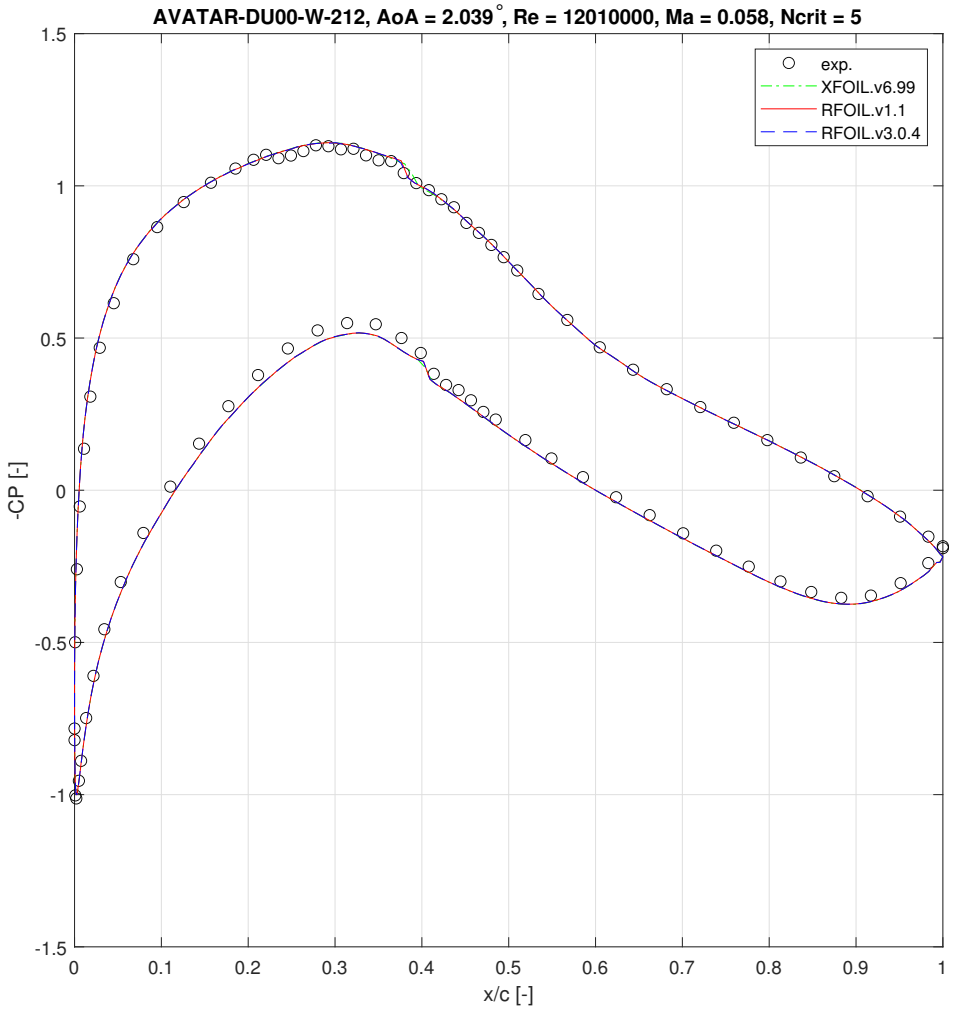

Figure C.340: Comparison between experimental and numerical pressure distributions for the AVATAR-DU00-W-212 airfoil at a Reynolds number of 8970000, and at an angle of attack and a Mach number of 3.036° and 0.043, respectively.

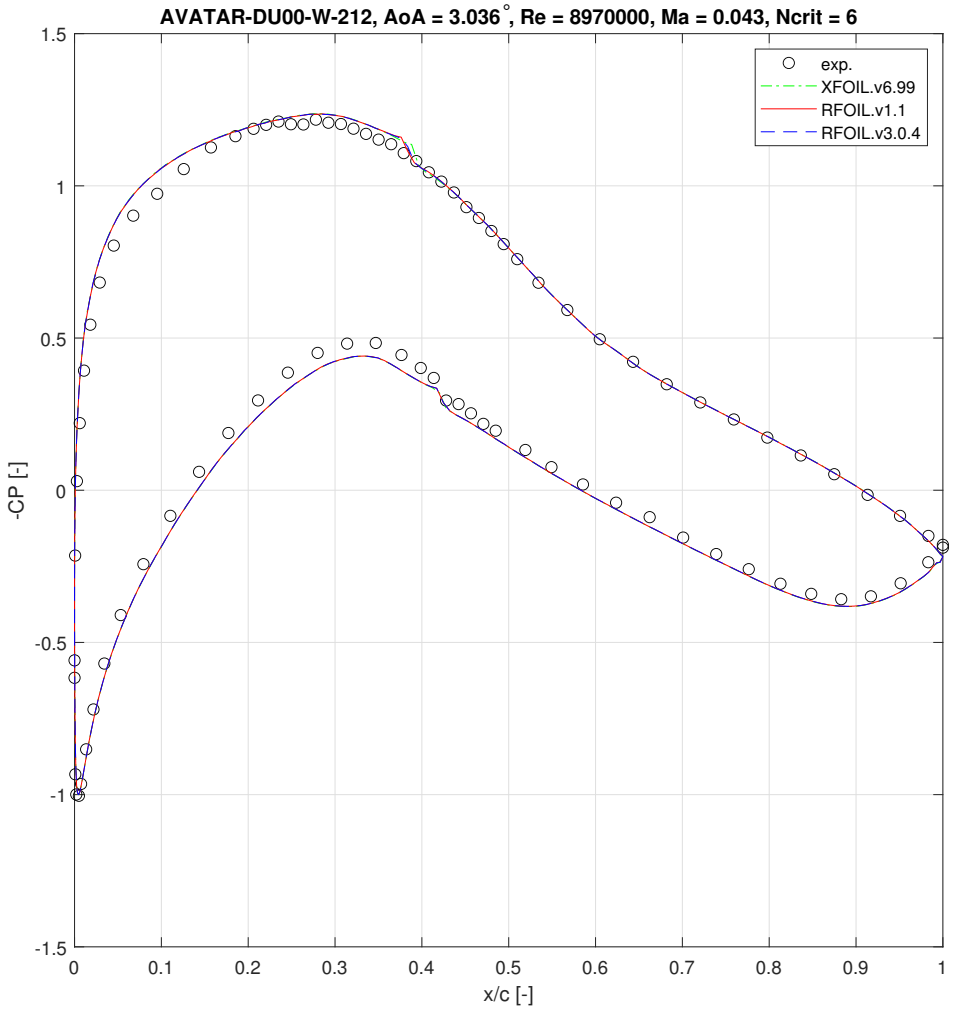

Figure C.341: Comparison between experimental and numerical pressure distributions for the AVATAR-DU00-W-212 airfoil at a Reynolds number of 15000000, and at an angle of attack and a Mach number of 3.037° and 0.081, respectively.

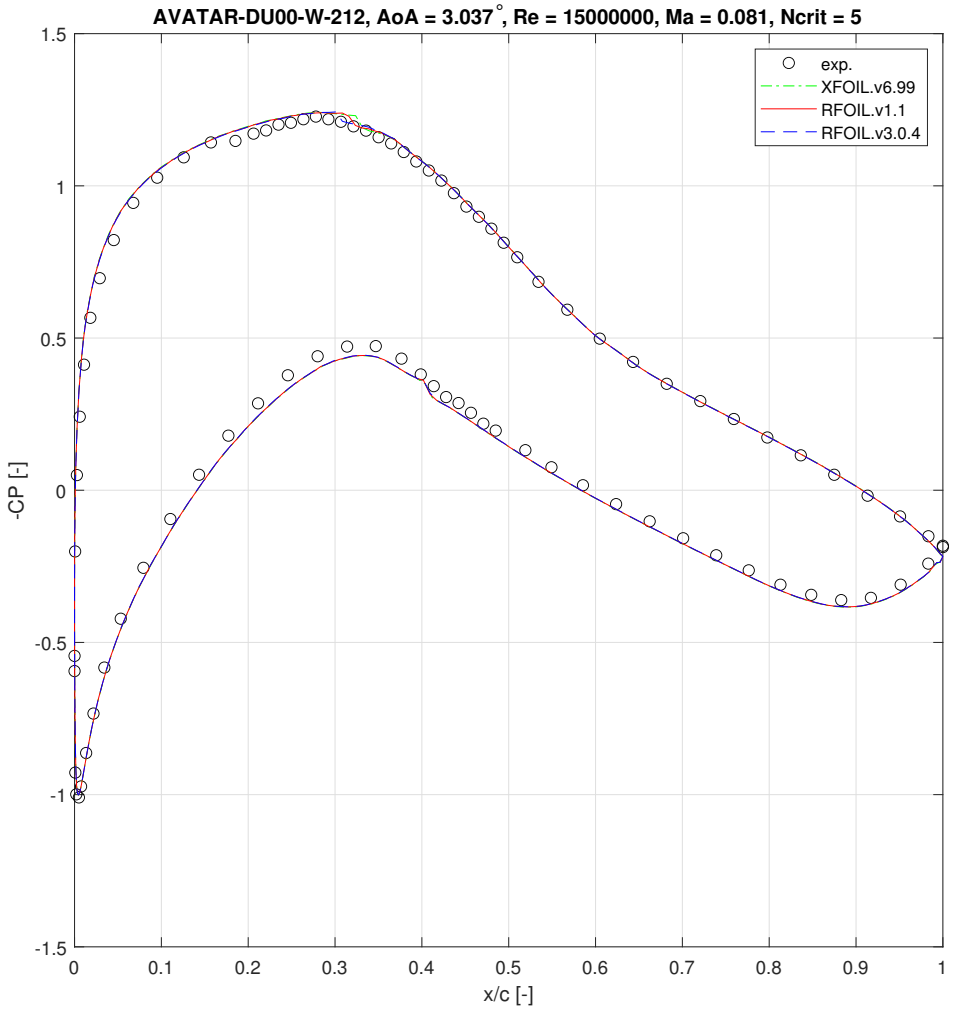

Figure C.342: Comparison between experimental and numerical pressure distributions for the AVATAR-DU00-W-212 airfoil at a Reynolds number of 5930000, and at an angle of attack and a Mach number of 3.037° and 0.029, respectively.

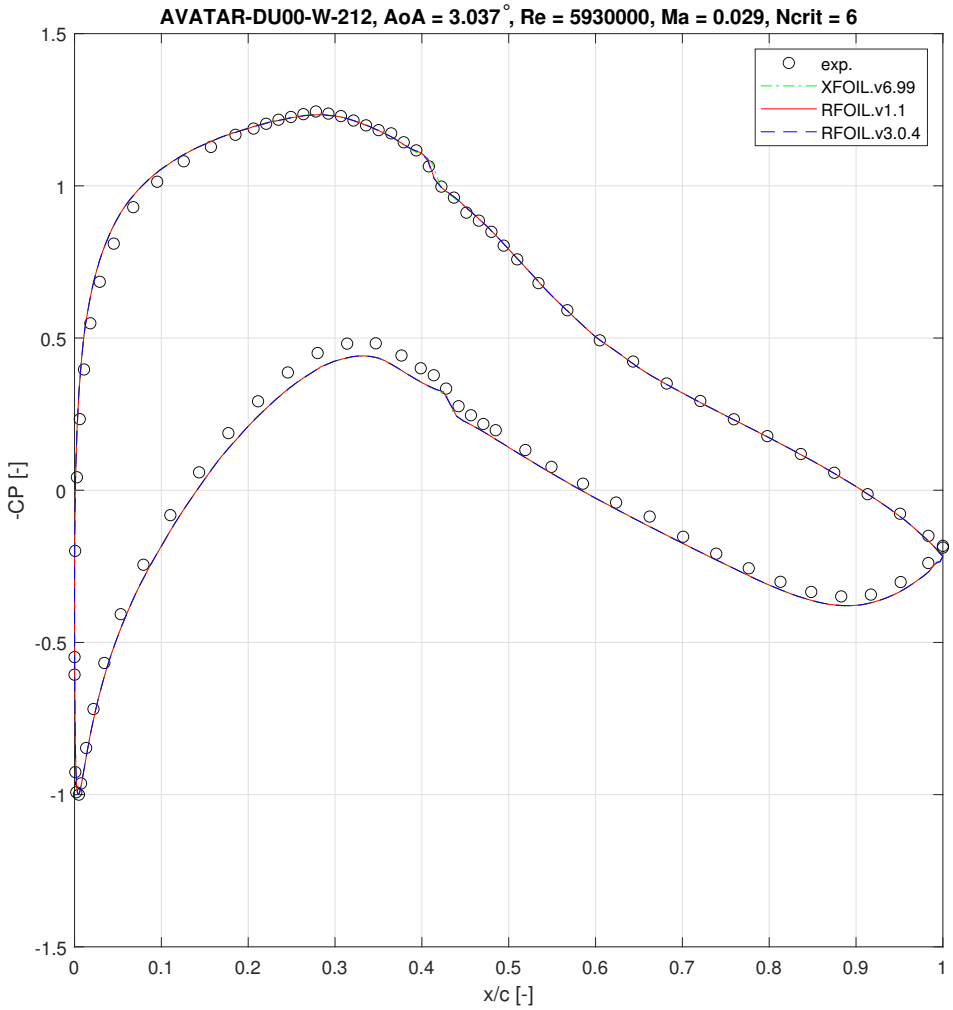

Figure C.343: Comparison between experimental and numerical pressure distributions for the AVATAR-DU00-W-212 airfoil at a Reynolds number of 5980000, and at an angle of attack and a Mach number of 3.037° and 0.055, respectively.

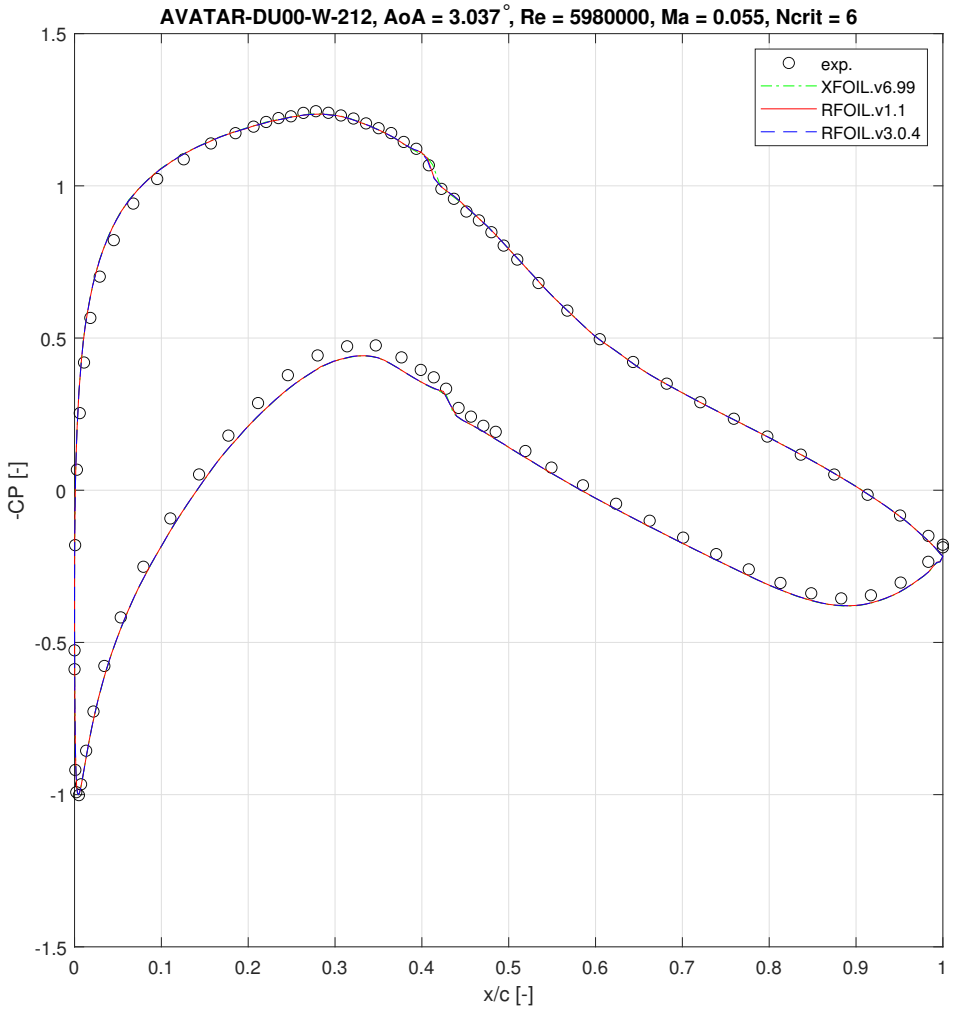

Figure C.344: Comparison between experimental and numerical pressure distributions for the AVATAR-DU00-W-212 airfoil at a Reynolds number of 2990000, and at an angle of attack and a Mach number of 3.038° and 0.073, respectively.

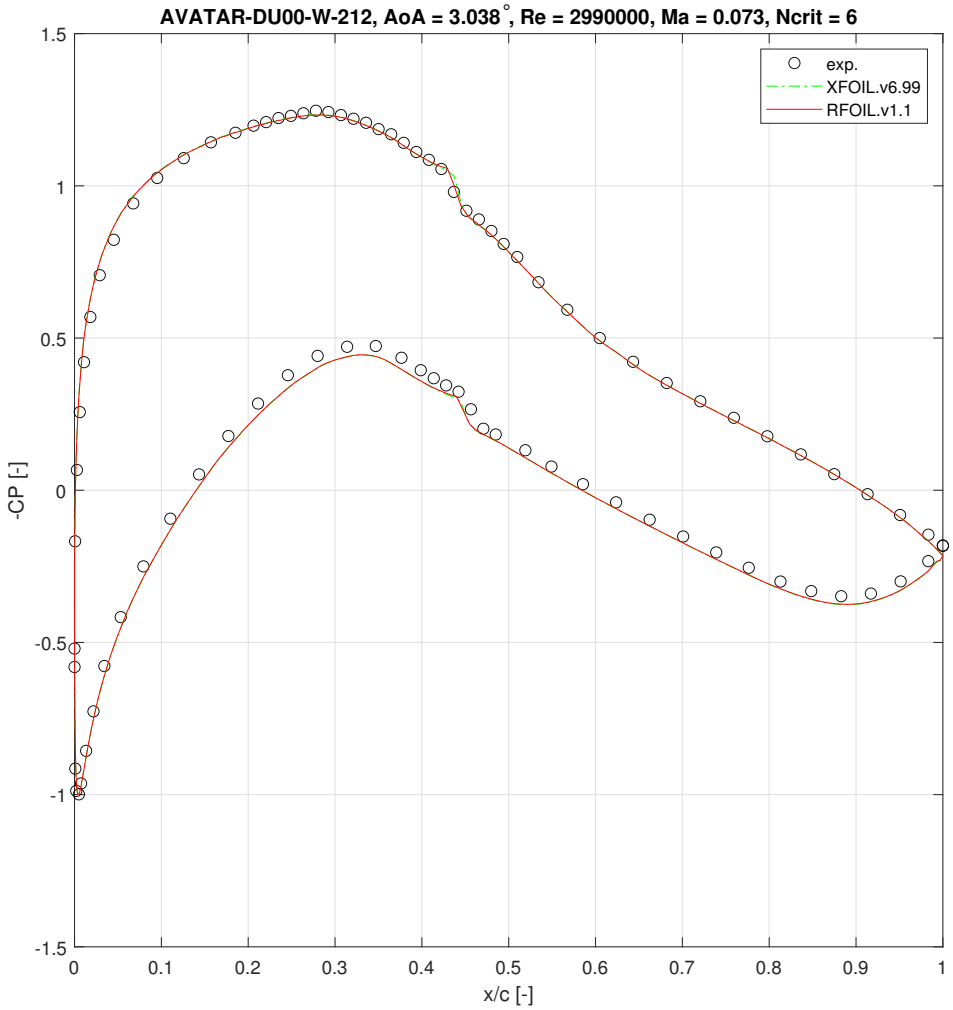

Figure C.345: Comparison between experimental and numerical pressure distributions for the AVATAR-DU00-W-212 airfoil at a Reynolds number of 8950000, and at an angle of attack and a Mach number of 3.038° and 0.082, respectively.

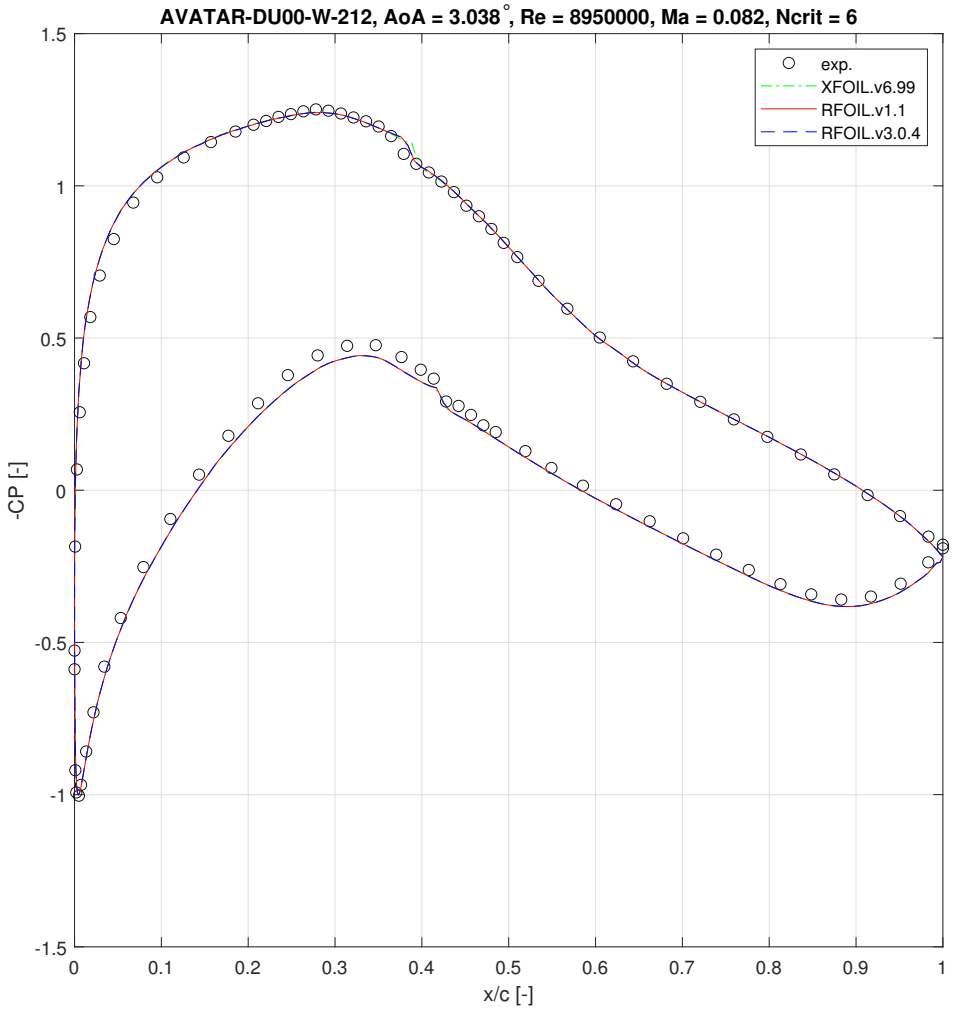

Figure C.346: Comparison between experimental and numerical pressure distributions for the AVATAR-DU00-W-212 airfoil at a Reynolds number of 12020000, and at an angle of attack and a Mach number of 3.039° and 0.058, respectively.

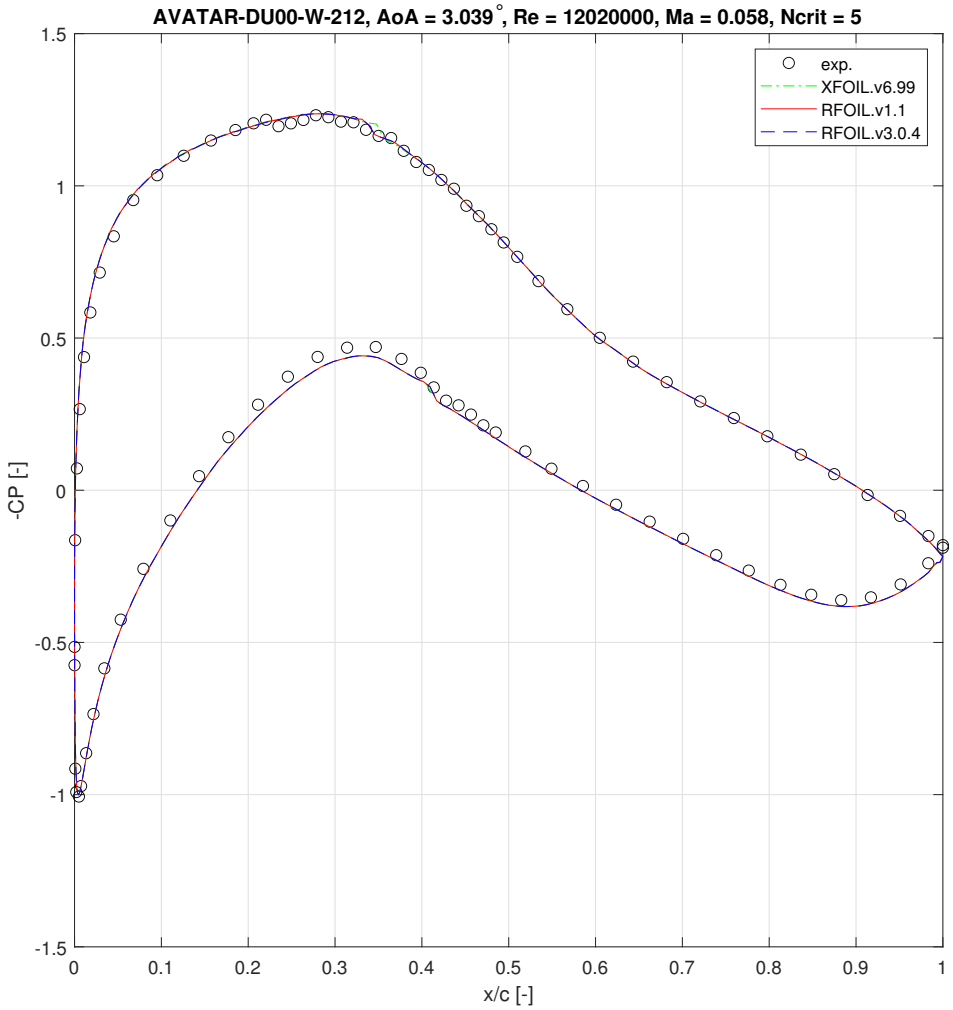

Figure C.347: Comparison between experimental and numerical pressure distributions for the AVATAR-DU00-W-212 airfoil at a Reynolds number of 11990000, and at an angle of attack and a Mach number of 3.537° and 0.058, respectively.

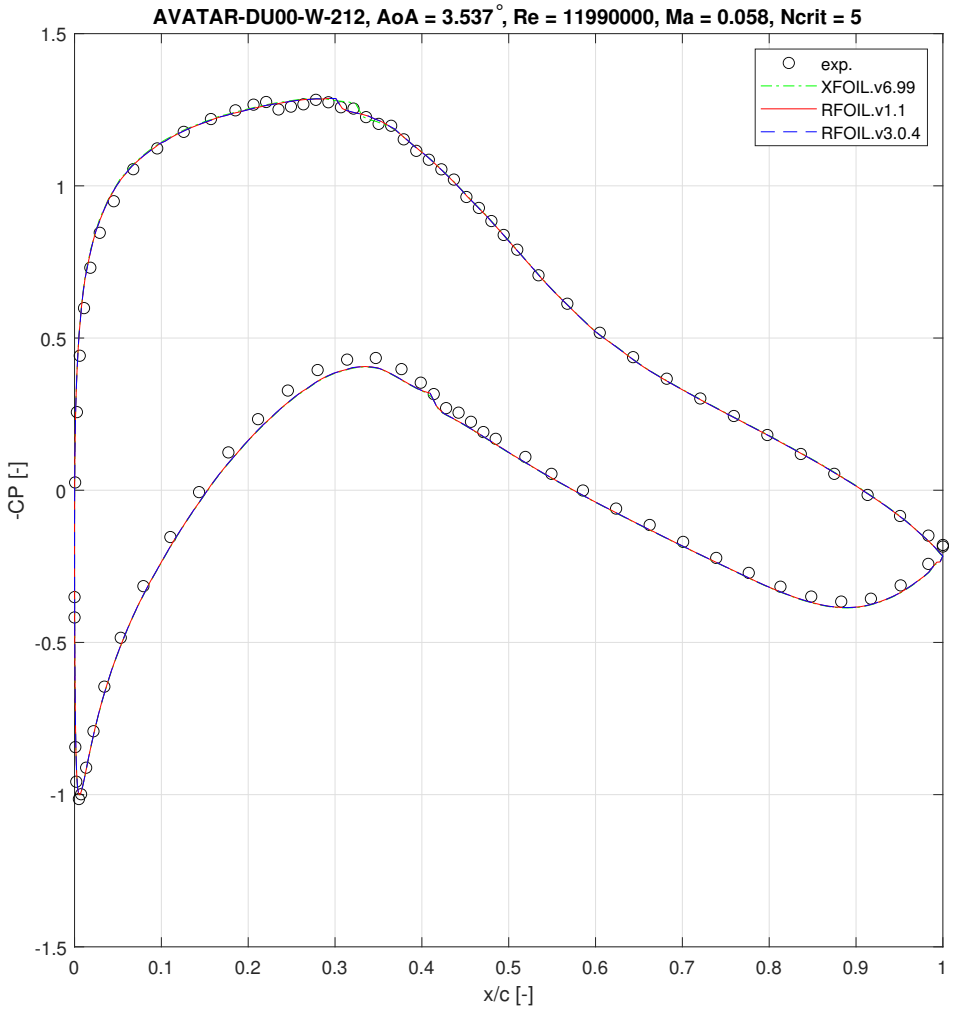

Figure C.348: Comparison between experimental and numerical pressure distributions for the AVATAR-DU00-W-212 airfoil at a Reynolds number of 14990000, and at an angle of attack and a Mach number of 3.543° and 0.081, respectively.

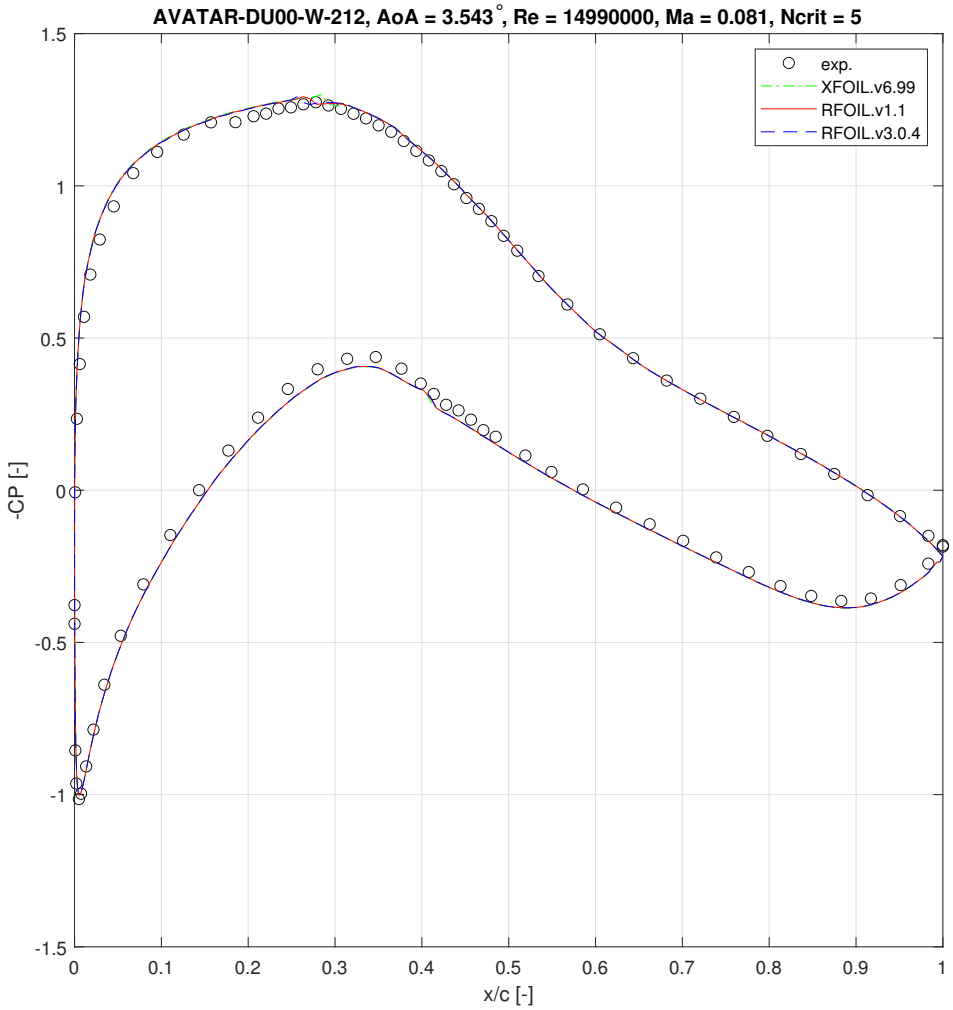

Figure C.349: Comparison between experimental and numerical pressure distributions for the AVATAR-DU00-W-212 airfoil at a Reynolds number of 14970000, and at an angle of attack and a Mach number of 3.746° and 0.081, respectively.

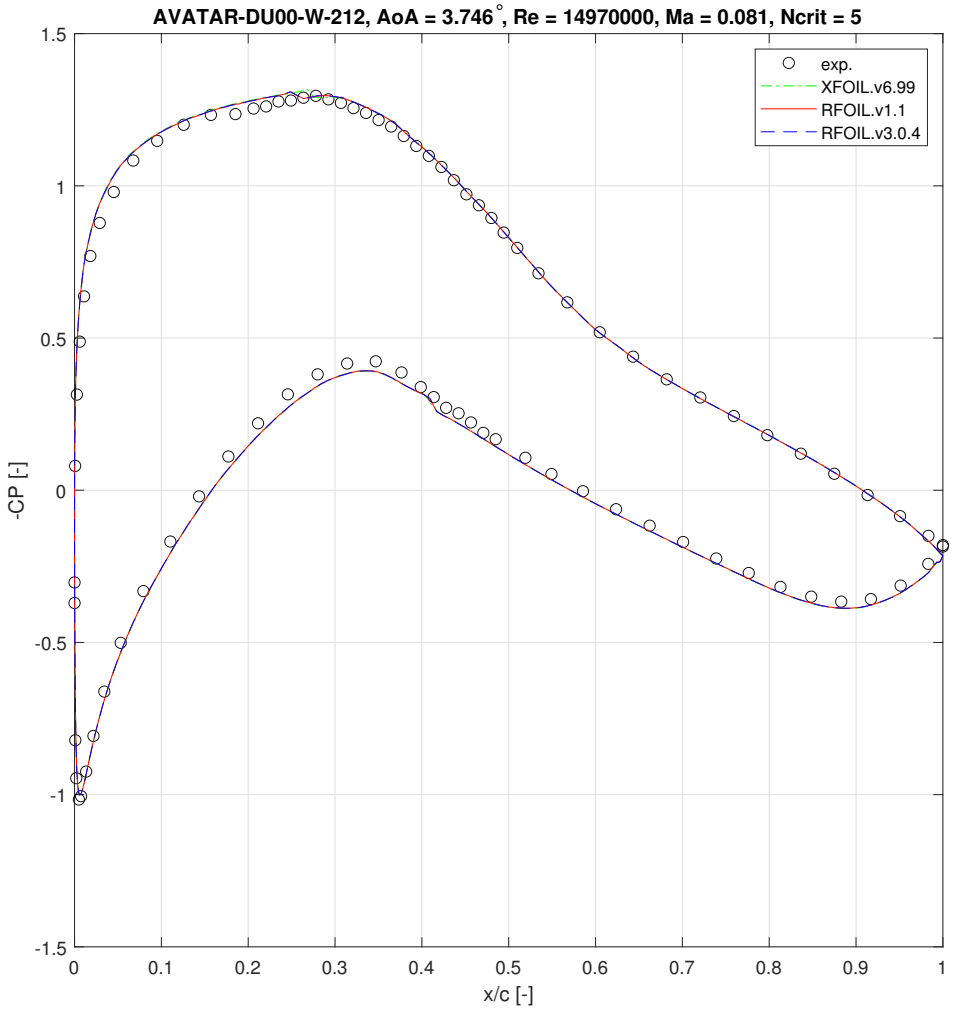

Figure C.350: Comparison between experimental and numerical pressure distributions for the AVATAR-DU00-W-212 airfoil at a Reynolds number of 11980000, and at an angle of attack and a Mach number of 4.038° and 0.058, respectively.

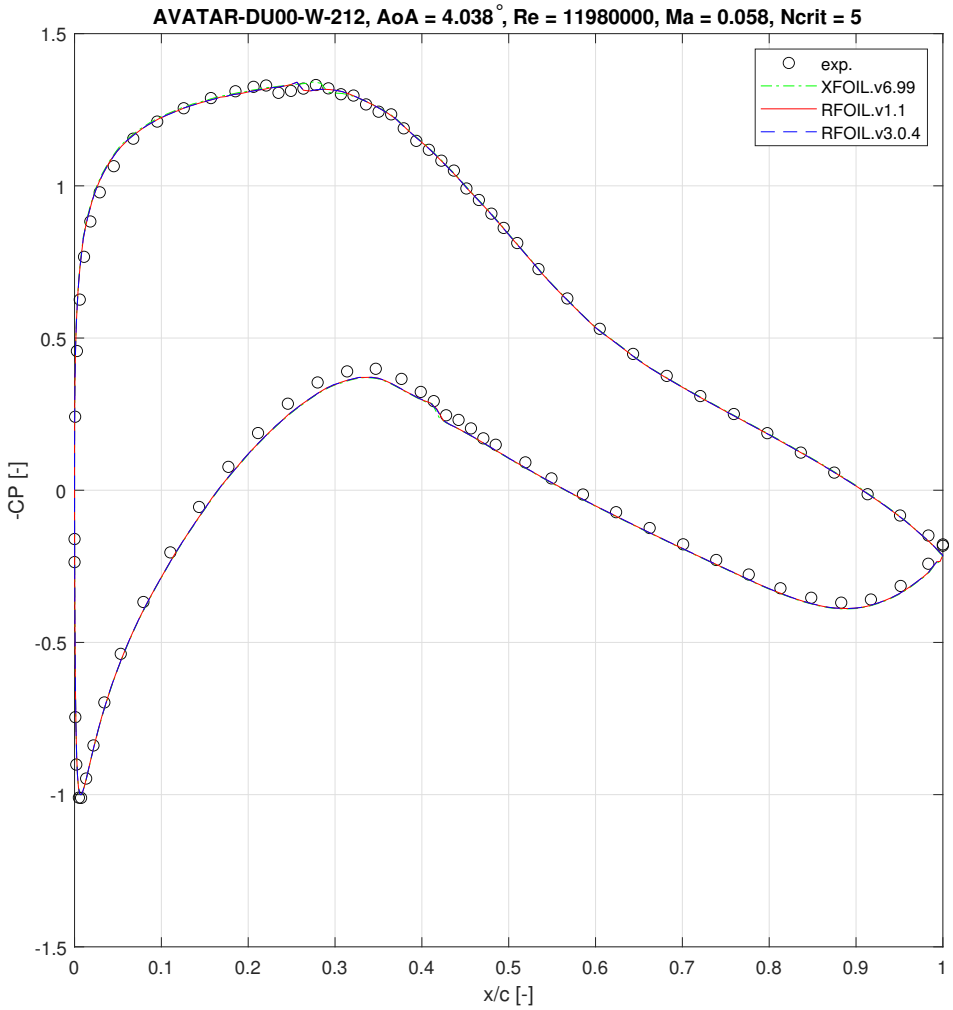

Figure C.351: Comparison between experimental and numerical pressure distributions for the AVATAR-DU00-W-212 airfoil at a Reynolds number of 9000000, and at an angle of attack and a Mach number of 4.048° and 0.043, respectively.

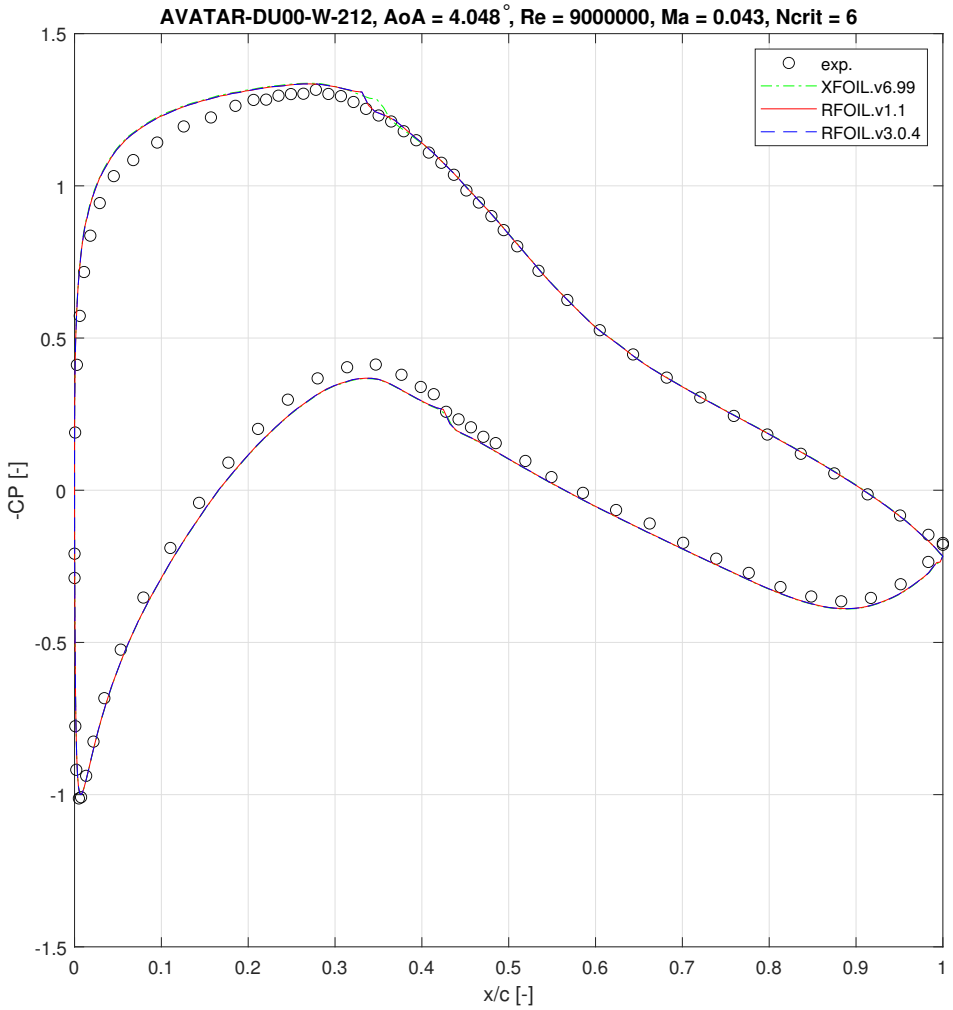

Figure C.352: Comparison between experimental and numerical pressure distributions for the AVATAR-DU00-W-212 airfoil at a Reynolds number of 5990000, and at an angle of attack and a Mach number of 4.049° and 0.029, respectively.

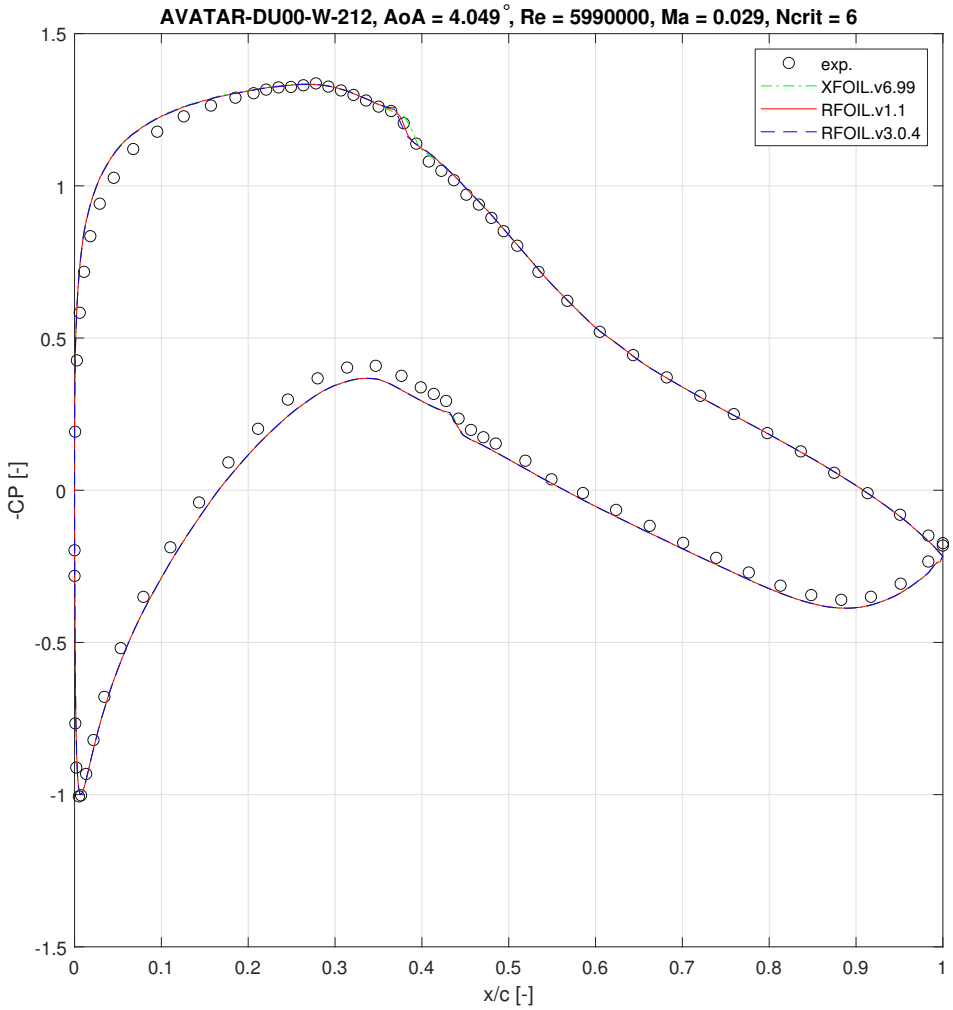

Figure C.353: Comparison between experimental and numerical pressure distributions for the AVATAR-DU00-W-212 airfoil at a Reynolds number of 2990000, and at an angle of attack and a Mach number of 4.051° and 0.073, respectively.

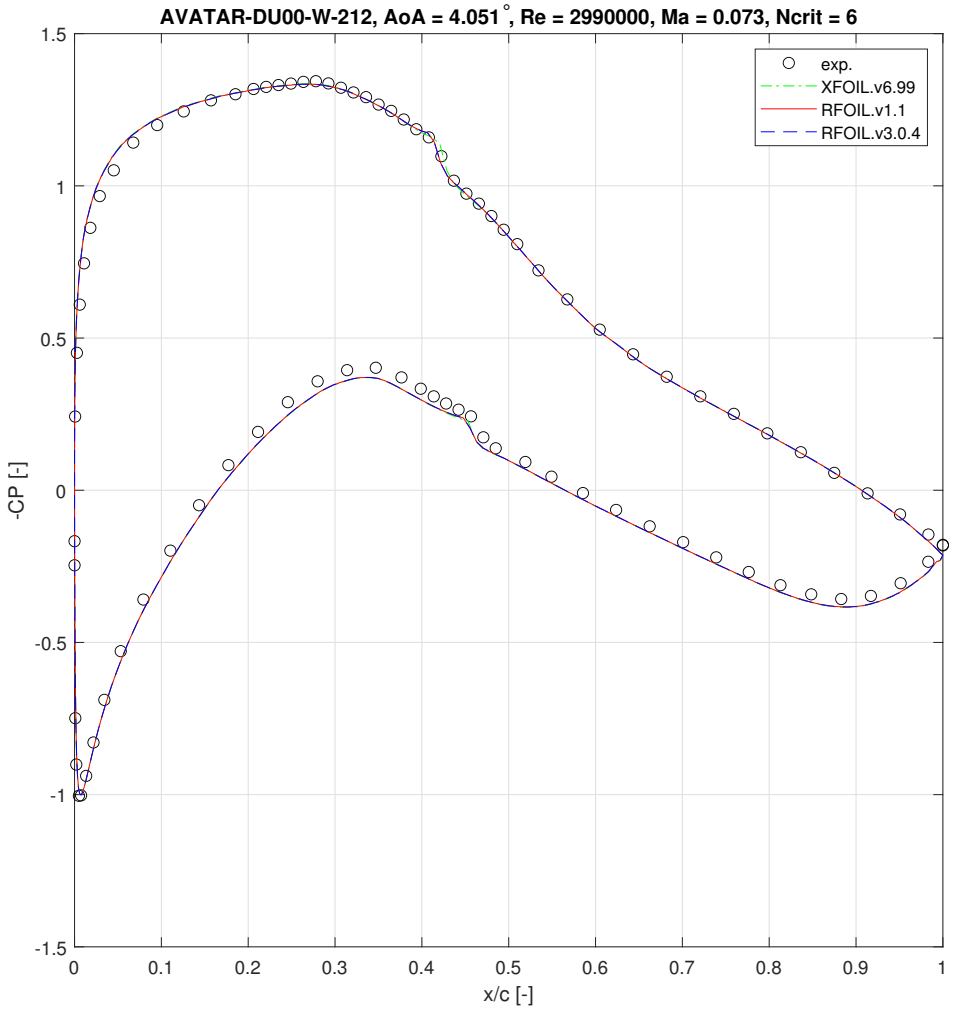

Figure C.354: Comparison between experimental and numerical pressure distributions for the AVATAR-DU00-W-212 airfoil at a Reynolds number of 5990000, and at an angle of attack and a Mach number of 4.051° and 0.055, respectively.

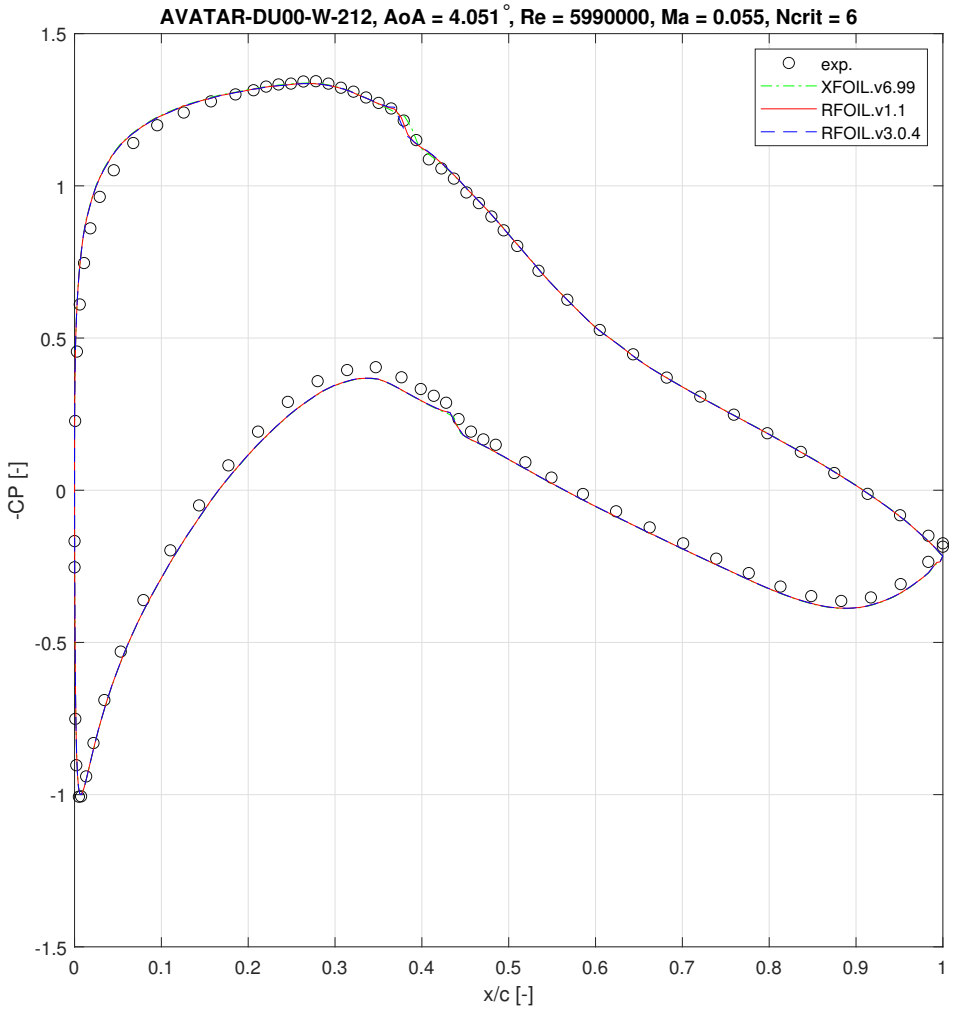

Figure C.355: Comparison between experimental and numerical pressure distributions for the AVATAR-DU00-W-212 airfoil at a Reynolds number of 8980000, and at an angle of attack and a Mach number of 4.051° and 0.083, respectively.

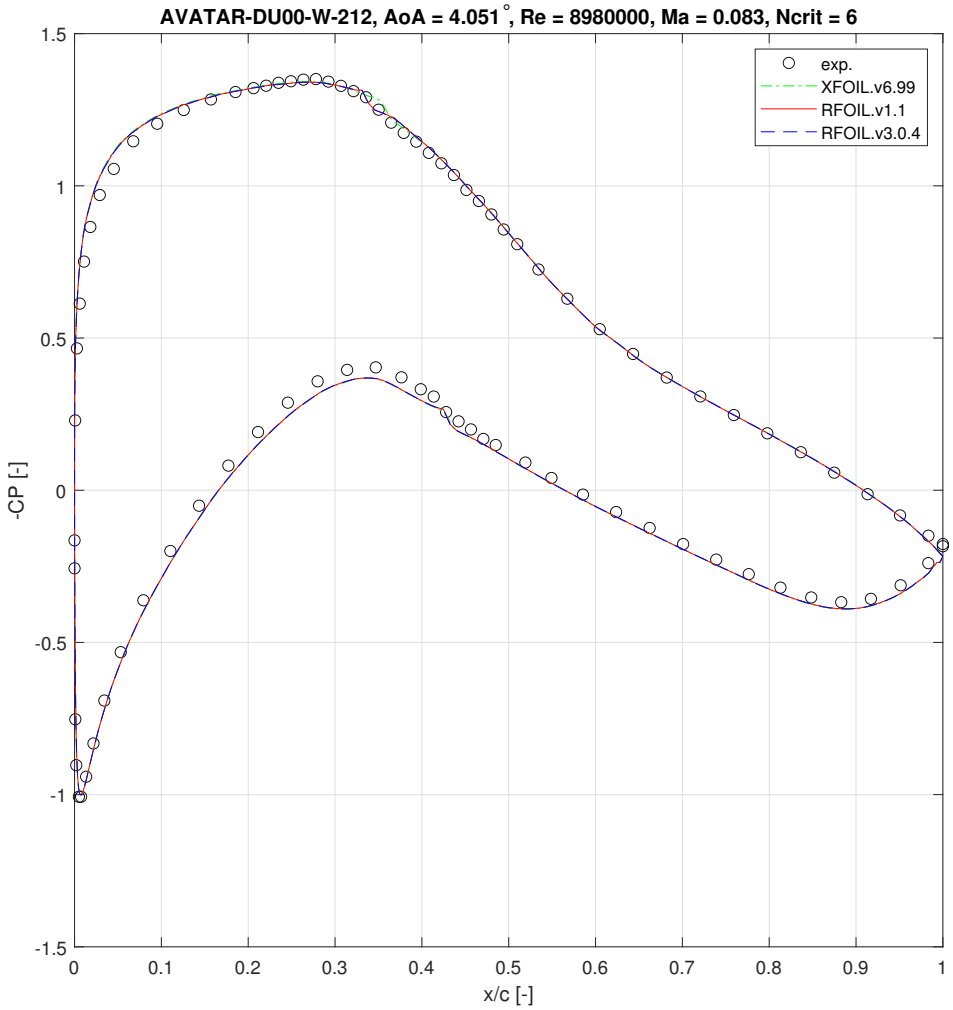

Figure C.356: Comparison between experimental and numerical pressure distributions for the AVATAR-DU00-W-212 airfoil at a Reynolds number of 9020000, and at an angle of attack and a Mach number of 4.051° and 0.083, respectively.

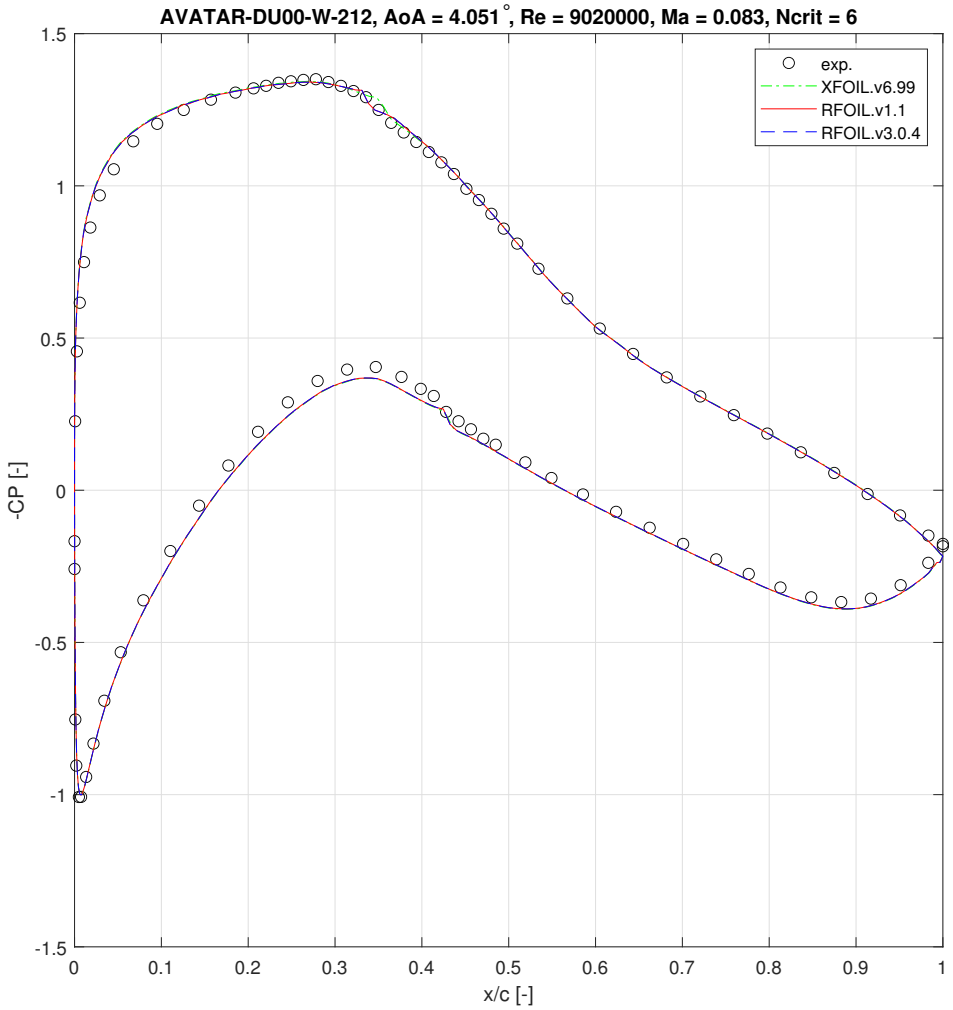

Figure C.357: Comparison between experimental and numerical pressure distributions for the AVATAR-DU00-W-212 airfoil at a Reynolds number of 14980000, and at an angle of attack and a Mach number of 4.050° and 0.081, respectively.

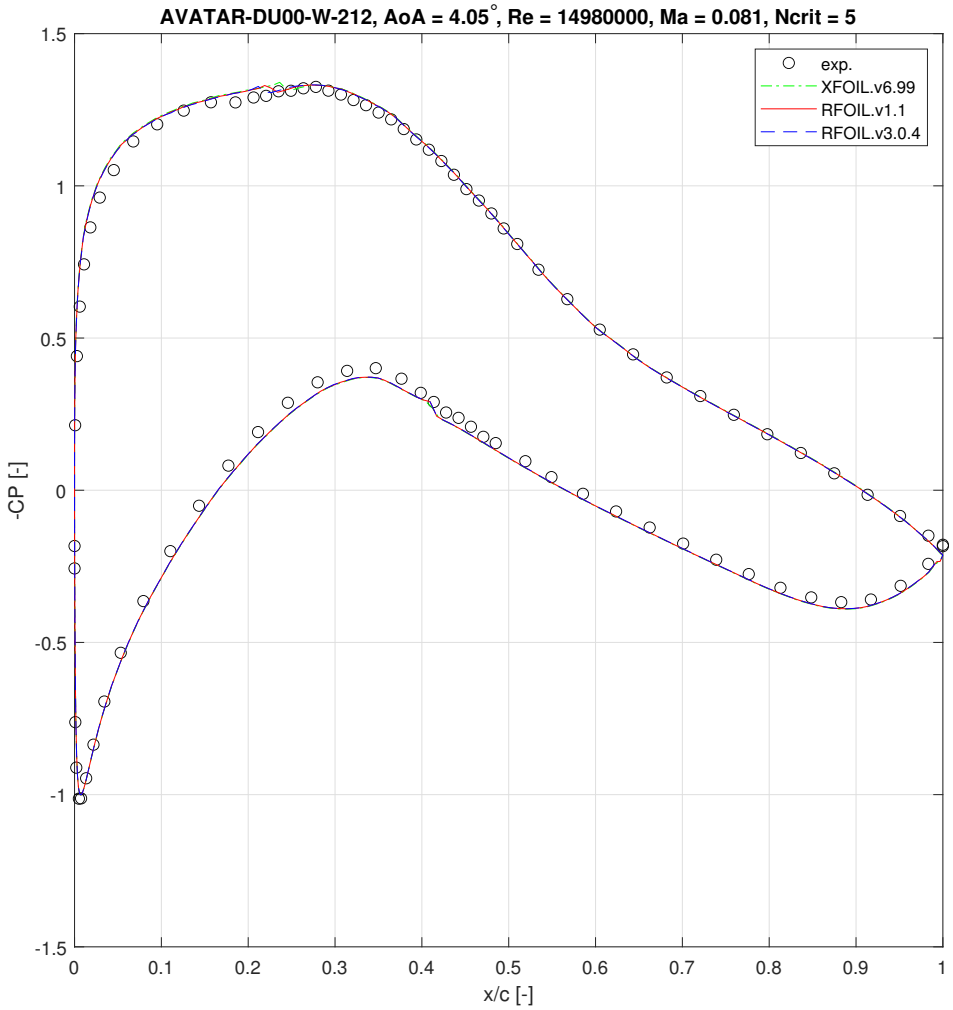

Figure C.358: Comparison between experimental and numerical pressure distributions for the AVATAR-DU00-W-212 airfoil at a Reynolds number of 6000000, and at an angle of attack and a Mach number of 4.252° and 0.029, respectively.

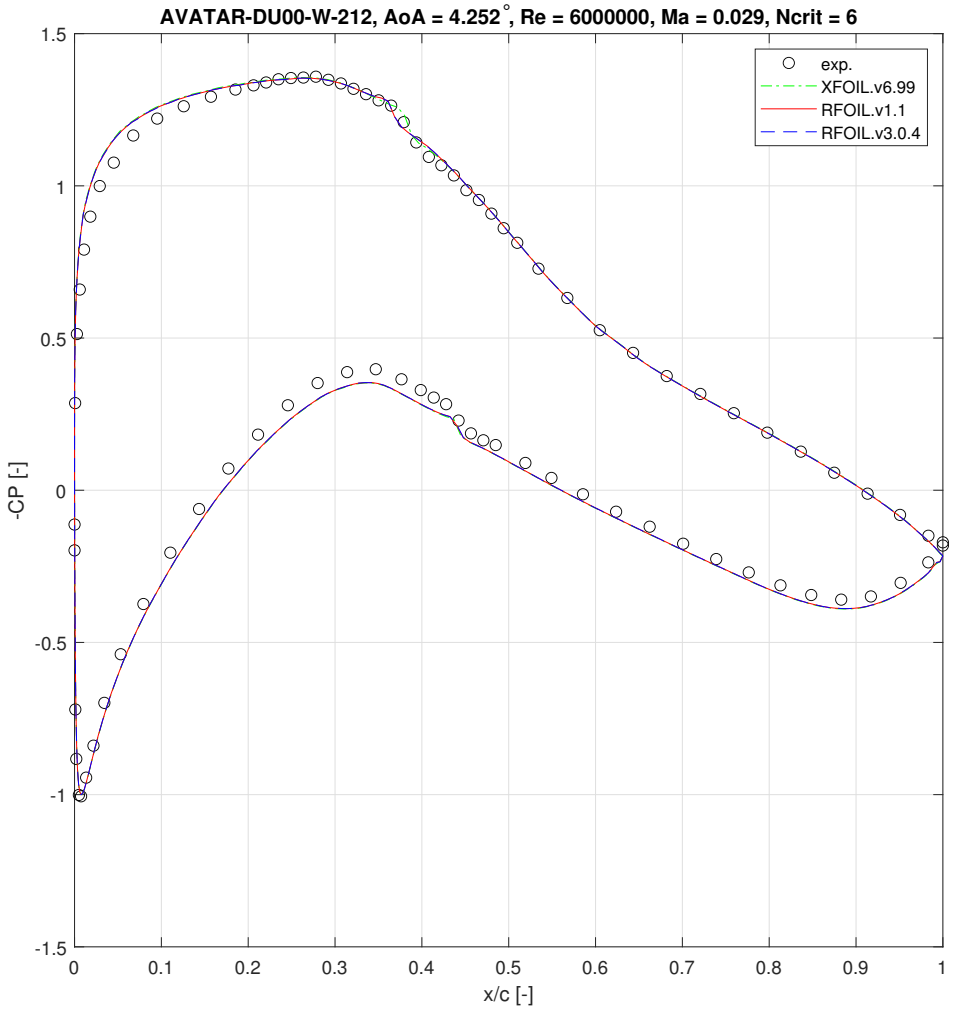

Figure C.359: Comparison between experimental and numerical pressure distributions for the AVATAR-DU00-W-212 airfoil at a Reynolds number of 15000000, and at an angle of attack and a Mach number of 4.253° and 0.081, respectively.

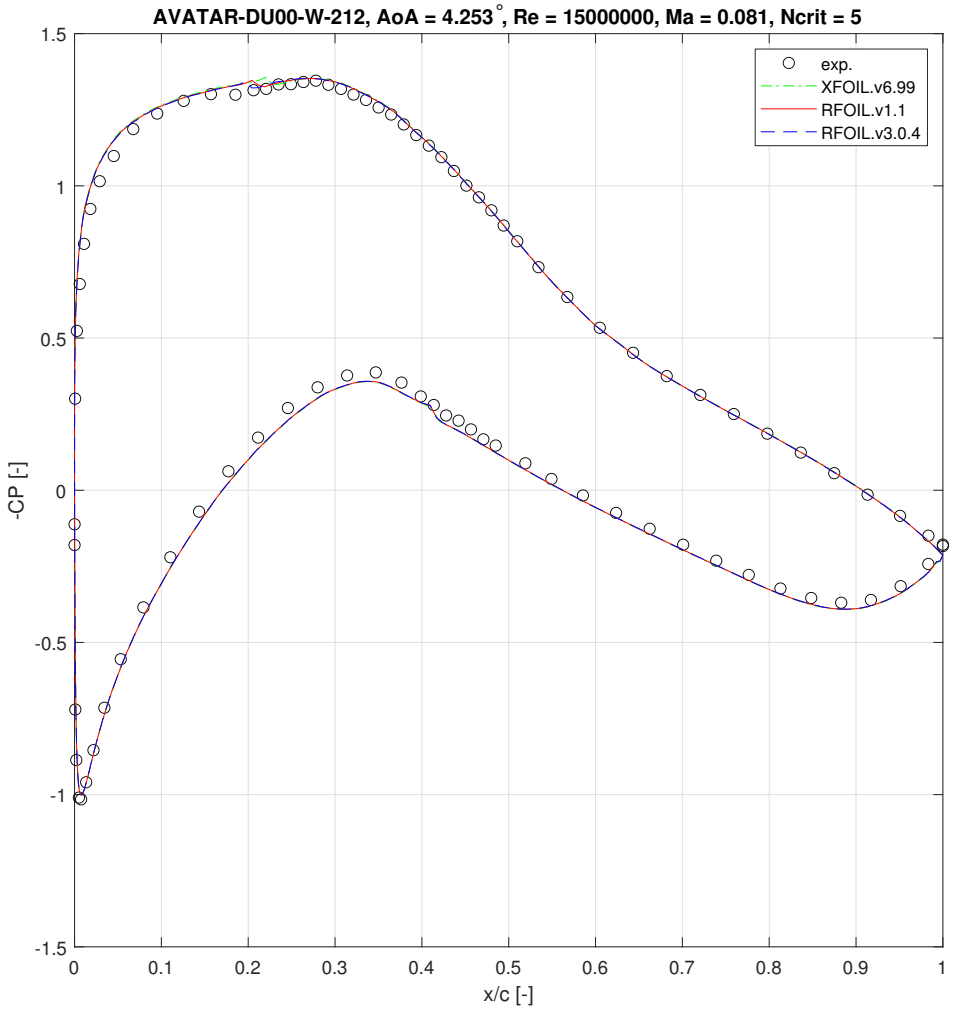

Figure C.360: Comparison between experimental and numerical pressure distributions for the AVATAR-DU00-W-212 airfoil at a Reynolds number of 6000000, and at an angle of attack and a Mach number of 4.455° and 0.029, respectively.

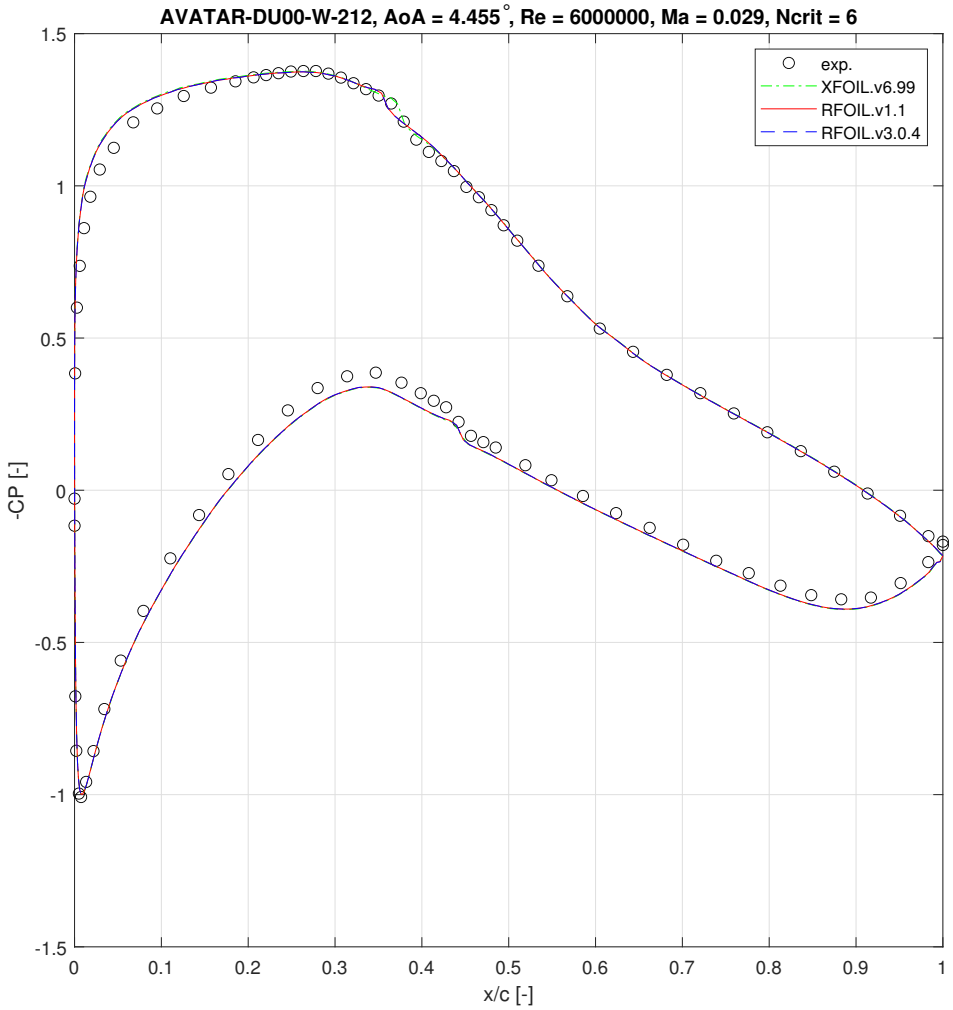

Figure C.361: Comparison between experimental and numerical pressure distributions for the AVATAR-DU00-W-212 airfoil at a Reynolds number of 11960000, and at an angle of attack and a Mach number of 4.535° and 0.057, respectively.

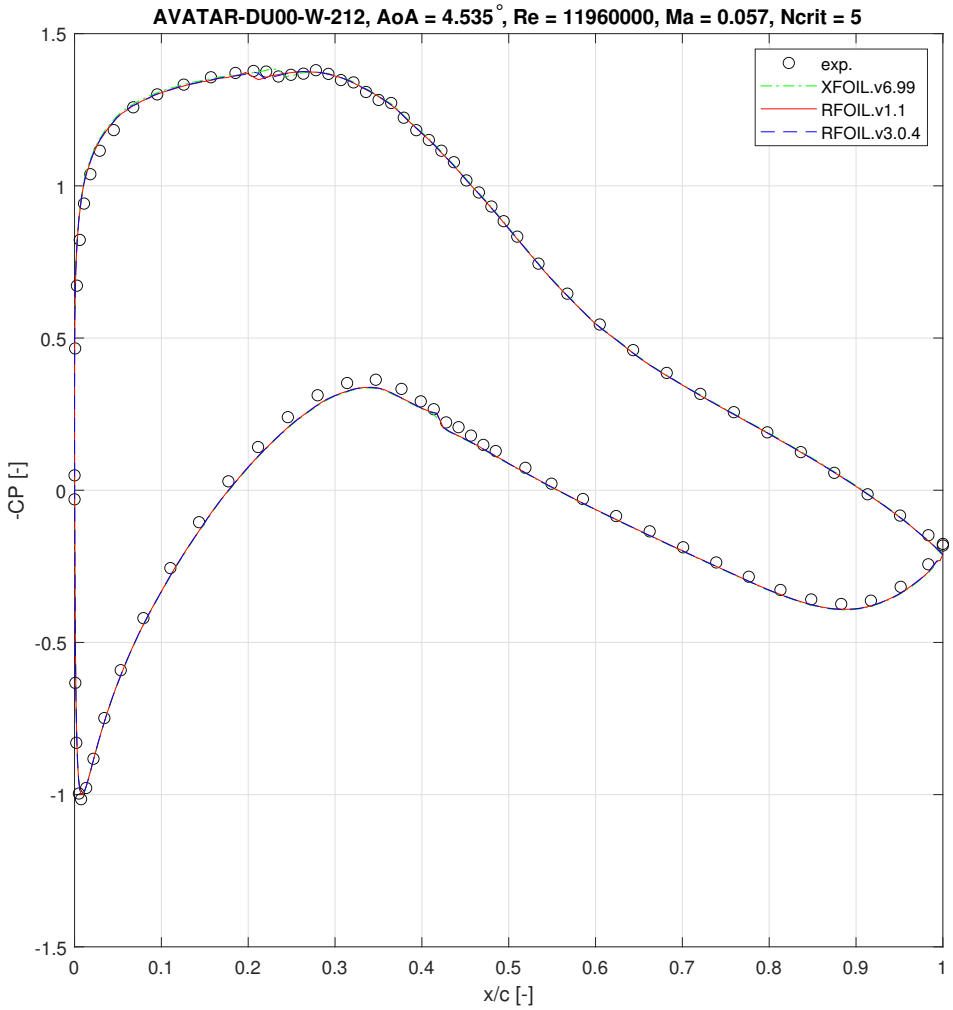

Figure C.362: Comparison between experimental and numerical pressure distributions for the AVATAR-DU00-W-212 airfoil at a Reynolds number of 8980000, and at an angle of attack and a Mach number of 4.555° and 0.043, respectively.

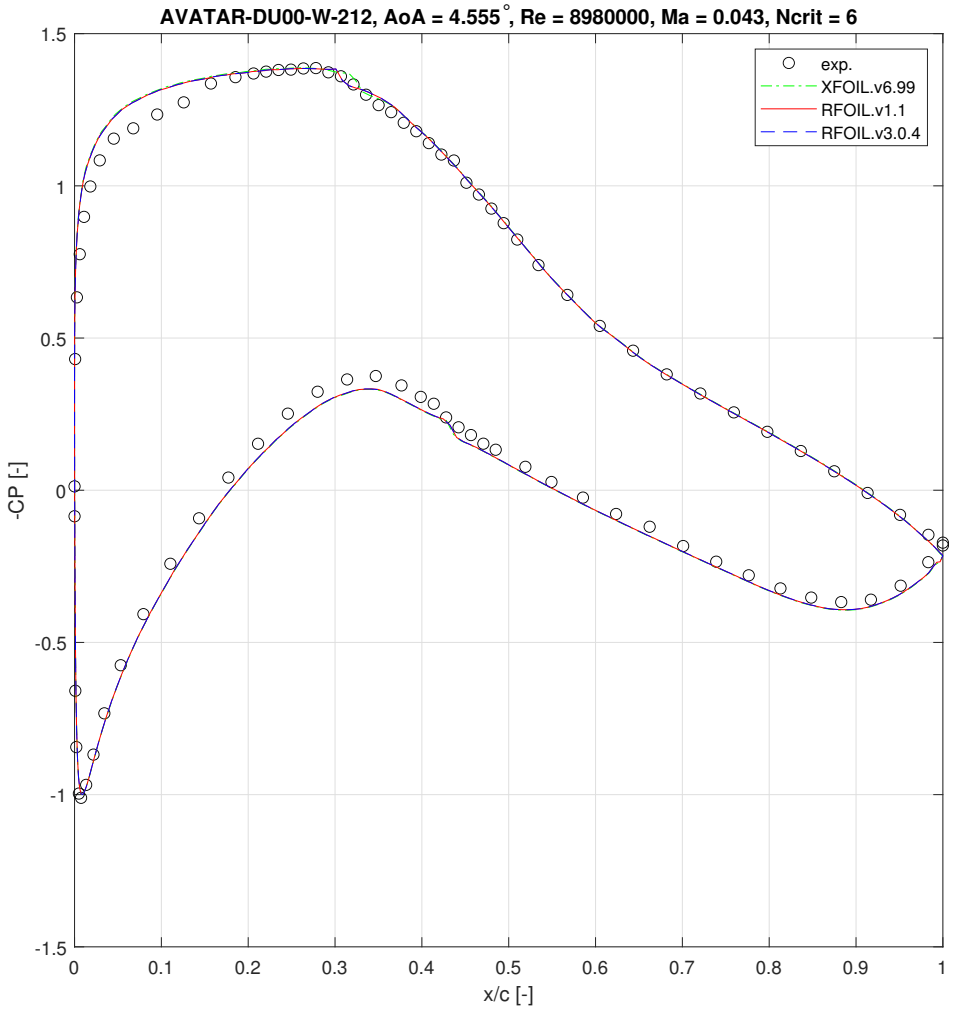

Figure C.363: Comparison between experimental and numerical pressure distributions for the AVATAR-DU00-W-212 airfoil at a Reynolds number of 14990000, and at an angle of attack and a Mach number of 4.557° and 0.081, respectively.

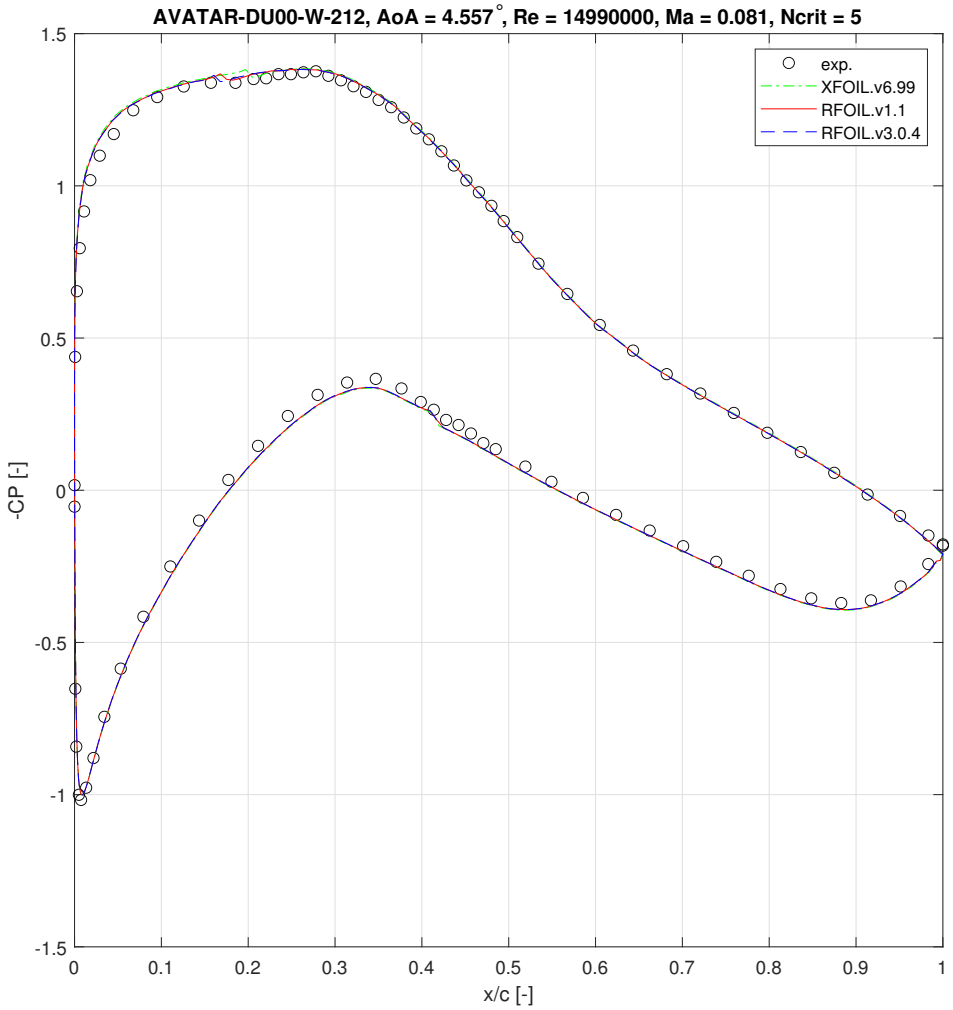

Figure C.364: Comparison between experimental and numerical pressure distributions for the AVATAR-DU00-W-212 airfoil at a Reynolds number of 6000000, and at an angle of attack and a Mach number of 4.557° and 0.055, respectively.

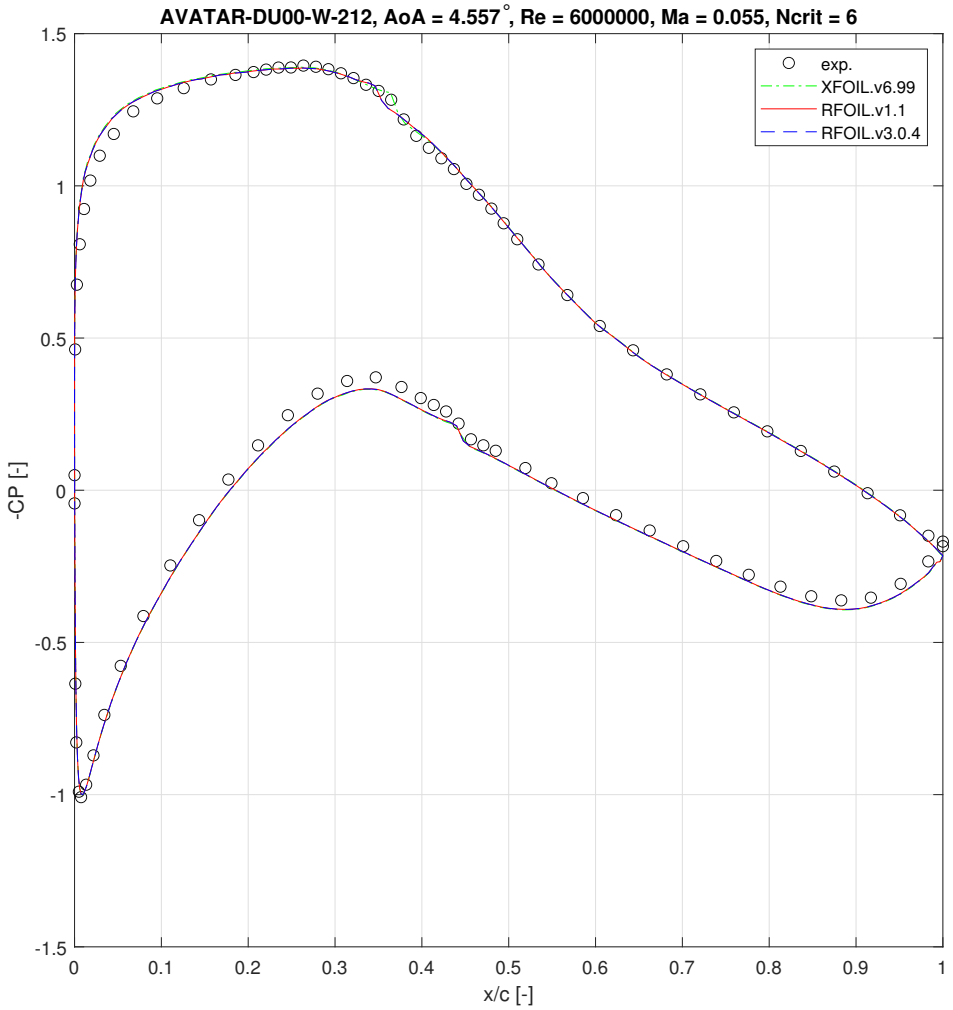

Figure C.365: Comparison between experimental and numerical pressure distributions for the AVATAR-DU00-W-212 airfoil at a Reynolds number of 9010000, and at an angle of attack and a Mach number of 4.557° and 0.083, respectively.

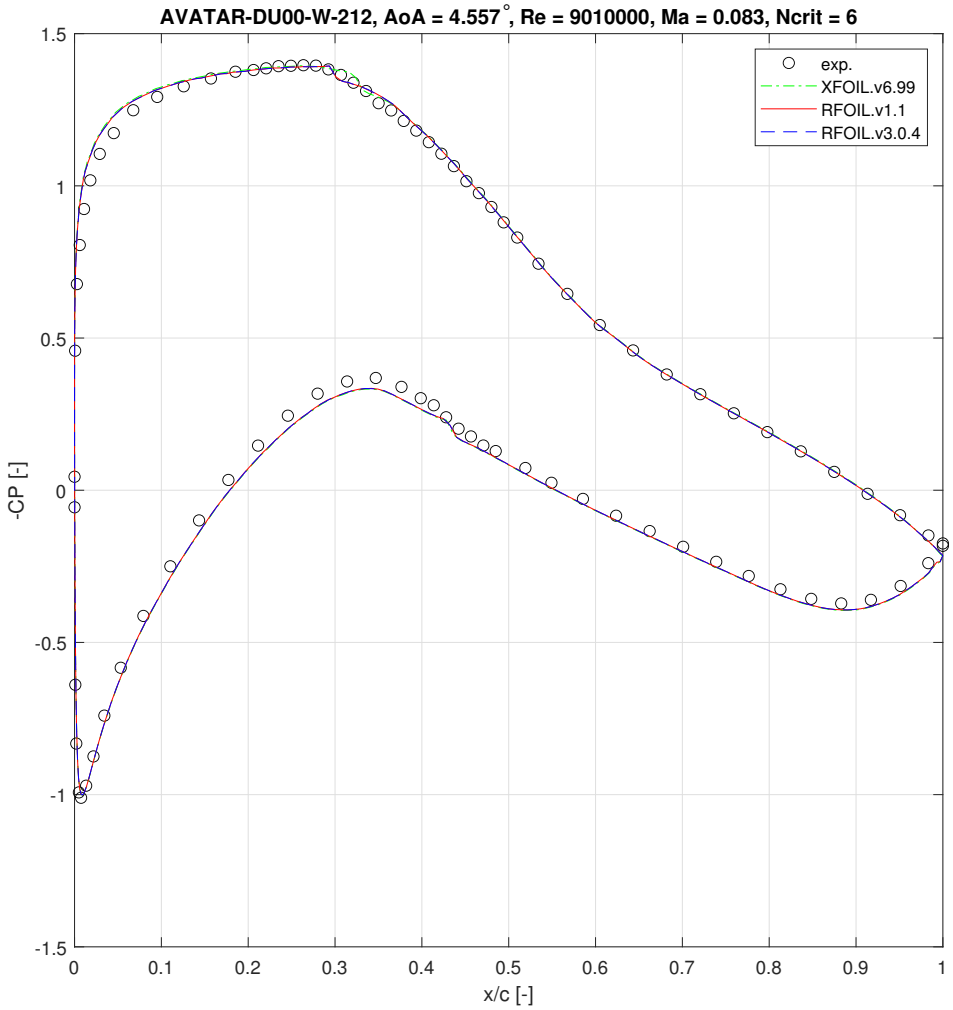

Figure C.366: Comparison between experimental and numerical pressure distributions for the AVATAR-DU00-W-212 airfoil at a Reynolds number of 11980000, and at an angle of attack and a Mach number of 4.833° and 0.058, respectively.

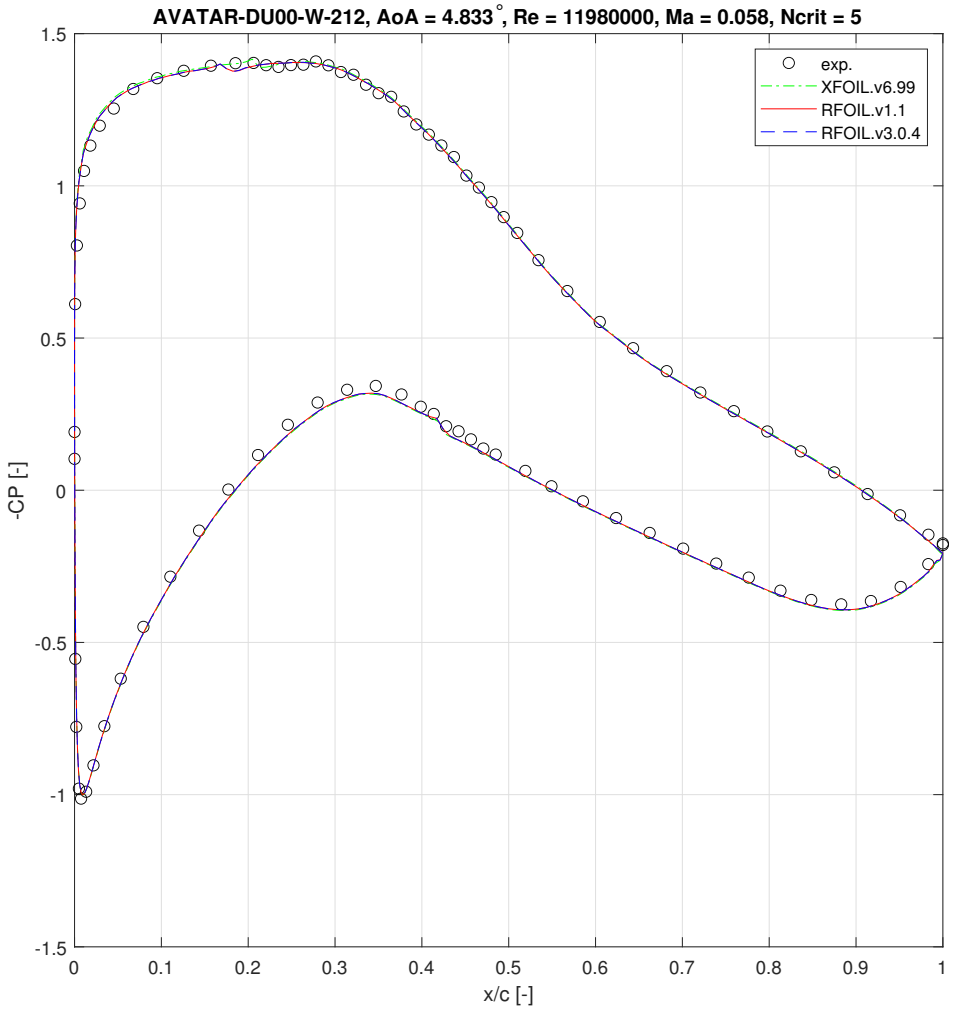

Figure C.367: Comparison between experimental and numerical pressure distributions for the AVATAR-DU00-W-212 airfoil at a Reynolds number of 8980000, and at an angle of attack and a Mach number of 4.859° and 0.043, respectively.

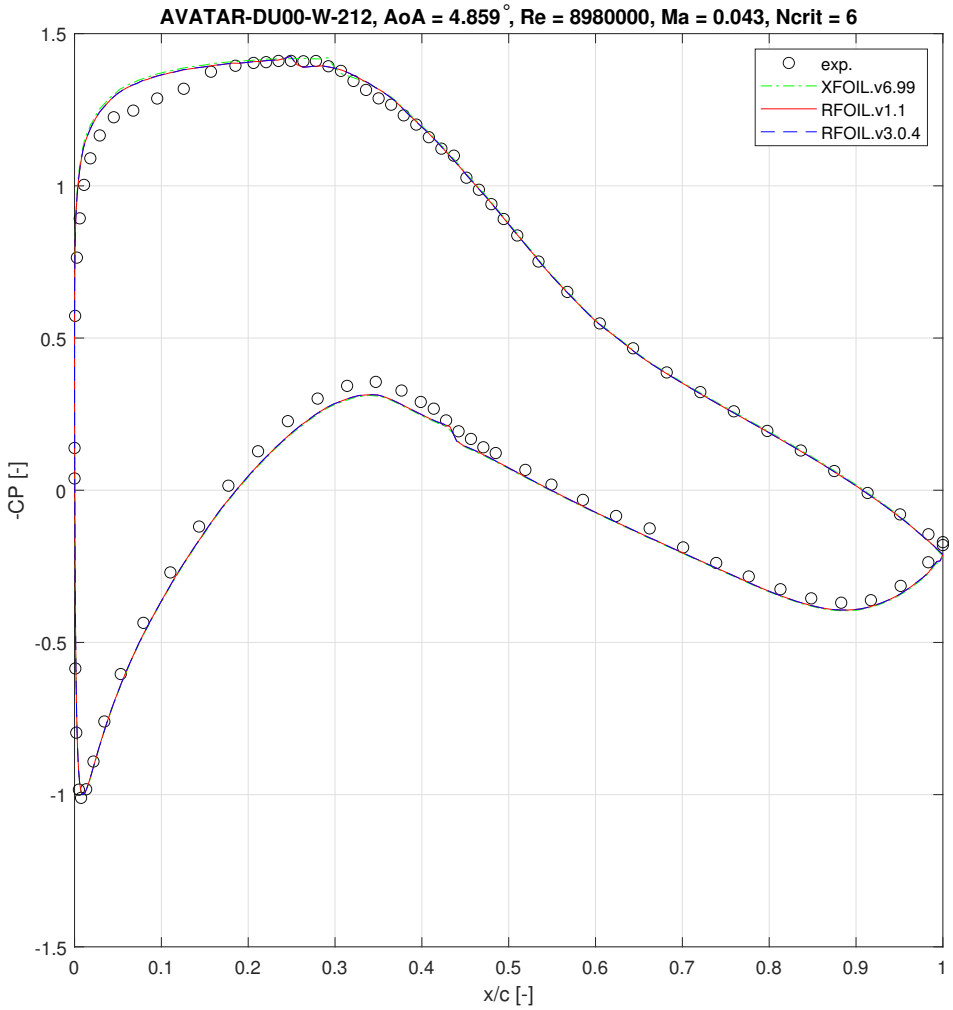

Figure C.368: Comparison between experimental and numerical pressure distributions for the AVATAR-DU00-W-212 airfoil at a Reynolds number of 15010000, and at an angle of attack and a Mach number of 4.861° and 0.082, respectively.

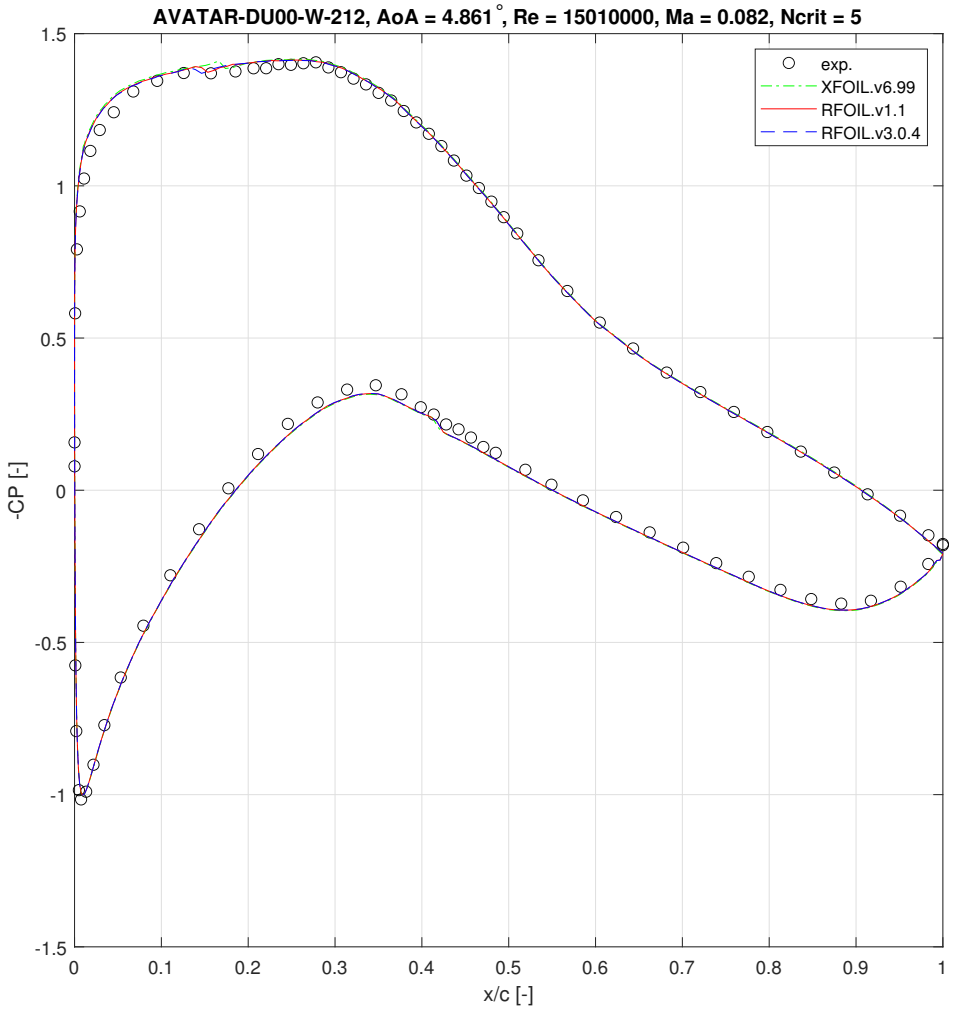

Figure C.369: Comparison between experimental and numerical pressure distributions for the AVATAR-DU00-W-212 airfoil at a Reynolds number of 6020000, and at an angle of attack and a Mach number of 4.861° and 0.055, respectively.

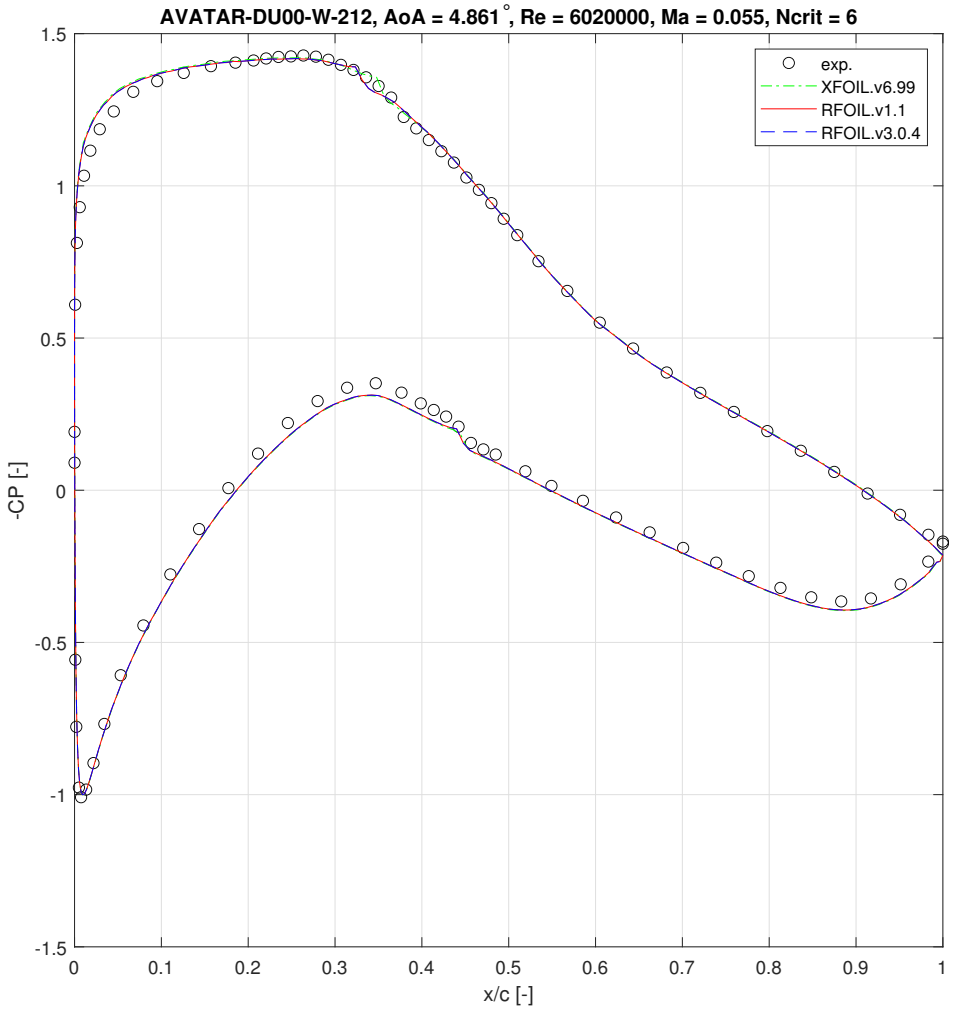

Figure C.370: Comparison between experimental and numerical pressure distributions for the AVATAR-DU00-W-212 airfoil at a Reynolds number of 9000000, and at an angle of attack and a Mach number of 4.861° and 0.083, respectively.

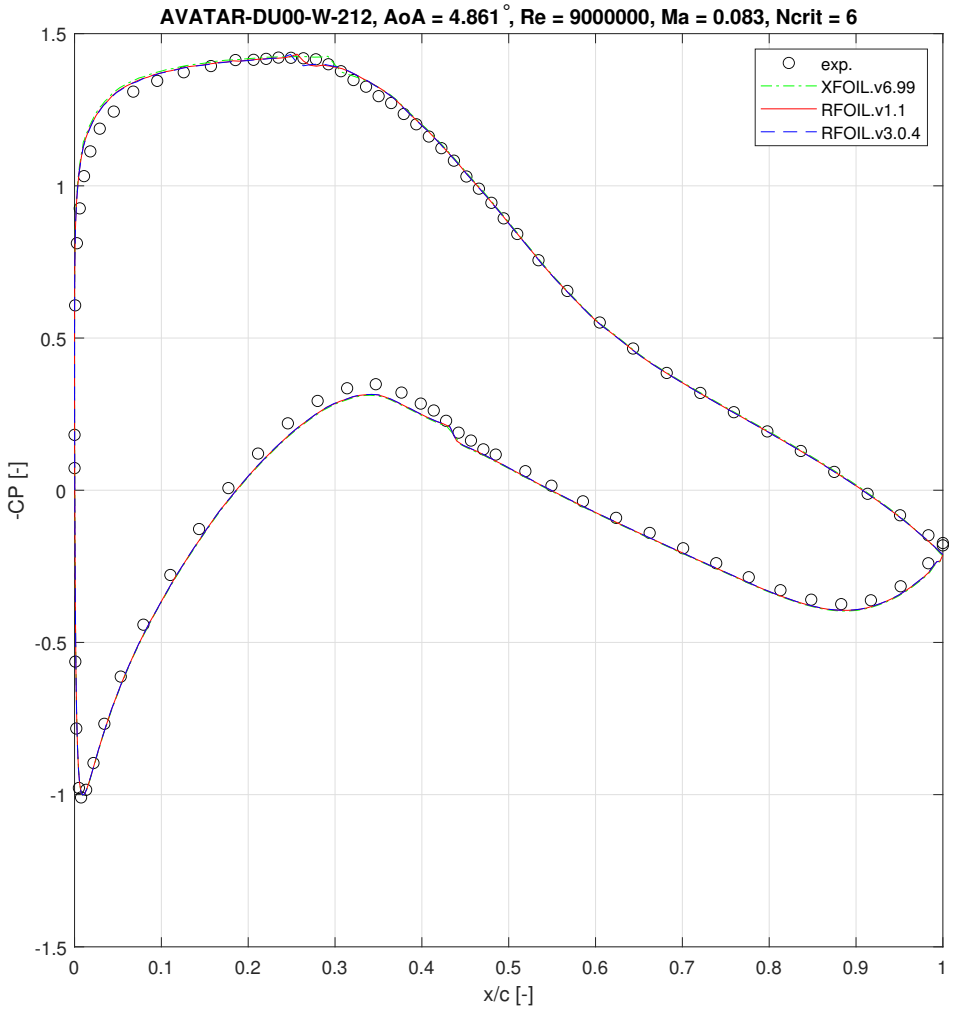

Figure C.371: Comparison between experimental and numerical pressure distributions for the AVATAR-DU00-W-212 airfoil at a Reynolds number of 6000000, and at an angle of attack and a Mach number of 4.860° and 0.029, respectively.

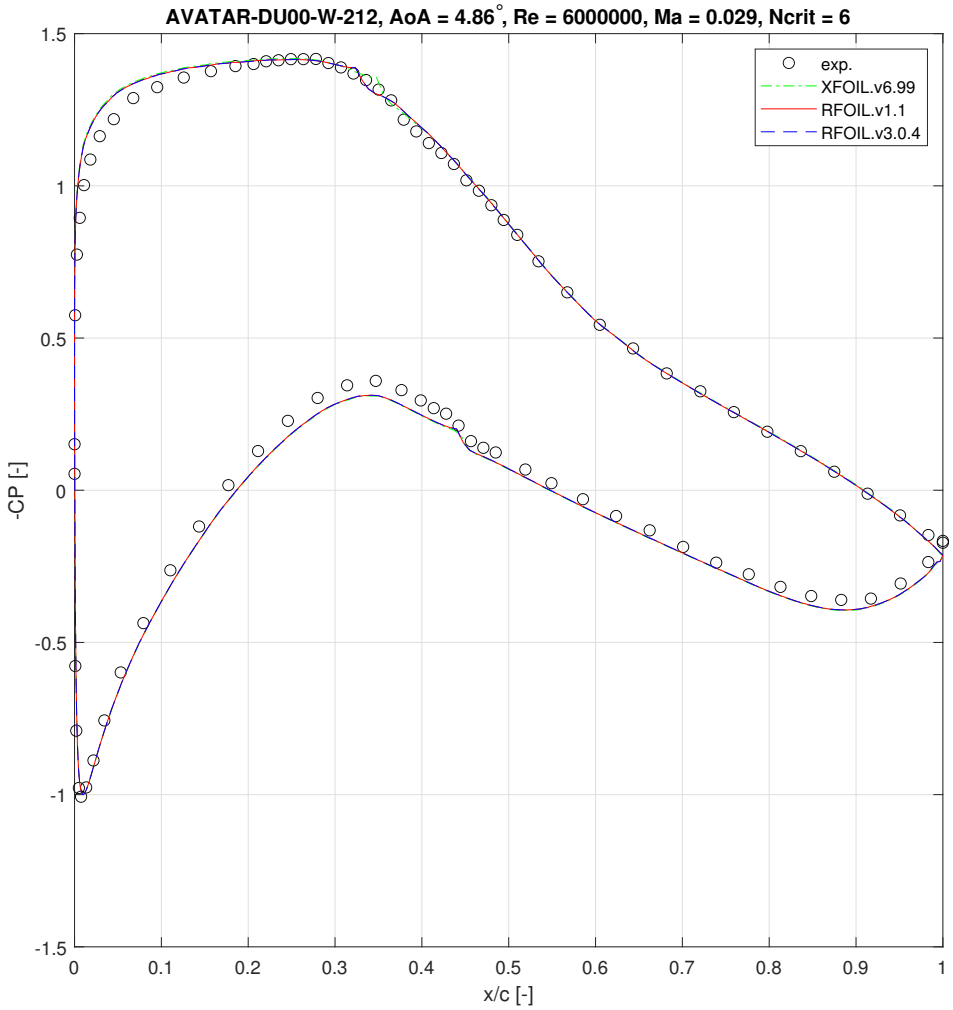

Figure C.372: Comparison between experimental and numerical pressure distributions for the AVATAR-DU00-W-212 airfoil at a Reynolds number of 11980000, and at an angle of attack and a Mach number of 5.035° and 0.058, respectively.

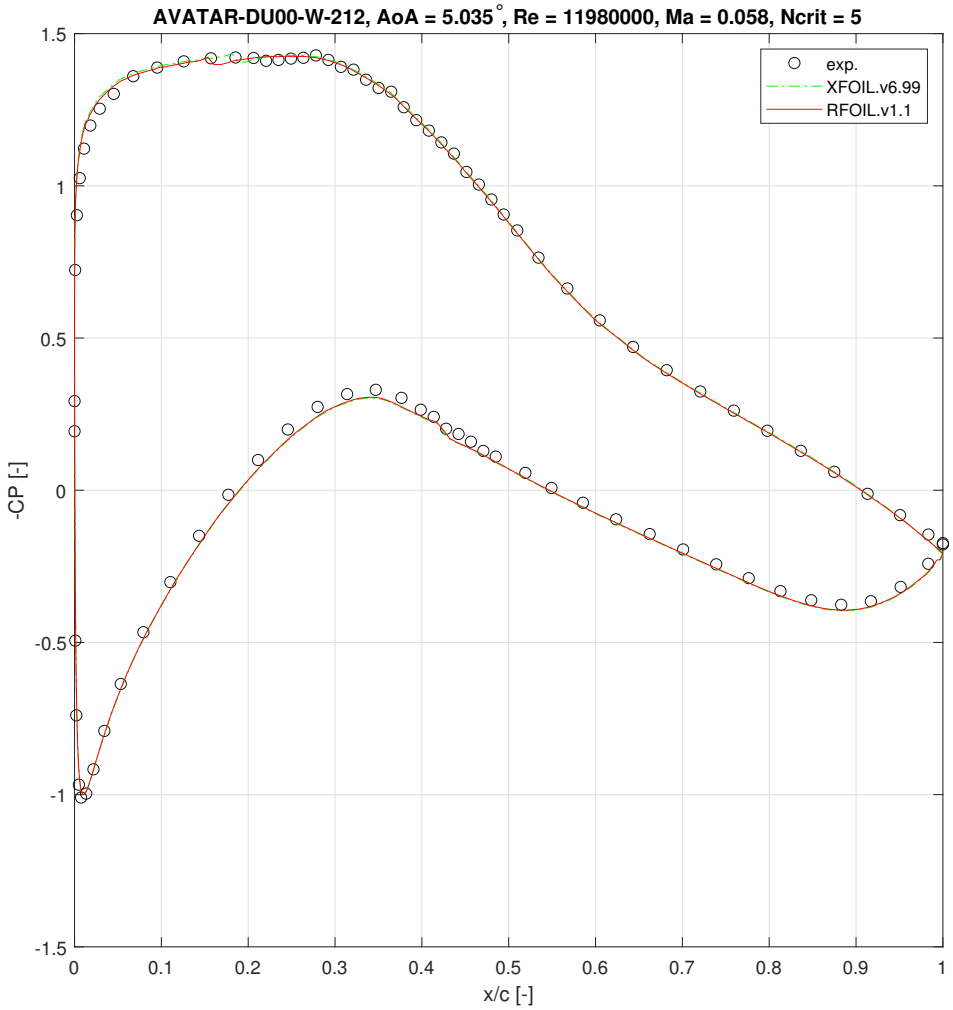

Figure C.373: Comparison between experimental and numerical pressure distributions for the AVATAR-DU00-W-212 airfoil at a Reynolds number of 8990000, and at an angle of attack and a Mach number of 5.061° and 0.043, respectively.

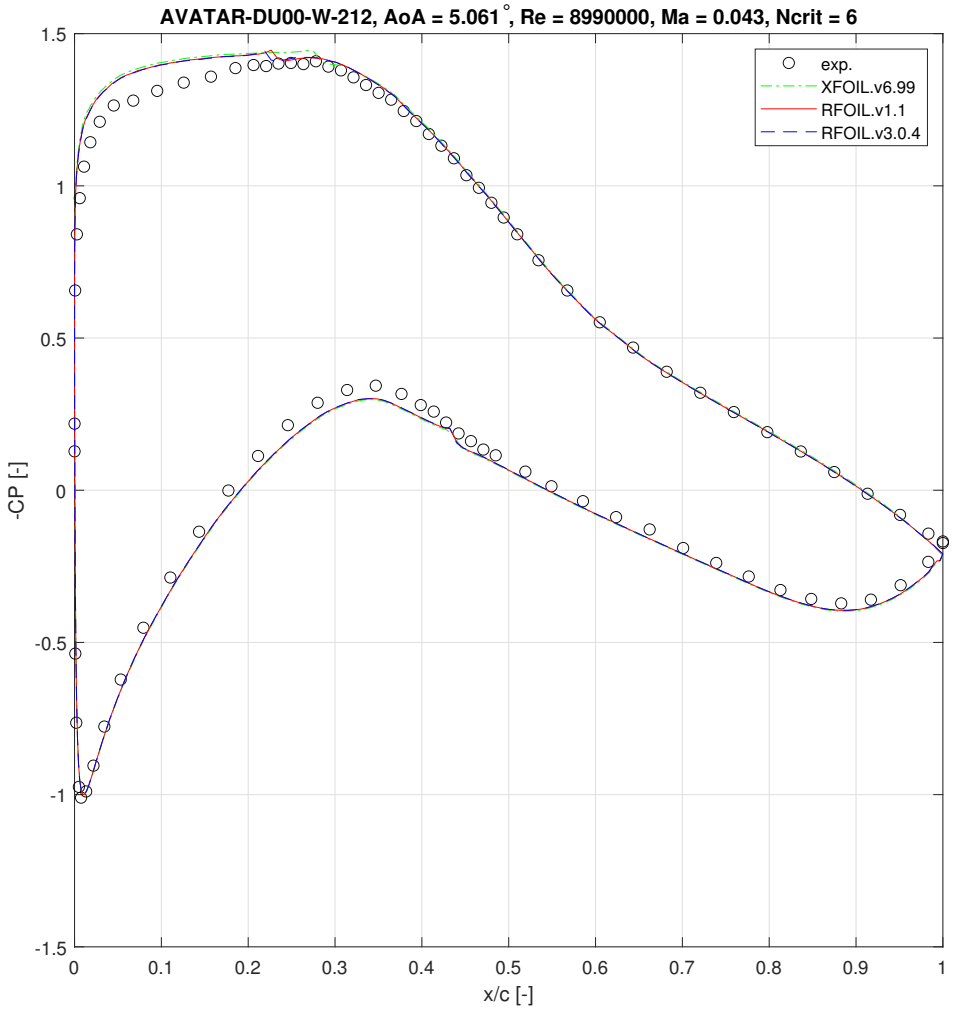

Figure C.374: Comparison between experimental and numerical pressure distributions for the AVATAR-DU00-W-212 airfoil at a Reynolds number of 6050000, and at an angle of attack and a Mach number of 5.062° and 0.029, respectively.

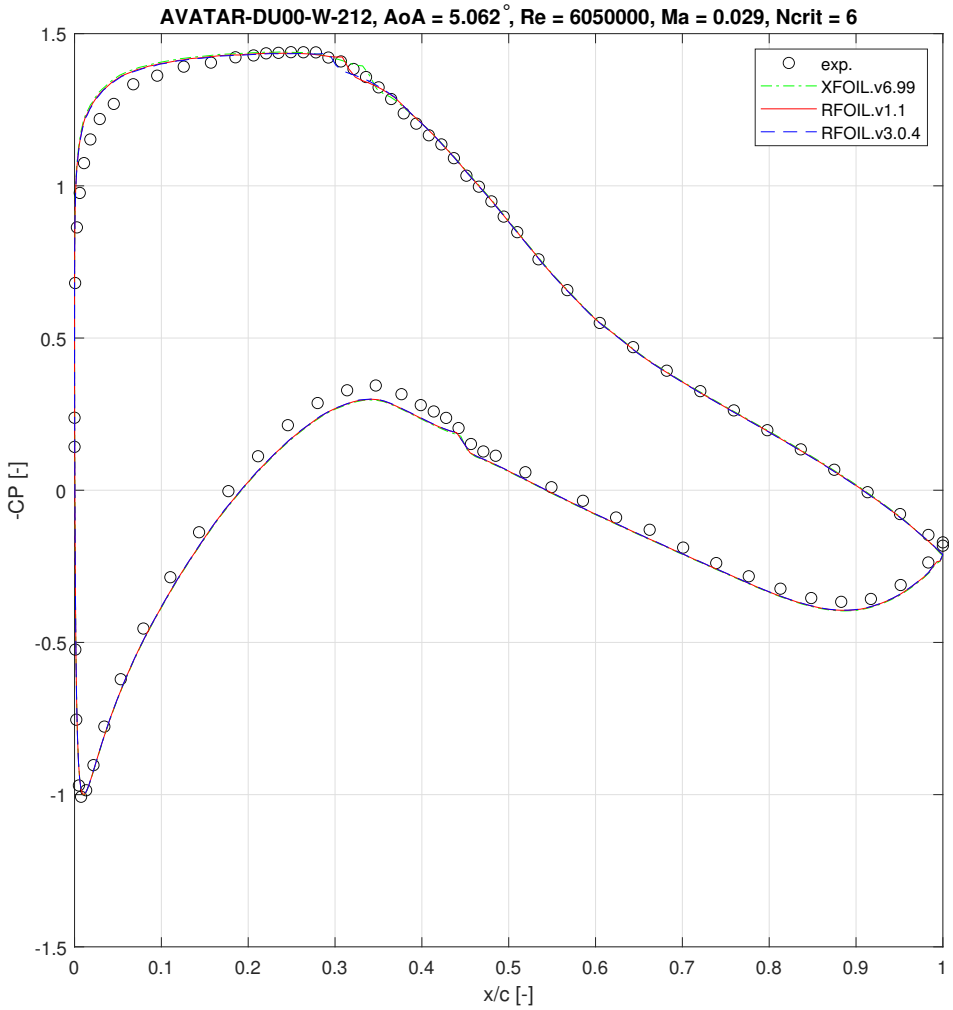

Figure C.375: Comparison between experimental and numerical pressure distributions for the AVATAR-DU00-W-212 airfoil at a Reynolds number of 5970000, and at an angle of attack and a Mach number of 5.063° and 0.054, respectively.

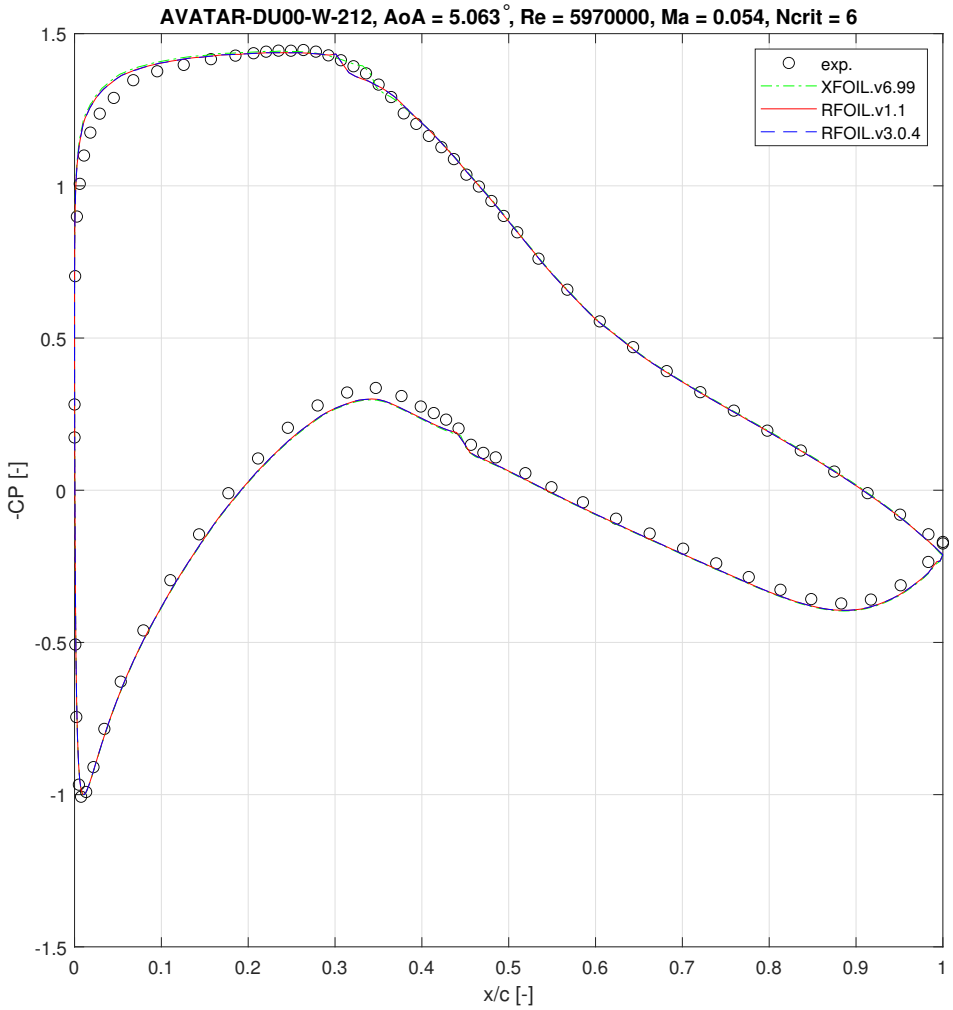

Figure C.376: Comparison between experimental and numerical pressure distributions for the AVATAR-DU00-W-212 airfoil at a Reynolds number of 8990000, and at an angle of attack and a Mach number of 5.063° and 0.083, respectively.

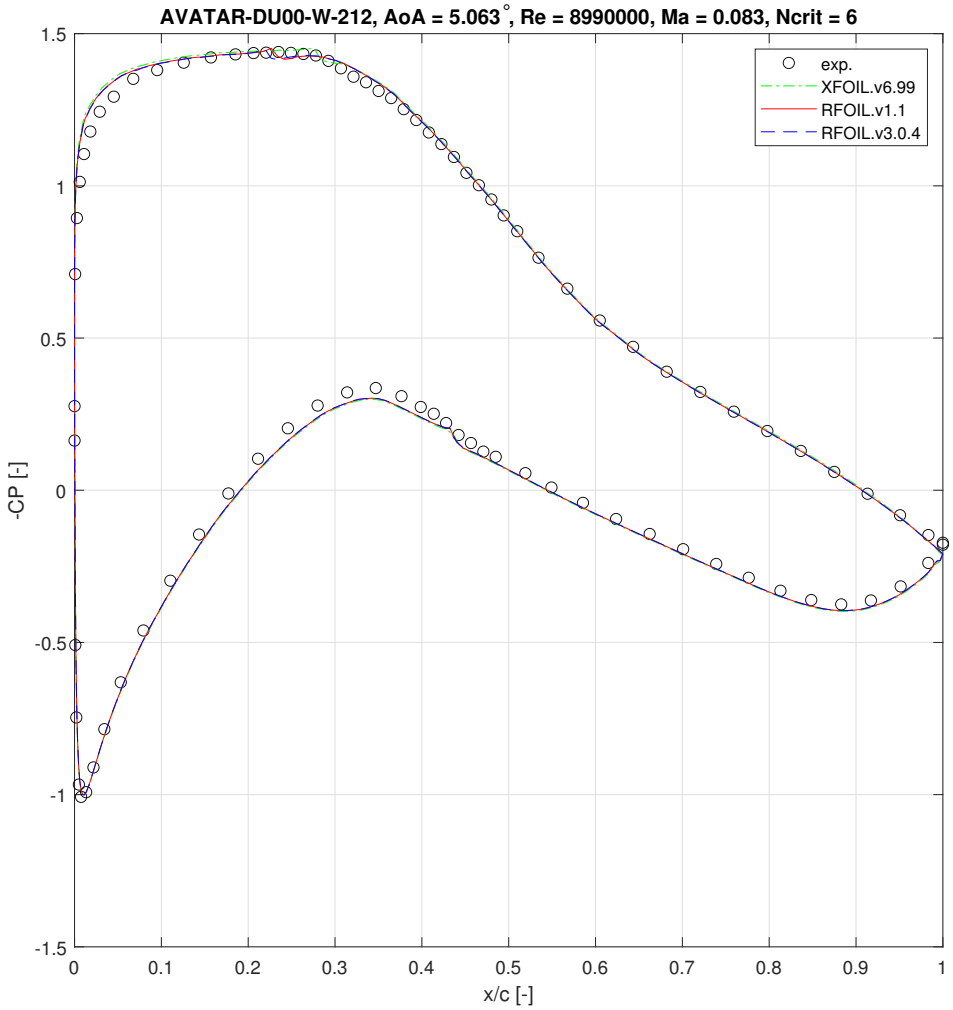

Figure C.377: Comparison between experimental and numerical pressure distributions for the AVATAR-DU00-W-212 airfoil at a Reynolds number of 15010000, and at an angle of attack and a Mach number of 5.064° and 0.081, respectively.

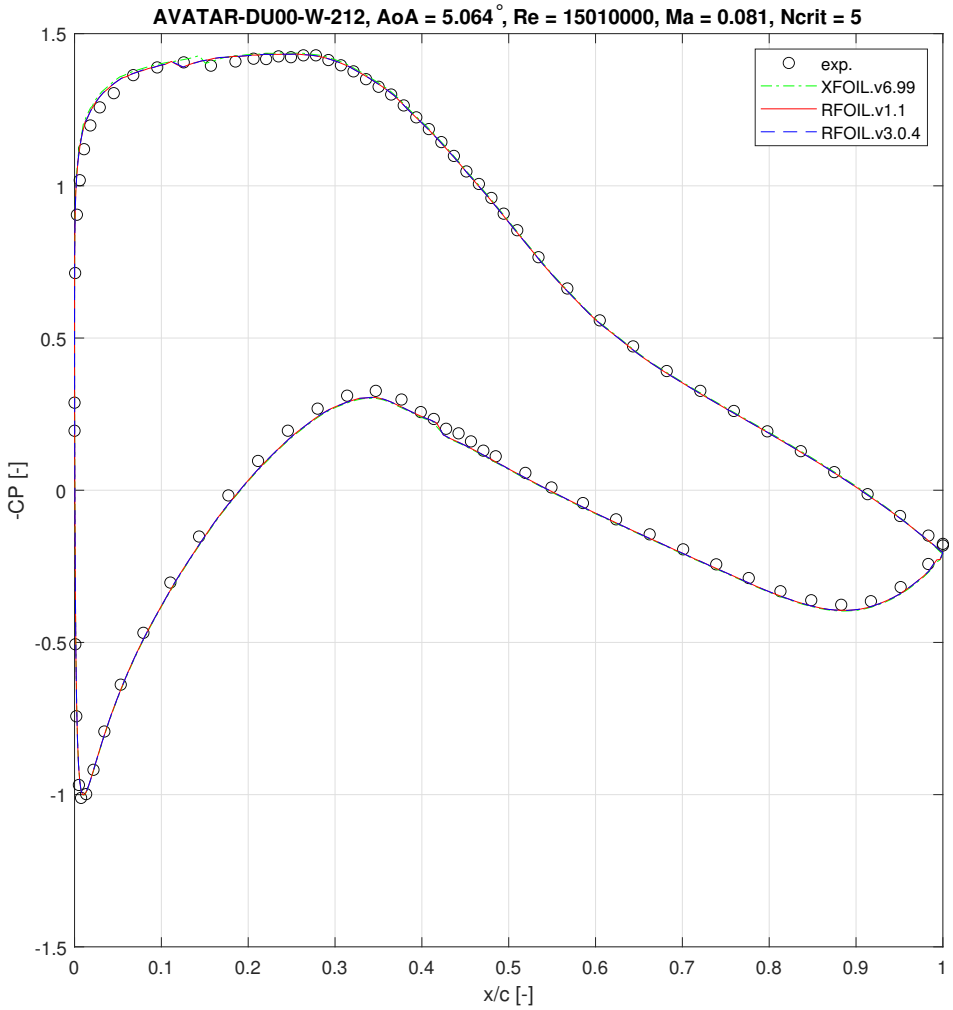

Figure C.378: Comparison between experimental and numerical pressure distributions for the AVATAR-DU00-W-212 airfoil at a Reynolds number of 2980000, and at an angle of attack and a Mach number of 5.064° and 0.073, respectively.

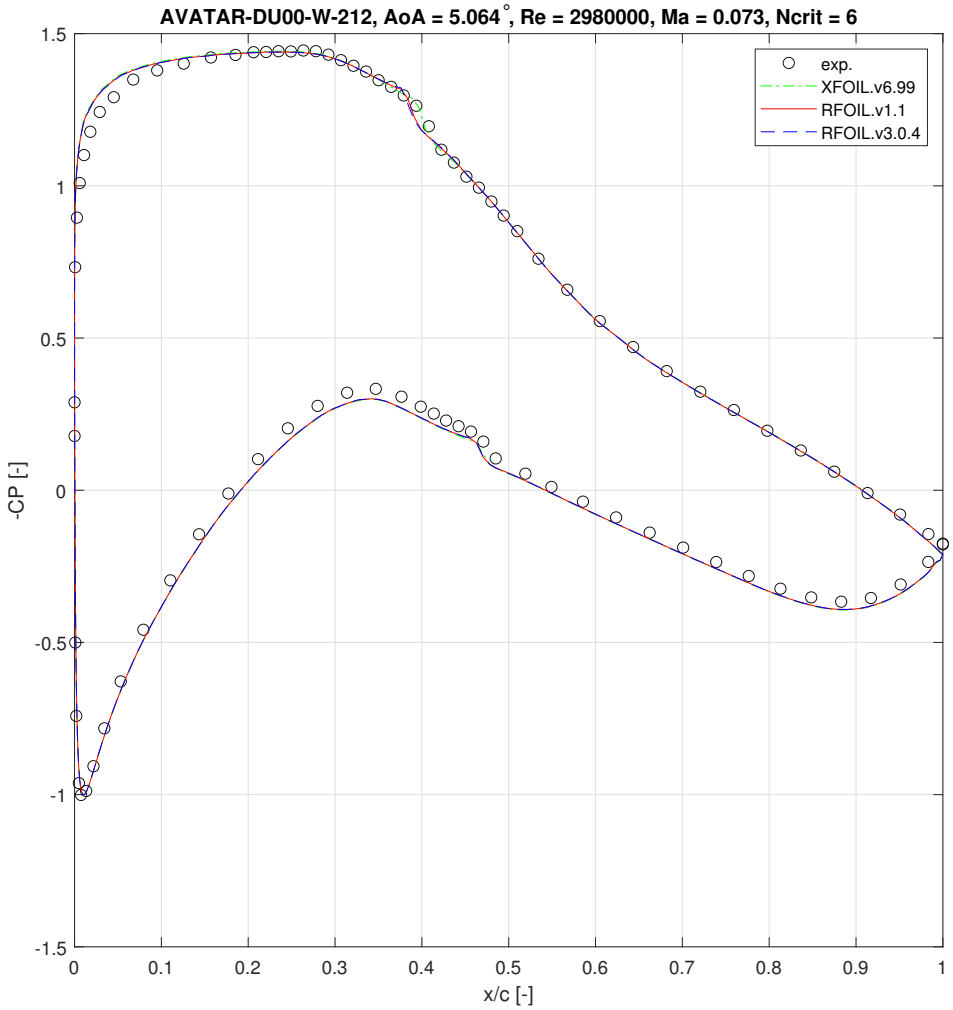

Figure C.379: Comparison between experimental and numerical pressure distributions for the AVATAR-DU00-W-212 airfoil at a Reynolds number of 6020000, and at an angle of attack and a Mach number of 5.064° and 0.055, respectively.

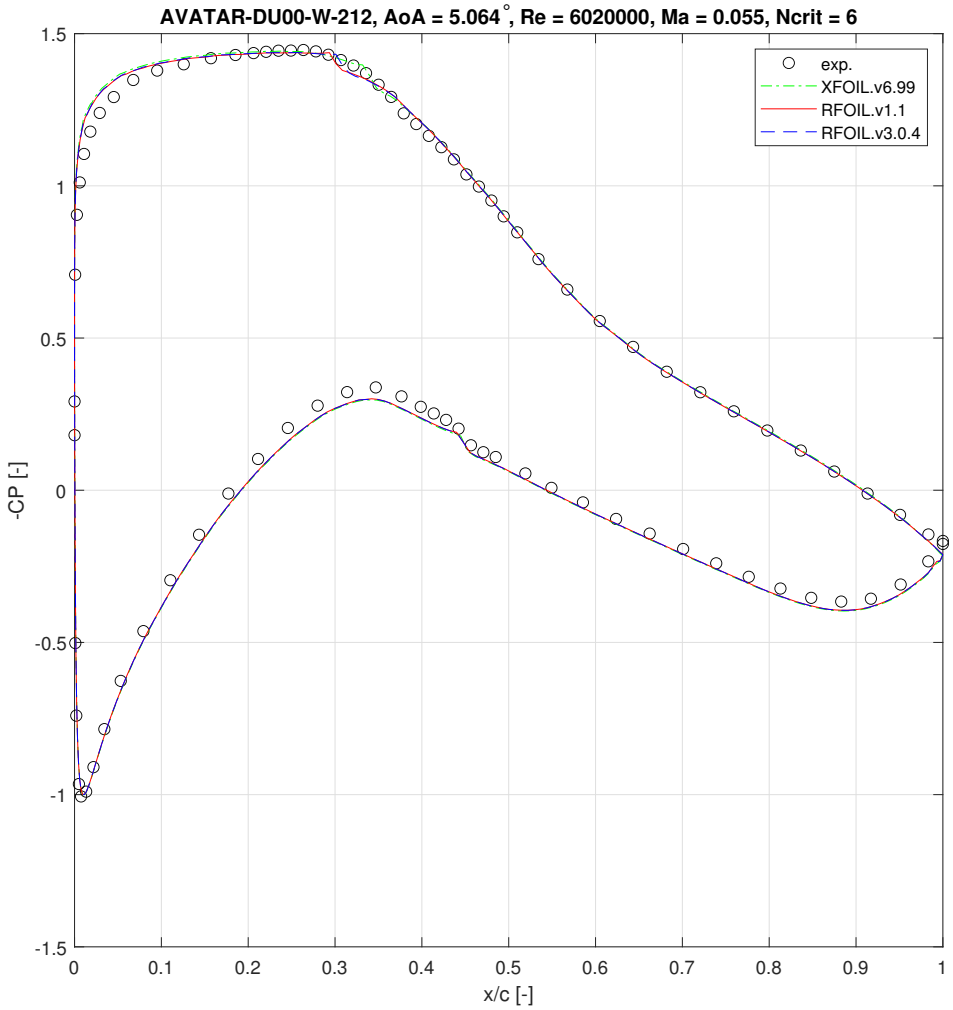

Figure C.380: Comparison between experimental and numerical pressure distributions for the AVATAR-DU00-W-212 airfoil at a Reynolds number of 8990000, and at an angle of attack and a Mach number of 5.264° and 0.043, respectively.

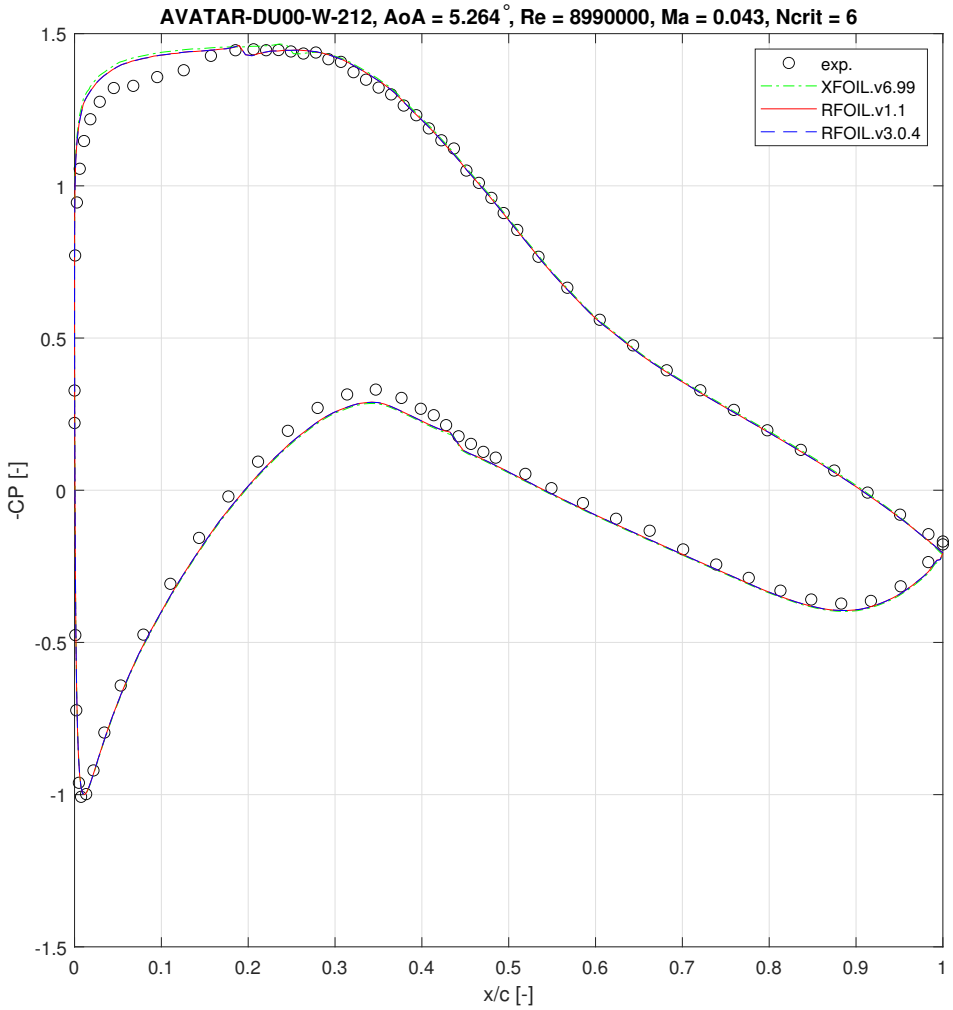

Figure C.381: Comparison between experimental and numerical pressure distributions for the AVATAR-DU00-W-212 airfoil at a Reynolds number of 2980000, and at an angle of attack and a Mach number of 5.266° and 0.073, respectively.

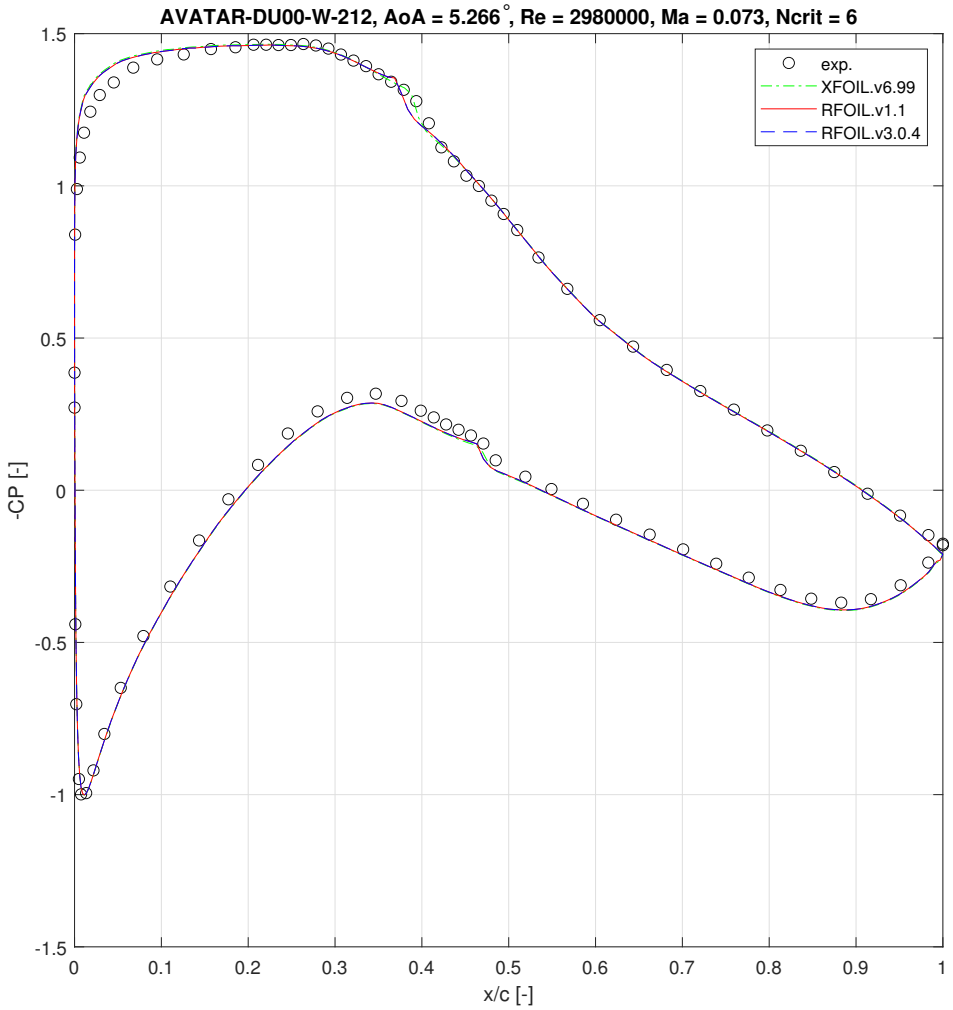

Figure C.382: Comparison between experimental and numerical pressure distributions for the AVATAR-DU00-W-212 airfoil at a Reynolds number of 6010000, and at an angle of attack and a Mach number of 5.266° and 0.055, respectively.

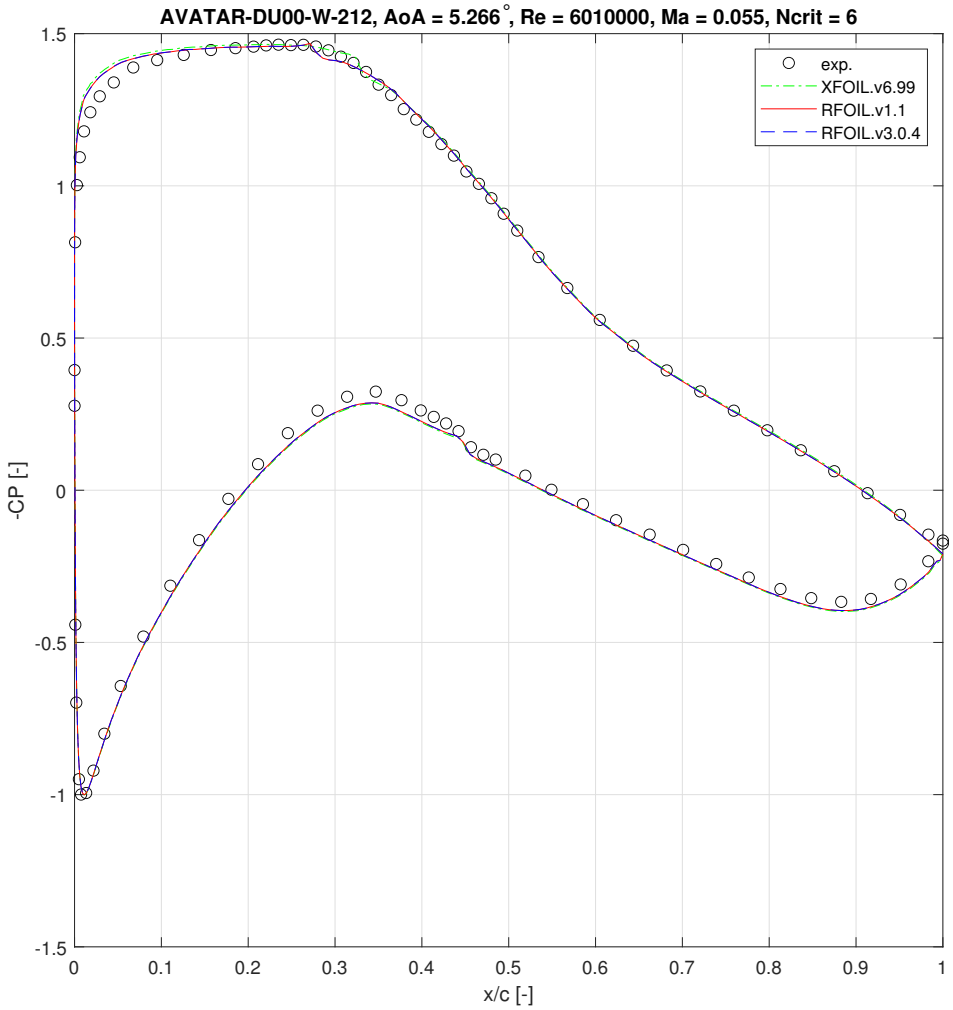

Figure C.383: Comparison between experimental and numerical pressure distributions for the AVATAR-DU00-W-212 airfoil at a Reynolds number of 8990000, and at an angle of attack and a Mach number of 5.266° and 0.083, respectively.

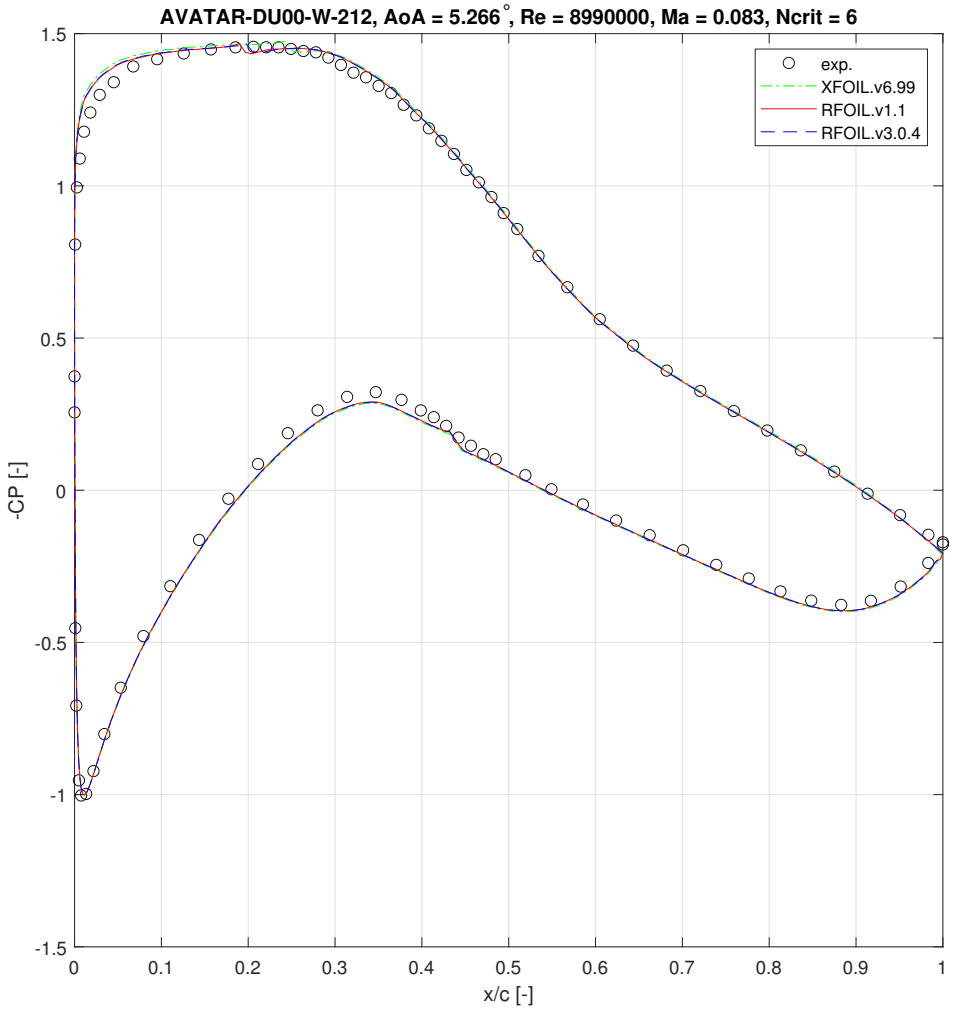

Figure C.384: Comparison between experimental and numerical pressure distributions for the AVATAR-DU00-W-212 airfoil at a Reynolds number of 2980000, and at an angle of attack and a Mach number of 5.469° and 0.073, respectively.

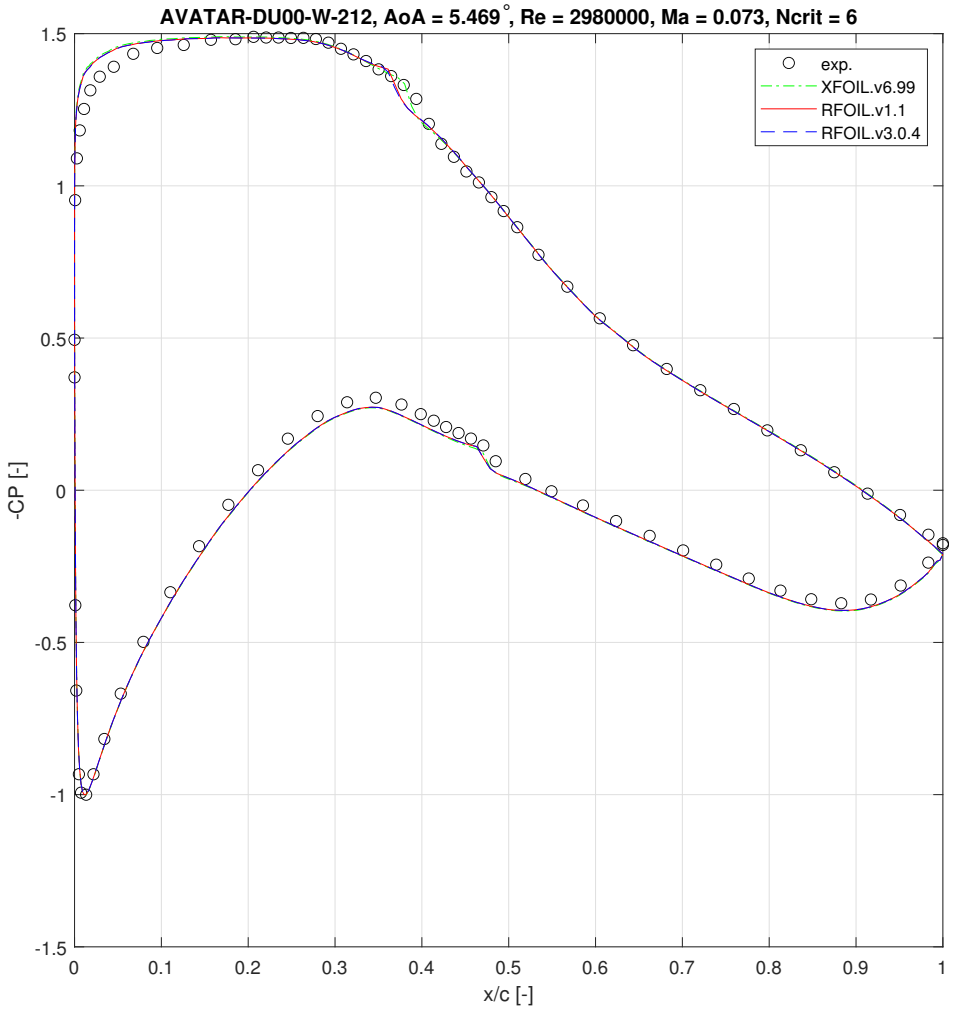

Figure C.385: Comparison between experimental and numerical pressure distributions for the AVATAR-DU00-W-212 airfoil at a Reynolds number of 8980000, and at an angle of attack and a Mach number of 5.567° and 0.043, respectively.

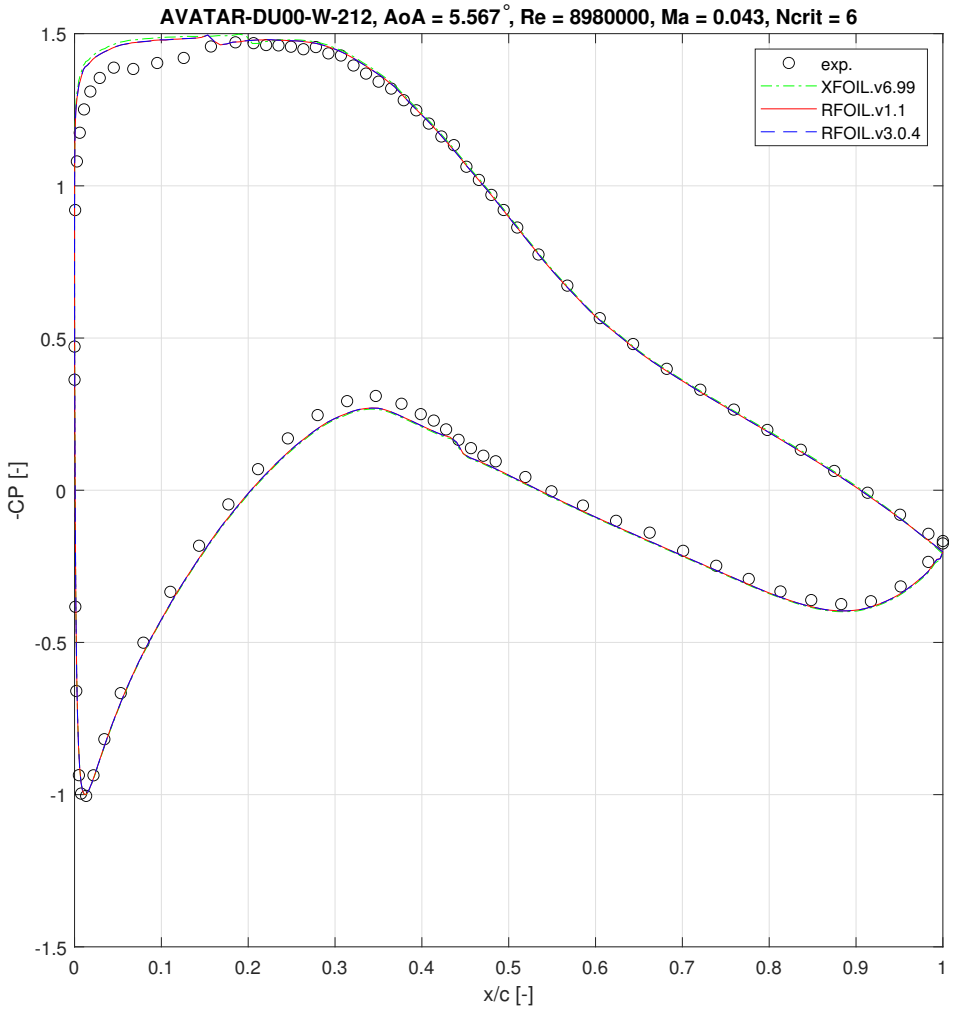

Figure C.386: Comparison between experimental and numerical pressure distributions for the AVATAR-DU00-W-212 airfoil at a Reynolds number of 6040000, and at an angle of attack and a Mach number of 5.568° and 0.029, respectively.

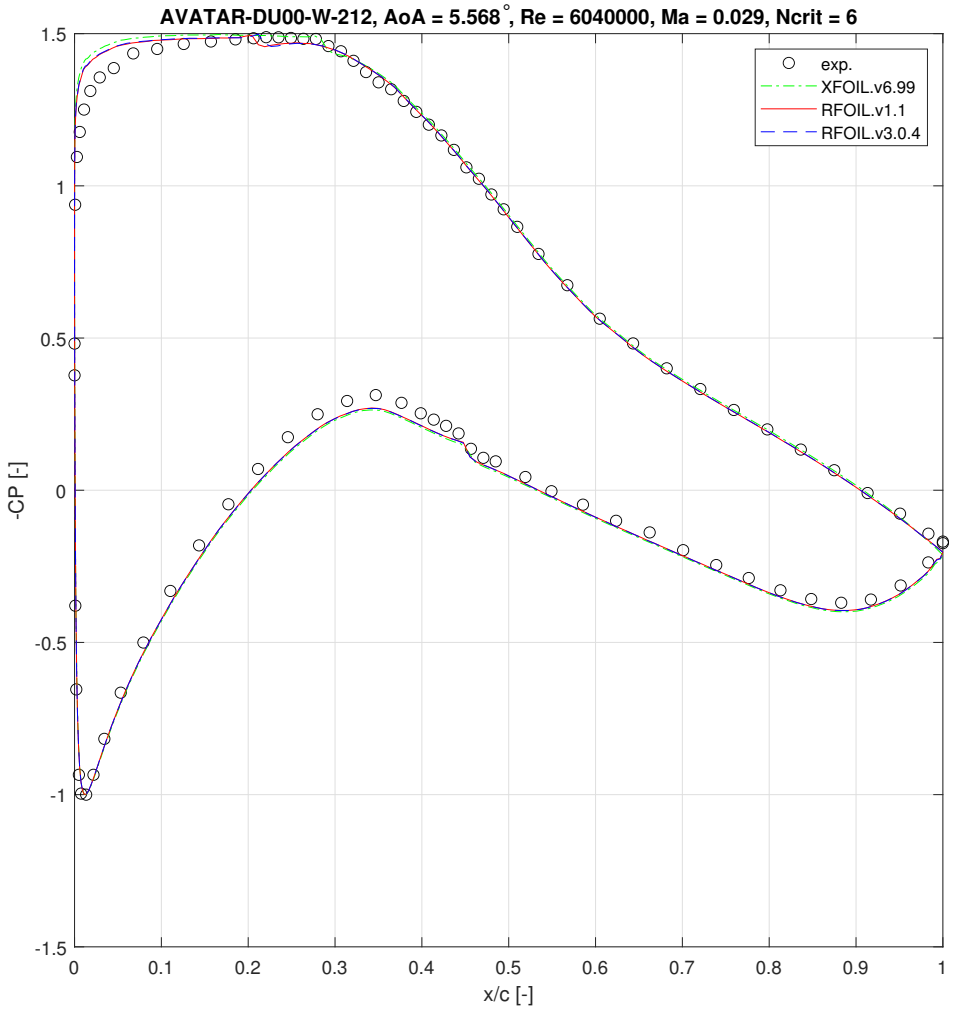

Figure C.387: Comparison between experimental and numerical pressure distributions for the AVATAR-DU00-W-212 airfoil at a Reynolds number of 9000000, and at an angle of attack and a Mach number of 5.568° and 0.044, respectively.

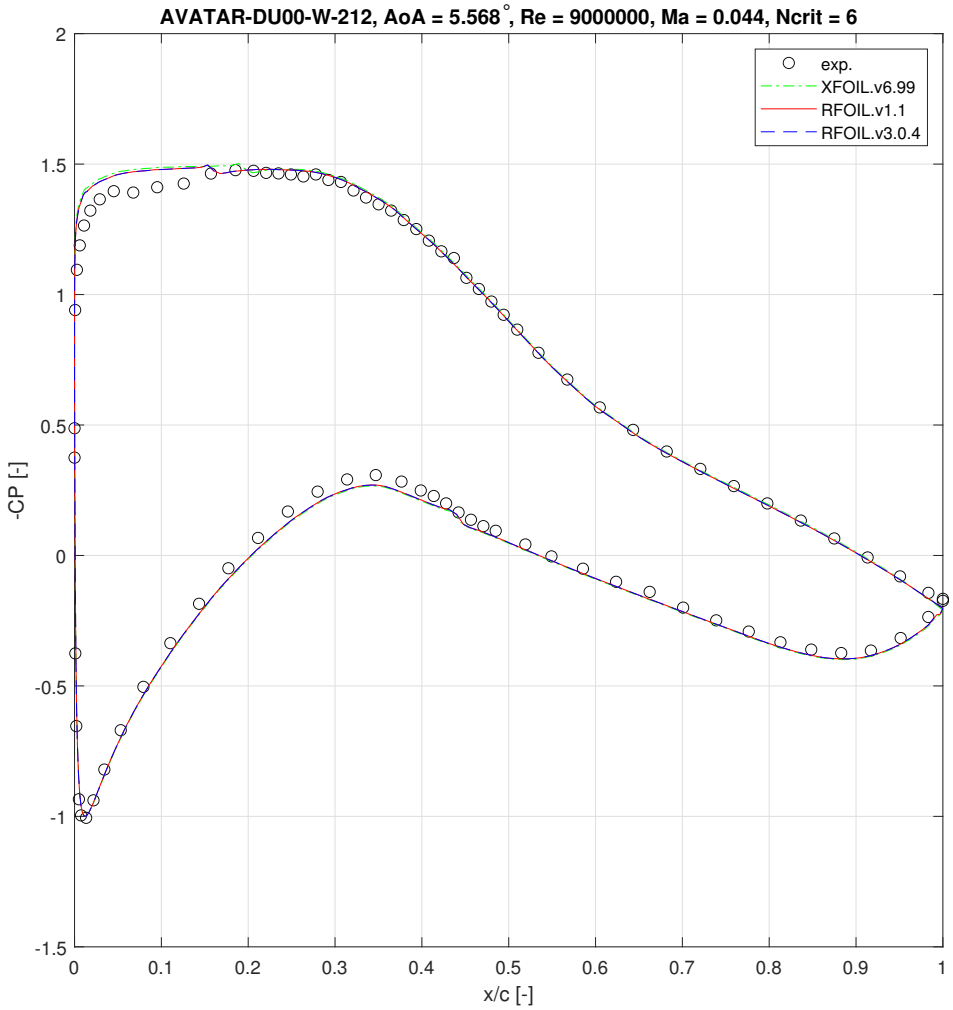

Figure C.388: Comparison between experimental and numerical pressure distributions for the AVATAR-DU00-W-212 airfoil at a Reynolds number of 5980000, and at an angle of attack and a Mach number of 5.570° and 0.055, respectively.

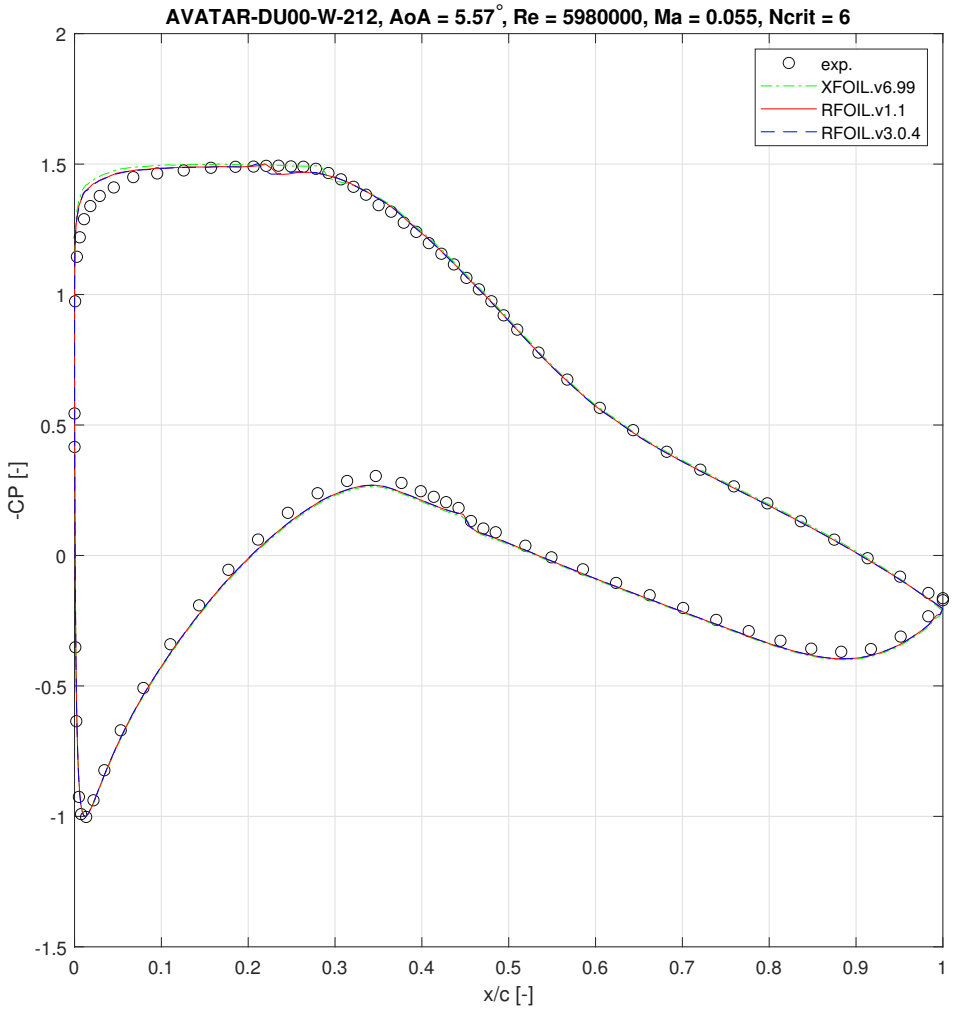

Figure C.389: Comparison between experimental and numerical pressure distributions for the AVATAR-DU00-W-212 airfoil at a Reynolds number of 8970000, and at an angle of attack and a Mach number of 5.570° and 0.083, respectively.

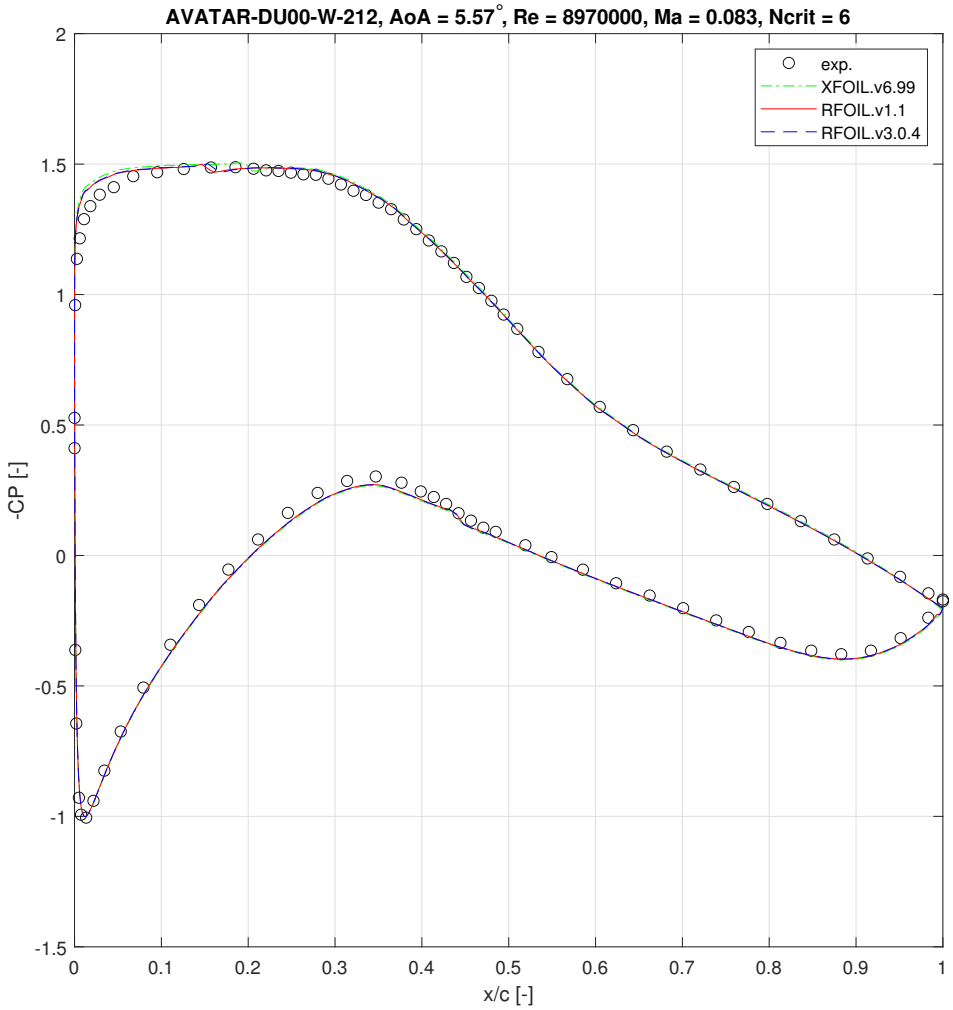

Figure C.390: Comparison between experimental and numerical pressure distributions for the AVATAR-DU00-W-212 airfoil at a Reynolds number of 2990000, and at an angle of attack and a Mach number of 5.672° and 0.074, respectively.

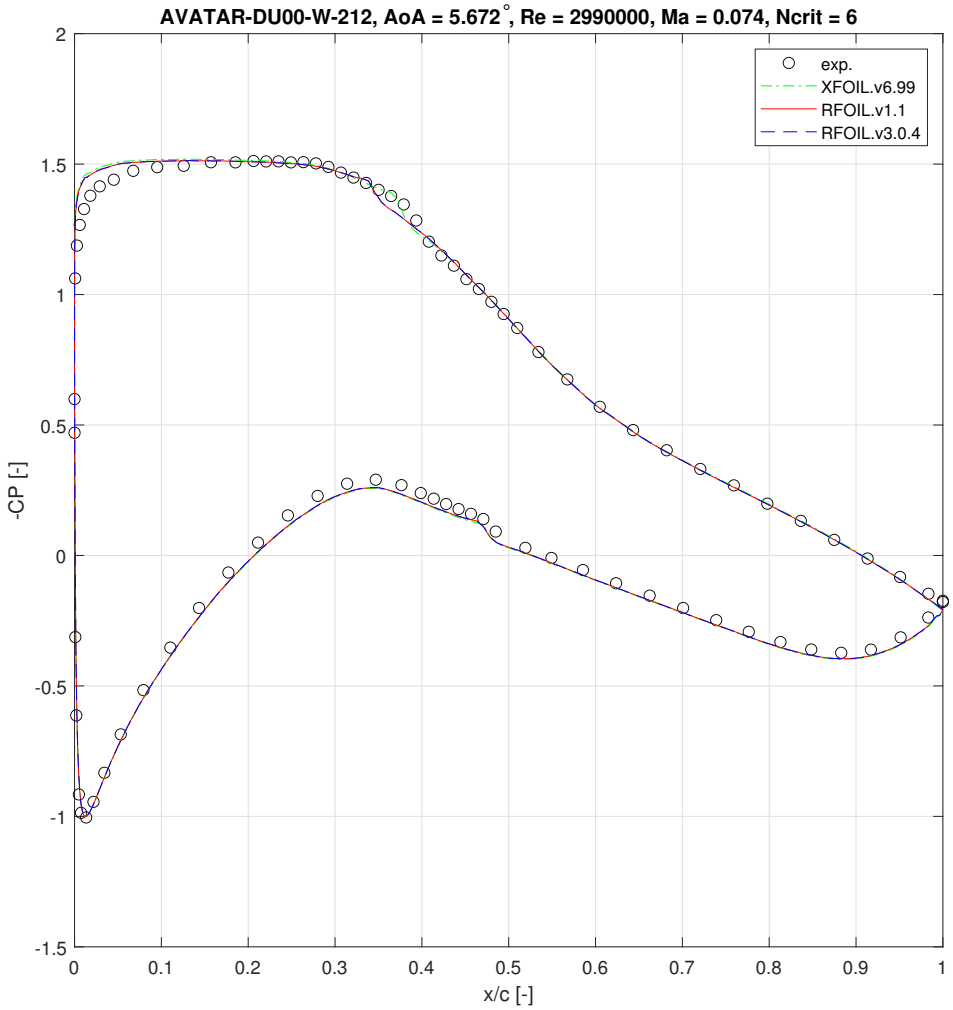

Figure C.391: Comparison between experimental and numerical pressure distributions for the AVATAR-DU00-W-212 airfoil at a Reynolds number of 2980000, and at an angle of attack and a Mach number of 5.874° and 0.074, respectively.

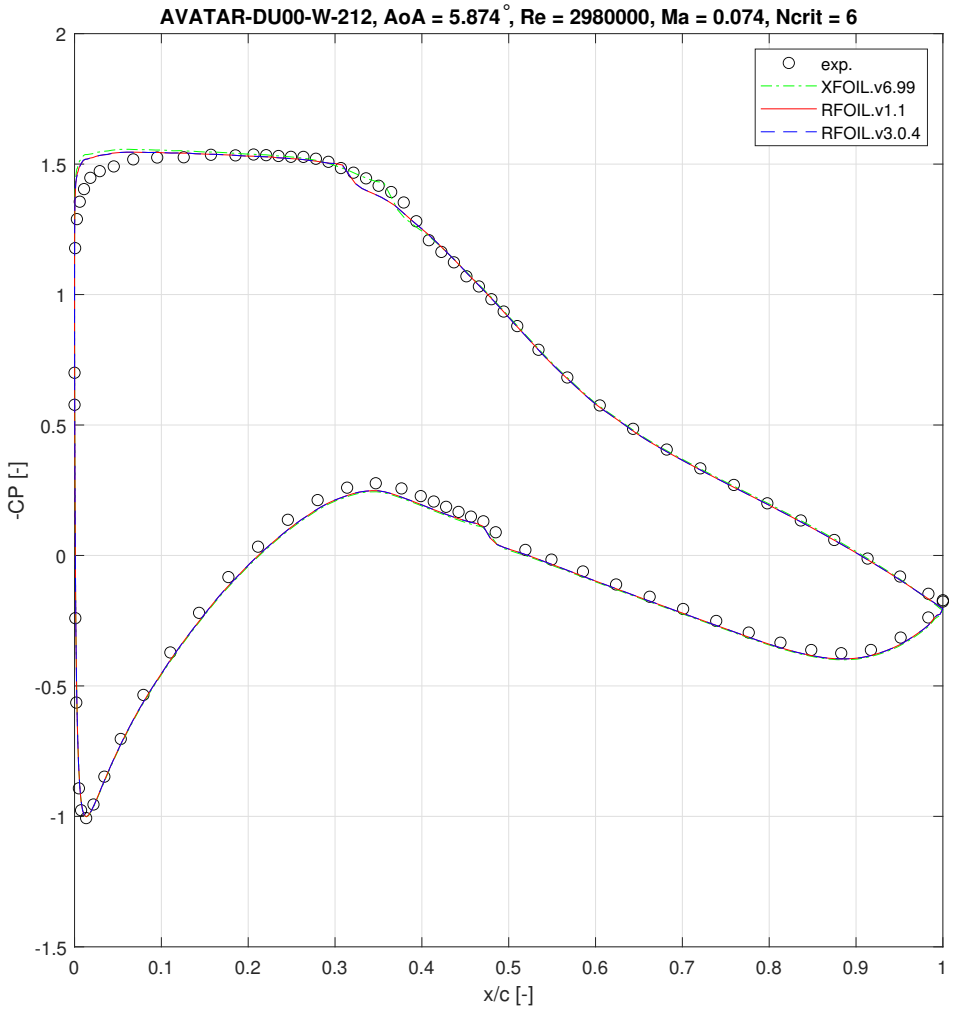

Figure C.392: Comparison between experimental and numerical pressure distributions for the AVATAR-DU00-W-212 airfoil at a Reynolds number of 12020000, and at an angle of attack and a Mach number of 6.034° and 0.058, respectively.

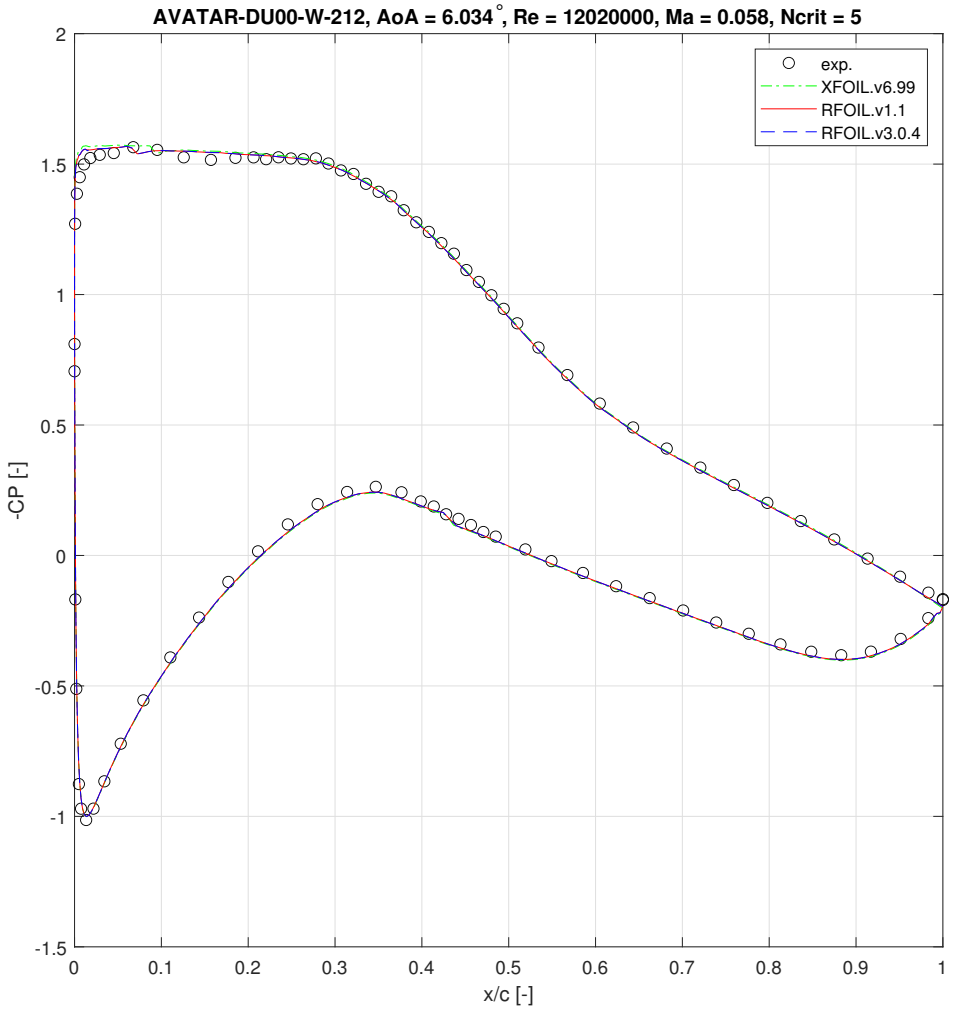

Figure C.393: Comparison between experimental and numerical pressure distributions for the AVATAR-DU00-W-212 airfoil at a Reynolds number of 9000000, and at an angle of attack and a Mach number of 6.073° and 0.044, respectively.

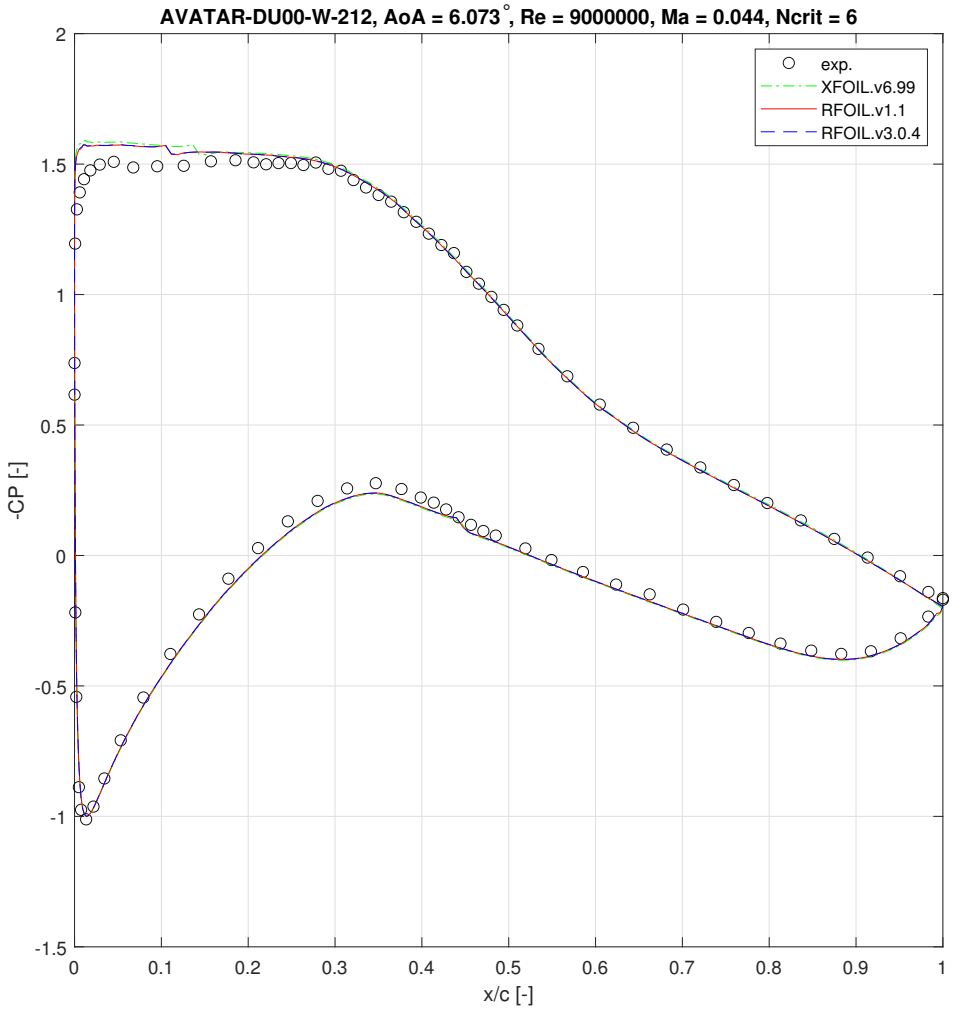

Figure C.394: Comparison between experimental and numerical pressure distributions for the AVATAR-DU00-W-212 airfoil at a Reynolds number of 9010000, and at an angle of attack and a Mach number of 6.073° and 0.043, respectively.

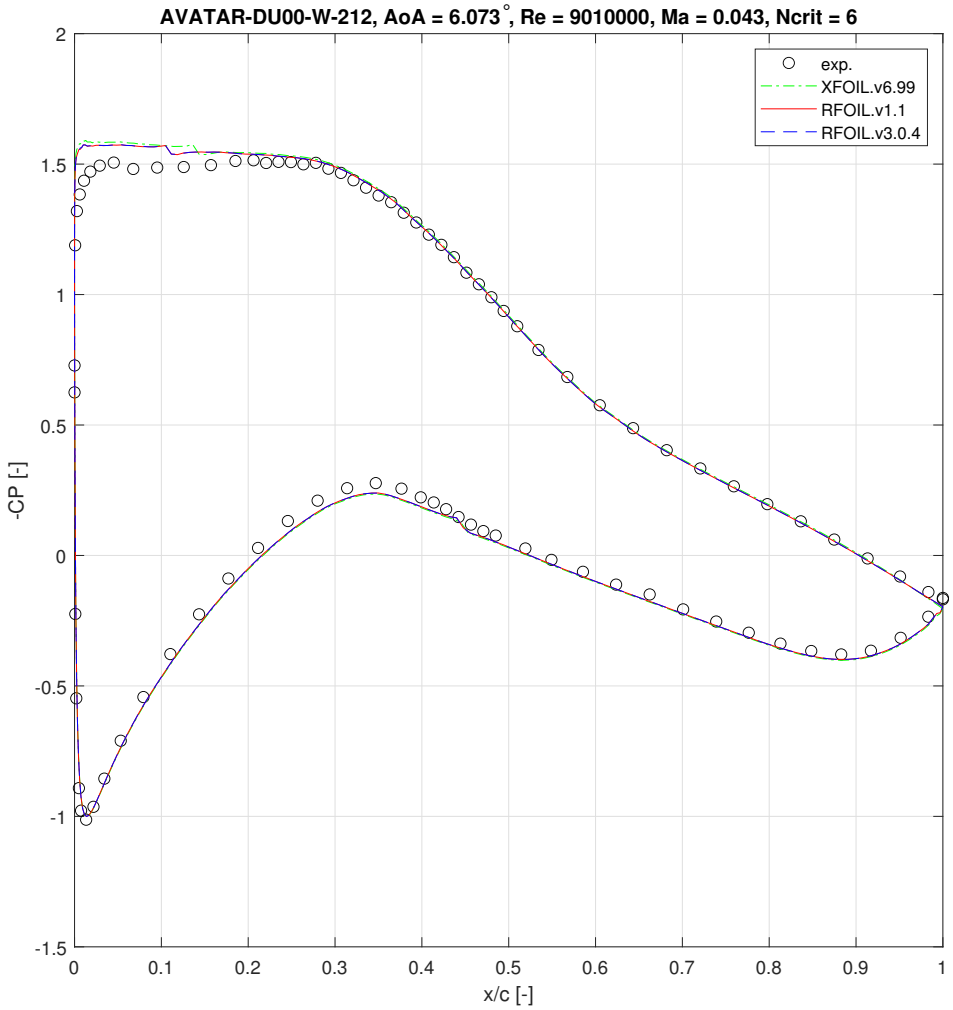

Figure C.395: Comparison between experimental and numerical pressure distributions for the AVATAR-DU00-W-212 airfoil at a Reynolds number of 5990000, and at an angle of attack and a Mach number of 6.075° and 0.029, respectively.

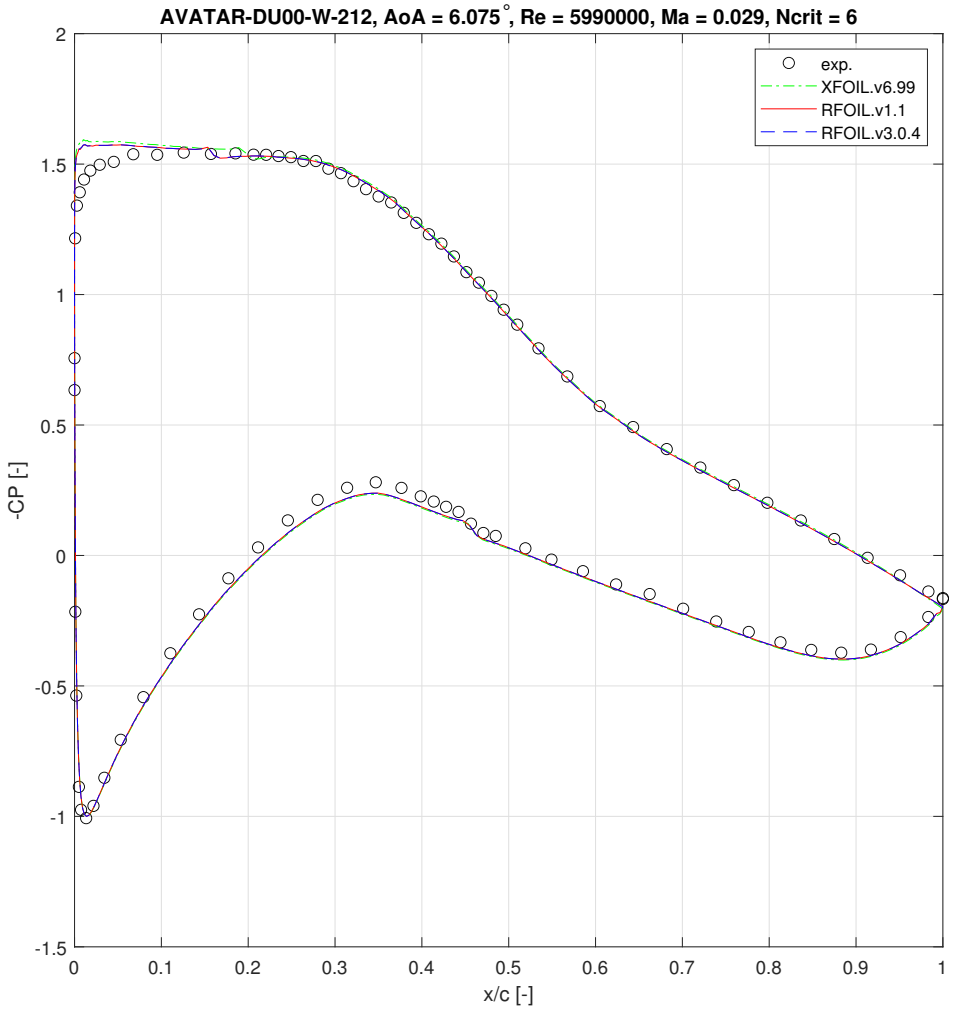

Figure C.396: Comparison between experimental and numerical pressure distributions for the AVATAR-DU00-W-212 airfoil at a Reynolds number of 15020000, and at an angle of attack and a Mach number of 6.076° and 0.081, respectively.

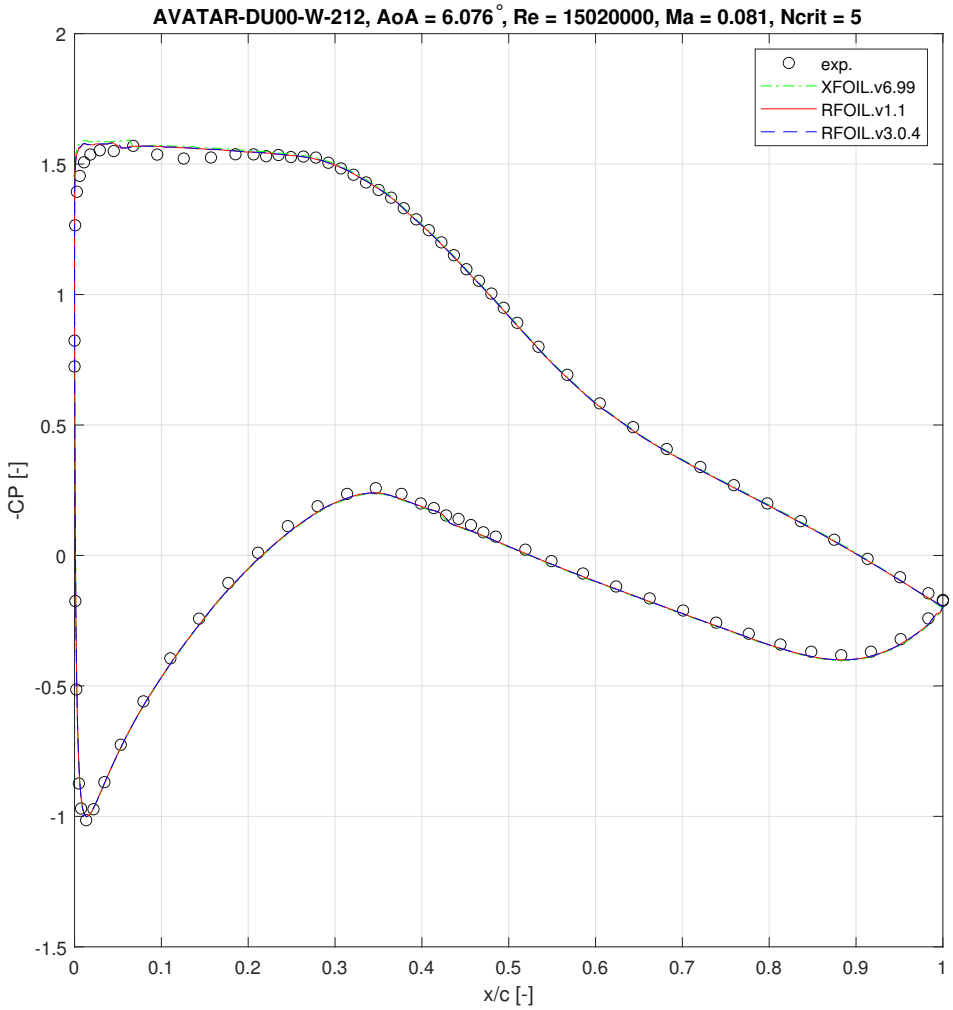

Figure C.397: Comparison between experimental and numerical pressure distributions for the AVATAR-DU00-W-212 airfoil at a Reynolds number of 5970000, and at an angle of attack and a Mach number of 6.076° and 0.055, respectively.

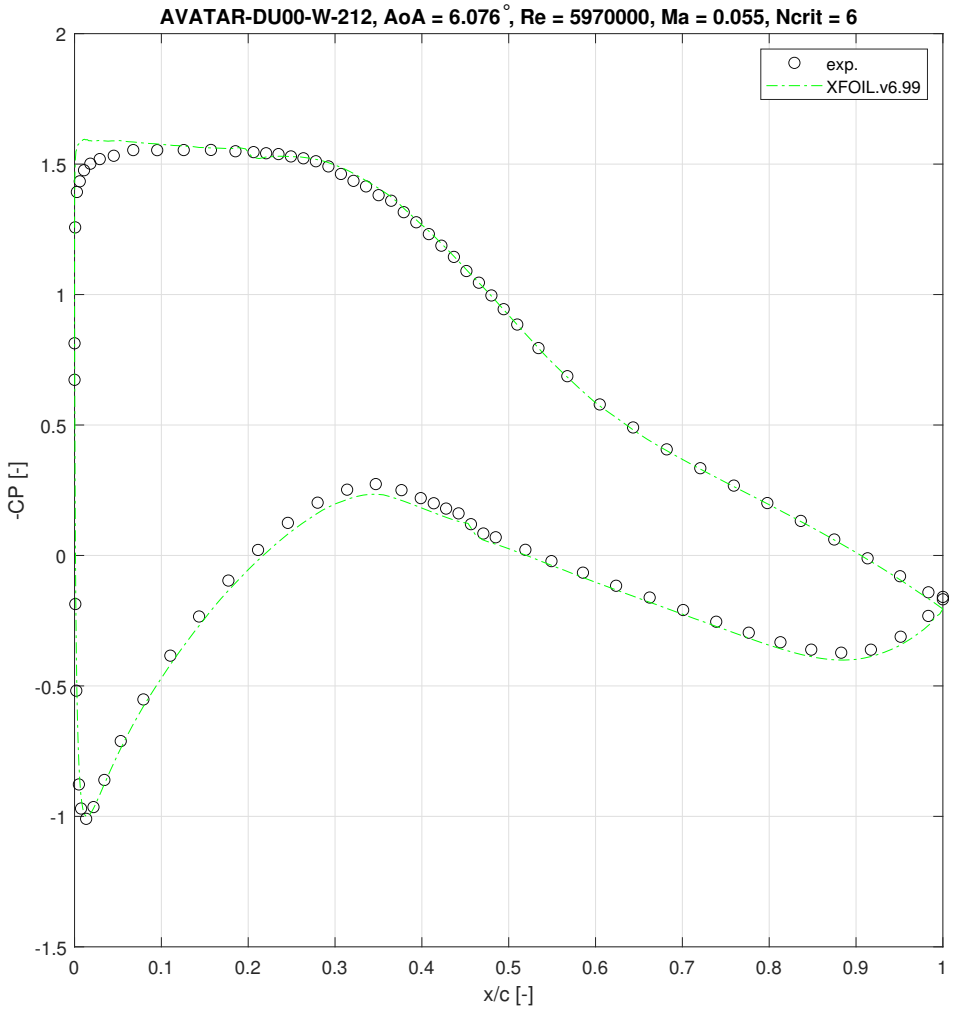

Figure C.398: Comparison between experimental and numerical pressure distributions for the AVATAR-DU00-W-212 airfoil at a Reynolds number of 6010000, and at an angle of attack and a Mach number of 6.076° and 0.055, respectively.

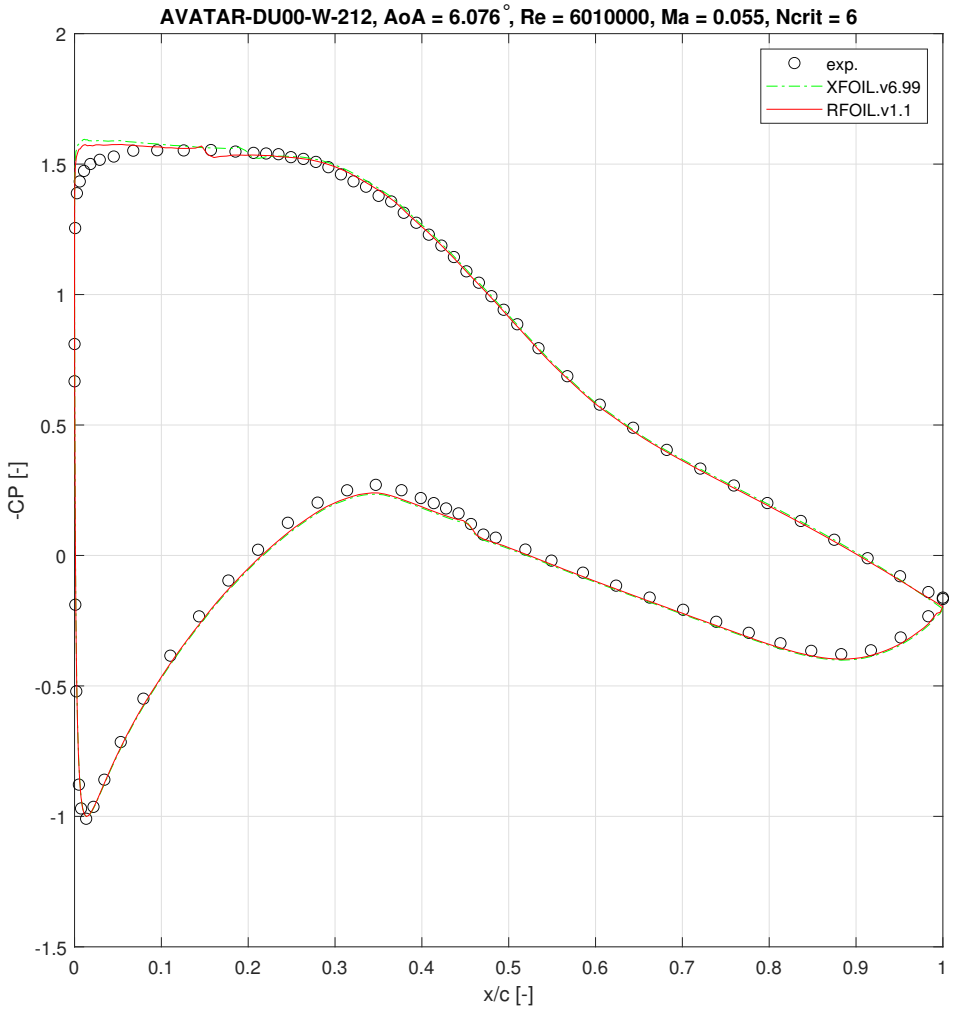

Figure C.399: Comparison between experimental and numerical pressure distributions for the AVATAR-DU00-W-212 airfoil at a Reynolds number of 8990000, and at an angle of attack and a Mach number of 6.076° and 0.083, respectively.

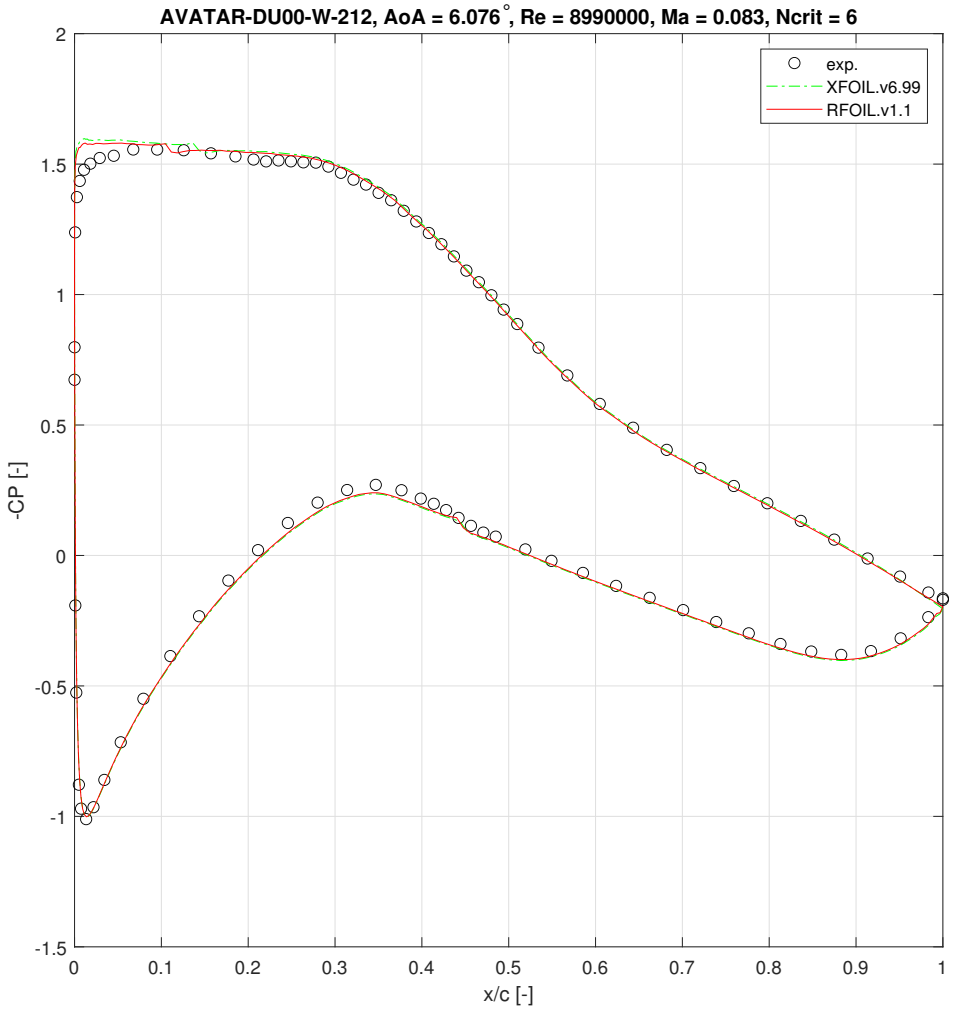

Figure C.400: Comparison between experimental and numerical pressure distributions for the AVATAR-DU00-W-212 airfoil at a Reynolds number of 2970000, and at an angle of attack and a Mach number of 6.077° and 0.073, respectively.

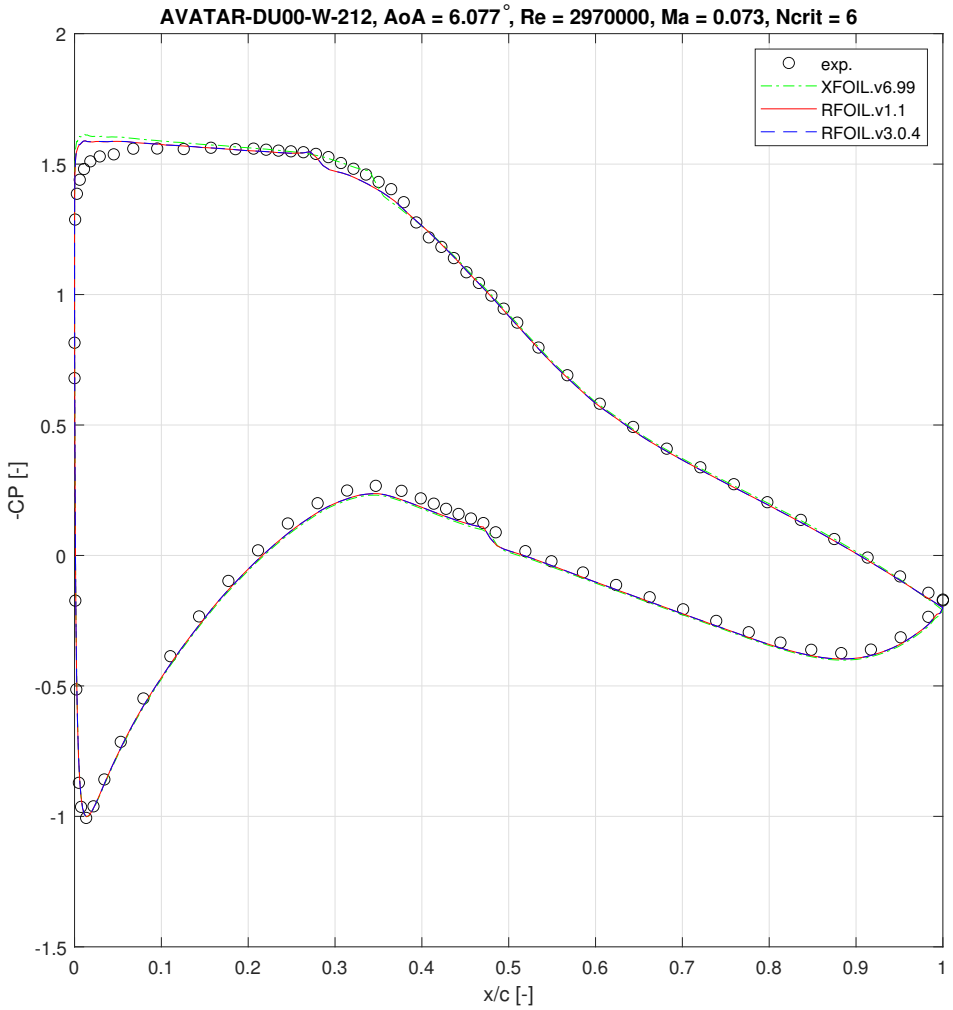

Figure C.401: Comparison between experimental and numerical pressure distributions for the AVATAR-DU00-W-212 airfoil at a Reynolds number of 2990000, and at an angle of attack and a Mach number of 6.077° and 0.074, respectively.

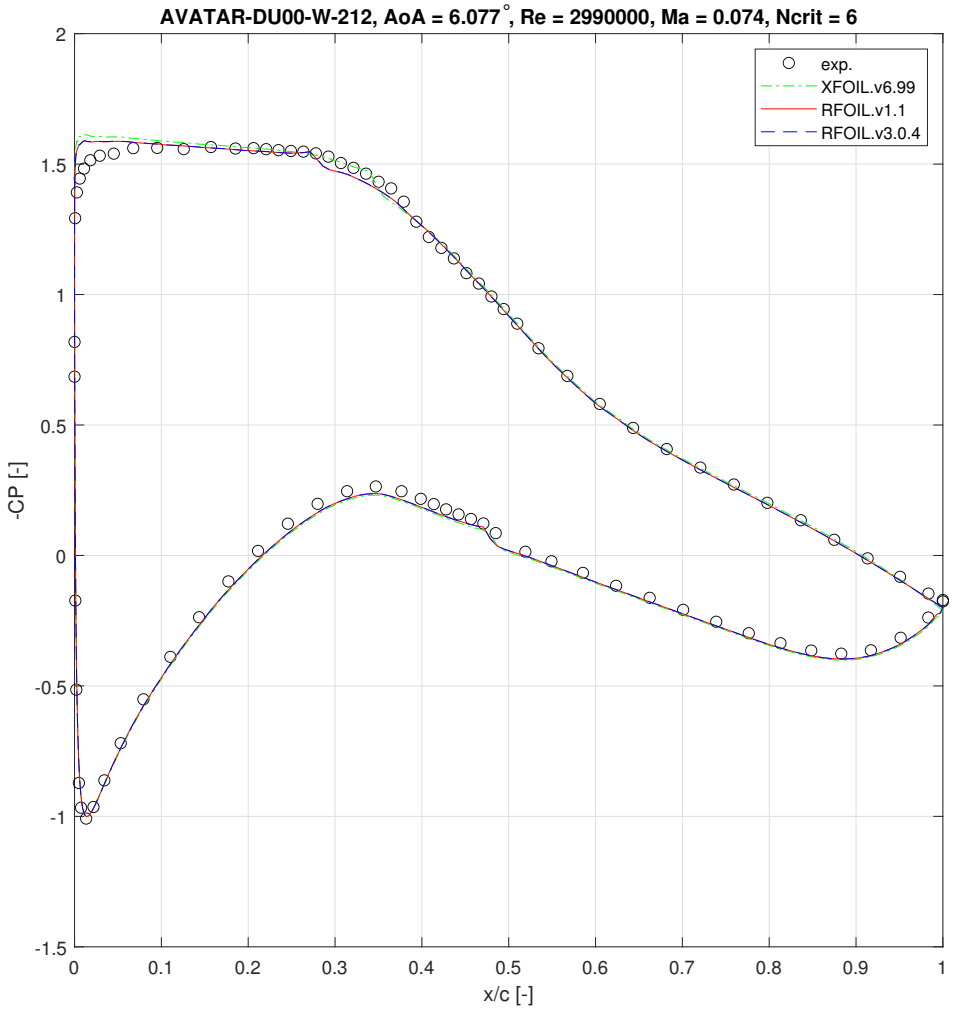

Figure C.402: Comparison between experimental and numerical pressure distributions for the AVATAR-DU00-W-212 airfoil at a Reynolds number of 2990000, and at an angle of attack and a Mach number of 6.279° and 0.074, respectively.

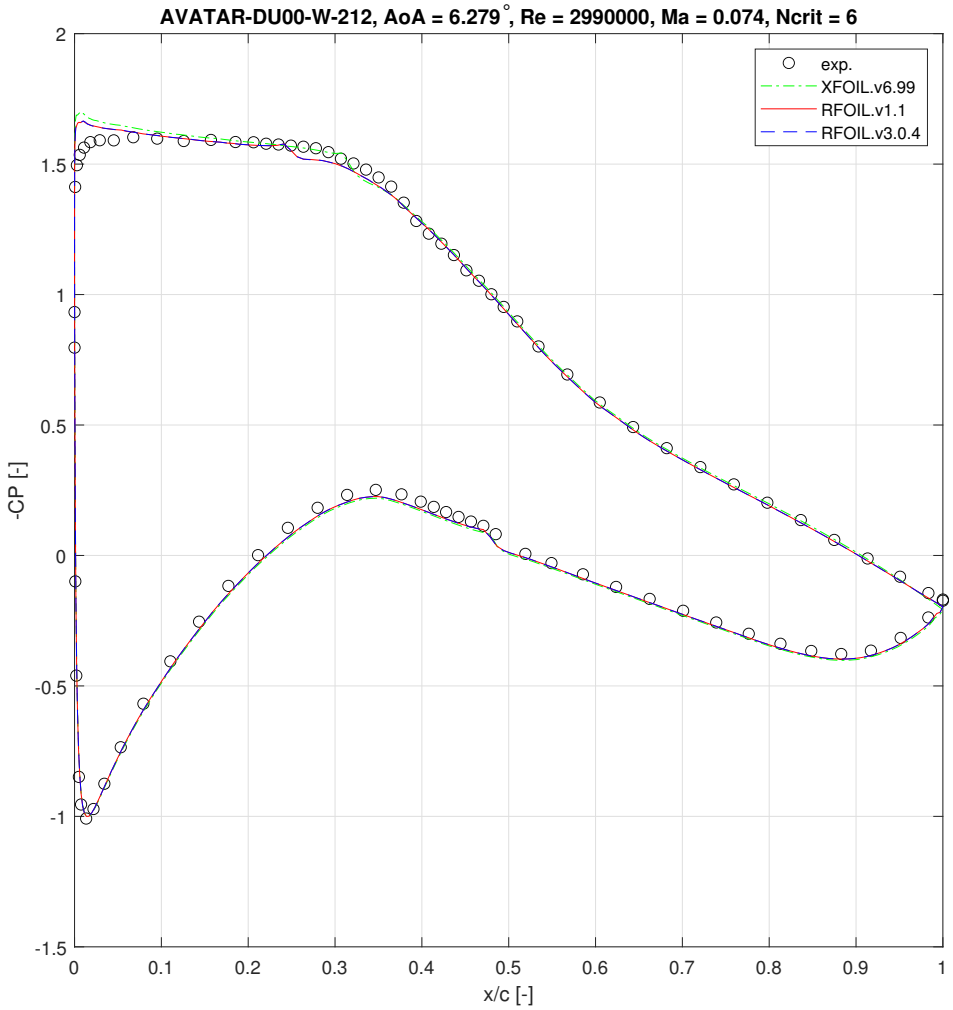

Figure C.403: Comparison between experimental and numerical pressure distributions for the AVATAR-DU00-W-212 airfoil at a Reynolds number of 2990000, and at an angle of attack and a Mach number of 6.482° and 0.074, respectively.

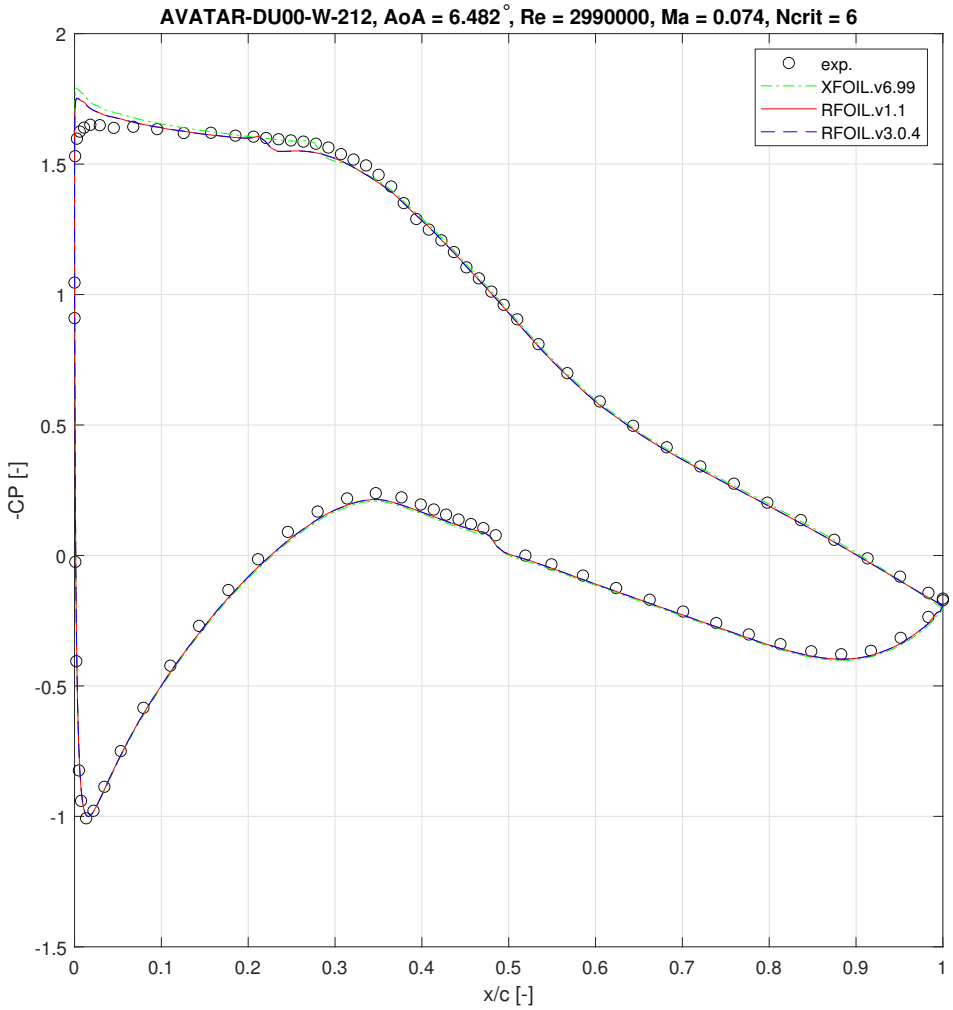

Figure C.404: Comparison between experimental and numerical pressure distributions for the AVATAR-DU00-W-212 airfoil at a Reynolds number of 3000000, and at an angle of attack and a Mach number of 6.684° and 0.074, respectively.

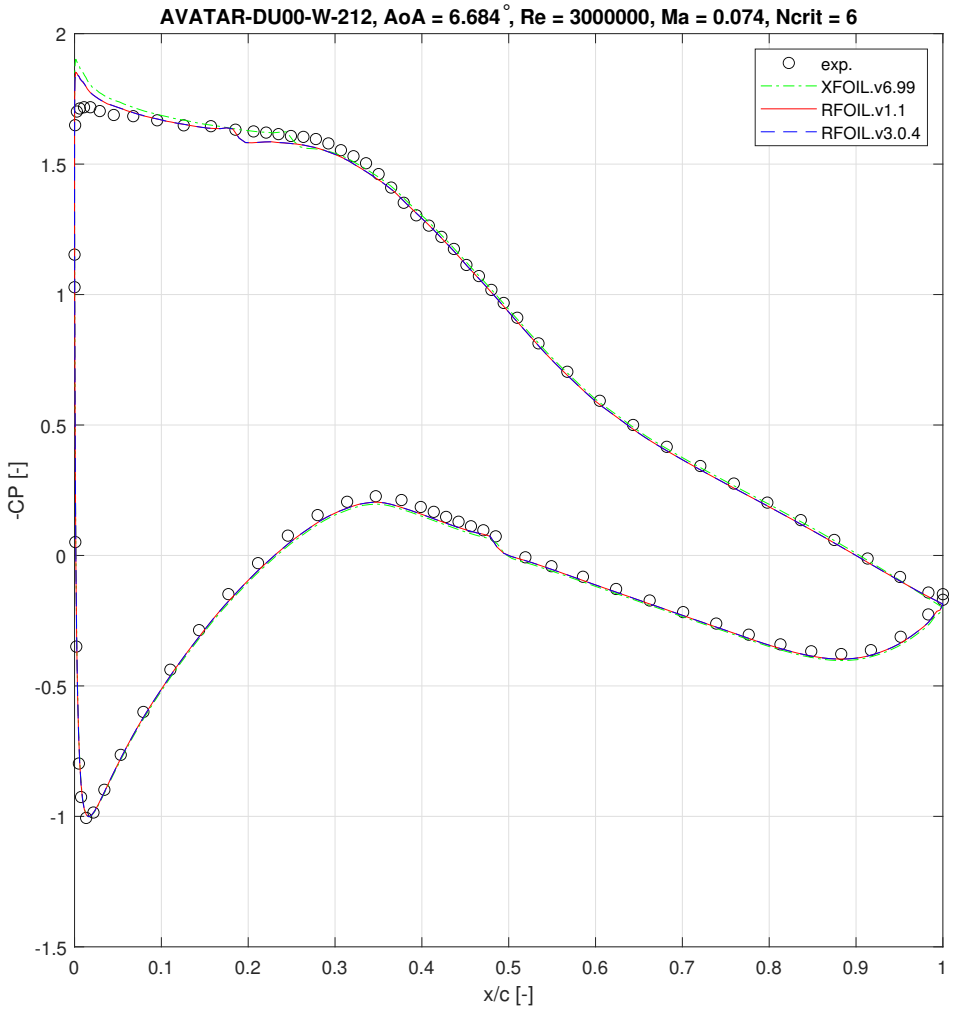

Figure C.405: Comparison between experimental and numerical pressure distributions for the AVATAR-DU00-W-212 airfoil at a Reynolds number of 3000000, and at an angle of attack and a Mach number of 6.887° and 0.074, respectively.

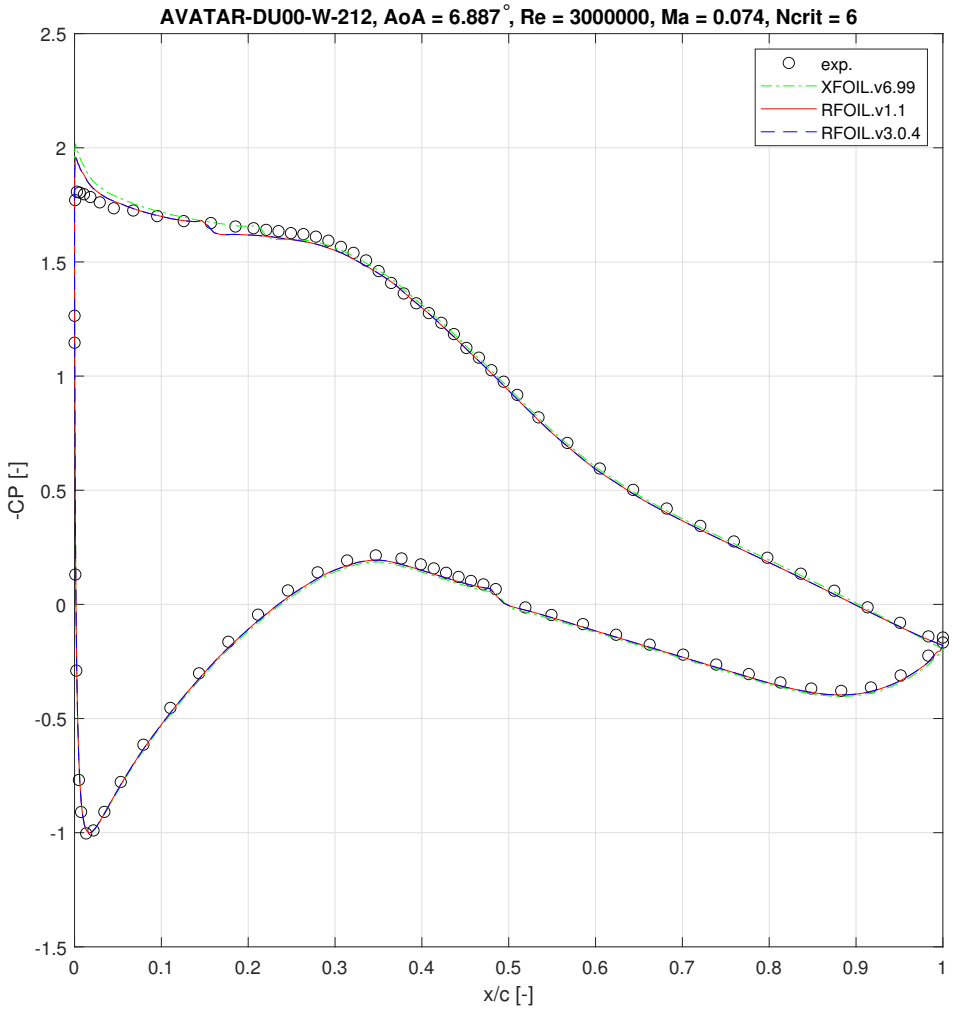

Figure C.406: Comparison between experimental and numerical pressure distributions for the AVATAR-DU00-W-212 airfoil at a Reynolds number of 11970000, and at an angle of attack and a Mach number of 7.034° and 0.058, respectively.

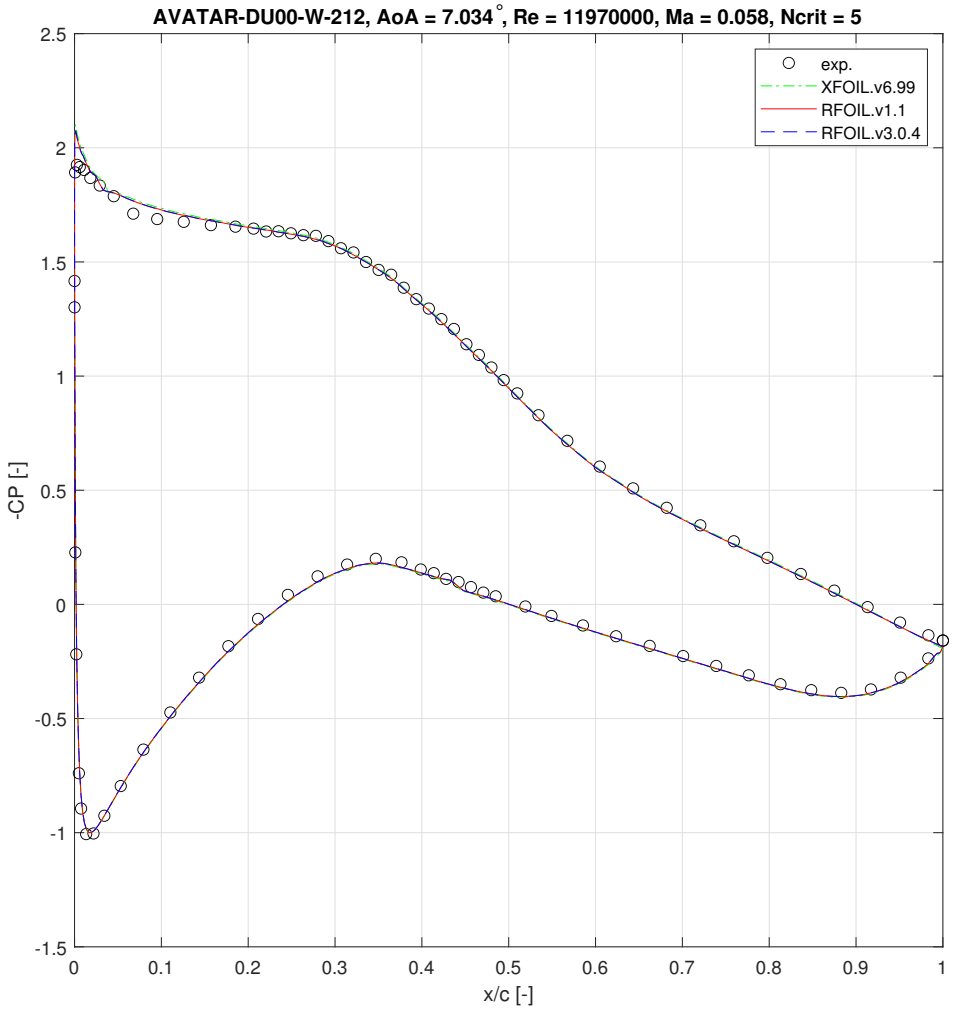

Figure C.407: Comparison between experimental and numerical pressure distributions for the AVATAR-DU00-W-212 airfoil at a Reynolds number of 5980000, and at an angle of attack and a Mach number of 7.086° and 0.029, respectively.

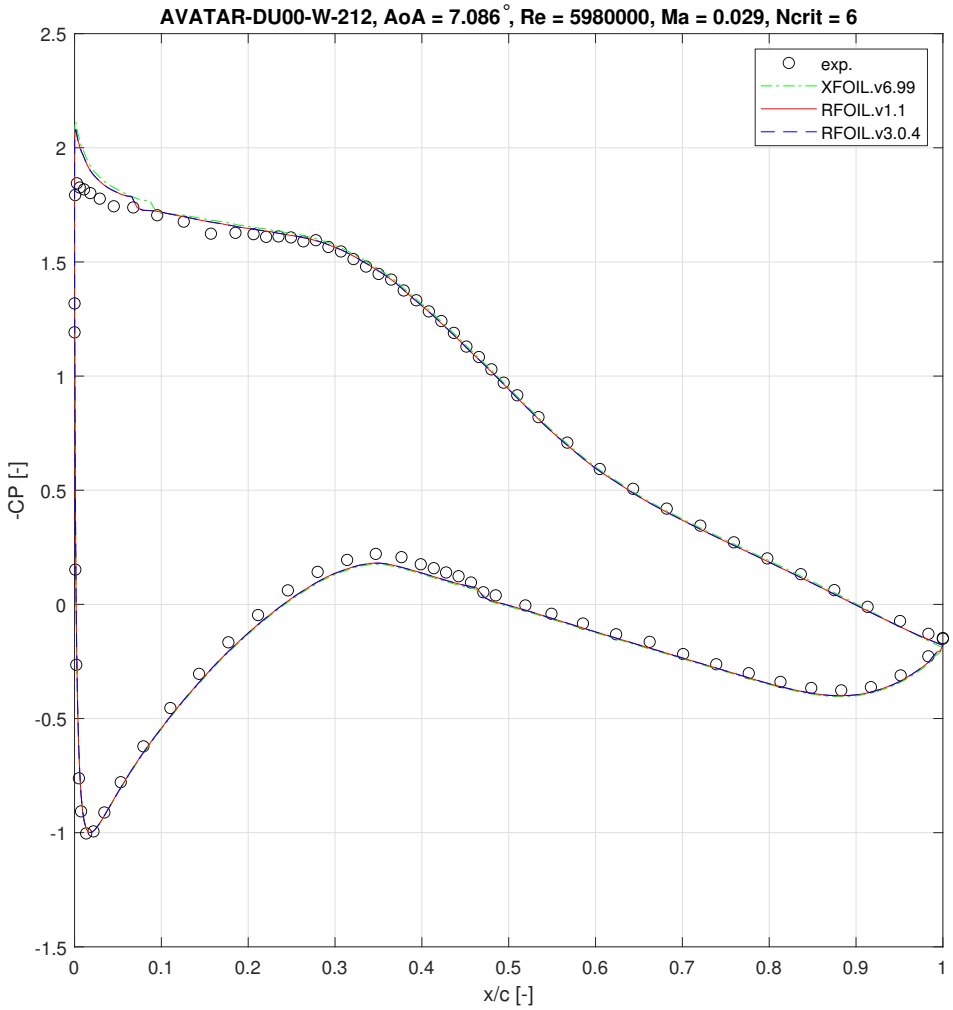

Figure C.408: Comparison between experimental and numerical pressure distributions for the AVATAR-DU00-W-212 airfoil at a Reynolds number of 8970000, and at an angle of attack and a Mach number of 7.086° and 0.043, respectively.

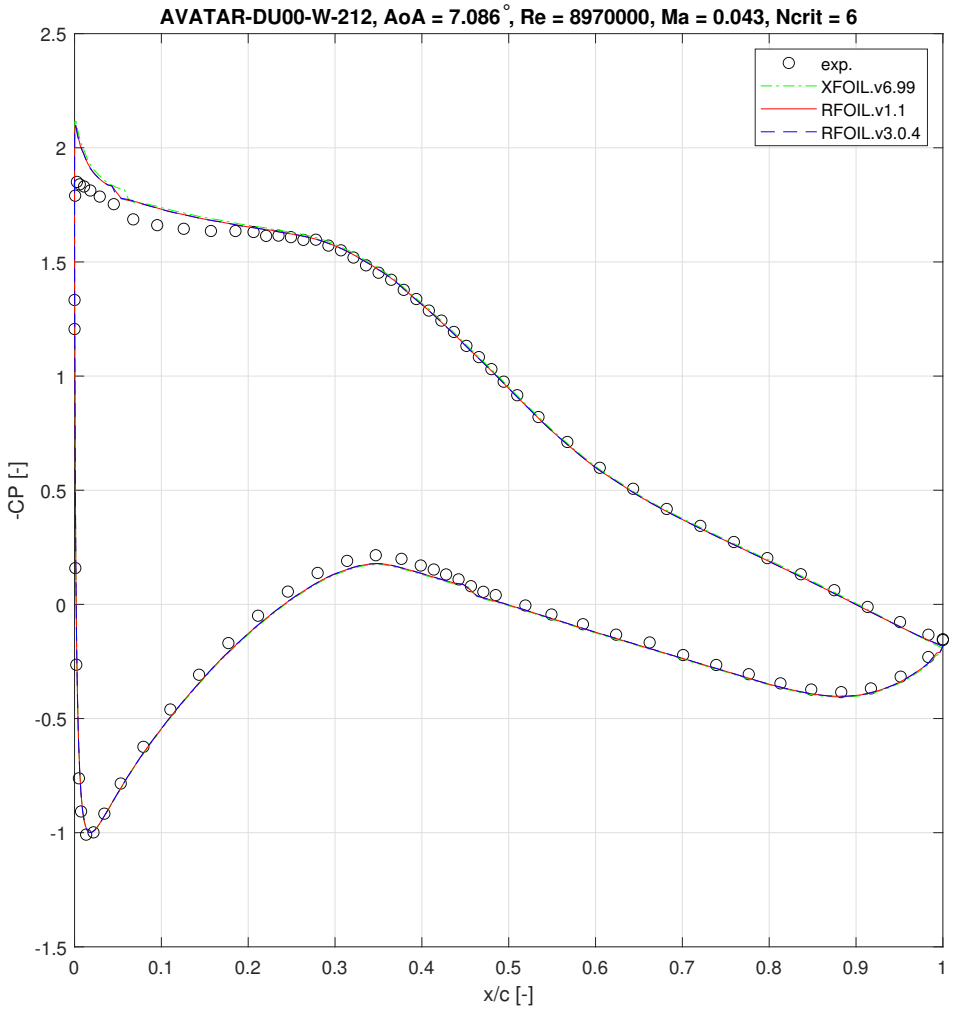

Figure C.409: Comparison between experimental and numerical pressure distributions for the AVATAR-DU00-W-212 airfoil at a Reynolds number of 6000000, and at an angle of attack and a Mach number of 7.087° and 0.055, respectively.

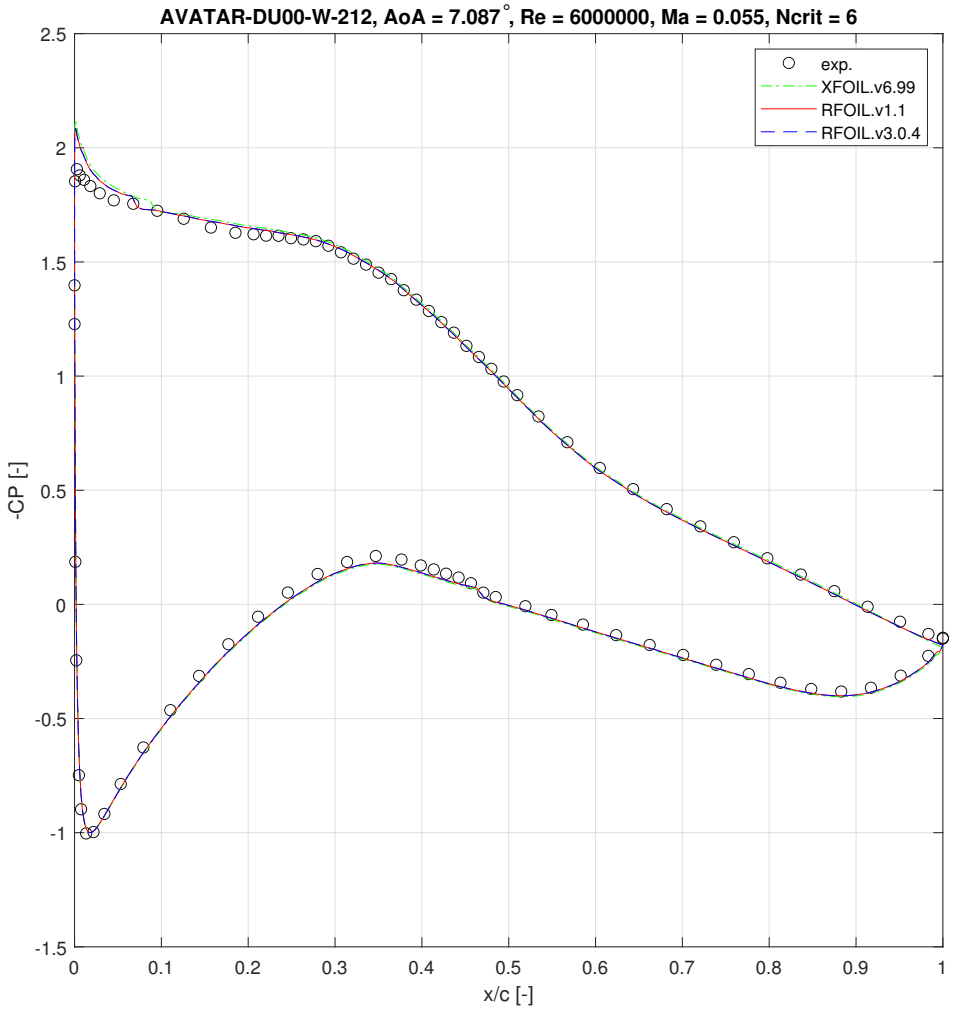

Figure C.410: Comparison between experimental and numerical pressure distributions for the AVATAR-DU00-W-212 airfoil at a Reynolds number of 15000000, and at an angle of attack and a Mach number of 7.088° and 0.081, respectively.

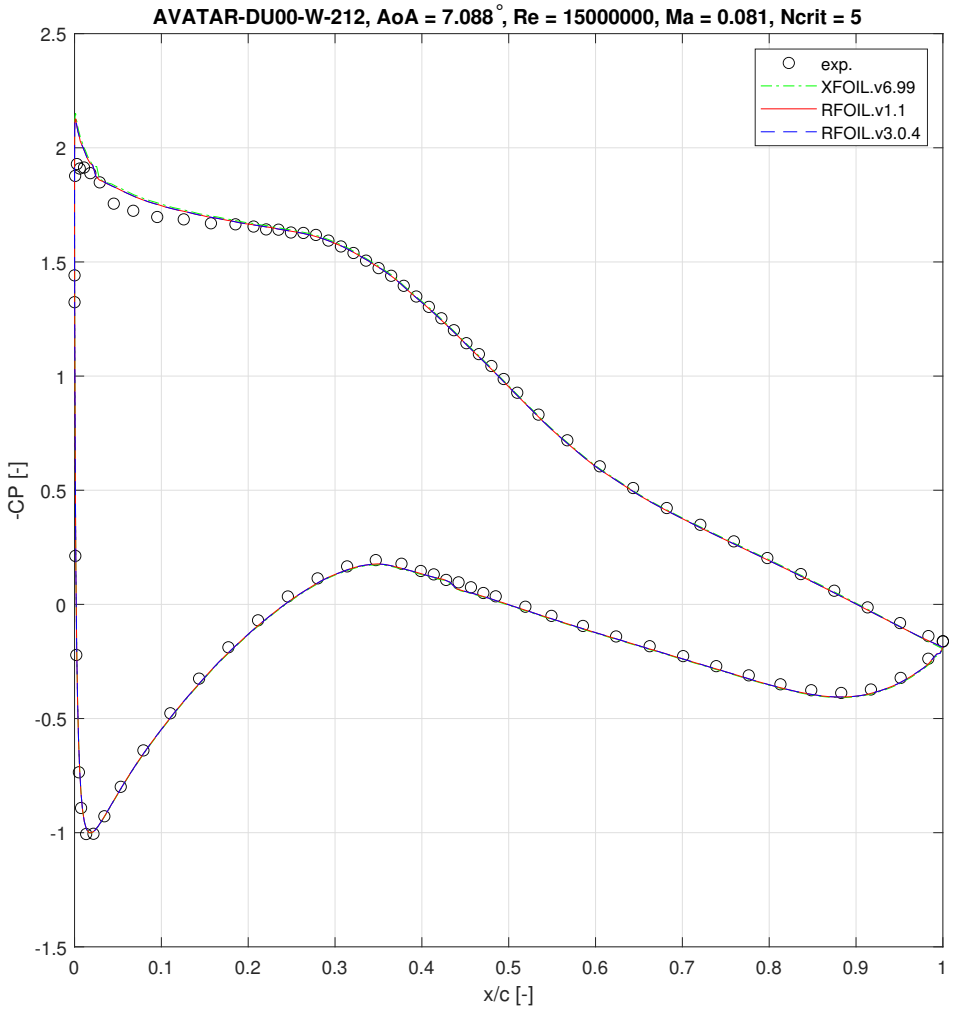

Figure C.411: Comparison between experimental and numerical pressure distributions for the AVATAR-DU00-W-212 airfoil at a Reynolds number of 9000000, and at an angle of attack and a Mach number of 7.088° and 0.083, respectively.

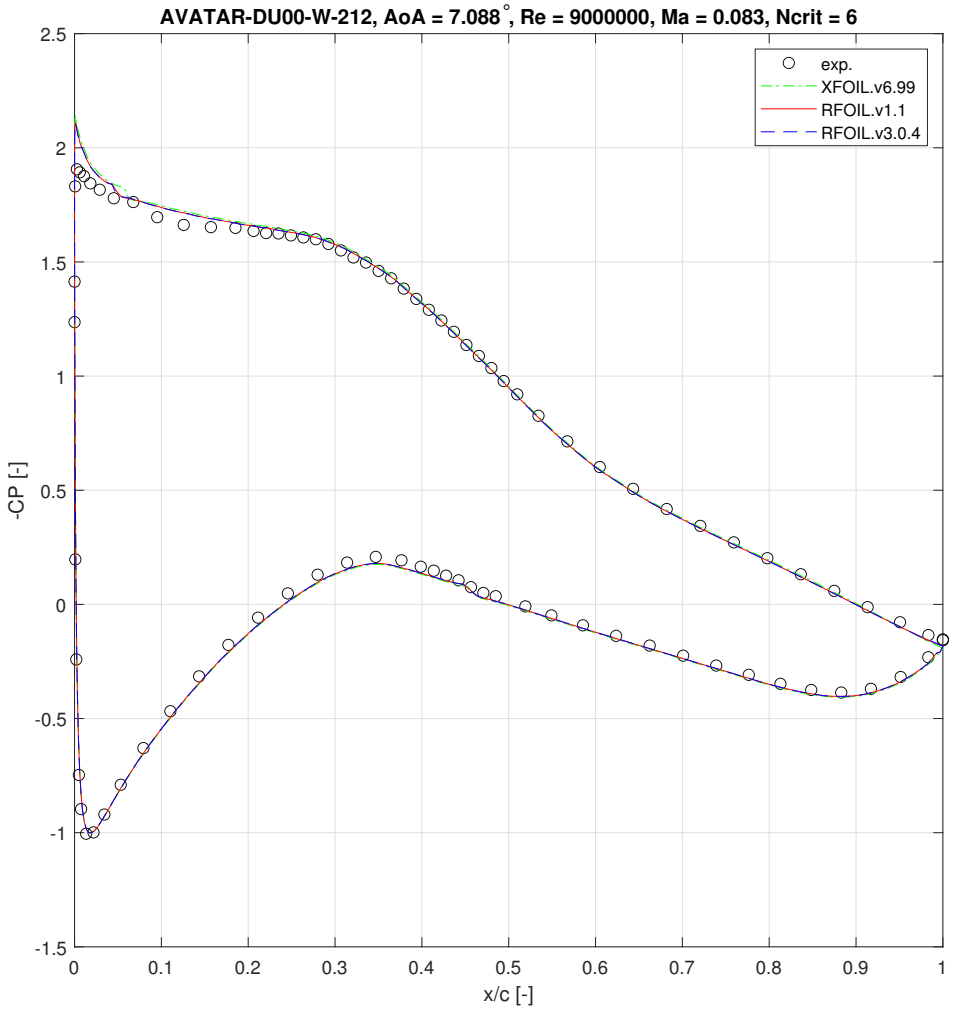

Figure C.412: Comparison between experimental and numerical pressure distributions for the AVATAR-DU00-W-212 airfoil at a Reynolds number of 2970000, and at an angle of attack and a Mach number of 7.089° and 0.073, respectively.

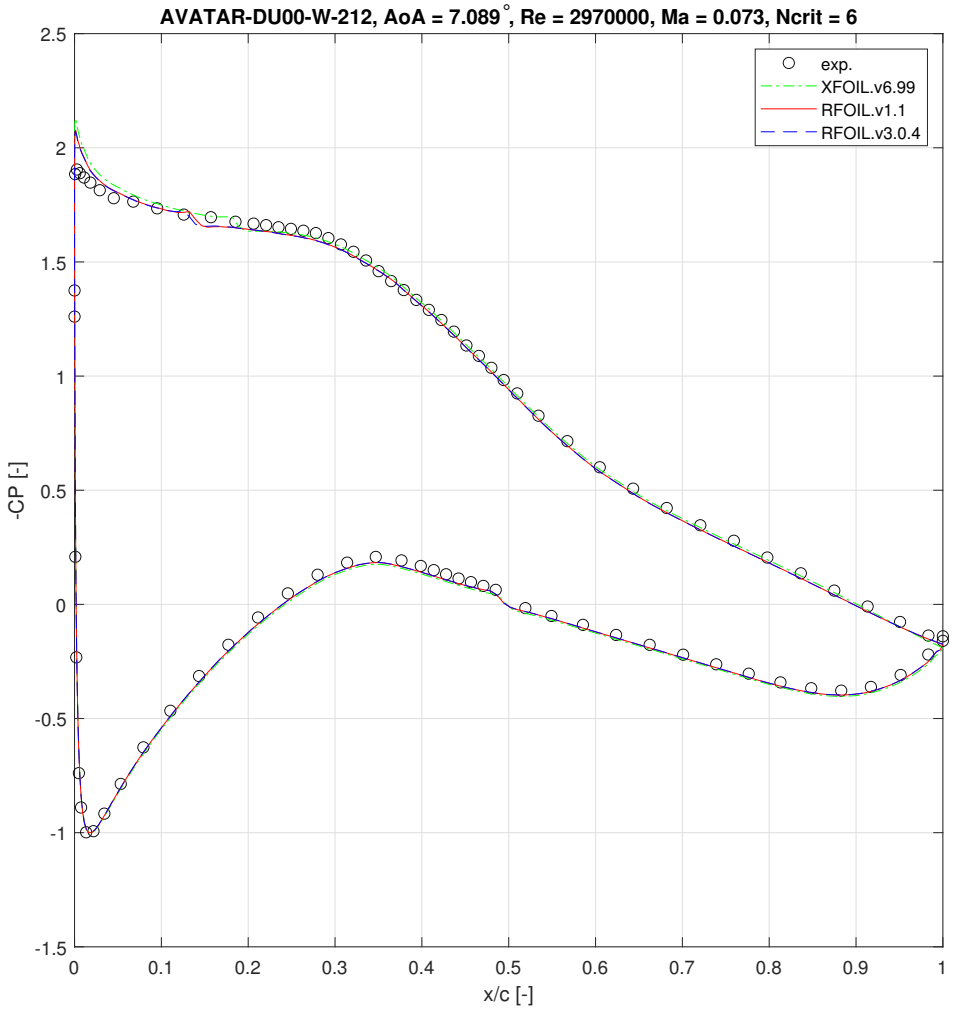

Figure C.413: Comparison between experimental and numerical pressure distributions for the AVATAR-DU00-W-212 airfoil at a Reynolds number of 3000000, and at an angle of attack and a Mach number of 7.594° and 0.074, respectively.

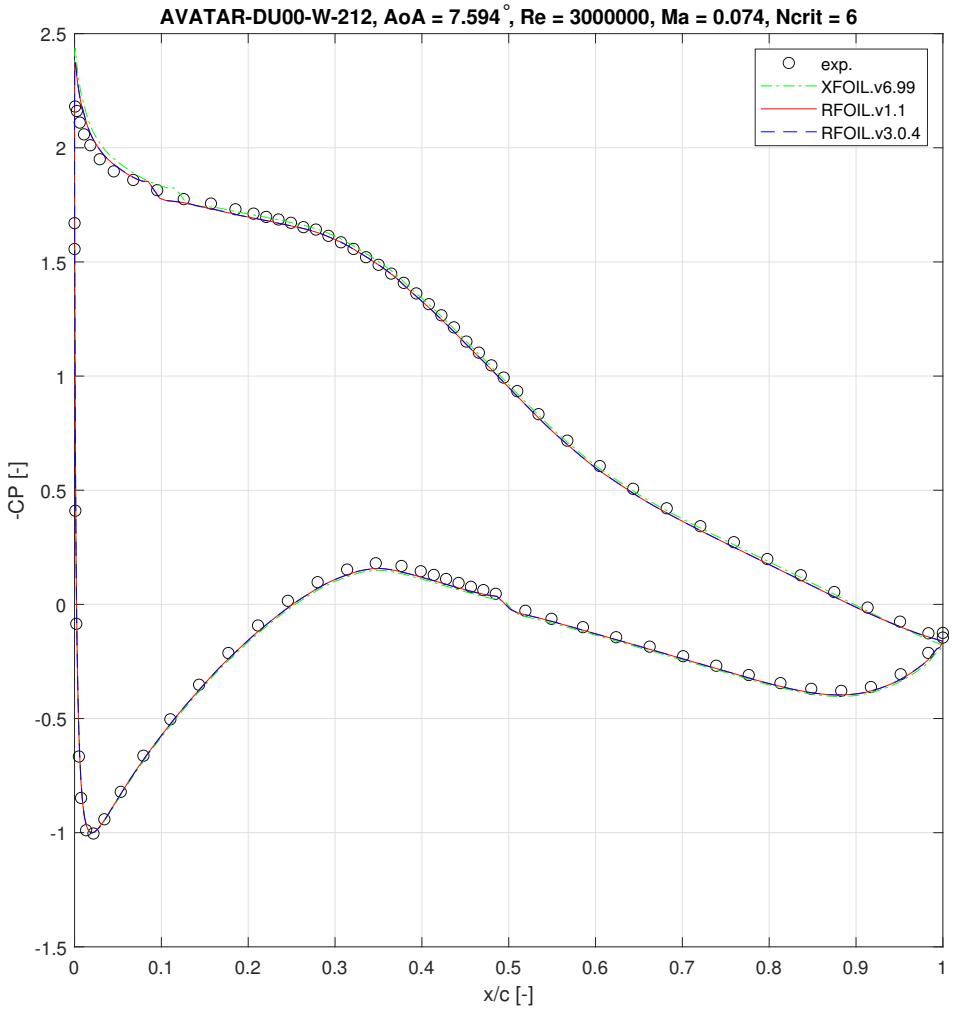

Figure C.414: Comparison between experimental and numerical pressure distributions for the AVATAR-DU00-W-212 airfoil at a Reynolds number of 3000000, and at an angle of attack and a Mach number of 7.897° and 0.074, respectively.

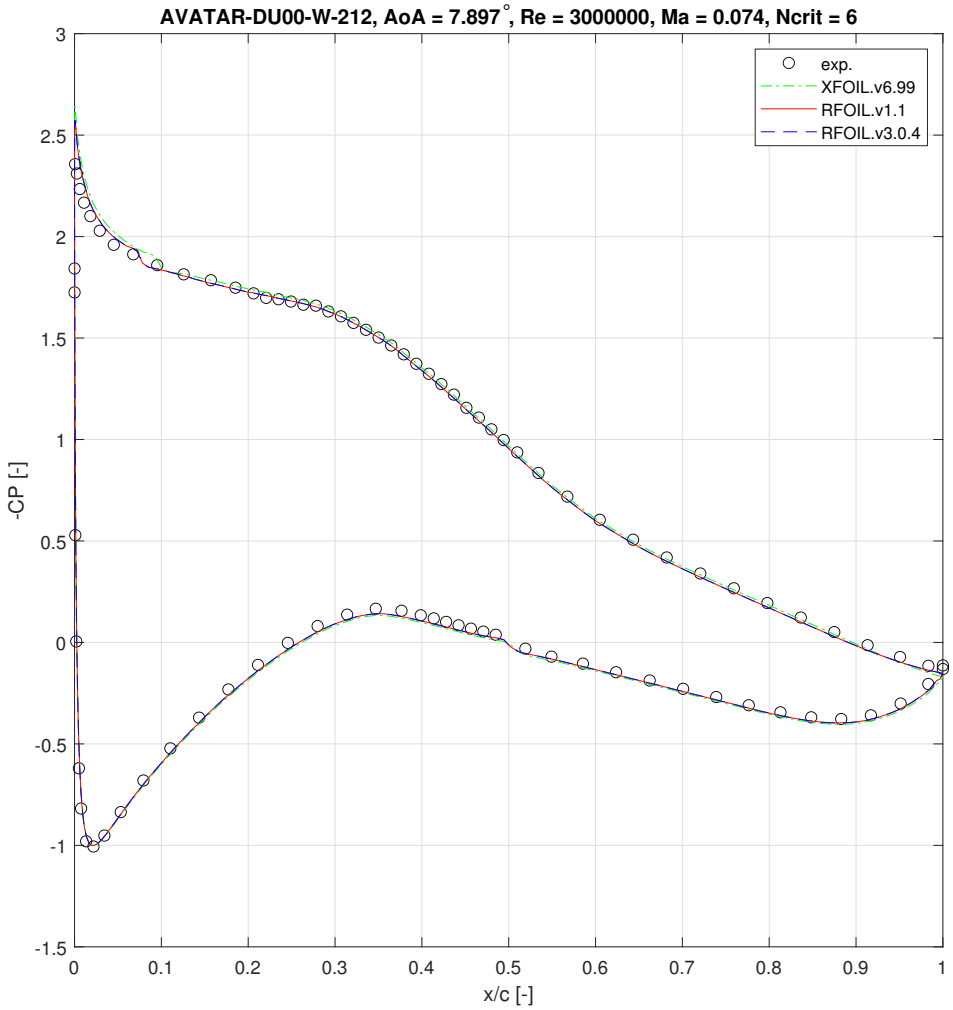

Figure C.415: Comparison between experimental and numerical pressure distributions for the AVATAR-DU00-W-212 airfoil at a Reynolds number of 12020000, and at an angle of attack and a Mach number of 8.031° and 0.058, respectively.

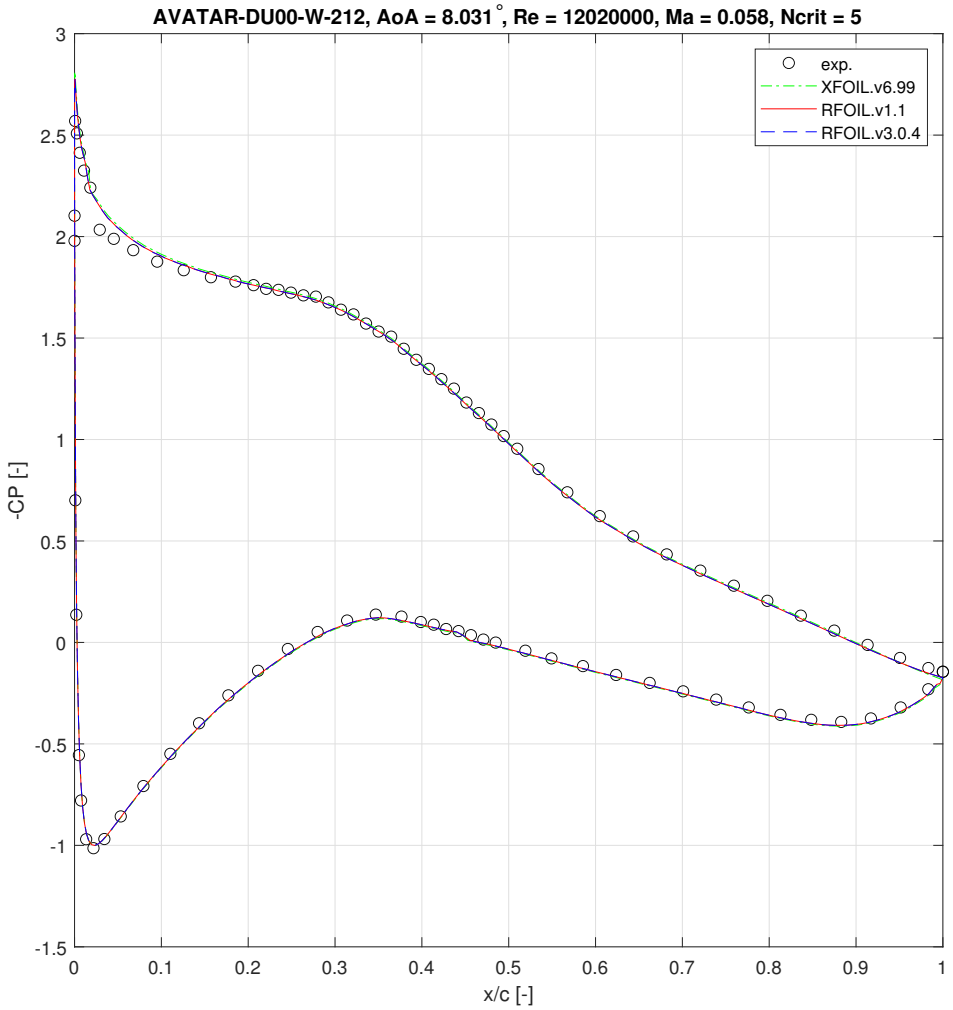

Figure C.416: Comparison between experimental and numerical pressure distributions for the AVATAR-DU00-W-212 airfoil at a Reynolds number of 6010000, and at an angle of attack and a Mach number of 8.097° and 0.029, respectively.

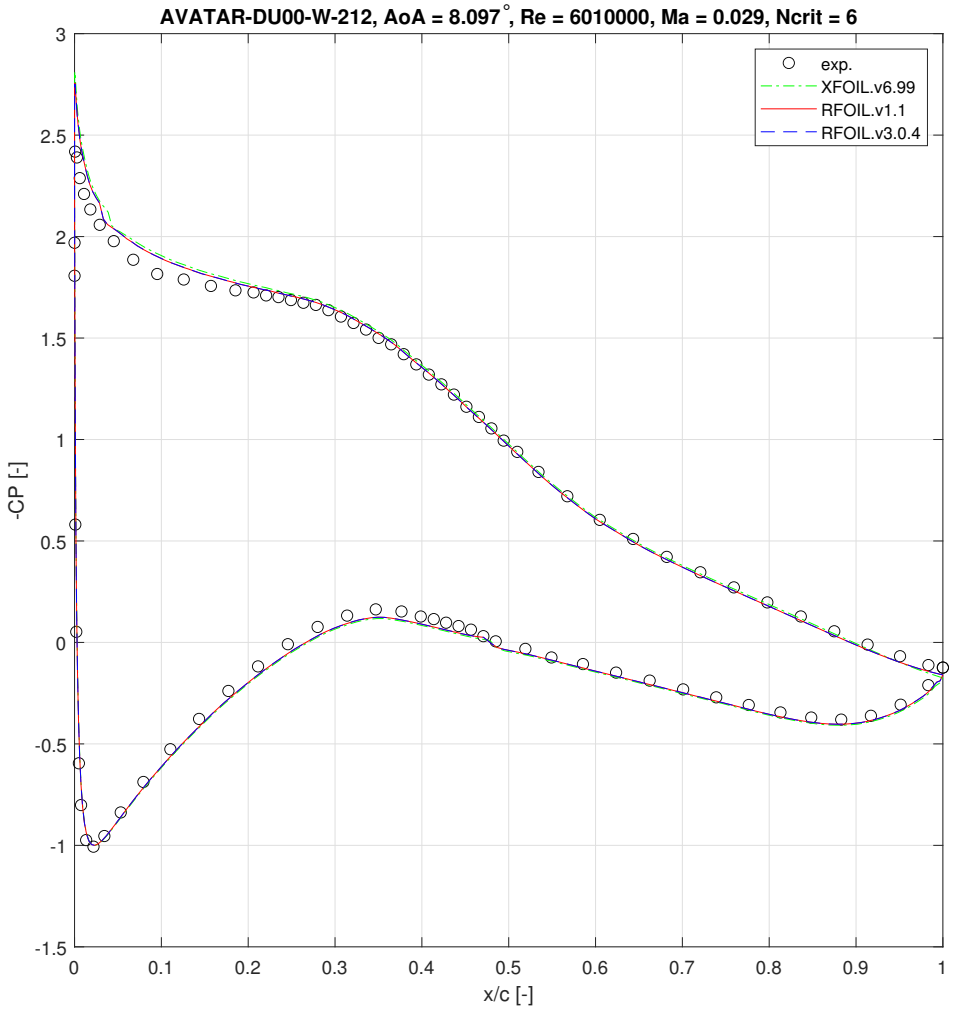

Figure C.417: Comparison between experimental and numerical pressure distributions for the AVATAR-DU00-W-212 airfoil at a Reynolds number of 6010000, and at an angle of attack and a Mach number of 8.098° and 0.055, respectively.

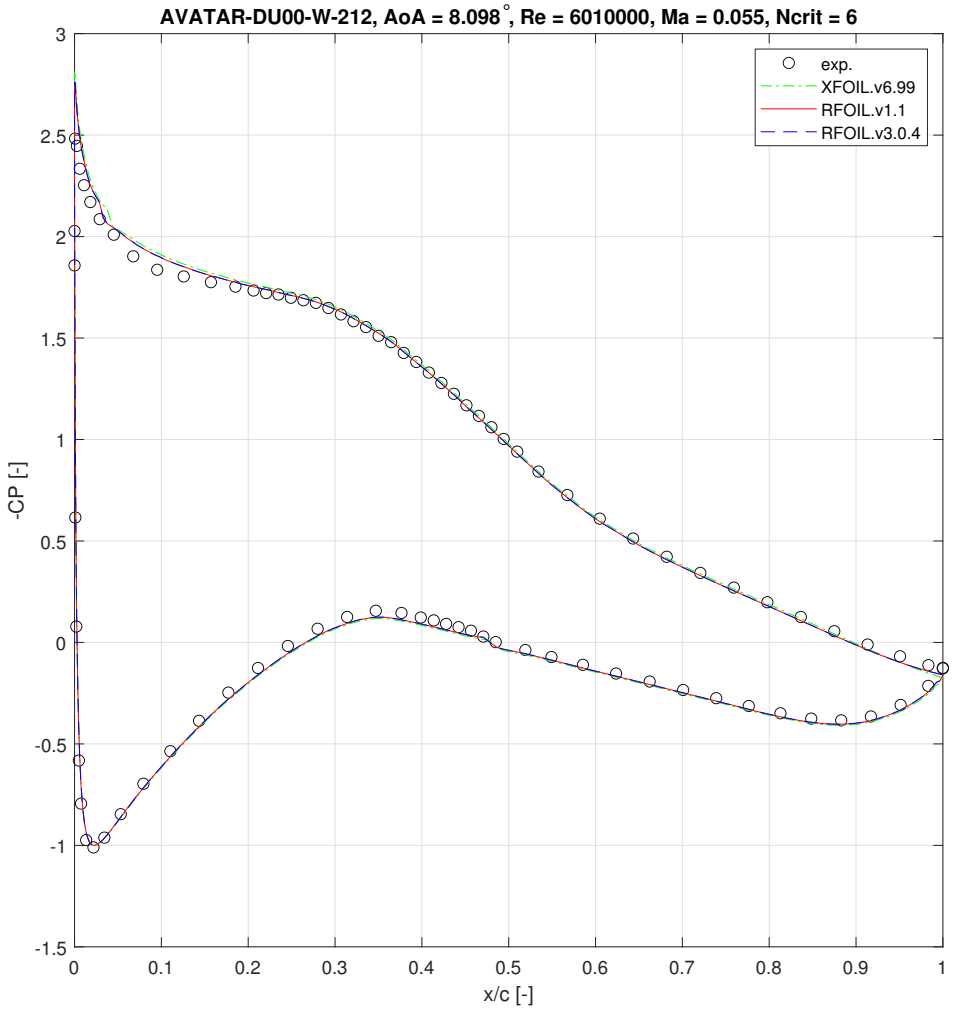

Figure C.418: Comparison between experimental and numerical pressure distributions for the AVATAR-DU00-W-212 airfoil at a Reynolds number of 9010000, and at an angle of attack and a Mach number of 8.098° and 0.043, respectively.

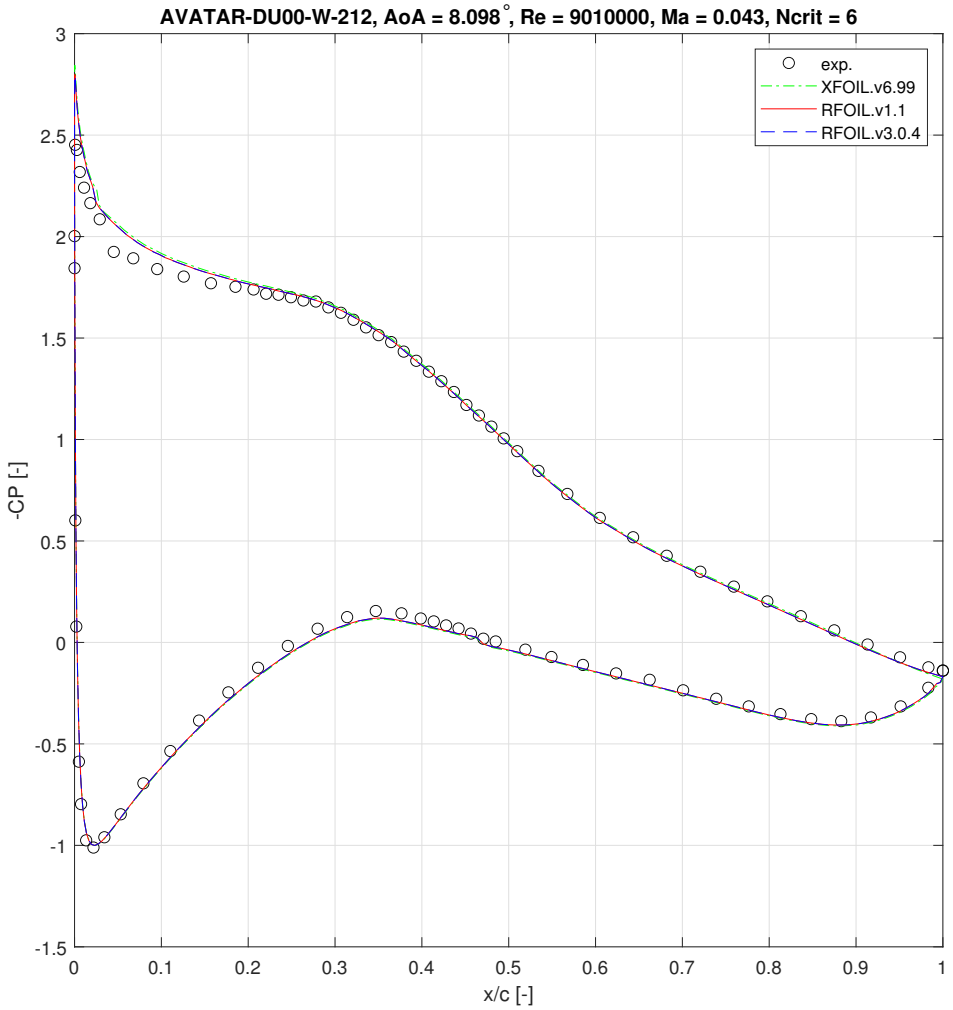

Figure C.419: Comparison between experimental and numerical pressure distributions for the AVATAR-DU00-W-212 airfoil at a Reynolds number of 2970000, and at an angle of attack and a Mach number of 8.099° and 0.073, respectively.

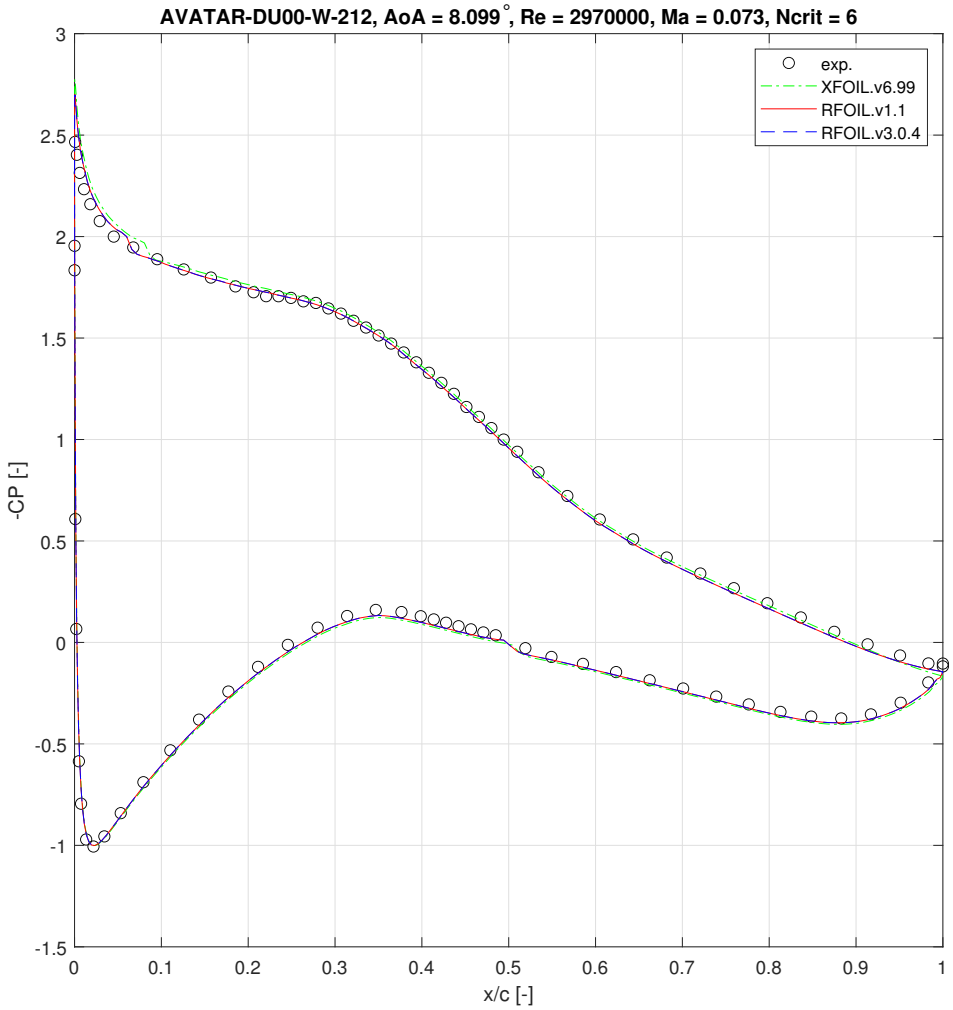

Figure C.420: Comparison between experimental and numerical pressure distributions for the AVATAR-DU00-W-212 airfoil at a Reynolds number of 9000000, and at an angle of attack and a Mach number of 8.099° and 0.083, respectively.

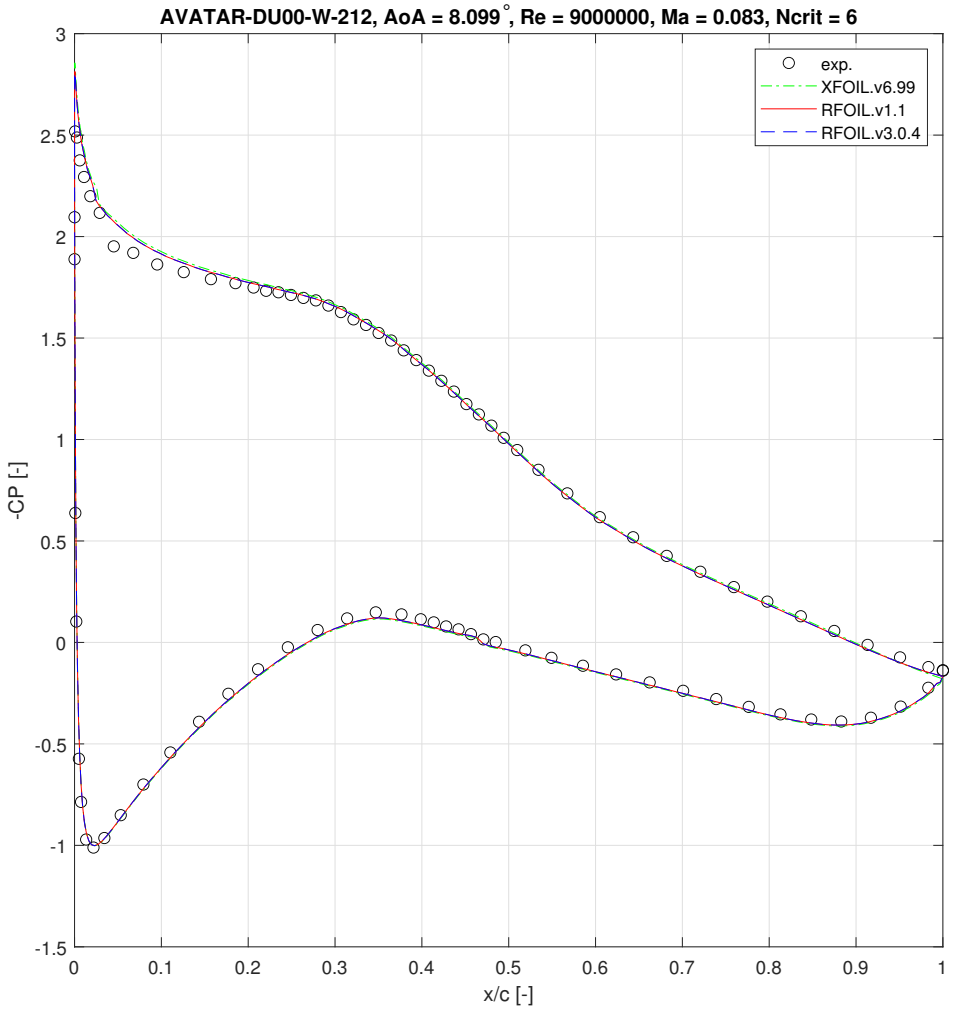

Figure C.421: Comparison between experimental and numerical pressure distributions for the AVATAR-DU00-W-212 airfoil at a Reynolds number of 14960000, and at an angle of attack and a Mach number of 8.101° and 0.081, respectively.

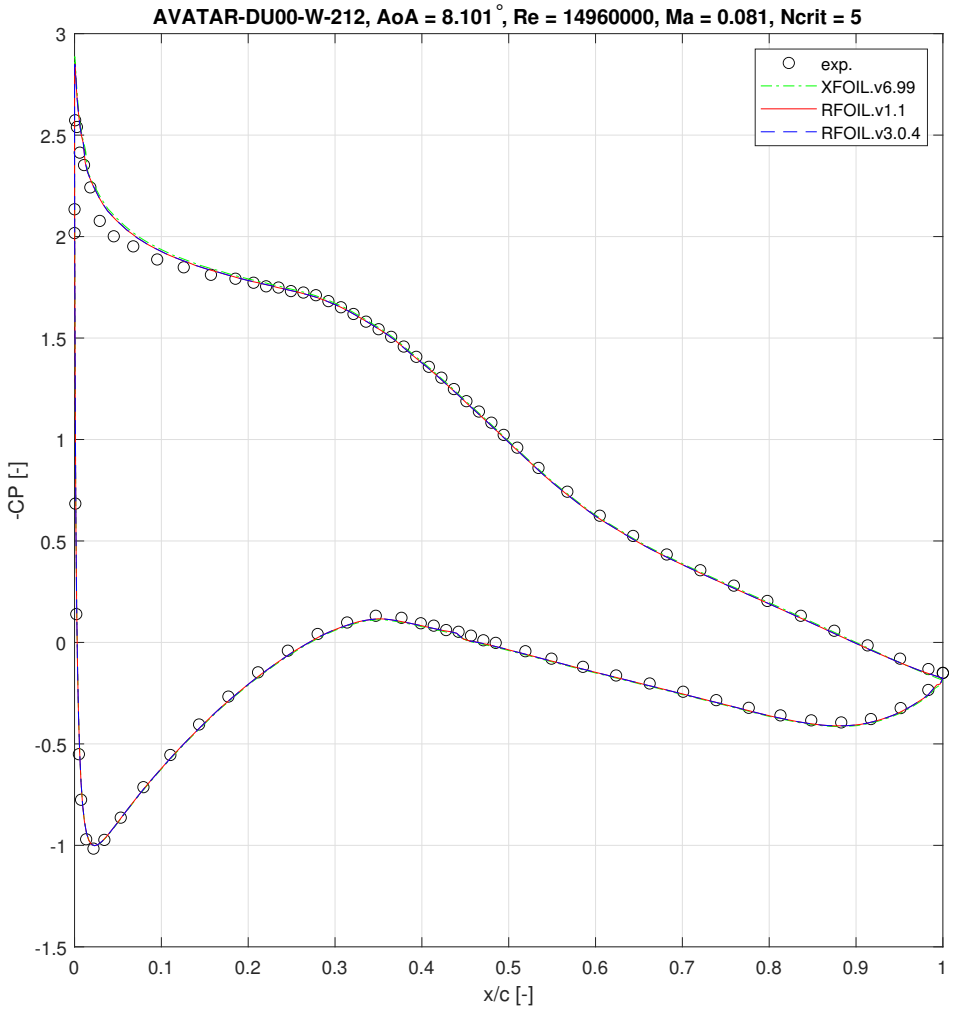

Figure C.422: Comparison between experimental and numerical pressure distributions for the AVATAR-DU00-W-212 airfoil at a Reynolds number of 11990000, and at an angle of attack and a Mach number of 9.029° and 0.058, respectively.

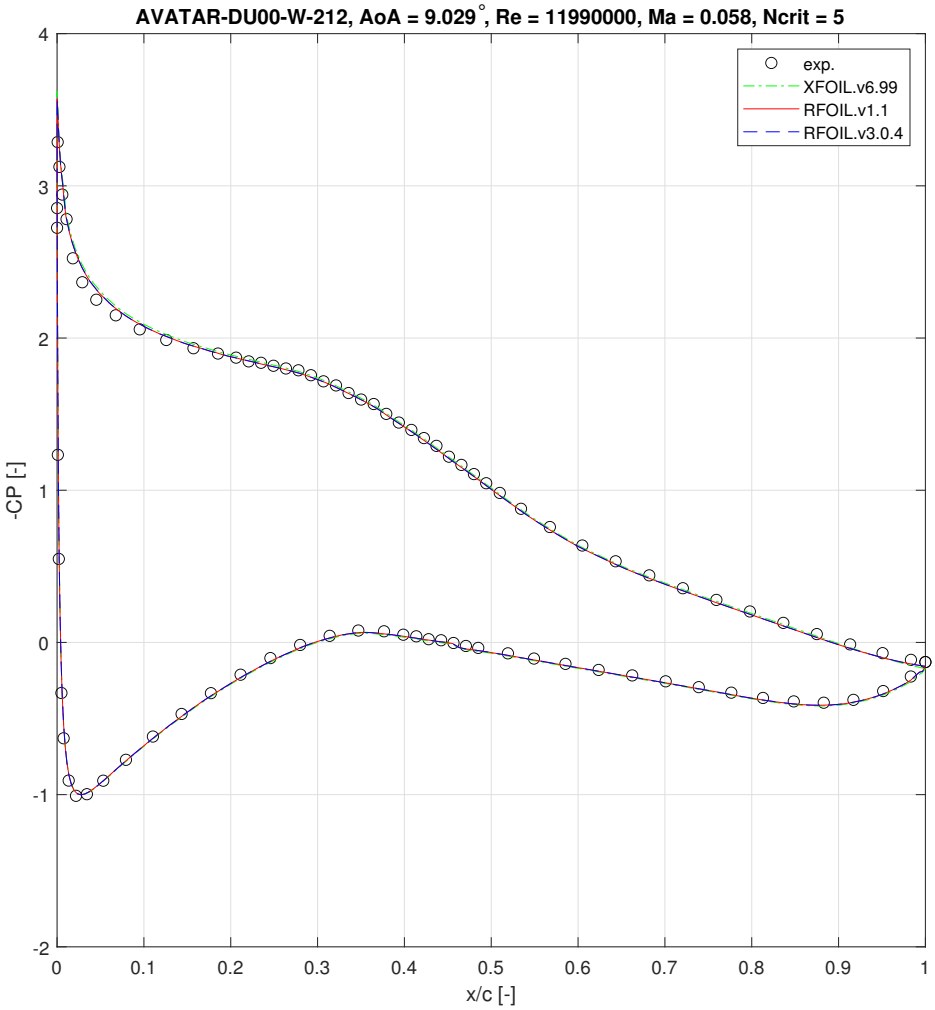

Figure C.423: Comparison between experimental and numerical pressure distributions for the AVATAR-DU00-W-212 airfoil at a Reynolds number of 2990000, and at an angle of attack and a Mach number of 9.108° and 0.074, respectively.

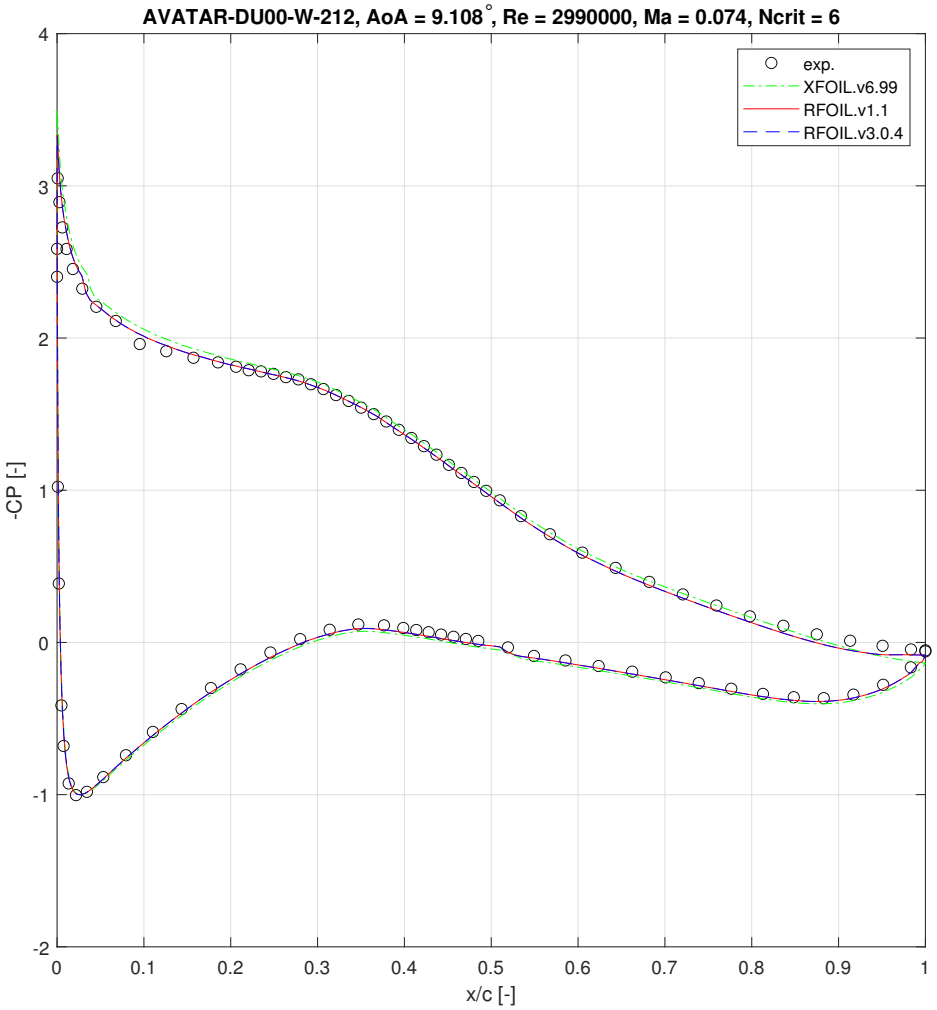

Figure C.424: Comparison between experimental and numerical pressure distributions for the AVATAR-DU00-W-212 airfoil at a Reynolds number of 6010000, and at an angle of attack and a Mach number of 9.108° and 0.029, respectively.

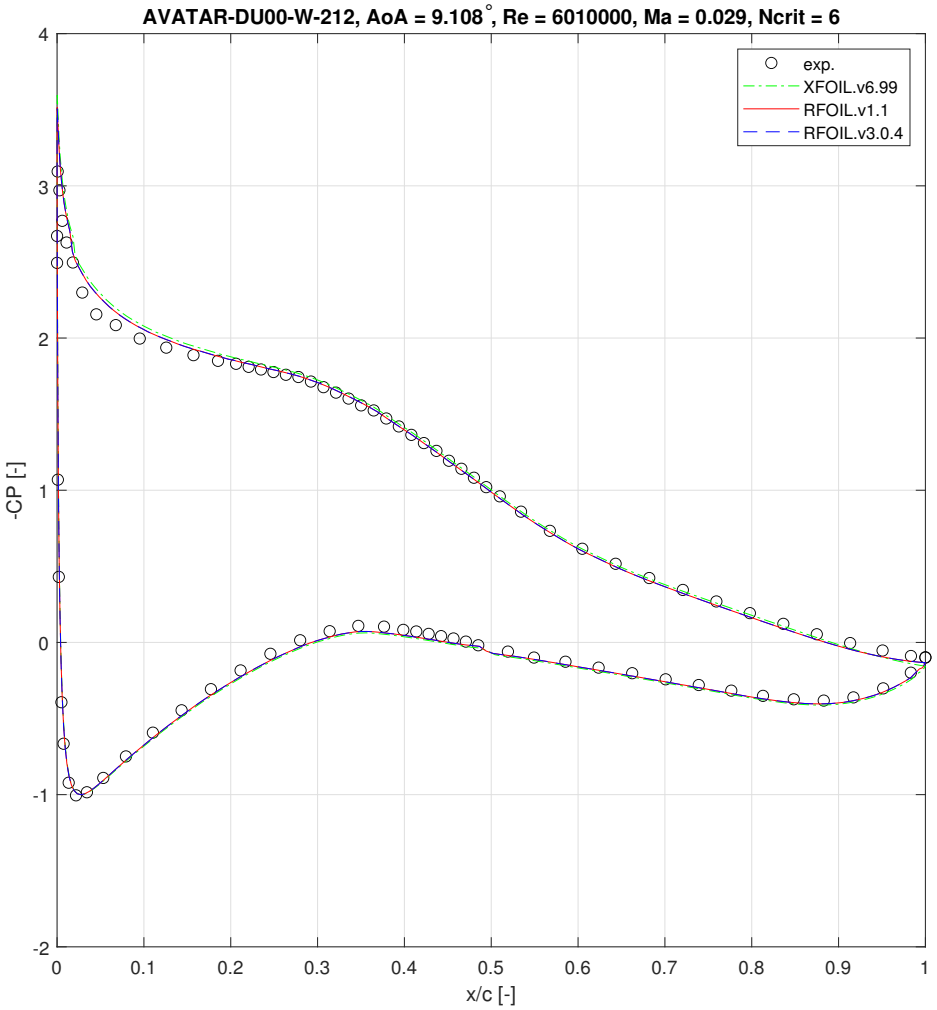

Figure C.425: Comparison between experimental and numerical pressure distributions for the AVATAR-DU00-W-212 airfoil at a Reynolds number of 5990000, and at an angle of attack and a Mach number of 9.109° and 0.055, respectively.

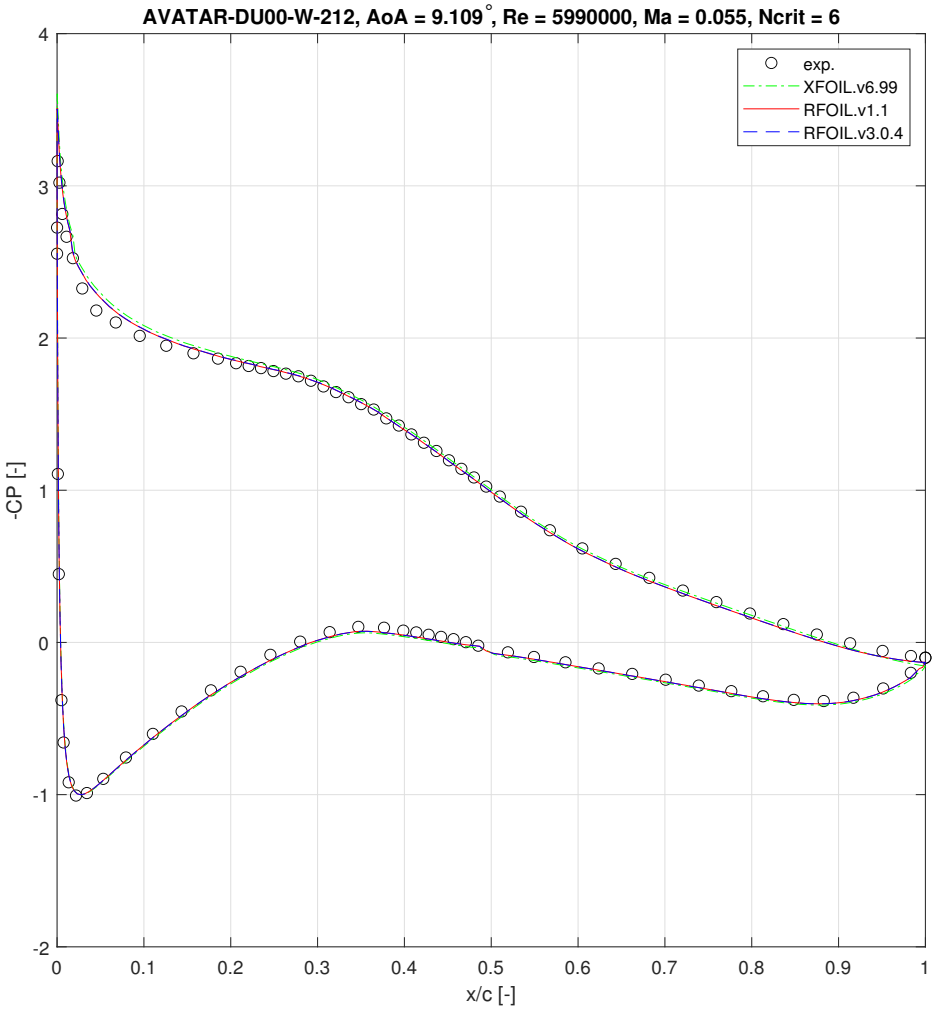

Figure C.426: Comparison between experimental and numerical pressure distributions for the AVATAR-DU00-W-212 airfoil at a Reynolds number of 8980000, and at an angle of attack and a Mach number of 9.111° and 0.082, respectively.

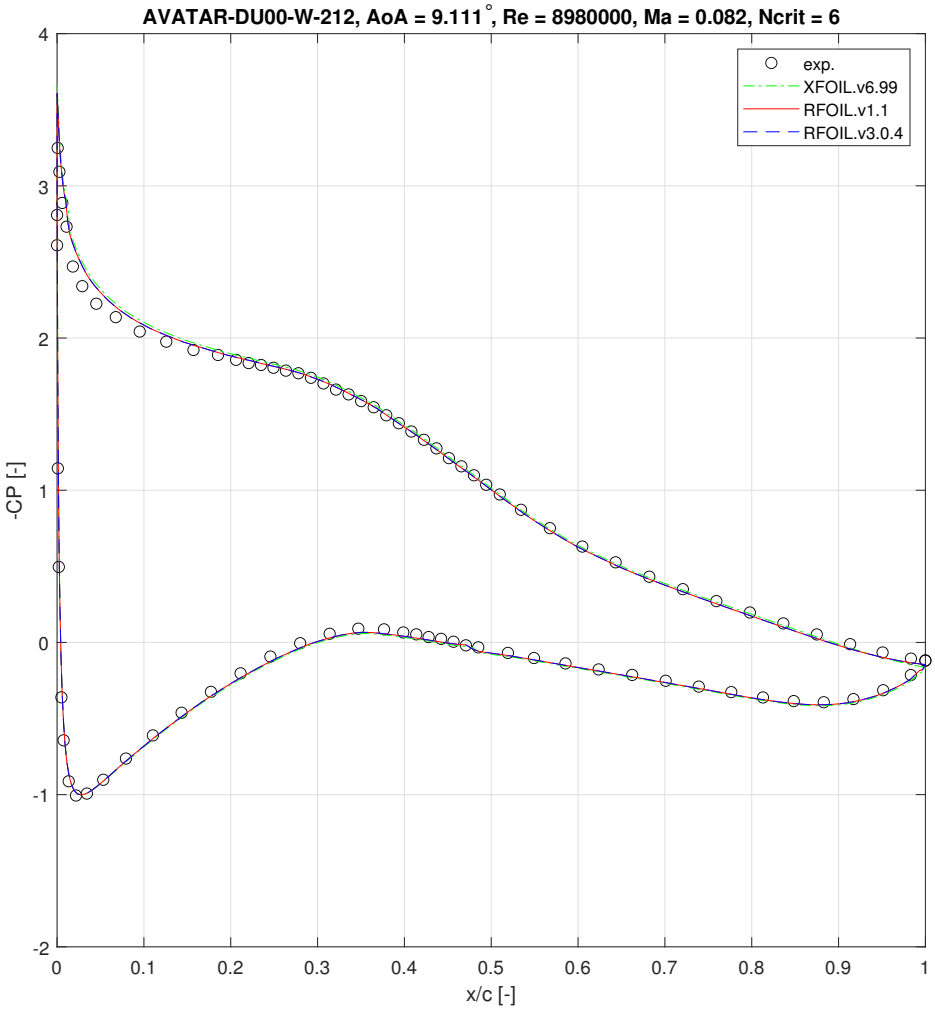

Figure C.427: Comparison between experimental and numerical pressure distributions for the AVATAR-DU00-W-212 airfoil at a Reynolds number of 15020000, and at an angle of attack and a Mach number of 9.113° and 0.081, respectively.

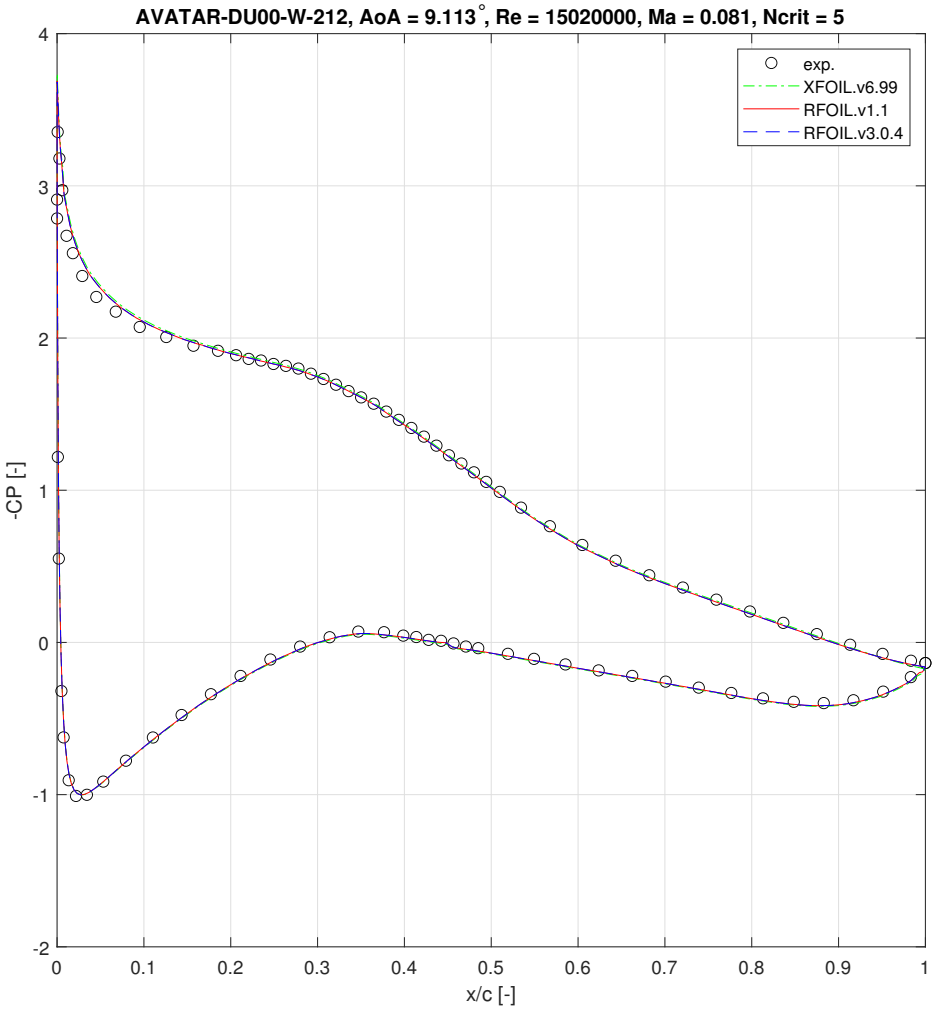

Figure C.428: Comparison between experimental and numerical pressure distributions for the AVATAR-DU00-W-212 airfoil at a Reynolds number of 9000000, and at an angle of attack and a Mach number of 9.110° and 0.043, respectively.

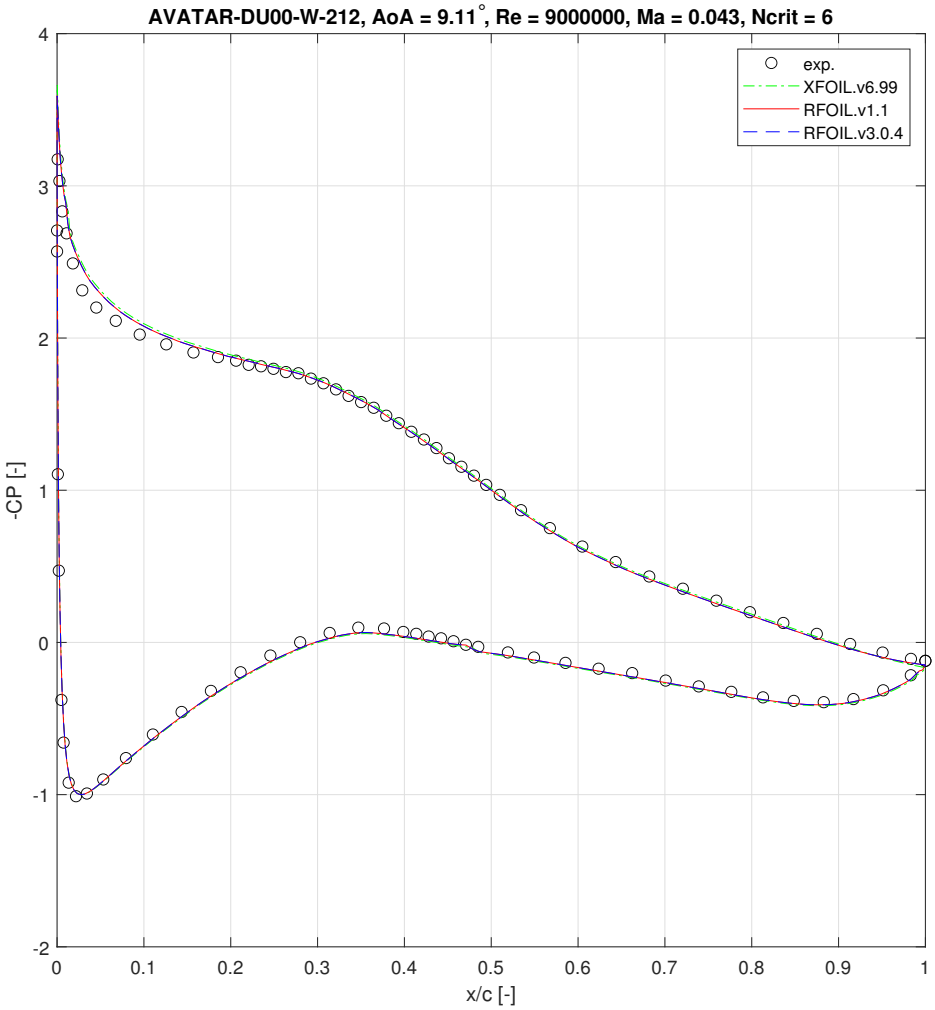

Figure C.429: Comparison between experimental and numerical pressure distributions for the AVATAR-DU00-W-212 airfoil at a Reynolds number of 3010000, and at an angle of attack and a Mach number of 9.713° and 0.074, respectively.

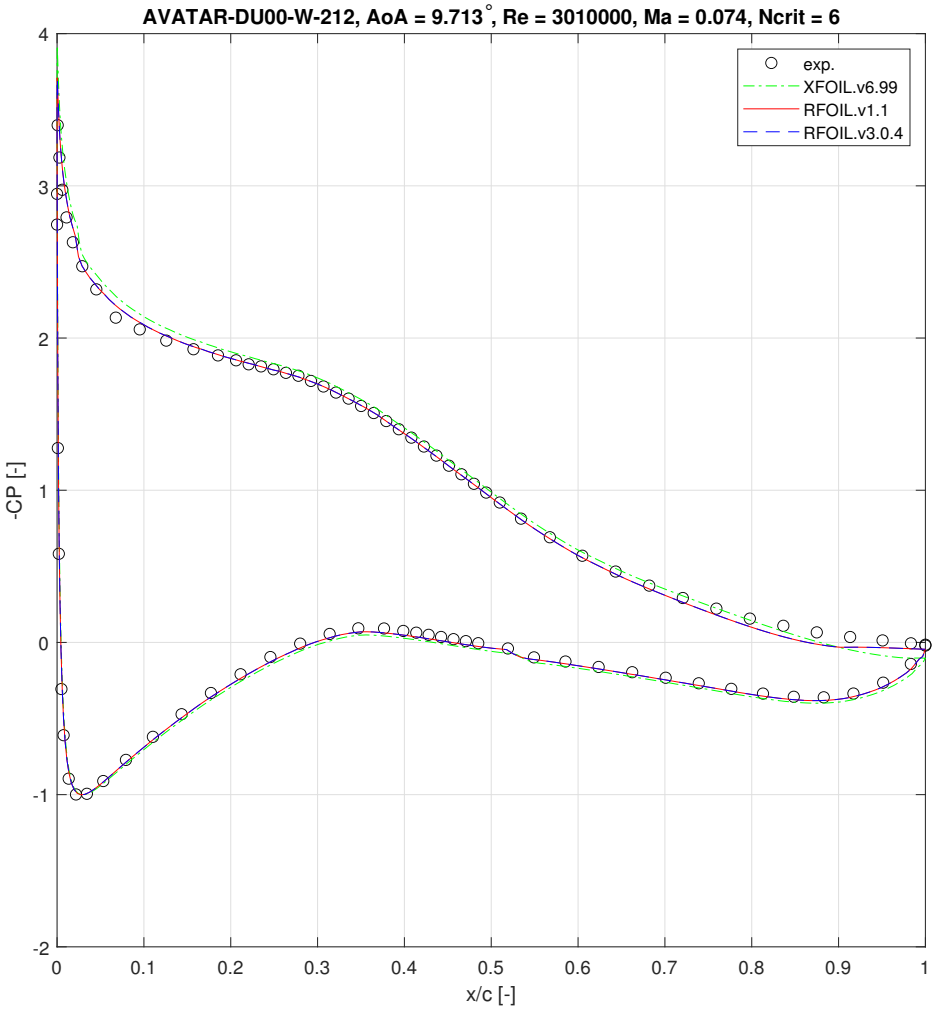

Energy & Materials Transition

Westerduinweg 3
1755 LE Petten
www.tno.nl

TNO innovation for life